

Special Collection on Tumor Suppressors

Small-bodied mammals that display exceptional longevity, see Lambert et al. - "Adaptive sequence convergence of the tumor suppressor ADAMTS9 between small-bodied mammals displaying exceptional longevity."

Tumor Suppressors

AGING

AGING

www.aging-us.com

EDITORIAL BOARD

EDITORS-IN-CHIEF

Jan Vijn - Albert Einstein College of Medicine, Bronx, NY, USA

David A. Sinclair - Harvard Medical School, Boston, MA, USA

Vera Gorbunova - University of Rochester, Rochester, NY, USA

Judith Campisi - The Buck Institute for Research on Aging, Novato, CA, USA

Mikhail V. Blagosklonny - Roswell Park Cancer Institute, Buffalo, NY, USA

EDITORIAL BOARD

Frederick Alt - Harvard Medical School, Boston, MA, USA

Vladimir Anisimov - Petrov Institute of Oncology, St.Petersburg, Russia

Johan Auwerx - Ecole Polytechnique Federale de Lausanne, Switzerland

Andrzej Bartke - Southern Illinois University, Springfield, IL, USA

Nir Barzilai - Albert Einstein College of Medicine, Bronx, NY, USA

Elizabeth H. Blackburn - University of California, San Francisco, CA, USA

Maria Blasco - Spanish National Cancer Center, Madrid, Spain

Vilhelm A. Bohr - National Institute on Aging, NIH, Baltimore, MD, USA

William M. Bonner - National Cancer Institute, NIH, Bethesda, MD, USA

Robert M. Brosh, Jr. - National Institute on Aging, NIH, Baltimore, MD, USA

Anne Brunet - Stanford University, Stanford, CA, USA

Rafael de Caba - NIA, NIH, Baltimore, MD, USA

Ronald A. DePinho - Dana-Farber Cancer Institute, Boston, MA, USA

Jan van Deursen - Mayo Clinic, Rochester, MN, USA

Lawrence A. Donehower - Baylor College of Medicine, Houston, TX, USA

Caleb E. Finch - University of Southern California, Los Angeles, CA, USA

Toren Finkel - National Institutes of Health, Bethesda, MD, USA

Luigi Fontana - Washington University, St. Louis, MO, USA

Claudio Franceschi - University of Bologna, Bologna, Italy

David Gems - Inst. of Healthy Ageing, Univ. College London, UK

Myriam Gorospe - National Institute on Aging, NIH, Baltimore, MD, USA

Leonard Guarente - MIT, Cambridge, MA, USA

Andrei Gudkov - Roswell Park Cancer Institute, Buffalo, NY, USA

Michael Hall - University of Basel, Basel, Switzerland

Philip Hanawalt - Stanford University, CA, USA

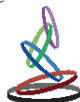
Nissim Hay - University of Illinois at Chicago, Chicago, IL, USA

Siegfried Hekimi - McGill University, Montreal, Canada
Stephen L. Helfand - Brown University, Providence, RI, USA
Jan H.J. Hoeijmakers - Erasmus MC, Rotterdam, The Netherlands
John O. Holloszy - Washington University, St. Louis, MO, USA
Stephen P. Jackson - University of Cambridge, Cambridge, UK
Heinrich Jasper - The Buck Institute for Research on Aging, Novato, CA, USA
Pankaj Kapahi - The Buck Institute for Research on Aging, Novato, CA, USA
Jan Karlseder - The Salk Institute, La Jolla, CA, USA
Cynthia Kenyon - University of California San Francisco, San Francisco, CA, USA
James L. Kirkland - Mayo Clinic, Rochester, MN, USA
Guido Kroemer - INSERM, Paris, France
Titia de Lange - Rockefeller University, New York, NY, USA
Arnold Levine - The Institute for Advanced Study, Princeton, NJ, USA
Michael P. Lisanti - University of Salford, Salford, UK
Lawrence A. Loeb - University of Washington, Seattle, WA, USA
Valter Longo - University of Southern California, Los Angeles, CA, USA
Gerry Melino - University of Rome, Rome, Italy
Simon Melov - The Buck Institute for Research on Aging, Novato, CA, USA
Alexey Moskalev - Komi Science Center of RAS, Syktyvkar, Russia
Masashi Narita - University of Cambridge, Cambridge, UK
Andre Nussenzweig - National Cancer Institute, NIH, Bethesda, MD, USA
William C. Orr - Southern Methodist University, Dallas, TX, USA
Daniel S. Peepker - The Netherlands Cancer Institute, Amsterdam, The Netherlands
Thomas Rando - Stanford University School of Medicine, Stanford, CA, USA
Michael Ristow - Swiss Federal Institute of Technology, Zurich, Switzerland
Igor B. Roninson - Ordway Research Institute, Albany, NY, USA
Michael R. Rose - University of California, Irvine, CA, USA
K Lenhard Rudolph - Hannover Medical School, Hannover, Germany
Paolo Sassone-Corsi - University of California, Irvine, CA, USA
John Sedivy - Brown University, Providence, RI, USA
Manuel Serrano - Spanish National Cancer Research Center, Madrid, Spain
Gerald S. Shadel - Yale University School of Medicine, New Haven, CT, USA
Norman E. Sharpless - University of North Carolina, Chapel Hill, NC, USA
Vladimir P. Skulachev - Moscow State University, Moscow, Russia
Sally Temple - NY Neural Stem Cell Institute, Albany, NY, USA
George Thomas - University of Cincinnati, Cincinnati, OH, USA
Jonathan L. Tilly - Massachusetts General Hospital, Boston, MA, USA
John Tower - University of Southern California, LA, CA, USA
Eric Verdin - University of California, San Francisco, CA, USA
Thomas von Zglinicki - Newcastle University, Newcastle, UK
Alex Zhavoronkov - Insilico Medicine, Baltimore, MD, USA

Aging (ISSN: 1945 - 4589) is published monthly by Impact Journals, LLC.
6666 East Quaker St., Suite 1B, Orchard Park, NY 14127

Abstracted and/or indexed in: PubMed/Medline (abbreviated as "Aging (Albany NY)"), PubMed Central (abbreviated as "Aging (Albany NY)"), Web of Science/Science Citation Index Expanded (abbreviated as Aging-US) & listed in the Cell Biology-SCIE and Geriatrics & Gerontology category, Scopus /Rank Q1(the highest rank) (abbreviated as Aging)- Aging and Cell Biology category, Biological Abstracts, BIOSIS Previews, EMBASE, META (Chan Zuckerberg Initiative), Dimensions (Digital Science's).

This publication and all its content, unless otherwise noted, is licensed under CC-BY 3.0 Creative Commons Attribution License.
Impact Journals, LLC meets Wellcome Trust Publisher requirements.
IMPACT JOURNALS is a registered trademark of Impact Journals, LLC.



Editorial and Publishing Office Aging

6666 E. Quaker St., Suite 1,
Orchard Park, NY 14127
Phone: 1-800-922-0957
Fax: 1-716-508-8254
e-Fax: 1-716-608-1380

Submission

Please submit your manuscript on-line at <http://aging.msubmit.net>

Editorial

For editorial inquiries, please call us or email editors@impactaging.com

Production

For questions related to preparation of your article for publication, please call us or email krasnova@impactaging.com

Indexing

If you have questions about the indexing status of your paper, please email kurenova@impactaging.com

Billing/Payments

If you have questions about billing/invoicing or would like to make a payment, please call us or email payment@impactaging.com

Media

If you have questions about post publication promotion, Altmetric, video interviews or social media, please email media@impactjournals.com

Printing

Each issue or paper can be printed on demand. To make a printing request, please call us or email printing@impactjournals.com

Publisher's Office

Aging is published by Impact Journals, LLC
To contact the Publisher's Office, please email: publisher@impactjournals.com, visit www.impactjournals.com, or call 1-800-922-0957

Aging (ISSN: 1945 - 4589) is published twice a month by Impact Journals, LLC.
6666 East Quaker St., Suite 1B, Orchard Park, NY 14127

Abstracted and/or indexed in: PubMed/Medline (abbreviated as "Aging (Albany NY)"), PubMed Central (abbreviated as "Aging (Albany NY)"), Web of Science/Science Citation Index Expanded (abbreviated as Aging-US) & listed in the Cell Biology-SCIE and Geriatrics & Gerontology category, Scopus /Rank Q1(the highest rank) (abbreviated as Aging) - Aging and Cell Biology category, Biological Abstracts, BIOSIS Previews, EMBASE, META (Chan Zuckerberg Initiative), Dimensions (Digital Science's).

This publication and all its content, unless otherwise noted, is licensed under CC-BY 3.0 Creative Commons Attribution License.
Impact Journals, LLC meets Wellcome Trust Publisher requirements.

IMPACT JOURNALS is a registered trademark of Impact Journals, LLC.



Table of Contents

Adaptive sequence convergence of the tumor suppressor ADAMTS9 between small-bodied mammals displaying exceptional longevity

[Originally published in Volume 9, Issue 2 pp 573-582](#)

Mir 145/143: tumor suppressor, oncogenic microenvironmental factor or ...both?

[Originally published in Volume 8, Issue 5 pp 1153-1155](#)

p63 expression confers significantly better survival outcomes in high-risk diffuse large B-cell lymphoma and demonstrates p53-like and p53-independent tumor suppressor function

[Originally published in Volume 8, Issue 2 pp 345-365](#)

The PTEN tumor suppressor gene and its role in lymphoma pathogenesis

[Originally published in Volume 7, Issue 12 pp 1032-1049](#)

The p53 tumor suppressor protein protects against chemotherapeutic stress and apoptosis in human medulloblastoma cells

[Originally published in Volume 7, Issue 10 pp 854-867](#)

MDL-1, a growth- and tumor-suppressor, slows aging and prevents germline hyperplasia and hypertrophy in *C. elegans*

[Originally published in Volume 6, Issue 2 pp 98-117](#)

Immortalization of MEF is characterized by the deregulation of specific miRNAs with potential tumor suppressor activity

[Originally published in Volume 3, Issue 7 pp 665-671](#)

Insights from model organisms on the functions of the tumor suppressor protein LKB1: Zebrafish chips in

[Originally published in Volume 3, Issue 4 pp 363-367](#)

MKK4 as oncogene or tumor suppressor: In cancer and senescence, the story's getting old

[Originally published in Volume 2, Issue 11 pp 752-753](#)

Tumor suppressors revival in CLL

[Originally published in Volume 9, Issue 6 pp 1473-1474](#)

SOCS1 regulates senescence and ferroptosis by modulating the expression of p53 target genes

[Originally published in Volume 9, Issue 10 pp 2137-2162](#)

Premature aging and cancer development in transgenic mice lacking functional CYLD

[Originally published in Volume 11, Issue 1 pp 127-159](#)

Long noncoding RNA LINCo0963 induces NOP2 expression by sponging tumor suppressor miR-542-3p to promote metastasis in prostate cancer

[Originally published in Volume 12, Issue 12 pp 11500-11516](#)

The association between KLF4 as a tumor suppressor and the prognosis of hepatocellular carcinoma after curative resection

[Originally published in Volume 12, Issue 15 pp 15566-15580](#)

Aerobic exercise induces tumor suppressor p16^{INK4a} expression of endothelial progenitor cells in human skeletal muscle

[Originally published in Volume 12, Issue 20 pp 20226-20234](#)

CPEB3 functions as a tumor suppressor in colorectal cancer via JAK/STAT signaling

[Originally published in Volume 12, Issue 21 pp 21404-21422](#)

Extracellular vesicle derived miR-544 downregulates expression of tumor suppressor promyelocytic leukemia zinc finger resulting in increased peritoneal metastasis in gastric cancer

[Originally published in Volume 12, Issue 23 pp 24009-24022](#)

MITF functions as a tumor suppressor in non-small cell lung cancer beyond the canonically oncogenic role

[Originally published in Volume 13, Issue 1 pp 646-674](#)

Tumor suppressor DCAF15 inhibits epithelial-mesenchymal transition by targeting ZEB1 for proteasomal degradation in hepatocellular carcinoma

[Originally published in Volume 13, Issue 7 pp 10603-10618](#)

SPRY4 suppresses proliferation and induces apoptosis of colorectal cancer cells by repressing oncogene *EZH2*

[Originally published in Volume 13, Issue 8 pp 11665-11677](#)

miR-144-3p inhibited the growth, metastasis and epithelial-mesenchymal transition of colorectal adenocarcinoma by targeting ZEB1/2

[Originally published in Volume 13, Issue 13 pp 17349-17369](#)

CircSPIDR acts as a tumour suppressor in cervical adenocarcinoma by sponging miR-431-5p and regulating SORCS1 and CUBN expression

[Originally published in Volume 13, Issue 14 pp 18340-18359](#)

Downregulation of ZC3H13 by miR-362-3p/miR-425-5p is associated with a poor prognosis and adverse outcomes in hepatocellular carcinoma

[Originally published in Volume 14, Issue 5 pp 2304-2319](#)

miRNA-142-3p functions as a potential tumor suppressor directly targeting FAM83D in the development of ovarian cancer

[Originally published in Volume 14, Issue 8 pp 3387-3399](#)

Wild type and gain of function mutant TP53 can regulate the sensitivity of pancreatic cancer cells to chemotherapeutic drugs, EGFR/Ras/Raf/MEK, and PI3K/mTORC1/GSK-3 pathway inhibitors, nutraceuticals and alter metabolic properties

[Originally published in Volume 14, Issue 8 pp 3365-3386](#)

Adaptive sequence convergence of the tumor suppressor ADAMTS9 between small-bodied mammals displaying exceptional longevity

Matthew J. Lambert¹ and Christine V. Portfors¹

¹School of Biological Sciences, Washington State University, Vancouver, WA 98686, USA

Correspondence to: Matthew J. Lambert; email: Matthew.Lambert@wsu.edu

Keywords: ADAMTS9; convergent evolution, longevity, naked mole-rat, microbats

Received: January 6, 2017

Accepted: February 11, 2017

Published: February 26, 2017

ABSTRACT

Maximum lifespan varies by two orders of magnitude across mammals. How such divergent lifespans have evolved remains an open question, with ramifications that may potentially lead to therapies for age-related diseases in humans. Several species of microbats as well as the naked mole-rat live much longer than expected given their small sizes, show reduced susceptibility to neoplasia, and largely remain healthy and reproductively capable throughout the majority of their extended lifespans. The convergent evolution of extreme longevity in these two groups allows for the opportunity to identify potentially important aging related genes that have undergone adaptive sequence convergence in these long-lived, yet small-bodied species. Here, we have tested 4,628 genes for evidence of convergence between the microbats and naked mole-rat. We find a strong signal of adaptive sequence convergence in the gene A disintegrin-like and metalloprotease with thrombospondin type 1 motifs 9 (ADAMTS9). We also provide evidence that the shared substitutions were driven by selection. Intriguingly, ADAMTS9 is a known inhibitor of the mTor pathway and has been implicated in several aging related processes.

INTRODUCTION

For several decades, it has been well recognized that there is strong correlation between lifespan and body mass [1,2], with larger species typically living longer than smaller species. There are, however, several species that violate this general rule, living much longer than expected given their small size and high metabolic rates. Of particular interest are the microbats, several species of which demonstrate longer maximum lifespans than any other mammals when controlling for body size [3]. In addition to their exceptional longevity, microbats appear to be resistant to neoplasia [4, 5] and remain healthy and reproductively capable throughout the majority of their lives [6].

Much like the microbats, *Heterocephalus glaber* (naked mole-rat) lives approximately three times longer than expected given its small size [7], is remarkably resistant to neoplasia [8-10] and displays no symptoms of aging well into its second decade [11].

Although once thought to be rare, there have been numerous recent studies demonstrating adaptive sequence convergence between a variety of species displaying convergent traits. These studies have highlighted genes that have been repeatedly targeted during the evolution of a given trait. For example, the evolution of echolocation in bats and toothed whales appears to be driven, in part, by common mutations in the genes *Prestin* [12, 13] and *Cdh23* [14, 15]; cardiac glycoside toxin resistance in numerous disparate vertebrates and invertebrates can be explained by identical amino acid substitutions in the enzyme Na⁺/K⁺-ATPase [16]; and the repeated convergent evolution of the sodium ion transporter NaV1.7 in hibernating mammals and mole-rats is believed to impart insensitivity to the accumulation of CO₂ [17]. These studies, and many others, demonstrate that common selective pressures can drive common mutations in relevant genes.

The evolution of extreme longevity in microbats and the naked mole-rat is likely attributable to a lack of

extrinsic sources of mortality in these species. Bats, being nocturnal and capable of flight, generally contend with few predators. Likewise, the naked mole-rat lives in subterranean burrows where the risk of predation is low. Several theories of aging suggest that a lack of extrinsic sources of mortality will result in selection for longer lifespan [8, 18]. For example, according to the antagonistic pleiotropy (AP) theory of aging, a mutation can be beneficial during development, but have late-onset deleterious effects [19]. AP is expected to be more prevalent in species with high levels of extrinsic mortality since most individuals are unlikely to survive long after reaching sexual maturity, therefore there will be little pressure to select against the deleterious effects that manifest later in life. Also, the disposable soma theory of aging suggests that there exists a trade-off between growth/development and repair/maintenance [20]. In species that contend with many predators, it should be beneficial to allocate resources to grow and develop as quickly as possible rather than to invest in repair and maintenance since longevity is already unlikely. According to both theories, for species that contend with numerous extrinsic sources of mortality, the decline in fitness due to aging is minimal, so selection is inefficient at promoting mutations that increase longevity. However, for species that exist in relatively safe niches, like microbats and the naked mole-rat, the strength of selection to delay senescence will be much stronger, as individuals that live longer will have higher lifetime reproductive fitness. We hypothesize that the pressure to delay senescence shared by microbats and naked mole-rat may have led to convergent sequence evolution in key longevity promoting genes. The identification of genes that have undergone convergent evolution in these long-lived

species would provide a better understanding of the genetics of longevity and could potentially identify therapeutic targets for cancer and other age-related illnesses.

Here we tested for adaptive convergent sequence evolution between microbats and the naked mole-rat in almost 5,000 genes conserved across a wide-range of mammals. We found that A disintegrin-like and metalloprotease with thrombospondin type 1 motifs 9 (ADAMTS9) displays numerous convergent substitutions between the long-lived species that were likely driven by positive selection.

RESULTS

The goal of this study was to determine if any genes display evidence of adaptive sequence convergence between long-lived microbats and the naked mole-rat. We tested for convergence in 4,628 1:1 ortholog groups between 3 microbat species (*Myotis lucifugus*, *Myotis brandtii* and *Eptesicus fuscus*), and the naked mole-rat. Additionally, as outgroup species, we included sequences from 11 small-bodied rodents and laurasiatherian mammals with at least acceptable longevity data curated in the AnAge database [21]. The relationship between the 15 species is shown in the phylogeny in Figure 1a. Importantly, none of these additional species demonstrate exceptional longevity (Fig. 1b). The requirement that sister species to microbats and naked mole-rat be small-bodied and not long-lived allowed us to control for body size and phylogeny while giving us the opportunity to test for convergence in the long-lived species as compared to normal aging species.

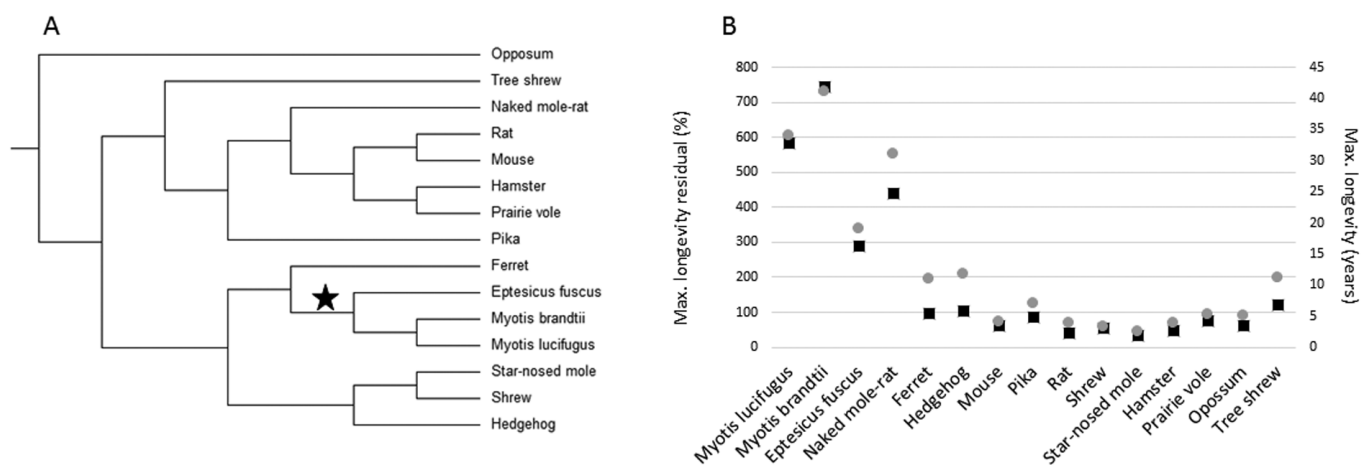


Figure 1. Small-bodied mammals that display exceptional longevity. (A) The accepted tree topology for the 15 species included in this study. (B) Maximum longevity residual (left axis, black boxes) and maximum longevity (right axis, grey circles) of the 15 species. Maximum longevity residual (tmax) is the percentage of the expected maximum longevity given adult body size (M), derived from the mammalian allometric equation: $tmax = 4.88M^{0.153}$ [30].

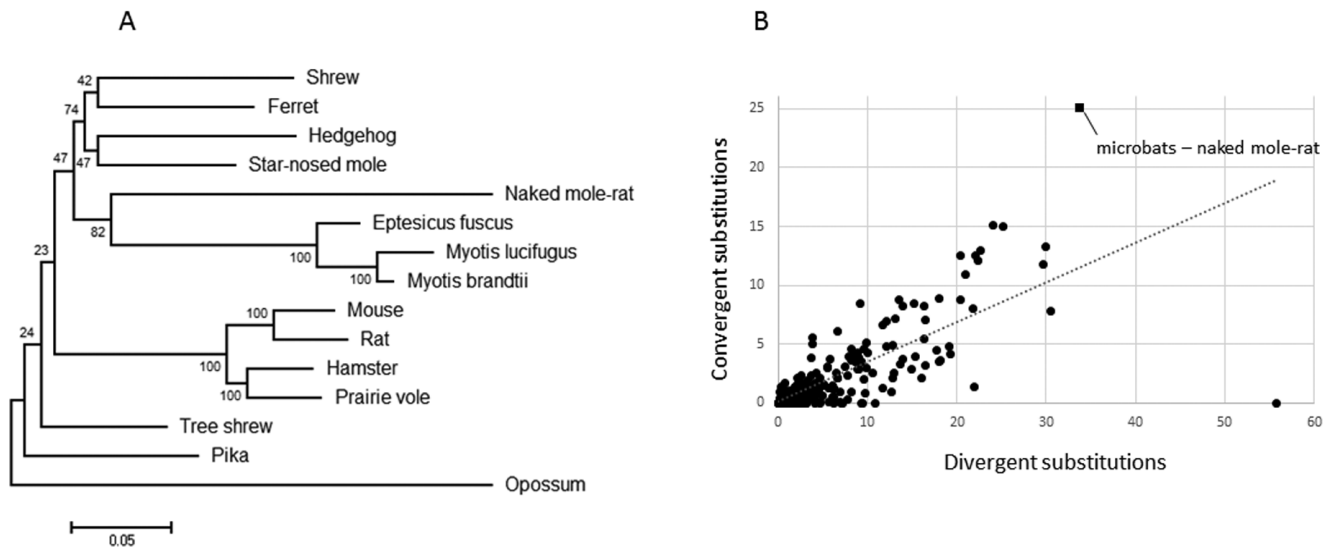


Figure 2. Evidence for ADAMTS9 sequence convergence in long-lived mammals. (A) Maximum-likelihood gene tree constructed using the best fitting nucleotide substitution model (GTR+G) demonstrates a monophyletic grouping of the long-lived mammals. (B) Plot of the numbers of divergent versus convergent substitutions occurring between all independent pairs of branches of the species tree. The microbat-naked mole-rat comparison has the highest level of convergence as well as the largest distance from the trendline.

Initially, we constructed maximum likelihood gene trees based on nucleotide alignments for each of the 4,628 ortholog groups. These trees were then parsed programmatically, searching for instances in which the long-lived mammals (naked mole-rat, *Myotis davidii*, *Myotis lucifugus* and *Eptesicus fuscus*) formed a monophyletic group, to the exclusion of their true closest relatives (rodents and carnivores/insectivores for the naked mole-rat and microbats, respectively). We found that only one gene, ADAMTS9, violated the known species tree in such a manner (Fig. 2a), suggesting sequence convergence between the naked mole-rat and microbats occurred during the evolution of this gene. To determine which sites were responsible for the observed grouping of the long-lived species, we used a maximum likelihood approach to reconstruct all ancestral amino acid sequences at interior nodes of the accepted phylogeny. These ancestral sequences were used to map and count all pairwise convergent substitutions (mutations from the ancestral state that lead to identical amino acids) shared between the microbats and naked mole-rat. Although, the microbats and naked mole-rat share 21 convergent substitutions in this gene (Table 1), which is far more than any other instance of sequence convergence described to date, it may be possible that this represents a normal level of background convergence if for example ADAMTS9 is rapidly evolving. However, Castoe et al. [22] developed

a method to generate an empirical null distribution for the expected level of convergence for a given gene, provided a sufficient number of taxa are included. Briefly, the number of divergent (mutations that lead to different amino acids at homologous sites in the species being compared) and convergent substitutions are estimated for every pair of branches in a phylogeny. It has previously been demonstrated that the number of divergent substitutions reliably predict the number of convergent substitutions, therefore excess convergence between any two branches would appear as an outlier with a higher convergent to divergent substitution ratio than all other pairwise comparisons between branches [22]. This method allowed us to distinguish between rapid evolution and potential adaptive convergence. To test this, we used the program Grand-conv [23, 24], which estimates the posterior numbers of convergent and divergent substitutions shared between all pairs of branches in the given phylogeny. We found that the convergence between the naked mole-rat and microbats exceeded expectations given the phylogeny (Fig. 2b), again suggesting sequence convergence between the long-lived species. In addition, using the methods of Zhang and Kumar [25], we found that the level of convergence between microbats and naked mole-rat exceeds random expectations ($p < .001$), indicating a significant amount of convergence.

Table 1. ADAMTS9 convergent sites. The numbers at the top of each column indicate the amino acid position in the alignment.

	54	236	244	324	362	512	558	565	775	838	884	890	1110	1314	1319	1489	1497	1597	1675	1765	1933
Naked mole-rat	V	R	R	V	P	S	D	Q	A	K	V	R	Q	R	R	R	E	R	A	S	T
Eptesicus fuscus	V	R	R	V	P	S	D	Q	A	K	V	R	Q	R	R	R	E	R	A	S	T
Myotis brandtii	V	R	R	V	P	S	D	Q	A	K	V	R	Q	R	R	-	-	R	A	S	T
Myotis lucifugus	V	V	Q	V	P	S	D	Q	A	K	V	R	Q	R	R	R	E	R	A	S	T
Rat	I	K	K	I	S	P	-	-	T	S	I	R	E	Q	T	K	D	Q	T	N	L
Mouse	I	K	K	I	Y	P	H	R	T	S	I	K	E	Q	T	K	D	Q	T	N	K
Prairie vole	I	K	K	I	S	P	H	R	T	S	I	K	E	Q	T	K	D	Q	T	N	K
Hamster	I	K	K	I	S	P	H	R	T	N	I	K	E	Q	R	K	D	Q	T	N	K
Star-nosed mole	I	K	K	I	S	S	P	R	T	N	V	K	E	Q	S	K	D	K	T	K	K
Shrew	-	K	K	I	S	X	L	R	T	N	V	K	E	Q	S	X	X	K	T	L	K
Ferret	I	K	K	I	S	P	-	R	T	N	I	K	E	Q	S	K	D	K	T	E	K
Tree shrew	V	K	K	I	X	P	X	X	T	X	-	K	E	Q	S	K	E	K	X	X	K
Hedgehog	-	S	K	I	S	Y	H	R	X	N	V	K	E	Q	D	K	D	K	T	N	K
Opossum	-	K	R	V	A	P	H	R	T	N	I	S	A	R	R	K	D	K	T	K	K
Pika	I	S	K	V	S	P	H	R	T	N	I	K	E	Q	M	K	D	K	A	Q	K

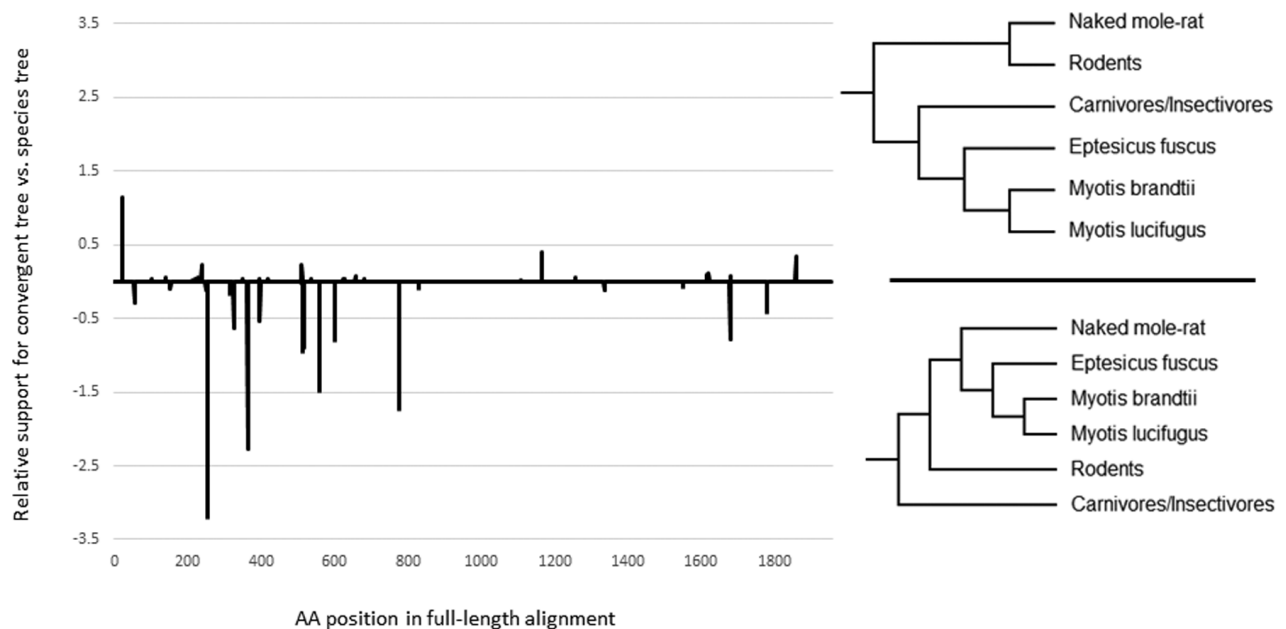


Figure 3. The relationship between sequence convergence and positive selection. Relative support for convergent tree and species tree topologies for all positively selected sites along the *ADAMTS9* gene sequence. The values are the difference between site-wise log likelihood scores for the species tree and the convergent tree. Negative values indicate more support for the convergent tree.

Notably, the addition of the moderately long-lived rodent, *Cavia porcellus* (guinea pig), and megabats, *Pteropus alecto* and *Pteropus vampyrus*, disrupted the monophyletic grouping of the naked mole-rat and micro-

bats in maximum-likelihood gene trees based on amino acid alignments (Not shown). However, even with the inclusion of these moderately long-lived mammals we still found that the naked mole-rat and microbats share

16 convergent substitutions (Supplemental Table 1), which remains significant using the method of Zhang and Kumar [25]. Furthermore, estimates of posterior numbers of divergent versus convergent changes still suggest sequence convergence between the naked mole-rat and microbats even when the megabats and guinea pig were included (Supplemental Fig. 1).

Lastly, to test if the observed sequence convergence may be due to positive selection, we employed a unique multistep approach. First, all sites with significant evidence for positive selection along the ancestral microbat branch (indicated by a star in Fig. 1a) were identified with the program TreeSAAP [26], producing a list of 77 sites. These 77 sites were then extracted from the original alignment and used to create a new alignment that consisted only of the sites with evidence of positive selection in microbats. Next, we calculated site-wise log-likelihood values for the convergent gene tree (Fig. 2a) and compared these to site-wise log likelihood values for the accepted species tree (Fig. 1a), using the positively selected sites alignment. If the observed convergence was due to chance, we would expect the positively selected sites to support the accepted species topology. However, we found that the opposite is true, the sites with evidence of positive selection strongly favored the convergent topology (Fig. 3). Indeed, an approximately unbiased test suggests that the convergent tree was much more likely than the accepted species tree ($P = .886$ and $P = .114$, respectively), suggesting that the convergence between the long-lived species was driven by selection.

DISCUSSION

We tested 4,628 genes for evidence of adaptive sequence convergence between long-lived, small-bodied mammals. We found evidence for an enrichment of convergent substitutions between the microbats and the naked mole-rat in the gene ADAMTS9. ADAMTS9 is the most widely conserved member of the ADAMTS family and has recently been reported to be a novel tumor suppressor that is downregulated in several varieties of human cancer [27]. Intriguingly, ADAMTS9 inhibits tumor growth by blocking the mTOR pathway [28], which has long been known to be associated with aging [29]. In addition to its role in tumor suppression, ADAMTS9 has also been implicated in several age-related conditions including arthritis [30], type 2 diabetes [31, 32], age-related macular degeneration [33, 34] and menopause [35]. Furthermore, in *C. elegans* the loss of GON-1, the roundworm homolog of ADAMTS9, alters lifespan and promotes dauer formation [36]. These

effects are likely due to modified insulin and insulin-like ortholog secretion and altered insulin/IGF-1 signaling, which is also known to contribute to aging [37].

Although, it may be possible that the observed convergent changes shared by microbats and the naked mole-rat may be the product of some non-adaptive force rather than selection for increased longevity, several lines of evidence suggest otherwise. First, the convergent substitutions are distributed along the length of the coding sequence, eliminating gene conversion or alternate exon usage as possible causes. Second, the convergent topology was strongly favored when only sites with evidence of positive selection occurring on the long-lived microbat branch were considered, suggesting that the convergence was indeed driven by selection. Finally, ADAMTS9 has previously been implicated in several aging processes and age-related diseases [27, 30-37], supporting the hypothesis that modulation of ADAMTS9 function alters lifespan. Together, this evidence suggests that ADAMTS9 has been repeatedly targeted by selection for increased longevity in microbats and the naked mole-rat.

As yet, we can provide no explanation for how the convergent evolution of ADAMTS9 has promoted longevity in microbats and the naked mole-rat. However, it is rather intriguing that ADAMTS9 is a known inhibitor of the mTor pathway. The hyperfunction theory of aging posits that aging is due to the prolonged activity of growth-promoting pathways, such as mTor [38]. According to this theory, aging itself is not a program, but rather aging is a harmful continuation of developmental programs after growth has ended [39]. This hypothesis is supported by several lines of evidence that have identified mTor activity as a driver of senescence [29, 40-43]. Therefore, it is a distinct possibility that the convergent evolution of ADAMTS9 in long-lived species may have altered this gene's function such that it now serves to slow the effects of mTor, preventing the declines normally associated with aging. Indeed, the author of the hyperfunction theory has recently speculated that the extraordinary longevity of microbats and the naked mole-rat may be due to selection for a "decelerator of mTor" [44].

Given the role of ADAMTS9 in such a wide range of age-related conditions, its direct effect on lifespan in *C. elegans* and its ability to modulate mTOR and insulin/IGF-1 signaling, it is likely that the convergent evolution of ADAMTS9 may be, in part, responsible for the exceptional longevity and resistance to neoplasia found in microbats and the naked mole-rat.

MATERIALS AND METHODS

Ensembl Compara [45] was used to identify all 1:1 orthologs from the species *Myotis lucifugus*, *Pteropus vampyrus*, *Erinaceus europaeus*, *Mustela putorius*, *Sorex araneus*, *Mus musculus*, *Rattus norvegicus*, *Ochotona princeps*, *Cavia porcellus* and *Monodelphis domestica*. This generated a list of 5109 1:1 ortholog groups from these species. Amino acid and coding sequences for the species listed above were downloaded from Ensembl version 84. For the species *Myotis brandtii*, *Eptesicus fuscus*, *Miniopterus natalensis*, *Pteropus alecto*, *Condylura cristata*, *Mesocricetus auratus*, *Microtus ochrogaster* and *Heterocephalus glaber*, orthologs were identified with a reciprocal best hit approach. For example, the naked mole-rat orthologs were identified by first using blastp to align the 5,109 *Cavia porcellus* protein sequences from Ensembl against all naked mole-rat refSeq sequences. The top naked mole-rat hits were then aligned against all *Cavia porcellus* protein sequences from Ensembl. All instances in which the reciprocal blast alignments identified the same sequences were included for further study, all others were discarded. This reduced the number of 1:1 ortholog groups to 4,978.

Amino acid sequences for each of the 4,978 1:1 ortholog groups were aligned with Muscle [46]. TrimAl [47] was used to filter alignments with mean percentage identity below 60%. This left 4,628 high quality multiple sequence alignments. Pal2Nal [48] was then used to create codon oriented nucleotide alignments for the 4,628 ortholog groups. We then constructed Maximum-likelihood gene trees in PhyML 3.0 [49] using the best fitting nucleotide substitution model for each gene as indicated by jModelTest 2 [50]. A custom perl script was used to analyze the resulting Newick files, searching for monophyletic groupings of the long-lived species.

PAML, specifically the program CodeML, [51] was used to reconstruct ancestral amino acid sequences at all interior nodes of the species tree for ADAMTS9. We then used custom Perl scripts to map and count all convergent substitutions occurring between the naked mole-rat and microbat branches. Since detection of convergent and divergent substitutions is critically dependent upon alignment quality we used PRANK [52], a phylogeny aware alignment tool, to generate a second ADAMTS9 multiple sequence alignment. Differences between the Muscle and PRANK alignments were minimal and both recovered the same 21 convergent substitutions between microbats and naked mole-rat.

Both the Muscle and PRANK ADAMTS9 amino acid multiple sequence alignments, the accepted tree

topology and the program Grand-conv were used to estimate the posterior numbers of convergent and divergent substitutions. The two alignments produced identical results. To determine which sites were subject to positive selection along the microbat lineage we used the program TreeSAAP. The ADAMTS9 nucleotide multiple sequence alignment and the accepted species tree were used as input. We only considered radical substitutions (categories 6-8) with Z-scores greater than 3.09. PhyML was used to calculate site-wise log likelihood values for both the convergent tree and a constrained species tree using a multiple sequence alignment containing only sites with evidence of positive selection as indicated by TreeSAAP. An approximately unbiased test comparing the likelihood of the convergent and species trees was conducted in ConSel [53].

AUTHOR CONTRIBUTIONS

MJL and CVP conceived of the study. MJL performed all analyses. MJL and CVP wrote the manuscript.

CONFLICTS OF INTEREST

The authors declare that there are no conflicts of interest.

FUNDING

Funding provided by Washington State University from the Herbert L. Eastlick Distinguished Professorship to CVP.

REFERENCES

1. Promislow DE. On size and survival: progress and pitfalls in the allometry of life span. *J Gerontol.* 1993; 48:B115–23. doi: 10.1093/geronj/48.4.B115
2. de Magalhães JP, Costa J, Church GM. An analysis of the relationship between metabolism, developmental schedules, and longevity using phylogenetic independent contrasts. *J Gerontol A Biol Sci Med Sci.* 2007; 62:149–60. doi: 10.1093/gerona/62.2.149
3. Podlutzky AJ, Khritankov AM, Ovodov ND, Austad SN. A new field record for bat longevity. *J Gerontol A Biol Sci Med Sci.* 2005; 60:1366–68. doi: 10.1093/gerona/60.11.1366
4. Buckles EL. Chiroptera (bats). In: Fowler ME, Miller RE (eds.). *Zoo and wildlife medicine*, Volume 8. St. Louis (MO): Elsevier; 2014. p. 285–286.
5. Chu P, Shuo Y, Wang F, Jeng C, Pang V, Chang P, Chin S, Liu C. Spontaneous neoplasms in zoo mammals, birds, and reptiles in Taiwan—a 10 year survey. *Anim*

- Biol. 2012; 62:95–110.
doi: 10.1163/157075611X616941
6. Brunet-Rossini A, Wilkinson G. Methods for age estimation and the study of senescence in bats. T. Kunz, S. Parsons (Eds.), *Ecological and Behavioral Methods for the Study of Bats*, The Johns Hopkins University Press, Baltimore, MD, USA. 2009; pp. 315–325.
 7. Buffenstein R, Jarvis JU. The naked mole rat--a new record for the oldest living rodent. *Sci SAGE KE*. 2002; 2002:pe7. doi: 10.1126/sageke.2002.21.pe7
 8. Buffenstein R. The naked mole-rat: a new long-living model for human aging research. *J Gerontol A Biol Sci Med Sci*. 2005; 60:1369–77.
doi: 10.1093/gerona/60.11.1369
 9. Liang S, Mele J, Wu Y, Buffenstein R, Hornsby PJ. Resistance to experimental tumorigenesis in cells of a long-lived mammal, the naked mole-rat (*Heterocephalus glaber*). *Aging Cell*. 2010; 9:626–35.
doi: 10.1111/j.1474-9726.2010.00588.x
 10. Delaney MA, Nagy L, Kinsel MJ, Treuting PM. Spontaneous histologic lesions of the adult naked mole rat (*Heterocephalus glaber*): a retrospective survey of lesions in a zoo population. *Vet Pathol*. 2013; 50:607–21. doi: 10.1177/0300985812471543
 11. Edrey YH, Hanes M, Pinto M, Mele J, Buffenstein R. Successful aging and sustained good health in the naked mole rat: a long-lived mammalian model for biogerontology and biomedical research. *ILAR J*. 2011; 52:41–53. doi: 10.1093/ilar.52.1.41
 12. Liu Y, Cotton JA, Shen B, Han X, Rossiter SJ, Zhang S. Convergent sequence evolution between echolocating bats and dolphins. *Curr Biol*. 2010; 20:R53–54. doi: 10.1016/j.cub.2009.11.058
 13. Liu Z, Qi FY, Zhou X, Ren HQ, Shi P. Parallel sites implicate functional convergence of the hearing gene prestin among echolocating mammals. *Mol Biol Evol*. 2014; 31:2415–24. doi: 10.1093/molbev/msu194
 14. Shen YY, Liang L, Li GS, Murphy RW, Zhang YP. Parallel evolution of auditory genes for echolocation in bats and toothed whales. *PLoS Genet*. 2012; 8:e1002788.
doi: 10.1371/journal.pgen.1002788
 15. Lambert M, Nevue A, Portfors C. Contrasting patterns of adaptive sequence convergence among echolocating mammals. *Gene*. 2017; 605:1-4. doi: 10.1016/j.gene.2016.12.017.
 16. Ujvari B, Casewell NR, Sunagar K, Arbuckle K, Wüster W, Lo N, O'Meally D, Beckmann C, King GF, Deplazes E, Madsen T. Widespread convergence in toxin resistance by predictable molecular evolution. *Proc Natl Acad Sci USA*. 2015; 112:11911–16.
doi: 10.1073/pnas.1511706112
 17. Liu Z, Wang W, Zhang TZ, Li GH, He K, Huang JF, Jiang XL, Murphy RW, Shi P. Repeated functional convergent effects of NaV1.7 on acid insensitivity in hibernating mammals. *Proc Biol Sci*. 2013; 281:20132950. doi: 10.1098/rspb.2013.2950
 18. Ricklefs RE. Evolutionary theories of aging: confirmation of a fundamental prediction, with implications for the genetic basis and evolution of life span. *Am Nat*. 1998; 152:24–44. doi: 10.1086/286147
 19. Williams GC. Pleiotropy, natural selection and the evolution of senescence. *Evolution*. 1957; 11:398–411. doi: 10.2307/2406060
 20. Kirkwood TB. Evolution of ageing. *Nature*. 1977; 270:301–04. doi: 10.1038/270301a0
 21. Tacutu R, Craig T, Budovsky A, Wuttke D, Lehmann G, Taranukha D, Costa J, Fraifeld VE, de Magalhães JP. Human Ageing Genomic Resources: integrated databases and tools for the biology and genetics of ageing. *Nucleic Acids Res*. 2013; 41:D1027–33. doi: 10.1093/nar/gks1155
 22. Castoe TA, de Koning AP, Kim HM, Gu W, Noonan BP, Naylor G, Jiang ZJ, Parkinson CL, Pollock DD. Evidence for an ancient adaptive episode of convergent molecular evolution. *Proc Natl Acad Sci USA*. 2009; 106:8986–91. doi: 10.1073/pnas.0900233106
 23. Qian C, de Koning AP. Rapid Discovery of Convergent Molecular Evolution Across Entire Phylogenies. 2015. University of Calgary. <http://lab.jasondk.io>.
 24. Qian C, Bryans N, Kruykov I, de Koning AP. Visualization and analysis of statistical signatures of convergent molecular evolution. 2015. University of Calgary. <http://lab.jasondk.io>.
 25. Zhang J, Kumar S. Detection of convergent and parallel evolution at the amino acid sequence level. *Mol Biol Evol*. 1997; 14:527–36.
doi: 10.1093/oxfordjournals.molbev.a025789
 26. Woolley S, Johnson J, Smith MJ, Crandall KA, McClellan DA. TreeSAAP: selection on amino acid properties using phylogenetic trees. *Bioinformatics*. 2003; 19:671–72. doi: 10.1093/bioinformatics/btg043
 27. Peng L, Yang Z, Tan C, Ren G, Chen J. Epigenetic inactivation of ADAMTS9 via promoter methylation in multiple myeloma. *Mol Med Rep*. 2013; 7:1055–61.
 28. Du W, Wang S, Zhou Q, Li X, Chu J, Chang Z, Tao Q, Ng EK, Fang J, Sung JJ, Yu J. ADAMTS9 is a functional tumor suppressor through inhibiting AKT/mTOR pathway and associated with poor survival in gastric cancer. *Oncogene*. 2013; 32:3319–28. doi: 10.1038/onc.2012.359

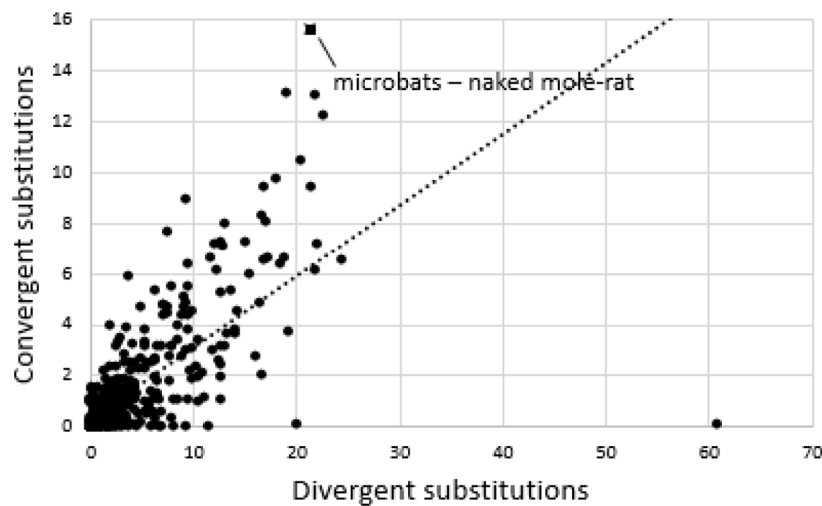
29. Vellai T, Takacs-Vellai K, Zhang Y, Kovacs AL, Orosz L, Müller F. Genetics: influence of TOR kinase on lifespan in *C. elegans*. *Nature*. 2003; 426:620. doi: 10.1038/426620a
30. Yaykasli KO, Hatipoglu OF, Yaykasli E, Yildirim K, Kaya E, Ozsahin M, Uslu M, Gunduz E. Leptin induces ADAMTS-4, ADAMTS-5, and ADAMTS-9 genes expression by mitogen-activated protein kinases and NF- κ B signaling pathways in human chondrocytes. *Cell Biol Int*. 2015; 39:104–12. doi: 10.1002/cbin.10336
31. Keaton JM, Cooke Bailey JN, Palmer ND, Freedman BI, Langefeld CD, Ng MC, Bowden DW. A comparison of type 2 diabetes risk allele load between African Americans and European Americans. *Hum Genet*. 2014; 133:1487–95. doi: 10.1007/s00439-014-1486-5
32. Kong X, Zhang X, Xing X, Zhang B, Hong J, Yang W. The Association of Type 2 Diabetes Loci Identified in Genome-Wide Association Studies with Metabolic Syndrome and Its Components in a Chinese Population with Type 2 Diabetes. *PLoS One*. 2015; 10:e0143607. doi: 10.1371/journal.pone.0143607
33. Whitmore SS, Braun TA, Skeie JM, Haas CM, Sohn EH, Stone EM, Scheetz TE, Mullins RF. Altered gene expression in dry age-related macular degeneration suggests early loss of choroidal endothelial cells. *Mol Vis*. 2013; 19:2274–97.
34. Helisalmi S, Immonen I, Losonczy G, Resch MD, Benedek S, Balogh I, Papp A, Berta A, Uusitupa M, Hiltunen M, Kaarniranta K. ADAMTS9 locus associates with increased risk of wet AMD. *Acta Ophthalmol*. 2014; 92:e410. doi: 10.1111/aos.12341
35. Pyun JA, Kim S, Cho NH, Koh I, Lee JY, Shin C, Kwack K. Genome-wide association studies and epistasis analyses of candidate genes related to age at menarche and age at natural menopause in a Korean population. *Menopause*. 2014; 21:522–29. doi: 10.1097/GME.0b013e3182a433f7
36. Yoshina S, Mitani S. Loss of *C. elegans* GON-1, an ADAMTS9 Homolog, Decreases Secretion Resulting in Altered Lifespan and Dauer Formation. *PLoS One*. 2015; 10:e0133966. doi: 10.1371/journal.pone.0133966
37. Tatar M, Bartke A, Antebi A. The endocrine regulation of aging by insulin-like signals. *Science*. 2003; 299:1346–51. doi: 10.1126/science.1081447
38. Blagosklonny MV. Answering the ultimate question “what is the proximal cause of aging?”. *Aging (Albany NY)*. 2012; 4:861–77. doi: 10.18632/aging.100525
39. Blagosklonny MV. Aging is not programmed: genetic pseudo-program is a shadow of developmental growth. *Cell Cycle*. 2013; 12:3736–42. doi: 10.4161/cc.27188
40. Demidenko ZN, Blagosklonny MV. Growth stimulation leads to cellular senescence when the cell cycle is blocked. *Cell Cycle*. 2008; 7:3355–61. doi: 10.4161/cc.7.21.6919
41. Demidenko ZN, Zubova SG, Bukreeva EI, Pospelov VA, Pospelova TV, Blagosklonny MV. Rapamycin decelerates cellular senescence. *Cell Cycle*. 2009; 8:1888–95. doi: 10.4161/cc.8.12.8606
42. Demidenko ZN, Shtutman M, Blagosklonny MV. Pharmacologic inhibition of MEK and PI-3K converges on the mTOR/S6 pathway to decelerate cellular senescence. *Cell Cycle*. 2009; 8:1896–900. doi: 10.4161/cc.8.12.8809
43. Wesierska-Gadek J. mTOR and its link to the picture of Dorian Gray - re-activation of mTOR promotes aging. *Aging (Albany NY)*. 2010; 2:892–93. doi: 10.18632/aging.100240
44. Blagosklonny MV. Big mice die young but large animals live longer. *Aging (Albany NY)*. 2013; 5:227–33. doi: 10.18632/aging.100551
45. Vilella AJ, Severin J, Ureta-Vidal A, Heng L, Durbin R, Birney E. EnsemblCompara GeneTrees: Complete, duplication-aware phylogenetic trees in vertebrates. *Genome Res*. 2009; 19:327–35. doi: 10.1101/gr.073585.107
46. Edgar RC. MUSCLE: multiple sequence alignment with high accuracy and high throughput. *Nucleic Acids Res*. 2004; 32:1792–97. doi: 10.1093/nar/gkh340
47. Capella-Gutiérrez S, Silla-Martínez JM, Gabaldón T. trimAl: a tool for automated alignment trimming in large-scale phylogenetic analyses. *Bioinformatics*. 2009; 25:1972–73. doi: 10.1093/bioinformatics/btp348
48. Suyama M, Torrents D, Bork P. PAL2NAL: robust conversion of protein sequence alignments into the corresponding codon alignments. *Nucleic Acids Res*. 2006; 34:W609–12. doi: 10.1093/nar/gkl315
49. Guindon S, Dufayard JF, Lefort V, Anisimova M, Hordijk W, Gascuel O. New algorithms and methods to estimate maximum-likelihood phylogenies: assessing the performance of PhyML 3.0. *Syst Biol*. 2010; 59:307–21. doi: 10.1093/sysbio/syq010
50. Darriba D, Taboada GL, Doallo R, Posada D. jModelTest 2: more models, new heuristics and parallel computing. *Nat Methods*. 2012; 9:772. doi: 10.1038/nmeth.2109
51. Yang Z. PAML 4: phylogenetic analysis by maximum likelihood. *Mol Biol Evol*. 2007; 24:1586–91. doi: 10.1093/molbev/msm088

52. Löytynoja A. Phylogeny-aware alignment with PRANK. *Methods Mol Biol.* 2014; 1079:155–70. doi: 10.1007/978-1-62703-646-7_10
53. Shimodaira H, Hasegawa M. CONSEL: for assessing the confidence of phylogenetic tree selection. *Bioinformatics.* 2001; 17:1246–47. doi: 10.1093/bioinformatics/17.12.1246

SUPPLEMENTARY MATERIAL

Supplemental Table 1. ADAMTS9 convergent sites. The numbers at the top of each column indicate the amino acid position in the alignment.

	54	236	244	362	512	775	838	890	1110	1342	1489	1497	1597	1675	1765	1933
Naked mole-rat	V	R	R	P	S	A	K	R	Q	G	R	E	R	A	S	T
Eptesicus fuscus	V	R	R	P	S	A	K	R	Q	G	R	E	R	A	S	T
Myotis brandtii	V	R	R	P	S	A	K	R	Q	G	-	-	R	A	S	T
Myotis lucifugus	V	V	Q	P	S	A	K	R	Q	G	R	E	R	A	S	T
Pteropus vampyrus	I	K	K	S	P	T	N	K	E	S	K	D	K	T	N	K
Pteropus alecto	I	K	K	S	P	T	N	K	E	S	K	D	K	T	N	K
Guinea pig	Q	D	F	L	P	T	N	K	E	S	K	D	Q	T	N	K
Mouse	I	K	K	Y	P	T	S	K	E	S	K	D	Q	T	N	K
Rat	I	K	K	S	P	T	S	R	E	S	K	D	Q	T	N	L
Hamster	I	K	K	S	P	T	N	K	E	S	K	D	Q	T	N	K
Prairie vole	I	K	K	S	P	T	S	K	E	S	K	D	Q	T	N	K
Pika	I	S	K	S	P	T	N	K	E	G	K	D	K	A	Q	K
Shrew	-	K	K	S	X	T	N	K	E	N	X	X	K	T	L	K
Ferret	I	K	K	S	P	T	N	K	E	G	K	D	K	T	E	K
Tree shrew	V	K	K	X	P	T	X	K	E	S	K	E	K	X	X	K
Hedgehog	-	S	K	S	Y	X	N	K	E	S	K	D	K	T	N	K
Star-nosed mole	I	K	K	S	S	T	N	K	E	N	K	D	K	T	K	K
Opossum	-	K	R	A	P	T	N	S	A	N	K	D	K	T	K	K



Supplemental Figure 1. Evidence for ADAMTS9 sequence convergence in long-lived mammals. Plot of the numbers of divergent versus convergent substitutions occurring between all independent pairs of branches of the species tree.

Mir 145/143: tumor suppressor, oncogenic microenvironmental factor or ...both?**Mario Cioce, Sabrina Strano, Paola Muti, and Giovanni Blandino**

An interesting debate is emerging from the recent literature regarding the role of mir-143/145 in tumor initiation/progression. Herein, we aim to contribute our experience and observations to this ongoing debate. We will start from the experimental data presented in the outstanding work of the Tyler Jacks lab, by Dimitrova, Gocheva and colleagues [6]. They show, in a kRAS/p53 murine model of lung adenocarcinoma, that the contribution of the microRNA 143/145 cluster to lung cancer development is non-cell autonomous with the expression of mir143/145 from the tumor micro-environment resulting protumorigenic. More specifically, higher expression of microRNA 143/145 by endothelial cells would be pivotal in tumor progression by favoring tumor angiogenesis in a lung tissue specific fashion. The authors conclude, and their conclusion is shared by Almeida and Calin in a commentary on Genome Biology [1], that mir-143/145 is a non-cell autonomous oncogenic factor rather than a tumor suppressor, with their speculation further supported by the absence of tumor development in mice devoid of such microRNAs and by their lack of expression in murine epithelial cell lines [6]. This is in apparent contrast to what was published by our group and by many others, who provided evidence for the roles that mir-143/145 play as tumor suppressors in human tumors of epithelial origin, including and not limited to cervical, colon, gastric, breast and pancreatic carcinomas, NSCLC and malignant pleural mesothelioma (reviewed in Das and Pillai, 2015) [5].

In their commentary, Almeida and Calin claim that the "heterogeneity" of the human tumors collected for the human studies has prevented to provide a precise definition of the mir143/145 role. They basically substantiate such observation with the possibility that, in unfractionated human tumor tissues, residual expression of mir-143/145 by stromal component may escape the analysis of unfractionated human tumors. Even though this is certainly possible, we will try to provide a "parallel" and not mutually exclusive vision to integrate the ongoing discussion, starting from the work by Dimitrova et al. [6].

First, the data supporting a non-cell autonomous oncogenic role for the mir143/145 derive from a murine

system. Dimitrova and coworkers employed an excellent albeit limited experimental system. In fact, while mice were engineered to express/not express specific tumor suppressors or oncogenes, represent an invaluable tool to study tumor progression, however there is little doubt left that such a system may reflect, at its best, one or few subtypes of its human counterparts of which it may recapitulate a gross history. Second, the mentioned data stem from the use of transgenic mice (Kras^{G12D/+}, p53^{-/-}). Such a model basically represents a "frozen status", again, corresponding only to a specific subset of the modeled tumors and "addicted" to the absence or expression of specific molecular lesions. Thus, engineered mice may not adequately represent the interpatient heterogeneity of human lung tumors. From this perspective, heterogeneity, more than representing an "Achille's Heel" of the mir-143/145 studies in human tumors, may represent an added welcome level of complexity toward understanding the "real life" modulation of such a miRNA locus. Third, by manipulating the levels of microRNA 143/145 into MEFs (Mouse Embryo Fibroblasts), Dimitrova and coworkers conclude that no tumor suppressor activity can be ascribed to the microRNA 143/145 in such cells. Now, it is pleonastic to note that MEFs represent a totally different experimental system from the human epithelial tumors, in terms of embryonal origin and histotype. Thus, it is far from appropriate to draw conclusions regarding functions of the microRNA143/145 locus in human epithelial tumors from experiments performed by inducing deletion of the microRNAs into murine cells of non-epithelial origin. Fourth, and here we come to addressing the system we and many others have employed recently, where matched human specimens have been used. In all the cases, deep downregulation of the miRNA-143-145 expression as compared to normal matched tissues was observed. This occurred in extremely different tumors in terms of history, tissue of origin, and aggressiveness. In fact, both miR-143 and miR-145 were broadly described as downregulated in a plethora of solid tumors, including and not limited to breast, lung, colon (n=43 matched tissues), prostate, the gastrointestinal system, ovary, cervix, head and neck, bladder, thyroid, pituitary and gonads, germ-cell tumors (GCTs), gallbladder cancer, renal cell carcinoma,

osteosarcoma, and neuroblastoma, mesothelioma (reviewed in Das and Pillai, 2015) [5] and thymic epithelial tumors [9]. Notably in most of the work mentioned, matched normal vs tumor samples were analyzed and, despite the fact that the analyzed tumors were very different in terms of history, tissue of origin, aggressiveness, mir143/145 levels, were invariably lower in the transformed tissues.

Rather convincing evidence supporting the tumor suppressor role of mir-143/145 in human malignancies comes from data showing that the downregulation of mir-143/145 is dynamic and correlates with the history of the disease. For example, Slaby et al. showed that downregulation of mir-145 was deeper in relapsing ccRCC as compared to the primary tumor, and, even deeper, in their metastatic counterparts [16]. Along the same line, reduced expression of mir-145 strongly correlated with shorter disease-free survival in prostate and small cell carcinoma of the cervix [2, 10]. Interestingly, by using in situ hybridization of >100 formalin fixed matched breast cancer specimens, Sempere and coworkers found that mir-145 was strongly downregulated in breast tumor tissues with its expression higher in the vessels and myoepithelial compartment of normal breast tissues but strongly reduced in the same compartments within the transformed tissues. However, there are not in enough samples to draw statistical conclusions [14]. On an even broader perspective, a relatively large study on postmenopausal women has recently been published where lower levels of mir-145 in circulating leukocytes were clearly shown to represent prognostic indicators linked to breast cancer progression [12]. Furthermore, dynamic reduction of mir-143/145 staining was observed upon exposure of rats to cigarette smoke [11]. Now, if increased expression of the mir-145 in stromal/endothelial human components would be oncogenic, as shown by Dimitrova et al. in the murine experimental system, it appears slightly counterintuitive that its levels were progressively downregulated in relapsing disease, metastatic disease, or upon stress stimuli conferring clear protumorigenic properties. Indeed, all these processes require a dynamic rearrangement of stromal cell subpopulations and neo-angiogenesis and this may likely lead to detectable changes of microRNA 143/145 expression. Thus, there generally appears to be a profound difference between human and murine tissues.

On a different note, other evidence point to active control of mir-143/145 levels within epithelial tumors and cell lines, in a protumorigenic direction. For example, we have shown that the mir-143/145 promoter is actively hyper-methylated in mesothelioma cancer

cell lines and that hyper-methylation of this promoter correlates with the progressive downregulation of the mir-143/145 in brain metastases of lung tumors, as opposed to primary lung tumors and, lastly, to normal lung tissue [7]. Furthermore, treatment with histone deacetylase inhibitors and de-methylating agents or ectopic restoration of the miRNA levels correlates with lack of tumorigenicity in vivo [7] and similar results were shown in Burkitt's lymphoma cells [8]. The tumor specimens used in the mentioned studies were composed for a large portion of tumor tissue (typically 85-90% of the total tissue) and represented the results of the analysis from many different institutions. Notably, in most of the mentioned studies, the levels of mir-143-145 were in no case undetectable but rather significantly lower than their matched normal tissues. In regards to the cell lines, it may be interesting to note that in vitro grown human cell lines are virtually devoid of any significant stroma component, due to the long adaptation to in vitro growth. Thus, the described dynamic downregulation of the mir-143-145 taking place in the cell lines of the mentioned work may represent an intrinsic property of the transformed epithelial cells.

On the other hand, Almeida and Calin suggest the use of FACS-sorted cell subpopulations and/or the use of laser microdissection to better study the function of microRNAs, in order to ensure cell subpopulations homogeneity. In support of the latter, it is worth mentioning that, in head and neck cancer, ALDH+ve/CD44⁺ cancer stem cells exhibited low levels of miR-145 [18]. Similarly, chemoresistant ABCG2 expressing glioma with decreased levels of the microRNAs 143/145 positively correlated with poor prognosis [15]. Thus, there is increasing evidence for a cell-subpopulation restricted expression of the microRNAs, possibly modulated by external stimuli affecting the progression of the disease. However, the current repertoire of cell surface markers generally used to purify cell subpopulations is still very limited in terms of specificity, and to be able to narrow down a pure, functionally homogeneous cell subpopulations with absolute specificity and enough sensitivity. Thus we note that, the purification of cell subpopulations based on the current repertoire of cell surface markers and/or functional assays may not favorably deal with the intrinsic tumor heterogeneity of the cell subpopulations composing the tumor, which takes place at a single cell level, as shown by single-cell RNAseq studies [3, 13].

Finally, the observation that increased miR-145 could force [17] differentiation of ES cells into the mesoderm and ectoderm lineages may reconcile with the observed

expression of mir-145 into the lung endothelial cells of the vessels of the transgenic kRAS/p53 mice, given the mesodermal derivation of endothelial cells in mouse. We are of the opinion that the use of matched human tissues may constitute an experimental system capable of capturing the complex modulation of the miRNA 143/145 in human tumors and may complement the observations performed in a single mouse strain, engineered to express frequent mutations in a time- and space- restricted manner. Therefore, the precise definition of the mir-143/145 contribution to oncogenesis is still ongoing...

REFERENCES

1. Almeida MI and Calin GA. *Genome medicine*. 2016; 8:29.
2. Avgeris M, et al. *British journal of cancer*. 2013; 108:2573-2581.
3. Buettner F, et al. *Nature biotechnology*. 2015; 33:155-160.
4. Ciocce M, et al. *Oncogene*. 2014; 33:5319-5331.
5. Das AV and Pillai RM. *Cancer cell international*. 2015; 15:92.
6. Dimitrova N, et al. *Cancer discovery*. 2016; 6:188-201.
7. Donzelli S, et al. *Oncotarget*. 2015; 6:35183-35201. doi: 10.18632/oncotarget.5930.
8. Ferreira AC, et al. *Annals of hematology*. 2014; 93:983-993.
9. Ganci F, et al. *Lung cancer*. 2014; 85:197-204.
10. Huang L, et al. *PLoS one*. 2012; 7:e33762.
11. Izzotti A, et al. *FASEB journal*. 2009; 23:806-812.
12. Muti P, et al. *Cancer Epidemiol Biomarkers Prev*. 2014; 23: 2471-2481.
13. Patel AP, et al. *Science*. 2014; 344:1396-1401.
14. Sempere LF, et al. *Cancer research*. 2007; 67:11612-11620.
15. Shi L, et al. *Neuromolecular Med*. 2014; 16:517-528.
16. Slaby O, et al. *Genes, chromosomes & cancer*. 2012; 51: 707-716.
17. Xu N, et al. *Cell*. 2009; 137:647-658.
18. Yu CC, et al. *Cancer research*. 2013; 73:3425-3440.

Giovanni Blandino: Oncogenomic and Epigenetic Unit, Regina Elena, National Cancer Institute, Rome, 00144 Italy

Correspondence: Giovanni Blandino

Email: blandino@ifo.it

Acknowledgements: We thank all the authors and collaborators whose work was mentioned here and we also apologize for the ones not mentioned here, for brevity. We thankfully acknowledge the help of Ms Tania Merlino (Regina Elena Cancer Institute) for proofreading the present manuscript.

Keywords: miR-143/145, cancer, tumor suppressor, microenvironment

Received: May 15, 2016

Published: May 18, 2016

p63 expression confers significantly better survival outcomes in high-risk diffuse large B-cell lymphoma and demonstrates p53-like and p53-independent tumor suppressor function

Zijun Y. Xu-Monette^{1*}, Shanxiang Zhang^{2*}, Xin Li^{1*}, Ganiraju C. Manyam³, Xiao-xiao Wang¹, Yi Xia¹, Carlo Visco⁴, Alexandar Tzankov⁵, Li Zhang³, Santiago Montes-Moreno⁶, Karen Dybkaer⁷, April Chiu⁸, Attilio Orazi⁹, Youli Zu¹⁰, Govind Bhagat¹¹, Kristy L. Richards¹², Eric D. Hsi¹³, William W.L. Choi¹⁴, J. Han van Krieken¹⁵, Jooryung Huh¹⁶, Maurilio Ponzoni¹⁷, Andrés J.M. Ferreri¹⁷, Xiaoying Zhao¹⁸, Michael B. Møller¹⁹, Ben M. Parsons²⁰, Jane N. Winter²¹, Miguel A. Piris⁶, L. Jeffrey Medeiros¹, and Ken H. Young^{1,22}

¹Department of Hematopathology, The University of Texas MD Anderson Cancer Center, Houston, TX 77030, USA

²University of Indiana School of Medicine, Indianapolis, IN 46202, USA

³Department of Bioinformatics and Computational Biology, The University of Texas MD Anderson Cancer Center, Houston, TX 77030, USA

⁴San Bortolo Hospital, Vicenza, Italy

⁵University Hospital, Basel, Switzerland

⁶Hospital Universitario Marques de Valdecilla, Santander, Spain

⁷Aalborg University Hospital, Aalborg, Denmark

⁸Memorial Sloan-Kettering Cancer Center, New York, NY 10065, USA

⁹Weill Medical College of Cornell University, New York, NY 10065, USA

¹⁰The Methodist Hospital, Houston, TX 77030, USA

¹¹Columbia University Medical Center and New York Presbyterian Hospital, New York, NY 10032, USA

¹²University of North Carolina School of Medicine, Chapel Hill, NC 27513, USA

¹³Cleveland Clinic, Cleveland, OH 44195, USA

¹⁴University of Hong Kong Li Ka Shing Faculty of Medicine, Hong Kong, China

¹⁵Radboud University Nijmegen Medical Centre, Nijmegen, Netherlands

¹⁶Asan Medical Center, Ulsan University College of Medicine, Seoul, Korea

¹⁷San Raffaele H. Scientific Institute, Milan, Italy

¹⁸Zhejiang University School of Medicine, Zhejiang, China

¹⁹Odense University Hospital, Odense, Denmark

²⁰Gundersen Medical Foundation, La Crosse, WI 54601, USA

²¹Feinberg School of Medicine, Northwestern University, Chicago, IL 60611, USA

²²The University of Texas School of Medicine, Graduate School of Biomedical Sciences, Houston, TX 77030, USA

*These authors contributed equally to this work.

Key words: p63, DLBCL, p53, TP53 mutation, MDM2

Received: 01/15/16; **Accepted:** 01/26/16; **Published:** 02/14/16

Correspondence to: Ken H. Young, MD; **E-mail:** khyoung@mdanderson.org

Copyright: Xu-Monette et al. This is an open-access article distributed under the terms of the Creative Commons Attribution License, which permits unrestricted use, distribution, and reproduction in any medium, provided the original author and source are credited

Abstract: The role of p53 family member, p63 in oncogenesis is the subject of controversy. Limited research has been done on the clinical implications of p63 expression in diffuse large B-cell lymphoma (DLBCL). In this study, we assessed p63 expression in *de novo* DLBCL samples (n=795) by immunohistochemistry with a pan-p63-monoclonal antibody and correlated it with other clinicopathologic factors and clinical outcomes. p63 expression was observed in 42.5% of DLBCL, did not correlate with p53 levels, but correlated with p21, MDM2, p16^{INK4A}, Ki-67, Bcl-6, IRF4/MUM-1 and CD30 expression, *REL* gains, and *BCL6* translocation. p63 was an independent favorable prognostic factor in DLBCL, which was most significant in patients with International Prognostic Index (IPI) >2, and in activated-B-cell-like DLBCL patients with wild-type *TP53*. The prognostic impact in germinal-center-B-cell-like DLBCL was not apparent, which was likely due to the association of p63 expression with high-risk IPI, and potential presence of Δ Np63 isoform in *TP63* rearranged patients (a mere speculation). Gene expression profiling suggested that p63 has both overlapping and distinct functions compared with p53, and that p63 and mutated p53 antagonize each other. In summary, p63 has p53-like and p53-independent functions and favorable prognostic impact, however this protective effect can be abolished by *TP53* mutations.

INTRODUCTION

TP63, a member of the *TP53* gene family, encodes p63 with 2 types of isoforms: a form with the N-terminal transactivation (TA) domain (TAp63) and a truncated form without the N-terminus (Δ Np63). Both TAp63 and Δ Np63 have isoforms α , β , γ , δ , and ϵ owing to alternative splicing at the 3' end [1-5]. p63 shares structural and sequence homology with p53 and p73, the third member of the p53 family [1, 6]. Like p53, TAp63 has been implicated in cell cycle arrest and apoptosis in response to DNA damage, ectoderm development, maternal reproduction and metabolism, dependent or independent of p53-functions [1, 7-13]. For example, TAp63 can transactivate some well-known p53 target genes including *CDKN1A*, *BAX* and *MDM2* [1, 14]. Moreover, p53-dependent apoptosis in response to DNA damage required p63 and p73 in mouse developing brain and embryonic fibroblasts [7]. However, in a mouse model p63 and p73 did not contribute to p53 tumor suppression function in lymphoma development [15]. Δ Np63, on the other hand, interacts with p53, TAp63, and TAp73 in a dominant-negative fashion to inhibit their tumor-suppressive functions [3]. It is generally believed that TAp63, like p53, is a tumor suppressor, whereas Δ Np63 has a critical role in epidermal development and functions as an oncogene in a mouse model [16-19]. Furthermore, the α , β , γ , δ , and ϵ isoforms of TAp63 and Δ Np63 have differential functions [5, 14, 20-24].

In normal human tissues, p63 expression is tissue-specific and restricted to epithelial cells, certain subpopulations of basal cells, and occasionally cells in the germinal centers of lymph nodes [1, 25, 26]. Accordingly, in tumors structural disruption of *TP63* and aberrant p63 expression are commonly seen in squamous cell and transitional cell carcinomas, but are also observed in non-Hodgkin lymphomas, predominantly in

In basal epithelial cells and squamous cell carcinomas, the Δ Np63 isoform, especially Δ Np63 α , is predominantly expressed, possibly due to the increased Δ Np63 stability caused by the lack of the transactivation domain which is indispensable for proteasome-dependent MDM2-independent degradation of p63 [24, 31]. In contrast, TAp63 is present mostly in epithelial lining cells at lower levels under normal physiological conditions, and in adenocarcinoma, thymoma and lymphoma cells; TAp63 accumulates in response to genotoxic stress [24, 26]. Although p63 expression has been shown in a few studies to indicate a poor prognosis in some carcinomas [32-34], its prognostic significance in DLBCL is unclear.

DLBCL is the most common type of non-Hodgkin lymphoma and can be divided into germinal center B-cell-like (GCB) and activated B-cell-like (ABC) subgroups by gene expression profiling [35]. Numerous genetic factors affecting the prognosis of DLBCL have been identified [36]. In our previous study, *TP53* mutations were detected in approximately 20% of *de novo* DLBCL cases and conferred a worse prognosis among DLBCL patients treated with rituximab, cyclophosphamide, doxorubicin, vincristine, and prednisolone (R-CHOP) [37]. Overexpression of mutated but not wild-type p53 (WT-p53) protein is also associated with a poor prognosis in DLBCL patients [38]. The dysregulation, expression, and clinical implications of p63 in DLBCL are less clear than those of p53; likewise, p63's role in tumorigenesis and its functional relationship with p53 are not well understood. p63, predominantly TAp63 (likely TAp63 β and/or TAp63 γ) but not Δ Np63 or p63 α , was found expressed in 15.1% to 52.5% of DLBCLs at higher levels than in normal lymphoid tissues [21, 25-27, 39]. Truncated p63 homologous to Δ Np63 due to *TP63* gene rearrangements was also reported in 1.2%-5% of DLBCL, exclusive of GCB subtype [40, 41].

Conflicting results showing the effect of p63 expression on patients' prognosis have been reported [21, 27, 39, 42, 43], likely owing to small number of patients (fewer than 100) in each study, the use of different cutoffs for p63 positivity, the differential functions and complicated interactions of multiple p63 isoforms [23, 43].

To fill this knowledge gap, we studied the prognostic effects of p63 expression correlating with *TP53* status in a multicenter cohort of patients with well-characterized *de novo* DLBCL treated with R-CHOP. We found that p63 expression conferred better clinical outcomes in DLBCL which however could be compromised or abolished by the difference in International Prognostic Index (IPI) scores and/or the presence of *TP53* mutations. We further investigated p63-associated biology to understand possible underlying molecular mechanisms.

RESULTS

p63 expression in DLBCL

We observed nuclear expression of p63 at variable levels in tumor cells of 317 (61%) of 520 samples from patients in the training set and 180 (65%) of 275 samples from patients in the validation set. Representative immunohistochemical stains are shown in Fig 1A, B and the histograms of p63 expression by immunohistochemistry are shown in Fig 1C, D. The mean number of p63 positive tumor cells in the training set was 18%, which was significantly higher than that of WT-p53 ($P=0.017$) but significantly lower than that of mutated p53 (MUT-p53, $P<0.0001$, Fig 1E) (Supplemental Fig 1A, B) [37, 38], although the *TP63* mRNA levels were significantly lower than the *TP53*

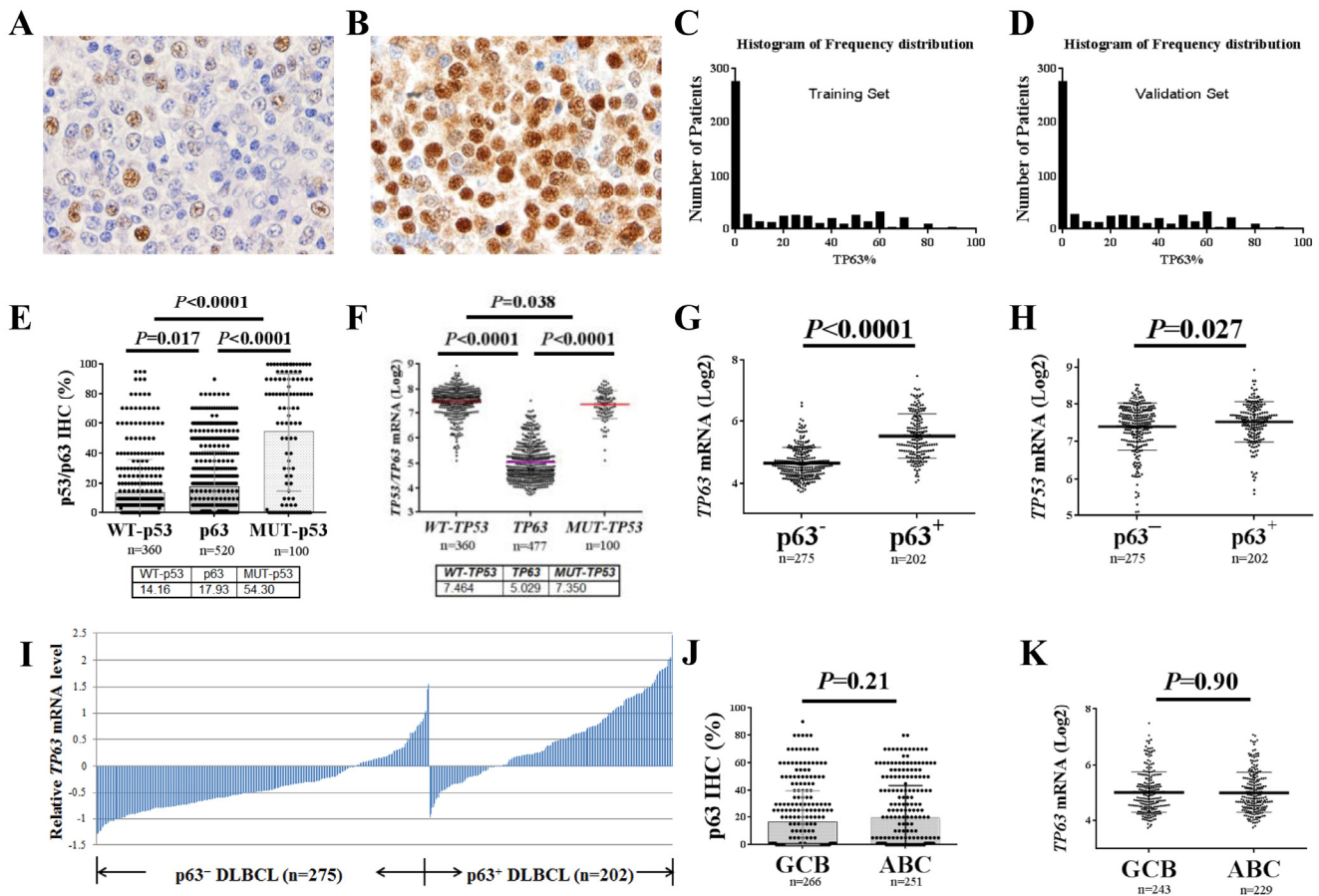


Figure 1. p63 expression in diffuse large B-cell lymphoma (DLBCL) in comparison with p53 expression. (A-B) Representative immunohistochemistry staining for p63 (10% and 95%) in DLBCL. **(C-D)** Histograms of p63 expression in the training and validation sets. **(E)** Comparisons between p63 and p53 expression levels in DLBCL. **(F)** Comparisons between *TP63* and *TP53* mRNA levels in DLBCL. **(G)** $p63^+$ DLBCL had significantly higher levels of *TP63* mRNA compared with $p63^-$ DLBCL. **(H)** $p63^+$ DLBCL had significantly higher *TP53* mRNA levels compared with $p63^-$ DLBCL. **(I)** Expression of p63 protein correlated with *TP63* mRNA levels. The *TP63* mRNA expression levels (Log2 values) were retrieved from the gene expression profiling data. The mean values of 3 probe-sets (1555581_a_at, 207382_at, 209863_s_at) for each patient were used. The relative mRNA level refers to the difference between the *TP63* mRNA level for each patient and the mean *TP63* mRNA level for the entire cohort. **(J-K)** Comparisons of p63 protein and *TP63* mRNA expression levels between germinal center B-cell-like (GCB) and activated B-cell-like (ABC) subtypes of DLBCL patients.

mRNA levels ($P < 0.0001$, Fig 1F). p63 protein expression significantly correlated with *TP63* mRNA (Spearman rank correlation: $r = 0.596$, $P < 0.0001$).

Owing to the significantly lower level of p63 compared with MUT-p53 expression in DLBCL and the exclusion of potential false-positive cases, we used a cutoff value of 5% of tumor cells being p63-positive for p63 expression in DLBCL ($p63^+$: $>5\%$). Using this cutoff, 221 patients (42.5%) in the training set, and 130 (47%) of 275 patients in the validation set had $p63^+$ DLBCL. The $p63^+$ group showed a significantly higher mean *TP63* mRNA level compared with the $p63^-$ group (unpaired *t* test, $P < 0.0001$, Fig 1G) and *TP53* mRNA level (Fig 1H). Transcriptional activation appeared to be the most common mechanism for p63 expression in this study of DLBCL (Fig 1I). No significant difference in the expression levels of p63/*TP63* was observed between the GCB and ABC subtypes of tumor samples, either at the protein (16.66% vs. 19.26%, $P = 0.21$) or mRNA ($P = 0.90$) levels (Fig 1J, K).

Clinical and pathobiological features of $p63^+$ DLBCL

We compared the clinicopathologic features of patients with $p63^+$ and $p63^-$ DLBCL. The $p63^+$ group more often had male ($P = 0.0056$) and patients with small (< 5 cm) tumors ($P = 0.05$) than did the $p63^-$ group. In addition, a higher proportion (41.9%) of $p63^+$ patients had an IPI score > 2 compared with $p63^-$ patients (34.4%), but this difference was not significant ($P = 0.086$); however, by unpaired *t* test, patients with IPI scores > 2 showed significantly higher mean levels of p63 ($P = 0.05$, Fig 2A) and MUT-p53 ($P = 0.011$, figure not shown) than did patients with IPI scores ≤ 2 . When DLBCL cases were stratified into the GCB and ABC subtypes, in GCB-DLBCL $p63^+$ compared with $p63^-$ patients was associated with IPI scores > 2 , small tumors, and possibly stage III/IV disease ($P = 0.06$), whereas in ABC-DLBCL $p63^+$ patients had higher percentages of male gender and extranodal DLBCL (44% compared with the 31% in $p63^-$ ABC-DLBCL) (Table 1). In contrast, WT-p53 overexpression was more common in nodal DLBCL (data not shown).

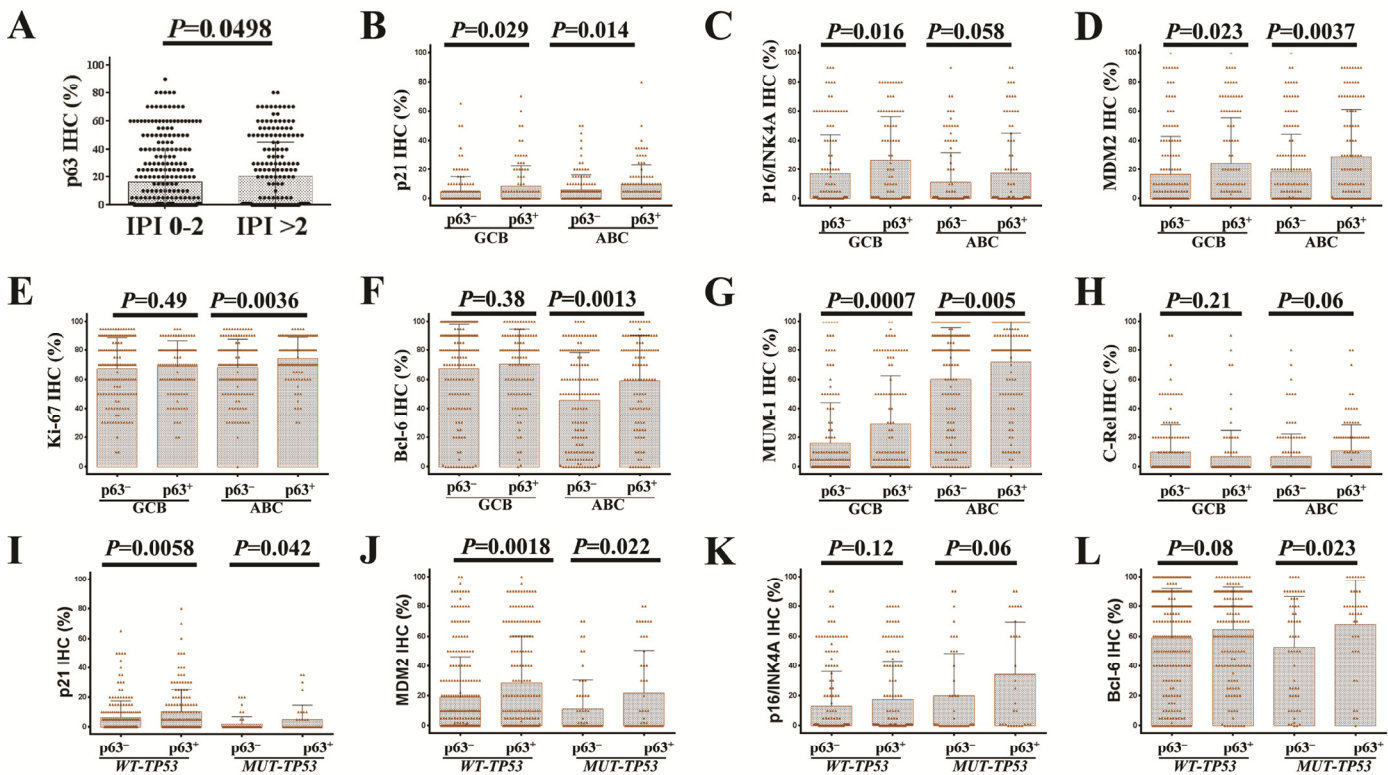


Figure 2. Correlations between p63 expression and other tumor associated factors. (A) The group with high International Prognostic Index (IPI) scores had a significantly higher mean level of p63 expression. (B-D) p63 expression was associated with significantly higher levels of p21, MDM2, and p16-INK4a in both germinal center B-cell like (GCB) and activated B-cell like (ABC) subtypes of DLBCL patients. (E-F) p63 expression was associated with significantly higher levels Ki-67 and Bcl-6 in ABC-DLBCL. (G) p63 expression was associated with significantly higher levels of IRF4/MUM-1 in both GCB and ABC subtypes of DLBCL patients. (H) $p63^+$ ABC-DLBCL was associated with a trend toward higher c-Rel level. (I-J) The association of p63 expression with p21 and MDM2 is independent of p53 mutation status. (K-L) p53 mutation status did not impact the association with increased p16-INK4a, Bcl-6 and IRF4/MUM-1 (figure not shown) levels.

Table 1. Clinical characteristics of patients with *de novo* DLBCL in the training cohort

	DLBCL			GCB-DLBCL			ABC-DLBCL			<i>P</i> 3	<i>P</i> 4
	p63 ⁺	p63 ⁻	<i>P</i> 1	p63 ⁺	p63 ⁻	<i>P</i> 2	p63 ⁺	p63 ⁻			
	N (%)	N (%)		N (%)	N (%)		N (%)	N (%)			
Patients	221	299		110	156		110	141	.59		
Age (yr)											
< 60	92 (42)	133 (45)	.52	52 (47)	84 (54)	.29	39 (35)	47 (33)	.73	.075	
≥ 60	129 (58)	166 (55)		58 (53)	72 (46)		71 (65)	94 (67)			
Sex											
Female	76 (34)	139 (46)	.0056	41 (37)	68 (44)	.30	34 (31)	70 (50)	.0028	.32	
Male	145 (66)	160 (54)		69 (63)	88 (56)		76 (69)	71 (50)			
Stage											
I-II	94 (44)	141 (49)	.30	50 (48)	89 (59)	.06	44 (41)	51 (37)	.54	.34	
III-IV	119 (56)	148 (51)		55 (52)	61 (41)		63 (59)	86 (63)			
B symptoms											
No	136 (63)	183 (65)	.63	73 (67)	101 (70)	.67	62 (58)	81 (60)	.76	.17	
Yes	79 (37)	97 (35)		35 (32)	43 (30)		44 (42)	53 (40)			
Serum LDH											
Normal	79 (39)	107 (39)	.97	42 (42)	56 (39)	.70	37 (36)	51 (39)	.71	.40	
Elevated	124 (61)	169 (61)		58 (58)	86 (61)		65 (64)	81 (61)			
No. of extranodal sites											
0-1	156 (75)	228 (79)	.27	79 (78)	121 (81)	.56	76 (71)	106 (77)	.30	.23	
≥ 2	53 (25)	61 (21)		22 (22)	28 (19)		31 (29)	32 (23)			
Performance status											
0-1	164 (85)	225 (83)	.66	78 (85)	119 (86)	.76	85 (84)	104 (79)	.35	.90	
≥ 2	30 (15)	46 (17)		14 (15)	19 (14)		16 (16)	27 (21)			
Size of largest tumor											
< 5cm	106 (65)	120 (55)	.05	56 (70)	62 (55)	.04	49 (59)	58 (54)	.51	.14	
≥ 5cm	58 (35)	99 (45)		24 (30)	50 (45)		34 (41)	49 (46)			
IPI score											
0-2	125 (58)	189 (66)	.086	65 (61)	111 (75)	.025	59 (55)	76 (56)	.90	.32	
3-5	90 (42)	99 (34)		41 (39)	38 (25)		49 (45)	61 (44)			
Therapy response											
CR	178 (81)	227 (76)	.21	87 (79)	118 (76)	.51	90 (82)	104 (74)	.13	.61	
PR	24	43		13	19		11	24			
SD	8	13		6	7		2	6			
PD	11	16		4	12		7	7			
Primary origin											
Nodal	131 (60)	193 (66)	.16	69 (64)	97 (64)	1.0	62 (56)	95 (69)	.048	.27	
Extranodal	88 (40)	99 (34)		39 (36)	55 (36)		48 (44)	43 (31)			
Ki-67											
< 70%	66 (30)	119 (40)	.0016	41 (37)	64 (42)	.45	24 (22)	55 (39)	.004	.018	
≥ 70%	155 (70)	175 (60)		69 (63)	88 (58)		86 (78)	86 (61)			
TP53 mutations											
WT-TP53	154 (80)	206 (77)	.65	70 (74)	105 (76)	.76	83 (85)	100 (79)	.38	.059	
MUT-TP53	40 (21)	60 (23)		25 (26)	34 (24)		15 (15)	26 (21)			
MYC translocation											
No	138 (89)	158 (88)	.86	62 (89)	73 (80)	.20	75 (89)	85 (95)	.15	1	
Yes	17 (11)	22 (12)		8 (11)	18 (20)		9 (11)	4 (5)			
BCL2 translocation											
No	159 (84)	187 (81)	.44	68 (74)	74 (64)	.18	90 (94)	113 (97)	.31	.0002	
Yes	30 (16)	44 (19)		24 (26)	41 (36)		6 (6)	3 (3)			
BCL6 translocation											
No	98 (60)	145 (74)	.0041	54 (69)	83 (78)	.16	43 (51)	61 (69)	.0016	.016	
Yes	66 (40)	51 (26)		24 (31)	23 (22)		42 (49)	28 (31)			
REL gains											
Normal	140 (86)	216 (92)	.068	62 (77)	118 (92)	.003	77 (94)	98 (92)	.036	.0001	
Amplification/ polysomy	23 (14)	19 (8)		18 (23)	10 (8)		5 (6)	9 (8)			
REL amplification											
No	156 (95)	227 (97)	.60	72 (91)	121 (95)	.40	83 (99)	106 (99)	1.0	.03	
Yes	8 (5)	8 (3)		7 (9)	7 (5)		1 (1)	1 (1)			
CD30 expression											
-	175 (79)	259 (88)	.0048	86 (78)	133 (88)	.06	88 (80)	125 (89)	.049	.87	
+	46 (21)	34 (12)		24 (22)	19 (12)		22 (20)	15 (11)			
p53 expression											
< 20%	116 (61)	172 (66)	.27	57 (61)	89 (66)	.40	59 (62)	83 (66)	.48	1.0	
≥ 20%	74 (39)	87 (34)		37 (39)	45 (34)		37 (38)	42 (34)			

Abbreviations: DLBCL, diffuse large B-cell lymphoma; GCB, germinal center B-cell-like; ABC, activated B-cell-like; LDH, lactate dehydrogenase; IPI, International Prognostic Index; CR, complete remission; PR, partial response; SD, stable disease; PD, progressive disease.

Note: *P* values indicate the significance of differences in the positivity frequencies of listed parameters between 2 groups. *P*1 values are for comparisons between overall p63⁺ and p63⁻ DLBCL patients; *P*2 values are for comparisons between p63⁺ and p63⁻ GCB-DLBCL patients; *P*3 values are for comparisons between p63⁺ and p63⁻ ABC-DLBCL patients; *P*4 values are for comparisons between p63⁺ GCB-DLBCL and p63⁺ ABC-DLBCL patients. For therapy response, we calculated *P* values by comparing CR to other responses.

When correlating p63 expression with other genetic abnormalities and immunohistochemical biomarkers in DLBCL, we found that the p63⁺ group had higher frequencies of *BCL6* translocation and CD30 positivity (21% compared with the 12% in p63⁻ patients) (Table 1), as well as elevated expression levels of Bcl-6, IRF4/MUM-1, p21, MDM2, p16-INK4a, and Ki-67 (in ABC-DLBCL only); most of these associations were independent of *TP53* mutation status (Fig 2B-L). In addition, p63 expression was associated with *REL* gains (including amplification and polysomies) in both the GCB and ABC subsets. No significant differences in frequencies of *TP53* mutations, *MYC* or *BCL2* translocations, or the expression levels of p53, Myc, or Bcl-2, were observed between the p63⁺ and p63⁻ groups.

p63 expression confers better clinical outcomes, more apparently in high-risk DLBCL and ABC-DLBCL

Univariate survival analysis in the training set

With a median follow-up of 62 months, p63⁺ DLBCL patients showed better progression-free survival (PFS, $P=0.05$) compared with p63⁻ DLBCL patients (Fig 3a, b). When patients with low-risk (IPI score ≤ 2) and high-risk DLBCL (IPI score >2) were analyzed separately (Fig 3c, d), p63 expression showed prognostic significance only in the high-risk group and correlated with significantly better overall survival (OS) ($P=0.006$) and PFS ($P=0.0043$).

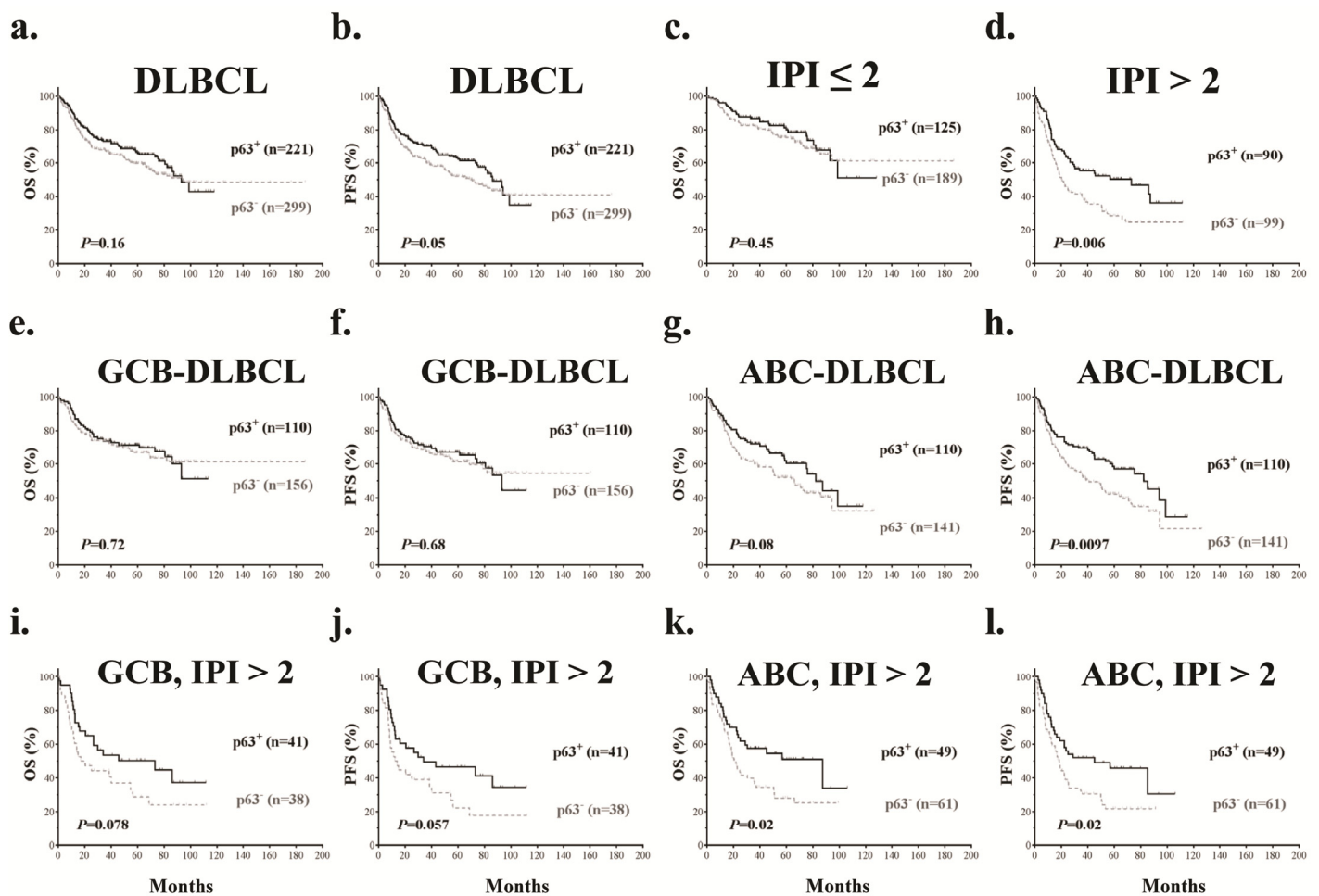


Figure 3. Prognostic analysis of p63 expression in DLBCL. (a-b) p63 expression correlated with significantly better progression-free survival (PFS) but not overall survival (OS) in DLBCL. (c-d) p63 expression correlated with significantly better overall survival in DLBCL patients with IPI scores > 2 but not in DLBCL patients with IPI scores ≤ 2 . (e-h) p63 expression correlated with significantly better PFS in ABC- but not GCB-DLBCL patients. (i-j) p63 expression was associated with trends towards better survival outcomes in GCB-DLBCL patients with IPI scores > 2 . (k-l) p63 expression correlated with significantly better survival outcomes in ABC-DLBCL patients with IPI scores > 2 .

Table 2. Multivariate survival analysis

Variable	OS			PFS		
	HR	95% CI	P	HR	95% CI	P
Overall DLBCL						
IPI >2	3.08	2.21-4.38	< .0001	2.84	2.08-3.89	< .0001
p63 ⁺	.62	.45- .87	.006	.66	.48- .90	.009
Female sex	.86	.62-1.20	.37	.92	.67-1.26	.60
Tumor size ≥5 cm	1.30	.94-1.79	.11	1.26	.93-1.70	.14
B symptoms present	1.32	.95-1.85	.10	1.24	.90-1.71	.18
GCB-DLBCL						
IPI >2	4.00	2.36-6.79	< .0001	3.44	2.27-5.21	< .0001
p63 ⁺	.64	.41- .99	.045	.67	.42-1.09	.11
Female sex	.94	.61-1.45	.78	1.00	.67-1.50	.99
Tumor size ≥5 cm	1.53	.92-2.54	.10	1.46	.92-2.34	.11
B symptoms present	1.08	.69-1.70	.74	1.21	.74-1.98	.44
ABC-DLBCL						
IPI >2	2.35	1.61-3.43	< .0001	2.23	1.57-3.16	< .0001
p63 ⁺	.56	.38- .83	.004	.58	.40- .83	.003
Female sex	.77	.52-1.15	.20	.78	.54-1.12	.17
Tumor size ≥5 cm	1.03	.58-1.56	.88	.99	.66-1.47	.94
B symptoms present	1.06	.72-1.58	.76	1.14	.79-1.64	.49
DLBCL with WT-TP53						
IPI >2	3.29	2.21-4.88	< .0001	3.21	2.18-4.72	< .0001
p63 ⁺	.61	.40- .91	.015	.63	.43- .92	.016
p53 ⁺	.97	.62-1.52	.90	.91	.60-1.40	.68
Female sex	.91	.61-1.36	.65	.85	.57-1.26	.42
Tumor size ≥5 cm	1.19	.81-1.76	.38	1.11	.76-1.62	.59
B symptoms present	1.45	.97-2.17	.07	1.48	1.00-2.20	.049
DLBCL with MUT-TP53						
IPI >2	2.43	1.17-5.05	.017	2.11	1.07-4.18	.032
p63 ⁺	.70	.34-1.44	.33	.72	.36-1.44	.36
p53 ⁺	3.16	1.17-8.52	.023	2.30	.97-5.45	.06
Female sex	1.02	.50-2.11	.96	1.12	.57-2.20	.75
Tumor size ≥5 cm	1.57	.77-3.20	.21	1.85	.95-3.63	.07
B symptoms present	1.19	.54-2.60	.67	1.03	.49-2.17	.93

Abbreviations: DLBCL, diffuse large B-cell lymphoma; ABC, activated B-cell-like; OS, overall survival; PFS, progression-free survival; HR, hazard ratio; CI, confidence interval; IPI, International Prognostic Index.

When analyzed in GCB- and ABC-DLBCL subsets separately, patients with p63⁺ ABC-DLBCL showed significantly better PFS ($P=0.0097$) and a trend of better OS ($P=0.08$) compared with p63⁻ ABC-DLBCL patients. In contrast, in GCB-DLBCL, p63 expression did not show significant impact on OS or PFS (Fig 3e-h). Consistently, survival analysis based on *TP63* mRNA levels showed that *TP63* mRNA expression correlated with favorable OS and significantly better PFS in ABC-DLBCL patients only ($P=0.06$ and $P=0.036$ respectively, Supplemental Fig S1D-G).

Since the p63⁺ GCB-DLBCL group had a higher portion of patients with high-risk DLBCL (Table 1) which may have confounded the analysis [44], patients with low-risk and high-risk DLBCL were analyzed separately. In GCB-DLBCL patients with IPI scores >2, p63⁺ GCB-DLBCL patients showed trends of better OS and PFS ($P=0.078$ and $P=0.057$ respectively) (Fig 3i-j). Similarly, the prognostic impact of p63 expression in ABC-DLBCL patients was more apparent in those with IPI scores >2 (Fig 3k-l); For ABC-DLBCL patients with IPI scores ≤ 2, OS and PFS rates were higher for p63⁺

patients but not the differences were not significant ($P=0.48$ and $P=0.12$ respectively).

Multivariate survival analysis

We performed multivariate survival analysis for p63 expression adjusting clinical parameters including IPI score, sex, tumor size and B symptoms. p63 expression was found to be an independent prognostic factor for better OS in the overall DLBCL, GCB-DLBCL and ABC-DLBCL sets, and an independent prognostic factor for better PFS in the overall DLBCL and ABC-DLBCL sets but not in the GCB-DLBCL set (Table 2).

Validation set

Similar to the training set, no significant difference was observed in p63 expression between the GCB and ABC subtypes ($P=0.68$). These similar prognostic impacts as in the training set were all significant with a $\geq 5\%$ cutoff value for p63 expression ($P=0.02$, $P=0.047$, and $P=0.0007$ for PFS in DLBCL, ABC-DLBCL and high-risk DLBCL respectively. Supplemental Fig S2). A multivariate survival analysis indicated that after adjusting clinical parameters, p63 expression $\geq 5\%$ was an independent favorable prognostic factor in overall DLBCL and ABC-DLBCL but not in GCB-DLBCL (data not shown).

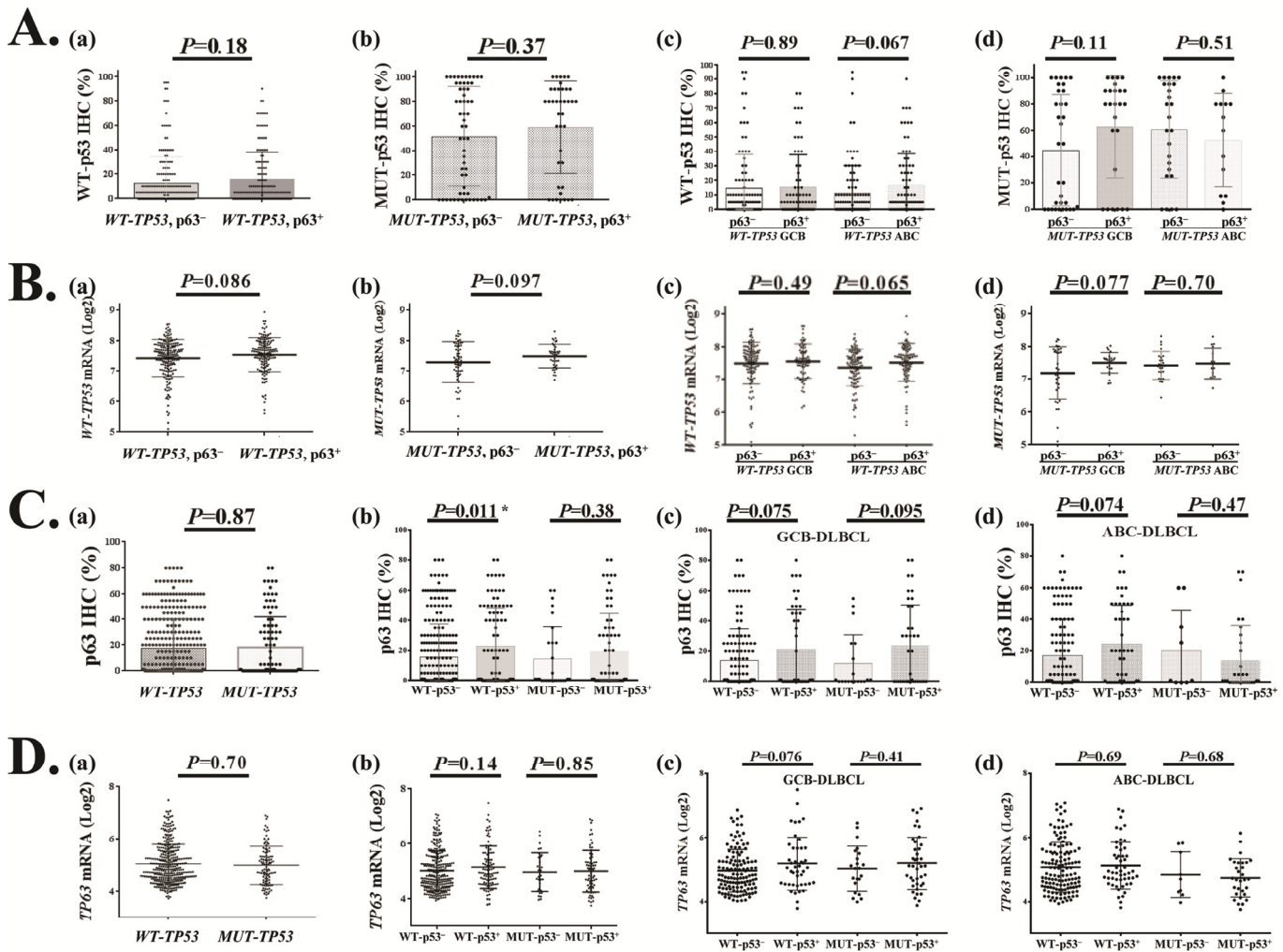


Figure 4. Relationship between TP63/p63 and TP53/p53 expression in DLBCL. (A) Comparison of wild-type (WT) or mutated (MUT) p53 protein expression between p63⁺ and p63⁻ patients with DLBCL or GCB/ABC subtypes of DLBCL. (B) Comparison of TP53 mRNA expression between p63⁺ and p63⁻ patients with WT-TP53 or MUT-TP53 and GCB/ABC DLBCL. (C) Comparison of p63 protein expression between WT-TP53 and MUT-TP53 DLBCL, and between p53⁺ and p53⁻ patients with DLBCL or GCB/ABC subtypes of DLBCL. (D) Comparison of TP63 mRNA expression between WT-TP53 and MUT-TP53 DLBCL, and between p53⁺ and p53⁻ patients with DLBCL or GCB/ABC subtypes of DLBCL.

Relationships with *TP53* mutations and p53 expression

Non-significant correlation with p53 expression and correlation with *TP53* mRNA

By Spearman rank correlation *TP63* mRNA showed correlation with *TP53* mRNA levels in the overall DLBCL set ($r=0.091$, $P=0.048$) and *WT-TP53* subset ($r=0.106$, $P=0.044$) but not in the *MUT-TP53* subset. In contrast, p63 expression did not show significant correlation with overall p53 ($r=0.071$, $P=0.132$), *WT-p53* ($r=0.08$, $P=0.135$), or *MUT-p53* ($r=0.072$, $P=0.481$). Using unpaired *t*-tests, p63 expression did not correlate with p53 levels (Supplemental Fig S1C), but was associated with elevated *TP53* mRNA levels (Fig 1H). Analysis in GCB/ABC DLBCL subsets with *WT-*

p53 or *MUT-p53* showed no significant correlations between p63 positivity and *WT-p53*/*MUT-p53* expression levels (Table 1, Fig 4A, B). However, the *WT-p53*⁺ ($\geq 20\%$ [38]) compared with the *WT-p53*⁻ DLBCL group had a significantly higher mean level of p63 protein (Fig 4C(b)) but not *TP63* mRNA (Fig 4D).

Prognostic impact of p63 expression in the presence of *WT-TP53* or *MUT-TP53*

The clinicopathologic features of patients with p63⁺ or p63⁻ DLBCL with *WT-TP53* or *MUT-TP53* are shown in Table 3. p63 expression was associated with significantly better OS and PFS in patients with *WT-TP53* and IPI scores >2 (Fig 5A, B) and in ABC-DLBCL patients with *WT-TP53* (Fig 5C, D), and favorable trends in patients with *MUT-p53*⁺ GCB-DLBCL (Fig 5G, H).

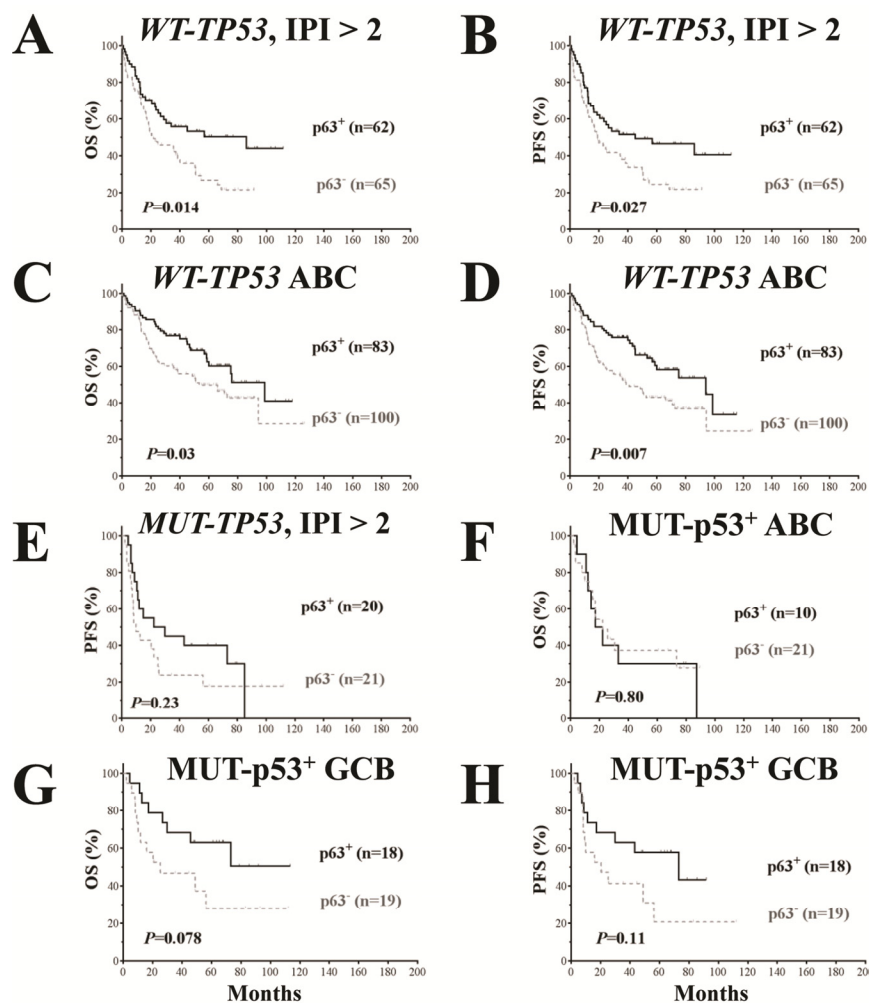


Figure 5. Prognostic analysis for p63 expression in DLBCL patients with wild-type and mutated *TP53*. (A-B) p63 expression correlated with significantly better survival outcomes in patients with high-risk (IPI > 2) DLBCL and *WT-TP53*. (C-D) p63 expression correlated with significantly better survival outcomes in patients with ABC-DLBCL and *WT-TP53*. (E) In patients with high-risk (IPI > 2) DLBCL and *MUT-TP53*, p63 expression did not correlate with survival outcomes although showed a trend toward better PFS. (F) p63 expression did not correlate with survival outcomes in patients with ABC-DLBCL and *MUT-p53* overexpression. (G-H) p63 expression was associated with trends toward better survival outcomes in GCB-DLBCL patients with *MUT-p53* overexpression (marginal *P* values).

Table 3. Clinical characteristics of DLBCL patients with wild-type *TP53* (WT-*TP53*) or mutated *TP53* (MUT-*TP53*)

Characteristic	WT- <i>TP53</i>		<i>P</i>	MUT- <i>TP53</i>		<i>P</i>
	p63 ⁺ N (%)	p63 ⁻ N (%)		p63 ⁺ N (%)	p63 ⁻ N (%)	
Patients	154	206		40	60	
Age (y)						
< 60	62 (40)	87 (42)	.75	16 (40)	25 (42)	1.0
≥ 60	92 (60)	119 (58)		24 (60)	35 (58)	
Gender						
Male	106 (69)	107 (52)	.0013	24 (60)	36 (60)	1.0
Female	48 (31)	99 (48)		16 (40)	24 (40)	
Stage						
I-II	62 (42)	97 (49)	.21	17 (43)	28 (47)	.68
III-IV	84 (58)	100 (51)		23 (58)	32 (53)	
B symptoms						
No	100 (67)	196 (66)	.92	23 (59)	38 (68)	.37
Yes	50 (33)	65 (34)		16 (41)	18 (32)	
LDH						
Normal	58 (41)	82 (44)	.66	12 (32)	19 (33)	.93
Elevated	82 (59)	105 (56)		25 (68)	38 (67)	
No. of extranodal sites						
0-1	105 (73)	155 (78)	.30	29 (74)	46 (78)	.68
≥ 2	38 (27)	43 (22)		10 (26)	13 (22)	
Performance status						
0-1	117 (87)	231 (85)	.62	30 (88)	50 (86)	.78
≥ 2	18 (13)	28 (15)		4 (12)	8 (14)	
Size of largest tumor						
< 5cm	81 (68)	90 (58)	.079	18 (58)	23 (48)	.38
≥ 5cm	38 (32)	66 (42)		13 (42)	25 (52)	
IPI risk group						
0-2	87 (58)	132 (67)	.10	19 (49)	38 (64)	.12
3-5	62 (42)	65 (33)		20 (51)	21 (36)	
Therapy response						
CR	126 (82)	163 (79)	.59	27 (68)	35 (58)	.40
PR	16	24		7	13	
SD	3	7		3	3	
PD	9	12		3	9	
Ki-67						
< 70%	50 (33)	83 (41)	.10	9 (22)	17 (29)	.64
≥ 70%	104 (67)	119 (59)		31 (78)	42 (71)	
Primary origin						
Nodal	91 (40)	134 (66)	.21	25 (37)	39 (70)	.54
Extranodal	61 (60)	68 (66)		15 (63)	17 (30)	
DLBCL subtypes						
GCB	70 (46)	105 (51)	.34	25 (62)	34 (57)	.68
ABC	83 (54)	100 (49)		15 (38)	26 (43)	
<i>BCL6</i> translocation						
-	73 (63)	97 (70)	.21	17(57)	35 (85)	.007
+	43 (37)	41 (30)		13(43)	6 (15)	
CD30						
-	120 (78)	178 (89)	.0085	32 (80)	54 (92)	.13
+	34 (22)	23 (11)		8 (20)	5 (8.5)	
p53 expression						
< 20%	106 (70)	154 (77)	.18	10 (26)	18 (31)	.65
≥ 20%	45 (30)	47 (23)		29 (74)	40 (69)	

Abbreviations: DLBCL, diffuse large B-cell lymphoma; R-CHOP, rituximab with cyclophosphamide, doxorubicin, vincristine, and prednisone; LDH, lactate dehydrogenase; IPI, international prognostic index; CR, complete remission; PR, partial response; SD, stable disease; PD, progressive disease; GCB, germinal center B-cell-like; ABC, activated B-cell-like.

Table 4. Genes differentially expressed between patients with p63⁺ and p63⁻ DLBCL

Function categories	p63 ⁺ DLBCL FDR < 0.20		p63 ⁺ DLBCL with <i>MUT-TP53</i> FDR < 0.05, fold change > 1.68		p63 ⁺ ABC-DLBCL with <i>WT-TP53</i> FDR < 0.20	
	Upregulated	Downregulated	Upregulated	Downregulated	Upregulated	Downregulated
Signaling, immune response, inflammation	<i>FLJ23834</i> , <i>TRAF1</i>	<i>SGPP1</i>			<i>FOXD1</i> , <i>PDE7A</i>	<i>GABRR2</i> , <i>MS4A2</i> , <i>COMMD5</i>
Development, differentiation	<i>SOX4</i> , <i>FOXC1</i>			<i>ZNF141</i> , <i>BACH2</i>	<i>SOX4</i> , <i>EPHA4</i>	
Cell growth and proliferation, gene expression, metabolism	<i>H2AFB1/2/3</i>	<i>MSI2</i> , <i>TBC1D1</i> , <i>ZNF652</i> , <i>TOR1AIP1</i> , <i>ZMYM2</i>		<i>STRBP</i> , <i>CDC2L5</i> , <i>DDX18</i> , <i>MSI2</i> , <i>ZNF439</i> , <i>ZNF91</i> , <i>ZNF226</i> , <i>MTMR2</i>	<i>MEF2C</i> , <i>DCN</i> , <i>CCND2</i> , <i>KDM2B</i> , <i>RPS15</i> , <i>NFYB</i> , <i>DDX3Y</i> , <i>FOXD1</i> , <i>UTY</i>	
Apoptosis, cell death, DNA damage response	<i>TP63</i> , <i>BCL2L1</i> , <i>ZAK</i> , <i>RFFL</i> , <i>ATG4B</i> , <i>MKL1</i> , <i>HIPK2</i>	<i>C13orf15</i>	<i>TP63</i>		<i>TP63</i> , <i>MKL1</i>	
Protein folding, protein translocation, heat shock	<i>PPIL6</i>	<i>HSF2</i> , <i>SEC62</i>				
Transport, mobility, cell adhesion	<i>KCNMA1</i> , <i>ATP2B1</i> , <i>KIF21A</i> , <i>ANKH</i> , <i>TRPM4</i>	<i>VAMP1</i>		<i>ITGB1</i> , <i>CXCR4</i>	<i>ECM2</i> , <i>RHOBTB3</i>	
lncRNA and other unknown function	<i>COBLL1</i> , <i>NCRNA00173</i>	<i>C17orf58</i> , <i>C8orf6</i>		<i>SETD5</i> , <i>SLMO2</i>	<i>DNAJC5B</i> , <i>TMEM57</i> , <i>ANUBL1</i> , <i>IQCK</i>	<i>C10orf53</i>

Abbreviations: DLBCL, diffuse large B-cell lymphoma; FDR, false discovery rate; lncRNA, long noncoding RNA.

Multivariate survival analysis

We further performed multivariate survival analysis including p63 expression, p53 overexpression, and clinical parameters in the *WT-TP53* and *MUT-TP53* subsets individually. In the *WT-TP53* subset, p63 expression but not WT-p53 overexpression remained as an independent prognostic factor for better OS and PFS; in the *MUT-TP53* subset, MUT-p53 overexpression but not p63 expression was an independent prognostic factor for poorer PFS (borderline *P* value for OS) (Table 2).

Gene expression profiling signature of p63 expression

To gain insights into the potential molecular mechanisms underlying the prognostic observation, we performed a series of GEP analyses comparing p63⁺ and

p63⁻ patients in the overall DLBCL group and various subsets stratified by GCB/ABC subtype, *TP53* mutation and p53 overexpression status (Fig 6A-H, Supplemental Fig S3A-D). Counts of significant differentially expressed genes (DEGs) between compared groups with different false discovery rate (FDR) thresholds are listed in Supplemental Table S1. Largely, whether p63 expression was associated with distinct GEP signatures did not correlated with whether p63 showed apparent prognostic effects, and the GEP signature of p63 expression in the *MUT-TP53* subset was much more prominent (Fig 6B, Table 4) than that in the *WT-TP53* subset (7 genes only with a FDR threshold of 0.30, figure not shown). However, after dividing the *WT-TP53* subset into GCB and ABC subtypes of DLBCL patients, p63 expression showed GEP signatures, more distinctive in ABC than in GCB (Fig 6C, Supplemental Fig S3A), which was opposite to the pattern for overall

ABC and GCB (only few DEGs in ABC compared to the distinct GEP signature in GCB, Supplemental Table S1). The p63 GEP signatures in the *MUT-TP53* and *WT-TP53* subsets had both similarity (upregulated *ATP2A2* and downregulated *ZNF652*) and difference (three genes, *GABBR2*, *PDHAI1* and *NFYB*, showed opposite up- or down-regulation). Reinforcing the idea that p63 GEP signatures are more highlighted in the absence of WT-p53 activities as shown in the *MUT-TP53* subset, we further found that in WT-p53⁻ ABC-DLBCL but not in WT-p53⁺ ABC-DLBCL, p63 expression was associated with significant DEGs (Supplemental Fig S3B, Supplemental Table S3).

To gain insights into the functional relationship between p53 and p63, we further analyzed the overlap and difference between the p53 [37, 38] and p63 GEP signatures. The results (Table 5) suggest p63 expression

had a WT-p53-like GEP signature either in the context of *WT-TP53* (such as *CTAG2*, *SOX4* and *ELL2*, accounting for approximately 21% of the DEGs between *WT-TP53/p63*⁺ and *WT-TP53/p63*⁻) or *MUT-TP53* (such as *DSE*, *ATM*, *CDK13*, *CD47*, *ELF1*, *DYRK1A* [45], *PFDN4*, and *TMEM97*, accounting for approximately 4% of the DEGs between *MUT-TP53/p63*⁺ and *MUT-TP53/p63*⁻), yet remained some *MUT-p53*-like GEP signature mainly in the context of *MUT-TP53* (such as *CAMTA1* resembling the *MUT-p53* GEP signature, and *ABHD11*, *KCNN3*, *MART3*, and *MRPL30* opposite to the *WT-p53* GEP signature; accounting for approximately 1.4% of the DEGs between *MUT-TP53/p63*⁺ and *MUT-TP53/p63*⁻). Moreover, only in the p63⁺ but not in the p63⁻ subset, expression of WT-p53 or *MUT-p53* was associated with distinct GEP signatures (Fig 6G, H), which may suggest that p63 is important for p53 activities.

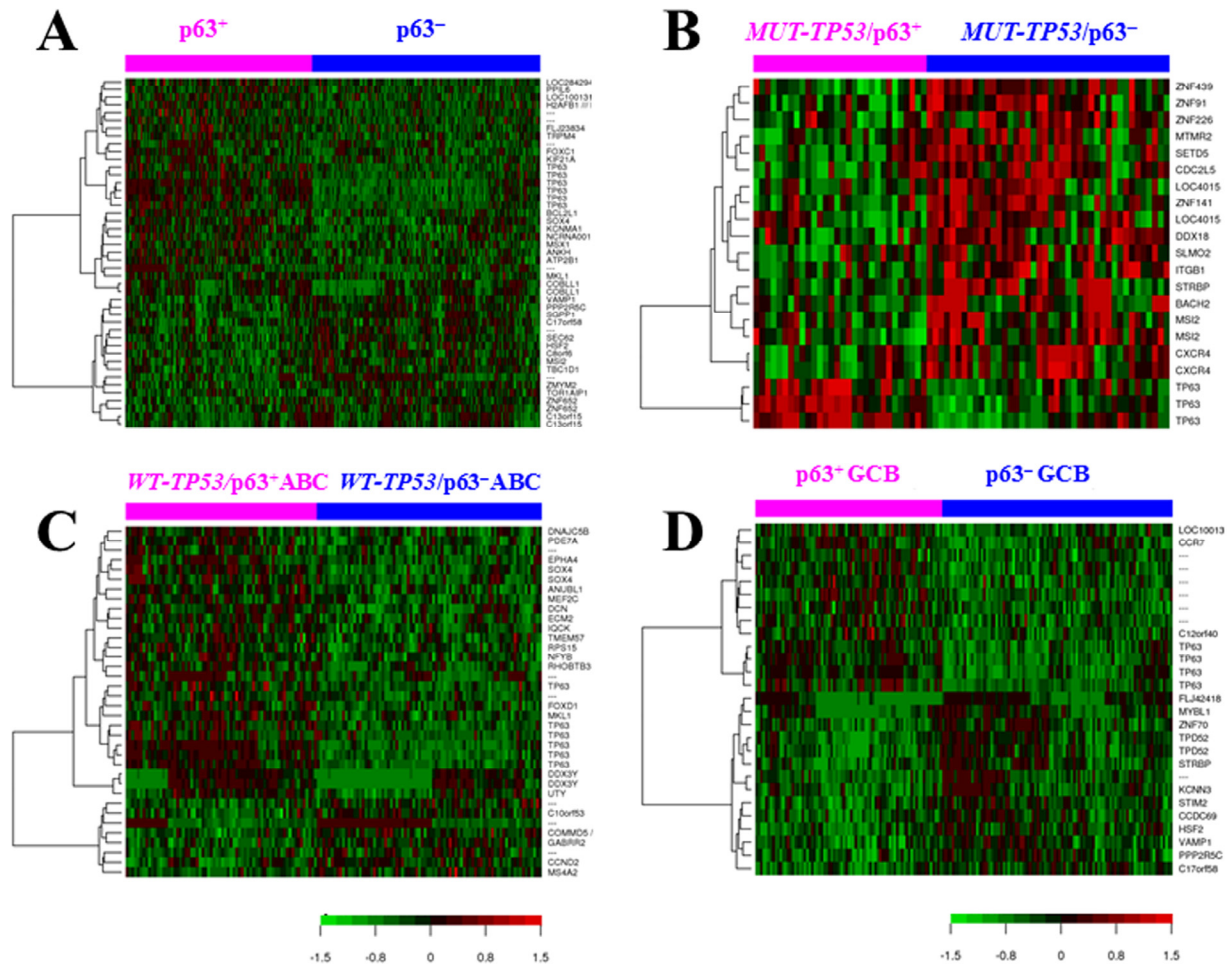


Figure 6. Gene expression profiling analysis. (A) Heatmap for comparison between p63⁺ and p63⁻ DLBCL patients (false discovery rate < 0.15). (B) Heatmap for comparison between p63⁺ and p63⁻ DLBCL patients with *MUT-TP53* (false discovery rate < 0.05, fold change >1.68). (C) Heatmap for comparison between p63⁺ versus p63⁻ patients with ABC-DLBCL and *WT-TP53* (false discovery rate < 0.20). (D) Heatmap for comparison between p63⁺ versus p63⁻ patients with GCB-DLBCL (false discovery rate < 0.05).

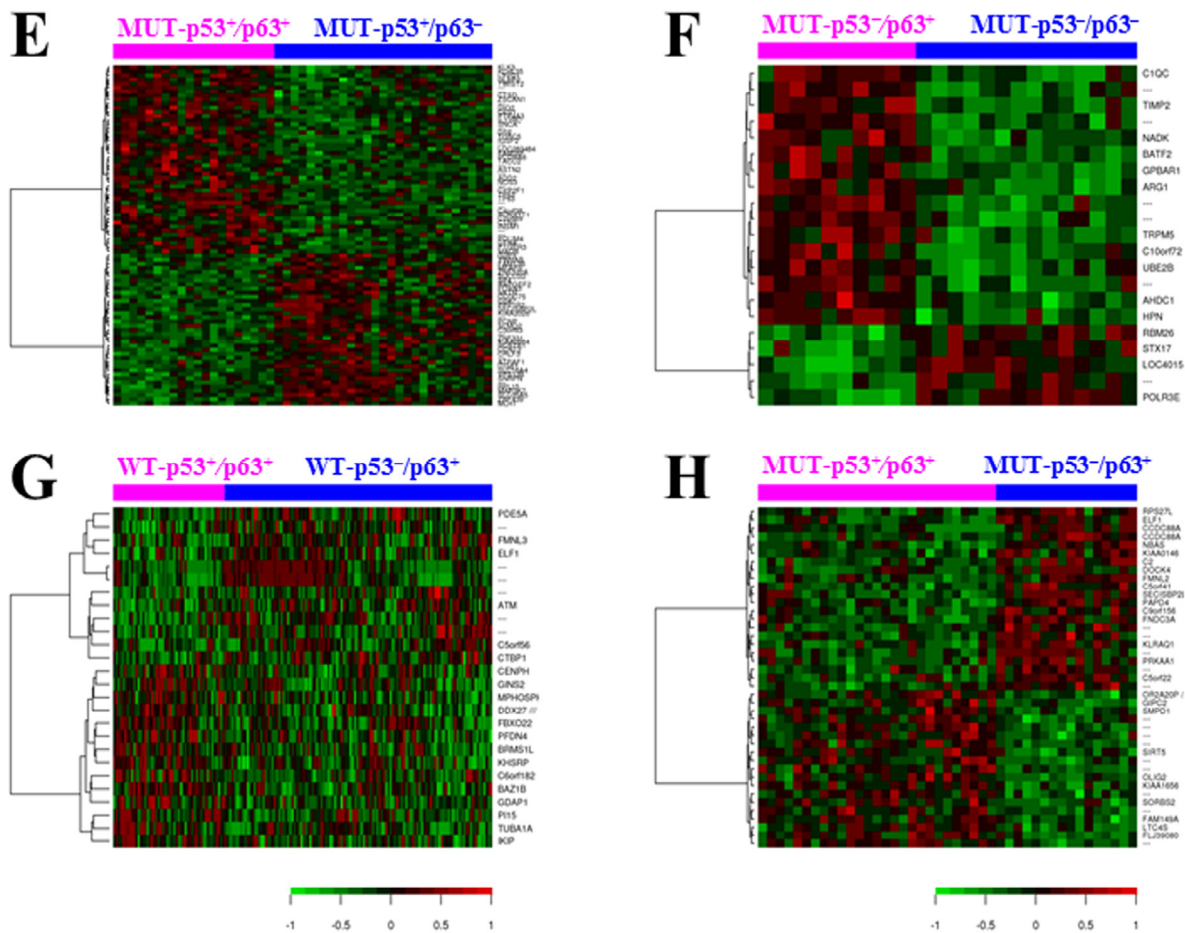


Figure 6. Gene expression profiling analysis. (E) Heatmap for comparison between $p63^+$ and $p63^-$ DLBCL patients with MUT-p53 overexpression (false discovery rate < 0.15). (F) Heatmap for comparison between $p63^+$ and $p63^-$ DLBCL patients with no or low (< 20%) expression levels of MUT-p53 (false discovery rate < 0.10). (G) Heatmap for comparison between WT-p53⁺ ($\geq 20\%$) and WT-p53⁻ (< 20%) DLBCL patients with p63 expression (false discovery rate < 0.30). (H) Heatmap for comparison between MUT-p53⁺ ($\geq 20\%$) and MUT-p53⁻ (< 20%) DLBCL patients with p63 expression (false discovery rate < 0.20).

We also compared the p63 GEP signature with the MDM2 GEP signature [38], and found 21 DEGs were common between the GEP signatures of p63 and MDM2 expression, among which 16 DEGs were not shared by the p53 GEP signature (Table 5).

Although the p53 and p63 GEP signatures overlapped, majority of the DEGs were not shared. Nonetheless, a p53-like tumor suppressor role of p63 was suggested by the p63 GEP signatures, including downregulation of *CCND2* (in WT-TP53/p63⁺ ABC-DLBCL), *CDC27* and *MYCT1* (in WT-TP53/p63⁺ GCB-DLBCL), *CDC2L5/CDK13* and *CXCR4* (in MUT-TP53/p63⁺ DLBCL). TP53 mutations were associated with increased CXCR4 levels especially in GCB-DLBCL as previously reported

[46]), *ELF1* which encodes a transcription factor that activates *LYN* and *BLK* (in MUT-TP53/p63⁺ GCB-DLBCL), *MYBL1* and *STRBP* which play roles in proliferation and growth (in MUT-TP53/p63⁺ GCB-DLBCL), antiapoptotic *C9orf82* and *BCOR* (which encodes an interacting corepressor of BCL6 required for germinal center formation and may influence apoptosis) (in MUT-TP53/p63⁺ ABC-DLBCL), as well as upregulation of *HIPK2* (which promotes apoptosis through the activation of p53/TP53) (in p63⁺ DLBCL) and *WWOX* (which functions synergistically with p53/TP53 to control genotoxic stress-induced cell death) (in MUT-TP53/p63⁺ ABC-DLBCL) (Supplemental Fig S3C-D).

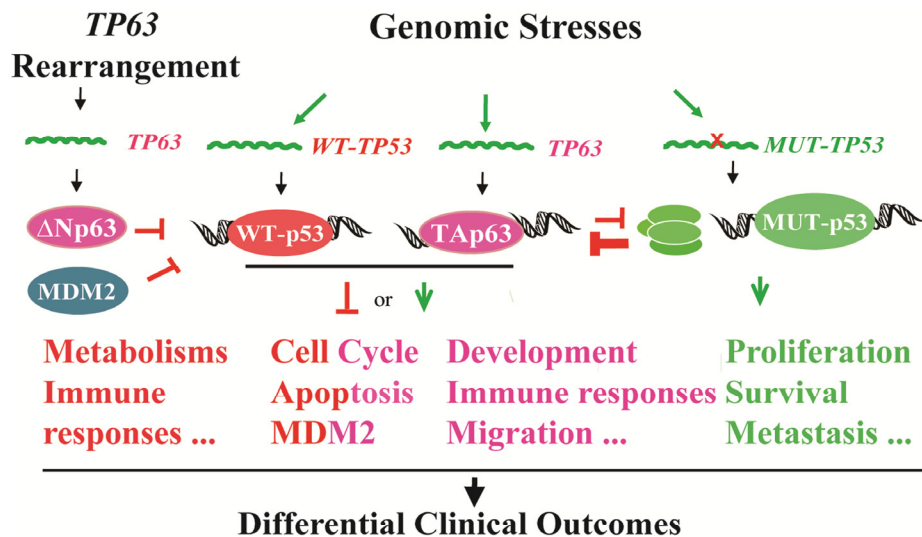
Table 5 Lists of differentially expressed genes between p63⁺ and p63⁻ DLBCL that are also in the p53 signatures and MDM2 signatures

Common genes shared by the p63 ⁺ and p53 ⁺ signatures						
<i>WT-TP53</i> WT-p53 ⁺ vs WT-p53 ⁻		<i>MUT-TP53</i> MUT-p53 ⁺ vs WT-p53 ⁻ <i>MUT-TP53</i> vs <i>WT-TP53</i>				
Same		Same				
Up ↑	<i>DSE</i>	↑ in <i>MUT-TP53/p63⁺</i> vs <i>MUT-TP53/p63⁻</i> ↑ in <i>MUT-p53⁺/p63⁺</i> vs <i>MUT-p53⁺/p63⁻</i>	<i>BCAS1</i>	↑ in p63 ⁺ GCB vs p63 ⁻ GCB		
	<i>ELL2</i>	↑ in <i>WT-TP53/p63⁺</i> vs <i>WT-TP53/p63⁻</i>				
	<i>FDXR</i>	↑ in <i>WT-p53⁻/p63⁺ ABC</i> vs <i>WT-p53⁻/p63⁻ ABC</i>				
	<i>GRRP1</i>	↑ in <i>MUT-TP53/p63⁺</i> vs <i>MUT-TP53/p63⁻</i>				
	<i>HPGD</i>	↑ in <i>MUT-TP53/p63⁺</i> vs <i>MUT-TP53/p63⁻</i>				
	<i>PFDN4</i>	↑ in <i>MUT-TP53/p63⁺</i> vs <i>MUT-TP53/p63⁻</i>				
	<i>SOX4</i>	↑ in p63 ⁺ vs p63 ⁻ ↑ in <i>WT-TP53/p63⁺</i> vs <i>WT-TP53/p63⁻</i> ↑ in <i>WT-p53⁻/p63⁺ ABC</i> vs <i>WT-p53⁻/p63⁻ ABC</i>				
	Down ↓	<i>ATM</i>		↓ in <i>MUT-TP53/p63⁺</i> vs <i>MUT-TP53/p63⁻</i>	<i>CAMTA1</i>	↓ in <i>MUT-TP53/p63⁺</i> vs <i>MUT-TP53/p63⁻</i> ↓ in <i>MUT-TP53/p63⁺ GCB</i> vs <i>MUT-TP53/p63⁻ GCB</i>
		<i>C3orf63</i>		↓ in <i>MUT-p53⁺/p63⁺</i> vs <i>MUT-p53⁺/p63⁻</i>		
		<i>CCDC69</i>		↓ in p63 ⁺ GCB vs p63 ⁻ GCB		
<i>CD47</i>		↓ in <i>MUT-p53⁺/p63⁺</i> vs <i>MUT-p53⁺/p63⁻</i>				
<i>CDC2L5/C</i>		↓ in <i>MUT-TP53/p63⁺</i> vs <i>MUT-TP53/p63⁻</i>				
<i>DK13</i>		↓ in <i>MUT-TP53/p63⁺ GCB</i> vs <i>MUT-TP53/p63⁻ GCB</i>				
<i>DCLRE1C</i>		↓ in <i>MUT-TP53/p63⁺</i> vs <i>MUT-TP53/p63⁻</i> ↓ in <i>MUT-TP53/p63⁺ GCB</i> vs <i>MUT-TP53/p63⁻ GCB</i>				
<i>DYRK1A</i>		↓ in <i>MUT-TP53/p63⁺</i> vs <i>MUT-TP53/p63⁻</i>				
<i>ELF1</i>		↓ in <i>MUT-TP53/p63⁺</i> vs <i>MUT-TP53/p63⁻</i> ↓ in <i>MUT-TP53/p63⁺ GCB</i> vs <i>MUT-TP53/p63⁻ GCB</i> ↓ in p63 ⁺ GCB vs p63 ⁻ GCB				
<i>ESR2</i>		↓ in p63 ⁺ GCB vs p63 ⁻ GCB				
<i>HCG18</i>		↓ in <i>WT-TP53/p63⁺</i> vs <i>WT-TP53/p63⁻</i>				
<i>HERC4</i>		↓ in <i>MUT-TP53/p63⁺</i> vs <i>MUT-TP53/p63⁻</i> ↓ in <i>MUT-TP53/p63⁺ GCB</i> vs <i>MUT-TP53/p63⁻ GCB</i>				
<i>ITCH</i>		↓ in <i>MUT-TP53/p63⁺</i> vs <i>MUT-TP53/p63⁻</i>				
<i>LOC645513</i>		↓ in <i>MUT-TP53/p63⁺</i> vs <i>MUT-TP53/p63⁻</i>				
<i>ORC4L</i>		↓ in <i>MUT-TP53/p63⁺</i> vs <i>MUT-TP53/p63⁻</i>				
<i>PPP1R2</i>		↓ in <i>MUT-TP53/p63⁺</i> vs <i>MUT-TP53/p63⁻</i>				
<i>TBC1D1</i>		↓ in p63 ⁺ vs p63 ⁻ ↓ in p63 ⁺ GCB vs p63 ⁻ GCB				
<i>PXK</i>		↓ in p63 ⁺ GCB vs p63 ⁻ GCB				
<i>TMCC1</i>		↓ in <i>MUT-TP53/p63⁺ ABC</i> vs <i>MUT-TP53/p63⁻ ABC</i>				
<i>ZCCHC7</i>		↓ in <i>MUT-TP53/p63⁺</i> vs <i>MUT-TP53/p63⁻</i>				
<i>ZNF221</i>	↓ in <i>WT-p53⁻/p63⁺ ABC</i> vs <i>WT-p53⁻/p63⁻ ABC</i>					
Opposite		Opposite				
Up ↑	<i>KCNN3</i>	↓ in p63 ⁺ GCB vs p63 ⁻ GCB	<i>CTAG2</i>	↓ in <i>WT-p53⁻/p63⁺ ABC</i> vs <i>WT-p53⁻/p63⁻ ABC</i>		
	<i>KIAA0564</i>	↓ in <i>MUT-TP53/p63⁺</i> vs <i>MUT-TP53/p63⁻</i> ↓ in <i>MUT-p53⁺/p63⁺</i> vs <i>MUT-p53⁺/p63⁻</i>		<i>TMEM97</i>	↓ in <i>MUT-TP53/p63⁺</i> vs <i>MUT-TP53/p63⁻</i>	
	<i>MATR3</i>	↓ in <i>MUT-TP53/p63⁺</i> vs <i>MUT-TP53/p63⁻</i>		<i>SLC16A1</i>	↓ in p63 ⁺ GCB vs p63 ⁻ GCB	
	<i>MRPL30</i>	↓ in <i>MUT-TP53/p63⁺</i> vs <i>MUT-TP53/p63⁻</i>				
Down ↓	<i>ABHD11</i>	↑ in <i>MUT-TP53/p63⁺ ABC</i> vs <i>MUT-TP53/p63⁻ ABC</i>				

Common genes shared by the p63 ⁺ and MDM2 ⁺ signatures				
<i>WT-TP53</i> MDM2 ⁺ vs MDM2 ⁻		<i>MUT-TP53</i> MDM2 ⁺ vs MDM2 ⁻		
Same		Same		
Up ↑	<i>FAM83A</i>	↑ in <i>MUT-TP53/p63</i> ⁺ ABC vs <i>MUT-TP53/p63</i> ⁻ ABC		
	<i>FDXR</i>	↑ in WT-p53 ⁻ /p63 ⁺ ABC vs WT-p53 ⁻ /p63 ⁻ ABC		
	<i>MICAL2</i>	↑ in <i>MUT-TP53/p63</i> ⁺ GCB vs <i>MUT-TP53/p63</i> ⁻ GCB		
Down ↓	<i>PCBP3</i>	↑ in <i>MUT-TP53/p63</i> ⁺ vs <i>MUT-TP53/p63</i> ⁻		
	<i>TCEB3</i>	↑ in p63 ⁺ vs p63 ⁻		
	<i>ATM</i>	↓ in <i>MUT-TP53/p63</i> ⁺ vs <i>MUT-TP53/p63</i> ⁻		
	<i>BPTF</i>	↓ in <i>MUT-TP53/p63</i> ⁺ vs <i>MUT-TP53/p63</i> ⁻	<i>ATG7</i>	↓ in p63 ⁺ GCB vs p63 ⁻ GCB
	<i>BRWD1</i>	↓ in p63 ⁺ GCB vs p63 ⁻ GCB	<i>ATP5C1</i>	↓ in <i>MUT-TP53/p63</i> ⁺ vs <i>MUT-TP53/p63</i> ⁻
	<i>CD22</i>	↓ in p63 ⁺ GCB vs p63 ⁻ GCB		↓ in <i>MUT-TP53/p63</i> ⁺ GCB vs <i>MUT-TP53/p63</i> ⁻ GCB
	<i>DHX36</i>	↓ in <i>MUT-TP53/p63</i> ⁺ vs <i>MUT-TP53/p63</i> ⁻	<i>EIF2A</i>	↓ in <i>MUT-TP53/p63</i> ⁺ vs <i>MUT-TP53/p63</i> ⁻
	<i>EIF2A</i>	↓ in <i>MUT-TP53/p63</i> ⁺ vs <i>MUT-TP53/p63</i> ⁻	<i>PAK2</i>	↓ in <i>MUT-TP53/p63</i> ⁺ vs <i>MUT-TP53/p63</i> ⁻
	<i>NKTR</i>	↓ in <i>MUT-TP53/p63</i> ⁺ vs <i>MUT-TP53/p63</i> ⁻	<i>PRICKLE4/TOMM6</i>	↓ in <i>MUT-TP53/p63</i> ⁺ ABC vs <i>MUT-TP53/p63</i> ⁻ ABC
		↓ in MUT-p53 ⁺ /p63 ⁺ vs MUT-p53 ⁺ /p63 ⁻		
		↓ in <i>MUT-TP53/p63</i> ⁺ GCB vs <i>MUT-TP53/p63</i> ⁻ GCB		
		↓ in <i>MUT-TP53/p63</i> ⁺ vs <i>MUT-TP53/p63</i> ⁻		
		↓ in MUT-p53 ⁻ /p63 ⁺ vs MUT-p53 ⁻ /p63 ⁻		
		↓ in <i>MUT-TP53/p63</i> ⁺ vs <i>MUT-TP53/p63</i> ⁻		
	↓ in <i>MUT-TP53/p63</i> ⁺ vs <i>MUT-TP53/p63</i> ⁻			
<i>WT-TP53</i> MDM2 ⁺ vs <i>MUT-TP53</i> MDM2 ⁺				
Same				
Down ↓	<i>LPP</i>	↓ in p63 ⁺ GCB vs p63 ⁻ GCB		

On the other hand, some DEGs promoting tumor cell survival were also shown in the comparison between overall p63⁺ and p63⁻ DLBCL patients, which may be due to the oncogenic function provided by MUT-p53 or p63 isoforms in the p63⁺ DLBCL subsets. For example, antiapoptotic *BCL2L1*, *RFFL* (which negatively regulates p53, CASP8 and CASP10 through proteasomal degradation), *ATG4B* (required for autophagy), and *MKLI* (which suppresses TNF-induced cell death by inhibiting caspase activation) were up-

regulated in p63⁺ DLBCL compared with p63⁻ DLBCL, whereas *C13orf15/RGCC* (in response to DNA damage) was downregulated in p63⁺ DLBCL patients (Table 4). Cytokine/receptor genes *IL17RC*, *IL4*, *IL4I1* and *IL8RB/CXCR2* which have been associated with poorer prognosis in cancers, were upregulated in *MUT-TP53/p63*⁺ compared with *MUT-TP53/p63*⁻ DLBCL (Supplemental Table S2); *MLL2* was upregulated in p63⁺ patients with ABC-DLBCL and *MUT-TP53* (Supplemental Fig S3D).



p63 (TAp63 mostly) expression has significant favorable impact on clinical outcomes of DLBCL, but the protective effect can be abolished by *TP53* mutations, or compounded by the presence of $\Delta Np63$ in some GCB-DLBCLs.

Figure 7. A hypothetical model illustrating the regulation and roles of p53 and p63 in DLBCL lymphomagenesis and clinical outcomes suggested by our clinical and biological data.

DISCUSSION

Abnormal p63 expression patterns instead of *TP63* mutations have been found to be important for tumorigenesis [5]. Little data are available with conflicting results regarding p63 expression and its prognostic role [27, 39, 43]. We found that p63 expression correlated with a superior survival in ABC-DLBCL with *WT-TP53* and in high-risk (IPI >2) DLBCL (regardless GCB or ABC), which is consistent with a previous study in high-intermediate and high risk DLBCL [27]. The association of p63 expression with high-risk IPI in GCB-DLBCL, and thus affecting its apparent prognostic effects in GCB and overall DLBCL, may contribute to the inconsistent findings from previous studies.

The prognostic effect of p63 expression suggests that p63 has a tumor suppressor role for DLBCL, although its protective effect can be antagonized or abolished by *TP53* mutations and high-risk DLBCL associated biology. In our cohort, p63 expression was associated with increased levels of IRF4/MUM-1, p21, MDM2, and p16-INK4a resembling that of WT-p53 yet independent of p53 mutation status. GEP analysis showed that compared to the prominent p63 GEP signature within the *MUT-TP53* subset, the comparison

between p63⁺ and p63⁻ patients with *WT-TP53* had much fewer DEGs; DEGs were shown within the WT-p53⁻ but not WT-p53⁺ ABC-DLBCL subset. These results may suggest that the tumor suppressor function of p63 may overlap with (and is probably weaker than) that of WT-p53, and when *TP53* was mutated, p63 functions as a supplemental tumor suppressor alternative to WT-p53. However, MUT-p53 function remained or dominated p63 function in certain *MUT-TP53* cases (Table 5), likely due to the significantly higher levels of MUT-p53 than p63 [47]. In addition to the GEP results as above, p63 expression correlated with *MDM2* upregulation and *BCL2* and *MDM4* downregulation ($P=0.0174$, $P=0.0487$ and $P=0.090$ respectively) resembling WT-p53 expression GEP signature (although the FDRs for the comparison between p63⁺ and p63⁻ DLBCL were higher). In contrast, *CDKN1A/p21*, *MCL1*, *B2M*, and *FYB* showed great variation even opposite up/down regulation between the WT-p53⁺ and the p63⁺ GEP signature. These phenomena may be explained by the remained MUT-p53-like function in the *MUT-TP53*/p63⁺ cases, whereas *TP63* mutations and expression of different p63 isoforms may not be significant factors as suggested by the previous studies [5, 25, 43] and our preliminary data of *TP63* mutations in DLBCL (unpublished data).

These observations in DLBCL may support previous functional studies, which showed that TAp63 α and TAp63 γ (but not Δ Np63) could induce apoptosis at lesser levels than WT-p53 [48]; TAp63, and also TAp73, together with p53, may transactivate a group of common target genes in response to DNA damage, including damage resulting from exposure to doxorubicin, a component of R-CHOP; ¹ TAp63 and MUT-p53 antagonize each other mainly in the regulation of metastasis and tumor dissemination [5]; p53 mutants may bind directly to p63 and inhibit the p63-mediated transcription of p53 target genes [49, 50]. Strategies to overcome MUT-p53 interaction with p63, decrease MUT-p53 levels and enhance p63 levels may have therapeutic value [47]. On the other hand, in mouse embryonic fibroblasts, p63 and p73 are required for p53-dependent apoptosis in response to DNA damage [7]. This may explain why our GEP comparisons between p53⁺ and p53⁻ DLBCL showed DEGs within the p63⁺ but not p63⁻ subset. Moreover, our data suggested that p63 act together with p53 in some essential pathways yet also function independently in many processes such as development, immune response and chemokinesis. Large variations between p63 signatures in the overall DLBCL patient population and in the GCB and ABC subsets may also imply a wide range of p63 activities. These characteristics of p63 function compared with p53, as well as association with high Ki-67 (consistent with previous studies [21, 43]) and high IPI may explain the limitation of p63's apparent prognostic effect in DLBCL.

It is also possible that the correlation between p63 expression and better survival outcomes may be also influenced by the escape from MDM2-mediated degradation. In our cohort, the p63's protective effects on patient survival were independent of MDM2 expression, yet GEP signatures were only shown in MDM2^{low} but not in MDM2^{high} subsets (data not shown), suggesting that MDM2 may suppress p63 function but the suppression is not significant to the p63's protective effect. Conversely, p63 may have confounded the MDM2's prognostic effect in DLBCL just as that of WT-p53 [38], suggested by the common genes shared by the MDM2 and p63 GEP signatures (Table 5). Previous studies have suggested that p63 degradation is independent of MDM2 [24, 31] and that MDM2 increases the protein level and transcriptional activity of p63 [51]. The MDM2 inhibitor p14ARF directly interacts with and impairs p63 transcriptional activity [52]. On the other hand, it has also been shown that MDM2 transports p63 out of nucleus and inhibits its transcription function [53].

Yang *et al.* speculated that p63 expression in cancer cells was due to *TP63* gene amplification by genomic

instability [3], and other researches showed that p63 expression was regulated via mRNA stability [4, 19]. *TP63* rearrangements have been reported in 1.2-5% of DLBCL (exclusive of GCB subtype) and also in 5.8% of peripheral T-cell lymphomas, which resulted in a truncated p63 protein lacking the TA domain [40, 41]. Our data showed the associations of p63 expression with *BCL6* (mapped to 3q27) translocations, which appears to suggest the possibility of concurrent translocation of *TP63* gene (mapped to 3q27-28) due to chromosomal proximity in p63⁺ DLBCL subsets. In these cases it is possible that expressed p63 had oncogenic function like Δ Np63, which may explain the oncogenic DEGs in the p63 GEP signatures, and the lack of p63's prognostic significance in GCB-DLBCL. In addition, genomic stress similar to that inducing p53 may also be the cause of p63 expression in subsets of p63⁺ DLBCL [54], since our data showed correlation between the *WT-TP53* and *TP63* mRNA levels, and both WT-p53 and p63 expression were associated with increased IRF4/MUM-1 and Ki-67 expression. Fig 7 illustrates these potential causes for p63 expression and possible relationships between p63 and WT-p53/MUT-p53 function. Understanding the mechanisms regulating *TP63* may lead to therapeutic strategies. In DLBCL cell lines, FOXP1, directly represses *TP63* and cooperate with NF- κ B signaling to promote lymphoma cell survival [42]. Consistently, our GEP data also suggest that molecules related to B-cell receptor signaling may be potential targets which suppresses p63 expression, as in GCB-DLBCL and *MUT-TP53/p63*⁺ DLBCL, p63 expression was associated with downregulation of *SYK* and *ELF1* respectively (suggesting decreased B-cell receptor signaling).

In conclusion, we demonstrated the correlation of p63 expression and better survival outcomes in patients with high-risk DLBCL, ABC-DLBCL with *WT-TP53*, and biology associated with p63 expression supporting p63's tumor suppressor role in DLBCL. This study helps identify a subgroup of patients with better prognosis among patients who have ABC-DLBCL or high-risk DLBCL. Targeting p63 expression and function may be a novel therapeutic strategy for particular subgroups of DLBCL patients.

MATERIALS AND METHODS

Patients. A total of 795 patients with *de novo* DLBCL from 20 medical centers treated with R-CHOP were studied, randomly divided into a training set (n=520) and a validation set (n=275). The diagnostic criteria, selection process, therapy, and treatment response have been described previously [37]. The study was approved as being of minimal or no risk or as exempt by the

institution review boards of all participating medical centers.

Immunohistochemistry. Tissue microarrays prepared from the diagnostic formalin-fixed, paraffin-embedded (FFPE) tissue blocks of all patients studied were stained with an anti-p63 antibody (4A4, Santa Cruz Biotechnology, Santa Cruz, CA) which can detect all p63 isoforms. Expression levels of p63 were determined by estimating the percentage of p63-positive tumor cells in the tissue array cores. X-tile software and receiver operating characteristic curve analysis by GraphPad Prism 6 Software were used to determine the percentage of p63-positive cells with maximal discriminatory power for the separation of DLBCL patients into 2 different prognostic groups. Evaluation of other biomarkers by immunohistochemistry was also performed on tissue microarrays using corresponding antibodies: p53 (DO-7, Dako, Carpinteria, CA), MDM2 (IF2, Calbiochem, Billerica, MA), p21 (Dako), Bcl-2 (Clone-124, Dako, Carpinteria, CA), Ki-67 (Dako), CD30 (clone BerH2, Dako), Bcl-6 (Dako), FOXP1 (Abcam), IRF4/MUM1 (Dako), CD10 (56C6, Vantana), c-Rel (Dako), and CXCR4 (Abcam, San Francisco, CA). Details of immunohistochemistry procedures and scoring processes have been described previously [38, 44, 55-58].

***TP53* and *TP63* sequencing, fluorescence *in situ* hybridization.** Genomic DNA samples were extracted from FFPE tissues, and the *TP53* coding region and splice site sequence were determined for 460 patients in the training set using a p53 AmpliChip (Roche Molecular Systems, Pleasanton, CA) as described previously [37]. *TP63* coding region sequence was analyzed by Sanger sequencing method. *MYC*, *BCL2*, *BCL6*, and *REL* gene arrangements and copy number aberrations were detected by fluorescence *in situ* hybridization [56, 59, 60].

Gene expression profiling. Gene expression profiling was performed on Affymetrix GeneChips HG-U133 Plus Version 2.0 (Affymetrix, Santa Clara, CA) using total RNAs as described previously [37, 55]. The CEL files are deposited in the National Center for Biotechnology Information Gene Expression Omnibus repository (GSE#31312). The microarray data were quantified and normalized by the frozen robust multiarray analysis (RMA) algorithm. The differentially expressed genes were identified by using multiple *t*-tests.

Statistical analysis. The clinical and pathologic features at the time of presentation were compared between various DLBCL subgroups by using the chi-square test and unpaired *t* test. Correlation between expression of different genes or proteins was evaluated by Spearman

rank correlation. Overall survival (OS) was calculated from the date of diagnosis to the date of last follow-up or death. Progression-free survival (PFS) was calculated from the date of diagnosis to the date of disease progression or death. OS and PFS curves of the various groups were analyzed by GraphPad Prism 6 software using the Kaplan-Meier method, and differences were compared with use of the log-rank (Cox-Mantel) test. Multivariate analysis was conducted by using the Cox proportional hazards regression model with the SPSS software version 19.0 (IBM, Armonk, NY). Any difference with a *P* value of < 0.05 was considered statistically significant.

Authorship

Contribution: Z.Y.X-M, S.Z., and K.H.Y designed and conducted the research and performed the statistical analysis; Z.Y.X-M, S.Z., X.L., G.C.M., X.W., Y.X., C.V., A.T., S.M.M., K.D., A.C., A.O., Y.Z., G.B., K.L.R., E.D.H., W.W.L.C., J.H.K., J.H., M.P., A.J.M.F., X.Z., M.B.M., F.B., B.M.P., M.A.P., J.N.W., L.J.M., and K.H.Y. contributed vital new reagents, resources, technology, and analytical tools; Z.Y.X-M, S.Z., C.V., A.T., S.M.M., K.D., A.C., A.O., Y.Z., G.B., K.L.R., E.D.H., W.W.L.C., J.H.K., J.H., M.P., A.J.M.F., X.Z., M.B.M., F.B., B.M.P., M.A.P., J.N.W., and K.H.Y. collected clinical and follow-up data under approval by the Institutional Review Boards and the material transfer agreement; Z.Y.X-M, S.Z., L.J.M., and K.H.Y. wrote and edited the manuscript; and all authors contributed vital strategies, participated in discussions, and provided scientific input.

Funding

This study was supported by the National Cancer Institute/National Institutes of Health (R01CA138688 and 1RC1CA146299 to K.H.Y.). K.H.Y. is supported by The University of Texas MD Anderson Cancer Center Lymphoma Moonshot Program, Institutional Research and Development Fund, an Institutional Research Grant Award, an MD Anderson Cancer Center Lymphoma Specialized Programs on Research Excellence (SPORE) Research Development Program Award, an MD Anderson Cancer Center Myeloma SPORE Research Development Program Award, and partially supported by the National Cancer Institute/National Institutes of Health (P50CA136411 and P50CA142509). G.M. is supported by a grant from the Michael and Susan Dell Foundation. Z.Y.X-M is the recipient of the Shannon Timmins Leukemia Fellowship and the Harold C. and Mary L. Daily Endowment Fellowships Award at The University of Texas MD Anderson Cancer Center.

Conflict of interest statement

KHY receives research support from Roche Molecular System, Gilead Sciences Pharmaceutical, Seattle Genetics, Dai Sanyo Pharmaceutical, Adaptive Biotechnology, Incyte Pharmaceutical, and HTG Molecular Diagnostics.

REFERENCES

1. Su X, Chakravarti D and Flores ER. p63 steps into the limelight: crucial roles in the suppression of tumorigenesis and metastasis. *Nat Rev Cancer*. 2013; 13:136-143.
2. Yang A and McKeon F. P63 and P73: P53 mimics, menaces and more. *Nat Rev Mol Cell Biol*. 2000; 1:199-207.
3. Yang A, Kaghad M, Wang Y, Gillett E, Fleming MD, Dotsch V, Andrews NC, Caput D and McKeon F. p63, a p53 homolog at 3q27-29, encodes multiple products with transactivating, death-inducing, and dominant-negative activities. *Molecular cell*. 1998; 2:305-316.
4. Cho SJ, Jung YS and Chen X. Poly (C)-binding protein 1 regulates p63 expression through mRNA stability. *PLoS one*. 2013; 8:e71724.
5. Pflaum J, Schlosser S and Muller M. p53 Family and Cellular Stress Responses in Cancer. *Front Oncol*. 2014; 4:285.
6. Levine AJ, Tomasini R, McKeon FD, Mak TW and Melino G. The p53 family: guardians of maternal reproduction. *Nat Rev Mol Cell Biol*. 2011; 12:259-265.
7. Flores ER, Tsai KY, Crowley D, Sengupta S, Yang A, McKeon F and Jacks T. p63 and p73 are required for p53-dependent apoptosis in response to DNA damage. *Nature*. 2002; 416:560-564.
8. Venkatanarayan A, Raulji P, Norton W, Chakravarti D, Coarfa C, Su X, Sandur SK, Ramirez MS, Lee J, Kingsley CV, Sananikone EF, Rajapakshe K, Naff K, et al. IAPP-driven metabolic reprogramming induces regression of p53-deficient tumours in vivo. *Nature*. 2015; 517:626-630.
9. Mills AA, Zheng B, Wang XJ, Vogel H, Roop DR and Bradley A. p63 is a p53 homologue required for limb and epidermal morphogenesis. *Nature*. 1999; 398:708-713.
10. Suh EK, Yang A, Kettenbach A, Bamberger C, Michaelis AH, Zhu Z, Elvin JA, Bronson RT, Crum CP and McKeon F. p63 protects the female germ line during meiotic arrest. *Nature*. 2006; 444:624-628.
11. Yang A, Schweitzer R, Sun D, Kaghad M, Walker N, Bronson RT, Tabin C, Sharpe A, Caput D, Crum C and McKeon F. p63 is essential for regenerative proliferation in limb, craniofacial and epithelial development. *Nature*. 1999; 398:714-718.
12. Sun R, Zhang Y, Lv Q, Liu B, Jin M, Zhang W, He Q, Deng M, Liu X, Li G, Li Y, Zhou G, Xie P, et al. Toll-like receptor 3 (TLR3) induces apoptosis via death receptors and mitochondria by up-regulating the transactivating p63 isoform alpha (TAP63alpha). *J Biol Chem*. 2011; 286:15918-15928.
13. Levrero M, De Laurenzi V, Costanza A, Gong J, Wang JY and Melino G. The p53/p63/p73 family of transcription factors: overlapping and distinct functions. *J Cell Sci*. 2000; 113:1661-1670.
14. Dohn M, Zhang S and Chen X. p63alpha and DeltaNp63alpha can induce cell cycle arrest and apoptosis and differentially regulate p53 target genes. *Oncogene*. 2001; 20:3193-3205.
15. Perez-Losada J, Wu D, DelRosario R, Balmain A and Mao JH. p63 and p73 do not contribute to p53-mediated lymphoma suppressor activity in vivo. *Oncogene*. 2005; 24:5521-5524.
16. Chakrabarti R, Wei Y, Hwang J, Hang X, Andres Blanco M, Choudhury A, Tiede B, Romano RA, DeCoste C, Mercatali L, Ibrahim T, Amadori D, Kannan N, et al. DeltaNp63 promotes stem cell activity in mammary gland development and basal-like breast cancer by enhancing Fzd7 expression and Wnt signalling. *Nat Cell Biol*. 2014; 16:1004-1015, 1001-1013.
17. Su X, Chakravarti D, Cho MS, Liu L, Gi YJ, Lin YL, Leung ML, El-Naggar A, Creighton CJ, Suraokar MB, Wistuba I and Flores ER. TAP63 suppresses metastasis through coordinate regulation of Dicer and miRNAs. *Nature*. 2010; 467:986-990.
18. Guo X, Keyes WM, Papazoglu C, Zuber J, Li W, Lowe SW, Vogel H and Mills AA. TAP63 induces senescence and suppresses tumorigenesis in vivo. *Nat Cell Biol*. 2009; 11:1451-1457.
19. Xu E, Zhang J, Zhang M, Jiang Y, Cho SJ and Chen X. RNA-binding protein RBM24 regulates p63 expression via mRNA stability. *Mol Cancer Res*. 2014; 12:359-369.
20. Truong AB, Kretz M, Ridky TW, Kimmel R and Khavari PA. p63 regulates proliferation and differentiation of developmentally mature keratinocytes. *Genes Dev*. 2006; 20:3185-3197.
21. Hedvat CV, Teruya-Feldstein J, Puig P, Capodici P, Dudas M, Pica N, Qin J, Cordon-Cardo C and Di Como CJ. Expression of p63 in diffuse large B-cell lymphoma. *Appl Immunohistochem Mol Morphol*. 2005; 13:237-242.
22. Danilova N, Sakamoto KM and Lin S. p53 family in development. *Mech Dev*. 2008; 125:919-931.
23. Wolff S, Talos F, Palacios G, Beyer U, Dobbelsstein M and Moll UM. The alpha/beta carboxy-terminal domains of p63 are required for skin and limb development. New insights from the Brdm2 mouse which is not a complete p63 knockout but expresses p63 gamma-like proteins. *Cell Death Differ*. 2009; 16:1108-1117.
24. Okada Y, Osada M, Kurata S, Sato S, Aisaki K, Kageyama Y, Kihara K, Ikawa Y and Katoh I. p53 gene family p51(p63)-encoded, secondary transactivator p51B(TAP63alpha) occurs without forming an immunoprecipitable complex with MDM2, but responds to genotoxic stress by accumulation. *Exp Cell Res*. 2002; 276:194-200.
25. Di Como CJ, Urist MJ, Babayan I, Drobnjak M, Hedvat CV, Teruya-Feldstein J, Pohar K, Hoos A and Cordon-Cardo C. p63 expression profiles in human normal and tumor tissues. *Clin Cancer Res*. 2002; 8:494-501.
26. Nylander K, Vojtesek B, Nenutil R, Lindgren B, Roos G, Zhanxiang W, Sjoström B, Dahlqvist A and Coates PJ. Differential expression of p63 isoforms in normal tissues and neoplastic cells. *J Pathol*. 2002; 198:417-427.
27. Hallack Neto AE, Siqueira SA, Dulley FL, Ruiz MA, Chamone DA and Pereira J. p63 protein expression in high risk diffuse large B-cell lymphoma. *J Clin Pathol*. 2009; 62:77-79.
28. Alexandrova EM and Moll UM. Role of p53 family members p73 and p63 in human hematological malignancies. *Leuk Lymphoma*. 2012; 53:2116-2129.
29. Aubry MC, Roden A, Murphy SJ, Vasmatzis G, Johnson SH, Harris FR, Halling G, Knudson RA, Ketterling RP and Feldman AL. Chromosomal rearrangements and copy number abnormalities of TP63 correlate with p63 protein expression in lung adenocarcinoma. *Mod Pathol*. 2015; 28:359-366.
30. Gedert H, Kiel S, Heep HJ, Gabbert HE and Sarbia M. The role of p63 and deltaNp63 (p40) protein expression and gene

- amplification in esophageal carcinogenesis. *Hum Pathol.* 2003; 34:850-856.
31. Ying H, Chang DL, Zheng H, McKeon F and Xiao ZX. DNA-binding and transactivation activities are essential for Tap63 protein degradation. *Mol Cell Biol.* 2005; 25:6154-6164.
32. Lo Muzio L, Santarelli A, Caltabiano R, Rubini C, Pieramici T, Trevisiol L, Carinci F, Leonardi R, De Lillo A, Lanzafame S, Bufo P and Piattelli A. p63 overexpression associates with poor prognosis in head and neck squamous cell carcinoma. *Hum Pathol.* 2005; 36:187-194.
33. Stetsenko GY, Malekirad J, Paulson KG, Iyer JG, Thibodeau RM, Nagase K, Schmidt M, Storer BE, Argenyi ZB and Nghiem P. p63 expression in Merkel cell carcinoma predicts poorer survival yet may have limited clinical utility. *Am J Clin Pathol.* 2013; 140:838-844.
34. Takahashi Y, Noguchi T, Takeno S, Kimura Y, Okubo M and Kawahara K. Reduced expression of p63 has prognostic implications for patients with esophageal squamous cell carcinoma. *Oncol Rep.* 2006; 15:323-328.
35. Alizadeh AA, Eisen MB, Davis RE, Ma C, Lossos IS, Rosenwald A, Boldrick JC, Sabet H, Tran T, Yu X, Powell JJ, Yang L, Marti GE, et al. Distinct types of diffuse large B-cell lymphoma identified by gene expression profiling. *Nature.* 2000; 403:503-511.
36. Testoni M, Zucca E, Young KH and Bertoni F. Genetic lesions in diffuse large B-cell lymphomas. *Ann Oncol.* 2015. 26:1069-1080
37. Xu-Monette ZY, Wu L, Visco C, Tai YC, Tzankov A, Liu WM, Montes-Moreno S, Dybkaer K, Chiu A, Orazi A, Zu Y, Bhagat G, Richards KL, et al. Mutational profile and prognostic significance of TP53 in diffuse large B-cell lymphoma patients treated with R-CHOP: report from an International DLBCL Rituximab-CHOP Consortium Program Study. *Blood.* 2012; 120:3986-3996.
38. Xu-Monette ZY, Moller MB, Tzankov A, Montes-Moreno S, Hu W, Manyam GC, Kristensen L, Fan L, Visco C, Dybkaer K, Chiu A, Tam W, Zu Y, et al. MDM2 phenotypic and genotypic profiling, respective to TP53 genetic status, in diffuse large B-cell lymphoma patients treated with rituximab-CHOP immunochemotherapy: a report from the International DLBCL Rituximab-CHOP Consortium Program. *Blood.* 2013; 122:2630-2640.
39. Park CK and Oh YH. Expression of p63 in reactive hyperplasias and malignant lymphomas. *J Korean Med Sci.* 2005; 20:752-758.
40. Vasmataz G, Johnson SH, Knudson RA, Ketterling RP, Braggio E, Fonseca R, Viswanatha DS, Law ME, Kip NS, Ozsan N, Grebe SK, Frederick LA, Eckloff BW, et al. Genome-wide analysis reveals recurrent structural abnormalities of TP63 and other p53-related genes in peripheral T-cell lymphomas. *Blood.* 2012; 120:2280-2289.
41. Scott DW, Mungall KL, Ben-Neriah S, Rogic S, Morin RD, Slack GW, Tan KL, Chan FC, Lim RS, Connors JM, Marra MA, Mungall AJ, Steidl C, et al. TBL1XR1/TP63: a novel recurrent gene fusion in B-cell non-Hodgkin lymphoma. *Blood.* 2012; 119:4949-4952.
42. van Keimpema M, Gruneberg LJ, Mokry M, van Boxtel R, Koster J, Coffey PJ, Pals ST and Spaargaren M. FOXP1 directly represses transcription of proapoptotic genes and cooperates with NF-kappaB to promote survival of human B cells. *Blood.* 2014; 124:3431-3440.
43. Fukushima N, Satoh T, Sueoka N, Sato A, Ide M, Hisatomi T, Kuwahara N, Tomimasu R, Tsuneyoshi N, Funai N, Sano M, Tokunaga O and Sueoka E. Clinico-pathological characteristics of p63 expression in B-cell lymphoma. *Cancer Sci.* 2006; 97:1050-1055.
44. Hu S, Xu-Monette ZY, Tzankov A, Green T, Wu L, Balasubramanyam A, Liu WM, Visco C, Li Y, Miranda RN, Montes-Moreno S, Dybkaer K, Chiu A, et al. MYC/BCL2 protein coexpression contributes to the inferior survival of activated B-cell subtype of diffuse large B-cell lymphoma and demonstrates high-risk gene expression signatures: a report from The International DLBCL Rituximab-CHOP Consortium Program. *Blood.* 2013; 121:4021-4031; quiz 4250.
45. Zhang Y, Liao JM, Zeng SX and Lu H. p53 downregulates Down syndrome-associated DYRK1A through miR-1246. *EMBO reports.* 2011; 12:811-817.
46. Chen J, Xu-Monette ZY, Deng L, Shen Q, Manyam GC, Martinez-Lopez A, Zhang L, Montes-Moreno S, Visco C, Tzankov A, Yin L, Dybkaer K, Chiu A, et al. Dysregulated CXCR4 expression promotes lymphoma cell survival and independently predicts disease progression in germinal center B-cell-like diffuse large B-cell lymphoma. *Oncotarget.* 2015; 6:5597-5614. DOI: 10.18632/oncotarget.3343.
47. Li Y and Prives C. Are interactions with p63 and p73 involved in mutant p23 gain of oncogenic function? *Oncogene.* 2007; 26:2220-2225.
48. Dietz S, Rother K, Bamberger C, Schmale H, Mossner J and Engeland K. Differential regulation of transcription and induction of programmed cell death by human p53-family members p63 and p73. *FEBS Lett.* 2002; 525:93-99.
49. Gaiddon C, Lokshin M, Ahn J, Zhang T and Prives C. A subset of tumor-derived mutant forms of p53 down-regulate p63 and p73 through a direct interaction with the p53 core domain. *Mol Cell Biol.* 2001; 21:1874-1887.
50. Strano S, Fontemaggi G, Costanzo A, Rizzo MG, Monti O, Baccarini A, Del Sal G, Levrero M, Sacchi A, Oren M and Blandino G. Physical interaction with human tumor-derived p53 mutants inhibits p63 activities. *J Biol Chem.* 2002; 277:18817-18826.
51. Calabro V, Mansueto G, Parisi T, Vivo M, Calogero RA and La Mantia G. The human MDM2 oncoprotein increases the transcriptional activity and the protein level of the p53 homolog p63. *J Biol Chem.* 2002; 277:2674-2681.
52. Calabro V, Mansueto G, Santoro R, Gentilella A, Pollice A, Ghioni P, Guerrini L and La Mantia G. Inhibition of p63 transcriptional activity by p14ARF: functional and physical link between human ARF tumor suppressor and a member of the p53 family. *Mol Cell Bio.* 2004; 24:8529-8540.
53. Kadakia M, Slader C and Berberich SJ. Regulation of p63 function by Mdm2 and MdmX. *DNA Cell Biol.* 2001; 20:321-330.
54. Gonfloni S, Di Tella L, Caldarola S, Cannata SM, Klinger FG, Di Bartolomeo C, Mattei M, Candi E, De Felici M, Melino G and Cesareni G. Inhibition of the c-Abl-Tap63 pathway protects mouse oocytes from chemotherapy-induced death. *Nature medicine.* 2009; 15:1179-1185.
55. Visco C, Li Y, Xu-Monette ZY, Miranda RN, Green TM, Li Y, Tzankov A, Wen W, Liu WM, Kahl BS, d'Amore ES, Montes-Moreno S, Dybkaer K, et al. Comprehensive gene expression profiling and immunohistochemical studies support application of immunophenotypic algorithm for molecular subtype classification in diffuse large B-cell lymphoma: a report from the International DLBCL Rituximab-CHOP Consortium Program Study. *Leukemia.* 2012; 26:2103-2113.
56. Tzankov A, Xu-Monette ZY, Gerhard M, Visco C, Dirnhofer S, Gisin N, Dybkaer K, Orazi A, Bhagat G, Richards KL, Hsi ED, Choi

WW, van Krieken JH, et al. Rearrangements of MYC gene facilitate risk stratification in diffuse large B-cell lymphoma patients treated with rituximab-CHOP. *Mod Pathol.* 2014; 27:958-971.

57. Ok CY, Chen J, Xu-Monette ZY, Tzankov A, Manyam GC, Li L, Visco C, Montes-Moreno S, Dybkaer K, Chiu A, Orazi A, Zu Y, Bhagat G, et al. Clinical Implications of Phosphorylated STAT3 Expression in De Novo Diffuse Large B-cell Lymphoma. *Clin Cancer Res.* 2014; 20:5113-5123.

58. Hu S, Xu-Monette ZY, Balasubramanyam A, Manyam GC, Visco C, Tzankov A, Liu WM, Miranda RN, Zhang L, Montes-Moreno S, Dybkaer K, Chiu A, Orazi A, et al. CD30 expression defines a novel subgroup of diffuse large B-cell lymphoma with favorable prognosis and distinct gene expression signature: a report from the International DLBCL Rituximab-CHOP Consortium Program Study. *Blood.* 2013; 121:2715-2724.

59. Visco C, Tzankov A, Xu-Monette ZY, Miranda RN, Tai YC, Li Y, Liu WM, d'Amore ES, Li Y, Montes-Moreno S, Dybkaer K, Chiu A, Orazi A, et al. Patients with diffuse large B-cell lymphoma of germinal center origin with BCL2 translocations have poor outcome, irrespective of MYC status: a report from an International DLBCL rituximab-CHOP Consortium Program Study. *Haematologica.* 2013; 98:255-263.

60. Xu-Monette ZY, Dabaja BS, Wang X, Tu M, Manyam GC, Tzankov A, Xia Y, Li Zhang, Visco C, Dybkaer K, Yin L, Chiu A, Orazi A, et al. Clinical features, tumor biology and prognosis associated with MYC rearrangement and overexpression in diffuse large B-cell lymphoma patients treated with rituximab-CHOP. *Modern Pathology.* 2015; 28:1555-1573.

SUPPLEMENTAL DATA

Please browse the Full Text version of this manuscript to see Supplemental Figures and Tables.

The PTEN tumor suppressor gene and its role in lymphoma pathogenesis

Xiaoxiao Wang^{1,2}, Huiqiang Huang², and Ken H. Young^{1,3}

¹Department of Hematopathology, The University of Texas M. D. Anderson Cancer Center, Houston, TX 77230, USA;

²Department of Medical Oncology, Sun Yat-Sen University Cancer Center, Guangzhou, Guangdong, China;

³The University of Texas Graduate School of Biomedical Science, Houston, TX 77230, USA

Key words: PTEN, tumor suppressor, PI3K, AKT, mTOR, lymphoid malignancies, diffuse large B-cell lymphoma

Key points: PTEN deficiency is related to poor clinical outcomes in patients with a variety of tumors

Nuclear and cytoplasmic PTEN has distinct functions in tumor suppression

Received: 09/04/15; **Accepted:** 11/02/15; **Published:** 12/10/15

Correspondence to: Ken H. Young, MD/PhD; **E-mail:** khyoung@mdanderson.org

Copyright: Wang et al. This is an open-access article distributed under the terms of the Creative Commons Attribution License, which permits unrestricted use, distribution, and reproduction in any medium, provided the original author and source are credited

Abstract: The phosphatase and tensin homolog gene *PTEN* is one of the most frequently mutated tumor suppressor genes in human cancer. Loss of *PTEN* function occurs in a variety of human cancers via its mutation, deletion, transcriptional silencing, or protein instability. *PTEN* deficiency in cancer has been associated with advanced disease, chemotherapy resistance, and poor survival. Impaired *PTEN* function, which antagonizes phosphoinositide 3-kinase (PI3K) signaling, causes the accumulation of phosphatidylinositol (3,4,5)-triphosphate and thereby the suppression of downstream components of the PI3K pathway, including the protein kinase B and mammalian target of rapamycin kinases. In addition to having lipid phosphorylation activity, *PTEN* has critical roles in the regulation of genomic instability, DNA repair, stem cell self-renewal, cellular senescence, and cell migration. Although *PTEN* deficiency in solid tumors has been studied extensively, rare studies have investigated *PTEN* alteration in lymphoid malignancies. However, genomic or epigenomic aberrations of *PTEN* and dysregulated signaling are likely critical in lymphoma pathogenesis and progression. This review provides updated summary on the role of *PTEN* deficiency in human cancers, specifically in lymphoid malignancies; the molecular mechanisms of *PTEN* regulation; and the distinct functions of nuclear *PTEN*. Therapeutic strategies for rescuing *PTEN* deficiency in human cancers are proposed.

INTRODUCTION

The phosphatase and tensin homolog gene, *PTEN*, is one of the most commonly mutated tumor suppressors in human malignancies [1-5], and complete loss of *PTEN* protein expression is significantly associated with advanced cancer and poor outcome [6, 7]. The importance of *PTEN* as a tumor suppressor is further supported by the fact that germline mutations of *PTEN* commonly occur in a group of autosomal dominant syndromes, including Cowden Syndrome, which are characterized by developmental disorders, neurological deficits, and an increased lifetime risk of cancer and are

collectively referred to as *PTEN* hamartoma tumor syndromes (PHTS) [8, 9].

Biochemically, *PTEN* is a phosphatase that dephosphorylates phosphatidylinositol (3,4,5)-triphosphate (PIP₃), the lipid product of class I phosphoinositide 3-kinase (PI3K) [10]. To date, *PTEN* is the only lipid phosphatase known to counteract the PI3K pathway. Unsurprisingly, loss of *PTEN* has a substantial impact on multiple aspects of cancer development. Strikingly, *PTEN* has distinct growth-regulatory roles depending on whether it is in the cytoplasm or nucleus. In the cytoplasm, *PTEN* has

intrinsic lipid phosphatase activity that negatively regulates the cytoplasmic PI3K/AKT pathway, whereas in the nucleus, PTEN has AKT-independent growth activities. The continued elucidation of the roles of nuclear PTEN will help uncover the various functions of this essential tumor suppressor gene.

In this review, we describe the molecular basis of PTEN loss, discuss the regulation of PTEN expression in lymphoid malignancies, and summarize potential therapeutic targets in PTEN-deficient cancers.

STRUCTURE AND FUNCTION OF PTEN

PTEN structure

PTEN is a tumor suppressor gene located on chromosome 10q23.31 that encodes for a 403-amino acid protein that has both lipid and protein phosphatase activities. *PTEN* gene and protein structures are shown in Figure 1. The *PTEN* protein contains a sequence motif

that is highly conserved in members of the protein tyrosine phosphatase family. Structurally, the *PTEN* protein is composed of two major functional domains (a phosphatase domain and a C2 domain) and three structural regions (a short N-terminal phosphatidylinositol [4,5]-bisphosphate [PIP₂]-binding domain, a C-terminal tail containing proline-glutamic acid-serine-threonine sequences, and a PDZ-interaction motif) [11]. The PIP₂-binding site and adjacent cytoplasmic localization signal are located at the protein's N-terminal [12, 13].

The PI3K/PTEN/AKT/mTOR pathway

PTEN's tumor-suppressing function largely relies on the protein's phosphatase activity and subsequent antagonism of the PI3K/AKT/mammalian target of rapamycin (mTOR) pathway. Following *PTEN* loss, excessive PIP₃ at the plasma membrane recruits and activates a subset of pleckstrin homology domain-containing proteins to the cell membrane. These proteins

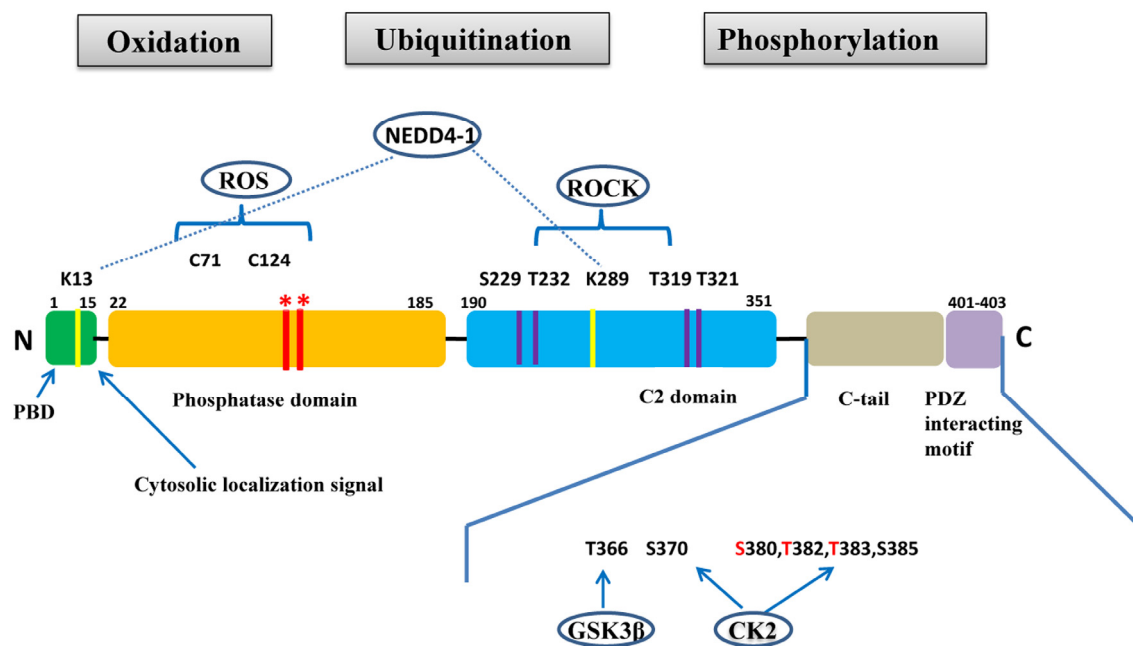


Figure 1. PTEN gene and protein structures. The *PTEN* protein is composed of 403 amino acids and contains an N-terminal PIP₂-binding domain (PBD), a phosphatase domain, a C2 domain, a C-terminal tail containing proline–glutamic acid–serine–threonine sequences, and a PDZ interacting motif at the end. *Mutations on the phosphatase domain that disrupt *PTEN*'s phosphatase activity include the C124S mutation, which abrogates both the lipid and protein phosphatase activity of *PTEN*, and the G129E mutation, which abrogates only the lipid phosphatase activity of *PTEN*. The C-terminal tail residues phosphorylated by glycogen synthase kinase 3 β (GSK3 β) and casein kinase 2 (CK2) are shown. Mutations of S380, T382, and T383 (referred to as the STT) can destabilize *PTEN* and increase its phosphatase activity. The PIP₂-binding site and adjacent cytoplasmic localization signal are located at the N-terminal. The N-terminal poly-basic region appears to selectively interact with PIP₂ and contribute to the nuclear accumulation of *PTEN*. Ubiquitination of *PTEN* has also been found on K13 and K289.

include phosphoinositide-dependent kinase-1 and AKT family members [14, 15]. AKT activation also leads to the activation of the mTOR kinase complex 1 through the inhibition of the phosphorylation of tuberous sclerosis complex tumor suppressors and consequent activation of the small GTPase rat sarcoma (RAS) homologue enriched in brain. The active mTOR complex 1 phosphorylates the p70 ribosomal protein S6 kinase (S6K) and inhibits 4E-binding protein 1 to activate protein translation [16]. Accordingly, the PTEN/PI3K/AKT/mTOR pathway is emerging as a vital target for anti-cancer agents, especially in tumors with mTOR pathway activation.

AKT-independent roles of PTEN

Although AKT pathway activation can explain many of the phenotypes associated with PTEN inactivation, *PTEN* gene targeting and genetic activation of *AKT* do not have completely overlapping biological consequences. Using transcriptional profiling, Vivanco et al. identified a new PTEN-regulated pathway, the Jun-N-terminal kinase (JNK) pathway, which was constitutively activated upon PTEN knockdown [17]. In the study, PTEN null cells had higher JNK activity than PTEN positive cells did, and genetic analysis indicated that JNK functioned parallel to and independently of AKT. Thus, the blockade of PI3K signaling may shift the survival signal to the AKT-independent PTEN-regulated pathway, implicating JNK and AKT as complementary signals in PIP₃-driven tumorigenesis and suggest that JNK may be a therapeutic target in *PTEN* null tumors.

In addition to its lipid phosphatase function, PTEN also has lipid phosphatase-independent roles. PTEN has been shown to inhibit cell migration through its C2 domain, independent of PTEN's lipid phosphatase activity [18]. In breast cancer, PTEN deficiency has been shown to activate, in a manner dependent on its protein phosphatase activity, the SRC proto-oncogene, non-receptor tyrosine kinase (SRC), thereby conferring resistance to human epidermal growth factor receptor 2 inhibition [19]. Furthermore, PTEN has been shown to directly bind to tumor protein 53 (p53), regulate its stability, and increase its transcription, thereby increasing P53 protein levels [20].

PTEN REGULATION

Genetic alteration of *PTEN*

PTEN loss of function occurs in a wide spectrum of human cancers through various genetic alterations that include point mutations (missense and nonsense mutations), large chromosomal deletions (homozygous/

heterozygous deletions, frameshift deletions, in-frame deletions, and truncations), and epigenetic mechanisms (e.g., hypermethylation of the *PTEN* promoter region) [21]. Somatic mutations are the main drivers of PTEN inactivation in human cancers, and have been reviewed extensively [22].

PTEN's tumor suppressor function is usually abrogated following mutations in its phosphatase domain, which is encoded by exon 5 [23] (Figure 1). These mutations typically include a C124S mutation that abrogates both lipid and protein phosphatase activity and a G129E mutation that abrogates lipid phosphatase but not protein phosphatase activity [24]. Although the N-terminal phosphatase domain is principally responsible for PTEN's physiological activity, approximately 40% of tumorigenic *PTEN* mutations occur in the C-terminal C2 domain (corresponding to exons 6, 7, and 8) and in the tail sequence (corresponding to exon 9), which encode for tyrosine kinase phosphorylation sites. This suggests that the C-terminal sequence is critical for maintaining PTEN function and protein stability [21, 23, 25, 26]. However, many tumor-derived *PTEN* mutants retain partial or complete catalytic function, suggesting that alternative mechanisms can lead to PTEN inactivation.

Transcriptional regulation

In addition to gene mutations, complete or partial loss of PTEN protein expression may impact PTEN's tumor suppression ability. The regulation of PTEN's functions and signaling pathway is shown in Figure 2. Positive regulators of PTEN gene expression include early growth response protein 1, peroxisome proliferator-activated receptor γ (PPAR γ) and P53, which have been shown to directly bind to the PTEN promoter region [27-29]. Early growth response protein 1, which regulates PTEN expression during the initial steps of apoptosis, has been shown to directly upregulate the expression of PTEN in non-small cell lung cancer. PPAR γ is a ligand-activated transcription factor with anti-inflammatory and anti-tumor effects. The activation of its selective ligand, rosiglitazone, leads to the binding of PPAR γ at two PTEN promoter sites, PPAR response element 1 and PPAR response element 2, thus upregulating PTEN and inhibiting PI3K activity. Negative regulators of PTEN gene expression include mitogen-activated protein kinase kinase-4, transforming growth factor beta (TGF- β), nuclear factor of kappa light polypeptide gene enhancer in B-cells (NF- κ B), IGF-1, the transcriptional cofactor c-Jun proto-oncogene, and the B-cell-specific Moloney murine leukemia virus insertion site 1 (BMI1) proto-oncogene, which have been shown to suppress PTEN expression in

several cancer models [30-32]. Research found that IGF-1 could affect cell proliferation and invasion by suppressing PTEN's phosphorylation. In pancreatic cancers, TGF- β significantly suppresses PTEN protein levels concomitant with the activation of AKT through transcriptional reduction of PTEN mRNA—induced growth promotion. c-Jun negatively regulates the expression of PTEN by binding to the activator protein 1 site of the PTEN promoter, resulting in the concomitant activation of the AKT pathway. *PTEN* transcription is also directly repressed by the leukemia-associated factor ecotropic virus integration site 1 protein in the hematopoietic system [33].

Intriguingly, recent studies reported a complex crosstalk between PTEN and other pathways. For example, RAS

has been found to mediate the suppression of PTEN through a TGF- β dependent mechanism in pancreatic cancer [34], and the mitogen-associated protein kinase/extracellular signal-related kinase pathway has been found to suppress PTEN transcription through c-Jun [35]. Finally, the stress kinase pathways including mitogen-activated protein kinase kinase kinase 4 and JNK promote resistance to apoptosis by suppressing PTEN transcription via direct binding of NF- κ B to the PTEN promoter [36]. These findings suggest that the pathways that are negatively regulated by PTEN can in turn regulate PTEN transcription, indicating a potential feedback loop. Studies have also shown that CpG islands hypermethylated in the *PTEN* promoter lead to the silencing of *PTEN* transcription in human cancer [37].

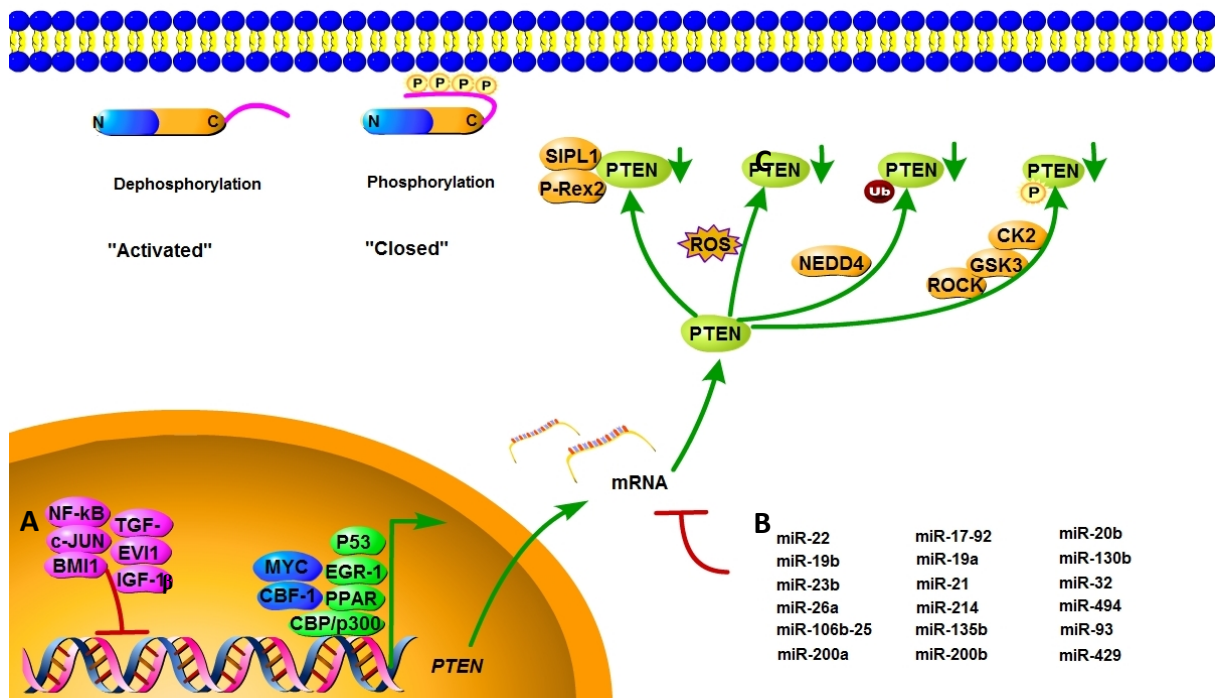


Figure 2. Mechanisms of PTEN regulation. PTEN is regulated at different levels. (A) PTEN mRNA transcription is activated by early growth response protein 1, P53, MYC, PPAR γ , C-repeat binding factor 1, and others, and inhibited by NF- κ B, proto-oncogene c-Jun, TGF- β , and BMI-1. (B) PTEN mRNA is also post-transcriptionally regulated by PTEN-targeting miRNAs, including miR-21, miR-17-92, and others. (C) Active site phosphorylation, ubiquitination, oxidation, acetylation, and protein-protein interactions can also regulate PTEN activity. The phosphorylation leads to a “closed” state of PTEN and maintains PTEN stability. Dephosphorylation of the C-terminal tail opens the PTEN phosphatase domain, thereby activating PTEN.

Table 1. MiRNAs which downregulate PTEN expression in human cancers

miRNA	Locus	Expression status	Tumor type	Reference
MiR-21	17q23.1	Upregulated	Colorectal, bladder, and hepatocellular cancer	[112-114]
MiR-19a	13q31.3	Upregulated	Lymphoma and CLL	[87, 115]
MiR-19b	Xq26.2	Upregulated	Lymphoma	[87]
MiR-22	17p13.3	Upregulated	Prostate cancer and CLL	[116, 117]
MiR-32	9q31.3	Upregulated	Hepatocellular carcinoma	[118]
MiR-93	7q22.1	Upregulated	Hepatocellular carcinoma	[119]
MiR-494	14q32.31	Upregulated	Cervical cancer	[120]
MiR-130b	22q11.21	Upregulated	Esophageal carcinoma	[121]
MiR-135b	1q32.1	Upregulated	Colorectal cancer	[122]
MiR-214	1q24.3	Upregulated	Ovarian cancer	[123]
MiR-26a	3p22.2 (MIR26A1) 12q14.1(MIR26A2)	Upregulated	Prostate cancer	[113]
MiR-23b	9q22.32	Upregulated	Prostate cancer	[114]

Abbreviations: CLL, chronic lymphocytic leukemia.

Translational and post-translational regulation

MicroRNAs (miRNAs) are a class of endogenous, 20- to 25-nucleotide single-stranded non-coding RNAs that repress mRNA translation by base-pairing with target mRNAs [38]. Various miRNAs are known to impact PTEN expression in both normal and pathological conditions. In multiple human cancers, PTEN expressions are downregulated by miRNAs, which are shown in Table 1.

Post-translational modifications, such as active site phosphorylation, ubiquitination, oxidation, and acetylation, can also regulate PTEN activity [39]. In its inactivated state, PTEN is phosphorylated on a cluster of serine and threonine residues located on its C-terminal tail, leading to a “closed” PTEN state in which PTEN protein stability is maintained. As PTEN is being activated, dephosphorylation of its C-terminal tail opens its phosphatase domain, thereby increasing PTEN acti-

vity (Figure 2). The phosphorylation of PTEN at specific residues of the C-terminal tail (Thr366, Ser370, Ser380, Thr382, Thr383, and Ser385) is associated with increased protein stability, whereas phosphorylation at other sites may decrease protein stability. Although S370 and S385 have been identified as the major sites for PTEN phosphorylation, mutations of these residues have minimal effects on PTEN function, whereas mutations of S380, T382, and T383 can destabilize PTEN and increase its phosphatase activity, thereby enhancing PTEN’s interaction with binding partners [40]. The “open” state of PTEN is more susceptible to ubiquitin-mediated proteasome degradation [13]. One recently identified E3 ligase of PTEN is neural precursor cell-expressed, developmentally down-regulated 4, E3 ubiquitin protein ligase 1 (NEDD4-1), which mediates PTEN mono- and poly-ubiquitination [41] (Figure 3). In cancer, the inhibition of NEDD4-1, whose expression has been found to be inversely correlated with PTEN levels in bladder cancer, may

upregulate PTEN levels [42]. Two major conserved sites for PTEN are K13 and K289, and ubiquitination of these sites is indispensable for the nuclear-cytoplasmic shuttling of PTEN (Figure 1).

Protein-protein interactions

PTEN contains a 3-amino acid C-terminal region that is able to bind to PDZ domain-containing proteins [43, 44]. PDZ domains are involved in the assembly of multi-protein complexes that may control the localization of PTEN and its interaction with other proteins. A number of PTEN-interacting proteins have been shown to regulate PTEN protein levels and activities. These interactions, which help recruit PTEN to the membrane, can be negatively modulated by the phosphorylation of PTEN on its C terminus [40, 45]. The phosphorylation of the C terminal end of PTEN has been attributed to the activities of casein kinase 2 and glycogen synthase kinase 3 β [46, 47]. In addition, evidence suggests that the C2 domain of PTEN can be phosphorylated by RhoA-associated kinase, which may have important roles in the regulation of chemoattractant-induced PTEN localization [48] (Figure 2).

Acetylation and oxidation also contribute to PTEN activity regulation. PTEN's interaction with nuclear histone acetyltransferase-associated p300/cAMP response element-binding protein (CREB)-binding protein (CBP)-associated factor can promote PTEN acetylation, and this acetylation negatively regulates the catalytic activity of PTEN [49]. Studies have shown that the PTEN protein becomes oxidized in response to the endogenous generation of the reactive oxygen species (ROS) stimulated by growth factors and insulin, and this oxidation correlates with a ROS-dependent activation of downstream AKT phosphorylation [50, 51]. Other studies have shown that the PIP₃-dependent Rac exchange factor 2 and SHANK-associated RH domain interactor proteins bind directly to PTEN to inhibit its lipid phosphatase activity [52, 53]. High P53 expression triggers proteasome degradation of the PTEN protein [54]. In addition to antagonizing the AKT-mouse double minute 2 homolog pathway in a phosphatase-dependent manner, PTEN also can interact with P53 directly in a phosphatase-independent manner, thereby stabilizing P53 [55, 56].

PTEN IN THE NUCLEUS

Growing evidence suggests that the translocation of PTEN from the nucleus to the cytoplasm leads to malignancy. In the nucleus, PTEN has important tumor-

suppressive functions, and the absence of nuclear PTEN is associated with aggressive disease in multiple cancers [57-59], implying that nuclear PTEN is a useful prognostic indicator. PTEN is predominantly localized to the nucleus in primary, differentiated, and resting cells, and nuclear PTEN is markedly reduced in rapidly cycling cancer cells [60, 61], which suggests that PTEN localization is related to cell differentiation status and cell cycle stage. High expression levels of nuclear PTEN have been associated with cell-cycle arrest at the G0/G1 phase, indicating a role of nuclear PTEN in cell growth inhibition [62]. PTEN's cytoplasmic and nuclear functions are shown in Figure 3.

PTEN enters the nucleus via its calcium-dependent interaction with the major vault protein [63], through passive diffusion [64], and by a Ran-GTPase-dependent pathway [65]. Moreover, monoubiquitination mediates PTEN's nuclear import, whereas polyubiquitination leads to PTEN's degradation in the cytoplasm [66] (Figure 3). The nuclear exportation of PTEN via a chromosome region maintenance 1-dependent mechanism during the G1-S phase transition is directly regulated by S6K, a downstream effector of the PI3K signaling pathway [67] (Figure 3). Thus, PTEN is preferentially expressed in the cytoplasm of tumor cells in which PI3K signaling is frequently activated. Nuclear PTEN has an essential role in the maintenance of chromosomal stability. First, PTEN directly interacts with centromere protein C in a phosphatase-independent manner. Second, PTEN transcriptionally regulates DNA repair by upregulating RAD51 recombinase in a phosphatase-dependent manner [68] (Figure 3). The disruption of nuclear PTEN results in centromere breakage and massive chromosomal aberrations. Nuclear PTEN may also play an important part in transcription regulation by negatively modulating the transcriptional activity of the androgen receptor, hepatocyte growth factor receptor, NF- κ B, CREB, and activator protein 1. Moreover, nuclear PTEN has been shown to promote p300/CREB-binding protein-mediated p53 acetylation in the response to DNA damage [69, 70].

Most of the functions of nuclear PTEN are independent of its phosphatase activity and do not involve the PI3K/AKT pathway. Not only PTEN but also activated PI3K and functional PIP₃ have been detected in the nucleus [71], indicating that nuclear PI3K signaling mediates PTEN's antiapoptotic effect through nuclear PIP₃ and nuclear AKT. Nevertheless, only limited evidence suggests that nuclear PTEN has lipid phosphatase functions, as the nuclear pool of PIP₃ is insensitive to PTEN [72].

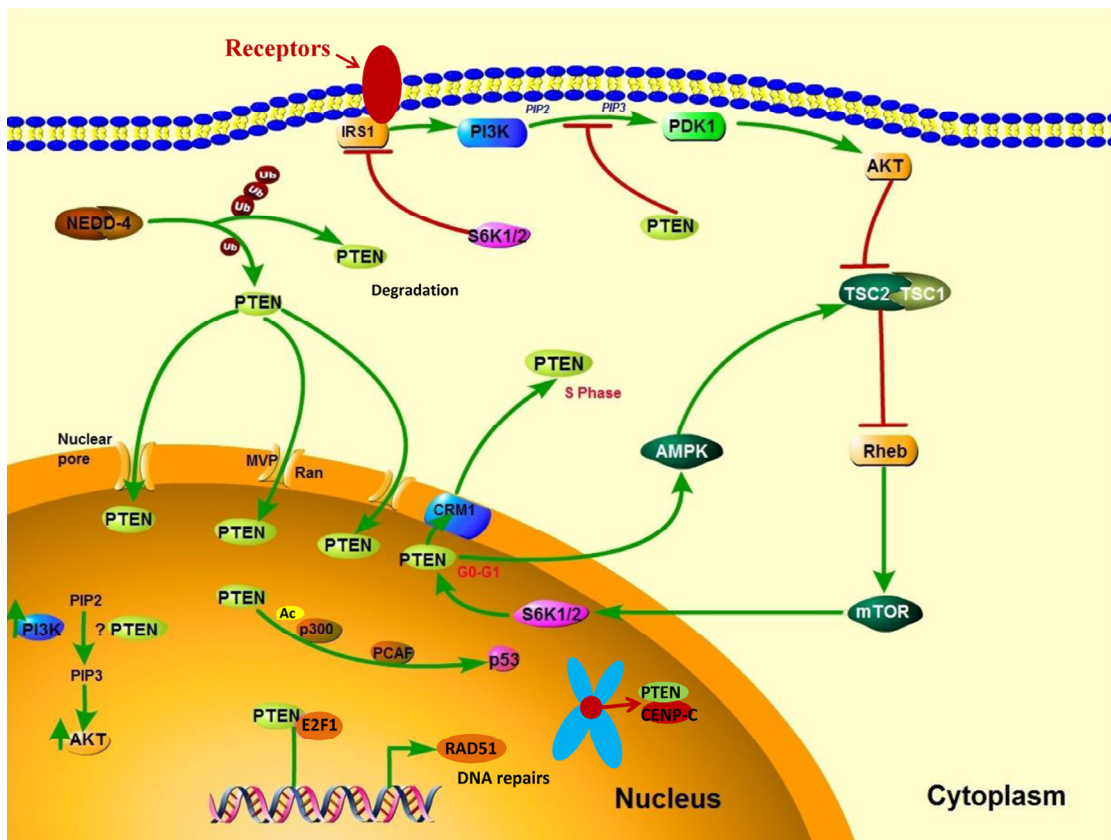


Figure 3. PTEN's cytoplasmic and nuclear functions. In the cytoplasm, PI3K is activated downstream of receptors that include receptor tyrosine kinases, G protein-coupled receptors, cytokine receptors, and integrins. PI3K activation converts PIP₂ to PIP₃, thereby leading to AKT activation, which enhances cell growth, proliferation, and survival. PTEN dephosphorylates PIP₃ and consequently suppresses the PI3K pathway. NEDD4-1 is an E3 ligase of PTEN that mediates PTEN ubiquitination. Polyubiquitination of PTEN leads to its degradation in the plasma, whereas monoubiquitination of PTEN increases its nuclear localization. PTEN can translocate into the nucleus through various mechanisms, including passive diffusion, Ran- or major vault protein-mediated import, and a monoubiquitination-driven mechanism. In the nucleus, PTEN promotes p300-mediated P53 acetylation in response to DNA damage to control cellular proliferation. Nuclear PTEN is also involved in maintaining genomic integrity by binding to centromere protein C (CENPC) and in DNA repair by upregulating RAD51 recombinase (RAD51).

PTEN DEFICIENCY IN LYMPHOMA

PTEN deficiency in T-cell acute lymphoblastic leukemia

PI3K signaling are frequently activated in T-cell acute lymphoblastic leukemia (T-ALL), which mainly due to the absent of PTEN function. Studies have shown that *PTEN* inactivation plays a prominent role in human T-ALL cell lines and primary patients [73-76]. Moreover, *PTEN* mutations have been shown induced resistance to γ -secretase inhibitors, which derepress the constitutively activated NOTCH1 signaling in T-ALL [77]. However, the *PTEN* mutations detected in these studies vary widely. Gutierrez et al. reported that T-ALL patients

had a *PTEN* mutation rate of 27% and a *PTEN* deletion rate of 9%, whereas Gedman et al. reported that 27 of 43 (63%) pediatric T-ALL specimens had *PTEN* mutations. In the latter study, the high frequency of *PTEN* mutations may have been due to the fact that approximately 50% of the specimens were patients with relapsed disease. Interestingly, all mutations were identified in the C2 domain of PTEN [75, 76], not in the phosphatase domain as has been reported for other solid tumors [78].

PTEN deficiency in diffuse large B-cell lymphoma

Published reports of *PTEN* gene alterations in lymphoid malignancies are summarized in Table 2. Studies have

reported unexpectedly low frequencies of *PTEN* mutations in DLBCL patients, ranging from 3% to 22% [79-83]. Lenz et al. performed gene expression profiling

in primary DLBCL and found that a recurrently altered minimal common region containing *PTEN* was lost in 11% GCB-DLBCL but not in other subtypes, suggesting

Table 2. Reported *PTEN* gene alterations in lymphoid malignancies

Alteration type	Exon	Domain	Disease	Frequency, %	Notes	Ref
Cell lines						
Del	3-9	PHOS, C2	DLBCL	28.6 (4/14)	Del in 4 of 11 GCB-DLBCL	[85]
Mut	2-5	PHOS, C2	DLBCL	35.7 (5/14)	Mut in 4 of 11 GCB- and 1 of 3 ABC-DLBCL	
Del and Mut	2-7	PHOS, C2		22.2 (6/27)		[82]
Biopsy tissue						
Del			DLBCL	15.3 (4/26)	Heterozygous Del in 3 of 18 GCB- and 1 of 8 ABC-DLBCL	[85]
Del	1	PB	NHL	3.4 (1/29)		[81]
Mut	5, 6	PHOS, C2		6.9 (2/29)		
Del and Mut	1, 8	PHOS, C2	NHL	4.6 (3/65)		[82]
Mut	8	C2	DLBCL	5 (2/39)		[79]
Del			GCB-DLBCL	13.9 (10/72)	Homozygous Del in 2, heterozygous Del in 8	[84]
Mut	1, 2, 7	PB, PHOS, C2	NHL	10 (4/40)		[109]
Mut	7	C2	T-ALL	8 (9/111)		[74]
Del	NA		T-ALL	8.7 (4/46)	Homozygous Del in 2, heterozygous Del in 2	[76]
Mut	7	C2		27.3 (12/44)		
Del and Mut			T-ALL	62.7 (27/43)	Homozygous Del in 8	[75]

Abbreviations: Del, deletion; PHOS, phosphatase; DLBCL, diffuse large B-cell lymphoma; GCB, germinal B-cell-like; Mut, mutation; ABC, activated B-cell-like; NHL, non-Hodgkin lymphoma; T-ALL, T-cell acute lymphoblastic leukemia; AML, acute myeloid leukemia; ALL, acute lymphoblastic leukemia; PB, phosphatidylinositol (4,5)-bisphosphate-binding; NA, not applicable.

that the alteration is exclusive to GCB-DLBCL [84]. More recently, Pfeifer and Lenz found that mutations involving both the phosphatase domain and C2 domain of *PTEN* were prominent in GCB-DLBCL cell lines. Interestingly, 7 of the 11 GCB-DLBCL cell lines had complete loss of PTEN function, whereas all ABC-DLBCL cell lines expressed PTEN, suggesting that *PTEN* mutation may be related to PTEN loss in GCB-DLBCL [85] (Table 2). In the GCB-DLBCL cell lines, PTEN loss was inversely correlated with the constitutive activation of the PI3K/AKT signaling pathway, whereas GCB-DLBCL cell lines with PTEN expression rarely had PI3K/AKT activation. In contrast, all ABC-DLBCL cell lines had PI3K/AKT activation regardless of PTEN status, which suggests that the activation of PI3K/AKT in GCB-DLBCL results from PTEN deficiency. Further, gene set enrichment analysis revealed that the MYC target gene set was significantly downregulated after PTEN induction. Also, inhibition of PI3K/AKT with either PTEN re-expression or PI3K inhibition significantly downregulated MYC expression, suggesting that PTEN loss leads to the upregulation of MYC through the constitutive activation of PI3K/AKT in DLBCL [85].

Although several studies have identified discrepancies in PTEN deficiency between DLBCL subtypes, few studies have investigated PTEN localization in different subcellular compartments, not to mention the prognostic value such information would have in de novo cases. Fridberg et al. found a trend towards a stronger staining intensity of cytoplasmic and nuclear PTEN in 28 non-GCB-DLBCL patients [59], most importantly, they found that the absence of nuclear PTEN expression was correlated with worse survival. This interesting evidence should be corroborated in a larger number of primary samples in further studies.

PTEN deficiency in other lymphomas

Previous studies of mantle cell lymphoma (MCL) showed that although the disease had no detectable genetic alterations of PTEN, it did have extremely low protein expression of PTEN. To determine whether the PI3K/AKT signaling pathway is involved in the pathogenesis of MCL, Rudelius et al. investigated pAKT and PTEN expression in primary MCL specimens and cell lines. Of the 31 MCL specimens, 6 had markedly decreased PTEN expression; of the 4 MCL cell lines, 3 had complete loss of PTEN expression [86]. The authors found no phosphatidylinositol 3-kinase catalytic subunit (*PIK3CA*) mutations in the primary specimens or cell lines, suggesting that loss of PTEN activates the PI3K/AKT pathway in MCL.

Loss of PTEN protein expression has also been reported in 32% of patients with primary cutaneous DLBCL–leg type and 27% of patients with primary cutaneous follicle center lymphomas. Remarkably, both the expression of miR-106a and that of miR-20a were significantly related to PTEN protein loss ($P < 0.01$). Moreover, low PTEN mRNA levels were significantly associated with shorter disease-free survival [87].

PTEN AND SPECIFIC PI3K ISOFORMS

PI3K comprises a regulatory p85 subunit and a catalytic p110 subunit. Of particular interest, Class IA PI3Ks include three p110 isoforms (p110 α , p110 β , and p110 δ), are primarily responsible for phosphorylating PIP₂. *PIK3CA*, the gene encoding the p110 α isoform is frequently mutated in various human cancers [88]. In one study, 59% of cases with mutant *PIK3CA* had increased p-AKT levels. Therefore, the constitutive activation of PI3K is another way by which the PTEN pathway can be disturbed in cancer. In their study of 215 DLBCL patients, Abubaker et al. reported that 8% had *PIK3CA* mutations and 37% had loss of PTEN. Both *PIK3CA* mutation and loss of PTEN were correlated with poor survival. However, correlation analysis revealed that most of the *PIK3CA* mutations occurred in cases with PTEN expression ($P = 0.0146$). Accordingly, 17 cases with *PIK3CA* mutations were screened for *PTEN* mutations, and none harbored both *PIK3CA* and *PTEN* mutations [89]. This suggests that *PIK3CA* mutation likely functions as an oncogene in DLBCL by contributing to PI3K pathway activation independently of PTEN deficiency.

Both p110 α and p110 β may generate distinct pools of PIP₃. In response to stimuli, p110 α produces an acute flux of PIP₃, which is efficiently coupled to AKT phosphorylation. In contrast, p110 β has been proposed to generate a basal level of PIP₃ with little effect on AKT phosphorylation [90]. Moreover, cells with AKT phosphorylation induced by PTEN loss were sensitive to a p110 β -specific inhibitor but not a p110 α inhibitor both in vitro and in vivo [91, 92], which suggests that the enhancement of basal PIP₃ drive oncogenesis in the absence of PTEN. Another study indicated that *PTEN*-mutant endometrioid endometrial carcinoma cells may not be sufficiently sensitive to the inhibition of p110 β alone and that combined targeted agents may be required for effective treatment [93]. This finding may have been due to the fact that mutations of *PTEN* and *PIK3CA* frequently coexist in endometrioid endometrial carcinoma. In contrast, cells with wild-type PTEN seem to engage the p110 α or p110 δ isoforms. Accordingly, clinical trials of isoform-specific inhibitors are warranted.

Table 3. Preclinical studies of targeted therapeutics in PTEN-deficient tumors

Inhibitor type	Drug	Study notes	Ref
<i>Class I-PI3K</i>			
Pan	Buparlisib (BKM120)	The drug elicited response in some PTEN-deficient tumors and induced cell death in DLBCL cell lines.	[124]
Pan	SAR245408 (XL147)	The drug significantly inhibited tumor growth in a PTEN-deficient prostate cancer model.	[109]
p110 α	BYL719	The drug had antitumor activity in cell lines harboring <i>PIK3CA</i> mutations but not in PTEN-deficient solid tumors	[110]
p110 β	AZD6482 (KIN-193)	The drug substantially inhibited tumor growth in PTEN-deficient cancer models.	[98]
p110 β	GSK2636771	<i>PTEN</i> -mutant EEC cell lines were resistant to the drug; the drug decreased cell viability only when combined with a p110 α selective inhibitor.	[93]
p110 β/δ	AZD8186	The drug inhibited the growth of PTEN-deficient prostate tumors.	[102]
p110 α/β	CH5132799	The drug inhibited the growth of some PTEN-deficient tumors in vitro.	[103]
p110 γ/δ	IPI-145	The drug significantly inhibited the Loucy cell lines in T-ALL.	[100]
<i>PI3K/mTOR</i>	SF1126	The drug significantly reduced the viability of PTEN-deficient but not PTEN-positive GCB-DLBCL cells.	[104]
<i>PI3K/HDAC</i>	CUDC-907	The drug inhibited growth in multiple cell lines; cell lines with <i>PIK3CA</i> or <i>PTEN</i> -mutation induced loss of PTEN were markedly sensitive to the drug.	[105]
<i>AKT</i>	MK-2206	The drug had antitumor activity in breast cancer cell lines with <i>PTEN</i> or <i>PIK3CA</i> mutations.	[106]
<i>mTORC1</i>	Everolimus (RAD001)	PTEN-deficient prostate cancer had greater sensitivity to the drug; glioblastoma cell lines were resistant to the drug.	[107]
	Temsirolimus (CCI-779)	Multiple PTEN-deficient cell lines were remarkably sensitive to the drug.	[108]

Abbreviations: DLBCL, diffuse large B-cell lymphoma; EEC, endometrioid endometrial carcinoma; MCL, mantle cell lymphoma; GCB, germinal B-cell-like.

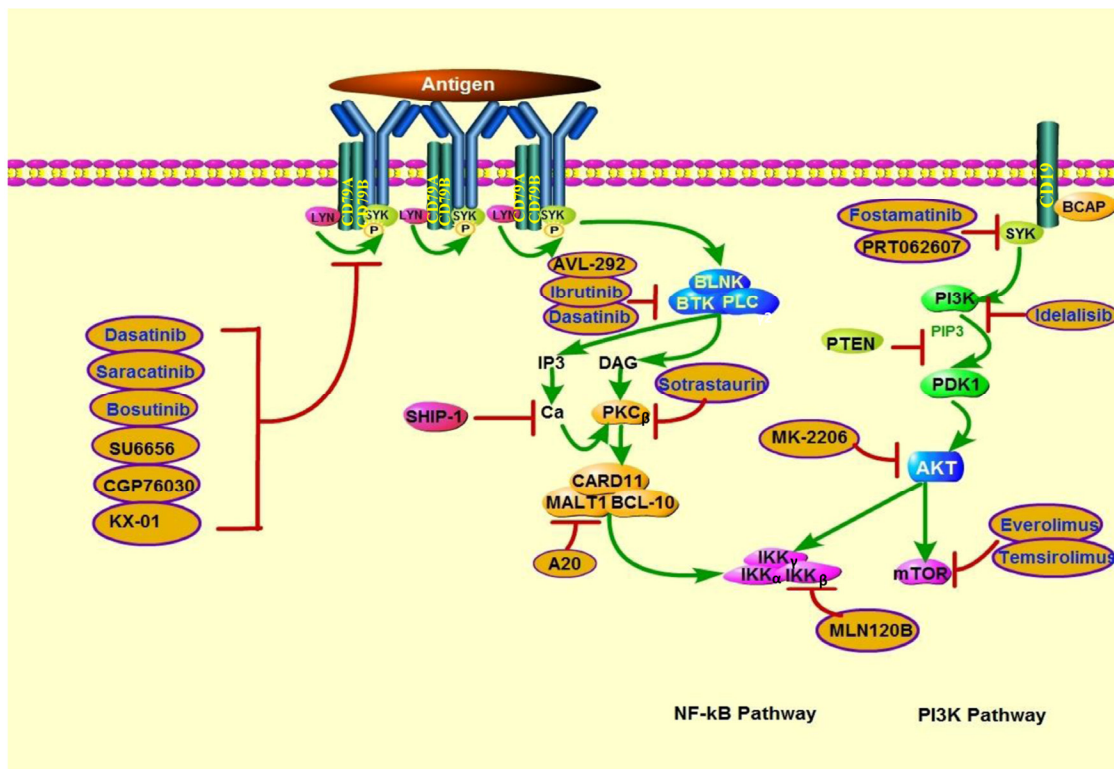


Figure 4. Actions of therapeutics targeting PTEN deficiency in lymphoid malignancies. PTEN deficiency is associated with increased sensitivity to PI3K, AKT, and mTOR inhibitors. In addition, because PI3K is involved in BCR signaling activation, BCR pathway inhibitors may also be effective in PTEN-deficient lymphoid malignancies. SRC family kinase inhibitors include dasatinib (which can also inhibit BTK), saracatinib, bosutinib, SU6656, CGP76030, and KX-01. BTK inhibitors include ibrutinib and AVL-292. Sotrastaurin is a PKC β inhibitor; A20, a MALT1 paracaspase inhibitor; and MLN120B, an IKK β inhibitor. SYK inhibitors include fostamatinib and PRT062607. Idelalisib is a PI3K δ -specific inhibitor. MK-2206 is an AKT inhibitor. mTOR inhibitors include everolimus and temsirolimus.

ENGAGEMENT OF THE PI3K PATHWAY IN B-CELL RECEPTOR SIGNALING

The survival of the majority of B-cell malignancies depends on functional B-cell receptor (BCR) signaling. The successful use of a Bruton tyrosine kinase (BTK) inhibitor to target the BCR pathway in DLBCL has yielded profound discoveries regarding the genetic and biochemical basis of BCR signaling. During BCR signaling, the SRC family kinase LYN phosphorylates the transmembrane protein cluster of differentiation 19, which recruits PI3K to the BCR. The transduction of BCR signaling finally results in the activation of the NF- κ B, PI3K, mitogen-associated protein kinase, and nuclear factor of activated T cells pathways, which

promote the proliferation and survival of normal and malignant B cells.

BCR signaling is directly affected by frequent mutations in CD79A (immunoglobulin α) and CD79B (immunoglobulin β)-mainly CD79B-which occur in approximately 20% of patients with ABC-DLBCL [94]. Tumor cells harboring CD79B mutations have longer and stronger activation of AKT signaling. Moreover, ABC-DLBCL cell lines with mutated CD79B are more sensitive to PI3K inhibition than those with wild-type CD79B are. Thus, CD79B mutations might be responsible for preventing the negative regulation that interferes with PI3K-dependent pro-survival BCR signaling [95].

Table 4. Preclinical studies of targeted therapeutics in PTEN-deficient tumors

Inhibitor type	Drug	Patient population	Phase	Identifier
PI3K	GSK2636771	Patients with advanced solid tumors with PTEN deficiency	1/2a	NCT01458067
	BKM120	Patients with recurrent glioblastoma with PTEN mutations or homozygous deletion of PTEN or with PTEN-negative disease	1b/2	NCT01870726
	BKM120	Patients with advanced, metastatic, or recurrent endometrial cancers with PIK3CA gene mutation, PTEN gene mutation, or null/low PTEN protein expression	2	NCT01550380
	AZD8186	Patients with advanced CRPC, sqNSCLC, TNBC, or known PTEN-deficient advanced solid malignancies	1	NCT01884285
PI3K/mTOR	BEZ235	Patients with advanced TCC; group 1 includes patients with no PI3K pathway activation, no loss of PTEN, and no activating PIK3CA mutation; group 2 includes patients with PI3K pathway activation as defined by PIK3CA mutation and/or PTEN loss	2	NCT01856101
	BEZ235	Patients with relapsed lymphoma or multiple myeloma	1	NCT01742988
AKT	MK-2206	Patients with previously treated metastatic colorectal cancer enriched for PTEN loss and PIK3CA mutation	2	NCT01802320
	MK-2206	Patients with advanced breast cancer with a PIK3CA mutation, AKT mutation, and/or PTEN loss or mutation	2	NCT01277757
	Pazopanib + everolimus	Patients with PI3KCA mutations or PTEN loss and advanced solid tumors refractory to standard therapy	1	NCT01430572
	Trastuzumab +RAD001	Patients with HER-2–overexpressing, PTEN-deficient metastatic breast cancer progressing on trastuzumab-based therapy	1/2	NCT00317720
	GDC-0068/ GDC-0980 +abiraterone	Patients previously treated prostate cancer with PTEN loss (currently in phase II)	1b/2	NCT01485861

Rapamycin (Temsirolimus)	Patients with advanced cancer and PI3K mutation and/or PTEN loss	1/2	NCT00877773
Ipatasertib (GDC- 0068) + paclitaxel	Patients with PTEN-low metastatic TNBC	2	NCT02162719

Abbreviations: CRPC, castrate-resistant prostate cancer; sqNSCLC, squamous non-small cell lung cancer; TNBC, triple-negative breast cancer; TCC, transitional cell carcinoma; HER-2, human epidermal growth factor receptor 2.

Previous studies have demonstrated that the transgenic expression of the constitutively active form of the PI3K catalytic subunit or PTEN knockout can rescue mature B cells from conditional BCR ablation. Moreover, BCR signaling is required for PI3K pathway engagement in both GCB-DLBCL and ABC-DLBCL. Specifically, PI3K engages BCR signaling by indirectly contributing to NF- κ B activity in ABC-DLBCL, whereas in GCB-DLBCL, PI3K pathway activation but not NF- κ B activity is required for survival. Briefly, the “chronic” BCR signaling in ABC-DLBCL is characterized by the many pathways involved with the CARD11-mediated activation of NF- κ B signaling, whereas the “tonic” BCR signaling in GCB-DLBCL is characterized by the constitutive activation of PI3K in promoting survival [96, 97].

Given these findings, the combination of PI3K pathway inhibitors with BCR pathway inhibitors may enhance the treatment response of PTEN-deficient tumors.

THERAPIES TARGETING FUNCTIONAL LOSS OF PTEN IN LYMPHOMA

PI3K/AKT/mTOR pathway inhibitors

Owing to PI3K’s critical roles in human cancers, PI3K targeting is one of the most promising areas of anticancer therapy development. Since the absent of PTEN is concomitant with PI3K signaling activation, inhibitors that targeting this pathway might play a significant role in the treatment of PTEN-deficient tumors. Growing evidence indicates that multiple solid tumor cell lines and several lymphoid malignancy cell lines with PTEN-deficient are hypersensitive to PI3K inhibitors, which are summarized in Tables 3 and Figure 4.

In addition to PI3K pan-inhibition, several isoform-selective PI3K inhibitors have been shown to repress the viability of PTEN-deficient tumors. Notably, the p110 β -specific PI3K inhibitor AZD6482 (KIN-193)

displayed remarkable antitumor activity in PTEN-null tumors but failed to block the growth of PTEN-wild-type tumors in mouse models [98]. However, another separate study showed that endometrioid endometrial cancer with *PTEN* mutation were resistant to p110 β -selective inhibition, cell lines’ viability was decreased only when p110 β -selective inhibition was combined with p110 α -selective inhibition. Recent findings have highlighted that there is a complex interplay between the Class I PI3K isoforms, inhibition of either α or β single isoform might be compensated by reactivation of another isoform at last [99]. Furthermore, it has been proposed that the dual γ/δ inhibitor CAL-130, specifically targeting p110 γ and p110 δ isoforms in *PTEN* deleted T-ALL cell lines [100]. By contrast, Lonetti et al. recently indicated that PI3K pan-inhibition developed the highest cytotoxic effects when compared with both selective isoform inhibition and dual p110 γ/δ inhibition, in T-ALL cell lines with or without *PTEN* deletion [101]. Nevertheless, which class of agents among isoform-specific or pan-inhibitors can achieve better efficacy is still controversial. Other target treatments including AKT, mTOR, dual PI3K/AKT and dual PI3K/mTOR inhibitors also show promising antitumor activity in cell line studies, and some of them have been testing under clinical trials [102-111] (Table 3, 4).

CONCLUSION

In summary, recent studies have identified PTEN as a tumor suppressor gene in various human cancers. It is clear that PTEN is far more than a cytosolic protein that acts as a lipid phosphatase to maintain PIP₃ levels. Therefore, we must reconsider the distinct roles PTEN have in specific subcellular compartments, identify the mechanisms underlying PTEN’s shuttling between different compartments, and investigate the significance of these mechanisms in predicting disease outcome. Future studies will further elucidate the mechanistic basis of PTEN deficiency in lymphoid malignancies, thereby aiding in the clinical management of lymphoid malignancies with PTEN loss or alteration.

Funding

This study was supported by the National Cancer Institute/National Institutes of Health (R01CA138688 and 1RC1CA146299 to KHY). XW is a recipient of hematology and oncology scholarship award. KHY is supported by The University of Texas MD Anderson Cancer Center Lymphoma Moonshot Program and Institutional Research and Development Award, an MD Anderson Cancer Center Lymphoma Specialized Programs on Research Excellence (SPORE) Research Development Program Award, an MD Anderson Cancer Center Myeloma SPORE Research Development Program Award, a Gundersen Lutheran Medical Foundation Award, and partially supported by the National Cancer Institute/National Institutes of Health (P50CA136411 and P50CA142509), and by MD Anderson's Cancer Center Support Grant CA016672.

Author contributions

Conception, design, manuscript writing and final approval of manuscript: XW and KHY.

Conflict of interest statement

KHY receives research support from Roche Molecular System, Gilead Sciences Pharmaceutical, Seattle Genetics, Dai Sanyo Pharmaceutical, Adaptive Biotechnology, Incyte Pharmaceutical and HTG Molecular Diagnostics.

REFERENCES

1. Wang SI, Puc J, Li J, Bruce JN, Cairns P, Sidransky D and Parsons R. Somatic mutations of PTEN in glioblastoma multiforme. *Cancer research*. 1997; 57:4183-4186.
2. Tashiro H, Blazes MS, Wu R, Cho KR, Bose S, Wang SI, Li J, Parsons R and Ellenson LH. Mutations in PTEN are frequent in endometrial carcinoma but rare in other common gynecological malignancies. *Cancer research*. 1997; 57:3935-3940.
3. Rasheed BKA, Stenzel TT, McLendon RE, Parsons R, Friedman AH, Friedman HS, Bigner DD and Bigner SH. PTEN gene mutations are seen in high-grade but not in low-grade gliomas. *Cancer research*. 1997; 57:4187-4190.
4. Wang SI, Parsons R and Ittmann M. Homozygous deletion of the PTEN tumor suppressor gene in a subset of prostate adenocarcinomas. *Clinical Cancer Research*. 1998; 4:811-815.
5. Cairns P, Evron E, Okami K, Halachmi N, Esteller M, Herman JG, Bose S, Wang SI, Parsons R and Sidransky D. Point mutation and homozygous deletion of PTEN/MMAC1 in primary bladder cancers. *Oncogene*. 1998; 16:3215-3218.
6. Nagata Y, Lan KH, Zhou X, Tan M, Esteva FJ, Sahin AA, Klos KS, Li P, Monia BP, Nguyen NT, Hortobagyi GN, Hung MC and Yu D. PTEN activation contributes to tumor inhibition by trastuzumab, and loss of PTEN predicts trastuzumab resistance in patients. *Cancer cell*. 2004; 6:117-127.
7. Berns K, Horlings HM, Hennessy BT, Madiredjo M, Hijmans EM, Beelen K, Linn SC, Gonzalez-Angulo AM, Stenke-Hale K, Hauptmann M, Beijersbergen RL, Mills GB, van de Vijver MJ, et al. A functional genetic approach identifies the PI3K pathway as a major determinant of trastuzumab resistance in breast cancer. *Cancer cell*. 2007; 12:395-402.
8. Trotman LC, Niki M, Dotan ZA, Koutcher JA, Di Cristofano A, Xiao A, Khoo AS, Roy-Burman P, Greenberg NM, Van Dyke T, Cordon-Cardo C and Pandolfi PP. Pten dose dictates cancer progression in the prostate. *PLoS biology*. 2003; 1:385-396.
9. Di Cristofano A, Pesce B, Cordon-Cardo C and Pandolfi PP. Pten is essential for embryonic development and tumour suppression. *Nature genetics*. 1998; 19:348-355.
10. Maehama T and Dixon JE. The tumor suppressor, PTEN/MMAC1, dephosphorylates the lipid second messenger, phosphatidylinositol 3,4,5-trisphosphate. *The Journal of biological chemistry*. 1998; 273:13375-13378.
11. Lee JO, Yang H, Georgescu MM, Di Cristofano A, Maehama T, Shi Y, Dixon JE, Pandolfi P and Pavletich NP. Crystal structure of the PTEN tumor suppressor: implications for its phosphoinositide phosphatase activity and membrane association. *Cell*. 1999; 99:323-334.
12. Denning G, Jean-Joseph B, Prince C, Durden DL and Vogt PK. A short N-terminal sequence of PTEN controls cytoplasmic localization and is required for suppression of cell growth. *Oncogene*. 2007; 26:3930-3940.
13. Leslie NR, Batty IH, Maccario H, Davidson L and Downes CP. Understanding PTEN regulation: PIP2, polarity and protein stability. *Oncogene*. 2008; 27:5464-5476.
14. Guertin DA and Sabatini DM. Defining the role of mTOR in cancer. *Cancer cell*. 2007; 12:9-22.
15. Manning BD and Cantley LC. AKT/PKB signaling: Navigating downstream. *Cell*. 2007; 129:1261-1274.
16. Ma XM and Blenis J. Molecular mechanisms of mTOR-mediated translational control. *Nature reviews Molecular cell biology*. 2009; 10:307-318.
17. Vivanco I, Palaskas N, Tran C, Finn SP, Getz G, Kennedy NJ, Jiao J, Rose J, Xie WL, Loda M, Golub T, Mellinghoff IK, Davis RJ, et al. Identification of the JNK signaling pathway as a functional target of the tumor suppressor PTEN. *Cancer cell*. 2007; 11:555-569.
18. Raftopoulou M, Etienne-Manneville S, Self A, Nicholls S and Hall A. Regulation of cell migration by the C2 domain of the tumor suppressor PTEN. *Science*. 2004; 303:1179-1181.
19. Zhang SY, Huang WC, Li P, Guo H, Poh SB, Brady SW, Xiong Y, Tseng LM, Li SH, Ding ZX, Sahin AA, Esteva FJ, Hortobagyi GN, et al. Combating trastuzumab resistance by targeting SRC, a common node downstream of multiple resistance pathways. *Nature medicine*. 2011; 17:461-U101.
20. Tang Y and Eng C. PTEN autoregulates its expression by stabilization of p53 in a phosphatase-independent manner. *Cancer research*. 2006; 66:736-742.
21. Waite KA and Eng C. Protean PTEN: form and function. *American journal of human genetics*. 2002; 70:829-844.
22. Keniry M and Parsons R. The role of PTEN signaling perturbations in cancer and in targeted therapy. *Oncogene*. 2008; 27:5477-5485.
23. Zhang S and Yu D. PI(3)king apart PTEN's role in cancer. *Clinical cancer research : an official journal of the American Association for Cancer Research*. 2010; 16:4325-4330.

24. Liaw D, Marsh DJ, Li J, Dahia PL, Wang SI, Zheng Z, Bose S, Call KM, Tsou HC, Peacocke M, Eng C and Parsons R. Germline mutations of the PTEN gene in Cowden disease, an inherited breast and thyroid cancer syndrome. *Nature genetics*. 1997; 16:64-67.
25. Sansal I and Sellers WR. The biology and clinical relevance of the PTEN tumor suppressor pathway. *Journal of clinical oncology : official journal of the American Society of Clinical Oncology*. 2004; 22:2954-2963.
26. Chalhoub N and Baker SJ. PTEN and the PI3-kinase pathway in cancer. *Annual review of pathology*. 2009; 4:127-150.
27. Patel L, Pass I, Coxon P, Downes CP, Smith SA and Macphie CH. Tumor suppressor and anti-inflammatory actions of PPARgamma agonists are mediated via upregulation of PTEN. *Current biology : CB*. 2001; 11:764-768.
28. Virolle T, Adamson ED, Baron V, Birle D, Mercola D, Mustelin T and de Belle I. The Egr-1 transcription factor directly activates PTEN during irradiation-induced signalling. *Nature cell biology*. 2001; 3:1124-1128.
29. Stambolic V, MacPherson D, Sas D, Lin Y, Snow B, Jang Y, Benchimol S and Mak TW. Regulation of PTEN transcription by p53. *Molecular cell*. 2001; 8(2):317-325.
30. Gericke A, Munson M and Ross AH. Regulation of the PTEN phosphatase. *Gene*. 2006; 374:1-9.
31. Lau MT, Klausen C and Leung PC. E-cadherin inhibits tumor cell growth by suppressing PI3K/Akt signaling via beta-catenin-Egr1-mediated PTEN expression. *Oncogene*. 2011; 30:2753-2766.
32. Meng X, Wang Y, Zheng X, Liu C, Su B, Nie H, Zhao B, Zhao X and Yang H. shRNA-mediated knockdown of Bmi-1 inhibit lung adenocarcinoma cell migration and metastasis. *Lung cancer*. 2012; 77:24-30.
33. Yoshimi A, Goyama S, Watanabe-Okochi N, Yoshiki Y, Nannya Y, Nitta E, Arai S, Sato T, Shimabe M, Nakagawa M, Imai Y, Kitamura T and Kurokawa M. Evi1 represses PTEN expression and activates PI3K/AKT/mTOR via interactions with polycomb proteins. *Blood*. 2011; 117:3617-3628.
34. Chow JY, Quach KT, Cabrera BL, Cabral JA, Beck SE and Carethers JM. RAS/ERK modulates TGFbeta-regulated PTEN expression in human pancreatic adenocarcinoma cells. *Carcinogenesis*. 2007; 28(11):2321-2327.
35. Vasudevan KM, Burikhanov R, Goswami A and Rangnekar VM. Suppression of PTEN expression is essential for antiapoptosis and cellular transformation by oncogenic ras. *Cancer research*. 2007; 67:10343-10350.
36. Xia DR, Srinivas H, Ahn YH, Sethi G, Sheng XY, Yung WKA, Xia QH, Chiao PJ, Kim H, Brown PH, Wistuba II, Aggarwal BB and Kurie JM. Mitogen-activated protein kinase kinase-4 promotes cell survival by decreasing PTEN expression through an NF kappa B-dependent pathway. *Journal of Biological Chemistry*. 2007; 282:3507-3519.
37. Leslie NR and Foti M. Non-genomic loss of PTEN function in cancer: not in my genes. *Trends in pharmacological sciences*. 2011; 32:131-140.
38. Bartel DP. MicroRNAs: target recognition and regulatory functions. *Cell*. 2009; 136:215-233.
39. Tamguney T and Stokoe D. New insights into PTEN. *J Cell Sci*. 2007; 120):4071-4079.
40. Vazquez F, Ramaswamy S, Nakamura N and Sellers WR. Phosphorylation of the PTEN tail regulates protein stability and function. *Molecular and cellular biology*. 2000; 20:5010-5018.
41. Wang XJ, Trotman LC, Koppie T, Alimonti A, Chen ZB, Gao ZH, Wang JR, Erdjument-Bromage H, Tempst P, Cordon-Cardo C, Pandolfi PP and Jiang XJ. NEDD4-1 is a proto-oncogenic ubiquitin ligase for PTEN. *Cell*. 2007; 128:129-139.
42. Drinjakovic J, Jung H, Campbell DS, Strohlic L, Dwivedy A and Holt CE. E3 ligase Nedd4 promotes axon branching by downregulating PTEN. *Neuron*. 2010; 65:341-357.
43. Georgescu MM, Kirsch KH, Akagi T, Shishido T and Hanafusa H. The tumor-suppressor activity of PTEN is regulated by its carboxyl-terminal region. *Proceedings of the National Academy of Sciences of the United States of America*. 1999; 96:10182-10187.
44. Wu X, Hepner K, Castelino-Prabhu S, Do D, Kaye MB, Yuan XJ, Wood J, Ross C, Sawyers CL and Whang YE. Evidence for regulation of the PTEN tumor suppressor by a membrane-localized multi-PDZ domain containing scaffold protein MAGI-2. *Proceedings of the National Academy of Sciences of the United States of America*. 2000; 97:4233-4238.
45. Vazquez F, Grossman SR, Takahashi Y, Rokas MV, Nakamura N and Sellers WR. Phosphorylation of the PTEN tail acts as an inhibitory switch by preventing its recruitment into a protein complex. *Journal of Biological Chemistry*. 2001; 276:48627-48630.
46. Al-Khoury AM, Ma YL, Togo SH, Williams S and Mustelin T. Cooperative phosphorylation of the tumor suppressor phosphatase and tensin homologue (PTEN) by casein kinases and glycogen synthase kinase 3 beta. *Journal of Biological Chemistry*. 2005; 280:35195-35202.
47. Miller SJ, Lou DY, Seldin DC, Lane WS and Neel BG. Direct identification of PTEN phosphorylation sites. *FEBS letters*. 2002; 528:145-153.
48. Li Z, Dong XM, Wang ZL, Liu WZ, Deng N, Ding Y, Tang LY, Hla T, Zeng R, Li L and Wu DQ. Regulation of PTEN by Rho small GTPases. *Nature cell biology*. 2005; 7:399-U342.
49. Okumura K, Mendoza M, Bachoo RM, DePinho RA, Cavenee WK and Furnari FB. PCAF modulates PTEN activity. *Journal of Biological Chemistry*. 2006; 281:26562-26568.
50. Leslie NR, Bennett D, Lindsay YE, Stewart H, Gray A and Downes CP. Redox regulation of PI 3-kinase signalling via inactivation of PTEN. *Embo J*. 2003; 22:5501-5510.
51. Seo JH, Ahn Y, Lee SR, Yeol Yeo C and Chung Hur K. The major target of the endogenously generated reactive oxygen species in response to insulin stimulation is phosphatase and tensin homolog and not phosphoinositide-3 kinase (PI-3 kinase) in the PI-3 kinase/Akt pathway. *Mol Biol Cell*. 2005; 16:348-357.
52. Fine B, Hodakoski C, Koujak S, Su T, Saal LH, Maurer M, Hopkins B, Keniry M, Sulis ML, Mense S, Hibshoosh H and Parsons R. Activation of the PI3K Pathway in Cancer Through Inhibition of PTEN by Exchange Factor P-REX2a. *Science*. 2009; 325:1261-1265.
53. He L, Ingram A, Rybak AP and Tang D. Shank-interacting protein-like 1 promotes tumorigenesis via PTEN inhibition in human tumor cells. *The Journal of clinical investigation*. 2010; 120:2094-2108.
54. Tang Y and Eng C. p53 down-regulates phosphatase and tensin homologue deleted on chromosome 10 protein stability partially through caspase-mediated degradation in cells with proteasome dysfunction. *Cancer research*. 2006; 66:6139-6148.
55. Mayo LD, Dixon JE, Durden DL, Tonks NK and Donner DB. PTEN protects p53 from Mdm2 and sensitizes cancer cells to chemotherapy. *The Journal of biological chemistry*. 2002; 277:5484-5489.

56. Freeman DJ, Li AG, Wei G, Li HH, Kertesz N, Lesche R, Whale AD, Martinez-Diaz H, Rozengurt N, Cardiff RD, Liu X and Wu H. PTEN tumor suppressor regulates p53 protein levels and activity through phosphatase-dependent and -independent mechanisms. *Cancer cell*. 2003; 3:117-130.
57. Tachibana M, Shibakita M, Ohno S, Kinugasa S, Yoshimura H, Ueda S, Fujii T, Rahman MA, Dhar DK and Nagasue N. Expression and prognostic significance of PTEN product protein in patients with esophageal squamous cell carcinoma. *Cancer*. 2002; 94:1955-1960.
58. Zhou XP, Loukola A, Salovaara R, Nystrom-Lahti M, Peltomaki P, de la Chapelle A, Aaltonen LA and Eng C. PTEN mutational spectra, expression levels, and subcellular localization in microsatellite stable and unstable colorectal cancers. *The American journal of pathology*. 2002; 161:439-447.
59. Fridberg M, Servin A, Anagnostaki L, Linderot J, Berglund M, Soderberg O, Enblad G, Rosen A, Mustelin T, Jerkeman M, Persson JL and Wingren AG. Protein expression and cellular localization in two prognostic subgroups of diffuse large B-cell lymphoma: higher expression of ZAP70 and PKC-beta II in the non-germinal center group and poor survival in patients deficient in nuclear PTEN. *Leuk Lymphoma*. 2007; 48:2221-2232.
60. Gimm O, Perren A, Weng LP, Marsh DJ, Yeh JJ, Ziebold U, Gil E, Hinze R, Delbridge L, Lees JA, Mutter GL, Robinson BG, Komminoth P, et al. Differential nuclear and cytoplasmic expression of PTEN in normal thyroid tissue, and benign and malignant epithelial thyroid tumors. *American Journal of Pathology*. 2000; 156:1693-1700.
61. Perren A, Komminoth P, Saremaslani P, Matter C, Feurer S, Lees JA, Heitz PU and Eng C. Mutation and expression analyses reveal differential subcellular compartmentalization of PTEN in endocrine pancreatic tumors compared to normal islet cells. *The American journal of pathology*. 2000; 157:1097-1103.
62. Ginn-Pease ME and Eng C. Increased nuclear phosphatase and tensin homologue deleted on chromosome 10 is associated with G0-G1 in MCF-7 cells. *Cancer research*. 2003; 63:282-286.
63. Minaguchi T, Waite KA and Eng C. Nuclear localization of PTEN is regulated by Ca²⁺ through a tyrosil phosphorylation-independent conformational modification in major vault protein. *Cancer research*. 2006; 66:11677-11682.
64. Liu FH, Wagner S, Campbell RB, Nickerson JA, Schiffer CA and Ross AH. PTEN enters the nucleus by diffusion. *Journal of cellular biochemistry*. 2005; 96:221-234.
65. Gil A, Andres-Pons A, Fernandez E, Valiente M, Torres J, Cervera J and Pulido R. Nuclear localization of PTEN by a ran-dependent mechanism enhances apoptosis: Involvement of an N-terminal nuclear localization domain and multiple nuclear exclusion motifs. *Mol Biol Cell*. 2006; 17:4002-4013.
66. Trotman LC, Wang X, Alimonti A, Chen Z, Teruya-Feldstein J, Yang H, Pavletich NP, Carver BS, Cordon-Cardo C, Erdjument-Bromage H, Tempst P, Chi SG, Kim HJ, et al. Ubiquitination regulates PTEN nuclear import and tumor suppression. *Cell*. 2007; 128:141-156.
67. Liu JL, Mao Z, LaFortune TA, Alonso MM, Gallick GE, Fueyo J and Yung WKA. Cell cycle-dependent nuclear export of phosphatase and tensin homologue tumor suppressor is regulated by the phosphoinositide-3-kinase signaling cascade. *Cancer research*. 2007; 67:11054-11063.
68. Shen WH, Balajee AS, Wang J, Wu H, Eng C, Pandolfi PP and Yin Y. Essential role for nuclear PTEN in maintaining chromosomal integrity. *Cell*. 2007; 128:157-170.
69. Li AG, Piluso LG, Cai X, Wei G, Sellers WR and Liu X. Mechanistic insights into maintenance of high p53 acetylation by PTEN. *Molecular cell*. 2006; 23:575-587.
70. Gu TT, Zhang Z, Wang JL, Guo JY, Shen WH and Yin YX. CREB Is a Novel Nuclear Target of PTEN Phosphatase. *Cancer research*. 2011; 71:2821-2825.
71. Tanaka K, Horiguchi K, Yoshida T, Takeda M, Fujisawa H, Takeuchi K, Umeda M, Kato S, Ihara S, Nagata S and Fukui Y. Evidence that a phosphatidylinositol 3,4,5-trisphosphate-binding protein can function in nucleus. *Journal of Biological Chemistry*. 1999; 274:3919-3922.
72. Lindsay Y, McCoull D, Davidson L, Leslie NR, Fairservice A, Gray A, Lucocq J and Downes CP. Localization of agonist-sensitive PtdIns(3,4,5)P3 reveals a nuclear pool that is insensitive to PTEN expression. *J Cell Sci*. 2006; 119:5160-5168.
73. Silva A, Yunes JA, Cardoso BA, Martins LR, Jotta PY, Abecasis M, Nowill AE, Leslie NR, Cardoso AA and Barata JT. PTEN posttranslational inactivation and hyperactivation of the PI3K/Akt pathway sustain primary T cell leukemia viability. *The Journal of clinical investigation*. 2008; 118:3762-3774.
74. Palomero T, Sulis ML, Cortina M, Real PJ, Barnes K, Ciofani M, Caparros E, Buteau J, Brown K, Perkins SL, Bhagat G, Agarwal AM, Basso G, et al. Mutational loss of PTEN induces resistance to NOTCH1 inhibition in T-cell leukemia. *Nat Med*. 2007; 13:1203-1210.
75. Larson Gedman A, Chen Q, Kugel Desmoulin S, Ge Y, LaFiura K, Haska CL, Cherian C, Devidas M, Linda SB, Taub JW and Matherly LH. The impact of NOTCH1, FBW7 and PTEN mutations on prognosis and downstream signaling in pediatric T-cell acute lymphoblastic leukemia: a report from the Children's Oncology Group. *Leukemia*. 2009; 23:1417-1425.
76. Gutierrez A, Sanda T, Grebliunaite R, Carracedo A, Salmena L, Ahn Y, Dahlberg S, Neuberg D, Moreau LA, Winter SS, Larson R, Zhang J, Protopopov A, et al. High frequency of PTEN, PI3K, and AKT abnormalities in T-cell acute lymphoblastic leukemia. *Blood*. 2009; 114:647-650.
77. Liu X, Karnell JL, Yin B, Zhang R, Zhang J, Li P, Choi Y, Maltzman JS, Pear WS, Bassing CH and Turka LA. Distinct roles for PTEN in prevention of T cell lymphoma and autoimmunity in mice. *The Journal of clinical investigation*. 2010; 120:2497-2507.
78. Bonneau D and Longy M. Mutations of the human PTEN gene. *Human mutation*. 2000; 16:109-122.
79. Gronbaek K, Zeuthen J, Guldberg P, Ralfkiaer E and Hou-Jensen K. Alterations of the MMAC1/PTEN gene in lymphoid malignancies. *Blood*. 1998; 91:4388-4390.
80. Dahia PL, Aguiar RC, Alberta J, Kum JB, Caron S, Sill H, Marsh DJ, Ritz J, Freedman A, Stiles C and Eng C. PTEN is inversely correlated with the cell survival factor Akt/PKB and is inactivated via multiple mechanisms in haematological malignancies. *Human molecular genetics*. 1999; 8:185-193.
81. Nakahara Y, Nagai H, Kinoshita T, Uchida T, Hatano S, Murate T and Saito H. Mutational analysis of the PTEN/MMAC1 gene in non-Hodgkin's lymphoma. *Leukemia*. 1998; 12:1277-1280.
82. Sakai A, Thieblemont C, Wellmann A, Jaffe ES and Raffeld M. PTEN gene alterations in lymphoid neoplasms. *Blood*. 1998; 92:3410-3415.
83. Butler MP, Wang SI, Chaganti RS, Parsons R and Dalla-Favera R. Analysis of PTEN mutations and deletions in B-cell non-Hodgkin's lymphomas. *Genes, chromosomes & cancer*. 1999; 24:322-327.

84. Lenz G, Wright GW, Emre NC, Kohlhammer H, Dave SS, Davis RE, Carty S, Lam LT, Shaffer AL, Xiao W, Powell J, Rosenwald A, Ott G, et al. Molecular subtypes of diffuse large B-cell lymphoma arise by distinct genetic pathways. *Proceedings of the National Academy of Sciences of the United States of America*. 2008; 105:13520-13525.
85. Pfeifer M and Lenz G. PI3K/AKT addiction in subsets of diffuse large B-cell lymphoma. *Cell cycle*. 2013; 12:3347-3348.
86. Rudelius M, Pittaluga S, Nishizuka S, Pham TH, Fend F, Jaffe ES, Quintanilla-Martinez L and Raffeld M. Constitutive activation of Akt contributes to the pathogenesis and survival of mantle cell lymphoma. *Blood*. 2006; 108:1668-1676.
87. Battistella M, Romero M, Castro-Vega LJ, Gapihan G, Bouhidel F, Bagot M, Feugeas JP and Janin A. The High Expression of the microRNA 17-92 Cluster and its Paralogs, and the Down-Regulation of the Target Gene PTEN are Associated with Primary Cutaneous B-cell Lymphoma Progression. *The Journal of investigative dermatology*. 2015; 135:1659-1667.
88. Samuels Y, Wang Z, Bardelli A, Silliman N, Ptak J, Szabo S, Yan H, Gazdar A, Powell SM, Riggins GJ, Willson JK, Markowitz S, Kinzler KW, et al. High frequency of mutations of the PIK3CA gene in human cancers. *Science*. 2004; 304:554.
89. Abubaker J, Bavi P, Al-Harbi S, Siraj A, Al-Dayel F, Uddin S and Al-Kuraya K. PIK3CA mutations are mutually exclusive with PTEN loss in diffuse large B-cell lymphoma. *Leukemia*. 2007; 21:2368-2370.
90. Knight ZA, Gonzalez B, Feldman ME, Zunder ER, Goldenberg DD, Williams O, Loewith R, Stokoe D, Balla A, Toth B, Balla T, Weiss WA, Williams RL, et al. A pharmacological map of the PI3-K family defines a role for p110 alpha in insulin signaling. *Cell*. 2006; 125:733-747.
91. Jia SD, Liu ZN, Zhang S, Liu PX, Zhang L, Lee SH, Zhang J, Signoretti S, Loda M, Roberts TM and Zhao JJ. Essential roles of PI(3)K-p110 beta in cell growth, metabolism and tumorigenesis. *Nature*. 2008; 454:776-U102.
92. Edgar KA, Wallin JJ, Berry M, Lee LB, Prior WW, Sampath D, Friedman LS and Belvin M. Isoform-Specific Phosphoinositide 3-Kinase Inhibitors Exert Distinct Effects in Solid Tumors. *Cancer research*. 2010; 70:1164-1172.
93. Weigelt B, Warne PH, Lambros MB, Reis-Filho JS and Downward J. PI3K pathway dependencies in endometrioid endometrial cancer cell lines. *Clin Cancer Res*. 2013; 19:3533-3544.
94. Davis RE, Ngo VN, Lenz G, Tolar P, Young RM, Romesser PB, Kohlhammer H, Lamy L, Zhao H, Yang Y, Xu W, Shaffer AL, Wright G, et al. Chronic active B-cell-receptor signalling in diffuse large B-cell lymphoma. *Nature*. 2010; 463:88-92.
95. Kloo B, Nagel D, Pfeifer M, Grau M, Duwel M, Vincendeau M, Dorken B, Lenz P, Lenz G and Krappmann D. Critical role of PI3K signaling for NF-kappaB-dependent survival in a subset of activated B-cell-like diffuse large B-cell lymphoma cells. *Proceedings of the National Academy of Sciences of the United States of America*. 2011; 108:272-277.
96. Chen L, Juszczynski P, Takeyama K, Aguiar RC and Shipp MA. Protein tyrosine phosphatase receptor-type O truncated (PTPROt) regulates SYK phosphorylation, proximal B-cell-receptor signaling, and cellular proliferation. *Blood*. 2006; 108:3428-3433.
97. Chen LF, Monti S, Juszczynski P, Daley J, Chen W, Witzig TE, Habermann TM, Kutok JL and Shipp MA. SYK-dependent tonic B-cell receptor signaling is a rational treatment target in diffuse large B-cell lymphoma. *Blood*. 2008; 111:2230-2237.
98. Li B, Sun A, Jiang W, Thrasher JB and Terranova P. PI-3 kinase p110beta: a therapeutic target in advanced prostate cancers. *Am J Clin Exp Urol*. 2014; 2:188-198.
99. Schwartz S, Wongvipat J, Trigwell CB, Hancox U, Carver BS, Rodrik-Outmezguine V, Will M, Yellen P, de Stanchina E, Baselga J, Scher HI, Barry ST, Sawyers CL, et al. Feedback Suppression of PI3K alpha Signaling in PTEN-Mutated Tumors Is Relieved by Selective Inhibition of PI3K beta. *Cancer cell*. 2015; 27:109-122.
100. Subramaniam PS, Whye DW, Efimenko E, Chen J, Tosello V, De Keersmaecker K, Kashishian A, Thompson MA, Castillo M, Cordon-Cardo C, Dave UP, Ferrando A, Lannutti BJ, et al. Targeting Nonclassical Oncogenes for Therapy in T-ALL. *Cancer cell*. 2012; 21:459-472.
101. Lonetti A, Cappellini A, Sparta AM, Chiarini F, Buontempo F, Evangelisti C, Evangelisti C, Orsini E, McCubrey JA and Martelli AM. PI3K pan-inhibition impairs more efficiently proliferation and survival of T-cell acute lymphoblastic leukemia cell lines when compared to isoform-selective PI3K inhibitors. *Oncotarget*. 2015; 6:10399-10414. DOI: 10.18632/oncotarget.3295.
102. Hancox U, Cosulich S, Hanson L, Trigwell C, Lenaghan C, Ellston R, Dry H, Crafter C, Barlaam B, Fitzek M, Smith PD, Ogilvie D, D'Cruz C, et al. Inhibition of PI3Kbeta signaling with AZD8186 inhibits growth of PTEN-deficient breast and prostate tumors alone and in combination with docetaxel. *Mol Cancer Ther*. 2015; 14:48-58.
103. Tanaka H, Yoshida M, Tanimura H, Fujii T, Sakata K, Tachibana Y, Ohwada J, Ebiike H, Kuramoto S, Morita K, Yoshimura Y, Yamazaki T, Ishii N, et al. The selective class I PI3K inhibitor CH5132799 targets human cancers harboring oncogenic PIK3CA mutations. *Clinical cancer research : an official journal of the American Association for Cancer Research*. 2011; 17:3272-3281.
104. Garlich JR, De P, Dey N, Su JD, Peng X, Miller A, Murali R, Lu Y, Mills GB, Kundra V, Shu HK, Peng Q and Durden DL. A vascular targeted pan phosphoinositide 3-kinase inhibitor prodrug, SF1126, with antitumor and antiangiogenic activity. *Cancer research*. 2008; 68:206-215.
105. Qian C, Lai CJ, Bao R, Wang DG, Wang J, Xu GX, Atoyan R, Qu H, Yin L, Samson M, Zifcak B, Ma AW, DellaRocca S, et al. Cancer network disruption by a single molecule inhibitor targeting both histone deacetylase activity and phosphatidylinositol 3-kinase signaling. *Clinical cancer research : an official journal of the American Association for Cancer Research*. 2012; 18:4104-4113.
106. Hirai H, Sootome H, Nakatsuru Y, Miyama K, Taguchi S, Tsujioka K, Ueno Y, Hatch H, Majumder PK, Pan BS and Kotani H. MK-2206, an allosteric Akt inhibitor, enhances antitumor efficacy by standard chemotherapeutic agents or molecular targeted drugs in vitro and in vivo. *Molecular cancer therapeutics*. 2010; 9:1956-1967.
107. Baselga J, Campone M, Piccart M, Burris HA, 3rd, Rugo HS, Sahmoud T, Noguchi S, Gnant M, Pritchard KI, Lebrun F, Beck JT, Ito Y, Yardley D, et al. Everolimus in postmenopausal hormone-receptor-positive advanced breast cancer. *The New England journal of medicine*. 2012; 366:520-529.
108. Elit L. CCI-779 Wyeth. *Curr Opin Investig Drugs*. 2002; 3:1249-1253.
109. Reynolds CP, Kang MH, Carol H, Lock R, Gorlick R, Kolb EA, Kurmasheva RT, Keir ST, Maris JM, Billups CA, Houghton PJ and

Smith MA. Initial testing (stage 1) of the phosphatidylinositol 3' kinase inhibitor, SAR245408 (XL147) by the pediatric preclinical testing program. *Pediatric blood & cancer*. 2013; 60:791-798.

110. Furet P, Guagnano V, Fairhurst RA, Imbach-Weese P, Bruce I, Knapp M, Fritsch C, Blasco F, Blanz J, Aichholz R, Hamon J, Fabbro D and Caravatti G. Discovery of NVP-BYL719 a potent and selective phosphatidylinositol-3 kinase alpha inhibitor selected for clinical evaluation. *Bioorg Med Chem Lett*. 2013; 23:3741-3748.

111. Hall CP, Reynolds CP and Kang MH. Modulation of glucocorticoid resistance in pediatric T-cell Acute Lymphoblastic Leukemia by increasing BIM expression with the PI3K/mTOR inhibitor BEZ235. *Clinical cancer research: an official journal of the American Association for Cancer Research*. 2015; in press.

112. Yang Y, Yang JJ, Tao H and Jin WS. MicroRNA-21 controls hTERT via PTEN in human colorectal cancer cell proliferation. *Journal of physiology and biochemistry*. 2015; 71:59-68.

113. Yang X, Cheng Y, Li P, Tao J, Deng X, Zhang X, Gu M, Lu Q and Yin C. A lentiviral sponge for miRNA-21 diminishes aerobic glycolysis in bladder cancer T24 cells via the PTEN/PI3K/AKT/mTOR axis. *Tumour biology : the journal of the International Society for Oncodevelopmental Biology and Medicine*. 2015; 36:383-391.

114. Meng F, Henson R, Wehbe-Janek H, Ghoshal K, Jacob ST and Patel T. MicroRNA-21 regulates expression of the PTEN tumor suppressor gene in human hepatocellular cancer. *Gastroenterology*. 2007; 133:647-658.

115. Calin GA, Liu CG, Sevignani C, Ferracin M, Felli N, Dumitru CD, Shimizu M, Cimmino A, Zupo S, Dono M, Dell'Aquila ML, Alder H, Rassenti L, et al. MicroRNA profiling reveals distinct signatures in B cell chronic lymphocytic leukemias. *Proceedings of the National Academy of Sciences of the United States of America*. 2004; 101:11755-11760.

116. Tian L, Fang YX, Xue JL and Chen JZ. Four microRNAs promote prostate cell proliferation with regulation of PTEN and its downstream signals in vitro. *PLoS one*. 2013; 8:e75885.

117. Palacios F, Prieto D, Abreu C, Ruiz S, Morande P, Fernandez-Calero T, Libisch G, Landoni AI and Oppezio P. Dissecting chronic lymphocytic leukemia microenvironment signals in patients with unmutated disease: microRNA-22 regulates phosphatase and tensin homolog/AKT/FOXO1 pathway in proliferative leukemic cells. *Leukemia & lymphoma*. 2015:1-6.

118. Yan SY, Chen MM, Li GM, Wang YQ and Fan JG. MiR-32 induces cell proliferation, migration, and invasion in hepatocellular carcinoma by targeting PTEN. *Tumour biology: the journal of the International Society for Oncodevelopmental Biology and Medicine*. 2015; 36:4747-4755.

119. Ohta K, Hoshino H, Wang J, Ono S, Iida Y, Hata K, Huang SK, Colquhoun S and Hoon DS. MicroRNA-93 activates c-Met/PI3K/Akt pathway activity in hepatocellular carcinoma by directly inhibiting PTEN and CDKN1A. *Oncotarget*. 2015; 6:3211-3224. DOI: 10.18632/oncotarget.3085.

120. Yang YK, Xi WY, Xi RX, Li JY, Li Q and Gao YE. MicroRNA494 promotes cervical cancer proliferation through the regulation of PTEN. *Oncology reports*. 2015; 33:2393-2401.

121. Yu TT, Cao RS, Li S, Fu MG, Ren LH, Chen WX, Zhu H, Zhan Q and Shi RH. MiR-130b plays an oncogenic role by repressing PTEN expression in esophageal squamous cell carcinoma cells. *BMC cancer*. 2015; 15:29.

122. Xiang SJ, Fang JQ, Wang SY, Deng B and Zhu L. MicroRNA-135b regulates the stability of PTEN and promotes glycolysis by

targeting USP13 in human colorectal cancers. *Oncology reports*. 2015; 33:1342-1348.

123. Yang H, Kong W, He L, Zhao JJ, O'Donnell JD, Wang J, Wenham RM, Coppola D, Kruk PA, Nicosia SV and Cheng JQ. MicroRNA expression profiling in human ovarian cancer: miR-214 induces cell survival and cisplatin resistance by targeting PTEN. *Cancer research*. 2008; 68:425-433.

124. Zang C, Eucker J, Liu H, Coordes A, Lenarz M, Possinger K and Scholz CW. Inhibition of pan-class I phosphatidylinositol-3-kinase by NVP-BKM120 effectively blocks proliferation and induces cell death in diffuse large B-cell lymphoma. *Leuk Lymphoma*. 2014; 55:425-434.

The p53 tumor suppressor protein protects against chemotherapeutic stress and apoptosis in human medulloblastoma cells

Sarah Wayne^{1#}, Aisha Naeem^{1#}, Muhammad Umer Choudhry^{1#}, Erika Parasido¹, Lucas Tricoli¹, Angiela Sivakumar¹, John P. Mikhael¹, Venkata Yenugonda¹, Olga C. Rodriguez¹, Sana D. Karam², Brian R. Rood³, Maria Laura Avantaggiati^{1*}, and Chris Albanese^{1,4,*}

¹Lombardi Comprehensive Cancer Center and Department of Oncology, Georgetown University Medical Center, Washington, DC 20057, USA;

²Department of Radiation Oncology, University of Colorado, Denver, CO 80208, USA;

³Center for Cancer and Immunology Research, Children's National Medical Center, Washington, DC 20057, USA;

⁴Department of Pathology, Georgetown University Medical Center, Washington, DC 20057, USA.

[#]These authors contributed equally

^{*}Equal Senior Author Contributions

Key words: p53, apoptosis, autophagy, medulloblastoma, Endonuclease G, BIK, p63, p73

Received: 08/30/15; **Accepted:** 10/02/15; **Published:** 10/27/15

Correspondence to: Chris Albanese, PhD; **E-mail:** albanese@georgetown.edu

Copyright: Wayne et al. This is an open-access article distributed under the terms of the Creative Commons Attribution License, which permits unrestricted use, distribution, and reproduction in any medium, provided the original author and source are credited

Abstract: Medulloblastoma (MB), a primitive neuroectodermal tumor, is the most common malignant childhood brain tumor and remains incurable in about a third of patients. Currently, survivors carry a significant burden of late treatment effects. The p53 tumor suppressor protein plays a crucial role in influencing cell survival in response to cellular stress and while the p53 pathway is considered a key determinant of anti-tumor responses in many tumors, its role in cell survival in MB is much less well defined. Herein, we report that the experimental drug VMY-1-103 acts through induction of a partial DNA damage-like response as well induction of non-survival autophagy. Surprisingly, the genetic or chemical silencing of p53 significantly enhanced the cytotoxic effects of both VMY and the DNA damaging drug, doxorubicin. The inhibition of p53 in the presence of VMY revealed increased late stage apoptosis, increased DNA fragmentation and increased expression of genes involved in apoptosis, including *CAPN12* and *TRPM8*, *p63*, *p73*, *BIK*, *EndoG*, *CIDEB*, *P27^{Kip1}* and *P21^{Cip1}*. These data provide the groundwork for additional studies on VMY as a therapeutic drug and support further investigations into the intriguing possibility that targeting p53 function may be an effective means of enhancing clinical outcomes in MB.

INTRODUCTION

Medulloblastoma (MB) is a primitive neuroectodermal tumor that arises from granule neuron precursors in the cerebellum or from neural stem cells of the rhombic lip and is the most frequently diagnosed malignant brain tumor in children [1]. Approximately 70% of MB cases occur in children under the age of 10. While less common, MB is also seen in patients between 20 and 44 years of age, with incidences falling off significantly thereafter. A combination of surgery, radiotherapy, and

chemotherapy has contributed to improved treatment outcomes, resulting in a 70-80% five-year disease-free patients with medulloblastoma remain significant and recurrence is frequently observed. As with many malignancies, disease recurrence is nearly always fatal, and late mortality remains a serious health issue in long-term MB survivors [2]. Moreover, current therapies result in significant negative impacts on neurological, cognitive and social development, especially in the youngest affected children. Significant efforts are therefore underway to develop more effective and less toxic MB treatments.

The efficacy of many anti-tumor agents relies on their ability to trigger the tumor suppressive activities of p53, which leads to the induction of cell death, frequently via cellular pathways of apoptosis, senescence or mitotic catastrophe. While the activity of the p53 tumor suppressor protein is highly complex [3], its expression is induced by a broad array of cell stressors including DNA-damaging chemotherapeutic drugs and can be an excellent target for therapeutic intervention ([4], see also [3]). Impairment of p53 signaling by gene mutation or gene silencing/loss has been shown to contribute to the induction, progression and/or recurrence of many tumor types and can confer resistance to tumor therapy. p53 plays unique roles in neural development. For example, p53 has been directly implicated in neurogenesis as well as in neural stem cell self-renewal, neurite outgrowth and axonal regeneration (reviewed in [5]), and acetylation of p53 is required for the induction of neurite outgrowth [6]. Despite this knowledge and that related to the role of p53 in many malignancies, the function of p53 in MB remains under-explored. For example, unlike lung, pancreas and bladder cancers, only a minority of primary MB patients present with p53 mutation or loss, with reported frequencies between 7% [7] and 15% [8]. Interestingly, while the frequency of p53 mutations increases upon recurrence, the percentage of cells with nuclear p53 also increases, rising from 26% at diagnosis to 33% at relapse [8], suggesting that certain mechanisms underlying p53 function may still be intact. Importantly, the MAGIC consortium identified chromosome 17 deletions, where the p53 locus is located, to be associated with chromothripsis (chromosomal fragmentation) in Group 3 MB [9], while reduced expression of p53 was seen in Group 4 MB [10]. Collectively, these findings highlight the complex and poorly defined role for p53 in human MB, and support the need for mechanistic studies into p53 activity as a possible therapeutic effector protein.

The *in vitro* [11-13] and *in vivo* [14] anti-tumor activities of an experimental CDK inhibitor, VMY-1-103 (VMY), have previously been described by us in both prostate and other solid tumors [11, 13, 15] and in MB [12, 14]. Our previous MB studies established that the extrinsic apoptotic pathway was induced by VMY, as was mitotic catastrophe in a subset of the cells [12]. In the present study, we sought to further define the molecular and genetic mechanisms by which VMY induces MB cell death. Herein, we show in both p53-wild type (D556) and p53-mutant (DAOY) MB cell lines that treatment with VMY resulted in the translocation of p53 into the nucleus, an induction of γ H2AX, a decrease in MDM2 protein levels and activation of non-survival macro-autophagy.

Interestingly, suppression of p53 function via shRNA knockdown or treatment with the p53 inhibitory compound Pifithrin- α (Pif) [16] resulted in significant increases in cell death following treatment with either VMY or doxorubicin. Gene expression analyses performed on D556 cells treated with VMY and Pif versus VMY alone revealed a significant increase in genes associated with apoptosis and necrosis, including the calcium pathway signaling genes *CAPN12* and *TRPM8* suggesting alterations in intracellular calcium signaling may play a role in enhancing cell death. In addition, p63 and its transcriptional target the pro-apoptotic gene *BIK* were induced, as were p73 and its target, the caspase-independent intranucleosomal DNase, *Endonuclease-G* (Endo-G) [17].

Given the difficulties in effectively treating MB, especially recurrent disease, targeting p53 in combination with chemotherapy potentially represents a new treatment strategy for medulloblastoma.

RESULTS

Treatment of MB cells induces a durable cytotoxic effect

We have previously reported that VMY induces MB cell death [12, 14]. To test whether VMY's antiproliferative effects were sustained after removal of the compound, colony forming assays were performed. D556 cells were treated with VMY or its parent compound purvalanol B (PVB) for 18 hrs, at which point the media was changed and the cells were allowed to recover in the absence of the drugs until the control plate reached 80% confluency (approximately 3-5 days). VMY treatment resulted in a significant reduction in both the number of colonies (Fig 1A, B, C) as well as the number of cells per colony (Fig 1D) versus either DMSO- or PVB- treated D556 cells, which express wild type p53. The DNA damaging drug, doxorubicin (1 μ M), effectively killed all cells (not shown).

VMY induces a partial DNA damage-like response in DAOY and D556 MB cell lines

Our previous studies established that the induction of cell death in MB cells occurred, at least in part, through the extrinsic apoptotic pathway and mitotic disruption [12, 14]. To further investigate the mechanisms by which VMY impacts cell survival, we interrogated proteins involved in DNA damage response and stress signaling. Time course studies of VMY treatment were performed first in DAOY cells, which express mutant p53 (p53^{C252F}). Doxorubicin was used as a positive control for induction of a DNA damage response [18],

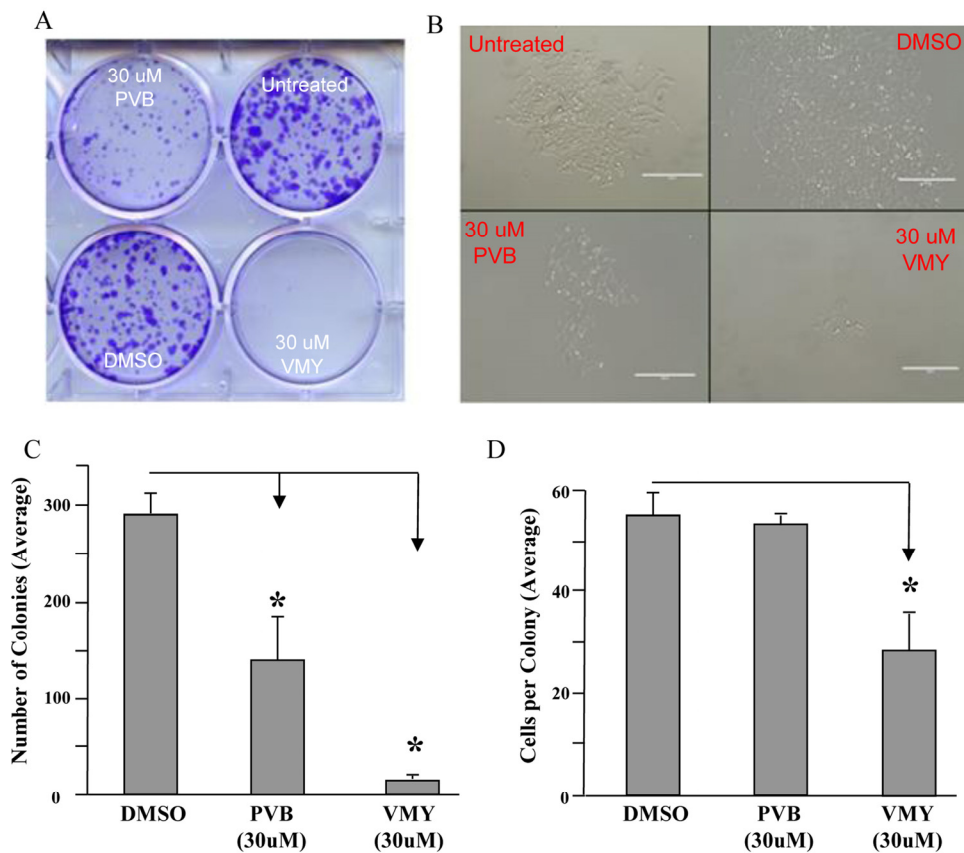


Figure 1. VMY induced cell death. The durability of effects of VMY on cell viability was determined via colony forming assays. D556 cells were treated with DMSO, PVB or VMY for 18 hrs. Fresh media was added and the cells cultured for an additional 3-5 days. (A) Cells stained with crystal violet. (B) Colonies as visualized by microscopy. (C) Quantification of colony number. (D) Quantification of cells per colony. The data are shown as average \pm standard deviation. PVB; purvalanol B, *; $p < 0.05$.

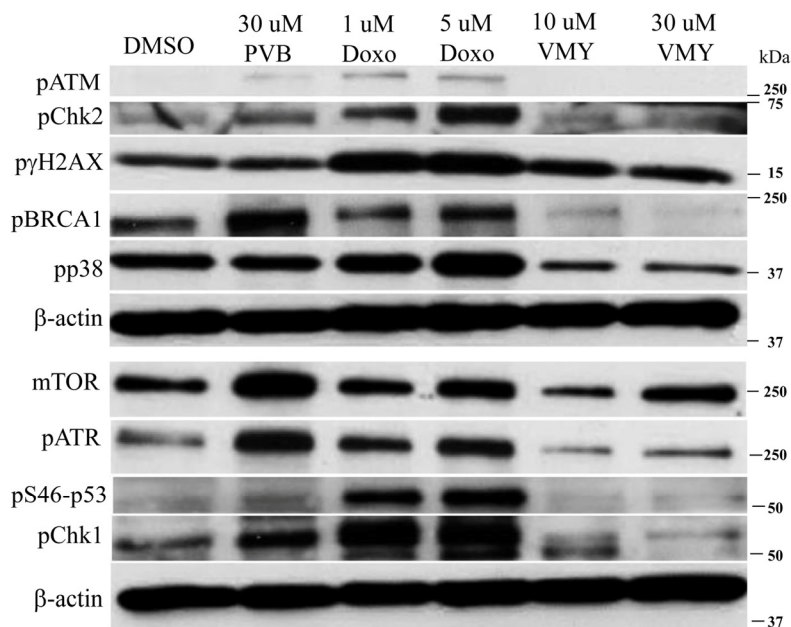


Figure 2. Effects of VMY on stress related proteins. DAOY cells were treated for 18 hrs with DMSO, PVB, VMY or doxorubicin at the concentrations listed and immunoblotting was performed for the proteins shown. β -actin was used as a loading control. PVB; purvalanol B, Doxo; doxorubicin.

and PVB was also tested. Compared to DMSO control, treatment with doxorubicin for 18 hours increased the levels of phosphorylated isoforms of ATM, Chk2, γ H2AX, BRCA1 and p38 (Fig. 2) as well as ATR, pS46-p53 and Chk1 (Fig 2). A modest increase in mTOR was also noted. In contrast, the levels of all of these proteins, with the exception of p- γ H2AX (Fig 2) and to a lesser extent mTOR, were reduced following treatment with VMY. Interestingly, PVB behaved in a

manner similar to doxorubicin despite the fact that PVB is an inefficient inhibitor of MB cell proliferation [12]. In contrast to DAOY cells, the levels of total- and phospho- p38 remained relatively constant in D556 cells and phospho-p38 decreased slightly following 18 hrs of VMY treatment (Fig 3A), however sustained induction of γ H2AX was confirmed by western blot and by immunofluorescence in both DAOY and D556 cells (Fig 3A, B).

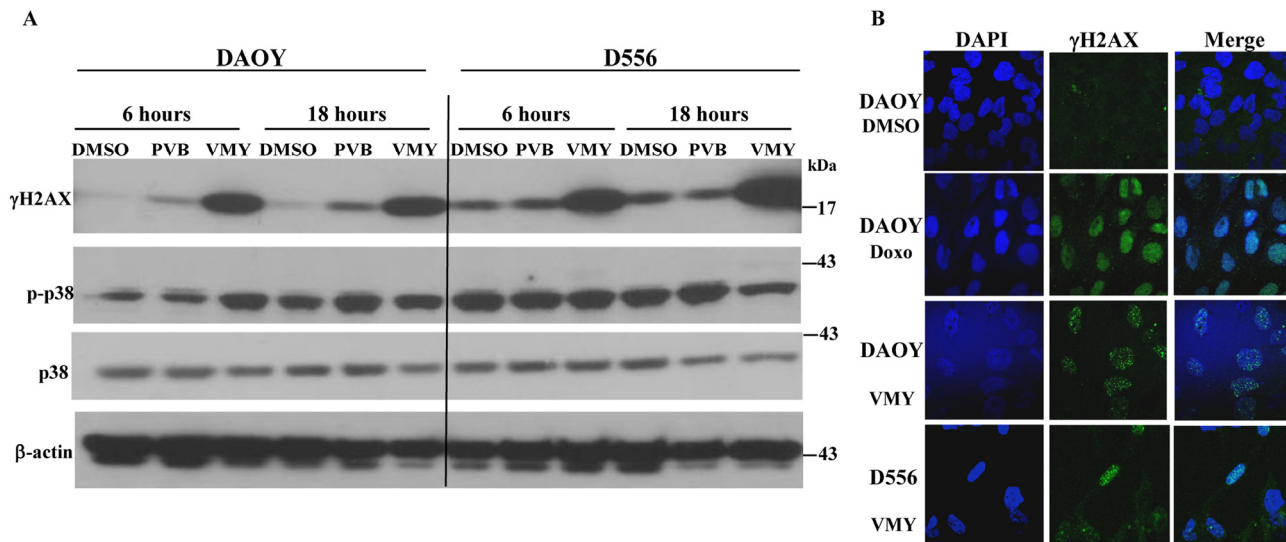


Figure 3. Effects of VMY on stress related proteins in MB cells. DAOY and D556 cells were treated with PVB or VMY. (A) Immunoblotting was performed for total and phosphorylated p38 and phosphorylated γ -H2AX following treatment for 6 or 18 hrs. (B) Immunofluorescence microscopy for γ -H2AX was performed on DAOY cells treated with 1 μ M doxorubicin for 18 hrs and DAOY and D556 cells treated with 10 μ M VMY for 18 hrs. DAPI was used to stain the nuclei. PVB; purvalanol B, Doxo; doxorubicin.

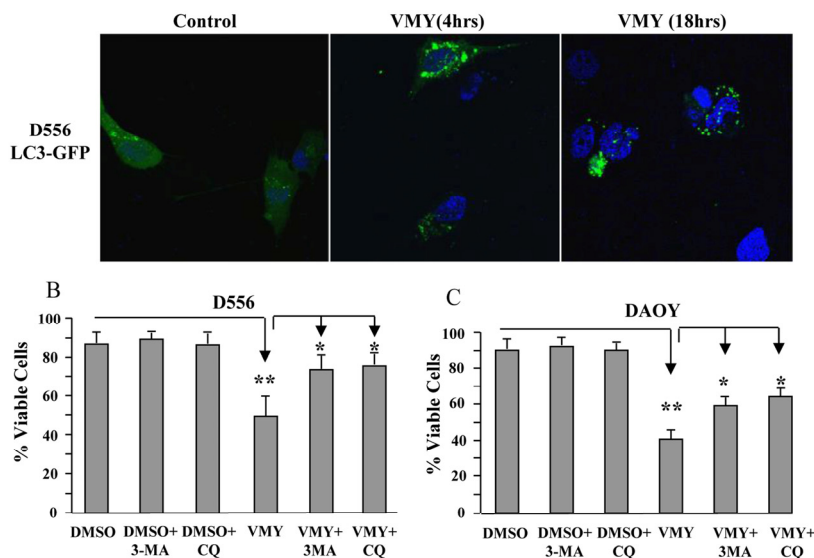


Figure 4. Induction of Autophagy by VMY reduces cell viability. (A) D556 cells, transfected with LC3-GFP, were treated with DMSO or VMY for 4 and 18 hrs. Autophagic LC3-GFP puncta were visualized by fluorescence microscopy. Cell nuclei were stained with DAPI. (B) D556 and (C) DAOY cells were treated with VMY for 18hrs in the presence or absence of 5 μ M 3-MA (an inhibitor of early autophagy) or 50 μ M chloroquine (an inhibitor of acidification of lysosomes and autophagosomes), and trypan blue viability assays were performed to establish cell viability. The data are shown as the average \pm standard deviation of N=3 separate experiments. *, $p < 0.05$, **, $p < 0.01$, 3-MA; 3-methyladenine, CQ; chloroquine.

VMY induces autophagy in MB cells

VMY has the ability to block proliferation in prostate cancer cells in part through the induction of catastrophic autophagy [15]. During autophagy, LC3-I (microtubule-associated protein 1 light chain 3) becomes lipidated by the class III phosphoinositide 3-kinase, Vps34, and re-localizes from the microtubules to autophagosomal membranes (reviewed in Kang, et al. [19]). We therefore studied the pattern of subcellular localization of LC3-I in MB cells. D556 cells were transiently transfected with an LC3-GFP expression vector and subjected to fluorescence microscopy as previously described [15]. VMY treatment induced LC3-GFP re-localization and concentration into prototypical autophagic puncta (Fig 4A) with an average of 6 puncta per VMY-treated, LC3-GFP positive cell at 4 hours and 7.8 puncta per cell at 18 hrs, versus an average of 2.3 puncta per cell in control cells (Fig 4A). Our previous data established that inhibition of autophagy protected against VMY-induced cell death in prostate cancer cells [15]. We therefore investigated whether inhibitors of early (3-methyladenine, 3-MA) or late (chloroquine, CQ) autophagy influenced cell survival. Using D556 and DAOY cells, trypan blue dye exclusion assays established that neither 3-MA nor CQ influenced survival in control cells, however significant increases ($p < 0.05$, $N = 3$ separate experiments) in cell viability were seen in both cell lines when treated with VMY and the inhibitors (Fig 4B, C).

Regulation of p53 activity is similar in DAOY and D556 MB cell lines

Our earlier investigations into the mechanisms by which VMY reduced overall cell survival in solid tumors clearly established a role for wild type p53 in inducing cell death through both apoptosis and catastrophic autophagy. For example, in adenocarcinoma cell lines with wild type p53, VMY caused a rapid induction of p53 protein levels whereas p53 levels remained constant in cells harboring p53 mutations [15]. Furthermore, the loss of p53 function via deletion, mutation or genetic silencing resulted in a complete loss of VMY-induced cytotoxicity in a variety of cancers, including prostate, breast and pancreas, while re-expression of wild type p53 in PC3 cells or treatment of DU145 cells with PRIMA1 restored VMY-induced autophagy and cell death [11, 15].

We therefore next investigated the effects of VMY on p53 expression in DAOY (p53 C242F mutant [20]) and D556 cells (p53 wild type). Unlike our previous findings in adenocarcinoma cells, p53 levels were high in both cell lines and were not affected by treatment with VMY (Supplemental Fig. 1). Similar results were seen with PVB (Supplemental Fig. 1). The levels of the p53-regulatory protein MDM2 were decreased in both cell lines (Fig 5A) and immunofluorescence microscopy demonstrated that p53 shifted from diffusely cytoplasmic with some nuclear positivity in control cells to

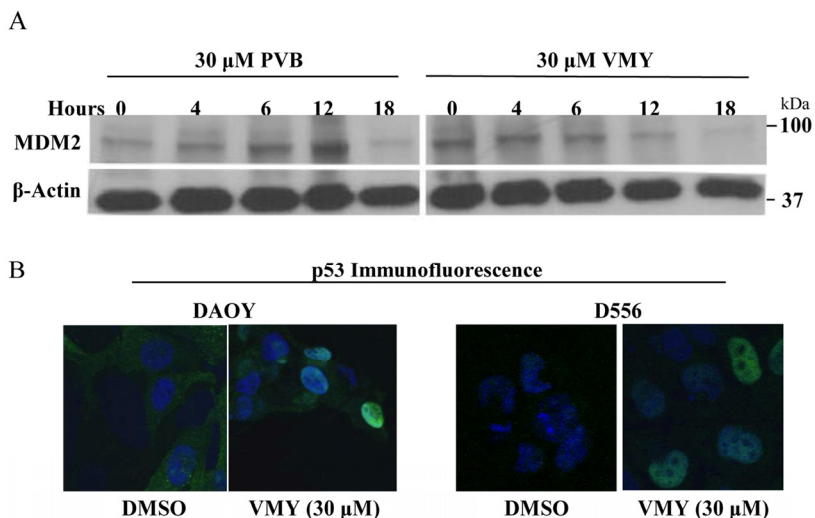


Figure 5. VMY alters the subcellular localization of p53. (A) Immunoblotting for MDM2 following exposure of D556 cells to PVB and VMY for the times indicated. β -actin was used as a loading control. (B) Immunofluorescence microscopy for p53 subcellular localization was performed on DAOY (left panels) and D556 (right panels). DAPI was used to stain the nuclei. PVB; purvalanol B.

predominantly nuclear in both cell lines following VMY treatment (Fig 5B). As both the wild type and mutant p53 proteins localize to the nucleus following exposure to VMY, these data suggest that both proteins may retain some functional activity.

The role of p53 in inducing cell death

To determine the role of p53 in regulating MB cell survival in the presence of VMY, p53 was genetically silenced with the previously validated p53 shRNA [15] or chemically inhibited by the p53-inhibitory compound, Pifithrin- α (Pif), which we have used in previous experiments to investigate p53's role in regulating autophagy [16]. The silencing of p53 by shRNA resulted

in up to a 68% decrease in p53 protein levels versus pLKO control across all treatment groups in both D556 and DAOY cells (Fig 6A). Surprisingly, both the genetic and chemical silencing of p53 led to significant increases in cell death by VMY as measured by colony forming assay (Fig 6B). Equally surprising was the observation that the loss of p53 failed to protect against cell death by doxorubicin (Fig 6B, C). Dose escalation experiments performed in D556 cells in the presence and absence of Pif established that the heightened chemosensitivity was consistent across a broad range of concentrations (Fig 6D). In addition, experiments performed in DAOY showed that cell-survival declined by 33 percent in VMY-treated cells with p53 shRNA knockdown compared to VMY-treated pLKO control cells (Sup Fig S2).

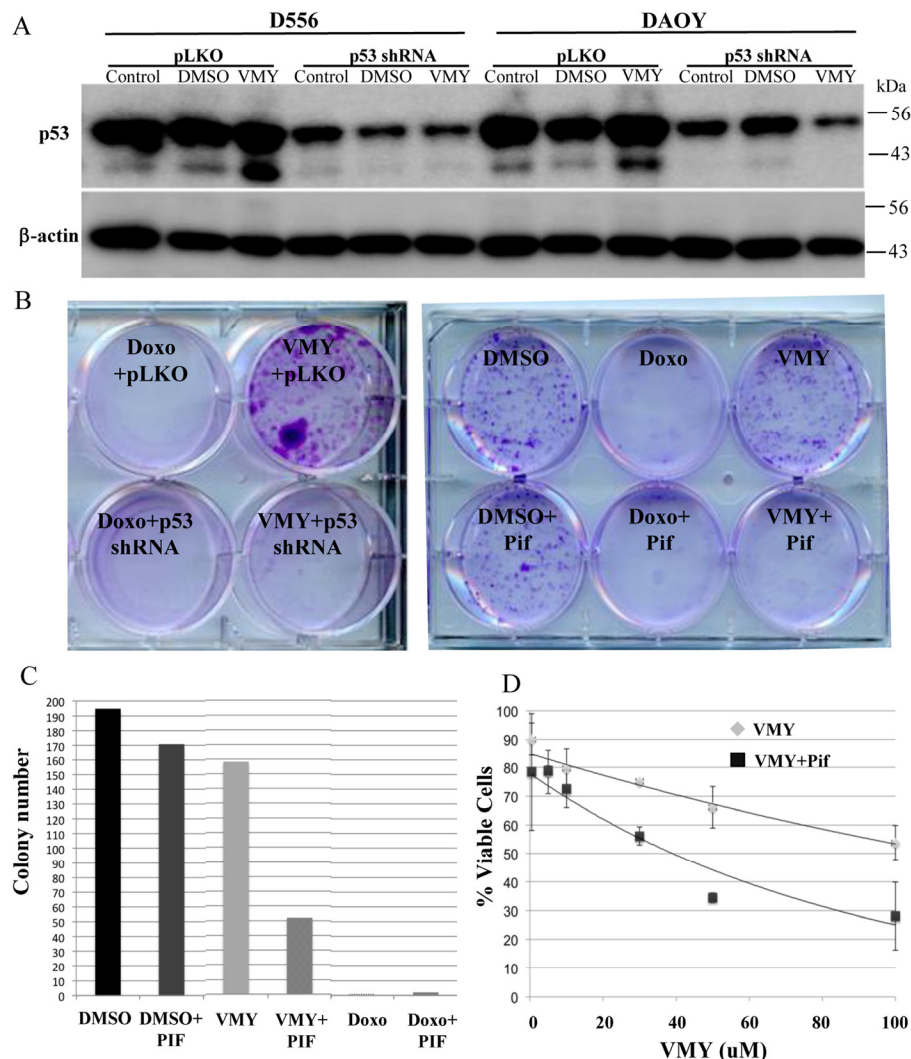


Figure 6. Effects of silencing of p53 on cell survival. (A) Genetic silencing of p53. D556 and DAOY cells were infected with p53siRNA or pLKO lentivirus'. The cells were left untreated or exposed for 18 hrs to DMSO or 30uM VMY as indicated, and western blots for p53 and β -actin were run. (B) The effects of p53shRNA knockdown (left) and Pifithrin (Pif, right) on cell viability were determined via colony forming assays. D556 cells were treated with DMSO, doxorubicin or VMY for 18 hrs. Fresh media was added and the cells cultured for an addition 3-5 days, followed by staining with crystal violet. (C) Quantification of the number of colonies in (B). (D) Dose response curves of D556 cells treated with VMY at the concentrations shown in the presence and absence of Pifithrin. The data are shown as average \pm standard deviation of N=3 separate experiments.

Table 1. Top 25 genes altered in the presence of Pifithrin α plus VMY vs. VMY alone.

Pif + VMY vs. VMY			
Up-regulated	Fold	Down-regulated	Fold
EndoG	8.77809E+30	FIGF	-6.10476E+11
CIDEB	1.9687E+12	ANGPT4	-6.017072518
PRSS54	1299.03	GSK3A	-5.35
BIK	19.44	INCA1	-5.18
MAP3K9	18.19	TNFSF14	-4.01
ERBB3	15.17	GDF15	-4.01
BRAT1	7.48	HGF	-3.89
CISH	6.73	BIRC3	-3.41
FADD	6.73	LIF	-2.85
TP63	6.63	NTF3	-2.77
CBX6	6.23	DRD2	-2.75
SRC	5.98	SNCG	-2.67
CBX7	5.98	MAGEA9	-2.67
HDAC4	5.24	ZNF385D	-2.67
RASSF4	4.49	CRIP3	-2.67
TRPM8	4.49	TNFSF15	-2.45
ERBB2	4.06	NAP1L6	-2.45
AKT1	3.84	TENC1	-2.33
UNC5B	3.83	NRCAM	-2.23
TNFRSF10D	3.74	DNAJB7	-2.21
NLRP12-14	3.74	MAGEB2	-2.19
TP73	3.74	PPAPDC2	-2.14
ARHGEF18	3.55	PRSS12	-2.14
TNFRSF25	3.49	CFLAR	-2.07
FASTK	3.48	GADD45A	-2.07

Loss of p53 in the presence of VMY alters calcium, p63 and p73 signaling pathways

In order to more completely define the mechanism underlying the paradoxical effect of p53 silencing, RNAseq next generation sequencing was performed on D556 cells treated with VMY in the presence or absence of Pif. RNA sequence analysis revealed an increase in expression of *calpain 12* in the VMY/Pif treated cells vs. VMY/DMSO control cells (Table 1). In addition, elevated expression of the transient receptor potential channel subfamily (*TRPM8*) gene was seen (Table 1), collectively suggesting that intracellular calcium signaling pathways were affected by p53 silencing. Dysregulation of the calcium signaling pathway downstream of stressors such as excitotoxicity can lead to necrotic cell death in neurons (reviewed in

[21, 22]), with one of the hallmarks of necrosis being Endo G induction and intranucleosomal DNA cleavage [22]. As both the pro-apoptosis regulatory genes p63 and p73 were induced by p53 silencing, as were possible downstream targets including Endo-G [23], the pro-apoptotic BH3-protein, BIK (Bcl-2-interacting killer) and CIDEB (cell death-inducing DFFA-like effector B), we assessed levels of late stage apoptosis and necrosis by flow cytometry, by gating for annexin V-positive/propidium iodide (PI)-positive cells. D556 cells were infected with either pLKO or p53shRNA as described above and treated for 18-hours with DMSO, 30uM VMY or 1uM doxorubicin, after which they were analyzed by flow cytometry as previously described [15]. While the annexin⁻/PI⁺ fraction of cells was unaffected, the silencing of p53 increased the proportion of annexin V⁺/PI⁺ cells following exposure to VMY or doxorubicin

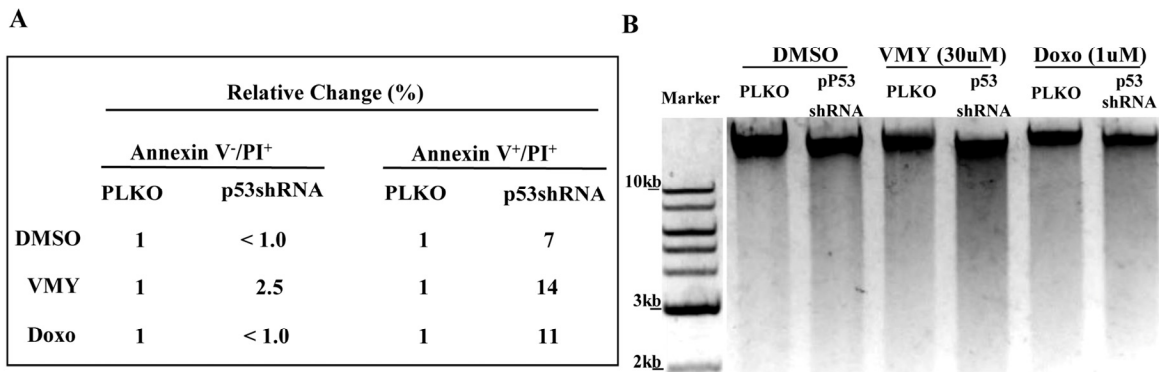


Figure 7. Effects of p53 knockdown on apoptosis and DNA fragmentation in D556 cells. (A) The proportion of cells undergoing apoptotic cell death as a result of p53 shRNA knockdown in D556 cells treated for 18 hrs with DMSO, VMY (30uM) or doxorubicin (1uM) as assessed using annexin V and propidium iodide (PI) staining and measured by flow cytometry. Data are shown as percent change in staining versus pLKO-control infected cells. (B) D556 cells were infected with pLKO or p53shRNA and treated with DMSO, VMY or doxorubicin for 18hrs. DNA fragmentation of nuclear DNA was assessed by ethidium bromide-agarose gel electrophoresis.

(Fig 7A). Finally, similar effects were seen using agarose gel electrophoresis assays where 18-hour treatment with VMY or doxorubicin plus p53shRNA resulted in enhanced DNA degradation, indicative of necrosis and apoptosis (Fig 7B).

Taken together, these experiments show that p53 protects against drug-induced cell death in medulloblastoma cells and its genetic- or chemical-suppression results in a significant increase in cell sensitivity to VMY and doxorubicin, an experimental and a clinical drug, respectively.

DISCUSSION

Necrosis, apoptosis and autophagy are activated under a variety of cell stress conditions (see references [24, 25] among others), however, little is known about how these complex and partially overlapping mechanisms are induced in medulloblastoma cells. In addition, to date, there have been few publications exploring the effects in medulloblastoma cells of the synthetic modulation of p53 activity during exposure to chemotherapeutic drugs.

We have recently shown in prostate cancer cell lines as well as in primary prostate cancer cells established using our conditional cell reprogramming approach [26, 27], that the induction of p53 by VMY was a prerequisite for inducing both autophagy and apoptosis, and that silencing p53 effectively blocked cell death [15]. Additionally, our earlier studies on VMY's effects

on MB established that this experimental drug induced apoptosis and mitotic catastrophe *in vitro* [12]. Furthermore, while our *in vivo* studies showed that 20 mg/kg of VMY administered three times per week for more than four weeks was well tolerated and was effective at treating a mouse model of SHH-driven medulloblastoma [14], a detailed investigation into the mechanism of VMY-induced cell death, and the role that p53 may play had not been explored. We now show that in MB cells, VMY induces the relocalization of p53 into the nucleus, an accumulation of γ H2AX, a decrease in MDM2 protein levels and activation of non-survival macro-autophagy. Since the protein levels of key stress-related proteins were reduced by VMY, the possibility existed that components of the CAP-dependent protein translation pathway may be inhibited by VMY. MNK1 is a target of p38 and MAPK and acts to increase CAP-dependent translation through the phosphorylation of the elongation factor eIF4E [28]. 4E-BP1 is a negative regulator of translation and phosphorylation of 4E-BP1 by mTOR inhibits its repressor function. Thus, if VMY negatively regulated CAP-dependent translation, the phosphorylation levels of 4E-BP1 and pMNK1 would be expected to reduce, however VMY increased the levels of these proteins in both D556 and DAOY cells (S.W and C.A, unpublished data). Interestingly, rather than protecting against chemotherapeutic cell killing, the suppression of p53 through shRNA knockdown or chemical inhibition by Pifithrin- α resulted in a significant increase in cell death by either VMY or doxorubicin, suggesting that p53 acts as a chemoprotective protein in these primitive neuroectoderm-derived cancer cells.

Regarding its function in the neuroectoderm, p53 performs roles different to those found in other tissues. In the past decade a role for p53 has emerged in neuronal differentiation, axon guidance, neurite outgrowth and axonal regeneration [29, 30]. Analysis of p53-dependent transcriptional activation in normal development *in vivo* by using a lacZ reporter gene under the control of a p53-responsive promoter showed that p53 activity was maximal during neuronal differentiation and clustered in areas that showed little correlation with the apoptosis normally ongoing in the developing nervous system [31, 32]. Furthermore, other studies have shown that approximately one quarter of

p53-null mice developed exencephaly due to cellular overgrowth, rather than decreased apoptosis [33, 34].

The dependence of neurite outgrowth and elongation on p53 has also been shown in the developing cerebellum. Gaub et al., 2010 showed that acetylated p53 is required for neurite outgrowth in cerebellar granule cell progenitors. Conversely, the loss of the function acetyl p53 mutant (K-R) inhibits physiological neurite outgrowth in those cells [35]. In cultured rat cerebellar granule cells, Maruoka et al., 2011, showed a p53-mediated neuroprotective effect against glutathione depletion-induced oxidative stress [36].

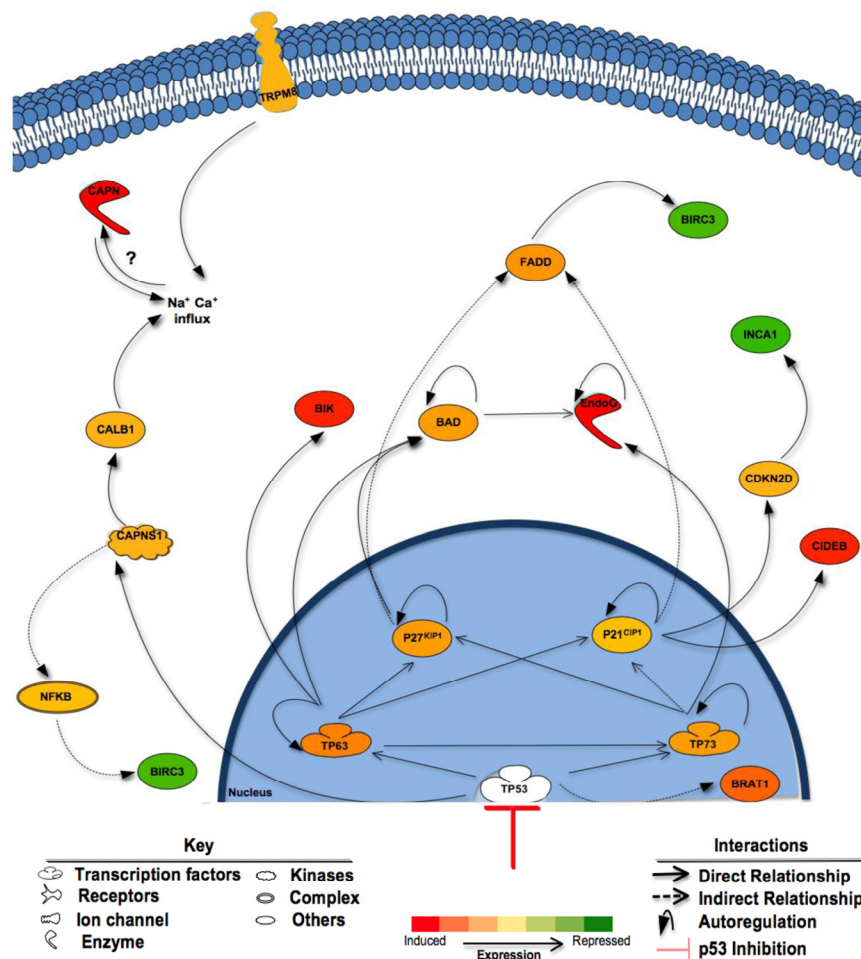


Figure 8. Proposed mechanisms of enhanced cell death following inhibition of p53. Shown are the effects of p53 suppression on components of cell death pathways in Pif + VMY vs. VMY treated D556 cells. p53 inhibition by Pifithrin resulted in the induction of *p63* and *p73* genes and subsequent enhanced cell death via apoptosis. Induction of the *p63* and *p73* genes leads to the activation of *p21^{CIP1}* and *p27^{KIP1}* both of which can indirectly trigger FADD, reducing the expression of BIRC3 (cIAP2). Induction of *p73* led to large increases in EndoG and CIDEB expression leading to DNA fragmentation while increased levels of *p63* induced apoptosis through BIRC3 and BIK, the latter of which along with TRPM8 can influence intracellular calcium levels. BAD; BCL2-Associated Agonist Of Cell Death, BIK; BCL2-Interacting Killer (Apoptosis-Inducing), BIRC3; baculoviral IAP repeat containing 3 (cIAP2), BRAT1; BRCA1-Associated ATM Activator 1, CAPN; Calpain, CALB1; Calbindin 1, CDKN2D; Cyclin-Dependent Kinase Inhibitor 2D (*p19^{Ink4D}*), CIDEB; Cell Death-Inducing DFFA-Like Effector B, EndoG; Endonuclease G, FADD; Fas-Associated Via Death Domain, INCA1; Inhibitor Of CDK, Cyclin A1 Interacting Protein 1, NF-KappaB; Nuclear Factor Of Kappa Light Polypeptide Gene Enhancer In B-Cells, TRPM8, Transient receptor potential cation channel subfamily M member 8.

Further validation of the role for p53 in neurite outgrowth and neuronal differentiation and maturation comes from studies establishing p53 as a downstream target of neurotrophic receptors. Loss of function experiments of p53 via either gene silencing or dominant negative p53 proteins lacking transactivation capacity have been shown to block NGF-dependent neurite outgrowth and differentiation in PC-12 cells [6, 37]. Another neurotrophic factor, BDNF, has also been shown to stimulate p53 phosphorylation and transcriptional activation in primary cortical neurons [30]. Activation of signaling molecules downstream of NGF or BDNF that are known to induce p53 post-translational modifications and enhance its transcriptional activity has been reported, including ERK1 and ERK2, p38MAPK, JNK1-2 (c-Jun N-terminal kinases 1-2), cytoskeleton remodeling genes, such as GAP-43, the actin-binding protein Coronin 1b and the RAS family member Rab13 [6, 38].

Unresolved however is an actual role for p53 in the biology of human MB. Frequencies of *p53* mutations are low in primary MB but increase significantly in recurrences, and mutant p53 proteins and Myc may collaborate to drive aggressive disease [8]. Additionally, modifications of p53 function are required in *Myc*- [39, 40] but not *Smoothed-* based mouse models to drive MB. The genetic silencing of *p53* in mice with conditional deletion of the *BRCA2-interacting protein (BCCIP)* gene also resulted in MB [41]; however the resulting tumor formation was predicated upon the loss of the BCCIP knockdown cassette, which restored BCCIP expression in the neuroectoderm, supporting a role for p53 in neuronal genomic stability. Interestingly, p53 expression levels are lower in group 4 MB, due to the iso-dicentric (17)(p11.2) recombination events frequently seen in this group [10]. However, neither the levels of p53 expression nor its subcellular localization were reported following chemotherapy. It should be noted that etoposide induced p53 activity in D283, MEDI and D458 MB cell lines *in vitro* [42] and the p53 target miR-34a was able to reduce the viability in the p53-impaired MB cell line, MEB-Med8a [43], however the effects of silencing of p53 *per se* were not reported. Furthermore, docosahexaenoic acid and etoposide were found to reduce the levels of MDM2 in both p53-mutant DAOY cells as well as in p53-wildtype D283 cells [44] and we also observe decreases in MDM2 with VMY, along with rapid translocation of p53 into the nucleus. Collectively these published studies and our new data suggest that components of the p53 pathway remain intact in a variety of p53-mutant and p53-wild type MB cells.

It was therefore surprising that rather than causing chemotherapeutic resistance, the suppression of p53

function by either shRNA knockdown or Pif sensitized DAOY and D556 cells to both VMY and doxorubicin. Mechanistically, the induction of the *p63* and *p73* and their targeted genes by VMY in the Pif-treated cells was one of the most prominent features (Table 1 and Figure 8). These p53 family-member genes, and their various splice variants, play both similar and distinct roles in development as well as in cancer (reviewed in [45]) and can interact with each other with a high degree of complexity. There is abundant evidence that modulation of p53 function can influence the activity of p63 and p73 (reviewed in [46]) and conversely that p63 and p73 can influence p53 activity in adult neural precursor cells [47]. While the mechanism(s) by which the genetic knockdown or chemical suppression of p53 regulates *p63* and *p73* expression in MB cells has yet to be elucidated, our data suggest that the induction of *p63* and *p73* following p53 suppression fundamentally alters the pro-apoptotic machinery in MB cells (Fig 8). It is also unknown whether the increased sensitivity seen in the cell lines tested extends to a broader array of clinical samples or to the chemo-radiation interventions currently used for treating MB. However as both DAOY and D556 cells show similar sensitivities to p53 functional blockade, the possibility exists that at least a subset of the p53 mutations found in MB patients may not adversely impact p53-targeting regimens. Additional experiments assessing whether the p53 mutant proteins identified in recurrent MB exhibit similar responses to combined p53 suppression and exposure to VMY, doxorubicin or other drugs are clearly warranted.

MATERIALS AND METHODS

Cell lines and cell culture. The human medulloblastoma (MB) cell lines D556 and DAOY were maintained in complete DMEM containing 10% FBS, L-glutamine, and 100 U/ml Penicillin-Streptomycin as previously described [12]. DNA STR fingerprint analyses were performed on both cell lines as a quality control measure. The DAOY data matched the ATCC database for this line, while early and late passage D556 cultures were compared with no significant changes observed and no matches with the available STR database (not shown).

Cell viability and growth. Cell viability was determined using trypan blue dye exclusion and viable and total cell counting using a hemocytometer as previously described [11, 12, 15].

Colony forming assays. A total of 1000 cells were plated in 6 well plates. Cells were allowed to adhere for 24 hrs before treatment, at which point they were

treated with VMY or Doxorubicin for 18 hrs. The media was changed after 18hrs and the plates were incubated in the absence of drug for 3-5 days to reach 80% confluency in the negative control wells. Cells were washed with PBS, fixed with 10% neutral buffered formalin solution for 15-30 minutes and stained with 0.5% (w/v) crystal violet for 30-60 minutes. The crystal violet was aspirated, cells were washed with PBS and dried for one hour before counting.

Flow cytometry. The prostate cells were fixed and stained with 20ug/ml propidium iodide (PI) and 5 U RNase A, and the DNA content and subG1 DNA fragmentation was measured using a FACStar Plus system (Becton-Dickson, Franklin Lakes, NJ) as previously described [11, 12]. Cellular apoptosis was also assessed by APC-Annexin V antibody (Biolegend, San Diego, CA) staining immediately after treatment with VMY and analyzed using FACStar Plus dual laser FACSrt system (Becton-Dickson, Franklin Lakes, NJ) as previously described by us [11, 12, 48, 49].

Immunoblotting. Protein extracts were prepared and separated on 4-20% Tris-glycine gels and electroblotted onto PVDF membranes as previously described [11, 12, 50]. Protein levels were assessed using antibodies against p53 (Millipore, Bellerica, MA #05-224), p-ATM (Cell Signaling, Danvers, MA #5883P), p-Chk2 (Cell Signaling, Danvers, MA #2661P), p-Chk1 (Cell Signaling, Danvers, MA #2348P), p38 (Cell Signaling, Danvers, MA #8690), histone γ -H2AX (Cell Signaling, Danvers, MA #7631), p-histone γ H2AX (Cell Signaling, Danvers, MA #9718P), p-BRCA1 (Ser1524) (Cell Signaling, Danvers, MA #9009P), p-P38 MAPK (Cell Signaling, Danvers, MA #9216S), mTOR (Cell Signaling, Danvers, MA #2983), p-ATR (Cell Signaling, Danvers, MA #2853P), p-p53 (Cell Signaling, Danvers, MA #9286P), p-MNK1 (cell signaling, #2111S), p-4E-BP1 (Cell Signaling, Danvers, MA #2855S), MDM2 (Santa Cruz Biotechnology, #sc-965), β -actin (Cell Signaling, Danvers, MA #4967). Densitometry was performed using ImageJ analysis software (NIH, Bethesda, MD) as previously described [11, 12, 50].

Immunofluorescent imaging. Cells were seeded on glass coverslips and treated with DMSO or VMY for 4 or 18 hrs. Cells were washed with PBS and fixed in 10% formalin for 10 min. The coverslips were washed three times with PBS, the cells were permeabilized with 0.1% Triton X-100 and washed three times with PBS. The samples were blocked with 1% BSA for 20 minutes and washed an additional three times in PBS. The cells were exposed to anti-p53 (1:150, Millipore #05-224) or anti- γ H2AX (1:150, Cell Signaling #7631) antibodies for 1

hr at room temperature. The slides were washed with PBS an additional three times and stained with the secondary antibody Alexa Fluor goat 488 anti-mouse (1:150, Life Technologies, A-10667) for 30 min at room temperature. Slides were then counter-stained with DAPI for 5 min. The coverslips were mounted onto glass slides with Tris-buffered fluoro-gel (Electron Microscopy Sciences). Confocal microscopy was performed on a Zeiss (Thornwood, NY) LSM510 Meta microscope using a 40x lens.

LC3-GFP. LC3 translocation was detected using the green fluorescent protein (GFP)-fused LC3 construct that was generously donated by Dr Robert Clarke [51]. Briefly, cells were seeded in 6 well plates containing glass coverslips and allowed to attach overnight. The LC3-GFP expression plasmid (14ug) was transfected using Lipofectamine LTX reagent (Life Technologies, Carlsbad, CA #15338-100) as previously described by us [15]. 24 hours after transfection, the cells were treated with VMY or vehicle. After 18 hours, the coverslips with attached cells were stained with DAPI and rinsed 3 times with PBS and the coverslips mounted. Imaging was performed by confocal microscopy as previously described [12, 15].

Autophagy inhibitors. For autophagy inhibition, 3-methyladenine (3-MA) (Sigma-Aldrich, St Louis, MO #M921) was used at 5mM and chloroquine diphosphate (CQ) (Sigma-Aldrich, St Louis, MO #C6628) was used at 50 μ M as previously described [15]. Cells were exposed to these inhibitors for 20 minutes prior to treatment with either DMSO or VMY [15].

p53 expression and shRNA knockdown. For lentivirus knockdown experiments, the p53shRNA and pLKO vectors were purchased commercially (Vector Biolabs, Philadelphia, PA, #1854) and used as described by the manufacturer as previously described [15]. Briefly, 293T cells (ATCC, Manassas, VA) were cotransfected with shRNA constructs along with the pHR'8.2 Δ R and pCMV-VSV-G helper constructs. After 24 hours, the media was changed and the virus-containing media was harvested after an additional 24 hours of incubation. The MB cells were seeded at 30% confluency and viral infections were performed for 72 hours prior to treatment with VMY or DMSO. Efficiency of the knockdown was monitored by p53 immunoblotting and quantification by ImageJ as previously described [15, 52, 53].

Chemical inhibition of p53. For chemical inhibition of p53, 30uM Pifithrin- α (Sigma-Aldrich, St Louis, MO #P4359) was added one hour prior to treatment with VMY, doxorubicin or DMSO.

DNA fragmentation. D556 cells were infected with pLKO or p53shRNA virus's for 72 hrs prior to treatment with VMY or DMSO. Doxorubicin was used as a positive control. The genomic DNA was isolated after 18 hr treatment with VMY or doxorubicin using the DNeasy blood and tissue kit (Qiagen, MD #69506). 500ng of DNA was run on 1% agarose gel containing ethidium bromide with the electrophoresis carried out at 100V for one hour.

RNAseq and pathway analyses. Total RNA was extracted from D556 cells treated with Pif and VMY as described above using an RNeasy Plus Mini Kit (Qiagen, MD, #74134) and submitted to Orogenetics Corporation (Norcross, GA USA) for RNA-Seq assays. Sequencing was performed on the Illumina HiSeq 2500 (20 million reads, Rapid run, Illumina, CA USA) with chemistry v1.0 and using the 2×106bp paired-end read mode and original chemistry from Illumina according to the manufacturer's instructions. The initial data analysis was started directly on the HiSeq 2500 System during the run. The HiSeq Control Software 2.0.5 in combination with RTA 1.17.20.0 (real time analysis) performed the initial image analysis and base calling. Quality control (QC) was performed using FastQC software. All the samples passed the "Basic Statistics", "Per Base Sequence Quality", "Per Sequence Quality Scores", "Per Base N Content", and "Sequence Length Distribution". No specific filtering was done for the samples. The final FASTQ files comprising the sequence information which was used for all subsequent bioinformatics analyses. Sequences were demultiplexed according to the 6bp index code with 1 mismatch allowed. After QC, Tophat2 was used for the alignment, and BAM files were obtained. Partek Genomics Suite (6.6 version 6.12.0713 software (Partek Inc.) was utilized to calculate RPKM as normalization, and fold changes were calculated based on the RPKM results. The pathways analysis was performed through the use of QIAGEN's Ingenuity[®] Pathway Analysis (Qiagen, Redwood City, CA).

ACKNOWLEDGEMENTS

Cell cycle analyses were performed in the Lombardi Comprehensive Cancer Center's Flow Cytometry Shared Resource, microscopy was performed in the Lombardi Comprehensive Cancer Center's Microscopy and Imaging Shared Resource, the DNA fingerprint analyses were done through the Lombardi Comprehensive Cancer Center's Tissue Culture Shared Resource and the RNAseq was performed through the Lombardi Comprehensive Cancer Center's Genomics and Epigenomics Shared Resource.

Funding

Funding was provided by; ABCC (Albanese), R01CA193698 (Avantaggiati) and NIH P30 CA51008-18 (Weiner). This work was also supported by the Paul Calabresi Career Development Award for Clinical Oncology (K12, Karam) an American Cancer Society Institutional Grant (Karam) and a Howard Hughes Medical Institute University Grant (Waye). We thank Milton Brown for supplying VMY-1-103.

Conflict of interest statement

Georgetown University has submitted a patent application on VMY-1-103 where V.Y. is an inventor.

REFERENCES

1. Samkari A, White JC and Packer RJ. Medulloblastoma: toward biologically based management. *Semin Pediatr Neurol.* 2015; 22:6-13.
2. Ning MS, Perkins SM, Dewees T and Shinohara ET. Evidence of high mortality in long term survivors of childhood medulloblastoma. *J Neurooncol.* 2015; 122:321-327.
3. Soussi T and Wiman KG. TP53: an oncogene in disguise. *Cell Death Differ.* 2015; 22:1239-1249.
4. Muller PA and Vousden KH. Mutant p53 in cancer: new functions and therapeutic opportunities. *Cancer Cell.* 2014; 25:304-317.
5. Quadrato G and Di Giovanni S. Gatekeeper between quiescence and differentiation: p53 in axonal outgrowth and neurogenesis. *Int Rev Neurobiol.* 2012; 105:71-89.
6. Di Giovanni S, Knights CD, Rao M, Yakovlev A, Beers J, Catania J, Avantaggiati ML and Faden AI. The tumor suppressor protein p53 is required for neurite outgrowth and axon regeneration. *Embo J.* 2006; 25:4084-4096.
7. Pfaff E, Remke M, Sturm D, Benner A, Witt H, Milde T, von Bueren AO, Wittmann A, Schottler A, Jorch N, Graf N, Kulozik AE, Witt O, Scheurlen W, von Deimling A, Rutkowski S, et al. TP53 mutation is frequently associated with CTNNB1 mutation or MYCN amplification and is compatible with long-term survival in medulloblastoma. *J Clin Oncol.* 2010; 28:5188-5196.
8. Hill RM, Kuijper S, Lindsey JC, Petrie K, Schwalbe EC, Barker K, Boulton JK, Williamson D, Ahmad Z, Hallsworth A, Ryan SL, Poon E, Robinson SP, Ruddle R, Raynaud FI, Howell L, et al. Combined MYC and P53 defects emerge at medulloblastoma relapse and define rapidly progressive, therapeutically targetable disease. *Cancer Cell.* 2015; 27:72-84.
9. Rausch T, Jones DT, Zapatka M, Stutz AM, Zichner T, Weischenfeldt J, Jager N, Remke M, Shih D, Northcott PA, Pfaff E, Tica J, Wang Q, Massimi L, Witt H, Bender S, et al. Genome sequencing of pediatric medulloblastoma links catastrophic DNA rearrangements with TP53 mutations. *Cell.* 2012; 148:59-71.
10. Bien-Willner GA and Mitra RD. Mutation and expression analysis in medulloblastoma yields prognostic variants and a putative mechanism of disease for i17q tumors. *Acta Neuropathol Commun.* 2014; 2:74.

11. Ringer L, Yenugonda VM, Ghosh A, Divito K, Trabosh V, Patel Y, Brophy A, Grindrod S, Lisanti MP, Rosenthal D, Brown ML, Avantaggiati ML, Rodriguez O and Albanese C. VMY-1-103, a dansylated analog of purvalanol B, induces caspase-3-dependent apoptosis in LNCaP prostate cancer cells. *Cancer Biol Ther.* 2010; 10:320-325.
12. Ringer L, Sirajuddin P, Heckler M, Ghosh A, Suprynowicz F, Yenugonda VM, Brown ML, Toretzky JA, Uren A, Lee Y, MacDonald TJ, Rodriguez O, Glazer RI, Schlegel R and Albanese C. VMY-1-103 is a novel CDK inhibitor that disrupts chromosome organization and delays metaphase progression in medulloblastoma cells. *Cancer Biol Ther.* 2011; 12:818-826.
13. Smahi A, Courtois G, Vabres P, Yamaoka S, Solange H, Munnich A, Israël A, Heiss NS, Klauk SKP and Wiemann S. Genomic rearrangement in NEMO impairs NF- κ B activation and is a cause of incontinentia pigmenti (IP). *Nature.* 2000; 405:466-472.
14. Sirajuddin P, Das S, Ringer L, Rodriguez O, Sivakumar A, Lee Y, Uren A, Fricke S, Rood B, Ozcan A, Wang SS, Karam S, Yenugonda VM, Salinas P, Petricoin EF, 3rd, Lisanti MP, et al. Quantifying the CDK inhibitor VMY-1-103's activity and tissue levels in an in vivo tumor model by LC-MS/MS and by MRI. *Cell Cycle.* 2012; 11:3801-3809.
15. Ringer L, Sirajuddin P, Tricoli L, Waye S, Parasido E, Lee RJ, Feldman A, Wu C-L, Dritschilo A, Lynch J, Schlegel R, Rodriguez O, Pestell RG, Avantaggiati ML and Albanese C. The Induction of the p53 Tumor Suppressor Protein Bridges the Apoptotic and Autophagic Signaling Pathways to Regulate Cell Death in Prostate Cancer Cells. *Oncotarget.* 2014; 5:10678-10691.
16. Garufi A, Pucci D, D'Orazi V, Cirone M, Bossi G, Avantaggiati ML and D'Orazi G. Degradation of mutant p53H175 protein by Zn(II) through autophagy. *Cell Death Dis.* 2014; 5:e1271.
17. Li LY, Luo X and Wang X. Endonuclease G is an apoptotic DNase when released from mitochondria. *Nature.* 2001; 412:95-99.
18. Petrucci LA, Pettersson F, Del Rincon SV, Guilbert C, Licht JD and Miller WH, Jr. Expression of leukemia-associated fusion proteins increases sensitivity to histone deacetylase inhibitor-induced DNA damage and apoptosis. *Mol Cancer Ther.* 2013; 12:1591-1604.
19. Kang R, Zeh HJ, Lotze MT and Tang D. The Beclin 1 network regulates autophagy and apoptosis. *Cell Death Differ.* 2011; 18:571-580.
20. Raffel C, Thomas GA, Tishler DM, Lasso S and Allen JC. Absence of p53 mutations in childhood central nervous system primitive neuroectodermal tumors. *Neurosurgery.* 1993; 33:301-305; discussion 305-306.
21. Hara MR and Snyder SH. Cell signaling and neuronal death. *Annu Rev Pharmacol Toxicol.* 2007; 47:117-141.
22. Fujikawa DG. The role of excitotoxic programmed necrosis in acute brain injury. *Comput Struct Biotechnol J.* 2015; 13:212-221.
23. Kitagawa K and Niikura Y. Caspase-independent mitotic death (CIMD). *Cell Cycle.* 2008; 7:1001-1005.
24. Galluzzi L, Vitale I, Abrams JM, Alnemri ES, Baehrecke EH, Blagosklonny MV, Dawson TM, Dawson VL, El-Deiry WS, Fulda S, Gottlieb E, Green DR, Hengartner MO, Kepp O, Knight RA, Kumar S, et al. Molecular definitions of cell death subroutines: recommendations of the Nomenclature Committee on Cell Death 2012. *Cell Death Differ.* 2012; 19:107-120.
25. Klionsky DJ, Abdalla FC, Abeliovich H, Abraham RT, Acevedo-Arozena A, Adeli K, Agholme L, Agnello M, Agostinis P, Aguirre-Ghiso JA, Ahn HJ, Ait-Mohamed O, Ait-Si-Ali S, Akematsu T, Akira S, Al-Younes HM, et al. Guidelines for the use and interpretation of assays for monitoring autophagy. *Autophagy.* 2012; 8:445-544.
26. Liu X, Ory V, Chapman S, Yuan H, Albanese C, Kallakury B, Timofeeva O, Nealon C, Dalic A, Simic V, Haddad B, Rhim J, Dritschilo A, Riegel A, McBride A and Schlegel R. ROCK inhibitor and feeder cells induce the conditional reprogramming of epithelial cells. *American Journal of Pathology.* 2012; 180:590-607.
27. Palechor-Ceron N, Suprynowicz FA, Upadhyay G, Dakic A, Minas T, Simic V, Johnson M, Albanese C, Schlegel R and Liu X. Radiation Induces Diffusible Feeder Cell Factor(s) That Cooperate with ROCK Inhibitor to Conditionally Reprogram and Immortalize Epithelial Cells. *Am J Pathol.* 2013; 183:1862-1870.
28. Bhat M, Robichaud N, Hulea L, Sonenberg N, Pelletier J and Topisirovic I. Targeting the translation machinery in cancer. *Nat Rev Drug Discov.* 2015; 14:261-278.
29. Arakawa H. p53, apoptosis and axon-guidance molecules. *Cell Death Differ.* 2005; 12:1057-1065.
30. Tedeschi A and Di Giovanni S. The non-apoptotic role of p53 in neuronal biology: enlightening the dark side of the moon. *EMBO Rep.* 2009; 10:576-583.
31. Komarova EA, Chernov MV, Franks R, Wang K, Armin G, Zelnick CR, Chin DM, Bacus SS, Stark GR and Gudkov AV. Transgenic mice with p53-responsive lacZ: p53 activity varies dramatically during normal development and determines radiation and drug sensitivity in vivo. *Embo J.* 1997; 16:1391-1400.
32. Gottlieb E, Haffner R, King A, Asher G, Gruss P, Lonai P and Oren M. Transgenic mouse model for studying the transcriptional activity of the p53 protein: age- and tissue-dependent changes in radiation-induced activation during embryogenesis. *Embo J.* 1997; 16:1381-1390.
33. Sah VP, Attardi LD, Mulligan GJ, Williams BO, Bronson RT and Jacks T. A subset of p53-deficient embryos exhibit exencephaly. *Nat Genet.* 1995; 10:175-180.
34. Armstrong JF, Kaufman MH, Harrison DJ and Clarke AR. High-frequency developmental abnormalities in p53-deficient mice. *Curr Biol.* 1995; 5:931-936.
35. Gaub P, Tedeschi A, Puttagunta R, Nguyen T, Schmandke A and Di Giovanni S. HDAC inhibition promotes neuronal outgrowth and counteracts growth cone collapse through CBP/p300 and P/CAF-dependent p53 acetylation. *Cell Death Differ.* 2010; 17(9):1392-1408.
36. Maruoka H, Sasaya H, Sugihara K, Shimoke K and Ikeuchi T. Low-molecular-weight compounds having neurotrophic activity in cultured PC12 cells and neurons. *J Biochem.* 2011; 150:473-475.
37. Knights CD, Catania J, Di Giovanni S, Muratoglu S, Perez R, Swartzbeck A, Quong AA, Zhang X, Beerman T, Pestell RG and Avantaggiati ML. Distinct p53 acetylation cassettes differentially influence gene-expression patterns and cell fate. *J Cell Biol.* 2006; 173:533-544.
38. Tedeschi A, Nguyen T, Puttagunta R, Gaub P and Di Giovanni S. A p53-CBP/p300 transcription module is required for GAP-43 expression, axon outgrowth, and regeneration. *Cell Death Differ.* 2009; 16:543-554.

39. Kawauchi D, Robinson G, Uziel T, Gibson P, Rehg J, Gao C, Finkelstein D, Qu C, Pounds S, Ellison DW, Gilbertson RJ and Roussel MF. A mouse model of the most aggressive subgroup of human medulloblastoma. *Cancer Cell*. 2012; 21:168-180.
40. Pei Y, Moore CE, Wang J, Tewari AK, Eroshkin A, Cho YJ, Witt H, Korshunov A, Read TA, Sun JL, Schmitt EM, Miller CR, Buckley AF, McLendon RE, Westbrook TF, Northcott PA, et al. An animal model of MYC-driven medulloblastoma. *Cancer Cell*. 2012; 21:155-167.
41. Huang YY, Dai L, Gaines D, Droz-Rosario R, Lu H, Liu J and Shen Z. BCCIP suppresses tumor initiation but is required for tumor progression. *Cancer Res*. 2013; 73:7122-7133.
42. Meley D, Spiller DG, White MR, McDowell H, Pizer B and See V. p53-mediated delayed NF-kappaB activity enhances etoposide-induced cell death in medulloblastoma. *Cell Death Dis*. 2010; 1:e41.
43. Fan YN, Meley D, Pizer B and See V. Mir-34a mimics are potential therapeutic agents for p53-mutated and chemoresistant brain tumour cells. *PLoS One*. 2014; 9:e108514.
44. Wang F, Bhat K, Doucette M, Zhou S, Gu Y, Law B, Liu X, Wong ET, Kang JX, Hsieh TC, Qian SY and Wu E. Docosahexaenoic acid (DHA) sensitizes brain tumor cells to etoposide-induced apoptosis. *Curr Mol Med*. 2011; 11:503-511.
45. Moll UM and Slade N. p63 and p73: roles in development and tumor formation. *Mol Cancer Res*. 2004; 2:371-386.
46. Pflaum J, Schlosser S and Muller M. p53 Family and Cellular Stress Responses in Cancer. *Front Oncol*. 2014; 4:285.
47. Fatt MP, Cancino GI, Miller FD and Kaplan DR. p63 and p73 coordinate p53 function to determine the balance between survival, cell death, and senescence in adult neural precursor cells. *Cell Death Differ*. 2014; 21:1546-1559.
48. Albanese C, D'Amico M, Reutens AT, Fu M, Watanabe G, Lee RJ, Kitsis RN, Henglein B, Avantaggiati M, Somasundaram K, Thimmapaya B and Pestell RG. Activation of the *cyclin D1* gene by the E1A-associated protein p300 through AP-1 inhibits cellular apoptosis. *J Biol Chem*. 1999; 274:34186-34195.
49. Albanese C, Wu K, D'Amico M, Jarrett C, Joyce D, Hughes J, Hult J, Sakamaki T, Fu M, Ben-Ze'ev A, Bromberg JF, Lamberti C, Verma U, Gaynor RB, Byers SW and Pestell RG. IKKalpha Regulates Mitogenic Signaling through Transcriptional Induction of Cyclin D1 via Tcf. *Mol Biol Cell*. 2003; 14:585-599.
50. Rodriguez OC, Choudhury S, Kolukula V, Vietsch EE, Catania J, Preet A, Reynoso K, Bargonetti J, Wellstein A, Albanese C and Avantaggiati ML. Dietary downregulation of mutant p53 levels via glucose restriction: mechanisms and implications for tumor therapy. *Cell Cycle*. 2013; 11:4436-4446.
51. Schwartz-Roberts JL, Shajahan AN, Cook KL, Warri A, Abu-Asab M and Clarke R. GX15-070 (obatoclax) induces apoptosis and inhibits cathepsin D- and L-mediated autophagosomal lysis in antiestrogen-resistant breast cancer cells. *Mol Cancer Ther*. 2013; 12:448-459.
52. Perez RE, Knights CD, Sahu G, Catania J, Kolukula VK, Stoler D, Graessmann A, Ogryzko V, Pishvaian M, Albanese C and Avantaggiati ML. Restoration of DNA-binding and growth-suppressive activity of mutant forms of p53 via a PCAF-mediated acetylation pathway. *J Cell Physiol*. 2010; 225:394-405.
53. Catalina-Rodriguez O, Kolukula VK, Tomita Y, Preet A, Palmieri F, Wellstein A, Byers S, Giaccia AJ, Glasgow E, Albanese C and Avantaggiati ML. The mitochondrial citrate transporter, CIC, is essential for mitochondrial homeostasis. *Oncotarget*. 2012; 3:1220-1235.

MDL-1, a growth- and tumor-suppressor, slows aging and prevents germline hyperplasia and hypertrophy in *C. elegans*

Michèle Riesen¹, Inna Feyst¹, Nattaphong Rattanavirotkul¹, Marina Ezcurra¹, Jennifer M.A. Tullet¹, Irene Papatheodorou², Matthias Ziehm², Catherine Au¹, Ann F. Gilliat¹, Josephine Hellberg¹, Janet M. Thornton², and David Gems¹

¹Institute of Healthy Ageing, and Research Department of Genetics, Evolution and Environment, University College London, London, United Kingdom;

²European Molecular Biology Laboratory, European Bioinformatics Institute, Wellcome Trust Genome Campus, Hinxton, Cambridge, United Kingdom

Key words: aging, *C. elegans*, FoxO, germline, hyperplasia, hypertrophy, Mad transcription factor

Received: 12/22/13; **Accepted:** 2/14/14; **Published:** 2/16/14

Correspondence to: David Gems, PhD; **E-mail:** david.gems@ucl.ac.uk

Copyright: © Riesen et al. This is an open-access article distributed under the terms of the Creative Commons Attribution License, which permits unrestricted use, distribution, and reproduction in any medium, provided the original author and source are credited

Abstract: In *C. elegans*, increased lifespan in *daf-2* insulin/IGF-1 receptor mutants is accompanied by up-regulation of the MDL-1 Mad basic helix-loop-helix leucine zipper transcription factor. Here we describe the role of *mdl-1* in *C. elegans* germline proliferation and aging. The deletion allele *mdl-1(tm311)* shortened lifespan, and did so significantly more so in long-lived *daf-2* mutants implying that *mdl-1(+)* contributes to effects of *daf-2* on lifespan. *mdl-1* mutant hermaphrodites also lay increased numbers of unfertilized oocytes. During aging, unfertilized oocytes in the uterus develop into tumors, whose development was accelerated by *mdl-1(tm311)*. Opposite phenotypes were seen in *daf-2* mutants, i.e. *mdl-1* and *daf-2* mutant germlines are hyperplastic and hypoplastic, respectively. Thus, MDL-1, like its mammalian orthologs, is an inhibitor of cell proliferation and growth that slows progression of an age-related pathology in *C. elegans* (uterine tumors). In addition, intestine-limited rescue of *mdl-1* increased lifespan but not to wild type levels. Thus, *mdl-1* likely acts both in the intestine and the germline to influence age-related mortality.

INTRODUCTION

In most animals, advancing age is accompanied by the deteriorative process of aging (senescence). Aging is the main cause of severe illness and death in humans, but the proximate biological mechanisms that cause it have proved difficult to identify. One approach to understand aging is to study simple model organisms [1], such as the nematode *Caenorhabditis elegans* which is particularly suitable for this purpose given e.g. its sequenced genome and very short lifespan (2-3 weeks). The identification from the 1980s onwards of many *C. elegans* mutants with altered aging rate [1] led to optimism that discovery of gene products of aging control genes would reveal the mechanisms of aging in this organism. Yet although many signaling pathways

and processes affecting aging rate have been identified, the nature of aging itself has remained obscure. For example, mutation of the *daf-2* insulin/IGF-1 receptor gene can more than double adult lifespan [2]. This increase requires the presence of the DAF-16 FoxO transcription factor [2-4], suggesting that transcriptional targets of DAF-16 encode proximal biochemical determinants of aging. But these target genes have proved to be very numerous [5, 6], 2,274 by one estimate [7], complicating the search for DAF-16 target genes that control aging. Understanding DAF-16/FoxO action is important, particularly because the role of insulin/IGF-1 signaling and FoxO in the control of aging shows evolutionary conservation, e.g. in the fruitfly *Drosophila* [8], and perhaps even in humans,

where age changes in allele frequency e.g. of the IGF-1 receptor and FoxO3A genes have been detected [1].

One approach to understand DAF-16 action is to map the gene regulatory network in which it acts. Previously we used a genome-wide approach to identify genes to which DAF-16 both binds and causes a change in gene expression [9]. This identified a mere 65 high confidence DAF-16 direct targets, which were enriched for genes encoding proteins involved in signaling and gene regulation, and transcription factors. Among the latter class was *mdl-1* (Mad-like 1), which encodes a basic helix-loop-helix (bHLH) TF homologous to mammalian Mad transcription factors [10] (Figure 1A). In mammals, Mad TFs act as heterodimers with Max bHLH TFs. Mad competes with Myc bHLH TFs to dimerize with Max, and bind to target genes containing E-box sequences (5'-CANNTG-3') [11]. Myc/Max dimers mainly activate gene expression, and are a major activator of cell proliferation of growth. By contrast, Mad/Max dimers mainly inhibit gene expression, antagonizing Myc/Max, and suppressing cell division and growth [11]. Inhibition of gene expression by Mad/Max is facilitated by recruitment of the Sin3 histone deacetylase (HDAC) corepressor complex. Myc TFs are potent oncogenes, while Mad TFs show some properties of tumor suppressors [11].

Our attention was drawn to *mdl-1* for several reasons. First, many genes that promote growth also promote aging [12]. Thus, growth suppressors activated by DAF-16 are candidates for downstream effectors slowing aging, and MDL-1, as a Mad TF, is a potential growth suppressor and, in fact, can suppress activated cMyc/Ras-induced cell transformation in mammalian cells [10]. Second, four mammalian Mad TFs, *mad1*, *mxl1*, *mad3* and *mad4*, are up-regulated by FoxO3a in a human colorectal adenocarcinoma cell line [13]. Thus, regulatory interactions between FoxO and Mad show at least some evolutionary conservation between nematodes and mammals. Consistent with this, in *C. elegans* *mdl-1* is an activator of intestinal expression of *ftn-1* (H ferritin, an iron storage protein) [14], while in mammals, Myc can repress H ferritin expression, which contributes to cell proliferation [15].

C. elegans possesses several Max-like (*mxl*) genes, including *mxl-1* which can form heterodimers with MDL-1 but, surprisingly, lacks Myc [10, 16, 17]. Previous RNAi screens have not detected major effects of expression knockdown of *mdl-1* or *mxl-1* (Wormbase.org). However, *mdl-1* exerts some influence upon the germline, as follows. Loss of *daf-2* inhibits lethal, *gld-1*-induced distal germline tumors via decreased cell division and increased DAF-16/p53-

dependent apoptosis [18], and *mdl-1* is a mediator of this inhibition [19]. Moreover, RNAi of *mdl-1* can reduce *daf-2* mutant longevity, but has little effect on lifespan in *daf-2*(+) worms [6].

In this study, we explore the possible role of *mdl-1* as a downstream effector of DAF-16 in the control of aging. In particular, we detail the phenotypic effects of mutation of *mdl-1*. We report that *mdl-1* acts as a repressor of germline hyperplasia and hypertrophy which otherwise contributes to age-related pathology in the germline.

RESULTS

mdl-1(tm311) increases production of unfertilized oocytes

To investigate *mdl-1* gene function, we studied the *mdl-1(tm311)* mutant allele, which contains a 471 bp base pair deletion that removes exon 2 of the gene (Figure 1A). This results in a frame shift after 51/281 amino acid residues and loss of the entire bHLH domain, implying that this is a null allele. The mutation was first backcrossed 6x into the *Caenorhabditis* Genetics Center wild type male stock to remove possible second site mutations, and ensure a wild type background [20]. Previous work on *mdl-1* and the function of Mad TFs in mammals led to several expectations about the possible effects of *mdl-1(0)*. First, since it is a DAF-16-activated gene, it might suppress *daf-2* mutant traits, e.g. constitutive dauer larva formation (Daf-c), stress resistance and increased longevity (Age). Second, since Mad TFs inhibit cell division and growth, *mdl-1(0)* might increase either somatic growth or germline proliferation.

We first examined effects of *mdl-1(0)* on somatic development and growth in wild type and *daf-2* mutant backgrounds. *mdl-1(0)* had no detectable effect on larval or adult growth (Figure 1B), but caused a slight reduction in constitutive dauer formation in *daf-2(m577)* mutants (Figure 1C). Next we probed the effects of *mdl-1* on the germline, first by looking at levels of fertility. The number of progeny produced by self-fertilized hermaphrodites was not affected by *mdl-1(0)*, either in terms of overall brood size or reproductive schedule (Figure 1D,E). As self sperm becomes depleted, N2 hermaphrodites start laying unfertilized oocytes [21]. Notably, *mdl-1(0)* caused a marked increase in the number of unfertilized oocytes laid, from 121 ± 15 to 219 ± 30 , an 81% increase (Figure 1D). *mdl-1*(RNAi) applied to RNAi-sensitive *rff-3(pk1426)* mutants also increased unfertilized oocyte number (data not shown).

In *daf-2(m577)* mutants, progeny number was also not different to N2, but the number of unfertilized oocytes laid was significantly reduced (Figure 1D,E), consistent with previous findings [22]. For convenience, to describe this mutant phenotype we introduce the term

Uno (abnormal in unfertilized oocyte production), and Uno-o, to describe mutants that are unfertilized oocyte over-producers (e.g. *mdl-1*), and Uno-d, to describe mutants that are unfertilized oocyte deficient (e.g. *daf-2*).

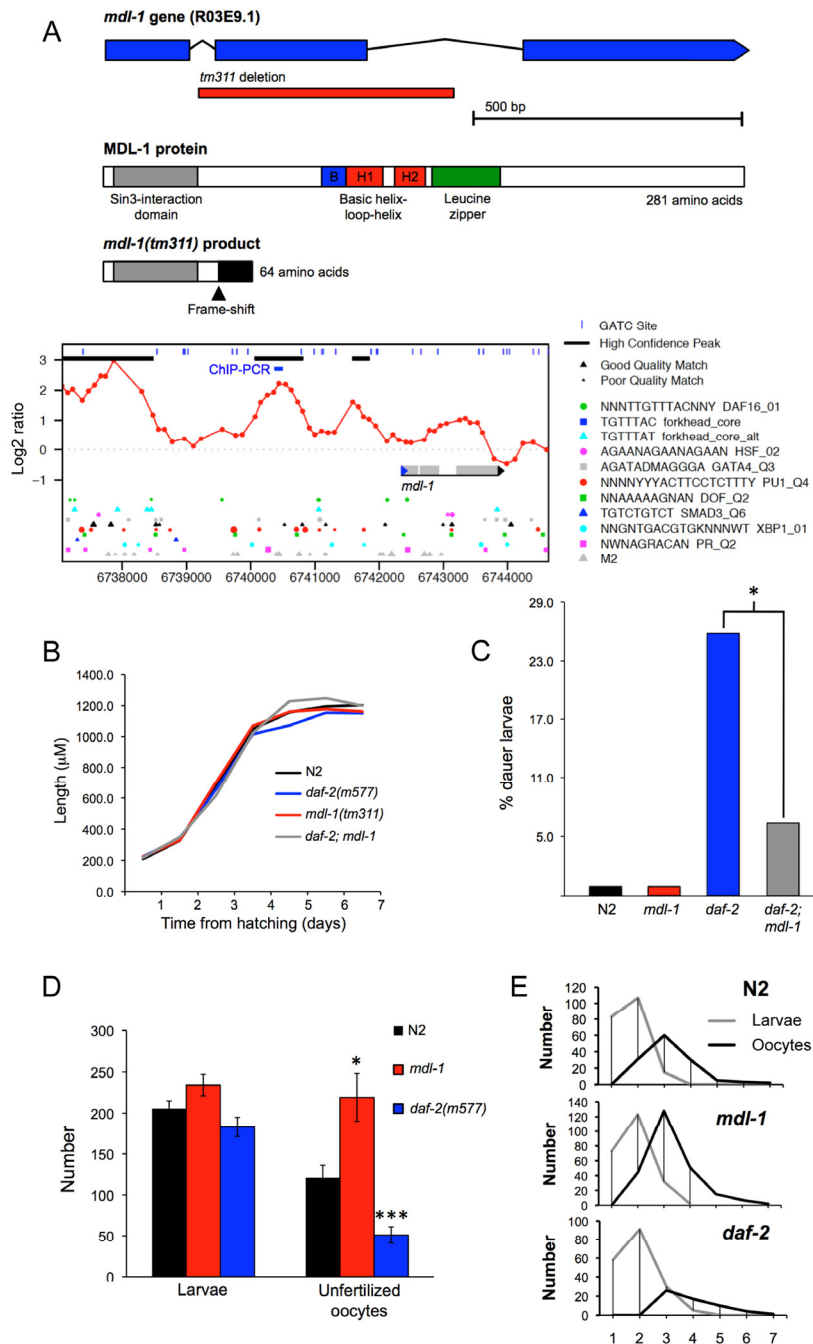


Figure 1. Phenotypic analysis of *mdl-1(tm311)* mutant. (A) *mdl-1* gene and protein description, including *tm311* deletion and effects on protein, DAF-16 binding sites (chromatin profile [DamID] data and DBEs) and site of ChIP analysis. For chromatin profile, y axis represents log₂ ratio of DAF-16 binding relative to control, and peaks correspond to potential DAF-16 binding sites [9]. (B–F). Phenotypic effects of *mdl-1(0)*. (B) Little effect on larval and adult growth. Samples sizes ranged from 23–39. (C) *mdl-1(0)* slightly reduces *daf-2(m577)* Daf-c, measured at 22.9°C. * 0.01 < *p* < 0.05 (Student’s *t* test). 4 trials conducted, in which *mdl-1(0)* reduced dauer formation in 3. (D, E) Effect of *mdl-1* and *daf-2* on fertility. Number of broods scored: N2, 19; *daf-2*, 20; *mdl-1*, 17. (D) Mean total progeny and unfertilized oocytes. * 0.01 < *p* < 0.05, *** *p* < 0.001 (Student’s *t* test). (E) Mean daily progeny and unfertilized oocyte numbers.

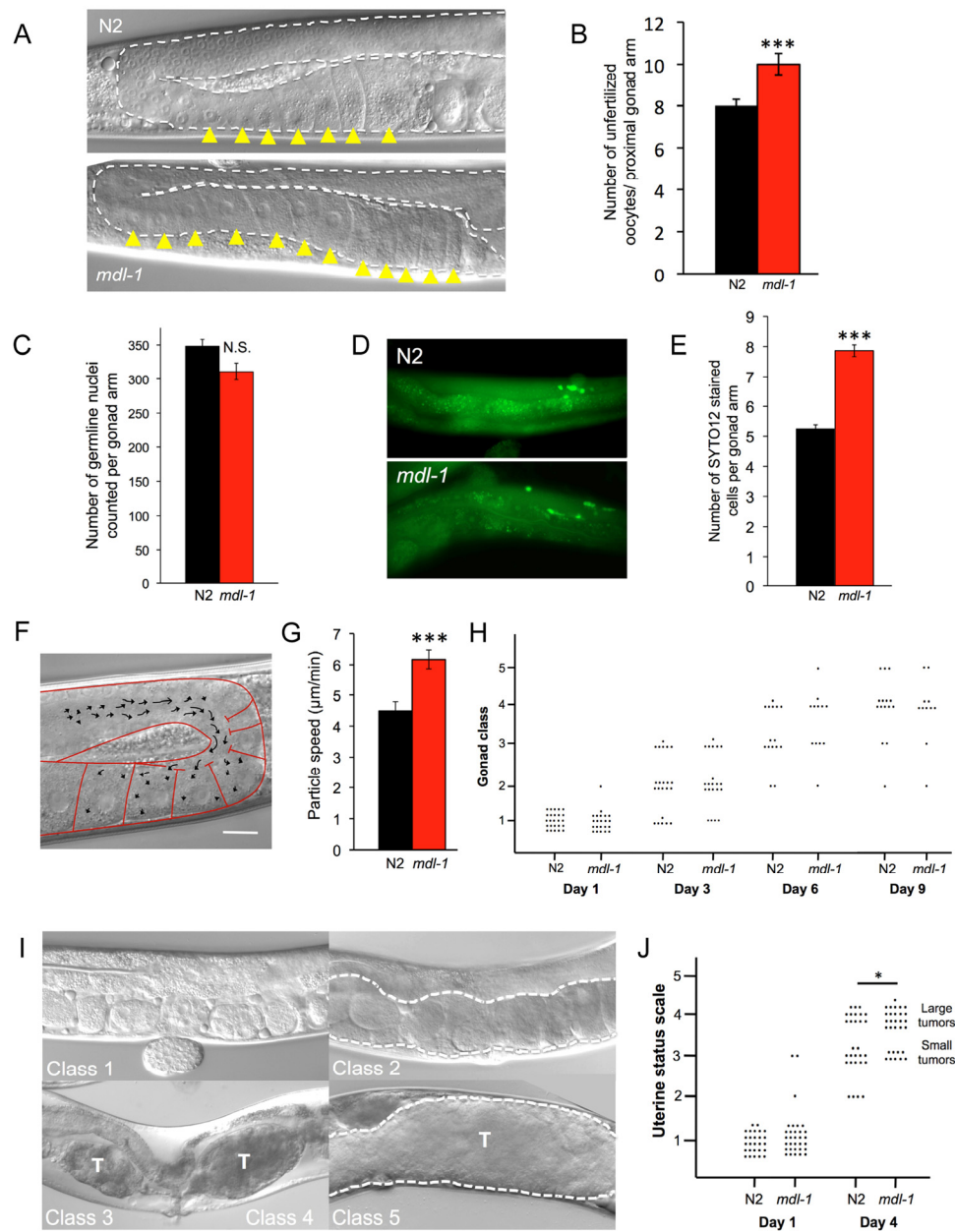


Figure 2. *mdl-1* causes hyperplasia and hypertrophy. (A, B) *mdl-1(0)* causes oocyte stacking in 1 day old worms. (A) Nomarski images. (B) Quantitation of stacking. Sample sizes: N2, 23; *mdl-1*, 17. *** $p < 0.001$ (Student's *t* test). (C) No effect of *mdl-1* on number of germline nuclei. $p > 0.05$ (Student's *t* test). (D, E) *mdl-1* increases levels of germline apoptosis. (D) Epifluorescence images of SYTO12 stained cells in young adult hermaphrodite germline. (E) Quantitated data. Number of gonads scored: N2, 153; *mdl-1*, 132. *** $p < 0.001$ (Student's *t* test). (F, G) *mdl-1* increases cytoplasmic streaming in the proximal gonad. (F) Single image obtained from a time-lapse recording. Arrows represent DIC-particle tracks. DIC-particles were tracked over a period of 1 minute. Scale bar: 20 μm . (G) Cytoplasmic streaming rate (mean particle speed \pm standard error). 30 particle speed measurements performed for each genotype. Number of worms examined: N2, 4; *mdl-1*, 3. *** $p < 0.001$ (Student's *t* test). (H) Absence of effect of *mdl-1(0)* on gonad disintegration (25°C). $p > 0.05$ for all comparisons of N2 vs. *mdl-1* of the same age (Wilcoxon Mann test). (I) Uterine status scale for quantitation of uterine tumor formation rate (5 classes). Class 1, normal uterus containing eggs (day 1 adult). Class 2, slightly abnormal uterine contents, but no tumor visible. Class 3, small tumor. Class 4, medium sized tumor. Class 5, large tumor, filling body cavity and squashing the intestine. Dotted line, outline of uterus. T, tumor. (J) *mdl-1(0)* increases uterine tumor formation (25°C), data summed from 3 trials. * $0.01 < p < 0.05$ (Wilcoxon Mann test).

***mdl-1(tm311)* causes germline hyperplasia and hypertrophy**

The *mdl-1* Uno-o phenotype suggests increased cell production in the germline distal to the spermatheca. To test this we compared proximal gonad contents in wild type and *mdl-1* animals on day 1 of adulthood. This revealed increased oocyte density, or stacking [23, 24], in *mdl-1* (Figure 2A,B), implying increased oocyte synthesis. This in turn suggests increased germ cell proliferation in the distal gonad. To probe this, we examined germ cell number by staining nuclei with the fluorescent DNA-binding dye 4',6-diamidino-2-phenylindole (DAPI), but no effect of *mdl-1* was detected (Figure 2C). However, an increase in the overall rate of germline cell turnover in *mdl-1* mutants could leave cell number unaffected.

If the distal proliferative zone is the source of germ cell nuclei, then the major sink is germline apoptosis. At least 50% [25] and as many as 97% [26] of germ cells undergo p53-independent, “physiological” apoptosis, their cytoplasm supplying expanding oocytes near the gonad bend. Using the SYTO 12 dye to detect apoptotic cell corpses, we found that *mdl-1* mutants showed a significant increase in apoptotic cell number in the germline in 3 out of 4 trials (Figure 2D, E).

The transfer of cytoplasm released by germ cells to nascent oocytes occurs by a process of cytoplasmic streaming (Figure 2F) [27]. We examined the effect of *mdl-1(0)* on the rate of cytoplasmic streaming in the mid-late pachytene region of the distal gonad, on day 1 of adulthood. Cytoplasmic streaming rate in *mdl-1* worms was significantly greater than in wild type (Figure 2G). Taken together, these results suggest that an increase in production of germ cells is matched by an increase in apoptosis, resulting in little change in overall germ cell number in the distal arm. Overall, this suggests that the increase in oocyte production is driven by a hyperplastic state in the distal gonad.

Next we studied the effect of *mdl-1* on pathologies of aging in the germline. The aging hermaphrodite gonad undergoes dramatic pathological changes. The distal gonad shrivels and eventually disintegrates [28, 29], while in the uterus large, amorphous masses (tumors) with very high DNA content develop [24, 29-31]. These tumors form from unfertilized oocytes which undergo multiple rounds of endoreduplication, and can grow to fill the entire body cavity in the mid-body. Continued germline apoptosis in late life contributes to gonad disintegration, and increased apoptosis rate is sufficient to increase gonad disintegration rate (Y. de la Guardia and D. Gems, unpublished). However, despite their

increased apoptosis rate (Figure 2D,E) gonad disintegration rate was not detectably altered in *mdl-1* mutants (Figure 2H).

Casual observation of *mdl-1* hermaphrodites under Nomarski microscopy suggested an increase in uterine tumors in these mutants. To verify this, we used a semi-quantitative approach [28] with a uterine status scale. According to the appearance of the uterus, worms were scored from 1 (healthy, no tumors) to 5 (large tumors) (Figure 2I) (see Materials and Methods). Using this scale to compare N2 and *mdl-1* mutants confirmed that uterine tumors grow significantly faster in *mdl-1* worms (Figure 2J).

***mdl-1* does not mediate effects of *daf-2* on germline proliferative status**

We next investigated whether MDL-1, like DAF-16, is an effector of *daf-2* mutant phenotypes. We first verified that DAF-16 acts directly on *mdl-1* to increase its expression, as predicted by mRNA and chromatin profiling studies [9]. Quantitative RT-PCR confirmed that *mdl-1* mRNA levels are higher in *daf-2* than in *daf-16*; *daf-2* strains (Figure 3A). Chromatin immunoprecipitation and PCR (ChIP-PCR) confirmed that DAF-16 binds to the *mdl-1* promoter (Figure 3B). This implies that *mdl-1* expression is activated by DAF-16 binding to its promoter.

mdl-1 mutants are Uno-o while *daf-2* mutants are Uno-d (Figure 1D,E) [22], and DAF-16 activates *mdl-1* expression (Figure 3A,B) [9]. This could imply that increased *mdl-1* activity in *daf-2* mutants reduces oocyte production. To test this we asked whether *mdl-1(tm311)* would suppress *daf-2* Uno-d, but it did not. Instead, *daf-2(m577)*; *mdl-1* worms were Uno-d (Figure 3C), i.e. *daf-2* is epistatic to *mdl-1*. *daf-2(m577)* also suppressed *mdl-1* effects on oocyte stacking and uterine tumor formation (data not shown). These results negate our hypothesis that *daf-2* Uno-d is caused by *mdl-1* over-activity. A different model was suggested by additional epistasis data as follows. In a *daf-2(+)* background, *daf-16* suppressed *mdl-1* Uno-o, consistent with the observation that *daf-16* over-expression in a *daf-2(+)* background can cause germline hyperplasia [32]. Thus, DAF-16 promotes oocyte production in a *daf-2(+)* background but inhibits it in a *daf-2(m577)* background (Figure 3D). Moreover, mutation of *daf-16* in a *daf-2*; *mdl-1* mutant did not restore MDL-1 Uno-o (Figure 3C). This suggests that MDL-1 suppresses the effect of DAF-16 on oocyte production in *daf-2(+)* worms, but plays no role in *daf-2* mutants (Figure 3D).

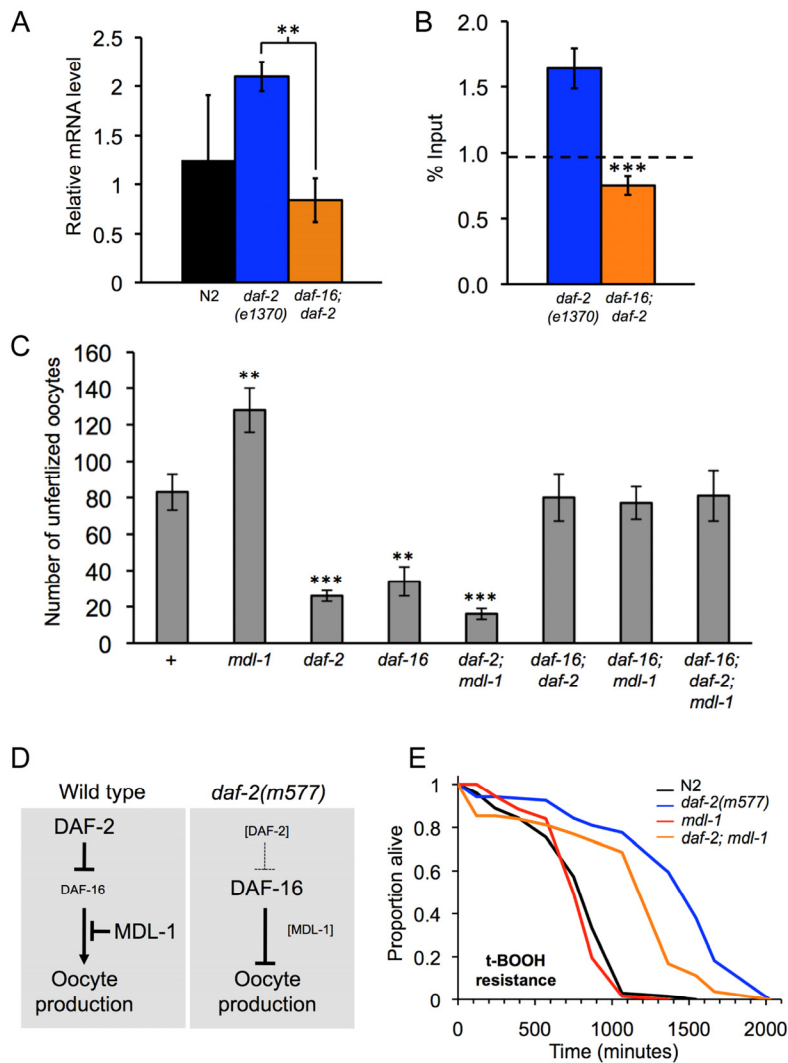


Figure 3. Distinct epistatic relationships between *daf-2* and *mdl-1* in hyperplasia and hypertrophy. (A, B). *mdl-1* is a direct transcriptional target of DAF-16. (A). *mdl-1* mRNA levels are increased in *daf-2* relative to *daf-2; daf-16* (Q-PCR data). ** 0.001 < p < 0.01. (B) DAF-16 binds to the *mdl-1* promoter (ChIP-PCR data). One experiment is shown which contained 3 immuno-precipitation replicates from the same chromatin preparation (error bars show the standard deviation between them). The dotted line shows the average inputs from 3 genes/genomic regions that do not show enrichment for DAF-16 binding in *daf-2* vs *daf-16; daf-2* in this particular trial, i.e. it reflects background DAF-16 binding levels. Significant DAF-16 binding was detected one of two additional trials. The position of the DAF-16 binding site detected is shown in Figure 1A. (C) *mdl-1*, *daf-2* and *daf-16* epistasis analysis with respect to unfertilized oocytes production (Uno). Total unfertilized oocyte production per worm was measured at 25°C. Means of 12 broods assessed; error bars, standard error. ** 0.001 < p < 0.01; *** p < 0.001 (Student's t test). (D) Model for interactions between DAF-2, DAF-16 and MDL-1, deduced from interactions between mutations. DAF-16 promotes oocyte production in *daf-2*(+) worms, but inhibits it in *daf-2*(*m577*) worms. MDL-1 acts via DAF-16 to inhibit oocyte formation in *daf-2*(+) worms, but does not influence oocyte production in *daf-2*(*m577*) worms. (E) Resistance to 7.5 mM *tert*-butylhydroperoxide (*t*-BOOH). Sample sizes (censored values): N2, 67 (7); *daf-2*(*m577*), 61 (8); *mdl-1*, 67 (8); *daf-2; mdl-1*, 70 (12). Probability of being the same: N2 vs. *mdl-1*, p = 0.24; *daf-2* vs. *daf-2; mdl-1*, p < 0.001 (log rank test).

daf-2 mutants exhibit various forms of stress resistance, including oxidative stress resistance (Oxr) [33]. We tested whether MDL-1 contributes to *daf-2* Oxr, specifically to *tert*-butylhydroperoxide (*t*-BOOH). In a wild-type background, *mdl-1(0)* did not affect Oxr, while *daf-2(m577)* markedly increased Oxr (Figure 3E). Notably, in a *daf-2(m577)* background, *mdl-1(0)* significantly decreased Oxr. This implies that MDL-1 contributes to *daf-2* Oxr.

MDL-1 contributes to *daf-2* mutant longevity by reducing baseline hazard

Next, we examined the effect of *mdl-1* on aging. First we compared effects of *mdl-1*(RNAi) on lifespan in *rrf-3* and *rrf-3; daf-2(e1368)* strains (25°C), and detected a reduction in lifespan only in the latter strain (data not shown), consistent with previous observations [6]. We then assessed the effect of *mdl-1(tm311)* on lifespan in wild-type or *daf-2(m577)* mutant backgrounds. *mdl-1* decreased lifespan in both wild-type and *daf-2* backgrounds, but the decrease was proportionally greater in the latter (Figure 4A, Table S1). This corresponded to a significantly greater *mdl-1*-induced increase in mortality in a *daf-2* background (4.5-fold vs 1.8-fold; significant interaction term, $p < 10^{-15}$, Cox proportional hazard analysis), suggesting that *mdl-1* activity contributes to the *daf-2* longevity increase.

To further characterize the effect of *mdl-1* on aging, we examined its effect on the pattern of age-specific mortality in wild-type and *daf-2(m577)* backgrounds.

Aging animal populations typically show exponential increases in mortality rate, and in *C. elegans* this occurs in two stages, with an initial faster exponential increase and a subsequent slower exponential increase [34, 35]. We fitted mortality data to a logistic model, which contains 3 components: a baseline hazard (initial mortality rate, parameter *a*), a mortality increase rate (parameter *b*) and a late-life mortality deceleration (parameter *s*).

In this analysis we wanted to probe whether *mdl-1(tm311)* shortens lifespan by accelerating aging or whether it could act by a life-shortening effect unrelated to aging. An effect of *mdl-1* on parameters *b* and *s* would imply an effect on aging, whereas an effect on parameter *a* could imply a non-aging related deleterious effect. In fact, *mdl-1* increased baseline hazard (*a*) without affecting the mortality increase rate (*b*) (Figure 4B-D). By contrast, relative to wild type, *daf-2(m577)* markedly decreased parameters *b* and *s*, while also slightly increasing parameter *a*. Reducing insulin/IGF-1 signaling has long been known to slow the age-related mortality rate increase [36]. In a *daf-2* background, *mdl-1(0)* again increased baseline hazard, and had no significant effect on parameters *b* and *s* ($p > 0.05$) (Figure 4C,D). In summary, this analysis confirms that *daf-2* increases lifespan by slowing demographic aging, while *mdl-1* shortens lifespan mainly by increasing baseline hazard. That *mdl-1* shortens lifespan more in a *daf-2* background could imply that MDL-1 contributes to *daf-2* longevity by reducing baseline hazard (see Discussion).

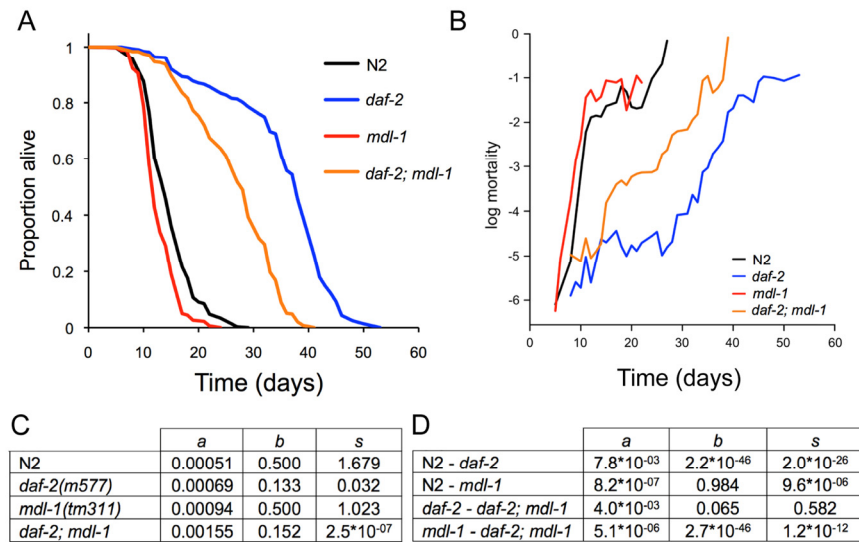


Figure 4. Effects of *mdl-1* on aging. (A) Effects of *mdl-1(tm311)* on lifespan (for statistics, see Table S1, combined data). (B) Effect of *mdl-1* on age-specific mortality profiles. (C, D) Mortality analysis using logistic model. (C) Estimated values of logistic model parameters. (D) Probability, *p*, of parameters in compared genotypes being the same, holding other parameters constant.

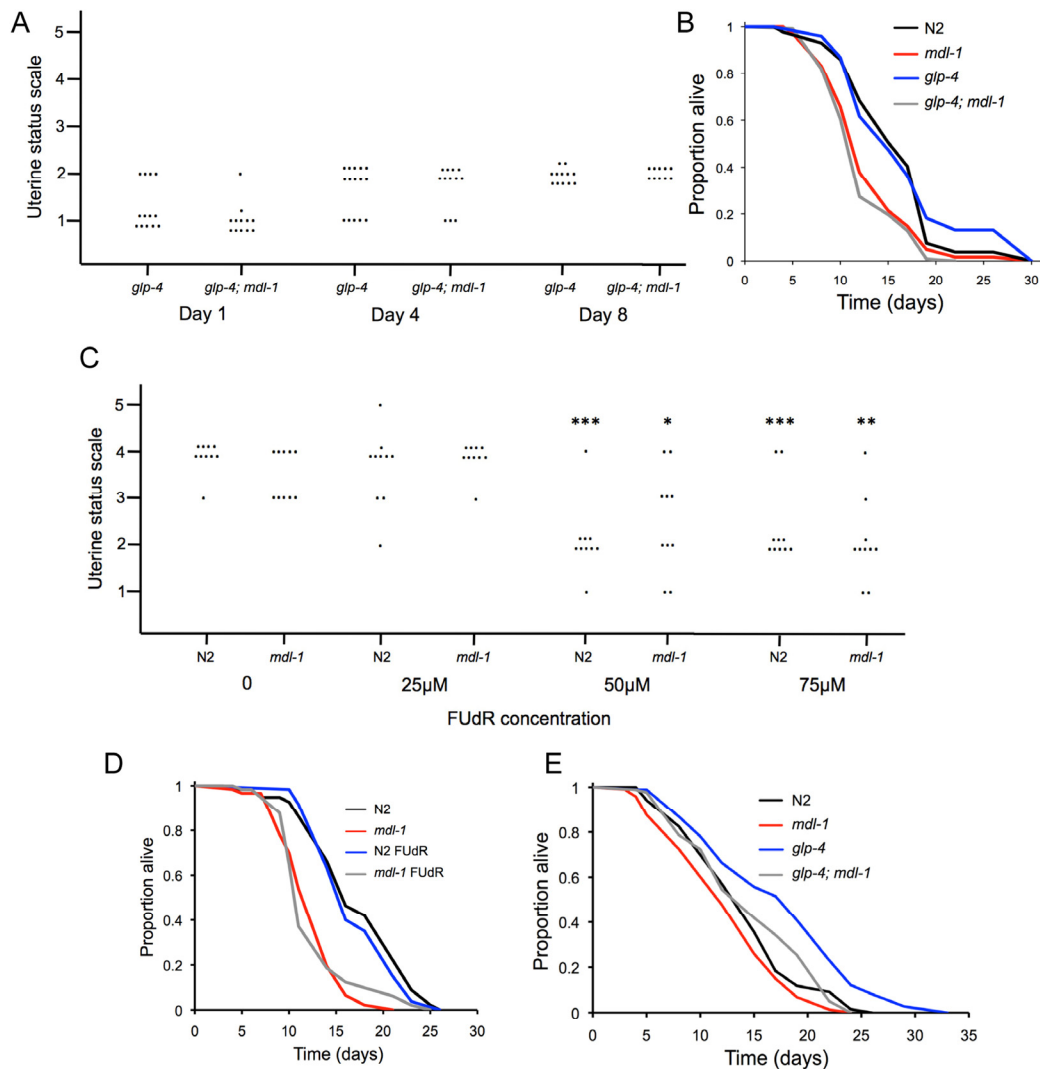


Figure 5. No effect of uterine tumors on lifespan. (A) Uterine tumors are not seen in *glp-4(bn2)* mutants (raised at 15°C to L4 then shifted to 25°C). Uterine classes 2-5 indicate presence of tumors. Each dot corresponds to a uterine status measurement. (B) *glp-4* does not suppress *mdl-1* effects on lifespan (for statistics, see Table S2, trial 1). (C) FUDR suppresses formation of uterine tumors at 50μM or greater. Stars represent a significant difference to worms of the same genotype in the absence of FUDR. No significant difference in tumor levels between N2 and *mdl-1* were detected at this age at any FUDR concentration. * 0.01 < *p* < 0.05; ** 0.001 < *p* < 0.01; *** *p* < 0.001 (Wilcoxon Mann test). (D) 50μM FUDR does not suppress *mdl-1* shortevity or increase N2 lifespan (for statistics, see Table S2, trial 1). (E) Effect of *mdl-1* on *glp-4* longevity (for statistics, see Table S2, trial 2).

Uterine tumors do not limit lifespan

mdl-1(0) accelerates formation of uterine tumors, which frequently grow very large, filling the body cavity in the mid-body region and squashing the intestine [31]. One possibility is that uterine tumors can contribute to mortality and that increased tumor formation in *mdl-1(0)* mutants causes a shortened lifespan. To test this, we examined the effect of *mdl-1* on lifespan in the

absence of uterine tumors. *glp-4(bn2)* mutants have a temperature-sensitive germline proliferation defect; if raised at 15°C to L4 and then switched to 25°C, oocyte production is blocked but longevity is not increased [7]. We first confirmed that *glp-4* blocks formation of uterine tumors (Figure 5A). We then compared lifespan in *glp-4*, *mdl-1* and *glp-4; mdl-1* worms. *glp-4* worms were normal-lived, but both *mdl-1* strains were similarly short lived (Figure 5B; Table S2).

We also blocked uterine tumor formation using the inhibitor of DNA replication 5-fluoro-deoxyuridine (FUdR), which is also commonly used to treat colorectal cancer. Application of FUdR at low concentrations (e.g. 10-25 μ M) from L4 stage is a convenient means to block progeny production, and has little effect on lifespan [37]. 50 μ M FUdR, but not lower FUdR concentrations, was sufficient to block formation of uterine tumors (Figure 5C). We then compared effects of 50 μ M FUdR on lifespan in wild type and *mdl-1* worms, and saw no effect on lifespan in either case (Figure 5D; Table S2). These results show that accelerated formation of uterine tumors do not cause the shorter lifespan of *mdl-1* worms. They also demonstrate that uterine tumors do not limit lifespan in wild type worms under standard culture conditions. This contrasts with the case of *daf-16* over-expression, where life shortening is suppressed by blocking germline hyperplasia either with *glp-1* or FUdR [32].

A number of interventions that remove the hermaphrodite germline cause increased lifespan, including raising *glp-4(bn2)* mutants at 25°C, and this effect is *daf-16* dependent [38, 39]. Notably, *mdl-1(0)* also reduced the longevity of *glp-4* mutants raised at 25°C (Figure 5E, Table S2). *mdl-1* shortened lifespan more in a *glp-4* background than in a wild-type background (Table S2). This suggests that *mdl-1(+)* contributes to *glp-4* longevity as well as *daf-2* longevity.

Evidence that *mdl-1* can act in the intestine to promote longevity

The intestine plays an important role in *daf-2* mutant longevity [40], and is a site of *mdl-1* expression [10]. One possibility is that *mdl-1* affects intestinal protein synthesis. Mutation of *daf-2* causes a global reduction in protein synthesis, which may contribute to longevity [41, 42]. In aging hermaphrodites, yolk proteins (vitellogenins) become very abundant indeed [43, 44], and this accumulation is suppressed *daf-2*, apparently by inhibition of protein translation in the intestine [45] where yolk is synthesized [46]. Thus, vitellogenin accumulation rate gives some indication of intestinal protein synthesis rate. However, *mdl-1(0)* did not alter vitellogenin accumulation, either in wild type or *daf-2* mutant backgrounds (Figure 6A,B). One possibility is that *mdl-1* mutants do synthesize more vitellogenin, but due to increased laying of unfertilized oocytes, this does not result in increased vitellogenin accumulation. To check this we compared sterile *glp-4* and *glp-4; mdl-1* worms (shifted at L4 to 25°C), but again no effect of *mdl-1* was seen (Figure 6A,B).

Next, we asked whether intestine-limited rescue of *mdl-1* using the *ges-1* promoter [47] would rescue *mdl-1* shortevity. A transgene array from which *mdl-1* was expressed using its own promoter was able to restore wild-type lifespan to *mdl-1(tm311)* mutants (Figure 6C; Table S3). Notably, *pges-1::mdl-1* too increased lifespan in *mdl-1* mutants, though the effect was smaller such that lifespan was not restored to wild type. This suggests short lifespan in *mdl-1* mutants is caused by loss of *mdl-1* from several sites, including the intestine. Possibly, a second site of action of *mdl-1* on lifespan is the germline, given its impact on that tissue.

The extent of loss of Myc among nematodes

One puzzle relating to *mdl-1* function is the absence of Myc in *C. elegans*. In mammals, the Mad/Max/Myc system works in concert with the Tor pathways to control growth [48]. *C. elegans* also lacks key components of the Tor pathway, including the Tsc1/Tsc2 complex [49], and 4E-BP [50] (Figure 7A). To try to understand the significance of the absence of Myc in the broader context of nematode gene loss, we tested for the presence of Myc, Tsc1, Tsc2 and 4E-BP throughout the Nematoda. It was previously noted that Myc orthologs are absent not only from *C. elegans* and *C. briggsae*, but also the filarial parasite *Brugia malayi* (nematode order Spirurida), and even the bilharzia parasite *Schistosoma mansoni* (phylum Platyhelminth) [51]. Searching the genomes of 13 nematode species, including representatives of the major nematode orders, no Myc orthologs were detected (Figure 7B). Myc was also absent from all 5 platyhelminth species examined. This implies that Myc evolved in the common ancestor of arthropods and chordates after divergence from the common ancestor of nematodes and platyhelminths, as previously suggested [51]. Thus, the Myc-less Mad-Max circuit in *C. elegans* appears to represent a more ancient regulatory system.

By contrast, both Tsc1/Tsc2 and 4E-BP were found in several nematode groups but were absent from many others, in a pattern indicating that each gene has been lost several times during nematode evolution. For Tsc1 and Tsc2, gene loss was correlated, i.e. both genes were either present or absent. There was no correlation between loss of Tsc1/Tsc2 and 4E-BP: nematode species exist with Tsc1/Tsc2 but lacking 4E-BP and vice versa. The distribution of Tsc1/Tsc2 is surprising in that most nematode and all platyhelminth groups lack this complex, apart from spirurid nematodes, and two rhabditid species. Sequence comparisons of Tsc1 and Tsc2 protein sequences from nematodes and other animal groups is consistent with multiple instances of gene loss (rather than horizontal gene transfer) (Figure 7C).

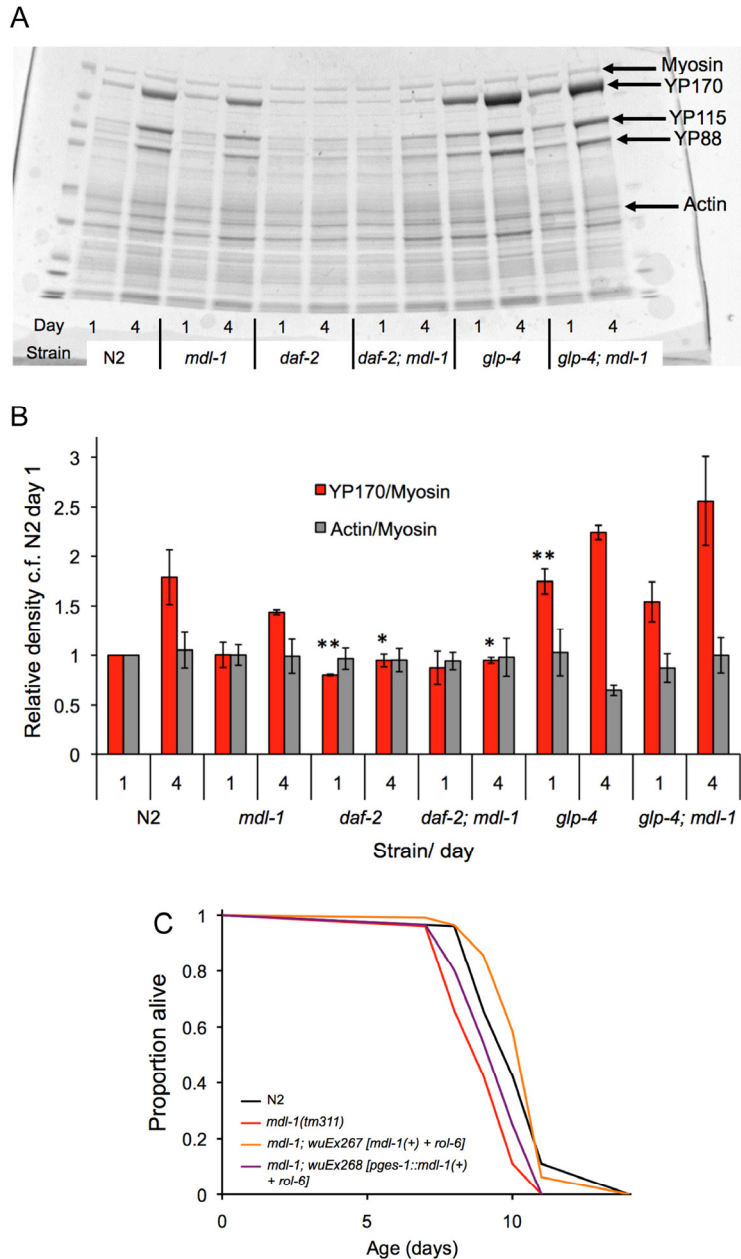


Figure 6. Tests for action of *mdl-1* in the intestine. (A,B) Effect of *mdl-1* on yolk accumulation. **(A)** Example of Coomassie stained gel with *C. elegans* protein extracts. **(B)** Bar graph data is derived from densitometric measurement of protein on gels (means of 3 biological replicates; error bars, standard error). It shows levels of the major yolk protein YP170 normalized to myosin levels (which are not expected to change), and again to levels in N2 on day 1. Actin/myosin ratio gives an indication of the reliability of myosin as a standard. * $0.01 < p < 0.05$; ** $0.001 < p < 0.01$, compared to N2 of the same age. **(C)** Effects on lifespan of *pges-1::mdl-1(+)* rescue of *mdl-1(0)* (for statistics, see Table S3, trial 2).

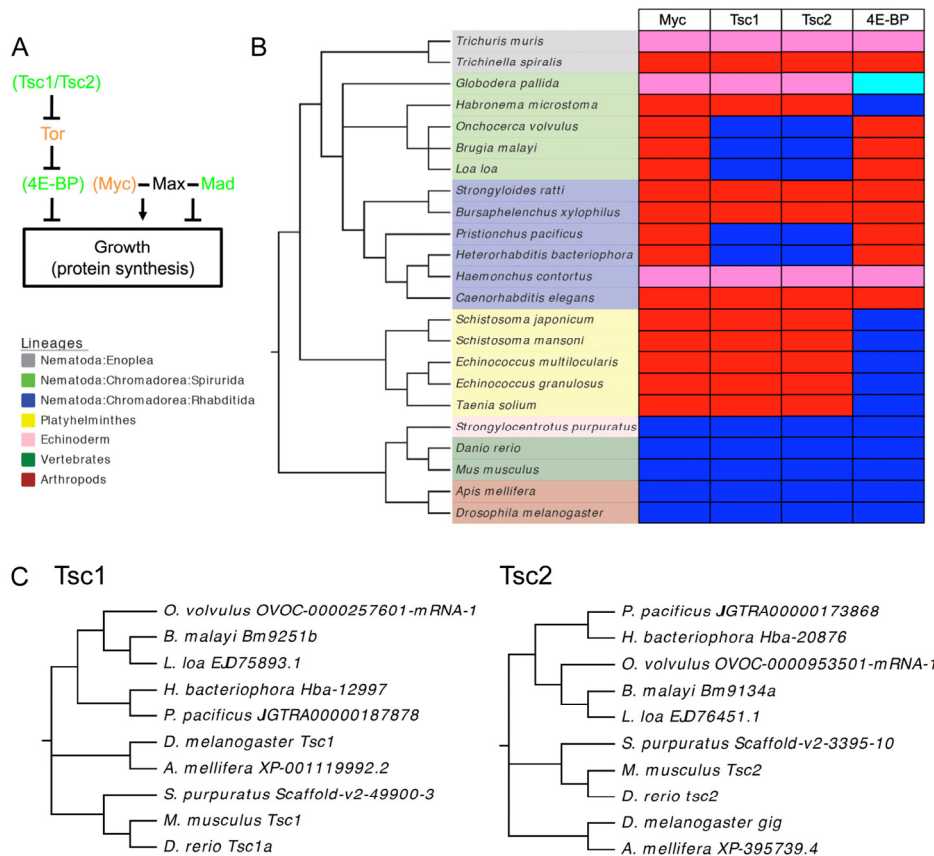


Figure 7. Extent of loss of Myc, Tsc1/Tsc2 and 4E-BP among the Nematoda. (A) Outline of missing elements of Tor and Myc/Max/Mad pathways in *C. elegans*. Green, tumor-suppressor/anti-aging; orange, oncogene/pro-aging. In brackets, proteins missing from *C. elegans*. **(B)** Presence and absence of Myc, Tsc1, Tsc2 and 4E-BP among nematodes and platyhelminths. Red, absent; dark blue, present; pink, not found; pale blue, putative but somewhat divergent 4E-BP. Not found: a caveat to this analysis may be the incompleteness of the genomic sequences of some of these species with draft assemblies being available for *G. pallida* and *H. contortus* and only contigs available for *T. muris*. **(C)** Phylogenograms of Tsc1 and Tsc2 sequences for nematodes and other animal groups. Note that species and sequence phylogenies correspond.

DISCUSSION

In this study we have shown that MDL-1 acts as an inhibitor of germline proliferation, and of oocyte hypertrophy, thereby inhibiting a salient aging-related pathology (uterine tumors). These properties of *mdl-1* mutants recapitulate effects of Mad TFs in mammals, e.g. mice lacking the Mad TF Mxi1 show hyperplasia in a number of tissues (e.g. prostatic epithelium), and are tumor prone [52]. We also confirm that MDL-1 inhibits aging, consistent with the observed association between tumor suppressors and inhibition of aging [53, 54].

Does *mdl-1* act downstream of *daf-16*?

Our initial hypothesis was that activation of *mdl-1* expression by DAF-16 contributes to *daf-2* longevity. The results of analysis of *mdl-1* expression (Figure 3A,B) and the effects on lifespan of *mdl-1(tm311)* (Figure 4A) are consistent with this hypothesis. We also noted that *mdl-1* and *daf-2* have opposing effects on the germline: *mdl-1(0)* causes Uno-o, increased oocyte stacking and increased uterine tumors (this study), while mutation of *daf-2* has opposite effects [22, 29]. This suggested that the effects of *daf-2* on the germline

might be mediated by *mdl-1*. However, epistasis analysis shows that this is not the case for oocyte production (Figure 3C). Instead *mdl-1* appears to have no effect on the germline in *daf-2* mutants, but to inhibit promotion of germline proliferation by DAF-16 in *daf-2(+)* worms (Figure 3D).

Does *mdl-1* affect aging?

The life-shortening effect of *mdl-1(0)* is mainly the result of increased base-line hazard (Figure 4B-D). This could imply that *mdl-1(0)* does not affect aging but, rather, shortens lifespan by causing a pathology that is distinct from aging. In similar fashion, a comparison of mortality in two groups of people during the 1940s, either in Australia or interned by the Japanese, showed increased base-line hazard but not increased demographic aging in the latter [55]. It is interesting to consider whether this necessarily means that the effect of *mdl-1* on lifespan does not involve an effect on aging. The impact of *mdl-1(0)* on lifespan is greater in a *daf-2* background, suggesting that MDL-1 does contribute to *daf-2* longevity, i.e. that *mdl-1* does affect aging. Arguably, the critical point here is that something that affects demographic aging necessarily affects biological aging, while something that affects base-line hazard may or may not affect biological aging. In other words, the biological process of aging is not always the same thing as demographic aging.

One working definition of biological aging is the set of endogenously generated pathologies that increase in later life [56]. In principle, interventions that reduce one or more age-related pathology (i.e. part or all of aging) could increase lifespan by reducing base-line hazard, demographic aging, or both. One possibility is that the wider the spectrum of age-related pathologies that an intervention suppresses, the more likely will a reduction in demographic aging be seen. In conclusion, *mdl-1(0)* may or may not affect aging. Its greater effect on *daf-2* could imply that it does; however, an alternative possibility is that *mdl-1(0)* causes a pathology that is distinct from those seen during aging, and that *daf-2(-)* slightly increases the severity of this pathology, or increases its effect on mortality.

Where and how does *mdl-1* act to impact lifespan?

The phenotype of *mdl-1(tm311)* mutants demonstrates that MDL-1 acts as a repressor of growth and proliferation in the germline. This is consistent with the role of Mad TFs as repressors of growth and proliferation in mammals [11]. A long-standing hypothesis about aging is that it is caused by molecular damage, but more recently it has been suggested that aging is caused by the

run on of developmental and reproductive processes in late life, leading e.g. to pathological hyperplasia, hypertrophy and atrophy [57-59]. The action of MDL-1 as a DAF-16-activated suppressor of growth is broadly consistent with this model.

The *mdl-1* mutant phenotype also suggests that this gene may affect lifespan through its effects on the germline. One possibility is that over-production of oocytes or increased formation of uterine tumors *per se* cause a decrease in lifespan. However, our findings argue against this: suppression of these effects in *mdl-1* mutants using *glp-4* or FUDR does not suppress the life-shortening effects of *mdl-1(0)* (Figure 5B,D). A second possibility is that *mdl-1(0)* affects signaling from the germline; removal of the germline can extend lifespan, and this effect is *daf-16* dependent [39]. Consistent with this possibility, *mdl-1(0)* shortens lifespan somewhat more in long-lived germlineless *glp-4* mutants than in otherwise wild-type worms (Figure 5E).

Another possible site of *mdl-1* action on lifespan is the intestine, which plays a significant role in the control of aging [40], and where *mdl-1* is expressed [10]. Notably, intestine-limited rescue of *mdl-1(+)* in otherwise *mdl-1(0)* worms was sufficient to modestly increase lifespan. However, how *mdl-1* acts in the intestine remains unclear. Mutation of *daf-2* increases intestinal expression of *ftn-1*, which encodes the iron storage protein ferritin. This increase is wholly *daf-16* dependent and partially *mdl-1* dependent [14]. Free iron is required for growth (e.g. ferroprotein synthesis) but also generates oxidative stress. Thus, increased activity of MDL-1 in *daf-2* mutants might retard intestinal aging as part of a program of suppression of protein biosynthesis. However, we did not detect an effect of *mdl-1* on accumulation of the most abundant protein class in *C. elegans* hermaphrodites, the vitellogenins (Figure 6A,B), which are synthesized in the intestine [46]. However, it remains possible that other aspects of protein synthesis are reduced by *mdl-1*.

Alternatively, mutation of *mdl-1* might increase levels of free iron in the intestine, perhaps accelerating aging by increasing oxidative damage, as suggested by the free radical theory. Consistent with this, *mdl-1(0)* partially suppress *daf-2* Oxr (Figure 3E), suggesting that MDL-1 promotes Oxr in *daf-2* mutants. However, *mdl-1(0)* alone did not affect Oxr; moreover, free iron levels appear to have little effect on aging under standard culture conditions [60]. More broadly, a range of studies suggest that oxidative damage is not a central determinant of aging, particularly in *C. elegans* [61, 62]. Together, these findings suggest that the intestine is one of several sites of action of *mdl-1* on lifespan.

The significance of uterine tumors in *C. elegans*

The oocyte-derived growths in the *C. elegans* uterus have been noted in previous studies and referred to as ‘*tumor-like*’ growths [30], *masses* [24] and *oocyte clusters* [29]. Dictionary definitions of the word *tumor* vary, but in the common understanding of *tumor*, as in “a growth — a mass of tissue — that has no function” [63], these entities are tumors, hence our use of the term in this study. Arguably, *C. elegans* uterine tumors are both different and similar to mammalian cancer. It seems likely that *C. elegans* uterine tumors result from aging-associated overgrowth rather than mutations in oncogenes or tumor suppressor genes. But much of mammalian cancer, like worm uterine tumors, is part of the aging process. While it is clear that aging and cancer are associated, the relationship between the two remains unclear. One possibility is that aging results in changes in tissue microenvironment, e.g. due to senescent cell accumulation, that create more permissive conditions for cancer growth [64]. Aging-related tumors can occur even in the absence of transforming mutation, as in benign prostatic hyperplasia (BPH). We postulate that *C. elegans* uterine tumors, like BPH, exemplify the non-mutational driven component of aging-associated cancer.

The regulatory network within which *mdl-1* might function

In mammals, Mad TFs act antagonistically to Myc TFs, which promote the cell cycle, growth and apoptosis, and reduce H ferritin expression [11, 15]. Consistent with this, MDL-1 inhibits germline growth and apoptosis (this study), and activates *fin-1* expression [14]. Moreover, in mammals over-expression of Myc can induce endomitosis and cause increased ploidy [65], often seen in tumors, and also in senescent cells [66, 67], while MDL-1 antagonizes growth of uterine tumors formed from endomitotic oocytes (this study). Thus, MDL-1 in *C. elegans* behaves as one would expect of an antagonist of Myc – which is perhaps surprising given that *C. elegans* does not possess Myc. Indeed, Myc appears to be absent from the entire Nematode phylum (this study) [51].

In mammals, the Tor pathway and Myc TFs work in concert to control protein synthesis. Myc TFs activate expression of translational machinery genes, including eIF4E, eIF4A and eIF4G, which are components of the eIF4F complex that promotes translational initiation [48]. *C. elegans* lacks many genes that are present in other animal phyla [68], which can limit its usefulness as a model organism. Besides Myc, this also affects the worm Tor pathway, which lacks several key proteins, notably Tsc1/Tsc2 and 4E-BP. Thus, *C. elegans* possesses what

appears to be a different version of the IIS/Tor/Mad network of higher animals. To fully understand the worm network requires understanding these differences.

Several interpretations have been made of the absence of Myc in *C. elegans*. First, that it reflects the relatively restricted *C. elegans* cell proliferation program [10]. Second, that in *C. elegans* the Myc role is played by a different bHLH TF, for example MML-1 (Myc and Mondo-like 1) [16]. However, arguing against this interpretation, MML-1 resembles Mondo rather than Myc, it dimerizes with MXL-2 while MDL-1 dimerizes with MXL-1, and deletion of *mxl-2* has only minor phenotypic effects (abnormal migration of ray 1 precursor cells in the male tail), and does not affect e.g. growth or lifespan [16].

Another possibility is that the Myc-less Mad-Max circuit ensures rapid growth, i.e. the nematode machinery for protein translation is, in the absence of DAF-16 and MDL-1, constitutively active. Consistent with this, Tsc1/Tsc2 and 4E-BP, which both antagonize growth, are absent from *C. elegans*, and most other nematodes (Figure 7B). Notably, in *Drosophila*, inhibition of growth resulting from reduced Tor kinase activity (e.g. by overexpression of Tsc1 and Tsc2) can be rescued by overexpression of dMyc [69]. An intriguing detail is the presence of Tsc1/Tsc2 in several spirurid nematodes (Figure 7B, Table S4); notably this group includes the longest lived nematode species known, e.g. the maximum lifespan of adult *Loa loa* is at least 20 years [70]. Another possibility is that the growth inhibitory functions of Tsc1/Tsc2 and 4E-BP have been taken over by DAF-16/FoxO, which is a major regulator of protein synthesis in *C. elegans* [41, 42, 45]. Thus, perhaps DAF-16 suppresses growth in soma and germline, while MDL-1 suppresses growth in the germline alone.

Conclusions

These results confirm that the Mad TF MDL-1 contributes to the *daf-2* longevity phenotype, and reveal a major role in inhibition of germline growth and reduction of uterine tumor development. They also suggest a role for intestinal MDL-1 in longevity assurance. The action of *mdl-1* as a DAF-16 activated gene that inhibits growth is broadly consistent with the possibility that the effects of insulin/IGF-1 signaling and DAF-16 on aging are a function of their effects on growth.

EXPERIMENTAL PROCEDURES

C. elegans culture and strains. Worms were cultured as previously described [71], at 20°C unless otherwise stated. Nematode strains used include N2 (wild type),

DR1567 *daf-2(m577)III*, SS104 *glp-4(bn2)I*, GA1200 *mdl-1(tm311)X* (6X out-crossed), GA91 *daf-16(mgDf50)I*; *daf-2(m577)*, GA1204 *daf-2(m577)*; *mdl-1(tm311)*, GA1208 *daf-16(mgDf50)*; *daf-2(m577)*; *mdl-1(tm311)*, GA1226 *daf-16(mgDf50)*; *mdl-1(tm311)*, GA1230 *glp-4(bn2)*; *mdl-1(tm311)*, GA1604 *mdl-1(tm311)*; *wuEx267[mdl-1 + rol-6(su1006)]*, GA1605 *mdl-1(tm311)*; *wuEx268[pges-1::mdl-1 + rol-6(su1006)]*. Primers to identify *mdl-1(tm311)* were atggaacagcaactcaaccttgg and ttaacttggagggtgattggcaag, and heterozygotes atgatgtgatctcgggctcg. Primers to genotype *daf-16(mgDf50)* were as described [72].

Strain construction. Multiple mutant strains were generated using standard genetic and molecular methodologies. Strains carrying mutations on the X chromosome (e.g. *mdl-1(tm311)*) were crossed with N2 males to generate hemizygous mutant males which were mated with L4 hermaphrodites of the strain carrying the second mutation of interest. F1 offspring were picked, and allowed to self-fertilise and 80 F2 were picked, allowed to lay eggs overnight, lysed and stored at -20°C. Genomic deletions were identified using PCR. In the presence of the temperature sensitive *daf-2(m577)* allele, F1 animals were shifted to 25°C to select for dauer formation in the F2, dauers were picked and left to recover at 15°C to lay eggs, the F2 were lysed and tested for deletions. The *daf-16(mgDf50)*; *daf-2(m577)*; *mdl-1(tm311)* triple mutant was constructed by mating *daf-16*; *daf-2* males with *daf-2*; *mdl-1* hermaphrodites. The F2 generation was cloned, lysed and offspring raised at 25°C. *daf-16(mgDf50)* homozygotes in the F3 were initially identified as non-dauer formers, and *mdl-1(tm311)* homozygotes identified by PCR.

mdl-1 transgenic lines were created by microinjection using PCR products and PCR fusion [73]. Primers used to make GA1604 were aaattgcatgcagagacg and gaaagatacggagggtgctg. Primers used to make GA1605 were ttgtctattggtatggctgc; ggttgagttgctgtccattacaaggaa tatccgcatctg; gcgctaccaataaggctaa; aatggaacagcaactc aacc; gaaagatacggagggtgctg; and tttaacaacagatccacag.

Staining protocols. To quantify germ cell number, nuclei were stained using DNA-binding dye 4',6-diamidino-2-phenylindole (DAPI). Animals were fixed in methanol, washed with M9 buffer and incubated in the dark in a 500ng/μl DAPI solution for 30 min. Thereafter they were washed again in M9 buffer. To quantify the number of apoptotic cells in living animals, nematodes were stained with SYTO 12 Green Fluorescent Nucleic Acid Stain (Molecular Probes). The animals were incubated in the dark in a 33μM SYTO 12 solution for 4 hr, and then placed on an OP50 lawn for 1 hr.

Quantitative RT-PCR and chromatin immunoprecipitation PCR (ChIP-PCR). RT-PCR and ChIP-PCR were performed largely as previously described [9, 74]. Primers for RT-PCR amplification from *mdl-1* mRNA were cccgttgcgtgtcattgt and atggattgtgagagtgtgagaat. Primers for ChIP-PCR of an *mdl-1* promoter region (Figure 1A) were ccccctcgttttccatgt and gccgctcgtccaatg.

Microscopy. Freshly prepared agar pads were created by dropping 35μl of 2% agarose onto a glass slide. Worms were anaesthetised using 5μl 0.2% levamisole. Nomarski microscopy was performed on a Zeiss Axioskop2 plus microscope with a Hamamatsu ORCA-ER digital camera C4742-95. Images were acquired using Volocity 5.5 software, with 10x eyepieces and a 40x objective lens. For body size measurements, worms were synchronized and hatched overnight in M9 buffer. The next day, ~30 worms per strain were imaged, and the remainder cultured on OP50 and thereafter imaged consecutively for 6 days. Volocity 5.5 was used to quantify the length of the worm from head to tail and the width across the pharyngeal-intestinal valve region.

Uterine tumor scoring system. Uterine status was scored from 1 to 5, where scores of 3-5 indicates the presence of a tumor. Class 1 denotes a normal, youthful uterus containing fertilized eggs and/or unfertilized oocytes of normal appearance. Class 2 denotes a uterus whose contents appear somewhat abnormal, but without a clear increase in size. Class 3 denotes a uterus containing a small tumor. Class 4 denotes a uterus containing a medium sized tumor, that does not fill the body cavity in the mid-body region. Class 5 denotes a uterus where the tumor is large, and fill the entire body cavity in the mid-body region, and even causes distension of the body wall. For the scoring, the tumor images was randomised, and the scoring was performed blinded by 3 different scorers. The non-parametric Wilcoxon test was used to compare tumor classes between worm strains and within the same strain on day 1 and day 4. The analysis was performed using the statistical programme JMP 9 (SAS Institute Inc.)

Fertility measurements. Brood sizes were assayed as previously described [22]. Briefly, 10-12 L4 hermaphrodites, raised at 20°C were cloned on individual plates, shifted to 25°C and transferred daily for 7 days. Plates were incubated at 20°C for 24 hr to allow offspring to hatch and then larvae, unfertilized oocytes and dead eggs were scored.

Yolk level measurements. For each test sample, 50 hermaphrodites at day 1 and 4 of adulthood were transferred into an Eppendorf tube filled with 1 ml M9

buffer. Worms were spun at 800 rpm for 2 min and supernatant removed, leaving 25 μ l. Then 25 μ l of 2x Laemmli buffer (Sigma) was added, and samples incubated at 70°C for 15 min, vortexed every other minute and then shifted to 95°C for 5 min. Lysates were centrifuged at 13,000 rpm at 4°C for 15 min. 20 μ l of each sample was loaded onto a Criterion XT Tris-Acetate gel. The gel was run at 200V in SDS-PAGE chamber with 1x 3-(N-morpholino) propanesulfonic acid (MOPS) buffer for 45 min. The gel was fixed in methanol, acetic acid and ultrapure water in ratio of 50:10:40 for 30 min. The fixing solution was then discarded and replaced with Coomassie fixation solution (50:3:40:10 methanol: Coomassie stock solution: ultrapure water: acetic acid). 12.0 g of Brilliant Blue R-250, 300 ml methanol and 60ml acetic acid were used to prepare Coomassie stock solution. The gel was incubated overnight in destaining solution (45:10:45 methanol: acetic acid: ultrapure water). Protein bands on the gel were visualised by a Image Quant GE Healthcare scanner system connected to a computer, and analysed by ImageQuant software with which densitometry was performed. Each experiment was done in triplicate.

Lifespan measurements. These were conducted as previously described [22]. Briefly, 5 plates per condition were seeded with OP50 2 days before the start of the experiment. 10 μ M FUdR was topically applied before beginning the trial. Animals were raised at 20°C, or for assays including *glp-4(bn2)* mutants, animals were raised at 15°C and switched to 25°C at L4 stage. All animals were transferred to fresh plates on day 5 and 10. Deaths were scored and losses due to causes other than death were censored. Lifespan data were deposited in SurvCurv [75] <IDs filled in proof>.

Dauer formation measurement. Dauer formation was assessed at 22.9°C as previously described [22]. Briefly, 12 L4s were picked and raised to adulthood at 20°C for 2 days. These gravid adults were then placed on 35mm plates to lay eggs for 6 hrs at the test temperature, after which the adults were removed and the larvae were allowed to develop at the test temperature. Dauers and normal larvae were scored 72 hr after the midpoint of the egg lay and the percentage dauer formation was calculated by dividing the number of dauer larvae by the total number of offspring.

Oxidative stress resistance. 1 day old adults were tested for resistance to 7.5 mM *tert*-butylhydroperoxide (*t*-BOOH) as previously described [33]. Briefly, L4 animals were picked from mixed stage plates raised at 20°C, then shifted to 25°C overnight. NGM agar was supplemented with 7.5 mM *t*-BOOH and the plates

were left to dry overnight. The next day, each plate was supplemented with a blob of densely grown OP50, and 15 young adults were added per plate. The trial was conducted at 25°C and animals were scored every 2 to 3 hr until the last animal had perished.

Bioinformatics. Myc, Tsc1, Tsc2 and 4E-BP orthologs were sought by local alignment searches of the 4 protein sequences to the gene models in *Mus musculus* using BLASTP searches. Since not all genomes were available in WormBase, orthologs for the parasitic helminths (*B. xylophilus*, *E. granulosus*, *E. multilocularis*, *T. solium*, *H. microstoma*, *S. mansoni* and *S. japonicum*) were derived from GeneDB. Orthologs for *G. pallida*, *H. contortus*, *O. volvulus*, *S. ratti* and *T. muris* were sought using the data available on the Sanger Institute Resources. Orthologs to *T. muris* were sought by local alignment searches of the 4 genes to contigs, using a “protein versus translated DNA” a TBLASTN search. Finally, orthologs of *P. pacificus* were sought among the gene predictions available from www.pristionchus.org. Multiple sequence alignments of the Tsc1/2 protein sequences were done using MUSCLE [76]. All trees were constructed and visualised as previously described [74].

Statistical analysis. Lifespans were analysed using the Cox Proportional Hazard method with the Efron approximation for ties of the survival package in R. The logistic mortality models were fitted to the lifespan data and parameter difference tested using the Survomatic R package. The body sizes were analysed using a linear regression model taking into account the trial as random factor in R. The Wilcoxon Mann test was used for tumors and the brood sizes were compared using a standard Student’s t Test.

ACKNOWLEDGEMENTS

We wish to thank Mikhail Nikiforov for useful discussion, and Filipe Cabreiro for comments on the manuscript. Some nematode strains used in this work were provided by the Caenorhabditis Genetics Center, which is funded by the National Institutes of Health National Center for Research Resources and the National Bioresource Project of Japan. This work was supported by the Wellcome Trust (Strategic Award), EMBL and the European Union (IDEAL).

Conflicts of Interest Statement

The authors of this manuscript have no conflict of interest to declare.

REFERENCES

1. Kenyon C. The genetics of ageing. *Nature*. 2010; 464:504-512.
2. Kenyon C, Chang J, Gensch E, Rudener A and Tabtiang R. A *C. elegans* mutant that lives twice as long as wild type. *Nature*. 1993; 366:461-464.
3. Lin K, Dorman JB, Rodan A and Kenyon C. *daf-16*: An HNF-3/forkhead family member that can function to double the life-span of *Caenorhabditis elegans*. *Science*. 1997; 278:1319-1322.
4. Ogg S, Paradis S, Gottlieb S, Patterson GI, Lee L, Tissenbaum HA and Ruvkun G. The Fork head transcription factor DAF-16 transduces insulin-like metabolic and longevity signals in *C. elegans*. *Nature*. 1997; 389:994-999.
5. McElwee J, Bubb K and Thomas J. Transcriptional outputs of the *Caenorhabditis elegans* forkhead protein DAF-16. *Aging Cell*. 2003; 2:111-121.
6. Murphy CT, McCarroll SA, Bargmann CI, Fraser A, Kamath RS, Ahringer J, Li H and Kenyon CJ. Genes that act downstream of DAF-16 to influence the lifespan of *C. elegans*. *Nature*. 2003; 424:277-284.
7. McElwee JJ, Schuster E, Blanc E, Thomas JH and Gems D. Shared transcriptional signature in *C. elegans* dauer larvae and long-lived *daf-2* mutants implicates detoxification system in longevity assurance. *J Biol Chem*. 2004; 279:44533-44543.
8. Partridge L, Alic N, Bjedov I and Piper MD. Ageing in *Drosophila*: the role of the insulin/Igf and TOR signalling network. *Exp Gerontol*. 2011; 46:376-381.
9. Schuster E, McElwee JJ, Tullet JMA, Doonan R, Matthijssens F, Reece-Hoyes JS, Hope IA, Vanfleteren JR, Thornton J and Gems D. DamID in *C. elegans* reveals longevity-associated targets of DAF-16/FoxO. *Mol Syst Biol*. 2010; 6:399.
10. Yuan J, Tirabassi RS, Bush AB and Cole MD. The *C. elegans* MDL-1 and MXL-1 proteins can functionally substitute for vertebrate MAD and MAX. *Oncogene*. 1998; 17:1109-1118.
11. Grandori C, Cowley SM, James LP and Eisenman RN. The Myc/Max/Mad network and the transcriptional control of cell behavior. *Ann Rev Cell Dev*. 2000; 16:653-699.
12. Gems D and Partridge L. Genetics of longevity in model organisms: Debates and paradigm shifts. *Annual Review of Physiology*. 2013; 75:621-644.
13. Delpuech O, Griffiths B, East P, Essafi A, Lam EW, Burgering B, Downward J and Schulze A. Induction of Mxi1-SR alpha by FOXO3a contributes to repression of Myc-dependent gene expression. *Mol Cell Biol*. 2007; 27:4917-4930.
14. Ackerman D and Gems D. Insulin/IGF-1 and hypoxia signaling act in concert to regulate iron homeostasis in *C. elegans*. *PLoS Genet*. 2012; 8:e1002498.
15. Le N and Richardson D. The role of iron in cell cycle progression and the proliferation of neoplastic cells. *Biochim Biophys Acta*. 2002; 1603:31-46.
16. Pickett CL, Breen KT and Ayer DE. A *C. elegans* Myc-like network cooperates with semaphorin and Wnt signaling pathways to control cell migration. *Dev Biol*. 2007; 310:226-239.
17. Grove CA, De Masi F, Barrasa MI, Newburger DE, Alkema MJ, Bulyk ML and Walhout AJ. A multiparameter network reveals extensive divergence between *C. elegans* bHLH transcription factors. *Cell*. 2009; 138:314-327.
18. Pinkston JM, Garigan D, Hansen M and Kenyon C. Mutations that increase the life span of *C. elegans* inhibit tumor growth. *Science*. 2006; 313:971-975.
19. Pinkston-Gosse J and Kenyon C. DAF-16/FOXO targets genes that regulate tumor growth in *Caenorhabditis elegans*. *Nat Genet*. 2007; 39:1403-1409.
20. Gems D and Riddle DL. Defining wild-type life span in *Caenorhabditis elegans*. *J Gerontol A Biol Sci Med Sci*. 2000; 55:B215-B219.
21. Ward S and Carrel JS. Fertilization and sperm competition in the nematode *Caenorhabditis elegans*. *Dev Biol*. 1979; 73:304-321.
22. Gems D, Sutton AJ, Sundermeyer ML, Larson PL, Albert PS, King KV, Edgley M and Riddle DL. Two pleiotropic classes of *daf-2* mutation affect larval arrest, adult behavior, reproduction and longevity in *Caenorhabditis elegans*. *Genetics*. 1998; 150:129-155.
23. Jud M, Razelun J, Bickel J, Czerwinski M and Schisa JA. Conservation of large foci formation in arrested oocytes of *Caenorhabditis* nematodes. *Dev Genes Evol*. 2007; 217:221-226.
24. Hughes SE, Huang C and Kornfeld K. Identification of mutations that delay somatic or reproductive aging of *Caenorhabditis elegans*. *Genetics*. 2011; 189:341-356.
25. Gumienny TL, Lambie E, Hartwig E, Horvitz HR and Hengartner MO. Genetic control of programmed cell death in the *Caenorhabditis elegans* hermaphrodite germline. *Development*. 1999; 126:1011-1022.
26. Jaramillo-Lambert A, Ellefson M, Villeneuve AM and Engebrecht J. Differential timing of S phases, X chromosome replication, and meiotic prophase in the *C. elegans* germ line. *Dev Biol*. 2007; 308:206-221.
27. Wolke U, Jezuit EA and Priess JR. Actin-dependent cytoplasmic streaming in *C. elegans* oogenesis. *Development*. 2007; 134:2227-2236.
28. Garigan D, Hsu A, Fraser A, Kamath R, Ahringer J and Kenyon C. Genetic analysis of tissue aging in *Caenorhabditis elegans*: a role for heat-shock factor and bacterial proliferation. *Genetics*. 2002; 161:1101-1112.
29. Luo S, Kleemann GA, Ashraf JM, Shaw WM and Murphy CT. TGF-beta and insulin signaling regulate reproductive aging via oocyte and germline quality maintenance. *Cell*. 2010; 143:299-312.
30. Golden T, Beckman K, Lee A, Dudek N, Hubbard A, Samper E and Melov S. Dramatic age-related changes in nuclear and genome copy number in the nematode *Caenorhabditis elegans*. *Aging Cell*. 2007; 6:179-188.
31. McGee MD, Day N, Graham J and Melov S. *cep-1/p53*-dependent dysplastic pathology of the aging *C. elegans* gonad. *Aging*. 2012; 4:256-269.
32. Qi W, Huang X, Neumann-Haefelin E, Schulze E and Baumeister R. Cell-nonautonomous signaling of FOXO/DAF-16 to the stem cells of *Caenorhabditis elegans*. *PLoS Genet*. 2012; 8:e1002836.
33. Tullet JM, Hertweck M, An JH, Baker J, Hwang JY, Liu S, Oliveira RP, Baumeister R and Blackwell TK. Direct inhibition of the longevity-promoting factor SKN-1 by insulin-like signaling in *C. elegans*. *Cell*. 2008; 132:1025-1038.
34. Johnson T, Wu D, Tedesco P, Dames S and Vaupel J. Age-specific demographic profiles of longevity mutants in *Caenorhabditis elegans* show segmental effects. *J Gerontol A Biol Sci Med Sci*. 2001; 56:B331-B339.
35. Vanfleteren JR, De Vreese A and Braeckman BP. Two-parameter logistic and Weibull equations provide better fits to survival data from isogenic populations of *Caenorhabditis*

- elegans* in axenic culture than does the Gompertz model. J Gerontol A Biol Sci Med Sci. 1998; 53:B393-B403.
36. Johnson TE. The increased lifespan of *age-1* mutants of *Caenorhabditis elegans* results from a lowering of the Gompertz rate of aging. Science. 1990; 249:908-912.
 37. Gandhi S, Santelli J, Mitchell DG, Stiles JW and Raosanadi D. A simple method for maintaining large, aging populations of *Caenorhabditis elegans*. Mech Ageing Dev. 1980; 12:137-150.
 38. Arantes-Oliveira N, Apfeld J, Dillin A and Kenyon C. Regulation of life-span by germ-line stem cells in *Caenorhabditis elegans*. Science. 2002; 295:502-505.
 39. Hsin H and Kenyon C. Signals from the reproductive system regulate the lifespan of *C. elegans*. Nature. 1999; 399:362-366.
 40. Libina N, Berman J and Kenyon C. Tissue-specific activities of *C. elegans* DAF-16 in the regulation of lifespan. Cell. 2003; 115:489-502.
 41. Depuydt G, Xie F, Petyuk VA, Shanmugam N, Smolders A, Dhondt I, Brewer HM, Camp DG, Smith RD and Braeckman BP. Reduced insulin/IGF-1 signaling and dietary restriction inhibit translation but preserve muscle mass in *Caenorhabditis elegans*. Mol Cell Proteomics. 2013.
 42. Stout GJ, Stigter EC, Essers PB, Mulder KW, Kolkman A, Snijders DS, van den Broek NJ, Betist MC, Korswagen HC, Macinnes AW and Brenkman AB. Insulin/IGF-1-mediated longevity is marked by reduced protein metabolism. Mol Syst Biol. 2013; 9:679.
 43. McGee MD, Weber D, Day N, Vitelli C, Crippen D, Herndon LA, Hall DH and Melov S. Loss of intestinal nuclei and intestinal integrity in aging *C. elegans*. Aging Cell. 2011; 10:699-710.
 44. Herndon L, Schmeissner P, Dudaronek J, Brown P, Listner K, Sakano Y, Paupard M, Hall D and Driscoll M. Stochastic and genetic factors influence tissue-specific decline in ageing *C. elegans*. Nature. 2002; 419:808-814.
 45. Depina A, Iser W, Park S, Maudsley S, Wilson M and Wolkow C. Regulation of *Caenorhabditis elegans* vitellogenesis by DAF-2/IIS through separable transcriptional and posttranscriptional mechanisms. BMC Physiol. 2011; 11:11.
 46. Kimble J, Sharrock, WJ. Tissue-specific synthesis of yolk proteins in *Caenorhabditis elegans*. Dev Biol. 1983; 96:189-196.
 47. Aamodt EJ, Chung MA and McGhee JD. Spatial control of gut-specific gene expression during *Caenorhabditis elegans* development. Science. 1991; 252:579-582.
 48. Lin C-J, Malina A and Pelletier J. c-Myc and eIF4F constitute a feedforward loop that regulates cell growth: implications for anticancer therapy. Cancer Res. 2009; 69:7491-7494.
 49. Kapahi P, Chen D, Rogers AN, Katewa SD, Li PW, Thomas EL and Kockel L. With TOR, less is more: a key role for the conserved nutrient-sensing TOR pathway in aging. Cell Metab. 2010; 11:453-465.
 50. Syntichaki P, Troulinaki K and Tavernarakis N. eIF4E function in somatic cells modulates ageing in *Caenorhabditis elegans*. Nature. 2007; 445:922-926.
 51. McFerrin LG and Atchley W. Evolution of the Max and Mix networks in animals. Genome Biol Evol. 2011; 3:915-937.
 52. Schreiber-Agus N, Meng Y, Hoang T, Hou H, Jr., Chen K, Greenberg R, Cordon-Cardo C, Lee HW and DePinho RA. Role of Mxi1 in ageing organ systems and the regulation of normal and neoplastic growth. Nature. 1998; 393:483-487.
 53. Blagosklonny MV. Cell cycle arrest is not yet senescence, which is not just cell cycle arrest: terminology for TOR-driven aging. Aging. 2012; 4:159-165.
 54. Budovsky A, Tacutu R, Yanai H, Abramovich A, Wolfson M and Fraifeld V. Common gene signature of cancer and longevity. Mech Ageing Dev. 2009; 130:33-39.
 55. Finch CE, Pike MC and Witten M. Slow mortality rate accelerations during aging in some animals approximate that of humans. Science. 1990; 249:902-905.
 56. Gems D. What is an anti-aging treatment? Exp Gerontol. 2014 (In press).
 57. Blagosklonny MV. Aging and immortality: quasi-programmed senescence and its pharmacologic inhibition. Cell Cycle. 2006; 5:2087-2102.
 58. Blagosklonny MV. Paradoxes of aging. Cell Cycle. 2007; 6:2997-3003.
 59. Gems D and de la Guardia Y. Alternative perspectives on aging in *C. elegans*: reactive oxygen species or hyperfunction? Antioxid Redox Signal. 2013; 19:321-329.
 60. Valentini S, Cabreiro F, Ackerman D, Alam MM, Kunze MBA, Kay CWM and Gems D. Manipulation of *in vivo* iron levels can alter resistance to oxidative stress without affecting ageing in the nematode *C. elegans*. Mech Ageing Dev. 2012; 133:282-290.
 61. Van Raamsdonk JM and Hekimi S. Reactive oxygen species and aging in *Caenorhabditis elegans*: causal or casual relationship? Antioxid Redox Signal. 2010; 13:1911-1953.
 62. Gems D and Doonan R. Antioxidant defense and aging in *C. elegans*: is the oxidative damage theory of aging wrong? Cell Cycle. 2009; 8:1681-1687.
 63. Vocabulary.com. (2013). tumor.
 64. Campisi J. Senescent cells, tumor suppression, and organismal aging: good citizens, bad neighbors. Cell. 2005; 120:513-522.
 65. Yin XY, Grove L, Datta NS, Long MW and Prochownik EV. C-myc overexpression and p53 loss cooperate to promote genomic instability. Oncogene. 1999; 18:1177-1184.
 66. Smogorzewska A and de Lange T. Different telomere damage signaling pathways in human and mouse cells. EMBO J. 2002; 21:4338-4348.
 67. Wagner M, Hampel B, Bernhard D, Hala M, Zwerschke W and Jansen-Durr P. Replicative senescence of human endothelial cells *in vitro* involves G1 arrest, polyploidization and senescence-associated apoptosis. Exp Gerontol. 2001; 36:1327-1347.
 68. Coghlan A. (2005). Nematode genome evolution. In: Community TCEr, ed. WormBook.
 69. Gallant P. Myc/Max/Mad in invertebrates: the evolution of the Max network. Curr Top Microbiol Immunol 2006; 302:235-253.
 70. Gems D. Longevity and ageing in parasitic and free-living nematodes. Biogerontology. 2000; 1:289-307.
 71. Brenner S. The genetics of *Caenorhabditis elegans*. Genetics. 1974; 77:71-94.
 72. Love D, Ghosh S, Mondoux M, Fukushige T, Wang P, Wilson M, Iser W, Wolkow C, Krause M and Hanover J. Dynamic O-GlcNAc cycling at promoters of *Caenorhabditis elegans* genes regulating longevity, stress, and immunity. Proc Natl Acad Sci U S A. 2010; 107:7413-7418.
 73. Hobert O. PCR fusion-based approach to create reporter gene constructs for expression analysis in transgenic *C. elegans*. Biotechniques. 2002; 32(4):728-730.
 74. Tullet JMA, Araiz C, Sanders MJ, Au C, Benedetto A, Papatheodorou I, Clark E, Schmeisser K, Jones D, Schuster EF, Thornton JM and Gems D. DAF-16/FoxO directly regulates an atypical AMP-activated protein kinase gamma isoform to

mediate the effects of insulin/IGF-1 signaling on aging in *C. elegans*. PLoS Genet. 2013; In press.

75. Ziehm M and Thornton JM. Unlocking the potential of survival data for model organisms through a new database and online analysis platform: SurvCurv. Aging Cell. 2013; 12:910-916.

76. Edgar RC. MUSCLE: a multiple sequence alignment method with reduced time and space complexity. BMC Bioinformatics. 2004; 5:113.

SUPPLEMENTAL TABLES

Table S1. Effect of *mdl-1* on life span in *C. elegans*. The trials were performed at 25°C without FUdR. Genotype: N2 wildtype, GA1200 *mdl-1(tm311)*, DR1567 *daf-2 (m577)*, GA1204 *daf-2(m577); mdl-1(tm311)*. *p*, log rank test. [n] biological replicates number. [C], combined data from 4 trials.

Genotype	Deaths/ censored	Mean life span (days)	% vs. wild type	<i>p</i> vs. wild type	% vs. <i>daf-2</i>	<i>p</i> vs. <i>daf-2</i>
Wild type	[C] 513/18	14.7				
	[1] 120/5	15.2				
	[2] 121/5	14.1				
	[3] 133/7	15.3				
	[4] 139/1	14.3				
<i>mdl-1(tm311)</i>	[C] 500/17	12.8	-13.1	<.0001		
	[1] 119/4	14.4	-5.4	0.0288		
	[2] 115/4	12.0	-15.1	<.0001		
	[3] 125/8	12.9	-16.0	<.0001		
	[4] 141/1	12.1	-15.5	<.0001		
<i>daf-2 (m577)</i>	[C] 412/57	35.2	+139.2	<.0001		
	[1] 87/26	31.0	+104.4	<.0001		
	[2] 86/3	34.0	+141.1	<.0001		
	[3] 121/8	35.1	+129.2	<.0001		
	[4] 118/20	39.2	+174.1	<.0001		
<i>daf-2(m577); mdl-1(tm311)</i>	[C] 438/78	26.6	+80.9	<.0001	-24.5	<.0001
	[1] 75/59	21.2	+39.4	<.0001	-31.7	<.0001
	[2] 113/1	28.0	+98.5	<.0001	-17.6	<.0001
	[3] 132/4	27.0	+76.4	<.0001	-22.9	<.0001
	[4] 118/14	28.3	+97.9	<.0001	-27.9	<.0001

Table S2. *glp-4(bn2)* and FUDR do not suppress *mdl-1* shortevity. Genotypes: N2 wildtype, GA1200 *mdl-1(tm311)*, SS104 *glp-4(bn2)*, GA1230 *glp-4; mdl-1*. p, log rank test. [n] biological replicates number. *glp-4* trial, worms raised at 15°C to L4, then shifted to 25°C.

Genotype	Deaths/ censored	Mean life span (days)	% vs. wild type	p vs. wild type	% vs. <i>glp-4</i>	p vs. <i>glp-4</i>
<i>glp-4</i> Trials (worms raised at 15°C, shifted at L4 stage to 25°C)						
Wild type	[1] 77/11	15.5				
	[2] 69/11	13.2				
<i>mdl-1(tm311)</i>	[1] 61/11	12.9	-17.0	0.0002		
	[2] 48/11	11.3	-14.5	0.0023		
<i>glp-4(bn2)</i>	[1] 86/14	15.7	+1.59	0.46		
	[2] 64/9	14.3	+8.4	0.43		
<i>glp-4; mdl-1</i>	[1] 120/4	12.3	-4.4	<0.0001	-21.6	<0.0001
	[2] 75/6	9.1	-19.2	<0.0001	-36.3	<0.0001
<i>glp-4</i> Trials (worms raised and maintained at 25°C)						
Wild type	[1] 87/7	12.2				
	[2] 78/12	14.2				
<i>mdl-1(tm311)</i>	[1] 78/19	11.4	-6.6	0.20		
	[2] 76/22	12.7	-10.7	0.05		
<i>glp-4(bn2)</i>	[1] 94/9	14.0	+14.8	0.0035		
	[2] 77/16	17.6	+24.0	0.0002		
<i>glp-4; mdl-1</i>	[1] 83/17	12.3	+0.8	0.21	-12.0	0.024
	[2] 70/17	15.0	-15.2	0.36	-14.7	0.0051
FUDR Trials						
Wild type	[1] 46/14	17.5				
	[2] 41/19	16.8				
<i>mdl-1(tm311)</i>	[1] 49/11	12.4	-41.1	<0.0001		
	[2] 49/11	13.3	-26.3	0.0027		
Wild type (50µM FUDR)	[1] 55/5	17.3	-1.2	0.55	-1.2	0.55
	[2] 57/3	14.6	-15.1	0.022	-15.1	0.022
<i>mdl-1(tm311)</i> (50µM FUDR)	[1] 54/6	12.7	-37.8	<0.0001	+2.4	0.80
	[2] 49/11	11.6	-44.8	<0.0001	-14.7	0.032

Table S1. Effect of *mdl-1* on life span in *C. elegans*.

Strain	Deaths/ censored	Mean life span (days)	% vs. wild type	<i>p</i> vs. wild type	% vs. <i>mdl-1</i>	<i>p</i> vs. <i>mdl-1</i>
Wild type	[C] 198/0 [1] 99/0 [2] 99/0	11.30 11.83 10.97				
<i>mdl-1(tm311)</i>	[C] 198/1 [1] 99/0 [2] 99/1	9.36 9.57 9.15	-17.97 -19.10 -15.20	<0.0001 <0.0001 <0.0001		
<i>mdl-1; wuEx267</i> <i>[mdl-1 rol-6]</i>	[C] 191/0 [1] 80/0 [2] 111/0	10.91 11.36 10.59	-3.45 -3.97 -1.85	0.0060 0.04 0.22	+19.55 +18.70 +15.74	<0.0001 <0.0001 <0.0001
<i>mdl-1; wuEx268</i> <i>[pges-1::mdl-1</i> <i>rol-6].</i>	[C] 210/0 [1] 94/0 [2] 116/0	9.97 10.47 9.56	-11.77 -11.50 -11.40	<0.0001 <0.0001 <0.0001	+9.51 +9.40 +4.48	<0.0001 <0.0001 0.0059

Immortalization of MEF is characterized by the deregulation of specific miRNAs with potential tumor suppressor activity

Milena Rizzo¹, Monica Evangelista¹, Marcella Simili¹, Laura Mariani¹, Letizia Pitto¹, Giuseppe Rainaldi^{1,2}

¹Laboratory of Gene and Molecular Therapy, Institute of Clinical Physiology, CNR, Pisa, Italy;

²Istituto Toscano Tumori, Firenze, Italy

Running title: MEF immortalization and microRNAs

Key words: mouse embryo fibroblasts, immortalization, microRNAs, genome instability

Received: 5/11/11; Accepted: 6/27/11; Published: 7/11/11

Correspondence to Giuseppe Rainaldi at, g.rainaldi@ifc.cnr.it

Copyright: © Rainaldi et al. This is an open-access article distributed under the terms of the Creative Commons Attribution License, which permits unrestricted use, distribution, and reproduction in any medium, provided the original author and source are credited

Abstract: The life span (Hayflick limit) of primary mouse embryo fibroblasts (MEF) in culture is variable but it is still unclear if the escape of the Hayflick limit is also variable. To address this point MEF were expanded every fifteen days (6T15) instead of every three days (6T3) until they became immortal. With this protocol MEF lifespan was extended and immortalization accordingly delayed. By testing a panel of genes (p19ARF, p16, p21) and miRNAs (miR-20a, miR-21, miR-28, miR-290) related to primary MEF senescence, a switch of p21 from up to down regulation, the down regulation of specific miRNAs as well as a massive shift from diploidy to hyperdiploidy were observed in coincidence with the resumption of cell proliferation. Collectively, these data indicate that the inactivation of genes and miRNAs, important in controlling cell proliferation, might be determinant for the escape from the Hayflick limit. In support of this hypothesis was the finding that some of the down regulated miRNAs transfected in immortalized MEF inhibited cell proliferation thus displaying a tumor suppressor-like activity.

INTRODUCTION

The Hayflick limit of primary mouse embryo fibroblasts (MEF) is variable since the growth conditions can either reduce or extend it [1-3]. We have reported that primary MEF expanded every three days (6T3 protocol) underwent four population cell doubling and thereafter cell proliferation was fully abolished and SA- β -gal⁺ cells induced [4]. However it is known that MEF senescence can be induced prematurely, before the end of the physiological lifespan, by cellular stresses such as the over expression [5] or down regulation [6] of single oncogenes and DNA damaging drugs [7-9]. Recently, it has been reported that miRNAs are involved in senescence of MEF as well as of human diploid fibroblasts [10, 11].

An unsolved question is which cells are able to escape the *in vitro* lifespan limit. So far, the molecular

characterization of immortalized MEF cell lines has shown that functional silencing of either the *INK4a/ARF* locus [12] or p53 [13] appears necessary to bypass senescence. A recurrent concept is that mutational events occurring in culture have a key role. If mutations confer a proliferative advantage, mutated cells can bypass the *in vitro* lifespan limit and rapidly replace the existing population [14, 15]. According to this view, the time spent in culture should affect immortalization. We modified the 6T3 expansion protocol of primary MEF [4] by lengthening the interval between passages (15 days versus 3 days) and reiterating it until MEF became immortal. Here we report that: i) the life span was extended up to 8 population cell doubling and immortalization was consequentially delayed; ii) p21 down regulation marks the switch from primary to immortalized MEF; iii) deregulation of genes and miRNAs which control

cell proliferation pathways correlate with the immortalization process; iv) down regulated miRNAs can behave as tumor suppressors.

RESULTS

1. The pro senescence axis p53/p21 is disrupted in immortalized MEF.

To investigate the relative importance of the time in culture versus the number of population cell doubling in the MEF immortalization process we modified the split time. MEF p0 (passage 0) were thawed, and expanded to obtain MEF p1. Thereafter MEF p1 were collected, diluted at the appropriate concentration (6×10^5) and grown for 15 days with a medium change every three days (6T15 protocol), before the next trypsinization and expansion. The 6T15 protocol was reiterated 10 times for a total of 150 days in culture. During the first three passages a reduced number of population cell doubling was observed; afterwards a population of proliferating MEF emerged, which rapidly increased (p5) and replaced the preexisting cell population (p10) (Fig. 1A). At the molecular level we found that both p19ARF and p16 were progressively up regulated during passages (with respect to the spontaneous level of MEF p0) (Fig. 1B). Vice versa the expression of p21 was biphasic: while it was up regulated till p3 it decreased thereafter with a clear switch toward under expression at p6 (Fig. 1B,C). As p21 is under the direct control of p53, a disruption of the p53/p21 axis can be hypothesized at the basis of immortalization.

2. Genome stability and miRNA signatures are modified in immortalized MEF.

The down regulation of p21 strongly suggests a loss of p53 activity. In accordance with the hypothesis, FACS analysis showed that while the DNA content distribution curve per cell of MEF p1 and MEF p5 were very similar and typical of diploid cells (Fig. 2A) a massive shift toward cells with higher DNA contents was observed in MEF p6 (Fig. 2B). Hyperdiploid cells, which emerged from diploid primary MEF, are indicative that genomic stability, controlled by p53 [16-18], is lost. It is of note that a stable hyperdiploid cell population is selected within four passages (p6-p10) (Fig. 2C). To strengthen the hypothesis of a functional loss of p53, in parallel we determined the expression profiles of p53 and of miR-34a directly controlled by p53. We found that p53 mRNA (Fig. 2D) and protein levels did not significantly change up to p6 (Fig. 2E); conversely miR-34a appears to increase till p4, starts to decrease at p5 to become markedly down regulated at

p6 (Fig. 2D) reinforcing the idea that p53 becomes non-functional.

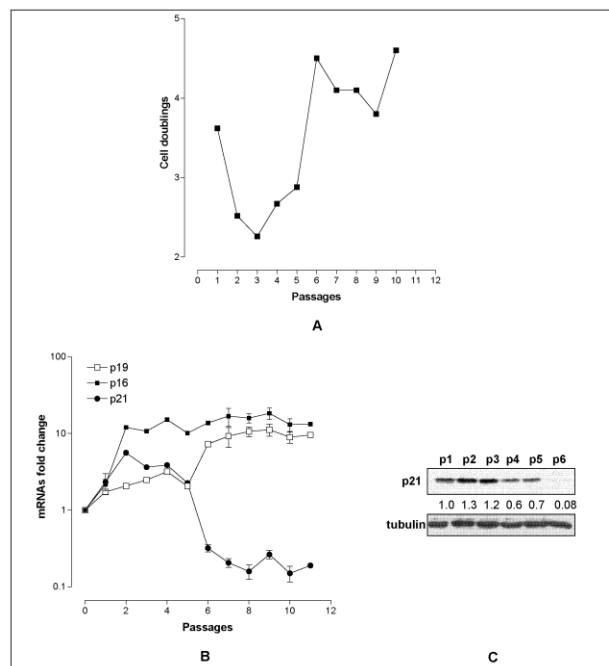


Figure 1. Characterization of MEF under 6T15 propagation regimen. (A) Proliferation curve of MEF expressed as cell doublings per passage. (B) Quantification of *p19ARF*, *p16* and *p21* transcripts per passage (each point represent one passage) normalized to that of MEF at passage 0. (C) p21 protein level at the various passages. The value reported under each lane represents the average of two independent experiments.

3. The senescence related miRNAs are down regulated in immortalized MEF.

As the p53/p21 axis of primary MEF was disrupted in immortalized MEF, we investigated whether the time course of the signatures of miRNAs related to either premature (miR-20a [19]) or replicative (miR-21, miR-28 [20], miR-290 [4]) primary MEF senescence were also modified. The analysis showed that while miR-20a and miR-290 were down regulated till p6 (Fig 3A) miR-21 and miR-28 were up regulated. It is worth noting that the up regulation of miR-21 and miR-28 is in agreement with findings in MEF replicative senescence, while miR-290 down regulation is the opposite of previous observations because we have shown that miR-290 steadily increased when either spontaneous or nocodazole-induced MEF G1 blocked tetraploid cells were present [4]. For that, we examined the cell cycle of p1-p5 MEF. We found that under 6T15 protocol no significant accumulation of G2/M cells was observed (Fig. 3B) suggesting that the failed accumulation of G2/M cells was responsible for the lack of miR-290 up

regulation. The miRNA signatures changed markedly after p6: while miR-20a and miR-290 remain down regulated, although to a lesser extent, miR-21 and miR-28 switched from up to down regulation (Fig. 3A). These data suggest that the deregulation of these two senescence related miRNAs, besides miR-34a, is involved in MEF immortalization.

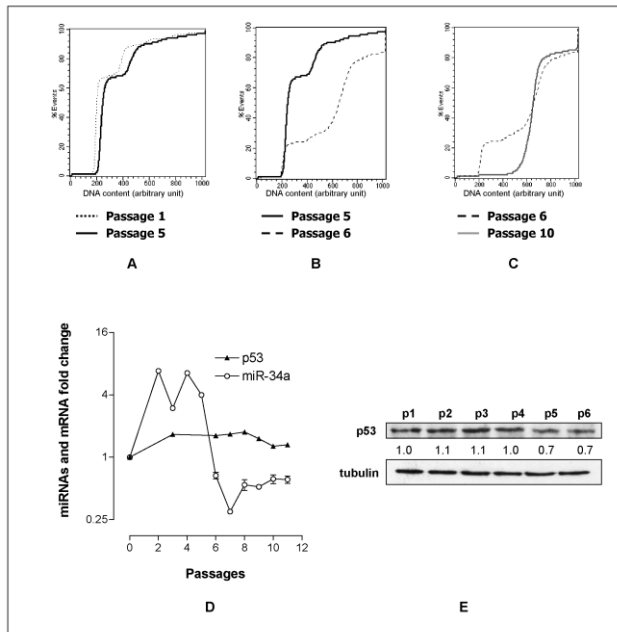


Figure 2. MEF immortalization is characterized by a p53-dependent events. DNA content profile per cell at p1/p5 (A), p5/p6 (B) and p6/p10 (C). (D) Fold change of miR-34a and p53 transcripts at various passages normalized to that of MEF at passage 0. (E) p53 protein level at the various passages. The value reported under each lane represents the average of two independent experiments.

4. The transfection of the down regulated miRNAs reduces the proliferation of immortalized MEF.

To investigate if the deregulated miRNAs play an active role in the immortalization, immortalized MEF (p10) were transfected with miR-21, miR-28 and miR-34. In addition we tested miR-20a and miR-290 whose expression was not affected by the immortalization. The proliferation data showed that miR-20a and miR-290 did not affect cell proliferation as expected, the down regulated miR-28 and miR-34 significantly reduced the proliferation of immortalized MEF with similar efficiency, while miR-21 did not inhibit cell proliferation (Fig. 3C). These data indicate that the re-expression of miR-34a and miR-28 (and consequently of their controlled pathways) was sufficient to reduce the proliferative rate of immortalized MEF and suggest

that miR-28, like the tumor suppressor miR-34a, could have a tumor suppressor activity.

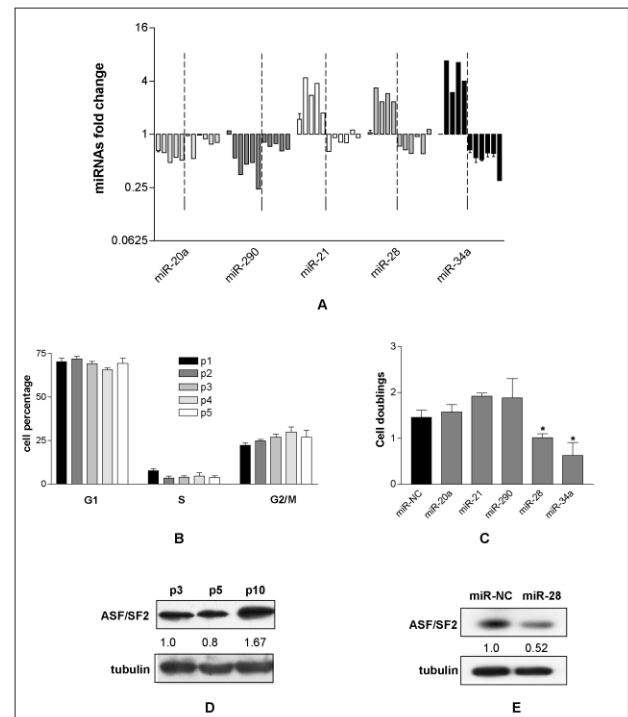


Figure 3. The re-expression of miRNAs down regulated in immortalized MEF reduces cell proliferation. (A) Quantification of miR-20a, miR-21, miR-28, miR-290 and miR-34a per passage normalized to that of MEF at passage 0. Dashed lines indicate the transition from passage 5 to 6. (B) Cell cycle phase distribution (%) of MEF from p1 to p5. (C) Population cell doubling of immortalized MEF after transfection of miR-NC, miR-20a, miR-21, miR-28, miR-290 and miR-34a. Each bar represents the mean \pm SD of three biological replicates (*= $p < 0.05$). (D) Expression of ASF/SF2 protein in primary (p3 and p5) and immortalized (p10) MEF. The value reported under each lane represents the average of two independent experiments. (E) Expression of ASF/SF2 after the transfection of immortalized MEF with either miR-NC or miR-28. The value reported under each lane represents the average of two independent experiments.

5. MiR-28 behaves as tumor suppressor miRNA.

It is well known that miR-34a has a widespread tumor suppressor activity [21, 22]. We show that it behaved as such in immortalized MEF as its re-expression inhibits cell proliferation, probably by partially restoring the p53 pathway. Interestingly miR-28, as far as we know, is not directly linked to the p53 controlled pathways. We have previously reported that in primary MEF miR-28 targets the proto-oncogenic splicing factor ASF/SF2 and that in turn miR-28 over-expression induces both apoptosis and senescence of primary MEF via ASF/SF2 down

regulation [20]. This prompted us to verify the expression of ASF/SF2 in primary and immortalized MEF. As expected the expression of ASF/SF2 was higher in immortalized than in primary MEF (Fig. 3D) suggesting a possible post transcriptional control of miR-28 on ASF/SF2 expression. To confirm the hypothesis, we transfected immortalized MEF (p10) with miR-28 and found 50% reduction of ASF/SF2 expression (Fig. 3E), suggesting that miR-28 control cell proliferation by targeting ASF/SF2. These results strengthen the idea that miR-28 has a tumor suppressor-like activity and might be suitable to be tested in tumor cell lines defective in miR-28 content.

DISCUSSION

The *in vitro* life span defines the number of population cell doubling which primary cells can undergo in culture. We have reported that MEF under the 6T3 expansion regimen were able to undergo four population cell doubling before achieving senescence. In this work we reported that by modifying the propagation regimen and growth conditions (6T15 protocol) MEF slowed down without reaching a complete cell proliferation block and restarted proliferation after about eight population cell doubling (passage 3). These results suggest that activation of p53 with the consequent induction of p21 in this case may favor proliferation arrest rather than senescence as previously described [23]. Interestingly the *in vitro* life span of MEF was extended both in terms of population cell doubling and in terms of days in culture, in keeping with the hypothesis that p53 activation, by inducing quiescence rather than senescence may increase the cell life span [24]. The immortalization process is delayed accordingly, suggesting that it does not strictly depend on the number of cell doubling or the time that the cells spend in culture (45 culture days in this case).

The spontaneous immortalization of primary MEF has been attributed to either the inactivation of p53 or the loss of the *INK4a/ARF* locus (p19ARF, p16) [25], two loci strictly related to cell proliferation. In this work we found that both loci were transcribed and translated during passages whereas p21 shifted from up to down regulation after p5. As p21 expression is mostly p53 dependent we argued that despite p53 continued to be expressed, it may not be functional any more. In support of this conclusion are the down regulation of the p53 dependent miR-34a and the loss of genomic stability revealed by the massive appearance of hyperdiploid cells [16-18]

A recurrent concept is that immortalization is due to mutations induced by DNA damage occurring during

the population expansion [14]. The loss of p53 activity found in immortalized MEF could be due to either point mutation or loss of one allele which appears to be sufficient to alter cell growth [15]. In any case the sharp increase of cell proliferation suggests that the immortalization process is caused by the concomitant alteration of multiple pathways. We found that the expression of miR-20a, miR-21, miR-28 and miR-290, all involved in MEF senescence, were deregulated in coincidence with p21 down regulation and increase of cell proliferation. As a high number of genes are potentially targeted by one miRNA [26], we argued that the deregulation of these miRNAs could be in part responsible for the absence of cell proliferation control characteristic of immortal cells. In particular we demonstrate that by replacing miR-28 and miR-34a, under expressed in immortalized MEF, cell proliferation was reduced suggesting that both miRNAs are implicated in immortalization. Evidence in support of an anti proliferative role of miR-28 is already available. We have shown in primary MEF that miR-28 targets the proto-oncogene ASF/SF2, a splicing factor involved in the alternative splicing of many transcripts [27, 28] and its over expression induces apoptosis and senescence by down regulating ASF/SF2 [20]. Our results demonstrate that also in immortalized MEF miR-28 targets ASF/SF2 suggesting that its tumor suppressor activity is due to ASF/SF2 inhibition, although other targets cannot be excluded.

The fact that the replacement of miR-28 in immortalized MEF reduced cell proliferation to the same extent as miR-34a further strengthens the hypothesis that miR-28 represents a novel TS miRNA. MiR-34a is a well known TS miRNA able to inhibit cell proliferation of a wide range of tumor cells [21, 29-31] as well as of human fibroblasts which extend their replicative capacity when treated with miR-34a antisense [32]. Conversely miR-290 and miR-20a involved in culture and stress induced senescence of primary MEF were not able to inhibit proliferation of immortal MEF in keeping with the idea that miRNAs behave differently in different cellular context [33]. In conclusion the delayed immortalization obtained with this protocol implies that point mutations; due to DNA damage accumulated during population expansion [14], are not the only molecular events at the basis of immortalization. The most notable feature which marks the immortalization process is the drastic p21 down regulation possibly due to p53 functional inactivation. Associated to the sudden down regulation of p21 was the induction of hyperploidy, suggesting that genomic instability and/or epigenetic changes are also responsible for the immortalization process. Interestingly, the switch of p21 expression was

accompanied by the change of the signature of miRNAs related to MEF senescence, including the p53-dependent miR-34 and miR-28 [20]. In particular, the down regulated miR-28, behaved as a TS miRNA, when transfected in immortalized MEF, analogously to the well known TS miR-34a, indicating that the comparison of the miRNA signature of primary versus immortalized cells could allow the identification of novel miRNAs with potential tumor suppressor-like activity.

MATERIALS AND METHODS

Reagents. miRNeasy mini kit, QuantiTect Reverse Transcription Kit, miScript Reverse Transcription Kit, miScript SYBR Green PCR Kit (QIAGEN, Milano, Italy); Dulbecco's Modified Eagle Medium-High Glucose (D-MEM-HG), foetal bovine serum (FBS) (Invitrogen, CA, USA); LightCycler 480 Probes Master, Universal ProbeLibrary LNA Probes; LightCycler 480 SYBR Green I Master (Roche Diagnostic, Mannheim, Germany); X-Gal (5-bromo-4-chloro-3-indolylb-D-galactoside); propidium iodide, anti- α -tubulin (Sigma-Aldrich Corporation, Missouri, USA); anti-p21 (Santa Cruz Biotechnology, Inc.); ECL, Hybond-C extra membranes (Amersham); anti-p53 (Cell Signaling Technology). The anti-ASF/SF2 was a gift of Dr. Adrian Krainer. miR-20a, miR-21, miR-28, miR-34, miR-290 and miR-NC (negative control) (GenePharma Shanghai, China)

Cells and culture conditions. MEF were isolated from 13.5d mouse embryos, expanded and then replated every three days (6T3 protocol). For 6T15 protocol MEF p1 were collected, diluted at the appropriate concentration (6×10^5) and grown for 15 days with a medium change every three days, before the next trypsinization and expansion. MEF were grown in Dulbecco's Modified Eagle Medium-high glucose (DMEM-HG)-10% FBS at 37°C in a humidified atmosphere containing 6% CO₂.

Cell proliferation. Cell proliferation was measured as number of population cell doubling per passage ($CD = \ln(N_f/N_i)/\ln 2$) where N_f is the final number of collected cells (day 3) and N_i the initial number of seeded cells (day 0).

MiRNAs transfection. Immortalized MEF (p10) were seeded at cell density of 1.0×10^5 per 30 mm diameter dish. After 24 hours cells were transfected with either miRNAs under test or a double-stranded oligonucleotide, named miR-NC. Briefly, 15 μ l Optimem and 25 μ l transfection buffer plus 80 nM miRNA were mixed with a solution of Gene Silencer (5 μ l) plus Optimem (25 μ l). After 15 minutes incubation,

Optimem was added up to 800 μ l. After 6 hours the medium was replaced with complete DMEM.

Quantification of miRNAs and genes with Q-Real-time PCR. Total RNA was extracted from 1×10^6 cells using the miRNeasy mini kit (Qiagen) following the manufacturer's recommendations. To quantify p19ARF, p16 and p21 transcripts, 1 μ g of total RNA was reverse transcribed using QuantiTect Reverse Transcription Kit (Qiagen). Real-time PCR (qRT-PCR) was carried out with LightCycler 480 (Roche) using LightCycler 480 SYBR Green I Master (Roche). Mature miR-20a, miR-21, miR-28, miR-34a and miR-290 were quantified using the miScript System: 1 μ g of total RNA was retrotranscribed with miScript Reverse Transcription Kit (Qiagen) and qRT-PCR was carried out using miScript SYBR Green PCR Kit (Qiagen). All reactions were performed in triplicate. Relative quantification of gene expression was calculated with the fit point method. Transcript values were normalized with those obtained from the amplification of the internal controls (GAPDH for transcripts and U6 for miRNAs). The following oligonucleotides were used: p19ARF, forward (F) (5'-CATGGGTCGCAGGTTCTTG-3') and reverse (R) (5'-GCTCGCTGTCTGG GTCTC-3'); p16, F (5'-CGACGGGCATAGCTTCAG-3') and R (5'-GCTCTGCTCTTGGGATTGG-3'); p21, F (5'-TCCACAGCGATATCCAGACA-3') and R (5'-GGACATCACCAGGATTGGAC-3'); p53, F (5'-ATGCCCATGCTACAGAGGAG-3') and R (5'-AGACTGGCCCTTCTTGGTCT-3'); GAPDH, F (5'-GCCTCCGTGTTCCCTACCC-3'), R (5'-TGCTGCTTCACCACCTTC-3'); miR-20a, F (5'-TAAAGTGCTTATAGTGCAGGTAG-3'); miR-21, F (5'-TAGCTTATCAGACTGATGTTGA-3'), miR-28, F (5'-AAGGAGCTCACAGTCTATTGAG-3'); miR-34a, F (5'-TGGCAGTGT CTTAGCTGGTTGT-3'); miR-290, F (5'-gctaattctctctgtatctgtccaa-3'); U6, F (5'-CGCAAGGATGACACGCAAATTC-3').

Western Blot analysis. Equivalent amounts of proteins were resolved on 10% SDS-PAGE gels and transferred to Hybond-C extra membranes by electro blotting. The resulting blots were blocked with 5% nonfat dry milk solution. Anti- α -tubulin (1:1000), anti-p53 (1:500), anti-p21 (1:1000), anti-ASF/SF2 (1:2000) were used. Incubation was performed overnight at 4°C and bands were revealed after incubation with the recommended secondary antibody coupled to peroxidase using ECL. Scanned images were quantified using scion Image software and normalized to α -tubulin.

Cell cycle. Samples of 5×10^5 of cells under test were fixed with 95% ethanol, stained with 50 μ g/ml propidium iodide (PI), incubated over night at 4°C and

cell cycle analyzed using a FACScalibur cytofluorimeter. The Kolmogorov-Smirnov Statistic was used to represent the DNA content profile of MEF at the various passages.

Statistical analysis. Data were analyzed using GraphPad Prism (GraphPad Software, Inc., San Diego, CA). Comparisons were evaluated by unpaired *t*-test. A value of $p < 0.05$ (*) was considered statistically significant.

ACKNOWLEDGEMENTS

This work was supported by Associazione Italiana per la Ricerca sul Cancro, AIRC [project no. 4753] and by Istituto Superiore di Sanità, ISS [project no. 527/A/3A/4].

REFERENCES

1. Parrinello S, Samper E, Krtolica A, Goldstein J, Melov S, Campisi J. Oxygen sensitivity severely limits the replicative lifespan of murine fibroblasts. *Nat Cell Biol.* 2003; 5:741-7.
2. Campisi J. Senescent cells, tumor suppression, and organismal aging: good citizens, bad neighbors. *Cell.* 2005; 120:513-22.
3. vom Brocke J, Schmeiser HH, Reinbold M, Hollstein M. MEF immortalization to investigate the ins and outs of mutagenesis. *Carcinogenesis.* 2006; 27:2141-7.
4. Pitto L, Rizzo M, Simili M, Colligiani D, Evangelista M, Mercatanti A, Mariani L, Cremisi F, Rainaldi G. miR-290 acts as a physiological effector of senescence in mouse embryo fibroblasts. *Physiol Genomics.* 2009; 39:210-8.
5. Serrano M, Lin AW, McCurrach ME, Beach D, Lowe SW. Oncogenic ras provokes premature cell senescence associated with accumulation of p53 and p16INK4a. *Cell.* 1997; 88:593-602.
6. Maeda T, Hobbs RM, Merghoub T, Guernah I, Zelent A, Cordon-Cardo C, Teruya-Feldstein J, Pandolfi PP. Role of the proto-oncogene *Pokemon* in cellular transformation and ARF repression. *Nature.* 2005; 433:278-85.
7. Di Micco R, Fumagalli M, Cicalese A, Piccinin S, Gasparini P, Luise C, Schurra C, Garre M, Nuciforo PG, Bensimon A, Maestro R, Pelicci PG, d'Adda di Fagagna F. Oncogene-induced senescence is a DNA damage response triggered by DNA hyper-replication. *Nature.* 2006; 444:638-42.
8. Yogev O, Anzi S, Inoue K, Shaulian E. Induction of transcriptionally active Jun proteins regulates drug-induced senescence. *J Biol Chem.* 2006; 281:34475-83.
9. Chen JH, Hales CN, Ozanne SE. DNA damage, cellular senescence and organismal ageing: causal or correlative? *Nucleic Acids Res.* 2007; 35:7417-28.
10. Bhaumik D, Scott GK, Schokrpur S, Patil CK, Orjalo AV, Rodier F, Lithgow GJ, Campisi J. MicroRNAs miR-146a/b negatively modulate the senescence-associated inflammatory mediators IL-6 and IL-8. *Aging (Albany NY).* 2009; 1:402-11.
11. Marasa BS, Srikantan S, Martindale JL, Kim MM, Lee EK, Gorospe M, Abdelmohsen K. MicroRNA profiling in human diploid fibroblasts uncovers miR-519 role in replicative senescence. *Aging (Albany NY).* 2010; 2:333-43.
12. Quelle DE, Zindy F, Ashmun RA, Sherr CJ. Alternative reading frames of the INK4a tumor suppressor gene encode two unrelated proteins capable of inducing cell cycle arrest. *Cell.* 1995; 83:993-1000.
13. Carnero A, Hudson JD, Hannon GJ, Beach DH. Loss-of-function genetics in mammalian cells: the p53 tumor suppressor model. *Nucleic Acids Res.* 2000; 28:2234-41.
14. Busuttill RA, Rubio M, Dolle ME, Campisi J, Vijg J. Oxygen accelerates the accumulation of mutations during the senescence and immortalization of murine cells in culture. *Aging Cell.* 2003; 2:287-94.
15. Odell A, Askham J, Whibley C, Hollstein M. How to become immortal: let MEFs count the ways. *Aging (Albany NY).* 2010; 2:160-5.
16. Borel F, Lohez OD, Lacroix FB, Margolis RL. Multiple centrosomes arise from tetraploidy checkpoint failure and mitotic centrosome clusters in p53 and RB pocket protein-compromised cells. *Proc Natl Acad Sci U S A.* 2002; 99:9819-24.
17. Vitale I, Galluzzi L, Senovilla L, Criollo A, Jemaa M, Castedo M, Kroemer G. Illicit survival of cancer cells during polyploidization and depolyploidization. *Cell Death Differ.* 2010.
18. Vitale I, Senovilla L, Jemaa M, Michaud M, Galluzzi L, Kepp O, Nanty L, Criollo A, Rello-Varona S, Manic G, Metivier D, Vivet S, Tajeddine N, Joza N, Valent A, Castedo M, Kroemer G. Multipolar mitosis of tetraploid cells: inhibition by p53 and dependency on Mos. *EMBO J.* 2010; 29:1272-84.
19. Poliseno L, Pitto L, Simili M, Mariani L, Riccardi L, Ciucci A, Rizzo M, Evangelista M, Mercatanti A, Pandolfi PP, Rainaldi G. The proto-oncogene LRF is under post-transcriptional control of miR-20a: implications for senescence. *PLoS One.* 2008; 3:e2542.
20. Verduci L, Simili M, Rizzo M, Mercatanti A, Evangelista M, Mariani L, Rainaldi G, Pitto L. MicroRNA (miRNA)-mediated interaction between leukemia/lymphoma-related factor (LRF) and alternative splicing factor/splicing factor 2 (ASF/SF2) affects mouse embryonic fibroblast senescence and apoptosis. *J Biol Chem.* 2010; 285:39551-63.
21. Yamakuchi M, Lowenstein CJ. miR-34, SIRT1 and p53: the feedback loop. *Cell Cycle.* 2009; 8:712-5.
22. Tazawa H, Tsuchiya N, Izumiya M, Nakagama H. Tumor-suppressive miR-34a induces senescence-like growth arrest through modulation of the E2F pathway in human colon cancer cells. *Proc Natl Acad Sci U S A.* 2007; 104:15472-7.
23. Demidenko ZN, Korotchikina LG, Gudkov AV, Blagosklonny MV. Paradoxical suppression of cellular senescence by p53. *Proc Natl Acad Sci U S A.* 2010; 107:9660-4.
24. Vigneron A, Vousden KH. p53, ROS and senescence in the control of aging. *Aging (Albany NY).* 2010; 2:471-4.
25. Kim H, You S, Farris J, Kong BW, Christman SA, Foster LK, Foster DN. Expression profiles of p53-, p16(INK4a)-, and telomere-regulating genes in replicative senescent primary human, mouse, and chicken fibroblast cells. *Exp Cell Res.* 2002; 272:199-208.
26. Lall S, Grun D, Krek A, Chen K, Wang YL, Dewey CN, Sood P, Colombo T, Bray N, Macmenamin P, Kao HL, Gunsalus KC, Pachter L, Piano F, Rajewsky N. A genome-wide map of conserved microRNA targets in *C. elegans*. *Curr Biol.* 2006; 16:460-71.
27. Krainer AR, Conway GC, Kozak D. The essential pre-mRNA splicing factor SF2 influences 5' splice site selection by activating proximal sites. *Cell.* 1990; 62:35-42.

- 28.** Krainer AR, Conway GC, Kozak D. Purification and characterization of pre-mRNA splicing factor SF2 from HeLa cells. *Genes Dev.* 1990; 4:1158-71.
- 29.** Ji Q, Hao X, Zhang M, Tang W, Yang M, Li L, Xiang D, Desano JT, Bommer GT, Fan D, Fearon ER, Lawrence TS, Xu L. MicroRNA miR-34 inhibits human pancreatic cancer tumor-initiating cells. *PLoS One.* 2009; 4:e6816.
- 30.** Liu C, Kelnar K, Liu B, Chen X, Calhoun-Davis T, Li H, Patrawala L, Yan H, Jeter C, Honorio S, Wiggins JF, Bader AG, Fagin R, Brown D, Tang DG. The microRNA miR-34a inhibits prostate cancer stem cells and metastasis by directly repressing CD44. *Nat Med.* 2011; 17:211-5.
- 31.** Hermeking H. The miR-34 family in cancer and apoptosis. *Cell Death Differ.* 2010; 17:193-9.
- 32.** Fujita K, Mondal AM, Horikawa I, Nguyen GH, Kumamoto K, Sohn JJ, Bowman ED, Mathe EA, Schetter AJ, Pine SR, Ji H, Vojtesek B, Bourdon JC, Lane DP, Harris CC. p53 isoforms Delta133p53 and p53beta are endogenous regulators of replicative cellular senescence. *Nat Cell Biol.* 2009; 11:1135-42.
- 33.** Rizzo M, Mariani L, Pitto L, Rainaldi G, Simili M. miR-20a and miR-290, multi-faceted players with a role in tumorigenesis and senescence. *J Cell Mol Med.* 2010; 14:2633-40.

Insights from model organisms on the functions of the tumor suppressor protein LKB1: Zebrafish chips in

Yme U. van der Velden and Anna-Pavlina G. Haramis

Department of Molecular Genetics, Netherlands Cancer Institute, Amsterdam, The Netherlands

Key words: LKB1, energy metabolism, cell polarity, animal models.

Received: 4/12/11; **Accepted:** 4/25/11; **Published:** 4/26/11

Corresponding author: Anna-Pavlina Haramis; **E-mail:** a.haramis@nki.nl

Copyright: © van der Velden and Haramis. This is an open-access article distributed under the terms of the Creative Commons Attribution License, which permits unrestricted use, distribution, and reproduction in any medium, provided the original author and source are credited

Abstract: The tumor suppressor LKB1 has emerged as a critical regulator of cell polarity and energy-metabolism. Studies in diverse model organisms continue to unravel the pathways downstream of LKB1; the emerging picture is that the outcomes of LKB1 signaling are mediated by a plethora of tissue-specific and context-dependent effectors.

INTRODUCTION

In 1998, the gene responsible for the rare dominantly inherited disorder Peutz-Jeghers syndrome [1], characterized by gastrointestinal hamartomatous polyposis and an increased predisposition to cancer [2], was identified as *LKB1*, which encodes a serine/threonine protein kinase. In addition to the familial syndrome, somatic mutations in *LKB1* were later found in over 30% of lung adenocarcinomas [3] and as the first identified recurrent mutation in endometrial cancer [4]. However clues as to its function were first discovered only in 2003, when it was identified as the long sought-after kinase that activates the alpha subunit of AMP-activated protein kinase (AMPK) [5],[6], linking LKB1 signaling to energy-metabolism control. Since then, LKB1 has been found to phosphorylate 12 other AMPK-related kinases including the microtubule-affinity-regulating kinase (MARK1-4), brain specific kinase (BRSK1-2), nuclear AMPK-related kinase (NUAK1-2), salt-inducible kinase (SIK1-3) and SNF-related kinase (SNRK) [7,8]. These results suggest that LKB1 is an upstream “master regulator” of energy homeostasis, cell polarity, DNA damage and cell cycle control [9].

Genetic analyses of LKB1 deficiency in higher eukaryotes have provided a framework to further dissect the functions of LKB1. However, the biology of LKB1 signaling appears to be highly complex, as loss of

LKB1 function in invertebrates and vertebrates have generated divergent results in different tissues and contexts. In this research perspective, we review the current understanding of LKB1 function in cellular polarity and energy metabolism derived from loss-of-function studies performed in different model organisms. For a more comprehensive overview of LKB1, we refer the reader to these recent excellent reviews [10,11,12,13,14,15]. In the last section we will discuss how the recently generated *Lkb1*-deficient zebrafish can provide a new tool to gain important insight into the function of this tumor suppressor protein.

LKB1 function during early development: polarization of the oocyte

Ten years before the human *LKB1* gene was cloned, the *C. elegans* homolog, abnormal embryonic PARTitioning of cytoplasm family member 4 (*par-4*), was retrieved from a maternal-effect-lethal screen for genes required for proper segregation of cytoplasmic factors in the first cell cycles of embryogenesis [16]. *par-4* mutant embryos had defects in several aspects of cell polarity and asymmetric cell division, which resulted in the formation of an amorphous mass of cells without distinct morphogenesis [17].

This function for LKB1 in polarization during early embryogenesis was subsequently found to be

conserved, at least in *Drosophila melanogaster*. The *Drosophila* egg is a highly polarized structure well before fertilization and the origin of this polarization might even be traced back to the first cell division of the cytotblast in the fly ovary [18]. Differentiation of germline cells into oocytes coincides with asymmetric localization of proteins and mRNAs that set up the anterior-posterior (A-P) and dorsal-ventral (D-V) axes within the oocyte [18]. *lkb1* mutant germline clones showed disrupted localization of various mRNAs resulting in defective oocyte polarity [19]. LKB1-deficiency in follicle cells also led to polarization defects including disorganization of the epithelial monolayer [19]. These polarity defects were not fully penetrant and it was suggested that LKB1 is essential for the establishment of epithelial polarity in the follicle, but not for its maintenance [20]. However, under conditions of glucose starvation, polarity defects were observed in all examined follicle cells, indicating that LKB1 is critical also for the maintenance of epithelial polarity in follicle cells upon energetic stress. As LKB1 is known to regulate energy homeostasis, as outlined in more detail below, this suggests that diverse LKB1 functions are connected under certain physiological conditions. Similar results were obtained for *ampka* mutant follicle cells [20]. Indeed, many aspects of the polarity defects in LKB1-deficient follicle cells were rescued by introduction of a phosphomimetic *ampka* mutant demonstrating the involvement of the LKB1-AMPK axis in polarization during early development [21].

Together, this illustrates the high conservation of LKB1 function in the earliest polarization processes in both worms and flies. Although it remains to be determined whether this function is also conserved in vertebrates, interestingly LKB1 is asymmetrically localized to the animal pole in the mouse oocyte [22].

LKB1 and cell polarization in later stages of development

LKB1 also has a conserved role in polarization during later stages of development. For example, loss of LKB1 signaling leads to impaired neuronal polarity in both invertebrates and vertebrates. In *C. elegans*, temperature-sensitive *par-4* mutants showed neuronal polarity defects in ventral cord neurons. This function was thought to be regulated by PAR-4-dependent phosphorylation of PAR-1, which is the homolog of human MAP/microtubule affinity-regulating kinases, MARK [23]. In *Drosophila*, depletion of LKB1 in neuroblasts caused polyploidism in larval brains, but via a Par1-independent mechanism [24]. Instead, defects in mitotic spindle formation and mislocalization of the

Baz/PAR-6/aPKC complex, a protein complex involved in cellular polarity, likely contributed to the reported phenotype [24]. In mice, conditional *lkb1* deletion in telencephalic progenitors led to impaired polarization of cortical neurons through impaired activation of the AMPK-related kinases SAD-A/B. Thus, LKB1 is required for polarization also in the vertebrate brain, although the molecular mechanisms involved are to a certain extent organism-specific [25].

In addition to neuronal polarization, LKB1 has been implicated in the polarization of epithelial structures, such as photoreceptors in the *Drosophila* eye. The *Drosophila* retina is derived from the eye imaginal disc, which is an epithelial structure. Eye-specific inactivation of LKB1 led to severe loss of polarity in photoreceptors at pupal stages [26]. Importantly, AMPK was not the primary LKB1 target in *Drosophila* eye development, but rather other AMPK-related kinases including SIK, NUA1 and PAR-1 [26]. In vertebrates, activation of LKB1 induced complete polarization of single intestinal epithelial cells in culture [27]. Furthermore, AMPK activation is required for tight-junction formation and polarization in the Madin-Darby Canine Kidney (MDCK) epithelial cell line, although this may not be exclusively dependent on LKB1 [28], [29]. LKB1 null mice do not survive beyond E10.5 and show several defects including mesenchymal cell death as well as neural tube and vascular abnormalities associated with increased VEGF signaling [30]. Somewhat unexpectedly, inactivation of *Lkb1* in several mouse tissues did not lead to gross epithelial polarity defects, with the notable exception of the pancreas [31,32].

Thus, it appears that LKB1 regulates polarization during development throughout the animal kingdom in a tissue- and context-dependent manner, and via phosphorylation of distinct substrates.

LKB1: a master regulator of energy homeostasis

Probably the best-studied function of LKB1 to date, at least in vertebrates, is the regulation of energy homeostasis, particularly through AMPK activation and the target of rapamycin (TOR) pathway [33,34]. Upon energetic stress induced by a variety of stimuli such as food-deprivation, exercise, osmotic stress and hypoxia, AMPK is phosphorylated and activated by LKB1. AMPK then phosphorylates tuberous sclerosis complex 2 (TSC2), which leads to inhibition of TOR complex 1 (TORC1) activity [34]. TORC1 activity is associated with cell growth and viability since TORC1 stimulates anabolic processes such as protein synthesis while inhibiting catabolic processes like the degradation of

cellular components by autophagy [35]. Thus, upon LKB1-dependent activation of AMPK, TORC1 signaling is inhibited, which promotes energy conservation under conditions of energetic stress.

Given the embryonic lethal phenotype of the knockout mouse, the role of LKB1 in energy homeostasis at the whole organism level in animals has only been studied in *C. elegans* and, more recently, in *D. rerio*. These studies, which are described in detail below, have revealed a far more complex role for LKB1 in energy homeostasis beyond only the regulation of TOR signaling via AMPK. Indeed, in addition to TSC2, AMPK has a multitude of direct substrates, many of which are also involved in metabolism control [11,14]. In *C. elegans*, larvae developmentally arrest and enter the so-called “dauer” phase under unfavorable environmental conditions. Dauer larvae do not feed, become stress-resistant, are extremely long-lived and “non-aging” [36]. In order to ensure long-term survival, fat is stored in the hypodermis, which is an organ akin to the skin of higher organisms [37]. Dauer larvae with compromised LKB1/AMPK signaling rapidly depleted hypodermic fat storages and die prematurely due to vital organ failure [38]. This inappropriate fat depletion was found to be due to increased activity of adipose triglyceride lipase (ATGL-1), a direct target of AMPK. Similar to this result in *C. elegans*, we recently reported that *lkb1* mutant zebrafish are also unable to cope with energetic stress [39]. Although *Lkb1* deficiency in *D. rerio* did not lead to overt developmental defects, *lkb1* mutants did fail to downregulate metabolism once the yolk, which provides energy in the first days of development, was consumed. These *lkb1* mutants exhibited hallmarks of a starvation response at the cellular and biochemical level, displayed profoundly decreased ATP levels and became energy-depleted much sooner than food-deprived wild type animals. Thus, in both worms and zebrafish, LKB1 is essential for control of whole-body energy homeostasis and adaptation of metabolism to changes in energy availability, which is essential for long-term viability of the organism.

Zebrafish *lkb1* mutants die two days after yolk absorption in stark contrast to wild-type larvae that can survive food deprivation for more than six days. Interestingly, two days of food deprivation did not lead to detectable AMPK phosphorylation in wild-type larvae, suggesting that deregulated AMPK signaling may not be the sole cause for impaired energy metabolism control in *lkb1* larvae. Furthermore, TOR signaling was not severely deregulated in *lkb1* mutants. Thus, we proposed that the AMPK-TORC1 axis might not be the critical or only effector of *Lkb1*-mediated

maintenance of whole-organism energy homeostasis, at least in this setting. Interestingly, recent work on the effect of *Lkb1* inactivation in mouse hematopoietic stem cells showed that, while LKB1 was critically required to regulate energy metabolism and maintain cell survival, the effects were again largely independent of AMPK and TORC1 signaling [40,41,42]. Together, these findings illustrate that *in vivo* LKB1 controls metabolism through several pathways in addition to TORC1 signaling and showcase the complexity of LKB1 biology.

A zebrafish perspective on LKB1

As zebrafish *lkb1* mutants survive embryonic development, unlike mice, they provide the first embryonic viable vertebrate model of homozygous *lkb1* deletion. This, combined with the many advantages of using zebrafish as a model organism, some of which are described below, should rapidly advance our understanding of LKB1 function.

One of the advantages of zebrafish is that the oocyte is externally fertilized, allowing early developmental processes, from fertilization onwards, to be easily analyzed. In addition, germline replacement methods [43] mean that an animal lacking both maternal and zygotic LKB1 can be generated. Maternal-zygotic zebrafish *lkb1* mutants will provide a system to address whether and how *Lkb1* functions in the first cleavage stages in vertebrates.

Another attractive feature of the zebrafish is their small size and transparency during development. In combination with the availability of numerous transgenic lines expressing tissue-specific fluorescently-labelled reporters, this allows real-time, *in vivo* visualization of various processes such as cell migration and organogenesis. Thus, questions pertaining to the biology of tissue physiology in a setting of *Lkb1*-deficiency can be addressed.

Although addressing whether neuronal polarity was impaired was beyond the scope of our previous study, it is still possible that *Lkb1* is required for polarization or asymmetric cell division in neuronal tissues in zebrafish, given this function is conserved in *C. elegans* and *Drosophila*. Should that be the case, the ease of performing forward genetic screens in zebrafish could help to dissect the pathway of neuronal polarization in vertebrates by identification of new proteins involved in this process.

Interestingly, we did not observe polarity defects in either the gut or the eye of zebrafish *lkb1* mutants, in

contrast to studies in human cell lines and *Drosophila* respectively, again highlighting the cell-type specificity and context-dependency of LKB1 function.

Since *Lkb1* deficiency leads to impaired metabolic control upon energetic stress, it will be interesting to determine whether *lkb1* mutants are hypersensitive to other types of stress, such as osmotic stress and DNA damage. Our preliminary results showed that *lkb1* mutants are hypersensitive to mechanical stress, but only when they are under energetic stress, again illustrating that the metabolic functions of *Lkb1* are tightly linked with other *Lkb1*-dependent processes.

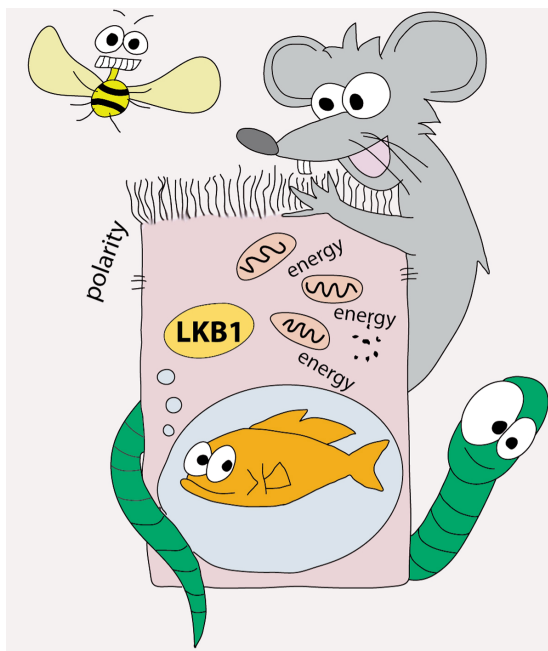


Figure 1. Studies of *LKB1*-deficiency in flies, worms, mice and zebrafish have revealed that the tumor suppressor *LKB1* has conserved and divergent roles in the regulation of cell polarization and energy metabolism processes.

Finally, since zebrafish *lkb1* mutants are embryonic viable they provide an excellent platform to conduct chemical genetic screens to identify molecular pathways that are regulated and/or cooperate with *Lkb1* and lead to deregulation of metabolism. These types of screens could also identify compounds that can modulate metabolism and may prove to be useful for inhibiting growth of *LKB1*-deficient tumors.

CONCLUSION

LKB1 is a tumor suppressor gene and is mutated in a wide variety of human cancers. Thus, deciphering its

function could have direct clinical implications. Given the complexity of *LKB1* function, which is illustrated by the diversity of its mutant phenotypes in a variety of model organisms and contexts, *lkb1* mutant zebrafish offer a powerful new tool for unraveling the numerous mechanisms and pathways regulated by *LKB1*. It also provides the unique opportunity to study *LKB1* function at the whole organism level in vertebrates.

ACKNOWLEDGEMENTS

The work on *LKB1* in the authors' laboratory was funded by a Netherlands Organization for Scientific Research Vidi Grant 91756322 to APGH.

CONFLICT OF INTERESTS STATEMENT

The authors of this manuscript have no conflict of interests to declare.

REFERENCES

1. Jegers H, Mc KV, Katz KH. Generalized intestinal polyposis and melanin spots of the oral mucosa, lips and digits; a syndrome of diagnostic significance. *N. Engl. J. Med.* 1949; 241:993, illust; passim.
2. Hemminki A, Markie D, Tomlinson I, Avizienyte E, Roth S, Loukola A, Bignell G, Warren W, Aminoff M, Hoglund P, Jarvinen H, Kristo P, Pelin K, Ridanpaa M, Salovaara R, Toro T, Bodmer W, Olschwang S, Olsen AS, Stratton MR, de la Chapelle A, Aaltonen LA. A serine/threonine kinase gene defective in Peutz-Jeghers syndrome. *Nature.* 1998; 391:184-187.
3. Sanchez-Cespedes M, Parrella P, Esteller M, Nomoto S, Trink B, Engles JM, Westra WH, Herman JG, Sidransky D. Inactivation of *LKB1/STK11* is a common event in adenocarcinomas of the lung. *Cancer Res.* 2002; 62:3659-3662.
4. Contreras CM, Gurumurthy S, Haynie JM, Shirley LJ, Akbay EA, Wingo SN, Schorge JO, Broaddus RR, Wong KK, Bardeesy N, Castrillon DH. Loss of *Lkb1* provokes highly invasive endometrial adenocarcinomas. *Cancer Res.* 2008; 68:759-766.
5. Hawley SA, Boudeau J, Reid JL, Mustard KJ, Udd L, Makela TP, Alessi DR, Hardie DG. Complexes between the *LKB1* tumor suppressor, *STRAD* alpha/beta and *MO25* alpha/beta are upstream kinases in the AMP-activated protein kinase cascade. *J. Biol.* 2003; 2:28.1-28.16.
6. Woods A, Johnstone SR, Dickerson K, Leiper FC, Fryer LG, Neumann D, Schlattner U, Wallimann T, Carlson M, Carling D. *LKB1* is the upstream kinase in the AMP-activated protein kinase cascade. *Curr. Biol.* 2003; 13:2004-2008.
7. Lizcano JM, Goransson O, Toth R, Deak M, Morrice NA, Boudeau J, Hawley SA, Udd L, Makela TP, Hardie DG, Alessi DR. *LKB1* is a master kinase that activates 13 kinases of the AMPK subfamily, including *MARK/PAR-1*. *Embo J.* 2004; 23:833-843.
8. Jaleel M, McBride A, Lizcano JM, Deak M, Toth R, Morrice NA, Alessi DR. Identification of the sucrose non-fermenting related kinase *SNRK*, as a novel *LKB1* substrate. *FEBS Lett.* 2005; 579:1417-1423.

9. Hezel AF, Bardeesy N. LKB1; linking cell structure and tumor suppression. *Oncogene*. 2008; 27:6908-6919.
10. Alessi DR, Sakamoto K, Bayascas JR. LKB1-dependent signaling pathways. *Annu. Rev. Biochem.* 2006; 75:137-163.
11. Shackelford DB, Shaw RJ. The LKB1-AMPK pathway: metabolism and growth control in tumour suppression. *Nat. Rev. Cancer*. 2009; 9:563-575.
12. Jansen M, Ten Klooster JP, Offerhaus GJ, Clevers H. LKB1 and AMPK family signaling: the intimate link between cell polarity and energy metabolism. *Physiol. Rev.* 2009; 89:777-798.
13. Shelly M, Poo MM. Role of LKB1 - SAD/MARK pathway in neuronal polarization. *Dev. Neurobiol.* 2011.
14. van Veelen W, Korsse SE, van de Laar L, Peppelenbosch MP. The long and winding road to rational treatment of cancer associated with LKB1/AMPK/TSC/mTORC1 signaling. *Oncogene*. 2011.
15. Mirouse V, Billaud M. The LKB1/AMPK polarity pathway. *FEBS Lett.* 2010.
16. Kempthues KJ, Priess JR, Morton DG, Cheng NS. Identification of genes required for cytoplasmic localization in early *C. elegans* embryos. *Cell*. 1988; 52:311-320.
17. Morton DG, Roos JM, Kempthues KJ. *par-4*, a gene required for cytoplasmic localization and determination of specific cell types in *Caenorhabditis elegans* embryogenesis. *Genetics*. 1992; 130:771-790.
18. Huynh JR, St Johnston D. The origin of asymmetry: early polarisation of the *Drosophila* germline cyst and oocyte. *Curr. Biol.* 2004; 14:R438-449.
19. Martin SG, St Johnston D. A role for *Drosophila* LKB1 in anterior-posterior axis formation and epithelial polarity. *Nature*. 2003; 421:379-384.
20. Mirouse V, Swick LL, Kazgan N, St Johnston D, Brenman JE. LKB1 and AMPK maintain epithelial cell polarity under energetic stress. *J. Cell Biol.* 2007; 177:387-392.
21. Lee JH, Koh H, Kim M, Kim Y, Lee SY, Karess RE, Lee SH, Shong M, Kim JM, Kim J, Chung J. Energy-dependent regulation of cell structure by AMP-activated protein kinase. *Nature*. 2007; 447:1017-1020.
22. Szczepanska K, Maleszewski M. LKB1/PAR4 protein is asymmetrically localized in mouse oocytes and associates with meiotic spindle. *Gene Expr. Patterns*. 2005; 6:86-93.
23. Kim JS, Hung W, Narbonne P, Roy R, Zhen M. *C. elegans* STRADalpha and SAD cooperatively regulate neuronal polarity and synaptic organization. *Development*. 2010; 137:93-102.
24. Bonaccorsi S, Mottier V, Giansanti MG, Bolkan BJ, Williams B, Goldberg ML, Gatti M. The *Drosophila* Lkb1 kinase is required for spindle formation and asymmetric neuroblast division. *Development*. 2007; 134:2183-2193.
25. Barnes AP, Lilley BN, Pan YA, Plummer LJ, Powell AW, Raines AN, Sanes JR, Polleux F. LKB1 and SAD kinases define a pathway required for the polarization of cortical neurons. *Cell*. 2007; 129:549-563.
26. Amin N, Khan A, St Johnston D, Tomlinson I, Martin S, Brenman J, McNeill H. LKB1 regulates polarity remodeling and adherens junction formation in the *Drosophila* eye. *Proc. Natl. Acad. Sci U.S.A.* 2009; 106:8941-8946.
27. Baas AF, Kuipers J, van der Wel NN, Batlle E, Koerten HK, Peters PJ, Clevers HC. Complete polarization of single intestinal epithelial cells upon activation of LKB1 by STRAD. *Cell*. 2004; 116:457-466.
28. Zhang L, Li J, Young LH, Caplan MJ. AMP-activated protein kinase regulates the assembly of epithelial tight junctions. *Proc. Natl. Acad. Sci U.S.A.* 2006; 103:17272-17277.
29. Zheng B, Cantley LC. Regulation of epithelial tight junction assembly and disassembly by AMP-activated protein kinase. *Proc. Natl. Acad. Sci U.S.A.* 2007; 104:819-822.
30. Ylikorkkala A, Rossi DJ, Korsisaari N, Luukko K, Alitalo K, Henkemeyer M, Makela TP. Vascular abnormalities and deregulation of VEGF in Lkb1-deficient mice. *Science*. 2001; 293:1323-1326.
31. Hezel AF, Gurumurthy S, Granot Z, Swisa A, Chu GC, Bailey G, Dor Y, Bardeesy N, Depinho RA. Pancreatic LKB1 deletion leads to acinar polarity defects and cystic neoplasms. *Mol. Cell. Biol.* 2008; 28:2414-2425.
32. Granot Z, Swisa A, Magenheimer J, Stolovich-Rain M, Fujimoto W, Manduchi E, Miki T, Lennerz JK, Stoeckert CJ, Jr., Meyuhos O, Seino S, Permutt MA, Piwnica-Worms H, Bardeesy N, Dor Y. LKB1 regulates pancreatic beta cell size, polarity, and function. *Cell Metab.* 2009; 10:296-308.
33. Shaw RJ. LKB1 and AMP-activated protein kinase control of mTOR signalling and growth. *Acta Physiol. (Oxf)*. 2009; 196:65-80.
34. Shaw RJ, Bardeesy N, Manning BD, Lopez L, Kosmatka M, Depinho RA, Cantley LC. The LKB1 tumor suppressor negatively regulates mTOR signaling. *Cancer Cell*. 2004; 6:91-99.
35. Wullschlegel S, Loewith R, Hall MN. TOR signaling in growth and metabolism. *Cell*. 2006; 124:471-484.
36. Klass M, Hirsh D. Non-ageing developmental variant of *Caenorhabditis elegans*. *Nature*. 1976; 260:523-525.
37. Burnell AM, Houthoofd K, O'Hanlon K, Vanfleteren JR. Alternate metabolism during the dauer stage of the nematode *Caenorhabditis elegans*. *Exp. Gerontol.* 2005; 40:850-856.
38. Narbonne P, Roy R. *Caenorhabditis elegans* dauers need LKB1/AMPK to ration lipid reserves and ensure long-term survival. *Nature*. 2009; 457:210-214.
39. van der Velden YU, Wang L, Zevenhoven J, van Rooijen E, van Lohuizen M, Giles RH, Clevers H, Haramis AP. The serine-threonine kinase LKB1 is essential for survival under energetic stress in zebrafish. *Proc. Natl. Acad. Sci U.S.A.* 2011; 108:4358-4363.
40. Gan B, Hu J, Jiang S, Liu Y, Sahin E, Zhuang L, Fletcher-Sanankone E, Colla S, Wang YA, Chin L, Depinho RA. Lkb1 regulates quiescence and metabolic homeostasis of haematopoietic stem cells. *Nature*. 2004; 428:701-704.
41. Gurumurthy S, Xie SZ, Alagesan B, Kim J, Yusuf RZ, Saez B, Tzatsos A, Ozsolak F, Milos P, Ferrari F, Park PJ, Shirihai OS, Scadden DT, Bardeesy N. The Lkb1 metabolic sensor maintains haematopoietic stem cell survival. *Nature*. 2004; 428:659-663.
42. Nakada D, Saunders TL, Morrison SJ. Lkb1 regulates cell cycle and energy metabolism in haematopoietic stem cells. *Nature*. 2004; 428:653-658.
43. Ciruna B, Weidinger G, Knaut H, Thisse B, Thisse C, Raz E, Schier AF. Production of maternal-zygotic mutant zebrafish by germ-line replacement. *Proc. Natl. Acad. Sci U.S.A.* 2002; 99:14919-14924.

MKK4 as oncogene or tumor suppressor: In cancer and senescence, the story's getting old

Steven C. Cunningham¹, Eike Gallmeier², and Scott E. Kern³

¹Department of Surgery, St. Agnes Hospital, Baltimore, MD 21229, USA

²Medizinische Klinik II, Klinikum der Universität München, Campus Großhadern, München, Germany

³Department of Oncology, Johns Hopkins University, Baltimore, MD 21231, USA

E-mail: to Steven Cunningham at scunning@stagnes.org

The MKK4 gene is selected against by inactivating mutations in a large number of different tumor types, eg, tumors of the pancreas, bile ducts, breast, colon, lungs, testes [1-3] at a remarkably consistent rate of approximately 5-10% of tumors, identifying and defining it, therefore, as a tumor-suppressor (or genome-maintenance) gene [4].

Yet, experimental evidence exists that supports a pro-oncogenic role for MKK4 [5, 6]. Finegan and Tournier [6], for example, recently used an inducible murine model of MKK4 homozygous deletion to evaluate the role of MKK4 in skin tumorigenesis. They found that skin-specific MKK4-null mice were resistant to carcinogen-induced tumorigenesis. While the paper is well written and the model well designed, the fundamental premise may well be flawed, especially concerning MKK4's role in tumorigenesis, perhaps misleading the line of experimentation. There should be no question that MKK4 is tumor-suppressive, not oncogenic. MKK4 is widely selected against by tumors (its low rate of homozygous loss may be accounted for by a higher rate of heterozygous loss that could rationalize frequent 17p loss in diverse human cancers[7]) and unsurprisingly patients whose tumors have loss of MKK4 show statistically significant decrease in survival in the best controlled studies, using calibrated immunohistochemistry in large numbers of patients [8], consistent with a tumor-suppressive role.

Similarly consistent with a growth-suppressive role of MKK4 are observations made regarding the relationship between MKK4 and senescence. One of the ways MKK4 may suppress tumors is by inhibiting cell proliferation during replicative senescence, a widely re-

cognized mechanism of tumor suppression. Marasa et al. [9] recently observed that MKK4 abundance increases in senescent fibroblasts. Overexpression of MKK4 decreased proliferation and promoted a senescent phenotype in young WI-38 human diploid fibroblasts and conversely, when MKK4 levels were lowered by several microRNAs targeting the MKK4 mRNA, the senescent phenotype was ameliorated and cells proliferated more rapidly [9]. In keeping with these observations, human tissue from older individuals was observed to express higher levels of MKK4 than corresponding tissue from young donors [9].

In the discussion of their inducible murine model of MKK4 homozygous deletion, Finegan and Tournier [6] rightly point out that there is conflicting literature regarding MKK4's role in tumorigenesis. The reason for the conflicting literature is largely because MKK4 is difficult to study experimentally. Their model would not be the first homozygous deletion model to model a population or a phenomenon that was not anticipated. For example, our own studies using homozygous MKK4-null cells engineered from the human pancreas cancer cell line PL-5 [10] showed that MKK4 deletion had a detrimental phenotype in a model of liver metastasis. Indeed experimental human data have shown that when tumors experiment with MKK4-null states, they are successful in developing a growth advantage allowing them to emerge through the clonal selection process in only 10% of cancers having 17p loss. We inferred from this observation that most tumor cells do not find the MKK4-null to be advantageous and that those PL-5 knock-out cells modeled this majority of cells. One may conclude from such a line of experimentation that the cell type-specific detrimental

phenotype that was modeled offered an important counterweight to the selective advantage achieved by cells experimenting with genetic null states during tumorigenesis, the resultant balance determining the low but remarkably consistent rate of observed biallelic MKK4 mutations [7, 10].

Because changes effected to this gene may have advantageous or deleterious effects on cells depending on the model, cancer investigators must rely on real tumors and not artificial models to guide experimental design and interpretation such that valuable research time, energy, and funding are not spent studying a phenomenon, viz, a “pro-oncogenic” function of MKK4, that common cancer sense should tell us does not likely exist. To put it colloquially, it does not matter how scientists vote regarding a pro-oncogenic or tumor-suppressive role of MKK4, because the tumors have already conducted that election in favor of the latter: MKK4 must be a tumor suppressor, as concluded from observations on wide varieties of examined tumors, which uniformly present evidence of having selected for its loss at a consistent rate. There is no convincing evidence from observations of tumor biology that MKK4 has any pro-oncogenic role. Scientists may argue for such a role, but the tumors have had their say, age-old dictators that they are.

REFERENCES

1. Teng DH, Perry WL, 3rd, Hogan JK, Baumgard M, Bell R, Berry S, Davis T, Frank D, Frye C, Hattier T, Hu R, Jammulapati S, Janecki T, Leavitt A, Mitchell JT, Pero R, Sexton D, Schroeder M, Su PH, Swedlund B, Kyriakis JM, Avruch J, Bartel P, Wong AK, and Tavtigian SV. Human mitogen-activated protein kinase kinase 4 as a candidate tumor suppressor. *Cancer Res.* 1997; 57: 4177-4182.
2. Su GH, Hilgers W, Shekher MC, Tang DJ, Yeo CJ, Hruban RH and Kern SE. Alterations in pancreatic, biliary, and breast carcinomas support MKK4 as a genetically targeted tumor suppressor gene. *Cancer Res.* 1998; 58: 2339-2342.
3. Parsons DW, Wang TL, Samuels Y, Bardelli A, Cummins JM, DeLong L, Silliman N, Ptak J, Szabo S, Willson JK, Markowitz S, Kinzler KW, Vogelstein B, Lengauer C, and Velculescu VE. Colorectal cancer: mutations in a signalling pathway. *Nature.* 2005; 436: 792.
4. Fearon ER Tumor-Suppressor Genes. In: B. Vogelstein and K. W. Kinzler (eds.), *The Genetic Basis of Human Cancer*, 2nd edition, pp. 197-206. New York: McGraw-Hill, 2002.
5. Wang L, Pan Y and Dai JL. Evidence of MKK4 pro-oncogenic activity in breast and pancreatic tumors. *Oncogene.* 2004; 23: 5978-5985.
6. Finegan KG and Tournier C. The mitogen-activated protein kinase kinase 4 has a pro-oncogenic role in skin cancer. *Cancer Res.* 70: 5797-5806.
7. Cunningham SC, Gallmeier E, Hucl T, Dezentje DA, Abdelmohsen K, Gorospe M and Kern SE. Theoretical proposal: allele dosage of MAP2K4/MKK4 could rationalize frequent 17p loss in diverse human cancers. *Cell Cycle.* 2006; 5: 1090-1093.
8. Cunningham SC, Kamangar F, Kim MP, Hammoud S, Haque R, Iacobuzio-Donahue C, Ashfaq R, Kern SE, Maitra A, Heitmiller RE, Choti MA, Lillemoe KD, Cameron JL, Yeo CJ, Montgomery E, and Schulick RD. Mkk4 Status Predicts Survival after Resection of Gastric Adenocarcinoma. *Arch Surg.* 2006; 141: 1095-1099.
9. Marasa BS, Srikantan S, Masuda K, Abdelmohsen K, Kuwano Y, Yang X, Martindale JL, Rinker-Schaeffer CW and Gorospe M. Increased MKK4 abundance with replicative senescence is linked to the joint reduction of multiple microRNAs. *Sci Signal.* 2009; 2: ra69.
10. Cunningham SC, Gallmeier E, Hucl T, Dezentje DA, Calhoun ES, Falco G, Abdelmohsen K, Gorospe M and Kern SE. Targeted deletion of MKK4 in cancer cells: a detrimental phenotype manifests as decreased experimental metastasis and suggests a counterweight to the evolution of tumor-suppressor loss. *Cancer Res.* 2006; 66: 5560-5564.

Tumor suppressors revival in CLL

Giovanna Carrà, Riccardo Tauli, Alessandro Morotti

Since the 2001 FDA approval of the BCR-ABL tyrosine kinase inhibitor, Imatinib, as the standard of treatment for Chronic Myeloid Leukemia (CML), these last 16 years have clearly showed the raise and the fall of strategies to target oncogenes in cancer. Beside the successful story of Imatinib in CML, no other drugs able to target oncogenes at the bench have shown such impressive results at the bedside. While various compounds have indeed clearly prompted themselves as effective drugs with promising clinical results, still the cure for cancer, meaning complete eradication, remains a mirage with these inhibitors.

Conversely, murine models have proven that the re-establishment of tumor suppressors in cancer remains the unique strong strategy to obtain cancer eradication: in a very simple, yet dramatically effective manner, the re-expression of p53 in various cancer models have indeed been associated with cancer exhaustion [1].

For many years, the strategies to target tumor suppressors have been neglected from drugs cocktails. The idea that tumor suppressors are involved in tumorigenesis through genetic impairments of both alleles and the lack of strategies to restore these genes in cancer cells have wiped out all the promises in targeting these genes. Yet, the mechanisms of tumor suppressors impairment in cancer have changed: it is now clear that even wild-type tumor suppressors can play an essential role in tumorigenesis, when functionally inhibited [2]. Mechanisms that promote tumor suppressors delocalization, degradation and/or inactivation inevitably result in tumor suppressors inhibition. The identification of tumors that depend on functionally inactive tumor suppressors is of extraordinary importance because these tumors can potentially benefit from therapies designed to restore the function of the inactive tumor suppressors.

Very recently, we have demonstrated that the de-ubiquitinase USP7, also known as HAUSP, is aberrantly expressed and active in Chronic Lymphocytic Leukemia (CLL) [3]. Besides being one of the hundreds of differentially expressed genes in a cancer, USP7 has the privilege of controlling the expression, localization and function of three major tumor suppressors: PTEN [4-5], p53 [6] and FOXO [7].

In this work, we demonstrated that CLL is characterized by an increased USP7 expression, through miRNA de-

regulation, and by aberrant USP7 regulation through Casein Kinase II. Consequently, USP7 was shown to promote PTEN delocalization from the nucleus with consequence loss of part of its tumor suppressive functions. Conversely, USP7 inhibitor restores PTEN nuclear pool with re-establishment of its tumor suppressive functions. In this work, we focused on the ability of USP7 to modulate PTEN in a p53 null scenario, which remains the most challenging battlefield for CLL therapy. However, it should be noted that USP7 is also well known to modulate p53 protein levels, as well [6]. USP7 promotes mdm2 de-ubiquitination, which in turn modulates p53 protein degradation. High levels of USP7 activation can indeed affect the mdm2/p53 network with potentially intriguing consequences on p53 protein levels and functional regulation. Similarly, USP7 was shown to modulate the mono-ubiquitination of FOXOs, very known tumor suppressors able to control cellular proliferation [7]. USP7 favors FOXOs nuclear exclusion and inactivation. While we did not investigate FOXO cellular compartmentalization and p53 protein levels in CLL, it could be speculated that high levels of USP7 may also affects FOXO localization and p53 protein levels in CLL.

Our published observation that USP7-PTEN is a targetable network in CLL [3], and the above speculations that USP7 may also affect p53 and FOXOs in the CLL context, attribute to USP7 a potential pivotal role in the functional regulation of three major tumor suppressors in CLL. Therefore, USP7 inhibitors may represent strong apoptotic inducers in CLL through: *i*) the reactivation of wild-type PTEN and, potentially, p53 and FOXO; *ii*) by-passing the resistance mediated by mutations/deletions of one of these tumor suppressors through the reactivation of the others, as we observed in the presence of p53 mutations [3].

In summary, our data clearly indicate that the characterization of molecular circuits involved in the control of oncosuppressor stability, localization and activity is critical to develop novel therapeutic strategies aimed at re-activating oncosuppressor functions. Thus, it is now advisable that USP7 inhibitors will be included among the drugs to be further investigated for their ability to positively modulate oncosuppressor regulatory networks in cancer.

REFERENCES

1. Ventura A, et al. Nature. 2007; 445:661–65. doi:10.1038/nature05541
2. Berger AH, et al. Nature. 2011; 476:163-69. doi:10.1038/nature10275
3. Carrà G, et al. Oncotarget. 2017; 8:35508-22. doi:10.18632/oncotarget.16348
4. Song MS, et al. Nature. 2008; 455:813-17. doi:10.1038/nature07290
5. Morotti A, et al. Leukemia. 2014; 28:1326-33. doi:10.1038/leu.2013.370
6. Cummins JM, et al. Nature. 2004; 428:1-486. doi:10.1038/nature02501
7. Van der Horst A, et al. Nature Cell Biol. 2006; 8:1064-73. doi 10.1038/ncb1469.

Alessandro Morotti: Department of Clinical and Biological Sciences, University of Turin, 10043 Turin, Italy

Correspondence: Alessandro Morotti

Email: alessandro.morotti@unito.it

Keywords: Chronic Lymphocytic Leukemia, tumor suppressors, USP7, PTEN, p53, FOXO

Copyright: Carrà et al. This is an open-access article distributed under the terms of the Creative Commons Attribution License (CC BY 3.0), which permits unrestricted use, distribution, and reproduction in any medium, provided the original author and source are credited

Received: June 14, 2017

Published: June 26, 2017

SOCS1 regulates senescence and ferroptosis by modulating the expression of p53 target genes

Emmanuelle Saint-Germain¹, Lian Mignacca¹, Mathieu Vernier², Diwakar Bobbala³, Subburaj Ilangumaran³ and Gerardo Ferbeyre¹

¹Département de Biochimie et Médecine Moléculaire; Université de Montréal, Montréal, Québec, H3C 3J7; Canada.

²Department of Biochemistry, Medicine & Oncology, Faculty of Medicine, McGill University, Goodman Cancer Research Centre, Montreal, Quebec, H3A 1A3, Canada

³Immunology Division, Department of Pediatrics, Faculty of Medicine, University of Sherbrooke, Sherbrooke, Quebec, J1K 2R1, Canada

Correspondence to: Gerardo Ferbeyre; email: g.ferbeyre@UMontreal.CA

Keywords: suppressor of cytokine signaling, tumor suppressor, ferroptosis, senescence, KAP1

Received: June 30, 2017 **Accepted:** October 15, 2017 **Published:** October 28, 2017

Copyright: Saint-Germain et al. This is an open-access article distributed under the terms of the Creative Commons Attribution License (CC BY 3.0), which permits unrestricted use, distribution, and reproduction in any medium, provided the original author and source are credited.

ABSTRACT

The mechanism by which p53 suppresses tumorigenesis remains poorly understood. In the context of aberrant activation of the JAK/STAT5 pathway, SOCS1 is required for p53 activation and the regulation of cellular senescence. In order to identify p53 target genes acting during the senescence response to oncogenic STAT5A, we characterized the transcriptome of STAT5A-expressing cells after SOCS1 inhibition. We identified a set of SOCS1-dependent p53 target genes that include several secreted proteins and genes regulating oxidative metabolism and ferroptosis. Exogenous SOCS1 was sufficient to regulate the expression of p53 target genes and sensitized cells to ferroptosis. This effect correlated with the ability of SOCS1 to reduce the expression of the cystine transporter SLC7A11 and the levels of glutathione. SOCS1 and SOCS1-dependent p53 target genes were induced during the senescence response to oncogenic STAT5A, RasV12 or the tumor suppressor PML. However, while SOCS1 sensitized cells to ferroptosis neither RasV12 nor STAT5A mimicked the effect. Intriguingly, PML turned cells highly resistant to ferroptosis. The results indicate different susceptibilities to ferroptosis in senescent cells depending on the trigger and suggest the possibility of killing senescent cells by inhibiting pathways that mediate ferroptosis resistance.

INTRODUCTION

p53 is by far the most commonly mutated gene in human cancers with mutations present in 36% of all patients [1]. p53 acts mainly as a transcription factor suggesting that p53-target genes should have important functions in cancer biology. Combining chromatin immunoprecipitation and gene expression data of different cellular models revealed a number of p53 target genes that range between 122 to 3697 genes with

little overlap between studies but including both genes that are activated or repressed by p53 [2,3,4,5]. A meta-analysis of different p53 and cell cycle regulatory networks revealed that p53 acts mainly as an activator through proximal promoter binding while gene repression is mostly indirect and dependent on the DREAM or RB/E2F complexes [5]. Identifying the key p53 targets that mediate tumor suppression and the cellular processes they regulate is a pressing goal for cancer research.

The tumor suppressor activity of p53 in mice does not correlate with the expression of p53 targets controlled by an acute DNA damage response [6]. For example, mice deficient for p21, Puma and Noxa, which are p53 target genes mediating cell cycle arrest and apoptosis, do not display the tumor prone phenotype typical of p53 null mice [7]. Genes controlling cell signalling, the cytoskeleton, DNA repair and ferroptosis were then identified as new candidates to mediate the tumor suppressor functions of p53 [4,6]. Genome wide analysis of p53 binding under conditions of acute or chronic stimulation revealed distinct p53 binding sites and regulated genes suggesting that upon chronic stimulation p53 DNA binding properties are regulated differently than in acute conditions [8]. The present state of knowledge indicates that context largely determines the transcriptional response to p53 activation. Hence, the identification of p53 targets in conditions where p53 regulates tumor suppression will help to identify important pathways and mechanisms to halt tumorigenesis.

Activation of p53 is often mediated by the DNA damage response that triggers a series of post-translational modifications on p53 preventing its degradation by E3 ubiquitin ligases such as MDM2 [9,10]. A similar mechanism is activated by the nucleolar protein p19ARF [11], the tumor suppressor PML [12] and several ribosomal proteins linking p53 activation to nucleolar stresses [13]. During cellular senescence induced by aberrant STAT5A stimulation both DNA damage and SOCS1 expression are required for p53 activation [14,15]. The specific role of SOCS1 in the senescence response to activated STAT5A and the p53 target genes modulated in this context remain for the most part unknown.

In order to identify and characterize p53 target genes whose regulation depends on SOCS1 we compared the transcriptome of cells that enter senescence in response to constitutive STAT5A-signaling with the transcriptome of cells that failed to do so due to inactivation of SOCS1. We define a set of SOCS1-dependent p53 target genes, some of which are downregulated in many human cancers. Interestingly, this set of genes included the ferroptosis regulators SLC7A11 and SAT1 as well as p53 target genes previously linked to the cellular response to oxidized phospholipids. Consistent with the gene expression analysis, overexpression of SOCS1 sensitized cells to ferroptosis. In contrast, induction of senescence by RasV12, STAT5A or PML did not sensitize cells to ferroptosis indicating different susceptibilities to ferroptosis depending on the senescence trigger. We also provide new insights into the mechanism of modulation of p53 by SOCS1 by showing that SOCS1

can stabilize p53 independently of its effects on serine 15-phosphorylation and that SOCS1 can form a complex with the p53 repressor KAP1.

RESULTS

SOCS1 inhibition affects a selective group of p53 target genes

To investigate how SOCS1 modulates the p53 pathway we used a model of oncogene-induced senescence where p53 activation is dependent on SOCS1 [14,15]. In this model, a constitutively active allele of STAT5A (cS5A) is introduced into human fibroblasts IMR90-E7. These cells express the papillomavirus protein E7 to inactivate the retinoblastoma tumor suppressor, allowing us to focus on the p53 pathway contribution to cellular senescence. Expression of cS5A in these cells induced a cell cycle arrest and reduced the expression of proliferation markers (MCM6 and phospho-histone H3) that was rescued by expression of a small hairpin RNA against SOCS1 (Figure 1A-C). Consistent with the reported role of SOCS1 in p53 phosphorylation at serine 15, cS5A failed to induce this modification in cells expressing the shRNA against SOCS1 (Figure 1D). We then compared the transcriptome of IMR90-E7 cells expressing cS5A and co-expressing an shRNA against SOCS1 or a non-targeted shRNA using RNA purified from cells 7 days after introduction of cS5A. The microarray data was deposited in NCBI's Gene Expression Omnibus (GEO) GSE98216. Genes whose expression changed +/- 1.5 fold were used for pathway analysis with the online bioinformatics platform DAVID. The most significant pathways regulated by SOCS1 in cells expressing cS5A are indicated in Figure 1E and S1. They include genes coding for secreted proteins (Figure S1A-C) and a few genes in the p53-signaling pathway (Figure 1E and Table 1). The bypass of senescence induced by cS5A and the inhibition of p53 activity was also confirmed by a second shRNA against SOCS1 (shS1b), (Figure S2). Therefore, although these results confirm the requirement for SOCS1 in p53 phosphorylation and the senescence response to aberrant STAT5A activation, the pattern of p53 target genes identified does not include the classic p53 target genes associated to the DNA damage response.

To further investigate whether SOCS1 modulates the p53 pathway, we performed Gene set enrichment analysis (GSEA) of the microarray data. We found that SOCS1-disabled cells have high levels of genes in the set TANG_SENESCENCE_TP53_TARGETS_DN that contain, genes upregulated by a dominant negative p53 in normal human fibroblasts (Figure 1F). This gene set mostly includes cell cycle regulated genes, which are

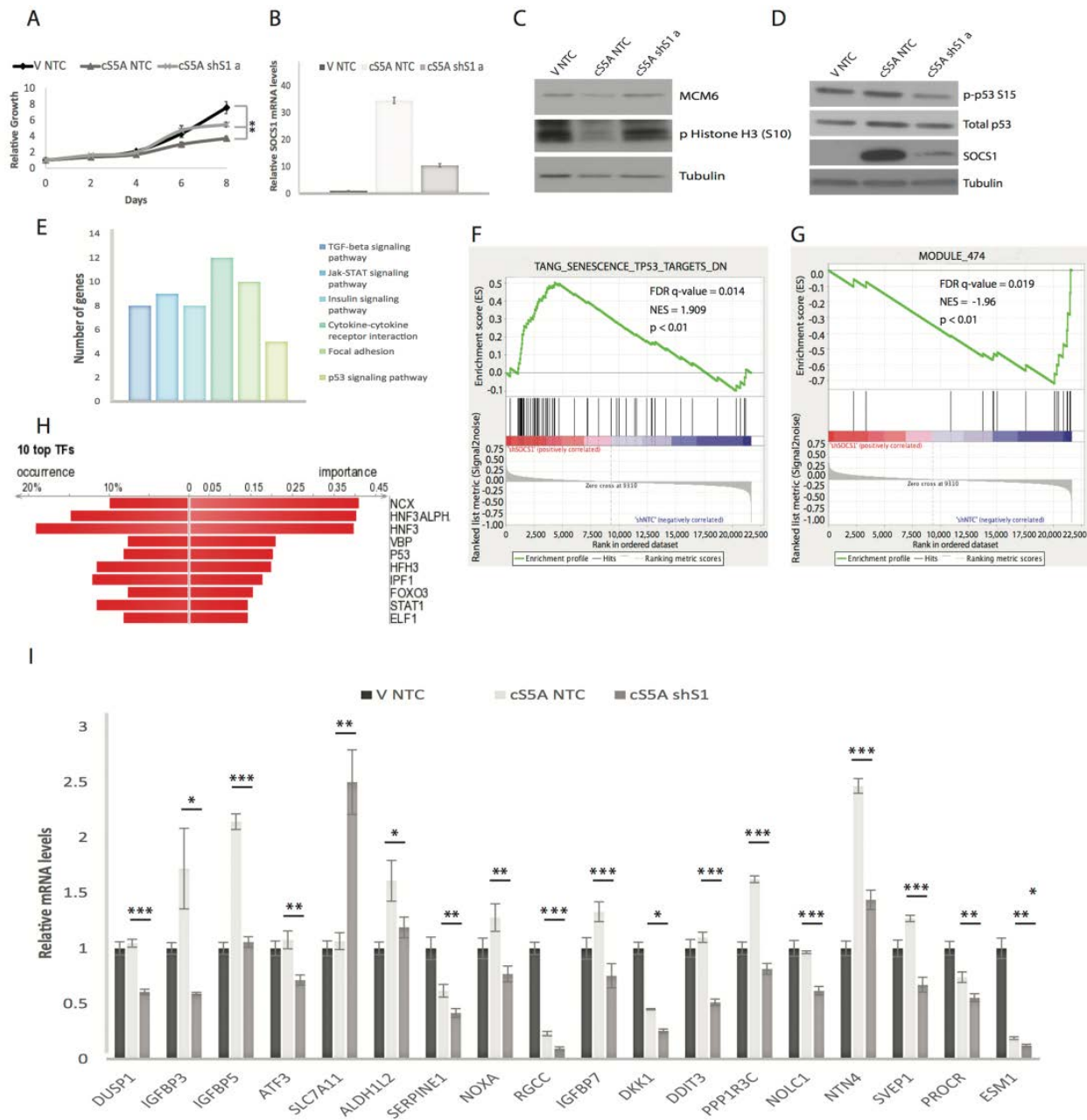


Figure 1. Microarray analysis identifies SOCS1-dependent p53 target genes. (A) Growth curves. Normal human fibroblasts (IMR90) expressing viral oncoprotein E7 were retrovirally infected with either an empty vector (V) or with constitutively activated STAT5A (cSSA) and with either a control shRNA (shNTC) or a shRNA against SOCS1 (shS1 a). Cells were counted and plated for the growth assay. (B) SOCS1 mRNA levels were measured by qPCR using cells collected 7 days post infection, as in (A). (C) Western blots of IMR90 cells at day 7 post infection, as described in (A) for MCM6, phosphorylated Histone H3 (S10) and Tubulin. (D) Western blots of IMR90 cells described in (A) for p53, phosphorylated p53 at serine 15 (p-p53 S15) and SOCS1 levels. (E) DAVID analysis (Kegg pathway) of Affymetrix microarray experiment performed on triplicates of IMR90 cells expressing E7 and either constitutively active STAT5A (cSSA) combined with a control shRNA (NTC) versus cells expressing cSSA combined with an shRNA against SOCS1 (shS1), collected 7 days after infection. (F) Gene Set Enrichment Analysis (GSEA) of differentially regulated genes between the conditions in (D). (G) GSEA of differentially regulated genes. (H) DiRE analysis of genes differentially regulated between cSSA NTC and cSSA shS1 conditions of the Affymetrix microarray analysis. (I) QPCR validation in IMR90 cells expressing the same constructs as mentioned in (A), for the p53 target genes identified by the microarray analysis. All experiments were performed three times, error bars indicate SD of triplicates (growth curves) or standard errors of triplicates (QPCR), * = $p < 0.05$, using the Student's t test. ** = $p < 0.01$, *** = $p < 0.005$.

Table 1. List of SOCS1-dependent p53 target genes identified by microarray analysis.

Reported p53 target genes	Fold Change	PMID
DDIT3	-1.79	16917513
GADD45B	-1.74	23948959
IGFBP3	-1.85	20182617
PMAIP1	-1.65	19641509
SERPINE1	-1.52	17882266
LOXL1	-1.81	16888633
DKK1	-2.37	16888633
GDF15	-1.65	16888633
DDB2	-1.47	16888633
SLC7A11	1.58	25799988
ALDH1L2	-1.42	25799988
ABHD4	-1.43	25799988
BCAT1	-1.44	25799988
LRP1	-1.53	25799988
DUSP1	-1.52	25799988
PROCR	-1.52	25799988
RGCC	-2.49	17146433
IGFBP7	-1.72	21095038
SAT1	-1.56	27698118

Of note, the microarray data indicates many more known p53 target genes regulated by SOCS1 than found by DAVID. Relevant references for those genes are indicated by their PMID.

known to be regulated by RB. However, the RB pathway was disabled in the IMR90-E7 cell line used in our experiments. These results thus imply a SOCS1-p53-dependent pathway that regulates cell cycle genes independently of the RB tumor suppressor. SOCS1-disabled cells also have a downregulation of the gene set MODULE_474 (<http://robotics.stanford.edu/~erans/cancer/>) containing several genes upregulated in senescent cells such as IGFBP2, 3, 5, 6 and 7, NOV and SOCS3 (Figure 1G). Further proof that SOCS1 controls the expression of p53 target genes was obtained using the platform DiRE that analyses the promoters of gene sets for signatures of transcription factors. P53 was one of the top transcription factors associated to transcriptome changes induced by an shRNA against SOCS1 (Figure 1H). In addition, this algorithm identified 12 new candidates for p53-target genes (Table 2). Many of

these genes are poorly expressed in human cancers suggesting that they could be novel tumor suppressors (Table 3). The microarray data was validated using qPCR for either known p53-target genes or the new candidates suggested by the DiRE platform (Figure 1I). We also used data in TCGA from hepatocellular carcinoma, a tumor type where promoter DNA methylation often silences SOCS1 expression [16]. We found a significant correlation between the expression of SOCS1 and the SOCS1-dependent p53 target genes defined in human fibroblasts (Figure 2). For several genes (SLC7A11, SAT1, SERPINE1, IGFBP7, GADD45 and ATF3) these correlations decreased in samples from p53 mutant tumors (Figure S3). Taken together, our results show that SOCS1 controls a unique set of p53 target genes.

To investigate the biological importance of SOCS1-dependent p53 target genes we analysed their overlap with gene sets mediating specific p53-dependent responses. First, genes regulated by SOCS1 matched gene sets that regulate the response to chemotherapy (Figure S4A), which is largely influenced by the p53 pathway [17]. Second, SOCS1-disabled cells expressed high levels of genes upregulated by a dominant negative BRCA1 allele (Figure S4B), which also disrupts the p53 pathway [18]. Third, SOCS1-disabled cells have a decrease in the expression of genes that blocked angiogenesis in endothelial cells (Figure S4C). These genes include IGFBP3 [19] and COL4A2 which encodes the potent antiangiogenic factor canstatin [20]. It is well known that p53 inhibits angiogenesis [21,22], and our gene expression data suggest that SOCS1 modulates this p53 function as well. Finally, SOCS1-regulated genes also overlapped with a set of genes induced by oxidized phospholipids (Figure S4D), which has been recently linked to iron-dependent cell death or ferroptosis [23]. P53 sensitizes cells to ferroptosis by repressing the cystine transporter SLC7A11 [4] and inducing the polyamine metabolic enzyme SAT1 [24]. The regulation of those two genes in cS5A expressing cells was SOCS1-dependent (Table 1) suggesting a role for SOCS1 in ferroptosis.

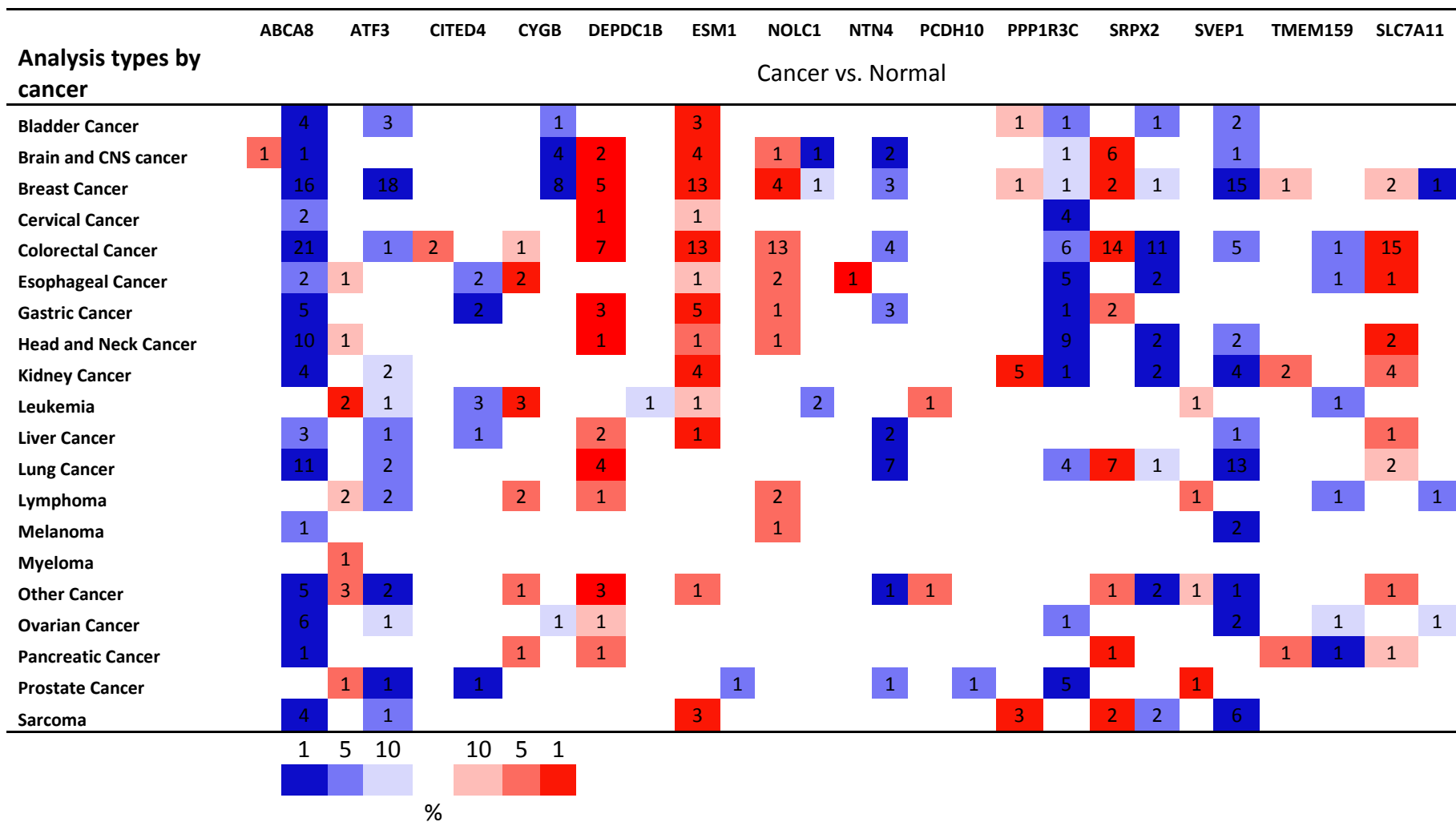
The inhibition of SOCS1 expression in IMR90-E7 bypasses cS5A-induced senescence, raising the possibility that the defects in p53 target gene expression we described above are the consequence of senescence inhibition and are not directly linked to SOCS1. In IMR90 cells, where the retinoblastoma pathway remains intact, inactivation of SOCS1 does not bypass cS5A-induced senescence [14]. This is due to the known fact that the RB pathway is sufficient to regulate senescence in the absence of p53 [25,26]. We thus took advantage of this fact to investigate whether expression of p53 target genes still required SOCS1 in these cells.

Table 2. List of potential SOCS1 dependent p53 target genes identified by DiRE analysis.

DiRE Analysis	Fold change	Function
ABCA8	-1.56	Transmembrane lipid transporter
ATF3	-1.69	Transcription factor, response to stress (16888633)
CITED4	-1.63	Transcriptional co-activator
CYGB	-1.51	Regulation of oxidative stress
DEPDC1B	1.62	Cell adhesion, mitosis regulation
ESM1	-1.53	Secreted factor, role in inflammation and cancer
KIAA1467	1.56	Uncharacterized protein
NOLC1	-1.87	Ribosome biosynthesis (21642980)
NTN4	-1.61	Role in metastasis (25590240)
PCDH10	-1.57	Cell adhesion and motility
PPP1R3C	-1.83	Regulation of glycogen metabolism
SRPX2	-1.83	Role in angiogenesis and migration
SVEP1	-1.67	Cell attachment
TMEM159	-1.73	Uncharacterized protein
ZNF2	-1.53	May be involved in transcriptional regulation

For previously linked p53 target genes, PMID is indicated in parenthesis as reference.

Table 3. Cancer vs. Normal expression of SOCS1-dependent p53 target genes identified by DiRE.



Red squares signal the number of studies showing upregulation and blue squares the number of studies showing downregulation. Cell color is determined by the best gene rank percentile for the analyses within the cell.

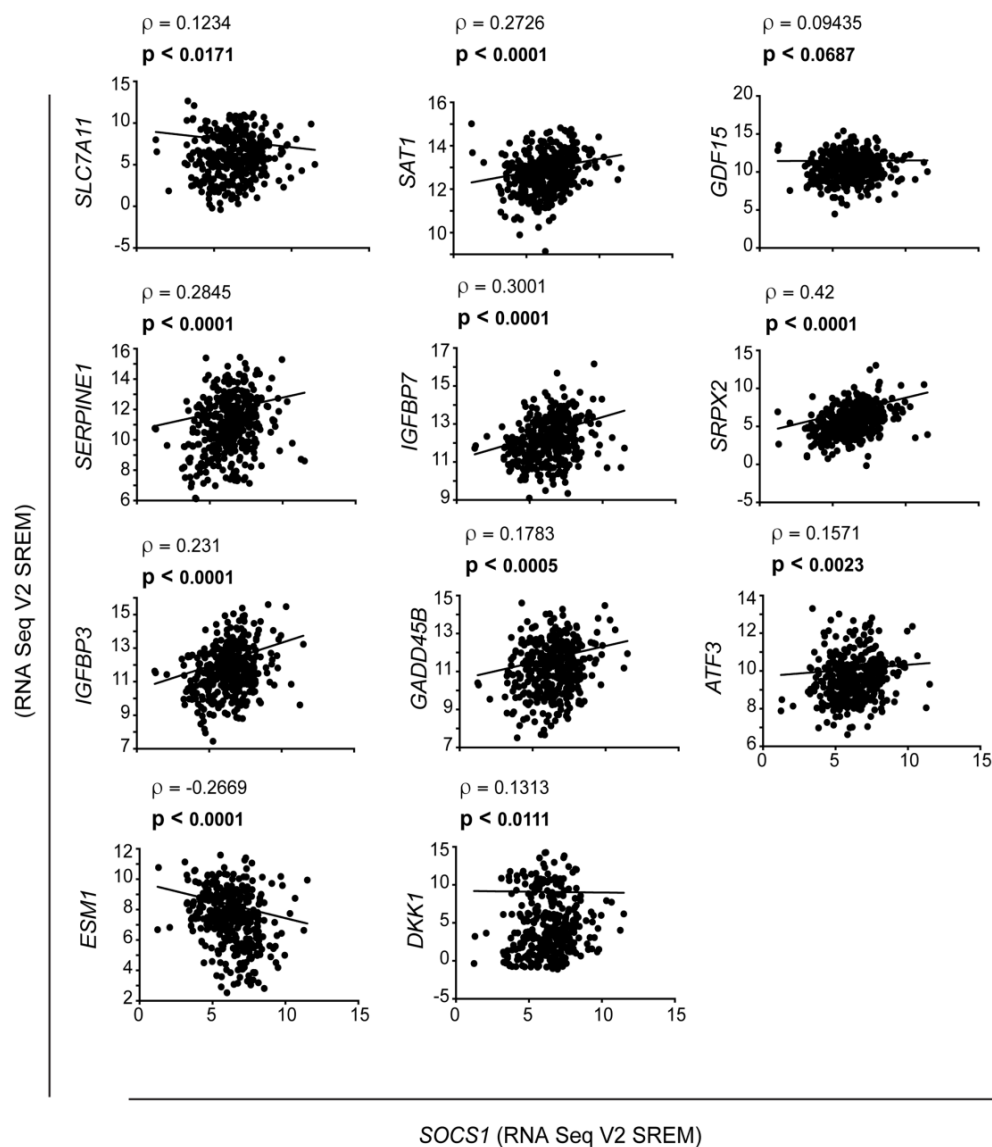


Figure 2. Correlation between SOCS1 and p53-target gene expression in hepatocellular carcinoma samples. The TCGA dataset human HCC specimens was analysed to determine the correlation between the expression of *SOCS1* (x-axis) and the indicated p53 target genes (y-axis), as indicated by the slope. The Spearman correlation (ρ) and the p values are given at the top of each plot.

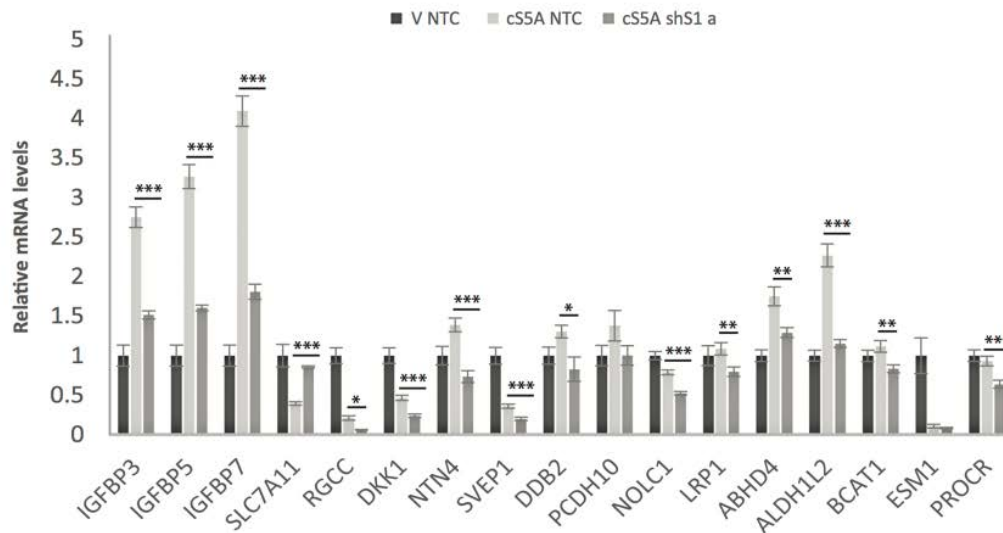
For most of the genes measured, disabling SOCS1 also inhibited the expression of p53 targets as well (Figure 3A-B) although cells remained senescent (Figure 3C-E). We conclude that the defects in p53 target gene expression we have seen after disabling SOCS1 are not the result of cell cycle re-entry after bypass of senescence and suggest a direct effect of SOCS1 on p53.

SOCS1 is sufficient to activate p53 and regulate the expression of its target genes

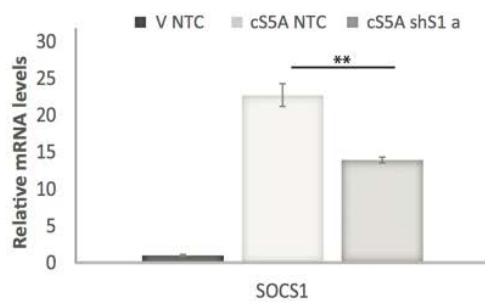
Previous research established a function for SOCS1 as an adaptor protein facilitating the phosphorylation of

p53 at serine 15 by the DNA damage response activated kinases ATM and ATR [14]. In culture, cells are exposed to high concentrations of oxygen and growth factors, increasing the probability of DNA damage by either replication stress or reactive oxygen species. We reasoned that enforcing SOCS1 expression might cooperate with these factors and engage the p53 pathway. Indeed, expressing SOCS1, in U2OS cells (Figure 4A-B) or IMR90 cells (Figure 4C-E) increased the expression of most of the genes that were positively regulated by p53 in c55A-induced senescence and decreased the expression of SLC7A11, a gene that is repressed by p53. As reported before, SOCS1 was sufficient to trigger senescence in close to 50% of the

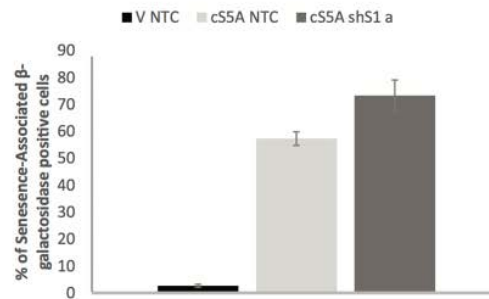
A



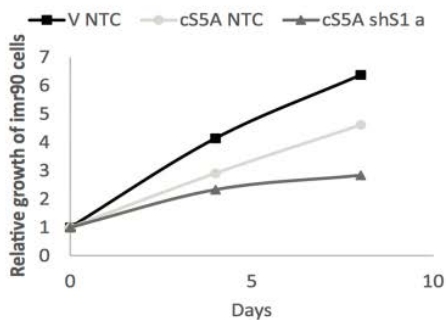
B



C



D



E

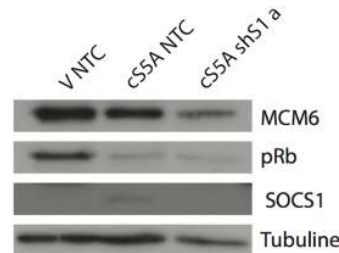


Figure 3. The regulation of p53 target genes by SOCS1 is not dependent on a disabled RB pathway. (A) QPCR validation of the p53 target genes identified by microarray analysis but in normal IMR90 fibroblasts expressing either an empty vector (V) or a constitutively activated STAT5A (cS5A) and with either a control shRNA (shNTC) or an shRNA against SOCS1 (shS1). Cells were collected 7 days after infection. (B) SOCS1 knockdown efficiency measured by qPCR in the conditions described in (A). (C) Status of the cells was assessed at the day of RNA collection (day 7 post infection) with a Senescence-Associated β -Galactosidase staining. Positively stained and unstained cells were counted under a light microscope in order to obtain the percentage of senescent cells. (D) Growth curves. Normal human fibroblasts (IMR90) were retrovirally infected with either an empty vector (V) or with constitutively activated STAT5A (cS5A) and with either a control shRNA (shNTC) or a shRNA against SOCS1 (shS1 a). Cells were counted and plated for the growth assay. (E) Western blots of senescence markers (MCM6, pRb and SOCS1) of cells as in (A). Tubulin was used as a loading control. All experiments were performed three times, error bars indicate the standard errors of triplicates, * = $p < 0.05$, using the Student's t test, ** = $p < 0.01$, *** = $p < 0.005$

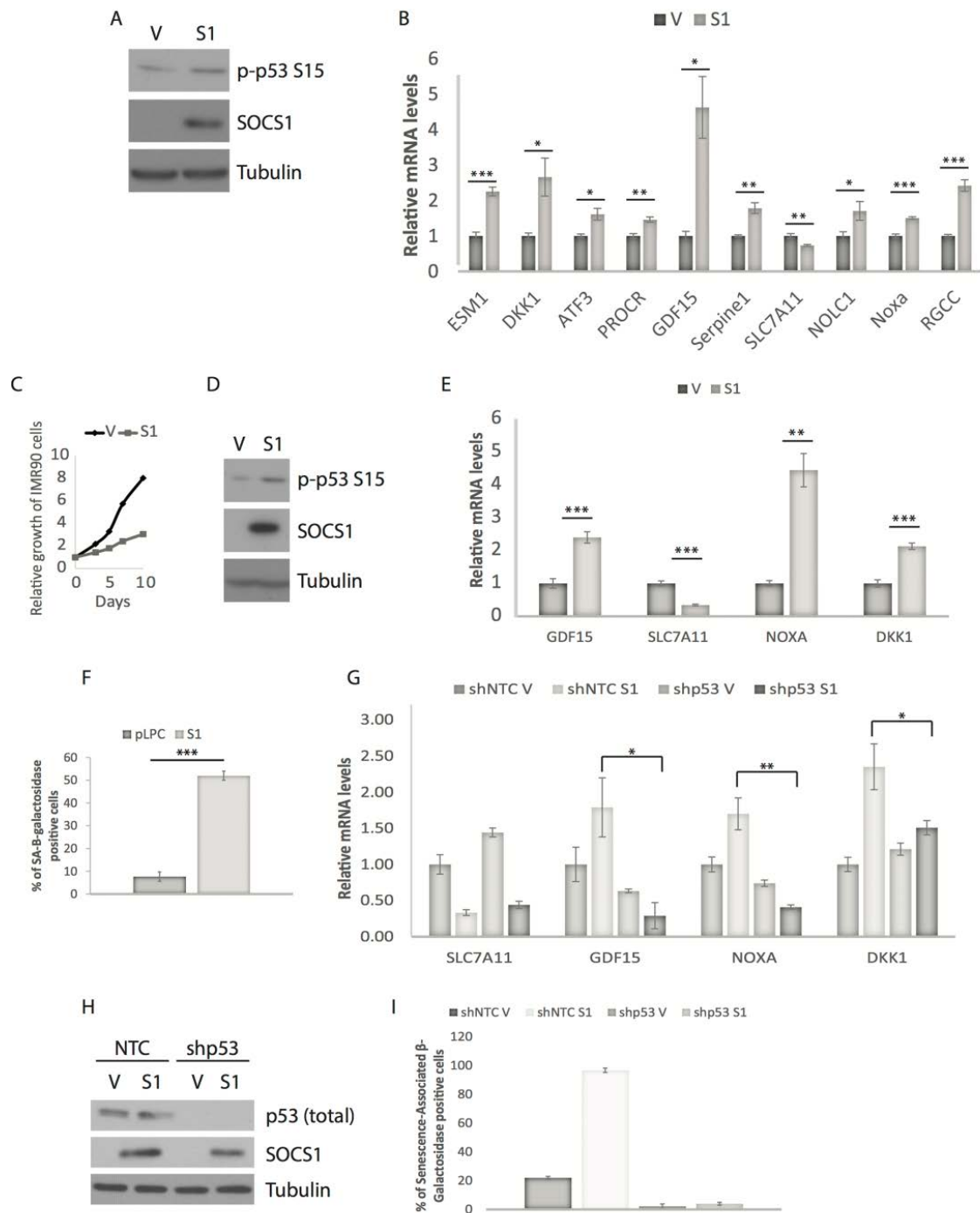


Figure 4. SOCS1 overexpression is sufficient to regulate the expression of SOCS1-dependent p53 target genes. (A) Western blots of SOCS1 and phospho-p53 (p-p53 S15) in U2OS cells expressing either empty vector (V) or SOCS1 (S1). (B) QPCR for p53 target genes in cells as in (A). Cells were collected at day 5 or 7 post-infection. (C) Growth curves of IMR90 cells expressing either empty vector (V) or SOCS1 (S1). (D) Western blots of SOCS1 and phospho-p53 (p-p53 S15) in IMR90 cells expressing either empty vector (V) or SOCS1 (S1). (E) QPCR for p53 target genes in cells as in (C). Cells were collected at day-7 post infection. (F) Senescence associated β -galactosidase of IMR90 cells expressing either empty vector (V) or SOCS1 (S1). Cells were fixed and stained at day 12 post- infection. (G) QPCR of IMR90 cells expressing either a control shRNA (shNTC) or a shRNA against p53 (shp53) combined with SOCS1 (S1) or empty vector (V) to confirm that the genes in (E) are targets of p53. (H) Western blots for the indicated proteins in IMR90 cells expressing a control shRNA (NTC) or an shRNA against p53 (shp53) and also infected with a SOCS1 expressing vector (S1) or a vector control (V). (I) Senescence-Associated β -Galactosidase staining. Positively stained and unstained cells were counted under a light microscope in order to obtain the percentage of senescent cells. All experiments were performed three times, error bars indicate the standard errors of triplicates, * = $p < 0.05$, using the Student's t test, **= $p < 0.01$, ***= $p < 0.005$.

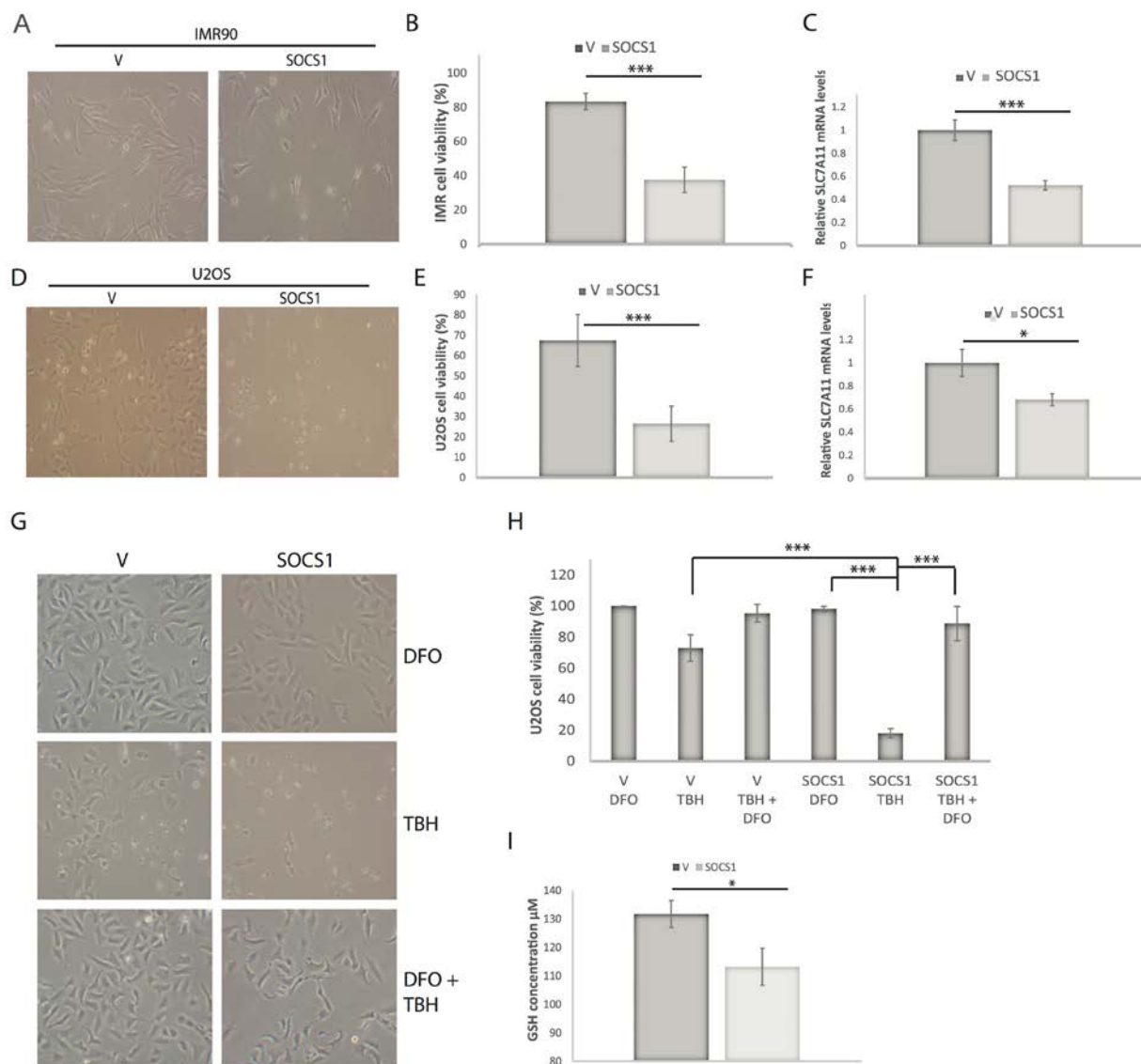


Figure 5. SOCS1 sensitizes cells to ferroptosis. (A) Representative photos of IMR90 cells expressing an empty vector (V) or SOCS1 (S1) and treated 24 hours after plating with 88 μ M tert-butyl-hydroperoxide (TBH). Cells were assayed for cell death 16 hours after treatment. (B) Quantification of cell viability portrayed in (A) by Trypan blue staining. (C) SLC7A11 mRNA levels measured by qPCR of IMR90 cells described in (A). (D) Representative photos of U2OS cancer cells expressing either V or S1 by retroviral infection and treated 24 hours after plating with 350 μ M TBH for 16 hours. (E) Quantification of cell viability of U2OS cells as portrayed in (D) by Trypan blue staining. (F) Relative SLC7A11 mRNA expression measured by qPCR in U2OS cells expressing either V or S1 as described in (D). (G) Representative photos of U2OS cancer cells expressing either V or S1 by retroviral infection and treated 24 hours after plating with either 350 μ M TBH alone, 100 μ M Deferoxamine mesylate (DFO) alone or the combination of both drugs. (H) Quantification of cell viability portrayed in (G) by Trypan blue cell counts. (I) GSH quantification in U2OS cells expressing either V or S1. All experiments were performed three times, error bars indicate the standard deviation of triplicates, * = $p < 0.05$, using the Student's t test, ** = $p < 0.01$, *** = $p < 0.005$.

cells overexpressing the protein (Figure 4F). The increase in expression of p53 target genes by SOCS1 was, for the most part, dependent on p53 since knockdown of p53 (Figure 4G-H) abolished their stimulation and prevented senescence (Figure 4I). However, the decrease in SLC7A11 was not blocked after knockdown of p53 suggesting that SOCS1

regulates the expression of this gene by additional mechanisms. Of note, not all p53 target genes that required SOCS1 in c55A-induced senescence were induced by SOCS1 expression alone. The following genes (IGFBP3, GFBP5, DUSP1, ALDH1L2, IGFBP7, DDIT3, PPP1R3C, NOLC1, NTN4 and SVEP1) were not significantly induced by SOCS1 in

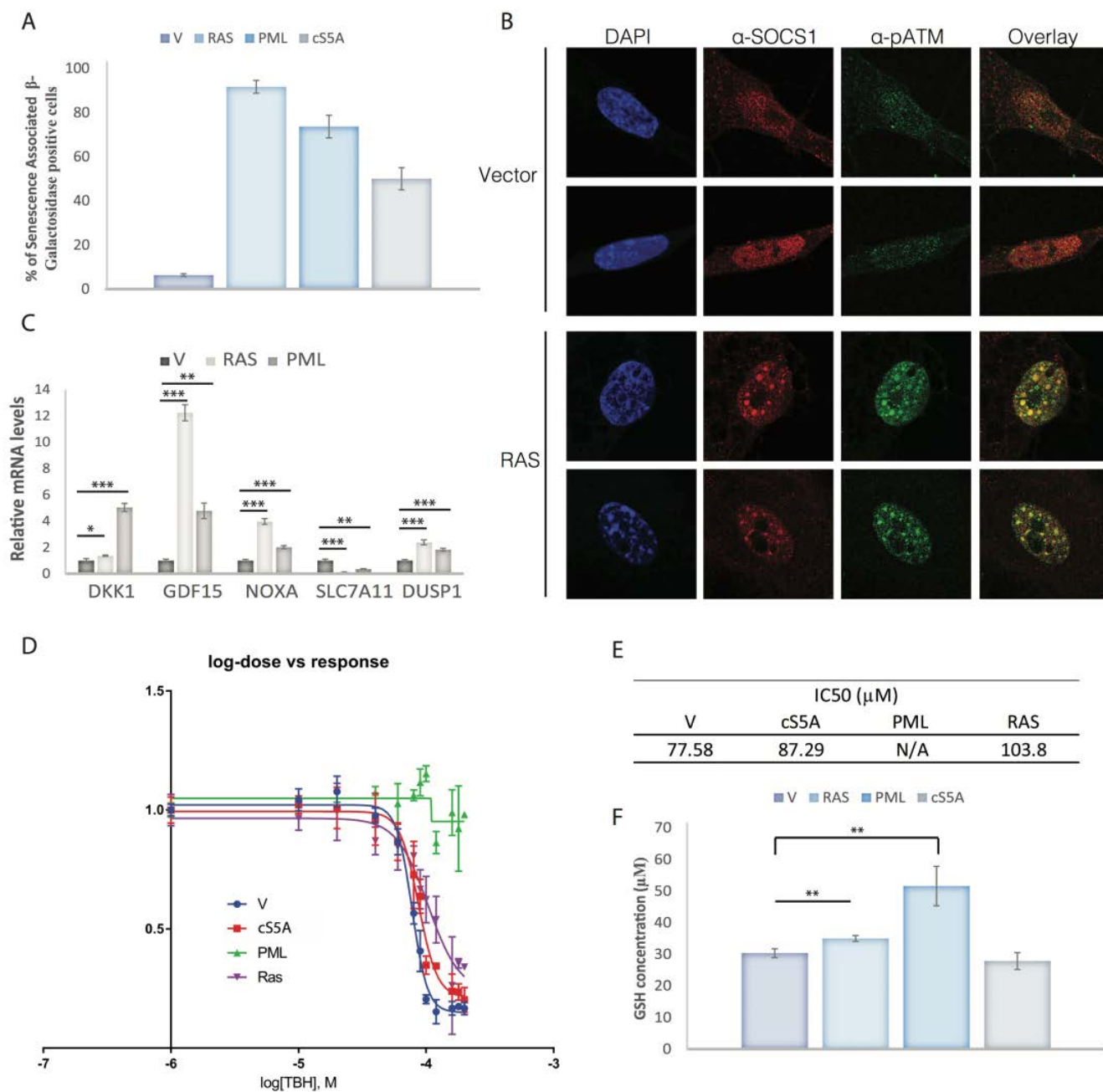


Figure 6. Ferroptosis sensitivity in senescent cells depends on the trigger. (A) Senescence was assessed by staining cells for the Senescence-Associated β -Galactosidase in IMR90 cells expressing either a control vector (V), the RASV12 oncogene (RAS), PML or STAT5A (c5SA). (B) Immunofluorescence of SOCS1 (anti-SOCS1) and phosphorylated ATM at S1981 (anti-ATM) in IMR90 cells rendered senescent by overexpressing the RASV12 oncogene compared to IMR90 expressing a control vector (Vector). (C) QPCR for mRNA levels of SOCS1-dependent p53 target genes in IMR90 cells expressing a control vector (V) or rendered senescent by overexpression of RASV12 (RAS) or PML (PML). (D) IC₅₀ curves of IMR90 cells overexpressing a control vector (V), the RASV12 oncogene (RAS), PML or STAT5A (c5SA). Cells were treated 24 hours after plating with 12 different doses (0, 10, 20, 40, 60, 80, 100, 120, 160, 180 and 200 μ M) of tert-butyl-hydroperoxide (TBH). Cells were fixed and stained with Crystal Violet to assess cell death 16 hours after treatment. The dye was then solubilized with acetic acid 10% and measured with a spectrophotometer. (E) The value of IC₅₀ of each condition graphed in D is presented. No IC₅₀ could be calculated for PML as it was resistant at the doses used. (F) GSH quantification in IMR90 cells rendered senescent by overexpression of RASV12, PML IV or STAT5A, compared with empty vector control (V). All experiments were performed three times, error bars indicate the standard deviation of triplicates, * = $p < 0.05$, using the Student's t test, ** = $p < 0.01$, *** = $p < 0.005$.

either U2OS or IMR90 cells. In addition, RGCC, ESM1, ATF3 and PROCR were induced in U2OS but not in IMR90 cells. These results indicate that SOCS1 partially reproduces oncogenic STAT5A signaling to p53 but additional STAT5A functions also contribute to p53 activation.

SOCS1 sensitizes cells to ferroptosis

The mechanisms by which p53 prevents tumor progression include apoptosis, senescence and ferroptosis [27,28]. The latter is an iron-dependent cell death mechanism that involves reactive oxygen species and lipid oxidation and that does not depend on caspases or Bcl2 family members Bak and Bax [28]. The SOCS1-dependent p53 target genes SLC7A11 [4] and SAT1 [24] play key roles in ferroptosis suggesting that SOCS1 could be a novel regulator of this process. As anticipated, expression of SOCS1 in U2OS or IMR90 cells sensitized them to the ferroptosis inducer tert-butyl-hydroperoxide (TBH). This effect of SOCS1 correlated with its ability to reduce the expression of the cystine transporter SLC7A11 (Figure 5A-F) and was efficiently blocked by treatment with deferoxamine, an iron chelator known to inhibit ferroptosis (Figure 5G-H and Figure S4). Ferroptosis depends on the actions of oxidized lipids, which are detoxified by the glutathione (GSH)-dependent enzyme GPX4 [29]. Cystine is used in the cells to generate cysteine, a metabolite required for the synthesis of glutathione (GSH). As expected, expression of SOCS1 reduced the levels of GSH (Figure 5I) explaining in part its ability to sensitize cells to ferroptosis.

The SOCS1-p53 axis is active in oncogene-induced senescence (OIS) but additional factors control ferroptosis in these cells

OIS is triggered by activated oncogenes and involves replication stress, mitochondrial dysfunction, reactive oxygen species and the DNA damage response [30,31,32]. We anticipated that SOCS1 is generally upregulated during OIS and not only in the specific case of c55A-induced senescence. This is because senescent cells secrete a variety of inflammatory mediators that activate JAK-STAT signaling [33], the major regulator of SOCS1 expression [14,34]. We thus induced senescence in IMR90 normal human fibroblasts with constitutively active RAS (RASV12), c55A or the tumor suppressor PML, that acts downstream of RAS and c55A to induce senescence (Figure 6A). As published before for cells expressing c55A [14], we found SOCS1 localizing with phospho-ATM [35] in DNA damage foci in senescent cells, which are known to contain phosphorylated p53 at serine 15 [36] (Figure 6B). Also, induction of senescence by RASV12 or PML

led to induction of SOCS1-dependent p53 target genes and the downregulation of the p53-repressible gene SLC7A11 (Figure 6C). Hence, despite the differences in the mechanisms triggering senescence by RasV12, STAT5A, SOCS1 or PML, they regulate a common set of p53 target genes.

Next, we performed ferroptosis assays in cells expressing RASV12, STAT5A or PMLIV using the ferroptosis inducer TBH and the ferroptosis inhibitor deferoxamine. For this assay we plated the same amount of cells for each condition and found that neither RasV12 nor STAT5A sensitized cells to ferroptosis, despite both having an increase in endogenous SOCS1 expression and a reduction in SLC7A11. Intriguingly, PML expression turned cells highly resistant to ferroptosis providing a mechanistic insight into a ferroptosis resistance pathway in senescent cells (Figure 6D-E). Glutathione levels correlated with ferroptosis resistance in senescent cells (Figure 6F) suggesting compensatory mechanisms of GSH biosynthesis as a possible mechanism for resistance to ferroptosis. Targeting anti-ferroptosis pathways activated in senescent cells might selectively kill them in the same way as targeting anti-apoptotic proteins.

SOCS1 activates p53 via both phosphorylation and stabilization

The pattern of p53 target genes regulated by SOCS1, including ferroptosis regulators, is unique and anticipates unique mechanisms of p53 activation by SOCS1. So far, SOCS1 has been linked to the regulation of serine 15 phosphorylation of p53 [14,15], a modification that is also efficiently induced during an acute DNA damage response, which does not necessarily evolve into a permanent senescent cell cycle arrest [37,38]. Therefore, the ability of SOCS1 to induce senescence must involve additional mechanisms capable of changing the quality of the p53 response.

To investigate how SOCS1 modulates p53 activity, we first induced endogenous p53 using the DNA damaging drug doxorubicin and measured both p53 phosphorylation and total p53 levels. SOCS1 expression increased p53 levels during the course of a doxorubicin treatment without changing the levels of serine 15-phosphorylation of p53, which are highly induced by the drug (Figure 7A and B). In other words, in the context of oncogenic stress that involves relatively modest rates of DNA damage, SOCS1 stimulates serine 15 phosphorylation of p53 by promoting p53-ATM interactions as described before [14]. In cells treated with doxorubicin, high levels of DNA damage maximally stimulate serine 15 phosphorylation of p53

in a SOCS1-independent manner but SOCS1 can still stabilize p53 in this condition.

In order to find additional mechanisms of p53 activation by SOCS1, we looked at the SOCS1 interactome [15]. Interestingly, KAP1, a repressor of p53 [39], immunoprecipitated with SOCS1 [15]. To confirm this finding we expressed wild type SOCS1 in U2OS cells and immunoprecipitated endogenous KAP1 using a specific antibody. We found SOCS1 in KAP1 immunoprecipitates but not in immunoprecipitates obtained with a control antibody (Figure 7C). The reciprocal co-IP analysis confirmed that endogenous KAP1 interacted with SOCS1 (Figure 7D). Next, we used a GST-pull-down assays with two fragments of KAP1 and an *in vitro* translated and ³⁵S labelled SOCS1. We found that the Bromo/PHD domain of KAP1 directly interacted with SOCS1 (Figure 7E-G). We thus propose that SOCS1 activates the senescence functions of p53 via two mechanisms (Figure 7H): 1) facilitating serine 15 phosphorylation of p53 and 2) p53 stabilization by interfering with KAP1. Together, these mechanisms can contribute to convert an acute p53 response into a chronic response characterized by the expression of a unique pattern of p53 target genes.

DISCUSSION

The tumor suppressor activity of the transcription factor p53 does not correlate with the expression of target genes induced by acute DNA damage [6]. The discovery and characterization of p53 targets in conditions of chronic stimulation of the p53 pathway should give critical insights into the mechanisms of tumor suppression by p53. Oncogene-induced senescence is a tumor suppressor mechanism where a lasting p53 response mediates a stable cell cycle arrest and the clearance of senescent cells, which prevents tumor progression [40]. The suppressor of cytokine signaling SOCS1 was previously shown to be required for p53 activation and senescence in response to constitutive JAK-STAT5 signaling [14,15,41,42]. However, the p53 target genes requiring SOCS1 remained poorly characterized. Here, we used RNA interference and transcriptome analysis to identify the set of SOCS1-dependent p53 target genes. Although SOCS1 was required for the expression of several previously identified p53 targets, most of the classic targets associated with acute DNA damage response such as p21 and MDM2 were not affected by SOCS1 inhibition (Table 1). In addition, bioinformatics analysis using the platform DiRE, uncovered several genes that required SOCS1 expression and contained p53-binding sites in their promoter regions (Table 2). This unbiased transcriptome analysis confirms that SOCS1 regulates

the p53 pathway and reveals a unique and interesting biology for the SOCS1-p53 axis.

The identification of SOCS1-dependent p53 targets links p53 to several interesting tumor suppression pathways. For example, DDIT-3 (also known as C/EBP Zeta) is a dominant negative inhibitor of C/EBP family of transcription factors [43]. This family is important for the expression of inflammatory cytokines in senescent cells that contribute to the SASP [44,45]. SOCS1 may regulate the SASP via p53 and DDIT-3 (Table 2). In addition, several SOCS1-dependent p53 targets are secreted proteins suggesting that the SOCS1-p53 pathway changes the quality of the SASP. They include the bona fide p53 targets IGFBP3, IGFBP7, SERPINE1/PAI1, DKK1 and GDF15 (Table 1) and the new candidate p53 targets ESM1 and SRPX2 (Table 2). Another interesting target is GADD45B that mediates activation of the p38MAPK pathway, which is required for OIS [46]. Perhaps the most intriguing connection found by our analysis involves the ferroptosis pathway. This form of cell death was linked to p53-dependent tumor suppression and involves the SOCS1-dependent p53 targets SLC7A11 [4] and SAT1 [24]. In addition, ferroptosis is mediated by oxidized lipids [23] and the overall gene expression pattern of SOCS1-expressing cells overlaps with genes regulated by oxidized lipids (Figure S3D). The SOCS1-dependent p53 targets DDIT3, PMAIP1, ATF3 and ESM1 are part of the gene set induced by oxidized phospholipids and therefore bona fide new candidates to regulate ferroptosis downstream the SOCS1-p53 axis.

SOCS1 does not only play a role in the senescence response to constitutively active JAK-STAT5 signaling. In cells expressing oncogenic RAS, SOCS1 is recruited to DNA damage foci, colocalizing with phospho-ATM. The extent to which SOCS1 modifies gene expression in RAS-induced senescence remains to be fully characterized. However, DKK1, GDF15, Noxa, Dusp1 and SLC7A11 were modulated in Ras- or PML-expressing cells in the same way as in cells expressing STAT5A or SOCS1. In contrast to SOCS1-cells, RAS- or STAT5A-senescent cells were not more sensitive to ferroptosis induced by TBH, suggesting that other pathways activated in these cells control ferroptosis. Intriguingly, PML expressing cells were highly resistant to ferroptosis providing a mechanistic insight into ferroptosis resistance pathways. In addition to influencing p53 target gene expression, SOCS1 could play a general role in senescence by stabilizing the interactions of p53 with protein complexes at DNA damage foci. This would allow the maintenance of a pool of pre-active p53 that can be slowly released during the senescence cell cycle arrest contributing to

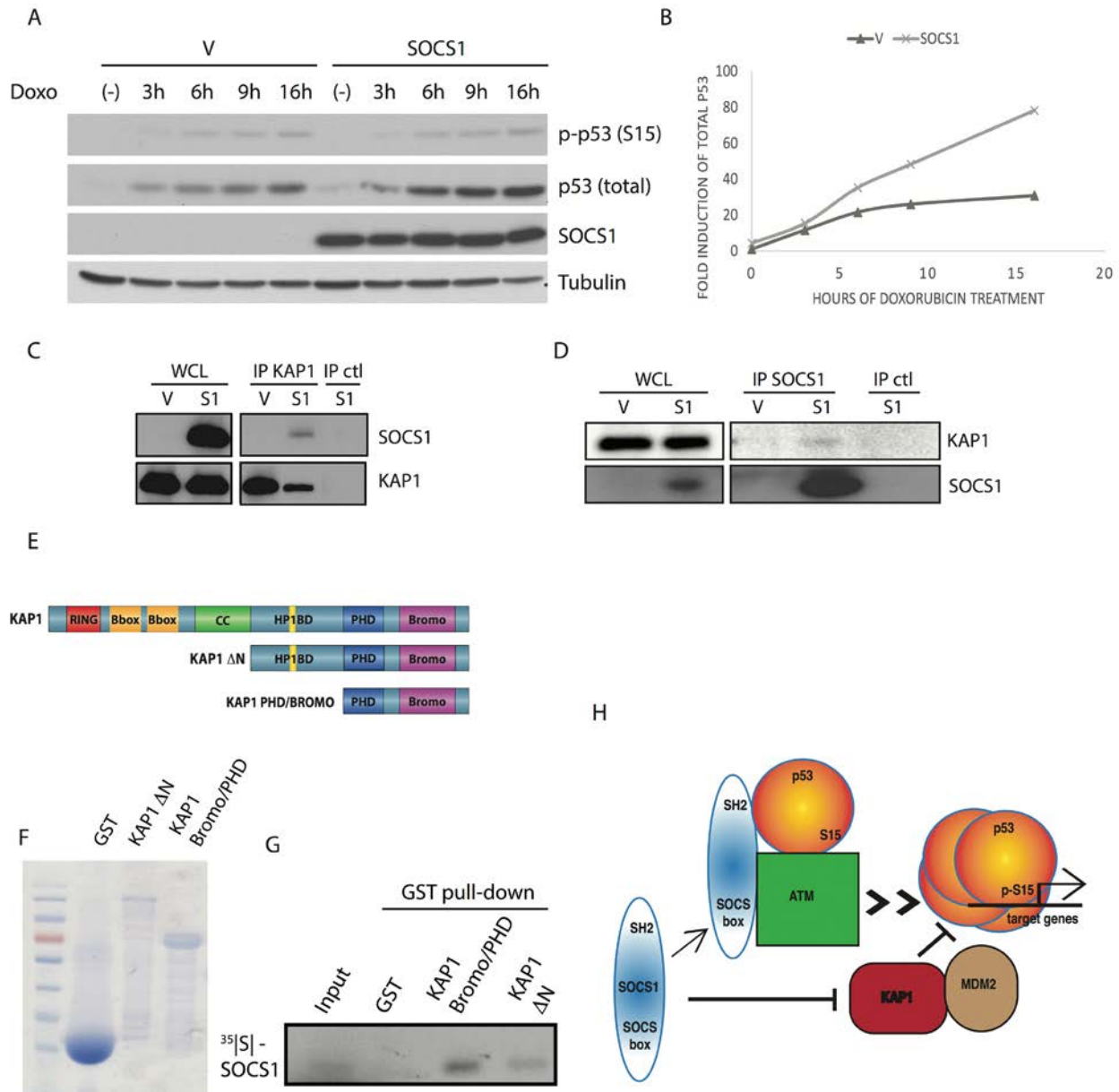


Figure 7. SOCS1 favors p53 accumulation in response to Doxorubicin. (A) Western blots of SOCS1, phosphorylated p53 at serine 15 [p-p53 (S15)] total p53 and tubulin in IMR90 cells expressing either empty vector (V) or SOCS1 and treated with doxorubicin (Doxo: 300 ng/mL) for 3, 6, 9, 16 hours or untreated (-). (B) Graphic representation of Western blots as in (A). Bands were quantified using image analysis software and normalized to tubulin, then plotted in a graph to show the kinetics of p53 stabilization. (C) Co-Immunoprecipitation of KAP1 with SOCS1. U2OS cell lysates of either empty vector cells (V) or SOCS1 overexpressing cells (S1) were immunoprecipitated with an antibody against KAP1 or a control antibody (IP ctl). Western blots against both KAP1 and SOCS1 were performed to confirm the presence of SOCS1 in complex with KAP1. Whole cell lysates (WCL) are used to control the expression of SOCS1 and KAP1 levels. (D) Co-immunoprecipitation as described in C. Cell lysates were immunoprecipitated with an antibody against SOCS1 or with a control antibody (IP ctl). Whole cell lysates (WCL) show the expression level of SOCS1 and KAP1. (E) Maps of the different KAP1 constructs used in experiments are depicted: KAP1 full length (KAP1), KAP1 with a deletion of its N-terminal RBCC domains (KAP1 Δ N) or KAP1 C-terminus including PHD and Bromo domains (KAP1 PHD/BROMO). (F) The constructs depicted in E. were expressed by IPTG induction in BL21 bacterial cells. Expression levels of the various constructs were assessed by migration of an SDS-PAGE gel and Coomassie staining. (G) GST pull down was performed on KAP1 constructs which were incubated with radiolabeled SOCS1. Autoradiography revealed the absence or presence of SOCS1 in each pull down. GST was used as a negative control. (H) Model for p53 activation by SOCS1 via two pathways.

generate a lasting chronic p53 response. Another function for maintaining p53 in DNA damage foci could be to suppress homologous recombination in cells arrested in G1 [47,48], an event that could lead to chromosome aberrations and potentially tumor development.

In summary, we report here that SOCS1 impacts the pattern of secreted products in cells with active p53 and is required for the expression of a selective set of p53 target genes including those involved in ferroptosis. SOCS1 can use several mechanisms to activate p53, including promotion of serine-15 phosphorylation by ATM/ATR kinases and inhibition of the p53 repressor KAP1. Further investigation of the SOCS1-p53 pathway will help to better understand p53 tumor suppression activity and provide insights for novel cancer therapies.

MATERIALS AND METHODS

Cell lines, reagents, growth analysis and senescence

U2OS were purchased from the American Type Culture Collection, (Manassas, VA) and normal human diploid fibroblasts IMR90 were purchased from the Coriell Institute (Camden, New Jersey, USA). IMR90 were cultured in DMEM supplemented with 10% fetal bovine serum (FBS; Wisent, Montréal, QC, Canada) and 1% penicillin G/streptomycin sulphate. U2OS were supplemented with 5% FBS (Wisent) and 5% Newborn Calf serum (Wisent), with 1% penicillin G/streptomycin sulphate and with 2mM L-glutamine. Tert-butyl Hydroperoxide was purchased from Sigma (cat #458139) and used at 350 μ M in U2OS cells and 88 μ M in IMR90 cells. Doxorubicin was purchased from Sigma. Growth curves and the senescence associated β -galactosidase were performed as previously described [49].

Plasmid constructions and viral gene transfer

Ca-STAT5A was previously described in [50]. pLPC-SOCS1 was previously described in [14]. pLPC PML IV and pBabe RASV12 were previously described in [49]. GST-KAP1 constructs were a kind gift of Dr. Xavier Masclé. Lentiviral shRNAs against SOCS1 were purchased from Sigma-Aldrich in the pLKO vector. ShSOCS1a (shS1) (TRCN0000356245, Sigma) has the following sequence:

CCGGCTGGTTGTTGTAGCAGCTTAACTCGAGTT
AAGCTGCTACAACAACCAGTTTTTTG and
shSOCS1b (TRCN0000057065, Sigma) has the
following sequence:
CCGGCTTCCGCACATTCCGTTCCGCACTCGAGTG
CGAACGGAATGTGCGGAAGTTTTTTG. shNTC has

the following sequence:
CCGGCAACAAGATGAAGAGCACCAACTCGAG
TTGGTGCTCTTCATCTTGTGTTTTT. pLXSN E7
was a kind gift from Dr. D. Galloway. Retroviral gene transduction was performed as previously described [49]. Lentiviral gene transduction was performed by co-transfecting 6 μ g of the lentiviral vector with the packaging vectors in 293T cells as follows: 3 μ g of the VSV-G envelope protein expression plasmid pMD2, 1.5 μ g of the regulator of virion expression (REV) expression plasmid pRSV and 1.5 μ g of gag/pol elements expression plasmid pMDLg/pRRE. 24 hours post transfection, media were changed and the supernatants (viral soup) were collected 48 hours post transfection, filtered through 0.45 μ m filters (Sarstedt) and added to target cells together with DMEM and 4 μ g/mL polybrene. Viruses were removed after 8 hours and replaced by fresh medium. Selection was started 24 hours post-infection. For triple infections in IMR90 cells, G418 (300 μ g/mL, 6 days) and puromycin (1.5 μ g/mL, 3 days) were used first. After puromycin selection was over, hygromycin (80 μ g/mL) was added for 4 days. Cells were selected for a total of 7 days before RNA collection. For U2OS and IMR90 single infections, puromycin was used at 3 μ g/mL for 3 days.

Ferroptosis cell death assays

U2OS and IMR90 cells were seeded 24 hours prior to treatments in 10 cm plates (Corning) at 60% confluence. Cells were then treated with 350 μ M (U2OS) or 88 μ M (IMR90) TBH (Sigma #458139) for 16 hours. Cell death was assessed by imaging the cells under a white-light microscope and by counting live and dead cells using Trypan-Blue (BioRad) and a cell counter. Supernatants were collected and added to trypsinized cells before counting. All assays were performed at least three times. For IC50 assays, 20 000 IMR90 cells of each condition were plated per well of a 48 well plate. Cells were plated 24 hours prior to TBH treatment. Cells were then treated with either: 0, 10, 20, 40, 60, 80, 90, 100, 120, 160, 180 or 200 μ M of TBH for 16 hours. Cells were then fixed with 1% glutaraldehyde in PBS and stained with Crystal Violet (Sigma #C0775). The dye was then resuspended in 10% acetic acid and dosed with a spectrophotometer. GraphPad Prism was used to generate IC50 curves and determine IC50 values.

Western blotting

Protein analysis was performed by lysing cells in Cell Lysis Buffer (20 mM Tris-HCl pH 7.5, 150 mM NaCl, 1 mM EDTA, 1 mM EGTA, 1% Triton X-100, 2.5 mM sodium pyrophosphate, 1 mM β -glycerolphosphate and a cocktail of protease inhibitors (Roche). Quantification

of protein content was performed with the Bradford method. Extracts were prepared with Laemmli buffer (1X final). For endogenous SOCS1 detection, 150 µg of total extract was loaded on a 12% SDS-PAGE gel and transferred on an Immobilon P membrane (Millipore). For SOCS1 overexpression and other protein detection, 50 µg of total cells extract was loaded on a 12% SDS polyacrylamide gel. Western blots were performed as described previously [14]. The following primary antibodies were used: anti-SOCS1, clone 4H1 MBL (cat #K0175-6) used at 1:1000 dilution overnight at 4 °C. Anti-phospho-p53 (Serine15), NEB (cat #9284) used at 1:1000 dilution overnight at 4 °C. Total p53 (DO1 clone), Santa Cruz biotechnology (cat# sc-126) used at 1:1000 overnight at 4 °C. Anti-MCM6, Bethyl (#A300-194A) used at 1:1000 overnight at 4°C. Anti-phosphorylated-Rb (Serine 795), Cell Signaling (#9301) used at 1:1000 overnight at 4°C. Anti-phosphorylated Histone H3 (Serine 10), Millipore (#6570) used at 1:1000 overnight at 4°C. Alpha Tubulin antibody clone B-5-1-2, Sigma (cat # T6074) used at 1:20,000 1 hour at Room Temperature and served as loading control. Signals were revealed by using secondary antibodies coupled to peroxidase (BioRad laboratories) and ECL (GE Healthcare, cat# RPN2106) or Clarity ECL (BioRad #cat 1705061).

Co-immunoprecipitation

U2OS cells were collected in Cell Lysis Buffer (20 mM Tris-HCl pH 7.5, 150 mM NaCl, 1 mM EDTA, 1 mM EGTA, 1% Triton X-100, 2.5 mM sodium pyrophosphate, 1 mM β-glycerolphosphate and a cocktail of protease inhibitors (Roche)) and protein concentration measured using the Bradford method. 2 mg of cell extract from each condition was used for IP and 50 µg was loaded as input (Whole Cell Lysate). Immunoprecipitation of either KAP1 (Bethyl #A300-274A) or SOCS1 (SantaCruz #sc-7005R) were performed at an antibody dilution of 1:200 overnight at 4°C. Protein A Sepharose 4B fast flow beads (Sigma #P9424) were used to immunoprecipitate antibody-protein complexes for 1 hour at 4°C. Beads were then washed four times with Cell Lysis Buffer and complexes were eluted by adding Laemmli 2X buffer directly to the beads. Samples were heated for 5 minutes at 100°C prior to loading on an SDS-PAGE gel for western blotting.

GST-pull-down

BL21 *E. coli* strain harboring each of the KAP1-GST-fusion vectors were grown at 37°C to an OD of 0.6 in 400 ml YTA 2X medium (16g/l tryptone, 10g/l yeast extract, 5g/l NaCl) and induced with 0.4 mM IPTG for 4 hr at 30°C. Cell pellets were resuspended in STE

buffer (10 mM Tris-HCl pH 8.0, 1 mM EDTA, 100 mM NaCl) supplemented with DTT (5mM) and a Protease Inhibitor Cocktail (Roche). Cells were lysed by adding 1mg/mL lysozyme and incubating 45 minutes on ice prior to sonicating with a microtip five times for 10 s. Extracts were centrifuged (13 000 rpm 10 minutes) and supernatants were incubated for 2 hr at 4°C with glutathione Sepharose-4B (Amersham) and washed four times with NETN buffer (10 mM Tris-HCl pH 8.0, 1 mM EDTA, 100 mM NaCl, 0.5% NP-40). Beads were resuspended in PBS after the last wash.

Briefly, ³⁵[S] Flag-SOCS1 was produced by *in vitro* transcription/translation (Promega #L1170) and incubated with GST, GST-KAP1, GST KAP1 PHD/BROMO or GST-KAP1 ΔN purified proteins bound to glutathione Sepharose-4B for 2 hr at 4°C. Equal amounts of GST fusion proteins were used as judged from SDS gel electrophoresis and Coomassie blue staining. Beads were washed 5 times with NETN buffer. Precipitates were eluted in 20 µl of SDS Sample Buffer and 10 µl of Bromophenol Blue and boiled for 5 min. Eluates (30 µl) were separated on SDS-PAGE, dried and exposed for autoradiography.

GSH quantification

Cells were collected in Cell Lysis Buffer (20 mM Tris-HCl pH 7.5, 150 mM NaCl, 1 mM EDTA, 1 mM EGTA, 1% Triton X-100, 2.5 mM sodium pyrophosphate, 1 mM β-glycerolphosphate and a cocktail of protease inhibitors (Roche)). GSH was then quantified with the QuantiChrom Glutathione (GSH) Assay Kit (BioAssay Systems, DIGT-250) following manufacturer's instructions. Quantification was normalized to total protein concentration of each sample.

Real-Time Quantitative PCR (qPCR)

Total RNA was isolated using Trizol (Invitrogen). Reverse transcription was performed using 5X All-In-One RT MasterMix (Abmgood) on 2 µg of total RNA in 20 µL final volume according to the kit's instructions. Reverse transcription products were diluted 10-fold in RNase free water before proceeding to qPCR. QPCR was performed using primers and probe sets from Roche Universal Probe Library (https://lifescience.roche.com/en_ca/brands/universal-probe-library.html?_ga=1.38905443.192324701.1470126343#overview). 96-well plate formats with SYBR-green technology was used as described previously [26]. Relative target-gene quantification was obtained by using the ΔΔCT method in a light Cycler 480 (Roche). The mRNA expressions were measured relative to the

Table 4.

Gene symbol	Forward primer	Reverse primer
DUSP1	caacgaggccattgactcataga	atggtggctgaccgggaaat
IGFBP3	tctcccaggctacaccaccaa	ggcatatttgagctccacattaacct
IGFBP5	ccgcgagcaagtcaagatcg	taggtctcctcggccatctca
ATF3	tgaggtttgccatccagaacaa	ttcatcttctcaggggtacc
SLC7A11	ctccatgaacgggtggtgttt	ccctctcgagacgcaacataga
ALDH1L2	tctggctttggaaaagacttagg	cctgatgatggtgttctctaat
Serpine1	cggtaagcaagtggacttttc	ggctcctttccaagcaagt
NOXA	gaagaaggcgcgcaagaacg	tgagtagcacactcgactcca
RGCC	cgccacttccactacgaggag	cactgaagctgaagctgttct
IGFBP7	cctgtcctcatctggaacaaggt	tctgaatggccaggtgtcc
DKK1	atgatcatagcacttggatggg	gcacaacacaatcctgaggcaca
DDIT3	catacatcaccacactgaaagca	gctggtctgatgcctgtttttgt
PPP1R3C	agcgggtgctggcttttagg	tggatctaaacctggatcattctg
NOLC1	gcggcagtggtagtttccaat	tgaagctttatcttctggcctga
NTN4	cgtgcacaataagagcgaacca	tgttcttacattcgatttacctg
SVEP1	tctgttggtttcccatacctg	ttatggagcccacaaaagactc
PROCR	aacattgctgccgatactgctg	tctggagcatatgaagtctttgga
ESM1	catggatggcatgaagtgtg	ccagatgccatgtcatgctcttt
IGFBP4	gcaacttccacccaagcag	cggtcacacaccagcactt
IGFBP6	aggaatccaggcacctctacca	agtccagatgtctacggcatgg
SOCS1	ggtcccctggtgtttgta	taggaggtgcgagttcaggt
GDF15	agtccggatactcacgccagaa	gcccgagagatacgcaggtg
GADD45B	tgcattgtctcctggtcacgaa	cccggcttcttcgcagtag

mRNAs of two housekeeping genes: HMBS and TBP. All forward and reverse primers are listed in Table 4.

Microarray analysis

RNA was collected from IMR90 cells expressing oncoprotein E7, seven days after co-infection with pWZL ca-STAT5A (5A) and pLKO shNTC or pWZL 5A and pLKO shSOCS1 a. Total RNA samples were isolated with the RNeasy mini kit (Qiagen) and sent to the Genome Quebec facility at McGill University for cRNA amplification and subsequent hybridization on GeneChip Human Gene 2.0 ST Array Affymetrix DNA Chip. Data were analyzed using Affymetrix Expression Console Software and Transcriptome Analysis Console (www.affymetrix.com). Each condition was analysed in biological triplicates and the cut-off applied for analysis was an ANOVA p-value <0.05 for genes that have a fold change $\geq \pm 1.5$. Data are available at <https://www.ncbi.nlm.nih.gov/geo/query/acc.cgi?acc=G>

SE98216 Further analysis were conducted with DiRE (<https://dire.dcode.org/>), Gene-Set Enrichment Analysis (GSEA) (<http://software.broadinstitute.org/gsea/index.jsp>) and DAVID database (<https://david.ncifcrf.gov/>). Genes identified by DiRE were further analysed with Oncomine (<https://www.oncomine.org/resource/login.html>).

Gene expression analysis in hepatocellular carcinoma (HCC) specimens

The correlation between *SOCS1* gene expression and that of p53 target genes related to ferroptosis was analysed using The Cancer Genome Atlas (TCGA) [51] provisional dataset containing 373 hepatocellular carcinoma (HCC) specimens, which was accessed via the cBioportal (<http://www.cbioportal.org>) [52]. The transcript levels were expressed as RNASeq V_e RESM (RNA-Seq by Expectation Maximization) [53]. The

downloaded data were plotted using the GraphPad Prism software to determine the Spearman correlation (ρ) and statistical significance (p).

ACKNOWLEDGEMENTS

We thank all members of the Ferbeyre laboratory for their useful comments.

CONFLICTS OF INTEREST

The authors have no conflict of interests to declare.

FUNDING

This work was funded by a grant from the Canadian Institute of Health and Research (CIHR-MOP229774) to GF.

REFERENCES

1. Lawrence MS, Stojanov P, Mermel CH, Robinson JT, Garraway LA, Golub TR, Meyerson M, Gabriel SB, Lander ES, Getz G. Discovery and saturation analysis of cancer genes across 21 tumour types. *Nature*. 2014; 505:495–501. <https://doi.org/10.1038/nature12912>
2. Wei CL, Wu Q, Vega VB, Chiu KP, Ng P, Zhang T, Shahab A, Yong HC, Fu Y, Weng Z, Liu J, Zhao XD, Chew JL, et al. A global map of p53 transcription-factor binding sites in the human genome. *Cell*. 2006; 124:207–19. <https://doi.org/10.1016/j.cell.2005.10.043>
3. Li M, He Y, Dubois W, Wu X, Shi J, Huang J. Distinct regulatory mechanisms and functions for p53-activated and p53-repressed DNA damage response genes in embryonic stem cells. *Mol Cell*. 2012; 46:30–42. <https://doi.org/10.1016/j.molcel.2012.01.020>
4. Jiang L, Kon N, Li T, Wang SJ, Su T, Hibshoosh H, Baer R, Gu W. Ferroptosis as a p53-mediated activity during tumour suppression. *Nature*. 2015; 520:57–62. <https://doi.org/10.1038/nature14344>
5. Fischer M, Grossmann P, Padi M, DeCaprio JA. Integration of TP53, DREAM, MMB-FOXM1 and RB-E2F target gene analyses identifies cell cycle gene regulatory networks. *Nucleic Acids Res*. 2016; 44:6070–86. <https://doi.org/10.1093/nar/gkw523>
6. Brady CA, Jiang D, Mello SS, Johnson TM, Jarvis LA, Kozak MM, Kenzelmann Broz D, Basak S, Park EJ, McLaughlin ME, Karnezis AN, Attardi LD. Distinct p53 transcriptional programs dictate acute DNA-damage responses and tumor suppression. *Cell*. 2011; 145:571–83. <https://doi.org/10.1016/j.cell.2011.03.035>
7. Valente LJ, Grabow S, Vandenberg CJ, Strasser A, Janic A. Combined loss of PUMA and p21 accelerates c-MYC-driven lymphoma development considerably less than loss of one allele of p53. *Oncogene*. 2016; 35:3866–71. <https://doi.org/10.1038/onc.2015.457>
8. Kirschner K, Samarajiwa SA, Cairns JM, Menon S, Pérez-Mancera PA, Tomimatsu K, Bermejo-Rodriguez C, Ito Y, Chandra T, Narita M, Lyons SK, Lynch AG, Kimura H, et al. Phenotype specific analyses reveal distinct regulatory mechanism for chronically activated p53. *PLoS Genet*. 2015; 11:e1005053. <https://doi.org/10.1371/journal.pgen.1005053>
9. Banin S, Moyal L, Shieh S, Taya Y, Anderson CW, Chessa L, Smorodinsky NI, Prives C, Reiss Y, Shiloh Y, Ziv Y. Enhanced phosphorylation of p53 by ATM in response to DNA damage. *Science*. 1998; 281:1674–77. <https://doi.org/10.1126/science.281.5383.1674>
10. Sakaguchi K, Herrera JE, Saito S, Miki T, Bustin M, Vassilev A, Anderson CW, Appella E. DNA damage activates p53 through a phosphorylation-acetylation cascade. *Genes Dev*. 1998; 12:2831–41. <https://doi.org/10.1101/gad.12.18.2831>
11. Pomerantz J, Schreiber-Agus N, Liégeois NJ, Silverman A, Alland L, Chin L, Potes J, Chen K, Orlow I, Lee HW, Cordon-Cardo C, DePinho RA. The Ink4a tumor suppressor gene product, p19Arf, interacts with MDM2 and neutralizes MDM2's inhibition of p53. *Cell*. 1998; 92:713–23. [https://doi.org/10.1016/S0092-8674\(00\)81400-2](https://doi.org/10.1016/S0092-8674(00)81400-2)
12. Bernardi R, Scaglioni PP, Bergmann S, Horn HF, Vousden KH, Pandolfi PP. PML regulates p53 stability by sequestering Mdm2 to the nucleolus. *Nat Cell Biol*. 2004; 6:665–72. <https://doi.org/10.1038/ncb1147>
13. Donati G, Peddigari S, Mercer CA, Thomas G. 5S ribosomal RNA is an essential component of a nascent ribosomal precursor complex that regulates the Hdm2-p53 checkpoint. *Cell Reports*. 2013; 4:87–98. <https://doi.org/10.1016/j.celrep.2013.05.045>
14. Calabrese V, Mallette FA, Deschênes-Simard X, Ramanathan S, Gagnon J, Moores A, Ilangumaran S, Ferbeyre G. SOCS1 links cytokine signaling to p53 and senescence. *Mol Cell*. 2009; 36:754–67. <https://doi.org/10.1016/j.molcel.2009.09.044>
15. Mallette FA, Calabrese V, Ilangumaran S, Ferbeyre G. SOCS1, a novel interaction partner of p53 controlling oncogene-induced senescence. *Aging (Albany NY)*. 2010; 2:445–52. <https://doi.org/10.18632/aging.100163>

16. Yoshikawa H, Matsubara K, Qian GS, Jackson P, Grooman JD, Manning JE, Harris CC, Herman JG. SOCS-1, a negative regulator of the JAK/STAT pathway, is silenced by methylation in human hepatocellular carcinoma and shows growth-suppression activity. *Nat Genet.* 2001; 28:29–35. <https://doi.org/10.1038/ng0501-29>
17. Khoo KH, Verma CS, Lane DP. Drugging the p53 pathway: understanding the route to clinical efficacy. *Nat Rev Drug Discov.* 2014; 13:217–36. <https://doi.org/10.1038/nrd4288>
18. Fabbro M, Savage K, Hobson K, Deans AJ, Powell SN, McArthur GA, Khanna KK. BRCA1-BARD1 complexes are required for p53Ser-15 phosphorylation and a G1/S arrest following ionizing radiation-induced DNA damage. *J Biol Chem.* 2004; 279:31251–58. <https://doi.org/10.1074/jbc.M405372200>
19. Liu B, Lee KW, Anzo M, Zhang B, Zi X, Tao Y, Shiry L, Pollak M, Lin S, Cohen P. Insulin-like growth factor-binding protein-3 inhibition of prostate cancer growth involves suppression of angiogenesis. *Oncogene.* 2007; 26:1811–19. <https://doi.org/10.1038/sj.onc.1209977>
20. Magnon C, Galaup A, Mullan B, Rouffiac V, Bouquet C, Bidart JM, Griscelli F, Opolon P, Perricaudet M. Canstatin acts on endothelial and tumor cells via mitochondrial damage initiated through interaction with alphavbeta3 and alphavbeta5 integrins. *Cancer Res.* 2005; 65:4353–61. <https://doi.org/10.1158/0008-5472.CAN-04-3536>
21. Yeh JR, Mohan R, Crews CM. The antiangiogenic agent TNP-470 requires p53 and p21CIP/WAF for endothelial cell growth arrest. *Proc Natl Acad Sci USA.* 2000; 97:12782–87. <https://doi.org/10.1073/pnas.97.23.12782>
22. Assadian S, El-Assaad W, Wang XQ, Gannon PO, Barrès V, Latour M, Mes-Masson AM, Saad F, Sado Y, Dostie J, Teodoro JG. p53 inhibits angiogenesis by inducing the production of Arresten. *Cancer Res.* 2012; 72:1270–79. <https://doi.org/10.1158/0008-5472.CAN-11-2348>
23. Kagan VE, Mao G, Qu F, Angeli JP, Doll S, Croix CS, Dar HH, Liu B, Tyurin VA, Ritov VB, Kapralov AA, Amoscato AA, Jiang J, et al. Oxidized arachidonic and adrenic PEs navigate cells to ferroptosis. *Nat Chem Biol.* 2017; 13:81–90. <https://doi.org/10.1038/nchembio.2238>
24. Ou Y, Wang SJ, Li D, Chu B, Gu W. Activation of SAT1 engages polyamine metabolism with p53-mediated ferroptotic responses. *Proc Natl Acad Sci USA.* 2016; 113:E6806–12. <https://doi.org/10.1073/pnas.1607152113>
25. Chicas A, Wang X, Zhang C, McCurrach M, Zhao Z, Mert O, Dickins RA, Narita M, Zhang M, Lowe SW. Dissecting the unique role of the retinoblastoma tumor suppressor during cellular senescence. *Cancer Cell.* 2010; 17:376–87. <https://doi.org/10.1016/j.ccr.2010.01.023>
26. Vernier M, Bourdeau V, Gaumont-Leclerc MF, Moiseeva O, Bégin V, Saad F, Mes-Masson AM, Ferbeyre G. Regulation of E2Fs and senescence by PML nuclear bodies. *Genes Dev.* 2011; 25:41–50. <https://doi.org/10.1101/gad.1975111>
27. Sinha VC, Qin L, Li Y. A p53/ARF-dependent anticancer barrier activates senescence and blocks tumorigenesis without impacting apoptosis. *Mol Cancer Res.* 2015; 13:231–38. <https://doi.org/10.1158/1541-7786.MCR-14-0481-T>
28. Jiang L, Hickman JH, Wang SJ, Gu W. Dynamic roles of p53-mediated metabolic activities in ROS-induced stress responses. *Cell Cycle.* 2015; 14:2881–85. <https://doi.org/10.1080/15384101.2015.1068479>
29. Yang WS, SriRamaratnam R, Welsch ME, Shimada K, Skouta R, Viswanathan VS, Cheah JH, Clemons PA, Shamji AF, Clish CB, Brown LM, Girotti AW, Cornish VW, et al. Regulation of ferroptotic cancer cell death by GPX4. *Cell.* 2014; 156:317–31. <https://doi.org/10.1016/j.cell.2013.12.010>
30. Mallette FA, Gaumont-Leclerc MF, Ferbeyre G. The DNA damage signaling pathway is a critical mediator of oncogene-induced senescence. *Genes Dev.* 2007; 21:43–48. <https://doi.org/10.1101/gad.1487307>
31. Bartkova J, Rezaei N, Liontos M, Karakaidos P, Kletsas D, Issaeva N, Vassiliou LV, Kolettas E, Niforou K, Zoumpourlis VC, Takaoka M, Nakagawa H, Tort F, et al. Oncogene-induced senescence is part of the tumorigenesis barrier imposed by DNA damage checkpoints. *Nature.* 2006; 444:633–37. <https://doi.org/10.1038/nature05268>
32. Di Micco R, Fumagalli M, Cicalese A, Piccinin S, Gasparini P, Luise C, Schurra C, Garre' M, Nuciforo PG, Bensimon A, Maestro R, Pelicci PG, d'Adda di Fagagna F. Oncogene-induced senescence is a DNA damage response triggered by DNA hyper-replication. *Nature.* 2006; 444:638–42. <https://doi.org/10.1038/nature05327>
33. Hubackova S, Novakova Z, Krejčíková K, Kosar M, Dobrovolná J, Dusková P, Hanzlíková H, Vancurova M, Barath P, Bartek J, Hodny Z. Regulation of the PML tumor suppressor in drug-induced senescence of human normal and cancer cells by JAK/STAT-mediated signaling. *Cell Cycle.* 2010; 9:3085–99. <https://doi.org/10.4161/cc.9.15.12521>








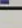
34. Tamiya T, Kashiwagi I, Takahashi R, Yasukawa H, Yoshimura A. Suppressors of cytokine signaling (SOCS) proteins and JAK/STAT pathways: regulation of T-cell inflammation by SOCS1 and SOCS3. *Arterioscler Thromb Vasc Biol.* 2011; 31:980–85. <https://doi.org/10.1161/ATVBAHA.110.207464>
35. Bakkenist CJ, Beumer JH, Schmitz JC. ATM serine-1981 phosphorylation is a plausible biomarker. *Cell Cycle.* 2015; 14:3207–08. <https://doi.org/10.1080/15384101.2015.1084205>
36. Al Rashid ST, Dellaire G, Cuddihy A, Jalali F, Vaid M, Coackley C, Folkard M, Xu Y, Chen BP, Chen DJ, Lilge L, Prise KM, Bazett Jones DP, Bristow RG. Evidence for the direct binding of phosphorylated p53 to sites of DNA breaks in vivo. *Cancer Res.* 2005; 65:10810–21. <https://doi.org/10.1158/0008-5472.CAN-05-0729>
37. Webley K, Bond JA, Jones CJ, Blaydes JP, Craig A, Hupp T, Wynford-Thomas D. Posttranslational modifications of p53 in replicative senescence overlapping but distinct from those induced by DNA damage. *Mol Cell Biol.* 2000; 20:2803–08. <https://doi.org/10.1128/MCB.20.8.2803-2808.2000>
38. Zhang XP, Liu F, Wang W. Two-phase dynamics of p53 in the DNA damage response. *Proc Natl Acad Sci USA.* 2011; 108:8990–95. <https://doi.org/10.1073/pnas.1100600108>
39. Wang C, Ivanov A, Chen L, Fredericks WJ, Seto E, Rauscher FJ 3rd, Chen J. MDM2 interaction with nuclear corepressor KAP1 contributes to p53 inactivation. *EMBO J.* 2005; 24:3279–90. <https://doi.org/10.1038/sj.emboj.7600791>
40. Xue W, Zender L, Miething C, Dickins RA, Hernando E, Krizhanovsky V, Cordon-Cardo C, Lowe SW. Senescence and tumour clearance is triggered by p53 restoration in murine liver carcinomas. *Nature.* 2007; 445:656–60. <https://doi.org/10.1038/nature05529>
41. Bouamar H, Jiang D, Wang L, Lin AP, Ortega M, Aguiar RC. MicroRNA 155 control of p53 activity is context dependent and mediated by Aicda and Socs1. *Mol Cell Biol.* 2015; 35:1329–40. <https://doi.org/10.1128/MCB.01446-14>
42. Mignacca L, Saint-Germain E, Benoit A, Bourdeau V, Moro A, Ferbeyre G. Sponges against miR-19 and miR-155 reactivate the p53-Socs1 axis in hematopoietic cancers. *Cytokine.* 2016; 82:80–86. <https://doi.org/10.1016/j.cyto.2016.01.015>
43. Ron D, Habener JF. CHOP, a novel developmentally regulated nuclear protein that dimerizes with transcription factors C/EBP and LAP and functions as a dominant-negative inhibitor of gene transcription. *Genes Dev.* 1992; 6:439–53. <https://doi.org/10.1101/gad.6.3.439>
44. Acosta JC, O’Loughlen A, Banito A, Guijarro MV, Augert A, Raguz S, Fumagalli M, Da Costa M, Brown C, Popov N, Takatsu Y, Melamed J, d’Adda di Fagagna F, et al. Chemokine signaling via the CXCR2 receptor reinforces senescence. *Cell.* 2008; 133:1006–18. <https://doi.org/10.1016/j.cell.2008.03.038>
45. Kuilman T, Michaloglou C, Vredeveld LC, Douma S, van Doorn R, Desmet CJ, Aarden LA, Mooi WJ, Peeper DS. Oncogene-induced senescence relayed by an interleukin-dependent inflammatory network. *Cell.* 2008; 133:1019–31. <https://doi.org/10.1016/j.cell.2008.03.039>
46. Takekawa M, Tatebayashi K, Itoh F, Adachi M, Imai K, Saito H. Smad-dependent GADD45beta expression mediates delayed activation of p38 MAP kinase by TGF-beta. *EMBO J.* 2002; 21:6473–82. <https://doi.org/10.1093/emboj/cdf643>
47. Willers H, McCarthy EE, Wu B, Wunsch H, Tang W, Taghian DG, Xia F, Powell SN. Dissociation of p53-mediated suppression of homologous recombination from G1/S cell cycle checkpoint control. *Oncogene.* 2000; 19:632–39. <https://doi.org/10.1038/sj.onc.1203142>
48. Dudenhöffer C, Rohaly G, Will K, Deppert W, Wiesmüller L. Specific mismatch recognition in heteroduplex intermediates by p53 suggests a role in fidelity control of homologous recombination. *Mol Cell Biol.* 1998; 18:5332–42. <https://doi.org/10.1128/MCB.18.9.5332>
49. Ferbeyre G, de Stanchina E, Querido E, Baptiste N, Prives C, Lowe SW. PML is induced by oncogenic ras and promotes premature senescence. *Genes Dev.* 2000; 14:2015–27.
50. Mallette FA, Gaumont-Leclerc MF, Huot G, Ferbeyre G. Myc down-regulation as a mechanism to activate the Rb pathway in STAT5A-induced senescence. *J Biol Chem.* 2007; 282:34938–44. <https://doi.org/10.1074/jbc.M707074200>
51. Wang F, Wang R, Li Q, Qu X, Hao Y, Yang J, Zhao H, Wang Q, Li G, Zhang F, Zhang H, Zhou X, Peng X, et al. A transcriptome profile in hepatocellular carcinomas based on integrated analysis of microarray studies. *Diagn Pathol.* 2017; 12:4. <https://doi.org/10.1186/s13000-016-0596-x>
52. Gao J, Aksoy BA, Dogrusoz U, Dresdner G, Gross B, Sumer SO, Sun Y, Jacobsen A, Sinha R, Larsson E, Cerami E, Sander C, Schultz N. Integrative analysis of complex cancer genomics and clinical profiles using

the cBioPortal. *Sci Signal*. 2013; 6:pl1.
<https://doi.org/10.1126/scisignal.2004088>

53. Li B, Dewey CN. RSEM: accurate transcript quantification from RNA-Seq data with or without a reference genome. *BMC Bioinformatics*. 2011; 12:323. <https://doi.org/10.1186/1471-2105-12-323>

SUPPLEMENTARY MATERIALS

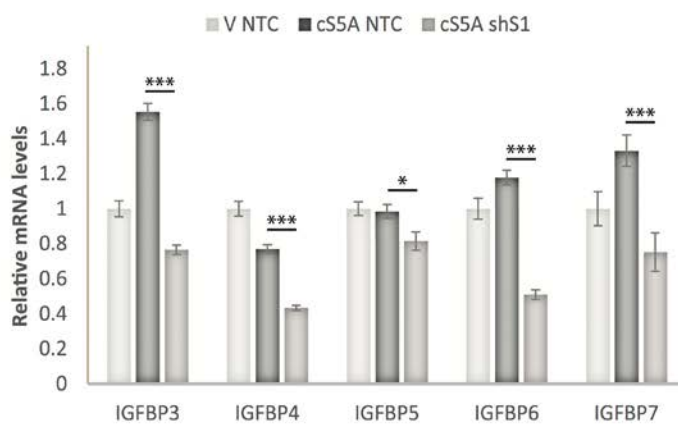
A

Category	Term	Genes	Count	%	P-Value	Benjamini
SP_PIR_KEY WORDS	Secreted		87	19.7	2.90E-15	1.10E-12
SP_PIR_KEY WORDS	signal		119	26.9	1.70E-10	3.30E-08
SP_PIR_KEY WORDS	glycoprotein		137	31	5.30E-08	7.00E-06
SP_PIR_KEY WORDS	disulfide bond		100	22.6	2.90E-07	2.80E-05
SP_PIR_KEY WORDS	egf-like domain		19	4.3	1.60E-06	1.20E-04
SP_PIR_KEY WORDS	extracellular matrix		18	4.1	1.20E-05	8.10E-04
SP_PIR_KEY WORDS	Growth factor binding		5	1.1	2.70E-04	1.50E-02
SP_PIR_KEY WORDS	cell adhesion		20	4.5	1.40E-03	6.60E-02

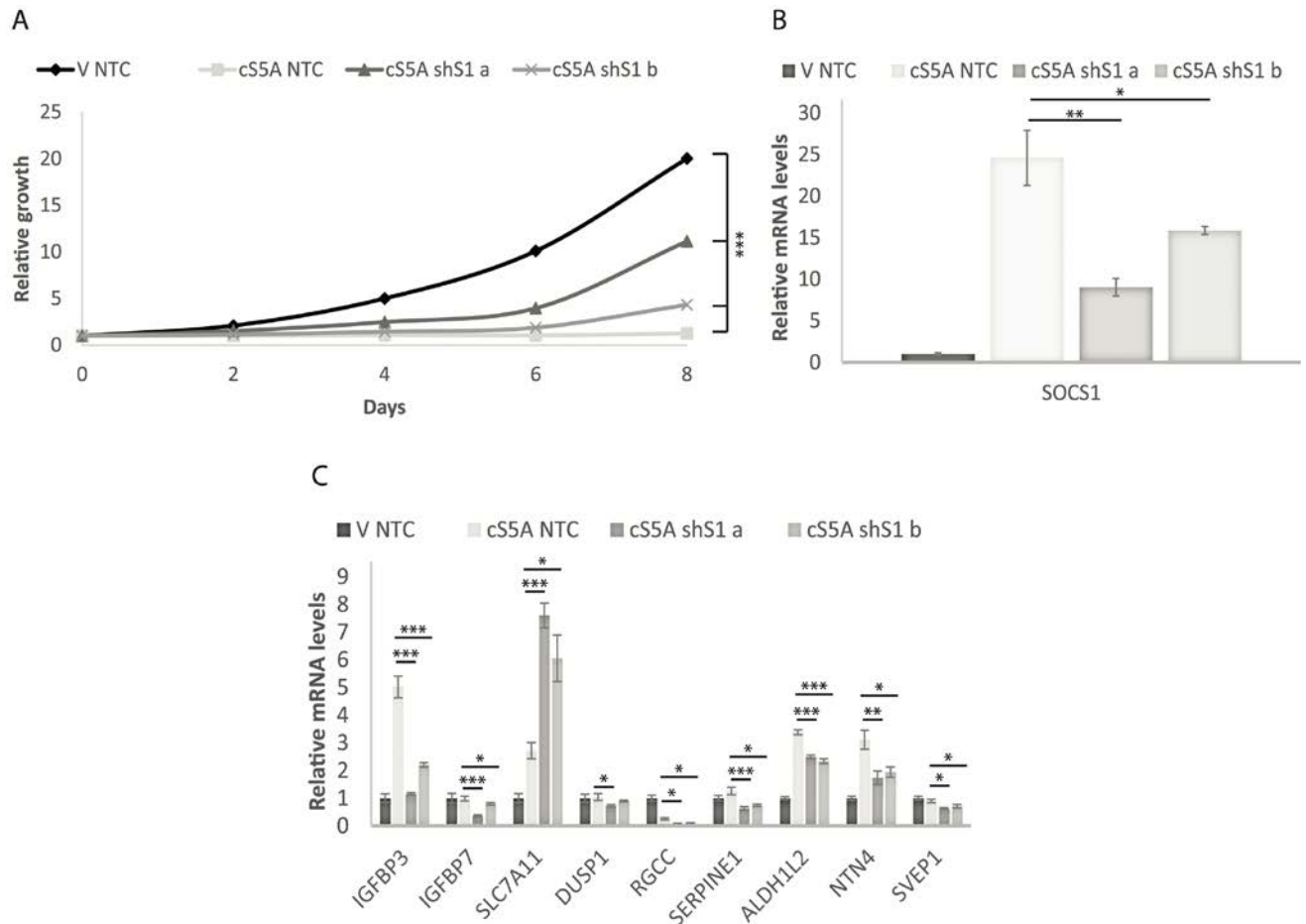
B

Genes from "Secreted" group	GENE NAME	Related Genes	Species
Kazal-type serine peptidase inhibitor domain 1	Kazal-type serine peptidase inhibitor domain 1	RG	Homo sapiens
connective tissue growth factor	connective tissue growth factor	RG	Homo sapiens
endothelial cell-specific molecule 1	endothelial cell-specific molecule 1	RG	Homo sapiens
insulin-like growth factor binding protein 3	insulin-like growth factor binding protein 3	RG	Homo sapiens
insulin-like growth factor binding protein 4	insulin-like growth factor binding protein 4	RG	Homo sapiens
insulin-like growth factor binding protein 5	insulin-like growth factor binding protein 5	RG	Homo sapiens
insulin-like growth factor binding protein 6	insulin-like growth factor binding protein 6	RG	Homo sapiens
insulin-like growth factor binding protein 7	insulin-like growth factor binding protein 7	RG	Homo sapiens

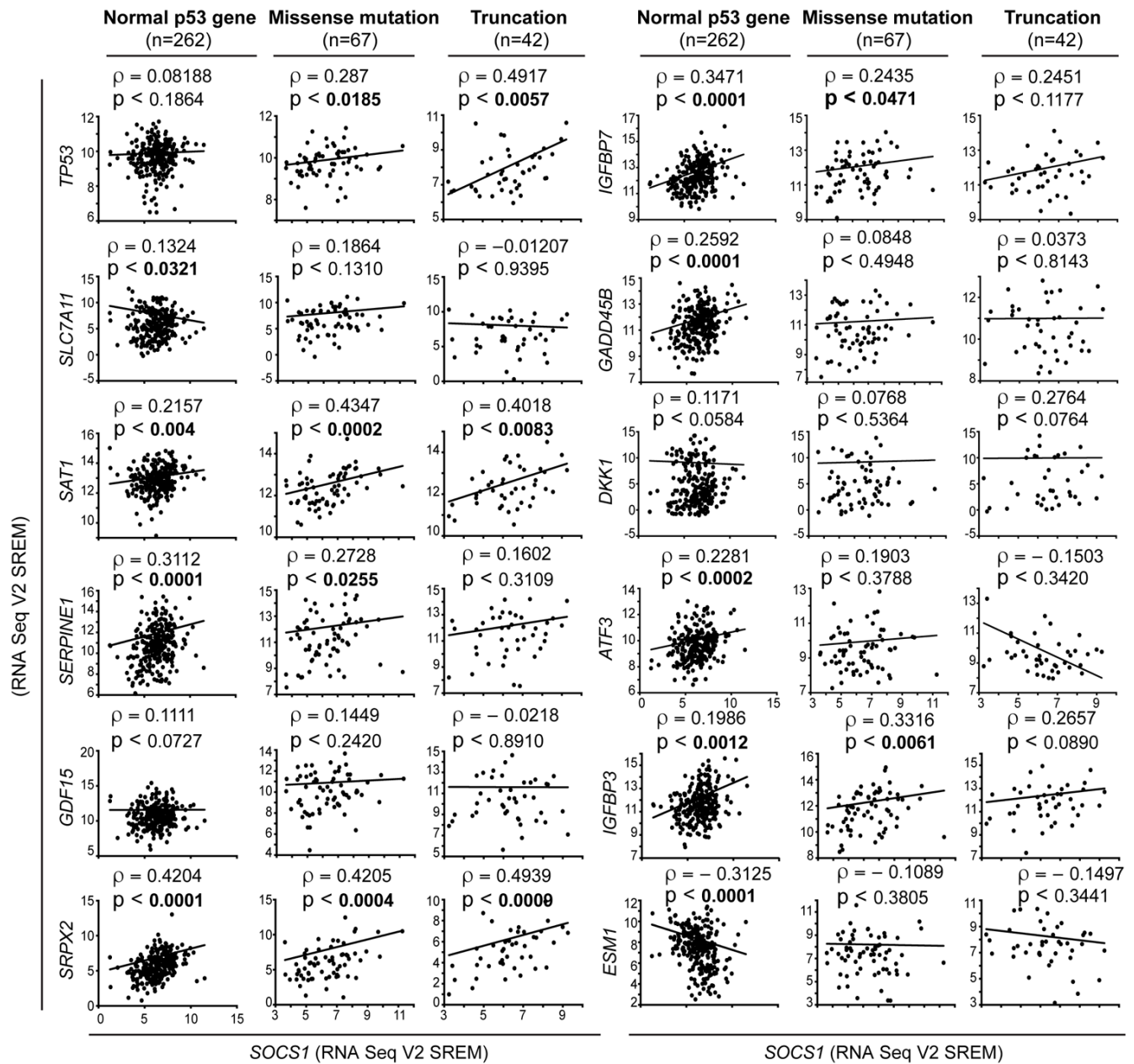
C



Supplementary Figure S1. David Analysis identifies Secreted proteins as differentially regulated in cells with SOCS1 knockdown. (A) DAVID Analysis of Key words category. (B) Genes differentially regulated in the "Secreted" category as identified by David Analysis. (C) QPCR validation of secreted factors of the IGFBP family identified by David Analysis in IMR90 cells expressing E7 in combination with either an empty vector (V) or with constitutively activated STAT5A (cS5A) and with either a control shRNA (shNTC) or an shRNA against SOCS1 (shS1). All experiments were performed three times, error bars indicate standard errors of triplicates *= $p < 0.05$, using the Student's t test, **= $p < 0.01$, ***= $p < 0.005$.

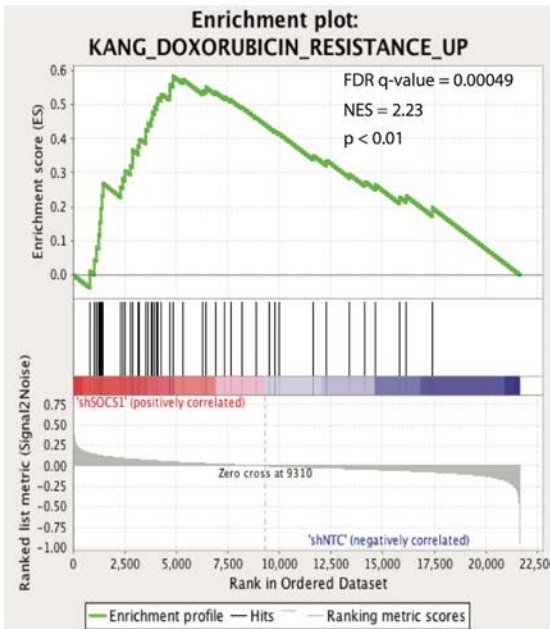


Supplementary Figure S2. Validation of SOCS1-dependent p53 target genes with two shRNAs against SOCS1. (A) Growth curves of IMR90 cells expressing E7 with either an empty vector (V) or with constitutively activated STAT5A (cS5A) and with either a control shRNA (NTC) or one of two shRNAs (shS1a or shS1b). (B) SOCS1 mRNA levels were measured by qPCR in IMR90 cells expressing the same constructs as described in (A) to assess SOCS1 knockdown efficiency. (C) QPCR of SOCS1-dependent p53 target genes in the conditions described previously. All experiments were performed three times, error bars indicate SD of triplicates (growth curves) or standard errors of triplicates (QPCR), *= p<0.05, using the Student's t test, **=p<0.01 and ***=p<0.005.

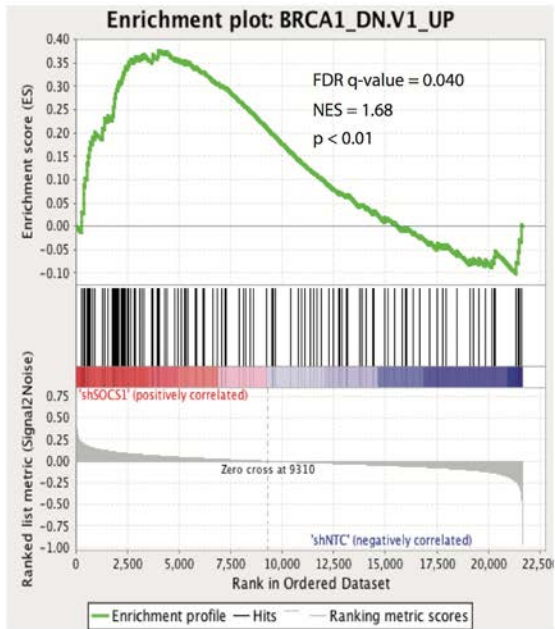


Supplementary Figure S3. Correlation between SOCS1 and p53-target gene expression in hepatocellular carcinoma samples separated according to p53 status. The Spearman correlation (ρ) and the p values are given at the top of each plot.

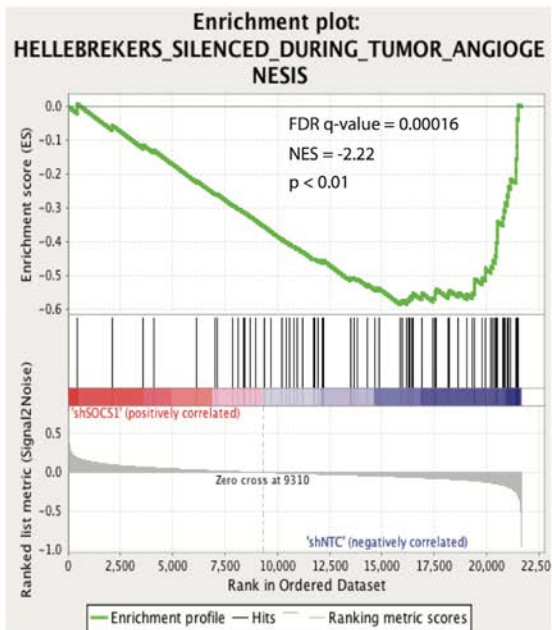
A



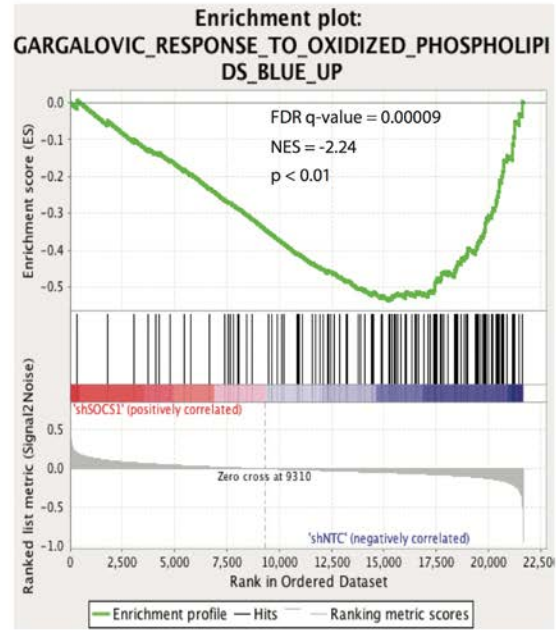
B



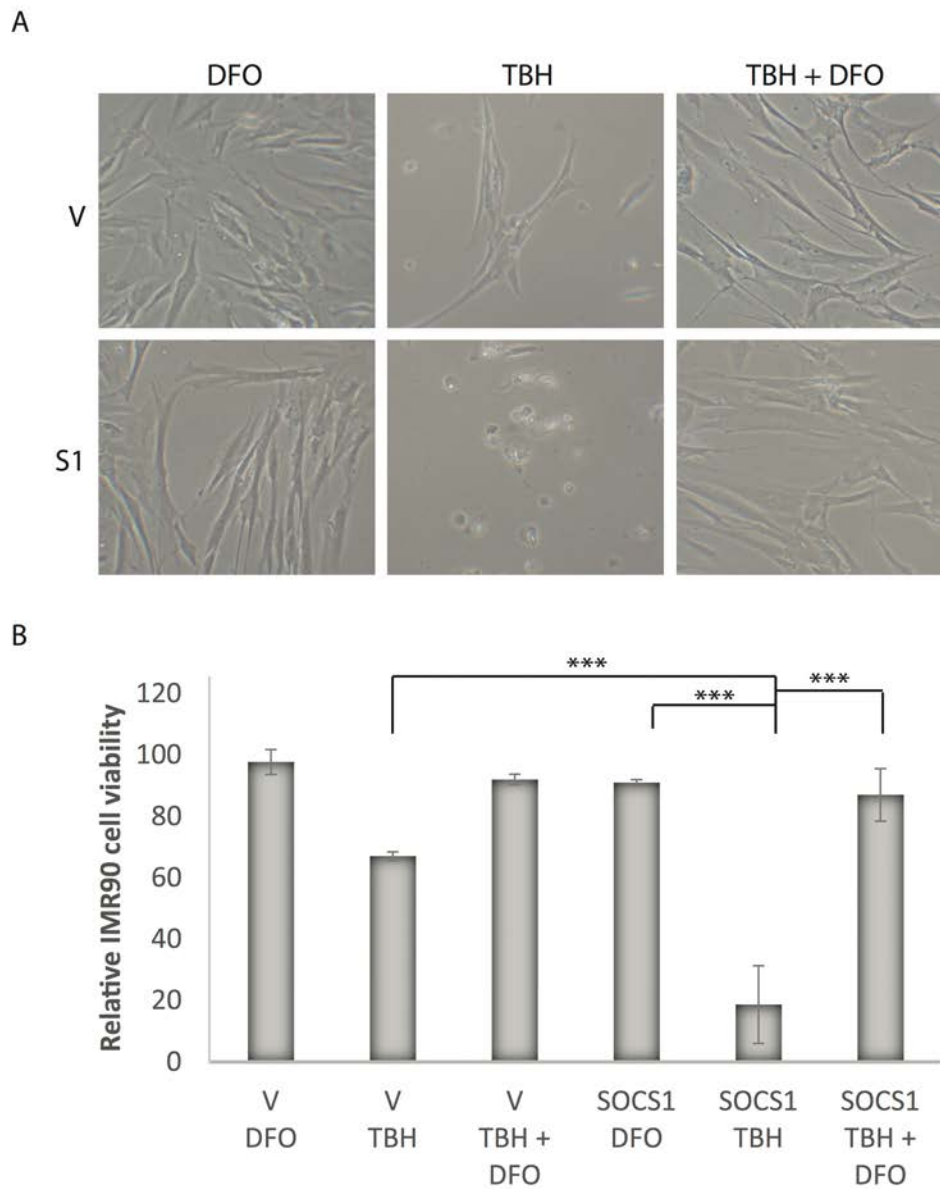
C



D



Supplementary Figure S4. GSEA analysis identifies genes sets associated with p53, angiogenesis and lipid oxidation as differentially regulated by SOCS1 knockdown. (A) Genes upregulated in a doxorubicin resistance context correlate with genes upregulated in presence of shSOCS1. **(B)** Genes upregulated in a BRCA1 dominant negative context are upregulated in presence of shSOCS1. **(C)** Genes silenced during tumor angiogenesis correlate with genes upregulated in the presence of SOCS1. **(D)** Genes upregulated in response to oxidized phospholipids are enriched in the presence of SOCS1.



Supplementary Figure S5. DFO rescues TBH-induced ferroptosis in IMR90 cells. (A) Representative photos of IMR90 cells expressing either V or S1 by retroviral infection and treated 24 hours after plating with either 88 μ M tert-butyl-hydroperoxide (TBH) alone, 100 μ M Deferoxamine mesylate (DFO) alone or the combination of both drugs. (B) Quantification of cell viability of cells portrayed in A. All experiments were performed three times, error bars indicate SD of triplicates, * = $p < 0.05$, using the Student's t test, ** = $p < 0.01$, *** = $p < 0.005$.

Premature aging and cancer development in transgenic mice lacking functional CYLD

Josefa P. Alameda^{1,2}, Ángel Ramírez^{1,2}, Rosa A. García-Fernández³, Manuel Navarro^{1,2}, Angustias Page^{1,2}, José C. Segovia⁴, Rebeca Sanchez⁴, Cristian Suárez-Cabrera^{1,2}, Jesús M. Paramio^{1,2}, Ana Bravo⁵, M. Jesús Fernández-Aceñero⁶, M. Llanos Casanova^{1,2}

¹Molecular Oncology Unit, Centro de Investigaciones Energéticas, Medioambientales y Tecnológicas (CIEMAT)/CIBERONC, 28040 Madrid, Spain

²Biomedical Research Institute I+12, 12 de Octubre University Hospital, 28040 Madrid, Spain

³Department of Animal Medicine and Surgery, Faculty of Veterinary, UCM, 28040 Madrid, Spain

⁴Division of Hematopoietic Innovative Therapies, CIEMAT/CIBERER/II-FJD, 28040 Madrid, Spain

⁵Department of Anatomy, Animal Production and Veterinary Clinical Sciences, Faculty of Veterinary Medicine, University of Santiago de Compostela, Lugo, Spain

⁶Servicio de Anatomía Patológica Hospital Clínico San Carlos, Departamento de Anatomía Patológica, Facultad de Medicina, UCM, Instituto de Investigación Sanitaria del Hospital Clínico San Carlos (IdISSC), 28040 Madrid, España

Correspondence to: M. Llanos Casanova; **email:** llanos.casanova@ciemat.es

Keywords: CYLD, premature aging, tumor suppressor, NF- κ B, keratinocyte differentiation, skin, inflammation.

Received: October 9, 2018

Accepted: December 17, 2018

Published: January 10, 2019

Copyright: Alameda et al. This is an open-access article distributed under the terms of the Creative Commons Attribution License (CC BY 3.0), which permits unrestricted use, distribution, and reproduction in any medium, provided the original author and source are credited.

ABSTRACT

CYLD is a deubiquitinating enzyme known for its role as a tumor suppressor whose mutation leads to skin appendages tumors and other cancers. In this manuscript we report that the tumor suppressor CYLD, similarly to other renowned tumor suppressor genes, protects from premature aging and cancer. We have generated transgenic mice expressing the mutant CYLD^{C/S} protein, lacking its deubiquitinase function, under the control of the keratin 5 promoter, the K5-CYLD^{C/S} mice. These mice express the transgene in different organs, including those considered to be more susceptible to aging, such as skin and thymus. Our results show that K5-CYLD^{C/S} mice exhibit epidermal, hair follicle, and sebaceous gland alterations; and, importantly, they show signs of premature aging from an early age. Typically, 3-month-old K5-CYLD^{C/S} mice exhibit a phenotype characterized by alopecia and kyphosis, and, the histological examination reveals that transgenic mice show signs of accelerated aging in numerous organs such as skin, thymus, pancreas, liver and lung. Additionally, they spontaneously develop tumors of diverse origin. Over-activation of the NF- κ B pathway, along with hyperactivation of Akt, JNK and c-Myc, and chronic inflammation, appear as the mechanisms responsible for the premature aging of the K5-CYLD^{C/S} mice.

INTRODUCTION

The *CYLD* gene [1, 2] encodes an enzyme (CYLD) that is ubiquitously expressed and contains a deubiquitinating (DUB) domain at the C-terminus, which removes lysine-63 linked polyubiquitin chains.

The first function described for CYLD was the inhibition of the nuclear factor (NF)- κ B pathway [1], and mutations that inactivate the carboxyl-terminal deubiquitinating domain of CYLD deregulate the NF- κ B activity, leading to the development of skin appendages tumors in patients of familial cylindromatosis [2].

The ubiquitous NF- κ B family of transcription factors is composed of dimers of five members, being the predominant dimer in skin p65/p50 [3]. In resting cells NF- κ B is maintained inactive and its activation by pro-inflammatory signals (such as cytokines IL-1 β and TNF- α in the canonical pathway), results in the phosphorylation and posterior degradation of the inhibitor of NF- κ B, I κ B, enabling a rapid nuclear entry of the NF- κ B dimers, and the consequent activation of specific target genes [3]. NF- κ B plays a crucial role in various biological processes, such as immune response and inflammation, and its dysregulated activity leads to the development of various autoimmune disorders, as well as to cancer development [4].

The skin is composed of three layers: epidermis, dermis and hypodermis; and also contains specialized structures, such as hair follicles (HF) and sebaceous and sweat glands. The balance between cell proliferation and differentiation of the epidermis must be maintained in order to preserve their functionality. The HF is a highly sensitive appendage undergoing continuous regeneration throughout life: HFs undergo periodic phases of rapid growth (anagen), apoptosis-driven regression (catagen) and relative quiescence (telogen). HF characteristics associated with each phase are morphologically distinct and distinguishable [5]. Loss of homeostasis of the epidermis and skin appendages leads to numerous skin alterations, such as alopecia, inflammatory diseases and non-melanoma skin cancer (NMSC). Our group and others have described that CYLD acts as a suppressor of the development and progression of the most aggressive form of the NMSC, i.e. skin squamous cell carcinomas (SCC) [6-9]. However, the role that CYLD plays *in vivo* in the epidermis and HF homeostasis has not been fully characterized.

In recent years, several genetic studies have associated the loss of CYLD functionality with the dysregulation of NF- κ B, JNK, c-Myc or Akt [10-12] and the development of different types of cancers of high prevalence in the population (multiple myeloma, hepatocarcinomas, lung, breast and gastric cancers, etc.) [13]. Therefore, it seems that CYLD, like other well-known tumor suppressor proteins such as Ink4a, Arf and PTEN, acts as a tumor suppressor in a variety of malignancies. It is interesting that these other renowned tumor suppressors develop important additional roles protecting from aging [14-16]. However, the possible role of CYLD as an aging guard has not been yet investigated.

The dual role of the tumor suppressors protecting from cancer and aging is not surprising, as it has been considered that age is the most significant risk factor for

cancer development [17]. It is remarkable that it is widely accepted that the activation of the NF- κ B signaling pathway is the driver of aging [18], since the genetic or pharmacological inhibition of NF- κ B results in the blocking of aging and even the reversion of tissue characteristics of old mice to those of young mice [19, 20]. Thus, the continuous NF- κ B hyperactivation has been directly linked to the aging process [4, 20]; moreover, abnormal NF- κ B activation is known to occur in diverse age-associated diseases (diabetes, osteoporosis, neurodegeneration etc.) [4].

It is relevant to mention that although there are many other molecules whose activation have been implicated in pro-aging and longevity processes, such as c-Myc, Akt and JNK, all of them converge in the activation or inhibition of NF- κ B signaling pathways respectively [4]. Also, chronic inflammation has been considered as a predominant and recurrent factor that is associated with the process of physiological and pathological aging, and, in this case, NF- κ B is also found on the axis of the inflammatory network of aging, since it is activated by innate/inflammatory responses, provoking a host defense mechanism, responsible for the release of SASP (senescence-associated secretory phenotype) molecules, principally IL-6 and TNF- α , which in turn favors the aging process and leads to the activation of many pro-inflammatory signaling pathways, mainly the NF- κ B pathway [21, 22].

We reasoned that CYLD, a tumor suppressor that is an inhibitor of NF- κ B activation, and consequently of inflammation, could also play an important role against aging. To study this possibility, we have generated a new model of transgenic mice, the K5-CYLD^{C/S} mice, carrying the mutant CYLD^{C/S} construct [6, 9, 23] under the regulatory elements of the keratin 5 (K5). These mice express a mutant CYLD^{C/S} protein defective in its DUB function in the skin and other numerous organs, and our results show that they exhibit signs of accelerated aging from very early ages; they also exhibit inflammation and develop spontaneous tumors in many organs. Therefore, our data indicate that CYLD, like other well-known tumor suppressor genes, also acts as an aging protector. Moreover, we propose that this is an important mechanism through which CYLD exerts its function as a tumor suppressor.

RESULTS

K5-CYLD^{C/S} transgenic mice have an impaired deubiquitination function

We have generated transgenic mice expressing a mutant CYLD protein (defective in the DUB function) under the control of the K5 promoter. The transgenic construct

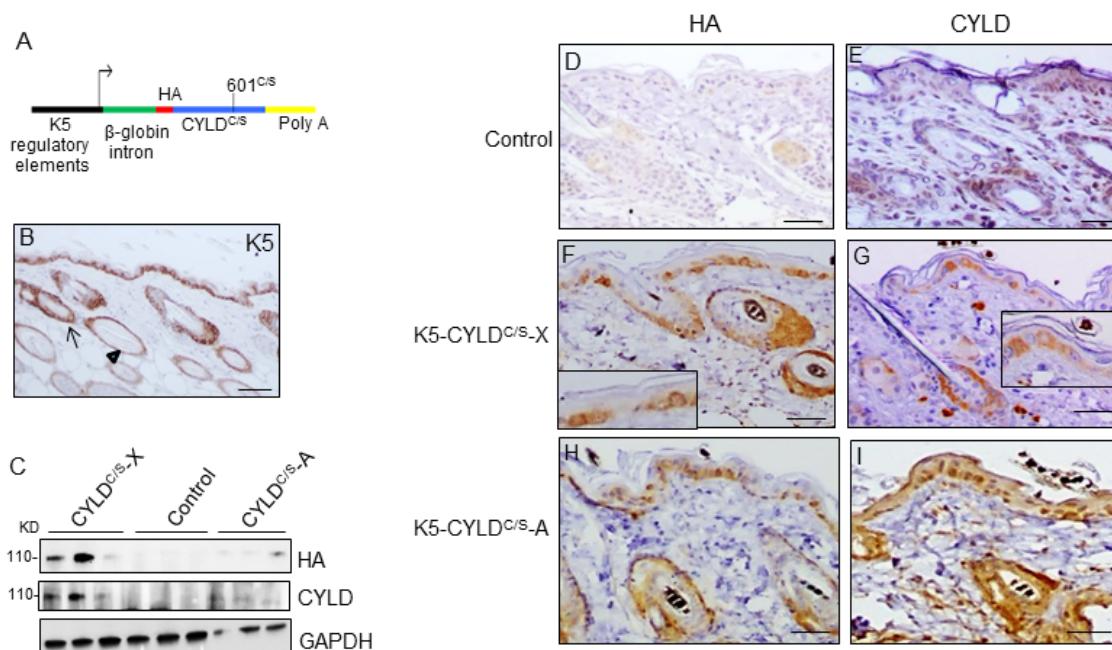


Figure 1. Analysis of the expression of the endogenous and the mutant CYLD protein in the K5-CYLD^{C/S} mice. (A) Scheme of the construction used to obtain the K5-CYLD^{C/S} mice. (B) Representative image showing the expression of K5 in the back skin of Control mice. Arrow: sebaceous gland; arrow head: ORS. (C) Analysis by WB of the expression of HA and CYLD in total protein extracts from the back skin of 30 day-old control and transgenic mice. Both lines of K5-CYLD^{C/S} mice express higher levels of CYLD than Controls. HA was not detected in Control mice. GAPDH was used as a loading control. Immunostaining -with HA (D, F, H) and CYLD (E, G, I) antibodies- of back skin samples from Control (D, E) and transgenic (K5-CYLD^{C/S}-X and K5-CYLD^{C/S}-A) mice (F-G, H-I, respectively). HA is not expressed in Control mice (D). In the K5-CYLD^{C/S} mice both, the expression of HA (F, H) and CYLD (G, I) follows the expression pattern of K5. Scale bars: 250µm (B); 150µm (D-I).

contains a mutant CYLD^{C/S} complementary DNA carrying a 601C/S point mutation in the cysteine box of the DUB domain (Fig. 1A), resulting in a catalytically inactive protein that acts as a dominant negative protein and is able to compete with the endogenous CYLD [2, 6, 9, 23]. The K5 derived sequences included in this construct drive transgene expression to the skin, specially to keratinocytes of the basal layer of the epidermis, the outer root sheath (ORS) of hair follicles, and the mitotically active basal cells of the secretory units that are the source of new secretory sebaceous glands [24] (Fig. 1B). K5 promoter also drives transgenic expression to other organs besides skin, i.e. tongue, palate, thymus, lung, stomach etc. [24] Two independent lines of transgenic mice were obtained, named as K5-CYLD^{C/S}-A and K5-CYLD^{C/S}-X. We verified by immunoblotting using two different antibodies (against CYLD or against the HA tag contained in the construct), that both lines expressed the transgene, although at different levels (Fig. 1C). The expression of the transgenic protein was also detected *in situ*, by immunohistochemical staining in different tissues (such as back and tail skin and tongue) of both lines of transgenic mice, and we found that it was

expressed following the K5 expression pattern (Fig. 1, F-I; Fig. S1). We also checked in both lines of transgenic mice, that, as expected, the CYLD^{C/S} mutant was catalytically inactive and inhibited the DUB function of the endogenous CYLD, as we previously described that occurred in the epidermal HaCaT-CYLD^{C/S} and PDVC57-CYLD^{C/S} cells [6, 9] (Fig. S2). The following analyses were performed in both lines of transgenic mice and obtained similar results.

CYLD controls hair follicle growth cycle

Young transgenic mice appeared normal and healthy; however, they showed an abnormal, untidy hair and patches of diffuse alopecia (Fig. 2A), visible from early age, i.e. 3-month-old mice. In addition, the histology of skin sections showed that while hair follicles in dorsal skin of 1-month-old Control mice had progressed to the anagen phase of the second hair growth cycle (Fig. 2B), as it occurs in normal mice at this age, HF in dorsal skin of 1-month-old transgenic mice remained in the first telogen phase (Fig. 2C). To ascertain whether CYLD had a role in hair follicle homeostasis and/or hair cycling, we depilated the dorsal skin of 7-week-old

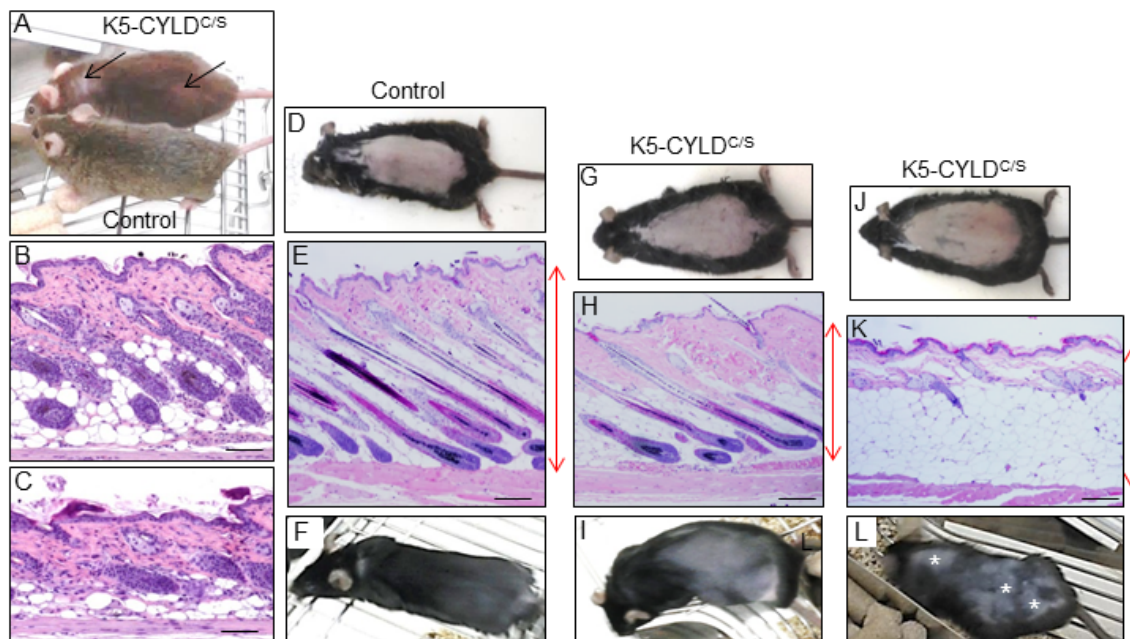


Figure 2. Analysis of the hair regrowth in Control and K5-CYLD^{C/S} mice. (A) Representative image of the patches of diffuse alopecia (arrows) of the transgenic mice (7-month-old mice are shown). (B, C) Representative images of the skin of 1-month-old mice. (D-L) Representative images of a hair growth experiment. The back of 7-week-old mice was shaved and the skin was collected 16 days after depilation. (D-F) Hair regrowth in Control mice. (G-L) Hair regrowth in the K5-CYLD^{C/S} mice. (D, G, J) Representative images of freshly depilated mice of the corresponding phenotypes (day 0 of the experiment). (E, F) 16 days after shaving Control HFs were in the anagen-catagen I phase (E) and mice exhibited a homogeneous hair regrowth (F). (H) Histology showing initiation of the anagen phase of the hair cycle 16 days after shaving the back of a transgenic mouse. The macroscopic view of this mouse showed that hair was very short and hardly visible (I). (K) Histology of a section of the back skin of a K5-CYLD^{C/S} mouse showing a delay in the growth of the new hair, so that 16 days after shaving it still remains in the telogen phase. (L) Macroscopically these areas correspond to those lacking hair in the back skin of the transgenic mouse (white asterisks). Red arrows show differences in the thickness of the skin between Control (E) and transgenic mice (H, K). Scale bars: 280 μ m.

mice (depilation allows the study of HF cycle in conditions of fully synchronized anagen [25]). Sixteen days later Control mice exhibited a homogenous short-haired layer (Fig. 2F), corresponding histologically to HF in the anagen-catagen I phase of the hair growth (Fig. 2E), while HFs of K5-CYLD^{C/S} mice had just entered the anagen phase (Fig. 2H) or still remained in the telogen phase (Fig. 2K) and, accordingly, hair was not visible yet or it had grown in a patched form (Fig. 2I and L). These histological differences were also reflected in the decrease in the skin thickness of the transgenic mice. Therefore, these findings indicate that CYLD is a positive stimulator of hair growth and that the DUB function of CYLD is essential for HF anagen induction of the second hair cycle.

K5-CYLD^{C/S} transgenic mice exhibit a premature aging skin phenotype

In addition to diffuse alopecia, young transgenic mice (8-12 months old, and even younger) also showed an

abnormal posture, characterized by excessive outward curvature of the spine (kyphosis) (Fig. S3). These features, alopecia and kyphosis in youth, are suggestive of premature aging. To check for the presence of other signs of accelerated aging in the K5-CYLD^{C/S} mice, histological analyses of the skins of mice at different ages were performed, as this organ is one of the first in which the signs of aging manifest (number and age of analyzed mice is showed, Table S1). We observed that at 1 month of age, in addition to the delay in the entry into the second hair growth cycle commented above (Fig. 2C), K5-CYLD^{C/S} mice presented a mild hyperplasia of the sebaceous glands, showing 6-8 mature sebaceous cells (Fig. 3B), versus 3-4 mature sebaceous cells in Control mice (Fig. 3A). Additionally, the interfollicular epidermis tended to be slightly thinner in the transgenic mice (compare Fig. 3D and E), and showed regions of thicker epidermis forming ridges of pyknotic keratinocytes (Fig. 3B and C). At 3 months of age, the skin phenotype of K5-CYLD^{C/S} mice was more obvious, showing a further pronounced thinning

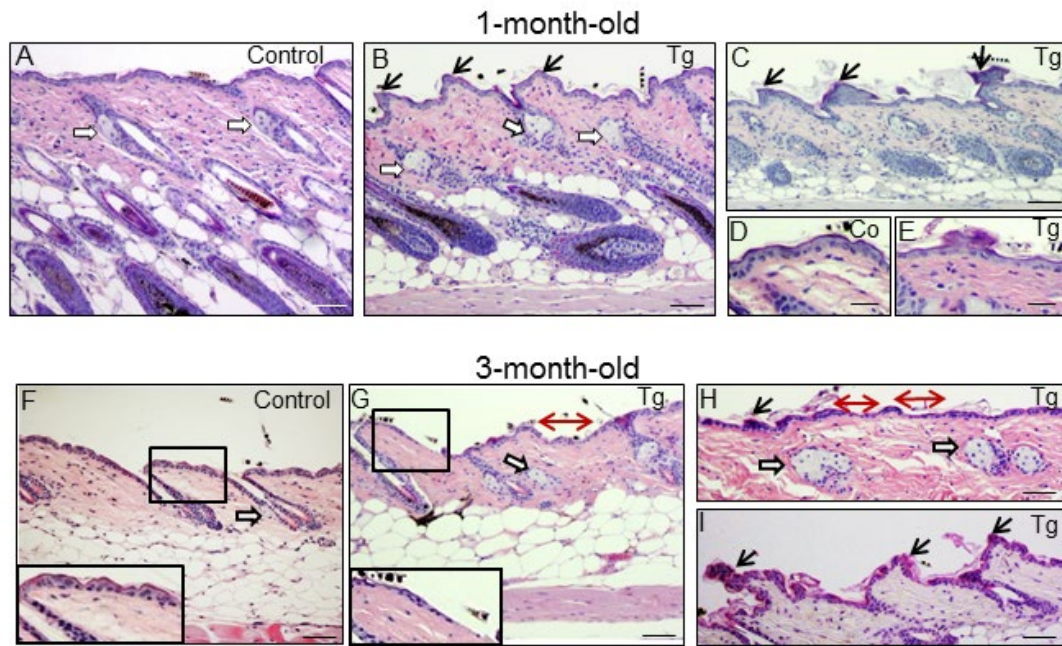


Figure 3. Histological alterations in the back skin of 1 and 3-month-old K5-CYLD^{C/S} mice. (A-E) Histology of the back skin of 1-month-old Control (A, D) and K5-CYLD^{C/S} mice (B, C, E). (A) Observe small sebaceous glands (white arrows) and HF in the anagen phase in Control mice. (B, C) Note in transgenic mice the presence of moderately hyperplastic sebaceous glands, epidermal ridges and HF initiating the anagen phase of the second hair growth cycle. (D, E) Slight thinning of the epidermis of K5-CYLD^{C/S} mice. (F-I) Histology of the back skin of 3-month-old Control (F) and K5-CYLD^{C/S} mice (G-I). (F) Note small sebaceous glands and telogenic HF in Control mice. (G-I) Observe marked epidermal atrophy; abundant epidermal ridges of pyknotic keratinocytes, increased hyperplasia of the sebaceous glands and areas with orphan sebaceous glands lacking hair follicles in transgenic mice. White arrows: sebaceous glands; black arrows: epidermal ridges of pyknotic keratinocytes; double-headed red arrows: areas of epidermal atrophy. Scale bars: 250 μm (C, F-H); 200 μm (A, B); 180 μm (I); 150 μm (D, E).

of the interfollicular epidermis, which presented areas with just one layer of flat keratinocytes, versus the 3 layers usually found in Control mice (compare insets in Fig. 3F and G); the epidermal ridges were more abundant (Fig. 3H and I), and orphan and hyperplastic sebaceous glands, with absence of HF were frequently observed (Fig. 3G and H), being macroscopically coincident with the incipient alopecia observed in the scalp of 3-month-old transgenic mice (not shown). Afterwards, additional young mice of 5- and 8-month-old were analyzed (Fig. 4 A-N; images of both K5-CYLD^{C/S}-X and -A mice are shown) and we found that the skin alterations of the transgenic mice were quickly emphasized as the mice grew; thus, 5-month-old K5-CYLD^{C/S} mice exhibited a very prominent phenotype, showing large areas of atrophic interfollicular epidermis in the back skin (Fig. 4B,C,E,I,J) alternating with regions of large epidermal ridges (Fig. 4 E, G) which often form foci of papillomatous hyperplasia, giving the appearance of a thin and wrinkled skin (Fig. 4 C, I, J). Also, transgenic mice showed scarcity of adipose tissue in the hypodermis (compare Fig. 4 F, G), which together with the atrophic epidermis contributes to the

thinning of the skin in these mice. In addition, these animals showed an important reduction in the number of hair follicles in the back skin (Fig. 4 B, C, J), as well as abundant hyperplastic and orphan sebaceous glands clustered in the dermis (Fig. 4 C-E; I, L-N). The analysis of the tail skin of the K5-CYLD^{C/S} mice revealed histological alterations similar to those in the back skin, i.e., hyperplasia of sebaceous glands, and thinning of the interfollicular epidermis (Fig. 4 K-N). In addition to these symptoms, the back skin of older transgenic mice (20-month-old) showed a striking lack of adipose tissue and the presence of profuse orphan sebaceous glands (Fig. 5 B-D) which resulted in the development of a severe alopecia of the K5-CYLD^{C/S} mice. Also, aggravation of the phenotypic alterations of the tail skin was detected in the 20-month-old transgenic mice (Fig. 5 F-H); however, 20-month-old Control littermates did not show these alterations neither in the back skin nor in the tail skin (Fig. 5).

Besides back and tail skin, other stratified epithelia of the K5-CYLD^{C/S} mice showed relevant alterations suggestive of early aging; it was the case of the palate,

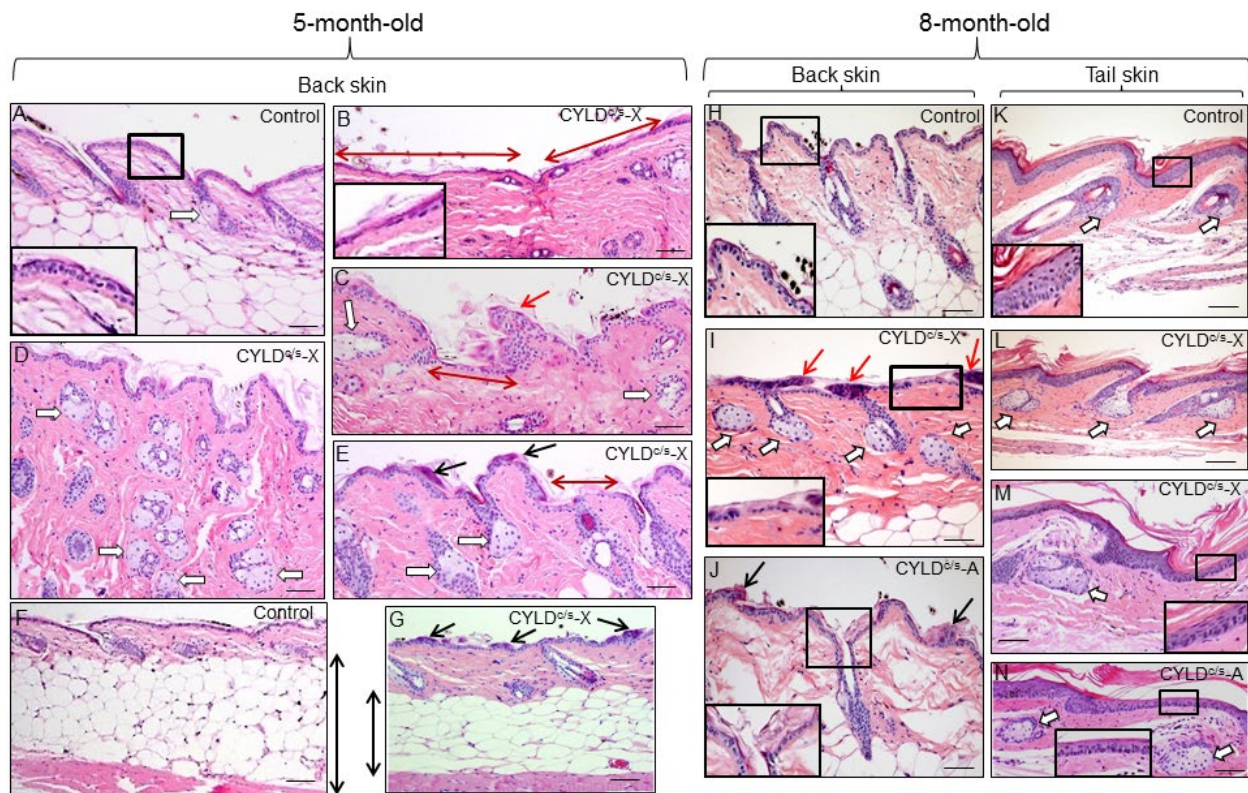


Figure 4. Histopathological signs of premature aging in the back skin of young (5- and 8-month-old) transgenic mice. Representative histology of the back skin of 5-month-old Control and transgenic mice (A-G). (A) Histology of the back skin of a Control mouse. Observe the presence of small sebaceous glands (white arrow) and 3 layers of keratinocytes in the interfollicular epidermis (higher magnification is showed in the inset). (B-E) The epidermis of the K5-CYLD^{C/S} mice shows frequent and extensive areas of atrophy (double-headed red arrows in B and C; also compare the inset in B with that of A); as well as papillomatous hyperplasia (red arrow in C) and epidermal ridges (black arrows in E and G). Abundant hyperplastic sebaceous glands -often orphan, were detected (white arrows in C-E). (F-G) Observe the scarce adipose tissue present in the skin of the transgenic mice (compare the length of the double-headed black arrows). Representative histology of the back skin of Control (H) and transgenic mice (I, J) of 8-month-old. Observe in the K5-CYLD^{C/S} mice the presence of papillomatous hyperplasia (red arrows in I); epidermal ridges (black arrows in J); abundant hyperplastic sebaceous glands (white arrows), some of them orphan (without HF) (I), and patchy epidermal atrophy associated to moderate hyperkeratosis (compare the inset in H with those of I and J). Representative histological images of the tail skin of Control (K) and transgenic mice (L-N). Note in the skin of transgenic mice the presence of hyperplastic sebaceous glands, most of them orphan (white arrows), and epidermal atrophy (compare the insets in K with those of M and N). Images of the histology of both K5-CYLD^{C/S-X} and K5-CYLD^{C/S-A} are shown. White arrows, sebaceous glands; black arrows: epidermal ridges; double-headed red arrows: areas of epidermal atrophy. Scale bars: 150 μ m (C, E); 180 μ m (A, B, D, I, J, L-N); 200 μ m (H, K) and (F, G) 350 μ m.

tongue and plantar skin; the epithelia of the snout and eyelids; also, the Meibomian glands presented a marked hyperplasia (Fig. S4).

Therefore, the signs of aging found in the skin of the K5-CYLD^{C/S} mice from 1 month of age can be considered characteristics of premature aging, as they were not manifested in the skin of Control mice until they were over 24 or 28 months old, suggesting that CYLD protects from aging. To further reinforce our findings, we analyzed the level of expression of classical molecular markers of aging, i.e., p16 and p19, and found that these were elevated in the skin of the

K5-CYLD^{C/S} mice (Fig. 5I); which strengthen our observations about the accelerated aging of the transgenic mice, since the levels of p16INK4a (and, to a lower extent, also p19ARF) increase with aging in almost all tissues analyzed both in mice and humans [26, 27]. Moreover, we analyzed levels of γ H2AX, a molecular marker of DSBs, whose elevation has been proposed as a molecular marker of aging [28], and found that levels of γ H2AX were also increased in the skin of the K5-CYLD^{C/S} mice (Fig. 5J).

Additionally, we have analyzed the level of expression of CYLD in the skin of Control mice at different ages

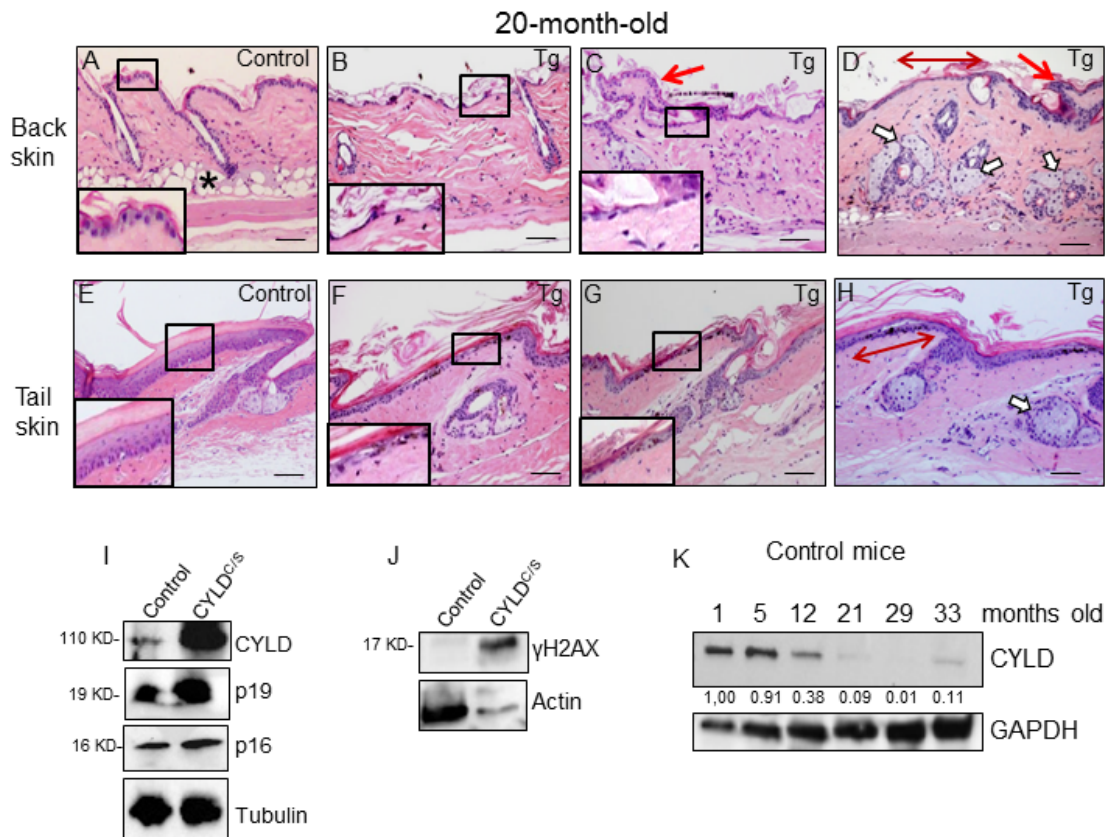


Figure 5. Histological and molecular signs of premature aging in the back skin of transgenic mice. (A-H) Representative histological images showing the back skin of 20-month-old Control mice (A) and the severe aging phenotype of the back skin of 20-month-old transgenic mice (B-D). (B-D) Note severe epidermal atrophy (compare insets in A with those of B and C; double-headed red arrow in D); foci of papillomatous hyperplasia (red arrows in C and D); numerous hyperplastic sebaceous glands, most of them orphan and grouped in the dermis (D); reduced number of HFs, and scarce or even lack of adipose tissue (compare A with B-D) in the back skin of the K5-CYLD^{C/S} mice. (E-H) Tail skin of Control (E) and transgenic (F-H) mice. Note the presence of hyperplastic sebaceous glands and extensive epidermal atrophy (compare inset in E with those in F and G) in the tail of the K5-CYLD^{C/S} mice. (I, J) WB of total protein extracts from skin of 12-month-old (I) and 6-month-old (J) showing elevated levels of p16, p19 and γH2AX in the K5-CYLD^{C/S} mice. Tubulin and Actin are used as control loading. (K) WB of total protein extracts from the skin of Control mice from 1 to 33 months of age showing the decreased expression of CYLD as mice age. GAPDH is used as a control loading. White arrows: sebaceous glands; red arrows: papillomatous hyperplasia; double-headed red arrows: areas of epidermal atrophy. Scale bars: 250 μm (A-D); 200 μm (E-H).

and found an important decrease in the amount of CYLD protein with aging, i.e. there was a diminished expression of CYLD in the skin of 12 month-old mice respect to that observed in younger mice (1-month-old); and, in aged mice (from 21-month-old), the expression of CYLD was hardly detected, being observed a decrease of more than 10 fold in the expression levels of CYLD (Fig. 5K). Therefore, all these results support the role of CYLD as a suppressor of aging in the skin.

Impaired differentiation of the epidermis of K5-CYLD^{C/S} mice

The analysis of the proliferation rate in the skin showed increased levels of BrdU and Ki67 staining in the

sebaceous glands of K5-CYLD^{C/S} mice (Fig. S5; S6 and S7), which is in accordance with its hyperplastic condition. No differences in apoptosis were found (measured by Caspase 3 cleaved immunostaining; data not shown). We then analyzed whether the differentiation of the epidermis of the K5-CYLD^{C/S} mice was affected by the lack of the DUB function of CYLD. The immunohistochemical examination of the early (K10, involucrin) and late (loricrin and filaggrin) differentiation markers showed a continuous and strong staining for all these markers in the suprabasal layers of the epidermis of Control mice; by contrast, the skin of K5-CYLD^{C/S} mice showed a pattern of discontinuous and scarce staining (Fig. 6 A-H). This deficiency in the epidermal differentiation of the skin of transgenic mice

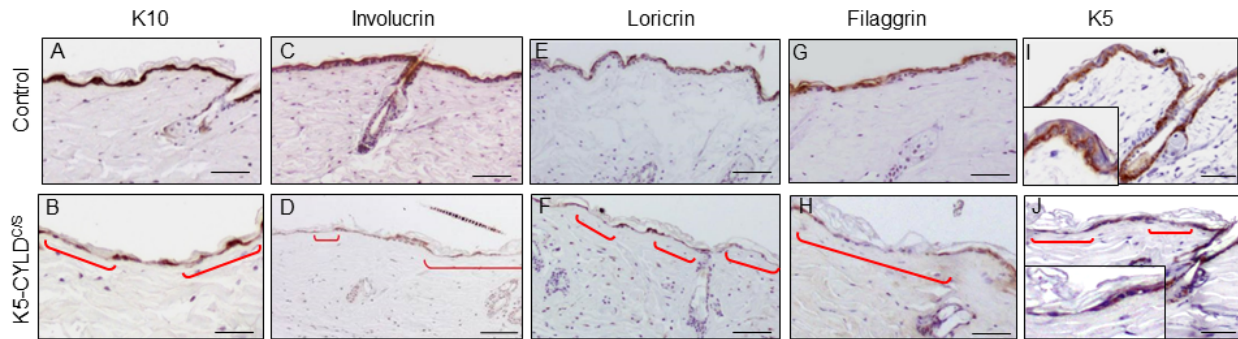


Figure 6. Deficient differentiation in the skin of K5-CYLD^{C/S} mice. Representative immunostainings of the back skin of 20-month-old mice (A-J). Observe the strong expression of the epidermal differentiation proteins Involucrin, Loricrin and Filaggrin in the suprabasal layers of the epidermis of Control mice (A,C,E,G); and the weak and discontinuous expression of these proteins in the epidermis of K5-CYLD^{C/S} mice (B,D,F,H), specially faint in the areas of epidermal atrophy (red brackets). (I, J) Representative images corresponding to the immunostaining of the back skin of Control (I) and transgenic (J) mice with the K5 specific antibody. (I) Strong K5 staining in basal keratinocytes of Control mice. A faint and patched expression is detected in the epidermis of the transgenic mice, especially in the regions of atrophic epidermis (indicated by red brackets). Scale bars: 180 μ m (A-H); 150 μ m (I, J).

was also confirmed by a semiquantitative analysis of the expression of these differentiation markers (Fig. S8). In addition, K5 staining of the basal layer of the epidermis of transgenic mice was also abnormal, showing areas of positive staining containing flat keratinocytes, with nuclei parallel to the basal membrane, alternating with no-staining skin, in which almost no keratinocytes were detected (Fig. 6J). This K5 staining pattern contrasted greatly with the continuous K5 expression found in the basal layer of the epidermis of Control littermates (Fig. 6I). Therefore, our results suggest that the atrophic skin of the transgenic mice is linked to alterations in the morphology of the basal keratinocytes and the impairment of the early and terminal epidermal differentiation.

The skin of K5-CYLD^{C/S} transgenic mice displays chronic activation of NF- κ B and other pro-aging pathways, along with increased inflammation

Searching for the mechanisms responsible for the premature aging of the skin of K5-CYLD^{C/S} mice, we first studied the activation of the NF- κ B signaling in the skin of 3-day-old mice and found that in the unstimulated, basal state, transgenic mice showed increased activation of NF- κ B (measured as P-p65 levels), as well as a long-lasting activation after 40 minutes of treatment with TNF- α (Fig. 7A). To analyze whether the hyperactivation of NF- κ B occurred only in newborn mice, coinciding with a rapid skin growth, we analyzed the activation of NF- κ B in the skin of older mice (20-month-old), and found that P-p65 was also increased in these transgenic mice (Fig. 7B). In addition, elevated phosphorylation of the inhibitor of NF- κ B, I κ B α , was detected (Fig. 7B), which may also

contribute to the increased levels of P-p65 observed. Thus, our results indicate that the skin of transgenic mice exhibit a constitutive activation of the NF- κ B canonical pathway, from birth to advanced age. Since a relevant mechanism through which NF- κ B activation promotes aging is by upregulating the expression of inflammatory cytokines, we analyzed by Western blot the expression of IL-6 and TNF- α in skin and found that they were significantly increased in that of transgenic mice (Fig. 7C); in addition, they were also increased in the serum of the K5-CYLD^{C/S} mice, mainly IL6 (Fig. S9). Although NF- κ B activation is the main regulator of aging, it has been described that the activation of other pathways, which in turn feeds the NF- κ B activation, such as Akt, JNK and c-Myc, also favors aging. In agreement with the reported negative regulation of JNK and c-Myc activation by CYLD [29], WB analysis of these molecules showed increased Akt, JNK and c-Myc activation (measured as levels of P-Akt, P-JNK and P-c-Myc respectively) in the skin of transgenic mice lacking the DUB function (Fig. 7 D-F).

K5-CYLD^{C/S} transgenic mice exhibit a premature aging of thymus

Together with the skin, other organ that is highly susceptible to premature aging is the thymus [19]. As the K5 promoter also drives transgene expression to this organ [24], we first analyzed whether the transgene was expressed in the thymus of the K5-CYLD^{C/S} mice, and found that it was mainly detected in the epithelial cells of the medullar area (Fig. 8B) of the thymus, coincident with the pattern of expression of K5 in this organ (Fig. 8C); WB also confirmed the expression of the transgene in the thymus of the K5-CYLD^{C/S} mice (Fig. 8D). Then,

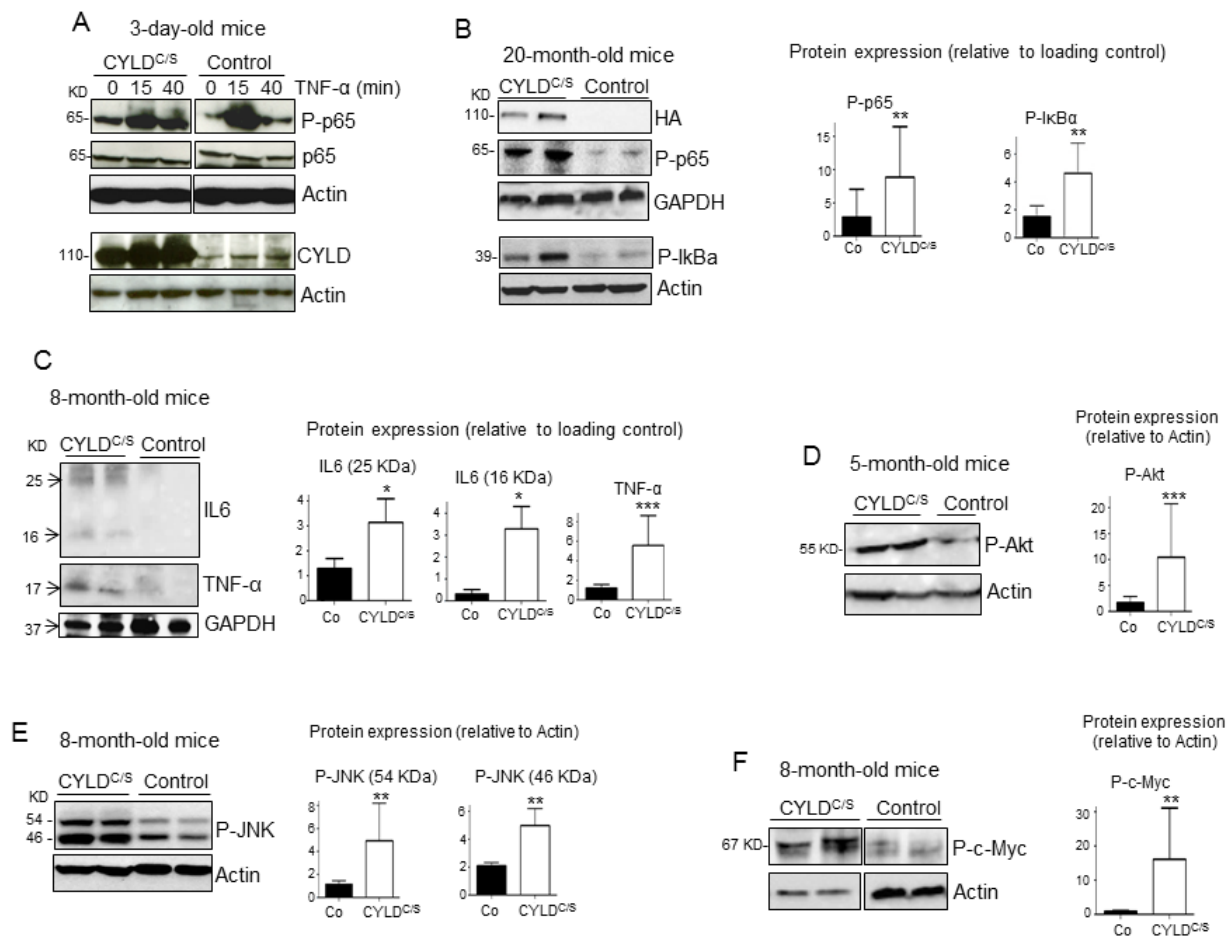


Figure 7. Overactivation of the NF- κ B, and other pro-aging pathways, along with increased IL6 and TNF- α expression in the skin of the K5-CYLD^{C/S} mice. (A) p65 and I κ B α phosphorylation kinetics in the back skin of 3-day-old Control and transgenic mice treated with TNF- α for the indicated times. (B) WB showing over-activation of the classical NF- κ B signaling pathway (P-p65 and P-I κ B α) in the skin of 20-month-old transgenic mice. (C) Increased expression of the inflammatory cytokines TNF- α and IL6 in the skin of the K5-CYLD^{C/S} mice. (D-F) WB showing the hyperactivation (phosphorylation) of Akt (D), JNK (E) and c-Myc (F) in the skin of adult K5-CYLD^{C/S} mice. Graphic representations of the densitometric analysis of western blots corresponding to extracts from 5-7 animals of each genotype are shown. Mann-Whitney U test was used for statistical analysis. (*p<0.05; **p<0.01; ***p<0.001).

we performed a histological analysis of the thymus at different ages (see Table S2) and found that in very young animals (2.5-months-old) alterations suggestive of premature aging took place. These changes consisted in the expansion of the cortical area, while a reduction of the medullar region occurred (Fig. 8F). Moreover, in 3.5 months-old transgenic mice an involution of the thymus was observed, as reflected by the atrophy of the organ and the infiltration of fat cells at expense of thymic tissue; by contrast, thymic involution was not observed in the thymus of aged-matched Control littermates (Fig. 8G and H), being the involution of the thymus considered as one of the most characteristic changes of the aging immune system [30, 31]. Since the NF- κ B pathway has been shown to be critically involved in thymic aging [32], we analyzed NF- κ B

activation by WB and found that it was overactivated in the thymus of the K5-CYLD^{C/S} mice (Fig. 8D), suggesting that, as in the skin, the overactivation of NF- κ B in the thymus could explain the accelerated aging of this organ. To further reinforce our findings, we analyzed the level of expression of CYLD in the thymus of Control mice at different ages and found that it decreases with aging, mainly from 7 months of age (Fig. 8I), reinforcing our finding of the role of CYLD as a protector of aging in the thymus.

K5-CYLD^{C/S} mice exhibit inflammation and other signals of premature aging in further organs

We found that, in addition to skin and thymus, K5-CYLD^{C/S} mice displayed signs of premature aging in

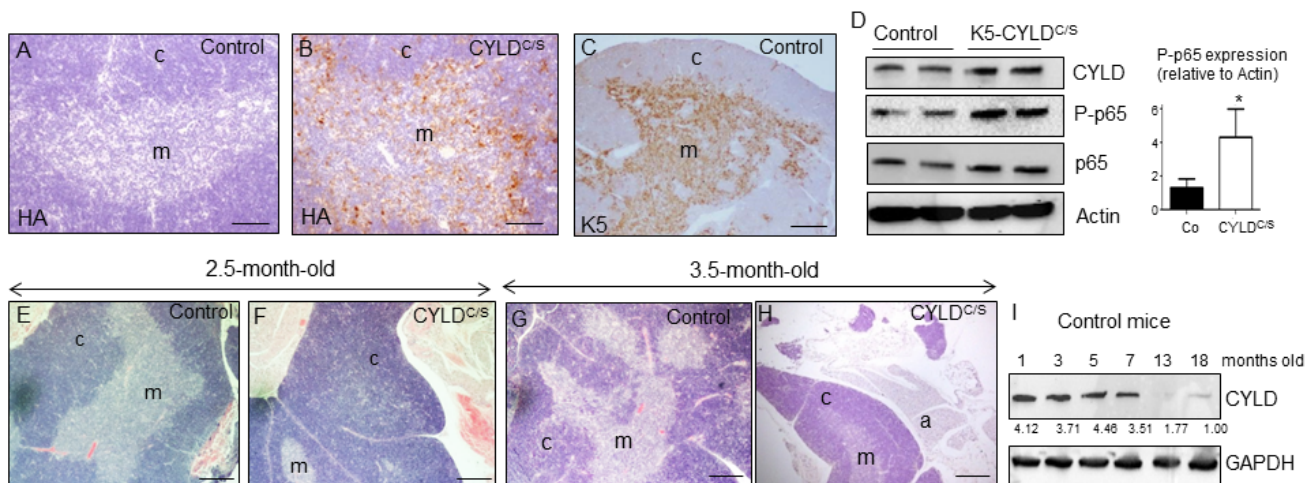


Figure 8. Premature thymic involution and over-activation of NF-κB in the thymus of K5-CYLD^{c/s} mice. (A-C) Analysis of the expression of the transgene by immunostaining with a specific antibody against the HA tag. Expression of HA is detected in the medulla of the thymus of the K5-CYLD^{c/s} mice (B), following the expression pattern of the K5 (C), while it is not detected in the Controls (A). (D) Analysis by WB of the expression of the transgene in protein extracts from isolated thymic cells of mice of 3.5-month-old. Note the overactivation of NF-κB (increased levels of P-p65) in the K5-CYLD^{c/s} mice. Mann-Whitney U test was used for statistical analysis. (*p<0.05). (E, F) Histological analysis of the thymus of 2.5-month-old mice. Observe the expansion of the cortical zone and reduction of the medullar region in the thymus of transgenic mice (F). (G, H) H&E staining of 3.5-month-old Control (G) and K5-CYLD^{c/s} mice (H) thymus. A representative image of the thymic atrophy and infiltration of white adipose tissue in the thymus of transgenic mice (H) is shown. (I) Western blot showing the decreased expression of CYLD with age in the thymus of control mice. M, medulla. C, cortex. a, adipose tissue. Scale bars: 200 μm (A, B); 300 μm (C); 350 μm (E-H).

other organs. Among them, it was remarkable the accelerated aging of the pancreas, liver, lung and stomach (Fig. 9). Features of early aging of the pancreas in the transgenic mice are the presence of huge islets of Langerhans detected in transgenic mice from 5-month-old (Fig. 9B, C and G), often observed in extrapancreatic locations, i.e. in the peripancreatic fat (Fig. 9D), and the mild chronic inflammation detected even in young mice (since 3-months-old) [33] (Fig. 9H). The liver of transgenic mice also exhibited marked aging-related lesions such as anisokaryosis,

anisocytosis, karyomegalia, and inter- and- intranuclear eosinophilic inclusions (Fig. 9I-K) as well as mild to moderate inflammation, i.e., multifocal chronic hepatitis (Fig. 9L). These alterations were not found in the liver of aged-matched Control littermates, with the exception of inflammatory cells that were sometimes detected, although in lower numbers than those found in the liver of transgenic mice (data not shown). Lungs of K5-CYLD^{c/s} mice showed moderate inflammation, consisting in BALF (Bronchus Associated Lymphoid Tissues) hyperplasia, which is typically found in lung of

Table 1. Number of tumors spontaneously developed in the K5-CYLD^{c/s} mice.

Genotype	Skin and HF Tumors	Lung ADC	Gastric ADC	Gastric Carcinoma <i>in situ</i>	HCC	Mammary ADC
Control	0/10	0/6	0/7	0/7	0/6	0/1
K5-CYLD ^{c/s}	2/10	4/6	3/8	1/8	2/6	1/2

Number of animals that have developed each type of tumor, as well as the number of mice that has been analyzed is shown. Mice of 8-29 months of age were analyzed.

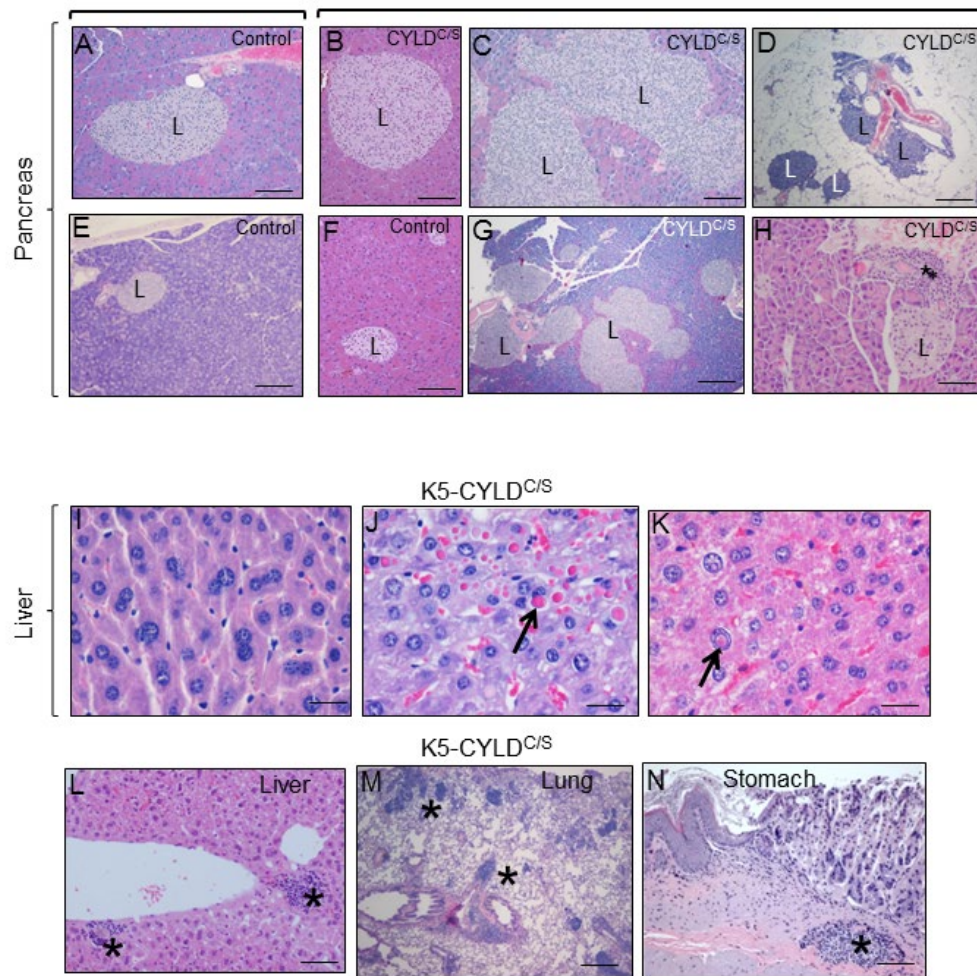


Figure 9. Alterations found in the pancreas, liver, lung and stomach of the K5-CYLD^{C/S} mice suggestive of early aging of the K5-CYLD^{C/S} mice. (A-H) Histopathologic analysis by H&E staining of pancreas from 5-month-old (B, F) and 12-month-old Control and transgenic mice. (A, E, F) Pancreas from Control mice: note the presence of Islets of Langerhans (L) of heterogeneous but moderate size. (B-D; G, H) Histology sections representatives of pancreas from K5-CYLD^{C/S} mice. Note the hyperplasia of the Islets of Langerhans (B, C, G, H). (D) Extrapancreatic location of the Islets of Langerhans, in the peripancreatic fat, observed in the K5-CYLD^{C/S} mice. (H) Foci of inflammation (asterisk) in the pancreas of K5-CYLD^{C/S} mice. (I-N) Histopathological analysis of liver, lung and stomach sections from different organs of 20-month-old K5-CYLD^{C/S} mice. (I-K) Representative images showing anisokariosis (I), eosinophilic intracytoplasmic inclusions (arrow in J), intranuclear eosinophilic inclusions (arrow in K), and inflammation foci (asterisks in L) in the liver. (M) Example of inflammation foci observed in the lung. (N) Stomach with an inflammation focus. The pancreas of 4 Control and 4 transgenic mice of 5- and 12-month-old were analyzed. Number of animals whose liver, lung and stomach has been analyzed is showed in Table 1. Asterisks: Inflammation. Scale bars: 250 μ m (A, B, D-F); 350 μ m (C); 500 μ m (G); 150 μ m (H; L-N); 40 μ m (I-K).

elderly mice, but it was observed in young transgenic mice (Fig. 9M); by contrast, Control age-matched littermates showed only a discrete inflammation in the lungs (not shown). Other organ showing evident lymphocyte infiltration was the stomach of K5-CYLD^{C/S} mice (Fig. 9N). Therefore, our results, showing several histological signs of aging in many organs of the transgenic mice, along with the chronic inflammation detected in those organs suggest that K5-CYLD^{C/S} mice undergo a systemic premature aging.

Aged K5-CYLD^{C/S} transgenic mice develop tumors in many organs

An important consequence of aging is the development of cancer [34]. Thus, a further confirmation of the premature aging of the K5-CYLD^{C/S} mice was the observation that transgenic animals (of both lines) develop spontaneous tumors of diverse origin when they reached about 8 months of age, while tumors were not detected in Control mice of similar age. The number

Spontaneous tumors arisen in transgenic mice

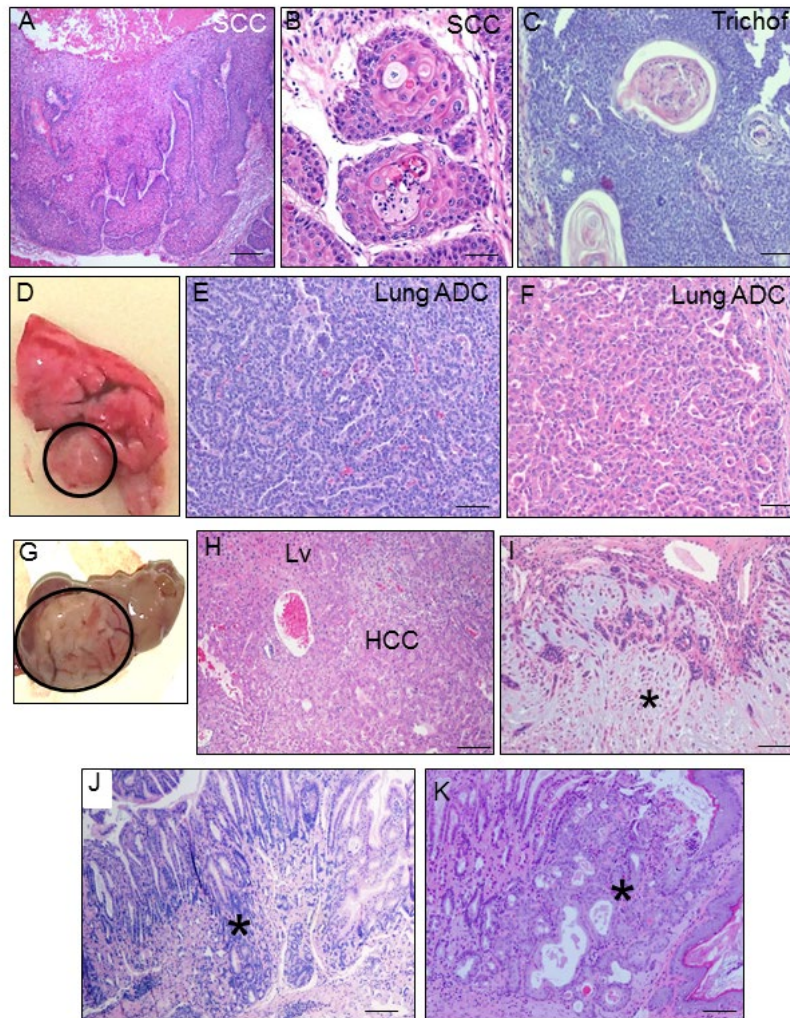


Figure 10. K5-CYLD^{C/S} mice develop spontaneous tumors in many organs. (A-C) Skin tumors. Infiltrating SCC arisen in the back skin of 8-month-old transgenic mouse (A, B). (C) Hair follicle derived tumor (trichofolliculoma) developed in the snout of a K5-CYLD^{C/S} mouse. (D) Macroscopic appearance of a lung adenocarcinoma. (E) Lung acinar adenocarcinoma. (F) Lung papillary adenocarcinoma. (G, H) Hepatocellular carcinoma (HCC); liver (Lv). (I) Mammary adenoepithelioma (asterisk). (J) Well differentiated gastric adenocarcinoma (asterisk). (K) *In situ* gastric carcinoma (asterisk). Scale bars: 500 μ m (A); 300 μ m (C, J, K); 200 μ m (E, F); 250 μ m (H, J); 100 μ m (B).

of tumors originated in K5-CYLD^{C/S} mice is summarized (Table 1). We observed the development of skin tumors, such as a squamous cell carcinoma (Fig. 10A and B) and a hair follicle-derived tumor (trichofolliculoma) (Fig. 10C). Pulmonary adenocarcinomas (acinar ADC and papillary-predominant ADC) were also detected (Fig. 10D-F). A differentiated hepatocellular carcinoma (HCC) and a hepatocellular adenoma were also found in two transgenic mice (Fig. 10G and H). K5-CYLD^{C/S} mice also exhibited well differentiated gastric adenocarcinomas (Fig. 10J) and one *in situ* gastric carcinoma (Fig. 10K). Other tumor less frequently

developed in K5-CYLD^{C/S} mice was a mammary adenomyoepithelioma (Fig. 10I). These findings indicate that the lack of the DUB function of CYLD makes transgenic mice more susceptible to the development of tumors, confirming *in vivo* the role of *Cyld* as a tumor suppressor gene in distinct organs.

Next, we performed immunostaining with the specific HA antibody to examine whether the transgene was expressed in these tumors; our data showed that the transgene was expressed in all tumors- as well as in the corresponding non tumoral tissues- except for the HCC, in which the transgene was not detected (Fig. 11).

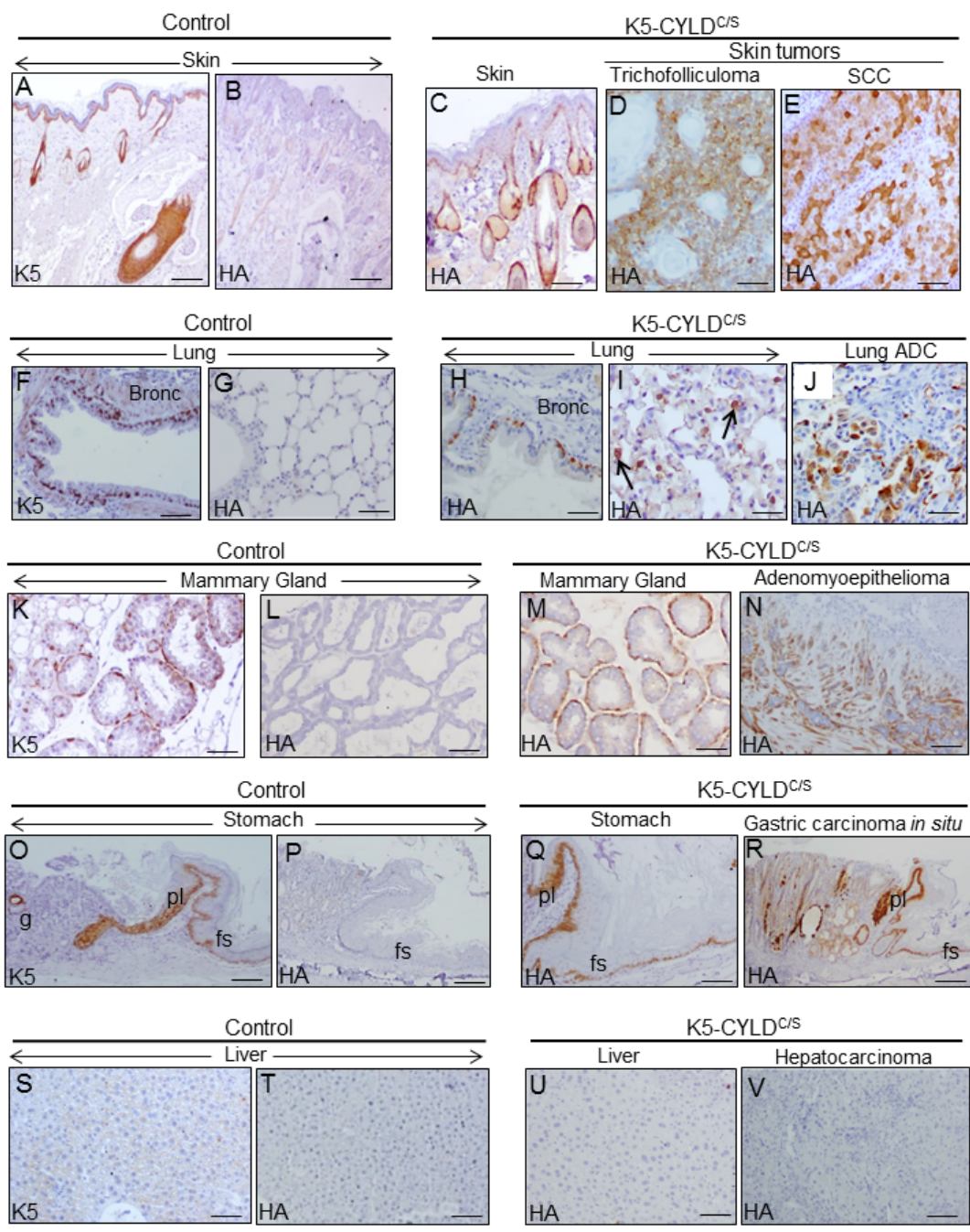


Figure 11. Analysis of the expression of the transgene in the tumors developed in the K5-CYLD^{C/S} mice and in their matched non tumoral tissue. Immunohistochemical staining with K5 and HA antibodies. (A, B) Snout sections from Control mice. K5 expression in the basal layer of the epidermis, HF and the immature cells of the sebaceous glands (A); HA is not detected (B). (C) HA expression in the snout of transgenic mice following the K5 expression pattern. HA expression in the trichofolliculoma of the snout (D) and in the SCC of the back skin of K5-CYLD^{C/S} mice (E). (F-G) K5 expression in the basal layer of the epithelium of bronchia and bronchioles of Control mice (F); no HA staining was observed (G). (H, I) HA in bronchia and bronchioles of transgenic mice (H) and in alveolar cells (I). (J) HA expression in the lung ADC. (K, L) K5 expression in the myoepithelial cells around the mammary secretory acini of Control mice (K); HA is not detected (L). (M) HA in the mammary secretory acini of lactating transgenic mice following the K5 expression patter. (N) HA expression in the mammary adenomyoepithelioma. (O, P) Stomach from a Control mice showing K5 expression in the aglandular epithelia (forestomach, fs), plica (pl), and in scattered glands (g) (O); HA is not expressed (P). (Q) Expression of HA in the stomach of transgenic mice following the K5 expression pattern. (R) Gastric carcinoma *in situ* expressing HA. (S, T) Neither K5 nor HA are expressed in the liver of Control mice. (U) HA is not detected in hepatocytes of K5-CYLD^{C/S} mice. (V) HA is not expressed in the hepatocarcinomas (HCC) of transgenic animals. Scale bars: 300 μ m (A-C; N, R); 150 μ m (D, E, I, J); 70 μ m (K-M); 250 μ m (G, O, P); 200 μ m (F, H, Q, V); 100 μ m (S-U). ADC: adenocarcinoma.

The reduction of NF- κ B activity decreases the expression of TNF- α and p16 in keratinocytes

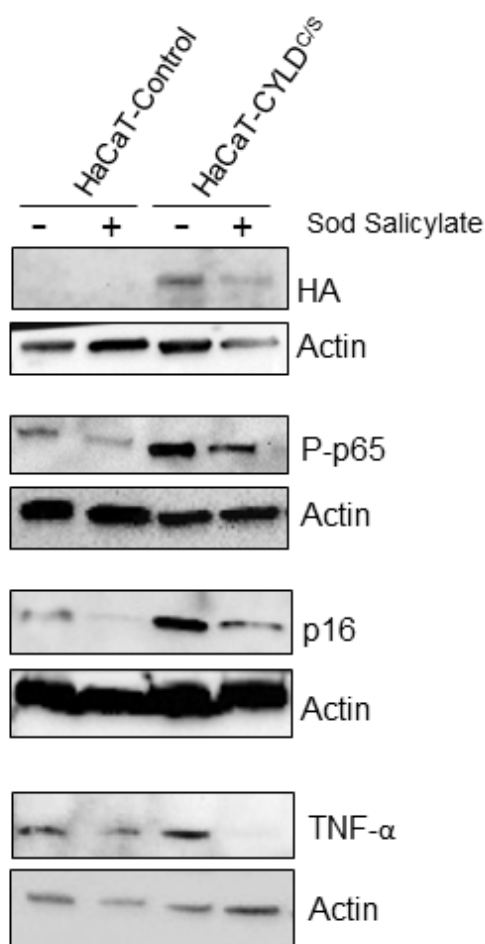


Figure 12. The reduction of the NF- κ B overactivation in keratinocytes expressing the CYLD^{C/S} mutant decreases the expression of the biomarker of aging p16 and TNF α . HaCaT (Control and CYLD^{C/S}) cells were treated with sodium salicylate for 48h when indicated (+). WB shows that HaCaT-CYLD^{C/S} cells exhibit increased levels of expression of P-p65, p16 and TNF α , but the treatment with sodium salicylate, which reduced P-p65 levels, also decreases p16 and TNF- α levels in these cells. Actin was used as a control loading.

To further reinforce our findings showing the role of CYLD as a protector from aging and tumor development, we analyzed the phenotype of the transgenic mice in a different genetic background (i.e., FVB/N background) and found that K5-CYLD^{C/S}/FVB/N mice develop similar alterations to those described above, i.e., they showed premature aging of skin and other organs (thymus, pancreas, stomach, lung etc.) (Fig. S10 and S11) and develop spontaneous tumors (from 8-10 months onwards), while their age-matched Control littermates do not show tumor development (Fig. S12).

To establish a causal relationship between CYLD lack of function, and NF- κ B activation and aging, we studied the properties of the HaCaT keratinocytes expressing the CYLD^{C/S} mutant [6, 9]. We checked that HaCaT-CYLD^{C/S} cells presented overactivation of the NF- κ B pathway (Fig. 12) and increased levels of p16 expression, whose increment is considered a biomarker of aging [26]. However, treatment of HaCaT keratinocytes with sodium salicylate reduced NF- κ B activation in both, Control and CYLD^{C/S} expressing cells, and reduced the overexpression of p16 found in the mutant HaCaT-CYLD^{C/S} keratinocytes to those levels showed in the HaCaT-Control cells (which contain a functional CYLD) (Fig. 12). In addition, we also found that NF- κ B inhibition in the HaCaT-CYLD^{C/S} cells reduces the expression of TNF- α (target of NF- κ B). Thus, our results in keratinocytes suggest a causal relationship between the lack of CYLD function, the NF- κ B hyperactivation, and the expression of aging hallmarks and inflammatory cytokines.

DISCUSSION

We have generated a new model of transgenic mice, the K5-CYLD^{C/S} mice, carrying the mutant CYLD^{C/S} construct [6] under the control of the keratin 5 (K5) promoter. The resultant CYLD^{C/S} mutant protein lacking the DUB function of CYLD, acts as a dominant negative of the endogenous CYLD. The study of our transgenic mice has allowed us to know that the DUB function of CYLD is essential for the maintenance of the homeostasis of the skin and other organs, including thymus, lung, stomach, etc. preventing the development of cancer. Notably, we have discovered a new function of CYLD as a suppressor of aging.

In the skin, we have found the importance of CYLD for the maintenance of hair follicle homeostasis and for the regulation of the hair growth cycle, showing that the DUB function of CYLD is essential for HF anagen induction of the second hair cycle. Moreover K5-CYLD^{C/S} mice show an early diffuse alopecia, progressive with age, which could be the result of both the constitutive activation of the canonical pathway of NF- κ B, and the increased expression of its targets, the pro-inflammatory cytokines TNF- α and IL-6, as inflammation is known to be linked to the development of the most common form of alopecia in humans, the androgenetic alopecia [35]. The K5-CYLD^{C/S} transgenic mice show in addition hyperplastic and orphan sebaceous glands, reminiscent of those found in another model of transgenic mice, the *Cyld*^{EA9/ Δ 9} mice, also deficient in its DUB function [36]. In both types of

transgenic mice the increased c-Myc activation found in skin could be mediating disorders of the sebaceous glands, as c-Myc has been characterized as a key regulator of homeostasis of these glands [37].

In addition to the skin appendages changes, the K5-CYLD^{C/S} mice show epidermal alterations, mainly impaired keratinocyte differentiation, thus confirming *in vivo* the results that our group have previously described using a model of skin equivalents of human HaCaT keratinocytes [9], in which we demonstrated that the overexpression of the wild-type CYLD (CYLD^{wt}) promoted keratinocyte differentiation, whereas the expression of the mutant CYLD^{C/S} prevented, through the activation of the JNK pathway, the epidermal differentiation [9]. Now our results *in vivo*, ratify the relevance of the DUB function of CYLD for epidermal differentiation, and also show the overactivation of JNK in the skin of transgenic mice.

A very relevant finding of our studies is that CYLD acts as a suppressor of aging, suggesting that CYLD is necessary to maintain the homeostasis of many organs, protecting them from premature aging. The anti-aging function of some well-known tumor suppressor genes (i.e. PTEN, Ink4/Arf) has been previously reported [16, 38], but the role of CYLD as an aging protector is a function not previously described. Supporting our results, CYLD deficiency in *Drosophila melanogaster* shortened life expectancy [39]. In addition, we show that levels of CYLD diminished in the skin and thymus of aged mice, as well as in the mammary gland (Alameda et al, not published) and other group has described it decreased expression in aged lungs [40].

One of the first manifestations of the early aging of the K5-CYLD^{C/S} mice is progressive diffuse alopecia, an alteration usually found in other models of mice exhibiting premature aging [41], and in progeria human diseases, such as Werner syndrome and Hutchinson-Gilford progeria [42]. Likewise, progressive hair loss related to age is also a hallmark of aging in humans [43]; as well as decreased hair growth [41], which we also find in our transgenic mice. Other symptoms of aging in both mice and humans are aging of the skin, mainly characterized by epidermal atrophy [44]; loss of panniculus adipose [45] and sebaceous gland hyperplasia [46]. We have observed all these signs of aging in the skin of young K5-CYLD^{C/S} mice (from 3 to 5 months of age), but they were not found in control mice of the same age; in fact these aging features are characteristics of 24-month-old control mice. Additionally the K5-CYLD^{C/S} mice show increased levels of both p16 and p19 in the skin, having been widely accepted that the expression of these proteins is augmented in aged tissues in both mice and humans [26,

27]. Also, the K5-CYLD^{C/S} mice show increased levels of γ H2AX, which is also considered a marker of aging [28]. Therefore, all these changes found in the skin of our transgenic mice lacking a functional CYLD suggest a role for CYLD as a protector of skin aging.

Chronic activation of NF- κ B in the skin appears as the key alteration causing the premature aging of this organ in K5-CYLD^{C/S} mice, as it has been described that the main mechanism responsible for both physiological and pathological aging is the activation of NF- κ B [18]. Accordingly, transgenic mice deficient in the p50 NF- κ B subunit also show hyperactivation of the classical pathway of NF- κ B and accelerated aging [47]. Although the skin of K5-CYLD^{C/S} mice show hyperactivation of other molecules, that also may favor aging (as JNK, Akt and c-Myc), it is interesting to note that the mechanism proposed through which the activation of these other pathways promotes aging is by activating NF- κ B in turn [4].

Besides the skin, other organs present accelerated aging in our transgenic mice, among them, the early aging of the thymus is very remarkable, appearing also in this case the NF- κ B over-activation as the likely mechanism causing the aging, as it has been previously reported that NF- κ B is critically involved in the aging of the thymus [19, 32]. The premature aging of other organs of the K5-CYLD^{C/S} mice could be the result of the early thymic involution (since it is considered one of the main regulators of physiological aging) as well as to the overexpression of TNF- α and IL-6, as it is known that these proinflammatory cytokines can affect distant organs causing systemic inflammation, compromising the homeostasis of the tissues and in turn promoting the accelerated aging [22]. Accordingly, elevated expression of TNF- α and IL-6 by the over-activation of NF- κ B has been proven to occur in both physiological aging and in progeria human diseases [48]. Our transgenic mice show inflammation and early aging in numerous organs (lung, stomach etc.), which could be due either to a systemic effect of TNF- α and IL-6 in the skin and/or to the expression of the transgene in these organs. These possibilities will be analyzed.

It is interesting that although there are two other models of transgenic mice that, similar to the K5-CYLD^{C/S} mice, express a mutated form of CYLD that causes the lack of DUB activity in the epidermis and other tissues (the CYLD^m [7] and the CYLD^{E Δ 9/ Δ 9} mice [36]); however, no premature aging has been described in neither of these two models. In the CYLD^m mice it was demonstrated the activation of JNK/AP1 in keratinocytes and skin tumors, though no significant increase in NF- κ B activation was detected. Activation of c-Myc was observed in the epidermis of the

CYLD^{EΔ9/Δ9} mice, and no reference to NF-κB overactivation is mentioned. Thus, it seems that the most likely reason for these other mice to age normally may be the absence of NF-κB hiperactivation. It also suggests that although both JNK and c-Myc activation might contribute to aging, the most important pro-aging pathway is that of NF-κB, as it has been widely demonstrated before [18].

A relevant phenotype of the K5-CYLD^{C/S} mice is also their susceptibility to spontaneously develop different types of tumors from an early age (8 months). Among them it has been shown the growth of skin tumors, which are likely the result of the molecular alterations observed in the skin of the transgenic mice, i.e. the overactivation of NF-κB, JNK, c-Myc and Akt. Different evidences support the role of these proteins in skin cancer development and progression, i.e., the activity of NF-κB increases with the skin tumor progression, supporting the pro-tumoral action of NF-κB in the cutaneous SCC [49]; also, NF-κB and JNK activation cause tumor development in familial cylindromatosis patients [1, 2]. The amplification or deregulation of c-Myc causes the genesis and tumor promotion of cutaneous SCC, and we have described the increased malignancy of cutaneous SCCs overexpressing c-Myc [50]. Our group has also found that the constitutive activation of Akt in the basal keratinocytes of the K5-myrAkt transgenic mice promotes the development and malignancy of cutaneous SCC [51].

But in addition to the skin tumors, other tumor types are found with a high frequency in the K5-CYLD^{C/S} mice, such as those developed in the lung, liver, and stomach. It is known that in addition to keratinocytes, the K5 regulatory elements direct the expression of the transgene to other cell types that express K5, including those in the mammary gland, stomach and lung [24]. Thus, the growth of tumors in these organs may be the direct consequence of the expression of the transgene. In fact, the lack of CYLD function has been detected in many human tumor cells of lung, stomach and breast cancer, in which the activation of NF-κB, JNK and/or c-Myc appears as the mechanisms through which CYLD downregulation promotes tumor development [10-12]. But, in addition, K5-CYLD^{C/S} mice form tumors derived from cells that do not express the transgenic protein, such as the hepatocytes. In these cases, tumors may develop as a consequence of the premature aging of the transgenic mice. In this context, it is remarkable that all types of tumors arise mainly in organs in which premature aging and inflammation has been noticed, such as in the skin, stomach, lung and liver. Therefore, it seems that tumor development could be the consequence of these pathologies, as the relationship

between aging, chronic inflammation and tumor development is well established [34, 52].

Thereby, the study of the K5-CYLD^{C/S} mice demonstrates the essential role of CYLD, *in vivo*, as a tumor suppressor of wide spectrum, providing an excellent model for studying, *in vivo*, the signaling pathways throughout CYLD exerts its tumor suppressor role in different types of cancer. In addition, our results suggest that the role of CYLD as an aging suppressor may be a mechanism through which CYLD acts as a tumor suppressor. In support of our hypothesis is the fact that although the function of CYLD as a tumor suppressor has been reported for different types of cancer [53]; however, none of the other two models of mutant CYLD transgenic mice (i.e. the CYLD^m and *Cyld*^{EΔ9/Δ9} mice) develop cancer spontaneously, strongly suggesting that the reason for this may be that they do not age prematurely. Therefore, the K5-CYLD^{C/S} mice constitute a suitable *in vivo* model for the study of the mechanisms through which NF-κB activation promotes aging, and to test putative targets aimed to delay the devastating effects of progeria syndromes. Moreover, the K5-CYLD^{C/S} mice offer a useful model for the study of the mechanisms involved in the chronological aging of the human skin, as it recapitulates its fundamental alterations.

MATERIALS AND METHODS

Generation of transgenic mice

HA-tagged murine CYLD^{C/S} [6] was placed under the control of a 5.2 kb 5'-upstream fragment of bovine K5 promoter and a rabbit β-globin intron (Figure 1A). Transgenic mice were generated by microinjection of this construct into B6D2F2 embryos using standard techniques. Mice were genotyped by PCR analysis of tail genomic DNA using primers specific for the rabbit β-globin intron. Wild type non-transgenic littermates were used as control animals. Two lines of transgenic mice were established (K5-CYLD^{C/S}-A and K5-CYLD^{C/S}-X). In addition, transgenic K5-CYLD^{C/S}-X mice were derived to FVB/N genetic background and analyzed.

Induced adult hair cycle

The hair parallel to the paravertebral line on the back skin of 7-week-old control and transgenic mice were removed. This procedure leads to synchronized development of anagen hair follicles. Tissues were obtained at days 16 and 21 after depilation and fixed in 10% buffered formalin. The distinct phases of hair follicle development were determined as previously described [5]. Body weight of the two groups of mice

was not significantly different at any point of time during the experiment. Six animals of each genotype were analyzed.

BrdU labeling

Mice received an intraperitoneal injection of BrdU 120 mg/kg body weight 1 h before sample harvesting. BrdU incorporation was detected by immunohistochemistry of paraffin-embedded sections using an anti-BrdU monoclonal antibody (Roche).

Isolation of thymic cells

Thymus from 1year old mice were collected and immersed in PBS, then mechanical disaggregation with syringe and filter system was performed.

Ethics statement

All animal experimental procedures were performed according to European and Spanish laws and regulations (2007/526/CE) and approved by the Ethics Committee for Animal Welfare of CIEMAT and by the legal authority (protocol code PROEX182/15).

Histology and immunohistochemistry

Mouse tissues were dissected and fixed in 10% buffered formalin or 70% ethanol and embedded in paraffin. Five μ m-thick sections were used for H&E staining or immunohistochemical preparations. Antibodies used in immunostaining were: antibodies against HA (3724, Cell Signaling Technology); CYLD (SAB4200061), Involucrin (I9018) and Sma (C-6198) (Sigma-Aldrich); K5, K10, Filaggrin and Loricrin (Covance).

Immunoblots and immunoprecipitation

Antibodies used in Western blots were: Actin (sc-1616), GAPDH (sc-25778), I κ B α (sc-371), p65 (sc-8008), Bcl-3 (sc-185) and P-c-Myc (sc-8000) (Santa Cruz Biotechnology); HA (3724), Ubiquitin (3936), P-Akt (4068), P-I κ B α (2859), P-JNK (4668) and P-p65 (3033) (Cell Signaling Technology); IL-6 (9324) (R&D Systems); CYLD (SAB4200061, Sigma-Aldrich); c-Myc (626802, Biologend); TNF- α (654250, Calbiochem); IKK γ (IMG-5480-2, Novus Biologicals); K63-Ubiquitin (ab179434), p19 (ab80) and p16 (ab51243) (Abcam) and γ H2AX (05-636) (Millipore). For immunoprecipitation 300 μ g cell lysate were incubated at 4°C overnight. Then washed, and performed the immunoblotting.

Determination of TNF- α and IL-6 in serum

Mice were anesthetized and blood were obtained (300 μ l) by puncture of the vein of the tail. Serum was stored at -20°C until assay. Serum from Control (n=16) and K5-CYLD^{C/S} (n=16) mice of 15-20 months of age were analyzed for the expression of both TNF- α and IL-6 cytokines (LEGENDplex Multi-Analyte Flow Assays Kit, Biologend). Cytokines were measured in a Tecan GENios Microplate Reader (Tecan Trading AG, Switzerland).

Cell culture and treatment

HaCaT cell lines of human keratinocytes were cultured in DMEM supplemented with 10% fetal calf serum. HaCaT-Control, HaCaT-CYLD^{C/S} cells have been previously described [54]; briefly, HaCaT-CYLD^{C/S} cells were transfected in a stable manner with the β -Actin-CYLD^{C/S} construct and are deficient in the DUB function of CYLD. Cells were grown in the presence of G418 (0.4mg/ml). When indicated, cells were incubated with 10mM sodium salicylate (S3007, Sigma-Aldrich) in DMEM for 48h.

Abbreviations

ORS: outer root sheath; HF: hair follicle; ADC: adenocarcinoma; HCC: hepatocarcinoma; SCC: squamous cell carcinoma; DUB: deubiquitinase; NMSC: non melanoma skin cancer.

AUTHOR CONTRIBUTIONS

Conception and design were performed by JPA and MLC. Data acquisition was performed by JPA, AR, AP, CS-C, JCS and RS. Data analysis was performed by JPA, AR, MN, JMP, RG-F; AB, MJF-A, Drafting of the manuscript was performed by MLC.

ACKNOWLEDGMENTS

We would like to thank Federico Sánchez-Sierra and Pilar Hernández for their histological processing of the samples; and Edilia de Almeida, Jesús Martínez-Palacio and the personnel of the CIEMAT Animal Unit for mice care.

CONFLICTS OF INTEREST

The authors declare that they have no competing interests.

FUNDING

This research was supported by grants from the Spanish Government and co-financed by Fondo Europeo de

Desarrollo Regional (FEDER): PI16/00161 from the Instituto de Salud Carlos III to M.L. Casanova; PI14/01403 from the Instituto de Salud Carlos III to A. Ramírez; PI17/00578 from the Instituto de Salud Carlos III to A. Ramírez and M. Navarro; and FEDER cofounded MINECO grant SAF2015-66015-R, ISCIII-RETIC RD12/0036/0009, PIE 15/00076 and CB/16/00228 to J.M. Paramio.

REFERENCES

1. Trompouki E, Hatzivassiliou E, Tschirritzis T, Farmer H, Ashworth A, Mosialos G. CYLD is a deubiquitinating enzyme that negatively regulates NF-kappaB activation by TNFR family members. *Nature*. 2003; 424:793–96. <https://doi.org/10.1038/nature01803>
2. Brummelkamp TR, Nijman SM, Dirac AM, Bernards R. Loss of the cylindromatosis tumour suppressor inhibits apoptosis by activating NF-kappaB. *Nature*. 2003; 424:797–801. <https://doi.org/10.1038/nature01811>
3. Ghosh S, Karin M. Missing pieces in the NF-kappaB puzzle. *Cell*. 2002 (Suppl); 109:S81–96. [https://doi.org/10.1016/S0092-8674\(02\)00703-1](https://doi.org/10.1016/S0092-8674(02)00703-1)
4. Tilstra JS, Clauson CL, Niedernhofer LJ, Robbins PD. NF-kB in aging and disease. *Aging Dis*. 2011; 2:449–65.
5. Straile WE, Chase HB, Arsenault C. Growth and differentiation of hair follicles between periods of activity and quiescence. *J Exp Zool*. 1961; 148:205–21. <https://doi.org/10.1002/jez.1401480304>
6. Alameda JP, Moreno-Maldonado R, Navarro M, Bravo A, Ramírez A, Page A, Jorcano JL, Fernández-Aceñero MJ, Casanova ML. An inactivating CYLD mutation promotes skin tumor progression by conferring enhanced proliferative, survival and angiogenic properties to epidermal cancer cells. *Oncogene*. 2010; 29:6522–32. <https://doi.org/10.1038/onc.2010.378>
7. Miliani de Marval P, Lutfeali S, Jin JY, Leshin B, Selim MA, Zhang JY. CYLD inhibits tumorigenesis and metastasis by blocking JNK/AP1 signaling at multiple levels. *Cancer Prev Res (Phila)*. 2011; 4:851–59. <https://doi.org/10.1158/1940-6207.CAPR-10-0360>
8. Masoumi KC, Shaw-Hallgren G, Massoumi R. Tumor Suppressor Function of CYLD in Nonmelanoma Skin Cancer. *J Skin Cancer*. 2011; 2011:614097. <https://doi.org/10.1155/2011/614097>
9. Alameda JP, Fernández-Aceñero MJ, Moreno-Maldonado R, Navarro M, Quintana R, Page A, Ramírez A, Bravo A, Casanova ML. CYLD regulates keratinocyte differentiation and skin cancer progression in humans. *Cell Death Dis*. 2011; 2:e208. <https://doi.org/10.1038/cddis.2011.82>
10. Deng LL, Shao YX, Lv HF, Deng HB, Lv FZ. Over-expressing CYLD augments antitumor activity of TRAIL by inhibiting the NF-kB survival signaling in lung cancer cells. *Neoplasma*. 2012; 59:18–29. https://doi.org/10.4149/neo_2012_003
11. Hayashi M, Jono H, Shinriki S, Nakamura T, Guo J, Sueta A, Tomiguchi M, Fujiwara S, Yamamoto-Ibusuki M, Murakami K, Yamashita S, Yamamoto Y, Li JD, et al. Clinical significance of CYLD downregulation in breast cancer. *Breast Cancer Res Treat*. 2014; 143:447–57. <https://doi.org/10.1007/s10549-013-2824-3>
12. Zhu M, Zhou X, Du Y, Huang Z, Zhu J, Xu J, Cheng G, Shu Y, Liu P, Zhu W, Wang T. miR-20a induces cisplatin resistance of a human gastric cancer cell line via targeting CYLD. *Mol Med Rep*. 2016; 14:1742–50. <https://doi.org/10.3892/mmr.2016.5413>
13. Mathis BJ, Lai Y, Qu C, Janicki JS, Cui T. CYLD-mediated signaling and diseases. *Curr Drug Targets*. 2015; 16:284–94. <https://doi.org/10.2174/1389450115666141024152421>
14. Carrasco-Garcia E, Moreno M, Moreno-Cugnon L, Matheu A. Increased Arf/p53 activity in stem cells, aging and cancer. *Aging Cell*. 2017; 16:219–25. <https://doi.org/10.1111/accel.12574>
15. Collado M, Blasco MA, Serrano M. Cellular senescence in cancer and aging. *Cell*. 2007; 130:223–33. <https://doi.org/10.1016/j.cell.2007.07.003>
16. Ortega-Molina A, Serrano M. PTEN in cancer, metabolism, and aging. *Trends Endocrinol Metab*. 2013; 24:184–89. <https://doi.org/10.1016/j.tem.2012.11.002>
17. Hsu T. Educational initiatives in geriatric oncology - Who, why, and how? *J Geriatr Oncol*. 2016; 7:390–96. <https://doi.org/10.1016/j.jgo.2016.07.013>
18. Osorio FG, Soria-Valles C, Santiago-Fernández O, Freije JM, López-Otín C. NF-kB signaling as a driver of ageing. *Int Rev Cell Mol Biol*. 2016; 326:133–74. <https://doi.org/10.1016/bs.ircmb.2016.04.003>
19. Osorio FG, Bárcena C, Soria-Valles C, Ramsay AJ, de Carlos F, Cobo J, Fueyo A, Freije JM, López-Otín C. Nuclear lamina defects cause ATM-dependent NF-kB activation and link accelerated aging to a systemic inflammatory response. *Genes Dev*. 2012; 26:2311–24. <https://doi.org/10.1101/gad.197954.112>

20. Adler AS, Sinha S, Kawahara TL, Zhang JY, Segal E, Chang HY. Motif module map reveals enforcement of aging by continual NF-kappaB activity. *Genes Dev.* 2007; 21:3244–57. <https://doi.org/10.1101/gad.1588507>
21. Chung HY, Cesari M, Anton S, Marzetti E, Giovannini S, Seo AY, Carter C, Yu BP, Leeuwenburgh C. Molecular inflammation: underpinnings of aging and age-related diseases. *Ageing Res Rev.* 2009; 8:18–30. <https://doi.org/10.1016/j.arr.2008.07.002>
22. Balistreri CR, Candore G, Accardi G, Colonna-Romano G, Lio D. NF-κB pathway activators as potential ageing biomarkers: targets for new therapeutic strategies. *Immun Ageing.* 2013; 10:24. <https://doi.org/10.1186/1742-4933-10-24>
23. Alameda JP, Fernández-Aceñero MJ, Quintana RM, Page A, Ramírez Á, Navarro M, Casanova ML. Functional inactivation of CYLD promotes the metastatic potential of tumor epidermal cells. *J Invest Dermatol.* 2013; 133:1870–78. <https://doi.org/10.1038/jid.2013.76>
24. Ramírez A, Bravo A, Jorcano JL, Vidal M. Sequences 5' of the bovine keratin 5 gene direct tissue- and cell-type-specific expression of a lacZ gene in the adult and during development. *Differentiation.* 1994; 58:53–64.
25. Chase HB. Growth of the hair. *Physiol Rev.* 1954; 34:113–26. <https://doi.org/10.1152/physrev.1954.34.1.113>
26. Krishnamurthy J, Torrice C, Ramsey MR, Kovalev GI, Al-Regaiey K, Su L, Sharpless NE. Ink4a/Arf expression is a biomarker of aging. *J Clin Invest.* 2004; 114:1299–307. <https://doi.org/10.1172/JCI22475>
27. Ressler S, Bartkova J, Niederegger H, Bartek J, Scharffetter-Kochanek K, Jansen-Dürr P, Wlaschek M. p16INK4A is a robust in vivo biomarker of cellular aging in human skin. *Aging Cell.* 2006; 5:379–89. <https://doi.org/10.1111/j.1474-9726.2006.00231.x>
28. Bohr VA. Deficient DNA repair in the human progeroid disorder, Werner syndrome. *Mutat Res.* 2005; 577:252–59. <https://doi.org/10.1016/j.mrfmmm.2005.03.021>
29. Reiley W, Zhang M, Sun SC. Negative regulation of JNK signaling by the tumor suppressor CYLD. *J Biol Chem.* 2004; 279:55161–67. <https://doi.org/10.1074/jbc.M411049200>
30. Aw D, Palmer DB. The origin and implication of thymic involution. *Aging Dis.* 2011; 2:437–43.
31. George AJ, Ritter MA. Thymic involution with ageing: obsolescence or good housekeeping? *Immunol Today.* 1996; 17:267–72. [https://doi.org/10.1016/0167-5699\(96\)80543-3](https://doi.org/10.1016/0167-5699(96)80543-3)
32. Bektas A, Zhang Y, Lehmann E, Wood WH 3rd, Becker KG, Madara K, Ferrucci L, Sen R. Age-associated changes in basal NF-κB function in human CD4+ T lymphocytes via dysregulation of PI3 kinase. *Aging (Albany NY).* 2014; 6:957–74. <https://doi.org/10.18632/aging.100705>
33. Slavin BG, Paaule WJ, Bernick S. Edited by Johnson John E., Jr. Morphological changes in the aging mammalian pancreas. In "Aging and Cell Structure", North Campus Library Plenum Press New York and London. 1945; 2: 198-206.
34. Zinger A, Cho WC, Ben-Yehuda A. Cancer and aging - the inflammatory connection. *Aging Dis.* 2017; 8:611–27. <https://doi.org/10.14336/AD.2016.1230>
35. Sueki H, Stoudemayer T, Kligman AM, Murphy GF. Quantitative and ultrastructural analysis of inflammatory infiltrates in male pattern alopecia. *Acta Derm Venereol.* 1999; 79:347–50. <https://doi.org/10.1080/000155599750010238>
36. Jin YJ, Wang S, Cho J, Selim MA, Wright T, Mosialos G, Zhang JY. Epidermal CYLD inactivation sensitizes mice to the development of sebaceous and basaloid skin tumors. *JCI Insight.* 2016; 1:e86548. <https://doi.org/10.1172/jci.insight.86548>
37. Arnold I, Watt FM. c-Myc activation in transgenic mouse epidermis results in mobilization of stem cells and differentiation of their progeny. *Curr Biol.* 2001; 11:558–68. [https://doi.org/10.1016/S0960-9822\(01\)00154-3](https://doi.org/10.1016/S0960-9822(01)00154-3)
38. Matheu A, Maraver A, Collado M, García-Cao I, Cañamero M, Borrás C, Flores JM, Klatt P, Viña J, Serrano M. Anti-aging activity of the Ink4/Arf locus. *Aging Cell.* 2009; 8:152–61. <https://doi.org/10.1111/j.1474-9726.2009.00458.x>
39. Xue L, Igaki T, Kuranaga E, Kanda H, Miura M, Xu T. Tumor suppressor CYLD regulates JNK-induced cell death in *Drosophila*. *Dev Cell.* 2007; 13:446–54. <https://doi.org/10.1016/j.devcel.2007.07.012>
40. Hinojosa CA, Akula Suresh Babu R, Rahman MM, Fernandes G, Boyd AR, Orihuela CJ. Elevated A20 contributes to age-dependent macrophage dysfunction in the lungs. *Exp Gerontol.* 2014; 54:58–66. <https://doi.org/10.1016/j.exger.2014.01.007>
41. Tyner SD, Venkatachalam S, Choi J, Jones S, Ghebranious N, Igelmann H, Lu X, Soron G, Cooper B,

- Brayton C, Park SH, Thompson T, Karsenty G, et al. p53 mutant mice that display early ageing-associated phenotypes. *Nature*. 2002; 415:45–53. <https://doi.org/10.1038/415045a>
42. Kamenisch Y, Berneburg M. Progeroid syndromes and UV-induced oxidative DNA damage. *J Invest Dermatol Symp Proc*. 2009; 14:8–14. <https://doi.org/10.1038/jidsymp.2009.6>
 43. Trüeb RM. Aging of hair. *J Cosmet Dermatol*. 2005; 4:60–72. <https://doi.org/10.1111/j.1473-2165.2005.40203.x>
 44. Rittié L, Fisher GJ. Natural and sun-induced aging of human skin. *Cold Spring Harb Perspect Med*. 2015; 5:a015370. <https://doi.org/10.1101/cshperspect.a015370>
 45. Kondratov RV, Kondratova AA, Gorbacheva VY, Vykhovanets OV, Antoch MP. Early aging and age-related pathologies in mice deficient in BMAL1, the core component of the circadian clock. *Genes Dev*. 2006; 20:1868–73. <https://doi.org/10.1101/gad.1432206>
 46. Montagna W, Carlisle K. Structural changes in aging human skin. *J Invest Dermatol*. 1979; 73:47–53. <https://doi.org/10.1111/1523-1747.ep12532761>
 47. Bernal GM, Wahlstrom JS, Crawley CD, Cahill KE, Pytel P, Liang H, Kang S, Weichselbaum RR, Yamini B. Loss of Nfkb1 leads to early onset aging. *Aging (Albany NY)*. 2014; 6:931–43. <https://doi.org/10.18632/aging.100702>
 48. Freund A, Orjalo AV, Desprez PY, Campisi J. Inflammatory networks during cellular senescence: causes and consequences. *Trends Mol Med*. 2010; 16:238–46. <https://doi.org/10.1016/j.molmed.2010.03.003>
 49. Budunova IV, Perez P, Vaden VR, Spiegelman VS, Slaga TJ, Jorcano JL. Increased expression of p50-NF-kappaB and constitutive activation of NF-kappaB transcription factors during mouse skin carcinogenesis. *Oncogene*. 1999; 18:7423–31. <https://doi.org/10.1038/sj.onc.1203104>
 50. Alameda JP, Gaspar M, Ramírez Á, Navarro M, Page A, Suárez-Cabrera C, Fernández MG, Mérida JR, Paramio JM, García-Fernández RA, Fernández-Aceñero MJ, Casanova ML. Deciphering the role of nuclear and cytoplasmic IKK α in skin cancer. *Oncotarget*. 2016; 7:29531–47. <https://doi.org/10.18632/oncotarget.8792>
 51. Segrelles C, García-Escudero R, Garín MI, Aranda JF, Hernández P, Ariza JM, Santos M, Paramio JM, Lorz C. Akt signaling leads to stem cell activation and promotes tumor development in epidermis. *Stem Cells*. 2014; 32:1917–28. <https://doi.org/10.1002/stem.1669>
 52. Munn LL. Cancer and inflammation. *Wiley Interdiscip Rev Syst Biol Med*. 2017; 9:e1370. <https://doi.org/10.1002/wsbm.1370>
 53. Massoumi R. CYLD: a deubiquitination enzyme with multiple roles in cancer. *Future Oncol*. 2011; 7:285–97. <https://doi.org/10.2217/fon.10.187>
 54. Alameda JP, Fernández-Aceñero MJ, Moreno-Maldonado R, Navarro M, Quintana R, Page A, Ramírez A, Bravo A, Casanova ML. CYLD regulates keratinocyte differentiation and skin cancer progression in humans. *Cell Death Dis*. 2011; 2:e208. <https://doi.org/10.1038/cddis.2011.82>

SUPPLEMENTARY MATERIAL

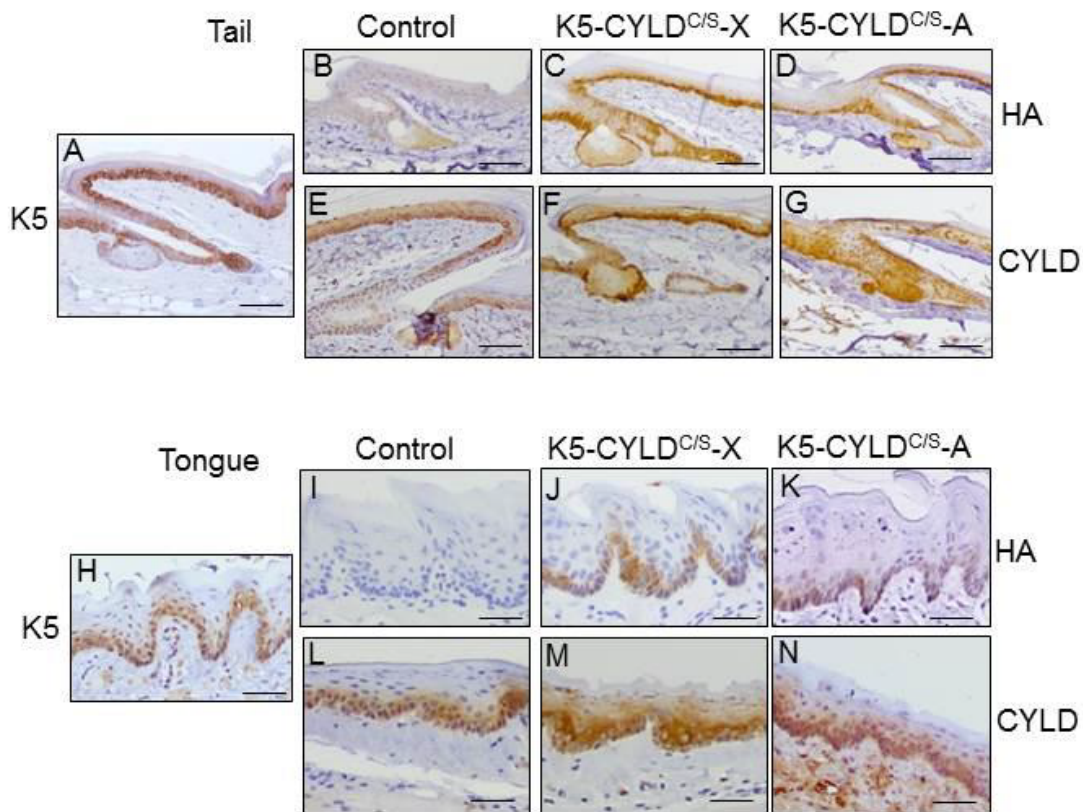


Figure S1. Analysis of the transgene expression in tail skin and tongue. (A) Representative staining of K5 in the skin of a control mouse. (B-D) HA and (E-G) CYLD expression in the tail skin of Control and transgenic mice. Observe that HA is not detected in Control sections (B), while HA expression in the tail of K5-CYLD^{C/S} mice follows the K5 expression pattern (C-D). (H) Representative sections showing the expression of K5 in the tongue of a control mouse. (I-K) HA and (L-N) CYLD expression in the tongue of Control and transgenic mice. HA is not expressed in the tongue of Control mice (I), while HA expression in the tongue of transgenic mice follows the K5 expression pattern in control mice (J, K). Sections correspond to 1-month-old mice. Scale bars: (A-D) 220 μ m; (E-G) 200 μ m; (H, J, K); 180 μ m; (I, L-N) 160 μ m.

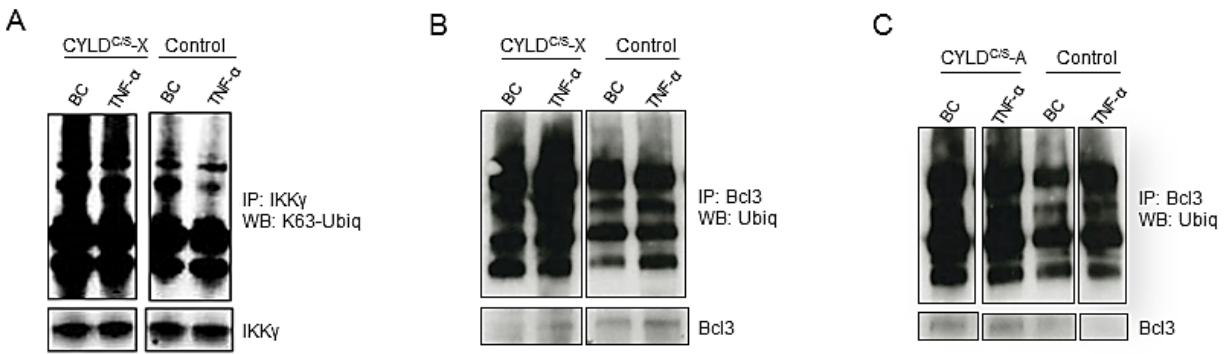


Figure S2. Lack of CYLD DUB function in the K5-CYLD^{C/S} mice. Functional analysis of the CYLD^{C/S} transgene, by IP of back skin protein extracts with an IKKγ or Bcl3 specific antibodies, in the presence and absence of TNF-α. Western blots using Ubiquitin and IKKγ specific antibodies are shown. **(A)** Observe the lack of DUB function in transgenic mice checked as elevated levels of polyubiquitinated IKKγ in both the basal condition (BC) and after TNF-α treatment. **(B, C)** Observe the increased levels of ubiquitinated Bcl3 in the back skin of transgenic mice in both states: without TNF-α stimulation (BC, basal condition), and after TNF-α treatment. Similar results were obtained for both K5-CYLD^{C/S-X} **(B)** and K5-CYLD^{C/S-A} **(C)** mice. BC: basal condition, i.e., without TNF-α stimulation. **(A, B)** when indicated, cells were incubated for 15 min with TNF-α treatment; **(C)** when indicated cells were incubated 40 min with TNF-α.



Figure S3. External phenotype of the K5-CYLD^{C/S} mice. Representative image showing kyphosis in the back of a transgenic mouse. Both Control and K5-CYLD^{C/S} mice are littermates of 11 months-old.

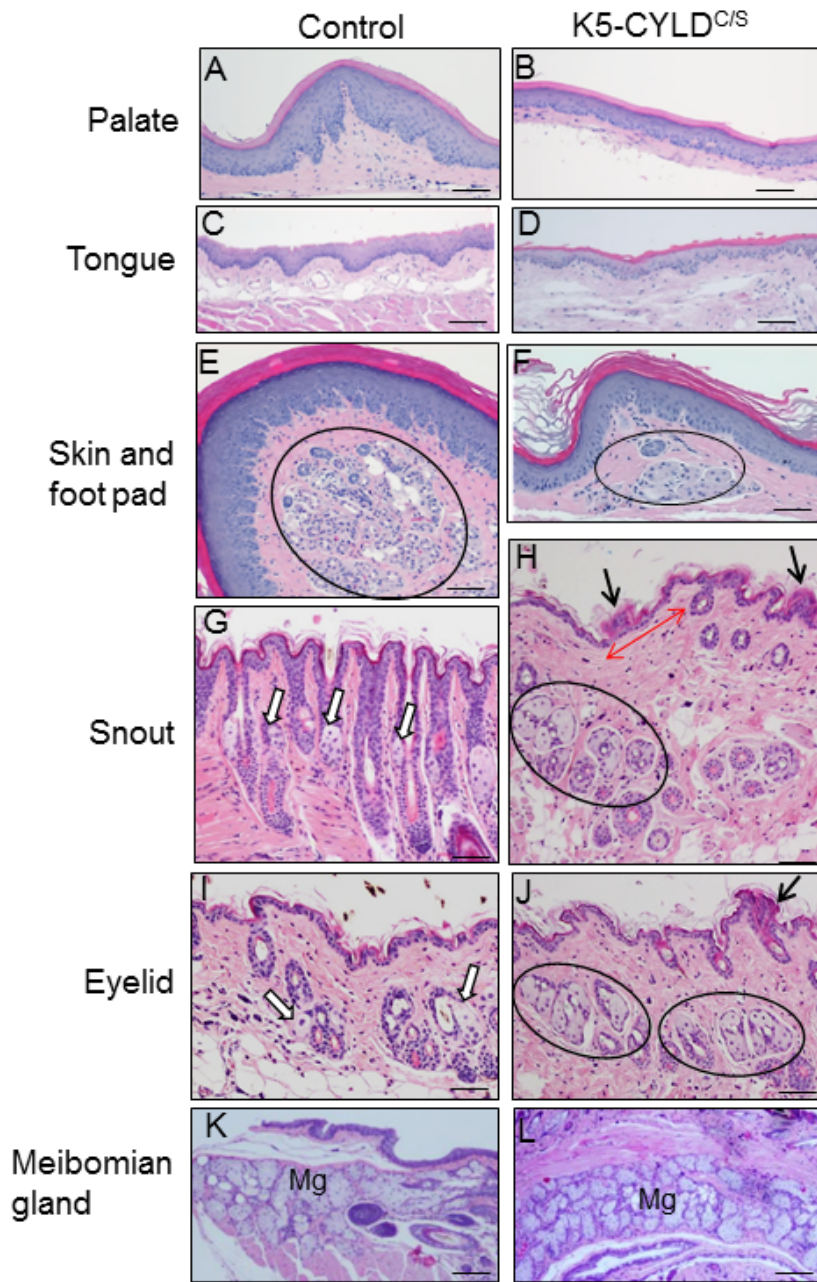


Figure S4. Histological analysis showing the premature aging of different epithelia of the K5-CYLD^{C/S} mice. Sections from both Control (A, C, E, G, I, K) and transgenic mice (B, D, F, H, J, L) of 5- (G-J) and 20-month-old are shown. (A, B) Palate epithelium; note the atrophy in that of K5-CYLD^{C/S} mice (B). (C, D) Stratified epithelium of the tongue. Note the thinning of the epithelium in transgenic mice (D). (E, F) Scarce eccrine glands in the hind limb foot pads of the K5-CYLD^{C/S} mice are appreciated (circle). (G, H) Snout skin of 5-month-old mice. Highly abundant hyperplastic sebaceous glands are observed in the transgenic mice (circles in H); additionally, an atrophic epidermal area (double-headed red arrow) and epidermal ridges (black arrows) are shown. Eyelid skin of 5-month-old mice (I, J); note the presence of numerous hyperplastic sebaceous glands in the K5-CYLD^{C/S} mice (enclosed in circles), in clear contrast with those found in the corresponding tissue of Control mice (I, white arrows). Also note the absence adipose tissue in the eyelid transgenic mice and the presence of epidermal ridges (J, black arrows). (K, L) Note the abundant hyperplastic Meibomian glands (Mg) found in the eyelids of K5-CYLD^{C/S} mice (L) compared to those in Control mice (K). Images from 20-month-old mice are showed, although similar alterations are found in young transgenic mice (from 3 months-old). Scale bars: 250 μ m (A-F, K, L); 150 μ m (G, H) 230 μ m (I, J).

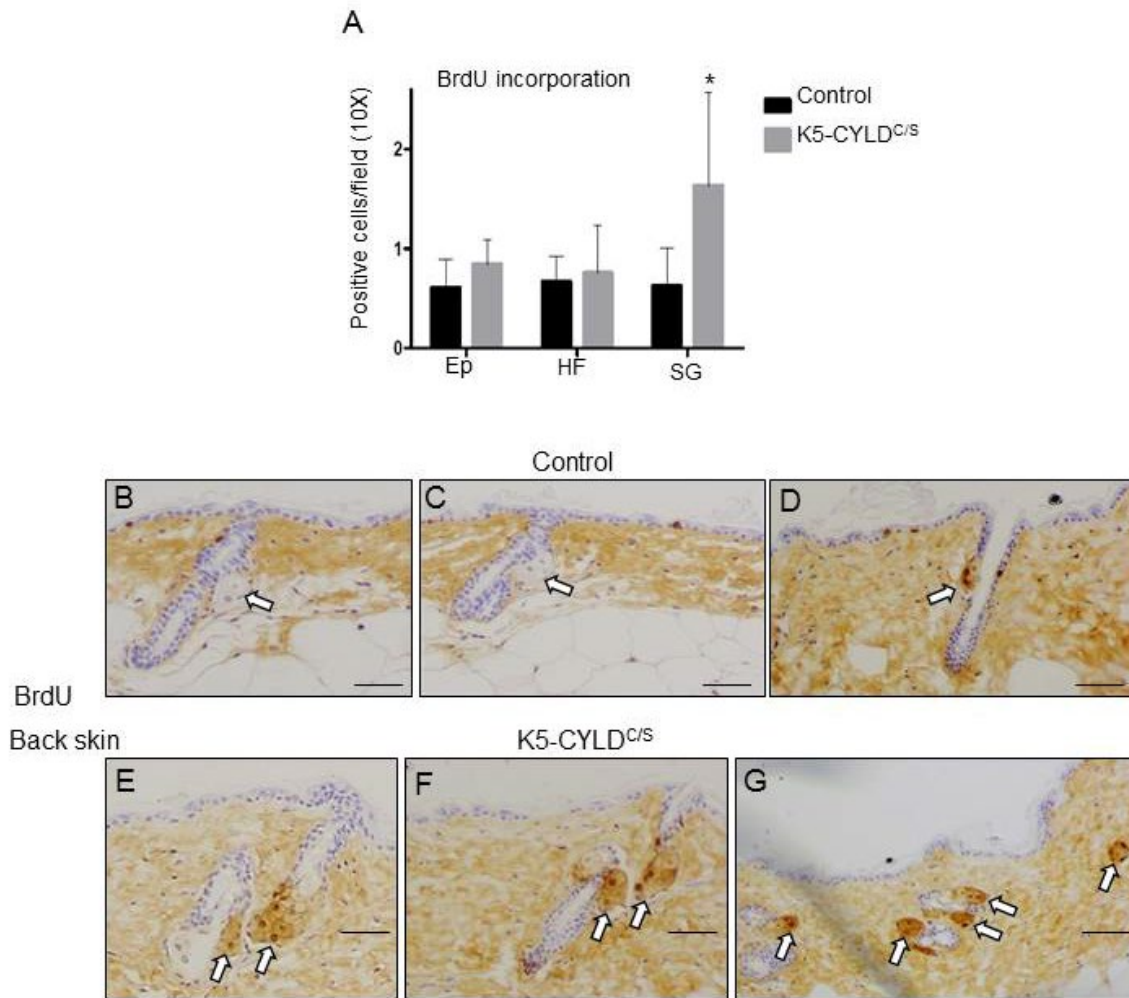


Figure S5. BrdU analysis in the back skin of Control and K5-CYLD^{C/S} mice. (A) BrdU incorporation in the back skin of 1-year-old mice. Note the increased proliferation of the sebaceous glands from transgenic mice (4 Control and 5 transgenic mice were analyzed; error bars represent SEM; *P* value by Bonferroni multiple comparisons test: two-way ANOVA). *P*<0.05. (B-G) Representative image showing the BrdU staining in Control (B-D) and transgenic (E-G) sections of back skin. Observe the increased BrdU incorporation in the sebaceous glands of the K5-CYLD^{C/S} mice. Scale bars: 150 μ m. Ep: epidermis; HF: hair follicles; SG: sebaceous glands.

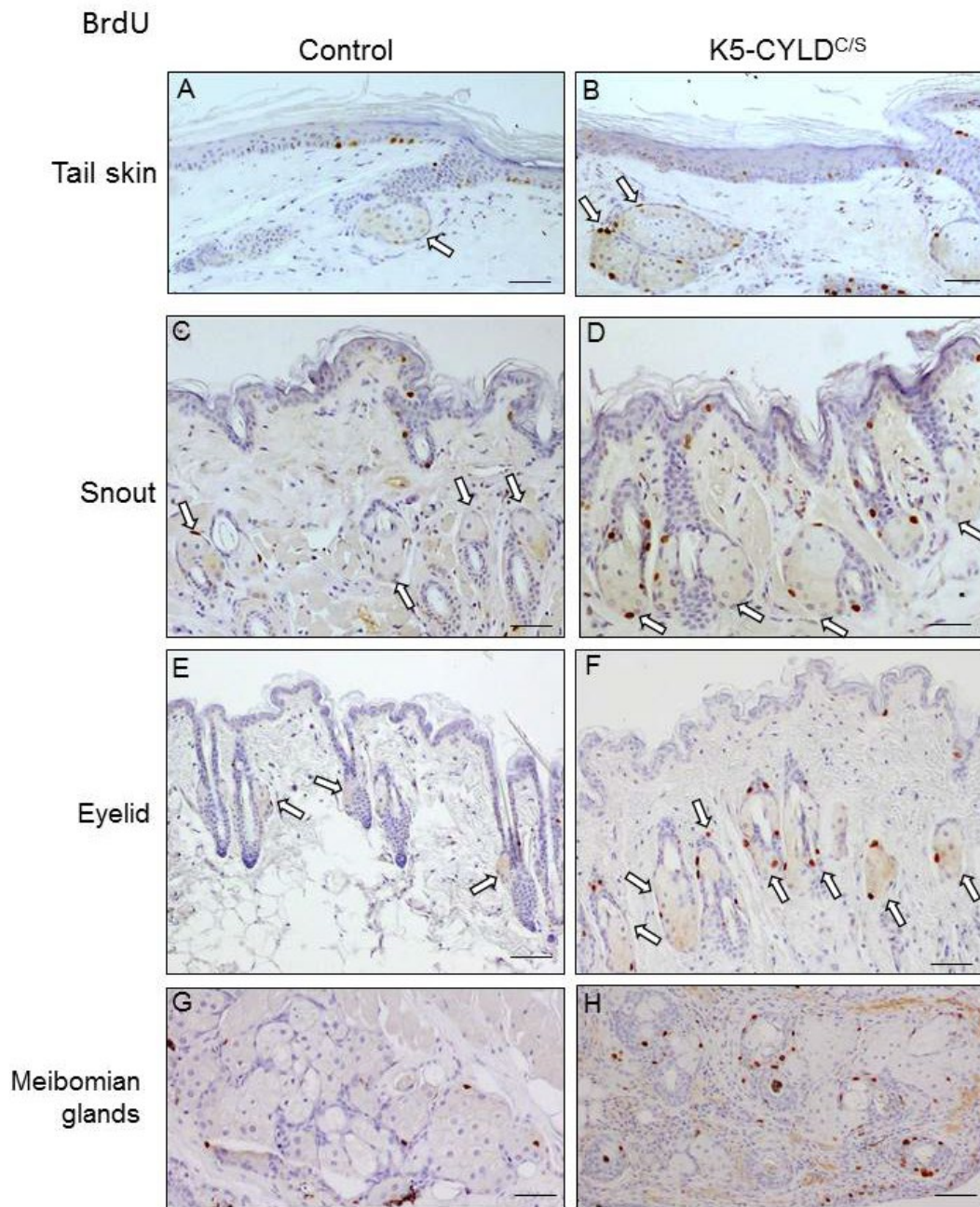


Figure S6. BrdU incorporation in the skin of Control and K5-CYLD^{C/S} mice. BrdU staining in Control (A, C, E, G) and transgenic (B, D, F, H) sections showing increased signal in the hyperplastic sebaceous glands of the tail, snout and eyelid skin of the K5-CYLD^{C/S} mice (B, D, F); as well as in the Meibomian glands (H) of the transgenic mice. White arrows point to sebaceous glands. Scale bars: 140 μ m (A-F); 110 μ m (G, H).

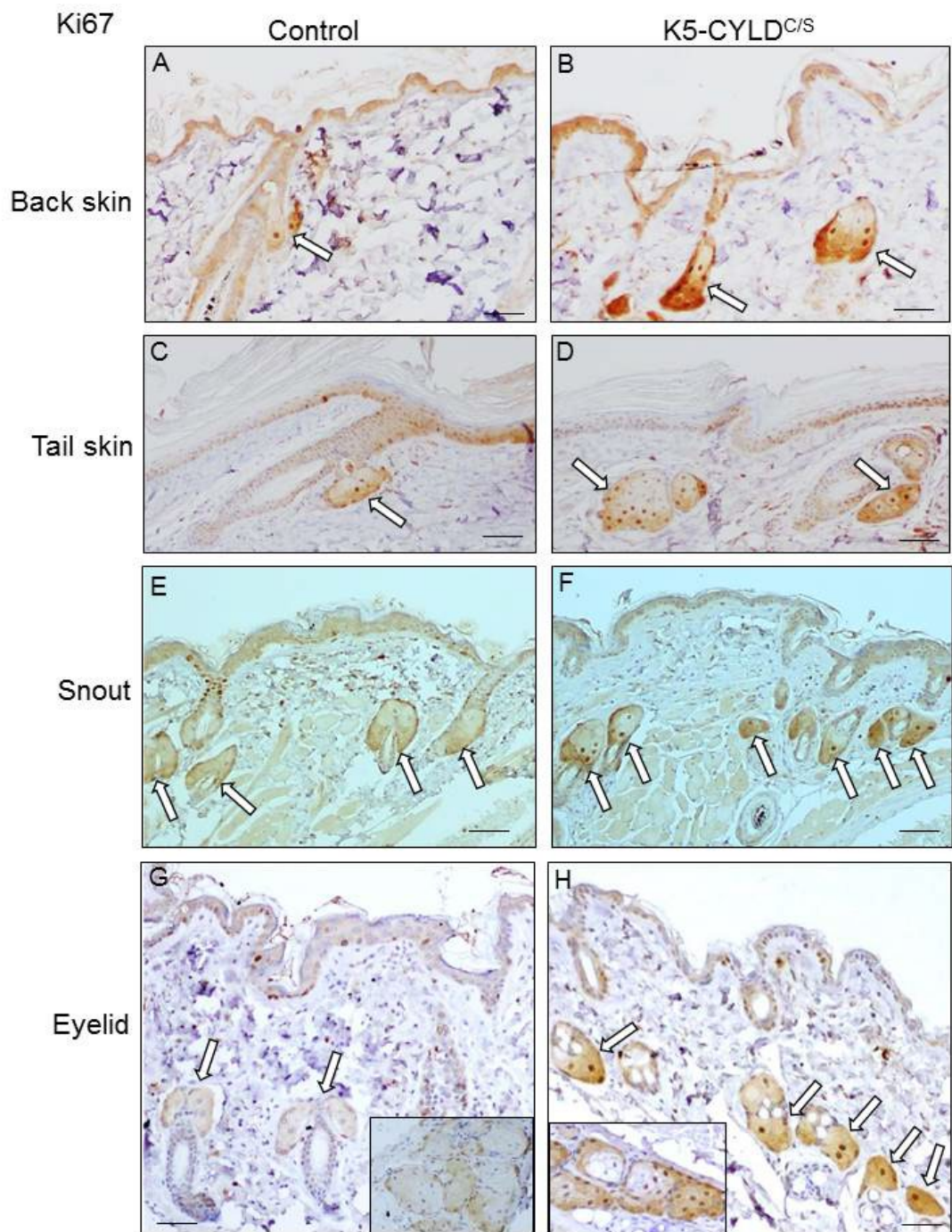


Figure S7. Analysis of cell proliferation in the skin of Control and K5-CYLD^{C/S} mice. Ki67 staining in Control (A, C, E, G) and transgenic (B, D, F, H) sections showing increased signal in the hyperplastic sebaceous glands of the back, tail, snout and eyelid skin of transgenic mice. Also note that Meibomian glands of the K5-CYLD^{C/S} mice are more proliferative than those of Control mice (compare insets in G and H). White arrows point to sebaceous glands. Scale bars: 160 μ m (A-F); 120 μ m (G, H).

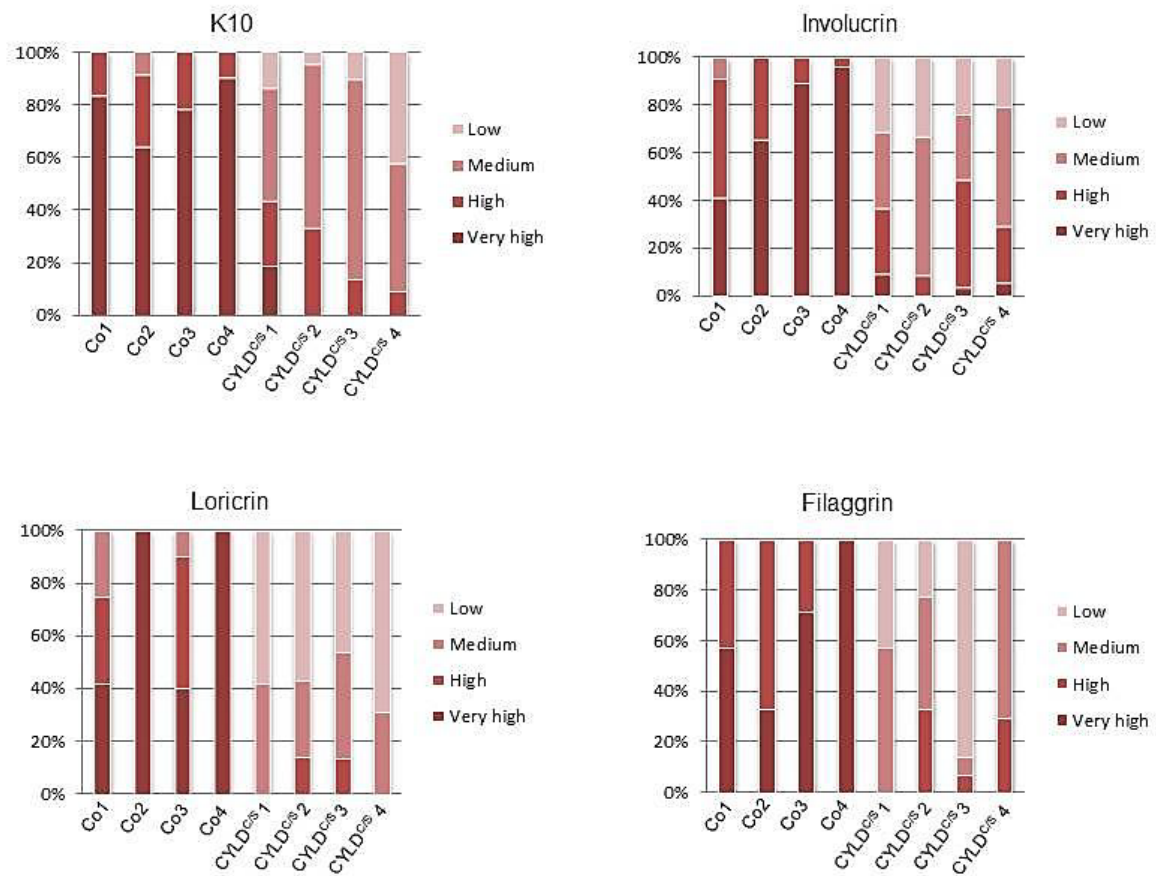


Figure S8. Semiquantitative analysis of the intensity of the expression of epidermal differentiation markers in Control and K5-CYLD^{C/S} mice. 10-15 fields, 10X magnification, corresponding to K10, Involucrin, Loricrin and Filaggrin immunostainings were analyzed and quantified as very high, high, medium or low expression. Analysis of the expression in 4 animals per genotype and staining is showed. Co: Control animals; CYLD^{C/S}: K5-CYLD^{C/S} transgenic mice.

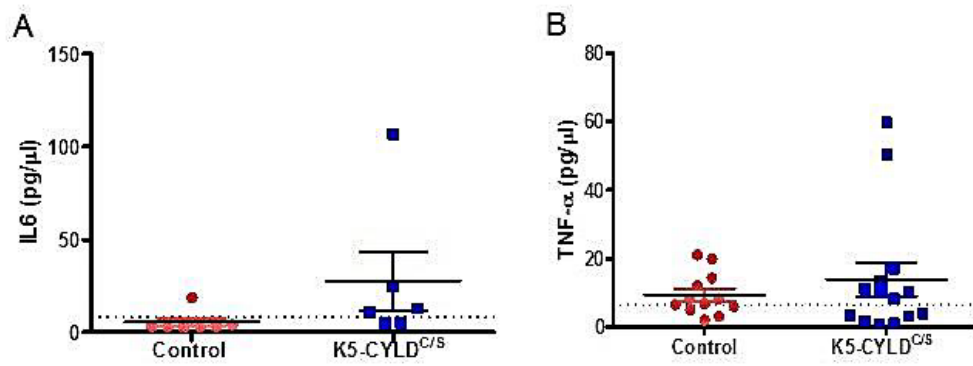


Figure S9. Increased levels of IL6 and TNF- α in the serum of K5-CYLD^{C/S} mice. IL6 (A) and TNF- α (B) serum levels from 8 Control and 8 transgenic mice of both 16 and 22 months-old (i.e., a total of 16 control and 16 transgenic animals) were analyzed. Results show increased levels of both cytokines in the serum of transgenic mice, mainly of IL-6.

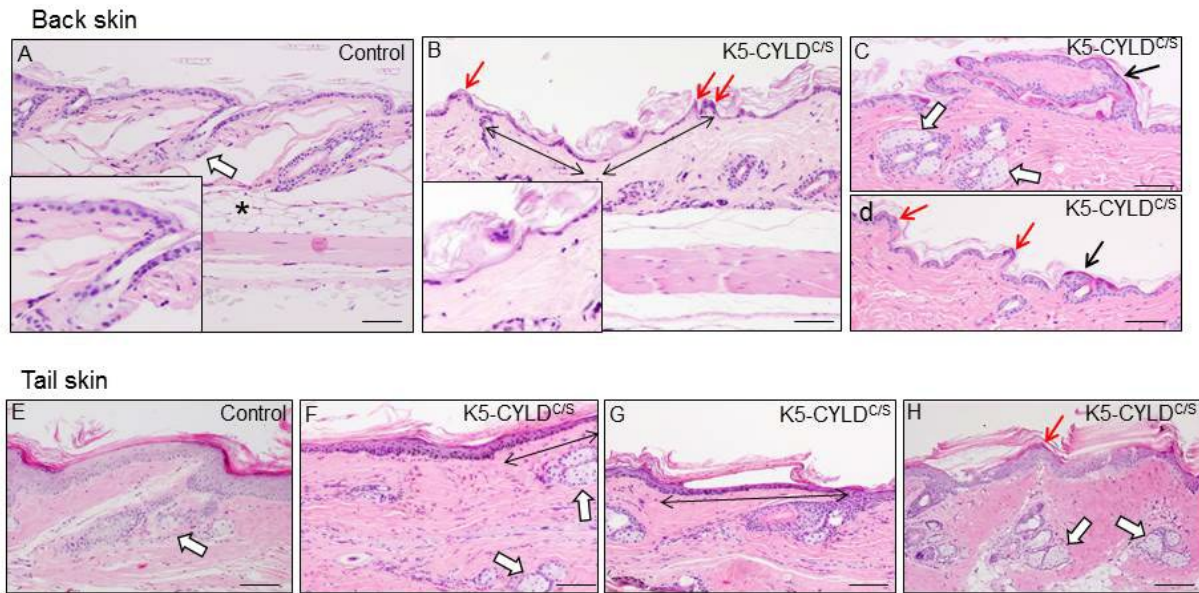


Figure S10. Phenotypic alterations in the skin of FVB/N-K5-CYLD^{C/S} mice indicating that premature aging signs are independent of their genetic background. Representative images showing the main histological alterations presented by K5-CYLD^{C/S} mice developed in a FVB/N genetic background (these are coincident with that observed in B6D2-transgenic mice). (A-D) Back skin sections from Control (A) and FVB/N-transgenic mice (B-D); (E-H) tail skin images from Control (E) and FVB/N-transgenic (F-H) mice. Observe areas of atrophy in the epidermis of the FVB/N-K5-CYLD^{C/S} mice (double-headed arrows in B,F,G; compare inserts in A,B); epidermal ridges of pyknotic keratinocytes (red arrows in B,D,H); papillomatous hyperplasia (black arrows in C, D); hyperplastic and orphan sebaceous glands (white arrows in C,F,H) compared with normal-size sebaceous glands in Control (white arrows in A, E). Reduced number of hair follicles (C, F, H), and scarce adipose tissue (B) is observed in FVB/N-transgenic mice; asterisk in (A) indicates fat tissue in Control mice hypodermis. Five animals of each genotype (18-20-month-old) were analyzed. Scale bars: 250 μ m (A-D); 300 μ m (E-H).

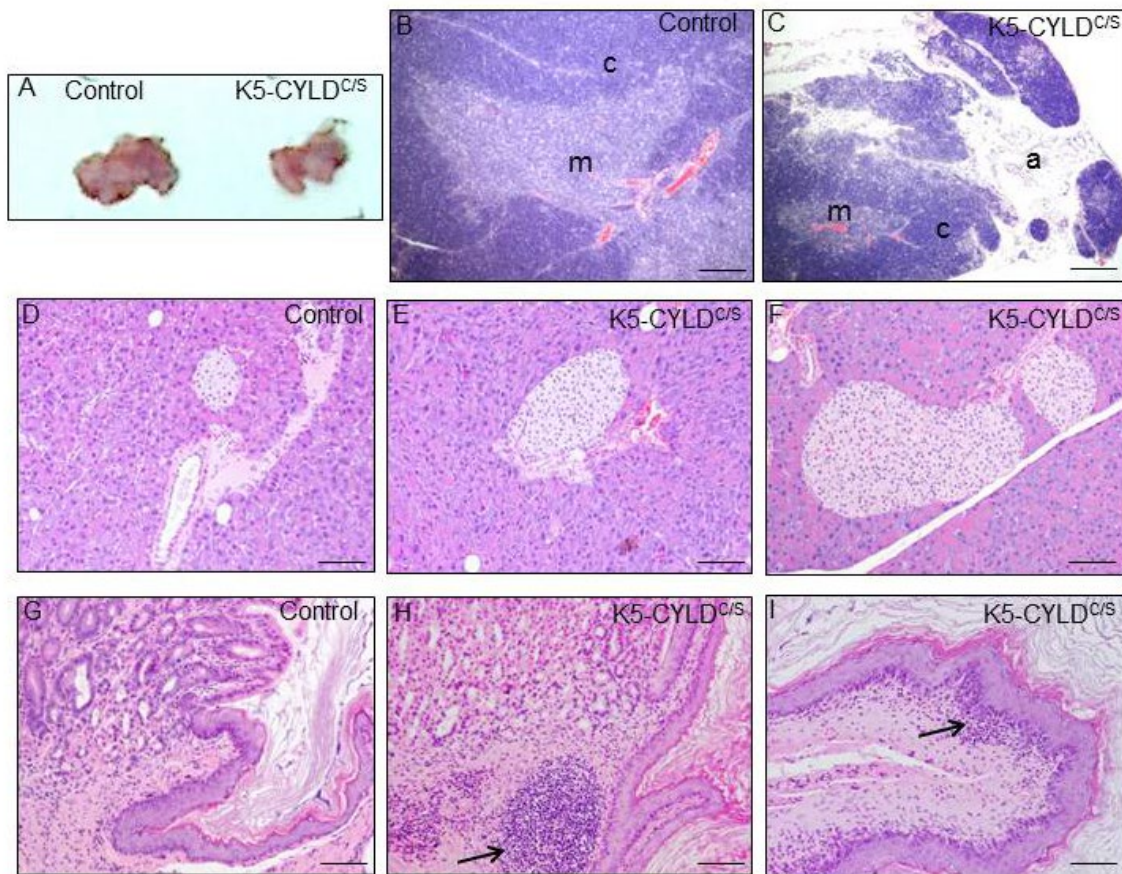


Figure S11. Signs of premature aging in the thymus, pancreas and stomach of FVB/N-K5-CYLD^{C/S} mice. (A) Representative images showing the smaller size of the thymus of 3-month-old FVB/N-transgenic mice. (B, C) Thymic atrophy and infiltration of white adipose tissue (A) in the thymus of FVB/N-transgenic mice (C) compared to thymus of age-matched Control mice (b). Histopathologic analysis of pancreas (D-F) and stomach (G-I) from 18-month-old Control (D, G) and FVB/N-transgenic (E, F, H, I) mice. Note the hyperplasia of the Islets of Langerhans in the FVB/N-K5-CYLD^{C/S} mice (E, F). (H, I) Representative images showing foci of inflammation in the stomach of FVB/N-transgenic mice (black arrows). Scale bars: 400 μ m (B, C); 200 μ m (D-F); 250 μ m (G-I).

A FVB/N-K5-CYLD^{C/S} mice develop spontaneous tumors

FVB/N Mouse genotype	Lung ADC	Mammary ADC
Control	0/5	0/3*
K5-CYLD ^{C/S-X}	2/5	1/3*

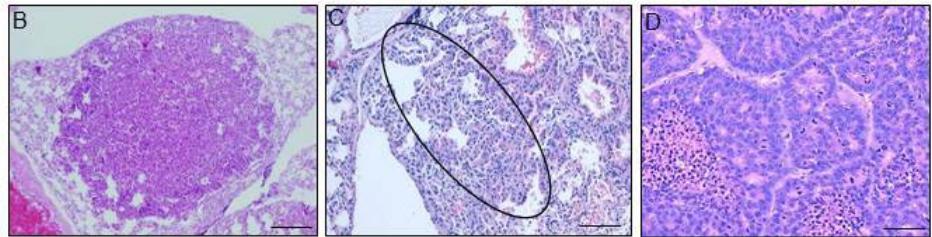


Figure S12. K5-CYLD^{C/S} mice develop spontaneous tumors independently of their genetic background. Control and transgenic mice (FVB/N background) were analyzed (3 females and 2 males). (A) Lung and mammary adenocarcinomas were detected in aging FVB/N-K5-CYLD^{C/S} mice. Number of animals that have developed each type of tumor, as well as the number of mice that have been analyzed is shown. (B) Image of lepidic lung adenocarcinoma developed in a FVB/-N-transgenic mouse. (C) Atypical adenomatous hyperplasia of lung in a FVB/N-K5-CYLD^{C/S} mouse (circle). (D) Mammary adenocarcinoma of high grade in a female FVB/N-transgenic mouse. ADC: Adenocarcinoma; (*): female mice. Scale bars: 500 μ m (A); 150 μ m (B, C).

Table S1. Number of mice whose skin has been analyzed.

Genotype	Age (months)							
	1 m	3 m	5 m	8 m	12m	20 m	21-24 m	25-30 m
Control	4	6	5	4	4	7	4	8
K5-CYLD^{C/S-X}	4	6	5	4	5	10	3	9

The number of animals analyzed at the indicated months of age is showed.

Table S2: Number of mice whose thymus has been analyzed.

Genotype	Age (months)			
	1m	2.5 m	3m	3.5m
Control	3	3	8	3
K5-CYLD^{C/S-X}	3	3	8	3

The number of animals analyzed at the indicated months of age is showed.

Long noncoding RNA LINC00963 induces NOP2 expression by sponging tumor suppressor miR-542-3p to promote metastasis in prostate cancer

Feng Sun^{1,*}, Ke Wu^{1,*}, Zhixian Yao^{1,*}, Xingyu Mu^{1,*}, Zhong Zheng¹, Menghao Sun¹, Yong Wang¹, Zhihong Liu¹, Yiyong Zhu¹

¹Department of Urology, Shanghai General Hospital, Shanghai Jiao Tong University School of Medicine, Shanghai 200080, China

*Equal contribution

Correspondence to: Zhihong Liu, Yiyong Zhu; **email:** drzhihongliu@sjtu.edu.cn, zyy1017@hotmail.com

Keywords: lncRNA LINC00963, miR-542-3p, NOP2, metastasis, prostate cancer

Received: December 16, 2019

Accepted: March 30, 2020

Published: June 17, 2020

Copyright: Sun et al. This is an open-access article distributed under the terms of the Creative Commons Attribution License (CC BY 3.0), which permits unrestricted use, distribution, and reproduction in any medium, provided the original author and source are credited.

ABSTRACT

Metastatic disease caused by castration-resistant prostate cancer (CRPC) is the principal cause of prostate cancer (PCa)-related mortality. CRPC occurs within 2–3 years of initiation of androgen deprivation therapy (ADT), which is an important factor of influencing PCa metastasis. Recent studies have revealed that non-coding RNAs in PCa can enhance metastasis and progression, while the mechanisms are still unclear. In this study, we reported that the long noncoding RNA-LINC00963 was increased in CRPC tissues and promoted migration of PCa cells in vitro and their metastasis in vivo. High levels of LINC00963 significantly decreased tumor suppressor miR-542-3p, whose levels in metastasis tissues were low compared to those in non-metastasis tissues. LINC00963 promotes and miR-542-3p inhibits metastasis. Furthermore, the expression levels of LINC00963 and miR-542-3p were positively and negatively associated with the expression of NOP2. We demonstrated that NOP2 promoted PCa by activating the epithelial-mesenchymal transition (EMT) pathway. For specific mechanism, dual luciferase reporter assays showed that miR-542-3p directly binds to both 3'-untranslated region (UTR) of LINC00963 and NOP2 mRNA. Taken together, our results show that LINC00963 acts as an inducer of PCa metastasis by binding miR-542-3p, thereby promoting NOP2. This axis may have diagnostic and therapeutic potential for advanced PCa.

INTRODUCTION

Prostate cancer (PCa) remains the second major cause of male cancer-associated death in the United States. Androgen-deprivation therapy (ADT) is the primary treatment for patients with biochemically relapsed and metastatic PCa [1, 2]. Unfortunately, research has consistently shown that after an initial sensitivity to ADT, most patients generate resistance and thus progress to castration-resistant prostate cancer (CRPC) [3, 4]. Novel therapeutic drugs, namely cabazitaxel, abiraterone, and enzalutamide, have prolonged the

survival of patients with CRPC [5–7]. However, outcomes for CRPC patients remain unsatisfying. CRPC is an essential cause of distant metastasis of prostate cancer, but the mechanism is still unclear [8, 9]. Hence, understanding the intrinsic mechanism of PCa metastasis is vitally crucial for future clinical management.

It has been observed for decades that non-protein-coding RNAs may possess significant cellular functions [10, 11]. The rapid advancement of high-resolution sequencing technologies allowed the detection of

thousands of novel transcripts, now identified as long noncoding RNAs (lncRNAs), which participate in a broad spectrum of biological pathways, from gene transcription to protein translation [12, 13]. Recent research has established that aberrant regulation of lncRNAs plays pivotal roles in cell proliferation, chemoresistance, and cancer metastasis in various malignancies [14, 15]. Further, lncRNAs can also function as competing endogenous RNAs (ceRNAs) by competitively binding to miRNAs and then modulating the targets of miRNAs, resulting in abnormal expression of downstream genes [11, 16, 17]. In terms of CRPC, several studies have indicated that lncRNA HOXD-AS1 (also known as HAGLR), PCAT1, and HORAS5 promote tumor proliferation and castration resistance and may serve as potential therapeutic targets [18–20]. In the same vein, ceRNA feedback loops like HOTAIR/EZH2/miR-193a, lncRNA CCAT1/DDX5/miR-28-5p have shown a substantial effect on CRPC progression [21, 22]. Contrary to previous views, Chen and Gu have suggested that lncRNA LBCS can actively suppress the viability of CRPC by repressing Androgen Receptor (AR) signaling [23]. Although the function of lncRNAs in PCa has been widely investigated, the role of lncRNA in the process of tumorigenesis and downstream regulation of metastasis is still poorly characterized. Therefore, it is of considerable significance to illustrate the function of lncRNAs and their potential for use as diagnostic and therapeutic targets in PCa metastasis.

RESULTS

LINC00963 is increased in CRPC tissues

After the transition to CRPC, PCa is prone to distant metastases. Thus, we explored the changes of lncRNAs between PCa and CRPC. As a CRPC mouse model, we used the TRAMP mouse model, in which the oncogene SV40 Tag is expressed under the control of the probasin promoter. As previously reported, TRAMP mice castrated at the age of 12 weeks gradually developed CRPC by the age of about 24 weeks (Figure 1A). These phenomena were also verified in the ProbCre/Pten^{fl/fl} prostate cancer model (Figure 1B). To identify lncRNAs that may be involved in the emergence of CRPC, we first analyzed RNA sequencing (RNA-seq) data of 3 CRPC tissues and 3 normal PCa tissues from the TRAMP and ProbCre/Pten^{fl/fl} mouse models. We found that the expression levels of 159 and 185 lncRNAs in CRPC tissues from the TRAMP mouse (Figure 1C) and the ProbCre/Pten^{fl/fl} mouse (Figure 1D) were significantly changed (Fold change > 2, P < 0.05) compared to those of normal PCa tissues. The expression levels of the top 10 increased and RT-qPCR examined decreased lncRNAs. The trends in the expression of lncRNAs in CRPC tissues

from TRAMP mice (Figure 1E) and ProbCre/Pten^{fl/fl} mice (Figure 1F) were in line with the RNA-seq data. To explore the crucial lncRNA, we took the two sets of differentially expressed lncRNAs together. The results showed that there are 36 repeated lncRNAs in RNA-seq data (Figure 1G) and singular repeated lncRNA in RT-qPCR assays (Figure 1H).

LINC00963 silencing inhibits CRPC cell metastasis

To investigate the functions of LINC00963 in PCa cells metastasis, we examined LINC00963 expression levels in the PCa cell lines DU 145 (PCa cells extracted from brain metastases) and PC-3 (PCa cells extracted from bone metastases). We compared them to those in the normal prostate cell line, RWPE-1. The RT-qPCR analysis showed that the levels of LINC00963 in DU 145 and PC-3 cells were significantly higher than those in RWPE-1 cells (Figure 2A). Then, we knocked down LINC00963 in DU 145 cells by transfection with the SH-LINC00963 lentivirus. The expression of LINC00963 was effectively decreased in cells transfected with the SH-LINC00963 lentivirus compared with that in cells transfected with the empty lentivirus vector (Figure 2B). Furthermore, transwell invasion assays showed that LINC00963 knockdown significantly inhibited DU 145 cell invasion (Figure 2C). AAV lentiviral can be used as a vector to regulate lncRNAs levels in vivo [24]. To examine the in vivo function of LINC00963, we generated the lentiviral vector contained GFP to down-regulate the expression of LINC01234 in the prostate gland. Following injection to the tail vein, SH-LINC00963 lentivirus effectively infected the prostate, produced considerable LINC00963-GFP signal (Figure 2D), and significantly decreased the amount of LINC00963 in vivo (Figure 2E). Low levels of LINC00963 also resulted in significantly prolonged survival time (Figure 2F). To investigate the role of LINC00963 in the onset of CRPC and PCa metastasis, we used SH-LINC00963 lentivirus to knock down LINC00963 during carcinogenesis of castrated TRAMP mice (Figure 2G). We injected SH-LINC00963 lentivirus every 3 days at 8 weeks after castration for a total of 4 times. Histopathological analysis revealed that, compared to that of the isotype vector controls, the downregulation of LINC00963 resulted in significantly reduced incidence of tumor draining lymph nodes (TdLNs), liver, lung, and bone metastases (Figure 2H). To verify these results, we used SH-LINC00963 lentivirus to knock down LINC00963 during carcinogenesis of castrated ProbCre/Pten^{fl/fl} mice and obtained similar results (Figure 2I). These results were also verified in the ProbCre/Pten^{fl/fl} prostate cancer mouse model (Figure 2J). Taken together, these results showed that silencing LINC00963 could effectively inhibit progression of PCa-CRPC-metastasis.

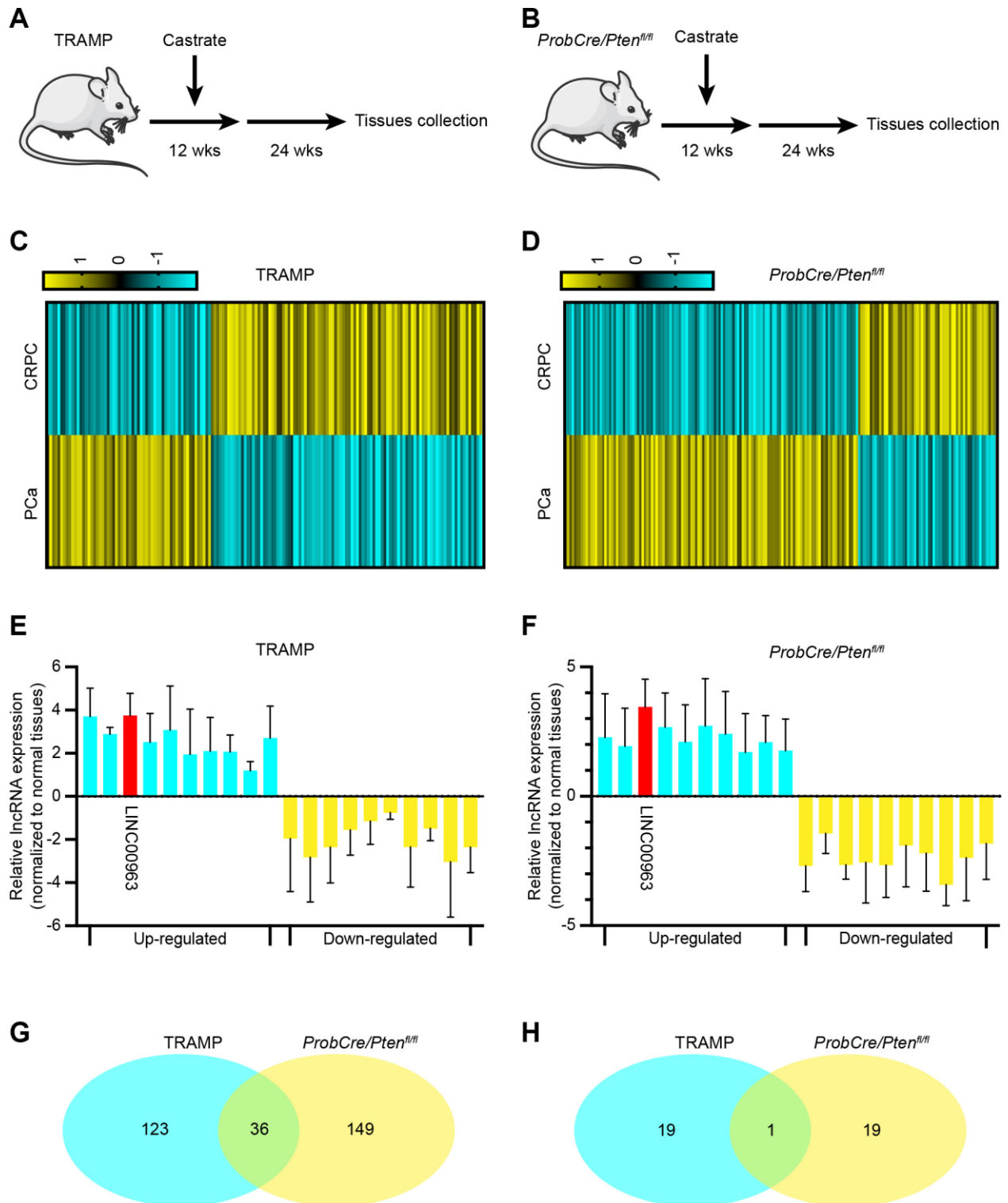


Figure 1. Long noncoding RNA LINC00963 is increased in castration-resistant prostate cancer (CRPC) tissues. (A, B) Experimental approach to construct CRPC mouse models; TRAMP mouse (A) and ProbCre/Pten^{fl/fl} mouse (B). (C, D) Heat map of differential expression of long noncoding RNAs (lncRNAs) in cells isolated from normal prostate cancer (PCa) and CRPC mouse models (C, TRAMP mouse; D, ProbCre/Pten^{fl/fl} mouse). (E, F) The expression of the 10 most apparent up- and decreased lncRNAs were analyzed by RT-qPCR in CRPC tissues and compared to those in normal PCa tissues (E, TRAMP mouse; F, ProbCre/Pten^{fl/fl} mouse). (G) Intersection of differentially expressed lncRNAs according to sequencing assays. (H) Intersection of differentially expressed lncRNAs according to RT-qPCR. Mean ± SEM.

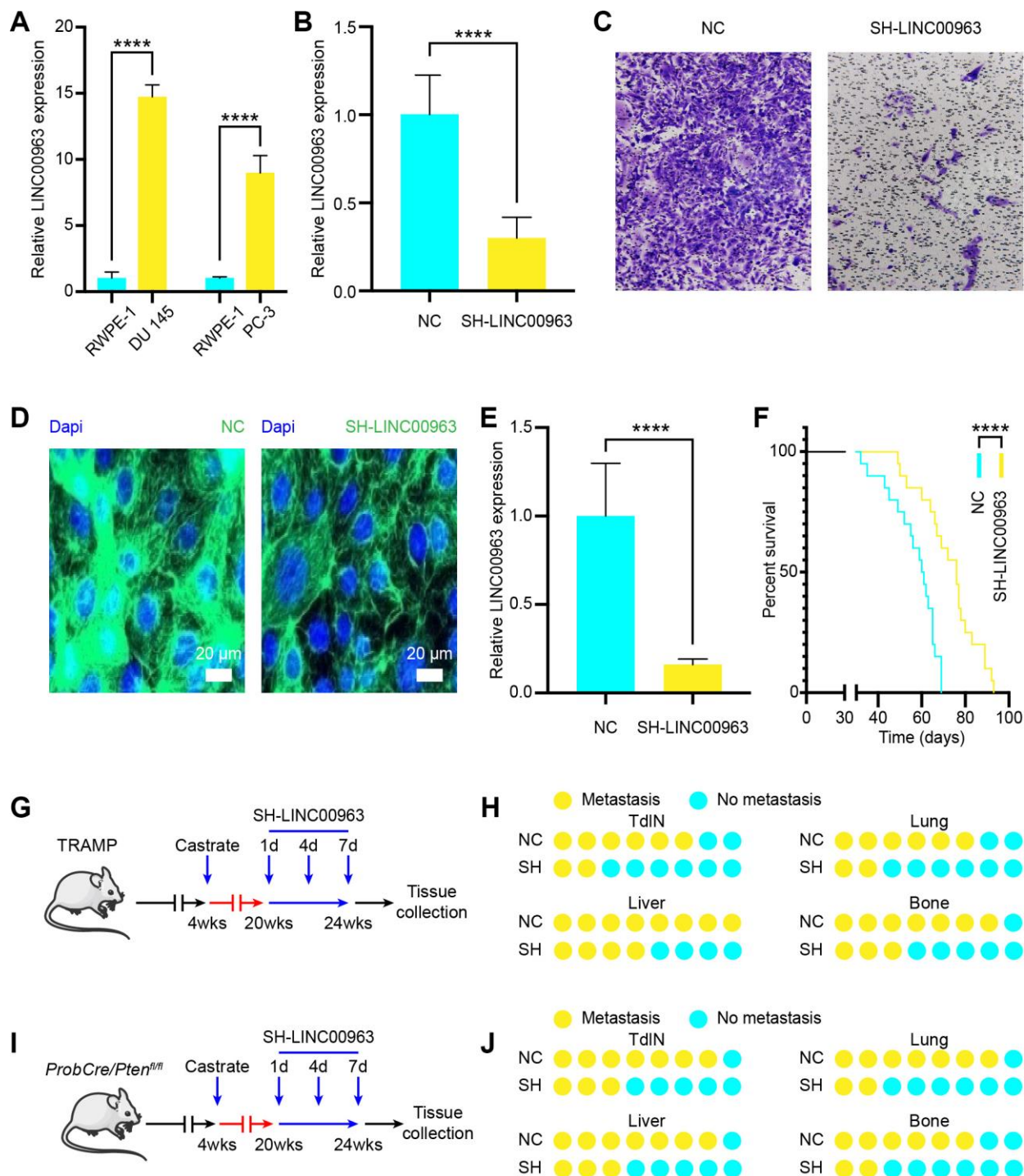


Figure 2. Effects of noncoding RNA LINC00963 on PCa cell metastasis in vitro and in vivo. (A) RT-qPCR analysis of LINC00963 expression in the PCa cell lines DU 145 and PC-3 compared to that of the normal prostate cell line RWPE-1. (B) LINC00963 expression in SH-LINC00963 Lentivirus and empty lentivirus vector-treated DU145 cells was tested using RT-qPCR. (C) Transwell invasion assays were performed to determine the invasion of SH-LINC00963 Lentivirus-transfected or empty lentivirus vector-transfected DU 145 cells. (D) A representative of the fluorescence image of LINC00963-GFP expression (green) and DAPI (blue) in SH-LINC00963 lentivirus-infected prostate of PCa mice. Scale bars = 20 μ m. (E) RT-qPCR analysis of LINC00963 expression in SH-LINC00963 Lentivirus-transfected or empty lentivirus vector-transfected PCa tissues. (F) Survival time of PCa mice injected with SH-LINC00963 Lentivirus or empty lentivirus vector. (G) Experimental approach to knock down LINC00963 in castrated TRAMP mice. (H) Incidence of TdLN, liver, lung, and bone metastases following injection with SH-LINC00963 Lentivirus or empty lentivirus vector in castrated TRAMP mice ($n = 10$, every group). (I) The experimental approach to knock down LINC00963 in castrated ProbCre/Pten^{fl/fl} mice. (J) Incidence of TdLN, liver, lung, and bone metastases following injection with SH-LINC00963 Lentivirus or empty lentivirus vector in castrated ProbCre/Pten^{fl/fl} mice ($n = 10$, every group). Mean \pm SEM, **** $P < 0.001$.

LINC00963 functions as a ceRNA and sponges miR-542-3p

Recent studies have shown that lncRNAs can regulate target gene expression by interacting with RNA-binding proteins, such as polycomb repressive complex 2 (PRC2), or by acting as ceRNAs for miRNAs [25]. To investigate the molecular mechanism by which LINC00963 promotes PC cell metastasis, we first analyzed its subcellular localization. RT-qPCR assayed the levels of LINC00963 in nuclear and cytoplasmic fractions. The isolated nuclear fraction displayed high levels of nuclear markers (U6 snRNA) but low levels of cytoplasmic markers (GAPDH). Furthermore, LINC00963 was found to be more abundant in the cytoplasm than in the nucleus (Figure 3A), suggesting that LINC00963 may regulate target gene expression at the posttranscriptional level. Indeed, RNA binding protein immunoprecipitation assays using PCa cell extracts revealed that LINC00963 binds directly to Ago2, a component of the RNA-induced silencing complex involved in miRNA-mediated repression of mRNAs (Figure 3B). This finding suggested that LINC00963 may function as a ceRNA of miRNAs. To examine this hypothesis, we used online bioinformatics databases (DIANA Tools: <http://diana.imis.athena-innovation.gr> and Starbase: <http://starbase.sysu.edu.cn/>) and observed that LINC00963 sequence contains potential miR-4731-5p, miR-511-3p, miR-542-3p, miR-1266-3p, miR-532-3p, and miR-10a-5p binding sites. We then performed dual luciferase reporter assays to confirm the prediction analysis. 293T cells were transfected with a luciferase plasmid harboring the sequence of LINC00963 together with plasmids encoding the miRNAs mentioned above or a control sequence. We found that miR-4731-5p, miR-511-3p, miR-542-3p, miR-1266-3p, miR-532-3p, and miR-10a-5p could suppress LINC00963-driven luciferase activity, and the suppression ability of miR-542-3p was stronger (Figure 3C). Hence, we chose miR-542-3p for further investigation and constructed a reporter construct in which the putative miR-542-3p binding site in the LINC00963 sequence was mutated by site-directed mutagenesis (Figure 3D). As expected, the miR-542-3p-mediated suppression of luciferase activity was abolished by the mutant LINC00963 (Figure 3E). In addition, RNA-binding protein immunoprecipitation experiments showed that LINC00963 and miR-542-3p were enriched in Ago2 immunoprecipitates compared to those of the control IgG (Figure 3F). We next evaluated the levels of miR-542-3p in DU 145 and PC-3 cells after knocking down the expression of LINC00963. Notably, the LINC00963 knockdown significantly increased the expression levels of miR-

542-3p (Figure 3G). Furthermore, we collected CRPC tissues from TRAMP and ProbCre/Pten^{fl/fl} mice and tested LINC00963/miR-542-3p levels by RT-qPCR. The results showed that there is a negative relationship between LINC00963 and miR-542-3p (Figure 3H and 3I). Taken together, these results showed that LINC00963 played as a sponge to decrease miR-542-3p.

MiR-542-3p overexpression inhibits PCa cell metastasis

To investigate the function of miR-542-3p in PCa cells, we examined miR-542-3p expression levels in the PCa cell lines DU 145 and PC-3 and compared them to the normal prostate cell line RWPE-1. The RT-qPCR analysis showed that the expression of miR-542-3p in DU 145 and PC-3 cells was significantly lower than that in RWPE-1 cells (Figure 4A). Then, we transfected DU 145 with OE-miR-542-3p lentivirus or with empty lentivirus vector and found that OE-miR-542-3p lentivirus effectively increased miR-542-3p (Figure 4B). Furthermore, transwell invasion assays showed that miR-542-3p overexpression significantly inhibited DU 145 cell invasion (Figure 4C). To examine the in vivo effects of miR-542-3p overexpression, we generated the lentiviral vector LV-miR-542-3p-GFP to overexpress miR-542-3p. Tail vein injection of LV-miR-542-3p-GFP effectively infected the prostate, produced considerable miR-542-3p-GFP signal (Figure 4D), and significantly increased the amount of miR-542-3p in vivo (Figure 4E). Furthermore, injected mice showed a significantly prolonged survival time (Figure 4F). To investigate the role of miR-542-3p in the onset of CRPC, we used LV-miR-542-3p-GFP to knock down miR-542-3p during carcinogenesis of castrated TRAMP mice (Figure 4G). We injected LV-miR-542-3p-GFP every 3 days at 8 weeks after castration for a total of four times. Histopathological analysis revealed that, compared to the isotype vector controls, overexpression of miR-542-3p resulted in significantly reduced incidence of TdLNs, liver, lung, and bone metastases in these mice (Figure 4H). To verify these results, we used LV-miR-542-3p-GFP to overexpress miR-542-3p during carcinogenesis of castrated ProbCre/Pten^{fl/fl} mice with similar results (Figure 4I). These results were also verified in the ProbCre/Pten^{fl/fl} prostate cancer mouse model (Figure 4J). Taken together, these results showed that overexpression miR-542-3p could effectively inhibit the metastasis of PCa.

NOP2 is a miR-542-3p target gene

To determine the target gene of miR-542-3p in PCa, we used RNA22 (<http://cm.jefferson.edu/rna22v1.0/>), miRmap (<http://mirmap.ezlab.org/>), microT

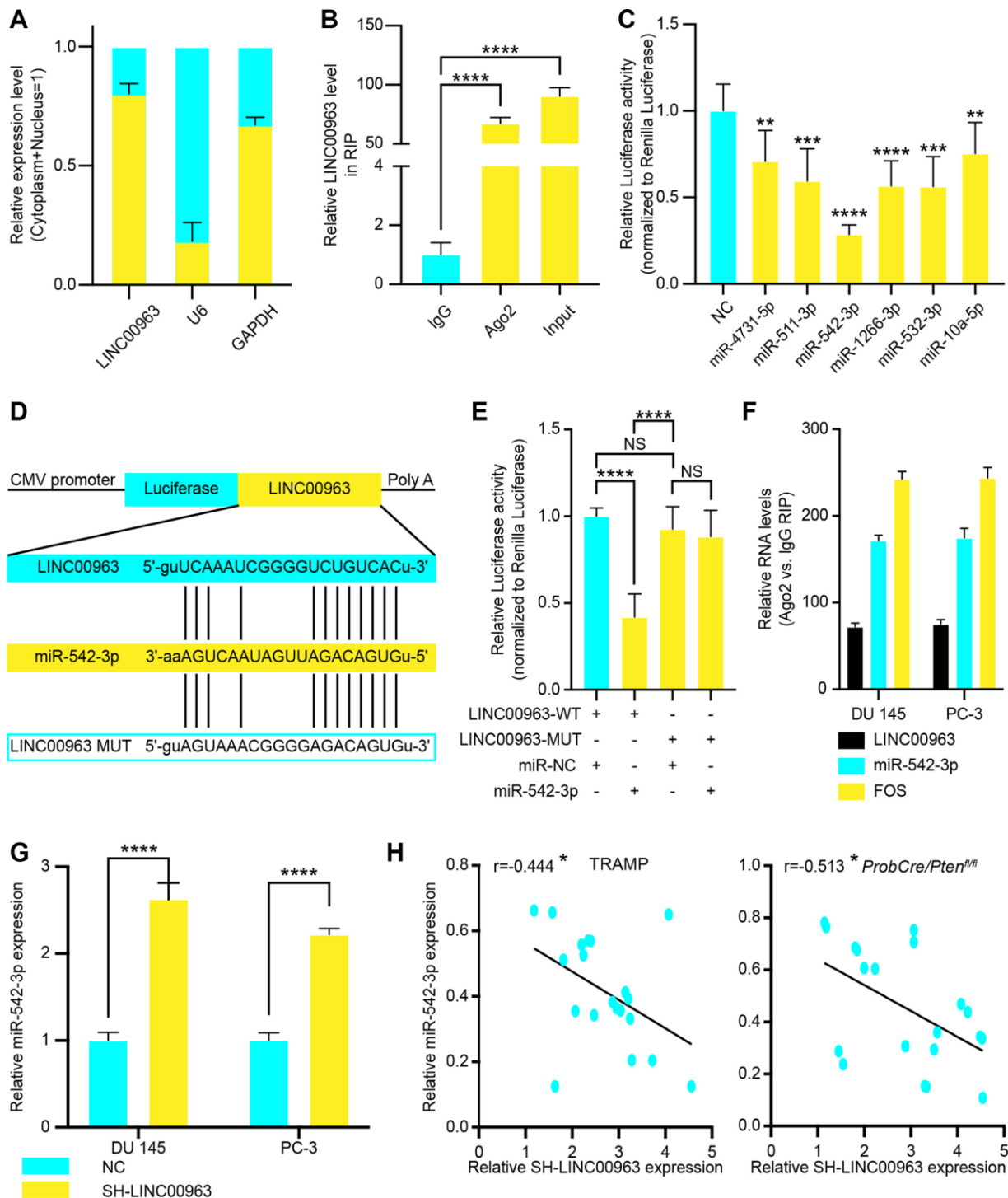


Figure 3. The relationship between long noncoding RNA LINC00963 and tumor suppressor miR-542-3p. (A) The quality of LINC00963 in DU 145 cytoplasmic and nuclear fractions. Levels of glyceraldehyde-3-phosphate dehydrogenase (GAPDH) mRNA and U6 snRNA in purified nuclear fractions were detected by reverse transcription quantitative polymerase chain reaction (RT-qPCR). (B) RIP experiments were performed in DU 145 cells, and the coprecipitated RNA was subjected to RT-qPCR for LINC00963. The fold enrichment of LINC00963 in argonaute 2 (Ago2) RIP is higher relative to that of its matching immunoglobulin (IgG) control. (C) The luciferase reporter plasmid (RLuc-LINC00963) was co-transfected into 293T cells with the 6 miRNA-coding plasmids. (D, E) The luciferase reporter plasmid containing wild-type (WT) or mutant (Mut) LINC00963 (D) was co-transfected into 293T cells with miR-542-3p or with an empty plasmid vector (E). (F) RNA levels in Ago2 immunoprecipitates are presented as fold enrichment relative to IgG immunoprecipitates. (G) RT-qPCR analysis of miR-542-3p expression in DU 145 and PC3 cells transfected with empty lentivirus vector or SH-LINC00963 Lentivirus. (H, I) Correlation of LINC00963 and miR-542-3p in CRPC tissues from TRAMP (H) and ProbCre/Pten^{fl/fl} mice (I). Mean \pm SEM, * $P < 0.05$, ** $P < 0.01$, *** $P < 0.005$, **** $P < 0.001$.

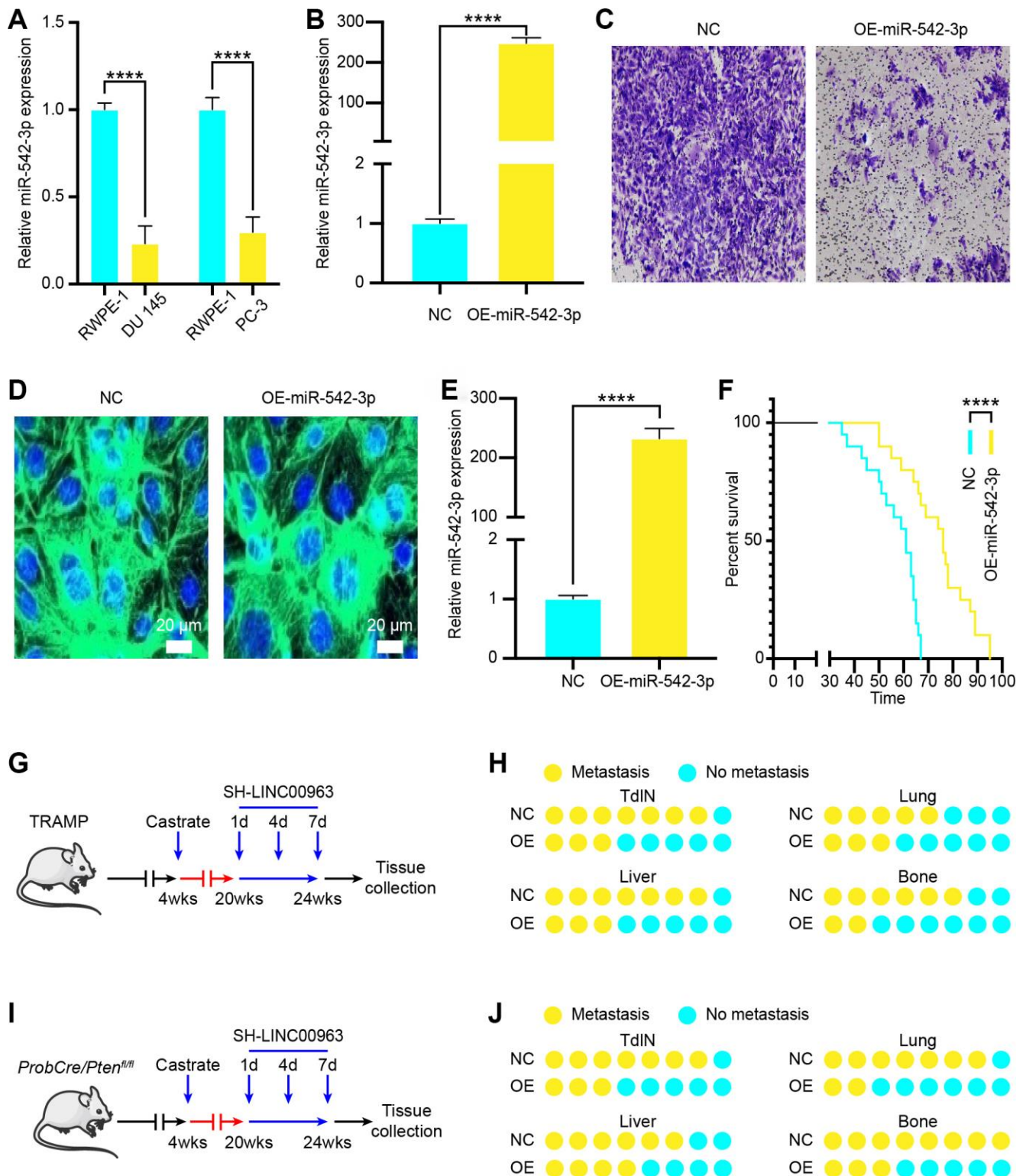


Figure 4. Effects of tumor suppressor miR-542-3p on PCa cell metastasis in vitro and in vivo. (A) RT-qPCR analysis of miR-542-3p expression in the PCa cell lines DU 145 and PC-3 compared to that of the normal prostate cell line RWPE-1. (B) MiR-542-3p expression in OE-miR-542-3p Lentivirus- and empty lentivirus vector-transfected DU145 was tested by RT-qPCR. (C) Transwell invasion assays were performed to determine the invasion of OE-miR-542-3p Lentivirus- or empty lentivirus vector-transfected DU 145 cells. (D) A representative fluorescence image of miR-542-3p expression (green) and DAPI (blue) in OE-miR-542-3p-GFP- or empty lentivirus vector-infected prostate of PCa mice. Scale bars = 20 μ m. (E) RT-qPCR analysis of miR-542-3p expression in OE-miR-542-3p Lentivirus- or empty lentivirus vector-transfected PCa tissues. (F) Survival time of PCa mice with OE-miR-542-3p Lentivirus- or empty lentivirus vector-transfected. (G) Experimental approach to knock down

miR-542-3p in castrated TRAMP mice. (H) Incidence of TdLNs, liver, lung, and bone metastases following OE-miR-542-3p Lentivirus–transfection or pcDNA-miR-542-3p lentivirus–transfection of castrated TRAMP mice (n = 10, every group). (I) Experimental approach to knock down miR-542-3p in castrated ProbCre/Pten^{fl/fl} mice. (J) Incidence of TdLNs, liver, lung, and bone metastases following OE-miR-542-3p Lentivirus–transfection or pcDNA-miR-542-3p lentivirus–transfection in castrated ProbCre/Pten^{fl/fl} mice (n = 10, every group). Mean ± SEM, ****P < 0.001.

(<http://www.microrna.gr/microT>), miRanda (<http://www.microrna.org/microrna/home.do>) and Target Scan (<http://www.targetscan.org/>) to predict potential miR-542-3p target genes (Figure 5A). This analysis showed that NOP2 was the only gene at the intersection of all databases, which is also a potential target gene of LINC00963. Next, these observations were echoed by RNA-seq, which revealed that the expression of NOP2 was reduced in DU 145 transfected with OE-miR-542-3p Lentivirus (Figure 5B). Then, we analyzed The Cancer Genome Atlas (TCGA) RNA-seq data and found that NOP2 was increased in PCa tissues (Figure 5C). Therefore, we chose NOP2 for further investigation and examined its expression levels in the PCa cell lines DU 145 and PC-3 and compared them to those in the normal prostate cell line RWPE-1. The RT-qPCR analysis showed that expression of NOP2 in DU 145 and PC-3 was significantly higher than that in RWPE-1 cells (Figure 5D). Then, we constructed a reporter construct in which the putative miR-542-3p binding site in the NOP2 sequence was mutated by site-directed mutagenesis (Figure 5E). As expected, the miR-542-3p–mediated suppression of luciferase activity was abolished by the mutant NOP2 (Figure 5F). We next evaluated the expression level of NOP2 in DU 145 and PC-3 cells after overexpression of miR-542-3p. Notably, miR-542-3p overexpression significantly decreased the expression levels of NOP2 (Figure 5G). Collectively, these data suggest that miR-542-3p decreases the expression levels of NOP2.

NOP2 is a miR-542-3p target gene and is indirectly regulated by LINC00963

As LINC00963 can sponge miR-542-3p, we next examined whether LINC00963 can regulate the expression of NOP2 by binding to miR-542-3p. We found that overexpression of miR-542-3p increased protein levels of NOP2 in DU 145 cells (Figure 6A). Next, we knocked down LINC00963 and found that decreased LINC00963 also significantly reduced NOP2 protein levels in DU 145 cells (Figure 6B). To determine whether miR-542-3p plays a role in the relationship between LINC00963 and NOP2, we co-transfected cells with SH-LINC00963 Lentivirus and the SH-miR-542-3p Lentivirus. The suppression of NOP2 mRNA in 293T cells and protein levels in DU 145 and PC-3 cells by SH-LINC00963 Lentivirus was effectively reversed by the SH-miR-542-3p

Lentivirus (Figure 6C and 6D). Collectively, these data suggest that LINC00963 modulates the expression of NOP2 by posttranscriptional regulation of miR-542-3p.

NOP2 promotes PCa metastasis by epithelial-mesenchymal transition (EMT) pathway

To investigate the oncogenic role of NOP2 in PCa, we overexpressed it in DU 145 cells, and positively-regulated genes were analyzed. The heat map showed that there were 82 genes highly increased in OE-NOP2 Lentivirus transfected cells (fold change > 2, P < 0.05 = (Figure 7A). We further analyzed the signaling pathways of these increased genes and found that the EMT signaling pathway was significantly activated (Figure 7B). Similarly, DU 145 cells were transfected with OE-NOP2 Lentivirus, and the EMT signaling pathway positively related protein, E-cadherin, was increased and the negatively related proteins N-cadherin and Vimentin were decreased (Figure 7C). To verify cancer promoting function of NOP2, we transfected DU 145 cells with SH-NOP2 Lentivirus to knock down its expression, which was confirmed by RT-qPCR (Figure 7D). Then, the transwell invasion assays showed that decreased NOP2 significantly inhibited DU 145 cell invasion (Figure 7E). NOP2 knockdown also resulted in a significantly prolonged survival of mice (Figure 7F). To examine its clinical significance, we analyzed NOP2 expression in PCa and normal tissues. The expression of NOP2 was found to be increased in PCa samples compared with normal tissues according to TCGA sequencing data, and NOP2 levels were positively related to Gleason score (Figure 7G). Moreover, the ROC curve analysis showed that NOP2 could be regarded as a potential diagnosis indicator of PCa (Figure 7J). These findings indicate that NOP2 behaves as an oncogene to promote PCa cell proliferation, and can serve as a clinical indicator.

DISCUSSION

Emerging data have shown that lncRNAs exert a crucial influence in human ailment and cellular function. Dysregulation of lncRNAs may also lead to tumorigenesis and cancer drug resistance [26, 27]. We discovered that LINC00963 is a novel CRPC–related lncRNA, which is significantly increased in PCa tissues and cell lines. Higher expression of

LINC00963 correlated with advanced TNM stage, larger tumor size, and positive lymph node invasion. Moreover, elevated LINC00963 expression was associated with shorter overall survival (OS) and

progression-free survival (PFS) time of patients with CRPC. Experiments in vitro and in vivo indicated that the inhibition of LINC00963 could restrain cell cycle and cell proliferation and enhance cell death, whereas

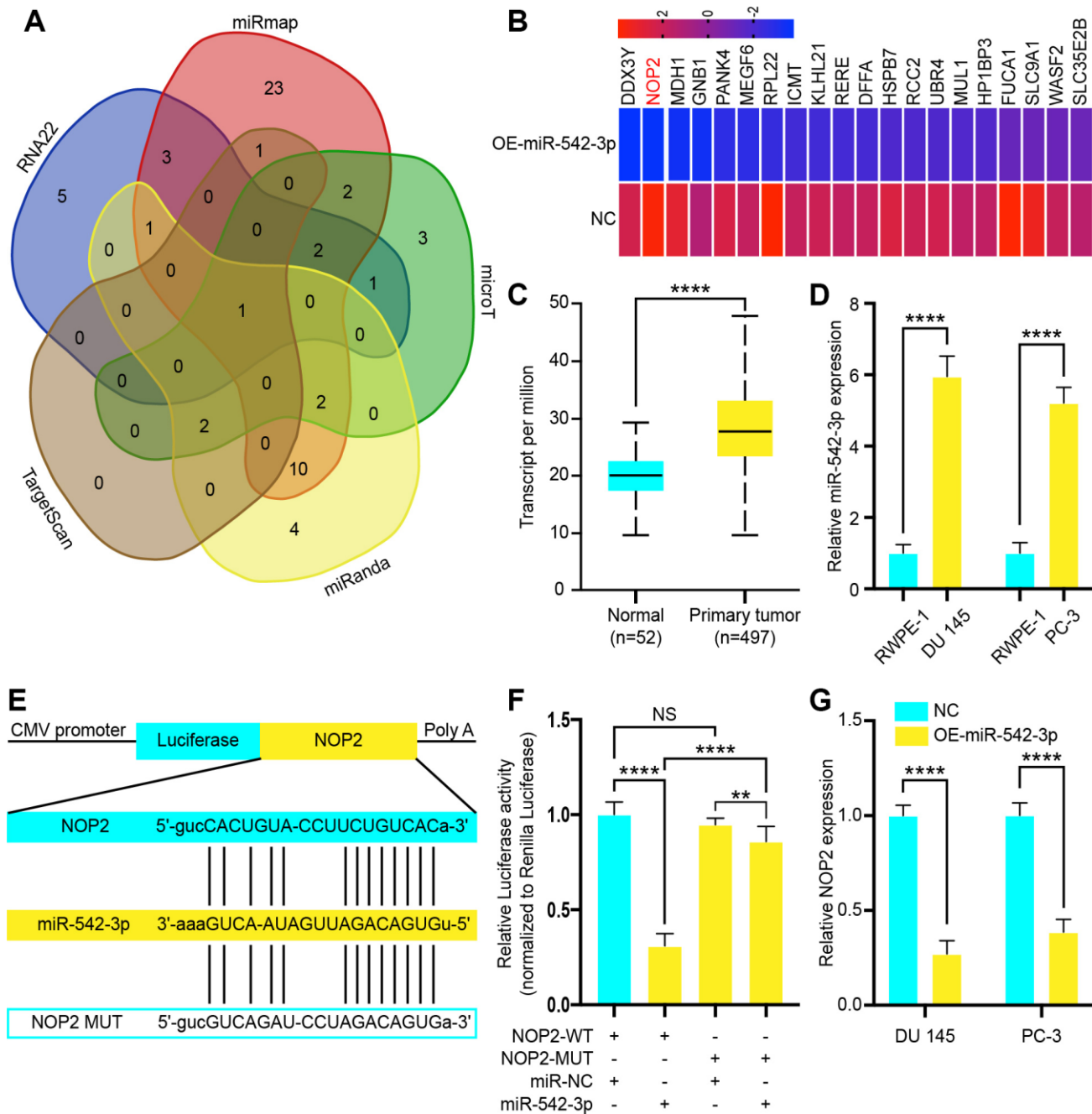


Figure 5. NOP2 is a target of tumor suppressor miR-542-3p and is suppressed by long noncoding RNA LINC00963 deletion. (A) Venn diagram of intersection target genes of miR-542-3p predicted by several bioinformatics databases. (B) Heat map of top 20 decreased genes in DU 145 cells after transfection with OE-miR-542-3p Lentivirus. (C) Relative expression of NOP2 in PCa tissues compared to that of normal tissue was analyzed by using the TCGA dataset. (D) RT-qPCR analysis of NOP2 expression in PCa cell lines the DU 145 and PC-3 cells compared to the normal prostate cell line RWPE-1. (E) Schematic view of miR-542-3p putative targeting site in the WT and Mut 3'-untranslated region (UTR) of *NOP2*. (F) Luciferase activity assay in 293 T cells transfected with luciferase report plasmids containing NOP2 3'UTR (WT or Mut), and control miRNA or miR-542-3p. (G) Relative mRNA levels of NOP2 in DU 145 and PC-3 cells transfected with control vector or OE-miR-542-3p Lentivirus. Mean \pm SEM, **P < 0.01, ****P < 0.0001, NS: no statistical significance.

overexpression of LINC00963 had the opposite effects. Collectively, these discoveries suggest the notion that LINC00963 possesses a critical role in PCa oncogenesis and could be considered as a novel treatment target in CRPC.

According to previous reports, there are novel and widespread interactive networks, including ceRNAs, where lncRNAs could interact with protein-coding mRNAs in a miRNA-dependent manner [28, 29]. For instance, lncRNA HOTAIR functions as a promoter of PCa cell proliferation by acting as a ceRNA for miR-

193a [21]. lncRNA CCAT1 promotes CRPC invasion and facilitates the expression of AR-regulated genes by acting as a ceRNA of miR-28-5p [22]. In this study, we confirmed that LINC00963 localized in the cytoplasm and that it interacts with Ago2 in PCa cells, suggesting its potential role as an endogenous miRNA sponge. After searching various bioinformatical databases and applying luciferase reporter assays, we confirmed that miR-542-3p is a novel target of LINC00963. Regarded as a tumor suppressor, miR-542-3p presents low expression in various types of human cancers.

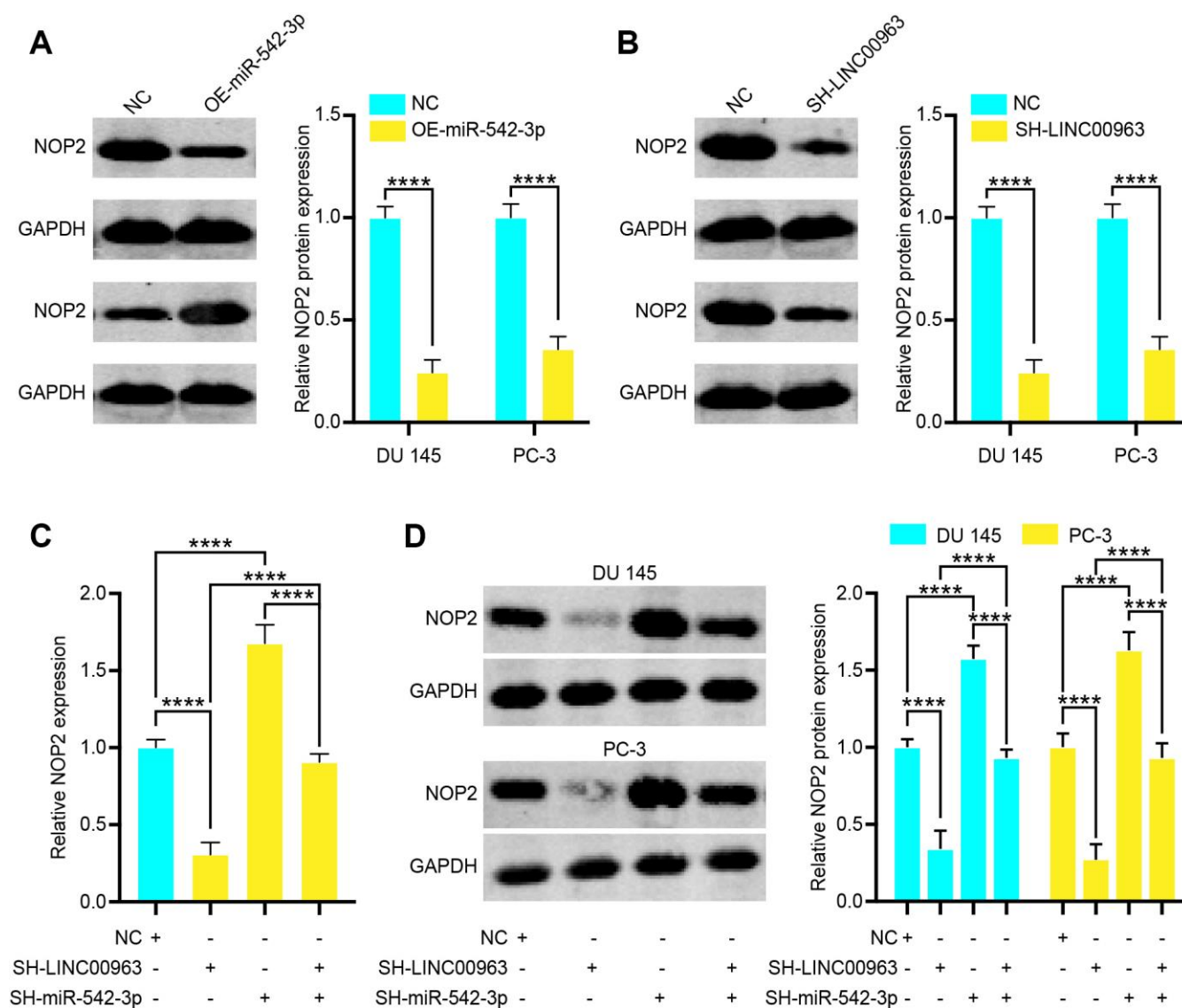


Figure 6. Long noncoding RNA LINC00963 functions as a competing endogenous RNA (ceRNA) and sponges tumor suppressor miR-542-3p to upregulate NOP2. (A) Relative protein levels of NOP2 in DU 145 cells transfected with empty vector lentivirus or OE-miR-542-3p lentivirus. (B) Relative protein levels of NOP2 in DU 145 cells transfected with empty vector lentivirus or SH-LINC00963 Lentivirus. (C, D) NOP2 mRNA (C) in 293T cells and protein level in DU 145 cells and PC-3 cells (D) following knockdown of LINC00963 and/or inhibition of miR-542-3p. Mean \pm SEM, ****P < 0.001.

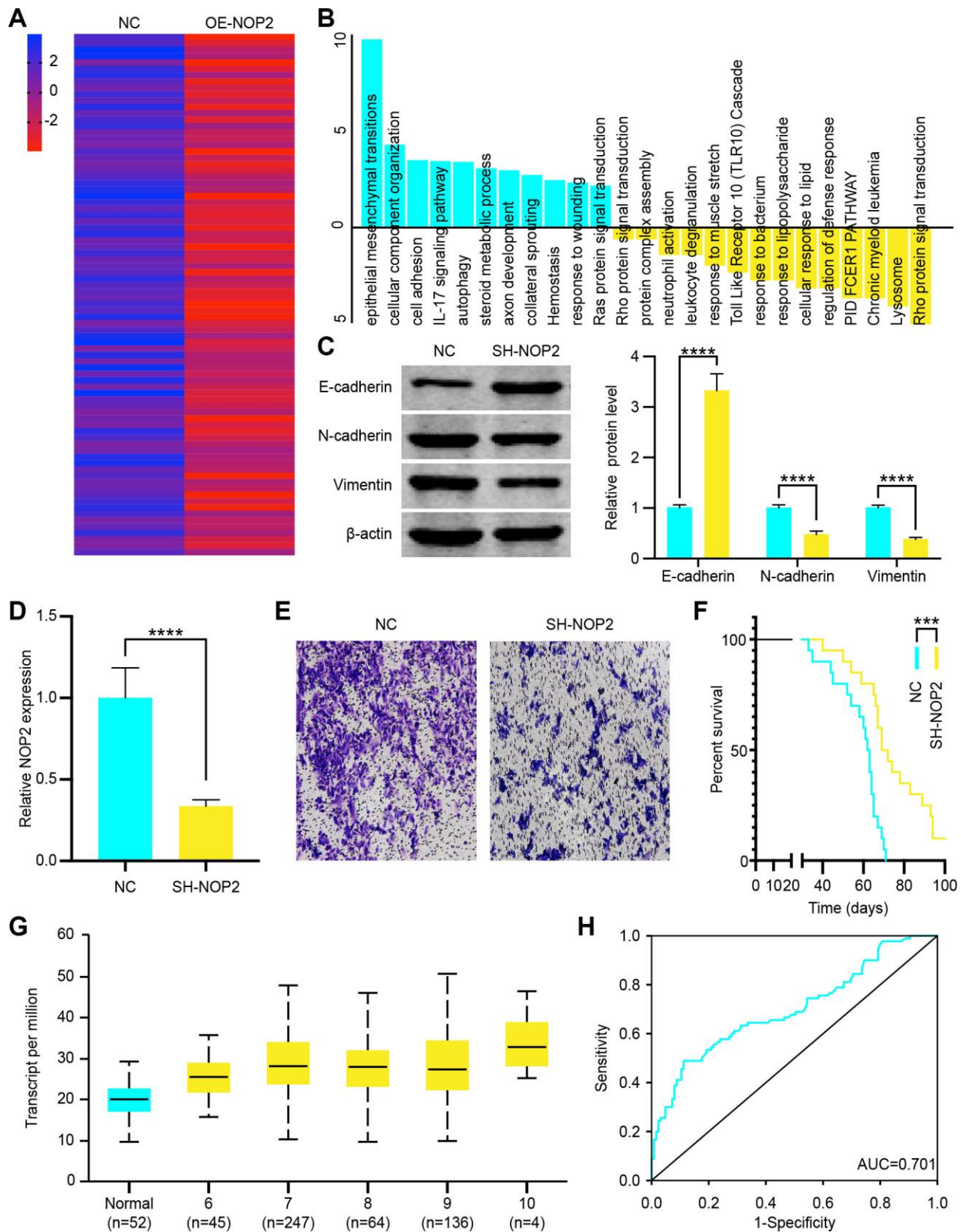


Figure 7. NOP2 promotes prostate cancer (PCa) cell progression through epithelial-mesenchymal transition (EMT) pathway. (A) Heat map of increased genes in DU 145 cells transfected with OE-NOP2 Lentivirus. (B) Gene enrichment analysis showed the signaling pathways activated or inhibited by NOP2 overexpression. (C) EMT related proteins (E-cadherin, N-cadherin, and vimentin) was examined by western blot in vector or OE-NOP2 Lentivirus transfected cells and the data were quantitated. (D) NOP2 expression in SH-NOP2 Lentivirus-

and pcDNA-NOP2 Lentivirus–transfected DU145 cells was examined by RT-qPCR. (E) Transwell invasion assays were performed to determine the invasion of SH-NOP2 Lentivirus–or pcDNA-NOP2 Lentivirus–transfected DU 145 cells. (F) Survival time of PCa mice transfected with SH-NOP2 Lentivirus or pcDNA-NOP2 Lentivirus. (G) Transcript levels of NOP2 in normal prostate tissues and PCa tissues and differential Gleason scores. (H) Receiver operation characteristic (ROC) curve analysis of the association of NOP2 with the diagnosis of PCa (AUC = 0.701). Mean ± SEM, ***P < 0.005, ****P < 0.001.

Lyu and colleagues have found that miR-542-3p inhibits breast cancer cell proliferation and HER3 signaling-induced chemo-resistance [30]. In addition, upregulating the expression of miR-542-3p could suppress the progression of colorectal cancer cells [31]. Furthermore, it has shown that miR-542-3p suppresses cell proliferation by inhibiting CDK14 in epithelial ovarian cancer [32]. In this study, we also found that miR-542-3p was significantly decreased in CRPC and increased miR-542-3p prevented PCa cell growth and increased the rate of apoptotic cell.

Generally, miRNA targets are an essential part of ceRNA networks where lncRNAs can exert their biological function. Using reliable online predicting tools, we revealed that NOP2 is one of the potential miR-542-3p targets. RNA-binding protein NOP2 can increase nucleolar activity and stimulate cell proliferation by influencing the cell cycle. In agreement with previous

research reporting NOP2 in hepatocellular carcinoma [33], we found that NOP2 was highly expressed in CRPC tissues compared with the normal ones. PCa patients with higher levels of NOP2 demonstrate poorer OS. Furthermore, we showed that knockdown of NOP2 repressed PCa cell growth and induced cell death. Rescue experiments also confirmed that after knocking down NOP2, the inhibition effect induced by miR-542-3p down-regulation partially reversed.

In summary, lncRNA-LINC00963 functions as a ceRNA that competitively binds to miR-542-3p, which then up-regulates NOP2 and promotes PCa metastasis via activating EMT signaling, which is the critical pathway regulating tumor metastasis in several cancers [34, 35]. The LINC00963/miR-542-3p/NOP2 axis was shown to be involved in the development of CRPC, and targeting this pathway might have therapeutic potential for CRPC (Figure 8).

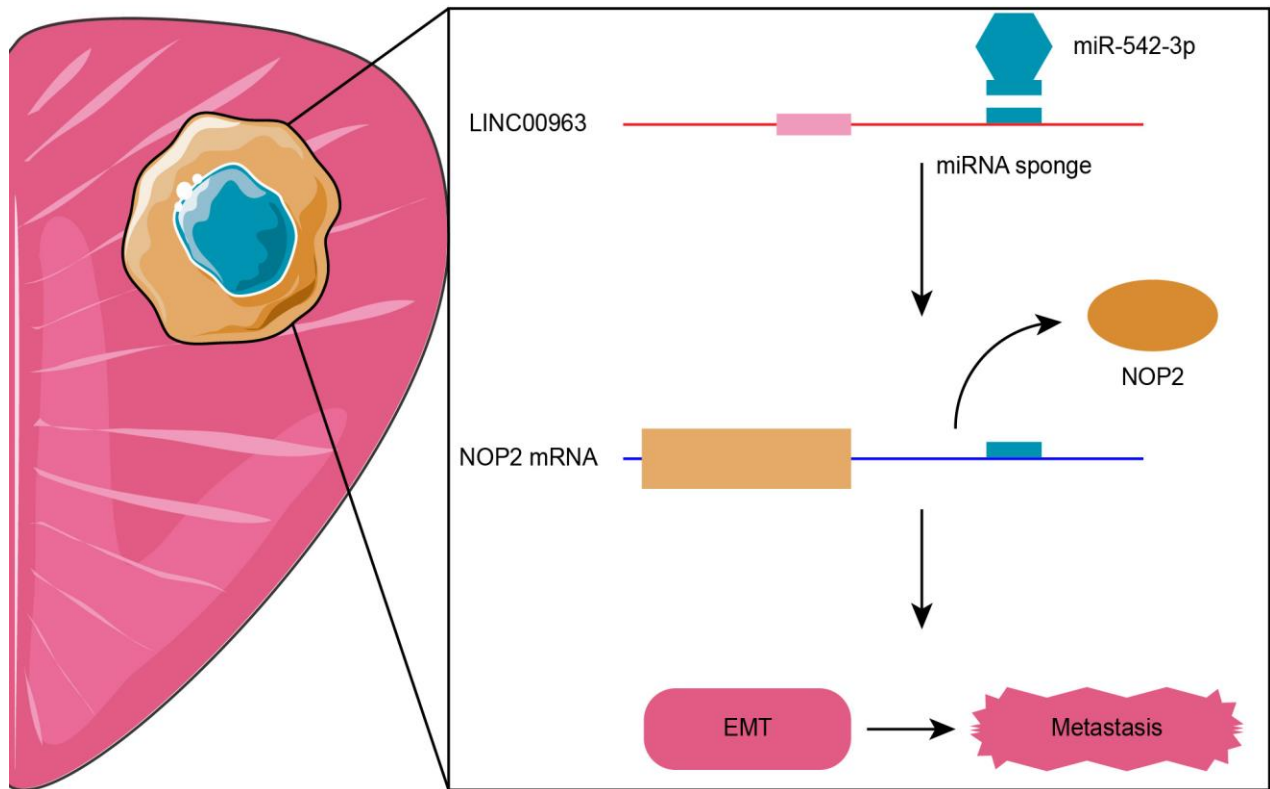


Figure 8. Proposed model of LINC00963/miR-542-3p/NOP2 axis-mediated epithelial-mesenchymal transition (EMT) pathway activation for promoting metastasis in prostate cancer (PCa).

MATERIALS AND METHODS

Animals

All animal studies were approved by the Institutional Animal Care and Use Committee of Shanghai Jiao Tong University. All mice were maintained in pathogen-free conditions and cared for in compliance with the ethical regulations at Shanghai General Hospital. Transgenic adenocarcinomas of mouse prostate (TRAMP) and ProbCre/Pten^{fl/fl} mice were provided by the Shanghai Model Organisms Center (Shanghai, China) sacrificed 12 weeks post-castration unless indicated otherwise [36]. We tested androgen to determine model successfully established. Prostates, TdLNs, livers, lungs, and bones were collected for hematoxylin and eosin (H&E) and immunohistochemistry staining. The diagnosis of tumor metastasis was made independently by two pathologists. The genetic background of all mice used in this study was C57BL/6.

Cell culture

Two human prostate cancer cell lines (DU 145, and PC-3) and a normal prostate cell line (RWPE-1) were purchased from the Institute of Biochemistry and Cell Biology of the Chinese Academy of Sciences (China). DU 145 and PC-3 cells were cultured in Ham's F12 medium and RWPE-1 cells were cultured in K-SFM medium supplemented with 10% fetal bovine serum (FBS), 100 mg/mL streptomycin (Invitrogen), and 100 U/mL penicillin in humidified air at 37 °C with 5% CO₂. All cell lines were authenticated by short tandem repeat DNA profiling.

RNA extraction and quantitative RT-qPCR assays

Total RNA was extracted from tissues or cultured cells using TRIzol reagent (Invitrogen) according to the manufacturer's instructions. RNA (1 mg) was reverse transcribed in a final volume of 20 mL using random primers under standard conditions using the PrimeScript RT Reagent Kit (TaKaRa). Real-time PCR analyses were performed with SYBR Premix Ex Taq (TaKaRa). Levels of LINC00963 (primer: forward 5'-TGGACA CCACTTTGCCCTTT-3', reverse: 5'-AGATGGGGCC CTTATCACCT-3') and NOP2 (primer: forward 5'-AAATGGGAGAAGGTGGCGTC-3', reverse: 5'-CTCTCGGACATTAACCCGCA-3') were normalized to the expression of glyceraldehyde-3-phosphate dehydrogenase (GAPDH). Primers for miR-542-3p (primer: forward 5'-TCGGGGATCATCATGTCACG-3', reverse: 5'-GAGTGGCTCCCAGACCTTTC-3') and U6 (miRNA0002-1-200) were purchased from RiboBio. RT-qPCR and data collection were conducted on an ABI 7500 real-time PCR system (Applied Biosystems).

RT-qPCR results were analyzed and expressed relative to the threshold cycle (Ct) values, and then converted to fold changes.

Transduction of BC cell lines and RNA extraction

The short hairpin RNA (shRNA) and green fluorescent protein (GFP)-labeled lentivirus vectors containing the miR-542-3p mimic lentivirus (OE-miR-542-3p), LINC00963 overexpression lentivirus (OE-LINC00963), NOP2 overexpression lentivirus (OE-NOP2), miR-542-3p inhibitor lentivirus (SH-miR-542-3p), LINC00963 silencing lentivirus (SH-LINC00963), NOP2 silencing lentivirus (SH-NOP2), and the corresponding control lentivirus (NC) were obtained from GeneChem (Shanghai, China). Cells were seeded in 6-well plates (5 × 10⁵ cells/well) before transduction. The shRNA transduction was conducted using the HiPerFect Transfection Reagent according to the manufacturer's instructions (Qiagen). Transduction with the lentiviral vectors was conducted using transduction reagents and 8 mg/ml polybrene (GeneChem) for 12 h. For viral transduction, cells were transduced with a multiplicity of infection (MOI) of 10,100 or 1,000. Overexpression, silencing, and the corresponding control stable cell lines were then established, and the efficiency of transduction was confirmed by RT-qPCR.

Cell migration and cell invasion assays

Transwell migration and invasion assays were performed as previously described. DU 145 were seeded in the upper chambers, and the conditioned medium was placed in the lower chambers. Cells were stained with crystal violet and observed under an optical microscope. All experiments were performed in triplicate.

Western blot assay and antibodies

DU 145 cells were lysed with RIPA extraction reagent (Beyotime) supplemented with a protease inhibitor cocktail (Roche). Cell protein lysates were separated by 10% sodium dodecyl sulfate-polyacrylamide gel electrophoresis (SDS-PAGE), transferred to 0.22 mm polyvinylidene fluoride membranes (Millipore), and probed with specific antibodies. Specific bands were detected by ECL chromogenic substrate and quantified by densitometry (Quantity One software, Bio-Rad). GAPDH antibody was used as the control. Antibodies against NOP2, GAPDH, E-cadherin, N-cadherin, vimentin, and β-actin were purchased from Cell Signaling Technology.

RNA immunoprecipitation

RNA immunoprecipitation was used to investigate whether LINC00963 could interact or bind with the

potential binding protein argonaute 2 (Ago2) in DU 145 and PC-3 cells. We used the EZMagna RIP Kit (Millipore) according to the manufacturer's instructions. DU 145 and PC-3 cells were lysed and incubated with protein A magnetic beads, which were conjugated with antibodies at 4 °C. After 3 to 6 hours, the beads were washed with wash buffer and then incubated with 0.1% SDS/0.5 mg·mL⁻¹ proteinase K for 30 minutes at 55 °C to remove proteins. Finally, immunoprecipitated RNA was subjected to RT-qPCR analysis to demonstrate the presence of LINC00963.

Luciferase assay

The complementary DNA fragment containing the wild-type or mutant LINC00963 fragment and the 3'-untranslated region (UTR) of *NOP2* was subcloned downstream of the luciferase gene within the pGL3-Basic luciferase reporter vector (Promega). Human 293T cells (1.0*10⁵) grown in a 24-well plate were co-transfected with 150 ng of either empty vector or miR-542-3p, 50 ng of firefly luciferase reporter comprising wild-type or mutant LINC01234 fragment, and the 3'-UTR of *NOP2* fragment using Lipofectamine 3000 (Invitrogen). Forty-eight hours after transfection, luciferase assay was determined using the dual luciferase kit (Promega). The relative firefly luciferase activities were normalized to those of Renilla luciferase. Transfection was performed in triplicate.

RNA sequencing

The RNA quality and integrity were analyzed by Qubit 2.0 (Life Technologies) and Bioanalyzer 2100 (Agilent). For library preparation, 3 µg total RNA was captured by NEBNext Oligo d (T) 25 beads (NEB), sheared to yield fragments of approximately 250 bp, and reverse transcribed using NEBNext RNA first and second Strand Synthesis Module (NEB, USA). The products were end-repaired, A-tailed, ligated to Illumina sequencing adapters and amplified by PCR. The quality of the sequencing library was assayed by using the Qubit 2.0 fluorometer (Life Technologies, USA) and the Bioanalyzer 2100 (Agilent) and then sequenced using an Illumina HiSeq X Ten with 2 × 150 bp paired-end sequencing, controlled by HiSeq Control Software (HCS). Raw sequence reads were initially examined using FastQC for quality control. Raw reads were processed to trim low-quality sequences and adapters using Trimmomatic. Clean reads were then mapped to hg19 for human samples and mm9 for mouse samples using STAR, and only uniquely mapped reads were kept. Read counts were calculated by htseq-count. Differential expression analysis was performed using DESeq2.

Statistical analysis

The significance of differences between groups was assessed by a paired, two-tailed Student *t*-test. The univariate and multivariate Cox proportional hazards model was used to determine the effects of variables on survival. The Kaplan-Meier method test was utilized for survival analysis. Spearman correlation analysis was used to calculate the correlation between LINC00963, miR-542-3p, and *NOP2*. All statistical analyses were performed using SPSS 17.0 software. A P value of < 0.05 determined statistical significance.

AUTHOR CONTRIBUTIONS

YYZ and ZHL conceived and designed the study. FS and KW performed the experiments and collected data. ZXY participated in RT-qPCR experiments, provided essential experimental materials and assisted in data analysis and interpretations. XYM, ZZ, MHS and YW drafted the manuscript. All authors read, reviewed, revised and approved the manuscript.

ACKNOWLEDGMENTS

The authors wish to thank the technical support provided by Shujie Xia from Shanghai General Hospital, Shanghai Jiaotong University, Shanghai, China.

CONFLICTS OF INTEREST

The authors declare that no conflicts of interests exist.

FUNDING

The reported work was supported in part by research grants from the Natural Science Foundation of China (no. 81672515), the Shanghai Pujiang Program (no. 16PJD039) and the Commission of Gaofeng Clinical Medicine Grant (no. 20172019).

REFERENCES

1. Malone S, Roy S, Eapen L, E C, MacRae R, Perry G, Bowen J, Samant R, Morgan S, Craig J, Malone K, Grimes S. Sequencing of androgen-deprivation therapy with external-beam radiotherapy in localized prostate cancer: a phase III randomized controlled trial. *J Clin Oncol*. 2020; 38:593–601. <https://doi.org/10.1200/JCO.19.01904> PMID:31829912
2. Xu X, Hou J, Lv J, Huang Y, Pu J, Wang L. Overexpression of lncRNA GAS5 suppresses prostatic epithelial cell proliferation by regulating COX-2 in

- chronic non-bacterial prostatitis. *Cell Cycle*. 2019; 18:923–31.
<https://doi.org/10.1080/15384101.2019.1593644>
PMID:30892130
3. ARv7 Is a Transcriptional Repressor in CRPC. *Cancer Discov*. 2019; 9:463.
<https://doi.org/10.1158/2159-8290.CD-RW2019-026>
 4. Sun J, Hu X, Gao Y, Tang Q, Zhao Z, Xi W, Yang F, Zhang W, Song Y, Song B, Wang T, Wang H. MYSM1-AR complex-mediated repression of akt/c-Raf/GSK-3 β signaling impedes castration-resistant prostate cancer growth. *Aging (Albany NY)*. 2019; 11:10644–63.
<https://doi.org/10.18632/aging.102482> PMID:31761786
 5. Metcalf CA 3rd, Svenson S, Hwang J, Tripathi S, Gangal G, Kabir S, Lazarus D, Cole R, Sweryda-Krawiec B, Shum P, Brown D, Case RI, van der Poll D, et al. Discovery of a novel cabazitaxel nanoparticle-drug conjugate (CRLX522) with improved pharmacokinetic properties and anticancer effects using a β -cyclodextrin-PEG copolymer based delivery platform. *J Med Chem*. 2019; 62:9541–59.
<https://doi.org/10.1021/acs.jmedchem.9b00892>
PMID:31593466
 6. Ploussard G. Re: Wnt-pathway activating mutations are associated with resistance to first-line abiraterone and enzalutamide in castration-resistant prostate cancer. *Eur Urol*. 2020; 77:393.
<https://doi.org/10.1016/j.eururo.2019.10.014>
PMID:31727449
 7. Davis ID, Stockler MR, Sweeney CJ. Enzalutamide in metastatic prostate cancer. Reply. *N Engl J Med*. 2019; 381:1494–95.
<https://doi.org/10.1056/NEJMc1910553>
PMID:31597033
 8. Stone L. CRPC-specific gene therapy. *Nat Rev Urol*. 2019; 16:206–07.
<https://doi.org/10.1038/s41585-019-0165-7>
PMID:30808987
 9. Peng R, Li Z, Lin Z, Wang Y, Wang W, Hu B, Wang X, Zhang J, Wang Y, Zhou R, Lu C, Shen Y, Wang J, Shi G. The HSP90 inhibitor 17-PAG effectively inhibits the proliferation and migration of androgen-independent prostate cancer cells. *Am J Cancer Res*. 2015; 5:3198–209.
PMID:26693070
 10. Davalos V, Esteller M. Disruption of long noncoding RNAs targets cancer hallmark pathways in lung tumorigenesis. *Cancer Res*. 2019; 79:3028–30.
<https://doi.org/10.1158/0008-5472.CAN-19-0910>
PMID:31201165
 11. Zhao J, Li L, Han ZY, Wang ZX, Qin LX. Long noncoding RNAs, emerging and versatile regulators of tumor-induced angiogenesis. *Am J Cancer Res*. 2019; 9:1367–81.
PMID:31392075
 12. Fanucchi S, Fok ET, Dalla E, Shibayama Y, Börner K, Chang EY, Stoychev S, Imakaev M, Grimm D, Wang KC, Li G, Sung WK, Mhlanga MM. Immune genes are primed for robust transcription by proximal long noncoding RNAs located in nuclear compartments. *Nat Genet*. 2019; 51:138–50.
<https://doi.org/10.1038/s41588-018-0298-2>
PMID:30531872
 13. Cirillo D, Blanco M, Armaos A, Bunes A, Avner P, Guttman M, Cerase A, Tartaglia GG. Quantitative predictions of protein interactions with long noncoding RNAs. *Nat Methods*. 2016; 14:5–6.
<https://doi.org/10.1038/nmeth.4100>
PMID:28032625
 14. Sun M, Gadad SS, Kim DS, Kraus WL. Discovery, annotation, and functional analysis of long noncoding RNAs controlling cell-cycle gene expression and proliferation in breast cancer cells. *Mol Cell*. 2015; 59:698–711.
<https://doi.org/10.1016/j.molcel.2015.06.023>
PMID:26236012
 15. Yousefi H, Maheronnaghsh M, Molaei F, Mashouri L, Reza Aref A, Momeny M, Alahari SK. Long noncoding RNAs and exosomal lncRNAs: classification, and mechanisms in breast cancer metastasis and drug resistance. *Oncogene*. 2020; 39:953–74.
<https://doi.org/10.1038/s41388-019-1040-y>
PMID:31601996
 16. Chen M, Xu Z, Zhang Y, Zhang X. LINC00958 promotes the Malignancy of nasopharyngeal carcinoma by sponging microRNA-625 and thus upregulating NUA1. *Onco Targets Ther*. 2019; 12:9277–90.
<https://doi.org/10.2147/OTT.S216342>
PMID:31819474
 17. Zhou K, Li S, Du G, Fan Y, Wu P, Sun H, Zhang T. LncRNA XIST depletion prevents cancer progression in invasive pituitary neuroendocrine tumor by inhibiting bFGF via upregulation of microRNA-424-5p. *Onco Targets Ther*. 2019; 12:7095–109.
<https://doi.org/10.2147/OTT.S208329> PMID:31564894
 18. Gu P, Chen X, Xie R, Han J, Xie W, Wang B, Dong W, Chen C, Yang M, Jiang J, Chen Z, Huang J, Lin T. lncRNA HOXD-AS1 regulates proliferation and chemoresistance of castration-resistant prostate cancer via recruiting WDR5. *Mol Ther*. 2017; 25:1959–73.
<https://doi.org/10.1016/j.ymthe.2017.04.016>
PMID:28487115
 19. Shang Z, Yu J, Sun L, Tian J, Zhu S, Zhang B, Dong Q, Jiang N, Flores-Morales A, Chang C, Niu Y. LncRNA

- PCAT1 activates AKT and NF- κ B signaling in castration-resistant prostate cancer by regulating the PHLPP/FKBP51/IKK α complex. *Nucleic Acids Res.* 2019; 47:4211–25.
<https://doi.org/10.1093/nar/gkz108>
PMID:30773595
20. Parolia A, Venalainen E, Xue H, Mather R, Lin D, Wu R, Pucci P, Rogalski J, Evans JR, Feng F, Collins CC, Wang Y, Crea F. The long noncoding RNA HORAS5 mediates castration-resistant prostate cancer survival by activating the androgen receptor transcriptional program. *Mol Oncol.* 2019; 13:1121–36.
<https://doi.org/10.1002/1878-0261.12471>
PMID:30776192
21. Ling Z, Wang X, Tao T, Zhang L, Guan H, You Z, Lu K, Zhang G, Chen S, Wu J, Qian J, Liu H, Xu B, Chen M. Involvement of aberrantly activated HOTAIR/EZH2/miR-193a feedback loop in progression of prostate cancer. *J Exp Clin Cancer Res.* 2017; 36:159.
<https://doi.org/10.1186/s13046-017-0629-7>
PMID:29141691
22. You Z, Liu C, Wang C, Ling Z, Wang Y, Wang Y, Zhang M, Chen S, Xu B, Guan H, Chen M. LncRNA CCAT1 promotes prostate cancer cell proliferation by interacting with DDX5 and MIR-28-5P. *Mol Cancer Ther.* 2019; 18:2469–79.
<https://doi.org/10.1158/1535-7163.MCT-19-0095>
PMID:31387890
23. Gu P, Chen X, Xie R, Xie W, Huang L, Dong W, Han J, Liu X, Shen J, Huang J, Lin T. A novel AR translational regulator lncRNA LBCS inhibits castration resistance of prostate cancer. *Mol Cancer.* 2019; 18:109.
<https://doi.org/10.1186/s12943-019-1037-8>
PMID:31221168
24. Dang Y, Loewen R, Parikh HA, Roy P, Loewen NA. Gene transfer to the outflow tract. *Exp Eye Res.* 2017; 158:73–84.
<https://doi.org/10.1016/j.exer.2016.04.023>
PMID:27131906
25. Pan H, Guo C, Pan J, Guo D, Song S, Zhou Y, Xu D. Construction of a competitive endogenous RNA network and identification of potential regulatory axis in gastric cancer. *Front Oncol.* 2019; 9:912.
<https://doi.org/10.3389/fonc.2019.00912>
PMID:31637209
26. Zhao H, Shi J, Zhang Y, Xie A, Yu L, Zhang C, Lei J, Xu H, Leng Z, Li T, Huang W, Lin S, Wang L, et al. LncTarD: a manually-curated database of experimentally-supported functional lncRNA-target regulations in human diseases. *Nucleic Acids Res.* 2020; 48:D118–D126.
<https://doi.org/10.1093/nar/gkz985>
PMID:31713618
27. Wei L, Wang X, Lv L, Liu J, Xing H, Song Y, Xie M, Lei T, Zhang N, Yang M. The emerging role of microRNAs and long noncoding RNAs in drug resistance of hepatocellular carcinoma. *Mol Cancer.* 2019; 18:147.
<https://doi.org/10.1186/s12943-019-1086-z>
PMID:31651347
28. Luo X, Wei J, Yang FL, Pang XX, Shi F, Wei YX, Liao BY, Wang JL. Exosomal lncRNA HNF1A-AS1 affects cisplatin resistance in cervical cancer cells through regulating microRNA-34b/TUFT1 axis. *Cancer Cell Int.* 2019; 19:323.
<https://doi.org/10.1186/s12935-019-1042-4>
PMID:31827397
29. Zhu H, Jin YM, Lyu XM, Fan LM, Wu F. Long noncoding RNA H19 regulates HIF-1 α /AXL signaling through inhibiting miR-20b-5p in endometrial cancer. *Cell Cycle.* 2019; 18:2454–64.
<https://doi.org/10.1080/15384101.2019.1648958>
PMID:31411527
30. Lyu H, Wang S, Huang J, Wang B, He Z, Liu B. Survivin-targeting miR-542-3p overcomes HER3 signaling-induced chemoresistance and enhances the antitumor activity of paclitaxel against HER2-overexpressing breast cancer. *Cancer Lett.* 2018; 420:97–108.
<https://doi.org/10.1016/j.canlet.2018.01.065>
PMID:29409974
31. Yuan L, Yuan P, Yuan H, Wang Z, Run Z, Chen G, Zhao P, Xu B. miR-542-3p inhibits colorectal cancer cell proliferation, migration and invasion by targeting OTUB1. *Am J Cancer Res.* 2017; 7:159–72.
PMID:28123857
32. Li J, Shao W, Feng H. MiR-542-3p, a microRNA targeting CDK14, suppresses cell proliferation, invasiveness, and tumorigenesis of epithelial ovarian cancer. *Biomed Pharmacother.* 2019; 110:850–56.
<https://doi.org/10.1016/j.biopha.2018.11.104>
PMID:30557834
33. Wang F, Yuan JH, Wang SB, Yang F, Yuan SX, Ye C, Yang N, Zhou WP, Li WL, Li W, Sun SH. Oncofetal long noncoding RNA PVT1 promotes proliferation and stem cell-like property of hepatocellular carcinoma cells by stabilizing NOP2. *Hepatology.* 2014; 60:1278–90.
<https://doi.org/10.1002/hep.27239>
PMID:25043274
34. Tian S, Peng P, Li J, Deng H, Zhan N, Zeng Z, Dong W. SERPINH1 regulates EMT and gastric cancer metastasis via the Wnt/ β -catenin signaling pathway. *Aging (Albany NY).* 2020; 12:3574–93.
<https://doi.org/10.18632/aging.102831>
PMID:32091407

35. Guo Q, Jing FJ, Xu W, Li X, Li X, Sun JL, Xing XM, Zhou CK, Jing FB. Ubenimex induces autophagy inhibition and EMT suppression to overcome cisplatin resistance in GC cells by perturbing the CD13/EMP3/PI3K/AKT/NF- κ B axis. *Aging (Albany NY)*. 2019; 12:80–105. <https://doi.org/10.18632/aging.102598>
PMID:[31895687](https://pubmed.ncbi.nlm.nih.gov/31895687/)
36. Grabowska MM, DeGraff DJ, Yu X, Jin RJ, Chen Z, Borowsky AD, Matusik RJ. Mouse models of prostate cancer: picking the best model for the question. *Cancer Metastasis Rev*. 2014; 33:377–97. <https://doi.org/10.1007/s10555-013-9487-8>
PMID:[24452759](https://pubmed.ncbi.nlm.nih.gov/24452759/)

The association between KLF4 as a tumor suppressor and the prognosis of hepatocellular carcinoma after curative resection

Min Xue^{1,*}, Chenhao Zhou^{2,*}, Yan Zheng^{3,*}, Ziping Zhang⁴, Shun Wang³, Yan Fu³, Manar Atyah², Xiaolong Xue¹, Le Zhu¹, Qiong Zhu Dong³, Huliang Jia³, Ning Ren^{2,4}, Ruolei Hu¹

¹Department of Biochemistry and Molecular Biology, Laboratory of Molecular Biology, Anhui Medical University, Hefei, China

²Department of Liver Surgery, Liver Cancer Institute, Zhongshan Hospital, Fudan University, Shanghai, China

³Department of General Surgery, Huashan Hospital and Cancer Metastasis Institute, Fudan University, Shanghai, China

⁴Institute of Fudan Minhang Academic Health System, Minhang Hospital, Fudan University, Shanghai, China

*Equal contribution

Correspondence to: Ruolei Hu, Ning Ren, Huliang Jia; **email:** shenghuahr@163.com, <https://orcid.org/0000-0001-5856-6814>; renning@fudan.edu.cn, jiahuliang@huashan.org.cn

Keywords: KLF4, hepatocellular carcinoma, prognosis, overall survival, recurrence-free survival

Received: December 27, 2019

Accepted: June 13, 2020

Published: August 5, 2020

Copyright: Xue et al. This is an open-access article distributed under the terms of the Creative Commons Attribution License (CC BY 3.0), which permits unrestricted use, distribution, and reproduction in any medium, provided the original author and source are credited.

ABSTRACT

Krüppel-like factor 4 (KLF4), a zinc-finger transcription factor in klfs family, is known for its crucial role in regulating cell growth, proliferation, and differentiation. This research aimed to explore the prognostic significance of KLF4 in hepatocellular carcinoma's (HCC) patients after curative resection and the role of KLF4 in HCC progression. There were 185 HCC patients who had hepatectomy from July 2010 to July 2011 included in this study. KLF4 expression was detected by microarray immunohistochemical technique, western blot, and qRT-PCR. Then, the correlation between the prognosis of patients and KLF4 expression was evaluated based on patients' follow-up data. The research found KLF4 expression was significantly downregulated in HCC tissues compared to para-tumorous tissues. More importantly, the overall survival rate (OS) and recurrence-free survival rate (RFS) of HCC patients with low KLF4 expression were both significantly decreased compared to those with a high level of KLF4. Further function and mechanism analysis showed that KLF4 could inhibit the proliferation, migration, invasion and epithelial-mesenchymal transition of HCC cells. The study revealed that KLF4 was not only a tumor suppressor in HCC but also can be regarded as a valuable prognostic factor and potential biological target for diagnosis and treatment in HCC patients.

INTRODUCTION

Hepatocellular carcinoma (HCC) is one of the most common types of cancer and ranks second in the leading causes of cancer-related death worldwide [1, 2]. Despite the great achievement in HCC treatment, the mortality in HCC patients remains high, which may be attributed to frequent tumor recurrence and distant metastasis. In addition to the critical role of early diagnosis and intervention in HCC treatment, post-operative monitoring also plays a significant role in im-

proving HCC patients' prognosis [3, 4]. However, there is a lack of prognosis markers for HCC patients receiving a hepatectomy, necessitating the investigation of clinically useful biomarkers for those patients.

Furthermore, due to the low early detection rate and complicated risk factors, the diagnosis of most HCC patients often occurs at an advanced stage with poor prognosis. Considering current medical capabilities, curative liver resection or radiofrequency ablation (RFA) is the first choice for early-stage HCC, but it is

restricted by many conditions such as age, tumor location, bilirubin level < 1.0mg/dL, and hepatic venous pressure < 10 mm Hg. The patients with HCC at early-stage received resection, liver transplantation or RFA with a 50–70% 5-year survival rate [5, 6]. Hence, it is important to explore more alternative clinical biomarkers, which can enhance the diagnosis and treatment in all stages of HCC. Not only radical surgery but also liver transplantation are the most essential treatments provided to patients diagnosed at early stages. Despite the emergence of some drug trials such as Sorafenib and Brivanib, no enhancement of the overall survival rate has been achieved yet [7–10]. With the development of tumor progression, HCC treatment faces a lot of challenges, especially in advanced stages of the disease. Therefore, it is urgent to explore latent molecular mechanisms of HCC progression, which would improve surgical treatment and prognosis of HCC patients.

The transcription factor Krüppel-like factor 4 (KLF4) with zinc-finger structure has specific binding sites and is a member of SP/KLF factors' family. It can regulate cell growth, proliferation, and differentiation in the process of development [11, 12]. In different kinds of tissues, KLF4 plays different roles, either acting as an oncogene or as a tumor suppressor [13, 14]. In cervical carcinoma, KLF4 as a tumor suppressor inhibited cell growth and tumor formation [15]. In lung cancer, KLF4 negatively regulated placenta-specific 8 (PLAC8) expression by binding to the promoter of PLAC8, which suppressed cell proliferation and apoptosis [16]. In addition, KLF4 negatively regulated podocalyxin-like 1 (PODXL) expression to inhibit human gastric cancer's tumorigenesis, invasion, and metastasis [17]. Judging from clinical and experimental data, KLF4 has an anti-cancer effect on suppressing tumor differentiation, proliferation, invasion, epithelial-mesenchymal transition (EMT), and metastasis [18–20]. In addition, recent studies have shown that KLF4 is a key regulator of monoglyceride lipase (MGLL) and plays an essential role in inhibiting HCC cell migration [21]. KLF4 can elevate miR-153, miR-506 and miR-200b levels to downregulate EMT-associated proteins [22]. Epithelial-mesenchymal transition (EMT) is a process of the transformation of epithelial phenotype to a mesenchymal phenotype. Multiple lines of evidence have demonstrated that EMT was strongly associated with cancer cell proliferation, invasion and metastasis [23, 24]. Recent studies have shown that KLF4 is a key negative regulator of EMT, and the expression of KLF4 is often decreased during the process of EMT [25]. In addition, E-cadherin was found to be the target gene of KLF4 in invasion and metastasis of breast cancer [26]. However, the prognostic value of KLF4 in

HCC patients and the influencing mechanism of KLF4 in the progression of HCC have been rarely explored.

In our research, we explored the prognostic values of KLF4 by analyzing the correlation between KLF4 and clinicopathologic features in HCC patients. In addition, we investigated the functions of cells by overexpressing and knocking-down KLF4 and the regulating effects of KLF4 on EMT in HCC cells. We determined KLF4 as an independent prognostic biomarker for HCC patients, and the inhibiting effect of KLF4 on EMT is expected to provide new therapeutic targets.

RESULTS

Different patterns were used for detecting KLF4 expression in HCC

KLF4 expression in most HCC cells (PLC/PRF/5, Hep3B, Huh7, HepG2, but except SMMC- 7721) was lower than in normal liver cells (L02) not only at mRNA level but also at the protein expression level (Figure 1A and 1B). Same KLF4 expression patterns were found in the TCGA database (<https://tcga-data.nci.nih.gov/tcga/>), with lower expression observed in many kinds of tumors including lung adenocarcinoma (LUAD), bladder urothelial carcinoma (BLCA), and cholangiocarcinoma (CHOL) (opposing to matched para-tumorous tissues) (Figure 1D).

Immunohistochemical staining intensity in a tissue microarray (TMA) was divided into four levels, which is our scoring criterion for KLF4 expression in tissues (Figure 1E). According to the score statistics of staining degree and the staining area, high KLF4 expression rate in para-tumorous tissues was 58.92% (109 of 185: 16 of strong and 93 of moderate) while high KLF4 expression rate in HCC tissues was 23.78% (44 of 185: 4 of strong and 40 of moderate), which showed KLF4 expression in tumor tissues is lower than the paired para-tumorous tissues (**P* <0.05) (Figure 1C). The results demonstrated that KLF4 may be a potential prognostic marker for those patients with HCC.

KLF4 expression is related to some clinicopathological features

Depending on the scores of immunohistochemical staining, 185 HCC patients were distributed into two groups: one group had high KLF4 expression and the other group had low KLF4 expression. High KLF4 expression group showed a statistical score of strong and moderate staining while the low KLF4 expression group showed a statistical score of weak and negative staining. Table 1 shows that low KLF4 expression was associated with many clinical phenotypes, such as vascular invasion (***P* <0.001), high alpha-fetoprotein

level ($*P = 0.012$), and advanced Barcelona Clinic Liver Cancer (BCLC) stage ($**P = 0.002$). There was no remarkable correlation between other clinical characteristics and KLF4 in our research.

The level of KLF4 expression was related with OS and RFS of HCC patients

The results showed a relation between the outcome of HCC and KLF4 expression when evaluating OS and

RFS of patients. Figure 2A showed HCC patients with high KLF4 expression in tumor tissues displayed a favorable prognosis in OS (OS, $***P < 0.001$) and RFS (RFS, $***P < 0.001$) analyses compared to those patients with low KLF4 expression.

From the analysis of the impact of different differentiation degree or BCLC stages on OS and RFS, we can see patients with higher KLF4 expression in “differentiation I-II” subgroups had a better OS

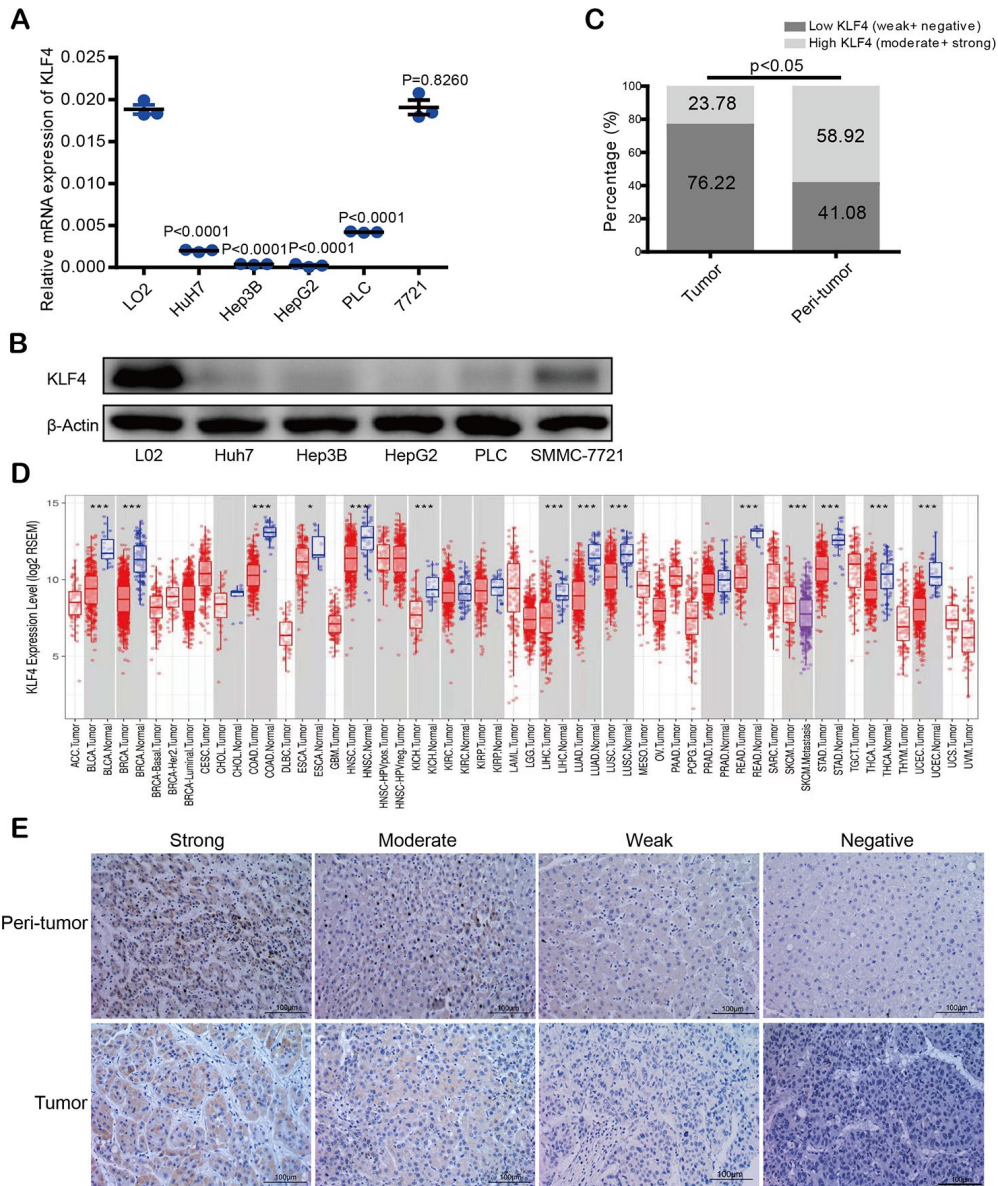


Figure 1. KLF4 expression in hepatocellular carcinoma (HCC) tissues and cell lines. (A) KLF4 expression was detected in the mRNA level among five HCC cell lines and one normal liver cell (L02). **(B)** KLF4 expression was detected in the protein level in six cell lines. The internal control was β -actin. **(C)** Immunohistochemical results were analyzed by chi-square test to compare the distribution of KLF4 in HCC tumors and adjacent tissues. **(D)** KLF4 expression was analyzed in tumor and para-tumorous tissues in TCGA tumors. **(E)** KLF4 expression was exhibited through characteristic photos of immunostaining in HCC tumor and para-tumorous tissues. Image scale= 100 μ m. $P < 0.05$ was considered statistically significant, $* P < 0.05$, $** P < 0.01$, $*** P < 0.001$.

Table 1. KLF4 expression in 185 HCC patients based on clinicopathologic characteristics.

Characteristics	Patients	KLF4 expression		P
	n (%)	Low (n = 141)	High (n = 44)	
Age, years				
≤ 50	94 (50.8)	69	25	
> 50	91 (49.2)	72	19	0.392
Gender				
Female	31 (16.8)	21	10	
Male	154 (83.2)	120	34	0.250
HBsAg				
Negative	26 (14.1)	20	6	
Positive	159 (85.9)	121	38	1.000
AFP, ng/ml				
≤ 20	70 (37.8)	46	24	
> 20	115 (62.2)	95	20	0.012*
Liver cirrhosis				
NO	29 (15.7)	21	8	
Yes	156 (84.3)	120	36	0.637
Tumor number				
Single	167 (90.3)	124	43	
Multiple	18 (9.7)	17	1	0.078
Tumor size, cm				
≤ 5	130 (70.3)	96	34	
> 5	55 (29.7)	45	10	0.264
Vascular invasion				
Absent	121 (65.4)	81	40	
Present	64 (34.6)	60	4	< 0.001***
Tumor differentiation				
I-II	136 (73.5)	99	37	
III-IV	49 (26.5)	42	7	0.080
BCLC stage				
0+A	39 (21.1)	22	17	
B+C	146 (78.9)	119	27	0.002**
Tumor capsule				
Complete	101 (54.6)	73	28	
None	84 (45.4)	68	16	0.225
ALT, U/L				
≤40	170 (91.9)	129	41	
>40	15 (8.1)	12	3	1.000

Abbreviations: HCC, hepatocellular carcinoma; HBsAg, hepatitis B surface antigen; AFP, α- fetoprotein; BCLC, Barcelona Clinic Liver Cancer; ALT, alanine aminotransferase. $P < 0.05$ was considered statistically significant, Pearson χ^2 tests. * $P < 0.05$, ** $P < 0.01$, *** $P < 0.001$.

(*** $P < 0.001$, Figure 2B) and RFS (** $P = 0.0029$, Figure 2D). However, differences in KLF4 expression of the “differentiation III-IV” subgroup failed to predict similar outcomes (Figure 2C and 2E). Then to further analyze the relationship between KLF4 and prognosis in different BCLC subgroups, results show the patients in all stages of BCLC with low KLF4 expression group had shorter OS (** $P = 0.0019$, Figure 2F and *** P

<0.0001, Figure 2G) and RFS (* $P = 0.0183$, Figure 2H and Figure 2I, ** $P = 0.0063$).

Low expression of KLF4 may mean poor prognosis for HCC patients

Table 2 showed the prognostic role of KLF4 in HCC patients. In univariate analysis, tumor size and the

degree of tumor differentiation were significantly related to HCC patients' OS and RFS. The OS was also significantly related to tumor number and microvascular invasion while RFS was also significantly associated with serum HBsAg level. However, other features including age, gender, ALT, liver cirrhosis, tumor encapsulation, and serum AFP level showed no significant prognostic associations with OS or RFS. A multivariate Cox regression analysis was then conducted with all the prognostic factors of $*P < 0.05$ in

univariate analysis. Based on the results, we concluded high KLF4 was identified as a positive prognostic factor for OS and RFS of HCC patients.

Prognostic prediction of nomograms for HCC based on KLF4 expression

Two new prognostic nomograms were built based on the results of univariate analysis to predict the OS and RFS of HCC patients, which aimed to further clarify the

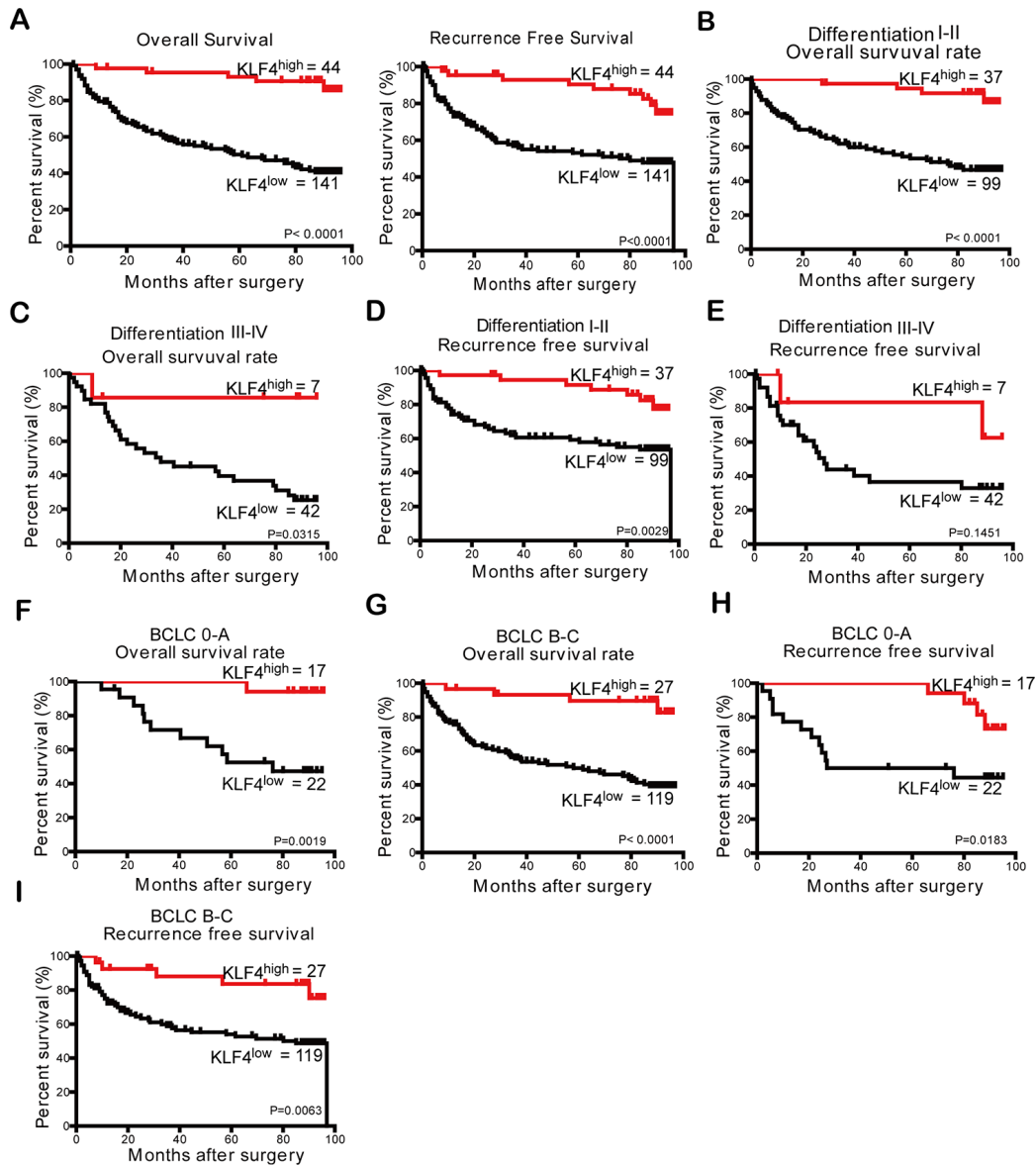


Figure 2. The prognostic analysis of KLF4 in HCC patients (n = 185) and subgroup analysis based on differentiation degree and BCLC stages. (A) According to KLF4 expression level in patients' tissues with HCC, the curves described OS and RFS of patients, respectively. The OS in (B) differentiation I-II patients and (C) differentiation III-IV patients was analyzed by Kaplan- Meier method. The RFS in (D) differentiation I-II patients and (E) differentiation III-IV patients were analyzed by Kaplan- Meier method. Kaplan- Meier method was employed to analyze the OS of patients in (F) BCLC 0-A group and (G) BCLC B-C group. The RFS of patients in two subgroups (H and I) of the BCLC stage was analyzed through Kaplan- Meier analysis. $P < 0.05$ was considered statistically significant.

Table 2. The prediction for OS and RFS of 185 HCC patients with univariate and multivariate analyses.

Variables	OS			RFS		
	Univariate	Multivariate		Univariate	Multivariate	
	<i>P</i>	HR (95% CI)	<i>P</i>	<i>P</i>	HR (95% CI)	<i>P</i>
Age (> 50 vs. ≤ 50)	0.619		NA	0.444		NA
Gender (male vs. female)	0.326		NA	0.756		NA
ALT, U/L (> 40 vs. ≤ 40)	0.462		NA	0.946		NA
AFP, ng/mL (> 20 vs. ≤ 20)	0.061		NA	0.488		NA
HBsAg (positive vs. negative)	0.276		NA	0.032	2.836 (1.138-7.067)	0.025
Liver cirrhosis (yes vs. no)	0.369		NA	0.169		NA
Tumor size, cm (> 5 vs. ≤ 5)	0.003	1.731 (1.101-2.722)	0.018	0.021	1.671 (1.017-2.746)	0.043
Tumor number (multiple vs. single)	0.004		NS	0.215		NA
Tumor differentiation (III-IV vs. I-II)	0.007		NS	0.010		NS
Tumor encapsulation (complete vs. none)	0.093		NA	0.090		NA
Vascular invasion (present vs. absent)	0.001		NS	0.402		NA
KLF4 (Low vs. High)	< 0.001	5.959 (2.366-15.004)	< 0.001	0.001	3.477 (1.720-7.027)	0.001

Abbreviations: OS, overall survival; RFS, recurrence-free survival; ALT, alanine aminotransferase; AFP, α-fetoprotein; HBsAg, hepatitis B surface antigen; CI, confidential interval; HR, hazard ratio. Data obtained from the Cox proportional hazards model; NS, not significant; NA, not adopted. $P < 0.05$ was regarded as statistically significant.

relationship between KLF4 expression and prognosis of patients (Figure 3A and 3B). As seen in Figure 3C–3F, the calibration curves were used to compare the value of nomograms-prediction and the actual observed value, and found the predicted results is similar to the actual results. The decision curve analyses were drawn to compare the prediction of clinical net benefits between prognostic nomograms and the BCLC staging. According to the comparison, it is found that prognostic nomograms has better prediction capability (Figure 3G–3J). To enhance the predictive accuracy of KLF4 for HCC, C-index (Harrell's concordance index) was employed to evaluate the performance. Table 3 showed the nomograms for OS and RFS (based on KLF4 expression) owned a better postoperative prediction effect compared to the BCLC staging (** $P < 0.001$).

KLF4 inhibits HCC cells proliferation

Based on the dysregulation of KLF4 expression in HCC patients, we further studied the effects of KLF4 on the biological behaviors of HCC cells. PLC/PRF/5 cells were transfected with pCDHCMV-MCS-EF1-Puro-KLF4 to select stable KLF4 overexpressed cells (OE-KLF4), while SMMC-7721 cells were transfected with pLKO.1-shRNA to select stable KLF4 silenced cells (sh-KLF4). The overexpression control (OE-NC) and shKLF4 control (sh-NC) were transfected with empty plasmids, respectively. The efficiency of overexpression or knockdown of KLF4 in PLC/PRF/5 and SMMC-7721 cells was detected by Western blot (Figure 4A). We applied the CCK8 assay to detect the cell proliferation rate. As shown in Figure 4B, the KLF4

overexpression could significantly reduce the cell proliferation activity in PLC/PRF/5 cells. While, KLF4 knockdown significantly improved the cell proliferation activity in SMMC-7721 cells. The results confirmed that KLF4 inhibits cell proliferation of HCC cells *in vitro*.

KLF4 inhibits HCC cells migration

Cell wound scratch and transwell assays were employed to explore the effects of KLF4 on cell motility. Compared to the control group, the cell wound scratch assay revealed that over-expressed KLF4 inhibited cell migration in PLC/PRF/5 cells, and knocked-down KLF4 promoted cell migration in SMMC-7721 cells, as shown in Figure 4C. Also, transwell assay showed that over-expressed KLF4 inhibited cell migration in PLC/PRF/5 cells and knocked-down KLF4 promoted cell migration in SMMC-7721 cells in comparison with the respective control group (Figure 4D). Thus, we concluded that KLF4 could inhibit HCC cell migration *in vitro*.

KLF4 inhibits the invasion of HCC cells

Transwell assay was used to investigate the effects on invasion by changing KLF4 expression. We found that up-regulated KLF4 expression in PLC/PRF/5 cells inhibited cell invasion, and decreased KLF4 expression in SMMC-7721 cells promoted cell invasion. These results illustrated that KLF4 inhibits the invasion of HCC cells *in vitro* (Figure 5A). Judging from the cellular morphology of SMMC-7721

cells with shKLF4, reduced KLF4 expression leads to the morphological transformation from the epithelial phenotype into the mesenchymal phenotype (Figure 5B). Western blot and qPCR assays showed that KLF4 overexpression in PLC/PRF/5 cells could effectively

upregulated the expression of E-cadherin. While KLF4 knockdown could significantly downregulate the expression of N-cadherin and Vimentin (Figure 5C). These results revealed that KLF4 exhibits the capacity to block the activation of EMT pathway.

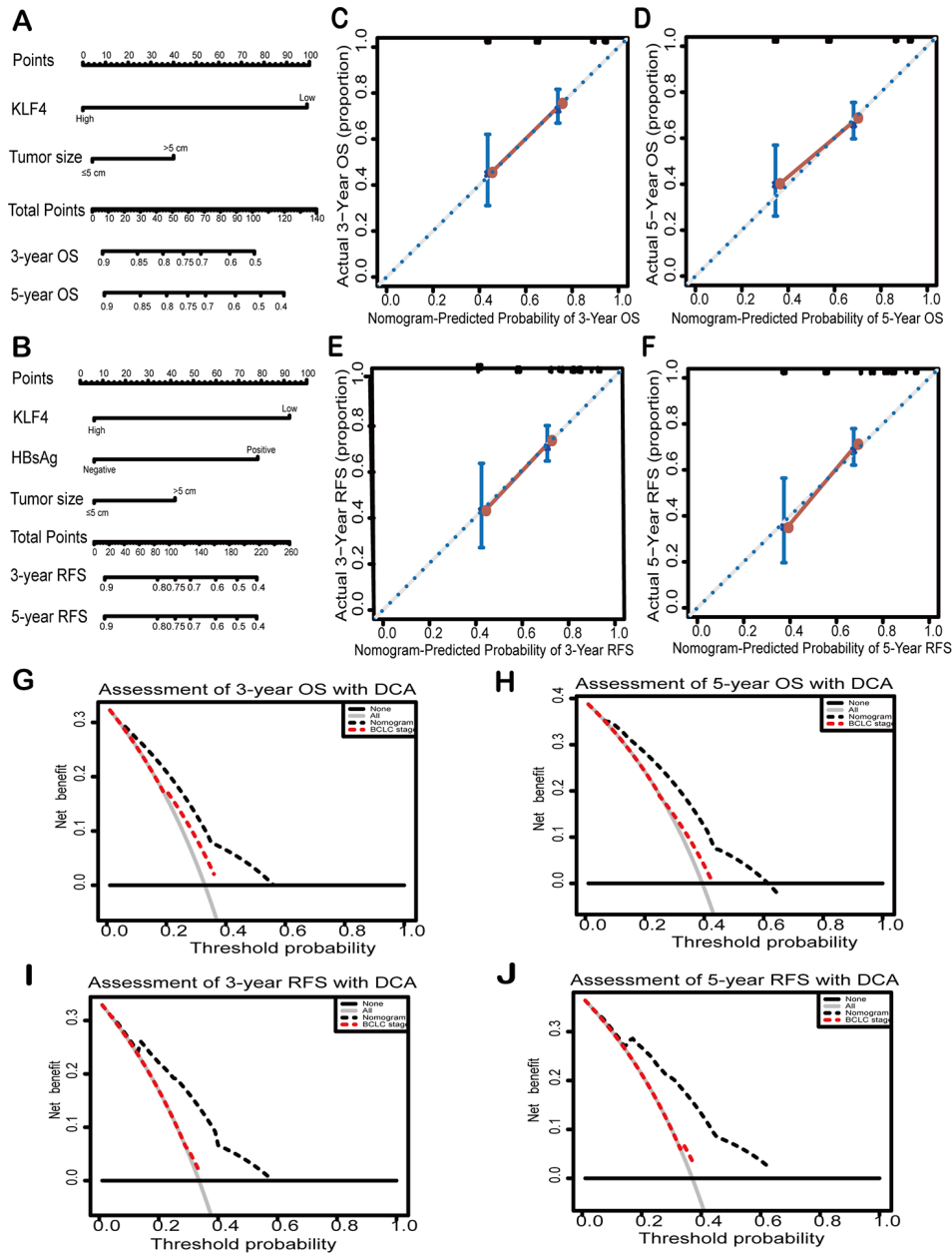


Figure 3. Nomograms and decision curves analyses were to further study the effect on the prognosis of KLF4. Pictures (A) and (D) showed the predictive analysis through prognostic nomogram. First, the plumb line between each factor and the point scale was drawn, and then got the point of each factor. The sum of the points of all factors is the total set of points. finally, a plumb line was drawn from all point scales to the probability scale to obtain the probability of OS or RFS. 3- year and 5- year OS (B and C) and 3-year and 5- year RFS (E and F) were shown by calibration curves. The X-axis represented the predicted value of OS or RFS by nomograms and the Y-axis represented actual OS or RFS. The clinical effects of different models were exhibited by decision curve analyses. The comparison of predictions between nomogram-predicted and conventional staging system for 3-year OS and RFS (G and H) and 5-year OS and RFS was shown (I and J). BCLC: Barcelona Clinic Liver Cancer staging. Dashed lines: The probability of the clinical net benefit crossing a certain threshold; the solid black horizontal line: to suppose no patients suffer the incident; the gray solid line: to assume all patients suffer the incident.

Table 3. The predicted comparison for OS and RFS between nomogram and BCLC stage in HCC patients.

Variables	Overall survival		Recurrence-free survival	
	C-index (95% CI)	P value	C-index (95% CI)	P value
BCLC stage	0.563 (0.525-0.601)		0.526 (0.478-0.574)	
Nomogram	0.681 (0.632-0.730)		0.686 (0.634-0.738)	
Nomogram vs. BCLC stage		< 0.001†		< 0.001†

Abbreviations: OS, overall survival; RFS, recurrence-free survival; C-index, concordance index; CI, confidence interval; TNM, Tumor-Nodes-Metastases; BCLC, Barcelona Clinic Liver Cancer.

†: Compared the C-index of nomogram with BCLC stage in patients with HCC.

DISCUSSION

HCC is one of the most common malignancies and ranks second among the leading causes of cancer-related deaths worldwide, and the morbidity and mortality of men with HCC are two to three times higher than that of women [1]. The low overall survival rate of liver cancer patients may be mainly attributed to cancer recurrence and distant metastasis [2, 27]. Increasing evidence suggested the abnormal expression of KLF4 was detected in many digestive system neoplasms. The point about KLF4 has been supported by a series of research. Shi et al reported that KLF4 repressed lactate dehydrogenase A (LDHA) expression level directly impacting aerobic glycolysis in pancreatic cancer [28]. The research of Zhao WD identified the functional role of KLF4 suppressing colorectal cancer progression [29]. KLF4 could also maintain homeostasis of gastric mucosa, and suppress gastric carcinogenesis and progression [30]. All these findings strengthen the suggestion that KLF4 plays a vital role in suppressing the development and progression in many kinds of tumors. So far, there are ambiguous for the mechanism of HCC progression and no satisfactory prognostic markers for HCC, which highlights the importance of research on the relevant mechanisms in HCC progression and potential biomarkers for HCC patients. Our results suggested KLF4 has the inhibitory effect in HCC progression and is associated with the prognosis of HCC patients receiving curative resection. Our results showed that KLF4 expression is decreased in HCC tissues compared to para-tumorous tissues. Similar results were also observed in the comparison of HCC cell lines with normal liver cell lines. Moreover, the staining results of immunohistochemistry (IHC) showed that KLF4 expression is predominantly decreased in tumor tissues, and lower KLF4 expression was associated with poorer prognosis of HCC patients, which indicated that KLF4 potentially acts as a prognostic marker for HCC patients.

The previous study showed that the transcription factor KLF4 is indispensable in maintaining vascular homeostasis as KLF4 transcriptionally upregulated

miR-15a to inhibit angiogenesis vascular endothelial cells [31]. It was reported that sustained KLF4 expression promotes ineffective tumor angiogenesis and diminishes tumor growth [32]. Interestingly, we also observed that KLF4 expression negatively correlated with vascular invasion, suggesting KLF4 may inhibit the tumor growth of HCC by regulating angiogenesis. KLF4 was reported to be a tumor suppressor in colorectal cancer, possibly through elevating the Von Hippel-Lindau gene product, pVHL [33]. In addition, KLF4 transactivated hepatocyte nuclear factor 6 (HNF-6) expression to block the dedifferentiation and progression of hepatocellular carcinoma [34]. Similar results were also observed in our study, which showed that the expression of KLF4 was lower in many types of TCGA tumors, such as LUAD, CHOL and BLCA (when compared to normal tissues). Also, aggressive tumor phenotypes such as advanced BCLC stages, high levels of AFP, present vascular invasion and poor differentiation were associated with low KLF4 expression. These results implied that KLF4 could be considered as a prognostic biomarker in HCC patients.

Research reports that the progression of hepatocellular carcinoma is a stepwise process of dedifferentiation, and well-differentiated HCC commonly appears in the early stage [35]. In our research, we explored the prognostic value of KLF4 in HCC patients through subgroup analysis. According to the analysis, patients with high KLF4 expression had longer OS and RFS in a well-differentiated group of HCC; whereas the correlation between KLF4 expression and prognosis was insignificant in the poorly differentiated subgroup. Patients with poor differentiation may affect the accuracy of KLF4 on prognostic assessment in patients with advanced HCC. Such results indicated KLF4 can act as a potential prognostic biomarker for patients with early HCC. To verify that KLF4 is not only a prognostic biomarker for early HCC patients, we analyzed the OS and RFS of patients in two subgroups of BCLC based on KLF4 expression. The results manifested that patients with high KLF4 expression had prolonged OS and RFS compared with the patients with low KLF4 expression in two subgroups of BCLC. According to

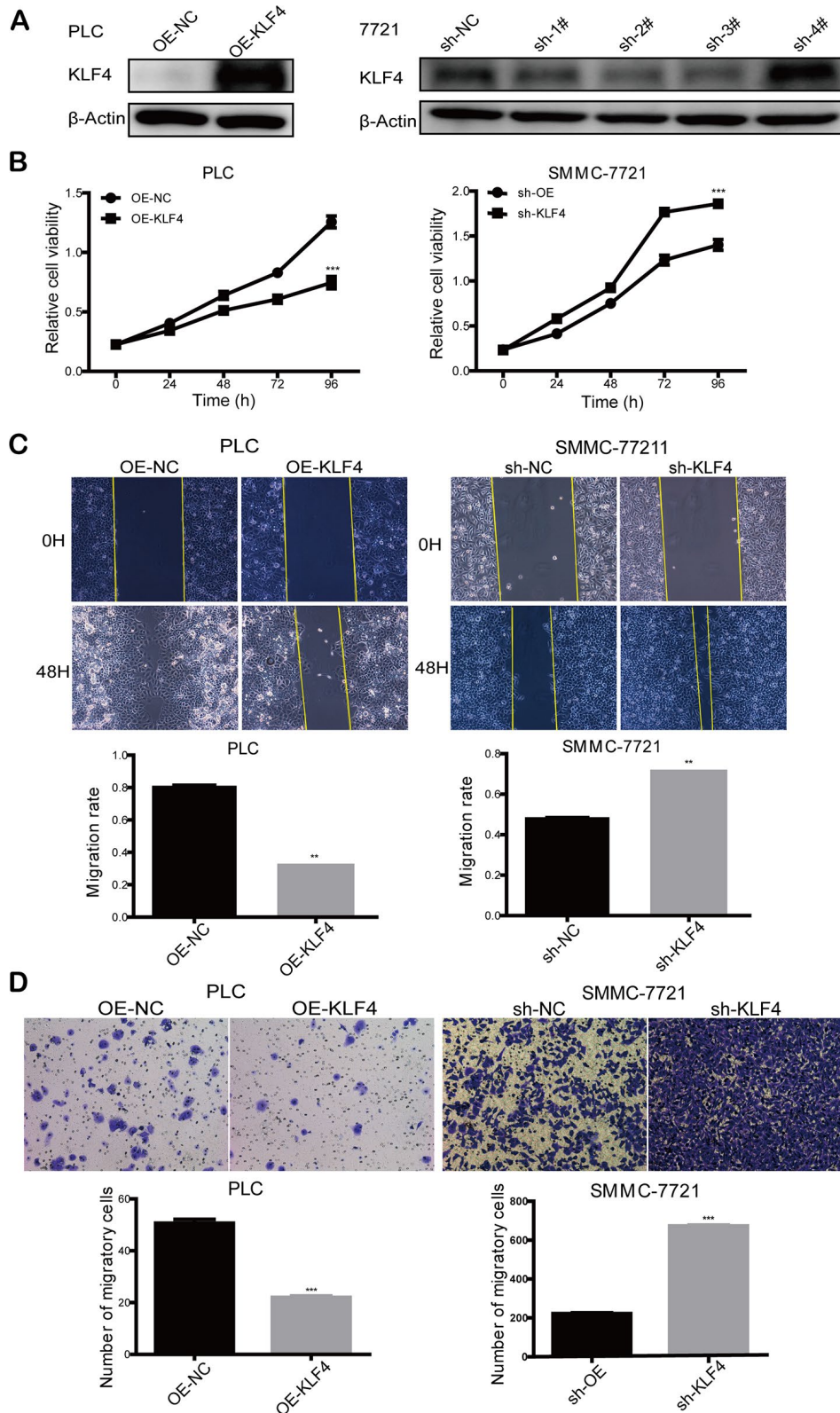


Figure 4. KLF4 inhibits the proliferation and migration ability of HCC cells. (A) Knockdown of KLF4 in SMMC-7721 and overexpression of KLF4 in PLC/PRF/5 was verified by western blot, and β -actin was used as an internal control in western blot assays. (B) CCK8 assay was implemented to detect the proliferation rate of steadily transfected SMMC-7721 and PLC/PRF/5. (C) Cell wound scratch assay and (D) transwell assay was executed to evaluate the migration rate of steadily transfected SMMC-7721 and PLC/PRF/5. Student's t-test was used in line charts and bar charts. $P < 0.05$ was considered statistically significant. * $P < 0.05$, ** $P < 0.01$, *** $P < 0.001$.

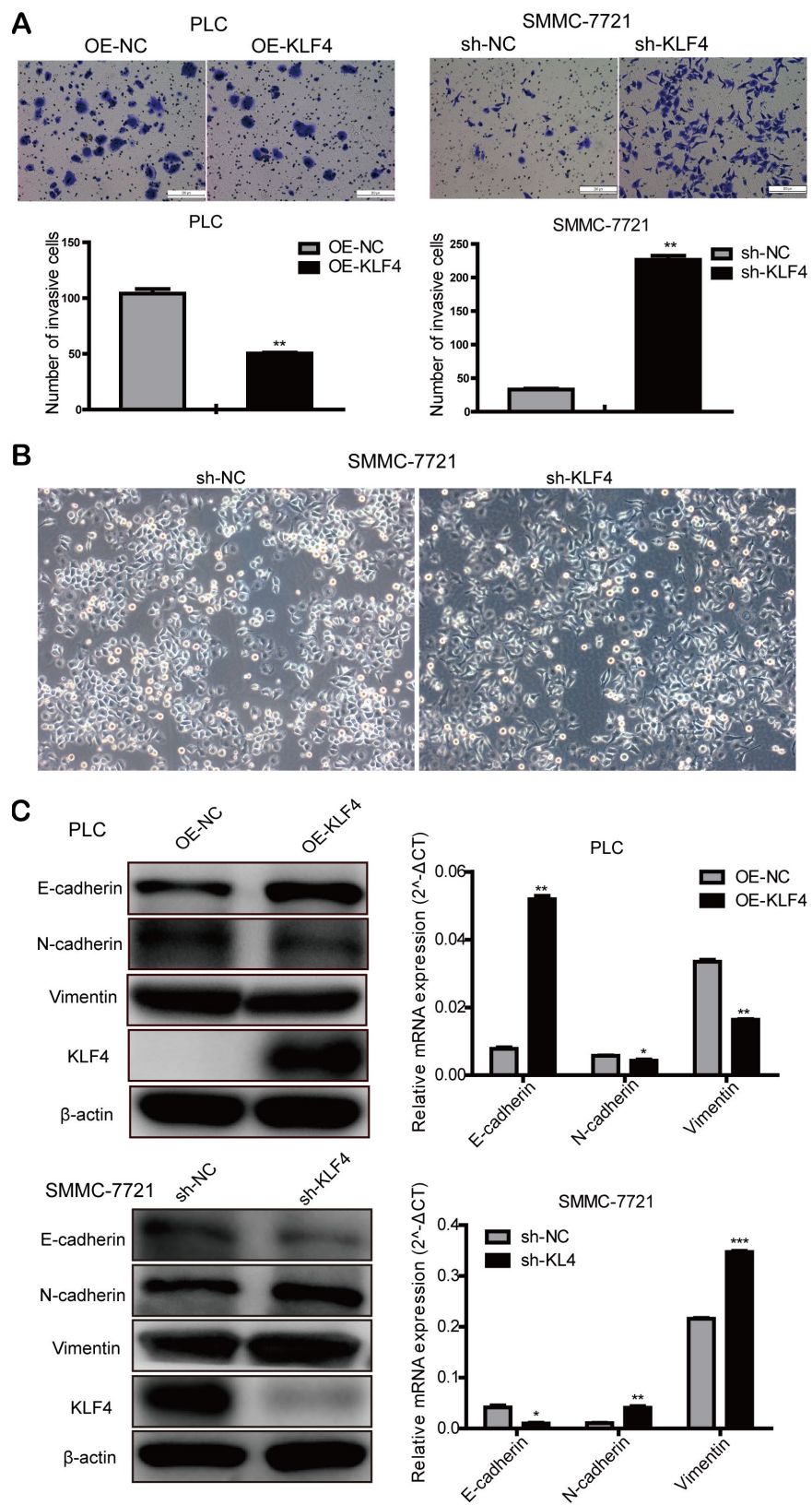


Figure 5. KLF4 inhibits the invasion of HCC cells. (A) Transwell assay was determined to detect the effect of KLF4 on cell invasion in PLC/PRF/5 and SMMC-7721 cells. Student's t-test was used in bar charts. (B) Changes in cell morphology in SMMC-7721 with shKLF4. (C) Western blot and qPCR were used to detect EMT-associated protein expression in steadily transfected PLC/PRF/5 and SMMC-7721 cells. $P < 0.05$ was considered statistically significant. * $P < 0.05$, ** $P < 0.01$, *** $P < 0.001$.

univariate and multivariate analysis, we concluded KLF4 was an independent prognostic factor regardless of HCC stage, tumor differentiation, and tumor size. Furthermore, the prognostic nomogram model based on KLF4 expression was employed to prove the prediction accuracy of KLF4 for HCC patients' OS and RFS. Then, we further studied the effects of KLF4 on the biological behaviors of HCC cells. Western blot and qPCR were used to detect KLF4 expression in HCC cell lines. Results show KLF4 expression in most HCC cells (PLC/PRF/5, Hep3B, Huh7, HepG2) was lower, while in SMMC-7721 cells was higher when compared to the normal liver cells (L02). Considering KLF4 expression levels in HCC cell lines, PLC/PRF/5 cells were selected to overexpress exogenous KLF4, and SMMC-7721 cells were transfected with shRNA of KLF4 to explore the effects of KLF4 on the biological behaviors of HCC cells. A series of in vitro study revealed that KLF4 overexpression inhibited cell proliferation, migration, and invasion of PLC/PRF/5 cells while KLF4 knock-down enhanced such activities in SMMC-7721 cells, which supported KLF4's antitumor function in HCC. Mounting research has shown that EMT plays a significant role in acquiring the capability of migration and invasion for cancer cell in cancer progression and metastasis[36, 37]. In addition, judging from the cellular morphology of SMMC-7721 cells with shKLF4, reduced KLF4 expression leads to the morphological transformation from the epithelial phenotype into the mesenchymal phenotype. Moreover, elevated KLF4 expression upregulated E-cadherin expression and decreased N-cadherin, Vimentin expression in PLC/PRF/5 cells, While reduced KLF4 expression downregulated E-cadherin expression and elevated N-cadherin, Vimentin expression in SMMC-7721 cells. These results demonstrated that KLF4 exhibits the capacity to inhibit HCC progression by blocking the activation of EMT pathway. Thereby, we regarded KLF4 as a tumor suppressor that could inhibit HCC progression.

However, there were some limitations in our research. Firstly, our results need to be further verified in a larger cohort of the patients considering the limited number of patients enrolled in this study. Secondly, this study was a retrospective analysis. Therefore, future prospective analysis to validate the results is needed. An independent cohort will also be needed to validate the findings, and the molecular mechanism of KLF4 inhibiting EMT in HCC progression should be further explored in future study.

In summary, we illustrated clearly that KLF4 as a suppressor can block the activation of EMT in HCC progression. And KLF4 is downregulated in HCC tumors and can be regarded as a prognostic factor to

predict OS and RFS of HCC patients after curative resection. In addition, the nomograms in this research can further improve the prediction for OS and RFS of HCC patients by integrating KLF4 and other independent clinical factors. Hence, KLF4 may be a potential therapeutic biomarker and prognostic indicator for HCC patients. The antitumor effect of KLF4 and the functional mechanisms need to be explored in future studies.

MATERIALS AND METHODS

Patient selected and follow-up

We completed a statistical analysis of registered information from 185 HCC patients in Zhongshan Hospital, Fudan University. All patients had a hepatectomy from July 2010 to July 2011. Patients' screening criteria were as follows: patients did not receive any systemic or local treatments nor experience extrahepatic metastases before the operation. All patients who underwent primary and therapeutic hepatectomy had a definite postoperative pathological diagnosis of HCC. These patients who all showed absolute follow-up data and clinicopathological features had no infection or inflammatory response other than viral hepatitis. The patients underwent a series of examinations such as alanine aminotransferase (ALT), liver cirrhosis, hepatitis B virus surface antigens (HBsAg), alpha-fetoprotein (AFP), tumor encapsulation, tumor number, tumor size, vascular invasion, differentiated degree, and Barcelona Clinic Liver Cancer staging (BCLC) within 3 days before the operation. All patients were followed up and received blood routine examination, blood biochemical examination, serological examination of tumor markers, abdominal ultrasound, and chest imaging examination. The follow-up time was defined as every three months for the first five years after surgery and once a year for the time after. The deadline for data collection was July 2018 or the time of death in deceased patients. The study was conducted with the patients' knowledge and permitted by the hospital ethics committee. The academic research was conducted under ethical standards.

Tissue samples and immunohistochemistry

The human HCC tissues microarray was made of the tumor tissues and para-carcinoma tissues collected from the 185 HCC patients after curative resection. We then sorted out and analyzed the corresponding information of tissue microarray. Tissue microarrays were constructed with surgical specimens fixed by formalin and embedded by paraffin. Anti-KLF4 antibody (ab215036; Abcam) was used for incubating sections. Immunohistochemical analysis was performed accord-

ing to the previous method [38]. Then, immunohistochemical results were assessed by two independent pathologists who did not have access to patients' information. The staining degree of KLF4 was scored semi-quantitatively as 3 for strong, 2 for moderate, 1 for weak, 0 for negative. The score of the staining area was calculated by the percentage of stained positive cells and was scored as 4 for >75%, 3 for 51%- 75%, 2 for 26%- 50%, 1 for 5%- 25%, 0 for <5%. The final results described each specimen through multiplying the staining degree score by the staining area score. The expression level of KLF4 in each specimen was evaluated according to the score value with 9- 12 as a strong level, 6- 8 as a moderate level, 1- 4 as a weak level, 0 as a negative level.

Cell culture and transfection

There are six types of cells (five types of liver cancer cells: SMMC- 7721, HepG2, Hep3B, Huh7, and PLC/PRF/5, and a normal liver cell (L02)) were included in the experiments and all cell identification reports were provided in supplementary materials. All these cells were acquired from the cell bank of the Chinese Academy of Sciences (Shanghai, China). All the cells were cultured with Dulbecco's Modified Eagle Medium (DMEM basic; Gibco). The concentration of fetal bovine serum (FBS; Gibco) in DMEM was 10%. These cells were then cultured at cell incubator (Thermo; America) with 5% CO₂ at 37°C. Lentiviral particles loaded the KLF4 overexpression plasmid (OE-KLF4) to infect PLC/PRF/5 cells, empty vectors (OE-NC) were used as overexpression control. SMMC- 7721 cells were infected with lentiviral particles, loading shRNA-KLF4 plasmid (sh-KLF4), and empty vector (sh-NC) as shRNA control.

RNA extraction and quantitative reverse transcription PCR (qRT-PCR)

Firstly, PBS was used to wash the collected HCC cells. Then, total RNA was extracted with the TRIzol reagent (Invitrogen, USA). Next, 1 µg of total RNA was used for reverse transcription with Reverse Transcription Reagent Kit (Takara, Japan). The mRNA expression of KLF4 was detected with TB Green qPCR Mix (Takara, Japan) on the basis of reagent supplying protocols. The primers were used for detection as follows: KLF4-forward: 5'-CAAGTCCC GCCGCTCCATTA-3'; KLF4-reverse: 5'-CCATCCACAGCCGTCCCAGT-3'; β-actin-forward: 5'-GGACCTGACTGACTACCTCAT-3'; β-actin-reverse: 5'-CGTAGCACAGCTTCTCCTTAAT-3'; E-cadherin-forward: 5'-CGAGAGCTACACG TTCACGG-3'; E-cadherin-reverse: 5'-GGGTGTCGA GGGAAAATAGG-3'; N-cadherin-forward: 5'-TGC GGTACAGTGTA ACTGGG-3'; N-cadherin-reverse: 5'-

GAAACCGGGCTATCTGCTCG-3'; Vimentin-forward: 5'-CGGGAGAAATTGCAGGAGGA-3'; Vimentin-reverse: 5'-AAGGTCAAGACGTGCCAGAG-3'. The conditions of the experimental reaction were: 1 cycle for 30 seconds (95 °C), 40 cycles of denaturation for 5 seconds (95 °C), and annealing for 34 seconds (60°C). Finally, the gene expression differences were analyzed according to the experimental results. Three repetitions were performed in the experiment.

Western blot

The protein expression level of KLF4 in the HCC cell lines was detected by Western blot. RIPA lysis buffer was employed to extract total protein of HCC cells, and then 10% SDS- PAGE were used to separate protein samples. The PVDF membrane (IPVH 00010; Millipore) with a pore size of 0.45µm was used to transfer the cell protein. After 5% defatted milk blocking for 90 minutes at room temperature, anti-KLF4 antibody (ab215036; Abcam) and anti-β-actin antibody (#13E5; CST) were used for incubating the membranes at 4°C overnight. On the second day, TBST (1% Tween diluted in TBS) was used to wash the membranes, then the membranes were incubated with diluted secondary antibodies (API32P; EMD Millipore) at room temperature for 90 minutes. Finally, the membranes were scanned with equipment (Image Quant LAS 4000; Sweden).

Cell proliferation assay

We employed CCK8 assay (<http://www.dojingdo.cn>) to detect the cell proliferation activity and viability of the selected SMMC- 7721 and PLC/PRF/5 cells. Counted cells were cultured with 96-well plates at 37 °C. The absorbance at 450nm was observed at different time points with each well injected into the 10ul CCK8 kit so that we can compare the rate of cell proliferation by the value of absorbance. Each well has three identical wells.

Cell migration and invasion assays

For cell wound scratch experiment, selected cells and cells of the control group were cultured in 6-well plates. Each well was covered with cells and scratched with white tips on the next day. Then pictures were taken at different time points. Cell migration and invasion was examined by transwell assays. Matrigel matrix basement membrane (#354234; Corning) was added into the chambers (8.0µm pores; Corning) before culturing cells in transwell invasion assay. For transwell migration and invasion assays, a certain amount of medium with serum was added to 24-well plate, then chambers were placed on the plate. The counted cells were cultured with serum-free DMEM in chambers for a

few hours, where they can migrate through the holes planting on the membranes of the chambers. Finally, the cells on the membranes were fixed with 4% paraformaldehyde and the fixed cells stained with crystal violet. The average number of cells in the five fields was regarded as the number of migrating cells.

Statistical analysis

Using the TCGA database, we estimated the differential expression of KLF4 between tumor tissues and para-tumorous tissues in different types of cancers with the method of the Wilcoxon test. The results were shown in box plots. The relationship between clinicopathologic features and KLF4 was evaluated by student's t-test and Pearson chi-square test. The OS and RFS were assessed by the Log-rank test and Kaplan Meier survival analysis. For other data, they were evaluated by means \pm standard deviation (SD), and SPSS 19.0 was used to complete the analysis. According to the distribution of data, student's t-test or Mann-Whitney U test was used for the comparison of differences between groups. The Cox proportional risk regression model was employed to perform univariate and multivariate analyses. The property of a nomogram was estimated according to three ways: the decision curve analysis (DCA), calibration curve and Concordance index (C-index). Only when $*P < 0.05$, results reached statistical significance.

AUTHOR CONTRIBUTIONS

Ruolei Hu, Ning Ren, Huliang Jia, and Min Xue contributed to the conception and design of research and completed the analysis and interpretation of data and drafted the manuscript. Ziping Zhang, Chenhao Zhou, Yan Zheng, and Qiongzhu Dong contributed to statistical analysis. Shun Wang, Yan Fu, Manar Atyah, Xiaolong Xue, Le Zhu corrected the text. All authors have accepted the final version of the manuscript.

CONFLICTS OF INTEREST

We guarantee that there are no conflicts of interest in the article.

FUNDING

The study is financially supported by the National Natural Science Foundation of China (grant No. 81800464 and 81872356), Shanghai Municipal Commission of Health and Family Planning (grant No. 201740238) and the China National Key Projects for Infectious Disease (2017ZX10203207004001).

REFERENCES

1. Bray F, Ferlay J, Soerjomataram I, Siegel RL, Torre LA, Jemal A. Global cancer statistics 2018: GLOBOCAN estimates of incidence and mortality worldwide for 36 cancers in 185 countries. *CA Cancer J Clin.* 2018; 68:394–424.
<https://doi.org/10.3322/caac.21492>
PMID:[30207593](https://pubmed.ncbi.nlm.nih.gov/30207593/)
2. Chen W, Zheng R, Baade PD, Zhang S, Zeng H, Bray F, Jemal A, Yu XQ, He J. Cancer statistics in China, 2015. *CA Cancer J Clin.* 2016; 66:115–32.
<https://doi.org/10.3322/caac.21338>
PMID:[26808342](https://pubmed.ncbi.nlm.nih.gov/26808342/)
3. Yang JD, Roberts LR. Hepatocellular carcinoma: a global view. *Nat Rev Gastroenterol Hepatol.* 2010; 7:448–58.
<https://doi.org/10.1038/nrgastro.2010.100>
PMID:[20628345](https://pubmed.ncbi.nlm.nih.gov/20628345/)
4. Llovet JM, Burroughs A, Bruix J. Hepatocellular carcinoma. *Lancet.* 2003; 362:1907–17.
[https://doi.org/10.1016/S0140-6736\(03\)14964-1](https://doi.org/10.1016/S0140-6736(03)14964-1)
PMID:[14667750](https://pubmed.ncbi.nlm.nih.gov/14667750/)
5. Kulik L, El-Serag HB. Epidemiology and management of hepatocellular carcinoma. *Gastroenterology.* 2019; 156:477–91.e1.
<https://doi.org/10.1053/j.gastro.2018.08.065>
PMID:[30367835](https://pubmed.ncbi.nlm.nih.gov/30367835/)
6. European Association for the study of the Liver, and European Organisation for Research and Treatment of Cancer. EASL-EORTC clinical practice guidelines: management of hepatocellular carcinoma. *J Hepatol.* 2012; 56:908–43.
<https://doi.org/10.1016/j.jhep.2011.12.001>
PMID:[22424438](https://pubmed.ncbi.nlm.nih.gov/22424438/)
7. Bruix J, Takayama T, Mazzaferro V, Chau GY, Yang J, Kudo M, Cai J, Poon RT, Han KH, Tak WY, Lee HC, Song T, Roayaie S, et al. Adjuvant sorafenib for hepatocellular carcinoma after resection or ablation (STORM): a phase 3, randomised, double-blind, placebo-controlled trial. *Lancet Oncol.* 2015; 16:1344–54.
[https://doi.org/10.1016/S1470-2045\(15\)00198-9](https://doi.org/10.1016/S1470-2045(15)00198-9)
PMID:[26361969](https://pubmed.ncbi.nlm.nih.gov/26361969/)
8. Palmer DH. Sorafenib in advanced hepatocellular carcinoma. *N Engl J Med.* 2008; 359:2498.
PMID:[19065750](https://pubmed.ncbi.nlm.nih.gov/19065750/)
9. Cheng AL, Kang YK, Chen Z, Tsao CJ, Qin S, Kim JS, Luo R, Feng J, Ye S, Yang TS, Xu J, Sun Y, Liang H, et al. Efficacy and safety of sorafenib in patients in the Asia-pacific region with advanced hepatocellular carcinoma: a phase III randomised, double-blind, placebo-controlled trial. *Lancet Oncol.* 2009; 10:25–34.

- [https://doi.org/10.1016/S1470-2045\(08\)70285-7](https://doi.org/10.1016/S1470-2045(08)70285-7)
PMID:[19095497](https://pubmed.ncbi.nlm.nih.gov/19095497/)
10. Kudo M, Han G, Finn RS, Poon RT, Blanc JF, Yan L, Yang J, Lu L, Tak WY, Yu X, Lee JH, Lin SM, Wu C, et al. Brivanib as adjuvant therapy to transarterial chemoembolization in patients with hepatocellular carcinoma: a randomized phase III trial. *Hepatology*. 2014; 60:1697–707.
<https://doi.org/10.1002/hep.27290>
PMID:[24996197](https://pubmed.ncbi.nlm.nih.gov/24996197/)
 11. Ghaleb AM, Yang VW. Krüppel-like factor 4 (KLF4): what we currently know. *Gene*. 2017; 611:27–37.
<https://doi.org/10.1016/j.gene.2017.02.025>
PMID:[28237823](https://pubmed.ncbi.nlm.nih.gov/28237823/)
 12. Farrugia MK, Vanderbilt DB, Salkeni MA, Ruppert JM. Kruppel-like pluripotency factors as modulators of cancer cell therapeutic responses. *Cancer Res*. 2016; 76:1677–82.
<https://doi.org/10.1158/0008-5472.CAN-15-1806>
PMID:[26964625](https://pubmed.ncbi.nlm.nih.gov/26964625/)
 13. Tetreault MP, Yang Y, Katz JP. Krüppel-like factors in cancer. *Nat Rev Cancer*. 2013; 13:701–13.
<https://doi.org/10.1038/nrc3582>
PMID:[24060862](https://pubmed.ncbi.nlm.nih.gov/24060862/)
 14. Evans PM, Liu C. Roles of krüppel-like factor 4 in normal homeostasis, cancer and stem cells. *Acta Biochim Biophys Sin (Shanghai)*. 2008; 40:554–64.
<https://doi.org/10.1111/j.1745-7270.2008.00439.x>
PMID:[18604447](https://pubmed.ncbi.nlm.nih.gov/18604447/)
 15. Yang WT, Zheng PS. Krüppel-like factor 4 functions as a tumor suppressor in cervical carcinoma. *Cancer*. 2012; 118:3691–702.
<https://doi.org/10.1002/cncr.26698>
PMID:[22170594](https://pubmed.ncbi.nlm.nih.gov/22170594/)
 16. Jia Y, Ying X, Zhou J, Chen Y, Luo X, Xie S, Wang QC, Hu W, Wang L. The novel KLF4/PLAC8 signaling pathway regulates lung cancer growth. *Cell Death Dis*. 2018; 9:603.
<https://doi.org/10.1038/s41419-018-0580-3>
PMID:[29789534](https://pubmed.ncbi.nlm.nih.gov/29789534/)
 17. Zhang J, Zhu Z, Wu H, Yu Z, Rong Z, Luo Z, Xu Y, Huang K, Qiu Z, Huang C. PODXL, negatively regulated by KLF4, promotes the EMT and metastasis and serves as a novel prognostic indicator of gastric cancer. *Gastric Cancer*. 2019; 22:48–59.
<https://doi.org/10.1007/s10120-018-0833-y>
PMID:[29748877](https://pubmed.ncbi.nlm.nih.gov/29748877/)
 18. Ghaleb AM, Nandan MO, Chanchevalap S, Dalton WB, Hisamuddin IM, Yang VW. Krüppel-like factors 4 and 5: the yin and yang regulators of cellular proliferation. *Cell Res*. 2005; 15:92–96.
<https://doi.org/10.1038/sj.cr.7290271> PMID:[15740636](https://pubmed.ncbi.nlm.nih.gov/15740636/)
 19. Yan Y, Li Z, Kong X, Jia Z, Zuo X, Gagea M, Huang S, Wei D, Xie K. KLF4-mediated suppression of CD44 signaling negatively impacts pancreatic cancer stemness and metastasis. *Cancer Res*. 2016; 76:2419–31.
<https://doi.org/10.1158/0008-5472.CAN-15-1691>
PMID:[26880805](https://pubmed.ncbi.nlm.nih.gov/26880805/)
 20. Yu F, Li J, Chen H, Fu J, Ray S, Huang S, Zheng H, Ai W. Kruppel-like factor 4 (KLF4) is required for maintenance of breast cancer stem cells and for cell migration and invasion. *Oncogene*. 2011; 30:2161–72.
<https://doi.org/10.1038/onc.2010.591>
PMID:[21242971](https://pubmed.ncbi.nlm.nih.gov/21242971/)
 21. Yang X, Zhang D, Liu S, Li X, Hu W, Han C. KLF4 suppresses the migration of hepatocellular carcinoma by transcriptionally upregulating monoglyceride lipase. *Am J Cancer Res*. 2018; 8:1019–29.
PMID:[30034939](https://pubmed.ncbi.nlm.nih.gov/30034939/)
 22. Li Q, Song W, Wang W, Yao S, Tian C, Cai X, Wang L. Suppression of epithelial-mesenchymal transition in hepatocellular carcinoma cells by krüppel-like factor 4. *Oncotarget*. 2016; 7:29749–60.
<https://doi.org/10.18632/oncotarget.8831>
PMID:[27102441](https://pubmed.ncbi.nlm.nih.gov/27102441/)
 23. Savagner P, Boyer B, Valles AM, Jouanneau J, Thiery JP. Modulations of the epithelial phenotype during embryogenesis and cancer progression. *Cancer Treat Res*. 1994; 71:229–49.
https://doi.org/10.1007/978-1-4615-2592-9_12
PMID:[7946950](https://pubmed.ncbi.nlm.nih.gov/7946950/)
 24. Nieto MA, Huang RY, Jackson RA, Thiery JP. EMT: 2016. *Cell*. 2016; 166:21–45.
<https://doi.org/10.1016/j.cell.2016.06.028>
PMID:[27368099](https://pubmed.ncbi.nlm.nih.gov/27368099/)
 25. Cui J, Shi M, Quan M, Xie K. Regulation of EMT by KLF4 in gastrointestinal cancer. *Curr Cancer Drug Targets*. 2013; 13:986–95.
<https://doi.org/10.2174/15680096113136660104>
PMID:[24168184](https://pubmed.ncbi.nlm.nih.gov/24168184/)
 26. Yori JL, Johnson E, Zhou G, Jain MK, Keri RA. Kruppel-like factor 4 inhibits epithelial-to-mesenchymal transition through regulation of e-cadherin gene expression. *J Biol Chem*. 2010; 285:16854–63.
<https://doi.org/10.1074/jbc.M110.114546>
PMID:[20356845](https://pubmed.ncbi.nlm.nih.gov/20356845/)
 27. Tang A, Hallouch O, Chernyak V, Kamaya A, Sirlin CB. Epidemiology of hepatocellular carcinoma: target population for surveillance and diagnosis. *Abdom Radiol (NY)*. 2018; 43:13–25.
<https://doi.org/10.1007/s00261-017-1209-1>
PMID:[28647765](https://pubmed.ncbi.nlm.nih.gov/28647765/)
 28. Shi M, Cui J, Du J, Wei D, Jia Z, Zhang J, Zhu Z, Gao Y, Xie K. A novel KLF4/LDHA signaling pathway regulates

- aerobic glycolysis in and progression of pancreatic cancer. *Clin Cancer Res*. 2014; 20:4370–80.
<https://doi.org/10.1158/1078-0432.CCR-14-0186>
PMID:[24947925](https://pubmed.ncbi.nlm.nih.gov/24947925/)
29. Zhao W, Hisamuddin IM, Nandan MO, Babbin BA, Lamb NE, Yang VW. Identification of krüppel-like factor 4 as a potential tumor suppressor gene in colorectal cancer. *Oncogene*. 2004; 23:395–402.
<https://doi.org/10.1038/sj.onc.1207067>
PMID:[14724568](https://pubmed.ncbi.nlm.nih.gov/14724568/)
30. Wei D, Gong W, Kanai M, Schlunk C, Wang L, Yao JC, Wu TT, Huang S, Xie K. Drastic down-regulation of krüppel-like factor 4 expression is critical in human gastric cancer development and progression. *Cancer Res*. 2005; 65:2746–54.
<https://doi.org/10.1158/0008-5472.CAN-04-3619>
PMID:[15805274](https://pubmed.ncbi.nlm.nih.gov/15805274/)
31. Zheng X, Li A, Zhao L, Zhou T, Shen Q, Cui Q, Qin X. Key role of microRNA-15a in the KLF4 suppressions of proliferation and angiogenesis in endothelial and vascular smooth muscle cells. *Biochem Biophys Res Commun*. 2013; 437:625–31.
<https://doi.org/10.1016/j.bbrc.2013.07.017>
PMID:[23867820](https://pubmed.ncbi.nlm.nih.gov/23867820/)
32. Hale AT, Tian H, Anih E, Recio FO 3rd, Shatat MA, Johnson T, Liao X, Ramirez-Bergeron DL, Proweller A, Ishikawa M, Hamik A. Endothelial kruppel-like factor 4 regulates angiogenesis and the notch signaling pathway. *J Biol Chem*. 2014; 289:12016–28.
<https://doi.org/10.1074/jbc.M113.530956>
PMID:[24599951](https://pubmed.ncbi.nlm.nih.gov/24599951/)
33. Gamper AM, Qiao X, Kim J, Zhang L, DeSimone MC, Rathmell WK, Wan Y. Regulation of KLF4 turnover reveals an unexpected tissue-specific role of pVHL in tumorigenesis. *Mol Cell*. 2012; 45:233–43.
<https://doi.org/10.1016/j.molcel.2011.11.031>
PMID:[22284679](https://pubmed.ncbi.nlm.nih.gov/22284679/)
34. Sun H, Tang H, Xie D, Jia Z, Ma Z, Wei D, Mishra L, Gao Y, Zheng S, Xie K, Peng Z. Krüppel-like factor 4 blocks hepatocellular carcinoma dedifferentiation and progression through activation of hepatocyte nuclear factor-6. *Clin Cancer Res*. 2016; 22:502–12.
<https://doi.org/10.1158/1078-0432.CCR-15-0528>
PMID:[26338995](https://pubmed.ncbi.nlm.nih.gov/26338995/)
35. Kojiro M. Histopathology of liver cancers. *Best Pract Res Clin Gastroenterol*. 2005; 19:39–62.
<https://doi.org/10.1016/j.bpg.2004.10.007>
PMID:[15757804](https://pubmed.ncbi.nlm.nih.gov/15757804/)
36. Aiello NM, Kang Y. Context-dependent EMT programs in cancer metastasis. *J Exp Med*. 2019; 216:1016–26.
<https://doi.org/10.1084/jem.20181827>
PMID:[30975895](https://pubmed.ncbi.nlm.nih.gov/30975895/)
37. Krebs AM, Mitschke J, Lasierra Losada M, Schmalhofer O, Boerries M, Busch H, Boettcher M, Mougiakakos D, Reichardt W, Bronsert P, Brunton VG, Pilarsky C, Winkler TH, et al. The EMT-activator Zeb1 is a key factor for cell plasticity and promotes metastasis in pancreatic cancer. *Nat Cell Biol*. 2017; 19:518–29.
<https://doi.org/10.1038/ncb3513>
PMID:[28414315](https://pubmed.ncbi.nlm.nih.gov/28414315/)
38. Dong Q, Zhu X, Dai C, Zhang X, Gao X, Wei J, Sheng Y, Zheng Y, Yu J, Xie L, Qin Y, Qiao P, Zhou C, et al. Osteopontin promotes epithelial-mesenchymal transition of hepatocellular carcinoma through regulating vimentin. *Oncotarget*. 2016; 7:12997–3012.
<https://doi.org/10.18632/oncotarget.7016>
PMID:[26824421](https://pubmed.ncbi.nlm.nih.gov/26824421/)

Note

You can find the publication record of corresponding author Ruolei Hu at:

<https://pubmed.ncbi.nlm.nih.gov/29152648/>

Aerobic exercise induces tumor suppressor p16^{INK4a} expression of endothelial progenitor cells in human skeletal muscle

Jinfu Wu^{1,2}, I-Shiung Cheng³, Suchada Saovieng^{2,8}, Wei-Horng Jean^{2,4}, Chung-Lan Kao⁵, Yung-Yang Liu⁶, Chih-Yang Huang⁷, Tania Xu Yar Lee², John L. Ivy⁹, Chia-Hua Kuo²

¹Laboratory of Regenerative Medicine in Sports Science, School of Physical Education and Sports Science, South China Normal University, Guangzhou, China

²Laboratory of Exercise Biochemistry, University of Taipei, Taipei, Taiwan

³Laboratory of Exercise Nutrition, National Taichung University of Education, Taichung, Taiwan

⁴Department of Anesthesiology, Far East Memorial Hospital, New Taipei, Taiwan

⁵Department of Physical Medicine and Rehabilitation, Taipei Veterans General Hospital and National Yang Ming University, Taipei, Taiwan

⁶Department of Chest Medicine, Taipei Veterans General Hospital and National Yang Ming University, Taipei, Taiwan

⁷Chinese Medicine, Hualien Tzu Chi Hospital, Tzu Chi Medical Foundation, Tzu Chi University, Hualien, Taiwan

⁸College of Sports Science and Technology, Mahidol University, Bangkok, Thailand

⁹Department of Kinesiology and Health Education, The University of Texas at Austin, TX 78712, USA

Correspondence to: Chia-Hua Kuo; email: kch@utapei.edu.tw

Keywords: cancer, tumor, cell cycle arrest, skeletal muscle

Received: March 9, 2020

Accepted: July 7, 2020

Published: October 26, 2020

Copyright: © 2020 Wu et al. This is an open access article distributed under the terms of the [Creative Commons Attribution License](https://creativecommons.org/licenses/by/3.0/) (CC BY 3.0), which permits unrestricted use, distribution, and reproduction in any medium, provided the original author and source are credited.

ABSTRACT

Aerobic exercise induces oxidative stress and DNA damage, nevertheless, lowers cancer incidence. It remains unclear how genetic stability is maintained under this condition. Here, we examined the dynamic change of the tumor suppressor p16^{INK4a} in cells of skeletal muscle among young men following 60-min of aerobic cycling at 70% maximal oxygen consumption ($\dot{V}O_{2max}$). Rg1 (5 mg, an immunostimulant ginsenoside) and placebo (PLA) were supplemented 1 h before exercise. Data from serial muscle biopsies shows unchanged p16^{INK4a+} cells after exercise followed by a considerable increase (+21-fold) in vastus lateralis muscle 3 h later. This increase was due to the accumulation of endothelial progenitor cells (p16^{INK4a+}/CD34⁺) surrounding myofibers and other infiltrated nucleated cells (p16^{INK4a+}/CD34⁻) in necrotic myofibers. During the Rg1 trial, acute increases of p16^{INK4a+} cells in the muscle occurred immediately after exercise (+3-fold) and reversed near baseline 3 h later. Rg1 also lowered IL-10 mRNA relative to PLA 3 h after exercise. Post-exercise increases in VEGF mRNA and CD163⁺ macrophages were similar for PLA and Rg1 trials. Conclusion: The marked increases in p16^{INK4a} protein expression of endothelial progenitor cells in skeletal muscle implicates a protective mechanism for maintaining genetic stability against aerobic exercise. Rg1 accelerates resolution of the exercise-induced stress response.

INTRODUCTION

Most of the cells within the human body are short-lived and age rapidly [1], where birth, aging, and death of cells are continuously occurring to sustain a stable cell population. Capillary endothelial cells have an average lifespan ranging from 2 to 15 days in mammalian tissues [1, 2]. Endothelial progenitor cells (CD34⁺) from bone marrow are responsible for the rapid replacement of unhealthy endothelial cells [3], as well as the donation of their nuclei to injured myofibers for regeneration [4]. We have recently reported various amounts of p16^{INK4a+} endothelial progenitor cells in more than 40% of capillaries surrounding myofibers in human skeletal muscle of young men between 20-25 years of age [5].

Given a huge amount of daily cell turnover in human adults, a random genetic mutation is unavoidable following numerous cell division. The protein p16^{INK4a}, known as a tumor suppressor, is a protein inhibitor of the DNA synthesis phase of the cell cycle expressed in replicable cells [6]. Both cellular senescence and stress elevate p16^{INK4a} protein in replicable cells, which induces cell cycle arrest [6, 7], and illustrates the protective role of p16^{INK4a} for the fidelity during cell division in large multicellular systems. Downregulation of p16^{INK4a} has been observed in a large number of tumors in humans.

Aerobic exercise transiently increases oxidative stress and DNA damage [8]. However, participating aerobic exercise is associated with lower cancer incidence in both animals and humans [9]. The underlying mechanism remains unclear. In this study, distribution of p16^{INK4a+} endothelial progenitor cells in vastus lateralis muscle were examined in young adults. Induction of cellular senescence facilitates immune clearance of unhealthy replicable cells by activating immune responses [10]. To further investigate the role of the immune system on dynamical changes of p16^{INK4a+} senescent cells, Rg1 was orally ingested 1 h before exercise [11, 12]. Rg1 is an immunostimulant during inflammation, which activates macrophage function [11, 13].

RESULTS

Endurance cycling at 70% $\dot{V}O_{2max}$ for 1 h does not produce significant increases in circulating LDH and myoglobin (Figure 1). The lipid peroxidation marker TBARS levels tends to increase by 35% during the PLA trial (Figure 1C). No detectable change in p16^{INK4a+} senescent cells was observed immediately after exercise (PLA trial). However, ~21-fold increases ($P < 0.01$) in p16^{INK4a+} senescent cells of skeletal muscle occurred 3 h

after exercise. During the Rg1 trial, ~3-fold increases ($P < 0.05$) in p16^{INK4a+} senescent cells of skeletal muscle were observed immediately exercise followed by ~40% decline 3 h after exercise ($P < 0.05$) (Figure 2A, 2C). CD34⁺ cell-to-fiber ratio of skeletal muscle was not altered after exercise (Figure 2B, 2D). A great portion of senescent cell accumulation in exercised muscle is contributed by increased senescent endothelial progenitor cells (p16^{INK4a+}/CD34⁺) (Figure 2E, 2G). Approximately 40% of the increases is associated with other types of nucleated cells (p16^{INK4a+}/CD34⁻) localized mostly in necrotic myofibers (Figure 2F, 2H).

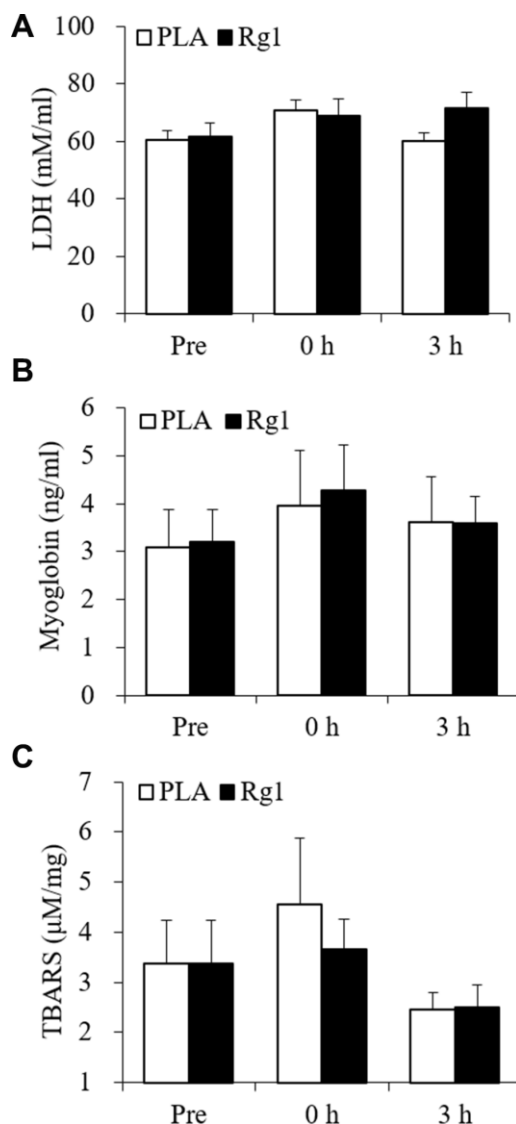


Figure 1. Plasma muscle damage markers unaltered following aerobic exercise. Lactate dehydrogenase (A), myoglobin (B), and TBARS (C) were not significantly increased after 1-h cycling exercise (70% $\dot{V}O_{2max}$). Data are expressed as mean and SEM. Abbreviation: TBARS, Thiobarbituric acid reactive substances.

Dramatic increases in p16^{INK4a+} cells 3 h after exercise is potently lowered by Rg1 supplementation ($P < 0.05$). A moderate correlation ($r = 0.29$, $p = 0.08$) was found between p16^{INK4a} positive cells and β -galactosidase positive cells of 36 biopsied muscle samples in men aged 20-26 y (Figure 3).

Aerobic cycling (70% $\dot{V}O_{2max}$) increased CD163⁺ macrophage infiltration into human skeletal muscle (Figure 4). Placebo (PLA) and Rg1 trials show a similar magnitude of cell infiltration (PLA: 0 h, +63%, $P <$

0.05; 3 h, +56%, $P < 0.05$; Rg1: 0 h, +92%, $P < 0.01$; 3 h, +70%, $P < 0.01$).

Data for exercise response in IL-10 mRNA, VEGF mRNA and PGC-1 α mRNA of skeletal muscle are shown in Figure 5. IL-10 mRNA did not change after an acute bout aerobic exercise, while Rg1 significantly decreased IL-10 mRNA expression 3 h after exercise (-60%, $P < 0.05$) (Figure 5A). Both VEGF mRNA (Figure 5B) and PGC-1 α mRNA (Figure 5C) increased significantly in challenged skeletal muscle. Similar

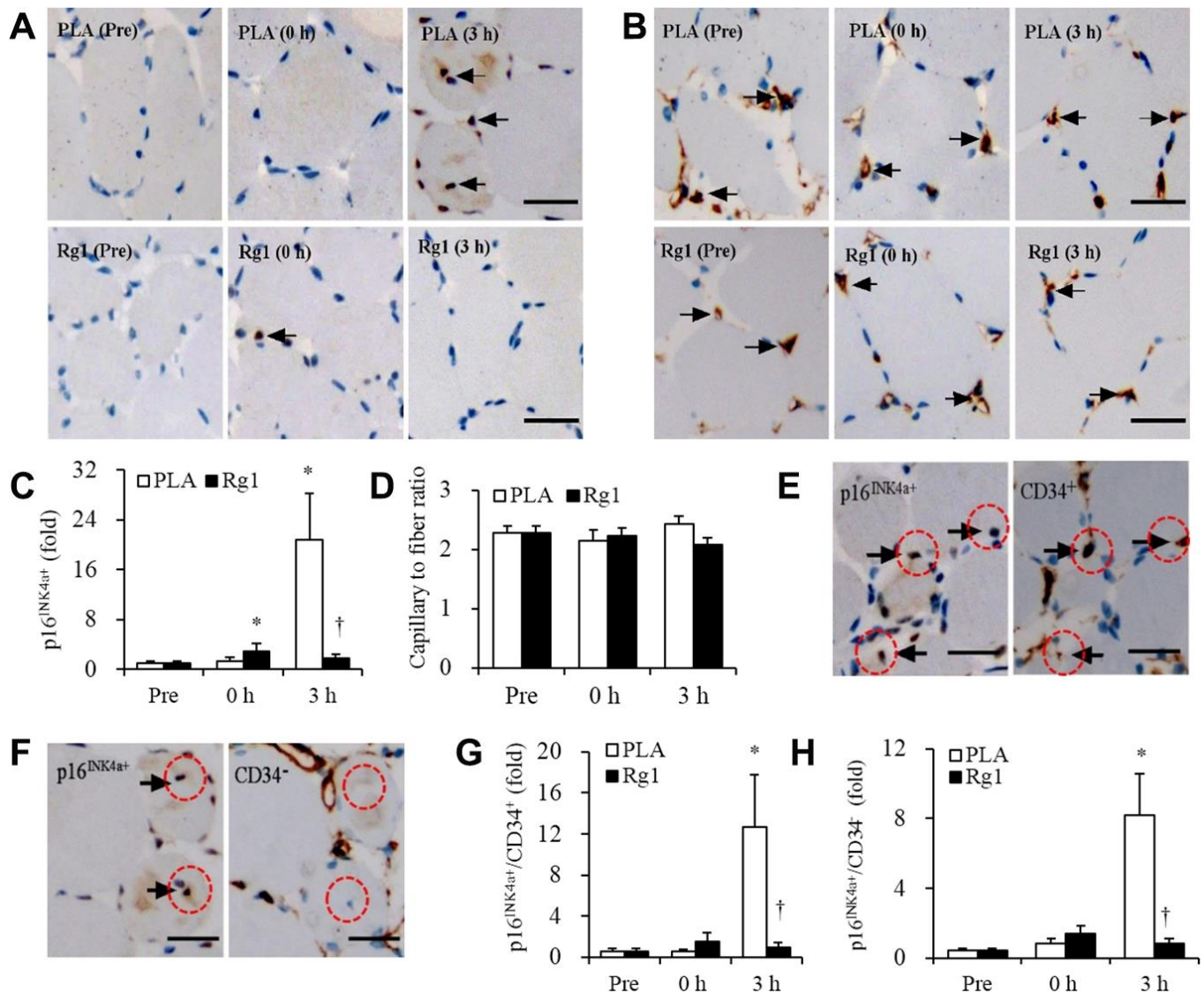


Figure 2. Massive increases of senescent endothelial progenitor cells in human skeletal muscle 3 h after aerobic exercise (70% $\dot{V}O_{2max}$). Approximately 21-fold increases in senescent endothelial progenitor cells occurred 3 h after 1-h cycling exercise (70% $\dot{V}O_{2max}$), while Rg1 supplementation advances the increase immediately after exercise (~3-fold) and decline to baseline 3 h after exercise (A, C). Total endothelial progenitor cells (CD34⁺) surrounding myofibers were unaltered after exercise for both trials (B, D). Approximately 60% of elevated senescent endothelial progenitor cells was contributed by endothelial progenitor cells (p16^{INK4a+} / CD34⁺) (E, G), while the rest of 40% was contributed by infiltrated nucleated cells (p16^{INK4a+} / CD34⁻) (F, H). Scale bar = 30 μ m. Data are expressed as mean and SEM. * Significant difference against Pre (Baseline), $P < 0.01$; † Significant difference against Placebo, $P < 0.01$. Abbreviation: PLA, Placebo.

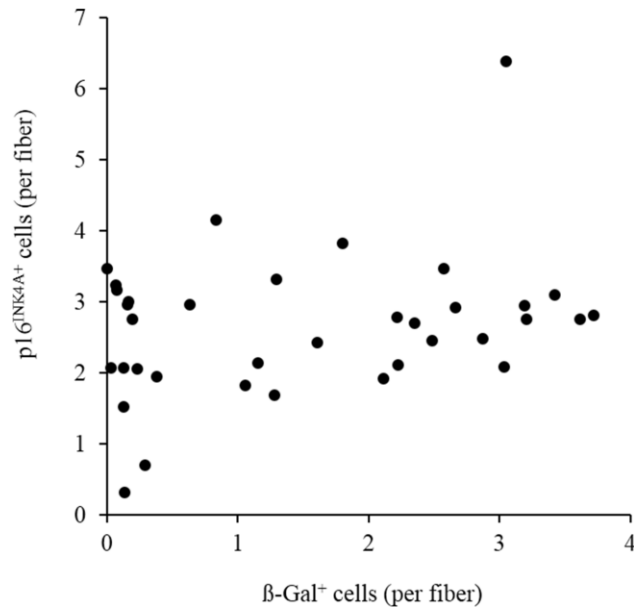


Figure 3. Moderate correlation ($r = 0.29$, $p = 0.08$) between p16^{INK4a} positive cells and β-galactosidase positive cells of 36 biopsied vastus lateralis muscle in men aged 20-26 y. Abbreviation: β-gal, β-galactosidase.

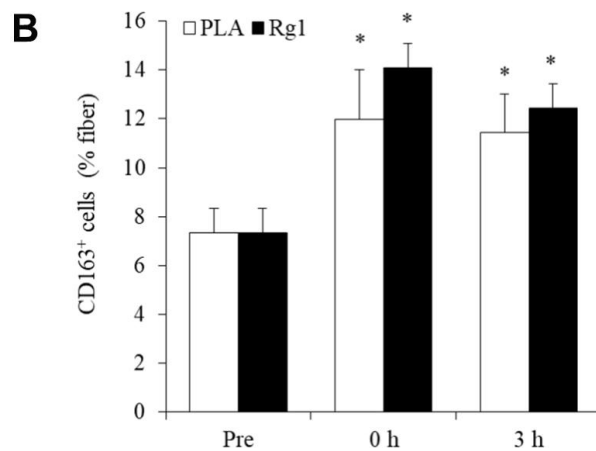
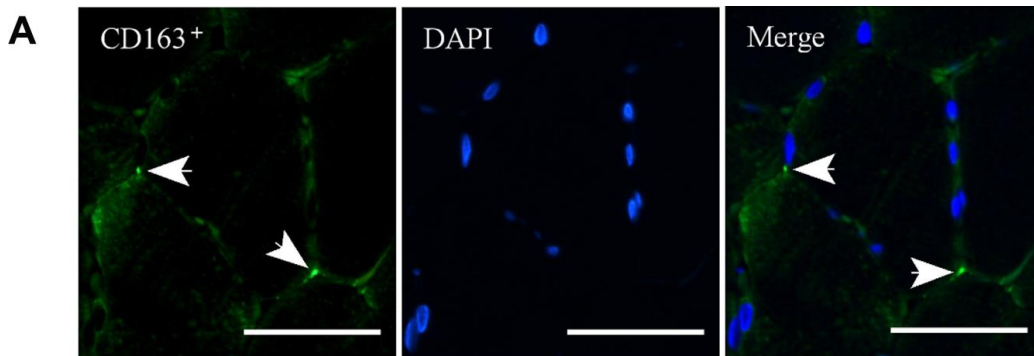


Figure 4. Aerobic exercise increases regenerative macrophage infiltration into human skeletal muscle. Arrows in the representative images indicate CD163⁺ cells (bright green) and nuclei (blue) surrounding myofibers in a muscle cross-section (A). This increase after 1-h cycling exercise (70% $\dot{V}O_{2max}$) was similar for both Placebo (PLA) and Rg1 trials (B). Scale bar = 50 μ m. Data are expressed as mean and SEM. * Significant difference against Pre (Baseline), $P < 0.01$. Abbreviation: PLA, Placebo.

increases were observed in VEGF mRNA of skeletal muscle for both PLA (0 h, +2-fold, $P < 0.01$; 3 h, +7-fold, $P < 0.01$) and Rg1 (0 h, +1-fold, $P < 0.05$; 3 h, +7-fold, $P < 0.01$) trials following exercise. PGC-1 α mRNA also shows similar increases for PLA (0 h, +1-fold, $P < 0.05$; 3 h, +13-fold, $P < 0.01$) and Rg1 (0 h, +1-fold, $P < 0.01$; 3 h, +14-fold, $P < 0.01$) trials.

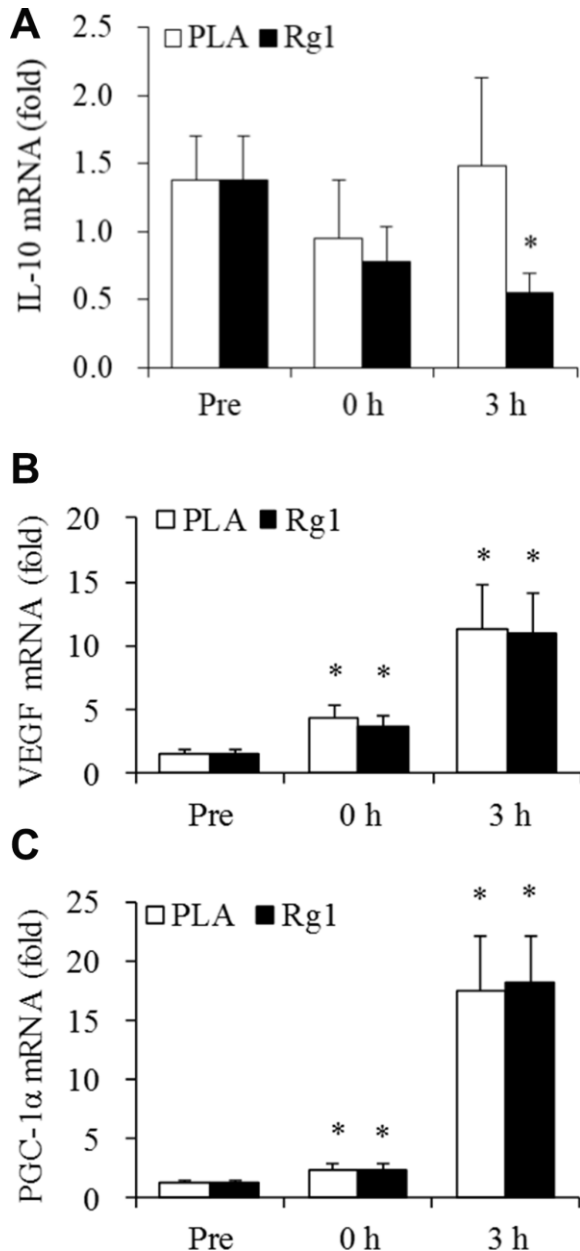


Figure 5. IL-10, VEGF, and PGC1-alpha expression after aerobic exercise. (A) Rg1 supplementation lowers IL-10 mRNA 3 h after exercise (-60%, $P < 0.05$). Dramatic elevations for VEGF mRNA (B) and PGC1-alpha mRNA (C) occurred 3 h after 1-h cycling exercise (70% $\dot{V}O_{2max}$). Data are expressed as mean and SEM. * Significant difference against Pre (Baseline), $P < 0.05$. Abbreviation: PLA, Placebo.

DISCUSSION

Aerobic exercise induces VEGF expression and stimulates angiogenesis [14]. During this process, endothelial progenitor cells are capable of self-replicating to increase cell number to renew damaged endothelial cells in the capillaries [15]. However, oxidative DNA damage is increased after an acute bout of aerobic exercise [8, 16]. In this study, we found a considerable rise in the tumor suppressor p16^{INK4a} protein expression in endothelial progenitor cells of human skeletal muscle after an acute bout of aerobic exercise (70% $\dot{V}O_{2max}$). Furthermore, the immunostimulant Rg1 accelerated the resolution of this stress response, evidenced by an earlier rise and fall of p16^{INK4a} cell number in exercised muscle. Stress that causes DNA damage results in the increased expression of the p16^{INK4a} protein, which is responsible for inhibition of cell division [6]. Thus, the transient increases in p16^{INK4a} protein expression may mirror the magnitude of stress-related DNA damage [16] and suggests a protective mechanism for maintaining genetic stability of replicable cells against aerobic exercise.

Increasing p16^{INK4a} protein expression is also known to stimulate tissue repair during inflammation [7, 17]. Inflammation is essential for recognition and phagocytic clearance of unhealthy cells that develops a senescence phenotype [18–20] followed by a protracted period of cell regeneration [21]. A recent study has reported an enhanced regenerative process after increasing p16^{INK4a} mesenchymal stem cells during muscle inflammation [22]. Taken together, these recent findings suggest a new role of stress-induced p16^{INK4a} protein expression in inflammation-mediated muscle regeneration. Rg1 is an immunostimulant that activates macrophage [11] and advances the progression of inflammation from M1 to M2 phenotype in exercised human skeletal muscle [23]. Therefore, pre-exercise Rg1 intake is likely to potentiate the inflammation response (preconditioning) and result in an early resolution of the exercise stress response.

M2 macrophage (CD163⁺) polarization occurs during the later period of inflammation, which is responsible for cell regeneration of muscle tissue after physical challenge [21, 24]. However, massive increases in p16^{INK4a} endothelial progenitor cells observed in the study was not directly associated with an exercise-induced increment of M2 macrophage in skeletal muscle. The magnitude of increase in M2 macrophage was similar for PLA and Rg1 trials, while the exercise-induced response of p16^{INK4a} cells in human skeletal muscle was lower than that in the PLA trial. However, our results do not preclude the possibility that accumulation of p16^{INK4a} endothelial progenitor cells

directly increase M2 macrophage activity in human skeletal muscle.

A limitation of the study is the difficulty in determining whether increased p16^{INK4a+} cells 3 h post-exercise was completely attributed cell senescence or simply due to a reversible induction of p16^{INK4a} protein expression of well-functioned endothelial progenitor cells. Cellular senescence is featured by an irreversible form of cell-cycle arrest after prolonged stress. It is not possible to determine whether p16^{INK4a+} cell number is representing of irreversible cell-cycle arrest in human muscle tissue, since both p16^{INK4a+} cell accumulation and p16^{INK4a+} cell removal (immune clearance) can occur in the same muscle tissue following exercise. In this study, a moderate correlation between p16^{INK4a} positive cells and β -galactosidase positive cells in 36 muscle samples suggests that p16^{INK4a} is not a perfect tissue senescence marker. This is in agreement with a previous study [25]. Whether p16^{INK4a} is a reliable cell senescence marker in human tissues cannot be settled in this study.

Another limitation is inadequate time points for muscle biopsies, which prevented us from delineating the timings of the rise-and-fall pattern for p16^{INK4a+} cell accumulation in exercising muscle. The acute response of p16^{INK4a} protein expression in endothelial cells of skeletal muscle after aerobic exercise is in sharp contrast to what has been observed after resistance exercise. We and others have previously shown decreased p16^{INK4a+} cells in muscle tissue of untrained active women and men after resistance training [5, 26]. Time required for resolution of the stress response and inflammation during and after exercise is associated with the magnitude of tissue damage, and varying by mode, intensity and duration of exercise. Furthermore, the local tissue response is influenced by distribution of the whole-body immune resource (white blood cells and stem cells from bone marrow). For example, aerobic exercise exerts a major challenge to the cardiopulmonary system in addition to skeletal muscle. The majority (> 60%) of white blood cells and stem cells are harbored in the lungs for constant local repair and regeneration [27, 28]. Aerobic exercise creates a competition between the lungs and muscle for immune resources for cell turnover [27]. In contrast, resistance exercise generates little challenge to the lungs, yet eccentric muscle contractions induce a substantial amount of muscle damage, which attracts more immune cells compared with aerobic exercise. Therefore, infiltration of immune cells into skeletal muscle after resistance exercise would be less likely to be compromised by competition with the lungs as occurs with aerobic exercise. Such differences can produce distinct rise-and-fall patterns for p16^{INK4a+} cells in human skeletal muscle [19, 29], and possibly explain the delayed

response of p16^{INK4a+} cells in human skeletal muscle after aerobic exercise.

CONCLUSIONS

We observed a considerable increase in p16^{INK4a} protein expression of endothelial progenitor cells in human skeletal muscle 3 h after aerobic exercise at 70% $\dot{V}O_{2max}$. The result of the study suggests that increased p16^{INK4a} expression is a protective mechanism to maintain genetic stability of replicable cells during regenerative phase after aerobic stress. Early resolution of this stress response occurs when the immunostimulant Rg1 is orally taken 1 h before exercise.

MATERIALS AND METHODS

Participants

Twelve healthy young men 20-23 years of age (weight: 51-95 kg; height: 161-190 cm) with $\dot{V}O_{2max}$ ranging between 43-55 ml⁻¹ kg⁻¹ min⁻¹ volunteered to participate in this study. Participants were untrained and recreationally active non-smokers. They were fully informed of the risks and discomfort associated with the study, and all provided written consent before participation. This study was conducted in accordance with the guidelines contained in the Declaration of Helsinki and was approved by the Institutional Review Board of University of Taipei, Taipei, Taiwan.

Experimental design

A placebo-controlled, counter-balanced, crossover study was conducted. Participants were randomized into one of two groups: PLA (5 mg of cellulose) and Rg1 (5 mg). Rg1 was obtained from NuLiv Science, Inc. (Brea, CA, USA). Participants randomly assigned to the PLA group received cellulose before trial one, and Rg1 before trial two. Accordingly, participants randomly assigned to the Rg1 group received Rg1 before trial one and cellulose before trial two. Trials one and two were separated by ten days. The Rg1 and cellulose were provided in capsules 1 h before exercise. Capsules were coded by number for later identification. Exercise consisted of 1 h of continuous cycling at 70% $\dot{V}O_{2max}$ on a cycle ergometer (Monark 839E, Stockholm, Sweden).

Experimental protocol

All participants were familiarized with the experimental procedures and equipment before testing started. Participants completed a $\dot{V}O_{2max}$ test using a graded exercise protocol on a cycle ergometer one week before starting the experimental trials. All participants consumed a standard isocaloric diet 12 h prior to each experimental

trial to limit any potential dietary effect that could influence the outcome of the study. Participants orally ingested 5 mg of Rg1 or PLA 1 h before cycling. After exercise, participants consumed a high carbohydrate meal (1.5 g carbohydrates per kg body weight: carbohydrate 80%, fat 8% and protein 12%; glycemic index: 80) within 10 min at the start of a 3-h recovery period. Water was provided ad libitum during and after the meal.

Muscle biopsy

Muscle samples were taken from vastus lateralis muscle before (Pre), immediately (0 h) and 3 h after the 1-h cycling exercise protocol. Biopsies were performed under local anesthesia (2% lidocaine) by a certified physician using an 18G Temno disposable cutting needle (Cardinal Health, Waukegan, IL, USA). Biopsies were taken from the vastus lateralis 3 cm in depth and 20 cm proximal to the knee. The baseline muscle biopsy (Pre) was conducted 3-4 weeks before the start of the first 1 h cycling exercise test. Two consecutive muscle biopsies were performed immediately (0 h) after and 3 h after each cycling test. The 0 h and 3 h biopsies were taken from opposite legs, but at the same position on the vastus lateralis. A portion of each muscle sample was immediately frozen in liquid nitrogen and stored at -70 °C until analyzed. The rest of the sample was immediately placed in a conical vial containing 10% formalin and used for immunohistochemical analysis. Paraffin-embedded tissue was sectioned no later than 3 h following muscle sample collection.

Immunohistochemistry

Serial sections of paraffin-embedded tissue were cut and analyzed for distribution of p16^{INK4a} and CD34 in the vastus lateralis muscle. Paraffin sections (8 µm thick) were labeled using immunohistochemistry for binding of human monoclonal antibody p16^{INK4a} (1:200, ab108349; Abcam, Cambridge, MA, USA) and CD34 (1:200, ab81289; Abcam, Cambridge, MA, USA). Immunofluorescence was used to detect regenerative macrophage CD163 (1:400, ab87099; Abcam, Cambridge, MA, USA) infiltration in the vastus lateralis after exercise. Optical images were analyzed using ImageJ (NIH, Bethesda, MD). Positive markers within cells were quantified and expressed as positive signal number/total skeletal muscle fiber number (%). An average of 600 muscle fibers per slide were included for analysis. All analyses were conducted by a specialist at the University of Taipei and a certified pathologist from Taipei Institute of Pathology with similar results. An additional 36 muscle biopsied samples were used to assess correlation between p16^{INK4a} positive cells and β-galactosidase positive cells (1: 150, NBP2-45731, Novus Biologicals, CO, USA).

Quantitative PCR

RNA was extracted from ~15 mg of skeletal muscle using TRI Reagent (T9424-200) (Sigma, St. Louis, MO, USA) for homogenization, followed by isopropanol precipitation, two ethanol washes, drying, and suspension in 20 µl nuclease-free water. One microgram of RNA in a total volume of 20 µl was reverse transcribed to cDNA using iScript cDNA Synthesis Kit (#170-8890) (Bio-Rad, Hercules, CA, USA). Real-time PCR was performed using MyiQ Single Color Real-Time PCR Detection System (Bio-Rad, Hercules, CA, USA), TaqMan Probe (Sigma-Aldrich, Singapore) and iQ Supermix kit (#170-8860) (Bio-Rad, Hercules, CA, USA). The PCR conditions for all genes consisted of one denaturing cycle at 90°C for 30 s, annealing at 60°C for 60 s and elongation at 72°C for 60 s. At the end of the PCR the samples were subjected to a melting curve analysis. To control for any variations due to efficiencies of the reverse transcription and PCR, 18S ribosomal RNA was used as an internal standard to determine relative expression levels of the target mRNAs. The primers and probes used to amplify target mRNA are 18S ribosomal (18S): Forward (5'-3'): ACAGGATTGACAGATTGAT AGCTC, Reverse (5'-3'): TCGCTCCACCAACTAAGA ACG, Probe (5'-3'): TGCACCACCACCCACGGAATC GAG; IL-10: Forward (5'-3'): CTTCCCTGTGAAAAC AAG, Reverse (5'-3'): AGACCTCTAATTTATGTCC TA, Probe (5'-3'): AGTCGCCACCCTGATGTCTC; VEGF: Forward (5'-3'): TGAGATCGAGTACATCTTC AAGCC, Reverse (5'-3'): GGCCTTGTTGAGGTTTGA TCC, Probe (5'-3'): CCTGTGTGCCCTGATGCGAT GCG; PGC-1α: Forward (5'-3'): CGAGGAATATCA GCACGAGAGG, Reverse (5'-3'): CATAAATCACAC GGCGCTCTTC, Probe (5'-3'): TGCCTTCTGCCTCTG CCTCTCCCTC.

Serum LDH, Myoglobin and TBARS

A colorimetric assay kit was used to detect serum LDH activity according to the manufacturer's instructions (Bio-Vision, # k726-500, CA, USA). Myoglobin was measured by ELISA using a commercially available kit (Immunology Consultants Laboratory, E-80MY, OR, USA). Serum samples were also used after further dilution for measurement of TBARS using a commercially available kit (Cayman Chemical, No. 10009055, MI, USA).

Statistical analysis

All data are expressed as means ± standard error. The data were analyzed using a two-factor repeated-measures ANOVA (SPSS 20.0). Post hoc paired comparison analysis was performed with the Fisher LSD method. Type I error of $P \leq 0.05$ was considered significant. $P \leq 0.1$ was considered moderately significant.

AUTHOR CONTRIBUTIONS

JW and CHK designed the experiments. JW, WHJ, CYH, TXYL, YYL, SS, and ISC performed the experiments. JW conducted the statistical analyses. JW and CHK wrote the manuscript. JLI help with the discussing, writing and editing of the manuscript. All authors read and approved the final manuscript.

CONFLICTS OF INTEREST

Chia-Hua Kuo and Jinfu Wu have submitted patents (Pub. No US2019/0374592 A1) for formulating senolytic ergogenic supplements with Nuliv Science related to the material studied. All other authors declare that they have no conflict of interest. The results of the study are presented clearly, honestly, and without fabrication, falsification, or inappropriate data manipulation. Publication fee is covered by funding agency listed above.

FUNDING

This study was sponsored by industrial research funds for product design from Joint fund of Nuliv Science Taiwan and Ministry of Science and Technology Taiwan (grant number: 106-2410-H-845), and the University of Taipei, Taiwan.

REFERENCES

1. Spalding KL, Bhardwaj RD, Buchholz BA, Druid H, Frisén J. Retrospective birth dating of cells in humans. *Cell*. 2005; 122:133–43.
<https://doi.org/10.1016/j.cell.2005.04.028>
PMID:16009139
2. Erben RG, Odörfer KI, Siebenhütter M, Weber K, Rohleder S. Histological assessment of cellular half-life in tissues in vivo. *Histochem Cell Biol*. 2008; 130:1041–46.
<https://doi.org/10.1007/s00418-008-0470-3>
PMID:18618128
3. Zampetaki A, Kirton JP, Xu Q. Vascular repair by endothelial progenitor cells. *Cardiovasc Res*. 2008; 78:413–21.
<https://doi.org/10.1093/cvr/cvn081> PMID:18349136
4. Zheng B, Cao B, Crisan M, Sun B, Li G, Logar A, Yap S, Pollett JB, Drowley L, Cassino T, Gharaibeh B, Deasy BM, Huard J, Péault B. Prospective identification of myogenic endothelial cells in human skeletal muscle. *Nat Biotechnol*. 2007; 25:1025–34.
<https://doi.org/10.1038/nbt1334> PMID:17767154
5. Yang C, Jiao Y, Wei B, Yang Z, Wu JF, Jensen J, Jean WH, Huang CY, Kuo CH. Aged cells in human skeletal muscle after resistance exercise. *Aging (Albany NY)*. 2018; 10:1356–65.
<https://doi.org/10.18632/aging.101472>
PMID:29953414
6. Sharpless NE. Ink4a/arf links senescence and aging. *Exp Gerontol*. 2004; 39:1751–59.
<https://doi.org/10.1016/j.exger.2004.06.025>
PMID:15582292
7. Sarkar-Agrawal P, Vergilis I, Sharpless NE, DePinho RA, Rütger TM. Impaired processing of DNA photoproducts and ultraviolet hypermutability with loss of p16INK4a or p19ARF. *J Natl Cancer Inst*. 2004; 96:1790–93.
<https://doi.org/10.1093/jnci/djh307> PMID:15572761
8. Tryfidou DV, McClean C, Nikolaidis MG, Davison GW. DNA damage following acute aerobic exercise: a systematic review and meta-analysis. *Sports Med*. 2020; 50:103–27.
<https://doi.org/10.1007/s40279-019-01181-y>
PMID:31529301
9. Ashcraft KA, Peace RM, Betof AS, Dewhirst MW, Jones LW. Efficacy and mechanisms of aerobic exercise on cancer initiation, progression, and metastasis: a critical systematic review of in vivo preclinical data. *Cancer Res*. 2016; 76:4032–50.
<https://doi.org/10.1158/0008-5472.CAN-16-0887>
PMID:27381680
10. Burton DG, Stolzing A. Cellular senescence: immunosurveillance and future immunotherapy. *Ageing Res Rev*. 2018; 43:17–25.
<https://doi.org/10.1016/j.arr.2018.02.001>
PMID:29427795
11. Fan ZH, Isobe K, Kiuchi K, Nakashima I. Enhancement of nitric oxide production from activated macrophages by a purified form of ginsenoside (Rg1). *Am J Chin Med*. 1995; 23:279–87.
<https://doi.org/10.1142/S0192415X9500033X>
PMID:8571924
12. Joo SS, Won TJ, Lee DI. Reciprocal activity of ginsenosides in the production of proinflammatory repertoire, and their potential roles in neuroprotection in vivo. *Planta Med*. 2005; 71:476–81.
<https://doi.org/10.1055/s-2005-864145>
PMID:15931589
13. Guo X, Zhang J, Liu M, Zhao GC. Protective effect of ginsenoside Rg1 on attenuating anti-GBM glomerular nephritis by activating NRF2 signalling. *Artif Cells Nanomed Biotechnol*. 2019; 47:2972–79.
<https://doi.org/10.1080/21691401.2019.1640712>
PMID:31322005
14. Tsai HH, Lin CP, Lin YH, Hsu CC, Wang JS. High-intensity interval training enhances mobilization/functionality of

- endothelial progenitor cells and depressed shedding of vascular endothelial cells undergoing hypoxia. *Eur J Appl Physiol.* 2016; 116:2375–88.
<https://doi.org/10.1007/s00421-016-3490-z>
PMID:27761657
15. Urbich C, Dimmeler S. Endothelial progenitor cells: characterization and role in vascular biology. *Circ Res.* 2004; 95:343–53.
<https://doi.org/10.1161/01.RES.0000137877.89448.78>
PMID:15321944
16. Wu J, Saovieng S, Cheng IS, Liu T, Hong S, Lin CY, Su IC, Huang CY, Kuo CH. Ginsenoside Rg1 supplementation clears senescence-associated β -galactosidase in exercising human skeletal muscle. *J Ginseng Res.* 2019; 43:580–88.
<https://doi.org/10.1016/j.jgr.2018.06.002>
PMID:31695564
17. Serrano M. Senescence helps regeneration. *Dev Cell.* 2014; 31:671–72.
<https://doi.org/10.1016/j.devcel.2014.12.007>
PMID:25535913
18. Kay MM. Mechanism of removal of senescent cells by human macrophages in situ. *Proc Natl Acad Sci USA.* 1975; 72:3521–25.
<https://doi.org/10.1073/pnas.72.9.3521>
PMID:1059140
19. Prata LG, Ovsyannikova IG, Tchkonina T, Kirkland JL. Senescent cell clearance by the immune system: emerging therapeutic opportunities. *Semin Immunol.* 2018; 40:101275.
<https://doi.org/10.1016/j.smim.2019.04.003>
PMID:31088710
20. Sagiv A, Biran A, Yon M, Simon J, Lowe SW, Krizhanovsky V. Granule exocytosis mediates immune surveillance of senescent cells. *Oncogene.* 2013; 32:1971–77.
<https://doi.org/10.1038/onc.2012.206> PMID:22751116
21. Tidball JG. Regulation of muscle growth and regeneration by the immune system. *Nat Rev Immunol.* 2017; 17:165–78.
<https://doi.org/10.1038/nri.2016.150> PMID:28163303
22. Chikenji TS, Saito Y, Konari N, Nakano M, Mizue Y, Otani M, Fujimiya M. p16^{INK4A}-expressing mesenchymal stromal cells restore the senescence-clearance-regeneration sequence that is impaired in chronic muscle inflammation. *EBioMedicine.* 2019; 44:86–97.
<https://doi.org/10.1016/j.ebiom.2019.05.012>
PMID:31129096
23. Hou CW, Lee SD, Kao CL, Cheng IS, Lin YN, Chuang SJ, Chen CY, Ivy JL, Huang CY, Kuo CH. Improved inflammatory balance of human skeletal muscle during exercise after supplementations of the ginseng-based steroid Rg1. *PLoS One.* 2015; 10:e0116387.
<https://doi.org/10.1371/journal.pone.0116387>
PMID:25617625
24. Wang Y, Wehling-Henricks M, Samengo G, Tidball JG. Increases of M2a macrophages and fibrosis in aging muscle are influenced by bone marrow aging and negatively regulated by muscle-derived nitric oxide. *Aging Cell.* 2015; 14:678–88.
<https://doi.org/10.1111/acer.12350> PMID:26009878
25. Dungan CM, Peck BD, Walton RG, Huang Z, Bamman MM, Kern PA, Peterson CA. In vivo analysis of γ H2AX+ cells in skeletal muscle from aged and obese humans. *FASEB J.* 2020; 34:7018–35.
<https://doi.org/10.1096/fj.202000111RR>
PMID:32246795
26. Justice JN, Gregory H, Tchkonina T, LeBrasseur NK, Kirkland JL, Kritchevsky SB, Nicklas BJ. Cellular senescence biomarker p16^{INK4a} cell burden in thigh adipose is associated with poor physical function in older women. *J Gerontol A Biol Sci Med Sci.* 2018; 73:939–45.
<https://doi.org/10.1093/gerona/glx134>
PMID:28658942
27. Adams GR, Zaldivar FP, Nance DM, Kodesh E, Radom-Aizik S, Cooper DM. Exercise and leukocyte interchange among central circulation, lung, spleen, and muscle. *Brain Behav Immun.* 2011; 25:658–66.
<https://doi.org/10.1016/j.bbi.2011.01.002>
PMID:21238578
28. Rochefort GY, Vaudin P, Bonnet N, Pages JC, Domenech J, Charbord P, Eder V. Influence of hypoxia on the domiciliation of mesenchymal stem cells after infusion into rats: possibilities of targeting pulmonary artery remodeling via cells therapies? *Respir Res.* 2005; 6:125.
<https://doi.org/10.1186/1465-9921-6-125>
PMID:16253136
29. Chang J, Wang Y, Shao L, Laberge RM, Demaria M, Campisi J, Janakiraman K, Sharpless NE, Ding S, Feng W, Luo Y, Wang X, Aykin-Burns N, et al. Clearance of senescent cells by ABT263 rejuvenates aged hematopoietic stem cells in mice. *Nat Med.* 2016; 22:78–83.
<https://doi.org/10.1038/nm.4010>
PMID:26657143

CPEB3 functions as a tumor suppressor in colorectal cancer via JAK/STAT signaling

Yuxin Fang^{1,*}, Qian Zhong^{1,*}, Yadong Wang¹, Chuncai Gu¹, Side Liu¹, Aimin Li¹, Qun Yan¹

¹Guangdong Provincial Key Laboratory of Gastroenterology, Department of Gastroenterology, Nanfang Hospital, Southern Medical University, Guangzhou 510515, China

*Equal contribution

Correspondence to: Qun Yan, Aimin Li, Side Liu; **email:** yq1107@smu.edu.cn, lam0725@smu.edu.cn, sideliu@smu.edu.cn

Keywords: tumor suppressor, metastasis, proliferation, post-transcriptional regulation, CPEB3

Received: December 21, 2019

Accepted: July 6, 2020

Published: November 3, 2020

Copyright: © 2020 Fang et al. This is an open access article distributed under the terms of the [Creative Commons Attribution License](https://creativecommons.org/licenses/by/3.0/) (CC BY 3.0), which permits unrestricted use, distribution, and reproduction in any medium, provided the original author and source are credited.

ABSTRACT

As RNA-binding proteins, cytoplasmic polyadenylation element binding proteins (CPEBs) have drawn increasing attention for their function of controlling gene expression related to malignant transformation via post-transcriptional regulation. However, the contribution of CPEB3 to malignant development in cancers is poorly understood. In this study, we explored the clinical, biological, and mechanical role of CPEB3 in colorectal cancer progression. We showed that colorectal cancer tissues exhibited dampened CPEB3 expression which was closely associated with poor prognosis in patients with colorectal cancer (47 vs. 62 months, $P = 0.035$, $n=99$). Down-regulation CPEB3 promoted proliferation, migration, and invasion in colorectal cancer cells and vice versa. Mechanistically, CPEB3 performed as an RNA binding protein binding to 3'UTR of JAK1 mRNA to inhibit JAK/STAT pathways in colorectal cancer cells. Knockdown of CPEB3 induced active JAK-STAT signaling, thereby triggering the proliferation and metastasis capacity of colorectal cancer cells. These results suggest that CPEB3 functions as a tumor suppressor in colorectal cancer through its post-transcriptional regulation of JAK/STAT signaling. **Implications:** This study identified a novel role of the RNA binding protein CPEB3 in inhibiting cell proliferation and migration as well as the underlining mechanisms in colorectal cancer cells.

INTRODUCTION

Colorectal cancer is extremely common and a serious health concern worldwide. Despite improvements in treatment, patients with advanced tumors still suffer from unsatisfactory prognosis [1, 2]. Hence, a better understanding of the molecular mechanisms contributing to colorectal cancer progression is critical for the development of more effective, targeted therapies.

Malignant transformation comprises a complicated process mediated by many pro- and anti-tumorigenic factors involving multiple signal pathways [3]. Although gene reprogramming at the transcriptional level has been widely studied, recent work indicates that

mRNA post-transcriptional regulation also constitutes an important step in the regulation of gene expression involved in malignant transformation [4, 5] as well as potentially in the oncogenesis of different cancers. Specifically, cytoplasmic polyadenylation element binding proteins (CPEBs) are RNA-binding proteins that interact with cytoplasmic polyadenylation element (CPE) or U-rich sequences in the 3' untranslated regions (UTRs) of specific mRNAs to activate or repress translation [6, 7]. The CPEB family consists of four members (CPEB1–4). The functions of CPEB1-mediated translation have been well characterized and include cell cycle [8], cellular senescence [9], and synaptic plasticity [10], but less is known regarding the effects of CPEB2–4 binding to target transcripts.

Decreased CPEB1 expression frequently occurs in ovarian and gastric tumors, as well as in breast, myeloma, and colorectal cancer cell lines. These reduced levels have been associated with malignant cell capacity to promote invasion and vascularization [11, 12]. Moreover, bioinformatics analysis based on 42 microarray studies showed ectopic mRNA expression of CPEB1-4 in 92 human cancers [13]. Notably, *CPEB3* mRNA is consistently down-regulated in digestive tract cancers, suggesting a potential role of CPEB3 in tumorigenesis. However, in contrast to CPEB1, evidence directly linking CPEB3 to malignancies remains limited.

In the present study, we confirmed that CPEB3 expression decreases in colorectal cancer tissues, a pattern that is closely associated with poor patient prognosis. CPEB3 down-regulation promotes colorectal cancer cell proliferation, migration, and invasion *in vitro* and *in vivo*, while up-regulation has an inhibitory effect. Furthermore, CPEB3 associates with tumor-related mRNAs in colorectal cancer cells, specifically targeting the 3'UTR of JAK1 mRNA to inhibit JAK/STAT pathways. Active JAK1 translation is induced when CPEB3 is down-regulated, causing abnormal JAK/STAT signaling activation in colorectal cancer. These findings highlight a novel role of CPEB3 post-transcriptional regulation in colorectal cancer and possibly in other digestive tract tumors.

RESULTS

CPEB3 is frequently down-regulated in colorectal cancer tissues

Based on previously published microarray data from the Oncomine database, we first analyzed *CPEB3* expression in colorectal cancer tissues and other tumors and identified 10 databases ($P < 0.0001$; Fold Change >2 ; Gene Rank $<10\%$) for further analysis (Figure 1A). Compared with peri-tumoral tissues, *CPEB3* mRNA expression was significantly decreased in colorectal cancer. The same phenomenon was also identified in other digestive duct tumors, including gastric, esophageal, and liver cancers. Analysis of *CPEB3* expression in The Cancer Gene Atlas revealed a similar declining trend in colorectal cancer tissues (Figure 1B, $P < 0.0001$). We then employed qRT-PCR, IHC, and WB on a panel of human colorectal cancer tissues ($n = 84$) from patients undergoing surgical resection in our hospital to further confirm CPEB3 ectopic expression. In 64 of 84 cancerous tissue samples, *CPEB3* mRNA expression decreased in relation to adjacent non-tumorous tissues ($P = 0.016$) (Figure 1C). The same outcome was confirmed using IHC and WB (Figure 1D, 1E).

Decreased CPEB3 expression is associated with poor prognosis in patients with colorectal cancer

To investigate the significance of CPEB3 expression in CRC, CPEB3 expression levels were further correlated with specific clinicopathologic features of 99 patients with CRC on the TMA. As shown in Table 1, we demonstrated the clinical significance of CPEB3 expression by demonstrating its close correlation with lymphatic metastasis ($P = 0.04$), distant metastasis ($P < 0.01$), and AJCC stages ($P = 0.026$). Further Kaplan-Meier analysis revealed that CPEB3 expression correlated significantly with prognosis. Patients in the low-expression group suffered from shorter OS compared with that in high expression group (47 vs. 62 months, $P = 0.035$, Figure 1F).

CPEB3 inhibits human colorectal cancer proliferation *in vitro*

Our transfection experiments to overexpress or knockdown CPEB3 in three colorectal cancer cell lines were controlled using qPCR and WB experiments (Figure 2A). Based on CCK-8 assay analysis, we found that CPEB3 overexpression significantly suppressed SW480 and LoVo cell proliferation rate at every experimental time point ($P < 0.001$, Figure 2B), whereas CPEB3 knockdown promoted growth rate. Colony formation assay also showed that CPEB3 significantly reduced cancer cell colonies and their size (Figure 2C). Compared with controls, CPEB3 impaired cell cycle progression via inducing G2/M phase arrest in LoVo and SW480 cells (Supplementary Figure 1).

Overexpression of CPEB3 inhibits a cluster of signaling pathways associated with tumor progression in colorectal cancer cells

The results of our Illumina whole-genome expression arrays showed that CPEB3 overexpression caused aberrant expression in 1279 genes (362 up-regulated and 917 down-regulated, fold change >1.5 or <0.67 and $P < 0.05$, Figure 3A). According to the analysis of The Cancer Genome Atlas (TCGA) database, overexpression of CPEB3 remarkably suppressed a series of signal pathways including several key carcinoma molecular pathways, such as cell adhesion, apoptosis, JAK/STAT signaling, Toll-Like-receptor signaling and so on (Figure 3B). Gene set enrichment analysis (GSEA) showed a clear stepwise decrease in average gene expression of the four tumor-related pathways from the control group to CPEB3-overexpressed group (Figure 3C). This outcome suggests that CPEB3 might be involved in the regulation of several tumor-related pathways relevant to tumor progression.

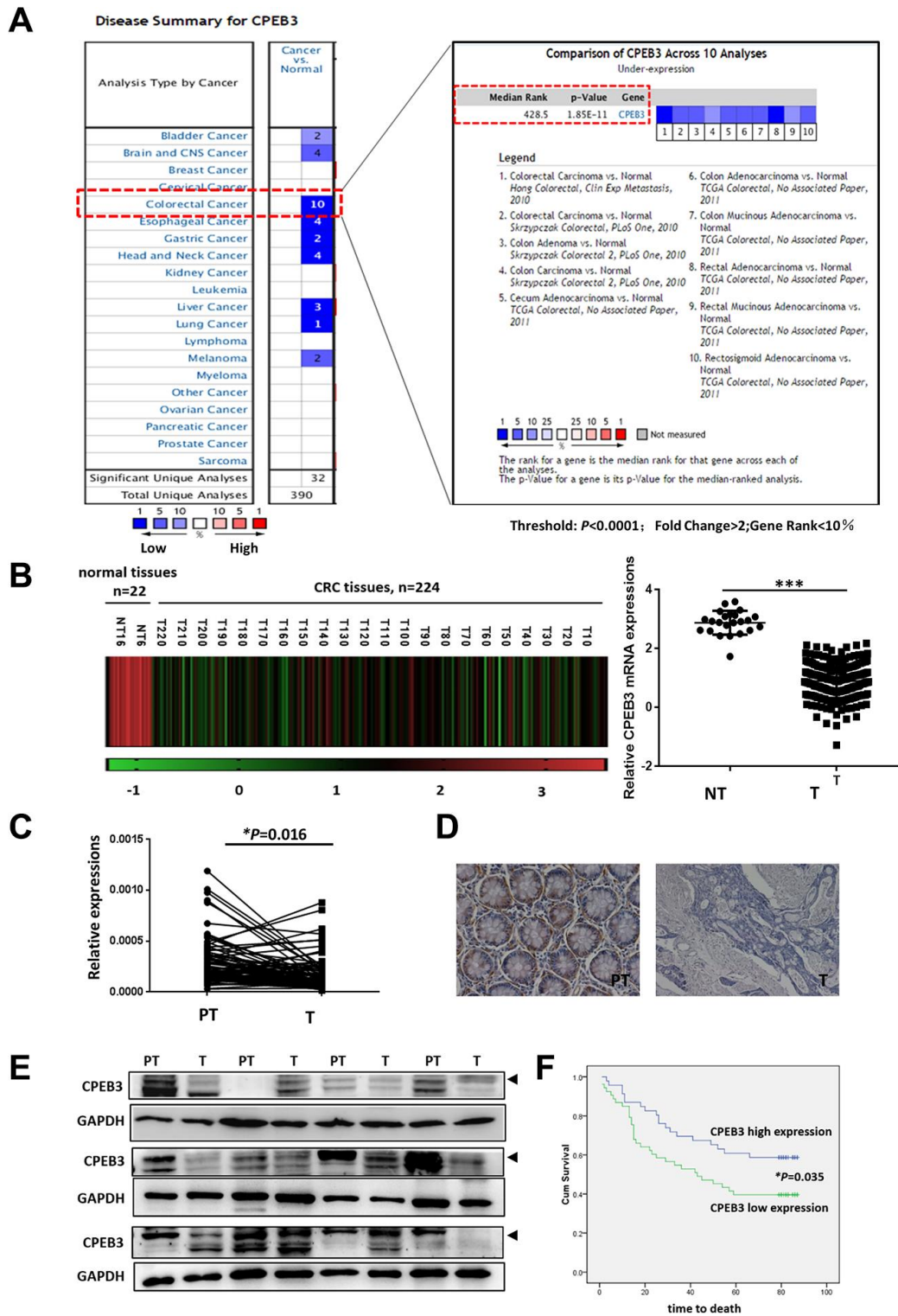


Figure 1. CPEB3 is frequently down-regulated in colorectal cancer tissues. (A) CPEB3 expression in colorectal cancer tissues and other tumors, based on previously published microarray data from the Oncomine database (threshold: $P < 0.0001$; fold change > 2 ; gene rank $< 10\%$). (B) Analysis of *CPEB3* gene expression in colorectal cancer and normal tissues in TCGA database ($n = 246$ [224 vs. 22]). (C) qPCR analysis of *CPEB3* mRNA expression in human colorectal cancer tissues and matched peri-tumoral tissues ($n = 84$). (D) Representative immunohistochemical staining of CPEB3 in human colorectal cancer tissues (right) and matched peri-tumoral tissues (left). (E) Western blotting analysis of CPEB3 in human colorectal cancer tissues and matched peri-tumoral tissues ($n = 12$). (F) Patients in the CPEB3 low-expression group tended to exhibit shorter OS than patients in the high-expression group by Kaplan-Meier analysis (47 vs. 62 months; $P = 0.035$).

Table 1. Association of CPEB3 expression with clinicopathological characteristics in 99 patients with CRC.

Variable	n	CPEB3		P
		Low (n = 53)	High (n = 46)	
Age (years)				
< 70 (45-69)	54	32	22	0.147
≥ 70 (70-91)	45	21	24	
Gender				
Male	58	30	28	0.411
Female	41	23	18	
Pathological grade				
Well	69	35	34	0.265
Moderate- Poor	30	18	12	
pT status				
T1-2	4	1	3	0.257
T3-4	95	52	43	
pN status				
N0	52	23	29	<u>0.040</u>
N1	47	30	17	
pM status				
M0	94	48	46	<u>0.040</u>
M1	5	5	0	
Tumor stage				
I/II	51	22	29	<u>0.026</u>
III/IV	48	31	17	
Tumor size				
≤ 5 cm	56	32	24	0.268
> 5 cm	43	21	22	
Tumor number				
Single	95	49	46	0.078
Multiple	4	4	0	

CPEB3 directly targets the 3'UTR of JAK1 and regulates colorectal cancer proliferation and metastasis via CPEB3/JAK/STAT axis

To obtain a genome-wide picture of potential CPEB3 targets in colorectal cancer, we performed RIP of CPEB3 extracted from SW480 cells. Assay validity was confirmed using snRNP70 (positive control) and IgG (negative control) antibodies for precipitation (Supplementary Figure 2A, 2B). Sequencing analysis of co-immunoprecipitated mRNAs showed that 1791 were significantly ($P < 1.00 \text{ E}-05$, Fold change > 5) linked to CPEB3 compared with the IgG group (Supplementary Figure 2C). Gene ontology analysis then demonstrated that CPEB3-targeted mRNAs were significantly enriched in biological processes relevant to RNA-binding, cell cycle, cellular response to stress, cellular metabolic process and so on (Figure 4A). We selected JAK1 for further analysis because the transcript was significantly enriched in CPEB3 immunoprecipitates according to the RIP-sequence (Figure 4B) and RIP-

qPCR analysis (Figure 4C). Besides, its downstream genes were significantly inhibited following CPEB3 overexpression according to the microarray analysis (Figure 3). The 3'UTR of JAK1 mRNA contains two potential CPEB3 binding sequences including one putative CPE and one U-rich sequence besides the polyadenylation signal (AAUAAA). To determine whether CPEB3 directly binds to JAK1 mRNA, reporter assay with firefly luciferase appended to mRNA of JAK1 3'UTR was performed and the results revealed markedly lower luciferase activity when the full-length sequence of JAK1 3'UTR was co-transfected with CPEB3. But this repression was abrogated when the two potential CPEB3 binding sequences was deleted (Figure 4D). Thus, CPEB3 binds to the JAK1 3'UTR.

As we have proved that reduced CPEB3 expression resulted in more aggressive proliferation and metastasis capacity in colorectal cancer cells and CPEB3 involved in the regulation of JAK/STAT signal pathway. We performed CCK-8 and transwell assays to analyze the

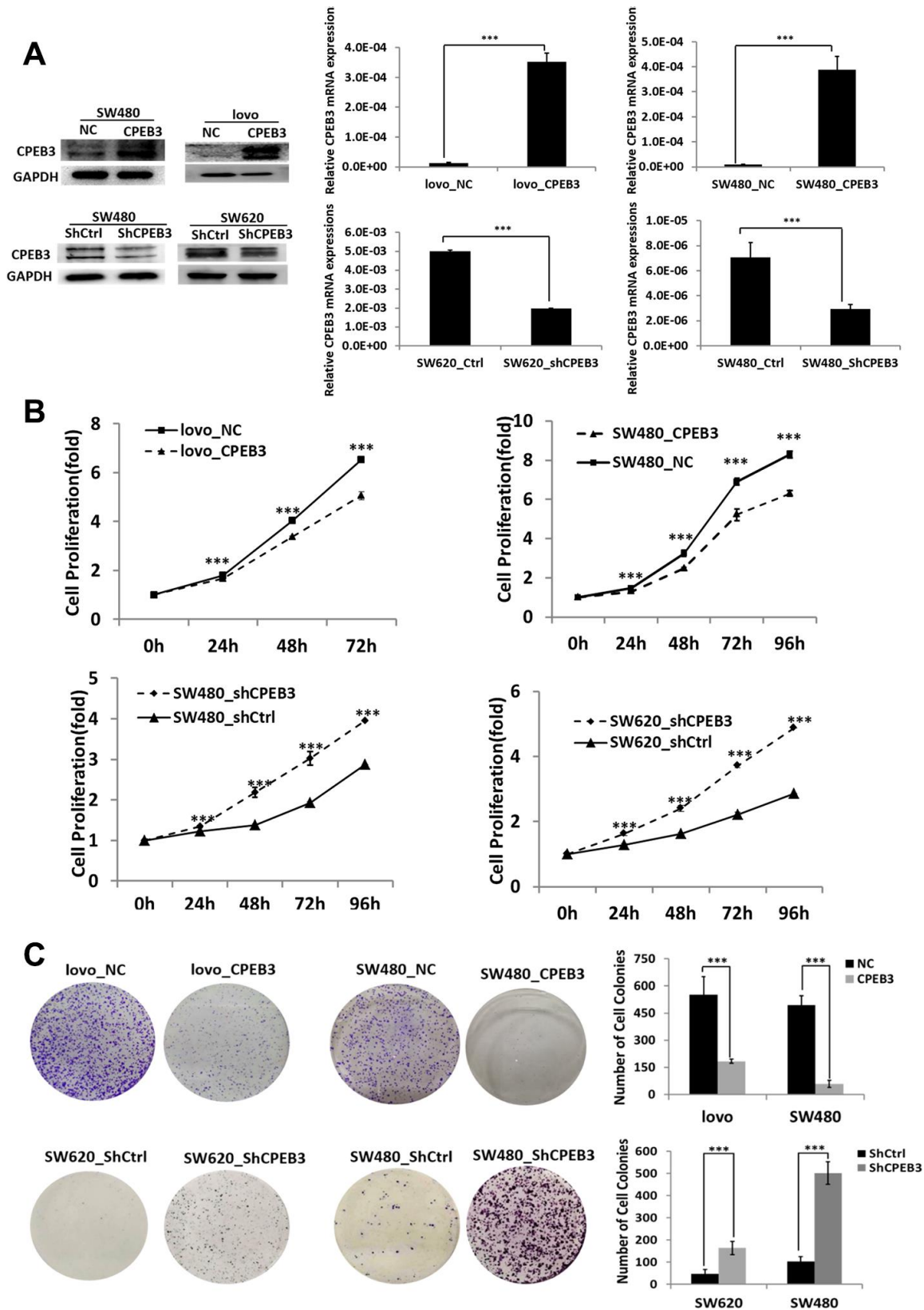


Figure 2. CPEB3 inhibits human colorectal cancer proliferation *in vitro*. (A) CPEB3 protein expressions of CRC cell lines were efficiently upregulated or downregulated after transfection as analyzed by Western blotting (left) and qPCR (right) detection (** $P < 0.01$, *** $P < 0.001$). (B, C) After effective up- or down-regulation of CPEB3, CCK-8 (B) and colony formation (C) assays were performed to explore the effect of CPEB3 on proliferative capacity of colorectal cancer cell line.

role of JAK/STAT in CPEB3-mediated cell proliferation and metastasis (Supplementary Figure 3). The results showed that inhibiting JAK/STAT attenuated the stimulatory effects of CPEB3-knockdown on proliferation, migration, and invasion (Figure 4E, 4F). Altogether, these results revealed that there is a mechanistic connection between CPEB3 and the JAK/STAT signal pathway, potentially via direct binding to JAK1 3'UTR in colorectal cancer cells.

CPEB3 inhibits human colorectal cancer proliferation and JAK/STAT pathway *in vivo*

For the tumorigenicity assay *in vivo*, SW480-CPEB3 and -NC cells as well as SW480-shCPEB3 and SW480-shControl cells were injected subcutaneously in the nude mice. Tumor volume was measured every 6 d and xenograft tumor growth curves were drawn 30 d post-injection. Tumor volume dropped significantly in the

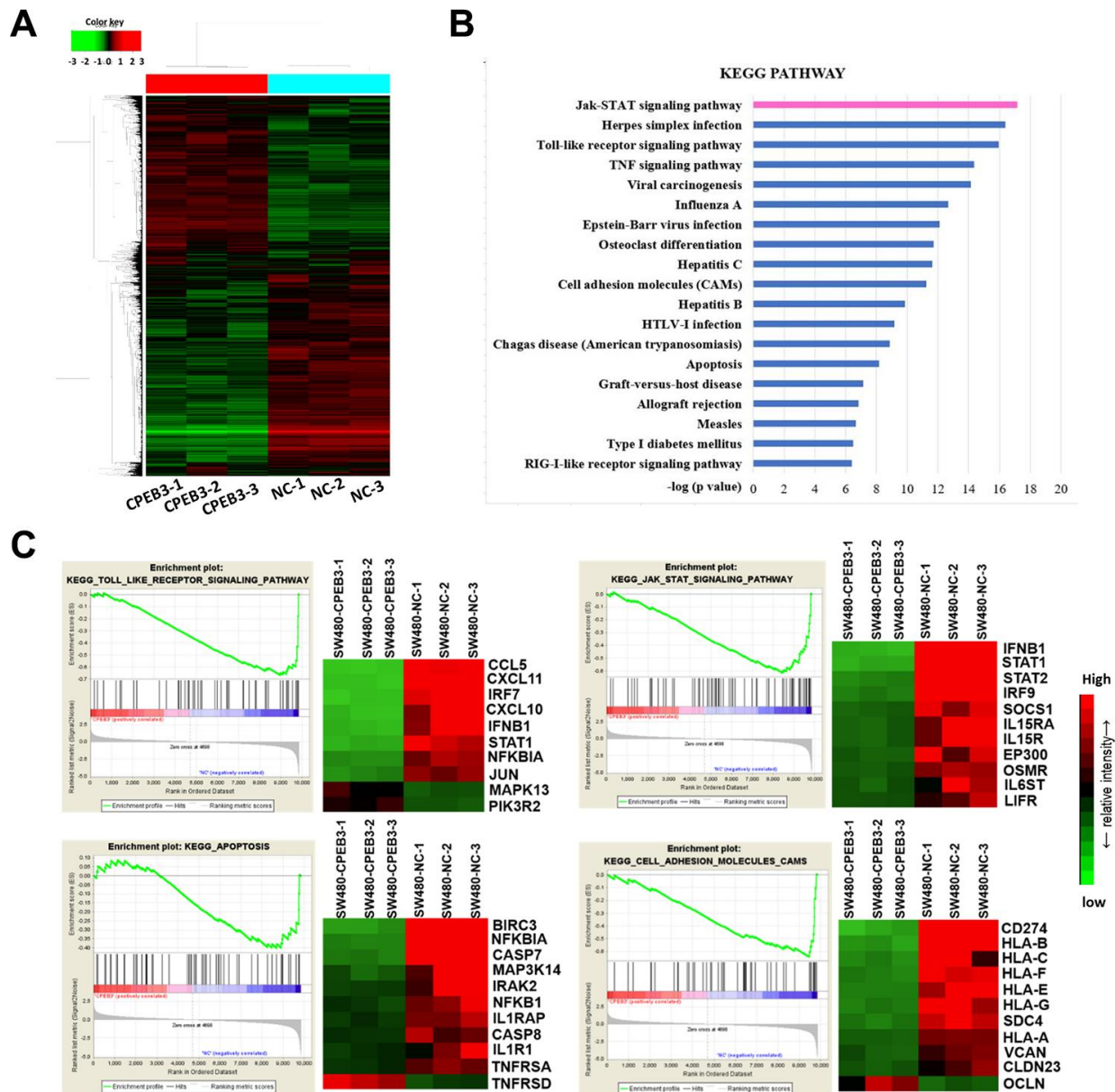


Figure 3. Overexpression of CPEB3 inhibits a cluster of signaling pathways associated with tumor progression in colorectal cancer cells. (A) Microarray analysis was applied to screen the mRNAs which can be regulated by CPEB3. (B) Canonical pathway enrichment of whole genome expression in SW480-CPEB3 and SW480-NC cell lines was analyzed based on KEGG pathway database. (C) Gene set enrichment analysis results for all fold changes calculated between SW480-CPEB3 and SW480-NC cells were shown on the left and the heatmap analysis of genes in each signaling pathway were displayed on the right. Red represents high expression levels and green represents low expression levels.

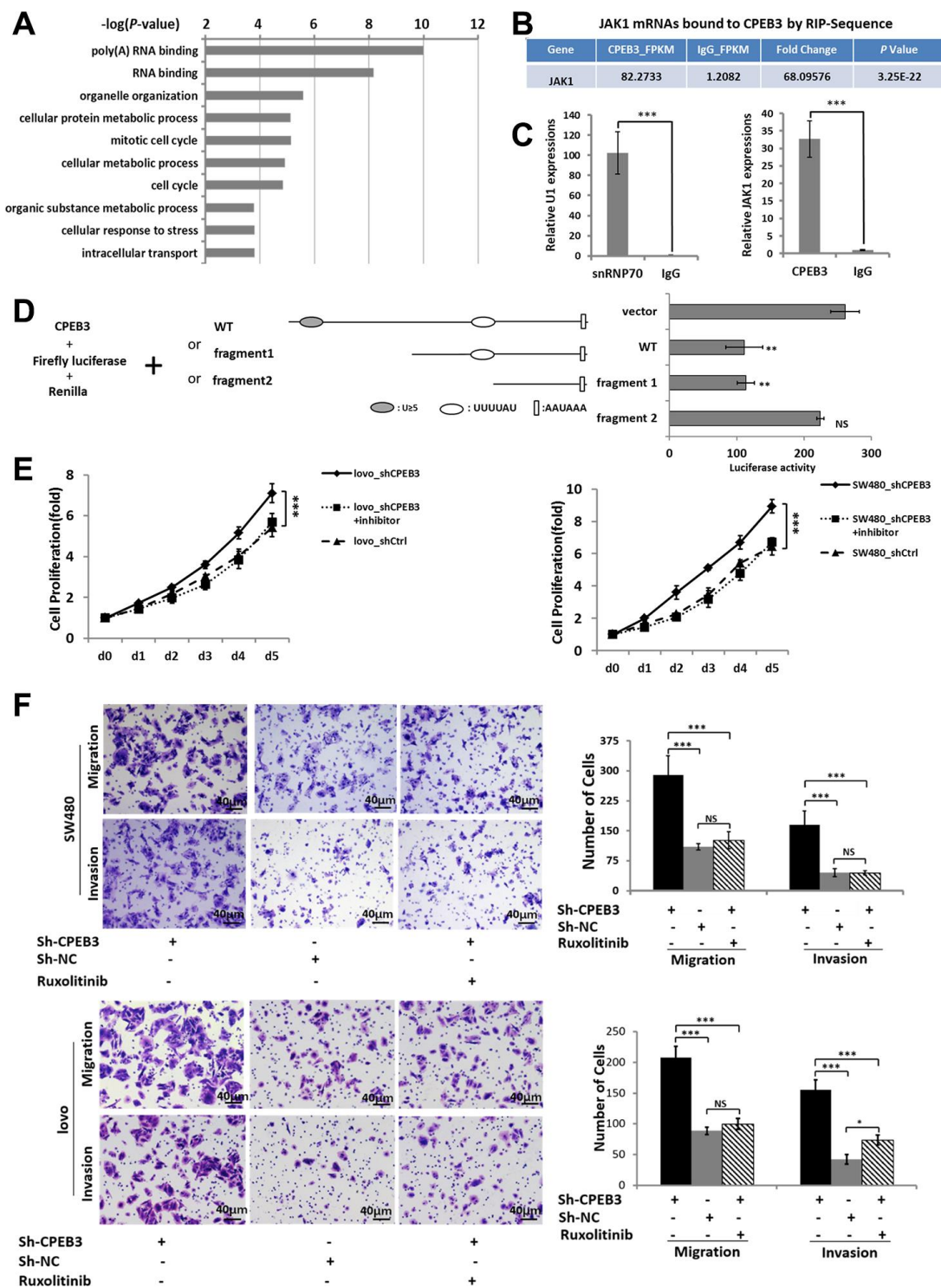


Figure 4. CPEB3 directly targets the 3'UTR of JAK1 and regulates colorectal cancer proliferation and metastasis via CPEB3/JAK/STAT axis. (A) High-throughput sequencing analysis of mRNAs bound to CPEB3 in SW480 cells showed the top 10 significantly enriched terms using Gene ontology analysis. (B) RNA immunoprecipitation and high-throughput sequencing analysis showed that JAK1 mRNA was significantly enriched in CPEB3 immunoprecipitates. (C) The combination of JAK1 mRNA and CPEB3 was further validated by RIP-qPCR. IgG and SnRNP70 are used as the negative and positive control respectively. Data are shown as mean \pm SD (** $P < 0.001$). (D) Luciferase reporter plasmid appended with different 3'UTR fragments of JAK1 mRNA were co-transfected with CPEB3 in the HEK-293T cell line, and luciferase activity was detected. Data are displayed as the means \pm SD (** $P < 0.01$, NS: No Significance). (E, F) Impairment of JAK/STAT pathway by Ruxolitinib could reverse the effect of CPEB3 down-regulation on proliferation ability by CCK-8 assay (E) as well as the migration and invasion ability by transwell assays (original magnification, $\times 400$) of colorectal cancer cell lines. (F).

CPEB3-overexpressing group compared with control (final volume: 0.155 cm³ vs. 0.543 cm³, $P = 0.008$), whereas the CPEB3-knockdown group had dramatically larger tumors than control (final volume: 1.338 cm³ vs. 0.592 cm³, $P = 0.000$) (Figure 5A, 5B). Histopathological detection of xenograft tumors showed that the CPEB3-overexpressing group exhibited weaker Ki67 staining than control, whereas the CPEB3-knockdown group had stronger Ki67 staining (Figure 5C). What's more, tumors from CPEB3 overexpressed group exhibited decreased activity of JAK/STAT signaling pathway, whereas CPEB3 knockdown promoted their activation (Figure 5D). These results indicated that CPEB3 inhibits colorectal cancer cell proliferation ability and JAK/STAT pathway *in vivo*.

DISCUSSION

Data accumulated in recent years support the role of post-transcriptional regulation in cancer oncogenesis [14]. RNA-binding proteins (RBPs) are emerging epigenetic post-transcriptional regulators involved in RNA processing, such as splicing, localization, stabilization, and translation. As a consequence, the abundance of RBPs and their constituents differentially affects RNA regulation [15–17]. Interplay between RBPs and RNAs is crucial for normal biological processes (e.g., brain and ovarian development) in addition to regulating tumor progression. CPEBs are RBPs with similar RNA-binding domains, through which they regulate CPE-containing mRNA translation. This capacity means they control the cell cycle, cellular differentiation, or synaptic plasticity.

Initial evidence linking CPEBs to cancer biology emerged from a meta-analysis of 42 studies comparing global gene expression in 92 human cancers with matched normal tissue [13, 18]. The findings strongly support a role of CPEBs in tumorigenesis. First, they showed that CPEB1 mRNA expression is reduced in reproductive-system and brain cancers. Additionally, CPEB4 mRNA is upregulated in pancreatic carcinomas and glioblastomas, while CPEB3 mRNA is consistently downregulated in digestive tract tumors. Subsequently, direct connections between ectopic CPEB1 expression and tumorous development were established [12, 19]. Ovarian and gastric cancer, as well as breast, myeloma, and colorectal cancer cell lines all display dampened CPEB1 expression [11, 12]. Mechanically, CPEB1 interactions with HIF-1 α mRNA appear to repress the latter's translation, thus inhibiting invasion and angiogenesis [20]. What's more, elevated CPEB4 expression correlates with increased malignancy, tumor growth, and vascularization in pancreatic ductal adenocarcinoma and glioblastoma [21]. However, we know considerably less about CPEB3's role in cancer

development compared with the body of work available for CPEB1 and CPEB4 [13, 22].

In this study, we showed that CPEB3 is frequently down-regulated in colorectal cancer tissues compared with matched peri-tumoral tissues. The clinical significance of CPEB3 expression is demonstrated by close correlations with lymphatic metastasis, distant metastasis, and tumor stage. Lower CPEB3 expression predicts shorter survival time in patients with colorectal cancer after surgical resection. As for the upstream regulatory mechanisms leading to decreased CPEB3 expression in cancers, one recent study by Lin et al. revealed that LncRNA SUMO1P3 promotes proliferation and inhibits apoptosis in colorectal cancer by epigenetically silencing CPEB3 [23]. Another recent study underlined the role of miRNA-301b-3p in the regulation of CPEB3/EGFR axis [24]. These results suggest a potential role of CPEB3 in cancers and highlight post-transcriptional regulation maybe an important controlling mechanism of CPEB3 expression.

In addition, CPEB3 attenuates colorectal cancer cell proliferation, while silencing the protein enhances proliferation rate *in vitro* and in athymic nude mice. Moreover, CPEB3 down-regulation in colorectal cancer cells increased migration and invasion, while up-regulation showed the opposite effect. Together, these results support conclusions from clinical data that CPEB3 is a tumor suppressor in colorectal cancer progression. Consistent with our results, previous research found that CPEB3 represses proliferation and metastasis in hepatocellular carcinoma cells [25]. Moreover, a microarray-based, high throughput screening study for unknown tumor-suppressor genes in colorectal cancer identified CPEB3 as one of four significantly down-regulated genes [26].

The recent development of large-scale quantitative methods, especially next-generation sequencing and modern protein mass spectrometry, facilitates genome-wide identification of RBPs, their protein cofactors, and their RNA targets [27–30]. Notable RBP-immunoprecipitation-based deep-sequencing approaches include crosslinking and immunoprecipitation followed by sequencing (CLIP-seq), RNA immunoprecipitation and sequencing (RIP-seq), as well as *in vitro* evolution methods. Studies using these techniques revealed that many RBPs bind to thousands of RNA targets in cells at defined binding sites [31, 32]. Here, we performed RIP-sequence to describe the RNA profiling directly binding to CPEB3. Consistent with other RBPs, CPEB3 binds to over 1000 RNAs; the most common targets are those encoding translation initiation factors and RNA-binding proteins, supporting the RNA-binding function of CPEBs. In addition, CPEB3 is associated with a gene

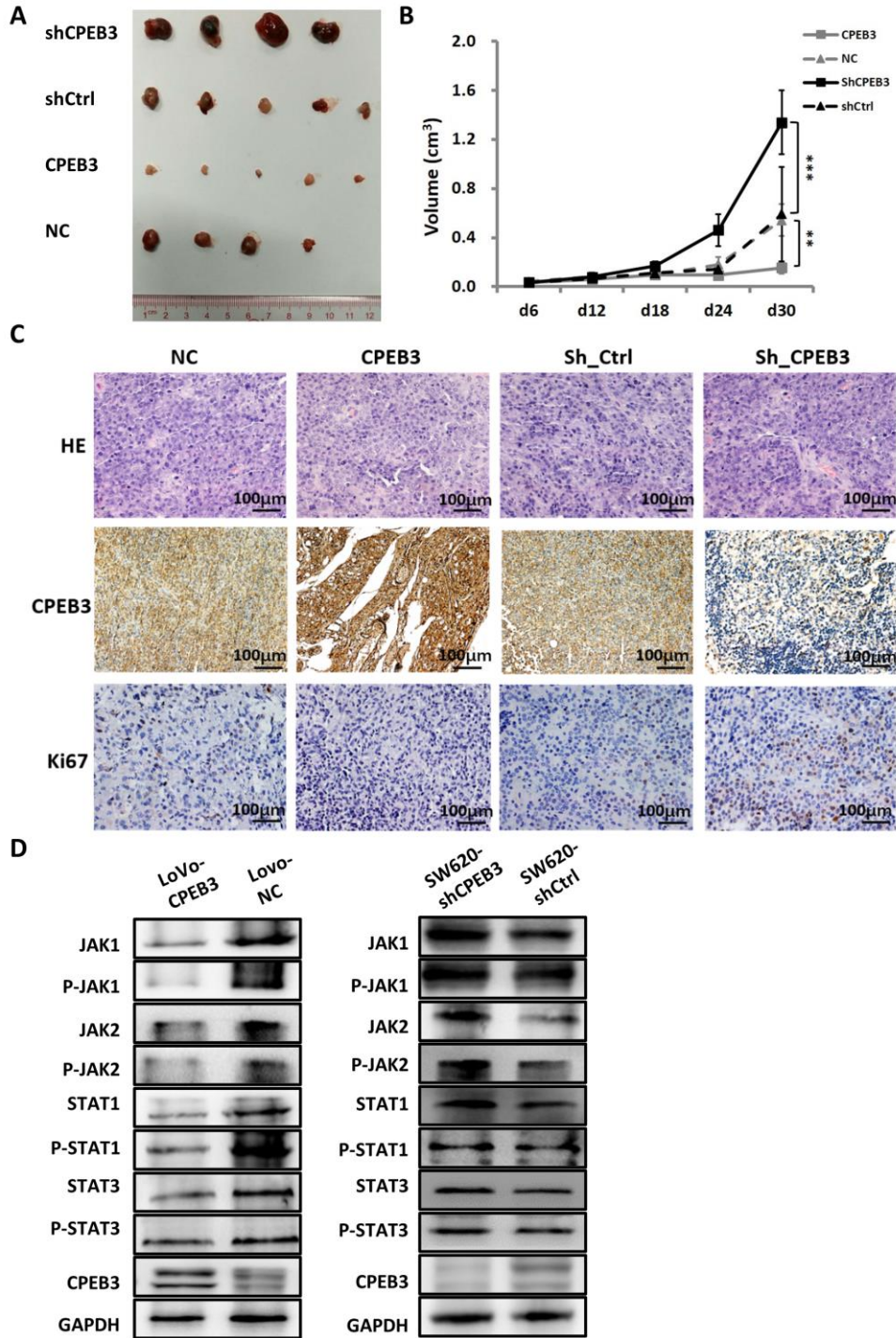


Figure 5. CPEB3 inhibits human colorectal cancer proliferation and JAK/STAT pathway *in vivo*. (A) Representative images of tumors formed in nude mice subcutaneously implanted with SW480-CPEB3, SW-NC, SW480-shCPEB3 and SW480-shCtrl cell lines. (B) Growth curves of implanted tumors in nude mice (** $P < 0.01$, *** $P < 0.001$). (C) Representative immunohistochemical images of tumor xenografts derived from SW480-CPEB3, SW-NC, SW480-shCPEB3 and SW480-shCtrl cell lines stained by anti-CD31 and anti-Ki67 antibodies (Original magnification, $\times 200$). (D) Western blots showed that CPEB3 overexpression suppressed JAK1 and phosphorylated JAK1, as well as molecules in the JAK/STAT pathway while CPEB3 knockdown promoted the activation of these genes.

cluster and signal pathways critical to cancer proliferation and metastasis, such as cellular protein metabolism, cell cycle (cyclins) and cellular stress response (autophagy-related factors, signal transducers and modulators).

Post-RNA-binding mechanisms of CPEB3 also remain poorly understood, especially in tumor development. Previous studies reported that CPEB3 depletion increases glutamate receptor 2 (GLUR2) mRNA translation [33] and CPEB3 inhibits translation of mRNA targets by localizing them to P bodies [34], suggesting that in neurons, CPEB3 has a negative regulatory role in post-transcription. However, another study demonstrated that CPEB3 can stimulate GLUA1 and GLUR2 translation, which suggests a positive regulation of its RNA targets [35]. In this study, whole-genome arrays revealed that CPEB3 overexpression in colorectal cancer cells down-regulated 226 genes by over two-fold, while up-regulating only 30 more. In addition, CPEB3 over-expressing colorectal cancer cells exhibited reduced activity in cancer-related signal pathways, including cell adhesion, apoptosis, JAK/STAT, and Toll-Like-receptor. Therefore, CPEB3 appears to exert primarily a negative effect on gene expression and tumor-related pathways in colorectal cancer cells.

JAKs are mediators of cytokine and growth hormone signaling. Activated JAKs phosphorylate signal transducer and activator of transcription (STAT) proteins, then translocate them from the cytoplasm to the nucleus. There, they bind canonical sequences and modulate transcription of genes involved in cell proliferation, differentiation, and apoptosis [36, 37]. Here, we showed that CPEB3 anti-tumor effects in colorectal cancer are likely mediated via regulating the JAK/STAT pathway. We already know that JAK/STAT signaling pathways are aberrantly activated in several types of cancers, playing a crucial role in promoting carcinogenesis [8, 38, 39]. Here, our microarray analysis showed that CPEB3 overexpression in SW480 cells decreased expression of multiple downstream genes related to the JAK/STAT pathway. Our RIP-sequencing and -qPCR also demonstrated that JAK1 is enriched in CPEB3 immunoprecipitates. Furthermore, CPEB3 down-regulation promoted JAK1, P-JAK1, and STAT protein expression, whereas CPEB3 overexpression had the opposite effect. Impairing the JAK/STAT signaling pathway reversed CPEB3-knockdown effects on proliferation, migration, and invasion in colorectal cancer cells. Finally, CPEB3 translationally repressed JAK1 mRNA through binding to 3'UTR.

Altogether, this study revealed that colorectal cancer tissues exhibit repressed CPEB3 expression, a

phenomenon that predicts poor prognosis in patients with colorectal cancer. In addition, CPEB3 is a tumor suppressor, inhibiting cell proliferation and migration in colorectal cancer cells through regulating the JAK/STAT pathway. However, as few preliminary cancer studies focus on CPEB3, many questions remain unanswered. For example, given the association of CPEB3 with numerous tumor-progression transcripts, we cannot exclude the possibility that other unidentified molecules or compensatory mechanisms may also contribute to aberrant colorectal cancer proliferation and metastasis. Furthermore, data from previously published microarray screening studies have indicated extensive CPEB3 deletion in digestive tract cancers [13]. Thus, the anti-tumorous effects of CPEB3 may not be restricted to colorectal cancer and requires further exploration in other digestive tract cancers.

MATERIALS AND METHODS

Patients and tissue samples

84 pairs of tumoral and peri-tumoral tissues for qRT-PCR, Immunohistochemistry (IHC) and Western blotting (WB) analysis were obtained from patients who underwent surgical resection at our institute's Department of General Surgery. A tissue microarray (TMA) including 99 pairs of CRC tissues with survival data were purchased from the China National Engineering Center for Biochip (Shanghai, China) and IHC detection and survival analysis were performed using the tissue microarray slides. Tumor stage was defined according to the American Joint Committee on Cancer (AJCC)/International Union against Cancer classification system [40]. All procedures were approved by the institutional ethics committee of Nanfang Hospital and all enrolled subjects provided written informed consent.

Cell culture and lentivirus infection

Human colorectal cancer cell lines LoVo, SW620, SW480 and human embryonic kidney-293T (HEK-293T) were obtained from the Shanghai Institute of Biochemistry and Cell Biology (Shanghai, China) and maintained in Dulbecco's modified Eagle's medium (DMEM; Invitrogen, Gaithersburg, MD, USA) containing 10% fetal calf serum (FCS; Hyclone, Logan, UT, USA), 100 IU/mL penicillin, and 100 µg/mL streptomycin. Cell lines were obtained in 2013, authenticated via short tandem repeat fingerprinting, and tested negative for mycoplasma contamination using Hoechst staining and PCR. Lentiviruses carrying full-length *CPEB3* or short hairpin RNA (shRNA) sequences were targeted against human *CPEB3* mRNA and matched negative controls (NC) were constructed

by the Shanghai Institute of Biochemistry and Cell Biology. The stable cell lines were established as previously described [41]. To obtain stable transfectants, 5 µg/mL puromycin was added to the culture medium 72 h post-transfection. Cells were pretreated with a dimethylsulfoxide vehicle control or the JAK inhibitor ruxolitinib (3 µM, Selleck Chemicals, Houston, TX, USA) for 48 h prior to analysis.

RNA extraction, cDNA synthesis, and qRT-PCR

Total RNA was extracted using TRIzol (Invitrogen) for cDNA synthesis using random primers (Supplementary Table 1) and the TaKaRa PrimeScript RT reagent kit. Quantitative real-time PCR was performed in triplicate using SYBR Green on a Light Cycler 480 Real Time PCR System (Roche Diagnostics, Mannheim, Germany). Cycling conditions were as follows: 40 cycles of 95°C (30 s), 95°C (5 s), and 60°C (20 s), followed by one cycle of 65°C (15 s). *GAPDH* was used as the endogenous control and relative gene expression levels were calculated using the $2^{-\Delta\Delta Ct}$ method.

IHC

Tissue sections were deparaffinized in xylene and rehydrated using a graded ethanol series. They were then immersed in 0.1 M citrate (pH 6.0) at 120 °C for 10 min to retrieve antigens, incubated with 1% goat serum albumin to block nonspecific binding, then incubated with CPEB3 polyclonal rabbit anti-human IgG (1:50; Abcam, Cambridge, UK) at 4 °C overnight. Secondary antibody incubation was performed after the sections were kept at room temperature for 45 min. Reactions were developed using diaminobenzidine as a chromogenic substrate. Two observers independently scored sections to determine proportion of positively stained tumor cells (<5% = 0, 5–25% = 1, 26–50% = 2, 51–75% = 3, 76–100% = 4) and staining intensity (none = 0, weak = 1, moderate = 2, strong = 3). The percentage of positive cells of different intensity was multiplied by the corresponding intensity value to obtain the staining index, ranging from 0 to 12. Cutoff values for CPEB3 were chosen based on a measure of heterogeneity by log-rank test statistical analysis with regard to overall survival (OS). An optimal cutoff value was obtained, with scores of >3 and ≤3 defined as the high and low CPEB3 expression group, respectively.

WB

Cells were homogenized in RIPA lysis buffer (Millipore, Billerica, MA, USA) containing 1% Halt Protease and Phosphatase Inhibitor Cocktails (Thermo Scientific, Rockford, IL, USA) and incubated on ice for 30 min. After centrifugation, proteins in the supernatant

were quantified using a Pierce BCA Protein Assay Kit (Thermo Scientific). Equal amounts of proteins were fractionated using sodium dodecyl sulfate-polyacrylamide gel electrophoresis and transferred to polyvinylidene fluoride membranes (Bio-Rad Laboratories, Hercules, CA, USA). Membranes were then blocked with 5% non-fat milk in TBST (10 mM Tris-HCl [pH 8], 150 mM NaCl, 0.05% Tween 20) for 1 h, probed overnight with designated primary antibodies at 4 °C, then incubated with corresponding horseradish peroxidase (HRP)-conjugated secondary antibodies. Signals were developed using Immobilon Western chemiluminescent HRP substrate (Millipore) and scanned in a GeneGnome HR Bioimaging system (Syngene, Bristol, UK). *GAPDH* was used as an internal control.

Cell proliferation, colony formation, and cell cycle assay

Colorectal cancer cells (5000 cells/well) were seeded in 96-well plates. Proliferation rate was assessed at 24, 48, 72, and 96 h using the Cell Counting Kit-8 (CCK-8; Beyotime, China). Briefly, cells were incubated with 100 µL DMEM containing 10 µL CCK-8 at 37 °C for 2 h. Absorbance at 450 nm was measured using a microplate spectrometer (Molecular Devices, Sunnyvale, CA, USA). Each time point was assessed in replicates of five wells. For the colony formation assay, stable cell lines (200 cells/well) were seeded in six-well plates. After 2 weeks, cells were fixed in 4% paraformaldehyde and stained with crystal violet for 30 min at room temperature. Colonies consisting of >50 cells were counted. Three independent experiments were performed for each cell line. For cell cycle analysis, stable cell lines were trypsinized, rinsed in PBS, fixed in 70% cold ethanol at 4 °C overnight, and incubated with 0.1 mg/mL RNase A (Calbiochem, San Diego, CA, USA) at 37 °C for 30 min, then with 0.5 mg/mL propidium iodide in the dark at 4 °C for 30 min. Cell cycle distribution was measured using a BD LSRFortessa cell analyzer (BD Biosciences, San Jose, CA, USA) and analyzed using ModFit (Verity Software House, Topsham, ME, USA).

Migration and invasion assay

The migration and invasion assays were performed in 24-well plates with 8 µm polycarbonate nucleopore filters (3422, Corning, Armonk, NY, USA). The assay membrane was covered with 40 µL BD Matrigel (diluted 1:8 with serum-free medium) in advance. Stable cell lines (1×10^5 and 5×10^5 cells for migration and invasion assays, respectively) were resuspended with 200 µL serum-free medium and seeded in the upper chambers; lower chambers were filled with 500 µL medium

containing 10% FCS. After a 48 h incubation, cells adhering to the lower filter surface were fixed with 4% paraformaldehyde and stained with 0.5% crystal violet. Cells in five random fields (at $\times 200$ magnification) were counted under a light microscope. Experiments were independently replicated three times. Data are presented as the means \pm SD.

For the wound healing assay, stable cells were seeded into a six-well plate until 80% confluence. Monolayers were scratched with a 200 μ L pipette tip to generate wounds. Wells were washed thoroughly with PBS and incubated for another 48 h. Images were taken at 0, 24, and 48 h using a light microscope ($\times 200$ magnification). Wound width was measured in Image J (National Institutes of Health, Bethesda, MD, USA) using an average of three width measurements per picture. Experiments were performed in triplicate.

Tumorigenesis in nude mice

Tumorigenesis testing in nude mice was carried out in accordance with ARRIVE guidelines. Briefly, 4-week-old BALB/c male nude mice were purchased from the Experimental Animal Center of Southern Medical University (Guangzhou, China). Xenograft tumors were generated via subcutaneous injection of SW480 cells (3×10^6) stably expressing CPEB3 or CPEB3-shRNA in the right flank of nude mice. Mice were housed and maintained under specific pathogen-free conditions. Tumor nodules were examined every 6 d to evaluate volume using the following formula: tumor volume = (width² \times length)/2. Mice were sacrificed with cervical dislocation 30 d after inoculation; their tumors were excised, weighted, and frozen or fixed for IHC staining and WB examination. Experiments were approved by the Institutional Animal Care and Use Committee of Nanfang Hospital.

Luciferase reporter assay

HEK-293T cells (3×10^4) were seeded three times independently in 24-well plates. Adhered cells were transfected with 0.5 μ g plasmid expressing firefly luciferase reporter appended with human *JAK13* UTR mutants, 20 ng plasmid expressing *Renilla* luciferase, and 750 ng plasmid expressing CPEB3 (Obio Technology, Shanghai, China), using Lipofectamine 3000 (Invitrogen). At 24 h after transfection, luciferase activity was measured using the Dual-Luciferase reporter assay system (Promega, Madison, WI, USA).

Microarray

The GeneChip Human Genome U133 Plus 2.0 Array was used for transcriptome analysis. Briefly, total RNA

extracted from SW480-NC and SW480-CPEB3 was purified using RNeasy columns (Qiagen, Valencia, CA, USA). RNA per sample (0.1 μ g) was labeled using the MessageAmp Premier RNA Amplification Kit (Ambion, Austin, TX, USA). Biotin-labeled cRNA was obtained from T7-oligo (dT)-primed cDNA processed using the Affymetrix Hybridization, Wash, and Stain Kit, following manufacturer protocol. Finally, hybridized biotinylated cRNA was quantified with a GeneChip Scanner 3000 (Affymetrix).

Image signals were transformed to digital data using Affymetrix GeneChip Command Console. The data were analyzed with Affymetrix GeneChip Command Console Software. Raw data were normalized and perfect matches summarized through median polish using the Robust Multi-array Average algorithm. Differentially expressed genes were analyzed using R Significance Analysis of Microarrays. The significance threshold was q-value $< 5\%$ and Fold Change > 1.5 or < 0.67 .

RNA immunoprecipitation and gene sequencing (RIP-seq)

To obtain a genome-wide picture of potential CPEB3 targets in colorectal cancer, we performed RIP of CPEB3 extracted from SW480 cells. SW480 cells grown to 80% confluence were washed with cold PBS and collected via scraping. RNA immunoprecipitation was performed according to Magna RIP RNA-Binding Protein Immunoprecipitation Kit guidelines (Millipore). Briefly, cells were lysed in lysis buffer containing RNase inhibitor and a protease inhibitor cocktail. Magnetic beads were pre-incubated with 5 μ g anti-SNRNP70 antibody, anti-CPEB3 antibody, or rabbit IgG for 1 h at room temperature, and lysates were immunoprecipitated with beads at 4 $^{\circ}$ C overnight. Using RIP Lysate, RNA was extracted from Magna RIP beads for high-throughput sequencing or qRT-PCR detection.

For gene sequencing, RIP-RNAs were subjected to fragmentation, retrotranscription, modification, and PCR to construct the sample library. Cluster generation and sequencing primer hybridization was conducted according to the cBot User Guide. The cluster was processed using a high-throughput sequencing system (HiSeq 2500, Illumina, San Diego, CA, USA) following standard procedures.

For bioinformatics analysis, raw reads (23063600 for *CPEB3* and 21692675 for IgG) were preprocessed by moving the unqualified reads using fastx_tool kit. Approximately 61% of the clean reads for the *CPEB3* group and 33% for the IgG group were rRNAs (Supplementary Table 2). Clean reads were mapped to

ensemble HG19 mRNAs using TopHat (version 2.0.9). We obtained 4759549 mapped reads from the *CPEB3* group and 2300735 from the IgG group (Supplementary Table 3). Relative abundances were estimated using cufflinks (version 2.1.1). Fragment per kilobase of transcript per million mapped reads (FPKM) was calculated using the formula: $FPKM = \text{total exon fragments} / (\text{mapped reads (millions)} \times \text{exon length (kb)})$. Genes with significant differences were selected based on the threshold criteria of $P < 0.0001$ (10^{-4}) and fold changes >5 .

Statistical analysis

All statistical analyses were performed in SPSS version 19.0 (Chicago, IL, USA). Pearson's chi-square was used to analyze the relationship between *CPEB3* expression and the clinicopathological features of patients with colorectal cancer. Overall survival rates were calculated using the Kaplan-Meier method, and significance was determined using a log-rank test. Paired-sample t-tests were used to determine differences between cancerous and peri-tumoral tissues. All other between-group differences were analyzed with two-tailed independent Student's t-tests. Data are presented as the means \pm SD. Significance was set to $P < 0.05$.

AUTHOR CONTRIBUTIONS

QY and AL designed the experiments. SL and YF performed the experiments and wrote the manuscript. QZ and YW analyzed the data and provided administrative, technical, or material support. CG helped with acquisition of data and writing of the manuscript. All authors discussed the results and approved of the final version.

ACKNOWLEDGMENTS

We would like to thank the CapitalBio Corporation for technical support in bioinformatics analysis.

CONFLICTS OF INTEREST

The authors declare no conflicts of interest.

FUNDING

This work was supported by the National Natural Science Foundation of China (grant number 81902481); Science and Technology Planning Project of Guangdong Province (grant number 2017A020215046); Natural Science Foundation of Guangdong Province (grant number 2018030310030); Medical Scientific Research Foundation of Guangdong Province (grant number A2018177, A2017291); President Foundation

of Nanfang Hospital, Southern Medical University (grant number 2016C001) and Natural Science Foundation of Guangdong Province (grant number 2016A030313600)

REFERENCES

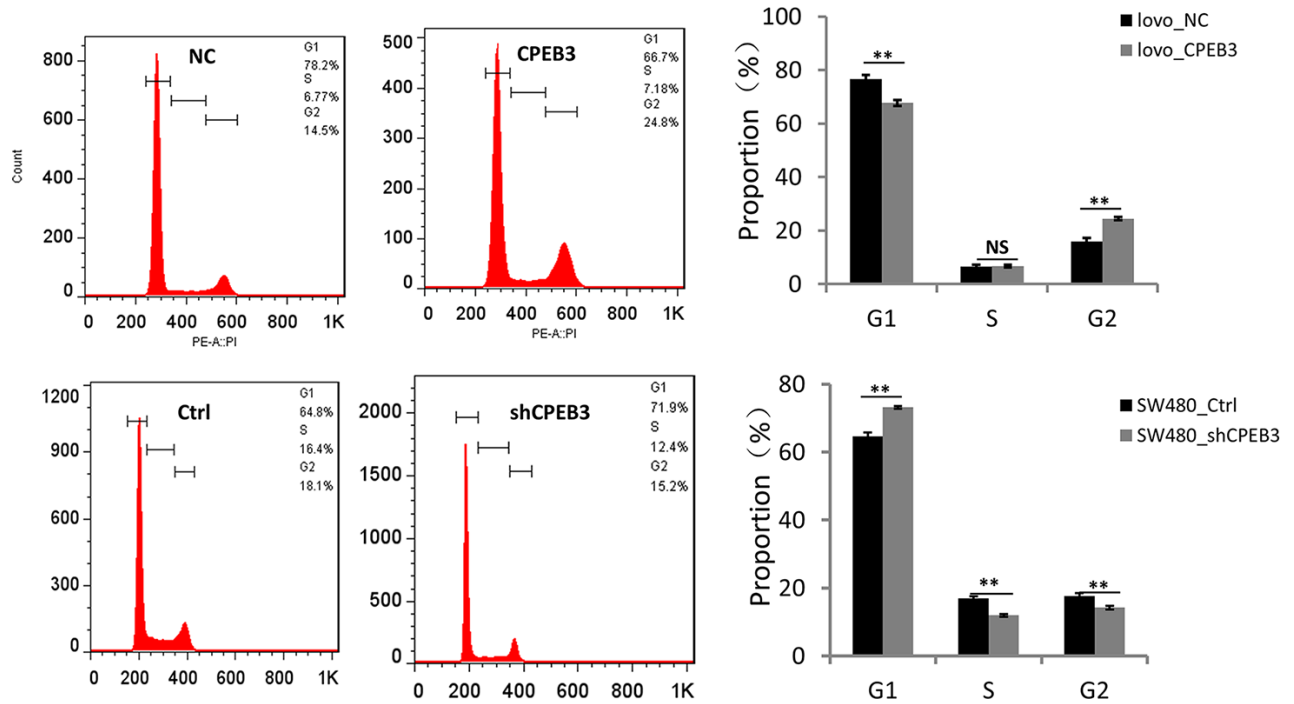
1. Shah MS, Fogelman DR, Raghav KP, Heymach JV, Tran HT, Jiang ZQ, Kopetz S, Daniel CR. Joint prognostic effect of obesity and chronic systemic inflammation in patients with metastatic colorectal cancer. *Cancer*. 2015; 121:2968–75. <https://doi.org/10.1002/cncr.29440> PMID:25975416
2. Hu JL, Wang W, Lan XL, Zeng ZC, Liang YS, Yan YR, Song FY, Wang FF, Zhu XH, Liao WJ, Liao WT, Ding YQ, Liang L. CAFs secreted exosomes promote metastasis and chemotherapy resistance by enhancing cell stemness and epithelial-mesenchymal transition in colorectal cancer. *Mol Cancer*. 2019; 18:91. <https://doi.org/10.1186/s12943-019-1019-x> PMID:31064356
3. Sakuma K, Sasaki E, Kimura K, Komori K, Shimizu Y, Yatabe Y, Aoki M. HNRNPLL, a newly identified colorectal cancer metastasis suppressor, modulates alternative splicing of CD44 during epithelial-mesenchymal transition. *Gut*. 2018; 67:1103–11. <https://doi.org/10.1136/gutjnl-2016-312927> PMID:28360095
4. Zanto TP, Hennigan K, Ostberg M, Clapp WC, Gazzaley A. Predictive knowledge of stimulus relevance does not influence top-down suppression of irrelevant information in older adults. *Cortex*. 2010; 46:564–74. <https://doi.org/10.1016/j.cortex.2009.08.003> PMID:19744649
5. Silvera D, Formenti SC, Schneider RJ. Translational control in cancer. *Nat Rev Cancer*. 2010; 10:254–66. <https://doi.org/10.1038/nrc2824> PMID:20332778
6. McGrew LL, Dworkin-Rastl E, Dworkin MB, Richter JD. poly(A) elongation during xenopus oocyte maturation is required for translational recruitment and is mediated by a short sequence element. *Genes Dev*. 1989; 3:803–15. <https://doi.org/10.1101/gad.3.6.803> PMID:2568313
7. Hake LE, Richter JD. CPEB is a specificity factor that mediates cytoplasmic polyadenylation during Xenopus oocyte maturation. *Cell*. 1994; 79:617–27. [https://doi.org/10.1016/0092-8674\(94\)90547-9](https://doi.org/10.1016/0092-8674(94)90547-9) PMID:7954828
8. Pheffe TJ, Buchert M, Stuart E, Flanagan DJ, Faux M, Afshar-Sterle S, Walker F, Zhang HH, Nowell CJ, Jorissen R, Tan CW, Hirokawa Y, Eissmann MF, et al. Partial inhibition of gp130-jak-Stat3 signaling prevents

- Wnt- β -catenin-mediated intestinal tumor growth and regeneration. *Sci Signal*. 2014; 7:ra92.
<https://doi.org/10.1126/scisignal.2005411>
PMID:[25270258](https://pubmed.ncbi.nlm.nih.gov/25270258/)
9. Groppo R, Richter JD. CPEB control of NF-kappaB nuclear localization and interleukin-6 production mediates cellular senescence. *Mol Cell Biol*. 2011; 31:2707–14.
<https://doi.org/10.1128/MCB.05133-11>
PMID:[21536657](https://pubmed.ncbi.nlm.nih.gov/21536657/)
 10. Costa-Mattioli M, Sonenberg N, Richter JD. Translational regulatory mechanisms in synaptic plasticity and memory storage. *Prog Mol Biol Transl Sci*. 2009; 90:293–311.
[https://doi.org/10.1016/S1877-1173\(09\)90008-4](https://doi.org/10.1016/S1877-1173(09)90008-4)
PMID:[20374745](https://pubmed.ncbi.nlm.nih.gov/20374745/)
 11. Hansen CN, Ketabi Z, Rosenstierne MW, Palle C, Boesen HC, Norrild B. Expression of CPEB, GAPDH and U6snRNA in cervical and ovarian tissue during cancer development. *APMIS*. 2009; 117:53–59.
<https://doi.org/10.1111/j.1600-0463.2008.00015.x>
PMID:[19161537](https://pubmed.ncbi.nlm.nih.gov/19161537/)
 12. Caldeira J, Simões-Correia J, Paredes J, Pinto MT, Sousa S, Corso G, Marrelli D, Roviello F, Pereira PS, Weil D, Oliveira C, Casares F, Seruca R. CPEB1, a novel gene silenced in gastric cancer: a drosophila approach. *Gut*. 2012; 61:1115–23.
<https://doi.org/10.1136/gutjnl-2011-300427>
PMID:[22052064](https://pubmed.ncbi.nlm.nih.gov/22052064/)
 13. D'Ambrogio A, Nagaoka K, Richter JD. Translational control of cell growth and malignancy by the CPEBs. *Nat Rev Cancer*. 2013; 13:283–90.
<https://doi.org/10.1038/nrc3485>
PMID:[23446545](https://pubmed.ncbi.nlm.nih.gov/23446545/)
 14. Sonenberg N, Hinnebusch AG. Regulation of translation initiation in eukaryotes: mechanisms and biological targets. *Cell*. 2009; 136:731–45.
<https://doi.org/10.1016/j.cell.2009.01.042>
PMID:[19239892](https://pubmed.ncbi.nlm.nih.gov/19239892/)
 15. Müller-McNicol M, Neugebauer KM. How cells get the message: dynamic assembly and function of mRNA-protein complexes. *Nat Rev Genet*. 2013; 14:275–87.
<https://doi.org/10.1038/nrg3434>
PMID:[23478349](https://pubmed.ncbi.nlm.nih.gov/23478349/)
 16. Mitchell SF, Parker R. Principles and properties of eukaryotic mRNPs. *Mol Cell*. 2014; 54:547–58.
<https://doi.org/10.1016/j.molcel.2014.04.033>
PMID:[24856220](https://pubmed.ncbi.nlm.nih.gov/24856220/)
 17. Shi R, Yu X, Wang Y, Sun J, Sun Q, Xia W, Dong G, Wang A, Gao Z, Jiang F, Xu L. Expression profile, clinical significance, and biological function of insulin-like growth factor 2 messenger RNA-binding proteins in non-small cell lung cancer. *Tumour Biol*. 2017; 39:1010428317695928.
<https://doi.org/10.1177/1010428317695928>
PMID:[28381175](https://pubmed.ncbi.nlm.nih.gov/28381175/)
 18. Rhodes DR, Kalyana-Sundaram S, Mahavisno V, Varambally R, Yu J, Briggs BB, Barrette TR, Anstet MJ, Kincead-Beal C, Kulkarni P, Varambally S, Ghosh D, Chinnaiyan AM. OncoPrint 3.0: genes, pathways, and networks in a collection of 18,000 cancer gene expression profiles. *Neoplasia*. 2007; 9:166–80.
<https://doi.org/10.1593/neo.07112> PMID:[17356713](https://pubmed.ncbi.nlm.nih.gov/17356713/)
 19. Burns DM, Richter JD. CPEB regulation of human cellular senescence, energy metabolism, and p53 mRNA translation. *Genes Dev*. 2008; 22:3449–60.
<https://doi.org/10.1101/gad.1697808> PMID:[19141477](https://pubmed.ncbi.nlm.nih.gov/19141477/)
 20. Hägele S, Kühn U, Böning M, Katschinski DM. Cytoplasmic polyadenylation-element-binding protein (CPEB)1 and 2 bind to the HIF-1alpha mRNA 3'-UTR and modulate HIF-1alpha protein expression. *Biochem J*. 2009; 417:235–46.
<https://doi.org/10.1042/BJ20081353> PMID:[18752464](https://pubmed.ncbi.nlm.nih.gov/18752464/)
 21. Ortiz-Zapater E, Pineda D, Martínez-Bosch N, Fernández-Miranda G, Iglesias M, Alameda F, Moreno M, Eliscovich C, Eyrales E, Real FX, Méndez R, Navarro P. Key contribution of CPEB4-mediated translational control to cancer progression. *Nat Med*. 2011; 18:83–90.
<https://doi.org/10.1038/nm.2540> PMID:[22138752](https://pubmed.ncbi.nlm.nih.gov/22138752/)
 22. Fernández-Miranda G, Méndez R. The CPEB-family of proteins, translational control in senescence and cancer. *Ageing Res Rev*. 2012; 11:460–72.
<https://doi.org/10.1016/j.arr.2012.03.004>
PMID:[22542725](https://pubmed.ncbi.nlm.nih.gov/22542725/)
 23. Lin H, Guo Q, Lu S, Chen J, Li X, Gong M, Tang L, Wen J. LncRNA SUMO1P3 promotes proliferation and inhibits apoptosis in colorectal cancer by epigenetically silencing CPEB3. *Biochem Biophys Res Commun*. 2019; 511:239–45.
<https://doi.org/10.1016/j.bbrc.2019.02.006>
PMID:[30799082](https://pubmed.ncbi.nlm.nih.gov/30799082/)
 24. Liu F, Zhang G, Lv S, Wen X, Liu P. miRNA-301b-3p accelerates migration and invasion of high-grade ovarian serous tumor via targeting CPEB3/EGFR axis. *J Cell Biochem*. 2019; 120:12618–27.
<https://doi.org/10.1002/jcb.28528> PMID:[30834603](https://pubmed.ncbi.nlm.nih.gov/30834603/)
 25. Zou CD, Zhao WM, Wang XN, Li Q, Huang H, Cheng WP, Jin JF, Zhang H, Wu MJ, Tai S, Zou CX, Gao X. MicroRNA-107: a novel promoter of tumor progression that targets the CPEB3/EGFR axis in human hepatocellular carcinoma. *Oncotarget*. 2016; 7:266–78.
<https://doi.org/10.18632/oncotarget.5689>
PMID:[26497556](https://pubmed.ncbi.nlm.nih.gov/26497556/)

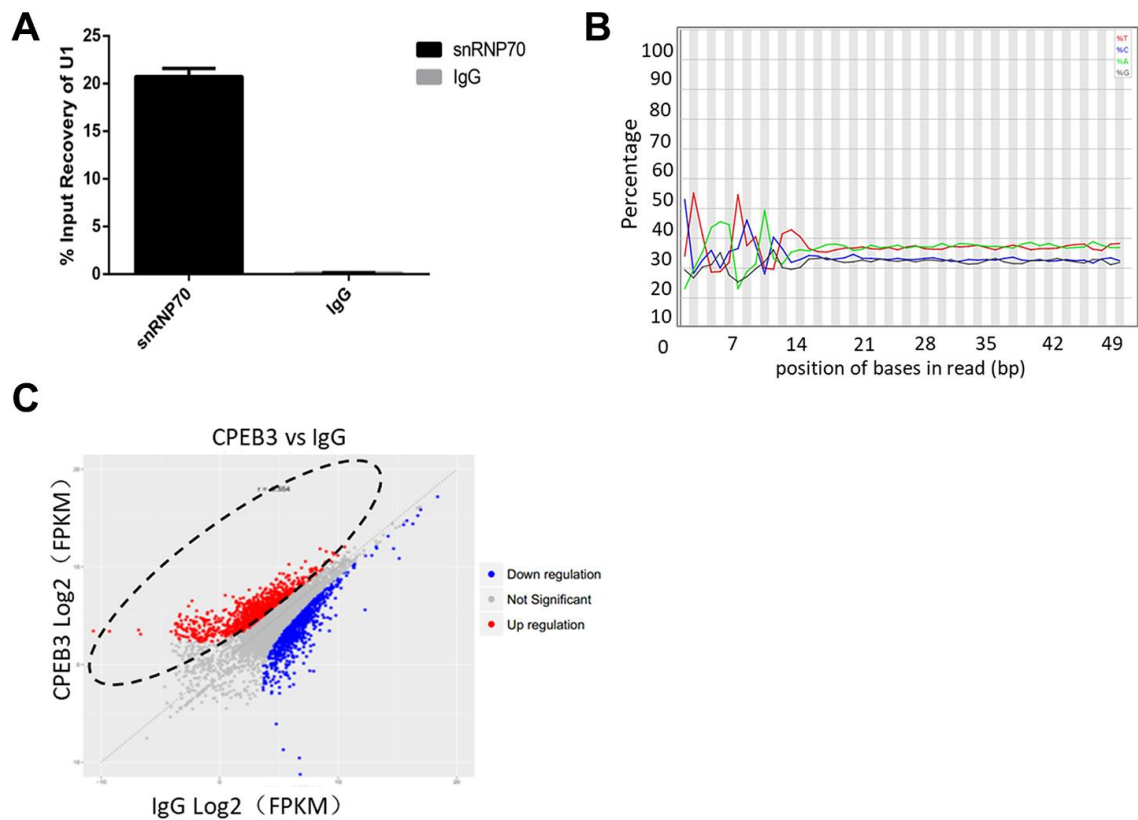
26. Wang X, Zbou C, Qiu G, Fan J, Tang H, Peng Z. Screening of new tumor suppressor genes in sporadic colorectal cancer patients. *Hepatogastroenterology*. 2008; 55:2039–44. PMID:[19260473](https://pubmed.ncbi.nlm.nih.gov/19260473/)
27. Mann M. Functional and quantitative proteomics using SILAC. *Nat Rev Mol Cell Biol*. 2006; 7:952–8. <https://doi.org/10.1038/nrm2067> PMID:[17139335](https://pubmed.ncbi.nlm.nih.gov/17139335/)
28. Wang Z, Gerstein M, Snyder M. RNA-Seq: a revolutionary tool for transcriptomics. *Nat Rev Genet*. 2009; 10:57–63. <https://doi.org/10.1038/nrg2484> PMID:[19015660](https://pubmed.ncbi.nlm.nih.gov/19015660/)
29. Ascano M, Hafner M, Cekan P, Gerstberger S, Tuschl T. Identification of RNA-protein interaction networks using PAR-CLIP. *Wiley Interdiscip Rev RNA*. 2012; 3:159–77. <https://doi.org/10.1002/wrna.1103> PMID:[22213601](https://pubmed.ncbi.nlm.nih.gov/22213601/)
30. König J, Zarnack K, Luscombe NM, Ule J. Protein-RNA interactions: new genomic technologies and perspectives. *Nat Rev Genet*. 2012; 13:77–83. <https://doi.org/10.1038/nrg3141> PMID:[22251872](https://pubmed.ncbi.nlm.nih.gov/22251872/)
31. Stoltenburg R, Reinemann C, Strehlitz B. SELEX—a (r)evolutionary method to generate high-affinity nucleic acid ligands. *Biomol Eng*. 2007; 24:381–403. <https://doi.org/10.1016/j.bioeng.2007.06.001> PMID:[17627883](https://pubmed.ncbi.nlm.nih.gov/17627883/)
32. Ray D, Kazan H, Cook KB, Weirauch MT, Najafabadi HS, Li X, Gueroussov S, Albu M, Zheng H, Yang A, Na H, Irimia M, Matzat LH, et al. A compendium of RNA-binding motifs for decoding gene regulation. *Nature*. 2013; 499:172–77. <https://doi.org/10.1038/nature12311> PMID:[23846655](https://pubmed.ncbi.nlm.nih.gov/23846655/)
33. Huang YS, Kan MC, Lin CL, Richter JD. CPEB3 and CPEB4 in neurons: analysis of RNA-binding specificity and translational control of AMPA receptor GluR2 mRNA. *EMBO J*. 2006; 25:4865–76. <https://doi.org/10.1038/sj.emboj.7601322> PMID:[17024188](https://pubmed.ncbi.nlm.nih.gov/17024188/)
34. Ford L, Ling E, Kandel ER, Fioriti L. CPEB3 inhibits translation of mRNA targets by localizing them to P bodies. *Proc Natl Acad Sci USA*. 2019; 116:18078–87. <https://doi.org/10.1073/pnas.1815275116> PMID:[31416913](https://pubmed.ncbi.nlm.nih.gov/31416913/)
35. Pavlopoulos E, Trifilieff P, Chevaleyre V, Fioriti L, Zairis S, Pagano A, Malleret G, Kandel ER. Neuralized1 activates CPEB3: a function for nonproteolytic ubiquitin in synaptic plasticity and memory storage. *Cell*. 2011; 147:1369–83. <https://doi.org/10.1016/j.cell.2011.09.056> PMID:[22153079](https://pubmed.ncbi.nlm.nih.gov/22153079/)
36. O’Shea JJ, Gadina M, Schreiber RD. Cytokine signaling in 2002: new surprises in the jak/stat pathway. *Cell*. 2002; 109:S121–31. [https://doi.org/10.1016/s0092-8674\(02\)00701-8](https://doi.org/10.1016/s0092-8674(02)00701-8) PMID:[11983158](https://pubmed.ncbi.nlm.nih.gov/11983158/)
37. Xue X, Jungles K, Onder G, Samhoun J, Györfy B, Hardiman KM. HIF-3 α 1 promotes colorectal tumor cell growth by activation of JAK-STAT3 signaling. *Oncotarget*. 2016; 7:11567–79. <https://doi.org/10.18632/oncotarget.7272> PMID:[26871465](https://pubmed.ncbi.nlm.nih.gov/26871465/)
38. Slattery ML, Lundgreen A, Kadlubar SA, Bondurant KL, Wolff RK. JAK/STAT/SOCS-signaling pathway and colon and rectal cancer. *Mol Carcinog*. 2013; 52:155–66. <https://doi.org/10.1002/mc.21841> PMID:[22121102](https://pubmed.ncbi.nlm.nih.gov/22121102/)
39. Stuart E, Buchert M, Putoczki T, Thiem S, Farid R, Elzer J, Huszar D, Waring PM, Pheese TJ, Ernst M. Therapeutic inhibition of Jak activity inhibits progression of gastrointestinal tumors in mice. *Mol Cancer Ther*. 2014; 13:468–74. <https://doi.org/10.1158/1535-7163.MCT-13-0583-T> PMID:[24398427](https://pubmed.ncbi.nlm.nih.gov/24398427/)
40. Edge SB, Compton CC. The American Joint Committee on Cancer: the 7th edition of the AJCC cancer staging manual and the future of TNM. *Ann Surg Oncol*. 2010; 17:1471–4. <https://doi.org/10.1245/s10434-010-0985-4> PMID:[20180029](https://pubmed.ncbi.nlm.nih.gov/20180029/)
41. Li T, Lai Q, Wang S, Cai J, Xiao Z, Deng D, He L, Jiao H, Ye Y, Liang L, Ding Y, Liao W. MicroRNA-224 sustains Wnt/ β -catenin signaling and promotes aggressive phenotype of colorectal cancer. *J Exp Clin Cancer Res*. 2016; 35:21. <https://doi.org/10.1186/s13046-016-0287-1> PMID:[26822534](https://pubmed.ncbi.nlm.nih.gov/26822534/)

SUPPLEMENTARY MATERIALS

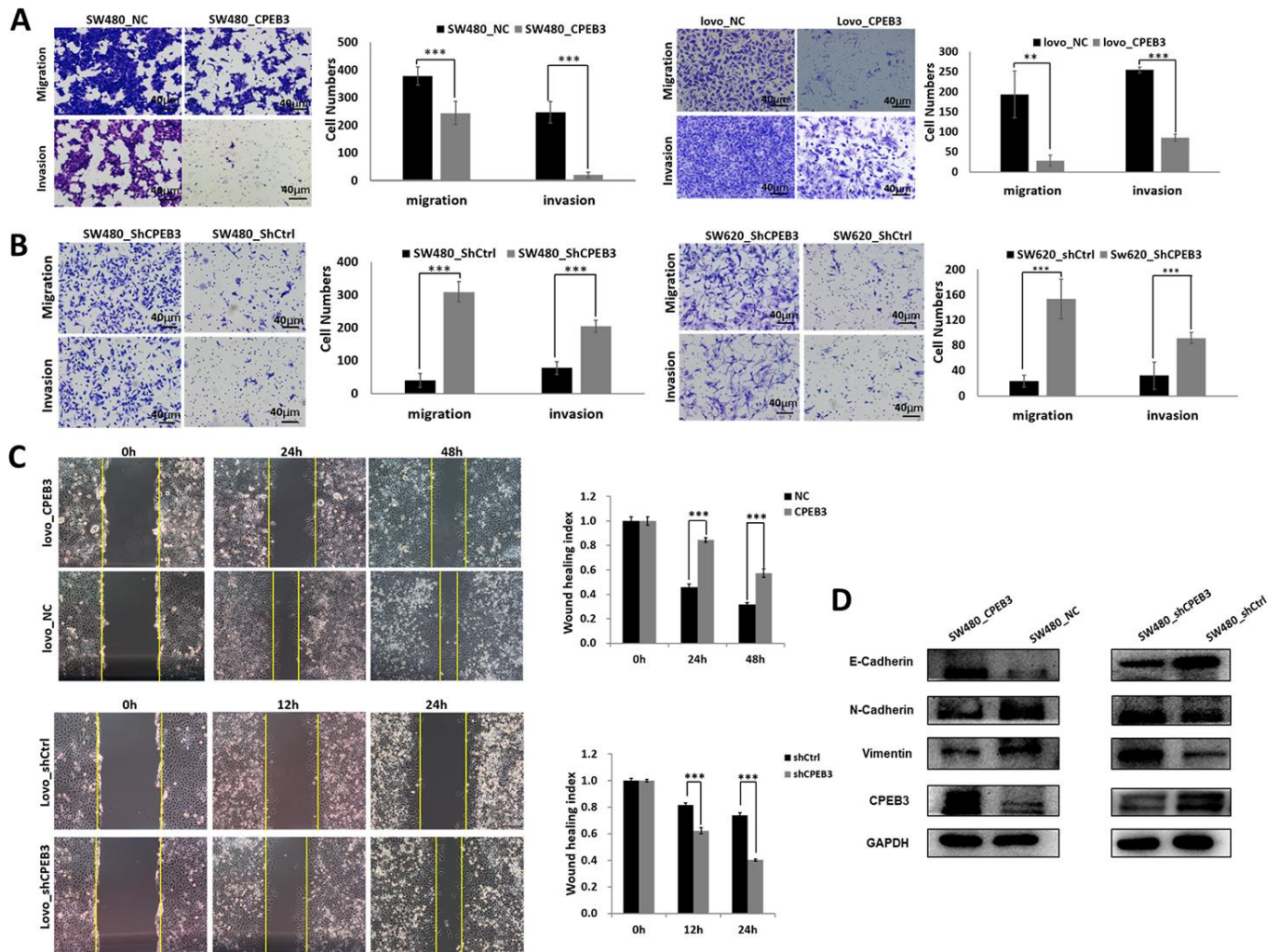
Supplementary Figures



Supplementary Figure 1. Up-regulation of CPEB3 in LoVo cells results in inhibition of cell cycle progression in G2/M phase as detected by flow cytometry.



Supplementary Figure 2. High-throughput sequencing analysis of mRNAs bound to CPEB3 in SW480 cells. (A) RNA extracts pre-incubated with IgG and SnRNP70 were used as negative and positive controls, respectively. (B) Sequence content across all in CPEB3 group. X axis represents the position of bases in reads (bp) and Y-axis represents the percentage of the bases in each position. (C) Scatter-plot of the read-densities for the mRNAs in the CPEB3 and the IgG group.



Supplementary Figure 3. CPEB3 inhibits metastasis of human colorectal cancer cells. (A) CPEB3 overexpression significantly suppressed migration and invasion capacity of SW480 and SW620 cells by transwell assays (original magnification, $\times 400$). (B) CPEB3 knockdown promoted migration and invasion ability of SW480 and SW620 cells (original magnification, $\times 400$). (C) *In vitro* wound healing assays showed that CPEB3 suppressed the migration ability of LoVo cells (original magnification, $\times 100$). (** $P < 0.01$, *** $P < 0.001$). (D) Metastasis-related markers were further confirmed by Western blotting.

Supplementary Tables

Supplementary Table 1. The upstream and downstream sequence of primers in Real time PCR.

Primer	Primer sequences	
	Forward	Reverse
CPEB3	5-CCAACCTGAGTCCAGCGTAT-3	5-AGGAGCGGTGATTCCATCT-3
MYC	5-GCCCCTCAACGTTAGCTTCA-3	5-AGTTCTCCTCCTCGTCGCAG-3
TGFB1	5-GATGTCACCGGAGTTGTGC-3	5-GAACCCGTTGATGTCCACTT-3
JAK1	5-ACTGAGGTGAACCTGGAGGC-3	5-ACTGCCAGCCGGAGG-3
SMAD2	5-GGAATTTGCTGCTCTTCTGG-3	5-CTGCCTTCGGTATTCTGCTC-3
STAT3	5-GAGCTGGCTGACTGGAAGAG-3	5-TGTTGACGGGTCTGAAGTTG-3
ATG3	5-TGCTATAAGCGGTGCAAACA-3	5-CGGCTTCCGTTATTCCTGTA-3
STAT6	5-CACTGGAAGCAGGAAGAACTCA-3	5-AGACACTTGGCCAGCCTCA-3
PIK3C3	5-TCATGGACAAGCTGTTACGG-3	5-TCAGCCACAGGAAGTACTG-3
RB1	5-CACATTCCTCGAAGCCCTTA-3	5-GTTGGTGTTGGCAGACCTTC-3
E2F3	5-TGCAGTCTGTCTGAGGATGG-3	5-GGTGCAGCTTTGGATCAGTT-3
GAPDH	5-GAAGGTGAAGGTCGGAGT-3	5-GAAGATGGTGATGGGATTTTC-3

Supplementary Table 2. Read count for sample (CPEB3) and control (IgG) in total, and in ribosomal RNAs (rRNAs).

Sample ID	Raw reads	Clean reads	Clean ratio*	rRNA trimed	rRNA ratio**
CPEB3	23063600	22537635	97.72%	8656239	61.59%
IgG	21692675	18560899	85.56%	12404800	33.17%

*: Clean ratio=(clean reads/Raw reads)%; **:rRNA ratio=[(Clean reads-rRNA trimed)/Clean reads]

Supplementary Table 3. Percentage of mapped reads in CPEB3 and control IgG group.

Sample ID	All reads	Mapped reads	Mapped ratio*
CPEB3	8656239	4759549	54.89%
IgG	12404800	2300735	18.55%

*: Mapped ratio= (Mapped reads/All reads)%

Extracellular vesicle derived miR-544 downregulates expression of tumor suppressor promyelocytic leukemia zinc finger resulting in increased peritoneal metastasis in gastric cancer

Wencheng Kong¹, Xinchun Liu¹, Guang Yin¹, Sixin Zheng¹, Akao Zhu¹, Panpan Yu¹, Yuqiang Shan¹, Rongchao Ying¹, Jian Zhang¹

¹Department of General Surgery, Affiliated Hangzhou First People's Hospital, Zhejiang University School of Medicine, Hangzhou 310006, Zhejiang Province, P.R. China

Correspondence to: Jian Zhang; email: zhangjianpw@163.com, <https://orcid.org/0000-0001-8246-8069>

Keywords: peritoneal metastasis, gastric cancer, PLZF, miR-544, extracellular vesicle

Received: March 11, 2020

Accepted: August 17, 2020

Published: November 18, 2020

Copyright: © 2020 Kong et al. This is an open access article distributed under the terms of the [Creative Commons Attribution License](https://creativecommons.org/licenses/by/3.0/) (CC BY 3.0), which permits unrestricted use, distribution, and reproduction in any medium, provided the original author and source are credited.

ABSTRACT

Peritoneal metastasis (PM) is the main cause of poor prognosis in patients with advanced gastric cancer (GC). Increasing evidence has suggested that cancer-associated EVs in body fluids may assist in the diagnosis and treatment of GC. Here, we investigated the role of GC-derived EVs in PM development. Our results demonstrate that expression of the tumor suppressor promyelocytic leukemia zinc finger (PLZF) is decreased in GC tissues and PM lesions from GC patients. PLZF suppression promoted migration and invasion of peritoneal mesothelial HMrSV5 cells, while PLZF overexpression suppressed HMrSV5 cell migration and invasion. Microarray analysis revealed significantly upregulated expression of several miRNAs in EVs isolated from GC patients with PM, including miR-544. The increased miR-544 expression was confirmed in GC tissues and PM-derived EVs. Transfection with miR-544 reduced PLZF expression in HMrSV5 cells, while miR-544 inhibition increased PLZF expression. Incubation of GC cells with peritoneal mesothelial HMrSV5 cells showed that miR-544 could be transferred from GC-derived EVs to peritoneal cells, where it suppressed the PLZF expression. These findings indicate that EV-mediated transfer of miR-544 decreases the PLZF expression in PM lesions, which suggests miR-544 could potentially serve as a diagnostic biomarker and therapeutic target for treatment of GC patients.

INTRODUCTION

Gastric cancer (GC) is the fourth most common cancer in the world, and the second leading cause of cancer-related deaths [1]. Although great progress has been made in chemotherapy, radiotherapy, and surgical techniques, the 5-year overall survival rates are still less than 25% [2–5]. Peritoneal metastases (PM) are the main cause of poor prognosis in advanced GC [6]; yet, there are no effective treatments for PM [7]. Hence, it is important to identify the mechanisms responsible for the PM development.

Extracellular vesicles (EVs), including exosomes and microvesicles, have 50 nm–1 µm in diameter, classic dish or cup morphology, and a double lipid layer [1]. EVs contain proteins, lipids, mRNA, DNA, and miRNA that can regulate gene expression [8]. EVs have been detected in body fluids including blood and urine, and may serve as potential biomarkers for various diseases, including cancer [1, 9]. For instance, exosomal miR-21-5p induces mesothelial-to-mesenchymal transition and promotes cancer peritoneal dissemination by targeting SMAD7 [10]. In addition, the expression of TRIM3 is decreased in serum EVs of GC patients [11]. Identification of

cancer-associated EVs in body fluids may assist in the diagnosis and treatment of GC.

Promyelocytic leukemia zinc finger (PLZF), also known as BTB-containing protein 16 (ZBTB16), is a transcription factor that functions as a tumor suppressor in carcinogenesis [12]. The loss of PLZF expression has been observed in melanoma, breast cancer, colorectal cancer, and prostate cancer [13–16]. A recent study has shown that the expression of PLZF is decreased in gastric cancer, suggesting that PLZF may serve as a potential therapeutic target in GC therapy [17]. However, the role of PLZF in peritoneal metastases in GC remains largely unknown.

In the present study, we investigated whether GC-derived EVs promote PM via regulating the expression of PLZF. For the first time, we showed novel data that EV-derived miR-544 mediated the PM in GC patients via suppressing the expression of PLZF in peritoneal mesothelial cells.

RESULTS

PLZF expression is decreased in GC tissues and PM lesions

We analyzed the expression of PLZF in GC patients. Compared with control tissues, PLZF mRNA and protein levels were significantly reduced in GC tissues (Figure 1A, 1B). However, no significant differences of PLZF mRNA and protein levels were found in GC tissues between GC patients with PM and without PM (Figure 1A, 1B). Furthermore, we compared the PLZF levels in PM lesions and normal peritoneal tissues. Remarkably, decreased mRNA and protein levels of PLZF were found in PM lesions compared to normal peritoneal tissues (Figure 1C, 1D), suggesting that the changes of PLZF in PM lesions of GC patients may be regulated by other mediators, such as EVs in the peritoneal fluid.

Peritoneal fluid in GC patients contains EVs

To explore the mechanism by which the PLZF expression is decreased in GC patients with PM, we first examined whether peritoneal fluid of GC patients with and without PM contains EVs. As shown in Figure 2A, many EVs were identified in the peritoneal fluid. Western blot analysis demonstrated that TSG101, CD63 and CD9, two commonly used EV markers, were present in EV fractions isolated from peritoneal fluids (Figure 2B), indicating that the peritoneal fluid contains EVs.

GC-associated EVs decrease PLZF expression in peritoneal mesothelial cells

We then investigated whether the GC-associated EVs might affect invasion and migration ability of human peritoneal mesothelial HMrSV5 cells. HMrSV5 cells were co-cultured with EVs isolated from peritoneal fluid from GC patients with and without PM. CCK-8 assay showed that EVs from GC patients with PM significantly increased the viability in HMrSV5 cells compared to that of EVs from GC patients without PM (Figure 3A). As shown in Figure 3B, HMrSV5 cells incubated with EVs isolated from peritoneal fluid from GC patients with PM had an increased invasive ability compared with cells incubated with EVs from patients without PM. In addition, HMrSV5 cells exhibited an increased migration when pretreated with EVs from GC patients with PM compared to those without PM (Figure 3C). Analysis of PLZF protein levels by immunofluorescence and western blotting showed that pretreatment of HMrSV5 cells with EVs from patients with PM reduced the PLZF levels compared to preincubation with EVs from patients without PM (Figure 3D, 3E). These findings suggest that the PM-derived EVs reduce the PLZF expression in peritoneal mesothelial cells, and promote GC peritoneal metastasis.

miR-544 suppresses PLZF in GC-derived EVs of PM patients

Having found that the GC-derived EVs decrease the PLZF expression in peritoneal mesothelial HMrSV5 cells, we next analyzed the EV PLZF levels in GC patients with and without PM. However, no significant differences were found in PLZF mRNA and protein levels in the EVs isolated from GC patients with and without PM (Figure 4A, 4B). Interestingly, microarray analysis of exosomal miRNAs of GC patients identified five miRNAs that may target PLZF, including miR-342, miR-223-3p, miR-19a-5p, miR-21-5p, and miR-544-5p; these miRNAs were upregulated in patients with PM. RT-PCR confirmed the increased expression of miR-223-3p, miR-21-5p, and miR-544-5p in EVs isolated from GC patients with PM compared to patients without PM (Figure 4C).

Since a previous report has indicated that PLZF is a target gene of miR-544 [18], we analyzed the PLZF regulation by miR-544 in HMrSV5 cells. RT-PCR analysis showed that transfection with miR-544 mimics significantly increased the level of miR-544, but transfection with miR-544 inhibitors significantly decreased the level of miR-544 (Figure 4D). Importantly, overexpression of miR-544 significantly suppressed the PLZF protein levels, while miR-544

inhibition increased the PLZF expression in HMrSV5 cells (Figure 4E). Together, these data indicate that PLZF is a target gene of miR-544 in peritoneal mesothelial cells, and in GC-derived EVs of PM patients.

miR-544 is transferred from GS-derived EVs to peritoneal cells

Since the GC-derived EVs could reduce the PLZF expression in HMrSV5 cells, we investigated whether

the GC-derived EVs could transfer miR-544 into peritoneum. We first evaluated the miR-544 expression in GC tissues and EVs from GS patients. Compared with adjacent normal tissues, the miR-544 levels were significantly increased in GC tissues (Figure 5A). Moreover, the miR-544 levels were significantly increased in the EVs isolated from GC patients with PM compared to patients without PM (Figure 5B).

Based on the above findings, we further explored the expression of miR-544 in GC cell lines. Compared to

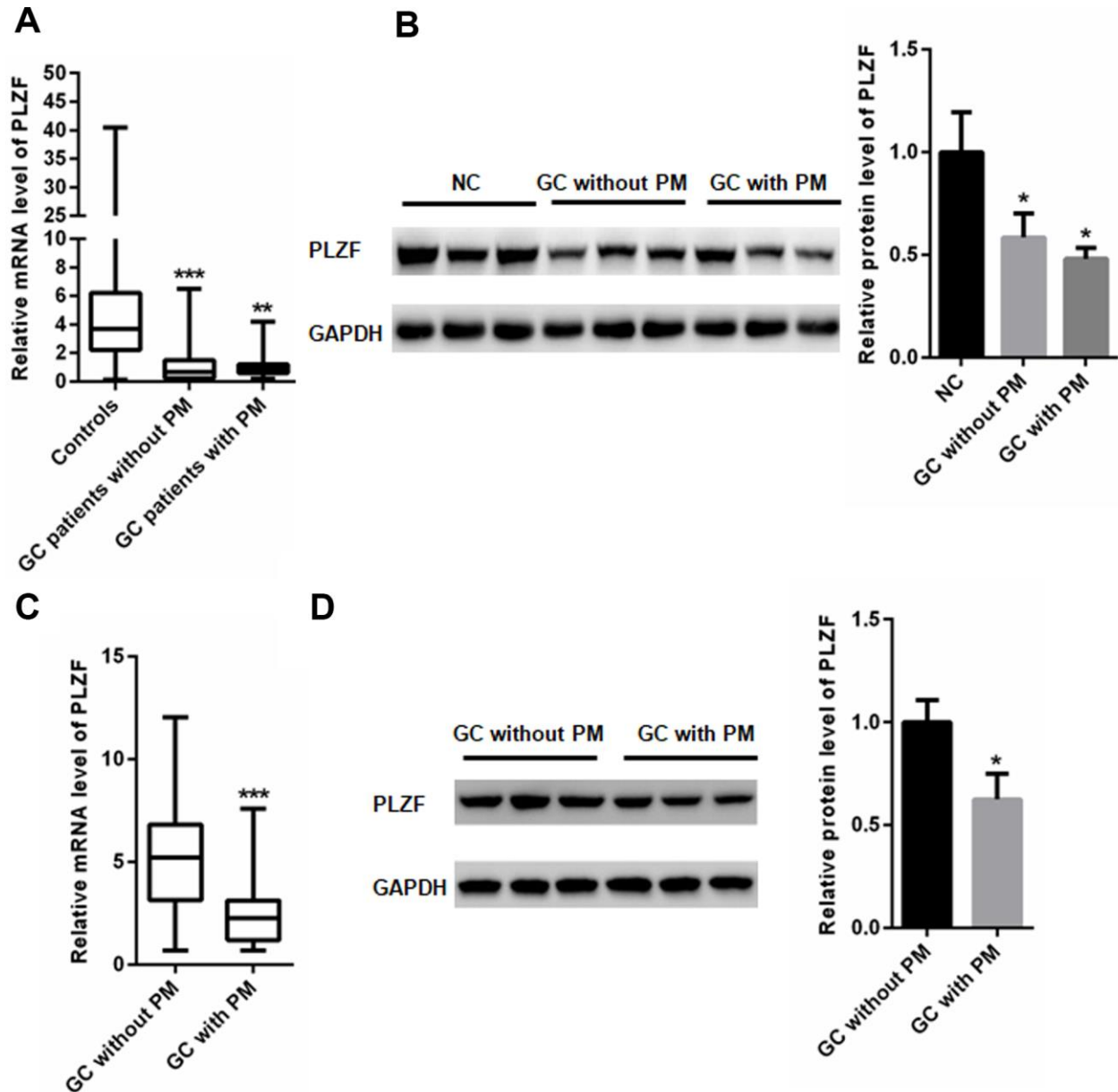


Figure 1. PLZF mRNA and protein levels in GC patients. (A) mRNA and (B) protein expression of PLZF in GC, and control adjacent tissues. (C) mRNA and (D) protein expression of PLZF in PM lesions and control tissues of GC patients. (n=68 for GC patients without PM, n=65 for GC patients with PM, one way ANOVA for A, B, two-tailed unpaired student's t-tests for C, D).

normal human gastric epithelial cell line GES-1, the miR-544 expression was significantly increased in gastric cancer cell lines, including MGC803, BGC823, MKN45, HGC27, and SGC7901 (Figure 5C). In addition, EVs isolated from the GC cell lines MGC803, BGC823, MKN45, HGC27, and SGC7901, demonstrated an increased miR-544 expression compared to GES-1 cells (Figure 5D). Since the EVs from MGC803EV cells exhibited the highest miR-544 levels (Figure 5D), MGC803 cells were used for further experiments.

EVs isolated from the gastric cancer MGC-803 cells and control gastric epithelial GES-1 cells were incubated with HMrSV5 cell culture supernatants. As shown in Figure 5E, PKH67 (green)-labeled EVs could be observed in HMrSV5 cells. Importantly, RT-PCR analysis demonstrated that the level of miR-544 increased in HMrSV5 cells co-cultured with MGC-803-derived EVs compared with GES-1-derived EVs. In addition, the PLZF levels were reduced in HMrSV5 cells co-cultured with MGC-803-derived EVs compared with GES-1-derived EVs (Figure 5F). These results indicated that miR-544 might be transferred from the GC-derived EVs to peritoneal cells, where it suppresses the PLZF expression.

Inhibition of miR-544 in MGC803 cells increases PLZF expression in HMrSV5 cells

To examine the possibility that the upregulation of miR-544 in HMrSV5 cells was directly due to the miR-544 transfer from MGC803 cells, we transfected MGC803 cells with a lentivirus construct that inhibits the miR-544 expression. RT-PCR analysis confirmed that the

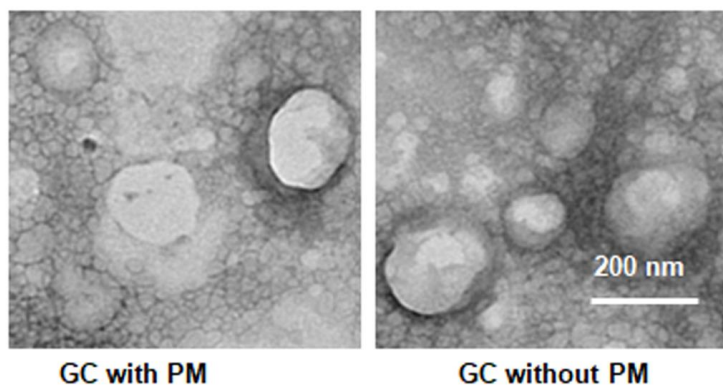
level of miR-544 was significantly decreased in MGC803 cells transfected with the Len-miR-544-inhibitor compared to the control vector Len-miR-544-NC (Figure 6A). Importantly, the PLZF expression was significantly increased in MGC803 cells transfected with Len-miR-544-inhibitor compared to Len-miR-544-NC (Figure 6B). In addition, the exosomal miR-544 derived from MGC803 cells transfected with Len-miR-544-inhibitor was significantly decreased compared to cells transfected with Len-miR-544-NC (Figure 6C). However, no changes in PLZF mRNA were found between the EVs derived from MGC803 cells transfected with Len-miR-544-inhibitor and Len-miR-544-NC (Figure 6D).

Next, HMrSV5 cells were co-cultured with EVs derived from MGC803 cells transfected with Len-miR-544-NC or Len-miR-544-inhibitor. As shown in Figure 6E, the miR-544 levels in the Len-miR-544-inhibitor group were distinctly decreased compared to the Len-miR-544-NC group. Moreover, the PLZF expression was increased in EVs isolated from MGC803 cells transfected with Len-miR-544-inhibitor compared to cells transfected with Len-miR-544-NC (Figure 6F). These results demonstrated that the exosomal miR-544 could be transferred from MGC803 cells to HMrSV5 cells.

miR-544 induces malignant phenotype of peritoneum cells by downregulating PLZF

The above findings demonstrated that miR-544 could be transferred from GC cells to peritoneum cells, but whether the transfer resulted in a malignant phenotype of HMrSV5 peritoneum cells has not been revealed. To

A



B

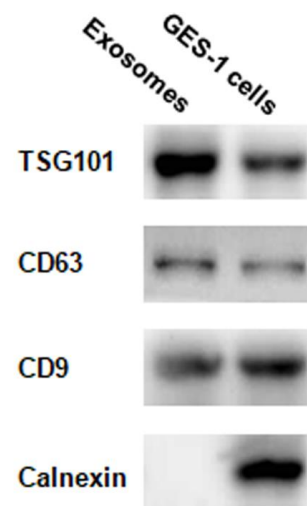


Figure 2. EVs identification in peritoneal fluid. (A) Transmission electron microscopy demonstrating many EVs <200 nm in diameter. (B) Western blotting illustrating the presence of TSG101 and CD63, two common EV markers, in EV fraction isolated from peritoneal fluid.

address this, we introduced a lentivirus vector overexpressing PLZF into HMrSV5 cells (Figure 7A). As shown in Figure 7B, PLZF overexpression significantly reduced migration and invasion of

HMrSV5 cells, indicating that PLZF functions as a tumor suppressor in peritoneum cells. In contrast, PLZF suppression by PLZF specific siRNA (Figure 7C), significantly increased HMrSV5 cell migration and

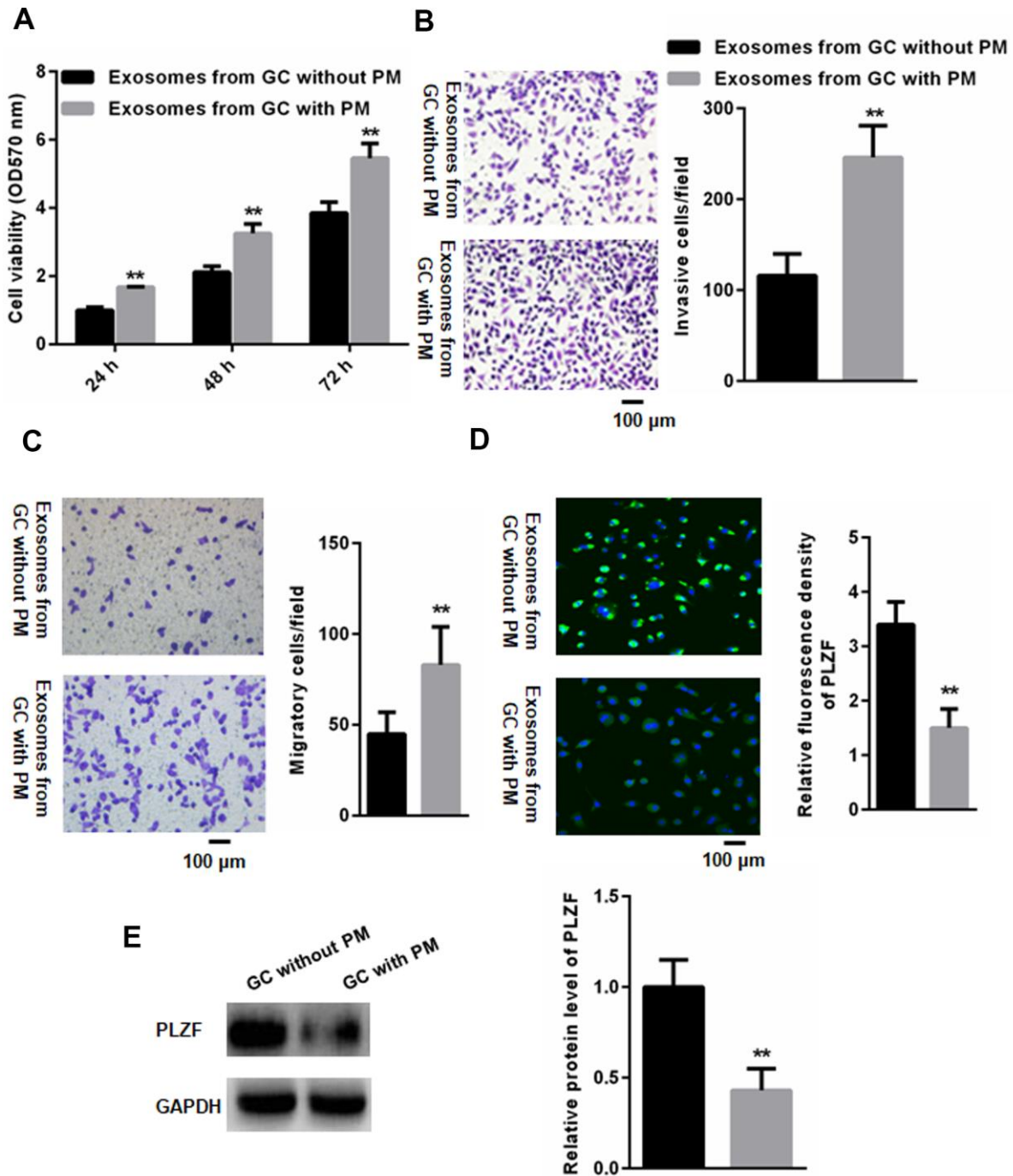


Figure 3. PM-derived EVs reduce PLZF expression in HMrSV5 cells and promote their invasive ability. (A) CCK-8 assay indicated that EVs isolated from GC patients with PM significantly increased the viability of HMrSV5 cells compared to that of without PM. (n=3, one way ANOVA) (B) Trans-well assay illustrating invasion of HMrSV5 cells incubated with EVs isolated from peritoneal fluid of GC patients with and without PM. (C) For migration assays, more adhesive HMrSV5 cells were found in those pretreated by EVs isolated from peritoneal fluid in GC patients with PM compared those without PM. (D) Immunofluorescence and (E) western blotting showing that pretreatment with EVs isolated from patients with PM reduces the PLZF expression in HMrSV5 cells. (n=3, Student's t-test for B, C, D, E).

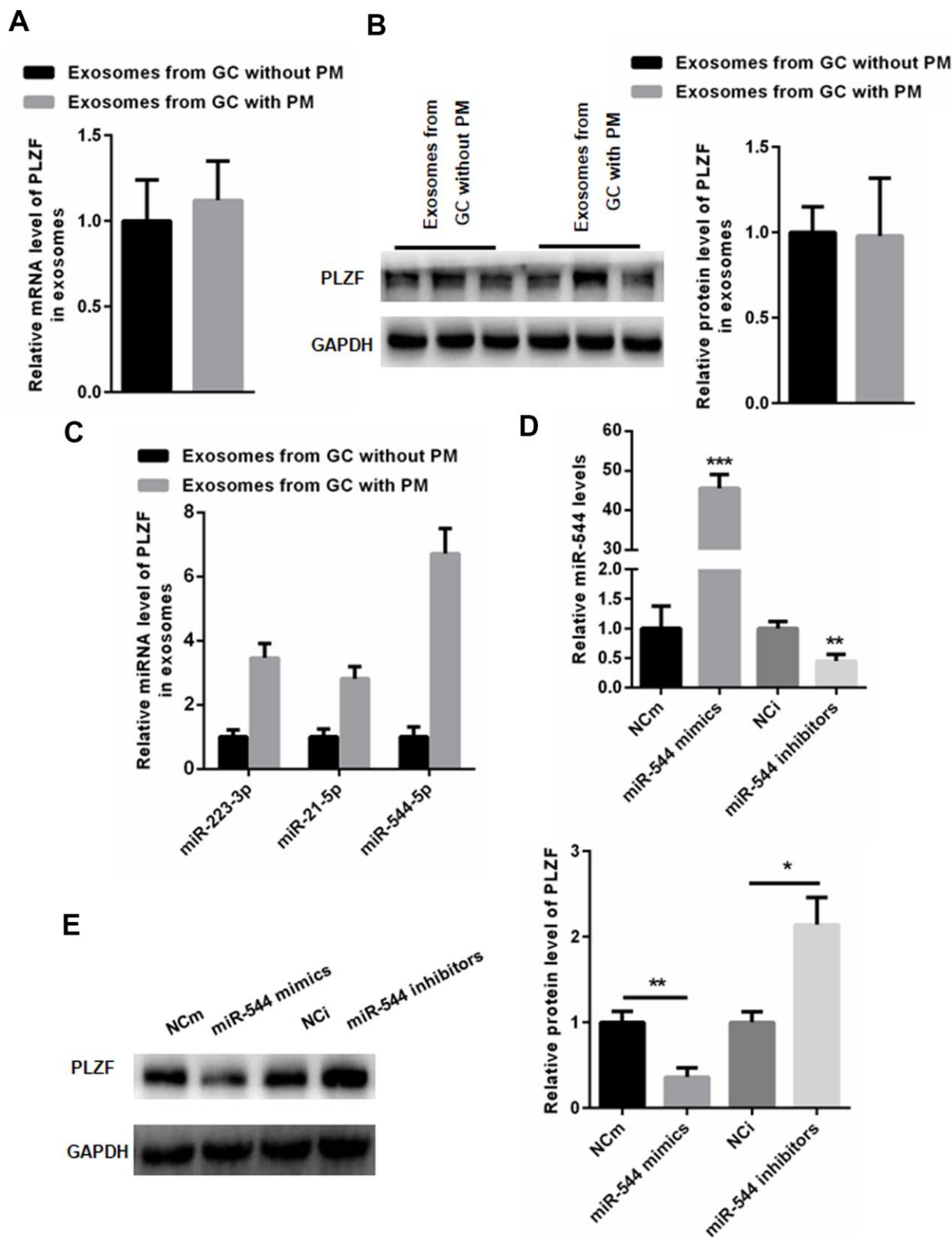


Figure 4. miR-544 from GC-derived EVs of PM patients reduces PLZF expression in HMrSV5 cells. (A) mRNA and (B) protein expression of PLZF in EVs isolated from GC patients with and without PM. (n=3, Student's t-test for A, B) (C) RT-PCR demonstrating increased levels of miR-223-3p, miR-21-5p, and miR-544-5p in EVs isolated from GC patients with PM. (D) RT-PCR of miR-544 in HMrSV5 cells transfected with miR-544 mimics or miR-544 inhibitors. (E) Western blotting of PLZF in HMrSV5 cells transfected with miR-544 mimics or miR-544 inhibitors. (n=3, one way ANOVA for C, D, E).

invasion (Figure 7D). Moreover, when PLZF was silenced, even transfection with Len-miR-544-inhibitor could not effectively reverse the increased HMrSV5 cell migration and invasion (Figure 7C, 7D). These data demonstrate that miR-544 induces the malignant phenotype of peritoneum cells via targeting PLZF.

DISCUSSION

Management of peritoneal metastasis (PM) in gastric cancer is still a great challenge in clinic. Without any treatment, the median overall survival is only 3-6 months in GC patients with PM [19]. PLZF is a

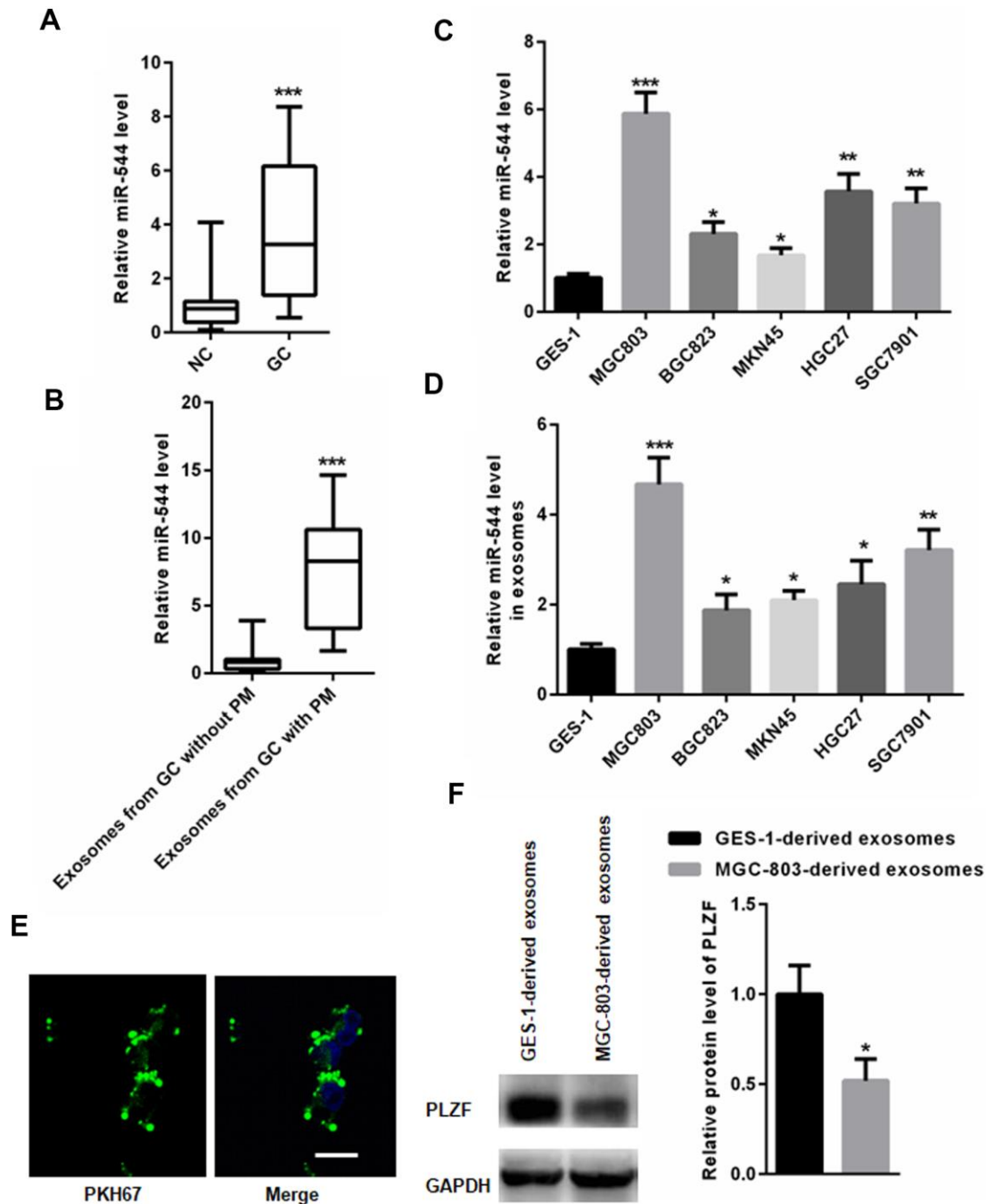


Figure 5. miR-544 is transferred from GS-derived EVs to peritoneal cells. (A) RT-PCR of miR-544 in GC tissues. (B) RT-PCR of miR-544 in EVs isolated from GC patients with and without PM. (n=68 for GC patients without PM, n=65 for GC patients with PM, two-tailed unpaired student's t-tests) (C) RT-PCR of miR-544 in GC cell lines MGC803, BGC823, MKN45, HGC27, and SGC7901. (D) RT-PCR of miR-544 in EVs isolated from GC and GES-1 cells. (E) PKH67-labeled EVs in HMrSV5 cells (bar represents 10 μ m). (F) PLZF expression in HMrSV5 cells co-cultured with MGC-803-and GES-1-derived EVs. (n=3, one way ANOVA for C, D, E and F).

transcription factor that functions as a tumor suppressor in various cancers [12, 20]. A previous study has shown that a low PLZF expression in GC tissues is associated with a poor prognosis in GC patients [17], but the role of PLZF in the process of PM in GC patients has not been explored.

We have found that the PLZF expression is decreased not only in GC tissues, but also in PM lesions of GC patients. In addition, silencing of PLZF promotes migration and invasion of peritoneum cells, while PLZF overexpression reduces their migration and invasion. These data indicate that the reduced

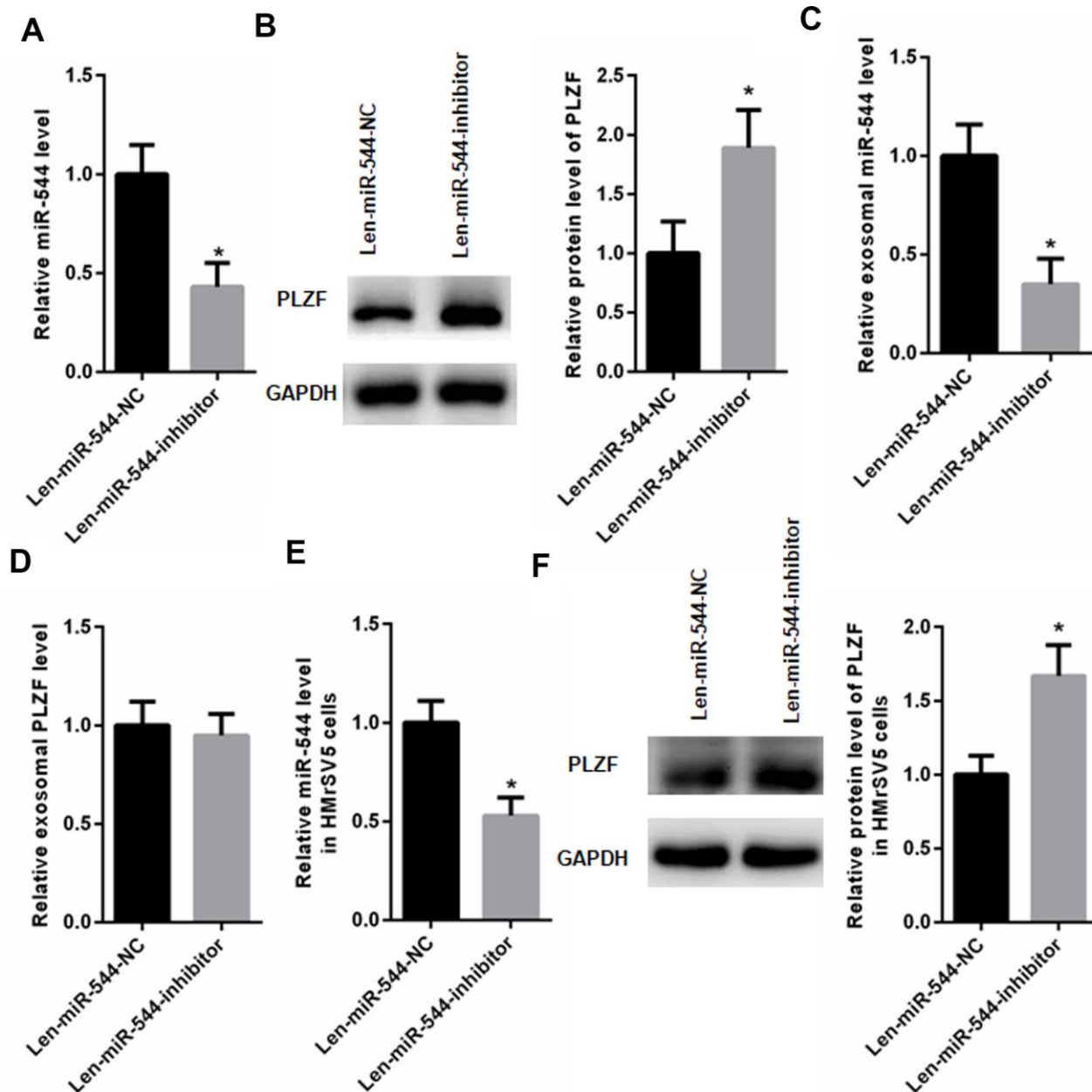


Figure 6. miR-544 inhibition increases PLZF expression in HMrsV5 cells. (A) RT-PCR of miR-544 in EVs isolated from MGC803 cells transfected with Len-miR-544-inhibitor or control Len-miR-544-NC. (B) Western blotting of PLZF in MGC803 cells transfected with Len-miR-544-inhibitor or Len-miR-544-NC. (C) RT-PCR of exosomal miR-544 derived from MGC803 cells transfected with Len-miR-544-inhibitor or Len-miR-544-NC. (D) PLZF mRNA in MGC803 cells transfected with Len-miR-544-inhibitor or Len-miR-544-NC. (E) RT-PCR of miR-544 in Len-miR-544-inhibitor group and Len-miR-544-NC group in HMrsV5 cells co-cultured with EVs derived from MGC803 Len-miR-544-NC or Len-miR-544-inhibitor. (F) PLZF expression in EVs isolated from MGC803 cells transfected with Len-miR-544-inhibitor or Len-miR-544-NC. (n=3, Student's t-test)

expression of PLZF can induce malignant changes in peritoneum cells.

Increasing evidence suggests that EVs play an important role in intercellular communication via transferring RNA, DNA and proteins [21, 22]. Thus, we hypothesized that the PM-derived EVs might be responsible for the decreased levels of PLZF in peritoneal tissues of GC patients. However, since there were no changes in the PLZF levels in EVs isolated from GC patients with and without PM, we speculated that the PLZF expression might be regulated by miRNAs present in the EVs. Indeed, microarray analysis showed that the expression of five miRNAs was significantly increased in EVs of GC patients with PM compared to patients without PM. Among the five upregulated miRNAs, miR-544 has

been previously reported to target the PLZF expression [18].

We have found that the expression of miR-544 is significantly increased in GC cells, tissues, and in GC/PM-derived EVs, compared to normal tissues and gastric epithelial cells. In addition, a co-incubation of peritoneum cells with exosomes isolated from GC cells and control gastric epithelial cells showed that the GC-derived EVs significantly suppressed the PLZF expression in peritoneum cells, indicating that EVs might be involved in GC peritoneal metastasis. Moreover, transfection with miR-544 mimics significantly reduced the PLZF expression in HMrSV5 peritoneum cells, while miR-544 inhibition increased the PLZF expression. These data indicate that miR-544 promotes peritoneal metastasis in GC.

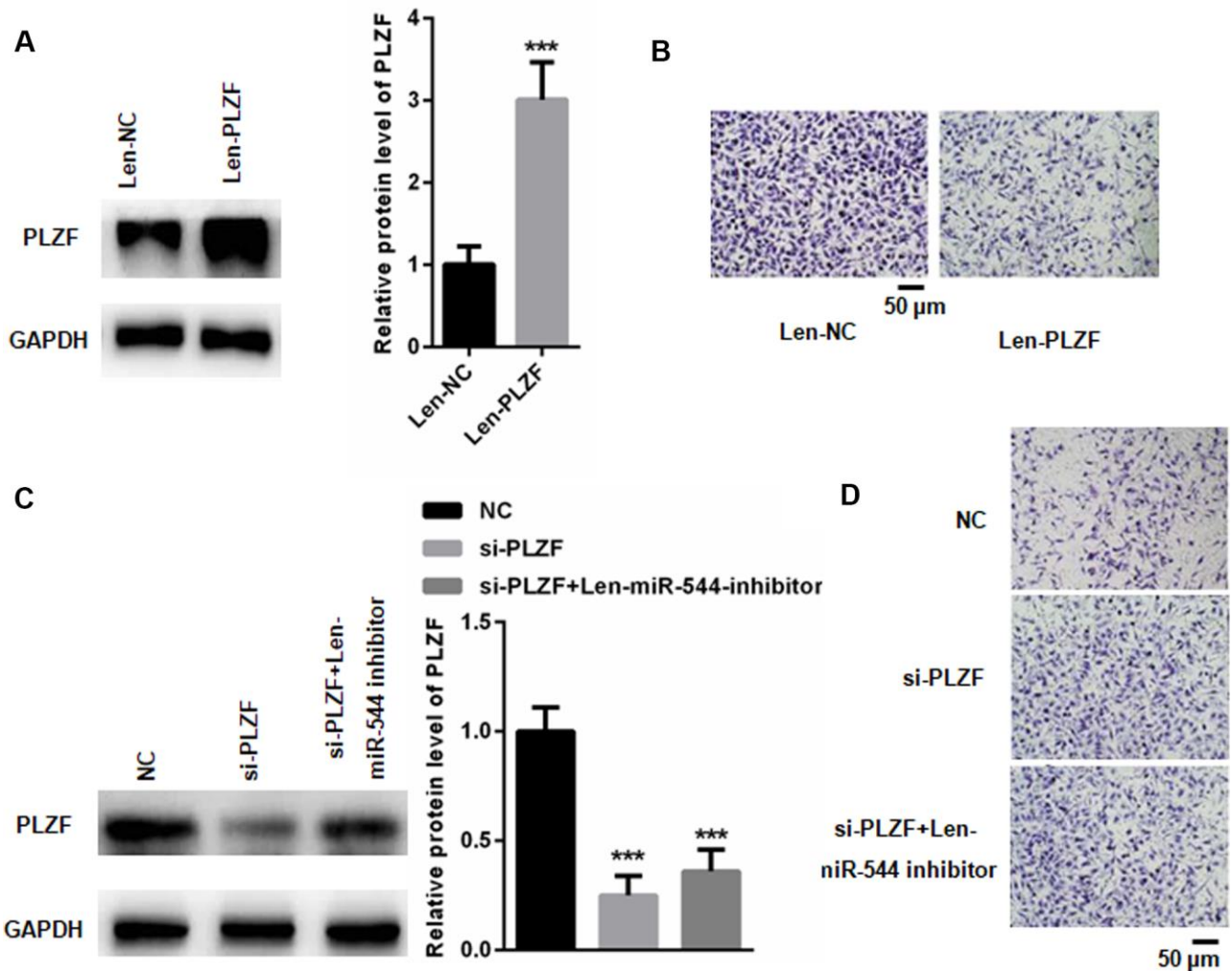


Figure 7. miR-544 induces malignant phenotype in HMrSV5 cells via targeting PLZF. (A) Western blotting of PLZF in Len-PLZF-transfected HMrSV5 cells overexpressing PLZF. (n=3, Student's t-test) (B) Migration and invasion of Len-PLZF-transfected HMrSV5 cells. (C) Western blotting of PLZF in PLZF siRNA-transfected HMrSV5 cells. (n=3, one way ANOVA) (D) Migration and invasion of PLZF siRNA-transfected HMrSV5 cells.

Our data showed that PLZF suppression increased the migratory and invasive capacity of HMrSV5 peritoneum cells. Importantly, inhibition of miR-544 could not reverse the PLZF silencing-induced increase in migration and invasion of HMrSV5 cells. These data strongly indicate that PLZF mediates peritoneal metastasis in GC via exosomal miR-544. It is widely accepted that PM occurs through the implantation of peritoneal free tumor cells [23, 24]. Therefore, elimination or reduction of peritoneal free tumor cells is necessary to prevent PM. Our data indicate that targeting miR-544 may serve as a target to reduce the peritoneal free tumor cells and PM development.

However, there are limitations in the current study. First, TEM pictures show a sub-population of EVs with size close to 200 nm, and the size of exosomes are defined as 30nm to 100 nm. It means that a subpopulation of microvesicles (100 nm to 1 μ m) is existed. Hence, it would be useful to analyze the size distribution of the EVs isolated from peritoneal fluid and culture media via Nanosight/DLS. Second, increasing evidence has shown that EVs taken up by endocytosis can be found within endosomes and lysosomes [25, 26]. Thereafter, once EVs are unable to escape the endosomal compartment, they will be degraded by lysosomes which then decrease functional delivery of EVs and their cargoes [27, 28]. Therefore, it would be great to show whether GC-derived EVs have the ability of endosomal escape after up taken by cells.

Altogether, our findings demonstrate that the PLZF expression is downregulated in GC tissues and peritoneal metastatic lesions of GC patients. Our data show that the PLZF expression is suppressed by miR-544, which can be transferred from GC-derived EVs to peritoneal cells. Furthermore, our results indicate that the EV-mediated transfer of miR-544 decreases the PLZF expression in peritoneal metastatic lesions, resulting in increased invasion potential. Thus, miR-544 might serve as a potential diagnostic biomarker and therapeutic target for GC patients.

MATERIALS AND METHODS

Patient samples

60 paired GC and adjacent non-cancer tissues from patients who underwent surgery at Affiliated Hangzhou First People Hospital were obtained between January 2018 and December 2018. At the same time, peritoneal lavage fluid was obtained. Laparoscopic observation or positive cytology of peritoneal lavage fluids was used for the diagnosis of peritoneal metastasis. Surgically resected samples, including primary tumors, paired adjacent non-cancerous tissues, suspicious peritoneal metastatic

lesions, and normal peritoneal tissues adjacent to the corresponding possible peritoneal metastasis sites were analyzed (Table 1). Exclusion criteria: (1) Patients who ever received chemotherapy or radiation therapy; (2) Patients with distant metastasis; (3) Patients with gastric stump carcinoma. Inclusion criteria: (1) Patients over 18 years old; (2) Patients with histologically proven adenocarcinoma of the stomach or esophagogastric junction (Siewert type 2 or 3); (3) Patients who received CT or PET-CT scan before surgery.

Cell culture

Human GC cell lines MGC803, BGC823, MKN45, HGC27, and SGC7901, normal human gastric epithelial cell line GES-1, and human peritoneal mesothelial cell line HMrSV5 were purchased from the Cell Center of Shanghai Institutes for Biological Sciences (Shanghai, China). All cell lines were cultured in RPMI-1640 (GE Healthcare Life Sciences, USA) supplemented with 10% fetal bovine serum (FBS; Invitrogen; Thermo Fisher Scientific, USA), streptomycin (100 mg/ml), and penicillin (100 U/ml) at 37° C in a humidified atmosphere containing 5% CO₂.

Isolation of EVs

EVs were isolated from peritoneal fluid samples by centrifuging at 2,000 g for 10 minutes. The supernatants were then filtered through 800 nm filter (Millipore, USA) to remove cell debris, and ultra-centrifuged at 150,000 g for 70 minutes at 4° C. In addition, EVs were isolated from GC cells cultured in RPMI-1640 supplemented with 10% exosome-free FBS (ExoPerfect™ Exo-free FBS, SUER250QY, Hangzhou Qiannuo Biotechnology Co., LTD, Hangzhou City, China) for 48 h, using the GET™ Exosome Isolation Kit (GET301-10, Genexosome Technologies, USA). In brief, 5ml of exosome concentration solution (ECS reagent) was added to 5ml of serum and was then diluted with 5ml of 1 × PBS. After adding 2.5 ml ECS reagent, the mixture was turned upside down, and then placed at 4° C for overnight. The mixture was centrifuged for 60 min at 10,000 g. The supernatant was discarded and EVs was rich in the precipitate. Then, 400 μ L of 1 × PBS was used to suspend the precipitate and EVs were collected for the subsequent experiments. The presence of isolated EVs was validated using an HT-7700 transmission electron microscope (Hitachi High-Technologies, Tokyo, Japan) (bar = 50 nm). Purified EVs were labeled with the PKH67 green fluorescent linker Mini Kit (Sigma, USA) according to the instructions. Briefly, EVs were suspended in 180 μ l of PBS with 20 μ l of 1:50 diluted PKH67. After 3 min of incubation at room temperature, 3.8 ml of exosome-free

Table 1. Characteristics of patients with gastric cancer.

Variable	Patients without PM	Patients with PM
Age (years)	68 (34-87)	65 (37-76)
Gender		
M	22	11
F	18	9
Depth of invasion		
pT1	8	
pT2	11	
pT3	10	
pT4	11	

medium was added to terminate the labeling reaction, and EVs were harvested and washed twice with PBS by centrifugation at 100,000 g for 1 h. After 48 h of co-culture, GC cells were washed twice with PBS, fixed with 4% paraformaldehyde for 10 min, washed twice or thrice with PBS for 10 min and then observed under a laser confocal microscope (Zeiss, Germany).

RNA isolation and qRT-PCR

RNA was extracted from EVs and cells using the miRNeasy Mini Kit (Qiagen, Hilden, Germany). Concentration and purity of RNA was determined by measuring the optical density at 260 and 280 nm. RNA reverse transcription was performed using the TaqMan™ MicroRNA Reverse Transcription Kit (Thermo Fisher Scientific USA). The reagent concentrations were 3.0 µl RNA, 3.0 µl RT primer, 0.3 µl dNTP, 3.0 µl MultiScribe Reverse Transcriptase, 1.5 µl 10e RT buffer, 1.01 µl Nuclease-free water. The temperature protocol used for RT was as follows 72° C for 10 min; 42° C for 60 min, 72° C for 5 min and 95° C for 2 min. SYBR Green Super mix (Biorad, USA) was used for real-time quantitative PCR. The PCR amplifications were performed in a 10 µl reaction system containing 5 µl SYBR Green Supermix, 0.4 µl forward primer, 0.4 µl reverse primer, 2.2 µl double distilled H₂O and 2 µl template cDNA. PCR reaction cycles were as follows: 95° C for 30 seconds, 45 cycles of 5 seconds at 95° C and 30 seconds at 60° C. Relative mRNA expression was normalized to U6 using the 2^{-ΔΔC_q} method [29]. The primers used in the present study were listed in Table 2. Cell migration assays were performed using Boyden chambers (8-µm pore filter; Corning Inc, USA). Cells (1 × 10⁵/well) were plated into the top chamber and 10% FBS containing medium was placed into the bottom chamber. After incubation at 37° C in 5% CO₂ for 12 h, the cells remaining at the upper surface of the membrane were removed with a cotton swab. The cells that migrated through the 8 µm sized pores and adhered to the lower surface of the

membrane were fixed with 4% paraformaldehyde, stained with crystal violet, and photographed.

Cell transfections

The lentivirus vector overexpressing PLZF (Len-PLZF), control vector (Len-NC), inhibitory miR-544 (Len-miR-544-inhibitor), and control miR (Len-miR-544-NC) were purchased from Genechem (Shanghai, China).

siRNA transfections, MGC-803 cells were seeded at the density of 10⁵ cells/well in a 6-well plate, and transfected with siRNA targeting PLZF or a non-specific siRNA at a final concentration at 20 nM, using the HiPerfect transfection reagent (Qiagen GmbH, Hilden, Germany).

Cell viability analysis

To examine cell viability, HMrSV5 cells were seeded in 96-well plates at a density of 1.0x10⁴ cells/per well. Exosomes from GC patients without PM or with PM were co-cultured with MGC-803 cells for 24, 48, 72 h. Then, Cell numbers were calculated using a hemocytometer and cell proliferation was analyzed using a Cell Counting Kit-8 (CCK-8, Dojindo Molecular Technologies, Inc., Kumamoto, Japan), according to the manufacturer's protocol.

Western blotting

Proteins were extracted using RIPA buffer (Beijing Solarbio Science and Technology Co., Ltd., Beijing, China). Equal amounts of protein (15 µg/lane) were separated by 10% SDS-PAGE, and transferred onto a PVDF membrane. The membranes were incubated with primary antibodies (RT, 2 h), washed in TBST, and incubated (RT, 2 h) with HRP-conjugated goat anti-rabbit IgG (1:5,000; ZB-2306, Zhongshan Gold Bridge Biological Technology Co., Beijing, China). After washing, the signal was detected using enhanced

Table 2. The primers used in the present study.

Primers	Sequence
PLZF-F	5'-TTTCAGCCATGAGTCCCACC-3'
PLZF-R	5'-CTCAACCTTGTCCCCATCC-3'
GAPDH-F	5'-CTAGCTGGCCCGATTCTCC-3'
GAPDH-R	5'-GCGCCCAATACGACCAAATC-3'
miR-544-RT	5'-GTCGTATCCAGTGCAGGGTCCGAGGTATTTCGACTGGATACGACGAACTT-3'
U6-RT	5'-GTCGTATCCAGTGCAGGGTCCGAGGTATTTCGACTGGATACGACAAAATG-3'
miR-544-F	5'-GCGCATTCTGCATTTTTAGC
U6-F	5'-GCGCGTCGTGAAGCGTTC-3'
Universal reverse primer	5'-GTGCAGGGTCCGAGGT-3'

chemiluminescence (Merck KGaA, Darmstadt, Germany). ImageJ 1.8.0 (National Institutes of Health, Bethesda, MD, USA) was used to quantify the relative protein levels. GAPDH was used as an internal control.

Statistical analysis

Data were expressed as the mean \pm standard error. Each experiment was carried out in triplicates. The two-tailed unpaired student's t-tests were used for comparisons of two groups. Multiple comparisons were performed using one-way one way ANOVA followed by Tukey's multiple comparison test; $P < 0.05$ was considered significant. The data were analyzed using SPSS software, version 20.0 (SPSS, Inc., Chicago, IL, USA).

AUTHOR CONTRIBUTIONS

W.K. and J.Z performed the experiments, analyzed the data, wrote the paper and gave final approval of the version to be published. X.L., G.Y., S.Z. and A.Z. collected patient samples. P.Y., Y.S., and R.Y. performed part of the RT-qPCR experiments and western blot analysis. All authors read and approved the final manuscript.

CONFLICTS OF INTEREST

We declare that we have no conflicts of interest.

FUNDING

This study was supported by Zhejiang Provincial Natural Science Foundation of China (Grant No. Q17H030001) and Zhejiang Medical and Health Research Project (Grant No. 2020KY700).

REFERENCES

1. Wang J, Lv B, Su Y, Wang X, Bu J, Yao L. Exosome-mediated transfer of lncRNA HOTTIP promotes

cisplatin resistance in gastric cancer cells by regulating HMGA1/miR-218 axis. *Onco Targets Ther.* 2019; 12:11325–38.

<https://doi.org/10.2147/OTT.S231846> PMID:[31908497](https://pubmed.ncbi.nlm.nih.gov/31908497/)

2. Wang Z, Chen JQ, Liu JL, Tian L. Issues on peritoneal metastasis of gastric cancer: an update. *World J Surg Oncol.* 2019; 17:215.

<https://doi.org/10.1186/s12957-019-1761-y>

PMID:[31829265](https://pubmed.ncbi.nlm.nih.gov/31829265/)

3. Zheng LN, Wen F, Xu P, Zhang S. Prognostic significance of Malignant ascites in gastric cancer patients with peritoneal metastasis: a systemic review and meta-analysis. *World J Clin Cases.* 2019; 7:3247–58.

<https://doi.org/10.12998/wjcc.v7.i20.3247>

PMID:[31667175](https://pubmed.ncbi.nlm.nih.gov/31667175/)

4. Dong D, Tang L, Li ZY, Fang MJ, Gao JB, Shan XH, Ying XJ, Sun YS, Fu J, Wang XX, Li LM, Li ZH, Zhang DF, et al. Development and validation of an individualized nomogram to identify occult peritoneal metastasis in patients with advanced gastric cancer. *Ann Oncol.* 2019; 30:431–38.

<https://doi.org/10.1093/annonc/mdz001>

PMID:[30689702](https://pubmed.ncbi.nlm.nih.gov/30689702/)

5. Fan S, Feng M, Wang M, Guan W. Extensive small bowel metastasis and peritoneal dissemination 1 year following curative gastrectomy for T1N1 gastric cancer: a case report. *Medicine (Baltimore).* 2019; 98:e13984.

<https://doi.org/10.1097/MD.0000000000013984>

PMID:[30702557](https://pubmed.ncbi.nlm.nih.gov/30702557/)

6. Kim M, Jeong WK, Lim S, Sohn TS, Bae JM, Sohn IS. Gastric cancer: development and validation of a CT-based model to predict peritoneal metastasis. *Acta Radiol.* 2020; 61:732–742.

<https://doi.org/10.1177/0284185119882662>

PMID:[31653185](https://pubmed.ncbi.nlm.nih.gov/31653185/)

7. Lee BE. Potential for peritoneal metastasis after gastric perforation induced by endoscopic submucosal dissection of early gastric cancer. *Gut Liver.* 2019; 13:481–82.

- <https://doi.org/10.5009/gnl19279>
PMID:31505906
8. Yang H, Zhang H, Ge S, Ning T, Bai M, Li J, Li S, Sun W, Deng T, Zhang L, Ying G, Ba Y. Exosome-derived miR-130a activates angiogenesis in gastric cancer by targeting C-MYB in vascular endothelial cells. *Mol Ther*. 2018; 26:2466–75.
<https://doi.org/10.1016/j.ymthe.2018.07.023>
PMID:30120059
 9. Chen KB, Chen J, Jin XL, Huang Y, Su QM, Chen L. Exosome-mediated peritoneal dissemination in gastric cancer and its clinical applications. *Biomed Rep*. 2018; 8:503–09.
<https://doi.org/10.3892/br.2018.1088>
PMID:29774141
 10. Li Q, Li B, Li Q, Wei S, He Z, Huang X, Wang L, Xia Y, Xu Z, Li Z, Wang W, Yang L, Zhang D, Xu Z. Exosomal miR-21-5p derived from gastric cancer promotes peritoneal metastasis via mesothelial-to-mesenchymal transition. *Cell Death Dis*. 2018; 9:854.
<https://doi.org/10.1038/s41419-018-0928-8>
PMID:30154401
 11. Fu H, Yang H, Zhang X, Wang B, Mao J, Li X, Wang M, Zhang B, Sun Z, Qian H, Xu W. Exosomal TRIM3 is a novel marker and therapy target for gastric cancer. *J Exp Clin Cancer Res*. 2018; 37:162.
<https://doi.org/10.1186/s13046-018-0825-0>
PMID:30031392
 12. Stopsack KH, Gerke T, Tyekucheva S, Mazzu YZ, Lee GM, Chakraborty G, Abida W, Mucci LA, Kantoff PW. Low expression of the androgen-induced tumor suppressor gene PLZF and lethal prostate cancer. *Cancer Epidemiol Biomarkers Prev*. 2019; 28:707–14.
<https://doi.org/10.1158/1055-9965.EPI-18-1014>
PMID:30602500
 13. Buluwela L, Pike J, Mazhar D, Kamalati T, Hart SM, Al-Jehani R, Yahaya H, Patel N, Sarwar N, Heathcote DA, Schwickerath O, Phoenix F, Hill R, et al. Inhibiting estrogen responses in breast cancer cells using a fusion protein encoding estrogen receptor-alpha and the transcriptional repressor PLZF. *Gene Ther*. 2005; 12:452–60.
<https://doi.org/10.1038/sj.gt.3302421>
PMID:15647773
 14. Hsieh CL, Botta G, Gao S, Li T, Van Allen EM, Treacy DJ, Cai C, He HH, Sweeney CJ, Brown M, Balk SP, Nelson PS, Garraway LA, Kantoff PW. PLZF, a tumor suppressor genetically lost in metastatic castration-resistant prostate cancer, is a mediator of resistance to androgen deprivation therapy. *Cancer Res*. 2015; 75:1944–48.
<https://doi.org/10.1158/0008-5472.CAN-14-3602>
PMID:25808865
 15. Mariani F, Sena P, Magnani G, Mancini S, Palumbo C, Ponz de Leon M, Roncucci L. PLZF expression during colorectal cancer development and in normal colorectal mucosa according to body size, as marker of colorectal cancer risk. *ScientificWorldJournal*. 2013; 2013:630869.
<https://doi.org/10.1155/2013/630869> PMID:24348178
 16. Xiao GQ, Unger P, Yang Q, Kinoshita Y, Singh K, McMahon L, Nastiuk K, Sha K, Krolewski J, Burstein D. Loss of PLZF expression in prostate cancer by immunohistochemistry correlates with tumor aggressiveness and metastasis. *PLoS One*. 2015; 10:e0121318.
<https://doi.org/10.1371/journal.pone.0121318>
PMID:25807461
 17. Wang JB, Jin Y, Wu P, Liu Y, Zhao WJ, Chen JF, De W, Yang F. Tumor suppressor PLZF regulated by lncRNA ANRIL suppresses proliferation and epithelial mesenchymal transformation of gastric cancer cells. *Oncol Rep*. 2019; 41:1007–1018.
<https://doi.org/10.3892/or.2018.6866> PMID:30431129
 18. Song W, Mu H, Wu J, Liao M, Zhu H, Zheng L, He X, Niu B, Zhai Y, Bai C, Lei A, Li G, Hua J. miR-544 regulates dairy goat male germline stem cell self-renewal via targeting PLZF. *J Cell Biochem*. 2015; 116:2155–65.
<https://doi.org/10.1002/jcb.25172> PMID:25808723
 19. Chan DY, Syn NL, Yap R, Phua JN, Soh TI, Chee CE, Nga ME, Shabbir A, So JB, Yong WP. Conversion surgery post-intraperitoneal paclitaxel and systemic chemotherapy for gastric cancer carcinomatosis peritonei. Are we ready? *J Gastrointest Surg*. 2017; 21:425–33.
<https://doi.org/10.1007/s11605-016-3336-3>
PMID:27981493
 20. Shen H, Zhan M, Zhang Y, Huang S, Xu S, Huang X, He M, Yao Y, Man M, Wang J. PLZF inhibits proliferation and metastasis of gallbladder cancer by regulating IFIT2. *Cell Death Dis*. 2018; 9:71.
<https://doi.org/10.1038/s41419-017-0107-3>
PMID:29358655
 21. Huang J, Shen M, Yan M, Cui Y, Gao Z, Meng X. Exosome-mediated transfer of miR-1290 promotes cell proliferation and invasion in gastric cancer via NKD1. *Acta Biochim Biophys Sin (Shanghai)*. 2019; 51:900–07.
<https://doi.org/10.1093/abbs/gmz077>
PMID:31435644
 22. Soeda N, Iinuma H, Suzuki Y, Tsukahara D, Midorikawa H, Igarashi Y, Kumata Y, Horikawa M, Kiyokawa T, Fukagawa T, Fukushima R. Plasma exosome-encapsulated microRNA-21 and microRNA-92a are promising biomarkers for the prediction of peritoneal recurrence in patients with gastric cancer. *Oncol Lett*. 2019; 18:4467–80.

- <https://doi.org/10.3892/ol.2019.10807>
PMID:[31611956](https://pubmed.ncbi.nlm.nih.gov/31611956/)
23. Miwa T, Kanda M, Umeda S, Tanaka H, Shimizu D, Tanaka C, Kobayashi D, Hayashi M, Yamada S, Nakayama G, Koike M, Kodera Y. Establishment of Peritoneal and Hepatic Metastasis Mouse Xenograft Models Using Gastric Cancer Cell Lines. *In Vivo*. 2019; 33:1785–1792.
<https://doi.org/10.21873/invivo.11669>
PMID:[31662503](https://pubmed.ncbi.nlm.nih.gov/31662503/)
24. Rau B, Brandl A, Piso P, Pelz J, Busch P, Demtröder C, Schüle S, Schlitt HJ, Roitman M, Tepel J, Sulkowski U, Uzunoglu F, Hünerbein M, et al, and Peritoneum Surface Oncology Group, and members of the StuDoQ|Peritoneum Registry of the German Society for General and Visceral Surgery (DGAV). Peritoneal metastasis in gastric cancer: results from the German database. *Gastric Cancer*. 2020; 23:11–22.
<https://doi.org/10.1007/s10120-019-00978-0>
PMID:[31228044](https://pubmed.ncbi.nlm.nih.gov/31228044/)
25. Heath N, Osteikoetxea X, de Oliveria TM, Lázaro-Ibáñez E, Shatnyeva O, Schindler C, Tigue N, Mayr LM, Dekker N, Overman R, Davies R. Endosomal escape enhancing compounds facilitate functional delivery of extracellular vesicle cargo. *Nanomedicine (Lond)*. 2019; 14:2799–814.
<https://doi.org/10.2217/nnm-2019-0061>
PMID:[31724479](https://pubmed.ncbi.nlm.nih.gov/31724479/)
26. Heusermann W, Hean J, Trojer D, Steib E, von Bueren S, Graff-Meyer A, Genoud C, Martin K, Pizzato N, Voshol J, Morrissey DV, Andaloussi SE, Wood MJ, Meisner-Kober NC. Exosomes surf on filopodia to enter cells at endocytic hot spots, traffic within endosomes, and are targeted to the ER. *J Cell Biol*. 2016; 213:173–84.
<https://doi.org/10.1083/jcb.201506084>
PMID:[27114500](https://pubmed.ncbi.nlm.nih.gov/27114500/)
27. Mathieu M, Martin-Jaular L, Lavieu G, Théry C. Specificities of secretion and uptake of exosomes and other extracellular vesicles for cell-to-cell communication. *Nat Cell Biol*. 2019; 21:9–17.
<https://doi.org/10.1038/s41556-018-0250-9>
PMID:[30602770](https://pubmed.ncbi.nlm.nih.gov/30602770/)
28. Mulcahy LA, Pink RC, Carter DR. Routes and mechanisms of extracellular vesicle uptake. *J Extracell Vesicles*. 2014; 3.
<https://doi.org/10.3402/jev.v3.24641>
PMID:[25143819](https://pubmed.ncbi.nlm.nih.gov/25143819/)
29. Livak KJ, Schmittgen TD. Analysis of relative gene expression data using real-time quantitative PCR and the 2⁻($\Delta\Delta C_T$) Method. *Methods*. 2001; 25:402–8.
<https://doi.org/10.1006/meth.2001.1262>
PMID:[11846609](https://pubmed.ncbi.nlm.nih.gov/11846609/)

MITF functions as a tumor suppressor in non-small cell lung cancer beyond the canonically oncogenic role

Yi-Jing Hsiao¹, Wen-Hsin Chang², Hsuan-Yu Chen³, Yin-Chen Hsu¹, Su-Chin Chiu⁴, Ching-Cheng Chiang¹, Gee-Chen Chang⁵, Yi-Ju Chen⁶, Chia-Yu Wang¹, Yan-Ming Chen¹, Chien-Yu Lin³, Yu-Ju Chen⁶, Pan-Chyr Yang^{7,8}, Jeremy J.W. Chen⁹, Sung-Liang Yu^{1,10,11}

¹Department of Clinical Laboratory Sciences and Medical Biotechnology, College of Medicine, National Taiwan University, Taipei, Taiwan

²Institute of Molecular Medicine, College of Medicine, National Taiwan University, Taipei, Taiwan

³Institute of Statistical Science, Academia Sinica, Taipei, Taiwan

⁴Inservice Master Program in Life Sciences, College of Life Sciences, National Chung-Hsing University, Taichung, Taiwan

⁵Division of Chest Medicine, Department of Internal Medicine, Taichung Veterans General Hospital, Taichung, Taiwan

⁶Institute of Chemistry, Academia Sinica, Taipei, Taiwan

⁷Institute of Biomedical Sciences, Academia Sinica, Taipei, Taiwan

⁸Department of Internal Medicine, National Taiwan University Hospital, Taipei, Taiwan

⁹Institute of Biomedical Sciences, National Chung-Hsing University, Taichung, Taiwan

¹⁰Department of Laboratory Medicine, National Taiwan University Hospital, Taipei, Taiwan

¹¹Centers for Genomic and Precision Medicine, National Taiwan University, Taipei, Taiwan

Correspondence to: Jeremy J.W. Chen, Sung-Liang Yu; **email:** jwchen@dragon.nchu.edu.tw, slyu@ntu.edu.tw

Keywords: FZD7, metastasis, transcriptome profiling, WNT pathway

Received: June 30, 2020

Accepted: September 9, 2020

Published: December 3, 2020

Copyright: © 2020 Hsiao et al. This is an open access article distributed under the terms of the [Creative Commons Attribution License](https://creativecommons.org/licenses/by/3.0/) (CC BY 3.0), which permits unrestricted use, distribution, and reproduction in any medium, provided the original author and source are credited.

ABSTRACT

Microphthalmia-associated transcription factor (MITF) is a critical mediator in melanocyte differentiation and exerts oncogenic functions in melanoma progression. However, the role of MITF in non-small cell lung cancer (NSCLC) is still unknown. We found that *MITF* is dominantly expressed in the low-invasive CL1-0 lung adenocarcinoma cells and paired adjacent normal lung tissues. *MITF* expression is significantly associated with better overall survival and disease-free survival in NSCLC and serves as an independent prognostic marker. Silencing *MITF* promotes tumor cell migration, invasion and colony formation in lung adenocarcinoma cells. In xenograft mouse model, *MITF* knockdown enhances metastasis and tumorigenesis, but decreases angiogenesis in the Matrigel plug assay. Whole transcriptome profiling of the landscape of MITF regulation in lung adenocarcinoma indicates that MITF is involved in cell development, cell cycle, inflammation and WNT signaling pathways. Chromatin immunoprecipitation assays revealed that MITF targets the promoters of *FZD7*, *PTGR1* and *ANXA1*. Moreover, silencing *FZD7* reduces the invasiveness that is promoted by silencing MITF. Strikingly, *MITF* has significantly inverse correlations with the expression of its downstream genes in lung adenocarcinoma. In summary, we demonstrate the suppressive role of MITF in lung cancer progression, which is opposite to the canonical oncogenic function of MITF in melanoma.

INTRODUCTION

Lung cancer is the leading cause of cancer-related death worldwide [1]. Approximately 85% of lung cancers are non-small cell lung cancer (NSCLC) including adenocarcinoma, squamous cell carcinoma and large cell carcinoma, and lung adenocarcinoma accounts for the majority of all lung cancer cases [2]. The 5-year survival rate of early stage NSCLC ranges from 41% to 90%, whereas tumor metastasis or recurrence leads to the high mortality of stage I patients after surgery [2, 3]. In addition, lymph node metastasis is also a prognostic predictor for NSCLC survival [4]. Metastasis involves oncogenic cell transformation, cell motility and invasion and angiogenesis [5, 6]. Through functional genomics studies and an isogenic metastasis cell model in CL1-0, CL1-1 and CL1-5 lung adenocarcinoma cell lines, we discovered several metastasis-related genes [7–9]. However, the detailed processes and molecular mechanisms in lung cancer metastasis are still unknown. A comprehensive understanding of the role of these novel genes in lung metastasis is critical for the development of prognostic markers and therapeutic strategies.

MITF is a leucine zipper transcription factor with a basic helix-loop-helix (bHLH-Zip) structure and is essential for the differentiation and development of various cell types, including melanocytes, retinal pigment epithelium, osteoclasts and mast cells [10, 11]. Moreover, oncogenic MITF mediates melanoma progression in a “rheostat model” [12, 13]. In this model, high activity levels of MITF promote proliferation and differentiation, while low MITF levels increase invasion and metastasis and reduce proliferation [10, 13, 14]. However, a recent study indicated that melanoma cells with genetic ablation of SMAD7 exhibited a dual invasive/proliferative phenotype without suppression of MITF [15]. MITF mediates diverse melanoma phenotypes defined by distinct gene expression profiles and confers plasticity to melanoma cells [16]. Beyond being an activator, MITF can act as a repressor on the same gene promoter, such as ERBIN by recruiting FHL2 [17]. Thus, MITF is not only a survival lineage-specific transcription factor, but also regulates DNA damage repair, senescence, cell cycle, stemness, metabolism and invasion. To control the survival and invasiveness of melanoma, MITF activates the antiapoptotic gene *BCL2* and the cell cycle regulators, *CDK2* and *CDKN1A* [18–20], whereas MITF suppresses invadopodia formation by upregulating *GMPT* and *DIAPH1* expression, which influences the activities of small GTPases and cytoskeleton remodeling [13, 21]. Comprehensive transcriptome analysis reveals that MITF is involved in melanoma progression [22–24]. Although MITF has been extensively investigated in the progression of the

melanocyte/melanoma lineage, few studies have demonstrated the role of MITF in lung cancer.

In this study, we identified differential expression of *MITF* in our lung cancer metastasis cell model by expression microarrays. The clinical relevance of *MITF* expression for survival in NSCLC is analyzed in patients and public databases. We manipulated *MITF* expression in lung adenocarcinoma cell lines and measured cell invasion and migration activities. The influence of MITF on tumorigenesis and angiogenesis was evaluated in a xenograft mouse model. The landscape of the MITF-regulated transcriptome was profiled by expression microarrays, and the significant regulatory network of MITF was identified by pathway analysis. We further identified several targets of MITF in lung adenocarcinoma and clarified their effects on cancer progression by utilizing *in vitro* and *in silico* analyses.

RESULTS

***MITF* expression is associated with better outcome in NSCLC**

In our previous studies, we utilized an expression microarray to profile the gene expression of isogenic lung adenocarcinoma cell lines with different invasive abilities (Figure 1A) [25]. In a comparison of the expression profiles of low-invasive CL1-0 cells and high-invasive CL1-5 cells, we found a gene, *MITF*, which had 7.5-fold lower expression in CL1-5 cells than in CL1-0 cells (Supplementary Figure 1A). *MITF* transcript expression was 25-fold higher in CL1-0 cells than in CL1-5 cells, as confirmed by RT-PCR, and the protein expression was markedly decreased in CL1-5 cells (Figure 1B). We found that *MITF* expression in adjacent normal tissues was significantly higher than that in NSCLC tumors ($p < 0.001$, Wilcoxon matched-pairs test) (Figure 1C). Next, we enrolled 70 NSCLC patients to evaluate *MITF* expression (Table 1). The patients with high *MITF* expression had significantly better overall survival (OS) and disease-free survival (DFS) than those with low *MITF* expression (OS, $p = 0.01$; DFS, $p = 0.02$, log-rank test) (Figure 1D, 1E). The *MITF* expression based dichotomy was not associated with age, sex, histology features, or clinicopathological stages (Supplementary Table 1). In univariate Cox regression analysis, the hazard ratio (HR) of *MITF* expression was significant (for OS, HR 0.51, 95% CI = 0.30 to 0.86, $p < 0.05$; for DFS, HR 0.54, 95% CI = 0.32 to 0.92, $p < 0.05$). In multivariate Cox regression analysis, the HR of *MITF* expression for OS remained significant (for OS, HR 0.52, 95% CI = 0.30 to 0.90, $p < 0.05$; for DFS, HR 0.61, 95% CI = 0.35 to 1.05, $p = 0.07$) (Table 2). These data indicated that *MITF* was a prognostic marker for lung cancer progression. To

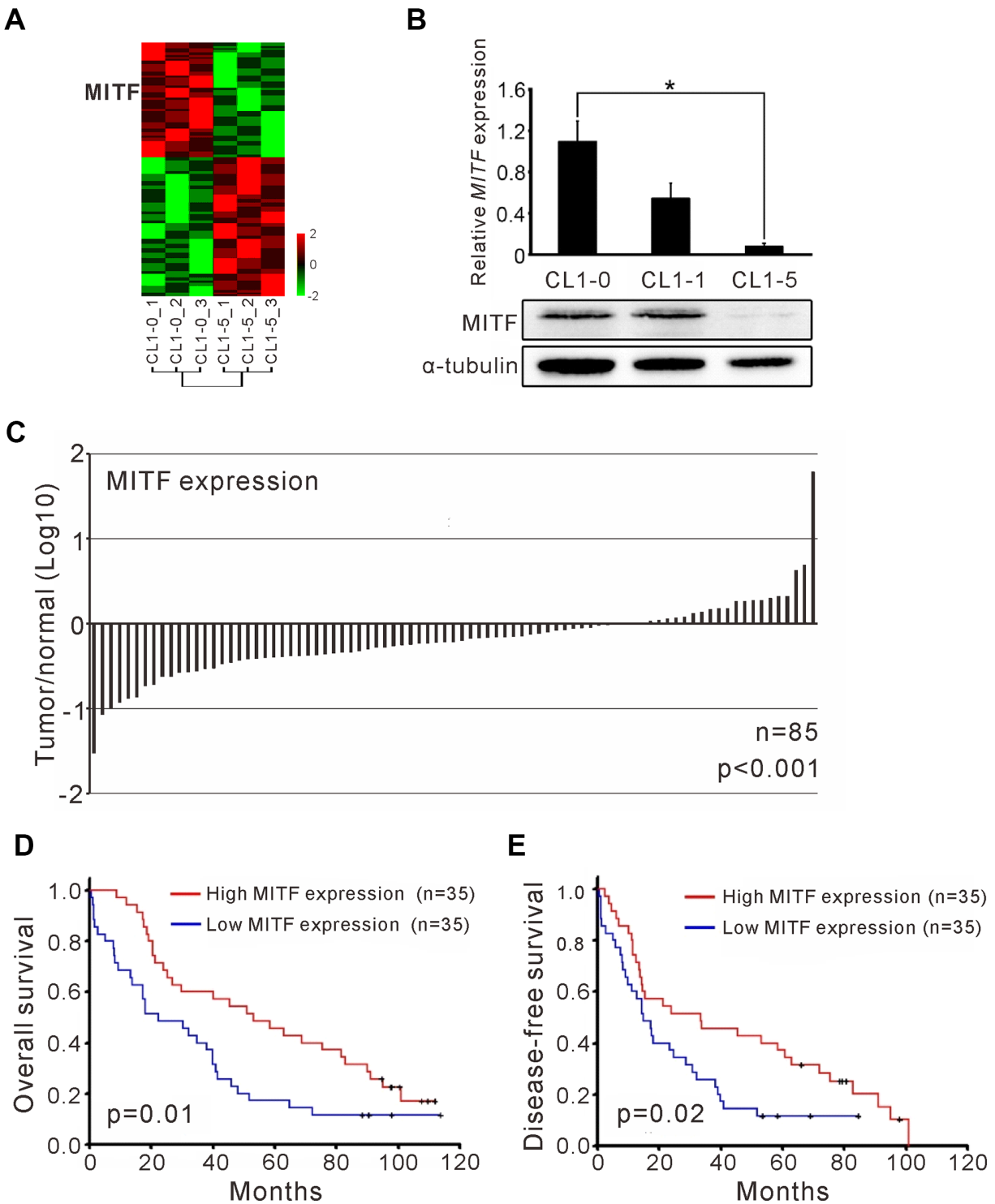


Figure 1. The *MITF* expression associated with cancer invasiveness and better outcome of NSCLC patients. (A) Heatmap of the gene expression profiles in CL1-0 and CL1-5 were presented. Each cell line was analyzed for three replicates and the significant microarray probes with 5-fold change were applied. *MITF* was one of the significant expressed genes. The scale was used the z-score. (B) *MITF* mRNA and protein level was measured by quantitative real-time PCR and immunoblot. * $p < 0.05$ (mean \pm SD, $n = 3$) (C) The ratio of *MITF* expression in tumor and adjacent normal parts of NSCLC patients ($n = 85$). The scale is the base 10 logarithm of the ratio of *MITF* expression. The difference of *MITF* expression between the two groups was estimated by Wilcoxon matched-pairs test. (D) Kaplan–Meier survival analysis estimated the overall survival of NSCLC patients by the *MITF* expression. (E) Kaplan–Meier survival analysis estimated the disease-free survival of NSCLC patients by the *MITF* expression. The *MITF* expression of clinical specimen was measured by real-time RT-PCR with TaqMan probe. The p-value for survival was estimated by log-rank test.

Table 1. Clinicopathologic characteristic of NSCLC patients (n=70).

Characteristic	Patients No. (%)
Age, mean (\pm SD)	67.48 \pm 10.21
Gender	
Male	59 (84.29)
Female	11 (15.71)
Stage	
I	34 (48.57)
II	7 (10.00)
III	29 (41.43)
Primary Tumor	
T1 and T2	60 (85.71)
T3 and T4	10 (14.29)
Regional Lymph Nodes	
N0	38 (54.29)
N1, N2, and N3	32 (45.71)
Cell Type	
Squamous cell carcinoma	19 (27.14)
Adenocarcinoma	42 (60.00)
Large cell carcinoma	7 (10.00)
Mixed (small/large cell carcinoma)	1 (1.43)
Bronchioloalveolar carcinoma	1 (1.43)

clarify the role of *MITF* in other populations, we analyzed available microarray datasets by the KM-plotter [26]. The results showed that *MITF* expression was significantly associated with OS and progression-free survival (PFS) in lung adenocarcinoma (p-value 0.047 was for OS and 0.034 for PFS, log-rank test) (Supplementary Figure 1B, 1C). Our data suggested that *MITF* was an independent prognostic marker for NSCLC and might have a suppressive role in lung cancer progression.

MITF suppresses the cell migration and invasion in lung adenocarcinoma cells

Given the existent transcripts of various *MITF* isoforms, the expression of different *MITF* isoforms in CL1-0 lung adenocarcinoma cells was measured. We found that *MITF-A* was the most abundant isoform in lung cancer cells, and *MITF-H*, *MITF-B* and *MITF-M* were the lesser abundant isoforms (Figure 2A). Next, the impact of *MITF* on invasiveness was evaluated. shMITF was transiently expressed in low-invasive CL1-0 cells and the number of invaded cells was increased in a dose-dependent manner (Figure 2B). The multiple

bands detected by high-resolution Western blotting demonstrated the isoform expression of *MITF*. Overexpression of *MITF-A* in highly invasive CL1-5 lung adenocarcinoma cells reduced cell invasive ability (Figure 2C). Next, we selected three clones stably expressing shMITF by antibiotics to avoid clonal bias (Supplementary Figure 2A). The three *MITF*-knockdown clones showed an increase in cell migration and invasion (Figure 2D). Introducing the *MITF-A* expressing plasmid into *MITF*-silenced cells reduced the migratory and invasive abilities by 60% and 80%, respectively (Figure 2E). *MITF* silencing promoted the anchorage-independent colony growth of CL1-0 cells (Figure 2F). However, *MITF* did not appear to affect cell proliferation (Supplementary Figure 2B). Taken together, the results indicated that *MITF* suppressed both cell migration and invasion in lung adenocarcinoma cells.

Silencing MITF promotes tumorigenesis and metastasis but suppresses angiogenesis

To investigate whether *MITF* plays a critical role in lung metastasis *in vivo*, we modified the method

Table 2. Univariate and multivariate Cox's regression analysis of the overall survival and disease-free survival prediction factors.

Univariate Cox's regression							
Variable		Overall survival			Disease-free survival		
		HR	95% CI	p-value	HR	95% CI	p-value
Age	<60	1			1		
	≥60	1.01	0.50-2.06	0.98	0.85	0.43-1.68	0.64
Gender	Male	1			1		
	Female	2.12	1.05-4.24	<0.05	1.54	0.77-3.08	0.22
Stage	I/II	1			1		
	III	3.36	1.97-5.74	<0.001	3.17	1.89-5.33	<0.001
Cell type	Adenocarcinoma	1			1		
	Others	1.18	0.70-1.99	0.54	1.20	0.71-2.03	0.50
MITF	High	1			1		
	Low	0.51	0.30-0.86	<0.05	0.54	0.32-0.92	<0.05

Multivariate Cox's regression							
Variable		Overall survival			Disease-free survival		
		HR	95% CI	p-value	HR	95% CI	p-value
Age	<60	1			1		
	≥60	1.31	0.63-2.72	0.48	0.98	0.49-1.98	0.96
Gender	Male	1			1		
	Female	1.94	0.93-4.06	0.08	1.52	0.74-3.11	0.25
Stage	I/II	1			1		
	III	3.57	2.06-6.20	<0.001	3.07	1.81-5.23	<0.001
Cell type	Adenocarcinoma	1			1		
	Others	1.05	0.61-1.83	0.86	1.10	0.61-1.86	0.82
MITF	High	1			1		
	Low	0.52	0.30-0.90	<0.05	0.61	0.35-1.05	0.07

HR, hazard ratio; CI, confident interval of hazard ratio.

developed by Zijlstra et al. [27]. The results showed that *MITF*-knockdown in CL1-0 cells significantly increased lung metastasis compared to the scramble control (Figure 3A). Moreover, we also found that reduced *MITF* expression strongly enhanced tumorigenesis in SCID mice ($p < 0.001$) (Figure 3B). New capillary formation was evaluated by the Matrigel plug assay *in vivo*. Interestingly, a more than 60% reduction in the number of CD31-positive stained endothelial cells in the *MITF*-knockdown tumors was observed at 10 days after injection (Figure 3C, 3D). Overall, *MITF* suppressed tumorigenesis and distal metastasis, but promoted angiogenesis *in vivo*.

MITF targets *ANXA1*, *FZD7* and *PTGR1*, and suppresses cell invasion by regulating *FZD7*

MITF is an important transcription factor in cell differentiation and cancer progression, and its transcriptional targets have been investigated in previous studies [12–14, 16, 17]. However, the landscape of MITF targets in NSCLC is not fully understood. Thus, we profiled the whole transcriptome of shMITF stably expressing cells and scramble cells by expression microarrays (Figure 4A). A total of 1,190 differentially expressed genes with greater than 2-fold changes were identified and applied for gene set enrichment analysis (GSEA) and MetaCore version

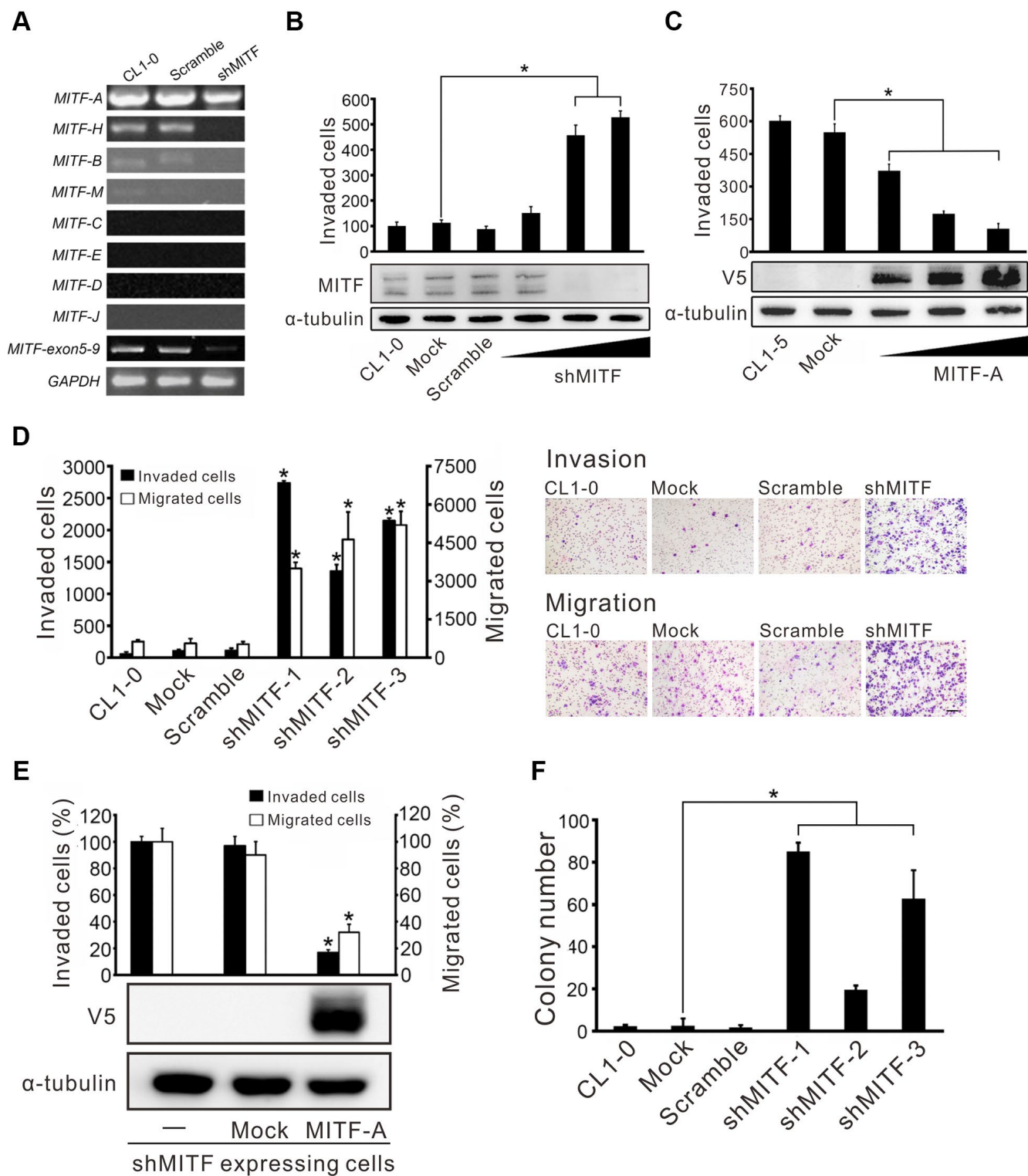


Figure 2. MIF promotes cell invasion and migration in lung adenocarcinoma cells. (A) The silencing efficiency of shMITF to different MIF isoforms in CL1-0 cells was measured by isoform-specific RT-PCR. Controls included RT-PCR for the common MIF exons 5-9 and GAPDH. (B) The cell invasive ability of CL1-0 cells was assayed after transiently delivering the shMITF expressing plasmids with different doses. Mock: vector transfectant; Scramble: scramble transfectant. * $p < 0.05$ (mean \pm SD, $n = 3$) (C) The cell invasive ability of CL1-5 cells was assayed after overexpression of MIF-A with different doses. * $p < 0.05$ (mean \pm SD, $n = 3$) (D) The cell invasive and migratory abilities of stably *MITF*-silenced cells were assayed by using Boyden chamber assays with and without Matrigel, respectively. * $p < 0.05$ (mean \pm SD, $n = 3$) (E) Re-expressed MIF-A in stably *MITF*-silenced cells were assayed for the cell invasion and migration. * $p < 0.05$ (mean \pm SD, $n = 3$) (F) The anchorage-independent colony formation ability of stably *MITF*-silenced cells was assayed. Scale bar, 100 μ m. * $p < 0.05$ (mean \pm SD, $n = 3$).

19.4 analysis [28, 29]. The resulting pathways were predominantly related to inflammation, development, cell signaling and cell cycle (Supplementary Tables 2, 3). We focused on several significant genes that were predicted targets of MITF and involved in those pathways. Real-time PCR and chromatin immunoprecipitation assays were performed to evaluate whether MITF regulated them directly. Compared to the scramble control, in *MITF*-silenced cells the frizzled homolog 7 (*FZD7*) and leukotriene B4 12-hydroxydehydrogenase (*PTGR1*) expression increased 3-fold and 5-fold, respectively, whereas annexin A1 (*ANXA1*) expression was suppressed approximately

25-fold (Figure 4B). Additionally, *VEGFC* and *PDGFC* in *MITF*-silenced cells decreased to approximately 0.02 of the expression in scramble cells, which was consistent with the *in vivo* angiogenesis results. Moreover, MITF was able to bind to the promoters of these genes, *ANXA1*, *FZD7* and *PTGR1* (Figure 4C). Additionally, the WNT signaling pathway was of interest because of its high ranking in the pathway analysis (Supplementary Tables 2, 3). Since *FZD7* is a transmembrane receptor in the WNT pathway, we further investigated whether MITF regulated cell invasion through *FZD7* in lung cancer cells. In Figure 4D, silencing of *MITF* resulted in an increase in *FZD7* protein.

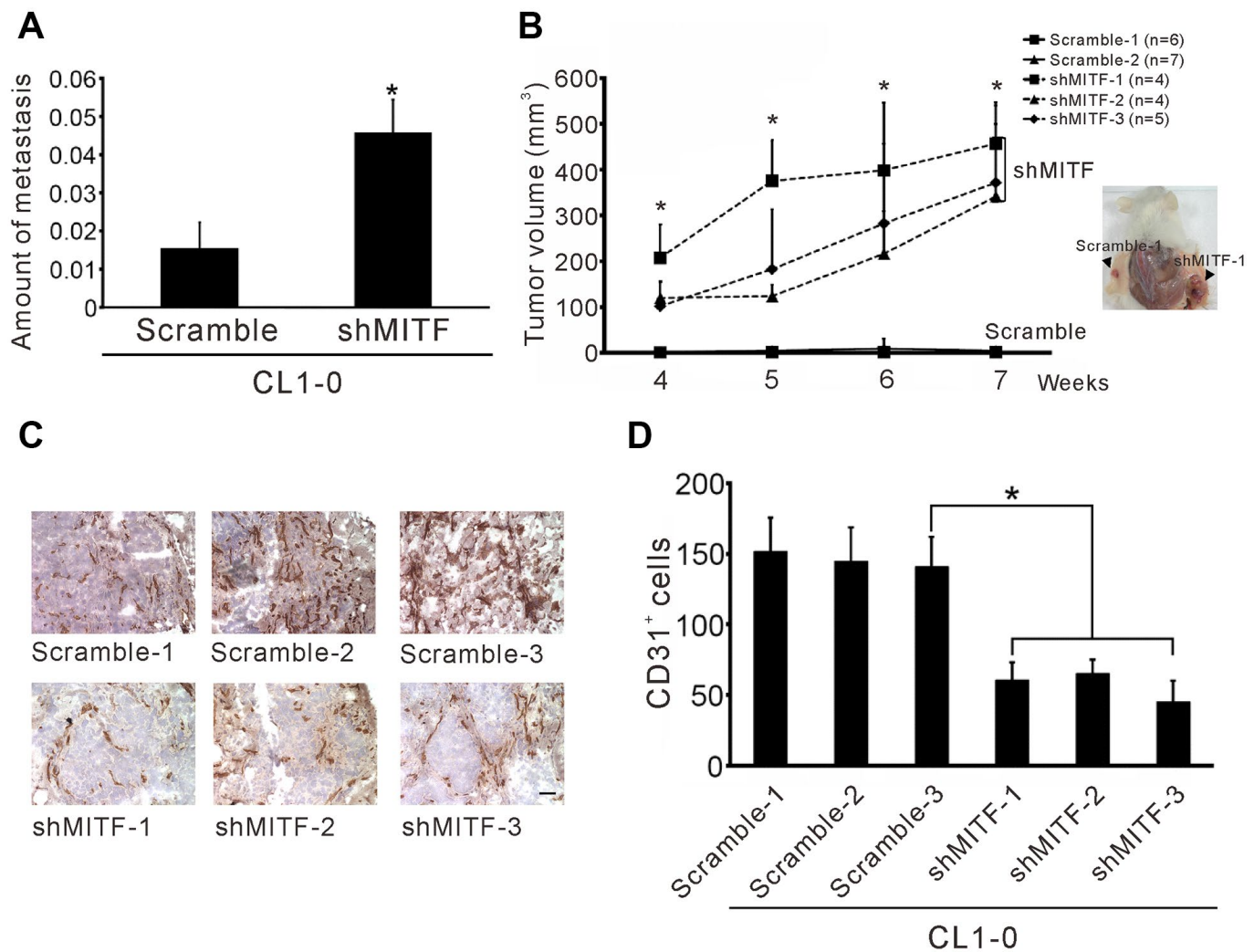


Figure 3. Knockdown of *MITF* increases metastasis and tumorigenesis but inhibits angiogenesis. (A) Intravenous injection with stable shMITF-harboring and scramble CL1-0 cells to SCID mice. The lung metastases were estimated by using real-time PCR for detection of the human *Alu* repeats. (B) Subcutaneous injection with stable shMITF-harboring cells into the right dorsal region and scramble cells into the left dorsal region of SCID mice. The tumor volume was measured every week. The mouse number of each group is listed on the plot. * $p < 0.05$ was calculated by ANOVA (mean \pm SD) (C) The cells mixed with Matrigel and injected subcutaneously. At 10 days, the plug was dissected and assayed the CD31 positive cells by immunohistochemistry. Scale Bar, 25 μ m. (D) The CD31 positive cells were counted by two blinded observers. A total of 21 fields/group (3 plugs \times 7 fields) were analyzed. * $p < 0.05$ (mean \pm SD).

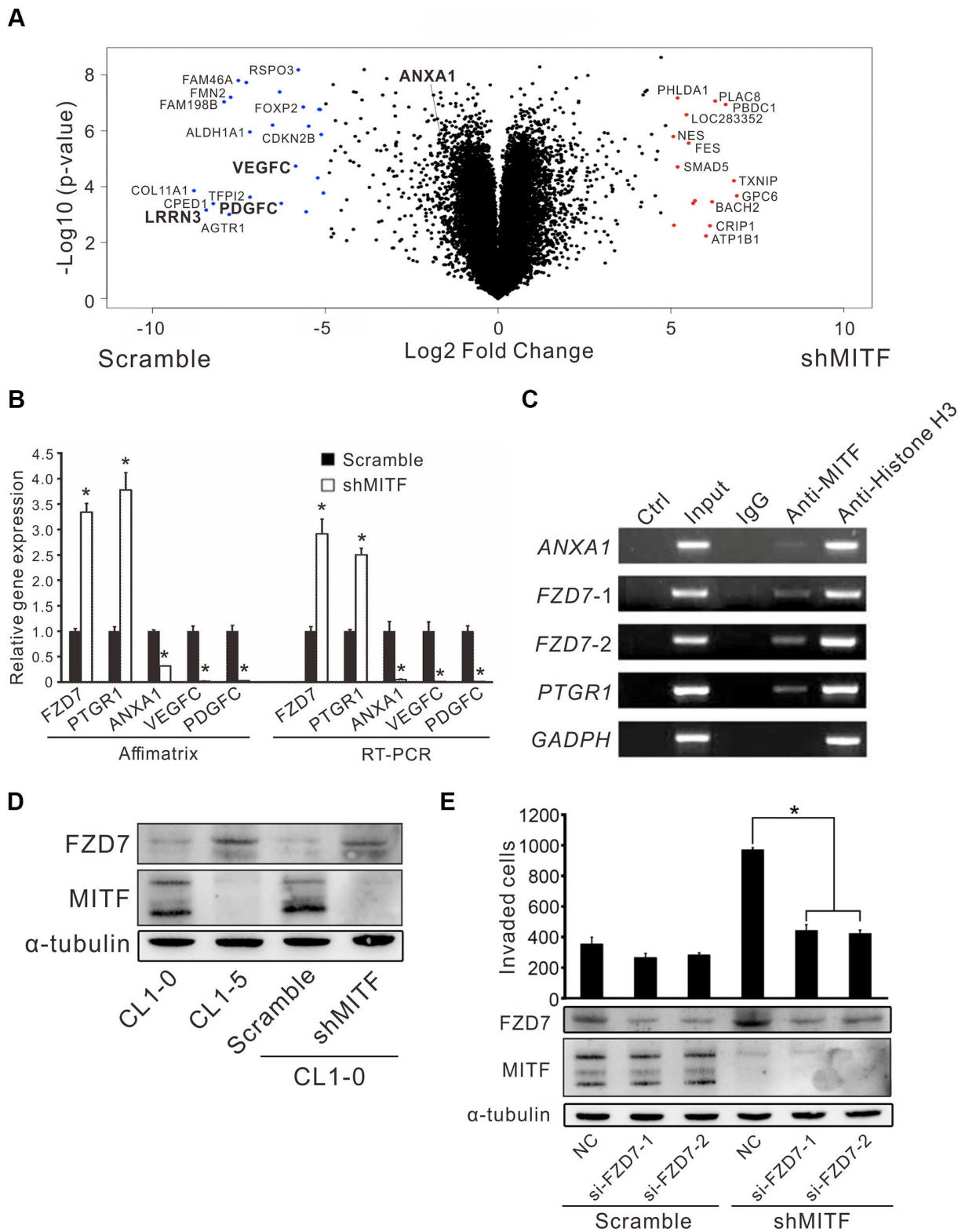


Figure 4. The regulation landscape and the direct targets of MITF. (A) The volcano plot showed the significant MITF-altered genes with log₂-fold-change. Red dot: genes with log₂-fold-change ≥ 5 , $p < 0.05$; Blue dot: genes with log₂-fold-change ≤ -5 , $p < 0.05$. (B) Relative gene expressions in CL1-0 scramble cells and stably MITF-silenced cells assayed by expression microarray and real-time RT-PCR. The scramble and three stably MITF-silenced clones were assayed in triplicate. * $p < 0.05$ (mean \pm SD, $n = 9$). (C) MITF binding targets identified by chromatin immunoprecipitation assay. (D) MITF negatively regulated FZD7 expression assayed by immunoblot. (E) The cell invasion of CL1-0 scramble cells and stably MITF-silenced cells assayed after silencing FZD7. * $p < 0.05$ (mean \pm SD, $n = 3$).

Furthermore, knockdown of *FZD7* with two independent siRNAs significantly inhibited shMITF-induced invasive ability (Figure 4E). These data suggested that MITF transcriptionally regulated *ANXA1*, *FZD7* and *PTGRI* and regulated cell invasion through *FZD7*.

Inverse correlations of *MITF* and *ANXA1* expression in lung adenocarcinoma and melanoma

To investigate the significance of *MITF* in malignancies, we analyzed The Cancer Genome Atlas (TCGA) database by OncoLnc and the pathology atlas [30, 31]. *MITF* is a well-known protumorigenic gene expressed in melanocytes. Indeed, *MITF* expression was significantly associated with poor outcome in skin cutaneous melanoma (SKCM) ($p < 0.05$, log-rank test) (Figure 5A and Supplementary Table 4). In contrast to melanoma patients, lung adenocarcinoma (LUAD) patients with high *MITF* expression had longer survival time than those with low *MITF* expression ($p < 0.05$, log-rank test) (Figure 5B and Supplementary Table 5). The results demonstrated an inverse association of *MITF* in lung adenocarcinoma.

The distinct functions of MITF in lung adenocarcinoma and melanoma attracted our interest. We hypothesized that the opposite transcriptional regulation of MITF resulted in different effects on these two malignancies. We evaluated the expression correlation of MITF and its targets between lung adenocarcinoma and melanoma by TCGA PanCancer Atlas database with cBioPortal analysis [32, 33]. We first found that *ANXA1* expression was positively correlated with MITF expression in lung adenocarcinoma (Spearman's correlation = 0.35, $q < 0.001$) but negatively correlated with MITF in melanoma (Spearman's correlation = -0.34, $q < 0.001$) (Figure 5C, 5D). Furthermore, we searched for genes that had a significant correlation with MITF expression in lung adenocarcinoma or melanoma. A total of 2,160 and 2,186 genes had significant correlations with MITF in LUAD and SKCM databases, respectively (Spearman's correlation > 0.3 or < -0.3 , q -value < 0.05) (Supplementary Figure 3). After intersecting and analyzing both gene sets, we further found that most of the genes with a positive correlation with MITF expression in lung adenocarcinoma had a negative correlation with MITF in melanoma (354 genes out of 446 total genes; $p = 1.01E-10$, Chi-square test) (Table 3). Conversely, there were 17 genes with a reverse correlation. Among these 371 genes, we found that *VEGFC*, *PDGFC* and *LRRN3* were extremely downregulated in MITF-silenced lung adenocarcinoma cells (\log_2 -fold-change < -5 , $p < 0.05$) (Figure 4A and Supplementary Table 6). Consistent with the TCGA database, MITF was positively correlated with *ANXA1*, *VEGFC*, *PDGFC* and *LRRN3*

in the East Asian cohort (Figure 5E) [34]. Furthermore, the expression levels of *ANXA1*, *VEGFC*, *PDGFC* and *LRRN3* were significantly positively associated with the survival of lung adenocarcinoma (Supplementary Figure 4A–4D). The results suggested that MITF has opposite functions in lung adenocarcinoma and melanoma, possibly by positively or negatively regulating its downstream targets.

DISCUSSION

MITF is a critical transcription factor that regulates the cell cycle, cell differentiation and cancer progression. The oncogenic role of MITF in melanoma is well defined, but the function of MITF in the NSCLC is still unclear. *MITF* contains several isoforms generated through differential use of alternative promoters that are controlled by tissue specificity, leading to MITF isoforms having distinct N-termini with a range of 419–526 amino acids [10]. MITF-A is the largest protein isoform and regulates kidney development [35]. Except for MITF-M, all isoforms contain exon 1B1b, which facilitates MITF interaction with RAG GTPases at the lysosomal surface and controls MITF nuclear-cytosol transportation [36, 37]. The expression of the shortest isoform *MITF-M* is limited to melanocytes and melanoma cells, but *MITF-A* is the major isoform expressed in our low-invasive lung adenocarcinoma cell line. *MITF-A* suppressed the invasive ability of CL1-5 cells in a dose-dependent manner that was distinct from the action of *MITF-M* in melanoma cells (Figure 2C).

Chromatin immunoprecipitation (ChIP) sequence analysis of melanoma cells indicates that MITF potentially binds between 12,000 and 100,000 genomic sites and that ~9400 of those lie within 20 kb of an annotated RefSeq gene, but genes may not obviously exhibit MITF regulation even though they have high levels of MITF occupancy at their promoter [22, 24]. We found that *ANXA1*, *FZD7* and *PTGRI* were MITF direct targets in CL1-0 cells, but these genes were not regulated in melanoma 501MEL cells [22]. However, the genes *ANXA1*, *PDGFC*, *VEGFC* and *LRRN3* were downregulated in CL1-0 shMITF-harboring cells, while they were upregulated in si-MITF melanoma 501MEL cells. In addition, they positively correlated with *MITF* in the LUAD TCGA database, but negatively correlated in the SKCM TCGA database. Accumulated data suggest that MITF executes tumor suppressive or oncogenic functions by switching its transcriptional role and targets in different malignancies.

ANXA1 is regarded as a proinvasive protein in melanoma and is correlated with poor outcome of lung cancer [38, 39], but it is associated with longer survival of NSCLC nonsmoking female and pancreatic ductal

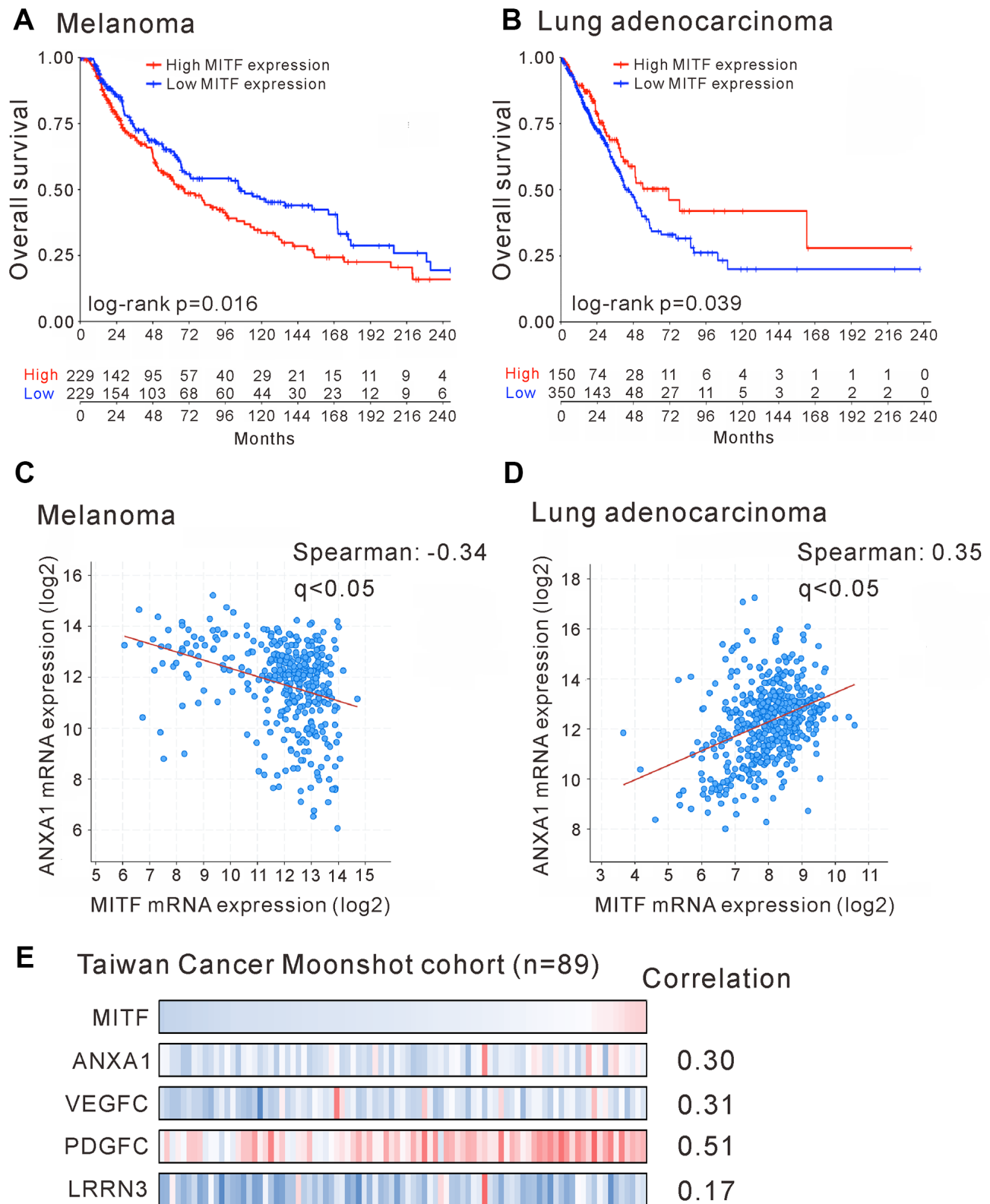


Figure 5. Reversal association and correlation of *MITF* in clinical significance. Kaplan-Meier survival estimated the association of *MITF* expression and survival of patients with skin cutaneous melanoma (SKCM) (A) or with lung adenocarcinoma (LUAD) (B) in TCGA database. The correlation of *MITF* and *ANXA1* expression in skin cutaneous melanoma (n = 363) (C) or in lung adenocarcinoma (n = 507) (D). The TCGA PanCancer Atlas database was analyzed by cBioPortal. (E) The mRNA log₂ T/N ratio of indicated genes of 89 lung adenocarcinoma patients from Taiwanese cohort and the Spearman's correlation with *MITF*. q < 0.05 was considered statistically significant.

Table 3. The number of genes with significantly positive or negative correlation with *MITF* expression in lung adenocarcinoma and melanoma.

		Lung Adenocarcinoma			<i>p</i> -value*
		Positive	Negative	Total	
Melanoma	Positive	67	17	84	1.01E-10
	Negative	354	8	362	
	Total	421	25	446	

The significant correlation were determined by q-value <0.05.

Positive: Spearman's correlation >0.3; Negative: Spearman's correlation <-0.3.

*Chi-square test was used for the statistical analyses.

adenocarcinoma patients [40, 41]. Knockdown of *ANXA1* in pancreatic ductal adenocarcinoma increases cell migration and invasion, but inhibits cell proliferation, which is similar to the phenotype at low levels of *MITF* in melanoma [41]. Although reduction of *ANXA1* in H1299 and A549 cells suppresses cell proliferation and invasion [42], in most cases, *ANXA1* acts as a tumor suppressor inhibiting tumor growth [43]. Due to its numerous, diverse, and sometimes opposing functions, *ANXA1* has been described as a “double-face” protein [44]. *PTGR1* is known as leukotriene B4 12-hydroxydehydrogenase (*LTB4DH*), which is capable of inhibiting lung cancer growth in nude mice and inactivating prostaglandins and the leukocyte chemoattractant leukotriene B4 (*LTB4*) [45, 46]. The tumor microenvironment of melanoma is shaped by the level of *MITF* expression and depletion of *MITF* stimulates the release of inflammatory cytokines such as *IL-6* and *IL-1 β* [47, 48]. We showed that *MITF* binds to the promoter of *PTGR1* and downregulates *PTGR1* expression in lung adenocarcinoma. The fundamental function of *PTGR1* in lung cancer progression is unclear but *MITF*-mediated inflammation involved in regulating *PTGR1* has been proposed.

β -Catenin activates *MITF* expression and acts as the coactivator for *MITF* to drive downstream gene expression [49, 50]. *Wnt3a* stabilizes the *MITF* protein and *MITF* enhances *WNT* signaling by driving lysosome biogenesis [51]. We found that *MITF* is involved in the canonical *WNT* pathway and binds to the promoter of *FZD7*. Supposedly, *MITF* enables transcriptional repression of *FZD7*, which encodes a receptor accounting for signaling canonical *WNT* pathways [52]. GSEA indicated that *WNT* signaling decreased in *MITF*-silenced cells, but depletion of *MITF* compromised the increase in *FZD7* expression. Downregulated *FZD7* rearranges the actin cytoskeleton and strengthens cell-cell adhesion by inhibiting *RhoA* and activating *Rac1* [53]. In agreement with that, *FZD7* is upregulated in *CL1-0* sh*MITF* cells and contributes to sh*MITF*-induced invasiveness (Figure 4E). In proliferative melanoma

cells, many *MITF* and *WNT* target genes are upregulated, but in the invasive melanoma cells, they are simultaneously downregulated [54]. After depletion of *MITF* expression in lung adenocarcinoma, cell proliferation was unaltered but tumorigenesis and metastases increased, although cell cycle and proliferation were enriched pathways. The rheostat model of *MITF* in lung adenocarcinoma is paradoxical, but the reciprocal regulation between *MITF* and *WNT* signaling matters.

The role of *MITF* in angiogenesis has been less investigated in lung adenocarcinoma. We found that the expression of the angiogenic factors *VEGFC* and *PDGFC* decreased over 60-fold in sh*MITF*-harboring cells compared with control cells. This result corresponds to less endothelial cell formation in sh*MITF* tumors. In contrast to their expression in lung adenocarcinoma, *VEGFC* and *PDGFC* are upregulated by silencing *MITF* in melanoma cells, which is in accordance with *MITF* low-expression promoting metastasis because angiogenesis usually accelerates metastasis [22]. However, the induction of vessel maturation and normalization accounts for the inhibition of both tumor growth and metastasis [55]. In cardiomyocytes, upregulated *MITF* increases *VEGF* production and promotes angiogenesis [56]. Moreover, the expression of *VEGFC* and *PDGFC* was associated with longer survival time of lung adenocarcinoma patients. Accordingly, *MITF*-mediated increase in angiogenesis in lung adenocarcinoma may be relevant to inhibition of both tumor growth and metastasis.

The transcriptional landscape of *MITF* regulation in lung adenocarcinoma was evaluated and was associated with inflammation, development, cell cycle and *WNT* signaling pathways, which is consistent with previous studies [10, 57]. However, we found that *MITF* plays a suppressive role in lung cancer progression and is a favorable prognostic marker for overall survival in NSCLC, which is contrary to the role of *MITF* in melanoma. In our study, we focused on *MITF*-mediated

metastasis. However, while some lung cancer patients responded to chemo-/radiotherapy, there was almost no response to chemo-/radiotherapy or any therapy in metastatic melanoma patients until vemurafenib received approval for melanoma treatment [58]. Therefore, the prognosis of lung cancer patients might be determined by their responses to chemo-/radiotherapy and might be associated with stem-like phenotype/MITF-low expression [59], whereas melanoma patients' prognosis might be determined largely by tumor growth and might be associated with differentiated state/MITF-high expression. Whether MITF regulates stemness and is associated with chemoresistance of lung cancer cells is an unanswered question. By analyzing both malignancies by microarrays and clinical datasets, we found an inverse pattern of gene expression and correlations with *MITF*. Although not all significantly MITF-correlated genes in clinical databases are transcriptional targets of MITF, they may be involved in the MITF regulation in some contexts. Approximately 83% of the genes that significantly correlate with *MITF* expression in the LUAD database have reverse correlations in SKCM (371 genes in total 446 genes) (Table 3). This finding is

in agreement with genes with opposite expression in CL1-0 cells and 501MEL cells. Among these genes, *ANXA1* is one of the MITF transcriptional targets. As expected, *ANXA1* plays multiple roles in cancer progression similar to MITF. We hypothesize that the transition between being an activator or a repressor and the selective regulation of downstream targets enable MITF to differentially regulate diverse functions in different malignancies, and *ANXA1* accounts at least in part for the diverse effects of MITF (Figure 6). Which function mediated by *ANXA1* in the context of MITF regulation in lung adenocarcinoma and melanoma progression, and how MITF regulates *ANXA1* warrant further investigation.

Collectively, our findings provide a new insight into the role of MITF (Figure 6). Knockdown of *MITF* increased cell invasiveness, tumorigenesis and metastasis, but decreased angiogenesis. *MITF* expression was significantly associated with favorable OS and DFS in NSCLC. Depletion of *MITF* enhanced cell invasion and migration by increasing *FZD7*, while knockdown of *FZD7* reduced shMITF-induced invasiveness. *MITF* had a positive correlation with its

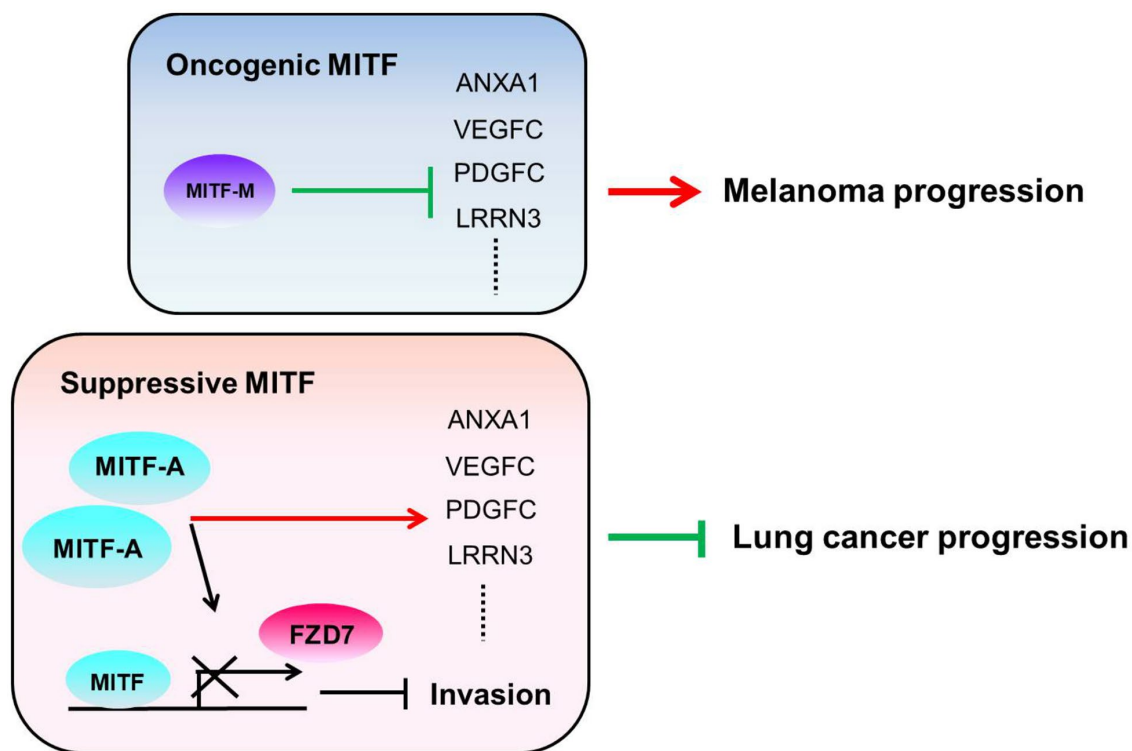


Figure 6. The illustration of the role of MITF in lung adenocarcinoma and melanoma. We hypothesize that the different MITF isoforms and their transcriptional regulations lead to opposite impacts on cancer progression. The dominant isoform *MITF-A* expresses in CL1-0 cells and inhibits cell invasion by repressing *FZD7* expression. Additionally, MITF activates *ANXA1*, *VEGFC*, *PDGFC* and *LRRN3* in lung adenocarcinoma, but suppresses *ANXA1*, *VEGFC*, *PDGFC* and *LRRN3* in melanoma. The red lines indicate the “activate” and the green lines indicate the “repress”.

target *ANXA1* in lung adenocarcinoma, but had an inverse correlation in melanoma. Our data suggest that *MITF* plays a suppressive role in lung cancer progression and serves as a prognostic marker of NSCLC. Further investigation is needed to elucidate the “rheostat model” of MITF in lung adenocarcinoma, and which transcriptional partners or modifications for MITF to shift its role in the progression of different malignancies.

MATERIALS AND METHODS

Patients and tissue specimens

A total of 70 treatment-naïve patients who underwent surgical resection and with histologically confirmed NSCLC were obtained from the Taichung Veterans General Hospital from November 1999 to August 2002. None of the patients had received neoadjuvant chemotherapy or radiation therapy. The clinicopathologic characteristic of them was shown in Table 1. Adjacent normal and tumor paired specimens of 85 NSCLC were obtained from another cohort. Informed consents were obtained from all patients and this investigation was approved by the Institutional Review Board of the Taichung Veterans General Hospital. All lung cancer patients were staged according to the American Joint Committee on Cancer Staging (AJCC) and the histology was performed with World Health Organization standards.

Cell culture and transfection

The human lung adenocarcinoma cell lines, CL1-0, CL1-1, and CL1-5 in ascending order of invasive competence were kind gifts from Professor Pan-Chyr Yang (National Taiwan University, Taipei, Taiwan) and were established in previously studies [60]. Cells were cultured in RPMI-1640 medium (Gibco, Life technologies, Carlsbad, CA) with 10% fetal bovine serum. Short hairpin RNA (shRNA) used in MITF (GenBank NM_000248) silencing studies was purchased from Open Biosystems (Huntsville, AL) [61]. The shRNA sequence targeting the human MITF gene is 5'-GCTAAAGTGATAGAAAGGCACCGCCTTAC CCAAGTAAAGCAGTACCTTTCTACCACTTTAGC-3' (the underline sequence matches MITF open reading frame nucleotide 94-122). A scrambled shRNA (5'-TGCTGTTGACAGTGAGCGATCTCGCTTGGGCGA GAGTAAGTAGTGAAGCCACAGATGTACTTACTC TCGCCAAGCGAGAGTGCCTACTGCCTCGGA-3') which does not match any known mammalian gene was used as the scramble control. CL1-0 cells were transfected with shRNAs using the Lipofectamine™ 2000 (Life technologies, Carlsbad, CA) and selected with 2.5 µg/ml puromycin (Sigma, St Louis, MO)

for stably MITF-silenced transfectants according to manufacturer's instructions. The full-length human *MITF-A* cDNA (GenBank NM_198159) was amplified from CL1-0 cells by RT-PCR and primers (forward primer: GCCATGCAGTCCGAATCGGG and reverse primer: ACAAGTGTGCTCCGCTCTTCCA) and cloned into the constitutive mammalian expression vector pEF6/V5-His TOPO (Life technologies, Carlsbad, CA).

Real-time RT-PCR

The mRNA expression level of MITF was detected by qRT-PCR on ABI prism 7900 sequence detection system (Applied Biosystems, Branchburg, NJ), performed in accordance with the manufacturer instructions. For the SYBR Green method, the MITF primers used were the following: forward primer MITF-F: 5'-CCGGCATTGTTGCTCAGA-3' and reverse primer MITF-R: 5'-AGACCCGTGGATGGAATA AGG-3' as well as the TATA box-binding protein (TBP) TBP-F: 5'-TTTTCTTGCTGCCAGTCTGGAC-3' and TBP-R: 5'-CACGAACCACGGCACTGA TT-3'. TBP was used as the internal control. For the TaqMan method, the sequences of customized MITF detection probes were as follows: MITF forward primer: 5'-CCGGCATTGTTGCTCAGA-3', reverse primer: 5'-ACTTGAAATGCAGGCTC-3', and the probe sequence: 5'-ACTTGAAATGCAGGCTC-3'. The TBP detection probe (Assay ID: Hs00427621_m1, Applied Biosystems, Branchburg, NJ) was used as the internal control. Other primers for MITF target genes were listed in Supplementary Table 7. All assays were performed in triplicate of three independent experiments.

Migration, invasion assays and colony formation

Transwell culture inserts (Costar, Cambridge, MA) were used for the assessment of cell migration and extracellular matrix invasion [8]. In migration assay, 1 × 10⁵ cells in 200 µl of serum-free RPMI were seeded on top of transwell and incubated for 8 hours. For invasion assay, the filter was coated with a thin layer of Matrigel matrix (R&D System, Minneapolis, MN). The 1 × 10⁵ cells were seeded onto the coated matrix and incubated for 18 hours. The number of migrated and invaded cells were counted at 200 × magnification under a light microscope. To determine anchorage independent colony formation assay, six-well plates were first layered with 1ml 0.7% low-melting point agarose in PBS. In the second layer, 100 cells per well were suspended in 1 ml RPMI containing 0.35% low-melting point agarose. 1ml RPMI was covered on the second layer. The plates were incubated for 4 weeks and then washed by PBS, fixed in 4% paraformaldehyde, and stained with 0.5% crystal violet. Colonies with a diameter greater than 1mm were counted under an inverted microscope.

Experimental metastasis assay *in vivo*

A single-cell suspension containing 1×10^6 cells in 100 μ l of PBS was injected into lateral tail vein of 6-week-old SCID mice. Mice were sacrificed after 10 weeks. The detection of human tumor cells in mouse lung was based on the human Alu element presented in mouse lung DNA extracts, which is modified from the method developed by Zijlstra et al. [27]. Genomic DNA was extracted from harvested tissues using the genomic DNA purification kit (Qiagen, Hilden, Germany). Primers specific for the human Alu element (reverse: 5-CGCCTGTAATCCCAGCTACT-3 and forward: 5-GATCTGGCTCACTGCAAC-3) and universal ProbeLibrary probe: #2 (Roche Diagnostics, Alameda, CA) were used to detect the human Alu repeats present in genomic DNA from mouse tissues. Each PCR contained 30 ng of genomic DNA was performed in a final volume of 20 μ l with the ABI prism 7900 system (Applied Biosystems, Branchburg, NJ). Mouse DNA was detected with mGAPDH primers (reverse: 5-AGCTTGTCATCAACGGGAAG-3 and forward: 5-TTGATGTTAGTGGGGTCTCG-3) and Universal ProbeLibrary probe: #9. The relative quantity of Alu against that of mouse GAPDH was defined as $-\Delta\text{CT} = -[\text{CT}_{\text{Alu}} - \text{CT}_{\text{GAPDH}}]$. Relative changes in metastasis were then calculated as $2^{-\Delta\text{CT}} \times K$, where K is a constant and the experimental samples in triplicate.

Angiogenesis and tumorigenesis *in vivo*

The 4×10^6 cells in 200 μ l PBS were subcutaneously injected into the dorsal region of SCID mice. Injected mice were examined every week for tumor appearance and tumor volumes were estimated from the length (a) and width (b) of the tumors using the formula $V = ab^2/2$. The 5×10^5 cells were mixed with 200 μ l growth factor reduced Matrigel (Becton Dickinson, Bedford, MA) and injected into the dorsal region of SCID mice. After 10 days, the Matrigel plug was dissected out, frozen, and fixed with acetone. Sections of the Matrigel plug (5 mm) were stained with an endothelium-specific anti-mouse CD31 monoclonal antibody (Abcam, Cambridge, England) for infiltrated endothelial cells. The CD31 positive cells were counted by blinded observers on a $200 \times$ microscopic field. A total of 21 fields/group (3 plugs \times 7 fields) were analyzed.

Microarray analysis

cRNA preparation and array hybridization were performed according to the Affymetrix GeneChip Expression Analysis Technical Manual. The biotinylated RNA was fragmented and hybridized overnight to Human genome U133 plus 2.0 GeneChip (Affymetrix, Santa Clara, CA). The raw data were processed using

GC-RMA algorithm. All hybridization experiments were performed in biological triplicate with cRNA probes prepared from three different MITF shRNA transfectants (shMITF-1, shMITF-2, shMITF-3) and three different scramble ones (scramble-1, scramble-2 and scramble-3). These array data had been uploaded into GEO with GSE146868.

Isoform-specific RT-PCR

Total RNA was isolated by the TRIzol reagent (Life Technologies, Carlsbad, CA) and reverse-transcribed using SuperScript™ II (Life Technologies, Carlsbad, CA) and random primers. Subsequently, 15 ng of the cDNA was used to analyze the presence of each isoform using PCR amplification. Isoform-specific 5' primers were used for each reaction with a common 3' primer (MITF-com R) in exon 5 (Supplementary Table 7) [62]. To detect total MITF expression, primers were designed to amplify a conserved fragment from exon 5 (forward: MITF-exon5 F) to exon 9 (reverse: MITF-exon9 R) and GAPDH was acted as an internal control. Cycling times and temperatures for PCR were 94° C for 30 sec, 55° C for 30 sec, and 72° C for 1 min for 35 cycles except 30 cycles for MITF exon 5-9. PCR products were resolved on a 2% agarose gel.

Chromatin immunoprecipitation assay and immunoblot

Transcription start sites of selected MITF-regulated genes were obtained from the Transcriptional Regulatory Element Database (<http://rulai.cshl.edu/cgi-bin/TRED/tred.cgi?process=home>). TRANSFAC Professional database (BioBase Biological Databases) was used to identify potential MITF binding sites for primer designed (Supplementary Table 8). The chromatin immunoprecipitation assay was performed according to the protocol of Upstate Biotechnology, Inc. (Lake Placid, NY). Briefly, the samples were sonicated to shear DNA to lengths between 200 and 1000 bps and then incubated for 16 hours at 4° C with mouse anti-MITF monoclonal antibody, rabbit anti-Histone H3 antibody and IgG (C5, Calbiochem, La Jolla, CA). Immune complexes were precipitated and the MITF-binding DNA was purified. The PCR was performed with primers flanking the putative MITF binding sites. The PCR product was analyzed by agarose gel electrophoresis. The immunoblot was performed as previously described [8]. Antibodies used for immunoblot were listed in Supplementary Table 9.

Statistical analysis

Overall survival curves were calculated by the Kaplan–Meier analysis, and the difference between survival

curves was tested by log-rank test. Each cutoff point for overall survival for definition of the high/low-MITF expression groups is listed in Supplementary Table 4 and Table 5. The univariate and multivariate Cox proportional hazards regression with covariates age, gender, cell types, stage, and *MITF* expression was performed to evaluate the prognostic abilities of variables. Student's t test, and Fisher's exact test were used to compare the difference between groups for continue or categorical data, respectively. All statistical analyses were done by SPSS (IBM, Chicago, IL) and SAS 9 (SAS Institute Inc., Cary, NC). All tests were two sided and p-value <0.05 was considered statistically significant.

AUTHOR CONTRIBUTIONS

Sung-Liang Yu and Jeremy J.W. Chen directed the project. Pan-Chyr Yang gave professional consultations. Wen-Hsin Chang, Ching-Cheng Chiang and Chia-Yu Wang performed and analyzed most of the experiments. Ching-Cheng Chiang and Su-Chin Chiu performed animal experiments. Yi-Jing Hsiao and Yin-Chen Hsu performed a clinical analysis of the public domain database. Gee-Chen Chang provided the clinical samples. Hsuan-Yu Chen and Chien-Yu Lin were responsible for the statistical analysis. Yan-Ming Chen analyzed the gene correlation. Yi-Ju Chen and Yu-Ju Chen provided and analyzed the transcriptome of the Taiwanese cohort. Yi-Jing Hsiao and Sung-Liang Yu drafted and edited the manuscript.

ACKNOWLEDGMENTS

We thank the Pharmacogenomics Laboratory of the National Core Facility for Biopharmaceuticals and the NGS and Microarray Core Facility of NTU Centers of Genomic and Precision Medicine for technical supports.

CONFLICTS OF INTEREST

The authors declare that there are no conflicts of interest.

FUNDING

This work was supported by Ministry of Science and Technology (MOST-96-2314-B-005-001, MOST108-2319-B-002-001), the Next-generation Pathway of Taiwan Cancer Precision Medicine Program (AS-KPQ-107-TCPMP) at Academia Sinica, and the "Center of Precision Medicine" from The Featured Areas Research Center Program within the framework of the Higher Education Sprout Project by the Ministry of Education (MOE) in Taiwan.

REFERENCES

1. Siegel RL, Miller KD, Jemal A. Cancer statistics, 2020. *CA Cancer J Clin.* 2020; 70:7–30. <https://doi.org/10.3322/caac.21590> PMID:31912902
2. Chansky K, Detterbeck FC, Nicholson AG, Rusch VW, Vallières E, Groome P, Kennedy C, Krasnik M, Peake M, Shemanski L, Bolejack V, Crowley JJ, Asamura H, Rami-Porta R, and IASLC Staging and Prognostic Factors Committee, Advisory Boards, and Participating Institutions. The IASLC lung cancer staging project: external validation of the revision of the TNM stage groupings in the Eighth edition of the TNM classification of lung cancer. *J Thorac Oncol.* 2017; 12:1109–21. <https://doi.org/10.1016/j.jtho.2017.04.011> PMID:28461257
3. Wang C, Wu Y, Shao J, Liu D, Li W. Clinicopathological variables influencing overall survival, recurrence and post-recurrence survival in resected stage I non-small-cell lung cancer. *BMC Cancer.* 2020; 20:150. <https://doi.org/10.1186/s12885-020-6621-1> PMID:32093621
4. Rusch VW, Crowley J, Giroux DJ, Goldstraw P, Im JG, Tsuboi M, Tsuchiya R, Vansteenkiste J, and International Staging Committee, and Cancer Research and Biostatistics, and Observers to the Committee, and Participating Institutions. The IASLC Lung Cancer Staging Project: proposals for the revision of the N descriptors in the forthcoming seventh edition of the TNM classification for lung cancer. *J Thorac Oncol.* 2007; 2:603–12. <https://doi.org/10.1097/JTO.0b013e31807ec803> PMID:17607115
5. Gupta GP, Massagué J. Cancer metastasis: building a framework. *Cell.* 2006; 127:679–95. <https://doi.org/10.1016/j.cell.2006.11.001> PMID:17110329
6. Akhtar M, Haider A, Rashid S, Al-Nabet AD. Paget's "seed and soil" theory of cancer metastasis: an idea whose time has come. *Adv Anat Pathol.* 2019; 26:69–74. <https://doi.org/10.1097/PAP.0000000000000219> PMID:30339548
7. Hsu CY, Chang GC, Chen YJ, Hsu YC, Hsiao YJ, Su KY, Chen HY, Lin CY, Chen JS, Chen YJ, Hong QS, Ku WH, Wu CY, et al. FAM198B is associated with prolonged survival and inhibits metastasis in lung adenocarcinoma via blockage of ERK-mediated MMP-1 expression. *Clin Cancer Res.* 2018; 24:916–26. <https://doi.org/10.1158/1078-0432.CCR-17-1347> PMID:29217529
8. Chen CC, Chen HY, Su KY, Hong QS, Yan BS, Chen CH, Pan SH, Chang YL, Wang CJ, Hung PF, Yuan S, Chang

- GC, Chen JJ, et al. Shisa3 is associated with prolonged survival through promoting β -catenin degradation in lung cancer. *Am J Respir Crit Care Med*. 2014; 190:433–44.
<https://doi.org/10.1164/rccm.201312-2256OC>
PMID:25036006
9. Hsiao YJ, Su KY, Hsu YC, Chang GC, Chen JS, Chen HY, Hong QS, Hsu SC, Kang PH, Hsu CY, Ho BC, Yang TH, Wang CY, et al. SPANXA suppresses EMT by inhibiting c-JUN/SNAI2 signaling in lung adenocarcinoma. *Oncotarget*. 2016; 7:44417–29.
<https://doi.org/10.18632/oncotarget.10088>
PMID:27323831
 10. Goding CR, Arnheiter H. MITF-the first 25 years. *Genes Dev*. 2019; 33:983–1007.
<https://doi.org/10.1101/gad.324657.119>
PMID:31123060
 11. Bharti K, Gasper M, Ou J, Brucato M, Clore-Gronenborn K, Pickel J, Arnheiter H. A regulatory loop involving PAX6, MITF, and Wnt signaling controls retinal pigment epithelium development. *PLoS Genet*. 2012; 8:e1002757.
<https://doi.org/10.1371/journal.pgen.1002757>
PMID:22792072
 12. Garraway LA, Widlund HR, Rubin MA, Getz G, Berger AJ, Ramaswamy S, Beroukhi R, Milner DA, Granter SR, Du J, Lee C, Wagner SN, Li C, et al. Integrative genomic analyses identify MITF as a lineage survival oncogene amplified in Malignant melanoma. *Nature*. 2005; 436:117–22.
<https://doi.org/10.1038/nature03664> PMID:16001072
 13. Carreira S, Goodall J, Denat L, Rodriguez M, Nuciforo P, Hoek KS, Testori A, Larue L, Goding CR. Mitf regulation of Dia1 controls melanoma proliferation and invasiveness. *Genes Dev*. 2006; 20:3426–39.
<https://doi.org/10.1101/gad.406406> PMID:17182868
 14. Vachtenheim J, Ondrušová L. Microphthalmia-associated transcription factor expression levels in melanoma cells contribute to cell invasion and proliferation. *Exp Dermatol*. 2015; 24:481–84.
<https://doi.org/10.1111/exd.12724> PMID:25866058
 15. Tuncer E, Calçada RR, Zingg D, Varum S, Cheng P, Freiberger SN, Deng CX, Kleiter I, Levesque MP, Dummer R, Sommer L. SMAD signaling promotes melanoma metastasis independently of phenotype switching. *J Clin Invest*. 2019; 129:2702–16.
<https://doi.org/10.1172/JCI94295> PMID:31039140
 16. Hartman ML, Czyz M. MITF in melanoma: mechanisms behind its expression and activity. *Cell Mol Life Sci*. 2015; 72:1249–60.
<https://doi.org/10.1007/s00018-014-1791-0>
PMID:25433395
 17. Rachmin I, Amsalem E, Golomb E, Beeri R, Gilon D, Fang P, Nechushtan H, Kay G, Guo M, Yiqing PL, Foo RS, Fisher DE, Razin E, Tshori S. FHL2 switches MITF from activator to repressor of erbin expression during cardiac hypertrophy. *Int J Cardiol*. 2015; 195:85–94.
<https://doi.org/10.1016/j.ijcard.2015.05.108>
PMID:26025865
 18. McGill GG, Horstmann M, Widlund HR, Du J, Motyckova G, Nishimura EK, Lin YL, Ramaswamy S, Avery W, Ding HF, Jordan SA, Jackson IJ, Korsmeyer SJ, et al. Bcl2 regulation by the melanocyte master regulator mitf modulates lineage survival and melanoma cell viability. *Cell*. 2002; 109:707–18.
[https://doi.org/10.1016/s0092-8674\(02\)00762-6](https://doi.org/10.1016/s0092-8674(02)00762-6)
PMID:12086670
 19. Du J, Widlund HR, Horstmann MA, Ramaswamy S, Ross K, Huber WE, Nishimura EK, Golub TR, Fisher DE. Critical role of CDK2 for melanoma growth linked to its melanocyte-specific transcriptional regulation by MITF. *Cancer Cell*. 2004; 6:565–76.
<https://doi.org/10.1016/j.ccr.2004.10.014>
PMID:15607961
 20. Carreira S, Goodall J, Aksan I, La Rocca SA, Galibert MD, Denat L, Larue L, Goding CR. Mitf cooperates with Rb1 and activates p21Cip1 expression to regulate cell cycle progression. *Nature*. 2005; 433:764–69.
<https://doi.org/10.1038/nature03269> PMID:15716956
 21. Bianchi-Smiraglia A, Bagati A, Fink EE, Moparthy S, Wawrzyniak JA, Marvin EK, Battaglia S, Jowdy P, Kolesnikova M, Foley CE, Berman AE, Kozlova NI, Lipchick BC, et al. Microphthalmia-associated transcription factor suppresses invasion by reducing intracellular GTP pools. *Oncogene*. 2017; 36:84–96.
<https://doi.org/10.1038/onc.2016.178> PMID:27181209
 22. Strub T, Giuliano S, Ye T, Bonet C, Keime C, Kobi D, Le Gras S, Cormont M, Ballotti R, Bertolotto C, Davidson I. Essential role of microphthalmia transcription factor for DNA replication, mitosis and genomic stability in melanoma. *Oncogene*. 2011; 30:2319–32.
<https://doi.org/10.1038/onc.2010.612> PMID:21258399
 23. Hoek KS, Schlegel NC, Eichhoff OM, Widmer DS, Praetorius C, Einarsson SO, Valgeirsdottir S, Bergsteinsdottir K, Schepsky A, Dummer R, Steingrimsdottir E. Novel MITF targets identified using a two-step DNA microarray strategy. *Pigment Cell Melanoma Res*. 2008; 21:665–76.
<https://doi.org/10.1111/j.1755-148X.2008.00505.x>
PMID:19067971
 24. Webster DE, Barajas B, Bussat RT, Yan KJ, Neela PH, Flockhart RJ, Kovalski J, Zehnder A, Khavari PA. Enhancer-targeted genome editing selectively blocks innate resistance to onco kinase inhibition. *Genome Res*. 2014; 24:751–60.

- <https://doi.org/10.1101/gr.166231.113>
PMID:[24443471](https://pubmed.ncbi.nlm.nih.gov/24443471/)
25. Chen CH, Chuang SM, Yang MF, Liao JW, Yu SL, Chen JJ. A novel function of YWHAZ/ β -catenin axis in promoting epithelial-mesenchymal transition and lung cancer metastasis. *Mol Cancer Res*. 2012; 10:1319–31.
<https://doi.org/10.1158/1541-7786.MCR-12-0189>
PMID:[22912335](https://pubmed.ncbi.nlm.nih.gov/22912335/)
26. Nagy Á, Lánckzy A, Menyhárt O, Gyórfy B. Validation of miRNA prognostic power in hepatocellular carcinoma using expression data of independent datasets. *Sci Rep*. 2018; 8:9227.
<https://doi.org/10.1038/s41598-018-27521-y>
PMID:[29907753](https://pubmed.ncbi.nlm.nih.gov/29907753/)
27. Zijlstra A, Mellor R, Panzarella G, Aimes RT, Hooper JD, Marchenko ND, Quigley JP. A quantitative analysis of rate-limiting steps in the metastatic cascade using human-specific real-time polymerase chain reaction. *Cancer Res*. 2002; 62:7083–92.
PMID:[12460930](https://pubmed.ncbi.nlm.nih.gov/12460930/)
28. Subramanian A, Tamayo P, Mootha VK, Mukherjee S, Ebert BL, Gillette MA, Paulovich A, Pomeroy SL, Golub TR, Lander ES, Mesirov JP. Gene set enrichment analysis: a knowledge-based approach for interpreting genome-wide expression profiles. *Proc Natl Acad Sci USA*. 2005; 102:15545–50.
<https://doi.org/10.1073/pnas.0506580102>
PMID:[16199517](https://pubmed.ncbi.nlm.nih.gov/16199517/)
29. Mootha VK, Lindgren CM, Eriksson KF, Subramanian A, Sihag S, Lehar J, Puigserver P, Carlsson E, Ridderstråle M, Laurila E, Houstis N, Daly MJ, Patterson N, et al. PGC-1 α -responsive genes involved in oxidative phosphorylation are coordinately downregulated in human diabetes. *Nat Genet*. 2003; 34:267–73.
<https://doi.org/10.1038/ng1180> PMID:[12808457](https://pubmed.ncbi.nlm.nih.gov/12808457/)
30. Anaya J. OncoLnc: linking TCGA survival data to mRNAs, miRNAs, and lncRNAs. *PeerJ Comput Sci*. 2016; 2:e67.
<https://doi.org/10.7717/peerj-cs.67>
31. Uhlen M, Zhang C, Lee S, Sjöstedt E, Fagerberg L, Bidkhori G, Benfeitas R, Arif M, Liu Z, Edfors F, Sanli K, von Feilitzen K, Oksvold P, et al. A pathology atlas of the human cancer transcriptome. *Science*. 2017; 357:eaan2507.
<https://doi.org/10.1126/science.aan2507>
PMID:[28818916](https://pubmed.ncbi.nlm.nih.gov/28818916/)
32. Cerami E, Gao J, Dogrusoz U, Gross BE, Sumer SO, Aksoy BA, Jacobsen A, Byrne CJ, Heuer ML, Larsson E, Antipin Y, Reva B, Goldberg AP, et al. The cBio cancer genomics portal: an open platform for exploring multidimensional cancer genomics data. *Cancer Discov*. 2012; 2:401–04.
<https://doi.org/10.1158/2159-8290.CD-12-0095>
PMID:[22588877](https://pubmed.ncbi.nlm.nih.gov/22588877/)
33. Gao J, Aksoy BA, Dogrusoz U, Dresdner G, Gross B, Sumer SO, Sun Y, Jacobsen A, Sinha R, Larsson E, Cerami E, Sander C, Schultz N. Integrative analysis of complex cancer genomics and clinical profiles using the cBioPortal. *Sci Signal*. 2013; 6:pl1.
<https://doi.org/10.1126/scisignal.2004088>
PMID:[23550210](https://pubmed.ncbi.nlm.nih.gov/23550210/)
34. Chen YJ, Roumeliotis TI, Chang YH, Chen CT, Han CL, Lin MH, Chen HW, Chang GC, Chang YL, Wu CT, Lin MW, Hsieh MS, Wang YT, et al. Proteogenomics of non-smoking lung cancer in east Asia delineates molecular signatures of pathogenesis and progression. *Cell*. 2020; 182:226–44.e17.
<https://doi.org/10.1016/j.cell.2020.06.012>
PMID:[32649875](https://pubmed.ncbi.nlm.nih.gov/32649875/)
35. Phelep A, Laouari D, Bharti K, Burtin M, Tammaccaro S, Garbay S, Nguyen C, Vasseur F, Blanc T, Berissi S, Langa-Vives F, Fischer E, Druilhe A, et al. MITF - a controls branching morphogenesis and nephron endowment. *PLoS Genet*. 2017; 13:e1007093.
<https://doi.org/10.1371/journal.pgen.1007093>
PMID:[29240767](https://pubmed.ncbi.nlm.nih.gov/29240767/)
36. Martina JA, Puertollano R. Rag GTPases mediate amino acid-dependent recruitment of TFEB and MITF to lysosomes. *J Cell Biol*. 2013; 200:475–91.
<https://doi.org/10.1083/jcb.201209135> PMID:[23401004](https://pubmed.ncbi.nlm.nih.gov/23401004/)
37. Ngeow KC, Friedrichsen HJ, Li L, Zeng Z, Andrews S, Volpon L, Brunson H, Berridge G, Picard S, Fischer R, Lisle R, Knapp S, Filippakopoulos P, et al. BRAF/MAPK and GSK3 signaling converges to control MITF nuclear export. *Proc Natl Acad Sci USA*. 2018; 115:E8668–77.
<https://doi.org/10.1073/pnas.1810498115>
PMID:[30150413](https://pubmed.ncbi.nlm.nih.gov/30150413/)
38. Boudhraa Z, Rondepierre F, Ouchchane L, Kintossou R, Trzeciakiewicz A, Franck F, Kanitakis J, Labeille B, Joubert-Zakeyh J, Bouchon B, Perrot JL, Mansard S, Papon J, et al. Annexin A1 in primary tumors promotes melanoma dissemination. *Clin Exp Metastasis*. 2014; 31:749–60.
<https://doi.org/10.1007/s10585-014-9665-2>
PMID:[24997993](https://pubmed.ncbi.nlm.nih.gov/24997993/)
39. Biaoxue R, Xiling J, Shuanying Y, Wei Z, Xiguang C, Jinsui W, Min Z. Upregulation of Hsp90-beta and annexin A1 correlates with poor survival and lymphatic metastasis in lung cancer patients. *J Exp Clin Cancer Res*. 2012; 31:70.
<https://doi.org/10.1186/1756-9966-31-70>
PMID:[22929401](https://pubmed.ncbi.nlm.nih.gov/22929401/)
40. Yang G, Chen Q, Xiao J, Zhang H, Wang Z, Lin X. Identification of genes and analysis of prognostic

- values in nonsmoking females with non-small cell lung carcinoma by bioinformatics analyses. *Cancer Manag Res.* 2018; 10:4287–95.
<https://doi.org/10.2147/CMAR.S174409>
PMID:[30349363](https://pubmed.ncbi.nlm.nih.gov/30349363/)
41. Liu QH, Shi ML, Bai J, Zheng JN. Identification of ANXA1 as a lymphatic metastasis and poor prognostic factor in pancreatic ductal adenocarcinoma. *Asian Pac J Cancer Prev.* 2015; 16:2719–24.
<https://doi.org/10.7314/apjcp.2015.16.7.2719>
PMID:[25854353](https://pubmed.ncbi.nlm.nih.gov/25854353/)
42. Fang Y, Guan X, Cai T, Long J, Wang H, Xie X, Zhang Y. Knockdown of ANXA1 suppresses the biological behavior of human NSCLC cells in vitro. *Mol Med Rep.* 2016; 13:3858–66.
<https://doi.org/10.3892/mmr.2016.5022>
PMID:[27035116](https://pubmed.ncbi.nlm.nih.gov/27035116/)
43. Foo SL, Yap G, Cui J, Lim LH. annexin-A1 - a blessing or a curse in cancer? *Trends Mol Med.* 2019; 25:315–27.
<https://doi.org/10.1016/j.molmed.2019.02.004>
PMID:[30871809](https://pubmed.ncbi.nlm.nih.gov/30871809/)
44. Shao G, Zhou H, Zhang Q, Jin Y, Fu C. Advancements of annexin A1 in inflammation and tumorigenesis. *Onco Targets Ther.* 2019; 12:3245–54.
<https://doi.org/10.2147/OTT.S202271> PMID:[31118675](https://pubmed.ncbi.nlm.nih.gov/31118675/)
45. Zhao Y, Weng CC, Tong M, Wei J, Tai HH. Restoration of leukotriene B(4)-12-hydroxydehydrogenase/15-oxo-prostaglandin 13-reductase (LTBDH/PGR) expression inhibits lung cancer growth in vitro and in vivo. *Lung Cancer.* 2010; 68:161–69.
<https://doi.org/10.1016/j.lungcan.2009.06.011>
PMID:[19595472](https://pubmed.ncbi.nlm.nih.gov/19595472/)
46. Jala VR, Bodduluri SR, Satpathy SR, Chheda Z, Sharma RK, Haribabu B. The yin and yang of leukotriene B₄ mediated inflammation in cancer. *Semin Immunol.* 2017; 33:58–64.
<https://doi.org/10.1016/j.smim.2017.09.005>
PMID:[28982616](https://pubmed.ncbi.nlm.nih.gov/28982616/)
47. Riesenbergs S, Groetchen A, Siddaway R, Bald T, Reinhardt J, Smorra D, Kohlmeyer J, Renn M, Phung B, Aymans P, Schmidt T, Hornung V, Davidson I, et al. MITF and c-Jun antagonism interconnects melanoma dedifferentiation with pro-inflammatory cytokine responsiveness and myeloid cell recruitment. *Nat Commun.* 2015; 6:8755.
<https://doi.org/10.1038/ncomms9755> PMID:[26530832](https://pubmed.ncbi.nlm.nih.gov/26530832/)
48. Tirosh I, Izar B, Prakadan SM, Wadsworth MH 2nd, Treacy D, Trombetta JJ, Rotem A, Rodman C, Lian C, Murphy G, Fallahi-Sichani M, Dutton-Regester K, Lin JR, et al. Dissecting the multicellular ecosystem of metastatic melanoma by single-cell RNA-seq. *Science.* 2016; 352:189–96.
<https://doi.org/10.1126/science.aad0501>
PMID:[27124452](https://pubmed.ncbi.nlm.nih.gov/27124452/)
49. Takeda K, Yasumoto K, Takada R, Takada S, Watanabe K, Udono T, Saito H, Takahashi K, Shibahara S. Induction of melanocyte-specific microphthalmia-associated transcription factor by Wnt-3a. *J Biol Chem.* 2000; 275:14013–16.
<https://doi.org/10.1074/jbc.c000113200>
PMID:[10747853](https://pubmed.ncbi.nlm.nih.gov/10747853/)
50. Schepsky A, Bruser K, Gunnarsson GJ, Goodall J, Hallsson JH, Goding CR, Steingrimsdottir E, Hecht A. The microphthalmia-associated transcription factor mitf interacts with beta-catenin to determine target gene expression. *Mol Cell Biol.* 2006; 26:8914–27.
<https://doi.org/10.1128/MCB.02299-05>
PMID:[17000761](https://pubmed.ncbi.nlm.nih.gov/17000761/)
51. Ploper D, Taelman VF, Robert L, Perez BS, Titz B, Chen HW, Graeber TG, von Euw E, Ribas A, De Robertis EM. MITF drives endolysosomal biogenesis and potentiates Wnt signaling in melanoma cells. *Proc Natl Acad Sci USA.* 2015; 112:E420–29.
<https://doi.org/10.1073/pnas.1424576112>
PMID:[25605940](https://pubmed.ncbi.nlm.nih.gov/25605940/)
52. Abu-Elmagd M, Garcia-Morales C, Wheeler GN. Frizzled7 mediates canonical Wnt signaling in neural crest induction. *Dev Biol.* 2006; 298:285–98.
<https://doi.org/10.1016/j.ydbio.2006.06.037>
PMID:[16928367](https://pubmed.ncbi.nlm.nih.gov/16928367/)
53. Asad M, Wong MK, Tan TZ, Choolani M, Low J, Mori S, Virshup D, Thiery JP, Huang RY. FZD7 drives in vitro aggressiveness in stem-a subtype of ovarian cancer via regulation of non-canonical Wnt/PCP pathway. *Cell Death Dis.* 2014; 5:e1346.
<https://doi.org/10.1038/cddis.2014.302>
PMID:[25032869](https://pubmed.ncbi.nlm.nih.gov/25032869/)
54. Hoek KS, Eichhoff OM, Schlegel NC, Döbbling U, Kobert N, Schaerer L, Hemmi S, Dummer R. In vivo switching of human melanoma cells between proliferative and invasive states. *Cancer Res.* 2008; 68:650–56.
<https://doi.org/10.1158/0008-5472.CAN-07-2491>
PMID:[18245463](https://pubmed.ncbi.nlm.nih.gov/18245463/)
55. Rolny C, Mazzone M, Tugues S, Laoui D, Johansson I, Coulon C, Squadrito ML, Segura I, Li X, Knevels E, Costa S, Vinckier S, Dresselaer T, et al. HRG inhibits tumor growth and metastasis by inducing macrophage polarization and vessel normalization through downregulation of PlGF. *Cancer Cell.* 2011; 19:31–44.
<https://doi.org/10.1016/j.ccr.2010.11.009>
PMID:[21215706](https://pubmed.ncbi.nlm.nih.gov/21215706/)
56. Qian L, Pan S, Shi L, Zhou Y, Sun L, Wan Z, Ding Y, Qian J. Downregulation of microRNA-218 is cardioprotective

- against cardiac fibrosis and cardiac function impairment in myocardial infarction by binding to MITF. *Aging* (Albany NY). 2019; 11:5368–88.
<https://doi.org/10.18632/aging.102112>
PMID:[31408435](https://pubmed.ncbi.nlm.nih.gov/31408435/)
57. Kawakami A, Fisher DE. The master role of microphthalmia-associated transcription factor in melanocyte and melanoma biology. *Lab Invest*. 2017; 97:649–56.
<https://doi.org/10.1038/labinvest.2017.9>
PMID:[28263292](https://pubmed.ncbi.nlm.nih.gov/28263292/)
58. Chapman PB, Hauschild A, Robert C, Haanen JB, Ascierto P, Larkin J, Dummer R, Garbe C, Testori A, Maio M, Hogg D, Lorigan P, Lebbe C, et al, and BRIM-3 Study Group. Improved survival with vemurafenib in melanoma with BRAF V600E mutation. *N Engl J Med*. 2011; 364:2507–16.
<https://doi.org/10.1056/NEJMoa1103782>
PMID:[21639808](https://pubmed.ncbi.nlm.nih.gov/21639808/)
59. Tsoi J, Robert L, Paraiso K, Galvan C, Sheu KM, Lay J, Wong DJ, Atefi M, Shirazi R, Wang X, Braas D, Grasso CS, Palaskas N, et al. Multi-stage differentiation defines melanoma subtypes with differential vulnerability to drug-induced iron-dependent oxidative stress. *Cancer Cell*. 2018; 33:890–904.e5.
<https://doi.org/10.1016/j.ccell.2018.03.017>
PMID:[29657129](https://pubmed.ncbi.nlm.nih.gov/29657129/)
60. Chu YW, Yang PC, Yang SC, Shyu YC, Hendrix MJ, Wu R, Wu CW. Selection of invasive and metastatic subpopulations from a human lung adenocarcinoma cell line. *Am J Respir Cell Mol Biol*. 1997; 17:353–60.
<https://doi.org/10.1165/ajrcmb.17.3.2837>
PMID:[9308922](https://pubmed.ncbi.nlm.nih.gov/9308922/)
61. Paddison PJ, Silva JM, Conklin DS, Schlabach M, Li M, Aruleba S, Baliya V, O’Shaughnessy A, Gnoj L, Scobie K, Chang K, Westbrook T, Cleary M, et al. A resource for large-scale RNA-interference-based screens in mammals. *Nature*. 2004; 428:427–31.
<https://doi.org/10.1038/nature02370> PMID:[15042091](https://pubmed.ncbi.nlm.nih.gov/15042091/)
62. Hershey CL, Fisher DE. Genomic analysis of the microphthalmia locus and identification of the MITF-J/Mitf-J isoform. *Gene*. 2005; 347:73–82.
<https://doi.org/10.1016/j.gene.2004.12.002>
PMID:[15715979](https://pubmed.ncbi.nlm.nih.gov/15715979/)

SUPPLEMENTARY MATERIALS

Supplementary Materials and Methods

Cell culture and transfection

The human lung adenocarcinoma cell lines, CL1-0, CL1-1, and CL1-5, in ascending order of invasive competence, were established in previously studies [1]. Cells were cultured in RPMI-1640 medium (Gibco, Life technologies, Carlsbad, CA) with 10% fetal bovine serum. Short hairpin RNA (shRNA) used in MITF (GenBank NM_000248) silencing studies was purchased from Open Biosystems (Huntsville, AL) [2]. The shRNA sequence targeting the human MITF gene is 5'-GCTAAAGTGATAGAAAGGCACCGCCTTACCCAAGTAAAGCAGTACCTTTCTACCACTTTAGC-3' (the underline sequence matches MITF open reading frame nucleotide 94-122). A scrambled shRNA (5'-TGCTGTTGACAGTGAGCGATCTCGCTTGGGCGAGAGTAAGTAGTGAAGCCACAGATGTACTTACTCTCGCCCAAGCGAGAGTGCCTACTGCCTCGGA-3') which does not match any known mammalian gene was used as the scramble control. CL1-0 cells were transfected with shRNAs using the Lipofectamine™ 2000 (Life technologies, Carlsbad, CA) and selected with 2.5 µg/ml puromycin (Sigma, St Louis, MO) for stably MITF-silenced transfectants according to manufacturer's instructions. The full-length human *MITF-A* cDNA (GenBank NM_198159) was amplified from CL1-0 cells by RT-PCR and primers (forward primer: GCCATGCAGTCCGAATCGGG and reverse primer: ACAAGTGTGCTCCGTCTCTTCCA) and cloned into the constitutive mammalian expression vector pEF6/V5-His TOPO (Life technologies, Carlsbad, CA).

Real-time RT-PCR

The mRNA expression level of MITF was detected by qRT-PCR on ABI prism 7900 sequence detection system (Applied Biosystems, Branchburg, NJ), performed in accordance with the manufacturer instructions. For the SYBR Green method, the MITF primers used were the following: forward primer MITF-F: 5'-CCGGCATTGTTGCTCAGA-3' and reverse primer MITF-R: 5'-AGACCCGTGGATGGAA TAAGG-3' as well as the TATA box-binding protein (TBP) TBP-F: 5'-TTTTCTTGCTGCCAGTCTGGAC-3' and TBP-R: 5'-CACGAACCACGGCACTGA TT-3'. TBP was used as the internal control. For the TaqMan method, the sequences of customized MITF detection probes were as follows: MITF forward primer: 5'-CCGGCATTGTTGCTCAGA-3', reverse primer: 5'-ACTTGAAATGCAGGCTC-3', and the

probe sequence: 5'- ACTTGAAATGCAGGCTC-3'. The TBP detection probe (Assay ID: Hs00427621_m1, Applied Biosystems, Branchburg, NJ) was used as the internal control. Other primers for MITF target genes were listed in Table S1. All experiments were performed in triplicate.

Cell proliferation

Cells from each clonal line were seeded onto 96-well plates (3×10³ cells/well). After culturing for various durations, cell proliferation was evaluated by thiazolyl bluetetrazolium bromide (MTT) assay according to the manufacturer's protocol (Chemicon, Temecula, CA). Briefly, 10 µl of the MTT solution (5mg/mL) was added to each well, the cells were cultured for another 4 hours at 37° C, and 100 µl of DMSO was added to each well and mixed vigorously to solubilize colored crystals produced within the cells. The absorbance at 570 nm (630 nm as the reference) was measured by using a multi-well scanning spectrophotometer Victor3 (Perkin-Elmer, Boston, MA). Experiments were performed three times in triplicate.

Statistical analysis

Overall survival curves were calculated by the Kaplan–Meier analysis, and the difference between survival curves was tested by log-rank test. Each cutoff point for overall survival for definition of the high/low-MITF expression groups is listed in Supplementary Table 7 and Table 8. The univariate and multivariate Cox proportional hazards regression with covariates age, gender, cell types, stage, and *MITF* expression was performed to evaluate the prognostic abilities of variables. Student's t test, and Fisher's exact test were used to compare the difference between groups for continue or categorical data, respectively. All statistical analyses were done by SPSS (IBM, Chicago, IL) and SAS 9 (SAS Institute Inc., Cary, NC). All tests were two sided and p-value <0.05 was considered statistically significant.

REFERENCES

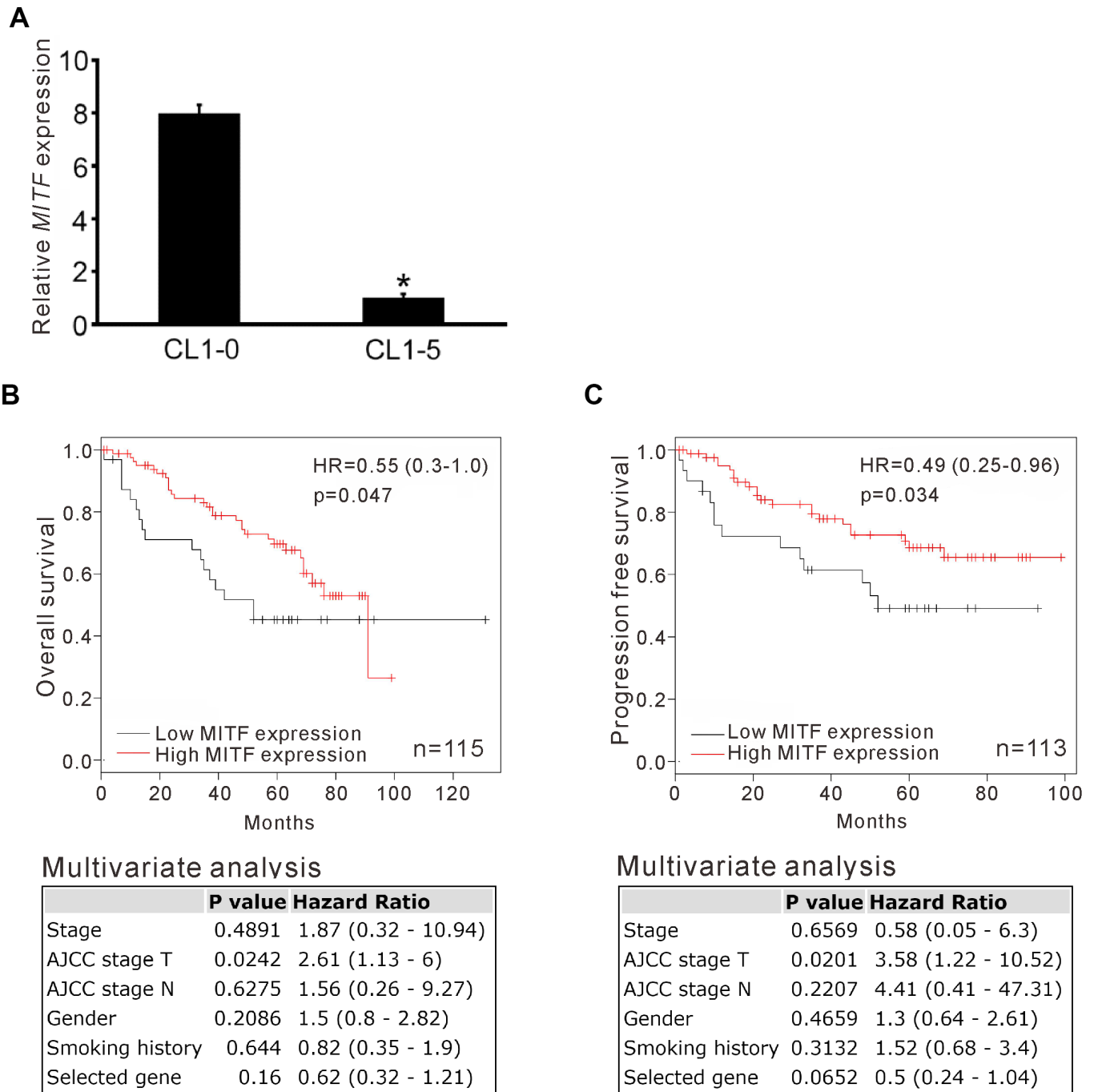
1. Chu YW, Yang PC, Yang SC, Shyu YC, Hendrix MJ, Wu R, Wu CW. Selection of invasive and metastatic subpopulations from a human lung adenocarcinoma cell line. *Am J Respir Cell Mol Biol*. 1997; 17:353–60. <https://doi.org/10.1165/ajrcmb.17.3.2837> PMID:9308922
2. Paddison PJ, Silva JM, Conklin DS, Schlabach M, Li M, Aruleba S, Balija V, O'Shaughnessy A, Gnoj L, Scobie K,

Chang K, Westbrook T, Cleary M, et al. A resource for large-scale RNA-interference-based screens in mammals. *Nature*. 2004; 428:427–31.
<https://doi.org/10.1038/nature02370>
PMID:[15042091](https://pubmed.ncbi.nlm.nih.gov/15042091/)

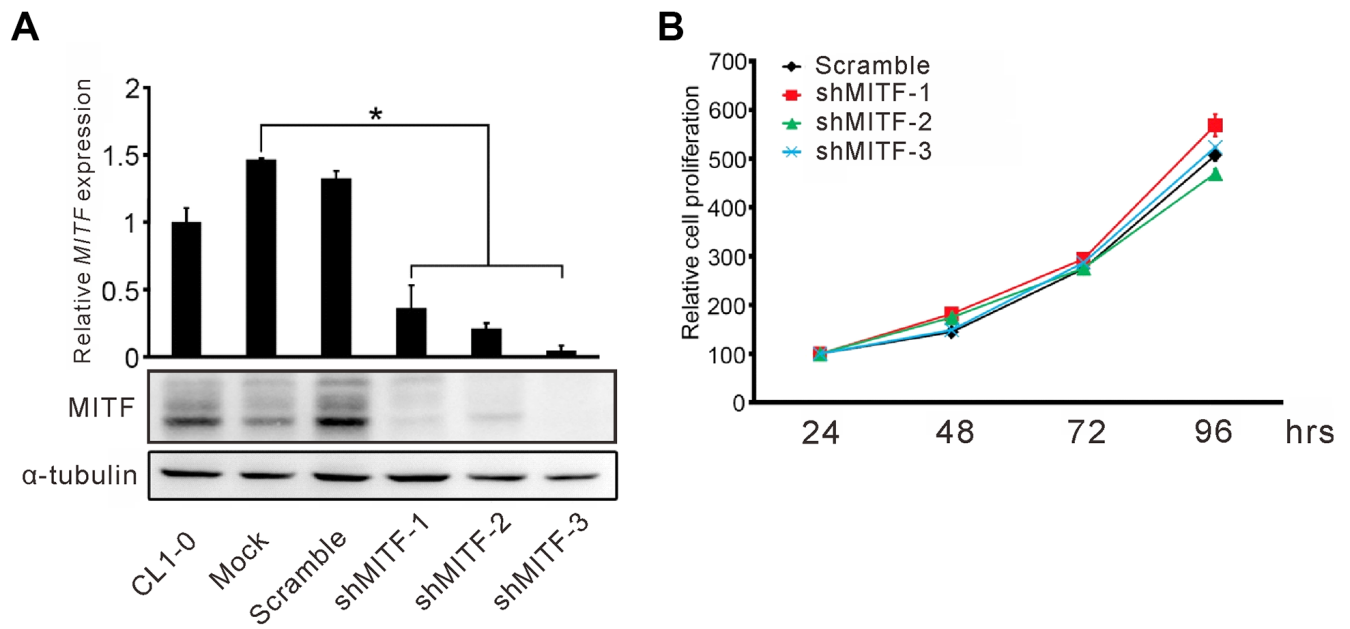
3. Strub T, Giuliano S, Ye T, Bonet C, Keime C, Kobi D, Le Gras S, Cormont M, Ballotti R, Bertolotto C, Davidson I.

Essential role of microphthalmia transcription factor for DNA replication, mitosis and genomic stability in melanoma. *Oncogene*. 2011; 30:2319–32.
<https://doi.org/10.1038/onc.2010.612>
PMID:[21258399](https://pubmed.ncbi.nlm.nih.gov/21258399/)

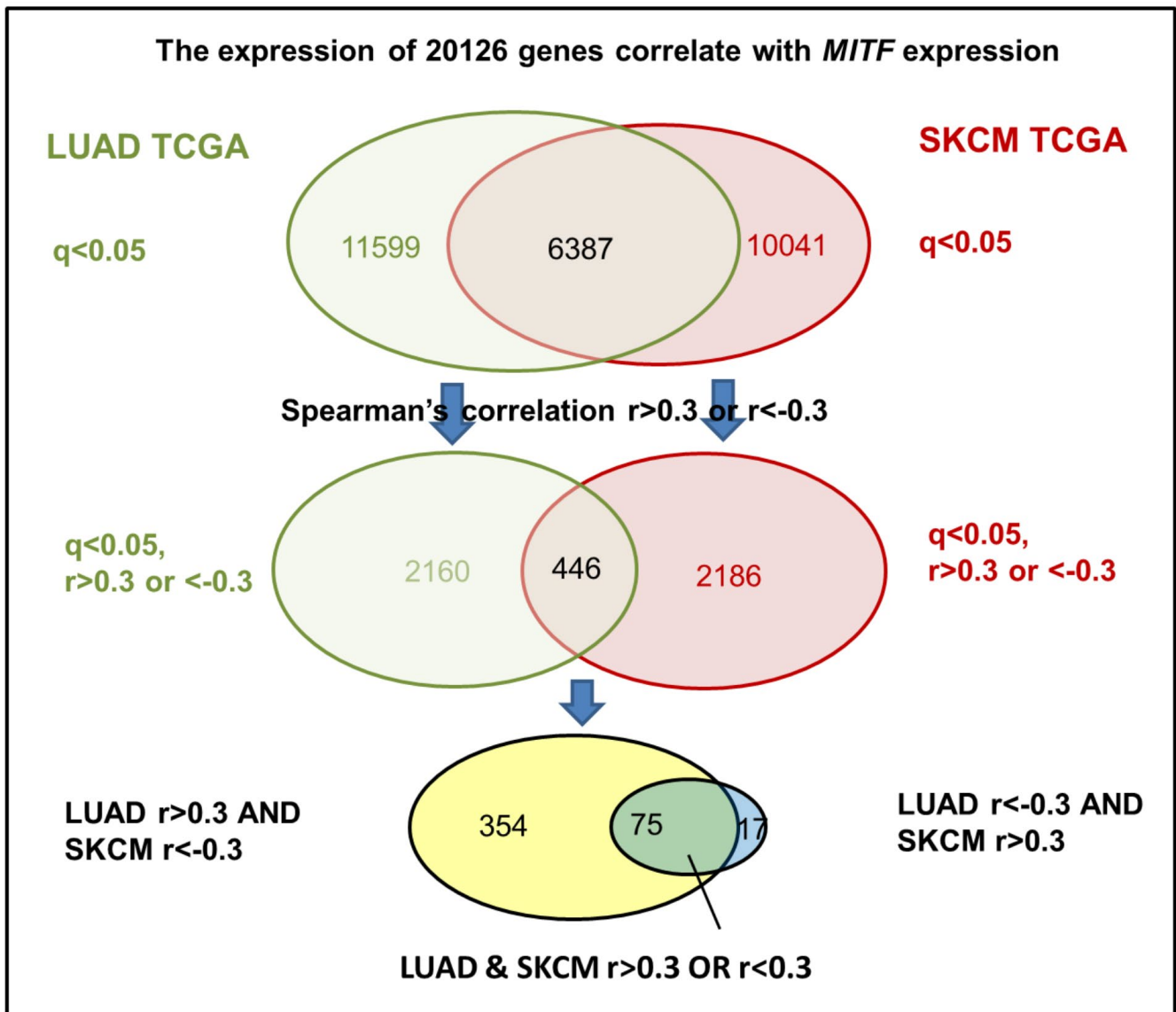
Supplementary Figures



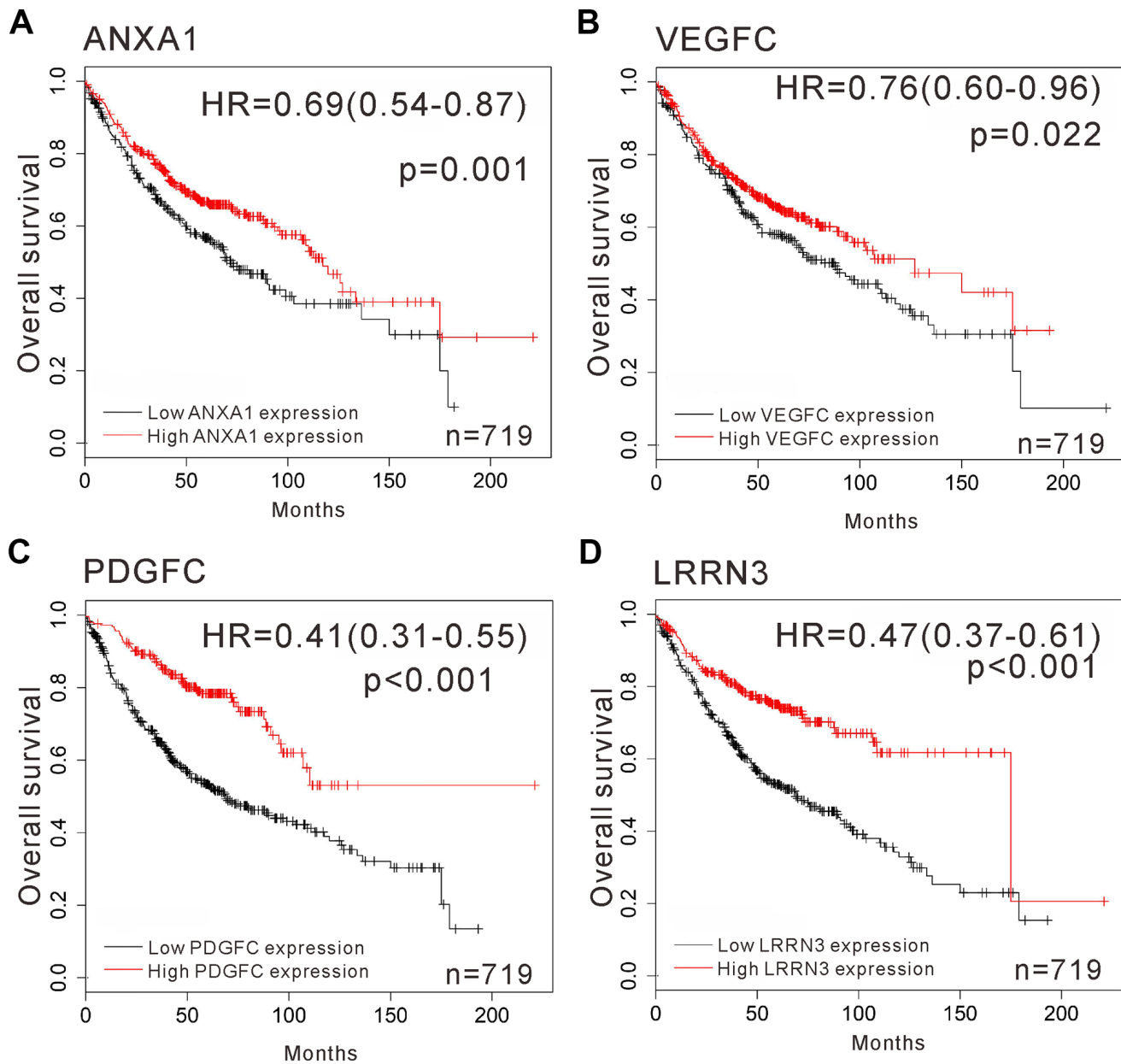
Supplementary Figure 1. MITF expression in an invasive cell line model and associated with survival in lung adenocarcinoma. (A) The relative MITF expression in low-invasive CL1-0 and high-invasive CL1-5 cells evaluated by expression microarray. (B, C) The survival curve of NSCLC was estimated with array probe of MITF (226066_at) by Kaplan-Meier plotter (<https://kmplot.com/>). The Hazard Ratio (HR) and p-value in the upper plots were estimated by univariate analysis and log-rank test, respectively. Lower panel listed the HR and p-value estimated by multivariate Cox's regression analysis.



Supplementary Figure 2. The stable MITF-knockdown clones were assayed the cell proliferation. (A) Stable-expressed shMITF in CL1-0 cells were established in culture with puromycin. **(B)** The cell proliferation was analyzed by MTT assay at indicated time points.



Supplementary Figure 3. The step-wise selection of Table 3. The spearman's correlations of *MITF* expression with 20,126 genes were sorted by cBioportal from the LUAD and SKCM TCGA datasets. The correlations with $q < 0.05$ and $r > 0.3$ or $r < -0.3$ were filtered and intersected by the two datasets. Only 75 genes had the same expression directions along with *MITF* expression in LUAD and SKCM datasets. In contrast, 371 genes showed inverse correlations. The final data was presented in Table 3.



Supplementary Figure 4. The correlation of overall survival and *ANXA1*, *VEGFC*, *PDGFC* and *LRRN3* expressions in lung adenocarcinoma by Kaplan-Meier analysis. The available microarray databases of lung adenocarcinoma analyzed by Kaplan-Meier plotter (<https://kmplot.com/>). The probe (A) *ANXA1* (201012_at), (B) *VEGFC* (209946_at), (C) *PDGFC* (218718_at) and (D) *LRRN3* (209840_s_at). The p-value was estimated by log-rank test. Univariate Cox's regression generated the hazard ratio.

Supplementary Tables

Supplementary Table 1. Characteristics of 70 NSCLC patients according to *MITF* expression.

Variables	High <i>MITF</i> expression	Low <i>MITF</i> expression	<i>p</i> -value
Age, mean (\pm SD)	69.07 \pm 9.29	65.88 \pm 10.95	0.19 [†]
Gender			
Male	32 (91.43)	27 (77.14)	0.19 [‡]
Female	3 (8.57)	8 (22.86)	
Stage			
I and II	23 (65.71)	18 (51.43)	0.33 [‡]
III	12 (34.29)	17 (48.57)	
Primary Tumor			
T1 and T2	30 (85.71)	30 (85.71)	1.00 [‡]
T3 and T4	5 (14.29)	5 (14.29)	
Regional Lymph Nodes			
N0	22 (62.86)	16 (45.71)	0.23 [‡]
N1, N2, and N3	13 (37.14)	19 (54.29)	
Cell Type			
Adenocarcinoma	20 (57.14)	22 (62.86)	
Squamous cell carcinoma	11 (31.43)	8 (22.86)	0.74 [‡]
Large cell carcinoma	3 (8.57)	4 (11.43)	
Mixed (small/large cell carcinoma)	0 (0.00)	1 (2.86)	
Bronchioloalveolar carcinoma	1 (2.86)	0 (0.00)	

[†]T test

[‡]Fisher's exact test

Supplementary Table 2. The enriched pathways in *MITF*-silenced cells by gene set enrichment analysis (GSEA).

Hallmark pathways	Size	ES	NES	NOM <i>p</i> -value	FDR <i>q</i> -value
Down-regulation					
Bile acid metabolism	109	-0.56	-1.45	0.024	0.41
IL2/STAT5 signaling	193	-0.50	-1.40	0.008	0.32
Wnt Beta-catenin signaling	41	-0.61	-1.38	0.061	0.25
Cholesterol homeostasis	71	-0.55	-1.35	0.061	0.24
Myogenesis	196	-0.47	-1.34	0.016	0.21
Upregulation					
Interferon-alpha response	92	0.74	1.81	0	0
E2F targets	190	0.56	1.51	0.002	0.07
Interferon-gamma response	194	0.54	1.45	0.006	0.09
Mitotic spindle	198	0.50	1.33	0.022	0.25
G2M checkpoint	185	0.49	1.29	0.054	0.32

Supplementary Table 3. Top 10 significantly enriched pathways of MITF by MetaCore analysis.

Pathway	FDR q-value
Gamma-secretase proteolytic targets	2.376E-05
Angiotensin II/ AGTR1 signaling via p38, ERK and PI3K	1.145E-04
Regulation of Beta-catenin activity	1.815E-04
Role of heterochromatin protein 1 (HP1) family in transcriptional silencing	1.815E-04
Gamma-Secretase regulation of cell development	1.815E-04
Angiotensin II/ AGTR1 signaling via JAK/STAT	5.292E-04
MAPK-mediated proliferation	6.296E-04
Alpha-2 adrenergic receptor regulation of ion channels	6.296E-04
Melanocyte development and pigmentation	8.655E-04
Thromboxane A2 signaling pathway	8.983E-04

Supplementary Table 4. Prognostic capability of MITF on the overall survival of melanoma patients from TCGA SKCM dataset.

Variable	Log-Rank P value	Hazard Ratio (95% CI)
10%	0.337	1.232 (0.805-1.884)
20%	0.442	1.139 (0.818-1.586)
30%	0.442	1.122 (0.837-1.504)
40%	0.194	1.200 (0.911-1.58)
50%	0.017 *	1.390 (1.062-1.819)
60%	0.058	1.298 (0.991-1.699)
70%	0.034 *	1.362 (1.024-1.812)
80%	0.215	1.228 (0.888-1.698)
90%	0.115	1.400 (0.921-2.127)

*P-value > 0.05 was considered statistically significant.

Supplementary Table 5. Prognostic capability of MITF on the overall survival of lung adenocarcinoma patients from TCGA LUAD dataset.

Variable	Log-Rank P value	Hazard Ratio (95% CI)
10%	0.228	0.730 (0.437-1.220)
20%	0.357	0.836 (0.570-1.225)
30%	0.039*	0.707 (0.508-0.984)
40%	0.251	0.838 (0.620-1.133)
50%	0.790	0.961 (0.718-1.286)
60%	0.863	0.974 (0.726-1.309)
70%	0.884	0.977 (0.713-1.339)
80%	0.783	0.951 (0.665-1.360)
90%	0.630	0.894 (0.567-1.410)

*P-value > 0.05 was considered statistically significant.

Supplementary Table 6. The expression of MITF downstream genes in lung adenocarcinoma and melanoma.

	Correlation with MITF expression*				Expression in MITF-silenced cells [§]			
	LUAD	q-value	SKCM	q-value	CL1-0	p-value	501MEL [#]	p-value
ANXA1	0.35	4.81E-15	-0.34	5.79E-10	-1.66	1.26E-06	1.98	2.16E-05
VEGFC	0.31	2.27E-11	-0.41	1.59E-14	-5.86	1.84E-05	0.93	0.35
PDGFC	0.40	7.61E-19	-0.48	1.91E-20	-5.31	1.66E-06	1.46	0.02
LRRN3	0.34	3.24E-14	-0.34	2.27E-10	-7.15	4.81E-06	3.10	2.91E-13

*Spearman's rank correlation coefficients were obtained from TCGA database by cBioPortal analysis. LUAD: lung adenocarcinoma. SKCM: skin cutaneous melanoma.

[§]Expression was log2 fold-change compared to control.

[#]Fold-change of gene expressions was obtained from siMITF and siLuc treated 501MEL human melanoma cells [3].

Supplementary Table 7. Primer sequences for real-time RT-PCR and MITF isoform-specific RT-PCR.

Gene	Primer sequence
MITF targeting genes	
<i>ANXA1</i>	F: TTCAATACCATCCTTACCACCAGAA R: CTCCAGGTCCAGAACTTTGTTC
<i>FZD7</i>	F: CGCCTCTGTTCGTCTACCTCTT R: TTCTCCAGCTTCTCGGTCTTG
<i>PTGR1</i>	F: TCAGGAGCTTCGCATGGAA R: CCTCTAAGACCCATTTTCAGCAAGT
MITF 5'-primers	
<i>MITF-A</i>	F: TGAAGAGCCCAAACCTATTACGA
<i>MITF-H</i>	F: GGAGGCGCTTAGAGTTCAGATG
<i>MITF-B</i>	F: CCAAAGTGCAAACGAAGGGTCTCA
<i>MITF-M</i>	F: CCTTCTCTTTGCCAGTCCATCTTC
<i>MITF-C</i>	F: CTTTCAGTGGTTTTCCACGAGCT
<i>MITF-E</i>	F: AGTAGCAGGGGTTAGTAGGTGGAT
<i>MITF-D</i>	F: GTTTTAACCTGACAGGCTTTGAATA
<i>MITF-J</i>	F: CTCTCCATGAGTCTGAGCATCTAA
<i>MITF-exon5</i>	F: CCAGCCAACCTTCCCAACATAAAA
MITF 3'-primers	
<i>MITF-com</i>	R: GATCAATCAAGTTTCCCGAGACAG
<i>MITF-exon9</i>	R: CCGGGGACACTGAGGAAAGGAG
<i>GAPDH</i>	F: GAAGGTGAAGGTCGGAGT R: GAAGATGGTGATGGGATTTC

Supplementary Table 8. Primers for chromatin immunoprecipitation assay of MITF.

Gene target* (Reference GenBank ID)	Primer sequence	Location#	Amplified length (bp)
<i>ANXA1</i> (NM_000700)	F: TTAAGTATGTCCCTAAAGTCACA R: TCAGCTATGTCCAAAAACAA	-441→-419 -123→-104	338
<i>FZD7-1</i> (NM_003507)	F: CTGGTTTCTAAGACGCATTA R: TTGGGGAGACTGGTTCTA	-1792→-1773 -1609→-1592	201
<i>FZD7-2</i>	F: AGCCTTTGCAGTCCTAAC R: GGAAAACTTTTACCCTGAA	-1237→-1220 -1012→-1031	207
<i>PTGRI</i> (NM_012212)	F: CCTGCCTTTGGACCCTTC R: GGAAATCTGAGTGCCTTTGTG	-420→-403 -152→-132	289
<i>GAPDH</i> (NM_002046)	F: AATTCCCATCTCAGTCGT R: CTACTTTCTCCCGCTTTTT	-385→-367 -172→-153	233

*The reference GenBank ID shows in the parenthesis.

#Nucleotide positions are numbered relative to the start site of transcription.

Supplementary Table 9. Antibodies for immunoblots.

Antibody	Clone	Dilution	Manufacturer	Cat No.
Anti-MITF	C17	1:100	Santa Cruz	SC-11002
Anti-MITF	C5	1:1000	Calbiochem	OP126L
Anti-FZD7		1:500	GeneTex	GTX64603
Anti- α -tubulin	DM1A	1:5000	Abcam	ab7291
Anti-V5		1:5000	Invitrogen	R960-25

Tumor suppressor DCAF15 inhibits epithelial-mesenchymal transition by targeting ZEB1 for proteasomal degradation in hepatocellular carcinoma

Xiao Dong^{1,*}, Yang Han^{2,*}, Encheng Zhang³, Yuqi Wang⁴, Pingzhao Zhang⁴, Chenji Wang⁴, Lin Zhong⁵, Qi Li¹

¹Department of Oncology, Shanghai General Hospital, Shanghai Jiao Tong University School of Medicine, Shanghai 200080, China

²Institute of Translational Medicine, Shanghai General Hospital, Shanghai Jiao Tong University School of Medicine, Shanghai 201620, China

³Department of Urology, Shanghai General Hospital, School of Medicine, Shanghai Jiao Tong University School of Medicine, Shanghai 200080, China

⁴State Key Laboratory of Genetic Engineering, Collaborative Innovation Center for Genetics and Development, School of Life Sciences, Fudan University, Shanghai 200438, China

⁵Department of Hepatobiliary and General Surgery, Shanghai General Hospital, Shanghai Jiao Tong University School of Medicine, Shanghai 200080, China

*Equal contribution

Correspondence to: Qi Li, Lin Zhong; **email:** leeqi@sjtu.edu.cn, zhonglin1@medmail.com.cn

Keywords: DCAF15, ZEB1, ubiquitination, epithelial-mesenchymal transition, hepatocellular carcinoma

Received: November 10, 2020

Accepted: March 4, 2021

Published: April 4, 2021

Copyright: © 2021 Dong et al. This is an open access article distributed under the terms of the [Creative Commons Attribution License](https://creativecommons.org/licenses/by/3.0/) (CC BY 3.0), which permits unrestricted use, distribution, and reproduction in any medium, provided the original author and source are credited.

ABSTRACT

Epithelial-mesenchymal transition (EMT) is an evolutionarily conserved developmental program that has been implicated in tumorigenesis and confers metastatic properties upon cancer cells. ZEB1 is a master transcription factor that activates the EMT process in various cancers. ZEB1 is reportedly degraded through the ubiquitin proteasome pathway, but the underlying molecular mechanism of this process remains largely unknown in hepatocellular carcinoma (HCC). Here, we identified ZEB1 as a substrate of the CRL4-DCAF15 (DDB1 and CUL4 associated factor 15) E3 ubiquitin ligase complex. DCAF15 acts as an adaptor that specifically recognizes the N-terminal zinc finger domain of ZEB1, then triggers its degradation via the ubiquitin-proteasome pathway. DCAF15 knockdown led to upregulation of ZEB1 and activation of EMT, whereas overexpression of DCAF15 suppressed ZEB1 and inhibited EMT. DCAF15 knockdown also promoted HCC cell proliferation and invasion in a ZEB1-dependent manner. In HCC patients, low DCAF15 expression was predictive of an unfavorable prognosis. These findings reveal the distinct molecular mechanism by which DCAF15 suppresses HCC malignancy and provides insight into the relationship between the CUL4-DCAF15 E3 ubiquitin ligase complex and ZEB1 in HCC.

INTRODUCTION

Hepatocellular carcinoma (HCC) is a highly aggressive malignant neoplasm and is the fifth leading cause of cancer-related death worldwide [1]. Hepatitis, liver cirrhosis and tumor occurrence are common indications

during the development of HCC [2]. Therapeutic strategies used to treat HCC entail both interdisciplinary and multidisciplinary approaches, including surgical resection, liver transplantation, radiofrequency ablation, chemotherapy, targeted medicine and immunological therapy [3]. Nevertheless, the prognosis for HCC

remains very poor, with a five-year survival rate that is below 12% [4]. The molecular mechanisms underlying HCC development and progression remain unclear. Consequently, there is an urgent need to identify specific biomarkers of HCC that will enable diagnosis early enough to improve prognosis.

Ubiquitin is covalently attached to substrate proteins through a cascade involving three enzymes: ubiquitin-activating enzyme (E1), ubiquitin-conjugating enzyme (E2) and ubiquitin-ligating enzyme (E3) [5]. The human genome encodes nearly 600 E3 ligases, including seven Cullin proteins (CUL1, CUL2, CUL3, CUL4A, CUL4B, CUL5, CUL7), which mediate nucleation events leading to the formation of a multi-subunit ubiquitin ligase [6]. DDB1 and CUL4 associated factor 15 (DCAF15) is a core component of the Cullin-RING E3 ligases-DCAF15 E3 ubiquitin ligase complex. This complex is composed of CUL4, DCAF15, DDB1 and DDA1 [7]. The Cullin 4 RING ligase (CRL4) contains two homogenous scaffolds, CUL4A and CUL4B, which bind DDB1 and the catalytic subunit RING-finger protein through its N-terminus and C-terminus, respectively [8]. The majority of CUL4A resides in the cytoplasm and regulates substrate ubiquitination; however, low levels of CUL4A are found in the nucleus, where it targets the nuclear proteins HOXA9 and p27 [9, 10]. DDB1 acts as a bridging factor between the Cullin scaffold and its substrate recognition subunit [11]. Earlier reports demonstrated that DDA1 directly binds to amino acids 390-460 of DCAF15 [12] and that DCAF proteins prompt E3 ubiquitin ligase complexes to ubiquitinate and target for degrading key substrates, including ZFP9, IKZF1, IKZF3 and RBM39 [7, 13, 14]. In addition, three aryl sulfonamides, E7820, indisulam and tasisulam, have been shown to induce degradation of RBM39 through recruitment of the CUL4-DDB1-DDA1-DCAF15 E3 ligase complex [15].

ZEB1 is a transcriptional regulator of epithelial-mesenchymal transition (EMT) [16]. To better understand the mechanism by which ZEB1 is degraded through the ubiquitin proteasome pathway, in the present study we surveyed a protein-protein interaction database to determine whether ZEB1 interacts with DCAF family proteins and assess its impact on the proliferation and invasiveness of HCC cells and the EMT process. Our findings provide a model for understanding the role of a DCAF15-ZEB1-EMT axis during the development of HCC.

RESULTS

DCAF15 forms a complex with ZEB1 in cells

To identify the molecular partners interacting with ZEB1, we surveyed a large-scale protein-protein

interaction database (<https://thebiogrid.org/124705/summary/homo-sapiens/dcaf15.html>) and noted that ZEB1 (red frame) is a potential interactor of DCAF15 (Figure 1). We then co-expressed Flag-DCAF15 and Myc-ZEB1 in 293T cells, after which the cells were harvested for co-immunoprecipitation (Co-IP) assays. The results indicated that Myc-ZEB1 was immunoprecipitated by Flag-DCAF15 (Figure 2A). Similarly, reciprocal Co-IP assays performed after co-transfecting cells with Flag-ZEB1 and Myc-DCAF15 showed that Myc-DCAF15 was immunoprecipitated by Flag-ZEB1 (Figure 2B), indicating exogenous interaction between these two proteins. We also observed that endogenous DCAF15 was efficiently immunoprecipitated by ZEB1 (Figure 2C) and that endogenous ZEB1 was efficiently immunoprecipitated by DCAF15 (Figure 2D), suggesting there is also endogenous interaction between ZEB1 and DCAF15.

To further investigate the intracellular interaction between ZEB1 and DCAF15, we examined their subcellular localization in two HCC cell lines (Hep-3B and SMMC-7721). After transfecting the cells with Flag-ZEB1 and Myc-DCAF15, they were immunofluorescence-stained with anti-Flag or anti-Myc antibodies. Upon visualization under a microscope, we observed that the exogenous ZEB1 and DCAF15 colocalized in the cytoplasm (Figure 2E). Taken together, these results strongly suggest that DCAF15 forms a complex with ZEB1 within the cytoplasm of HCC cells.

DCAF15 ubiquitinates and degrades ZEB1 protein

We next investigated whether DCAF15 promotes the ubiquitination and subsequent degradation of ZEB1 protein. Consistent with that idea, levels of Flag-ZEB1 were dose-dependently decreased by expression of Myc-DCAF15, and that effect was absent when cells were treated with a proteasomal inhibitor (MG132, Bortezomib or chloroquine). That all three inhibitors tested rescued ZEB1 from DCAF15-mediated degradation indicates that DCAF15 downregulates ZEB1 levels via the proteasomal degradation pathway (Figure 3A). To identify which ZEB1 domain interacts with DCAF15, we generated five ZEB1 deletion mutants: ZEB1- Δ 1 (amino acids 1-340), ZEB1- Δ 2 (amino acids 1-781), ZEB1- Δ 3 (amino acids 341-781), ZEB1- Δ 4 (amino acids 341-1,124) and ZEB1- Δ 5 (amino acids 782-1124) [17]. Subsequent Co-IP experiments revealed that the N-terminal zinc finger domain mediated interaction between ZEB1 and DCAF15, but not the Smad-binding domain, homeodomain, CtBP interaction domain, or C-terminal zinc finger domain (Figure 3B). In addition, knocking down endogenous DCAF15 using two targeted siRNAs

increased endogenous ZEB1 levels (Figure 3C) and markedly prolonged the half-life of endogenous ZEB1 in SMMC-7721 cells (Figure 3D and 3E).

To address the possibility that the elevated ZEB1 expression was mediated at the transcriptional level, we measured levels of DCAF15 and ZEB1 mRNA in SMMC-7721 cells after transiently treating them with DCAF15 siRNAs. We found that levels of DCAF15 mRNA were significantly decreased, while levels of

ZEB1 mRNA were little changed from control, indicating that the degradative effect of DCAF15 on ZEB1 is not mediated at the transcriptional level (Figure 3F). Instead, co-expression of HA-ubiquitin, Flag-ZEB1 and Myc-DCAF15 in HEK293T cells revealed that ZEB1 was robustly and dose-dependently poly-ubiquitinated (Figure 3G and 3H). These results suggest that DCAF15 triggers the ubiquitin-dependent proteasomal degradation pathway through recognition of the N-terminal zinc finger domain of ZEB1 protein.

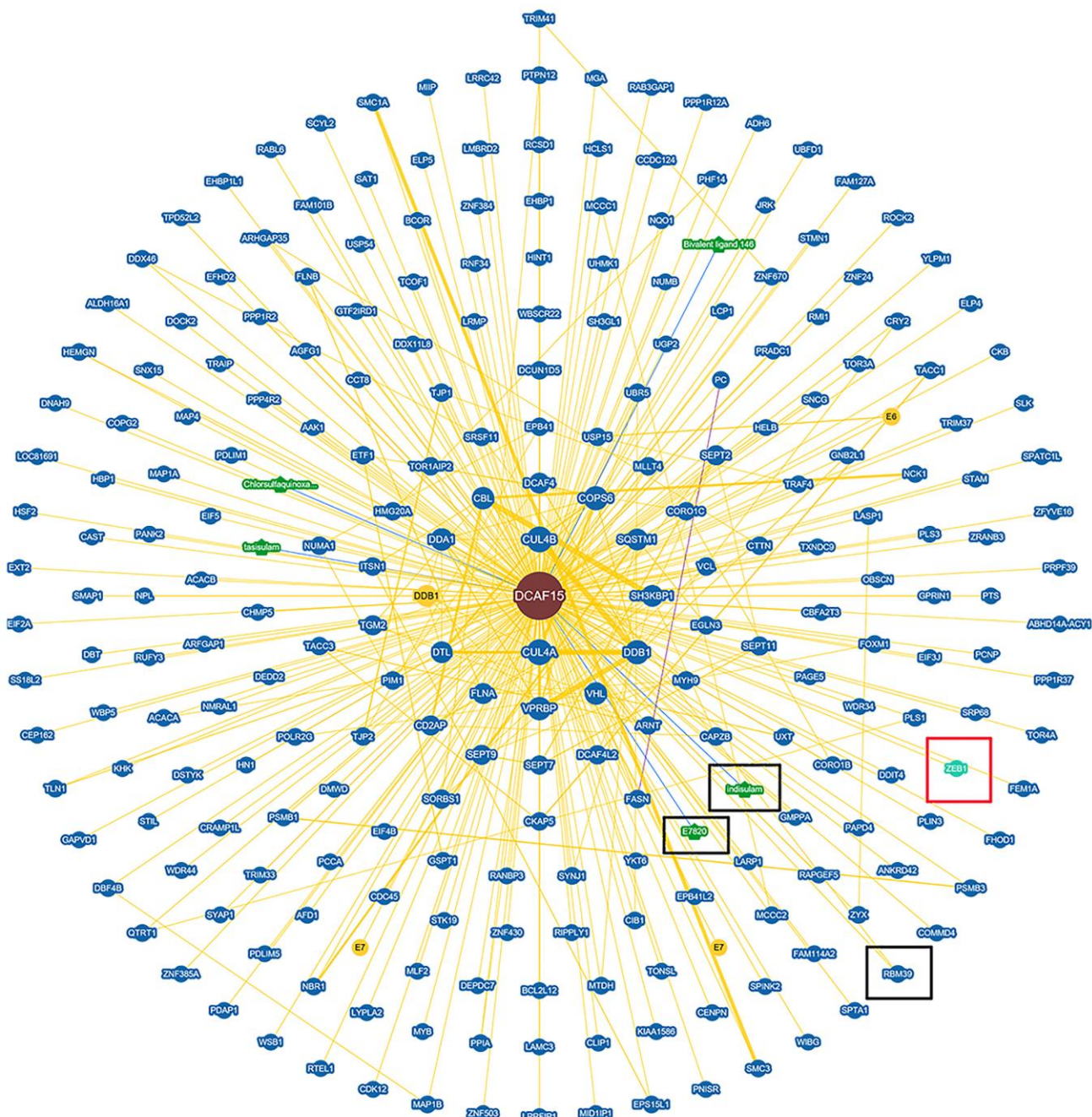


Figure 1. Protein network diagram shows potential interaction of DCAF15. Black frame indicates the interactors of DCAF15 reported. Red frame indicates ZEB1 is a potential interactor of DCAF15.

Ubiquitin is conjugated to its substrates by Cullin RING ligases (CRLs), which are multi-subunit ubiquitin ligases. CRLs are modular complexes that contain a common catalytic core but assemble with a diverse set of receptors that recruit specific substrates to the CRL's catalytic complex [6]. Within CRL4 (CUL4A and

CUL4B), DDB1 and DDA1 are adaptors, while DCAF15 is a substrate-specific receptor [7]. We first tested whether CUL4A binds ZEB1 within cells. As shown in Figure 4A, ZEB1 was not immunoprecipitated by Flag-CUL4A, indicating no binding between ZEB1 and CUL4A (Figure 4A). Likewise, exogenous CUL4B

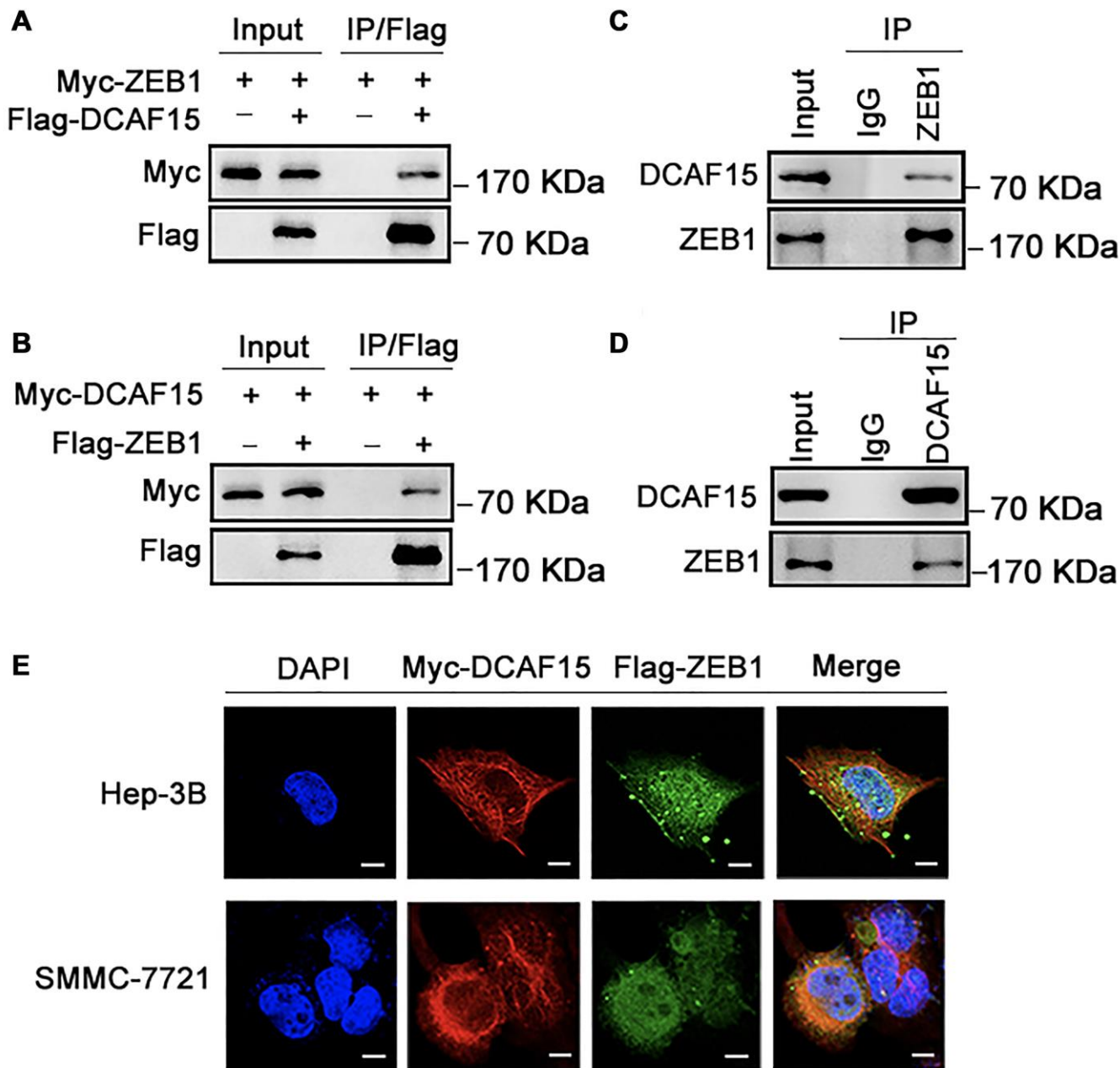


Figure 2. DCAF15 binds with ZEB1 protein. (A–B) Ectopically expressed DCAF15 and ZEB1 can bind with each other. (A) Flag-DCAF15 and Myc-ZEB1 were co-expressed in HEK293T cells, and immunoprecipitated with FLAG-M2 agarose beads. (B) Similar Co-IP assay was performed between Flag-ZEB1 and Myc-DCAF15. (C–D) Endogenous interaction between DCAF15 and ZEB1. (C) SMMC-7721 cells were treated with 10 μM MG132 for 6h. Cell lysates were precipitated using anti-ZEB1 antibody or with IgG (mock IP) and coprecipitated DCAF15 was detected by western blotting. (D) SMMC-7721 cells were treated with 10 μM MG132 for 6h. Cell lysates were precipitated using anti-DCAF15 antibody or with IgG (mock IP) and coprecipitated ZEB1 was detected by western blotting. (E) Flag-DCAF15 and Myc-ZEB1 were co-expressed in Hep3B and SMMC-7721 cells respectively and visualized by fluorescence microscopy. Scale bars, 30 μm.

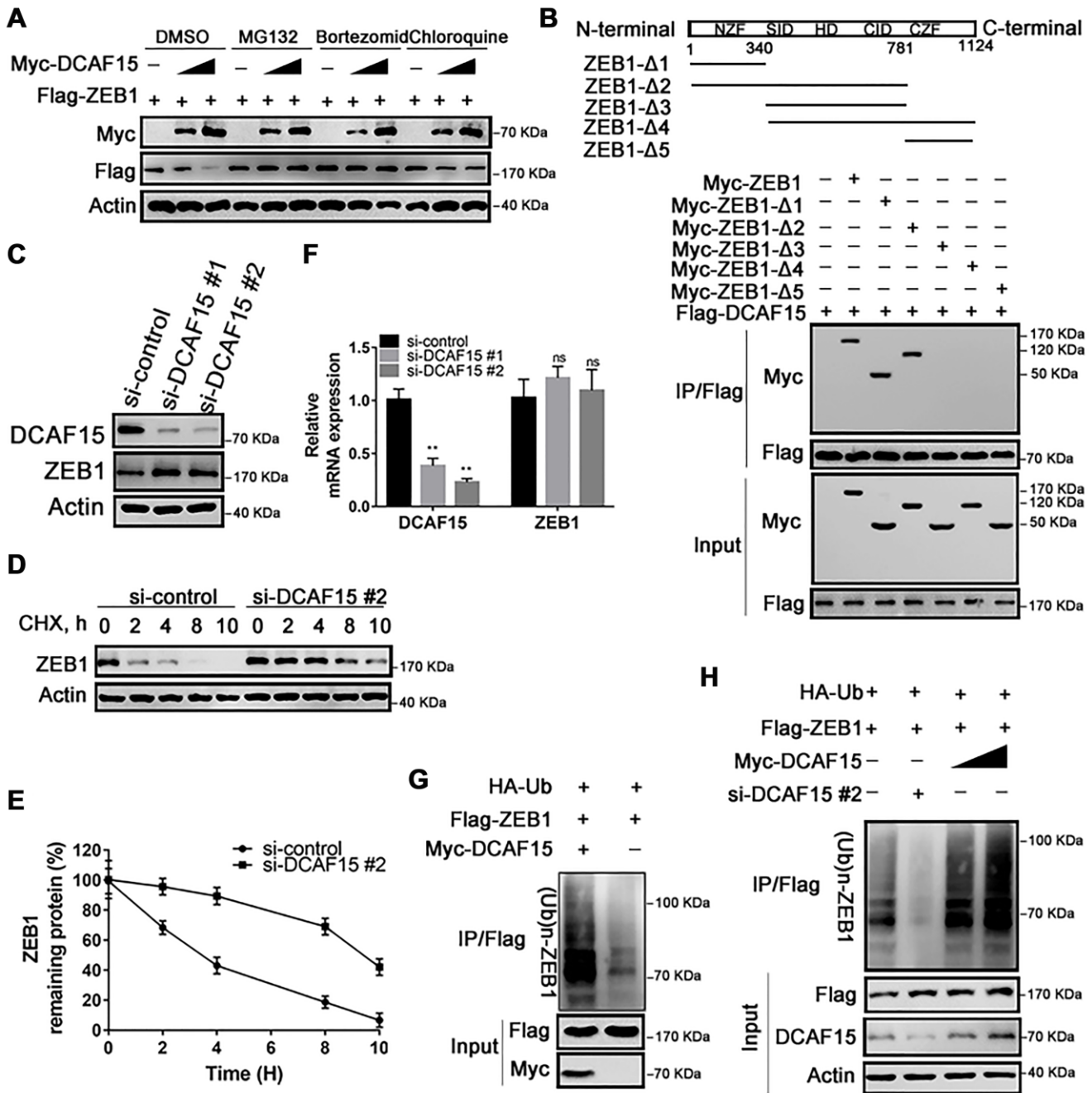


Figure 3. DCAF15 ubiquitinates and degrades ZEB1 protein. (A) DCAF15 regulates protein level of ZEB1 through the proteasome pathway. HEK293T cells were co-transfected with Flag-ZEB1 and increasing amounts of Myc-DCAF15. After 24h, cells were treated with DMSO, MG132, bortezomid or chloroquine respectively and detected by western blot. (B) HEK293T cells were transfected with Flag-DCAF15 and Myc-full-length or truncated ZEB1. After 24 h, cell lysates were immunoprecipitated using FLAG-M2 agarose beads. Immune complexes were analyzed by immunoblotting with the indicated antibodies (lower panel). Schematic diagram illustrating ZEB1 deletion mutants (upper panel). (C) SMMC-7721 cells were transfected with the control or two independent DCAF15 siRNAs, respectively. Cell lysates were analyzed via immunoblotting with the indicated antibodies. (D) SMMC-7721 cells were transfected with the control or DCAF15 siRNAs. After 24 h, cells were treated with cycloheximide (CHX) for indicated time-periods. Cell lysates were analyzed via immunoblotting with the indicated antibodies. (E) The relative intensities of ZEB1 protein were first normalized to the intensities of actin and then normalized to the value of the 0 h point. (F) qPCR validation of relative DCAF15 and ZEB1 mRNA levels in DCAF15 control and knockdown cells. GAPDH was used for normalization. (G) HEK293T cells were co-transfected with Flag-ZEB1, Myc-DCAF15 and HA-Ub. After 24 h, cells were treated with 10μM MG132 for 6 h. Cell lysates were immunoprecipitated using FLAG-M2 agarose beads and analyzed by immunoblotting with the indicated antibodies. (H) DCAF15 promotes ZEB1 ubiquitination. HEK293T cells were co-transfected with Flag-ZEB1, HA-Ub, si-DCAF15 #2 and increasing amounts of Myc-DCAF15. After 24h, cells were treated with MG132. The ZEB1 protein was immunoprecipitated using FLAG-M2 agarose beads. The ubiquitinated ZEB1 was analyzed by Western blotting.

did not bind ZEB1, nor did DDA1 or DDB1 (Figure 4B–4D). We only detected an interaction between endogenous ZEB1 and exogenous Flag-DCAF15

(Figure 2D). Moreover, when we knocked down endogenous CUL1, CUL2, CUL3, CUL4A, CUL4B or CUL5 using corresponding siRNAs in SMMC-7721

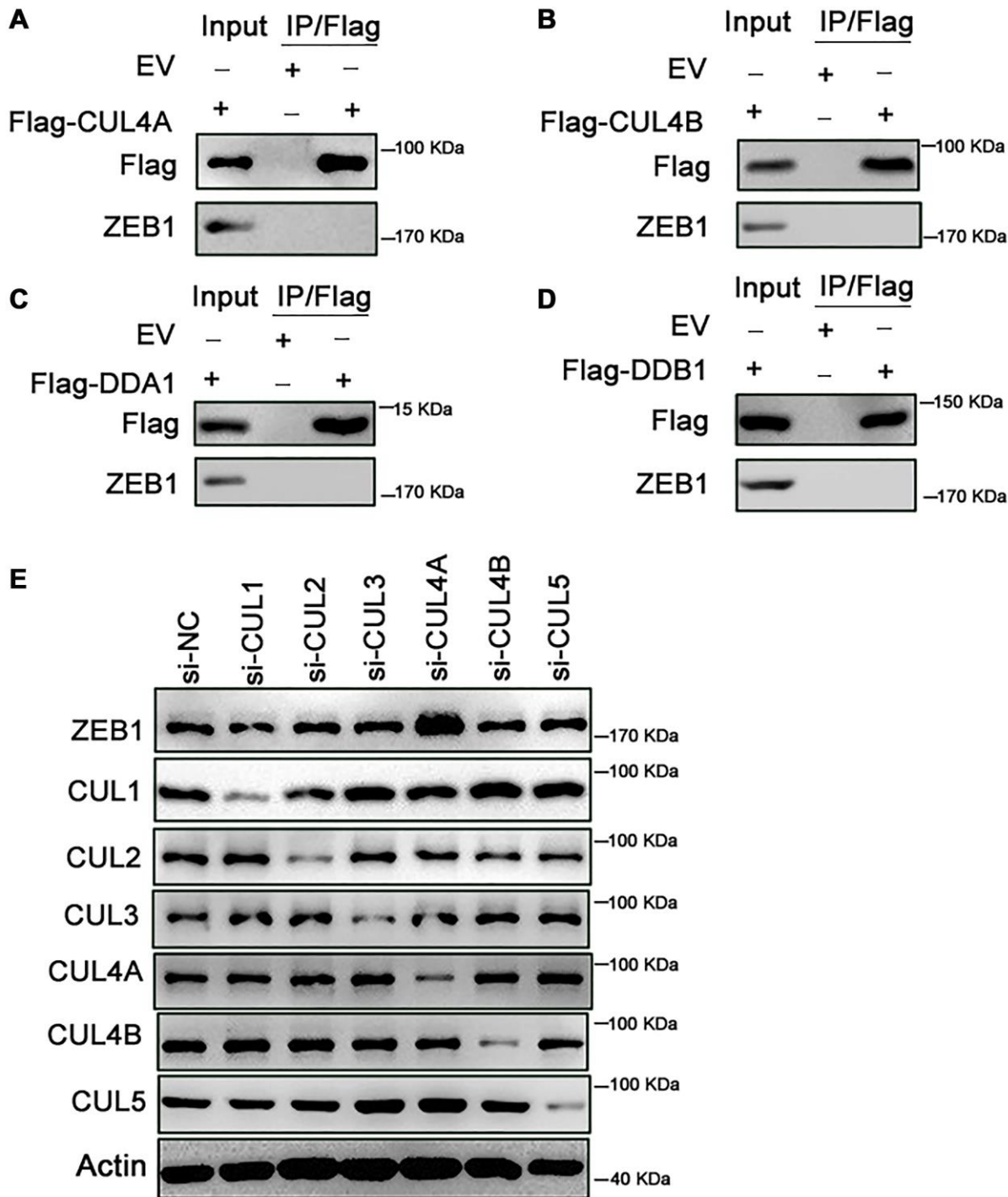


Figure 4. Knockdown of CUL4A promotes the stability of ZEB1. (A–D) HEK293T cells were transfected with Flag-CUL4A, Flag-CUL4B, Flag-DDA1 and Flag-DDB1 respectively. After 24h, cells were treated with 10 μ M MG132 for 6h. Cell lysates were immunoprecipitated using FLAG-M2 agarose beads and analyzed by immunoblotting with the indicated antibodies. (A) Ectopically expressed CUL4A didn't bind with endogenous ZEB1. (B) Ectopically expressed CUL4B didn't bind with endogenous ZEB1. (C) Ectopically expressed DDA1 didn't bind with endogenous ZEB1. (D) Ectopically expressed DDB1 didn't bind with endogenous ZEB1. (E) SMMC-7721 cells were transfected with the control or si-CUL1, si-CUL2, si-CUL3, si-CUL4B and si-CUL5 respectively. Cell lysates were analyzed by immunoblotting with the indicated antibodies. Expression of si-CUL1, si-CUL2, si-CUL3, si-CUL4B and si-CUL5 had no effect on ZEB1 degradation, in contrast, si-CUL4A promoted the ZEB1 protein expression.

cells and then measured the levels of ZEB1 and Cullin family members, we found that when cells were transfected with siCUL4A, ZEB1 levels were significantly higher than control (Figure 4E). By contrast, transfection of siRNAs targeting other Cullin family proteins had no effect on ZEB1 levels. Thus, only CUL4A appears to affect the stability of ZEB1 protein.

DCAF15 inhibits cell proliferation, migration and invasion by HCC cells

To explore the biological function of the DCAF15-ZEB1 axis in HCC, siRNAs targeting DCAF15 and ZEB1 were transiently transfected into SMMC-7721 cells (Figure 5A), after which CCK8 and colony formation assays were performed. The results showed that cell proliferation was inhibited by ZEB1 knockdown but promoted by DCAF15 knockdown. Moreover, the enhanced cell proliferation caused by DCAF15 knockdown could be reversed by ZEB1 co-knockdown (Figure 5B–5C). This suggests DCAF15 inhibits HCC cell proliferation.

We next performed transwell and wound healing assays to assess the impact of DCAF15 and ZEB1 on cell migration and invasion. We found that ZEB1 knockdown suppressed both migration and invasion by HCC cells, whereas DCAF15 knockdown had the opposite effect. Moreover, the enhanced migration and invasion caused by DCAF15 knockdown was reversed by ZEB1 co-knockdown (Figure 5D–5E), again demonstrating the functional interconnection of these two proteins.

DCAF15 inhibits EMT in HCC cells

Numerous studies have reported that EMT is necessary for cancer metastasis [18, 19]. To become highly mobile, epithelial cells are known to lose their polarity, which helps them acquire migratory and invasive capabilities. Upon DCAF15 overexpression, E-cadherin was upregulated while several mesenchymal markers, including N-cadherin, β -catenin, slug and vimentin, were all downregulated (Figure 6A–6B, 6E and 6G). Conversely, E-cadherin was downregulated when DCAF15 expression was suppressed, and the mesenchymal signals were correspondingly upregulated (Figure 6C–6D, 6F and 6H).

DCAF15 and ZEB1 are negatively correlated in HCC

Finally, we assessed DCAF15 and ZEB1 expression in tissue specimens from 40 HCC patients. As shown in Figure 7A–7B, DCAF15 levels were lower in HCC than in paired normal liver tissues. In addition, DCAF15 and ZEB1 levels were negatively correlated

in HCC tissues ($r = -0.46$, $p = 0.006$) (Figure 7C and 7D). We also used The Cancer Genome Atlas (TCGA) database to analyze the clinical prognostic significance of DCAF15 or ZEB1 mRNA expression. Kaplan-Meier analyses revealed that overall survival (OS) among HCC patients exhibiting low DCAF15 mRNA expression was poorer than among those exhibiting high DCAF15 mRNA expression, and that low DCAF15 or high ZEB1 mRNA expression was predictive of unfavorable OS in HCC patients (Supplementary Figure 1).

DISCUSSION

In this study, we showed that the DCAF15-CUL4 E3 ligase complex functions as a tumor suppressor that promotes ZEB1 ubiquitination and degradation, which suppresses malignant phenotypes such as cell proliferation, migration and invasion as well as EMT in HCC cells (Figure 8).

ZEB1 is a key transcriptional regulator in EMT, which consists of two zinc finger clusters and a centrally-located homeodomain capable of DNA binding [20, 21]. Previous studies have shown that ZEB1 is highly expressed in HCC and that its overexpression promotes tumor cell migration, invasion and metastasis through EMT [22–26]. CUL4A, a member of the Cullin family and a component of the E3 ubiquitin ligase complex, is necessary for the ubiquitination and degradation of proteins [27]. Numerous studies have elaborated on Cullin family proteins and their associated CRLs E3 ligases [28–31]. Among them, CUL4 related E3 ubiquitin ligases comprise a Cullin 4 scaffold and the triple β -propeller DDB1 adaptor. However, few substrate receptors have been identified [32]. DCAF15 was first detected as a vital ubiquitin ligase contributing to the cytotoxicity of indisulam (a carbonic anhydrase inhibitor)-induced RBM39 degradation [7, 15]. A subsequent kinetic analysis found that aryl sulfonamide and RBM39 bind to DCAF15 in a synergistic manner [33], and it was later demonstrated that E7070, an aryl sulfonamide drug, mediates ubiquitination and proteasomal degradation of PRPF39 by recruiting PRPF39 to the CUL4-DCAF15 E3 ubiquitin ligase [34]. A variety of substrate receptors have been described as targets of DCAF15; however, the biological and functional significance of this ubiquitination event requires further elucidation. To our knowledge, this is the first report revealing the critical role of DCAF15-ZEB1 binding in HCC. Our findings suggest *DCAF15* serves as a tumor suppressor gene in HCC and is negatively related to ZEB1 protein. These results provide a mechanistic explanation for the clinical observation that HCC patients have high levels of ZEB1 in their tissues.

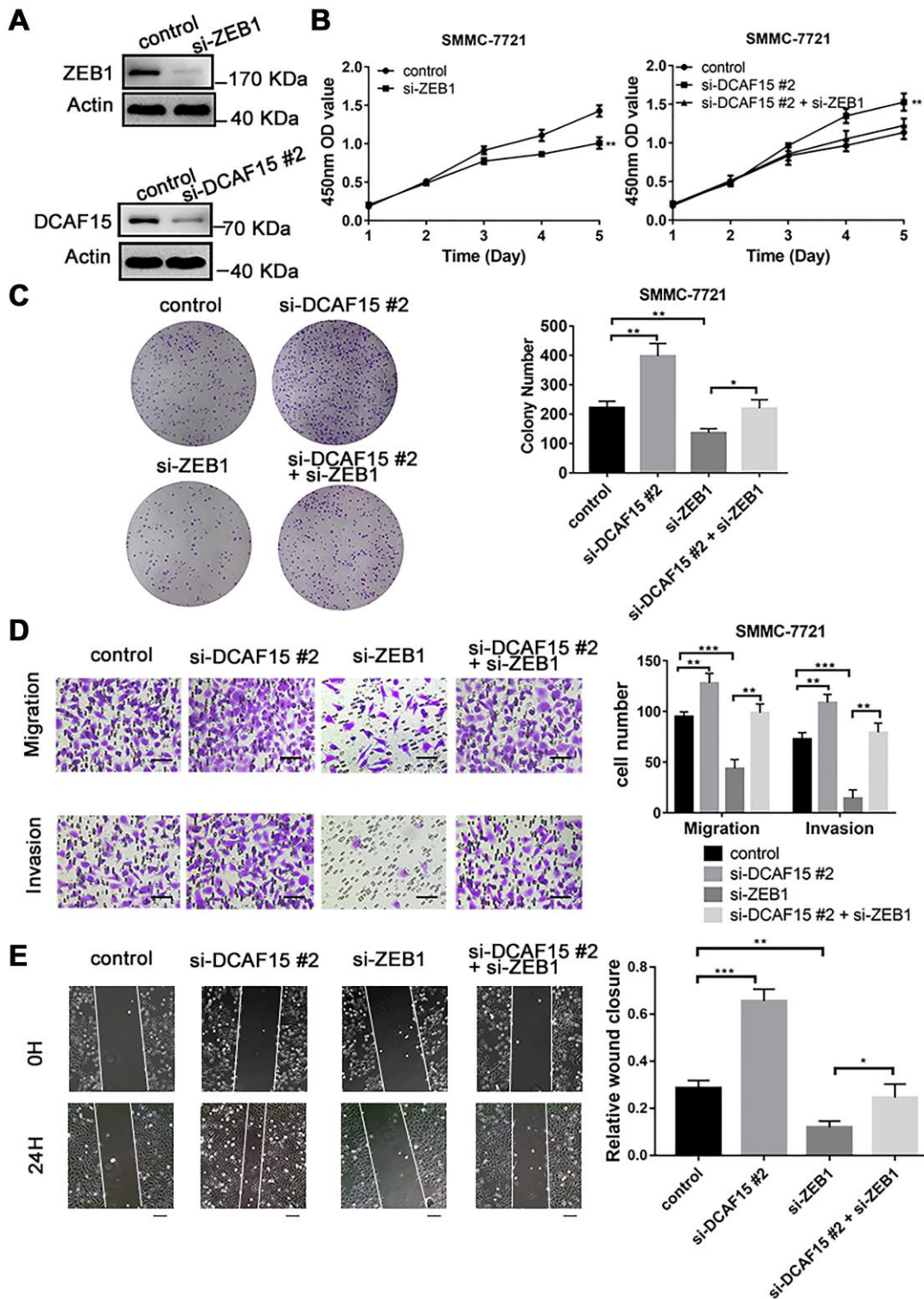


Figure 5. DCAF15 inhibits proliferation, migration, and invasion of HCC cells. (A) DCAF15 and ZEB1 was knocked down in SMMC-7721 cells by expressing siRNAs. Immunoblotting analyses were performed with the indicated antibodies. (B) CCK-8 assay was performed for cell proliferation of control, ZEB1-knockdown, DCAF15-knockdown and ZEB1- & DCAF15-knockdown SMMC-7721 cells. (C) The cells of (B) were plated and cultured on 6-well plates. Colony numbers were quantified. (D) The migration and invasion ability of the cells of (B) in were examined using the Transwell migration and invasion assay respectively. Cell numbers were quantified. Data are presented as mean \pm SD ($n = 3$). $**P < 0.01$, $***P < 0.001$. Scale bars, 50 μ m. (E) The cells of (B) were plated and cultured on 6-well plates. The cell layer was scratched with a 10 μ l pipette tip. For each sample, at least three scratched fields were photographed immediately (0 h) or 24 h after scratching. Photographs of representative images were taken at $\times 100$ magnification.

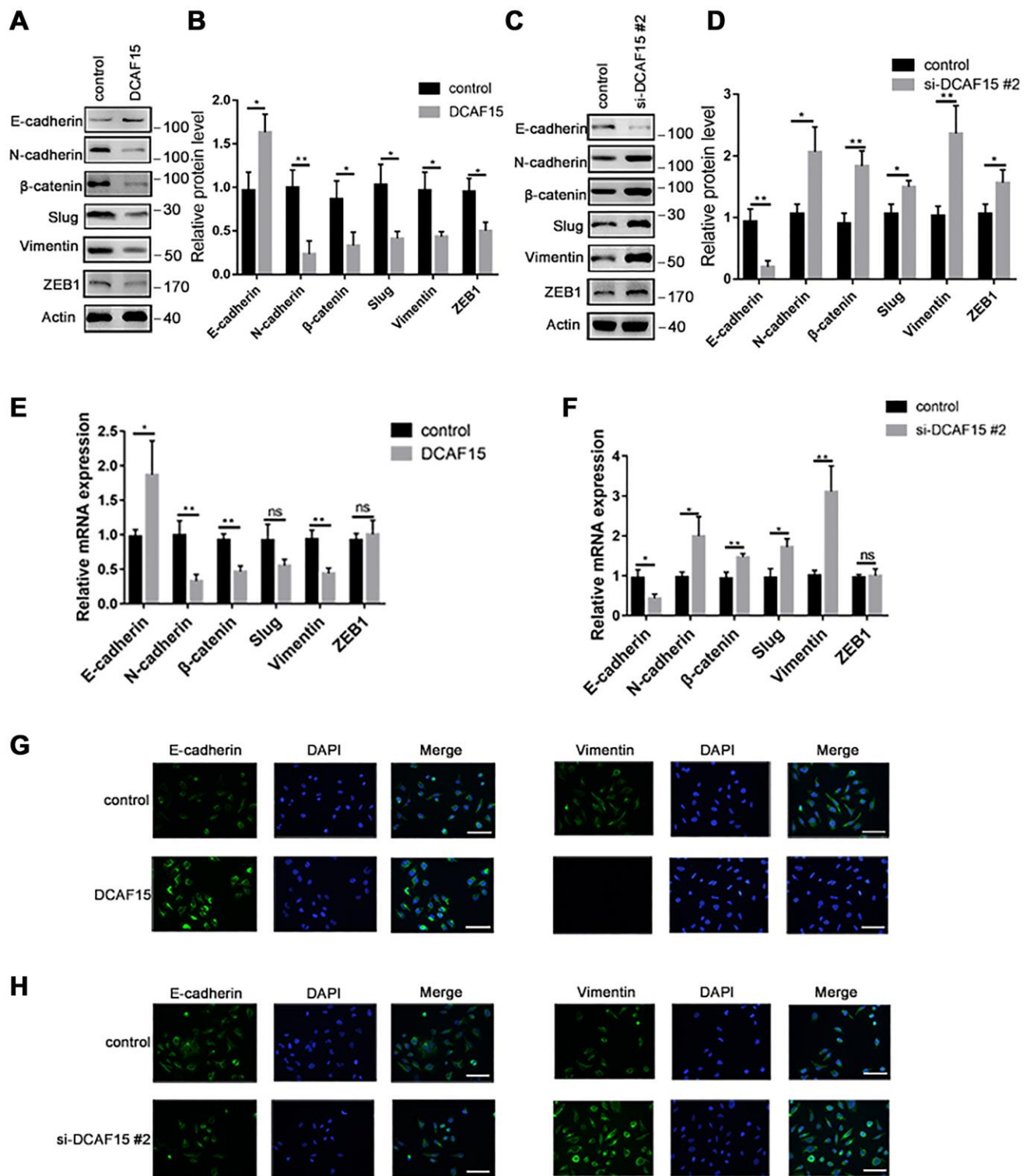


Figure 6. DCAF15 inhibits epithelial-mesenchymal transition (EMT) of HCC cells. (A–B) Western blot analysis showed the protein level of EMT markers after transfecting with control or DCAF15 overexpression plasmids in HCC cells. (C–D) Western blot analysis showed the protein level of EMT markers after transfecting with control or DCAF15 siRNA in HCC cells. (E) qPCR analysis showed relative mRNA level of EMT markers after transfecting with control or DCAF15 overexpression plasmids in HCC cells. (F) qPCR analysis showed relative mRNA level of EMT markers after transfecting with control or DCAF15 siRNA in HCC cells. (G) Protein level of E-cadherin and vimentin after transfecting with control or DCAF15 overexpression plasmids in HCC cells was visualized by fluorescence microscopy. Scale bars, 100 μ m. (H) Protein level of E-cadherin and vimentin after transfecting with control or DCAF15 siRNA in HCC cells was visualized by fluorescence microscopy. Scale bars, 100 μ m.

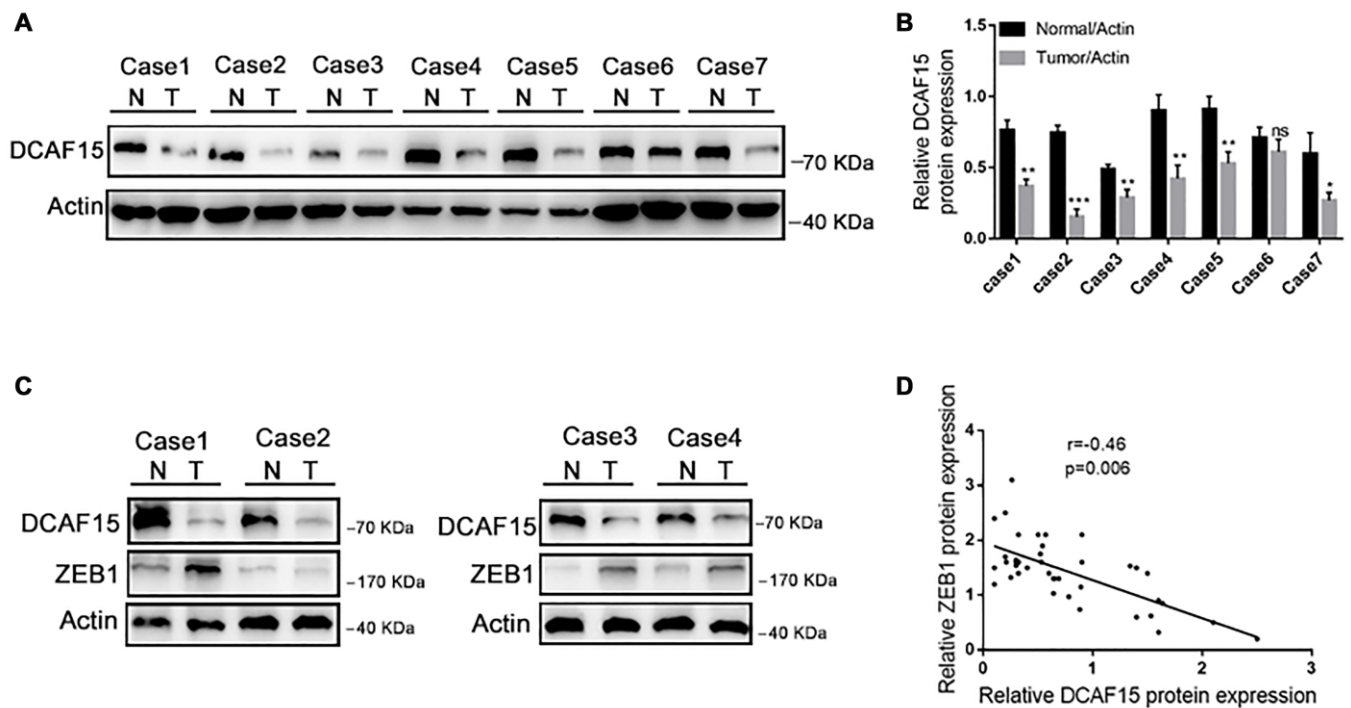


Figure 7. DCAF15 and ZEB1 protein levels negatively correlate in HCC patient specimens. (A–B) In random 7 HCC patient specimens, protein level of DCAF15 in tumor tissues is lower than in normal tissues. (C) Representative western blotting figures show protein expression of DCAF15 and ZEB1 in 40 HCC patient specimens. (D) Correlation analysis of the expression levels of DCAF15 and ZEB1 protein in 40 HCC patient specimens ($r = -0.46$, $p = 0.006$).

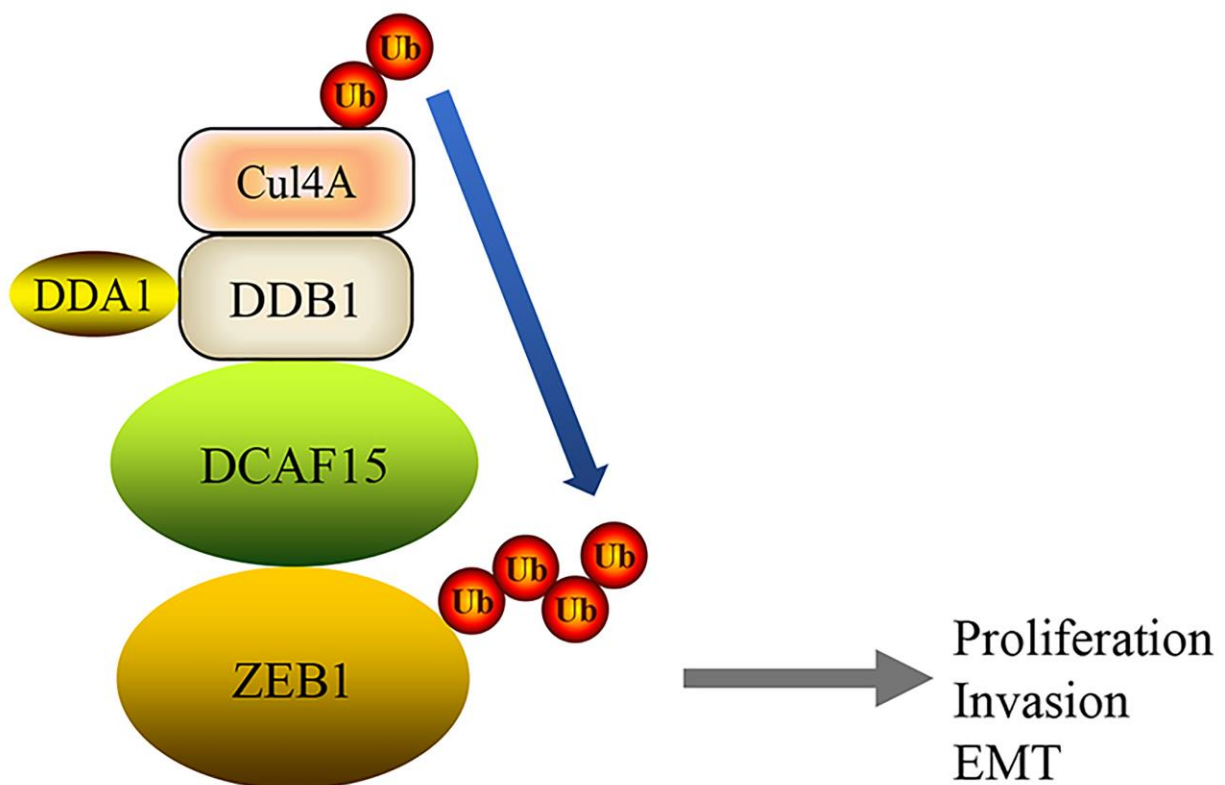


Figure 8. A mechanism of DCAF15 function as a tumor suppressor through ubiquitination and degradation of ZEB1 leads to proliferation, invasion and EMT of HCC.

In summary, our study demonstrates that ZEB1 is recognized by DCAF15 as a substrate in human HCC cells and offers new insight into the specific functions of DCAF15 in HCC and a unique DCAF15-ZEB1 axis in the E3 ubiquitin ligase system.

MATERIALS AND METHODS

Cell culture

Human HCC cell lines (SMMC-7721 and Hep-3B) and HEK293T cells were obtained from the Type Culture Collection of the Chinese Academy of Sciences (Shanghai, China). They were cultured in high-glucose Dulbecco's modified Eagle's medium (DMEM) (Gibco) supplemented with 10% fetal bovine serum (FBS) (Gibco), 100 mg/ml penicillin and streptomycin (Gibco) at 37°C in a humidified atmosphere containing 5% CO₂.

Plasmids Constructs

The DCAF15 and ZEB1 cDNAs were purchased from Genechem and subcloned into pCMV-Flag or pCMV-Myc expression vectors, respectively. ZEB1 deletion mutants were generated by PCR, and subcloned into pCMV-Myc expression vectors. All the constructs were confirmed by DNA sequencing.

RNA Interference

Human DCAF15 and Culling family siRNAs were purchased from GenePharma (Shanghai, China). siRNA transfection of cells was performed following the manufacturer's instructions. The siRNA oligos sequences information is provided in Supplementary Table 1. The cells were transiently transfected with siRNAs using Lipofectamine 2000 (Invitrogen) according to the manufacturer's instructions.

Western blotting analysis

Cells were washed three times with 1× phosphate buffer saline (PBS) for 5 min, and then lysed with ice-cold radioimmunoprecipitation buffer containing a protease inhibitor cocktail (Sigma-Aldrich) for 30 min. And the lysate containing protein was centrifuged, then analysis with Western blot. Cell lysates or immune-precipitates were resolved by SDS-PAGE and proteins were transferred onto polyvinylidene difluoride membranes. The membranes were then maintained in 5% non-fat milk blocking for 2 h, and incubated with primary antibody for 12 h and followed by secondary antibody for 1h at room temperature. The proteins bands were visualized using ECL chemiluminescence system (Santa Cruz). The following antibodies were used: DCAF15 (SAB1103260, Sigma), ZEB1 (4C4,

Novus), Myc (M4439; Sigma), Flag (F3165, Sigma), HA (M180-7; MLB), CUL1 (ab75817, Abcam), CUL2 (10981-2-AP, Proteintech), CUL3 (11107-1-AP, Proteintech), CUL4A (2715-S, EPITOMICS), CUL4B (12916-1-AP, Proteintech), CUL5 (ab34840, Abcam), and Actin (AC028; ABclonal). E-cadherin, N-cadherin, vimentin, β -catenin, and Slug antibodies were from CST (9782).

Immuno-precipitation analysis

To immune-precipitate the ectopically expressed Flag-tagged proteins, transfected cells were lysed in NP40 buffer. The whole-cell lysates were immune-precipitated with anti-Flag antibody-conjugated M2 agarose beads (Sigma) at 4°C overnight. After three washes with Flag lysis buffer, followed by two washes with BC100 buffer, the bound proteins were eluted using Flag-Peptide (Sigma)/BC100 for 5 h at 4°C. To immune-precipitate the endogenous proteins, cells were lysed with RIPA buffer. The supernatant was precleared with protein A/G beads (Sigma) and incubated with indicated antibodies overnight. Thereafter, protein A/G beads were applied at 4°C overnight. After 2 h of incubation, pellets were washed five times with lysis buffer and resuspended in sample buffer. And analysis with Western blot.

Immunofluorescence and confocal microscopy

Transfected cells were plated in glass-bottomed culture dishes (NEST) for 24 h. They were fixed with 4% paraformaldehyde, and then washed with PBS. After that, cells were permeabilized with 0.1% Triton X-100 for 15 min, and then washed with PBS. After treating the cells with blocking buffer (Beyotime) for 30 min, they were incubated with anti-Flag, anti-Myc, E-cadherin and vimentin, at 4°C overnight. Then, fluorescence labelled secondary antibodies were applied, and following DAPI was counterstained for 1 h at room temperature. An anti-fluorescence quencher was added dropwise and fixed with a coverslip. Images were taken using a confocal microscope (LSM710, Zeiss).

Quantitative RT-PCR (qRT-PCR)

Total RNA was extracted from transfected cells using the TRIzol reagent (Invitrogen), and the concentration was measured by NanoDrop1000 Spectrophotometer (Agilent, USA). cDNA was reversed transcribed by the Superscript RT kit (TOYOBO), according to the manufacturer's instructions. qRT-PCR amplification was performed using the SYBR Prime Script RT-qPCR kit (Takara, Japan). All quantization was normalized to the level of internal control GAPDH. The primer sequences for qRT-PCR were listed in Supplementary Table 1.

CCK-8 assay

1,000 cells were plated in 96-well plates in 100 μ l of media. 10 μ l Cell Counting Kit (CCK-8) (Yeasen) solution was added into medium for 30 min before measuring absorbance at a wavelength of 450 nm by a microplate reader (Thermo Scientific) daily for continuous 5 days.

Colony formation assay

Cells were seeded at 6-well plates with a density of 1×10^3 cells per well and then cultured for in complete medium for 10 days. Then, the colonies were fixed using 4% methyl alcohol for 20 min and stained with 5% crystal violet solution. Clones were photographed and counted to evaluate cell proliferation ability.

Migration and invasion assays

Migration and invasion chambers precoated with or without Matrigel (Corning) were prepared and placed into 24-well plates. Cells were digested into single cell suspension in 100 μ l serum-free medium and 1×10^5 cells were seeded into the upper chamber. And 700 μ l DMEM medium with 10% FBS was added into the lower chamber. After 24 h of incubation, cells that invaded through the filters were stained with using 4% methyl alcohol for 20 min and stained with 5% crystal violet solution. The non-invading cells were wiped out with a cotton swab. The membrane was randomly photographed by a microscope.

Wound healing assay

After transfected cells reaching 80% confluence, they were cultured with 1% fetal bovine serum for 12 h. The scratch was made by sterile pipette tips and mark the scratched point. The migration distance was photographed at 0 h and 24 h at the same location. The average migration distance was measured and analyzed.

Statistical analysis

Student's *t*-test was used for the two-group test, and one-way ANOVA was used for three or more groups test. Survival analysis was conducted using the Kaplan-Meier method. All data are shown as mean values \pm SEM for experiments performed with at least three replicates. SPSS 22.0 and GraphPad Prism 6.0 software were used for analyses. * represents $p < 0.05$; ** represents $p < 0.01$; *** represents $p < 0.001$.

AUTHOR CONTRIBUTIONS

Xiao Dong designed the study; Yang han, Lin Zhong and Encheng Zhang conducted the experiments; Yuqi Wang analyzed the data; Pingzhao Zhang wrote the manuscript; Chenji Wang and Qi Li revised the manuscript. Xiao Dong and Yang han contributed equally to this study. All authors read and approved the final manuscript.

ACKNOWLEDGMENTS

We thank Professor Lin Zhong for his work on HCC specimens.

CONFLICTS OF INTEREST

The authors declare no conflicts of interest.

FUNDING

This study was completely supported by the National Natural Science Foundation of China (No. 82073214 and NO. 81572310) and Outstanding disciplines leaders of Shanghai Municipal Commission of Health and Family Planning (No. 2018BR39).

REFERENCES

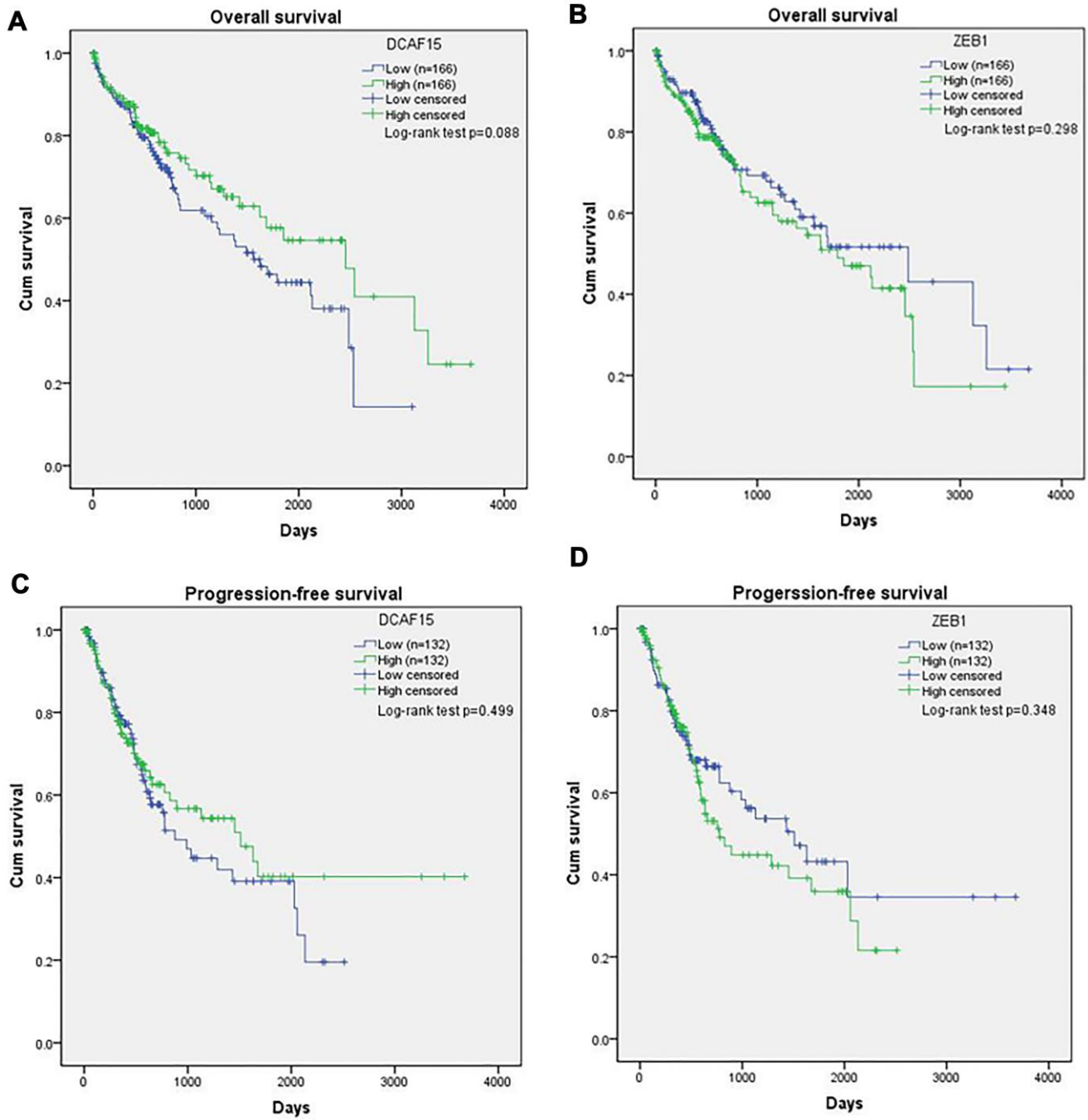
1. Siegel RL, Miller KD, Jemal A. Cancer statistics, 2019. *CA Cancer J Clin.* 2019; 69:7–34. <https://doi.org/10.3322/caac.21551> PMID:[30620402](https://pubmed.ncbi.nlm.nih.gov/30620402/)
2. Wallace MC, Preen D, Jeffrey GP, Adams LA. The evolving epidemiology of hepatocellular carcinoma: a global perspective. *Expert Rev Gastroenterol Hepatol.* 2015; 9:765–79. <https://doi.org/10.1586/17474124.2015.1028363> PMID:[25827821](https://pubmed.ncbi.nlm.nih.gov/25827821/)
3. Kirstein MM, Wirth TC. [Multimodal treatment of hepatocellular carcinoma]. *Internist (Berl).* 2020; 61:164–69. <https://doi.org/10.1007/s00108-019-00722-x> PMID:[31919533](https://pubmed.ncbi.nlm.nih.gov/31919533/)
4. Vande Lune P, Abdel Aal AK, Klimkowski S, Zarzour JG, Gunn AJ. Hepatocellular Carcinoma: Diagnosis, Treatment Algorithms, and Imaging Appearance after Transarterial Chemoembolization. *J Clin Transl Hepatol.* 2018; 6:175–88. <https://doi.org/10.14218/jcth.2017.00045> PMID:[29951363](https://pubmed.ncbi.nlm.nih.gov/29951363/)
5. Nakayama KI, Nakayama K. Ubiquitin ligases: cell-cycle control and cancer. *Nat Rev Cancer.* 2006; 6:369–81.

- <https://doi.org/10.1038/nrc1881>
PMID:16633365
6. Petroski MD, Deshaies RJ. Function and regulation of cullin-RING ubiquitin ligases. *Nat Rev Mol Cell Biol.* 2005; 6:9–20.
<https://doi.org/10.1038/nrm1547>
PMID:15688063
7. Han T, Goralski M, Gaskill N, Capota E, Kim J, Ting TC, Xie Y, Williams NS, Nijhawan D. Anticancer sulfonamides target splicing by inducing RBM39 degradation via recruitment to DCAF15. *Science.* 2017; 356:eaal3755.
<https://doi.org/10.1126/science.aal3755>
PMID:28302793
8. Jackson S, Xiong Y. CRL4s: the CUL4-RING E3 ubiquitin ligases. *Trends Biochem Sci.* 2009; 34:562–70.
<https://doi.org/10.1016/j.tibs.2009.07.002>
PMID:19818632
9. Zhang Y, Morrone G, Zhang J, Chen X, Lu X, Ma L, Moore M, Zhou P. CUL-4A stimulates ubiquitylation and degradation of the HOXA9 homeodomain protein. *EMBO J.* 2003; 22:6057–67.
<https://doi.org/10.1093/emboj/cdg577>
PMID:14609952
10. Li B, Jia N, Kapur R, Chun KT. Cul4A targets p27 for degradation and regulates proliferation, cell cycle exit, and differentiation during erythropoiesis. *Blood.* 2006; 107:4291–299.
<https://doi.org/10.1182/blood-2005-08-3349>
PMID:16467204
11. Hannah J, Zhou P. Distinct and overlapping functions of the cullin E3 ligase scaffolding proteins CUL4A and CUL4B. *Gene.* 2015; 573:33–45.
<https://doi.org/10.1016/j.gene.2015.08.064>
PMID:26344709
12. Ting TC, Goralski M, Klein K, Wang B, Kim J, Xie Y, Nijhawan D. Aryl Sulfonamides Degrade RBM39 and RBM23 by Recruitment to CRL4-DCAF15. *Cell Rep.* 2019; 29:1499–510.e1496.
<https://doi.org/10.1016/j.celrep.2019.09.079>
PMID:31693891
13. Lu G, Middleton RE, Sun H, Naniog M, Ott CJ, Mitsiades CS, Wong KK, Bradner JE, Kaelin WG Jr. The myeloma drug lenalidomide promotes the cereblon-dependent destruction of Ikaros proteins. *Science.* 2014; 343:305–09.
<https://doi.org/10.1126/science.1244917>
PMID:24292623
14. An J, Ponthier CM, Sack R, Seebacher J, Stadler MB, Donovan KA, Fischer ES. pSILAC mass spectrometry reveals ZFP91 as IMiD-dependent substrate of the CRL4(CRBN) ubiquitin ligase. *Nat Commun.* 2017; 8:15398.
<https://doi.org/10.1038/ncomms15398>
PMID:28530236
15. Uehara T, Minoshima Y, Sagane K, Sugi NH, Mitsushashi KO, Yamamoto N, Kamiyama H, Takahashi K, Kotake Y, Uesugi M, Yokoi A, Inoue A, Yoshida T, et al. Selective degradation of splicing factor CAPERalpha by anticancer sulfonamides. *Nat Chem Biol.* 2017; 13:675–80.
<https://doi.org/10.1038/nchembio.2363>
PMID:28437394
16. Zhang P, Sun Y, Ma L. ZEB1: at the crossroads of epithelial-mesenchymal transition, metastasis and therapy resistance. *Cell Cycle.* 2015; 14:481–87.
<https://doi.org/10.1080/15384101.2015.1006048>
PMID:25607528
17. Lehmann W, Mossmann D, Kleemann J, Mock K, Meisinger C, Brummer T, Herr R, Brabletz S, Stemmler MP, Brabletz T. ZEB1 turns into a transcriptional activator by interacting with YAP1 in aggressive cancer types. *Nat Commun.* 2016; 7:10498.
<https://doi.org/10.1038/ncomms10498>
PMID:26876920
18. Giannelli G, Koudelkova P, Dituri F, Mikulits W. Role of epithelial to mesenchymal transition in hepatocellular carcinoma. *J Hepatol.* 2016; 65:798–808.
<https://doi.org/10.1016/j.jhep.2016.05.007>
PMID:27212245
19. Liu Z, Wang Y, Dou C, Xu M, Sun L, Wang L, Yao B, Li Q, Yang W, Tu K, Liu Q. Hypoxia-induced up-regulation of VASP promotes invasiveness and metastasis of hepatocellular carcinoma. *Theranostics.* 2018; 8:4649–63.
<https://doi.org/10.7150/thno.26789>
PMID:30279729
20. Onder TT, Gupta PB, Mani SA, Yang J, Lander ES, Weinberg RA. Loss of E-cadherin promotes metastasis via multiple downstream transcriptional pathways. *Cancer Res.* 2008; 68:3645–54.
<https://doi.org/10.1158/0008-5472.can-07-2938>
PMID:18483246
21. Han L, Chen W, Xia Y, Song Y, Zhao Z, Cheng H, Jiang T. MiR-101 inhibits the proliferation and metastasis of lung cancer by targeting zinc finger E-box binding homeobox 1. *Am J Transl Res.* 2018; 10:1172–83.
PMID:29736210
22. Li L, Zheng YL, Jiang C, Fang S, Zeng TT, Zhu YH, Li Y, Xie D, Guan XY. HN1L-mediated transcriptional axis AP-2gamma/METTL13/TCF3-ZEB1 drives tumor growth and metastasis in hepatocellular carcinoma. *Cell Death Differ.* 2019; 26:2268–83.
<https://doi.org/10.1038/s41418-019-0301-1>
PMID:30778199

23. Sreekumar R, Emaduddin M, Al-Saihati H, Moutasim K, Chan J, Spampinato M, Bhome R, Yuen HM, Mescoli C, Vitale A, Cillo U, Rugge M, Primrose J, et al. Protein kinase C inhibitors override ZEB1-induced chemoresistance in HCC. *Cell Death Dis.* 2019; 10:703.
<https://doi.org/10.1038/s41419-019-1885-6>
PMID:[31543517](https://pubmed.ncbi.nlm.nih.gov/31543517/)
24. Han J, Xie C, Pei T, Wang J, Lan Y, Huang K, Cui Y, Wang F, Zhang J, Pan S, Liang Y, Zhen T, Song R, et al. Deregulated AJAP1/beta-catenin/ZEB1 signaling promotes hepatocellular carcinoma carcinogenesis and metastasis. *Cell Death Dis.* 2017; 8:e2736.
<https://doi.org/10.1038/cddis.2017.126>
PMID:[28383563](https://pubmed.ncbi.nlm.nih.gov/28383563/)
25. Chen J, Zhang L, Ma S, Lu G, Wang D. The aberrant expressions of MACC1, ZEB1, and KLF4 in hepatocellular carcinoma and their clinical significance. *Int J Clin Exp Pathol.* 2019; 12:3653–61.
PMID:[31934216](https://pubmed.ncbi.nlm.nih.gov/31934216/)
26. Chang L, Yuan Y, Li C, Guo T, Qi H, Xiao Y, Dong X, Liu Z, Liu Q. Upregulation of SNHG6 regulates ZEB1 expression by competitively binding miR-101-3p and interacting with UPF1 in hepatocellular carcinoma. *Cancer Lett.* 2016; 383:183–94.
<https://doi.org/10.1016/j.canlet.2016.09.034>
PMID:[27702662](https://pubmed.ncbi.nlm.nih.gov/27702662/)
27. Gupta A, Yang LX, Chen L. Study of the G2/M cell cycle checkpoint in irradiated mammary epithelial cells overexpressing Cul-4A gene. *Int J Radiat Oncol Biol Phys.* 2002; 52:822–30.
[https://doi.org/10.1016/s0360-3016\(01\)02739-0](https://doi.org/10.1016/s0360-3016(01)02739-0)
PMID:[11849807](https://pubmed.ncbi.nlm.nih.gov/11849807/)
28. Yang D, Zhao Y, Liu J, Sun Y, Jia L. Protective autophagy induced by RBX1/ROC1 knockdown or CRL inactivation via modulating the DEPTOR-MTOR axis. *Autophagy.* 2012; 8:1856–58.
<https://doi.org/10.4161/auto.22024>
PMID:[22965024](https://pubmed.ncbi.nlm.nih.gov/22965024/)
29. Liu M, Jiang K, Lin G, Liu P, Yan Y, Ye T, Yao G, Barr MP, Liang D, Wang Y, Gong P, Meng S, Piao H. Ajuba inhibits hepatocellular carcinoma cell growth via targeting of beta-catenin and YAP signaling and is regulated by E3 ligase Hakai through neddylation. *J Exp Clin Cancer Res.* 2018; 37:165.
<https://doi.org/10.1186/s13046-018-0806-3>
PMID:[30041665](https://pubmed.ncbi.nlm.nih.gov/30041665/)
30. Zhang L, Chen J, Ning D, Liu Q, Wang C, Zhang Z, Chu L, Yu C, Liang HF, Zhang B, Chen X. FBXO22 promotes the development of hepatocellular carcinoma by regulating the ubiquitination and degradation of p21. *J Exp Clin Cancer Res.* 2019; 38:101.
<https://doi.org/10.1186/s13046-019-1058-6>
PMID:[30808376](https://pubmed.ncbi.nlm.nih.gov/30808376/)
31. Yin J, Zhu JM, Shen XZ. The role and therapeutic implications of RING-finger E3 ubiquitin ligases in hepatocellular carcinoma. *Int J Cancer.* 2015; 136:249–57.
<https://doi.org/10.1002/ijc.28717>
PMID:[24420637](https://pubmed.ncbi.nlm.nih.gov/24420637/)
32. Jin J, Arias EE, Chen J, Harper JW, Walter JC. A family of diverse Cul4-Ddb1-interacting proteins includes Cdt2, which is required for S phase destruction of the replication factor Cdt1. *Mol Cell.* 2006; 23:709–21.
<https://doi.org/10.1016/j.molcel.2006.08.010>
PMID:[16949367](https://pubmed.ncbi.nlm.nih.gov/16949367/)
33. Du X, Volkov OA, Czerwinski RM, Tan H, Huerta C, Morton ER, Rizzi JP, Wehn PM, Xu R, Nijhawan D, Wallace EM. Structural Basis and Kinetic Pathway of RBM39 Recruitment to DCAF15 by a Sulfonamide Molecular Glue E7820. *Structure.* 2019; 27:1625–33.e1623.
<https://doi.org/10.1016/j.str.2019.10.005>
PMID:[31693911](https://pubmed.ncbi.nlm.nih.gov/31693911/)
34. Jia X, Pan L, Zhu M, Hu H, Zhai L, Liu J, Hu M, Liu B, Tan M. pSILAC method coupled with two complementary digestion approaches reveals PRPF39 as a new E7070-dependent DCAF15 substrate. *J Proteomics.* 2020; 210:103545.
<https://doi.org/10.1016/j.jprot.2019.103545>
PMID:[31626998](https://pubmed.ncbi.nlm.nih.gov/31626998/)

SUPPLEMENTARY MATERIALS

Supplementary Figure



Supplementary Figure 1. DCAF15 was associated with better prognosis for TCGA HCC patients. Kaplan-Meier analysis of OS and DFS in HCC patients. OS (A–B) and DFS (C–D) of patients according to different DCAF15 and ZEB1 RNA expression.

Supplementary Table

Supplementary Table 1. Primers used for RT-qPCR in cultured cell lines, and sequences of siRNAs.

Primers for RT-qPCR with cell lines samples		
Gene name	F: 5'-3'	R: 5'-3'
DCAF15	CGAGCCTGGCTATGTCAACT	TCTTGTGTCGTCCTCCAACATCAT
ZEB1	AGCAGTGAAAGAGAAGGGAATGC	GGTCCTCTTCAGGTGCCTCAG
E-cadherin	GCTTCAGTTCCGAGGTCTAC	GCCAGTGCATCCTTCAAATC
N-cadherin	GTGGAGGCTTCTGGTGAA AT	GGCTCGCTGCTTTCATACT
β-catenin	CATCTACACAGTTTGTGCTGCT	GCAGTTTTGTGTCAGTTCAGGGA
vimentin	GAGGAGATGCTCCAGAGAGA	TCCTGC AAGGATTCCACTTT
Slug	TGATGCCAGTCTAGGAAAT	AGTGAGGGCAAGAGAAAGG
GAPDH	GAAGGTGAAGGTCGGAGT	GAAGATGGTGATGGGATTTTC
Sequences of siRNAs		
Gene name	Sequence	
si-DCAF15 #1	GGGUGUGCGUGUCCCUCAA	
si-DCAF15 #2	AGUUCAACGUUCACAGCAA	
si-ZEB1	CCUAGUCAGCCACCUUUA	
siCUL1	CAACGAAGAGUUCAGGUUU	
siCUL2	GGAAGUGCAUGGUAAAUUU	
siCUL3	GAGAAGATGTACTAAATTC	
siCUL4A	GCACAGAUCCUCCGUUUA	
siCUL4B	UAAAUAAACCUCCUUGAUGA	
siCUL5	GACACGACGUCUUAUAUUA	

SPRY4 suppresses proliferation and induces apoptosis of colorectal cancer cells by repressing oncogene EZH2

Jia Guo^{1,*}, Huadong Zhu^{2,*}, Qiang Li³, Jianhua Dong³, Wei Xiong³, Kun Yu³

¹Department of Gastroenterology, Sunshine Union Hospital, Weifang 261000, China

²School of Life Science, Nanchang University, Nanchang 330031, China

³Department of Colorectal Cancer Surgery, Yunnan Cancer Hospital, The Third Affiliated Hospital of Kunming Medical University, Kunming 650118, China

*Equal contribution

Correspondence to: Kun Yu; **email:** yukun479@126.com, <https://orcid.org/0000-0003-3711-8320>

Keywords: colorectal cancer, SPRY4, EZH2, cell proliferation

Abbreviations: CRC: colorectal cancer; Ct: comparative threshold cycle; CCK-8: Cell Counting Kit-8; Oe-SPRY4: overexpress SPRY4; si-SPRY4: silence SPRY4

Received: September 13, 2020 **Accepted:** February 16, 2021 **Published:** April 20, 2021

Copyright: © 2021 Guo et al. This is an open access article distributed under the terms of the [Creative Commons Attribution License](https://creativecommons.org/licenses/by/3.0/) (CC BY 3.0), which permits unrestricted use, distribution, and reproduction in any medium, provided the original author and source are credited.

ABSTRACT

Colorectal cancer (CRC), a common malignant tumor in the digestive tract, is a leading cause of cancer-related death. *SPRY4* has been reported to act as a tumor suppressor gene in various tumors. This study aims to assess the role of *SPRY4* in colorectal cancer (CRC) and uncover its underlying mechanisms. Firstly, the expression levels of *SPRY4* were measured in CRC cell lines. *SPRY4*-overexpressing or silencing plasmids were transfected into CRC cells to regulate its expression level. CCK-8, colony formation, EdU assay, wound-healing and Transwell assays were performed to determine cell proliferation, invasion and migration abilities. Then, apoptosis was measured by flow cytometry analysis, and the expression of apoptosis-related protein was analyzed by western-blotting. Next, the *in vivo* tumorigenesis assay was performed in nude mice. According to the results, there was a lower expression of *SPRY4* in CRC cell lines compared with normal cell line, and the overexpression of *SPRY4* significantly suppressed cell proliferation, migration and invasion, and promoted apoptosis in SW480 cells. Moreover, the enhanced proliferation, invasion and migration upon *SPRY4* silencing was reversed by *EZH2* inhibition. In addition, we found that the overexpression of *SPRY4* inhibited tumorigenesis *in vivo* by diminishing the size and weight of the tumors. Our study indicates that *SPRY4* might be a potential tumor suppressor gene and prognostic factor for patients with CRC.

INTRODUCTION

Despite significant progress in therapeutic strategies has been achieved in recent years, colorectal cancer (CRC) still ranks the third most frequent tumor worldwide, followed by lung and breast carcinoma [1]. The mortality of CRC in developed countries is high, and is keeping an increasing tendency [2]. At present, there are over 1 million newly diagnosed cases each year, seriously threatening People's health and quality of life [3]. Therefore, in-depth exploration of the process and specific molecular mechanism of CRC is particularly

important, which may offer the references or strategies for updated treatments.

Sprouty (SPRY) are initially identified as the inhibitors of receptor tyrosine kinase regulating tracheal branching in *Drosophila* [4]. *SPRY4*, a membrane of SPRY family (*SPRY1-4*), is generally recognized as a regulator of receptor tyrosine kinases [5]. In addition, *SPRY4* also exerts regulatory effects on cell growth, differentiation, and metastasis during the development of malignant tumors in various types of cancers [6, 7]. *SPRY4* suppresses the migration and stem cell-related

properties of breast carcinoma cells and suppresses cell motility of prostate cancer cells [8–10]. Nevertheless, *SPRY4* acts as an oncogene to promote ovarian cancer invasion and accelerate human ovarian cancer progression [11]. Thus, *SPRY4* plays a dual role in human cancers and the function of *SPRY4* often varies among different tumor types. However, up to date, the role of *SPRY4* in CRC still remains unclear.

EZH2, a histone-lysine N-methyltransferase enzyme, has been documented to be associated with the occurrence and development of malignant tumors [12–14], and also be involved in the cellular biological functions of various cancers, including gastric cancer, hepatocellular carcinoma, bladder cancer, and nasopharyngeal cancer [15–18]. Furthermore, several studies have reported the abnormally high expression of *EZH2*, which is also positively correlated with the poor prognosis of CRC [19–21], indicating an important role of *EZH2* in CRC.

The aim of the present study is to explore the role of *SPRY4* during tumor progression of CRC *in vivo* and *in vitro*. In addition, this study also investigates the relationship between *SPRY4* and *EZH2* to further understand the potential regulatory mechanism.

RESULTS

Differential expression of *SPRY4* and *EZH2* between colorectal cancer cells and normal human colon cell

To explore the role of *SPRY4* in CRC, we first screened the expression level of *SPRY4* and *EZH2* in four human CRC cell lines, SW620, SW480, LOVO and HCT116, and a normal human colorectal epithelial cell line, NCM460, via western blotting and RT-qPCR. As shown in Figure 1A–1C, the translation and transcription levels of *SPRY4* genes between normal cell line and cancer cell lines were statistically different. In particular, NCM460 cell line exhibited the highest level of *SPRY4*, while SW480 exhibited the lowest. In contrast, the expression of *EZH2* gene was upregulated in all cancer cell lines, and SW480 showed the highest level (Figure 1D–1F). Therefore, we selected SW480 cell line to continue the investigation of *SPRY4*.

Effects of *SPRY4* overexpression on CRC cell proliferation

To examine the impacts of *SPRY4*, we constructed the overexpression plasmid of *SPRY4* and the enhanced expression of *SPRY4* was observed in transfected SW480 (Figure 2A–2C). Next, the effects of *SPRY4* overexpression on SW480 cell proliferation were determined by CCK8, colony formation and EdU

assays. As shown in Figure 2D, *SPRY4* overexpression dramatically suppressed the proliferation ability of SW480 cells in a time-dependent manner. Additionally, compared with negative control group, the number of cell colonies was also significantly reduced upon *SPRY4* overexpression (Figure 2E). Furthermore, EdU assay further revealed that overexpression of *SPRY4* obviously decreased the proliferation ability of SW480 cells (Figure 2F).

Effects of *SPRY4* overexpression on invasion and migration of CRC cell

We further evaluated the impacts of *SPRY4* on CRC cell mobility. As exhibited by the *in vitro* scratch assay (Figure 2G, 2I), wound closure of SW480 cell was decreased upon *SPRY4* overexpression, compared to the control. For the Transwell assay, SW480 cells with different treatments were allowed to invade for 48 h and a similar trend was also observed. The *SPRY4* overexpression treatment resulted in the least amount of cancer cells in the lower chamber (Figure 2H, 2J). Since matrix metalloproteinase 2 (MMP2) and MMP9 are the key members of the MMP family which can degrade the extracellular matrix, we continued to evaluate their expression mediated by *SPRY4* overexpression with western-blotting assay. As depicted in Figure 2K–2M, the expression of MMP2 and MMP9 was downregulated by *SPRY4*, which was only about half of that of control group. In general, these data indicated a preventive role of *SPRY4* against invasion and migration of CRC cells.

Effect of *SPRY4* overexpression on apoptosis in CRC cells

Next, we assessed the impacts of *SPRY4* on apoptosis in SW480 cells. As shown in Figure 3A, 3B, compared to the control group, *SPRY4* overexpression remarkably improved cell apoptosis rate. In addition, *SPRY4* overexpression upregulated the protein expressions of pro-apoptosis-related Bax and cleaved caspase-3 while down-regulated the anti-apoptosis-related Bcl-2 (Figure 3C–3F), which further demonstrated the promotive effect on cell apoptosis in SW480 cells.

SPRY4 reduced the expression of *EZH2* and MDM2

SW480 cells is a p53 double-mutant cell line, whereas the main target of MDM2 is wild-type p53 [22]. In addition, activated p53 was demonstrated to suppress *EZH2* gene expression through repression of the *EZH2* gene promoter, and *SPRY4* was reported to promote tumor cell proliferation by activating *EZH2* [23, 24], thus, the relationship among *SPRY4*, MDM2 and *EZH2* in SW480 cells aroused our interest. Intriguingly, we

observed a statistically significant inverse correlation between *SPRY4* and the expression of EZH2 and MDM2 (Figure 4A–4C). Upon *SPRY4* overexpression, the expression of EZH2 and MDM2 in SW480 were downregulated, which were similar with the treatment of GSK126 at 50 μ M, indicating an underlying inhibition role of *SPRY4* towards EZH2 and MDM2. Next, the immunoprecipitation assay was used to evaluate the association between EZH2 and MDM2, and western blot was used to measure the expression of EZH2 and MDM2. We found that EZH2 and MDM2 could bind to each other (Figure 4D, 4E). Thus, taking the important role of p53 into consideration, the functional role of *SPRY4* in CRC might be achieved partly through EZH2/MDM2/p53 axis.

The effects of *SPRY4* silencing on proliferation, invasion and apoptosis were partly via regulating EZH2

To further study the impacts of *SPRY4*, we successfully transfected SW480 cells with si-*SPRY4* plasmid (Figure 5A). The protein expression of EZH2 was demonstrated

to be up-regulated after transfection with si-*SPRY4* (Figure 5B). A series of cellular functional experiments showed that after *SPRY4* was knocked down, the proliferation of SW480 cells was greatly enhanced (reached ~200% after 72 h of incubation) and the inhibitory effects of GSK126 on cell proliferation in such cell were compromised. Similar trends were also observed in the wound-healing and Transwell assays. Compared with the GSK126 alone, GSK126 combined with si-*SPRY4* transfection enhanced cell migration and invasion (Figure 5D–5G), upregulated expression of MMP2 and MMP9 (Figure 5H–5J), and reduced level of apoptosis (Figure 6A, 6B), as well as upregulated the expression of Bcl-2 and decreased the expression of Bax and cleaved caspase-3 (Figure 6C–6F). These results again highlighted the *SPRY4* as a repressor to oncogene *EZH2*.

SPRY4 regulated tumorigenesis *in vivo*

To further investigate the effects of *SPRY4* on tumorigenesis *in vivo*, we have additionally constructed plasmids to overexpress *SPRY4* (Oe-*SPRY4*) or silence *SPRY4* (si-*SPRY4*), respectively. The SW480 cells

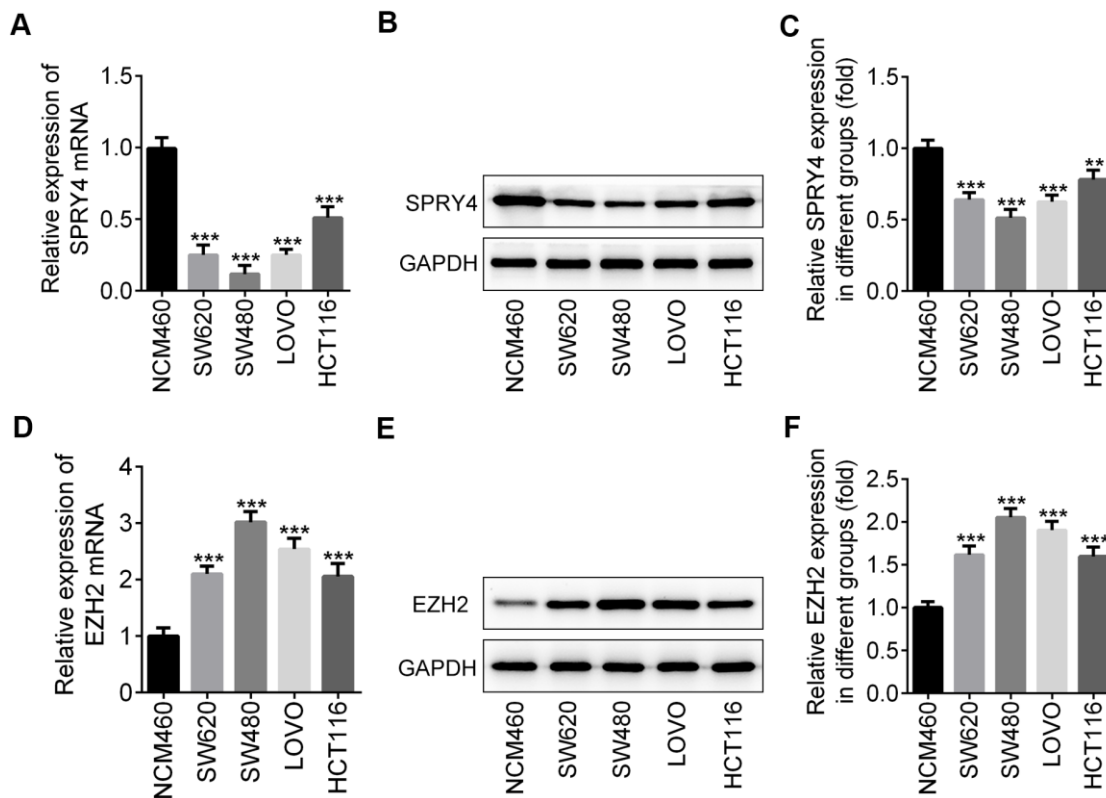


Figure 1. Differential expression of *SPRY4* and *EZH2* between colorectal cancer cells and normal human colon cell. From four human CRC cell lines, SW620, SW480, LOVO and HCT116, and a normal human colon mucosal epithelial cell line NCM460, we detected the mRNA level and protein expression of *SPRY4* using western blotting and RT-qPCR, respectively (A–C). The mRNA level and protein expression of *EZH2* were detected using western blotting and RT-qPCR, respectively (D–F). **, *** $p < 0.01, 0.001$ vs NCM460.

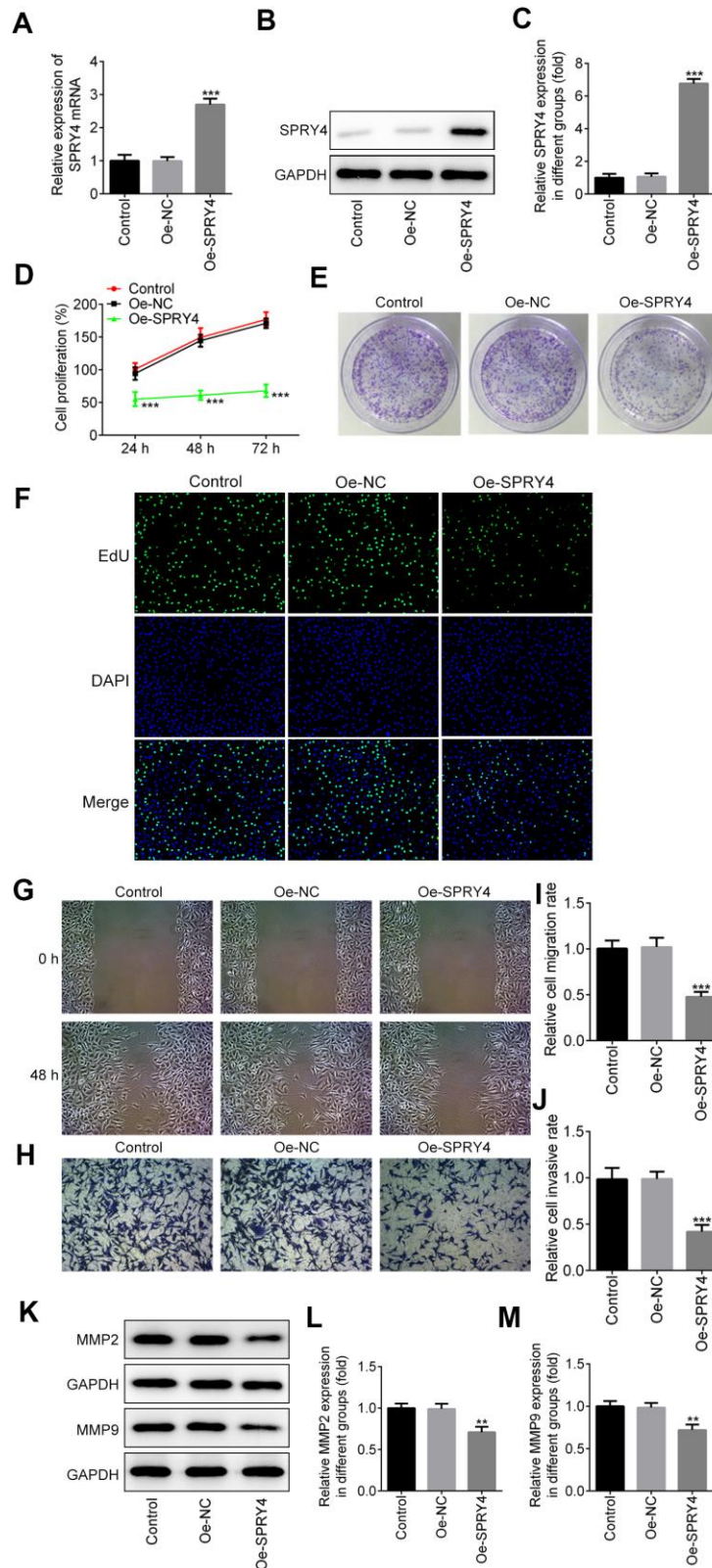


Figure 2. Effects of *SPRY4* overexpression on CRC cell proliferation, migration and invasion. The overexpression plasmid of *SPRY4* was constructed and transfected into SW480 cells. The mRNA level and protein expression of *SPRY4* were detected using RT-qPCR and western blotting, respectively (A–C). Cell proliferation ability was determined using CCK-8 assay (D), cell colony formation (E), and EdU assay (F). Wound-healing and Transwell assays were conducted to measure cell migration and invasion, respectively (G–J). Protein expression of MMP2 and MMP9 was detected by western blotting (K–M). **, *** $p < 0.01$, 0.001 vs Oe-NC.

transfected with Oe-*SPRY4* or si-*SPRY4* were subcutaneously implanted into the axilla of the nude mice. The weight of mice and the tumor volume were monitored before sacrifice. Our results showed that both tumor size and tumor weight were reduced by Oe-*SPRY4* and increased by si-*SPRY4*, especially, and the promotive effect of si-*SPRY4* on tumor size and tumor weight was partly reversed by GSK126 (Figure 7A–7D). The protein expression of EZH2 in tumor tissues was reduced in Oe-*SPRY4* group but increased in si-*SPRY4* group (Figure 7E, 7F), indicating the involvement of EZH2 in the antitumor activity of *SPRY4*. Immunohistochemistry assay indicated that the expression of Ki67 was remarkably increased upon si-*SPRY4*, which was also partly declined upon co-treatment of si-*SPRY4* and GSK126 (Figure 7G). Moreover, H&E staining was applied to observe the morphological changes in major organs in different groups. As shown in Figure 7H, the liver, lung and kidney were not injured in each group, indicating that cancer metastasis did not occur. Collectively, our data

demonstrated that the *SPRY4* regulated tumorigenesis *in vivo*.

DISCUSSION

Pathogenesis and metastasis of CRC generally coincides with the successive dysregulation of certain genes. Even though mounting evidence has highlighted the *SPRY4* functions as tumor suppressor, the effects and the mechanism of *SPRY4* in regulating CRC progression remain unclear. The purpose of this study is to clarify whether the suppressive role of *SPRY4* in tumorigenesis involves modulation of CRC. In order to assess the impacts of *SPRY4* on CRC, we first measured the mRNA and protein expression of *SPRY4* in CRC cell lines and the normal colorectal cell line. We demonstrated that differential expression modality between cancer cells and normal cells in *SPRY4*, which hinted that *SPRY4* might serve as a tumor suppressor gene that negatively regulates tumor development.

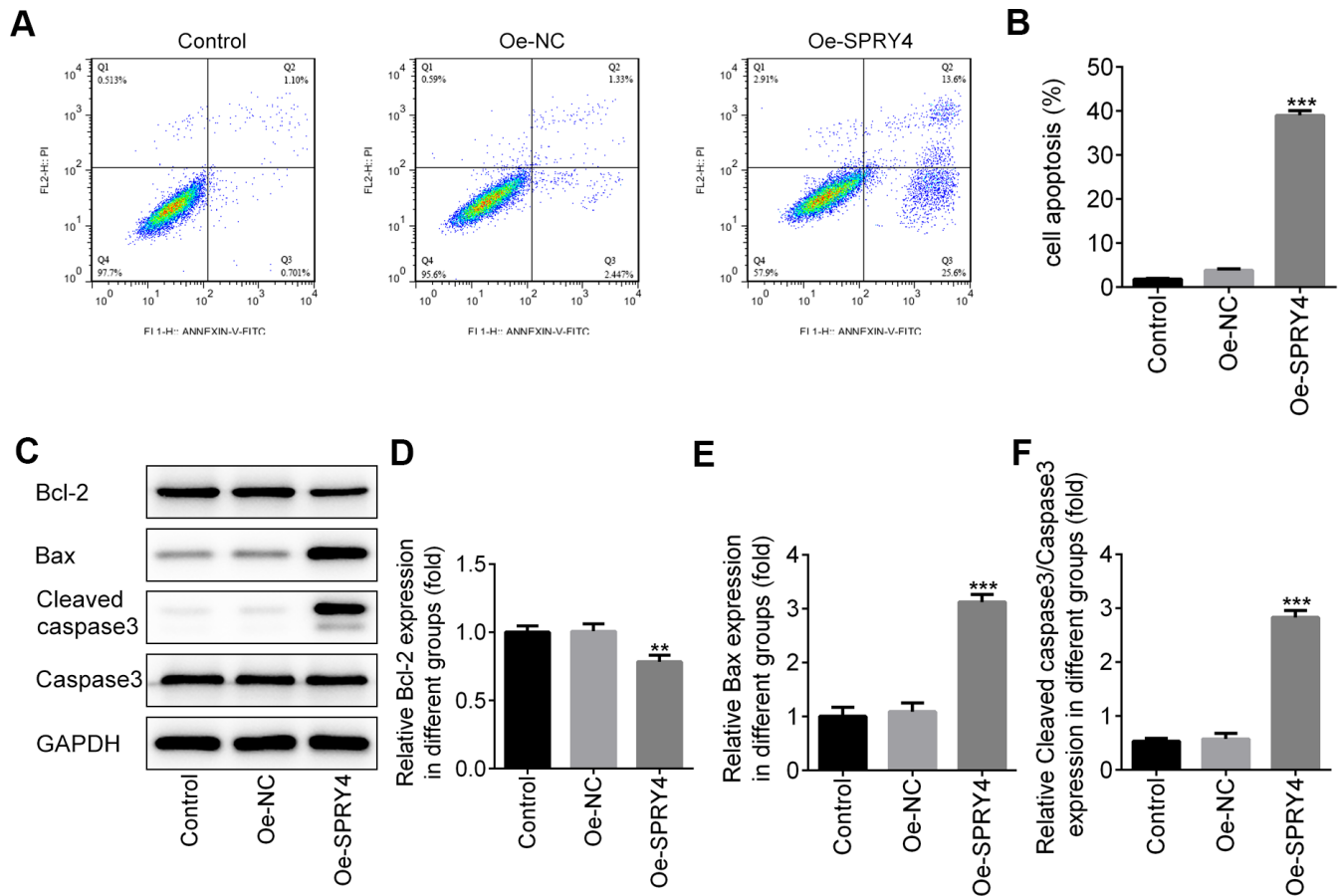


Figure 3. Effects of *SPRY4* overexpression on CRC cell apoptosis. The overexpression plasmid of *SPRY4* was constructed and transfected into SW480 cells. Then, cell apoptotic rate was analyzed using flow cytometry assay (A, B). Furthermore, the protein expressions of Bcl-2, Bax, Cleaved caspase-3 and caspase-3 were measured using western blotting (C–F). **, *** $p < 0.01, 0.001$ vs Oe-NC.

Then, to clarify the role of *SPRY4* in CRC, we explored the effects of *SPRY4* on CRC cellular biological activities. The uncontrolled proliferation of CRC cells is the main cause for tumor metastasis. Recently, much attention has been paid on the exploration of specific genes or drugs which have inhibitory effects on cell proliferation during the development of CRC. For example, high expression of ubiquitin-like modifier-activating enzyme 2 (UBA2) was reported to be associated with poor prognosis of patients with CRC. Further basic experiments exhibited that downregulated UBA2 could significantly inhibit the proliferation of CRC cell lines *in vitro* and suppress tumor growth *in vivo* [25], and butyrate could interrupt the metabolism of CRC cells and ultimately result in the suppression of cell proliferation by targeting pyruvate kinase M2, thus suppressing the development of CRC [26]. These existing evidence revealed that inhibition of cell over-proliferation is an alternative approach to discover the effective treatment for CRC therapy. In the present study, we found that the overexpression of *SPRY4* significantly reduced cell proliferation by inhibiting

cell viability and hindering colony formation of SW480 cells.

Apoptosis, as a process of the programmed cell death, is essential for the development and for the well-functioning of multicellular systems, and also is an important mechanism among anti-cancer research [27]. In this study, we found that overexpression of *SPRY4* significantly promoted cell apoptosis rate of SW480 cells. What's more, overexpression of *SPRY4* showed significant inhibitory effects on the expression of Bcl-2 and promotive effects on the expression of Bax and cleaved caspase-3. Caspase-3 is known as an executioner caspase, and exerts critical effects during cell apoptosis by cleaving many key cellular proteins, no matter through intrinsic mitochondrial pathway or the extrinsic death receptor pathway [28]. Bcl-2 is a critical anti-apoptotic gene which can inhibit cell apoptosis by reducing the generation of reactive oxygen and hindering the release of cytochrome C. While Bax is regarded as a pro-apoptotic gene as the anti-apoptotic activity of Bcl-2 can be abolished by Bax [29]. Thus, these

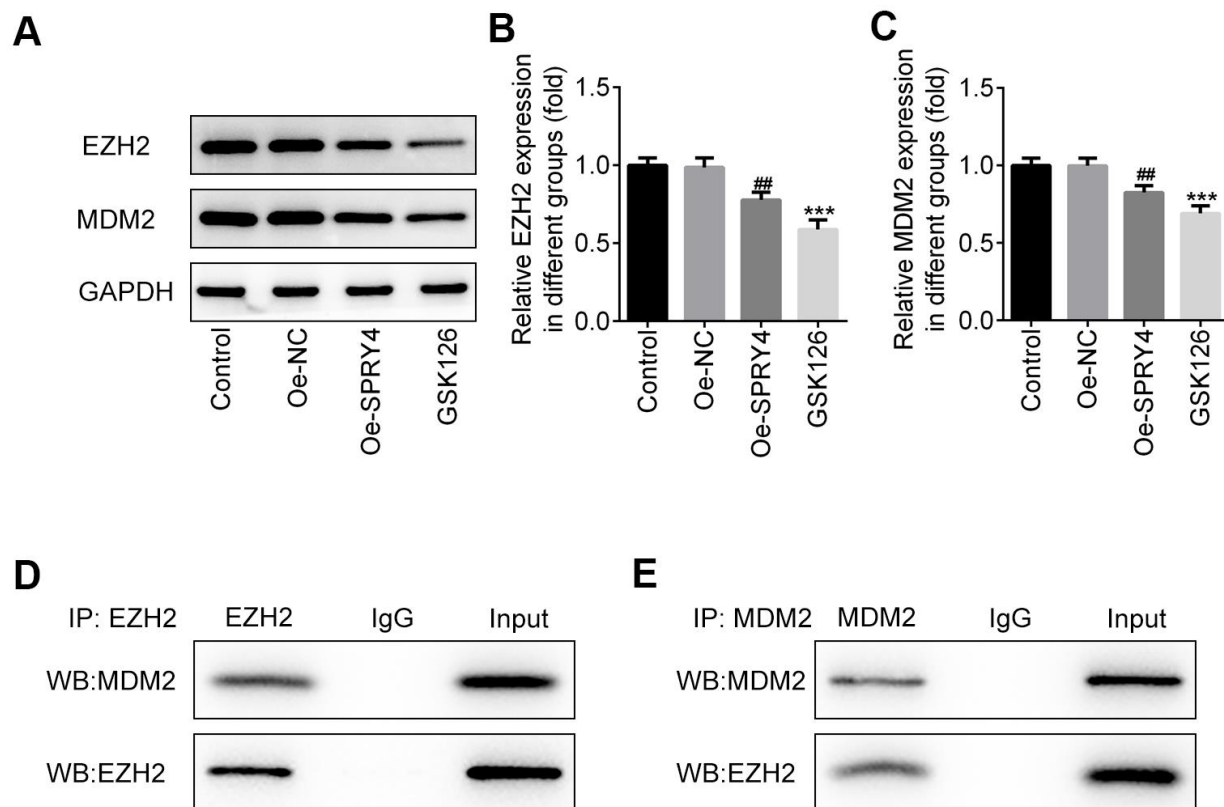


Figure 4. *SPRY4* reduced the expression of EZH2 and MDM2. SW480 cells were transfected with overexpression plasmid of *SPRY4* or co-treated with overexpression plasmid of *SPRY4* and GSK126 (an EZH2 inhibitor). In each group, protein expressions of EZH2 and MDM2 were detected using western blotting (A–C). Immunoprecipitation assay, followed by western blotting, was used to evaluate the association between EZH2 and MDM2 (D, E). *** $p < 0.001$ vs Control; ## $p < 0.01$ vs Oe-NC.

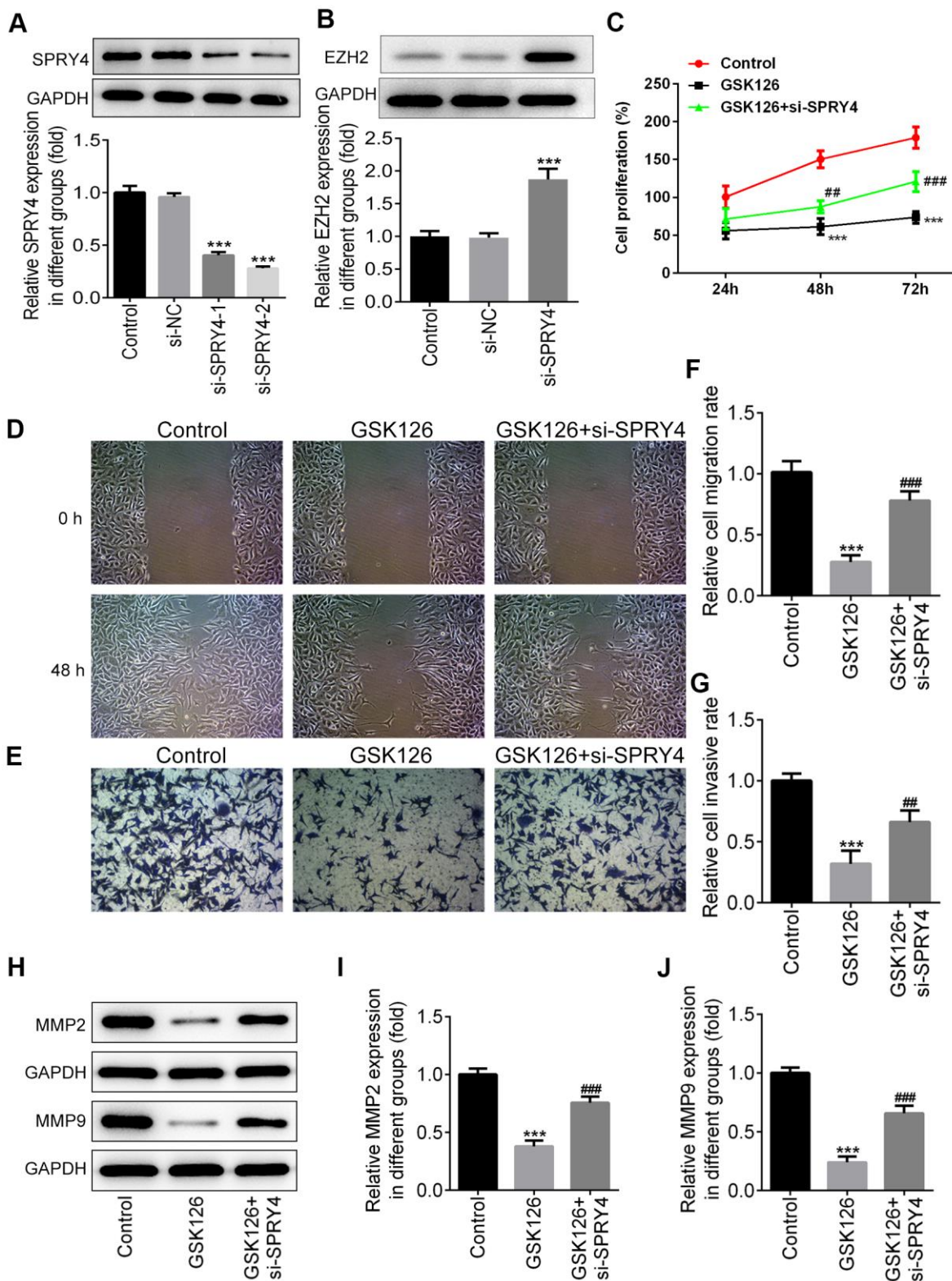


Figure 5. The function of *SPRY4* silence on proliferation, migration and invasion in SW480 cells. SW480 cells were transfected with si-*SPRY4* plasmid-1/2 and the empty plasmid, then the protein expression of *SPRY4* in different groups was measured using western blotting (A). After transfection, the protein expression of EZH2 was also measured using western blot (B). *** $P < 0.001$ vs si-NC. SW480 cells were treated with GSK126 or co-treated with GSK126 and si-*SPRY4*. CCK-8 assay was conducted to determine cell proliferation ability (C). Wound-healing and Transwell assays were performed to determine cell migration and invasion abilities (D–G). The protein expression of MMP2 and MMP9 was measured using western blotting (H–J). *** $p < 0.001$ vs Control; ##, ### $p < 0.01, 0.001$ vs GSK126.

results suggested that the overexpression of *SPRY4* might promote apoptosis in SW480 cells by upregulating Bax and caspase-3 while downregulating Bcl-2.

We next investigated the possible targets of *SPRY4* in CRC cells through analysis by immunoprecipitation and western blotting. Considering the important role of p53 for *SPRY4* and the close relationship among p53, MDM2 and EZH2, it is interesting to find that EZH2 is an appropriate theoretical candidate target of *SPRY4*. EZH2 is highly expressed in various malignant tumors and is closely involved in the occurrence and development of cancers. EZH2 activation can promote expansion of breast tumor initiating cells [30], whereas GSK126, the novel EZH2 inhibitor, exerts anticancer effects on gastric cancer and prostate cancer by inhibiting cell migration, invasion and angiogenesis [31, 32]. In the present study, both the expression of EZH2 and

MDM2 were downregulated upon *SPRY4* overexpression. Moreover, with the observation that GSK126 could mimic the inhibitory effect of *SPRY4* on EZH2 and MDM2, our work indicated that EZH2 might be a direct target of *SPRY4* in CRC. EZH2 was verified to bind to MDM2, and MDM2 could bind p53 to promote p53 degradation, which then influenced CRC progression [33, 34]. Thus, the antitumor effects of *SPRY4* might be achieved partly by regulating EZH2-mediated MDM2/p53 pathway. The more detailed information concerning on an in-depth research of the mechanism action of *SPRY4* is deserved to be investigated in the future.

Collectively, this study found that *SPRY4* might act as an anti-tumor gene in CRC and *SPRY4* exerted a suppressive effect on CRC progression via the inhibition of EZH2. This study suggests that *SPRY4* may serve as a promising candidate of therapeutic targets for CRC treatment.

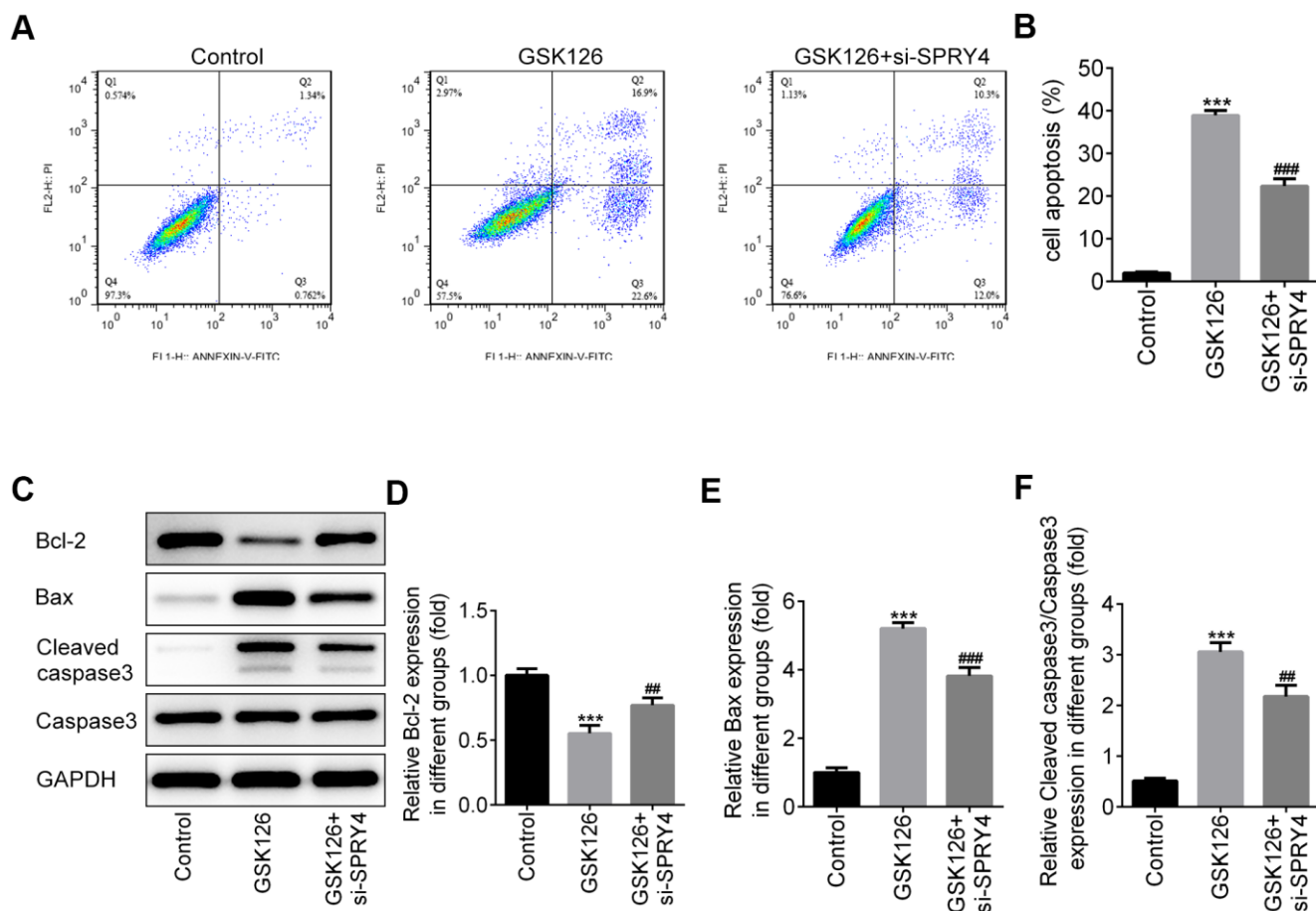


Figure 6. The function of *SPRY4* silence on apoptosis in SW480 cells. SW480 cells were treated with GSK126 or co-treated with GSK126 and si-*SPRY4*. Cell apoptotic rate was analyzed using flow cytometry assay (A, B). Moreover, the protein expressions of Bcl-2, Bax, Cleaved caspase-3 and caspase-3 were measured using western blotting (C-F). *** $p < 0.001$ vs Control; ##, ### $p < 0.01$, 0.001 vs GSK126.

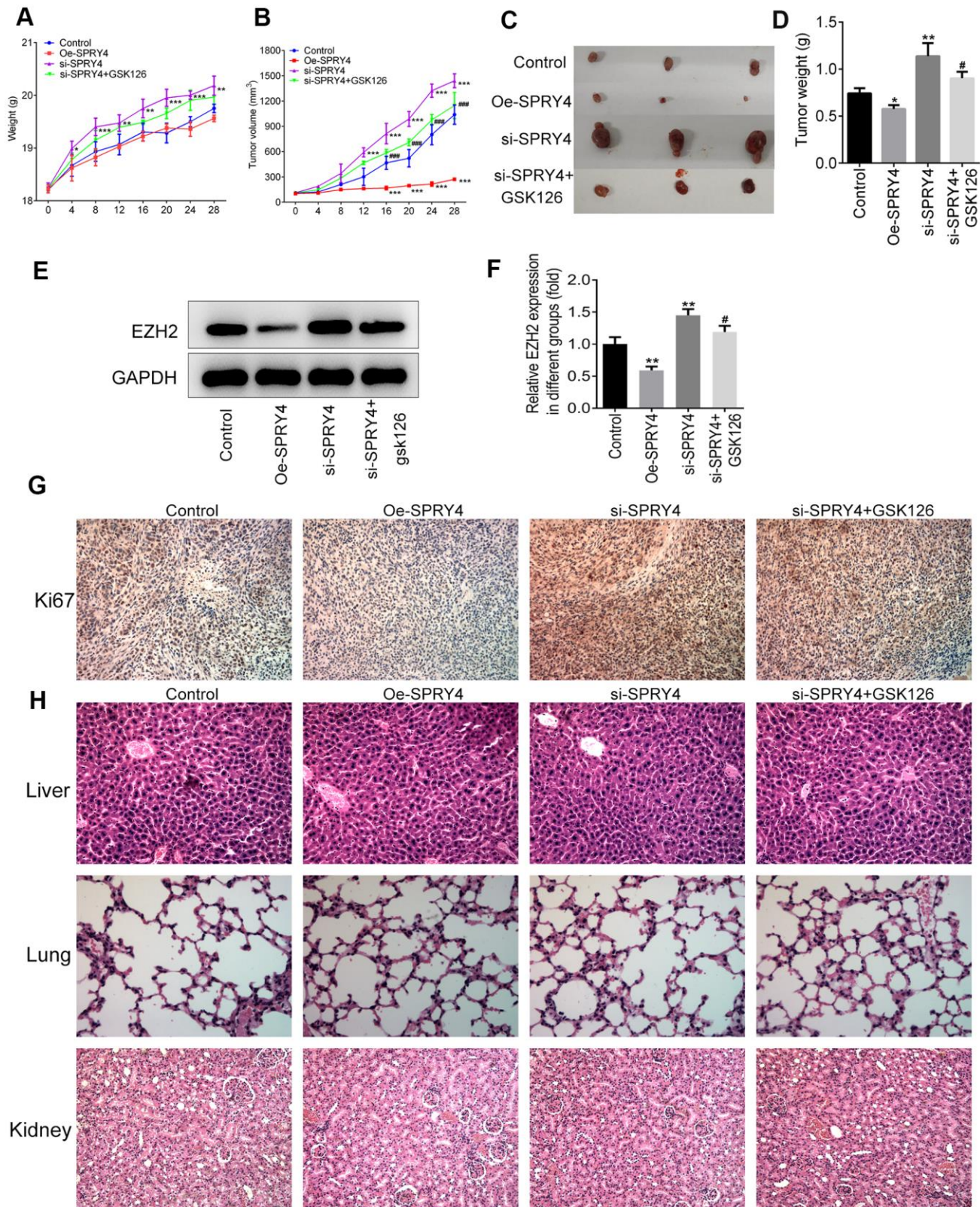


Figure 7. *SPRY4* regulated tumorigenesis *in vivo*. The SW480 cells transfected with Oe-SPRY4 or si-SPRY4 were subcutaneously implanted into the axilla of the nude mice. The weight and tumor volume of mice were monitored every four days (A, B). After sacrifice, the total tumors were separated from the mice and were weighed (C, D). The protein expression of EZH2 in tumor tissues was detected using western blot (E, F). The expression of Ki67 was analyzed by immunohistochemistry (G). This histology of liver, lung and kidney was measured by H&E staining (H). *, **, *** $p < 0.05, 0.01, 0.001$ vs Control; #, ### $p < 0.05, 0.001$ vs si-SPRY4.

MATERIALS AND METHODS

Cells

Human colorectal epithelial cell line NCM460 and colorectal cancer cell lines, including SW620, SW480, LOVO and HCT116, were obtained from American Type Culture Collection (ATCC, Manassas, VA, USA). All cells were cultured in complete Dulbecco's modified Eagle medium (DMEM; HyClone, Logan, UT) with 10 % fetal bovine serum (FBS; HyClone, Logan, UT).

Quantitative real-time PCR

Trizol reagent (Beyotime, Haimen, China) was applied to extract entire RNA. After determining the quality and concentration of the extracted RNA, 1 µg of RNA was reverse transcribed to complementary DNA (cDNA) by a reverse transcriptase (TaKaRa, Japan). Then, quantitative real time PCR (qRT-PCR) was conducted using the SYBR-Green method (Applied Biosystems, USA) to detect the expression level of corresponding genes following the manufacturer's guide. The primers used were listed as follows: *SPRY4* (forward-5'-TCTGACCAACGGCTCTTAGAC-3', reverse-5'-GTGCATAGTTGACCAGAGTC-3'), *EZH2* (forward 5'-TTGTTGGCGGAAGCGTGATAAATC-3', reverse-5'-TCCCTAGTCCCGCGCAATGAGC-3'), and *β-actin* (forward-5'-GCACCACACCTTCTACAATG-3', reverse-5'-TGCTTGCTGATCCACATCTG). RT-qPCR was performed in triplicate for each sample. The mRNA level of these genes was calculated using $2^{-\Delta\Delta CT}$ method and normalized to that of *β-actin* mRNA.

Western blotting

Total protein was extracted from the cells using lysis buffer containing proteinase inhibitor cocktail. The protein concentration was measured using the BCA protein assay kit (Beyotime, Haimen, China). Then, the same amount of protein was resolved by 12% SDS-PAGE and transferred to PVDF membranes, followed by blocking of 5 % skimmed milk for 2 h at room temperature. Subsequently, the membranes were incubated with primary antibodies at 4° C overnight. After horseradish peroxidase (HRP)-conjugated second incubation, the bands were developed by ECL assay (Beyotime, Haimen, China). The antibodies used were as followed: Anti-*SPRY4* antibody (ab59785), anti-*KMT6/EZH2* antibody (ab186006), anti-*MDM2* antibody (ab38618), anti-*Bcl-2* antibody (ab182858), anti-*Bax* antibody (ab32503), anti-*MMP2* antibody (ab215986), anti-*MMP9* antibody (ab219372), anti-Cleaved Caspase-3 antibody (ab32042), anti-*β-actin* antibody (ab8227) and Rabbit IgG, monoclonal- Isotype

Control (ab172730) were obtained from Abcam (MA, USA).

Cell transfection

Cell transfection was conducted using lipofectamine 2000 (Invitrogen, USA) in accordance with the guide of the manufacturer. The pcDNA3.1-*SPRY4* (Oe-*SPRY4*) and pcDNA3.1 negative control (Oe-NC) vectors were obtained from GenePharma (Shanghai, China). SW480 cells were transfected with 50 nM Oe-*SPRY4* and Oe-NC, respectively. 48 after transfection, the transfection efficacy was detected by qRT-PCR and western blotting.

Cell proliferation assay

Cell proliferation was determined using Cell Counting Kit-8 (CCK-8) assay. In brief, the transfected SW480 cells were inoculated into 96-well plates (2000 cells/well) and incubated in a humidified atmosphere with 5% CO₂ at 37° C. After incubation for various durations, 10 µl of CCK-8 agent was added into each well for a further 3 h's incubation. Afterwards, a microplate reader (Bio-Tek, USA) was used to detect the optical density of each well at 450 nm.

Colony formation assay

The transfected SW480 cells were seeded into 6-well plates (400 cells/well) and incubated for 2 weeks. During this period, culture medium was replaced every three days. At last, cells were fixed with 4 % paraformaldehyde and stained with 0.1 % crystal violet to observe the colony formation.

EdU assay

The transfected SW480 cells were inoculated into 24-well plates and cultured in a humidified atmosphere with 5% CO₂ at 37° C for 24 h. EdU (50 µmol/L) was added for a further incubation of 8 h. Afterwards, cells were fixed with 4% formaldehyde at room temperature for 15 min, followed by incubation with Triton X-100 for 15 min. Subsequently, cells were incubated with EdU agent and stained with DAPI. Finally, cells were observed under a confocal microscopy (Olympus, Japan).

Wound-healing assay

The transfected SW480 cells were seeded into 6-well plates. When 100% confluence achieved, a scratch was generated by using a 20 µl pipette tip. Then, the culture medium was replaced to DMEM without FBS. Cell images were obtained at 0 and 48 h under a light microscope (Olympus, Japan).

Transwell assay

The transfected SW480 cells suspended in FBS-free DMEM were inoculated into the upper chamber of a 24-well Transwell pre-coated with Matrigel (BD Biosciences, USA) at a density of 4×10^4 cells per well. The complete medium with 10% FBS was added to the lower chamber of the Transwell. 48 h later, the cells on the surface of the upper chamber were wiped out. The invasive cells were fixed with 4 % paraformaldehyde and were stained with 0.1 % crystal violet. The images were visualized using a light microscope (Olympus, Japan).

Flow cytometry analysis

The transfected SW480 cells were collected, washed with cold PBS, and re-suspended in 100 μ L of binding buffer. Subsequently, cells were stained with annexin V-FITC and propidium iodide (PI) according to the guide of the manufacturer. The signal was acquired by a FACS caliber flow cytometry and analyzed with FACS Diva software (BD Biosciences, USA).

In vivo tumor xenograft study

Male Balb/c nude mice at the age of 4-6 weeks were obtained from Shanghai SLAC laboratory animal co. Ltd (Shanghai, China). The animal experiments were carried out in accordance with the protocols approved by the Institutional Animal Care and Use Committee of The Affiliated Hospital of Kunming Medical University. SW480 cells were transfected with *SPRY4* knockdown plasmid or *SPRY4* overexpression plasmid. The transfected cells were subcutaneously injected into the axilla of the mice. GSK126 (an inhibitor of EZH2, Selleck) was administrated intravenously at a dose of 150 mg/kg. The tumor volume was calculated as follows: tumor volume = $1/2 \times \text{length} \times \text{width}^2$. After 28 days, the mice were euthanized, and the tumors were weighed and collected for further tests.

Hematoxylin-Eosin (H&E) staining

The tumor tissue samples were fixed in 4 % paraformaldehyde, dehydrated in ethanol and embedded in paraffin blocks. Then, the samples were cut into 5- μ m-thickness of sections. After staining with H&E reagent, the images were observed under a light microscope for randomly five fields.

Immunohistochemistry

The paraffin-embedded tissue samples were deparaffinized, rehydrated and subjected to antigen retrieval. After washing with PBS and blocked with

PBS containing 5% normal goat serum, the sections were washed with PBS and incubated with primary antibody against Ki67 and biotinylated secondary antibody (Santa Cruz, CA, USA). The sections were developed with DAB staining and hematoxylin counterstain. All images were photographed for five randomly fields.

Statistical analysis

Data were presented as mean \pm SEM. All the data were analyzed using the SPSS 18.0 statistical software. The differences among groups were determined using one way ANOVA analysis followed by Tukey's post hoc test. $p < 0.05$ was considered to indicate a statistically significant difference.

AUTHOR CONTRIBUTIONS

KY and JG contributed conception and design of the study. JG, HZ, QL, JD and WX performed the experiments and statistical analysis. KY wrote the first draft of the manuscript. JG, HZ and QL wrote sections of the manuscript. All authors contributed to manuscript revision, read and approved the submitted version.

CONFLICTS OF INTEREST

The authors declare that they have no conflicts of interest.

FUNDING

This study was supported by Yunnan Science and Technology Planning Project (NO. 2017FE467 (-072)).

REFERENCES

1. Siegel R, Ma J, Zou Z, Jemal A. Cancer statistics, 2014. *CA Cancer J Clin.* 2014; 64:9–29. <https://doi.org/10.3322/caac.21208> PMID:[24399786](https://pubmed.ncbi.nlm.nih.gov/24399786/)
2. Das V, Kalita J, Pal M. Predictive and prognostic biomarkers in colorectal cancer: A systematic review of recent advances and challenges. *Biomed Pharmacother.* 2017; 87:8–19. <https://doi.org/10.1016/j.biopha.2016.12.064> PMID:[28040600](https://pubmed.ncbi.nlm.nih.gov/28040600/)
3. Ferlay J, Soerjomataram I, Dikshit R, Eser S, Mathers C, Rebelo M, Parkin DM, Forman D, Bray F. Cancer incidence and mortality worldwide: sources, methods and major patterns in GLOBOCAN 2012. *Int J Cancer.* 2015; 136:E359–86. <https://doi.org/10.1002/ijc.29210> PMID:[25220842](https://pubmed.ncbi.nlm.nih.gov/25220842/)

4. Hacohen N, Kramer S, Sutherland D, Hiromi Y, Krasnow MA. Sprouty encodes a novel antagonist of FGF signaling that patterns apical branching of the drosophila airways. *Cell*. 1998; 92:253–63. [https://doi.org/10.1016/s0092-8674\(00\)80919-8](https://doi.org/10.1016/s0092-8674(00)80919-8) PMID:[9458049](https://pubmed.ncbi.nlm.nih.gov/9458049/)
5. Mason JM, Morrison DJ, Basson MA, Licht JD. Sprouty proteins: multifaceted negative-feedback regulators of receptor tyrosine kinase signaling. *Trends Cell Biol*. 2006; 16:45–54. <https://doi.org/10.1016/j.tcb.2005.11.004> PMID:[16337795](https://pubmed.ncbi.nlm.nih.gov/16337795/)
6. Masoumi-Moghaddam S, Amini A, Morris DL. The developing story of sprouty and cancer. *Cancer Metastasis Rev*. 2014; 33:695–720. <https://doi.org/10.1007/s10555-014-9497-1> PMID:[24744103](https://pubmed.ncbi.nlm.nih.gov/24744103/)
7. Tennis MA, Van Scoyk MM, Freeman SV, Vandervest KM, Nemenoff RA, Winn RA. Sprouty-4 inhibits transformed cell growth, migration and invasion, and epithelial-mesenchymal transition, and is regulated by Wnt7A through PPARgamma in non-small cell lung cancer. *Mol Cancer Res*. 2010; 8:833–43. <https://doi.org/10.1158/1541-7786.MCR-09-0400> PMID:[20501643](https://pubmed.ncbi.nlm.nih.gov/20501643/)
8. Vanas V, Mühlbacher E, Kral R, Sutterlüty-Fall H. Sprouty4 interferes with cell proliferation and migration of breast cancer-derived cell lines. *Tumour Biol*. 2014; 35:4447–56. <https://doi.org/10.1007/s13277-013-1587-0> PMID:[24402575](https://pubmed.ncbi.nlm.nih.gov/24402575/)
9. Wang J, Thompson B, Ren C, Ittmann M, Kwabi-Addo B. Sprouty4, a suppressor of tumor cell motility, is down regulated by DNA methylation in human prostate cancer. *Prostate*. 2006; 66:613–24. <https://doi.org/10.1002/pros.20353> PMID:[16388505](https://pubmed.ncbi.nlm.nih.gov/16388505/)
10. Jing H, Liaw L, Friesel R, Vary C, Hua S, Yang X. Suppression of Spry4 enhances cancer stem cell properties of human MDA-MB-231 breast carcinoma cells. *Cancer Cell Int*. 2016; 16:19. <https://doi.org/10.1186/s12935-016-0292-7> PMID:[26973433](https://pubmed.ncbi.nlm.nih.gov/26973433/)
11. So WK, Cheng JC, Liu Y, Xu C, Zhao J, Chang VT, Leung PC. Sprouty4 mediates amphiregulin-induced down-regulation of E-cadherin and cell invasion in human ovarian cancer cells. *Tumour Biol*. 2016; 37:9197–207. <https://doi.org/10.1007/s13277-016-4790-y> PMID:[26768617](https://pubmed.ncbi.nlm.nih.gov/26768617/)
12. Kuser-Abali G, Gong L, Yan J, Liu Q, Zeng W, Williamson A, Lim CB, Molloy ME, Little JB, Huang L, Yuan ZM. An EZH2-mediated epigenetic mechanism behind p53-dependent tissue sensitivity to DNA damage. *Proc Natl Acad Sci USA*. 2018; 115:3452–57. <https://doi.org/10.1073/pnas.1719532115> PMID:[29540569](https://pubmed.ncbi.nlm.nih.gov/29540569/)
13. Zhao Y, Ding L, Wang D, Ye Z, He Y, Ma L, Zhu R, Pan Y, Wu Q, Pang K, Hou X, Weroha SJ, Han C, et al. EZH2 cooperates with gain-of-function p53 mutants to promote cancer growth and metastasis. *EMBO J*. 2019; 38:e99599. <https://doi.org/10.15252/emboj.201899599> PMID:[30723117](https://pubmed.ncbi.nlm.nih.gov/30723117/)
14. Fillmore CM, Xu C, Desai PT, Berry JM, Rowbotham SP, Lin YJ, Zhang H, Marquez VE, Hammerman PS, Wong KK, Kim CF. EZH2 inhibition sensitizes BRG1 and EGFR mutant lung tumours to Topoll inhibitors. *Nature*. 2015; 520:239–42. <https://doi.org/10.1038/nature14122> PMID:[25629630](https://pubmed.ncbi.nlm.nih.gov/25629630/)
15. Chen DL, Ju HQ, Lu YX, Chen LZ, Zeng ZL, Zhang DS, Luo HY, Wang F, Qiu MZ, Wang DS, Xu DZ, Zhou ZW, Pelicano H, et al. Long non-coding RNA XIST regulates gastric cancer progression by acting as a molecular sponge of miR-101 to modulate EZH2 expression. *J Exp Clin Cancer Res*. 2016; 35:142. <https://doi.org/10.1186/s13046-016-0420-1> PMID:[27620004](https://pubmed.ncbi.nlm.nih.gov/27620004/)
16. Chen S, Pu J, Bai J, Yin Y, Wu K, Wang J, Shuai X, Gao J, Tao K, Wang G, Li H. EZH2 promotes hepatocellular carcinoma progression through modulating miR-22/galectin-9 axis. *J Exp Clin Cancer Res*. 2018; 37:3. <https://doi.org/10.1186/s13046-017-0670-6> PMID:[29316949](https://pubmed.ncbi.nlm.nih.gov/29316949/)
17. Ler LD, Ghosh S, Chai X, Thike AA, Heng HL, Siew EY, Dey S, Koh LK, Lim JQ, Lim WK, Myint SS, Loh JL, Ong P, et al. Loss of tumor suppressor KDM6A amplifies PRC2-regulated transcriptional repression in bladder cancer and can be targeted through inhibition of EZH2. *Sci Transl Med*. 2017; 9:eaai8312. <https://doi.org/10.1126/scitranslmed.aai8312> PMID:[28228601](https://pubmed.ncbi.nlm.nih.gov/28228601/)
18. Yu M, Li Y, Li M, Lu D. Eudesmin exerts antitumor effects by down-regulating EZH2 expression in nasopharyngeal carcinoma cells. *Chem Biol Interact*. 2019; 307:51–57. <https://doi.org/10.1016/j.cbi.2019.04.028> PMID:[31026422](https://pubmed.ncbi.nlm.nih.gov/31026422/)
19. Huang KB, Zhang SP, Zhu YJ, Guo CH, Yang M, Liu J, Xia LG, Zhang JF. Hotair mediates tumorigenesis through recruiting EZH2 in colorectal cancer. *J Cell Biochem*. 2019; 120:6071–77. <https://doi.org/10.1002/jcb.27893> PMID:[30362162](https://pubmed.ncbi.nlm.nih.gov/30362162/)
20. Chen Z, Yang P, Li W, He F, Wei J, Zhang T, Zhong J, Chen H, Cao J. Expression of EZH2 is associated with poor outcome in colorectal cancer. *Oncol Lett*. 2018; 15:2953–61.

- <https://doi.org/10.3892/ol.2017.7647>
PMID:[29435024](https://pubmed.ncbi.nlm.nih.gov/29435024/)
21. Wang D, Quiros J, Mahuron K, Pai CC, Ranzani V, Young A, Silveria S, Harwin T, Abnousian A, Pagani M, Rosenblum MD, Van Gool F, Fong L, et al. Targeting EZH2 reprograms intratumoral regulatory T cells to enhance cancer immunity. *Cell Rep.* 2018; 23:3262–74. <https://doi.org/10.1016/j.celrep.2018.05.050>
PMID:[29898397](https://pubmed.ncbi.nlm.nih.gov/29898397/)
 22. Rochette PJ, Bastien N, Lavoie J, Guérin SL, Drouin R. SW480, a p53 double-mutant cell line retains proficiency for some p53 functions. *J Mol Biol.* 2005; 352:44–57. <https://doi.org/10.1016/j.jmb.2005.06.033>
PMID:[16061257](https://pubmed.ncbi.nlm.nih.gov/16061257/)
 23. Zhou M, Zhang XY, Yu X. Overexpression of the long non-coding RNA SPRY4-IT1 promotes tumor cell proliferation and invasion by activating EZH2 in hepatocellular carcinoma. *Biomed Pharmacother.* 2017; 85:348–54. <https://doi.org/10.1016/j.biopha.2016.11.035>
PMID:[27899259](https://pubmed.ncbi.nlm.nih.gov/27899259/)
 24. Tang X, Milyavsky M, Shats I, Erez N, Goldfinger N, Rotter V. Activated p53 suppresses the histone methyltransferase EZH2 gene. *Oncogene.* 2004; 23:5759–69. <https://doi.org/10.1038/sj.onc.1207706>
PMID:[15208672](https://pubmed.ncbi.nlm.nih.gov/15208672/)
 25. He P, Sun X, Cheng HJ, Zou YB, Wang Q, Zhou CL, Liu WQ, Hao YM, Meng XW. UBA2 promotes proliferation of colorectal cancer. *Mol Med Rep.* 2018; 18:5552–62. <https://doi.org/10.3892/mmr.2018.9613>
PMID:[30387828](https://pubmed.ncbi.nlm.nih.gov/30387828/)
 26. Li Q, Cao L, Tian Y, Zhang P, Ding C, Lu W, Jia C, Shao C, Liu W, Wang D, Ye H, Hao H. Butyrate suppresses the proliferation of colorectal cancer cells via targeting pyruvate kinase M2 and metabolic reprogramming. *Mol Cell Proteomics.* 2018; 17:1531–45. <https://doi.org/10.1074/mcp.RA118.000752>
PMID:[29739823](https://pubmed.ncbi.nlm.nih.gov/29739823/)
 27. Ashkenazi A, Fairbrother WJ, Levenson JD, Souers AJ. From basic apoptosis discoveries to advanced selective BCL-2 family inhibitors. *Nat Rev Drug Discov.* 2017; 16:273–84. <https://doi.org/10.1038/nrd.2016.253> PMID:[28209992](https://pubmed.ncbi.nlm.nih.gov/28209992/)
 28. Riedl SJ, Shi Y. Molecular mechanisms of caspase regulation during apoptosis. *Nat Rev Mol Cell Biol.* 2004; 5:897–907. <https://doi.org/10.1038/nrm1496>
PMID:[15520809](https://pubmed.ncbi.nlm.nih.gov/15520809/)
 29. Reed JC. Proapoptotic multidomain bcl-2/bax-family proteins: mechanisms, physiological roles, and therapeutic opportunities. *Cell Death Differ.* 2006; 13:1378–86. <https://doi.org/10.1038/sj.cdd.4401975>
PMID:[16729025](https://pubmed.ncbi.nlm.nih.gov/16729025/)
 30. Chang CJ, Yang JY, Xia W, Chen CT, Xie X, Chao CH, Woodward WA, Hsu JM, Hortobagyi GN, Hung MC. EZH2 promotes expansion of breast tumor initiating cells through activation of RAF1- β -catenin signaling. *Cancer Cell.* 2011; 19:86–100. <https://doi.org/10.1016/j.ccr.2010.10.035>
PMID:[21215703](https://pubmed.ncbi.nlm.nih.gov/21215703/)
 31. Lin W, Chen Y, Zeng L, Ying R, Zhu F. [Effect of a novel EZH2 inhibitor GSK126 on prostate cancer cells]. *Zhejiang Da Xue Xue Bao Yi Xue Ban.* 2016; 45:356–63. PMID:[27868408](https://pubmed.ncbi.nlm.nih.gov/27868408/)
 32. Chen YT, Zhu F, Lin WR, Ying RB, Yang YP, Zeng LH. The novel EZH2 inhibitor, GSK126, suppresses cell migration and angiogenesis via down-regulating VEGF-A. *Cancer Chemother Pharmacol.* 2016; 77:757–65. <https://doi.org/10.1007/s00280-016-2990-1>
PMID:[26898301](https://pubmed.ncbi.nlm.nih.gov/26898301/)
 33. Li H, Zhang J, Tong JH, Chan AW, Yu J, Kang W, To KF. Targeting the oncogenic p53 mutants in colorectal cancer and other solid tumors. *Int J Mol Sci.* 2019; 20:5999. <https://doi.org/10.3390/ijms20235999>
PMID:[31795192](https://pubmed.ncbi.nlm.nih.gov/31795192/)
 34. Deisenroth C, Zhang Y. Ribosome biogenesis surveillance: probing the ribosomal protein-Mdm2-p53 pathway. *Oncogene.* 2010; 29:4253–60. <https://doi.org/10.1038/onc.2010.189>
PMID:[20498634](https://pubmed.ncbi.nlm.nih.gov/20498634/)

miR-144-3p inhibited the growth, metastasis and epithelial-mesenchymal transition of colorectal adenocarcinoma by targeting ZEB1/2

Taiyuan Li^{1,2,*}, Cheng Tang^{1,*}, Zhixiang Huang^{1,*}, Lingling Yang^{3,*}, Hua Dai⁴, Bo Tang¹, Benping Xiao⁵, Jianfeng Li¹, Xiong Lei^{1,2,&}

¹Department of General Surgery, The First Affiliated Hospital of Nanchang University, Nanchang 330006, Jiangxi, China

²Gastrointestinal Surgical Institute, Nanchang University, Nanchang 330006, Jiangxi, China

³Department of Gastroenterology, The Second Affiliated Hospital of Nanchang University, Nanchang 330006, Jiangxi, China

⁴Department of Pathology, The First Affiliated Hospital of Nanchang University, Nanchang 330006, Jiangxi, China

⁵Department of General Surgery, Jiangxi Pingxiang People's Hospital, Pingxiang 337000, Jiangxi, China

*Equal contribution

Correspondence to: Xiong Lei; email: leixionglinty@126.com, <https://orcid.org/0000-0002-4055-3414>

Keywords: colorectal cancer, miR-144-3p, epithelial-mesenchymal transition, metastasis, ZEB1/2

Received: November 23, 2020

Accepted: June 4, 2021

Published: July 5, 2021

Copyright: © 2021 Li et al. This is an open access article distributed under the terms of the [Creative Commons Attribution License](https://creativecommons.org/licenses/by/3.0/) (CC BY 3.0), which permits unrestricted use, distribution, and reproduction in any medium, provided the original author and source are credited.

ABSTRACT

miR-144-3p is aberrantly expressed in several types of human cancer and functions as a tumor suppressor by inhibiting metastasis. However, the clinical significance and biological function of miR-144-3p in colorectal adenocarcinoma (CRA) have yet to be elucidated. Here we reported that miR-144-3p expression level was significantly down-regulated in CRA tissues compared with matched noncancerous colorectal mucosae tissues. Low miR-144-3p expression was correlated with adverse clinicopathologic characteristics and poor prognosis of CRA patients. Cox regression analysis showed that low miR-144-3p expression was an independent risk factor for DFS and OS in CRA. *In vitro* and *in vivo* assays showed that miR-144-3p significantly inhibited proliferation, migration and invasion of CRA cells. In particular, miR-144-3p could suppress EMT process of CRA cells by regulating the cytoskeleton and EMT markers. Bioinformatics analysis indicated that EMT associated transcription factors ZEB1 and ZEB2 were potential targets of miR-144-3p, and miR-144-3p inhibited ZEB1 and ZEB2 expression and was negatively correlated with their expression in CRA. Finally, we confirmed that ZEB1 and ZEB2 down-regulation collaboratively mediated the inhibitory effect of miR-144-3p on proliferation, invasion and EMT of CRA cells. In conclusion, our study provided evidence that miR-144-3p could inhibit CRA cell proliferation, invasion and EMT by targeting ZEB1/2.

INTRODUCTION

Colorectal cancer (CRC) has become the second leading cause of cancer related death, accounting for about 1 in 10 cancer death [1]. About 98% of CRC histopathologic type is colorectal adenocarcinoma (CRA) [2]. Despite improved survival rate of CRA patients due to the

development of chemotherapeutic treatments and surgical technology, about 30% CRA patients present with metastasis at the time of diagnosis, which is the major obstacle to improving the prognosis of CRA patients [3]. The liver is the major organ for CRA metastasis, and liver metastasis would develop in about 15% of operable CRA patients and over 50% of inoperable CRA patients [4].

Tumor metastasis involves complex cascade, which is regulated by molecular mechanisms [5]. Therefore, understanding the molecular mechanisms of CRA metastasis cascade will help develop new targeted drugs and improve the survival rate of CRA patients.

Epithelial-mesenchymal transition (EMT) occurs in embryonic developmental stages (e.g. gastrointestinal and neuronal crest formation) and pathological or physiological processes (e.g. wound healing or fibrosis). EMT is often aberrantly activated in tumor cells to gain invasive ability for metastasis [6, 7]. The activation of EMT involves many intracellular signaling pathways that repress E-cadherin expression while up-regulate vimentin expression [8]. EMT associated transcriptional factors, such as SNAI, ZEB and TWIST, are aberrantly upregulated during EMT and participate in CRA metastasis [9]. Accumulating studies demonstrated that miRNAs modulate CRA metastasis via regulating EMT [10, 11].

miRNAs regulate gene expression by preventing translation or promoting mRNA degradation [12]. Alterations in miRNA expression profiles are related to the staging and prognosis of carcinomas [13–15]. Recent evidence showed that miR-144-3p may be a tumor suppressor [16–18]. In particular, miR-144-3p inhibited EMT process and cancer metastasis [18–20]. In addition, plasma miR-144-3p level was significantly lower in CRA patients than in healthy controls [21]. However, the significance of miR-144-3p in CRA remains unclear.

In this study, we investigated the expression profile and clinical significance of miR-144-3p in CRA patients and explored molecular mechanisms of miR-144-3p in CRA.

MATERIALS AND METHODS

Colorectal adenocarcinoma samples

Fresh frozen colorectal adenocarcinoma tissues (CRAT) and corresponding noncancerous colorectal mucosae tissues (NCMT) harvested from 160 CRA patients at the First Affiliated Hospital of Nanchang University from January 2009 to December 2011 were set as training cohort. In addition, matched NCMTs, CRATs, liver metastatic nodule (LMNs) were obtained from 8 patients with liver-only metastases. Another 140 matched fresh frozen CRATs and NCMTs from CRA patients undergoing radical resection between July 2011 and July 2013 at People's Hospital of Pingxiang were set as validation cohort. None of CRA patients had chemotherapy or radiotherapy before the surgery. This study was approved by Ethics Committee of First Affiliated Hospital of Nanchang University. All participants provided informed consent.

Follow-up study

Overall survival (OS) indicated the time from the surgery to tumor related death or the last follow-up if the patients survived [2]. Disease-free survival (DFS) indicated the time from the surgery till the patient survived without recurrence or metastasis [2]. All follow-up data were collected for further analysis.

Cell culture and transfection

Cancer cell lines HCT116, LoVo, SW480, HT-29, SW620 and colorectal mucosal cell line FHC were provided by American Type Culture Collection. Cell were cultured and cell transfection was performed with miR-144-3p mimic, inhibitor and their corresponding control sequences (RiboBio, Guangzhou, China) by using Lipofectamine (Invitrogen, Carlsbad, CA, USA).

PCR

Total RNA was extracted by using TRIzol (Invitrogen) and cDNA was synthesized by using cDNA kit (Toyobo, Japan). PCR analysis was performed by using SYBR[®]-Green Master kit (Toyobo) (details in Supplementary Materials).

Western blot analysis

Total proteins were extracted by using RIPA buffer (Beyotime Institute of Biotechnology, Jiangsu, China), and the details for Western blotting were shown in Supplementary Materials.

Immunohistochemistry (IHC)

The tissue sections were dewaxed, rehydrated, blocked, and then incubated with primary antibodies and horseradish peroxidase conjugated secondary antibody, sequentially (Zhongshan Goldenbridge Biotech, Beijing, China). The sections were then stained with 3,3'-diaminobenzidine substrate.

Cell proliferation assay

The proliferation ability of CRA cells was analyzed by methyl thiazolyl tetrazolium (MTT), EdU proliferation and colony formation analysis (details in Supplementary Materials).

Transwell and cell adhesion assays

Cell motility and invasive ability and cell adhesion were examined by transwell migration and invasion assay, cell-cell adhesion and cell-extracellular matrix (ECM) assay, respectively (details in Supplementary Materials).

Immunofluorescence (IF) and flow cytometry

The details of IF staining and flow cytometry of vimentin and E-cadherin were described in Supplementary Materials. Briefly, cells were fixed and incubated with rhodamine conjugated phalloidin (Solarbio, Beijing, China). The nuclei were stained with DAPI and cells were observed under fluorescence microscope (Nikon Corporation, Japan).

Animal experiments

CRA cells (5×10^6) were subcutaneously injected into left upper flank of nude male BALB/c mice (4-5 weeks old). Tumor volume was calculated with formula: tumor volume (cm^3) = (long axis \times short axis²)/2 [22]. After 6 weeks, tumor tissues were dissected. For *in vivo* metastatic assay, the spleen was exposed after anesthesia and the incision on left lateral flank in nude mice. One month after intrasplenic injection of 1×10^6 CRA cells, the mice were euthanized and liver specimens were collected to examine metastatic nodules.

Statistical analysis

All data were analyzed with software SPSS 18 (SPSS, Chicago, IL, USA). The differences between two groups were analyzed by *t* test or χ^2 test. Survival curve was calculated by Kaplan-Meier method. Factors associated with OS and DFS were identified by Cox proportional hazard regression analysis. $P < 0.05$ indicated significance.

Ethics approval and consent to participate

The study was approved by the Ethics Committee of the Institutional Review Boards of the First Affiliated Hospital of Nanchang University and Jiangxi Pingxiang People's Hospital, and was performed in accordance with the Declaration of Helsinki and current ethical guidelines. Prior informed consent was obtained from all participants.

Consent for publication

Patients provided written informed consent for publication. All authors have read and approved of publication of this manuscript.

Availability of data and materials

The datasets used and/or analyzed during the current study are openly available.

RESULTS

miR-144-3p was significantly downregulated in CRA

The analysis of 160 pairs of fresh frozen CRATs and corresponding NCMTs from training cohort showed that miR-144-3p level was lower in CRATs than in NCMTs (Figure 1A). Furthermore, miR-144-3p level was lower in CRATs with TNM stage III than in those with TNM stage I/II (Figure 1B). Moreover, analysis of 8 matched NCMTs, CRATs and LMNs demonstrated that miR-144-3p level gradually decreased from NCMTs, CRATs to LMNs (Figure 1C). Analysis of miR-144-3p level in CRATs and LMNs from the GEO dataset (GSE44121) showed that miR-144-3p level was lower in LMNs than in CRATs (Figure 1D).

Low miR-144-3p expression was associated with poor prognosis of CRA

Next we explored clinical significance of miR-144-3p in CRA following ReMARK guidelines for prognostic tumor biomarkers [23]. We found that miR-144-3p level was significantly lower in CRATs than in NCMTs (data not shown). According to relative miR-144-3p level in CRATs, CRA patients were further divided into low miR-144-3p expression group (\log_2 fold change of CRAT/NCMT ≤ -1) and high miR-144-3p expression group (\log_2 fold change of CRAT/NCMT > -1). First, we found no differences in clinicopathologic characteristics for CRA patients between training cohort and validation cohort (Table 1). In training cohort, miR-144-3p level was related to adverse clinicopathological features such as tumor size ($P=0.002$), pN stage ($P=0.002$), pT stage ($P=0.003$), distant metastasis ($P=0.004$) and lymphatic/microvascular/nerve invasion ($P=0.001$) (Table 2). Similarly, in validation cohort, miR-144-3p level was related to tumor differentiation ($P=0.011$), pT stage ($P=0.003$), pN stage ($P=0.027$), tumor size ($P=0.001$), distant metastasis ($P=0.018$) and lymphatic/microvascular/nerve invasion ($P<0.001$) (Table 3). Based on follow-up data, CRA patients in training cohort with low miR-144-3p level showed shorter OS ($P=0.006$) and shorter DFS ($P=0.002$) compared to patients with high miR-144-3p level (Figure 1E, 1F). CRA patients in validation cohort with low miR-144-3p level showed shorter OS ($P=0.007$) and DFS ($P=0.009$) compared to patients with high miR-144-3p level (Figure 1G, 1H). Furthermore, Cox proportional hazards regression model identified low miR-144-3p level as a risk factor for both OS and DFS (Tables 3, 4).

miR-144-3p inhibited CRA cell proliferation

Next we explored biological function of miR-144-3p in CRAPCR analysis of miR-144-3p expression in

CRA cell lines and colorectal mucosal cell line FHC showed lower expression of miR-144-3p in CRA cell lines than in FHC cell line (Figure 2A). In particular, HCT116 had the highest and Lovo had the lowest level of miR-144-3p, and they were selected for subsequent assays. Transfection of miR-144-3p mimic effectively increased miR-144-3p level in Lovo cells

and transfection of miR-144-3p inhibitor reduced miR-144-3p level in HCT116 cells (Figure 2B).

MTT assay showed that miR-144-3p mimic inhibited Lovo cell proliferation, while miR-144-3p inhibitor significantly promoted HCT116 cell proliferation (Figure 2C). Moreover, miR-144-3p mimic significantly

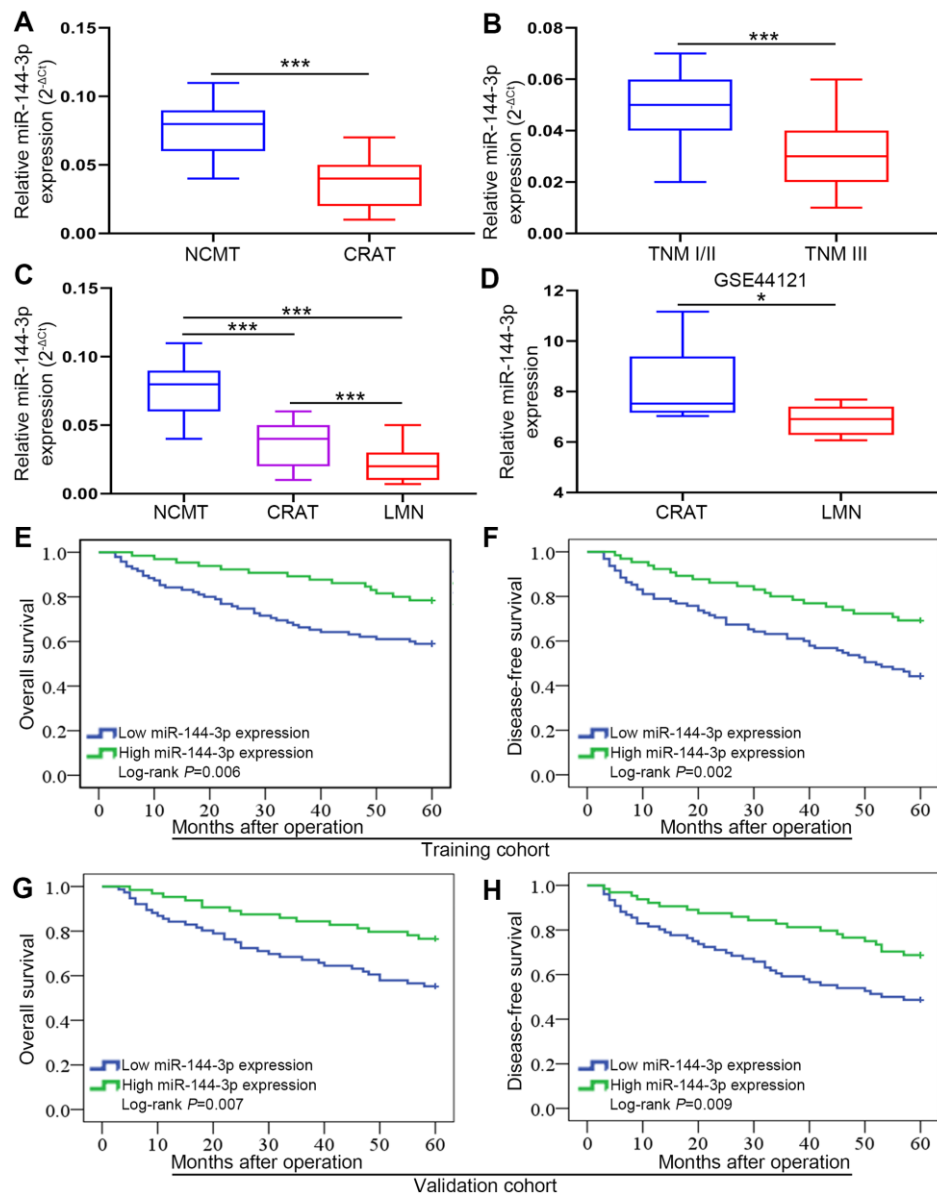


Figure 1. miR-144-3p expression was significantly downregulated and associated with poor prognosis in CRA. (A) miR-144-3p expression was significantly downregulated in CRATs. The levels of miR-144-3p in 160 paired CRATs and NCMTs from training cohort were determined by qRT-PCR. Data were analyzed using 2^{-ΔCt} method. (B) Expression levels of miR-144-3p in CRATs with advanced TNM stage (TNM III) were significantly lower than in early TNM stage (TNM I/II). (C) miR-144-3p expression level gradually increased from LMNs, CRATs to NCMTs. The expression levels of miR-144-3p were determined and compared in 8 matched NCMTs, CRATs, and LMNs. (D) Data from GSE44121 were used to compare miR-144-3p expression levels in LMNs and CRATs. Overall survival (E) and disease-free survival (F) were compared by Kaplan-Meier method based on miR-144-3p expression in the training cohort. Overall survival (G) and disease-free survival (H) were compared by Kaplan-Meier method based on miR-144-3p expression in the validation cohort. NCMTs, noncancerous colorectal mucosae tissues; CRATs, colorectal adenocarcinoma tissues; LMNs, liver metastatic nodules. *, P<0.05; ***, P<0.001.

Table 1. Clinicopathologic characteristics of patients with CRA in the training cohort and validation cohort.

Clinicopathologic parameters	Training cohort	Validation cohort	<i>P</i>
Gender			
Female	62	58	0.639
Male	98	82	
Age (y)			
≤60	71	60	0.816
>60	89	80	
CEA (ng/ml)			
≤5	68	65	0.560
>5	92	75	
Tumor differentiation			
I/II	75	62	0.728
III/IV	85	78	
Tumor site			
Colon	58	54	0.720
Rectum	102	86	
Tumor size			
≤5 cm	105	93	0.903
>5 cm	55	47	
pT stage			
T1/T2	52	51	0.542
T3/T4	108	89	
pN stage			
N0	72	66	0.729
N+	88	74	
Lymphatic/microvascular/nerve invasion			
Negative	66	55	0.814
Positive	94	85	
Distant metastasis			
Negative	76	72	0.563
Positive	84	68	

*, detected during the follow-up period.

inhibited colony formation of Lovo cells, while miR-144-3p inhibitor significantly enhanced colony formation of HCT116 cells (Figure 2D). Edu assay showed that miR-144-3p mimic reduced Lovo cell proliferation and miR-144-3p inhibitor increased HCT116 cell proliferation (Figure 2E). By using subcutaneous xenograft tumor model, we found that tumors derived from Lovo cells treated with miR-144-3p mimic were significantly smaller (Figure 2F). In contrast, miR-144-3p inhibitor promoted the growth of tumors derived from HCT116 cells (Figure 2F).

miR-144-3p inhibited CRA metastasis

Transwell migration assays showed that miR-144-3p mimic significantly inhibited Lovo cell migration,

while miR-144-3p downregulation in HCT116 significantly increased cell migration (Figure 3A). Transwell invasion assays showed similar results (Figure 3B). Adhesion assays showed that miR-144-3p mimic significantly enhanced cell-cell adhesion but decreased cell-ECM adhesion in Lovo cells. However, miR-144-3p inhibitor significantly decreased cell-cell adhesion but increased cell-ECM adhesion in HCT116 cells (Figure 3C, 3D). Furthermore, we found lower number of liver metastatic nodules from mice with the injection of Lovo cells transfected with miR-144-3p mimic and higher number of liver metastatic nodules from mice with the injection of HCT116 cells transfected with miR-144-3p inhibitor, compared to control mice (Figure 3E).

Table 2. Correlations between expression of miR-144-3p and clinicopathologic parameters of CRA patients in the training and validation cohort.

Clinicopathologic parameters	Training cohort				Validation cohort			
	n	miR-144-3p expression		P	n	miR-144-3p expression		P
		Low	High			Low	High	
Gender								
Female	62	40	22		58	27	31	
Male	98	55	43	0.324	82	49	33	0.168
Age (y)								
≤60	71	46	25		60	31	29	
>60	89	49	40	0.257	80	45	35	0.611
CEA (ng/ml)								
≤5	68	35	33		65	31	34	
>5	92	60	32	0.103	75	45	30	0.175
Tumor differentiation								
I/II	75	39	36		62	26	36	
III/IV	85	56	29	0.079	78	50	28	0.011
Tumor site								
Colon	58	31	27		54	34	20	
Rectum	102	64	38	0.315	86	42	44	0.119
Tumor size								
≤5 cm	105	53	52		93	41	52	
>5 cm	55	42	13	0.002	47	35	12	0.001
pT stage								
T1/T2	52	22	30		51	19	32	
T3/T4	108	73	35	0.003	89	57	32	0.003
pN stage								
N0	72	33	39		66	29	37	
N+	88	62	26	0.002	74	47	27	0.027
Lymphatic/microvascular/nerve invasion								
Negative	66	29	37		55	18	37	
Positive	94	66	28	0.001	85	58	27	<0.001
Distant metastasis								
Negative	76	36	40		72	32	40	
Positive	84	59	25	0.004	68	44	24	0.018

miR-144-3p inhibited EMT

Next, we wondered whether miR-144-3p inhibited CRA metastasis by suppressing EMT. We detected actin cytoskeleton of CRA cells based on F-actin staining, because actin transformation is involved in cell adhesion and migration and EMT [24, 25]. Compared to control cells, Lovo cells treated with miR-144-3p mimic showed a cobblestone shape and shrunk F-actin fiber (Figure 4A). In contrast, HCT116 cells treated with miR-144-3p inhibitor presented elongated shape and long F-actin

fibers (Figure 4A). Moreover, miR-144-3p mimic promoted E-cadherin expression but inhibited vimentin expression. Inversely, miR-144-3p inhibitor inhibited E-cadherin expression while enhanced vimentin expression (Figure 4B, 4C). Immunofluorescence staining for vimentin and E-cadherin showed similar results (Figure 4D). Flow cytometry showed higher E-cadherin expression and lower vimentin expression in Lovo cells treated with miR-144-3p mimic, while opposite results were shown in HCT116 cells treated with miR-144-3p inhibitor (Figure 4E).

Table 3. Cox proportional hazard regression analysis for OS in the training and validation cohort.

Parameters	Training cohort				Validation cohort			
	Univariate analysis	P	Multivariate analysis	P	Univariate analysis	P	Multivariate analysis	P
	HR (95% CI)		HR (95% CI)		HR (95% CI)		HR (95% CI)	
Gender (male vs female)	0.819 (0.476–1.409)	0.470		NA	1.183 (0.650-2.153)	0.583		NA
Age (y, >60 vs ≤60)	1.020 (0.593–1.756)	0.942		NA	1.497 (0.774-2.893)	0.230		NA
CEA (ng/ml) (ng/ml, >5 vs ≤5)	1.785 (0.993–3.210)	0.053		NA	1.490 (0.823-2.696)	0.188		NA
Tumor differentiation (III/IV vs I/II)	1.395 (1.081–1.800)	0.011	1.432 (0.776–2.643)	0.251	2.467 (1.357-4.485)	0.003	1.757 (0.936-3.297)	0.079
Tumor site (Colon vs Rectum)	1.194 (0.656–2.174)	0.563		NA	1.412 (0.790-2.522)	0.244		NA
Tumor size (cm, >5 vs ≤5)	1.302 (1.033–1.640)	0.025	2.336 (1.229–4.439)	0.010	1.934 (1.012-3.699)	0.046	1.717 (0.873-3.374)	0.117
pT stage (T3/T4 vs T1/T2)	1.849 (1.214–2.818)	0.004	1.686 (1.213–2.343)	0.002	2.317 (1.194-4.498)	0.013	2.449 (1.319-4.547)	0.005
pN stage (N+ vs N0)	2.172 (1.424–3.314)	<0.001	1.901 (1.241–2.913)	0.003	2.311 (1.242-4.302)	0.008	2.302 (1.180-4.492)	0.014
Lymphatic/microvascular/nerve invasion (Positive vs Negative)	2.144 (1.196–3.844)	0.010	2.318 (1.059–5.076)	0.035	2.132 (1.188-3.825)	0.011	2.367 (1.134-4.938)	0.022
miR-144-3p expression (High vs Low)	0.437 (0.237–0.806)	0.006	0.471 (0.254–0.874)	0.017	0.443 (0.241-0.814)	0.007	0.500 (0.283-0.884)	0.027

Table 4. Cox proportional hazard regression analysis for DFS in the training and validation cohort.

Parameters	Training cohort				Validation cohort			
	Univariate analysis	P	Multivariate analysis	P	Univariate analysis	P	Multivariate analysis	P
	HR (95% CI)		HR (95% CI)		HR (95% CI)		HR (95% CI)	
Gender (male vs female)	0.728 (0.459–1.154)	0.177		NA	1.230 (0.712-2.126)	0.459		NA
Age (y, >60 vs ≤60)	1.138 (0.714–1.814)	0.588		NA	1.661 (0.888-3.107)	0.113		NA
CEA (ng/ml) (ng/ml, >5 vs ≤5)	1.582 (0.975–2.568)	0.063		NA	1.625 (0.932-2.836)	0.087		NA
Tumor differentiation (III/IV vs I/II)	1.288 (1.018–1.630)	0.035	1.493 (0.844-2.641)	0.169	2.636 (1.484-4.682)	0.001	1.693 (0.924-3.104)	0.089
Tumor site (Colon vs Rectum)	1.097 (0.625–1.924)	0.747		NA	1.089 (0.631-1.880)	0.760		NA
Tumor size (cm, >5 vs ≤5)	1.304 (1.044–1.629)	0.019	1.489 (0.771–2.873)	0.236	1.826 (1.009-3.306)	0.047	1.569 (0.849-2.901)	0.151
pT stage (T3/T4 vs T1/T2)	1.765 (1.187–2.625)	0.005	1.593 (1.196–2.121)	0.001	1.954 (1.082-3.529)	0.026	1.968 (1.064-3.642)	0.031
pN stage (N+ vs N0)	2.027 (1.363–3.014)	<0.001	2.271 (1.260–4.092)	0.006	2.217 (1.222-4.022)	0.002	2.638 (1.499-4.643)	0.001
Lymphatic/microvascular/nerve invasion (Positive vs Negative)	2.241 (1.297–3.874)	0.004	2.408 (1.169–4.961)	0.017	2.303 (1.326-3.999)	0.003	2.169 (1.174-4.007)	0.013
miR-144-3p expression (High vs Low)	0.451 (0.269–0.754)	0.002	0.467 (0.276–0.789)	0.004	0.496 (0.289-0.852)	0.009	0.487 (0.265-0.896)	0.021

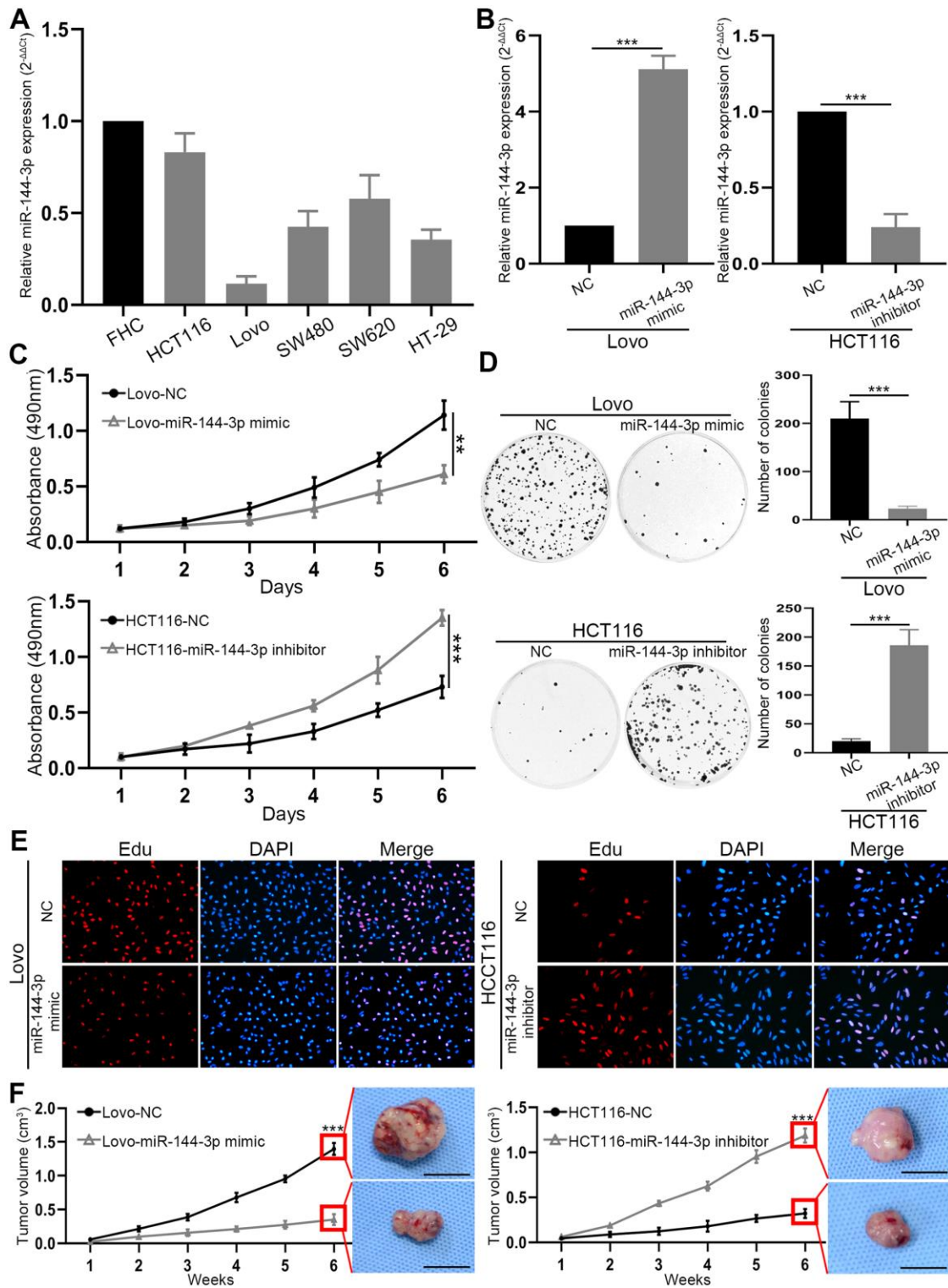


Figure 2. miR-144-3p was downregulated in CRA cell lines and inhibited CRA cell proliferation and growth. (A) miR-144-3p expression was downregulated in CRA cells lines HCT116, Lovo, SW480, SW620, HT-29 compared to normal colorectal mucosal cell line FHC. (B) qRT-PCR was performed to verify the efficiency of overexpression in Lovo cells transfected with miR-144-3p mimic and knockdown in HCT116 cells transfected with miR-144-3p inhibitor. (C) MTT assay of Lovo and HCT116 cell proliferation. (D) Colony formation assay of Lovo and HCT116 cells. (E) Edu assay of the proliferation ability of Lovo cells transfected with miR-144-3p mimic and HCT116 cells transfected with miR-144-3p inhibitor. (F) The growth curve showed the change of the volume of subcutaneous tumors from indicated CRA cells and the representative images of subcutaneous tumors harvested 6 weeks after CRA cell inoculation in the right panel. Scale bar: 1cm. NC, normal control. **, $P < 0.01$; ***, $P < 0.001$.

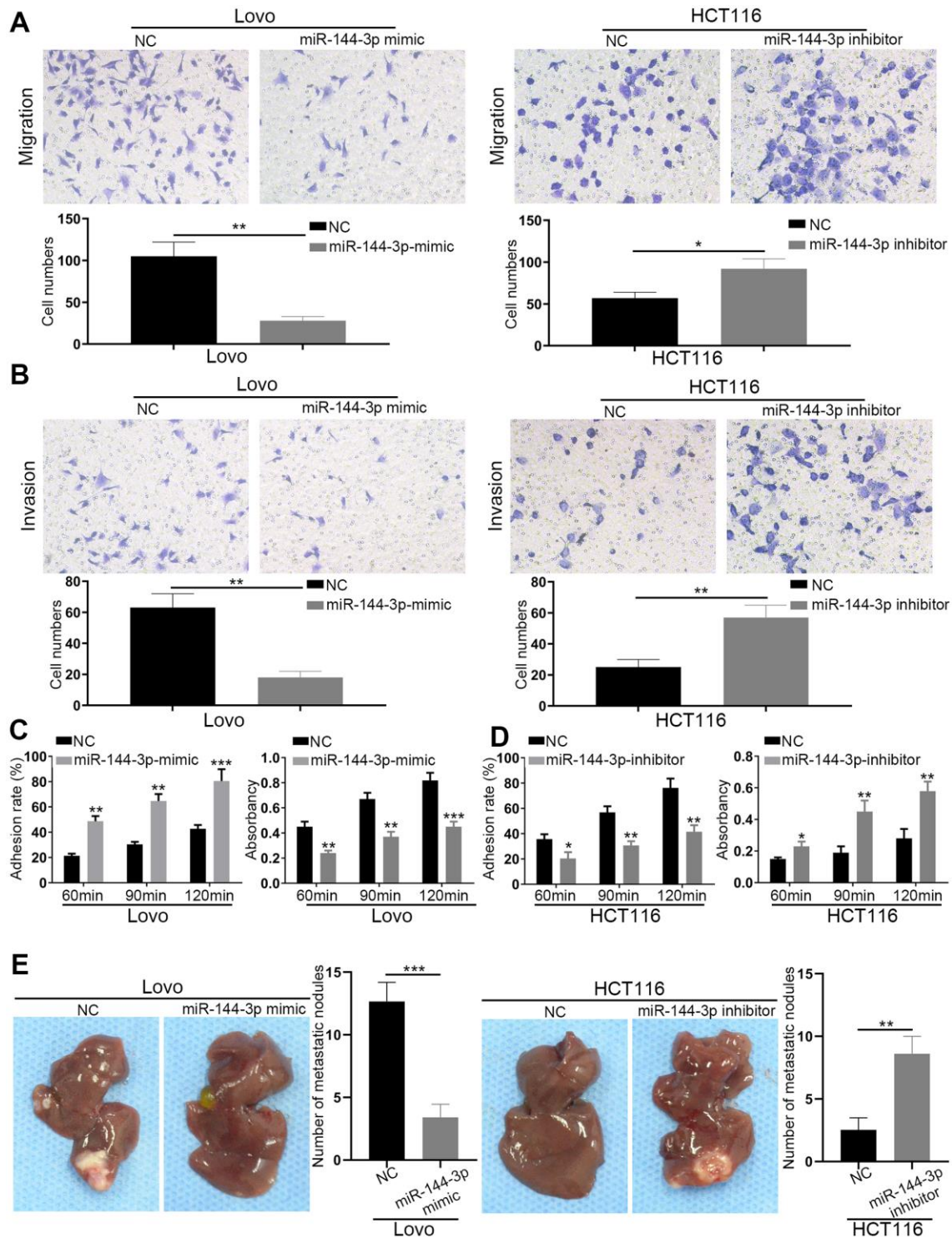


Figure 3. miR-144-3p inhibited CRA cell migration, invasion and tumor metastasis. (A) Transwell migration assay of migratory ability of Lovo cells transfected with miR-144-3p mimic and HCT116 cells transfected with miR-144-3p inhibitor. (B) Transwell invasion assay of invasive ability of Lovo cells transfected with miR-144-3p mimic and HCT116 cells transfected with miR-144-3p inhibitor. (C) Overexpression of miR-144-3p in Lovo cells significantly enhanced cell-cell adhesion and decreased cell-ECM adhesion. (D) Knockdown of miR-144-3p in HCT116 cells significantly inhibited cell-cell adhesion and increased the cell-ECM adhesion. (E) *In vivo* metastatic assays by splenic injection showed that miR-144-3p inhibited CRA liver metastasis. The number of liver metastatic nodules from mice with inoculation of Lovo^{miR-144-3p mimic} cells was significantly smaller than that from mice with inoculation of control cells, whereas the number of liver metastatic nodules from mice with inoculation of HCT116^{miR-144-3p inhibitor} cells was significantly larger than that from mice with inoculation of control cells. ECM, extracellular matrix. *, $P < 0.05$; **, $P < 0.01$; ***, $P < 0.001$.

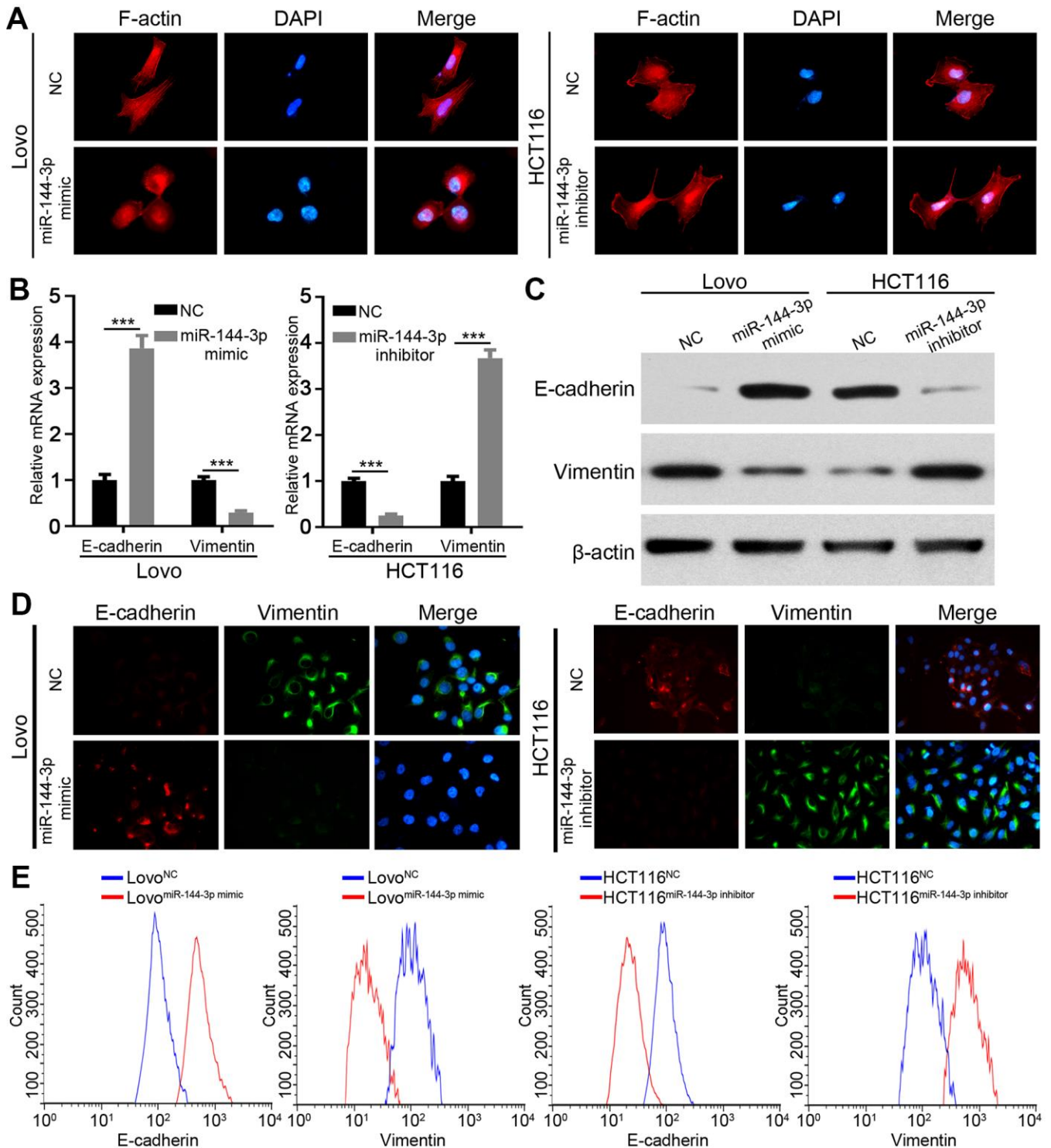


Figure 4. miR-144-3p inhibited EMT process of CRA cells. (A) Representative images of cytoskeleton showed that miR-144-3p affected polymerization of F-actin and cellular morphology of CRA cells. (B) qRT-PCR analysis of the expression level of epithelial marker E-cadherin and mesenchymal marker vimentin in CRA cells. (C) Western blot analysis of the expression level of E-cadherin and vimentin in CRA cells. (D) Representative IF images showed the expression of E-cadherin and vimentin in CRA cells. (E) Flow cytometry analysis of E-cadherin and Vimentin in CRA cells. The results showed that E-cadherin expression was enriched and vimentin expression was reduced in Lovo cells treated with miR-144-3p mimic, while opposite results were observed in HCT116 cells treated with miR-144-3p inhibitor. ***, $P < 0.001$.

ZEB1 and ZEB2 are direct targets of miR-144-3p

Next we attempted to identify the targets of miR-144-3p, and searched four databases, including TargetScan [26], miRDB [27], miRTarBase [28] and miRDIP, [29]. Among 78 genes predicted by all four databases, we focused on EMT key transcription factors ZEB1, ZEB2 [30, 31]. (Figure 5A). We constructed wild type (WT) luciferase reporter containing 3'-UTR of ZEB1/ZEB2 and mutant type (Mut) luciferase reporter containing mutant binding sequences of ZEB1/ZEB2 for miR-144-3p (Figure 5B). The results of luciferase reporter assay showed that miR-144-3p inhibited luciferase activity of ZEB1 and ZEB2 3'-UTR, but not that of mutant ZEB1 and ZEB2 3'-UTR (Figure 5C). qRT-PCR and Western blot analysis showed that miR-144-3p mimic significantly decreased ZEB1 and ZEB2 expression in Lovo cells while miR-144-3p inhibitor increased ZEB1 and ZEB2 expression in HCT116 cells (Figure 5D, 5E). Furthermore, miR-144-3p level showed negative correlation with ZEB1/2 levels in CRATs (Figure 5F).

ZEB forms a mutually inhibitory feedback loop with transcription factors OVOL1/2 [32]. Therefore, we examined the expression of transcription factors OVOL1/2. While miR-144-3p mimic induced the expression of OVOL1/2 in Lovo cells, miR-144-3p inhibitor suppressed OVOL1/2 expression in HCT116 cells (Figure 5G, 5H).

ZEB1 and ZEB2 abrogated the inhibition of CRA cell proliferation and invasion by miR-144-3p

Next, we upregulated ZEB1/2 expression in Lovo^{miR-144-3p mimic} cells and downregulated ZEB1/2 expression in HCT116^{miR-144-3p inhibitor} cells (Figure 6A, 6B). MTT assay showed that restoration of ZEB1 or ZEB2 could partly recover the proliferation of Lovo^{miR-144-3p mimic} cells (Figure 6C). However, when both ZEB1 and ZEB2 were elevated, the proliferation of Lovo^{miR-144-3p mimic} cells was completely restored (Figure 6C). In HCT116^{miR-144-3p inhibitor} cells, knockdown of ZEB1 or ZEB2 could partly inhibit enhanced proliferation, which could be fully suppressed by knockdown of both ZEB1 and ZEB2 (Figure 6D). Similarly, the restoration of ZEB1 or ZEB2 alone could partly recover the migration and invasion of Lovo^{miR-144-3p mimic} cells (Figure 6E). The migration and invasion of Lovo^{miR-144-3p mimic} cells were completely restored after the overexpression of both ZEB1 and ZEB2 (Figure 6E). In HCT116^{miR-144-3p inhibitor} cells, knockdown of ZEB1 or ZEB2 could partly inhibit enhanced migration and invasion (Figure 6F), whereas knockdown of both ZEB1 and ZEB2 completely suppressed cell migration and invasion (Figure 6F).

ZEB1 and ZEB2 mediated the inhibition of EMT by miR-144-3p

Finally, we examined whether miR-144-3p may inhibit EMT of CRA cells by targeting ZEB1 and ZEB2. In Lovo^{miR-144-3p mimic} cells, the upregulation of ZEB1 or ZEB2 alone could partly upregulate vimentin expression and partly inhibit E-cadherin expression (Figure 7A, 7B). When both ZEB1 and ZEB2 were upregulated, vimentin expression increased while E-cadherin expression decreased significantly (Figure 7A, 7B). In HCT116^{miR-144-3p inhibitor}, knockdown of ZEB1 or ZEB2 alone could partly downregulate vimentin expression and upregulate E-cadherin expression, but the effects were better after knockdown of both ZEB1 and ZEB2 (Figure 7A, 7B). Immunofluorescence and flow cytometry confirmed that ZEB1 and ZEB2 mediated the effect of miR-144-3p on EMT in CRA cells (Figure 7C, 7D).

Next we performed IHC to detect E-cadherin, vimentin, ZEB1 and ZEB2 in serial sections of NCMT and CRAT with high or low miR-144-3p expression level, and found that NCMT and CRAT with high miR-144-3p level had low levels of ZEB1, ZEB2 and vimentin and high level of E-cadherin, while CRAT with low miR-144-3p level exhibited opposite levels of these proteins (Figure 7E).

DISCUSSION

This study showed that miR-144-3p level in CRATs was lower compared to matched NCMTs, and was lower in CRATs with advanced TNM stage than in CRATs with early TNM stage. In addition, miR-144-3p level progressively decreased from matched NCMTs, CRATs to LMNs. These results suggest that miR-144-3p may modulate CRA metastasis.

miRNA expression level has been widely utilized to assess tumor pathological stages and clinical prognosis [33–35]. In this study, miR-144-3p level in CRA was significantly correlated to aggressive clinicopathological features and poor OS and DFS. In addition, low miR-144-3p level was a risk factor for OS and DFS in CRA. Therefore, miR-144-3p can be a prognostic biomarker for CRA patients after radical surgery.

Studies have shown that miR-144-3p could inhibit tumor proliferation, invasion and metastasis [36–38]. However, its biological function in CRA remains unclear. We demonstrated that miR-144-3p inhibited CRA cell proliferation, invasion and metastasis, indicating its pivotal role in CRA progression. miRNAs play critical role in regulating EMT during CRA development [39]. miR-144-3p could inhibit EMT and

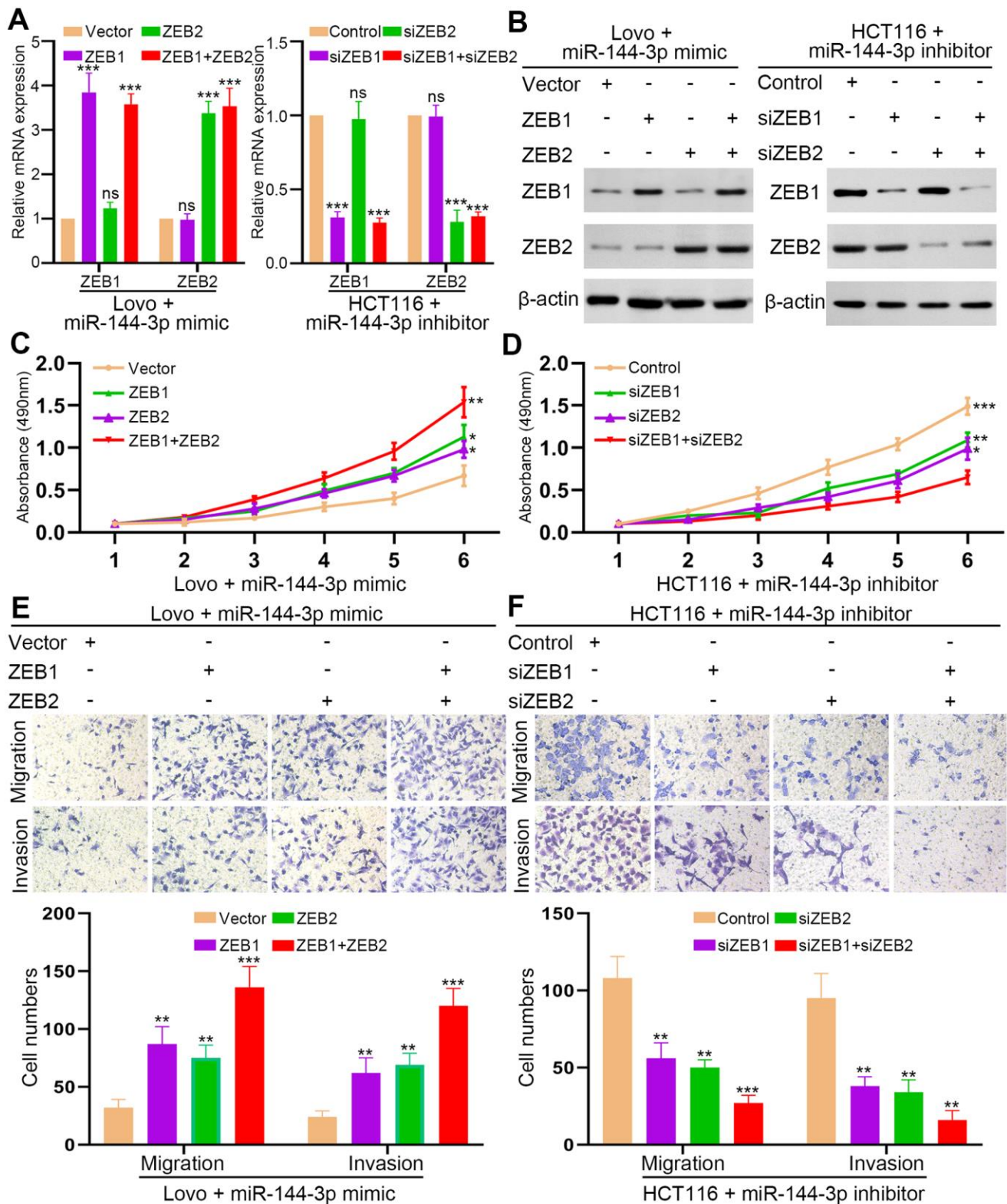


Figure 6. ZEB1 and ZEB2 collaboratively abrogated the inhibitory effect of miR-144-3p on CRA cell proliferation and invasion.

(A) qRT-PCR analysis of ZEB1, ZEB2 expression in Lovo^{miR-144-3p mimic} cells with overexpression of ZEB1 or/and ZEB2 and in HCT116^{miR-144-3p inhibitor} cells with knockdown of ZEB1 or/and ZEB2. (B) Western blot analysis of protein expression of ZEB1 and ZEB2 in indicated cells. (C) MTT assay of proliferation ability of Lovo^{miR-144-3p mimic} cells. (D) MTT assay of proliferation ability of HCT116^{miR-144-3p inhibitor} cells. (E) Transwell migration and invasion assays of the migration and invasion of Lovo^{miR-144-3p mimic} cells. (F) Transwell migration and invasion assay of HCT116^{miR-144-3p inhibitor} cells after knockdown of ZEB1 or/and ZEB2. *, $P < 0.05$; **, $P < 0.01$; ***, $P < 0.001$.

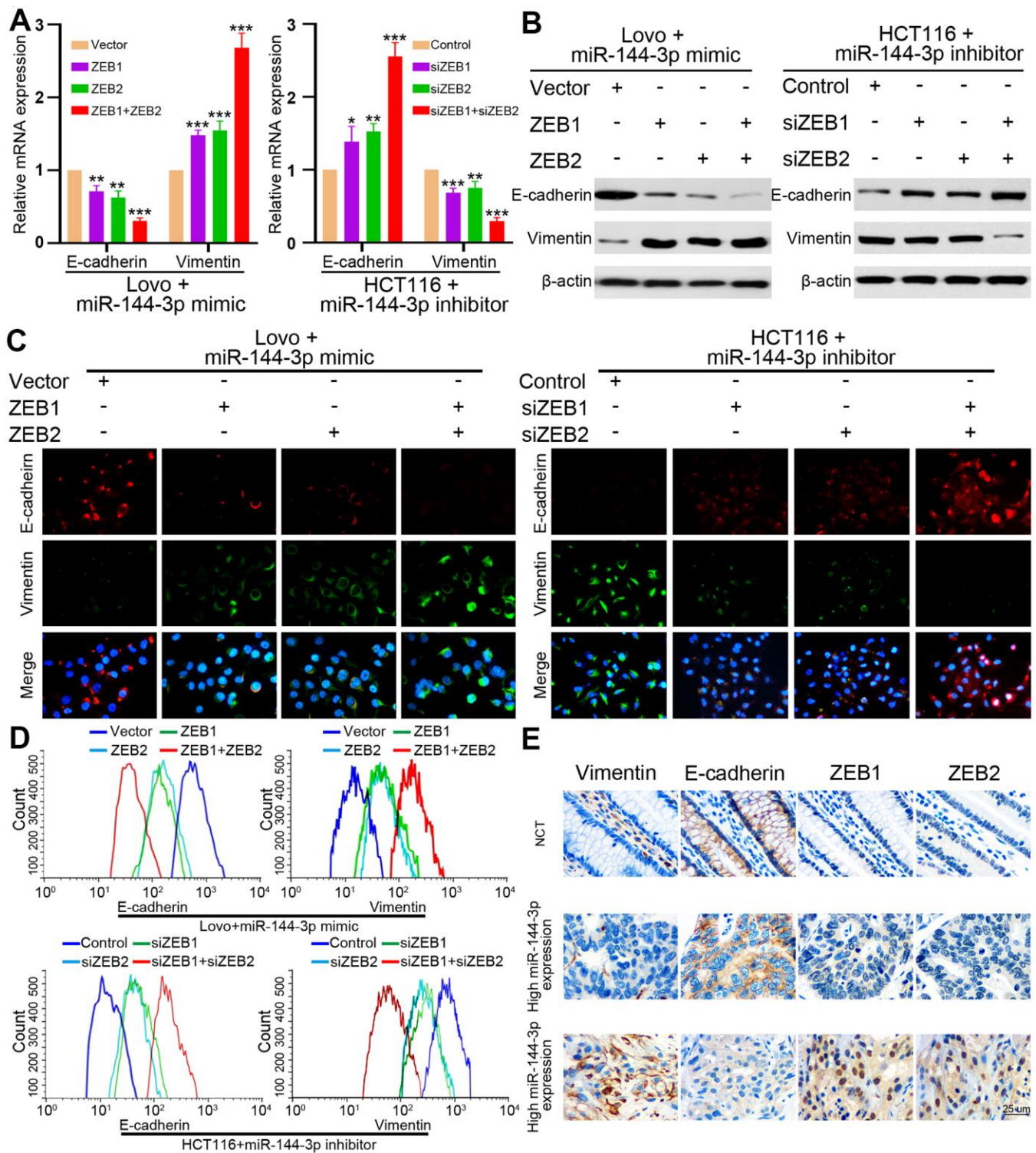


Figure 7. ZEB1 and ZEB2 collaboratively mediated the effect of miR-144-3p on CRA cell EMT. (A) qRT-PCR analysis of E-cadherin and vimentin expression in Lovo^{miR-144-3p mimic} cells with overexpression of ZEB1 or/and ZEB2, and in HCT116^{miR-144-3p inhibitor} cells with knockdown of ZEB1 or/and ZEB2. (B) Protein expression of E-cadherin and vimentin in indicated CRA cells was tested by Western blot analysis. Immunofluorescence (C) and flow cytometry (D) analysis of E-cadherin and vimentin expression in Lovo^{miR-144-3p mimic} cells with overexpression of ZEB1 or/and ZEB2, and in HCT116^{miR-144-3p inhibitor} cells with knockdown of ZEB1 or/and ZEB2. (E) Representative IHC images of serial sections showed the expression of E-cadherin, vimentin, ZEB1, ZEB2 in NCMTs and CRATs with high miR-144-3p expression or low miR-144-3p expression determined by the cut-off value of qRT-PCR. *, $P < 0.05$; **, $P < 0.01$; ***, $P < 0.001$.

metastasis of renal cell carcinoma, gastric cancer, and breast cancer [18–20]. In this study we found that miR-144-3p regulated cell cytoskeleton, decreased vimentin expression while increased E-cadherin expression in CRA cells. These results indicate that miR-144-3p may suppress CRA metastasis by inhibiting EMT process.

ZEB1 and ZEB2 are EMT-associated transcription factors involved in tumor metastasis [40–42]. Based on miRNA target prediction algorithms, both ZEB1 and ZEB2 were predicted to contain binding site of miR-144-3p. We demonstrated that miR-144-3p bound 3'-UTR of ZEB1 and ZEB2, and inhibited their expression in CRA. In addition, ZEB1 and ZEB2 are overexpressed in CRA and are related with poor prognosis for CRA patients [43, 44]. In this study, the levels of miR-144-3p and ZEB1/2 were negatively correlated in CRATs, indicating that miR-144-3p may downregulate ZEB1 and ZEB2 in CRA. We further confirmed that overexpression of ZEB1 or ZEB2 alone could only partly recover inhibitory effects of miR-144-3p on CRA cell proliferation, migration and invasion, while overexpression of both ZEB1 and ZEB2 abrogated inhibitory effects of miR-144-3p on CRA cell proliferation, migration and invasion. Although miR-144 downregulated ZEB1 and ZEB2 in various types of cancers [44, 45], this is the first study to investigate the interaction of ZEB1/2 and miR-144 in CRA. By rescue experiments, we confirmed that ZEB1 and ZEB2 downregulation collaboratively mediated inhibitory effects of miR-144-3p on EMT in CRA. Therefore, our study systematically explored the role of miR-144-3p in CRA.

CONCLUSIONS

In summary, miR-144-3p was downregulated in CRA and its downregulation was significantly correlated to poor prognosis of CRA patients. Moreover, miR-144-3p inhibited CRA cell proliferation, invasion, and EMT process *in vitro* and suppressed CRA metastasis *in vivo*. Furthermore, we revealed the mechanism that miRNA-144-3p inhibited ZEB1 and ZEB2 expression to suppress CRA growth and metastasis. Therefore, our study suggested that miR-144-3p could be a therapeutic target and prognostic marker for CRA.

Abbreviations

CRC: colorectal cancer; CRA: colorectal adenocarcinoma; qRT-PCR: quantitative real-time polymerase chain reaction; CRAT: colorectal adenocarcinoma tissues; NCMT: noncancerous colorectal mucosae tissues; DFS: disease free survival; OS: overall survival; EMT: epithelial-mesenchymal transition; IHC: Immunohistochemistry; IF: Immunofluorescence; ZEB1/2: zinc finger E-box binding homeobox 1/2.

AUTHOR CONTRIBUTIONS

Xiong Lei designed the experiments. Xiong Lei, Bo Tang, Zhixiang Huang, Cheng Tang, and Hua Dai performed experiments and analyzed data. Taiyuan Li, Xiong Lei, Cheng Tang, Benping Xiao, Hua Dai and Jianfeng Li provided patient samples and collected data. Xiong Lei wrote and revised the paper.

CONFLICTS OF INTEREST

The authors declare that they have no conflicts of interest.

FUNDING

This study was supported by the National Natural Science Foundation of China (grant no. 81702922), National Health Commission Foundation of Jiang Xi, China (grant no. 20191016), key project of Natural Science Foundation of Jiangxi, China (grant no. 20192ACBL21043).

Editorial note

*This corresponding author has a verified history of publications using a personal email address for correspondence.

REFERENCES

1. Bray F, Ferlay J, Soerjomataram I, Siegel RL, Torre LA, Jemal A. Global cancer statistics 2018: GLOBOCAN estimates of incidence and mortality worldwide for 36 cancers in 185 countries. *CA Cancer J Clin.* 2018; 68:394–424. <https://doi.org/10.3322/caac.21492> PMID:30207593
2. Lei X, Deng L, Liu D, Liao S, Dai H, Li J, Rong J, Wang Z, Huang G, Tang C, Xu C, Xiao B, Li T. ARHGEF7 promotes metastasis of colorectal adenocarcinoma by regulating the motility of cancer cells. *Int J Oncol.* 2018; 53:1980–96. <https://doi.org/10.3892/ijo.2018.4535> PMID:30132516
3. McQuade RM, Stojanovska V, Bornstein JC, Nurgali K. Colorectal Cancer Chemotherapy: The Evolution of Treatment and New Approaches. *Curr Med Chem.* 2017; 24:1537–57. <https://doi.org/10.2174/092986732466617011152436> PMID:28079003
4. Manfredi S, Lepage C, Hatem C, Coatmeur O, Faivre J, Bouvier AM. Epidemiology and management of liver metastases from colorectal cancer. *Ann Surg.* 2006; 244:254–59. <https://doi.org/10.1097/01.sla.0000217629.94941.cf>

- PMID:[16858188](https://pubmed.ncbi.nlm.nih.gov/16858188/)
5. Valastyan S, Weinberg RA. Tumor metastasis: molecular insights and evolving paradigms. *Cell*. 2011; 147:275–92.
<https://doi.org/10.1016/j.cell.2011.09.024>
PMID:[22000009](https://pubmed.ncbi.nlm.nih.gov/22000009/)
 6. Thiery JP, Acloque H, Huang RY, Nieto MA. Epithelial-mesenchymal transitions in development and disease. *Cell*. 2009; 139:871–90.
<https://doi.org/10.1016/j.cell.2009.11.007>
PMID:[19945376](https://pubmed.ncbi.nlm.nih.gov/19945376/)
 7. Yang J, Weinberg RA. Epithelial-mesenchymal transition: at the crossroads of development and tumor metastasis. *Dev Cell*. 2008; 14:818–29.
<https://doi.org/10.1016/j.devcel.2008.05.009>
PMID:[18539112](https://pubmed.ncbi.nlm.nih.gov/18539112/)
 8. Nieto MA, Huang RY, Jackson RA, Thiery JP. EMT: 2016. *Cell*. 2016; 166:21–45.
<https://doi.org/10.1016/j.cell.2016.06.028>
PMID:[27368099](https://pubmed.ncbi.nlm.nih.gov/27368099/)
 9. Vu T, Datta PK. Regulation of EMT in Colorectal Cancer: A Culprit in Metastasis. *Cancers (Basel)*. 2017; 9:171.
<https://doi.org/10.3390/cancers9120171>
PMID:[29258163](https://pubmed.ncbi.nlm.nih.gov/29258163/)
 10. Díaz-López A, Moreno-Bueno G, Cano A. Role of microRNA in epithelial to mesenchymal transition and metastasis and clinical perspectives. *Cancer Manag Res*. 2014; 6:205–16.
<https://doi.org/10.2147/CMAR.S38156>
PMID:[24812525](https://pubmed.ncbi.nlm.nih.gov/24812525/)
 11. Bonfrate L, Altomare DF, Di Lena M, Travaglio E, Rotelli MT, De Luca A, Portincasa P. MicroRNA in colorectal cancer: new perspectives for diagnosis, prognosis and treatment. *J Gastrointest Liver Dis*. 2013; 22:311–20.
PMID:[24078989](https://pubmed.ncbi.nlm.nih.gov/24078989/)
 12. Calin GA, Croce CM. MicroRNA signatures in human cancers. *Nat Rev Cancer*. 2006; 6:857–66.
<https://doi.org/10.1038/nrc1997> PMID:[17060945](https://pubmed.ncbi.nlm.nih.gov/17060945/)
 13. Liu W, Lu Y, Zhang D, Shi L, Zu G, Yan H, Sun D. MicroRNA-708 inhibits the proliferation and chemoresistance of pancreatic cancer cells. *Biocell*. 2020; 44:73–80.
<https://doi.org/10.32604/biocell.2020.08613>
 14. Wu J, Zhao Y, Li F, Qiao B. MiR-144-3p: a novel tumor suppressor targeting MAPK6 in cervical cancer. *J Physiol Biochem*. 2019; 75:143–52.
<https://doi.org/10.1007/s13105-019-00681-9>
PMID:[31016619](https://pubmed.ncbi.nlm.nih.gov/31016619/)
 15. Nicoloso MS, Spizzo R, Shimizu M, Rossi S, Calin GA. MicroRNAs—the micro steering wheel of tumour metastases. *Nat Rev Cancer*. 2009; 9:293–302.
<https://doi.org/10.1038/nrc2619>
PMID:[19262572](https://pubmed.ncbi.nlm.nih.gov/19262572/)
 16. Fei X, Hu W, Wang G, Su C, Huang X, Jiang Z. Effect of microRNA-143-3p- mediated CTNND1 on the biological function of lung cancer cells. *Biocell*. 2020; 44:81–88.
<https://doi.org/10.32604/biocell.2020.08125>
 17. Cheng ZX, Song YX, Wang ZY, Wang Y, Dong Y. miR-144-3p serves as a tumor suppressor by targeting FZD7 and predicts the prognosis of human glioblastoma. *Eur Rev Med Pharmacol Sci*. 2017; 21:4079–86.
PMID:[29028093](https://pubmed.ncbi.nlm.nih.gov/29028093/)
 18. Liu F, Chen N, Xiao R, Wang W, Pan Z. miR-144-3p serves as a tumor suppressor for renal cell carcinoma and inhibits its invasion and metastasis by targeting MAP3K8. *Biochem Biophys Res Commun*. 2016; 480:87–93.
<https://doi.org/10.1016/j.bbrc.2016.10.004>
PMID:[27717821](https://pubmed.ncbi.nlm.nih.gov/27717821/)
 19. Li B, Zhang S, Shen H, Li C. MicroRNA-144-3p suppresses gastric cancer progression by inhibiting epithelial-to-mesenchymal transition through targeting PBX3. *Biochem Biophys Res Commun*. 2017; 484:241–47.
<https://doi.org/10.1016/j.bbrc.2017.01.084>
PMID:[28111340](https://pubmed.ncbi.nlm.nih.gov/28111340/)
 20. Yu L, Yang Y, Hou J, Zhai C, Song Y, Zhang Z, Qiu L, Jia X. MicroRNA-144 affects radiotherapy sensitivity by promoting proliferation, migration and invasion of breast cancer cells. *Oncol Rep*. 2015; 34:1845–52.
<https://doi.org/10.3892/or.2015.4173>
PMID:[26252024](https://pubmed.ncbi.nlm.nih.gov/26252024/)
 21. Tan Y, Lin JJ, Yang X, Gou DM, Fu L, Li FR, Yu XF. A panel of three plasma microRNAs for colorectal cancer diagnosis. *Cancer Epidemiol*. 2019; 60:67–76.
<https://doi.org/10.1016/j.canep.2019.01.015>
PMID:[30925282](https://pubmed.ncbi.nlm.nih.gov/30925282/)
 22. Chang RM, Xiao S, Lei X, Yang H, Fang F, Yang LY. miRNA-487a Promotes Proliferation and Metastasis in Hepatocellular Carcinoma. *Clin Cancer Res*. 2017; 23:2593–604.
<https://doi.org/10.1158/1078-0432.CCR-16-0851>
PMID:[27827315](https://pubmed.ncbi.nlm.nih.gov/27827315/)
 23. McShane LM, Altman DG, Sauerbrei W, Taube SE, Gion M, Clark GM, and Statistics Subcommittee of the NCI-EORTC Working Group on Cancer Diagnostics. Reporting recommendations for tumor marker prognostic studies (REMARK). *J Natl Cancer Inst*. 2005; 97:1180–84.
<https://doi.org/10.1093/jnci/dji237>
PMID:[16106022](https://pubmed.ncbi.nlm.nih.gov/16106022/)
 24. Dongre A, Weinberg RA. New insights into the mechanisms of epithelial-mesenchymal transition and

- implications for cancer. *Nat Rev Mol Cell Biol.* 2019; 20:69–84.
<https://doi.org/10.1038/s41580-018-0080-4>
 PMID:[30459476](https://pubmed.ncbi.nlm.nih.gov/30459476/)
25. Lamouille S, Xu J, Derynck R. Molecular mechanisms of epithelial-mesenchymal transition. *Nat Rev Mol Cell Biol.* 2014; 15:178–96.
<https://doi.org/10.1038/nrm3758>
 PMID:[24556840](https://pubmed.ncbi.nlm.nih.gov/24556840/)
 26. Agarwal V, Bell GW, Nam JW, Bartel DP. Predicting effective microRNA target sites in mammalian mRNAs. *Elife.* 2015; 4:e05005.
<https://doi.org/10.7554/eLife.05005> PMID:[26267216](https://pubmed.ncbi.nlm.nih.gov/26267216/)
 27. Liu W, Wang X. Prediction of functional microRNA targets by integrative modeling of microRNA binding and target expression data. *Genome Biol.* 2019; 20:18.
<https://doi.org/10.1186/s13059-019-1629-z>
 PMID:[30670076](https://pubmed.ncbi.nlm.nih.gov/30670076/)
 28. Chou CH, Shrestha S, Yang CD, Chang NW, Lin YL, Liao KW, Huang WC, Sun TH, Tu SJ, Lee WH, Chiew MY, Tai CS, Wei TY, et al. miRTarBase update 2018: a resource for experimentally validated microRNA-target interactions. *Nucleic Acids Res.* 2018; 46:D296–302.
<https://doi.org/10.1093/nar/gkx1067> PMID:[29126174](https://pubmed.ncbi.nlm.nih.gov/29126174/)
 29. Tokar T, Pastrello C, Rossos AE, Abovsky M, Hauschild AC, Tsay M, Lu R, Jurisica I. mirDIP 4.1-integrative database of human microRNA target predictions. *Nucleic Acids Res.* 2018; 46:D360–70.
<https://doi.org/10.1093/nar/gkx1144>
 PMID:[29194489](https://pubmed.ncbi.nlm.nih.gov/29194489/)
 30. Cao H, Xu E, Liu H, Wan L, Lai M. Epithelial-mesenchymal transition in colorectal cancer metastasis: A system review. *Pathol Res Pract.* 2015; 211:557–69.
<https://doi.org/10.1016/j.prp.2015.05.010>
 PMID:[26092594](https://pubmed.ncbi.nlm.nih.gov/26092594/)
 31. Ahmadiankia N, Khosravi A. Significance of epithelial-to-mesenchymal transition inducing transcription factors in predicting distant metastasis and survival in patients with colorectal cancer: A systematic review and meta-analysis. *J Res Med Sci.* 2020; 25:60.
https://doi.org/10.4103/jrms.JRMS_174_19
 PMID:[33088297](https://pubmed.ncbi.nlm.nih.gov/33088297/)
 32. Mooney SM, Jolly MK, Levine H, Kulkarni P. Phenotypic plasticity in prostate cancer: role of intrinsically disordered proteins. *Asian J Androl.* 2016; 18:704–10.
<https://doi.org/10.4103/1008-682X.183570>
 PMID:[27427552](https://pubmed.ncbi.nlm.nih.gov/27427552/)
 33. White NM, Fatoohi E, Metias M, Jung K, Stephan C, Yousef GM. Metastamirs: a stepping stone towards improved cancer management. *Nat Rev Clin Oncol.* 2011; 8:75–84.
<https://doi.org/10.1038/nrclinonc.2010.173>
 PMID:[21045789](https://pubmed.ncbi.nlm.nih.gov/21045789/)
 34. Hayes J, Peruzzi PP, Lawler S. MicroRNAs in cancer: biomarkers, functions and therapy. *Trends Mol Med.* 2014; 20:460–69.
<https://doi.org/10.1016/j.molmed.2014.06.005>
 PMID:[25027972](https://pubmed.ncbi.nlm.nih.gov/25027972/)
 35. Shirafkan N, Mansoori B, Mohammadi A, Shomali N, Ghasbi M, Baradaran B. MicroRNAs as novel biomarkers for colorectal cancer: New outlooks. *Biomed Pharmacother.* 2018; 97:1319–30.
<https://doi.org/10.1016/j.biopha.2017.11.046>
 PMID:[29156521](https://pubmed.ncbi.nlm.nih.gov/29156521/)
 36. Liu JL, Li J, Xu JJ, Xiao F, Cui PL, Qiao ZG, Chen XD, Tao WD, Zhang XL. MiR-144 Inhibits Tumor Growth and Metastasis in Osteosarcoma via Dual-suppressing RhoA/ROCK1 Signaling Pathway. *Mol Pharmacol.* 2019; 95:451–61.
<https://doi.org/10.1124/mol.118.114207>
 PMID:[30674565](https://pubmed.ncbi.nlm.nih.gov/30674565/)
 37. Liu CL, Wang WH, Sun YL, Zhuang HW, Xu M, Chen HF, Liu JX. MiR-144-3p inhibits the proliferation and metastasis of pediatric Wilms' tumor cells by regulating Girdin. *Eur Rev Med Pharmacol Sci.* 2018; 22:7671–78.
https://doi.org/10.26355/eurev_201811_16384
 PMID:[30536309](https://pubmed.ncbi.nlm.nih.gov/30536309/)
 38. Tao P, Wen H, Yang B, Zhang A, Wu X, Li Q. miR-144 inhibits growth and metastasis of cervical cancer cells by targeting VEGFA and VEGFC. *Exp Ther Med.* 2018; 15:562–68.
<https://doi.org/10.3892/etm.2017.5392>
 PMID:[29387205](https://pubmed.ncbi.nlm.nih.gov/29387205/)
 39. Ma Y, Li W, Wang H. Roles of miRNA in the initiation and development of colorectal carcinoma. *Curr Pharm Des.* 2013; 19:1253–61.
<https://doi.org/10.2174/138161213804805784>
 PMID:[23092337](https://pubmed.ncbi.nlm.nih.gov/23092337/)
 40. Jolly MK, Celià-Terrassa T. Dynamics of Phenotypic Heterogeneity Associated with EMT and Stemness during Cancer Progression. *J Clin Med.* 2019; 8:1542.
<https://doi.org/10.3390/jcm8101542> PMID:[31557977](https://pubmed.ncbi.nlm.nih.gov/31557977/)
 41. Gregory PA, Bracken CP, Bert AG, Goodall GJ. MicroRNAs as regulators of epithelial-mesenchymal transition. *Cell Cycle.* 2008; 7:3112–18.
<https://doi.org/10.4161/cc.7.20.6851>
 PMID:[18927505](https://pubmed.ncbi.nlm.nih.gov/18927505/)
 42. Long ZH, Bai ZG, Song JN, Zheng Z, Li J, Zhang J, Cai J, Yao HW, Wang J, Yang YC, Yin J, Zhang ZT. miR-141 Inhibits Proliferation and Migration of Colorectal Cancer

- SW480 Cells. *Anticancer Res.* 2017; 37:4345–52.
<https://doi.org/10.21873/anticancerres.11828>
PMID:[28739727](https://pubmed.ncbi.nlm.nih.gov/28739727/)
43. Chen H, Lu W, Huang C, Ding K, Xia D, Wu Y, Cai M. Prognostic significance of ZEB1 and ZEB2 in digestive cancers: a cohort-based analysis and secondary analysis. *Oncotarget.* 2017; 8:31435–48.
<https://doi.org/10.18632/oncotarget.15634>
PMID:[28416756](https://pubmed.ncbi.nlm.nih.gov/28416756/)
44. Li MZ, Wang JJ, Yang SB, Li WF, Xiao LB, He YL, Song XM. ZEB2 promotes tumor metastasis and correlates with poor prognosis of human colorectal cancer. *Am J Transl Res.* 2017; 9:2838–51.
PMID:[28670373](https://pubmed.ncbi.nlm.nih.gov/28670373/)
45. Pan Y, Zhang J, Fu H, Shen L. miR-144 functions as a tumor suppressor in breast cancer through inhibiting ZEB1/2-mediated epithelial mesenchymal transition process. *Onco Targets Ther.* 2016; 9:6247–55.
<https://doi.org/10.2147/OTT.S103650>
PMID:[27785072](https://pubmed.ncbi.nlm.nih.gov/27785072/)

SUPPLEMENTARY MATERIALS

Cell lines

The normal colorectal mucosal cell line FHC, and colorectal adenocarcinoma (CRA) cell line SW480, SW620, HCT116, LoVo, HT-29 cell lines were purchased from the American Type Culture Collection (Manassas, VA, USA). Short tandem repeat (STR) DNA fingerprinting was used to authenticate all cell lines prior to commencement of the study. All cell lines were routinely cultured with RPMI-1640 (Gibco; Thermo Fisher Scientific Inc., Waltham, MA, USA) supplemented with 10% fetal bovine serum (HyClone; GE Healthcare Life Sciences, Logan, UT, USA), and maintained in a 5% CO₂ humidified incubator at 37° C.

qRT-PCR analysis

Total RNA was extracted using TRIzol reagent (Invitrogen; Thermo Fisher Scientific, Inc) according to the manufacturer's protocol. After determining the concentration, the RNA was then reverse transcribed to obtain cDNA using the universal cDNA synthesis kit (Toyobo, Osaka, Japan). qRT-PCR analysis was performed using the SYBR[®]-Green Realtime PCR Master Mix assay kit (Toyobo, Osaka, Japan). GAPDH and U6 were used as internal controls for gene mRNA and miRNA respectively. The primer sequences were as follows:

miR-144-3p: F: 5'-TACTGCATCAGGAACTGACTGGA-3'; R: 5'-GTGCAGGGTCCGAGGT-3'.

U6: F: 5'-GCTTCGGCAGCACATATACTAAAAT-3'; R: 5'-CGCTTCAGAAATTTGCGTGTTCAT-3'.

cadherin: F: 5'-CGAGAGCTACACGTTACACGG-3'; R: 5'-GGGTGTCGAGGGAAAAATAGG-3'.

Vimentin: F: 5'-AGTCCACTGAGTACCGGAGAC-3'; R: 5'-CATTTACGCATCTGGCGTTC-3'.

ZEB1: F: 5'-TTACACCTTTGCATACAGAACCC-3'; R: 5'-TTTACGATTACACCCAGACTGC-3'.

ZEB2: F: 5'-GGAGACGAGTCCAGCTAGTGT-3'; R: 5'-CCACTCCACCCCTCCCTTATTTTC-3'.

GAPDH: F: 5'-GCACCGTCAAGGCTGAGAAC-3'; R: 5'-TGGTGAAGACGCCAGTGGA-3'.

The results were analyzed using $2^{-\Delta Ct}$ or $2^{-\Delta\Delta Ct}$ method to determine the relative expression level of corresponding genes.

Western blot analysis

Total proteins were extracted by RIPA lysis buffer (Beyotime Institute of Biotechnology, Jiangsu, China). The protein concentrations were measured according to BCA method (Beyotime Institute of Biotechnology). A total of 50 µg protein was subjected to 12% sodium dodecyl sulfate-polyacrylamide gel electrophoresis and then transferred onto PVDF membranes (Millipore; Bedford, MA, USA). Then, the membranes were incubated with primary antibodies and subsequently incubated with the appropriate secondary antibodies (Cell Signaling Technology; Beverly, MA, USA). Bands were detected with enhanced chemiluminescence reagents (Thermo Fisher Scientific). β-actin (MilliporeSigma; St Louis, MO, USA) was used as a loading control. The primary antibodies used in this study were as follows: mouse anti-β-actin antibody (MilliporeSigma; St Louis, MO, USA), mouse anti-E-cadherin antibody (CST; Danvers, MA, USA), mouse anti-vimentin antibody (CST), rabbit anti-ZEB1 antibody (Affinity Biosciences, Jiangsu, China), rabbit anti-ZEB2 antibody (Affinity Biosciences).

Cell transfection

miR-144-3p mimic or inhibitor and their corresponding control sequences (RiboBio, Guangzhou, China) were transfected into the indicated CRA cells using Lipofectamine 3000 (Invitrogen; Thermo Fisher Scientific Inc) following the manufacturer's protocol. After 48h transfection, the transfected cells were harvested and verified their efficiency for subsequent experiments. For transfection of ZEB1 and ZEB2 ORF for ZEB1 and ZEB2 overexpression or short hairpin RNA (shRNA) for ZEB1 and ZEB2 knockdown, the lentiviral vectors encoding ZEB1 and ZEB2 ORF or shRNA-ZEB1/2 were synthesized and purchased from GenePharma Co., Ltd (Shanghai, China). The empty vector was used as the negative control. The sequences of shRNAs for ZEB1 and ZEB2 knockdown were as follows: shRNA-ZEB1: 5'-CCUAGUCAGCCACCUUUAATT-3'; shRNA-ZEB2: 5'-GUAAUGACUAGGGCUA UUA-3'. Lentiviral vectors were transfected into cells in 6-well plates using Lipofectamine[®] 3000 (Invitrogen, Thermo Fisher Scientific Inc.) according to the manufacturer's protocol. The efficiency of knockdown or overexpression of ZEB1 and ZEB2 was confirmed by qRT-PCR and western blot. The stably transfected cells were subjected to subsequent experiments.

Cell proliferation and colony formation assays

Methyl thiazolyl tetrazolium (MTT) assays and colony formation assays were used to determine CRA cell proliferation ability. For the MTT assays, 5×10^3 cells were seeded into each well of 96-well plates. 100 μ l fresh medium containing 0.5 mg/ml MTT (MilliporeSigma) was added into each well and incubated at 37° C for 4 h. The absorbance was measured at 570 nm. For the colony formation assay, about 500 cells were seeded into 35-mm cell-culture dishes (Corning Incorporated; Corning, NY, USA) and cultured for 2 weeks. The number of colonies per dish was calculated following being stained with crystal violet (Beyotime Institute of Biotechnology, Jiangsu, China). Only positive colonies (diameter > 40 μ m) were calculated and compared. The experiments were repeated three times.

EdU proliferation assays

Cell proliferation was detected using the incorporation of 5-ethynyl-2'-deoxyuridine (EdU) with the EdU Cell Proliferation Assay Kit (Ribobio, Guangzhou, China). Briefly, the indicated cells were seeded in 96-well plates and cultured in complete media under the condition of 5% CO₂, at 37° C. After incubation with 50 μ M EdU for 4h, the cells were fixed, permeabilized and stained with EdU in order according to the manufacturer's protocol. Then the cell nuclei were stained with DAPI at a concentration of 1 μ g/ml for 30 second. The typical images of the plates were taken using an inverted fluorescence microscope (Nikon Corporation, Tokyo, Japan). The experiments were repeated with three wells.

Transwell assay

Transwell migration and invasion assays were separately used to test CRA cell motility and invasion ability. Briefly, after pre-incubation with 10 μ g/ml Mitomycin-C for 1 h to inhibit cell proliferation, about 1×10^5 cells in serum free medium were placed into the upper chamber of the insert. The upper chamber of the insert was coated with Matrigel (BD Biosciences; Franklin Lakes, NJ, USA) used for Transwell invasion assays, while the upper chamber of the insert without Matrigel used for Transwell migration assays. Following incubation for 24 h, the number of cells that adhered to the lower membrane of the inserts was calculated after stained with 0.1% crystal violet (Beyotime Institute of Biotechnology). For each group, the assays were repeated three times, and five random fields of view were selected for analysis.

Adhesion assay

The adhesive ability of the CRA cells was analyzed by cell-extracellular matrix (ECM) and cell-cell adhesion

assays. For the cell-ECM adhesion assay, a 96-well plate was plated with fibronectin at 37° C for 60 min and washed twice with DMEM buffer supplied with 0.1% BSA (HyClone, GE Healthcare Life Sciences; Logan, UT, USA). The plates were blocked with DMEM buffer supplied with 0.5% BSA at 37° C in a 5% CO₂ incubator for 60 min. About 1×10^4 cells (100 μ l cells at a density of about 1×10^5 /ml) were added into each well of a 96-well plate (Costar; Corning Incorporated, Corning, NY, USA) and cultured at 37° C. Five wells for each group were determined at 60, 90 or 120 min. After remove of the non-adhesion cells, then 100 μ l fresh medium containing 0.5 mg/ml MTT (MilliporeSigma) was added into each well and incubated at 37° C for 4 hours. The wells were then added 100 μ l DMSO following remove of the medium and shaken at room temperature for 10 min. Finally, the absorbance was measured at 570 nm. For the cell-cell adhesion assay, sub-confluent (70-80%) cell layers were rinsed twice with Ca₂- and Mg₂-free PBS and separated by incubation in HBSS containing 1 mmol/L EDTA at 37° C for 20 min. And then, 100 μ l single cells at density of about 1×10^5 /ml were added into a 96-well plate (Corning Costar Incorporated) with a fully confluent single cell layer, and cultured at 37° C for 0-120 min. The non-adhesion cells were collected from the wells, and counted using an inverted TE-2000S microscope (Nikon Corporation). The adhesion rate was determined by calculating representative aliquots from each well on a hemacytometer. The adhesion rate was calculated at 60, 90 or 120 min as follow: $N_0 - N_t / N_0 \times 100\%$, where N_t is the number of non-adhesion cells at the incubation time t , and N_0 is the total number of cells added.

Immunofluorescence (IF)

The CRA cells were grown on the glass coverslips, and then fixed with 4% paraformaldehyde. After permeated in phosphate-buffered saline (PBS) with 0.2% Trion X-100, CRA cells were blocked for an hour with 1% bovine serum albumin (BSA), and then incubated with primary antibody overnight at 4° C. In the following day, the cells incubated with appropriate concentration of secondary antibody (Beyotime Institute of Biotechnology) and DAPI (Beyotime Institute of Biotechnology) separately. Images of the slides were captured using an inverted fluorescence microscope. Primary antibodies for E-cadherin, vimentin were purchased from Santa Cruz Biotechnology (Santa Cruz, CA, USA).

Flow cytometry

CRA cells were seeded in 6-well plates and incubated for 24 h. Then monocytes were washed and incubated with E-cadherin, vimentin antibody (CST; Danvers, MA, USA) at a dilution of 1:10 in phosphate buffered saline (PBS)-bovine serum albumin (BSA) for 30 min at 4° C.

Cells were incubated with an isotype immunoglobulin G (IgG) antibody as control. Cells were filtered through a 70 μ M cell strainer immediately prior to flow cytometry, which was carried out on a FACS caliber flow cytometer (BD Biosciences, San Jose, CA).

Luciferase reporter assay

Luciferase activity was assessed according to the Dual-Luciferase Reporter Assay protocol (Promega,

Madison, WI, USA) using a Veritas™ 96-well Microplate Luminometer (Promega) with substrate dispenser (Promega). 293T cells infected with miR-144-3p mimic or control were seeded in 96-well plates with 70% confluence. 12 hours later, the cells were co-transfected with 50 ng pGL3-UTR and 10 ng pRLTK by using Lipofectamine LTX. After transfection 24 hours, firefly and Renilla luciferase activities were measured. The Renilla luciferase activities were used to normalize transfection efficiency.

CircSPIDR acts as a tumour suppressor in cervical adenocarcinoma by sponging miR-431-5p and regulating *SORCS1* and *CUBN* expression

Junfen Xu¹, Weiguo Lu^{1,2,3}

¹Department of Gynecologic Oncology, Women's Hospital, Zhejiang University School of Medicine, Hangzhou 310006, Zhejiang, China

²Center of Uterine Cancer Diagnosis & Therapy of Zhejiang Province, Hangzhou 310006, Zhejiang, China

³Zhejiang University Cancer Center, Hangzhou 310006, Zhejiang, China

Correspondence to: Weiguo Lu; **email:** lbwg@zju.edu.cn

Keywords: CircSPIDR, cervical adenocarcinoma, miR-431-5p, *SORCS1*, *CUBN*, cell growth

Received: February 8, 2021

Accepted: June 19, 2021

Published: July 29, 2021

Copyright: © 2021 Xu and Lu. This is an open access article distributed under the terms of the [Creative Commons Attribution License](https://creativecommons.org/licenses/by/3.0/) (CC BY 3.0), which permits unrestricted use, distribution, and reproduction in any medium, provided the original author and source are credited.

ABSTRACT

To identify circular RNAs (circRNAs) with tumor suppressor activity against cervical adenocarcinoma, we compared the circRNA levels of cervical adenocarcinoma and normal cervical tissues. We found that circSPIDR was dramatically downregulated in cervical adenocarcinoma tissues. In cervical adenocarcinoma cells, overexpression of circSPIDR reduced cell viability, inhibited colony formation and promoted apoptosis, whereas knockdown of circSPIDR exerted the opposite effects. CircSPIDR overexpression also suppressed the tumorigenicity of cervical adenocarcinoma cells in a xenograft mouse model. CircSPIDR was found to sponge miR-431-5p, thereby de-repressing sortin-related VPS10 domain-containing receptor 1 (*SORCS1*) and cubilin (*CUBN*) and inhibiting the development of cervical adenocarcinoma. In clinical cervical samples, circSPIDR expression correlated negatively with miR-431-5p expression and positively with *SORCS1* and *CUBN* expression. These results demonstrated that circSPIDR suppresses cervical adenocarcinoma by competitively binding to miR-431-5p, thus upregulating *SORCS1* and *CUBN*. These findings suggest circSPIDR could serve as a novel therapeutic target for treatment of cervical adenocarcinoma patients.

INTRODUCTION

Cervical cancer is the fourth most common cancer and the fourth leading cause of cancer death in women worldwide [1]. In China, approximately 98,900 new cervical cancer cases were diagnosed and 30,500 women died of this disease in 2015 [2]. Overall, cervical squamous cell carcinoma is the primary pathological type of human cervical cancer, while cervical adenocarcinoma (CADC) is the second. In recent decades, the tumor screenings and human papillomavirus vaccination programs have greatly reduced the burden of cervical squamous cell carcinoma in developed countries; however, the incidence of CADC has increased during the same period worldwide [2, 3]. Thus, it is critical to determine the underlying

molecular mechanisms of CADC and develop effective therapies.

Circular RNAs (circRNAs) are regulatory RNAs characterized by covalent single-stranded loop structures generated via back-splicing or exon skipping of the precursor mRNA [4–7]. CircRNAs are naturally resistant to RNA exonucleases, are tissue- or cell type-specific [5, 8], and exert important functions in various human cancers [9, 10]. To date, circRNAs have largely been reported to serve as competing endogenous RNAs (ceRNAs). For example, circTP63 (an oncogene in lung squamous cell carcinoma), circ-ZKSCAN1 (a bladder cancer suppressor) and other cancer-related circRNAs such as CDR1as [11–13] and circAKT3 [14, 15] function as microRNA (miRNA) sponges that inhibit the effects

of miRNAs on their target genes. In addition to the ceRNA mechanism, circRNAs can sequester specific RNA-binding proteins to regulate gene expression [4, 16], and some of them can be translated into functional proteins [17–19]. Certain circRNAs have been identified as promising clinical molecular biomarkers for cancer diagnosis and treatment [20–22]. However, the functions of circRNAs in CADC remain to be elucidated.

In the present study, our main interest was to identify circRNAs with tumor suppressor functions in CADC. In a previous study using RNA-sequencing data from human CADC and normal cervical tissues (GSE No. 145372), we found that one of the most significantly downregulated circRNAs in CADC tissues was circSPIDR, - a circRNA derived from exons 6 and 7 of the human scaffold protein involved in DNA repair (SPIDR) gene. Thus, in the current study, we evaluated the effects of circSPIDR on cell proliferation, colony formation and apoptosis in CADC cells. Then, we examined the influence of circSPIDR on miRNAs and their target genes, and determined the effects of these genes on the malignant behaviors of CADC cells. Finally, we assessed the clinical importance of circSPIDR expression by evaluating its correlation with miRNA and target gene expression in a large cohort of primary CADC tissues. Our study suggested that circSPIDR is a tumor suppressor that may be a candidate for the diagnosis and treatment of CADC.

RESULTS

CircSPIDR is significantly down-regulated in CADC

We previously used transcriptome sequencing to determine the circRNA expression signatures of CADC patients [23], and found that a novel circRNA named circSPIDR was significantly downregulated in CADC tissues compared with normal cervical tissues (Figure 1A). CircSPIDR is derived from exons 6 and 7 of the human *SPIDR* gene, and is 352 nucleotides long (Figure 1B). To confirm our circRNA sequencing data, we used quantitative real-time PCR (qRT-PCR) to assess circSPIDR expression in another 40 human cervical samples (20 normal vs. 20 CADC tissues). CircSPIDR expression was much lower in CADC tissues than in normal control tissues (Figure 1C).

Characterization of circSPIDR in CADC cells

Next, we used Sanger sequencing to assess the structure of circSPIDR (Figure 1B). Northern blotting confirmed that circSPIDR could be detected at approximately 352 nucleotides with a probe targeting the back-spliced

junction in CADC cells (HeLa) and tissues (Figure 1D). A stability analysis of circSPIDR and *SPIDR* indicated that the loop structure of circSPIDR was resistant to digestion with RNase R exonuclease, while the linear *SPIDR* mRNA was degraded upon RNase R treatment (Figure 1E).

To determine whether head-to-tail splicing was the result of trans-splicing or genomic rearrangement, we designed divergent and convergent primers for circSPIDR. An RT-PCR analysis of reverse-transcribed RNA (cDNA) and genomic DNA (gDNA) from HeLa cells indicated that the divergent circSPIDR primers could amplify products from the cDNA, but not from the gDNA (Figure 1F). These results confirmed that circSPIDR is a stable circRNA expressed in CADC cells.

CircSPIDR exerts tumor-suppressive effects in CADC cells *in vitro* and *in vivo*

To evaluate the effects of circSPIDR on CADC cells, we conducted a circSPIDR expression vector and two specific siRNAs against circSPIDR. The overexpression plasmids and siRNAs were transfected into HeLa cells, and the cells were harvested for experiments after 48 h. The circSPIDR vector successfully increased circSPIDR expression rather than *SPIDR* mRNA expression in HeLa cells (Supplementary Figure 1A). CircSPIDR siRNA #1 and #2 specifically inhibited circSPIDR expression without influencing *SPIDR* mRNA expression (Supplementary Figure 1B). These results also indicated that *SPIDR* expression was not altered by circSPIDR expression.

We then performed Cell Counting Kit 8 (CCK-8) and colony formation assays. Which demonstrated that overexpression of circSPIDR significantly suppressed HeLa cell viability and colony formation (Figure 2A and 2B). Conversely, knockdown of circSPIDR significantly enhanced cell viability and colony formation (Figure 2C and 2D). A bromodeoxyuridine (BrdU) incorporation assay indicated that the percentage of the BrdU-positive (proliferating) cells was lower in circSPIDR-overexpressing HeLa cells than in vector control cells (Supplementary Figure 2). Apoptosis assays illustrated that circSPIDR overexpression remarkably increased the proportion of apoptotic HeLa cells (Figure 2E), whereas circSPIDR knockdown had the opposite effect (Figure 2F). These results indicated that circSPIDR significantly suppressed cell proliferation and induced apoptosis in HeLa cells.

To identify the effects of circSPIDR *in vivo*, we stably expressed circSPIDR or an empty vector in HeLa cells

using neomycin selection for 10 days. Then, we subcutaneously injected these cells into the right single flank of BALB/c nude mice ($n = 6/\text{group}$) to establish a xenograft tumor model. The tumors formed after one week, and the tumor size were monitored for the next five weeks. Tumors derived from circSPIDR overexpressing cells were much smaller than those derived from control cells (Figure 3A and 3B), suggesting that circSPIDR significantly inhibited tumor

growth. Immunohistochemical staining of the xenograft tumor tissues demonstrated that the proliferation marker Ki-67 was expressed at lower levels in the circSPIDR-overexpressing group (Figure 3C). In addition to generating the subcutaneous tumor model, we also intraperitoneally injected the two groups of cells into nude mice ($n = 5/\text{group}$), and found that the tumors were much smaller in the circSPIDR group than in the vector control group (Figure 3D and 3E). These results

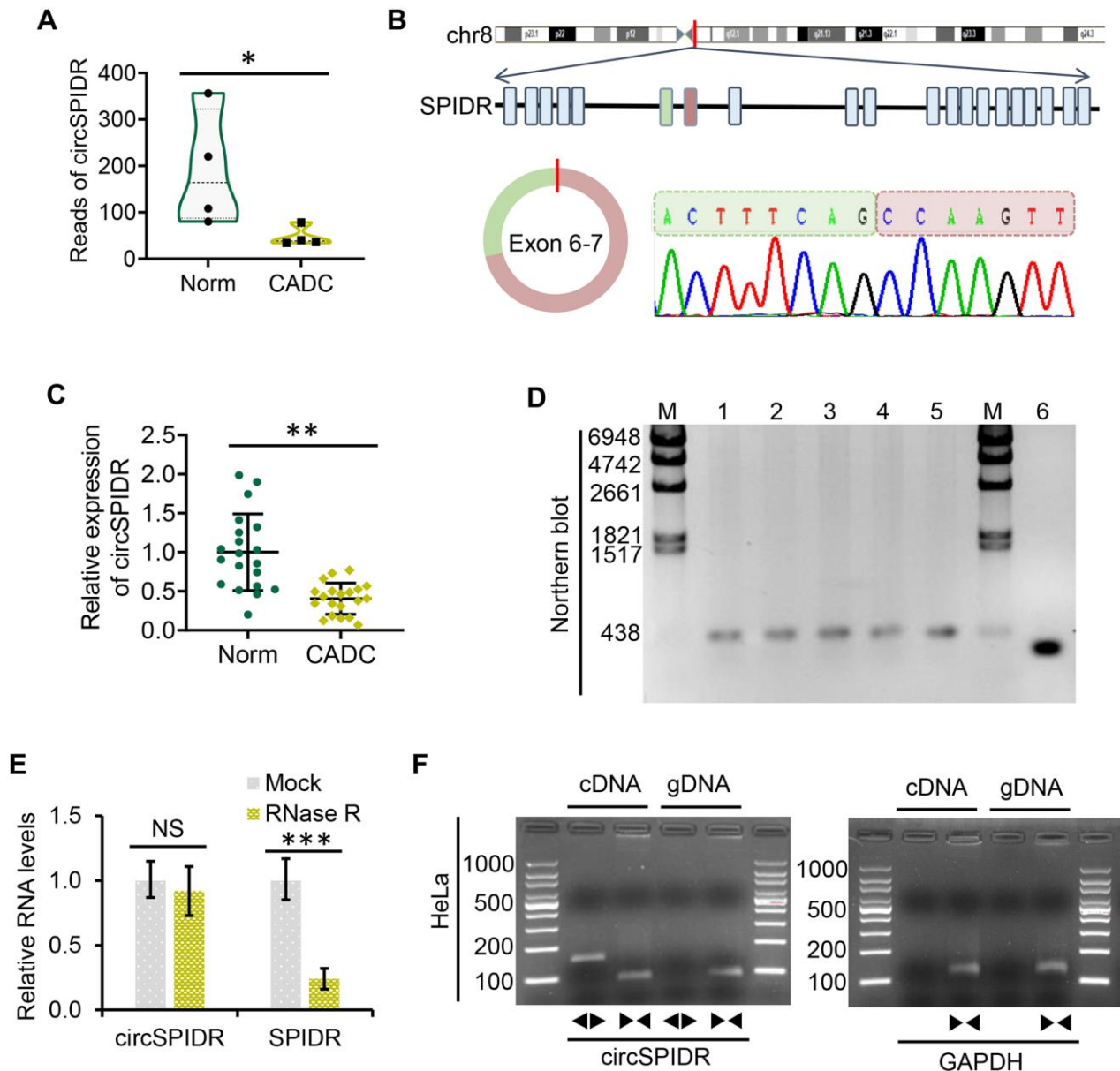


Figure 1. Characterization and validation of circSPIDR expression in CADC. (A) Violin plot showing the distribution of the RNA sequencing reads of circSPIDR in normal cervical tissues (Norm) and CADC tissues. (B) The genomic locus and generation of circSPIDR. CircSPIDR is produced from exons 6 and 7 of the human *SPIDR* gene. The back-splice junction sequence of circSPIDR was detected using Sanger sequencing. (C) qRT-PCR analysis of circSPIDR expression in 20 normal cervical tissues and 20 CADC tissues. (D) Northern blot of circSPIDR. Hybridization was performed with exon 6–7 junction probes. M, RNA marker; 1–3, HeLa cell repeats; 4, CADC tissue; 5, Normal cervical tissue; 6, RT-PCR products of probes. (E) qRT-PCR analysis of circSPIDR expression and *SPIDR* mRNA expression in HeLa cells with or without RNase R treatment. (F) RT-PCR products of circSPIDR and its linear isoform (*SPIDR*) in cDNA and gDNA from HeLa cells. *GAPDH* was used as a control. NS, not significant; * $P < 0.05$; ** $P < 0.01$; *** $P < 0.001$.

suggested that circSPIDR suppressed CADC tumor growth *in vitro* and *in vivo*.

CircSPIDR sponges miR-431-5p in CADC cells

One major function of circRNAs is to sponge miRNAs [24]. To identify miRNAs that could be targets of circSPIDR, we searched the miRanda bioinformatics prediction database. Then, we compared the results with

the differentially expressed miRNA signature of CADC patients from our previous miRNA sequencing data [25]. We found that circSPIDR possessed the conserved target site of miR-431-5p, and that miR-431-5p was upregulated in CADC tissues.

To test the hypothesis that circSPIDR sponges miR-431-5p, we first examined miR-431-5p levels in the same 40 human cervical samples assayed for circSPIDR

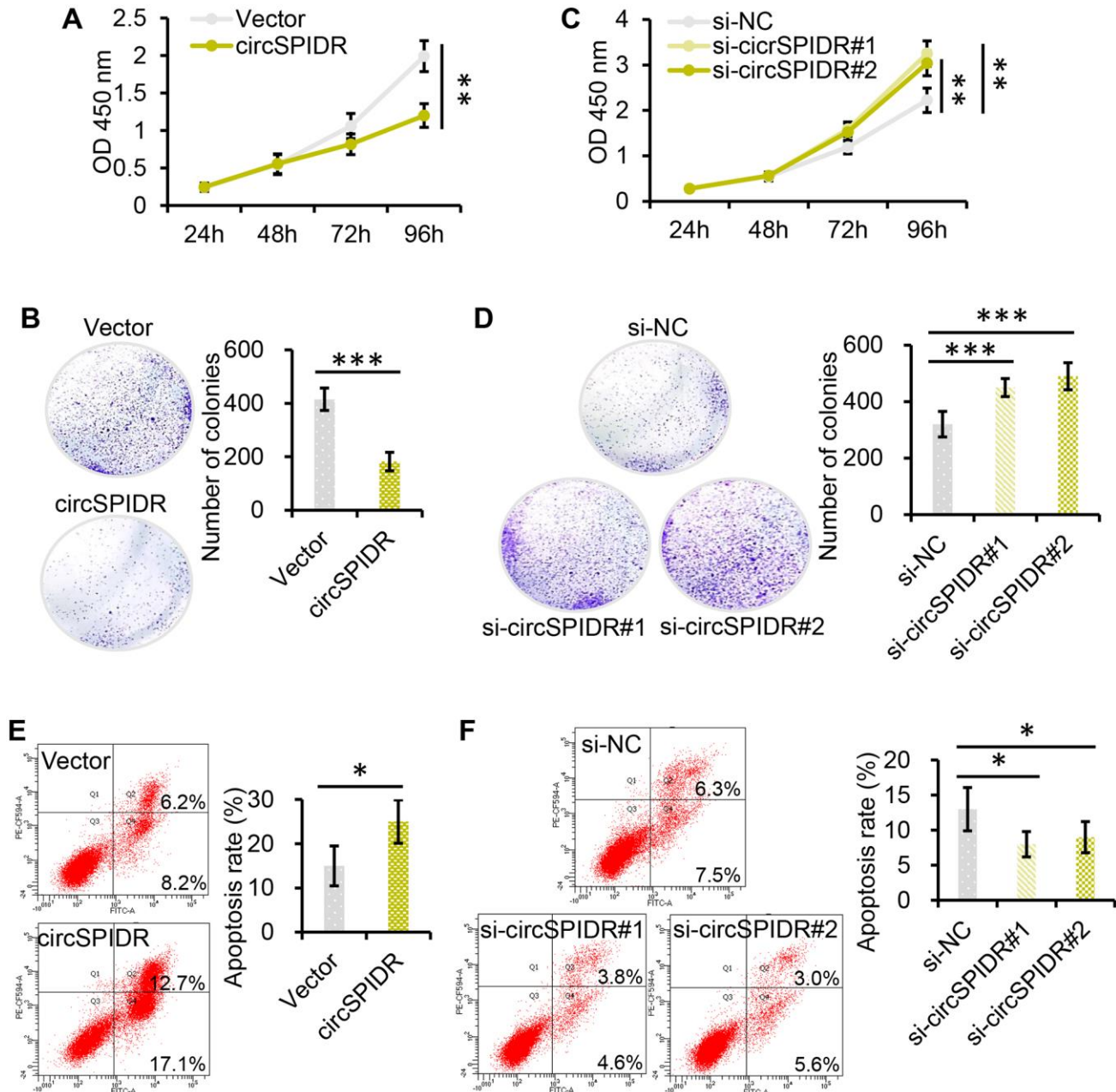


Figure 2. CircSPIDR inhibits cell growth and promotes apoptosis in CADC cells *in vitro*. (A, C) CCK-8 assays demonstrated that circSPIDR overexpression reduced HeLa cell viability (A), while circSPIDR inhibition with specific siRNAs (si-circSPIDR#1 or si-circSPIDR#2) increased HeLa cell viability (C). (B, D) Colony formation assays indicated that circSPIDR overexpression suppressed colony formation in HeLa cells (B), while circSPIDR inhibition promoted colony formation (D). (E, F) Representative images from flow cytometry analysis of apoptosis. Apoptotic cells were determined using Annexin V-FITC (X-axis) and PI (Y-axis) staining. CircSPIDR overexpression promoted HeLa cell apoptosis, while circSPIDR inhibition had the opposite effect. * $P < 0.05$; ** $P < 0.01$; *** $P < 0.001$.

expression above. The qRT-PCR results revealed that miR-431-5p expression was significantly greater in CADC tissues with lower circSPIDR expression (Figure 4A). Next, we assessed the effects of circSPIDR expression on miR-431-5p expression in HeLa cells,

and found that circSPIDR overexpression significantly reduced miR-431-5p expression, while circSPIDR knockdown increased miR-431-5p expression (Figure 4B). We then performed an RNA fluorescence *in situ* hybridization assay, which demonstrated that

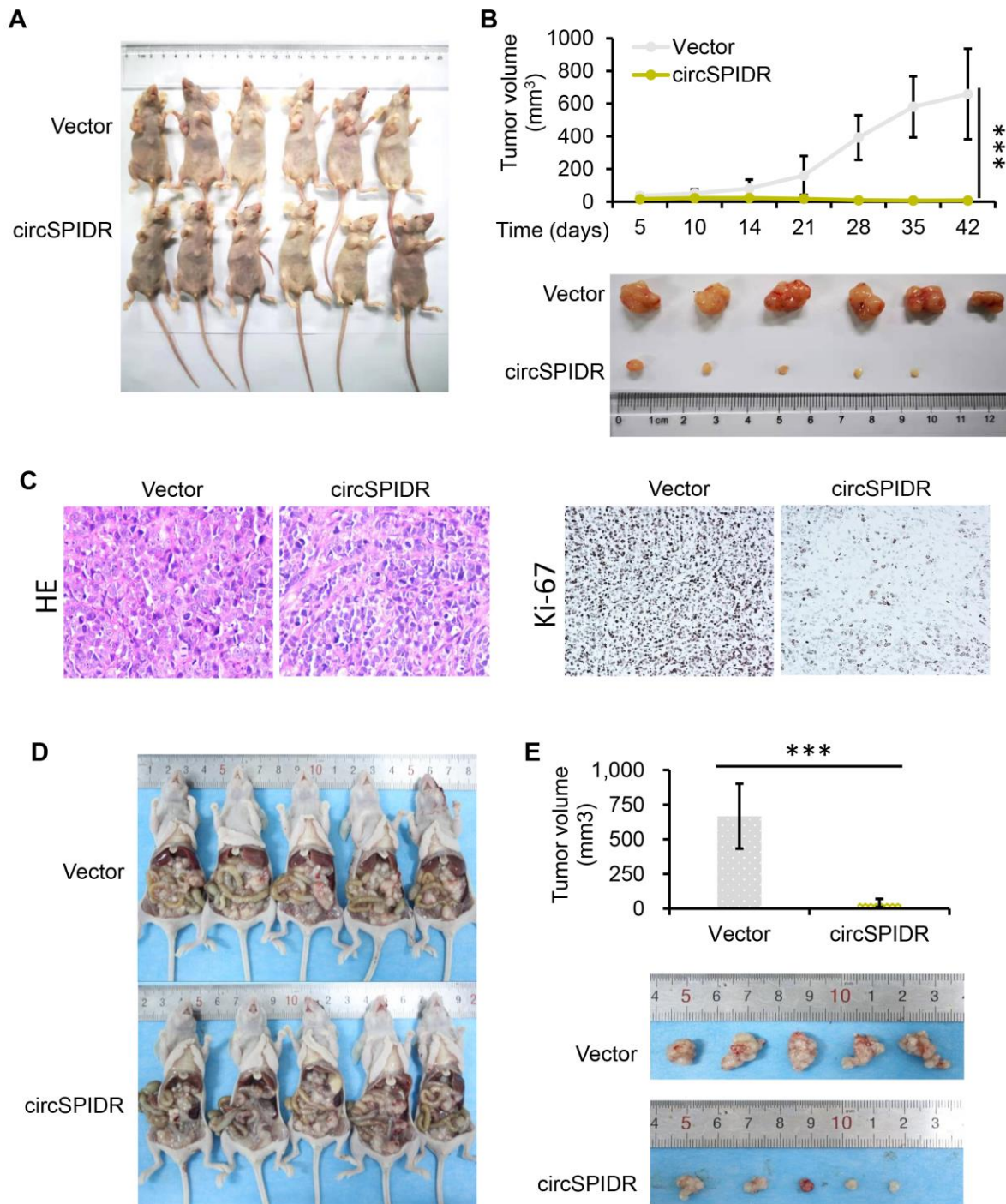


Figure 3. CircSPIDR overexpression inhibits HeLa cell growth *in vivo*. (A) HeLa cells expressing circSPIDR or the vector control were inoculated into BALB/c nude mice ($n = 6/\text{group}$) to establish subcutaneous xenograft tumors. Representative images of nude mice bearing CADC tumors are shown. (B) Growth curves and representative images of isolated xenograft tumours. The volume of the local tumors was measured. (C) Hematoxylin and eosin staining was performed and Ki-67 protein expression was evaluated in the xenograft tumors. (D, E) Representative images of nude mice intraperitoneally transplanted with HeLa/circSPIDR and HeLa/vector cells. *** $P < 0.001$.

circSPIDR co-localized with miR-431-5p in HeLa cells (Figure 4C). Of note, circSPIDR and miR-431-5p were localized in both the cytoplasm and the nucleus, indicating that these RNAs may have additional functions aside from serving as ceRNAs.

Subsequently, we performed a dual luciferase reporter assay in 293T cells transfected with miR-431-5p mimics and luciferase vectors fused with circSPIDR wild-type (wt) or mutant (mut) promoters. As shown in Figure 4D, when miR-431-5p mimics were present,

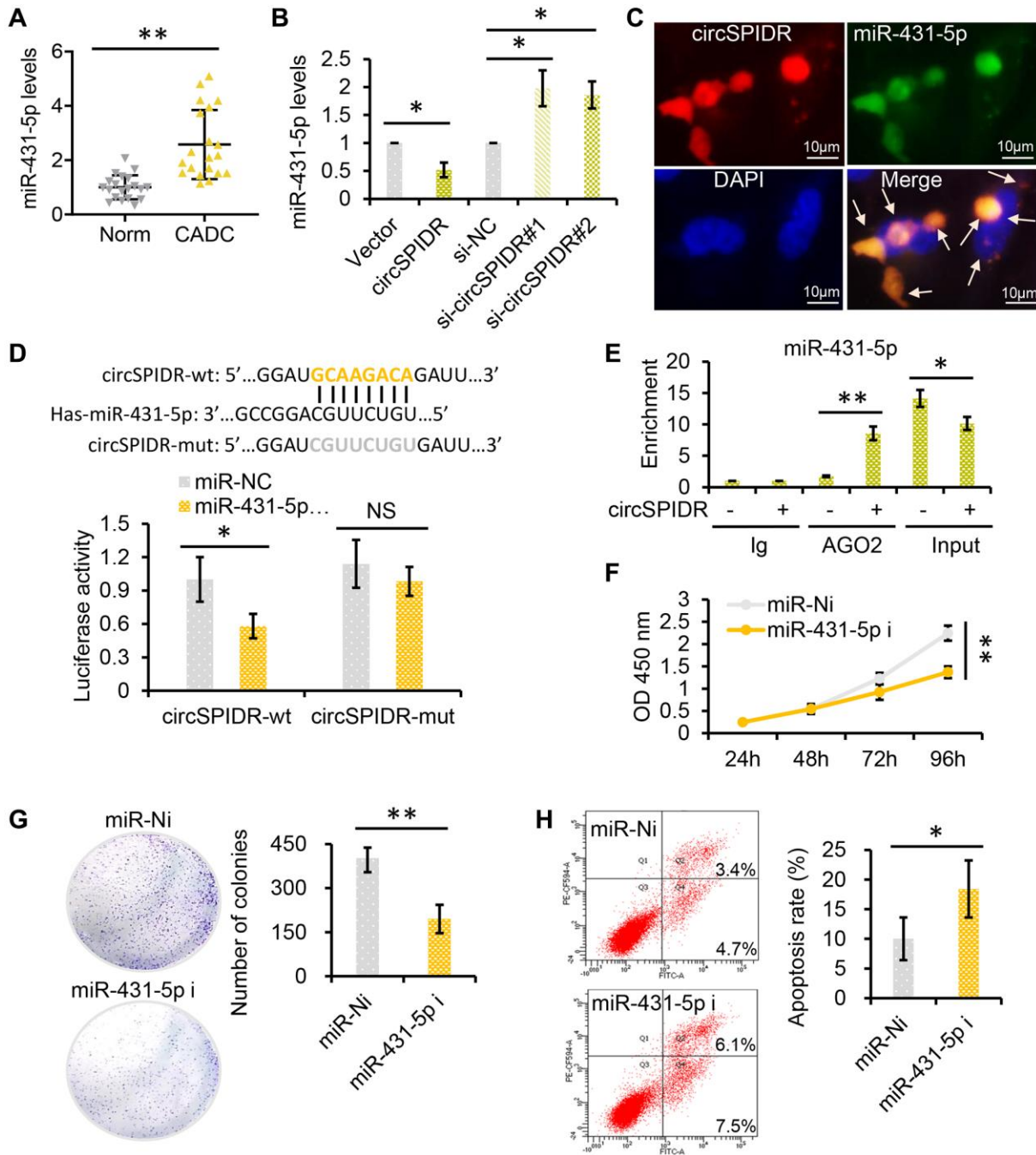


Figure 4. CircSPIDR directly binds to miR-431-5p as a miRNA sponge. (A) qRT-PCR analysis of miR-431-5p expression in 20 normal cervical tissues and 20 CADC tissues. (B) qRT-PCR analysis of miR-431-5p expression in HeLa cells transfected with circSPIDR, the vector, si-circSPIDR#1, si-circSPIDR#2 or si-NC. (C) RNA fluorescence *in situ* hybridization assay for circSPIDR and miR-431-5p in HeLa cells. (D) Schematic drawing showing the putative binding sites of miR-431-5p on circSPIDR. A luciferase reporter assay was performed to detect circSPIDR luciferase reporter activity in cells co-transfected with miR-431-5p mimics or miR-NC. (E) AGO2-RIP was conducted to detect circSPIDR luciferase reporter activity in HeLa cells transfected with circSPIDR or the vector. The enrichment of miR-431-5p was then assessed using qRT-PCR. (F-G) CCK-8 (F) and colony formation (G) assays of HeLa cells transfected with miR-431-5p inhibitors. (H) Apoptosis analysis of HeLa cells transfected with miR-431-5p inhibitors. NS, not significant; * $P < 0.05$; ** $P < 0.01$.

luciferase reporter activity was significantly reduced in the circSPIDR-wt group, but not in the circSPIDR-mut group. In addition, we performed an RNA immunoprecipitation for argonaute 2 (AGO2-RIP) assay in circSPIDR-overexpressing and control HeLa cells. The results revealed that circSPIDR and miR-431-5p were substantially enriched by AGO2 (Figure 4E). These findings indicated that circSPIDR could bind directly to miR-431-5p.

To explore the function of miR-431-5p in CADC cells, we treated HeLa cells with inhibitors of miR-431-5p. CCK-8 and colony formation assays demonstrated that miR-431-5p inhibitors significantly reduced the growth of HeLa cells (Figure 4F and 4G). In addition, miR-431-5p inhibitors promoted HeLa cell apoptosis (Figure 4H). Thus, miR-431-5p inhibition mimicked the phenotypic effects of circSPIDR overexpression in HeLa cells.

Next, we used miR-431-5p mimics to examine whether miR-431-5p overexpression could nullify the effects of circSPIDR overexpression in CADC cells. In rescue experiments, miR-431-5p overexpression reversed the circSPIDR-induced suppression of CADC cell proliferation and colony formation (Figure 5A and 5B). Co-transfection of circSPIDR with the miR-431-5p negative control (miR-NC) induced apoptosis in CADC cells, consistent with the effects of circSPIDR alone (see Figure 2E); however, miR-431-5p mimics impaired the apoptotic effects of circSPIDR (Figure 5C). These results demonstrated that miR-431-5p is the critical target of circSPIDR sponging activity in CADC.

CircSPIDR relieves the repression of *SORCS1* and *CUBN* by miR-431-5p in CADC cells

Based on the ceRNA theory, we hypothesized that circSPIDR could enhance the expression of miR-431-5p

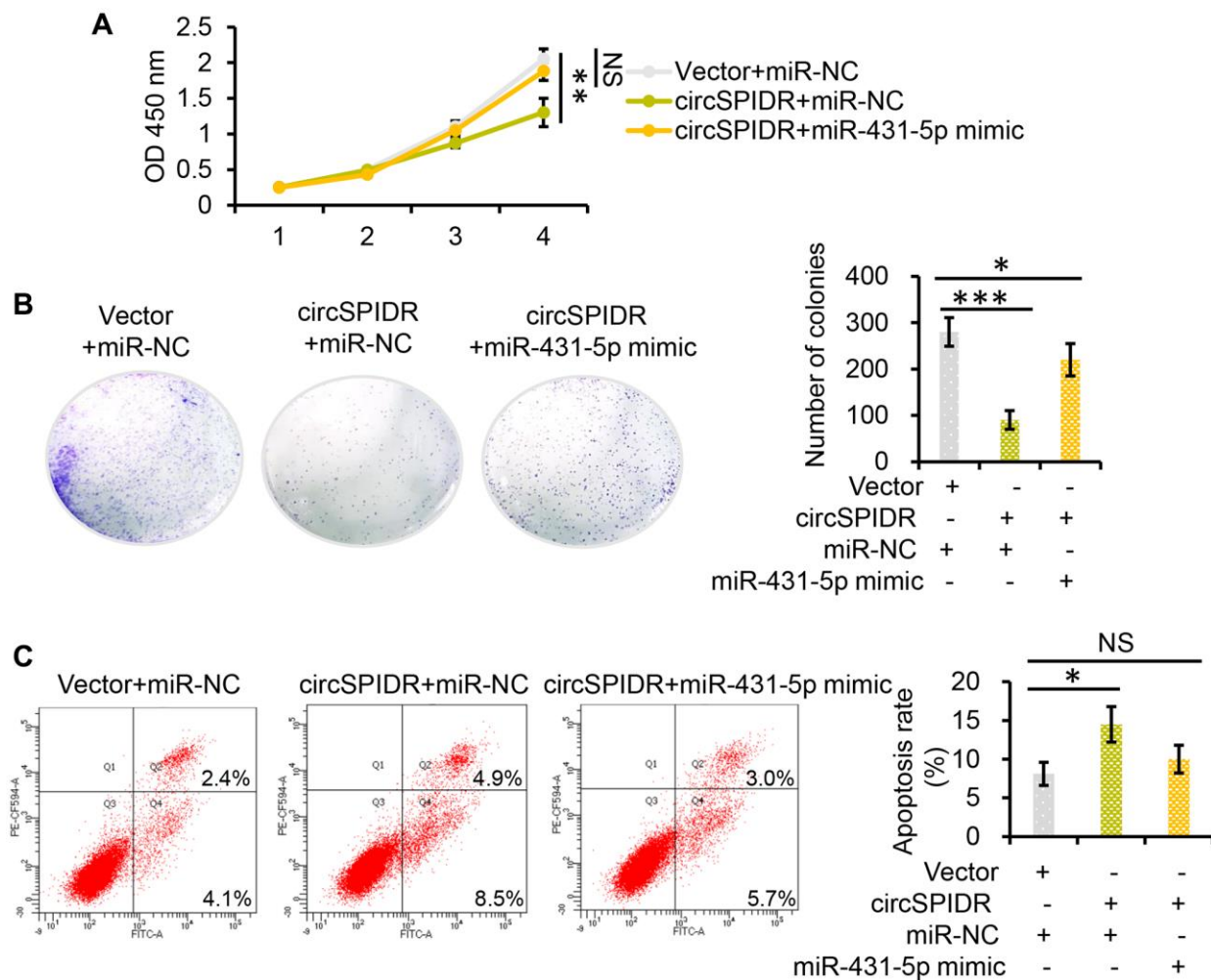


Figure 5. MiR-431-5p reverses the tumor-suppressive effects of circSPIDR in CADC cells. (A) CCK-8 assay evaluating the viability of HeLa cells co-transfected with circSPIDR and miR-431-5p mimics. (B) Colony formation assay in HeLa cells co-transfected with circSPIDR and miR-431-5p mimics. (C) Apoptosis analysis of HeLa cells co-transfected with circSPIDR and miR-431-5p mimics. NS, not significant; * $P < 0.05$; ** $P < 0.01$; *** $P < 0.001$.

target genes by sponging miR-431-5p. Using TargetScan and miRanda, we filtered the potential direct targets of miR-431-5p and mapped them to our previous transcriptome sequencing data for CADC [25]. We thus identified 16 putative miR-431-5p target genes that were significantly downregulated in CADC tissues: *ADD2*, *CDHR1*, *CUBN*, *DIRAS2*, *EFCAB1*, *KLF8*,

L3MBT4, *NXPH3*, *PLEKHG7*, *SCN3B*, *SHE*, *SORCS1*, *SOX5*, *TMEM213*, *WASF3* and *ZNF483*. (Figure 6A).

Next, we used miR-431-5p inhibitors to examine the effects of miR-431-5p on the expression of these genes in HeLa cells. Treatment of CADC cells with miR-431-5p inhibitors strongly increased the expression of

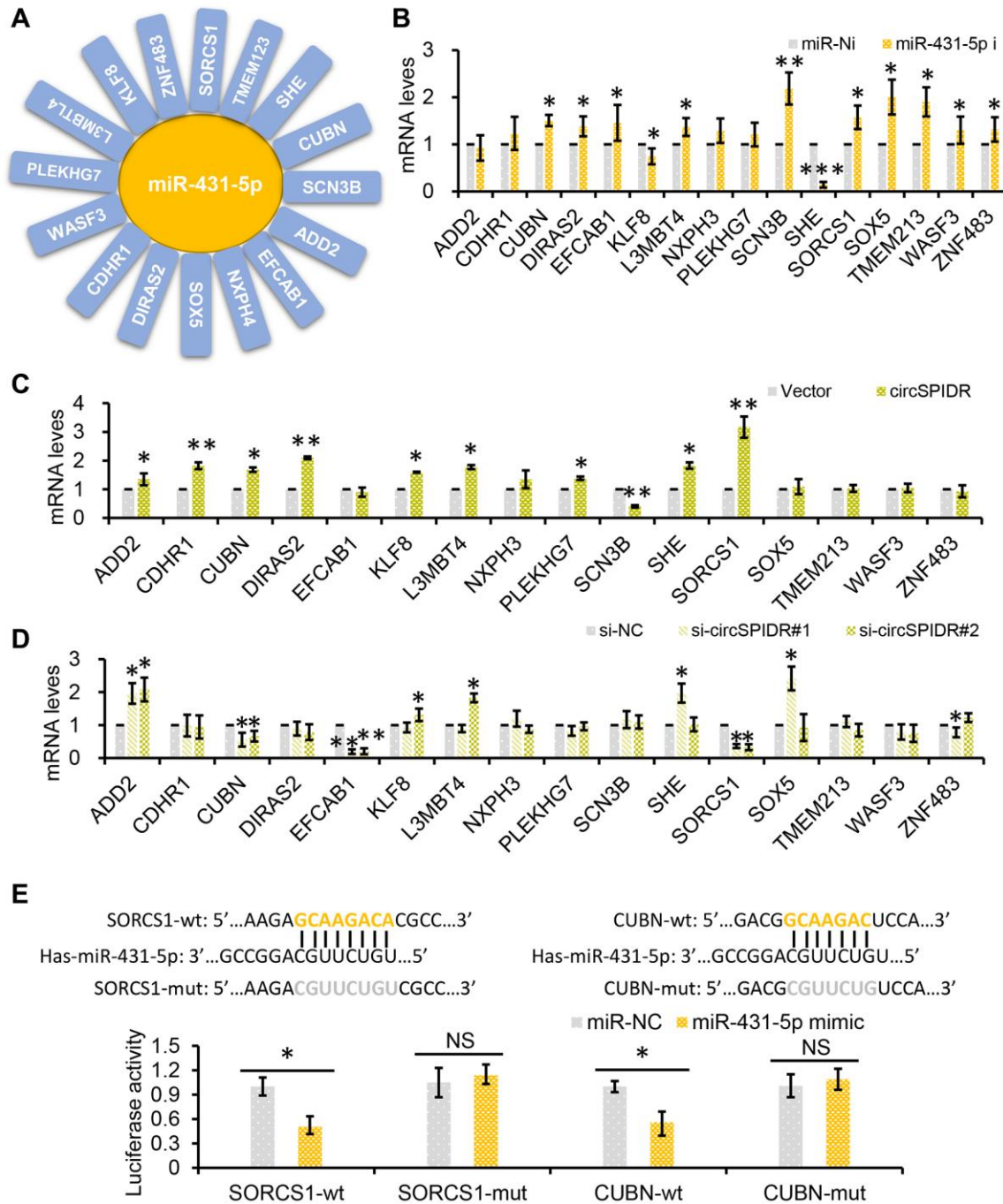


Figure 6. *SORCS1* and *CUBN* are the target genes of miR-431-5p and circSPIDR. (A) miR-431-5p-target gene regulatory network. (B) qRT-PCR analysis of candidate target gene expression in CADC cells transfected with miR-431-5p inhibitors. (C, D) qRT-PCR analysis of candidate target gene expression in CADC cells transfected with the circSPIDR expression vector (C) or siRNAs against circSPIDR (D). (E) Luciferase activity of the 3'UTRs of *SORCS1* and the *CUBN* in 293T cells co-transfected with miR-431-5p mimics. NS, not significant; * $P < 0.05$; ** $P < 0.01$.

CUBN, *DIRAS2*, *EFCAB1*, *L3MBT4*, *SCN3B*, *SORCS1*, *SOX5*, *TMEM213*, *WASF3* and *ZNF483*, but not the other genes (Figure 6B). However, overexpression of circSPIDR in HeLa cells only significantly upregulate *CUBN* (cubilin) and *SORCS1* (sortilin-related VPS10 domain-containing receptor 1), and knockdown of circSPIDR only significantly downregulated the same two genes (Figure 6C and 6D).

To verify that *SORCS1* and *CUBN* were the bona fide targets of miR-431-5p, we constructed *SORCS1* 3' untranslated region (UTR)-wt, *SORCS1* 3'UTR-mut, *CUBN* 3'UTR-wt, and *CUBN* 3'UTR-mut luciferase reporter systems and co-transfected them with miR-431-5p mimic into 293T cells. The miR-431-5p mimics significantly reduced the activities of the luciferase reporter vectors carrying *SORCS1* 3'UTR-wt or *CUBN* 3'UTR-wt sequences, but not of the vectors containing *SORCS1* 3'UTR- mut or *CUBN* 3'UTR- mut sequences (Figure 6E). Furthermore, inhibition of miR-431-5p markedly increased the protein levels of *SORCS1* and *CUBN* in CADC cells (Figure 7A). Consistently, overexpression of circSPIDR significantly increased the protein levels of *SORCS1* and *CUBN* in HeLa cells (Figure 7A).

To test whether *SORCS1* and *CUBN* were localized with the circSPIDR/miR-431-5p sponge complex, we performed an AGO2-RIP assay, which indicated that circSPIDR, miR-431-5p, *SORCS1* and *CUBN* were mainly enriched with AGO2 (Figures 4E, 7B). In addition, the up-regulation of *SORCS1* and *CUBN* in circSPIDR-overexpressing CADC cells could be partially reversed by co-transfection with miR-431-5p mimics (Figure 7C). Therefore, we considered *SORCS1* and *CUBN* as the major downstream targets of miR-431-5p and circSPIDR.

Next, we assessed the involvement of *SORCS1* and *CUBN* in circSPIDR/miR-431-5p signaling. The knockdown of *SORCS1* or *CUBN* using specific siRNAs significantly promoted cell survival and reduced apoptosis in CADC cells (Figure 7D, Supplementary Figure 3A and 3B). Moreover, *SORCS1* or *CUBN* knockdown partially reversed the proliferation-suppressive effects (Figure 7E) and abrogated the pro-apoptotic effects (Figure 7F, Supplementary Figure 4A) of miR-431-5p inhibitors. *SORCS1* and *CUBN* siRNAs reversed the suppression of cell proliferation (Figure 7G) and partially reversed the induction of apoptosis in circSPIDR-overexpressing HeLa cells (Figure 7H, Supplementary Figure 4B). These results suggested that *SORCS1* and *CUBN* are direct functional targets of circSPIDR/miR-431-5p signalling.

The clinical value of circSPIDR in human cervical samples

To explore the clinical value of circSPIDR, we collected an additional 57 normal human cervical tissues and 141 CADC tissues. A qRT-PCR analysis demonstrated that circSPIDR, *CUBN* and *SORCS1* were significantly down-regulated in CADC tissues compared with normal cervical tissues, while miR-431-5p was remarkably upregulated in CADC tissues (Figure 8A). To determine the correlation among these candidate biomarkers, we performed a Pearson's correlation analysis. CircSPIDR levels exhibited a significant inverse correlation with miR-431-5p levels (Figure 8B), but exhibited significant positive correlations with *SORCS1* (Figure 8C) and *CUBN* levels (Figure 8D). The expression of miR-431-5p correlated inversely with the levels of *SORCS1* (Figure 8E) and *CUBN* (Figure 8F).

In addition, we performed a receiver operating characteristic (ROC) curve analysis to determine their diagnostic value of these genes in identifying CADC. The area under the ROC curve (AUC, representing the average sensitivity for all possible specificity values) was 0.794 for circSPIDR, 0.787 for miR-431-5p, 0.741 for *SORCS1* and 0.711 for *CUBN*, where an AUC > 0.5 is considered significant (Figure 8G). These data revealed that circSPIDR, miR-431-5p, *SORCS1* and *CUBN* have good potential as diagnostic markers for CADC.

DISCUSSION

Numerous circRNAs serve as ceRNAs that bind to specific miRNAs and upregulate their target genes, thus promoting tumor development and progression [26–28]. For example, the well-known circRNA CDR1a competitively binds to miR-7 to promote the progression of many cancer types [11, 29–31]. Likewise, circTADA2A sponges miR-203a-3p, thus disinhibiting cyclic adenosine monophosphate responsive element binding protein 3 (CREB3) and increasing the malignant behavior of osteosarcoma [32]. We previously used RNA-sequencing to compare the circRNA, miRNA and mRNA signatures of CADC and normal cervical tissues, in order to identify potential oncogenic and tumor-suppressive circRNAs in CADC [23, 25]. We proposed that circEYA1 is a ceRNA that binds directly to miR-582-3p to enhance the expression of the miR-582-3p target gene C-X-C motif chemokine ligand 14 (CXCL14) [23]. In the same study, we also identified circSPIDR as a significantly downregulated circRNA in CADC tissues.

CircSPIDR is a novel human circRNA, so its functions had not previously been elucidated. Rat circSPIDR has

been reported to enhance axon regeneration after sciatic nerve injury partially by altering the phosphoinositide 3-kinase/AKT pathway in dorsal root ganglions [33]. In the present study, we confirmed that circSPIDR was

significantly downregulated in CADC tissues. Overexpression of circSPIDR reduced cell viability, inhibited colony formation and promoted apoptosis in CADC cells, while knockdown of circSPIDR had the

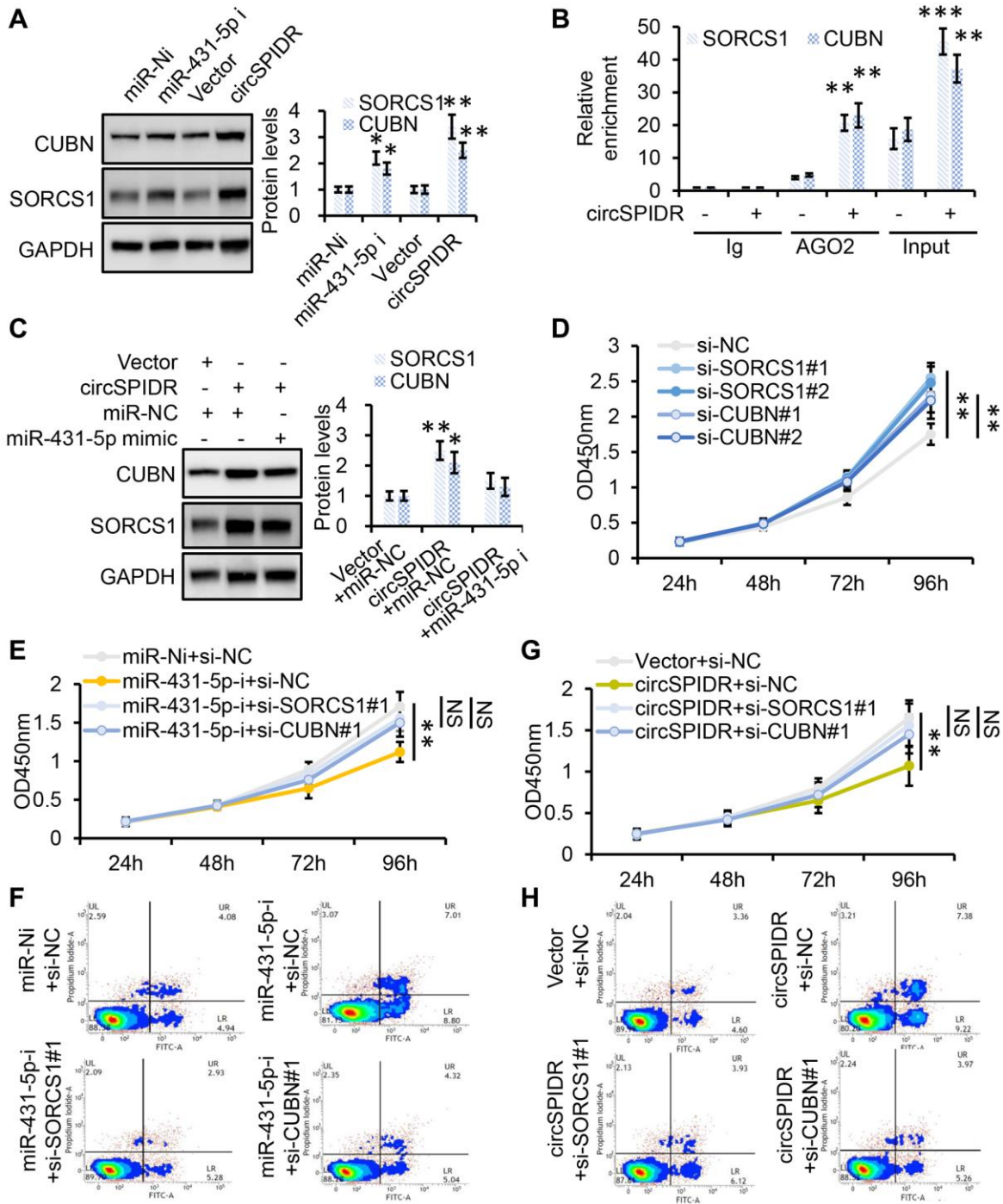


Figure 7. *SORCS1* and *CUBN* are the functional targets of circSPIDR/miR-431-5p signaling. (A) Western blot analysis of *SORCS1* and *CUBN* protein levels in CADC cells transfected with miR-431-5p inhibitors or the circSPIDR expression vector. (B) AGO2-RIP was performed using an anti-AGO2 antibody in HeLa cells transfected with circSPIDR or the vector. Then, qRT-PCR was used to assess and the enrichment of *SORCS1* and *CUBN*. (C) Western blot analysis of *SORCS1* and *CUBN* protein expression in CADC cells co-transfected with circSPIDR and miR-431-5p mimics. (D) CCK-8 assay in *SORCS1*- or *CUBN*-knockdown HeLa cells. (E, F) CCK-8 assay (E) and apoptosis assay (F) in HeLa cells following miR-431-5p inhibition and *SORCS1* or *CUBN* knockdown. (G, H) CCK-8 assay (G) and apoptosis assay (H) in HeLa cells following circSPIDR overexpression and *SORCS1* or *CUBN* knockdown. NS, not significant; * $P < 0.05$; ** $P < 0.01$; *** $P < 0.001$.

opposite effects. CircSPIDR suppressed CADC cell growth both *in vitro* and *in vivo*, suggesting that this circRNA is a tumor suppressor in CADC.

To explore the potential ceRNA mechanism of circSPIDR, we performed bioinformatic analyses, which indicated that miR-431-5p shares a binding site with circSPIDR. MiR-431-5p has not been well studied, although it has been proposed as a tumor suppressor in certain cancer types. For instance, miR-431-5p was found to be down-regulated in colon cancer [34] and lung cancer [35], and circ_0001742 was reported to promote tongue squamous cell carcinoma by suppressing miR-431-5p, thus de-repressing activating transcription factor 3 (ATF3) [36]. However, our experiments revealed that, miR-431-5p was significantly up-regulated in CADC tissues, promoted

CADC cell growth and reversed the tumor-suppressive effects of circSPIDR in HeLa cells. Luciferase reporter assays indicated that miR-431-5p reduced the activity of the circSPIDR-wt luciferase reporter, and AGO2-RIP analyses verified that circSPIDR could bind to miR-431-5p. These results suggested that circSPIDR bind to miR-431-5p to suppress CADC tumor growth.

We next searched for direct targets of miR-431-5p in HeLa cells, and identified *SORCS1* and *CUBN*. *SORCS1* is a sorting-related receptor that is involved in metabolic control [37] and has been associated with diabetes in mice and humans [38–41]. *SORCS1* was found to be hypermethylated in colorectal cancer tissues, and reduced *SORCS1* expression was identified as an independent prognostic factor in colorectal cancer patients [42]. *CUBN* is an intrinsic factor-vitamin B12

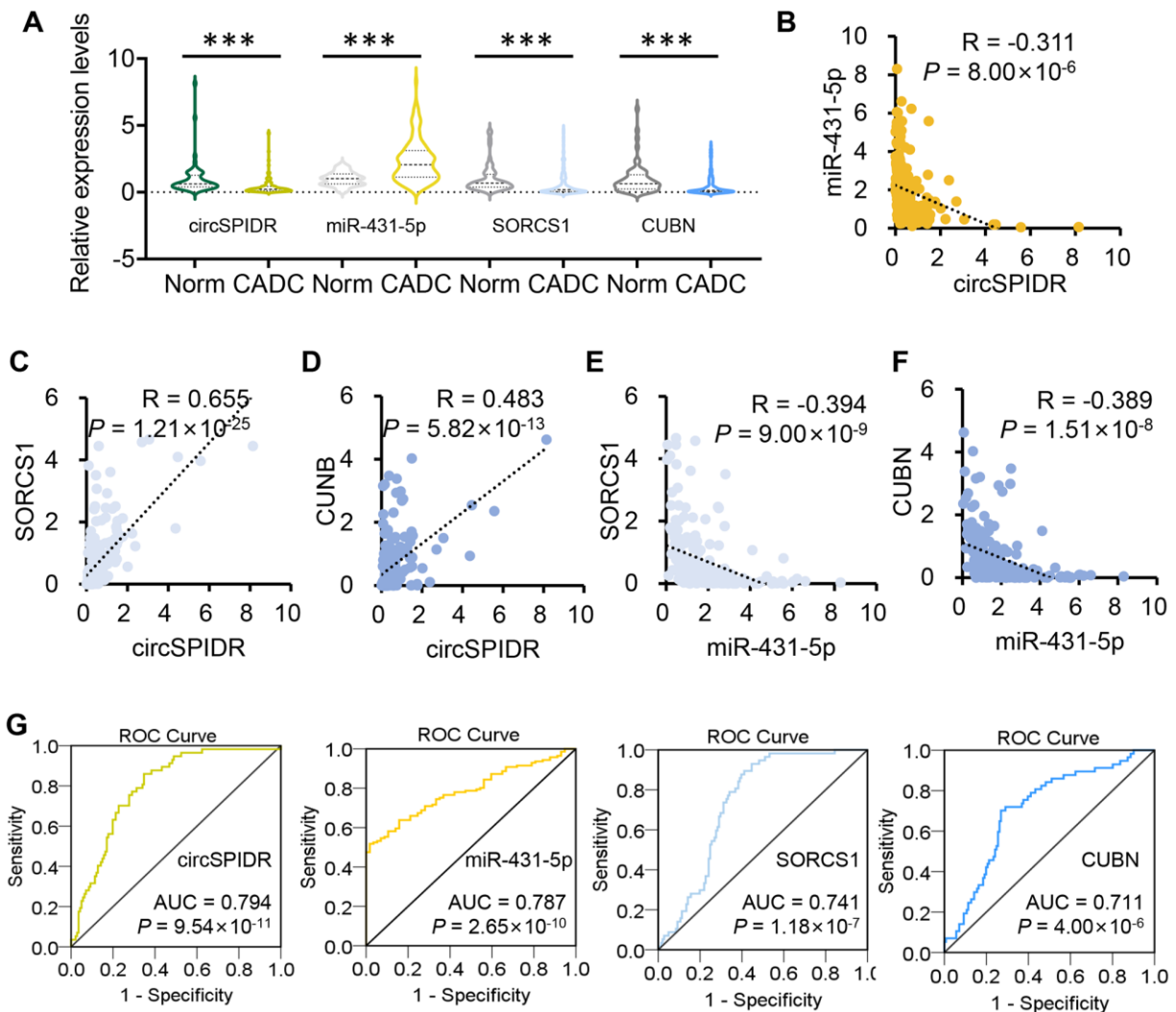


Figure 8. The clinical value of circSPIDR, miR-431-5p, SORCS1 and CUBN expression in CADC tissues. (A) Violin plots showing circSPIDR, miR-431-5p, SORCS1 and CUBN levels determined using qRT-PCR in 57 normal cervical tissues and 141 CADC tissues. (B–D) Pearson correlation analysis between circSPIDR levels and miR-431-5p (B), SORCS1 (C), CUBN (D) levels. (E, F) Pearson correlation analysis between miR-431-5p levels and SORCS1 (E) or CUBN (F) levels. (G) ROC curve analysis of circSPIDR, miR-431-5p, SORCS1 and CUBN detection for CADC diagnosis. *** $P < 0.001$.

receptor, and mutation of *CUBN* was found to cause megaloblastic anaemia 1 [43]. Positive *CUBN* expression was associated with a better prognosis in clear cell renal cell carcinoma patients [44]. Here, we found that *SORCSI* and *CUBN* were down-regulated in CADC tissues, negatively regulated by miR-431-5p and positively regulated by circSPIDR. Correlation analyses indicated that circSPIDR, miR-431-5p, *SORCSI* and *CUBN* levels were tightly correlated in CADC tissues. Moreover, ROC curve analyses suggested that circSPIDR, miR-431-5p, *SORCSI* and *CUBN* expression had good diagnostic potential in CADC patients.

One limitation of our study was that we only used HeLa cells, the currently available CADC cell line. However, we confirmed our observations both in a large cohort of clinical CADC tissues and in animal models, and obtained consistent results. Overall, our findings demonstrated that circSPIDR was significantly down-regulated in CADC tissues and could suppress CADC cell growth by competitively binding to miR-431-5p, thus de-repressing *SORCSI* and *CUBN*. Our study has provided insight into circRNA activity in CADC and revealed the potential of circSPIDR as a therapeutic target in this disease.

MATERIALS AND METHODS

Human tissue specimen collection and ethical approval

This study was approved by the Ethics Committee of Women's Hospital, Zhejiang University School of Medicine (IRB-2019062-R). Written informed consent was obtained from the patients. The study was performed in accordance with the Declaration of Helsinki. In total, 77 normal cervical tissues and 161 CADC tissues were obtained from Women's Hospital, Zhejiang University School of Medicine from 2009 to 2019. Among them, 40 samples (20 normal cervical tissues and 20 CADC tissues) were used for the initial analysis of circSPIDR and miR-431-5p expression, and while the remaining 198 samples were used for qRT-PCR verification of all the candidate genes.

Cell culture

The human CADC HeLa cell line was purchased from the Institute of Biochemistry and Cell Biology of the Chinese Academy of Sciences (Shanghai, China) and tested negative for mycoplasma contamination. HeLa cells were cultured in Minimum Essential Medium (Cellmax) with 10% fetal bovine serum (Sijiqing, China).

Plasmids, siRNAs, miRNA mimics and miRNA inhibitors

The circSPIDR expression plasmid, the siRNAs targeting circSPIDR, *SORCSI* and *CUBN*, the miR-431-5p mimics, the miR-431-5p inhibitors and the relevant negative controls (pEX-3 empty vector, si-NC, miR-NC, and miR-Ni) were all purchased from GenePharma (Shanghai, China). The circSPIDR overexpression plasmids and siRNAs were transfected into HeLa cells using X-tremeGENE HP DNA transfection reagent (Roche, USA) and DharmaFECT1 transfection reagent (Dharmacon), respectively. The transfection experiments were conducted as described previously [23].

RNA and gDNA extraction, RNase R treatment, RT-PCR, and qRT-PCR

The RNA and gDNA extraction, RNase R treatment, RT-PCR, and qRT-PCR were performed as previously reported [23]. The primers used in this study are listed in Supplementary Table 1.

Northern blotting

Total RNA was extracted from the indicated cells and tissues using TRIzol (Invitrogen) and digested with RNase R. Subsequently, a 15- μ g sample was loaded onto a 1% formaldehyde agarose gel and transferred to a Hybond N+ membrane (Amersham) via capillary transfer. Digoxigenin-deoxyuridine triphosphate (DIG-dUTP)-labeled circSPIDR probes were generated using a PCR DIG Probe Synthesis Kit (Roche) with the following primers: 5'-CCACAGCTAAGTTTCCCAGGAC-3' and 5'-TGAGGTGTATGCAAATGGTCT-3'. The PCR products were gel purified and sequenced prior to hybridization. Hybridization was performed with dUTP-labelled circSPIDR probes in DIG Easy Hyb buffer at 50°C overnight. The membrane was then washed and detected in accordance with the instructions for the DIG High Prime DNA Labeling and Detection Starter Kit II (Roche). Finally, the membrane was exposed to X-ray film for 10 min.

CCK-8 and colony formation assays

CCK-8 and colony formation assays were performed as previously reported [23].

Apoptosis assay

Treated cells were resuspended in binding buffer containing Annexin V-fluorescein isothiocyanate (FITC) and propidium iodide (PI) for 15 min in the dark

(MultiSciences, China). The apoptotic rate was detected with a FACSVerse or FACSCalibur flow cytometer (BD Biosciences).

BrdU assay

On the basis of the specifications of BrdU (Sigma), HeLa cell proliferation was assessed using a FITC-BrdU Cell Proliferation Detection Kit (KGA319-1, KeyGen Biotech, Nanjing, China). In brief, HeLa cells were incubated in a six-well plate and transfected with siRNAs or plasmids. After 48 h of transfection, 30 μ M BrdU was added and incubated with the cells for 2 h at 37°C. The cells were washed twice with phosphate-buffered saline and subsequently fixed with 4% paraformaldehyde overnight. Then, the cells were resuspended in 500 μ L of cell-penetrating fluid for 2 min at 0°C and treated with DNA denaturation working fluid for 30 min at 4°C. FITC-anti-BrdU (diluted 1:40) was mixed into the cell plate and incubated with the cells for 30 min at room temperature. The percentage of BrdU-positive cells was determined using a Flow Cytometer (BD, USA).

Xenograft model

The animal procedures were approved by the Institutional Animal Care and Use Committee of Zhejiang Chinese Medical University (IACUC-20190909-02). All the female BALB/c nude mice used in this study were obtained from Shanghai National Laboratory Animal Center (Shanghai, China). Each 4-week-old nude mouse was subcutaneously injected with 5×10^6 of the indicated cells suspended in 100 μ L of phosphate-buffered saline ($n = 6$ /group) or intraperitoneally transplanted with 8×10^6 cells suspended in 150 μ L phosphate-buffered saline ($n = 5$ /group). The mice were sacrificed after 42 days, and their tumors were processed for hematoxylin and eosin staining and Ki-67 detection. The tumor volume was determined as follows: Volume = (length \times width²)/2.

Luciferase activity assay

We used pmirGLO dual-luciferase vector (Promega, Madison, WI, USA) to construct different luciferase reporter vectors. We co-transfected 293T cells with 50 ng of the corresponding luciferase reporter vector, 50 nm miRNA mimics and 5 ng of a Renilla luciferase reporter vector (pRL-TK, Promega) for 24 h. Luciferase activity was assessed with a dual luciferase reporter assay kit (Promega, E2920). The relative firefly luciferase activity was then normalized to the corresponding Renilla luciferase activity.

RIP

The RIP experiment was performed with an EZ-Magna RIP Kit (Millipore, Billerica, MA, USA) according to the manufacturer's protocol. An anti-AGO2 antibody (Abcam) was used for the RIP. The purified RNA was confirmed using qRT-PCR analysis.

Fluorescence *in situ* hybridization

Cy3-labeled probe sequences for circSPIDR (5'-CY3-AUAGAACUUGGCUGAAAGUGUCUUUUGGUAA-G-3') and FITC-labeled probe sequences for hsa-miR-431-5p (5'-FITC-UGCAUGACGGCCUGCAAGACA-3') were synthesized by Sangon Biotech (Shanghai, China) and used to analyze the co-localization of circSPIDR and miR-431-5p in CADC cells. Hybridization was performed overnight using the circSPIDR and miR-431-5p probes, and images were acquired using a Nikon inverted fluorescence microscope (Olympus).

Western blotting

Total protein were extracted from treated HeLa cells. Then, equal amounts of protein were electrophoretically separated on a 8% sodium dodecyl sulfate polyacrylamide gel, and transferred to a polyvinylidene difluoride membrane. The membrane was blocked for nonspecific binding, incubated overnight with antibodies against SORCS1 (1:1000, Proteintech, 23002-1-AP), CUBN (1:500, Abcam, ab191073), or GAPDH (1:5000, Santa Cruz, sc-47724), and then incubated with a secondary antibody for 1 h. The bands of proteins were detected using SuperSignal West Pico Chemiluminescent Substrate (Pierce).

Statistical analysis

All experiments were performed at least three times independently, and images from one representative experiment are shown. Statistical analyses were carried out using SPSS version 24.0 or GraphPad Prism version 9.0. The results are presented as the mean \pm standard deviation. Differences between two groups were evaluated using a two-tailed Student's *t* test. The correlations among circSPIDR, miR-431-5p, *SORCS1* and *CUBN* levels in CADC patients were assessed using Pearson's correlation analysis. *P*-values ≤ 0.05 were defined as significant.

AUTHOR CONTRIBUTIONS

Junfen Xu and Weiguo Lu conceived and designed this study. Junfen Xu conducted the experiments and analyzed and checked the data. Weiguo Lu supervised

the whole project. Junfen Xu wrote the original draft. Weiguo Lu revised the manuscript. All authors read and approved the final manuscript.

CONFLICTS OF INTEREST

The authors declare no conflicts of interest related to this study.

FUNDING

This project was supported by the National Natural Science Foundation of China (Grant No. 82072855) to Doctor Junfen Xu, National Key Research and Development Program of China (Grant No. 2016YFC1302900) to Professor Weiguo Lu, the Fundamental Research Funds for the Central Universities (Grant No. 2019QNA7035 and 2021FZZX001-43) to Doctor Junfen Xu and Innovative Talent Plan of Zhejiang Health Science and Technology Project (Grant No. 2021RC086) to Doctor Junfen Xu.

REFERENCES

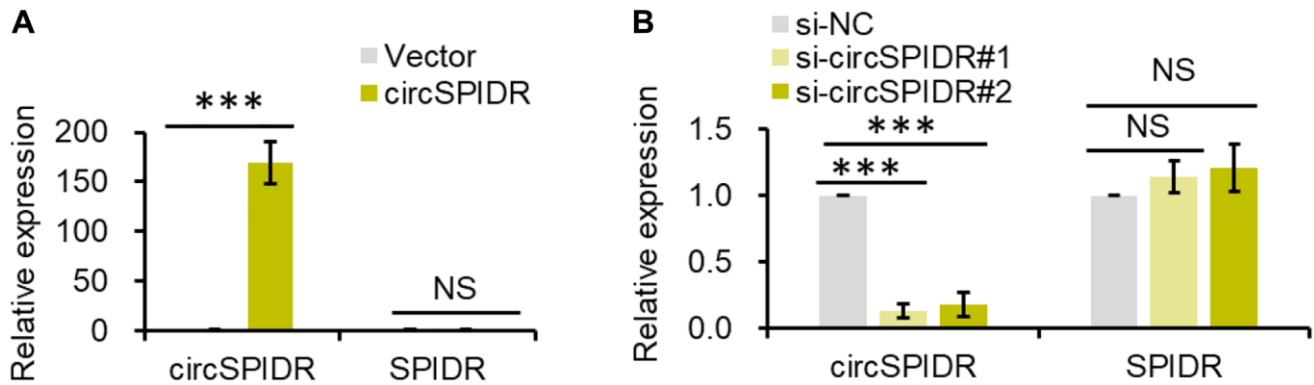
1. Bray F, Ferlay J, Soerjomataram I, Siegel RL, Torre LA, Jemal A. Global cancer statistics 2018: GLOBOCAN estimates of incidence and mortality worldwide for 36 cancers in 185 countries. *CA Cancer J Clin.* 2018; 68:394–424.
<https://doi.org/10.3322/caac.21492>
PMID:[30207593](https://pubmed.ncbi.nlm.nih.gov/30207593/)
2. Chen W, Zheng R, Baade PD, Zhang S, Zeng H, Bray F, Jemal A, Yu XQ, He J. Cancer statistics in China, 2015. *CA Cancer J Clin.* 2016; 66:115–32.
<https://doi.org/10.3322/caac.21338>
PMID:[26808342](https://pubmed.ncbi.nlm.nih.gov/26808342/)
3. Siegel RL, Miller KD, Jemal A. Cancer statistics, 2020. *CA Cancer J Clin.* 2020; 70:7–30.
<https://doi.org/10.3322/caac.21590>
PMID:[31912902](https://pubmed.ncbi.nlm.nih.gov/31912902/)
4. Jeck WR, Sharpless NE. Detecting and characterizing circular RNAs. *Nat Biotechnol.* 2014; 32:453–61.
<https://doi.org/10.1038/nbt.2890>
PMID:[24811520](https://pubmed.ncbi.nlm.nih.gov/24811520/)
5. Ashwal-Fluss R, Meyer M, Pamudurti NR, Ivanov A, Bartok O, Hanan M, Evtantal N, Memczak S, Rajewsky N, Kadener S. circRNA biogenesis competes with pre-mRNA splicing. *Mol Cell.* 2014; 56:55–66.
<https://doi.org/10.1016/j.molcel.2014.08.019>
PMID:[25242144](https://pubmed.ncbi.nlm.nih.gov/25242144/)
6. Memczak S, Jens M, Elefsinioti A, Torti F, Krueger J, Rybak A, Maier L, Mackowiak SD, Gregersen LH, Munschauer M, Loewer A, Ziebold U, Landthaler M, et al. Circular RNAs are a large class of animal RNAs with regulatory potency. *Nature.* 2013; 495:333–38.
<https://doi.org/10.1038/nature11928>
PMID:[23446348](https://pubmed.ncbi.nlm.nih.gov/23446348/)
7. Wilusz JE. A 360° view of circular RNAs: From biogenesis to functions. *Wiley Interdiscip Rev RNA.* 2018; 9:e1478.
<https://doi.org/10.1002/wrna.1478>
PMID:[29655315](https://pubmed.ncbi.nlm.nih.gov/29655315/)
8. Gao Y, Wang J, Zheng Y, Zhang J, Chen S, Zhao F. Comprehensive identification of internal structure and alternative splicing events in circular RNAs. *Nat Commun.* 2016; 7:12060.
<https://doi.org/10.1038/ncomms12060>
PMID:[27350239](https://pubmed.ncbi.nlm.nih.gov/27350239/)
9. Guarnerio J, Bezzi M, Jeong JC, Paffenholz SV, Berry K, Naldini MM, Lo-Coco F, Tay Y, Beck AH, Pandolfi PP. Oncogenic Role of Fusion-circRNAs Derived from Cancer-Associated Chromosomal Translocations. *Cell.* 2016; 165:289–302.
<https://doi.org/10.1016/j.cell.2016.03.020>
PMID:[27040497](https://pubmed.ncbi.nlm.nih.gov/27040497/)
10. Lasda E, Parker R. Circular RNAs: diversity of form and function. *RNA.* 2014; 20:1829–42.
<https://doi.org/10.1261/rna.047126.114>
PMID:[25404635](https://pubmed.ncbi.nlm.nih.gov/25404635/)
11. Li C, Li M, Xue Y. Downregulation of CircRNA CDR1as specifically triggered low-dose Diosbulbin-B induced gastric cancer cell death by regulating miR-7-5p/REGY axis. *Biomed Pharmacother.* 2019; 120:109462.
<https://doi.org/10.1016/j.biopha.2019.109462>
PMID:[31542615](https://pubmed.ncbi.nlm.nih.gov/31542615/)
12. Li Y, Zhang J, Pan S, Zhou J, Diao X, Liu S. CircRNA CDR1as knockdown inhibits progression of non-small-cell lung cancer by regulating miR-219a-5p/SOX5 axis. *Thorac Cancer.* 2020; 11:537–48.
<https://doi.org/10.1111/1759-7714.13274>
PMID:[31917898](https://pubmed.ncbi.nlm.nih.gov/31917898/)
13. Yuan W, Zhou R, Wang J, Han J, Yang X, Yu H, Lu H, Zhang X, Li P, Tao J, Wei J, Lu Q, Yang H, Gu M. Circular RNA Cdr1as sensitizes bladder cancer to cisplatin by upregulating APAF1 expression through miR-1270 inhibition. *Mol Oncol.* 2019; 13:1559–76.
<https://doi.org/10.1002/1878-0261.12523>
PMID:[31131537](https://pubmed.ncbi.nlm.nih.gov/31131537/)
14. Huang X, Li Z, Zhang Q, Wang W, Li B, Wang L, Xu Z, Zeng A, Zhang X, Zhang X, He Z, Li Q, Sun G, et al. Circular RNA AKT3 upregulates PIK3R1 to enhance cisplatin resistance in gastric cancer via miR-198 suppression. *Mol Cancer.* 2019; 18:71.
<https://doi.org/10.1186/s12943-019-0969-3>
PMID:[30927924](https://pubmed.ncbi.nlm.nih.gov/30927924/)

15. Xia X, Li X, Li F, Wu X, Zhang M, Zhou H, Huang N, Yang X, Xiao F, Liu D, Yang L, Zhang N. A novel tumor suppressor protein encoded by circular AKT3 RNA inhibits glioblastoma tumorigenicity by competing with active phosphoinositide-dependent Kinase-1. *Mol Cancer*. 2019; 18:131.
<https://doi.org/10.1186/s12943-019-1056-5>
PMID:[31470874](https://pubmed.ncbi.nlm.nih.gov/31470874/)
16. Garikipati VNS, Verma SK, Cheng Z, Liang D, Truongcao MM, Cimini M, Yue Y, Huang G, Wang C, Benedict C, Tang Y, Mallareddy V, Ibbett J, et al. Circular RNA CircFndc3b modulates cardiac repair after myocardial infarction via FUS/VEGF-A axis. *Nat Commun*. 2019; 10:4317.
<https://doi.org/10.1038/s41467-019-11777-7>
PMID:[31541092](https://pubmed.ncbi.nlm.nih.gov/31541092/)
17. Legnini I, Di Timoteo G, Rossi F, Morlando M, Briganti F, Sthandier O, Fatica A, Santini T, Andronache A, Wade M, Laneve P, Rajewsky N, Bozzoni I. Circ-ZNF609 Is a Circular RNA that Can Be Translated and Functions in Myogenesis. *Mol Cell*. 2017; 66:22–37.e9.
<https://doi.org/10.1016/j.molcel.2017.02.017>
PMID:[28344082](https://pubmed.ncbi.nlm.nih.gov/28344082/)
18. Rossi F, Legnini I, Megiorni F, Colantoni A, Santini T, Morlando M, Di Timoteo G, Dattilo D, Dominici C, Bozzoni I. Circ-ZNF609 regulates G1-S progression in rhabdomyosarcoma. *Oncogene*. 2019; 38:3843–54.
<https://doi.org/10.1038/s41388-019-0699-4>
PMID:[30670781](https://pubmed.ncbi.nlm.nih.gov/30670781/)
19. Pamudurti NR, Bartok O, Jens M, Ashwal-Fluss R, Stottmeister C, Ruhe L, Hanan M, Wyler E, Perez-Hernandez D, Ramberger E, Shenzen S, Samson M, Dittmar G, et al. Translation of CircRNAs. *Mol Cell*. 2017; 66:9–21.e7.
<https://doi.org/10.1016/j.molcel.2017.02.021>
PMID:[28344080](https://pubmed.ncbi.nlm.nih.gov/28344080/)
20. Meng S, Zhou H, Feng Z, Xu Z, Tang Y, Li P, Wu M. CircRNA: functions and properties of a novel potential biomarker for cancer. *Mol Cancer*. 2017; 16:94.
<https://doi.org/10.1186/s12943-017-0663-2>
PMID:[28535767](https://pubmed.ncbi.nlm.nih.gov/28535767/)
21. Tang W, Fu K, Sun H, Rong D, Wang H, Cao H. CircRNA microarray profiling identifies a novel circulating biomarker for detection of gastric cancer. *Mol Cancer*. 2018; 17:137.
<https://doi.org/10.1186/s12943-018-0888-8>
PMID:[30236115](https://pubmed.ncbi.nlm.nih.gov/30236115/)
22. Zhang HD, Jiang LH, Hou JC, Zhong SL, Zhou SY, Zhu LP, Li J, Wang DD, Sun DW, Ji ZL, Tang JH. Circular RNA hsa_circ_0052112 promotes cell migration and invasion by acting as sponge for miR-125a-5p in breast cancer. *Biomed Pharmacother*. 2018; 107:1342–53.
<https://doi.org/10.1016/j.biopha.2018.08.030>
PMID:[30257349](https://pubmed.ncbi.nlm.nih.gov/30257349/)
23. Xu J, Zhang Y, Huang Y, Dong X, Xiang Z, Zou J, Wu L, Lu W. circEYA1 Functions as a Sponge of miR-582-3p to Suppress Cervical Adenocarcinoma Tumorigenesis via Upregulating CXCL14. *Mol Ther Nucleic Acids*. 2020; 22:1176–90.
<https://doi.org/10.1016/j.omtn.2020.10.026>
PMID:[33312754](https://pubmed.ncbi.nlm.nih.gov/33312754/)
24. Hansen TB, Jensen TI, Clausen BH, Bramsen JB, Finsen B, Damgaard CK, Kjems J. Natural RNA circles function as efficient microRNA sponges. *Nature*. 2013; 495:384–88.
<https://doi.org/10.1038/nature11993>
PMID:[23446346](https://pubmed.ncbi.nlm.nih.gov/23446346/)
25. Xu J, Zou J, Wu L, Lu W. Transcriptome analysis uncovers the diagnostic value of miR-192-5p/HNF1A-AS1/VIL1 panel in cervical adenocarcinoma. *Sci Rep*. 2020; 10:16584.
<https://doi.org/10.1038/s41598-020-73523-0>
PMID:[33024199](https://pubmed.ncbi.nlm.nih.gov/33024199/)
26. Piwecka M, Glažar P, Hernandez-Miranda LR, Memczak S, Wolf SA, Rybak-Wolf A, Filipchyk A, Klironomos F, Cerda Jara CA, Fenske P, Trimbuch T, Zywitzka V, Plass M, et al. Loss of a mammalian circular RNA locus causes miRNA deregulation and affects brain function. *Science*. 2017; 357:eaam8526.
<https://doi.org/10.1126/science.aam8526>
PMID:[28798046](https://pubmed.ncbi.nlm.nih.gov/28798046/)
27. Zheng Q, Bao C, Guo W, Li S, Chen J, Chen B, Luo Y, Lyu D, Li Y, Shi G, Liang L, Gu J, He X, Huang S. Circular RNA profiling reveals an abundant circHIPK3 that regulates cell growth by sponging multiple miRNAs. *Nat Commun*. 2016; 7:11215.
<https://doi.org/10.1038/ncomms11215>
PMID:[27050392](https://pubmed.ncbi.nlm.nih.gov/27050392/)
28. Chen LL. The biogenesis and emerging roles of circular RNAs. *Nat Rev Mol Cell Biol*. 2016; 17:205–11.
<https://doi.org/10.1038/nrm.2015.32>
PMID:[26908011](https://pubmed.ncbi.nlm.nih.gov/26908011/)
29. Tang W, Ji M, He G, Yang L, Niu Z, Jian M, Wei Y, Ren L, Xu J. Silencing CDR1as inhibits colorectal cancer progression through regulating microRNA-7. *Oncotargets Ther*. 2017; 10:2045–56.
<https://doi.org/10.2147/OTT.S131597>
PMID:[28435295](https://pubmed.ncbi.nlm.nih.gov/28435295/)
30. Zhong Q, Huang J, Wei J, Wu R. Circular RNA CDR1as sponges miR-7-5p to enhance E2F3 stability and promote the growth of nasopharyngeal carcinoma. *Cancer Cell Int*. 2019; 19:252.
<https://doi.org/10.1186/s12935-019-0959-y>
PMID:[31582908](https://pubmed.ncbi.nlm.nih.gov/31582908/)

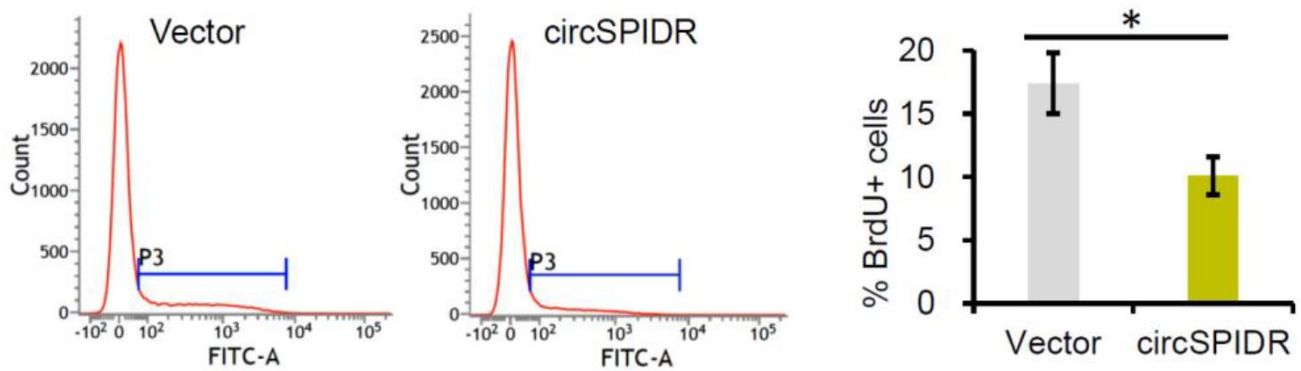
31. Yu L, Gong X, Sun L, Zhou Q, Lu B, Zhu L. The Circular RNA Cdr1as Act as an Oncogene in Hepatocellular Carcinoma through Targeting miR-7 Expression. *PLoS One*. 2016; 11:e0158347. <https://doi.org/10.1371/journal.pone.0158347> PMID:27391479
32. Wu Y, Xie Z, Chen J, Chen J, Ni W, Ma Y, Huang K, Wang G, Wang J, Ma J, Shen S, Fan S. Circular RNA circTADA2A promotes osteosarcoma progression and metastasis by sponging miR-203a-3p and regulating CREB3 expression. *Mol Cancer*. 2019; 18:73. <https://doi.org/10.1186/s12943-019-1007-1> PMID:30940151
33. Mao S, Huang T, Chen Y, Shen L, Zhou S, Zhang S, Yu B. Circ-Spindr enhances axon regeneration after peripheral nerve injury. *Cell Death Dis*. 2019; 10:787. <https://doi.org/10.1038/s41419-019-2027-x> PMID:31624232
34. Huang W, Zeng C, Hu S, Wang L, Liu J. ATG3, a Target of miR-431-5p, Promotes Proliferation and Invasion of Colon Cancer via Promoting Autophagy. *Cancer Manag Res*. 2019; 11:10275–85. <https://doi.org/10.2147/CMAR.S226828> PMID:31849517
35. Jiang Q, Cheng L, Ma D, Zhao Y. FBXL19-AS1 exerts oncogenic function by sponging miR-431-5p to regulate RAF1 expression in lung cancer. *Biosci Rep*. 2019; 39:BSR20181804. <https://doi.org/10.1042/BSR20181804> PMID:30610161
36. Hu YT, Li XX, Zeng LW. Circ_0001742 promotes tongue squamous cell carcinoma progression via miR-431-5p/ATF3 axis. *Eur Rev Med Pharmacol Sci*. 2019; 23:10300–12. https://doi.org/10.26355/eurrev_201912_19668 PMID:31841185
37. Hermey G, Riedel IB, Hampe W, Schaller HC, Hermans-Borgmeyer I. Identification and characterization of SorCS, a third member of a novel receptor family. *Biochem Biophys Res Commun*. 1999; 266:347–51. <https://doi.org/10.1006/bbrc.1999.1822> PMID:10600506
38. Subkhangulova A, Malik AR, Hermey G, Popp O, Dittmar G, Rathjen T, Poy MN, Stumpf A, Beed PS, Schmitz D, Breiderhoff T, Willnow TE. SORCS1 and SORCS3 control energy balance and orexigenic peptide production. *EMBO Rep*. 2018; 19:e44810. <https://doi.org/10.15252/embr.201744810> PMID:29440124
39. Clee SM, Yandell BS, Schueler KM, Rabaglia ME, Richards OC, Raines SM, Kabara EA, Klass DM, Mui ET, Stapleton DS, Gray-Keller MP, Young MB, Stoehr JP, et al. Positional cloning of Sorcs1, a type 2 diabetes quantitative trait locus. *Nat Genet*. 2006; 38:688–93. <https://doi.org/10.1038/ng1796> PMID:16682971
40. Goodarzi MO, Lehman DM, Taylor KD, Guo X, Cui J, Quiñones MJ, Clee SM, Yandell BS, Blangero J, Hsueh WA, Attie AD, Stern MP, Rotter JI. SORCS1: a novel human type 2 diabetes susceptibility gene suggested by the mouse. *Diabetes*. 2007; 56:1922–29. <https://doi.org/10.2337/db06-1677> PMID:17426289
41. Paterson AD, Waggott D, Boright AP, Hosseini SM, Shen E, Sylvestre MP, Wong I, Bharaj B, Cleary PA, Lachin JM, Below JE, Nicolae D, Cox NJ, et al, and MAGIC (Meta-Analyses of Glucose and Insulin-related traits Consortium), and Diabetes Control and Complications Trial/Epidemiology of Diabetes Interventions and Complications Research Group. A genome-wide association study identifies a novel major locus for glycemic control in type 1 diabetes, as measured by both A1C and glucose. *Diabetes*. 2010; 59:539–49. <https://doi.org/10.2337/db09-0653> PMID:19875614
42. Huang PZ, Peng SY, Yu HC, Huang L, Yao Q, Wang XL, Tan SY, Zhou JM, Wang PN, Huang AP, Bai LL, Luo YX, Huang MJ. Decreased expression of SorCS1 in colorectal cancer: An independent predictor of poor prognosis. *Neoplasma*. 2020; 67:119–28. https://doi.org/10.4149/neo_2019_190221N146 PMID:31829024
43. Aminoff M, Carter JE, Chadwick RB, Johnson C, Gräsbeck R, Abdelaal MA, Broch H, Jenner LB, Verroust PJ, Moestrup SK, de la Chapelle A, Krahe R. Mutations in CUBN, encoding the intrinsic factor-vitamin B12 receptor, cubilin, cause hereditary megaloblastic anaemia 1. *Nat Genet*. 1999; 21:309–13. <https://doi.org/10.1038/6831> PMID:10080186
44. Gremel G, Djureinovic D, Niinivirta M, Laird A, Ljungqvist O, Johannesson H, Bergman J, Edqvist PH, Navani S, Khan N, Patil T, Sivertsson Å, Uhlén M, et al. A systematic search strategy identifies cubilin as independent prognostic marker for renal cell carcinoma. *BMC Cancer*. 2017; 17:9. <https://doi.org/10.1186/s12885-016-3030-6> PMID:28052770

SUPPLEMENTARY MATERIALS

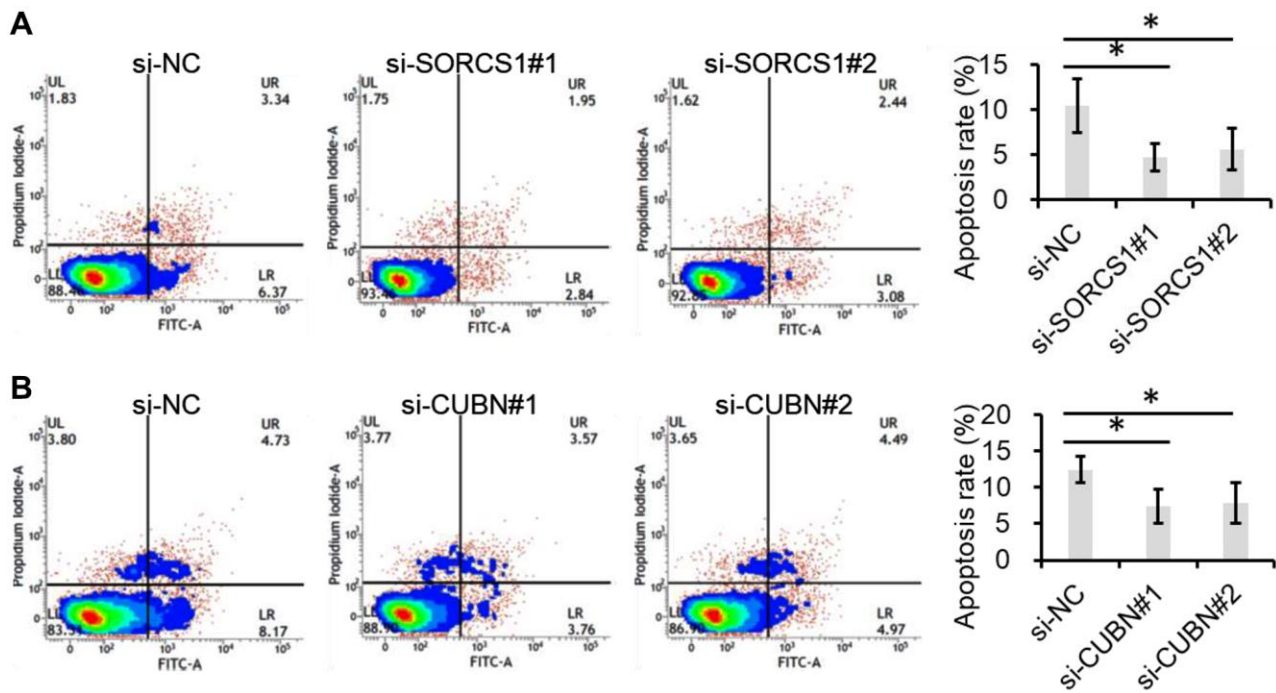
Supplementary Figures



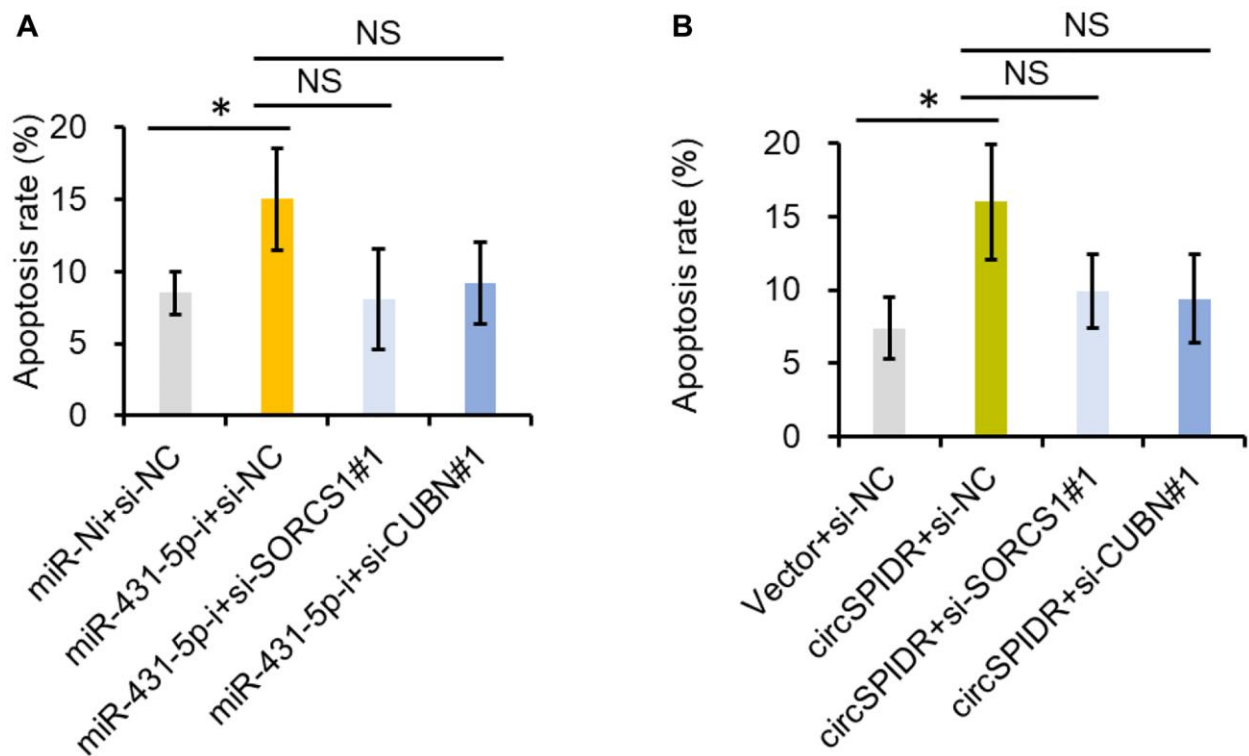
Supplementary Figure 1. Transfection efficiency of circSPIDR expression vector and siRNAs in HeLa cells. (A) The expression level of circSPIDR in HeLa cells after transfection with circSPIDR expression vector was detected by qRT-PCR. Vector was taken as empty vector control. (B) The expression level of circSPIDR in HeLa cells after transfection with circSPIDR siRNA#1 or #2 was detected by qRT-PCR. si-NC was taken as negative siRNA control. NS, not significant; *** $P < 0.001$.



Supplementary Figure 2. Overexpression of circSPIDR suppressed cell proliferation in HeLa cells by BrdU assay. The percentage of BrdU positive cells was shown. * $P < 0.05$.



Supplementary Figure 3. Knockdown of SORCS1 and CUBN decreased cell apoptosis in HeLa cells. (A) Cell apoptosis assay for HeLa cells with SORCS1 knockdown. (B) Cell apoptosis assay for HeLa cells with CUBN knockdown. * $P < 0.05$.



Supplementary Figure 4. miR-431-5p and circSPIDR contribute to cell apoptosis via targeting SORCS1 and CUBN. (A) Cell apoptosis assay for HeLa cells with miR-431-5p inhibitors and SORCS1 knockdown or CUBN knockdown. (B) Cell apoptosis assay for HeLa cells with circSPIDR and SORCS1 knockdown or CUBN knockdown. NS, not significant; * $P < 0.05$.

Supplementary Table

Supplementary Table 1. The primer sequences used in this study.

Primers	Strand	Sequences (5'-3')
circSPIDR	Forward	AAGACACTTTCAGCCAAGTTC
(divergent primers)	Reverse	CTCTCCATAATCTGTCTTGC
circSPIDR	Forward	ATTCAGAATCCCCTCACA
(convergent primers)	Reverse	CTGTTGATTTTGTCTTGG
SPIDR	Forward	ACTGGTGTGATCGTGTCTCTG
	Reverse	CGTGCACATTACCCAGCCTA
ADD2	Forward	CTCATTTTCTCCCAGCCTCG
	Reverse	GCCGCAGTTCCTTGACAAAA
CDHR1	Forward	TAATTGGTCTCGTCAGGCGG
	Reverse	GGGAGGGCAGAGACCACAAT
CUBN	Forward	AGGAACTGAGGAGGTGGACA
	Reverse	GACTGGAAGACGGCAGTGAA
DIRAS2	Forward	GAAGCTCTGAGCGGAGTTGT
	Reverse	AAACCTCAACACCAGGGAGC
EFCAB1	Forward	AGTAACTGAGACCTCACCGC
	Reverse	TGTCTGGCGCTCAGAGAATC
KLF8	Forward	TGTGGTATCTCCTCGTGGGT
	Reverse	GGTGGGGGCTATGAAAACCA
L3MBTL4	Forward	GTAGCTCGGTCGGCGTTG
	Reverse	TTGGGCTGTTTCATTGCCAC
NXPH3	Forward	GACCCCGAAAAGAGAAGGGG
	Reverse	ATAGAGGCTACCCTGCACCA
PLEKHG7	Forward	AAATTACCAGCTTCAGGGGCT
	Reverse	TGTGAAAAGTTCCACACGG
SCN3B	Forward	GATTCCAGTCGGAACGCAAC
	Reverse	GGGTAAGCTCAGCTCGGAAG
SHE	Forward	TGTGACCCTCAGGAAGGTTAAG
	Reverse	TCCTCTTCCAGTCTGCACCA
SORCS1	Forward	CTGCCGGCATTGTTGTTCAA
	Reverse	ACCACCTTCCTGTACCCAGT
SOX5	Forward	AGGTAGCCATGGTGACAAGC
	Reverse	ACAAGTCTCTTGCGTCAGCA
TMEM213	Forward	CTCAACGTGGACTTCTGCCCA
	Reverse	CATCAGTTTGTCCACACAGAGC
WASF3	Forward	TGAGCCAAAGTGGTGATGCT
	Reverse	CGGGGCTCAATGTTCTCTT
ZNF483	Forward	GCTCTACGCAATCCTAGCCA
	Reverse	AGTTATGTGCTCCACACAGCA
si-circSPIDR#1	Forward	AAAAGACACUUUCAGCCAATT
	Reverse	UUGGCUGAAAGUGUCUUUUTT
si-circSPIDR#2	Forward	CACUUUCAGCCAAGUUCUATT
	Reverse	UAGAACUUGGCUGAAAGUGTT
si-SORCS1#1	Forward	CCAACAAGCGUAAGAUAAUTT
	Reverse	AUUAUCUUACGCUUGUUGGTT

si-SORCS1#2	Forward	GCUGCCCUAUUGCUCACUATT
	Reverse	UAGUGAGCAAUAGGGCAGCTT
si-CUBN#1	Forward	GGAAUAUUCUAUGGCUCAATT
	Reverse	UUGAGCCAUAGAAUAUUCCTT
si-CUBN#2	Forward	GCAGACUACCCAAAUGAUATT
	Reverse	UAUCAUUUGGGUAGUCUGCTT

Downregulation of ZC3H13 by miR-362-3p/miR-425-5p is associated with a poor prognosis and adverse outcomes in hepatocellular carcinoma

Shuang Wu^{1,2}, Shihai Liu³, Yongxian Cao¹, Geng Chao¹, Peng Wang⁴, Huazheng Pan¹

¹Department of Clinical Laboratory, The Affiliated Hospital of Qingdao University, Qingdao 266003, Shandong, People's Republic of China

²Department of Medicine, Qingdao University, Qingdao 266071, Shandong, People's Republic of China

³Medical Animal Laboratory, The Affiliated Hospital of Qingdao University, Qingdao 266003, Shandong, People's Republic of China

⁴Department of Oncology, Weifang Yidu Central Hospital, Qingzhou 262509, Shandong, People's Republic of China

Correspondence to: Huazheng Pan; email: panhuazheng@qduhospital.cn

Keywords: miRNA, prognosis, HCC, m6A

Received: October 25, 2021

Accepted: February 22, 2022

Published: March 12, 2022

Copyright: © 2022 Wu et al. This is an open access article distributed under the terms of the [Creative Commons Attribution License](https://creativecommons.org/licenses/by/3.0/) (CC BY 3.0), which permits unrestricted use, distribution, and reproduction in any medium, provided the original author and source are credited.

ABSTRACT

Hepatocellular carcinoma (HCC) is notorious for its poor prognosis. Previous studies identified several N6-methyladenosine (m6A)-related genes that play key roles in the initiation and progression of HCC patients. In particular, the N6-methyladenosine RNA methylation regulator ZC3H13 could be a candidate as a novel biomarker and therapeutic target for hepatocellular carcinoma. In HCC, low expression of ZC3H13 was reported, but the molecular reason is unclear. In this study, we performed pan cancer analysis for ZC3H13 expression and prognosis using The Cancer Genome Atlas (TCGA) and Genotype-Tissue Expression (GTEx) data and found that ZC3H13 might be a potential tumor suppressor gene in HCC. Subsequently, miRNAs contributing to ZC3H13 downregulation were identified by a series of *in silico* analyses, including expression analysis, correlation analysis, and survival analysis. Finally, the miR-362-3p/miR-425-5p-ZC3H13 axis was identified as the most likely upstream miRNA-related pathway of ZC3H13 in HCC. Additionally, miR-362-3p/miR-425-5p mimic and inhibitor results were detected by quantitative real-time PCR (qPCR) analysis and western blotting. We identified an upstream regulatory mechanism of ZC3H13 in HCC, namely, the miR-362-3p/miR-425-5p-ZC3H13 axis. Moreover, the ZC3H13 level was significantly positively associated with tumor immune cell infiltration, biomarkers of immune cells, and immune checkpoint expression. Collectively, our findings elucidated that ncRNA-mediated downregulation of ZC3H13 was correlated with a poor prognosis and tumor immune infiltration in HCC. In conclusion, this study demonstrates that ZC3H13 is a direct target of miR-362-3p/miR-425-5p in liver hepatocellular carcinoma (LIHC) that regulates immune modulation in the microenvironment of LIHC.

INTRODUCTION

Hepatocellular carcinoma (HCC) is the third most common cause of cancer death worldwide [1]. To date, chronic hepatitis B and C virus (HBV/HCV) infection,

obesity, type 2 diabetes, alcohol abuse, smoking and aflatoxins have been clearly identified as risk factors for the development of liver cancer [2]. The difficulty in diagnosing hepatocellular carcinoma at an early stage is due to the lack of typical clinical symptoms in patients

with HCC. Once diagnosed, surgical resection is the most effective treatment [3]. Currently, with the advancement of medicine, considerable progress has been made in the diagnosis, treatment and prognosis, but the prognosis of HCC patients remains unsatisfactory, and more than 700,000 people still die each year [4]. Because of this high lethality rate and high risk of recurrence in postoperative patients, dynamic surveillance of hepatocellular carcinoma is necessary [5]. Therefore, identifying promising HCC prognostic biomarkers and developing effective therapeutic targets are the main tasks of current studies.

Tumorigenesis and progression are driven by a combination of genetic, epigenetic, and environmental factors. Epigenetic factors can be vividly likened to a bridge to describe the critical role of genetic and environmental factors [6]. N6-methyladenosine (m6A) was known for being the most important modification of mRNA and for its importance in post-transcriptional epigenetic modifications [7, 8].

Regulation of m6A methyltransferase (“writers”), m6A demethylase (“erasers”) and m6A read-binding protein (“readers”) together participate in M6A modification, forming a dynamic and reversible process [9]. Methyltransferases are responsible for adding a methyl group to the nitrogen on the sixth carbon of the aromatic ring of adenosine residues, hence the name “writers”. Factors with these roles include methyltransferase 14 (METTL14), VIRMA (formerly KIAA1429), putative RNA binding protein 15 (RBM15), Wilms tumor 1 associated protein (WTAP), and zinc finger CCCH type 13 containing (ZC3H13) [10].

ZC3H13, one of the “writers”, is involved in cancers. For example, Gong et al. demonstrated that ZC3H13 can be used as a negative regulator to assess the prognosis of breast cancer patients. The downregulation of ZC3H13 expression in breast cancer patients coincides with the fact that this downregulation promotes breast cancer invasion [11]. A recent report by Zhu et al. found that overexpression of ZC3H13 could impair the proliferation and invasion of colorectal cancer cells. It is possible that the mechanism involved is to act as an upstream regulator involved in the Ras-ERK signaling pathway to achieve the above inhibitory effects [12]. The current study suggests that ZC3H13 may act as an upstream regulator of the Ras-ERK signaling pathway to achieve inhibition of CRC invasion and proliferation.

Considering the widespread concern of the methyltransferase ZC3H13, researchers have proposed the following views: ZC3H13 is expected to be a marker for evaluating the prognosis of patients with

hepatocellular carcinoma [13]. However, the expression of ZC3H13 in patients with hepatocellular carcinoma remains controversial, which triggered us to delve into the expression level of ZC3H13 in patients with hepatocellular carcinoma and its regulatory factors.

To resolve the current controversy concerning the expression level of ZC3H13 in hepatocellular carcinoma, we further clarified whether ZC3H13 could be a prognostic marker to evaluate hepatocellular carcinoma patients. The present study is based on the TCGA dataset of the prognostic significance of low ZC3H13 levels in hepatocellular carcinoma. More meaningfully, we further explained the reason for the low expression of ZC3H13 at the miRNA level through bioinformatics and experimental verification, which provided a reliable theoretical basis for this study.

RESULTS

Pan cancer analysis of ZC3H13

In this study, the expression of ZC3H13 in different tumors was initially assessed by the Oncomine database. Among them, ZC3H13 was highly expressed in five cancers, including colorectal cancer, kidney cancer, lymphoma, melanoma and sarcoma. But downregulated in four cancers, brain and CNS cancer, liver cancer, lung cancer, and lymphoma (Figure 1A). Next, to make our analysis more reliable, the expression of ZC3H13 in different cancers was further validated by the GEPIA database. The results showed that ZC3H13 expression was significantly increased in patients with DLBC, ESCA, LAML, PAAD, SKCM, STAD and THYM (Figure 1B). In LIHC, ZC3H13 was significantly decreased (Figure 1C). Taken together, both database results confirmed that ZC3H13 is downregulated in HCC, suggesting that abnormal ZC3H13 may drive the carcinogenesis of HCC.

ZC3H13 can evaluate the prognosis of HCC patients

Next, the prognostic impact of different expression levels of ZC3H13 on patients with BRCA, KIRC, LIHC, LUAD and STAD were analyzed. (Figure 2). The two prognostic indicators were overall survival (OS) and progression-free survival (RFS). If OS is used as an evaluation criterion, ZC3H13 can be used to assess the prognosis of patients with KIRC (P = 5.2E-07) and LIHC (P = 0.013). Again, with RFS assessment, only ZC3H13 is eligible for assessing prognosis in patients with LIHC (P = 0.046). No statistical significance was observed for ZC3H13 in predicting the prognosis in patients with other cancer types. In conclusion, by synthesizing differential expression and prognostic analysis results, ZC3H13 has met the

screening criteria and can be used as a candidate factor to assess the prognosis of HCC patients.

MiR-362-3p/miR-425-5p is an upstream miRNA of ZC3H13

The ceRNA theory is used to describe the mechanism of regulating gene expression. Theoretically, ZC3H13 would be regulated by some ncRNAs; therefore, the upstream miRNAs to which ZC3H13 might be bound were first queried, and 12 miRNAs were identified (Table 1). Cytoscape software was used to establish the miRNA-ZC3H13 regulatory network (Figure 3A). Based on the mechanism by which miRNAs regulate target gene expression, a negative regulatory relationship should exist between miRNAs and ZC3H13; thus,

correlation analysis was performed. ZC3H13 was inhibited by upstream miR-362-3p or miR-425-5p (Figure 3B, 3E). No negative correlation was found between ZC3H13 and the other nine predicted miRNAs. miRNAs are upregulated in liver cancer patients and function as oncogenes in terms of prognostic value. The above results are consistent with bioinformatics analysis, supporting the ceRNA hypothesis. Finally, based on the correlation analysis and prognosis analysis results of miR-362-3p/miR-425-5p and ZC3H13, the status of miR-362-3p/miR-425-5p as the upstream regulator of ZC3H13 was determined.

Huh7 and Hep3B cells were transfected with miR-362-3p/miR-425-5p, and the effect on ZC3H13 expression levels was tested. The downregulation of ZC3H13

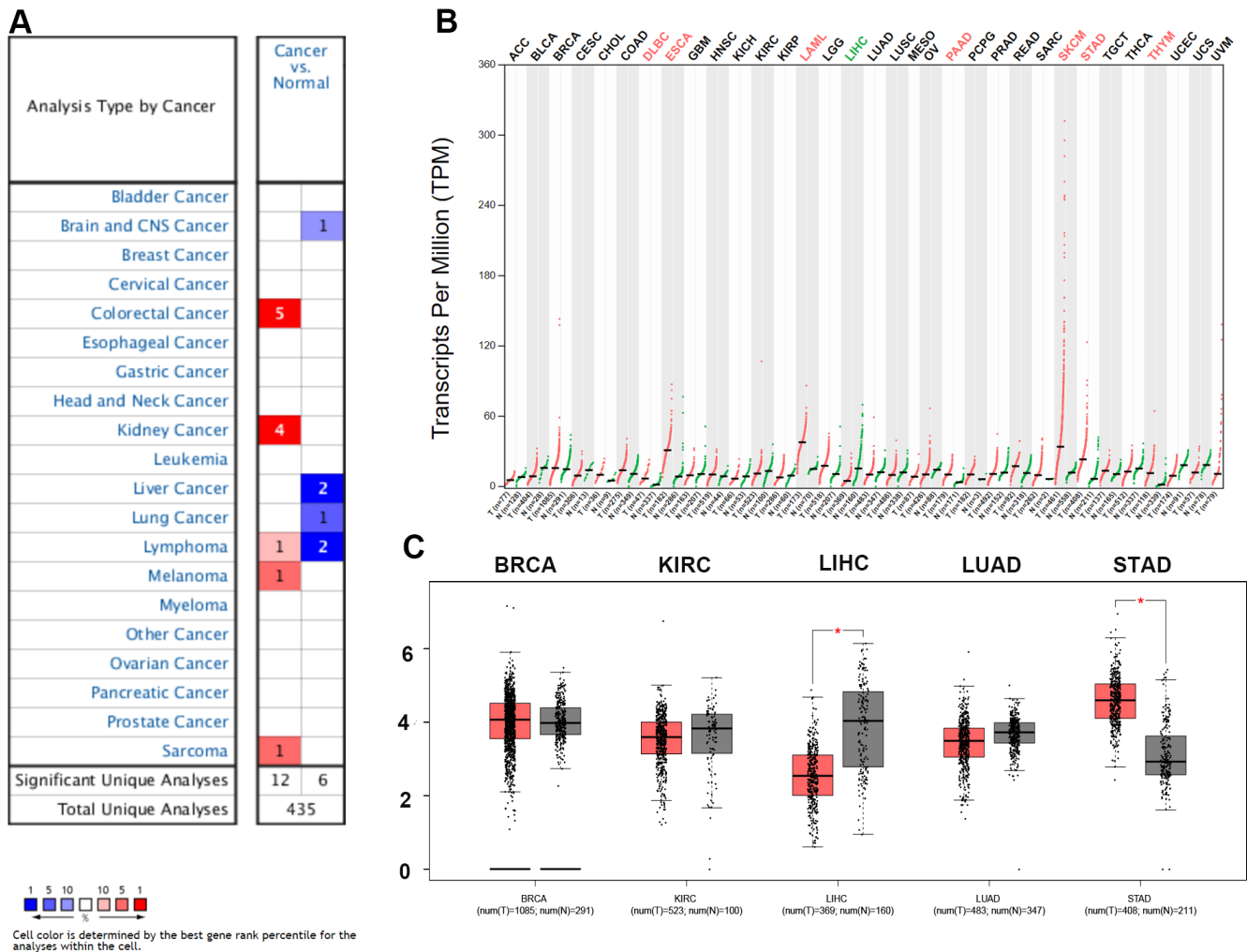


Figure 1. Expression analysis for ZC3H13 in multiple cancers. (A) mRNA expression levels of ZC3H13 in various types of cancer (OncoPrint). The threshold was designed with the following parameters: fold change = 2 and P value = 0.01. The cell number represents the number of datasets that meets the threshold. The color intensity (RED OR BLUE) is directly proportional to the significance level of upregulation or downregulation. (B, C) ZC3H13 expression in TCGA (BRCA, KIRC, LIHC, LUAD, STAD) tissues compared with the corresponding TCGA and GTEx normal tissues. *p value < 0.05.

expression was regulated by miR-362-3p/miR-425-5p mimics and qRT-PCR demonstrated that this reduction could be reversed by miR-362-3p/miR-425-5p inhibitors (Figure 3H, 3I). Furthermore, the protein levels of ZC3H13 were detected by western blotting. And the results were consistent with qRT-PCR results demonstrating that ZC3H13 protein levels were regulated by miR-362-3p/miR-425-5p mimics and inhibitors (Figure 3J). Strikingly, ZC3H13 was identified as a direct target of miR-362-3p/miR-425-5p, further corroborating the RNA-seq results (Figure 3).

Determining the function of ZC3H13 in HCC

To further explore the biological function and pathway analysis of the candidate factor ZC3H13 in HCC, TCGA sequencing data stored on LinkedOmics online tool were utilized. Red dots represent genes that are positively

correlated with ZC3H13, and green dots represent negative correlations (Figure 4A, $P < 0.05$). The genes that were ranked in the top 50 positively and negatively associated with ZC3H13 were presented in a heat map in Supplementary Figure 1. ZC3H13 is involved in biological functions such as phosphoinositide metabolism, Chagas disease, propionate metabolism and transcriptional dysregulation in cancer. Kyoto Encyclopedia of Genes and Genomes (KEGG) analysis showed that these genes were mainly enriched in the JAK-STAT signaling pathway and Hippo signaling pathway.

ZC3H13 positively correlates with immune cell infiltration in HCC

Studies have identified zinc finger proteins in other diseases, and they are increasingly recognized as drug

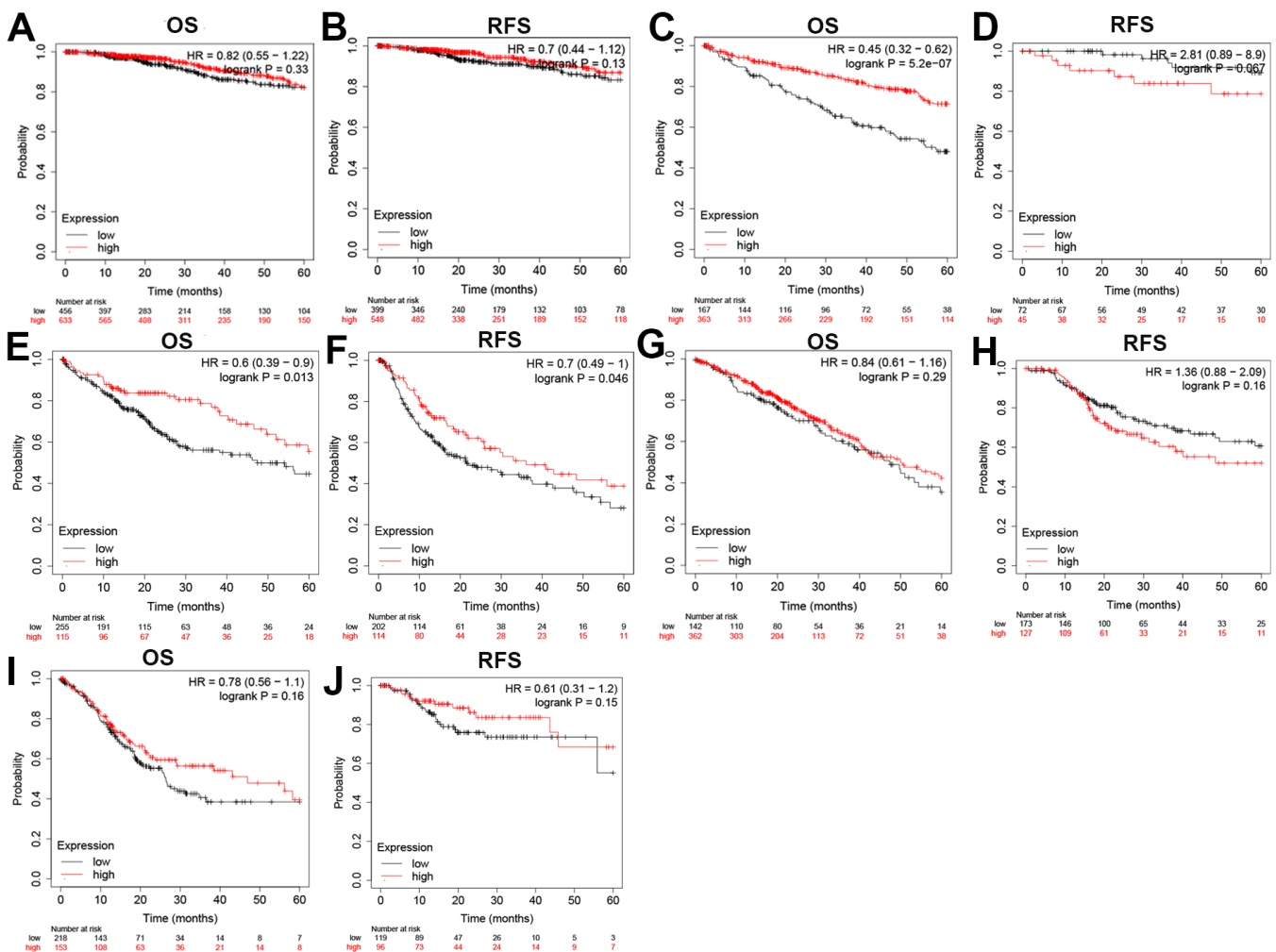


Figure 2. Overall survival (OS) and disease-free survival (RFS) analysis for ZC3H13 in various human cancers determined by the GEPIA database. The OS and RFS plots of ZC3H13 in BRCA (A, B). The OS and RFS plots of ZC3H13 in KIRC (C, D). The OS and RFS plots of ZC3H13 in LIHC (E, F). The OS and RFS plots of ZC3H13 in LUAD (G, H). The OS and RFS plots of ZC3H13 in STAD (I, J).

Table 1. The expression correlation between predicted miRNAs and ZC3H13 in HCC analyzed by starBase database.

GeneName	miRNAname	R-value	P-value
ZC3H13	hsa-miR-15a-5p	0.069	0.183
ZC3H13	hsa-miR-16-5p	0.173 ^a	8.29E-04 ^a
ZC3H13	hsa-miR-23a-3p	0.081	0.119
ZC3H13	hsa-miR-7-5p	0.026	0.616
ZC3H13	hsa-miR-15b-5p	0.021	0.691
ZC3H13	hsa-miR-23b-3p	0.036	0.492
ZC3H13	hsa-miR-195-5p	0.173 ^a	8.35E-04 ^a
ZC3H13	hsa-miR-424-5p	0.086	0.1
ZC3H13	hsa-miR-329-3p	0.006	0.905
ZC3H13	hsa-miR-497-5p	0.079	0.130
ZC3H13	hsa-miR-425-5p	-0.129 ^a	0.0128 ^{a*}
ZC3H13	hsa-miR-362-3p	-0.106 ^a	0.0417 ^{a*}

^aThese results are statistically significant.

*p value < 0.05; **p value < 0.01; ***p value < 0.001.

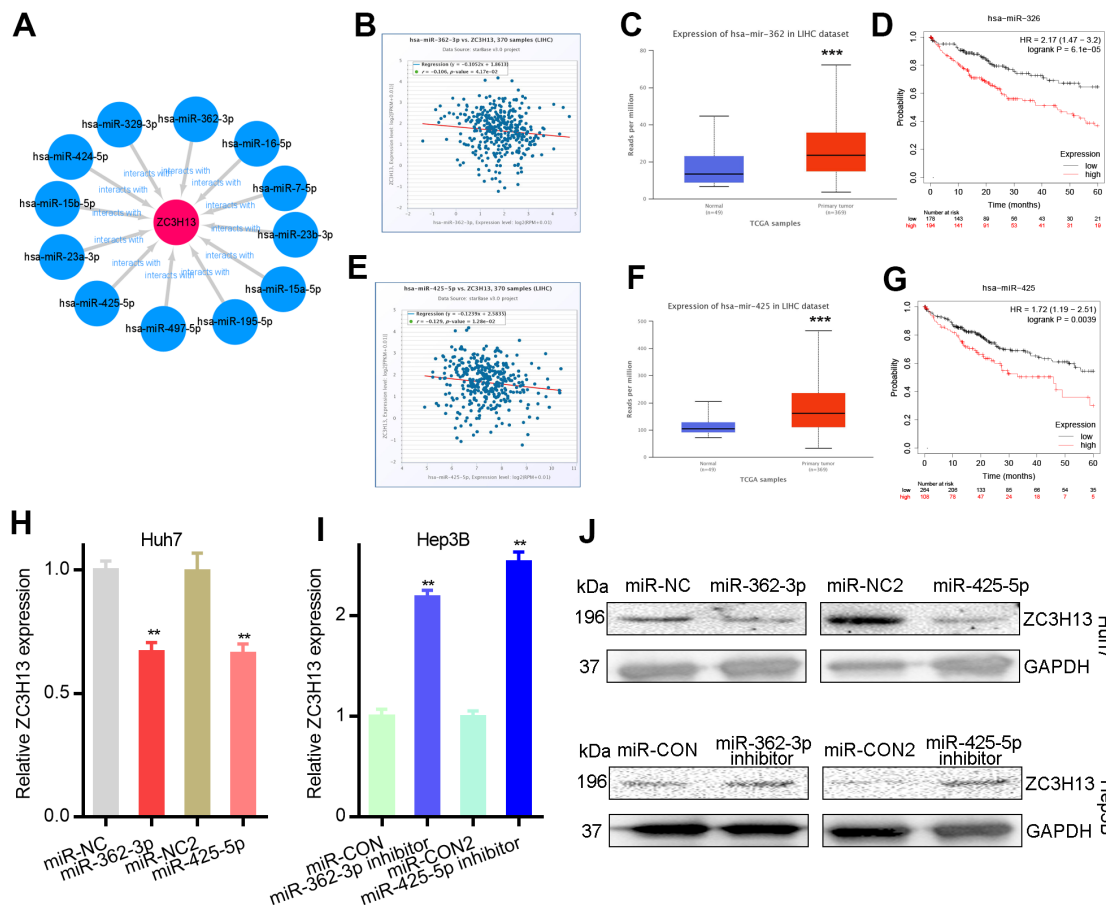
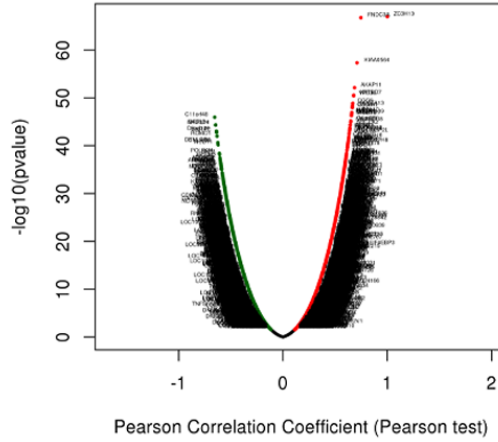


Figure 3. Mir-362-3p/mir-425-5p downregulates ZC3H13 in liver cancer. (A) The miRNA-ZC3H13 regulatory network established by Cytoscape software. (B) ZC3H13 is negatively correlated with miR-362-3p in LIHC analyzed by the starBase database. (C) Mir-362-3p is overexpressed in LIHC analyzed by UALCAN. (D) The prognostic value of miR-362-3p in HCC assessed by Kaplan–Meier plotter. (E) ZC3H13 is negatively correlated with miR-425-5p in LIHC analyzed by the starBase database. (F) Mir-425-5p is overexpressed in LIHC analyzed by UALCAN. (G) The prognostic value of miR-425-5p in HCC assessed by Kaplan–Meier plotter. (H, I) MiR-362-3p/miR-425-5p mimic and inhibitor results detected by qPCR. (J) MiR-362-3p/miR-425-5p mimic and inhibitor results detected by western blot. **P<0.01.

A

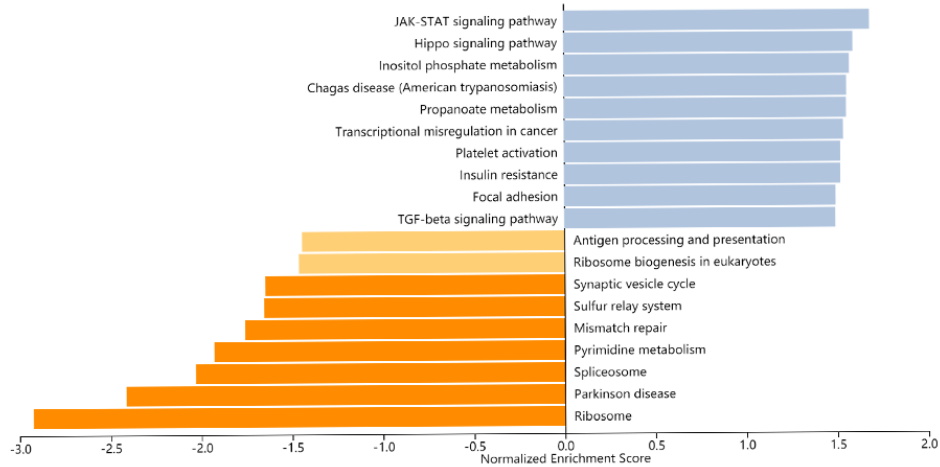
ZC3H13 Association Result



B

■ FDR ≤ 0.05 ■ FDR > 0.05

KEGG



Affinity Propagation Enrichment Results

C

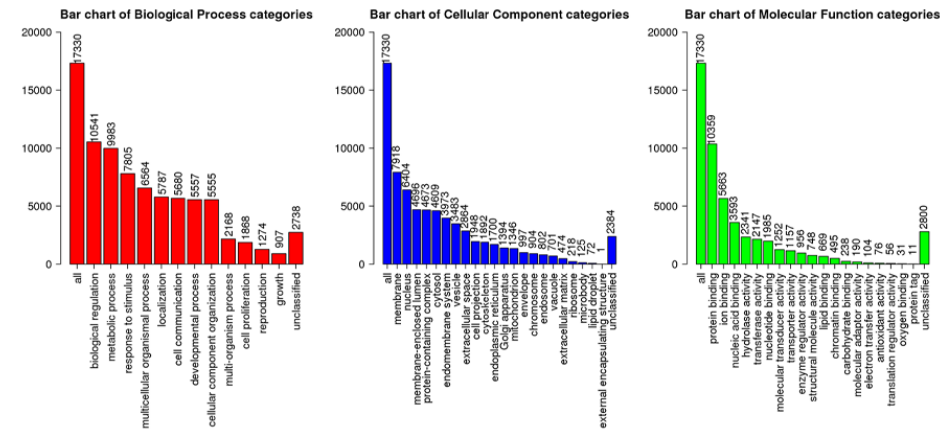


Figure 4. ZC3H13 coexpression genes in LIHC (LinkedOmics). (A) Global ZC3H13 highly correlated genes identified by the Pearson test in LIHC. Red and green dots represent positively and negatively significantly correlated genes with ZC3H13, respectively. (B) KEGG pathways of ZC3H13-correlated genes. (C) Gene Ontology of ZC3H13-correlated genes. KEGG: Kyoto Encyclopedia of Genes and Genomes; LIHC: Liver hepatocellular carcinoma.

targets [14]. As a typical zinc finger protein, ZC3H13 has a finger domain. Tumor-infiltrating immune cells are represented by six types, namely B cells, CD8+ T cells, CD4+ T cells, macrophages, neutrophils and dendritic cells. Clarifying tumor-infiltrating immune cell types may help to improve the survival prediction of HCC patients increasing the therapeutic effect. Therefore, we investigated the correlation between

ZC3H13 and tumor-infiltrating immune cells (Figure 5). The results revealed that the expression of ZC3H13 in HCC patients was significantly and positively correlated with four types of immune cell infiltration, including CD4+ T cells ($P = 2.32E-07$), macrophages ($P = 2.96E-03$), neutrophils ($P = 1.51E-09$) and dendritic cells ($P = 1.07E-03$). Among these immune cells, tumor-infiltrating neutrophils showed the strongest correlation.

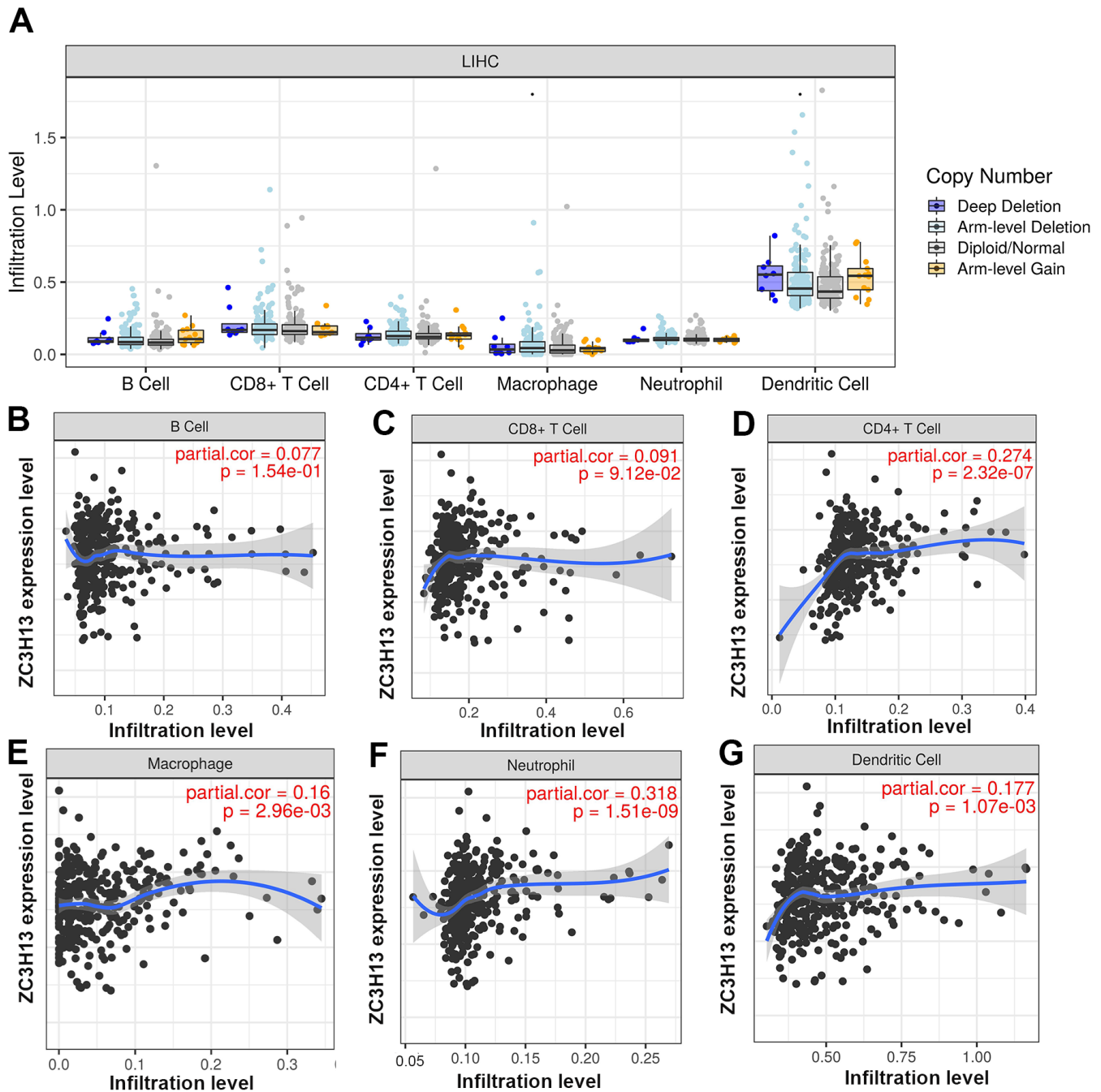


Figure 5. (A) The relationship of immune cell infiltration with ZC3H13 levels in HCC. (B–G) The infiltration level of various immune cells under different expression levels of ZC3H13 in HCC. The correlation of ZC3H13 expression level with B cell (B), CD8+T cell (C), CD4+T cell (D), macrophage (E), neutrophil (F), or dendritic cell (G) infiltration level in HCC.

Correlation analysis of ZC3H13 and immune cell biomarkers in HCC

Continuing the correlation analysis in the previous section, this study analyzed the correlation between ZC3H13 and biomarkers expressed by immune cells in patients with hepatocellular carcinoma. The biomarkers expressed on immune cells are listed in Table 2. For example, CD4 is a CD4⁺ T cell biomarker. Correlation analysis showed that ZC3H13 was significantly positively correlated with CD4⁺ T cell biomarkers ($R = 0.25$, $P = 1.60E-06$), M1 macrophage biomarkers ($R = 0.4$, $P = 1.20E-15$), M2 macrophage biomarkers ($R = 0.25$, $P = 1.10E-06$), neutrophil biomarkers ($R = 0.25$, $P = 7.50E-07$), and dendritic cell biomarkers ($R = 0.26$, $P = 4.00E-07$). These findings prompted us to consider that ZC3H13 may lead to different prognostic outcomes of patients by influencing the immune cells infiltrating hepatocellular carcinoma patients.

Relationship between ZC3H13 and immune checkpoints in HCC

PD1/PD-L1 and CTLA-4 are known to be key immune checkpoints, and they are responsible for tumor immune escape. We evaluated the correlation of ZC3H13 with these immune checkpoints in patients with hepatocellular carcinoma using bioinformatics. The analysis showed that the expression of ZC3H13 was significantly and positively correlated with PD-L1 in HCC ($R = 0.437$, $P = 1.73E-17$), which was adjusted by purity (Supplementary Figure 2). Consistent with the TIMER data analysis results, GEPIA database analysis found that ZC3H13 was positively correlated with PD-L1 ($R = 0.33$, $P = 6.3E-11$). In addition, no correlation was seen between ZC3H13 and PD1 and CTLA-4.

DISCUSSION

The liver has a unique anatomical feature of dual blood supply, making liver cancer patients prone to recurrence or metastasis after surgery. This situation contributes to most advanced HCC patients being prone to a poor prognosis; thus, effective HCC diagnostic and prognostic biomarkers must be identified [7, 15].

Presently, domestic and foreign researchers have proposed the following views: ZC3H13 has the potential to be a prognostic indicator or therapeutic target for hepatocellular carcinoma [13]. However, the role of ZC3H13 in hepatocellular carcinoma remains controversial. Liu Jun et al. evaluated the transcriptome data and corresponding clinical data of m6A methylation-related genes (including 15 genes) from the

TCGA database and found that ZC3H13 was upregulated in high-risk tumor patients and that ZC3H13 was associated with survival and prognosis, making it a potential predictor for patients with hepatocellular carcinoma [16]. However, Wu Xiaomin et al. also used The Cancer Genome Atlas (TCGA) database for bioinformatics analysis, but they proposed the opposite point of view: ZC3H13 was overexpressed in hepatocellular carcinoma patients, and they used m6A regulators such as YTHDF2, YTHDF1, METTL3, KIAA1429, and ZC3H13 as prognostic features, which could successfully distinguish high-risk patients with HCC [17]. Although the above articles reported the expression of ZC3H13 in HCC, they lacked the regulatory mechanism of ZC3H13 expression.

In the present study, also based on the TCGA dataset and bioinformatics analysis, ZC3H13 was expressed at low levels in HCC patients. ZC3H13 is a “protective factor” for patients with hepatocellular carcinoma, and patients with low ZC3H13 expression have a poor prognosis. To further elucidate the regulatory mechanism of ZC3H13, we explored upstream regulatory factors.

The ceRNA mechanism involves three levels of mRNA, miRNA and lncRNA and regulates gene expression [18, 19]. We predict upstream miRNAs that can regulate ZC3H13 through the starBase database. Finally, 12 miRNAs were obtained from the screening. Most miRNAs act as oncogene miRNAs in HCC. Considering the above analysis, after continuing to perform correlation analysis, expression analysis and survival analysis on this basis, we identified miR-362-3p/miR-425-5p as the ZC3H13 upstream oncogene miRNA with the most potential. Previous studies have reported that miR-362-3p/miR-425-5p exerts oncogenic effects by regulating HCC proliferation and migration. For example, miR-425-5p achieved its role in promoting the malignant progression of HCC by regulating RNF11 and was seen as a molecular target to predict the outcome of HCC patients [20]. Upregulation of miR-362-3p, which targets and regulates Tob2, thereby promoting the proliferation of hepatocellular carcinoma cells [21]. Li, Z et al. found that inhibition of Rab23 expression by overexpression of miR-362-3p inhibited the growth and proliferation of Hep3B cells *in vivo* [22].

The mechanism of ZC3H13 downregulation in HCC was explained by our results. MiR-362-3p/miR-425-5p bound to the ZC3H13 3' UTR (Supplementary Figure 3), validating database findings that miR-362-3p/miR-425-5p targets and regulates ZC3H13 expression. Additionally, miR-362-3p/miR-425-5p expression was inversely associated with ZC3H13 expression in HCC tissues.

Table 2. Correlation analysis between ZC3H13 and biomarkers of immune cells in HCC determined by GEPIA database.

Immune cell	Biomarker	R value	p value
B cell	CD19	-0.013	8.00E-01
	CD79A	0.1 ^a	4.80E-02* ^a
CD8+ T cell	CD8A	0.15 ^a	4.20E-03** ^a
	CD8B	0.033	5.20E-01
CD4+ T cell	CD4	0.25 ^a	1.60E-06*** ^a
	NOS2	0.29 ^a	1.70E-08*** ^a
M1 macrophage	IRF5	0.2 ^a	7.50E-05*** ^a
	PTGS2	0.4 ^a	1.20E-15*** ^a
	CD163	0.07	1.80E-01
M2 macrophage	VSIG4	0.18 ^a	3.90E-04*** ^a
	MS4A4A	0.25 ^a	1.10E-06*** ^a
	CEACAM8	0.078	1.30E-01
Neutrophil	ITGAM	0.24 ^a	2.30E-06*** ^a
	CCR7	0.25 ^a	7.50E-07*** ^a
	HLA-DPB1	0.17 ^a	1.10E-03** ^a
	HLA -DQB1	-0.078	1.30E-01
Dendritic cell	HLA-DRA	0.22 ^a	1.60E-05*** ^a
	HLA-DPA1	0.26 ^a	4.00E-07*** ^a
	CD1C	0.2 ^a	1.20E-04*** ^a
	NRP1	0.5 ^a	1.40E-24*** ^a
	ITGAX	0.28 ^a	7.60E-08*** ^a

^aThese results are statistically significant.

*p value < 0.05; **p value < 0.01; ***p value < 0.001.

Many studies have confirmed that the therapeutic efficacy and prognosis of cancer patients are closely related to tumor immune cell infiltration. Our work showed that ZC3H13 is positively associated with the following four types of immune cell infiltration in HCC: CD4+ T cells, macrophages, neutrophils and dendritic cells. More precisely, ZC3H13 was also positively correlated with the above biomarkers expressed on immune cells. These findings suggested that tumor immune infiltration may partially explain the different ZC3H13 expression levels affecting the prognosis of patients with hepatocellular carcinoma.

CONCLUSIONS

Considering the controversy over ZC3H13 expression in HCC patients, this study showed that ZC3H13 is downregulated in HCC and significantly associated with a poor prognosis in HCC. To elucidate the mechanism of ZC3H13 downregulation in hepatocellular carcinoma, the miR-362-3p/miR-425-5p-ZC3H13 axis was further evaluated. In addition, ZC3H13 may affect the prognosis of patients with hepatocellular carcinoma by increasing four tumor immune cell (CD4+ T cells, macrophages, neutrophils and dendritic cells)

infiltration and thus affecting the prognosis of patients with hepatocellular carcinoma. However, more basic trials and large clinical trials will make these findings even more convincing.

MATERIALS AND METHODS

Predicted upstream regulators of ZC3H13

StarBase (<http://starbase.sysu.edu.cn/>) searches were performed for microRNA targets using high-throughput CLIP-Seq experimental data and degradome experimental data, providing various visual interfaces to explore microRNA targets. The miRNA-mRNA module was used to analyze upstream miRNAs [23]. StarBase database involves PITA, RNA22, miRmap, microT, miRanda, PicTar, and TargetScan target gene prediction programs. Only target miRNAs validated by more than two prediction programs were considered as miRNAs meeting the screening criteria. The miRNAs screened above were considered candidate miRNAs of ZC3H13. And starBase was used to analyze the correlation between miR-362-3p/miR-425-5p and ZC3H13 in liver cancer patients. Comparison of miR-362-3p/miR-425-5p expression differences between hepatocellular

carcinoma patients and normal was also done through this website.

Oncomine analysis

The Oncomine database is a large oncology gene microarray database. Because it covers 65 gene microarray datasets, large-scale gene expression data are recognized and used by everyone. This study used it to analyze gene expression differences. It can also have functional modules such as identifying abnormal values and predicting co-expressed genes [24]. In this study, we analyzed the differences in expression of m6A-related genes in HCC patients and healthy individuals based on mRNA levels using the Oncomine database. Analysis was based on the following criteria: fold change = 2 and P value = 0.01.

GEPIA database analysis

GEPIA (<http://gepia.cancer-pku.cn/>) integrates TCGA cancer data with GTEx normal tissue data. By revealing driver genes, alleles, differential expression or oncogenic factors, it can provide key clues for our analysis of novel cancer targets and markers. Therefore, it is often used to address differential gene expression in cancer biology [25]. The expression of ZC3H13 in different types of human tumors was detected by GEPIA. In addition, the relationship of ZC3H13 with immune cell surface markers and immune checkpoints in patients with hepatocellular carcinoma was evaluated. The selection criteria were statistically significant with $R > 0.1$ and a p value < 0.05 .

Kaplan–Meier plotter analysis

The Kaplan–Meier plotter (<http://kmplot.com>) database is processed by a PostgreSQL server that integrates both gene expression and clinical data [26]. Gene expression data and recurrence-free and overall survival information were downloaded from GEO, EGA, and TCGA. To analyze the prognostic value of ZC3H13 and upstream miRNAs, samples of hepatocellular carcinoma patients were divided into two groups with high and low expression. The two cohorts were compared by Kaplan–Meier survival plots, and hazard ratios and log-rank P values were calculated using 95% confidence intervals. Survival time was selected as 60 months.

TIMER database analysis

The TIMER database (<https://cistrome.shinyapps.io/timer/>) stores a comprehensive resource of immune infiltrations of different cancer types. It is one of the common databases used to analyze tumor immune infiltrates. This study involved six immune cells

containing B cells, CD4+ T cells, CD8+ T cells, neutrophils, macrophages and dendrites [27]. We analyzed the correlation between ZC3H13 and immune cell infiltration levels or immune checkpoint expression levels in liver cancer patients. A p value < 0.05 was considered statistically significant.

Gene set enrichment analysis

LinkedOmics (<http://www.linkedomics.org>) has over a billion data points. Specifically, it contains the TCGA dataset covering 32 cancer types and stores multi-omic and clinical data on more than 10,000 patients [28]. The “LinkInterpreter” module can translate big data about ZC3H13 into biological functions and enumerate the most likely signaling pathways involved through its inherent pathway analysis and network analysis. It was used for Gene Ontology and Kyoto Encyclopedia of Genes and Genomes (KEGG) pathway analysis by Gene Set Enrichment Analysis (GSEA). In the “LinkFinder” module of LinkedOmics, we performed a statistical analysis of ZC3H13 co-expression using the Pearson test, and the results are presented in the form of volcano plots. The rank criterion was a false discovery rate (FDR) < 0.05 , and there were 500 simulations.

UALCAN database analysis

UALCAN (<http://ualcan.path.uab.edu/index.html>) is also based on the TCGA database of relevant cancer data. It is often used for online analysis and mining of cancer data [29]. It can perform commands such as expression profiling, survival analysis, correlation analysis, methylation levels and even target gene prediction. Gene expression of miR-362-3p/miR-425-5p in the LIHC TCGA dataset was explored using UALCAN. $P < 0.05$ indicated statistical significance.

Cell culture, cell transfection, RNA isolation and quantitative real-time PCR (qPCR) analysis

The HCC cell lines used in this study were purchased from the American Type Culture Collection and included Hep3B and Huh7 cells. All cancer cells survived in an environment based on high glucose Dulbecco’s modified Eagle’s medium (DMEM; Thermo Scientific) supplemented with 10% fetal bovine serum (FBS, Gibco), 0.1 mmol/L MEM nonessential amino acids (NEAA; Invitrogen) and 1% L-glutamine (Invitrogen). All the cell lines were cultured under growth conditions of 5% CO₂ in an incubator at 37° C and 100% humidity. The cells were transfected at a density of 2×10^6 /ml with the indicated miRNA mimics or inhibitors using Lipofectamine® 3000 (Invitrogen; Thermo Fisher Scientific, Inc.) as indicated by the manufacturer. After 48 hours, the cells were used for subsequent experiments.

Total RNA was extracted from HCC cells using TRIzol® Reagent (Invitrogen; Thermo Fisher Scientific, Inc.) following the manufacturer's instructions. First, total RNA (1 µg) was reverse transcribed into cDNA using the PrimeScript RT kit with gDNA Eraser (Takara Biotechnology Co., Ltd.) (Experimental conditions: 37° C for 15 minutes and 85° C for 5 seconds). Subsequently, qPCR was performed using TB Green Fast qPCR mix (Takara Biotechnology Co., Ltd.). The following primers were used for qPCR: ZC3H13 forward, 5'- AAAGGAGGGTTTACCAGAAGTG-3' and reverse, 5'- CGCTTCGGAGATTTGCTAGAC-3'; and GAPDH forward, 5'- GAAATCCCATCACCATC TTCCAGG-3' and reverse, 5'- GAGCCCCAGCCTTC TCCATG-3'. qPCR was performed under the following thermal cycling conditions: initial denaturation at 95° C for 2 min, followed by 40 cycles of 95° C for 20 s, 58° C for 20 s, and 72° C for 20 s. The mRNA expression levels were quantified using the 2- $\Delta\Delta$ Ct method and normalized to the internal reference gene GAPDH.

Western blotting

Cells were collected and washed twice with PBS. The cells were then lysed with RIPA lysis buffer containing protein inhibitors on ice for 30 minutes. The cell lysate was then centrifuged at 13 000 rpm for 30 minutes. Supernatants containing protein were collected, and the protein was quantitated using a Pierce BCA Protein Assay Kit (Thermo Fisher Scientific, Waltham, MA). SDS-PAGE involves the principle of separating proteins by electrophoresis according to their size. After electrophoresis, the proteins are transferred to polyvinylidene difluoride (PVDF) membranes. The membranes were blocked with 5% skim milk and shaken at room temperature for 30 minutes. The primary antibody targeting the protein of interest was incubated with the membrane overnight at 4° C with shaking. The next day, an HRP-labeled secondary antibody was used to detect the protein of interest. Finally, the bands were visualized using Pierce ECL (Thermo Fisher Scientific, Waltham, MA). All of the images were captured using the Molecular Imager ChemiDoc XRS+ (Bio-Rad, Hercules, CA).

Statistical analysis

Statistical analyses were automatically calculated from the aforementioned online databases and were divided into the following four aspects: (1) Comparison of mRNA expression using Student's t test; (2) Correlation of gene expression using Spearman's correlation to assess or infiltrate immune cells and Pearson's correlation method; (3) Fisher's exact test to measure gene enrichment; (4) a p value < 0.05 or a log rank p value < 0.05 was considered statistically significant.

Data availability

The datasets presented in this study can be found in publicly available databases. The names of the databases and their websites have been marked in the article.

Abbreviations

m6A: N6-methyladenosine; LIHC: liver hepatocellular carcinoma; HCC: hepatocellular carcinoma; HBV: hepatitis B virus; HCV: hepatitis C virus; TCGA: The Cancer Genome Atlas; GO: Gene Ontology; KEGG: Kyoto Encyclopedia of Genes and Genomes; ZC3H13: zinc finger CCCH-type containing 13; OS: Overall survival; RFS: Recurrence free survival; qPCR: Quantitative Real-time PCR; GSEA: Gene set enrichment analysis; RBM15: RNA-binding motif protein 15; METTL14: methyltransferase like 14; WTAP: Wilms tumor 1 associated protein; FTO: fat mass- and obesity-associated protein; ALKBH5: alkb homolog 5.

AUTHOR CONTRIBUTIONS

SW, and SHL conceived the project and wrote the manuscript. SW, SHL and GC participated in data analysis and experiments. YXC, and PW participated in discussion and language editing. HZP reviewed the manuscript. All authors contributed to the article and approved the submitted version.

ACKNOWLEDGMENTS

The authors thank the contributors of The Cancer Genome Atlas for their contribution to share the sequencing dataset on open access. The authors thank the contributors of related databases for their contribution to facilitate the analyses of The Cancer Genome Atlas datasets.

CONFLICTS OF INTEREST

The authors declare that they have no conflicts of interest.

FUNDING

This work was supported by National Natural Science Foundation of China (Grant No. 81402579), Natural Science Foundation of Shandong Province General Project (Grant No. ZR2020MH318), the Key Program of Research and Development Foundation of Shandong province (Grant No. 2017GSF18179), Source Innovation Foundation of Qingdao (Grant No. 18-2-2-79-jch), "Clinical Medicine + X" of Qingdao University (Grant No. CMX201729) and "Clinical Medicine + X" of the Affiliated Hospital of Qingdao University (Grant No. QDFY+X202101019).

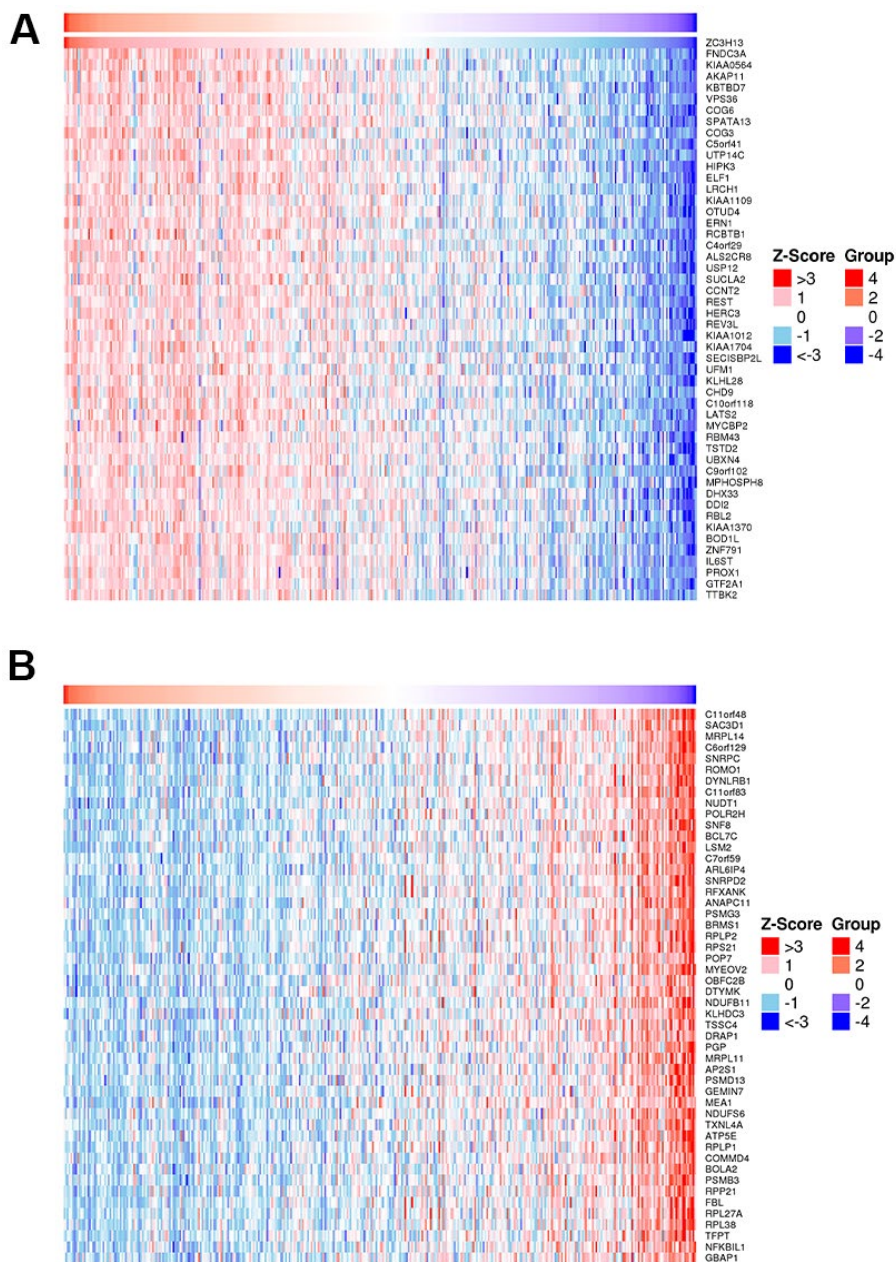
REFERENCES

1. Erratum: Global cancer statistics 2018: GLOBOCAN estimates of incidence and mortality worldwide for 36 cancers in 185 countries. *CA Cancer J Clin.* 2020; 70:313.
<https://doi.org/10.3322/caac.21609>
PMID:[32767693](https://pubmed.ncbi.nlm.nih.gov/32767693/)
2. Llovet JM, Kelley RK, Villanueva A, Singal AG, Pikarsky E, Roayaie S, Lencioni R, Koike K, Zucman-Rossi J, Finn RS. Hepatocellular carcinoma. *Nat Rev Dis Primers.* 2021; 7:6.
<https://doi.org/10.1038/s41572-020-00240-3>
PMID:[33479224](https://pubmed.ncbi.nlm.nih.gov/33479224/)
3. Chen HY, Chen YM, Wu J, Yang FC, Lv Z, Qian YG, Zheng SS. Effects of *HGF* gene polymorphisms and protein expression on transhepatic arterial chemotherapeutic embolism efficacy and prognosis in patients with primary liver cancer. *OncoTargets Ther.* 2017; 10:803–10.
<https://doi.org/10.2147/OTT.S115035> PMID:[28243116](https://pubmed.ncbi.nlm.nih.gov/28243116/)
4. Zhu XD, Sun HC. Emerging agents and regimens for hepatocellular carcinoma. *J Hematol Oncol.* 2019; 12:110.
<https://doi.org/10.1186/s13045-019-0794-6>
PMID:[31655607](https://pubmed.ncbi.nlm.nih.gov/31655607/)
5. de Jesus VH, Dettino AL. Update on hepatocellular carcinoma from the 2018 Gastrointestinal Cancer Symposium (ASCO GI). *J Hepatocell Carcinoma.* 2018; 5:87–90.
<https://doi.org/10.2147/JHC.S171396> PMID:[30324097](https://pubmed.ncbi.nlm.nih.gov/30324097/)
6. Geula S, Moshitch-Moshkovitz S, Dominissini D, Mansour AA, Kol N, Salmon-Divon M, Hershkovitz V, Peer E, Mor N, Manor YS, Ben-Haim MS, Eyal E, Yunger S, et al. Stem cells. m6A mRNA methylation facilitates resolution of naïve pluripotency toward differentiation. *Science.* 2015; 347:1002–6.
<https://doi.org/10.1126/science.1261417>
PMID:[25569111](https://pubmed.ncbi.nlm.nih.gov/25569111/)
7. He L, Li H, Wu A, Peng Y, Shu G, Yin G. Functions of N6-methyladenosine and its role in cancer. *Mol Cancer.* 2019; 18:176.
<https://doi.org/10.1186/s12943-019-1109-9>
PMID:[31801551](https://pubmed.ncbi.nlm.nih.gov/31801551/)
8. Du K, Zhang L, Lee T, Sun T. m⁶A RNA Methylation Controls Neural Development and Is Involved in Human Diseases. *Mol Neurobiol.* 2019; 56:1596–606.
<https://doi.org/10.1007/s12035-018-1138-1>
PMID:[29909453](https://pubmed.ncbi.nlm.nih.gov/29909453/)
9. Meyer KD, Jaffrey SR. Rethinking m6A Readers, Writers, and Erasers. *Annu Rev Cell Dev Biol.* 2017; 33:319–42.
<https://doi.org/10.1146/annurev-cellbio-100616-060758> PMID:[28759256](https://pubmed.ncbi.nlm.nih.gov/28759256/)
10. Knuckles P, Lence T, Haussmann IU, Jacob D, Kreim N, Carl SH, Masiello I, Hares T, Villaseñor R, Hess D, Andrade-Navarro MA, Biggiogera M, Helm M, et al. Zc3h13/Flacc is required for adenosine methylation by bridging the mRNA-binding factor Rbm15/Spenito to the m⁶A machinery component Wtap/Fl(2)d. *Genes Dev.* 2018; 32:415–29.
<https://doi.org/10.1101/gad.309146.117>
PMID:[29535189](https://pubmed.ncbi.nlm.nih.gov/29535189/)
11. Gong PJ, Shao YC, Yang Y, Song WJ, He X, Zeng YF, Huang SR, Wei L, Zhang JW. Analysis of N6-Methyladenosine Methyltransferase Reveals METTL14 and ZC3H13 as Tumor Suppressor Genes in Breast Cancer. *Front Oncol.* 2020; 10:578963.
<https://doi.org/10.3389/fonc.2020.578963>
PMID:[33363011](https://pubmed.ncbi.nlm.nih.gov/33363011/)
12. Zhu D, Zhou J, Zhao J, Jiang G, Zhang X, Zhang Y, Dong M. ZC3H13 suppresses colorectal cancer proliferation and invasion via inactivating Ras-ERK signaling. *J Cell Physiol.* 2019; 234:8899–907.
<https://doi.org/10.1002/jcp.27551>
PMID:[30311220](https://pubmed.ncbi.nlm.nih.gov/30311220/)
13. Liu GM, Zeng HD, Zhang CY, Xu JW. Identification of METTL3 as an Adverse Prognostic Biomarker in Hepatocellular Carcinoma. *Dig Dis Sci.* 2021; 66:1110–26.
<https://doi.org/10.1007/s10620-020-06260-z>
PMID:[32333311](https://pubmed.ncbi.nlm.nih.gov/32333311/)
14. Abbehausen C. Zinc finger domains as therapeutic targets for metal-based compounds - an update. *Metallomics.* 2019; 11:15–28.
<https://doi.org/10.1039/c8mt00262b>
PMID:[30303505](https://pubmed.ncbi.nlm.nih.gov/30303505/)
15. Wen J, Lv R, Ma H, Shen H, He C, Wang J, Jiao F, Liu H, Yang P, Tan L, Lan F, Shi YG, He C, et al. Zc3h13 Regulates Nuclear RNA m⁶A Methylation and Mouse Embryonic Stem Cell Self-Renewal. *Mol Cell.* 2018; 69:1028–38.e6.
<https://doi.org/10.1016/j.molcel.2018.02.015>
PMID:[29547716](https://pubmed.ncbi.nlm.nih.gov/29547716/)
16. Liu J, Sun G, Pan S, Qin M, Ouyang R, Li Z, Huang J. The Cancer Genome Atlas (TCGA) based m⁶A methylation-related genes predict prognosis in hepatocellular carcinoma. *Bioengineered.* 2020; 11:759–68.
<https://doi.org/10.1080/21655979.2020.1787764>
PMID:[32631107](https://pubmed.ncbi.nlm.nih.gov/32631107/)
17. Wu X, Zhang X, Tao L, Dai X, Chen P. Prognostic Value of an m6A RNA Methylation Regulator-Based Signature in Patients with Hepatocellular Carcinoma. *BioMed Res Int.* 2020; 2020:2053902.

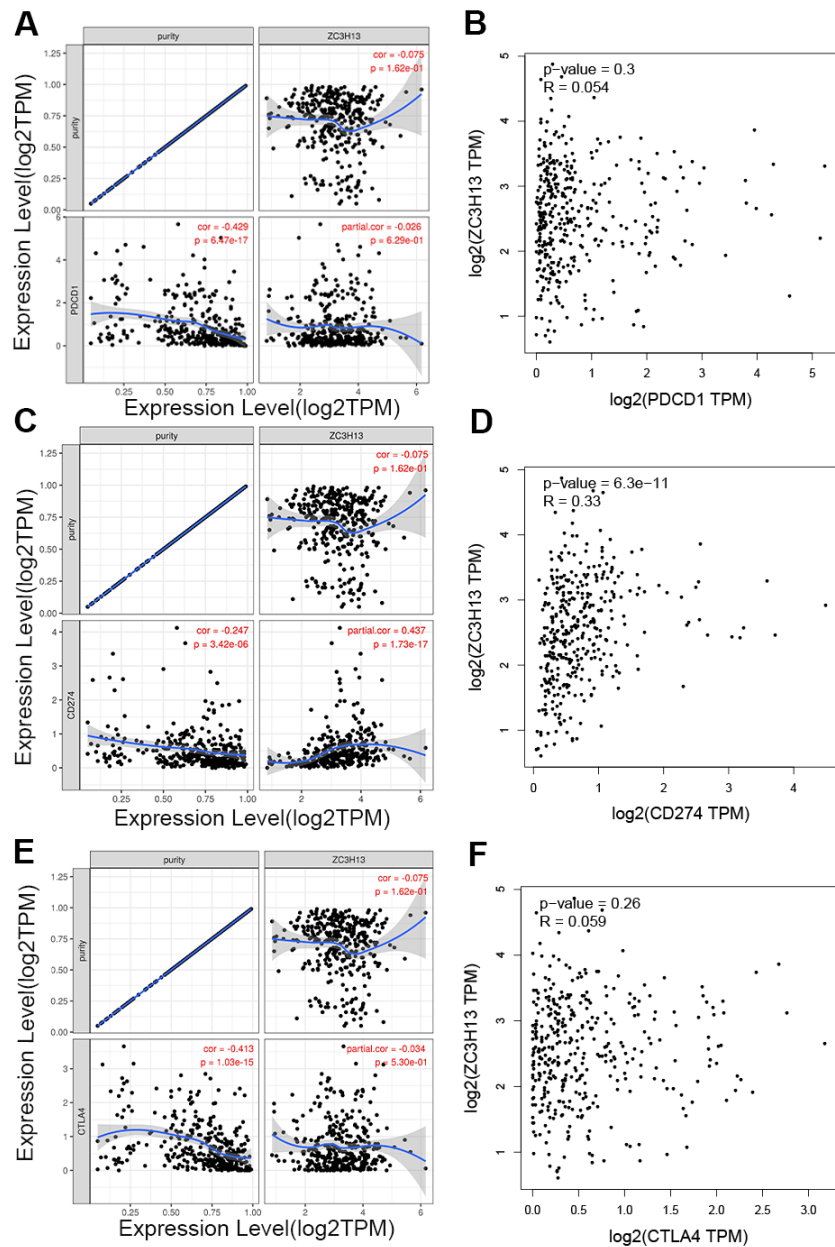
- <https://doi.org/10.1155/2020/2053902>
PMID:[32733931](https://pubmed.ncbi.nlm.nih.gov/32733931/)
18. Fiannaca A, Paglia L, Rosa M, Rizzo R, Urso A. miRTissue_{ce}: extending miRTissue web service with the analysis of ceRNA-ceRNA interactions. *BMC Bioinformatics*. 2020 (Suppl 8); 21:199.
<https://doi.org/10.1186/s12859-020-3520-z>
PMID:[32938402](https://pubmed.ncbi.nlm.nih.gov/32938402/)
19. Lou W, Wang W, Chen J, Wang S, Huang Y. ncRNAs-mediated high expression of SEMA3F correlates with poor prognosis and tumor immune infiltration of hepatocellular carcinoma. *Mol Ther Nucleic Acids*. 2021; 24:845–55.
<https://doi.org/10.1016/j.omtn.2021.03.014>
PMID:[34026328](https://pubmed.ncbi.nlm.nih.gov/34026328/)
20. Rao D, Guan S, Huang J, Chang Q, Duan S. miR-425-5p Acts as a Molecular Marker and Promoted Proliferation, Migration by Targeting RNF11 in Hepatocellular Carcinoma. *BioMed Res Int*. 2020; 2020:6530973.
<https://doi.org/10.1155/2020/6530973>
PMID:[33123581](https://pubmed.ncbi.nlm.nih.gov/33123581/)
21. Shen H, Li W, Tian Y, Xu P, Wang H, Zhang J, Li Y. Upregulation of miR-362-3p Modulates Proliferation and Anchorage-Independent Growth by Directly Targeting Tob2 in Hepatocellular Carcinoma. *J Cell Biochem*. 2015; 116:1563–73.
<https://doi.org/10.1002/jcb.25110>
PMID:[25649327](https://pubmed.ncbi.nlm.nih.gov/25649327/)
22. Li Z, Hu Y, Zeng Q, Wang H, Yan J, Li H, Yu Z. Circular RNA MYLK promotes hepatocellular carcinoma progression by increasing Rab23 expression by sponging miR-362-3p. *Cancer Cell Int*. 2019; 19:211.
<https://doi.org/10.1186/s12935-019-0926-7>
PMID:[31413665](https://pubmed.ncbi.nlm.nih.gov/31413665/)
23. Yang JH, Li JH, Shao P, Zhou H, Chen YQ, Qu LH. starBase: a database for exploring microRNA-mRNA interaction maps from Argonaute CLIP-Seq and Degradome-Seq data. *Nucleic Acids Res*. 2011 (Suppl 1); 39:D202–9.
<https://doi.org/10.1093/nar/gkq1056>
PMID:[21037263](https://pubmed.ncbi.nlm.nih.gov/21037263/)
24. Rhodes DR, Kalyana-Sundaram S, Mahavisno V, Varambally R, Yu J, Briggs BB, Barrette TR, Anstet MJ, Kincaid-Beal C, Kulkarni P, Varambally S, Ghosh D, Chinnaiyan AM. OncoPrint 3.0: genes, pathways, and networks in a collection of 18,000 cancer gene expression profiles. *Neoplasia*. 2007; 9:166–80.
<https://doi.org/10.1593/neo.07112>
PMID:[17356713](https://pubmed.ncbi.nlm.nih.gov/17356713/)
25. Tang Z, Li C, Kang B, Gao G, Li C, Zhang Z. GEPIA: a web server for cancer and normal gene expression profiling and interactive analyses. *Nucleic Acids Res*. 2017; 45:W98–102.
<https://doi.org/10.1093/nar/gkx247>
PMID:[28407145](https://pubmed.ncbi.nlm.nih.gov/28407145/)
26. Hou GX, Liu P, Yang J, Wen S. Mining expression and prognosis of topoisomerase isoforms in non-small-cell lung cancer by using OncoPrint and Kaplan-Meier plotter. *PLoS One*. 2017; 12:e0174515.
<https://doi.org/10.1371/journal.pone.0174515>
PMID:[28355294](https://pubmed.ncbi.nlm.nih.gov/28355294/)
27. Li T, Fan J, Wang B, Traugh N, Chen Q, Liu JS, Li B, Liu XS. TIMER: A Web Server for Comprehensive Analysis of Tumor-Infiltrating Immune Cells. *Cancer Res*. 2017; 77:e108–10.
<https://doi.org/10.1158/0008-5472.CAN-17-0307>
PMID:[29092952](https://pubmed.ncbi.nlm.nih.gov/29092952/)
28. Vasaikar SV, Straub P, Wang J, Zhang B. LinkedOmics: analyzing multi-omics data within and across 32 cancer types. *Nucleic Acids Res*. 2018; 46:D956–63.
<https://doi.org/10.1093/nar/gkx1090>
PMID:[29136207](https://pubmed.ncbi.nlm.nih.gov/29136207/)
29. Chandrashekar DS, Bashel B, Balasubramanya SA, Creighton CJ, Ponce-Rodriguez I, Chakravarthi BV, Varambally S. UALCAN: A Portal for Facilitating Tumor Subgroup Gene Expression and Survival Analyses. *Neoplasia*. 2017; 19:649–58.
<https://doi.org/10.1016/j.neo.2017.05.002>
PMID:[28732212](https://pubmed.ncbi.nlm.nih.gov/28732212/)

SUPPLEMENTARY MATERIALS

Supplementary Figures



Supplementary Figure 1. (A, B) Heatmaps showing the top 50 genes positively and negatively correlated with ZC3H13 in LIHC.



Supplementary Figure 2. Correlation of ZC3H13 expression with PD-1, PD-L1, and CTLA-4 expression in HCC. (A) Spearman correlation of ZC3H13 with the expression of PD-1 in HCC adjusted by purity using TIMER. (B) The expression correlation of ZC3H13 with PD-1 in HCC determined by the GEPIA database. (C) Spearman correlation of ZC3H13 with the expression of PD-L1 in HCC adjusted by purity using TIMER. (D) The expression correlation of ZC3H13 with PD-L1 in HCC determined by the GEPIA database. (E) Spearman correlation of ZC3H13 with the expression of CTLA-4 in HCC adjusted by purity using TIMER. (F) The expression correlation of ZC3H13 with CTLA-4 in HCC determined by the GEPIA database.

Binding Site of hsa-miR-362-3p on ZC3H13:

Show 10 entries

BindingSite	Class	Alignment
chr13:46537300-46537305[-]	6mer	Target: 5' cuAUUACUU-AAUCUGUGUGUu 3' miRNA : 3' acUUAGGAACUUAUCCACACAA 5'

Binding Site of hsa-miR-362-3p on ZC3H13:

Show 10 entries

BindingSite	Class	Alignment
chr13:46537403-46537410[-]	8mer	Target: 5' caucuacccaAAUGCAGGUGUGUa 3' miRNA : 3' acuuaggaacUUA--UCCACACAA 5'

Binding Site of hsa-miR-425-5p on ZC3H13:

Show 10 entries

BindingSite	Class	Alignment
chr13:46537291-46537297[-]	7mer-m8	Target: 5' uuAAUCUGUGUGUAGUGUCAUc 3' : miRNA : 3' agUUGCCUCACUAGCACAGUAA 5'

Supplementary Figure 3. The binding site of miR-362/miR-425 to ZC3H13 was determined by the starBase database.

miRNA-142-3p functions as a potential tumor suppressor directly targeting FAM83D in the development of ovarian cancer

Guangyu Gao^{1,*}, Xiaofei Guo^{2,*}, Wenyong Gu^{2,*}, Yufeng Lu¹, Zhigang Chen¹

¹Department of Oncology, The Second Affiliated Hospital of Soochow University, Suzhou 215004, China

²Department of Ultrasound, The Second Affiliated Hospital of Soochow University, Suzhou 215004, China

*Equal contribution

Correspondence to: Yufeng Lu, Zhigang Chen; **email:** luyufeng-011@163.com, 20185233105@stu.suda.edu.cn

Keywords: microRNA-142-3p, ovarian cancer, GEO, FAM83D, IHC

Received: January 19, 2022

Accepted: March 26, 2022

Published: April 22, 2022

Copyright: © 2022 Gao et al. This is an open access article distributed under the terms of the [Creative Commons Attribution License](https://creativecommons.org/licenses/by/3.0/) (CC BY 3.0), which permits unrestricted use, distribution, and reproduction in any medium, provided the original author and source are credited.

ABSTRACT

Background: FAM83D (family with sequence similarity 83, member D) is of particular interest in tumorigenesis and tumor progression. Ovarian cancer is the leading cause of cancer-related death in women all over the world. This study aims to research the association between FAM83D and ovarian cancer (OC).

Methods: The gene expression data of OC and normal samples (GSE81873 and GSE27651) was downloaded from Gene Expression Omnibus (GEO) dataset. The bioinformatics analysis was performed to distinguish two differentially expressed genes (DEGs), prognostic candidate genes and functional enrichment pathways. Immunohistochemistry (IHC), Quantitative Real-time PCR (qPCR), and luciferase reporter assays were utilized for further study.

Results: There were 56 DEMs and 63 DEGs in cancer tissues compared to normal tissues. According to the km-plot software, hsa-miR-142-3p and FAM83D were associated with the overall survival of patients with OC. Besides, Multivariate analysis included that hsa-miR-142-3p and FAM83D were independent risk factors for OC patients. Furthermore, qPCR demonstrated that miRNA-142-3p and FAM83D were differentially expressed in normal ovarian tissues (NOTs) and ovarian cancer tissues (OCTs). IHC results indicated that FAM83D was overexpressed in OCTs compared with NOTs. Last but not least, luciferase reporter assays verified that FAM83D was a direct target of hsa-miRNA-142-3p in OC cells.

Conclusions: The prognostic model based on the miRNA-mRNA network could provide predictive significance for the prognosis of OC patients, which would be worthy of clinical application. Our results concluded that miR-142-3p and its targets gene FAM83D may be potential diagnostic and prognostic biomarkers for patients with OC.

INTRODUCTION

Ovarian cancer (OC) is one of the main causes of female death. 70% of patients are in the advanced stage (clinical stage III ~ IV), and peritoneal metastasis is the characteristic metastasis symptom of patients with advanced OC. Although the incidence rate is not high, the mortality rate is 2.9%, which is the top ten of female malignant tumor mortality. For OC, the current standard

treatment is not optimistic [1]. One reason is that most patients are diagnosed only in the late stage of the disease. Standard treatment for OC usually includes surgery and platinum chemotherapy. Despite available treatments, the recurrence rate of OC is still high, and about 75% of advanced patients are incurable [2, 3]. Genomics research shows that there is no regulated gene mutation, and many clinical trials have failed to bring lasting clinical benefits [4]. Molecular typing of OC

through molecular expression differences, exploring the microenvironment characteristics of different molecular subtypes of OC, and formulating accurate treatment may be a feasible strategy to improve the dilemma of OC treatment.

Since the discovery of *lin-4* and *let-7*, the founding members of the microRNA (miRNA) family, hundreds of miRNAs have been found in viruses, plants, and animals by molecular cloning and bioinformatics methods [5]. There are more than 1000 known human miRNAs, which control more than 50% of mammalian protein-coding genes. MiRNAs can be overexpressed or inhibited in different diseases. It is a promising therapeutic research field to inhibit or replace microRNAs [6]. Although microRNA has only 20 nucleotides, it plays a key role in biological function by targeting plenty of mRNAs [7]. For example, one study found that miRNA-424-5p regulated ferroptosis by targeting Acyl-CoA Synthetase Long-Chain Family Member 4 in OC cells and indicated a potential therapeutic target for OC [8]. Wu et al. found that the downregulated microRNA-1301-3p inhibited lung carcinoma cell proliferation and migration and has a strong negative correlation with Polymerase I and transcript release factor [9]. Another study also indicated the expression level of miR-200-b control PD-L1 expression in lung carcinoma cells. Furthermore, it may function as a potential biomarker for PD-L1 expression in lung cancer patients [10]. These studies indicated that microRNAs may be related to the progression of cancer, and their mechanisms may take part in the pathogenesis of tumors via controlling cancer-associated genes.

In this article, DEGs and DEMs were selected by researching 1 OC mRNA microarray dataset and 1 miRNA dataset. We aimed to study the relationship between miR-142-3p, FAM83D (we identified), and the development of OC.

RESULTS

Identification of DEGs

We used GEO2R to analysis the DEMs and DEGs from the GSE81873 and GSE27651. Based on the cut-off criteria, 56 DEMs such as *hsa-microRNA-142-3p*, *hsa-microRNA-429*, *hsa-microRNA-199a-3p*, *hsa-microRNA-484*, *hsa-microRNA-139-5p*, *hsa-microRNA-483-5p*, *hsa-microRNA-423-5p*, *hsa-microRNA-342-3p*, *hsa-microRNA-885-5p*, and 63 DEGs were selected (Figure 1).

Gene ontology enrichment analysis

By utilizing FunRich and R software, we performed TF enrichment analysis (Figure 2A).

KEGG and GO function enrichment analyses were performed here. As for GO function analysis, three GO were selected: molecular function (MF), cellular component (CC), and biological process 156 (BP). Expression analysis showed that DEGs had the most uniquely enriched terms for Cell communication, Signal transduction, Regulation of nucleobase, nucleotide and nucleic acid metabolism, Cytoplasm, Nucleus, Cytosol, Membrane, Transcription factor activity, GTPase activity, Receptor signaling complex scaffold activity, Receptor signaling protein serine/threonine kinase activity, and CAMP-mediated signaling (Figure 2B–2D). Besides, DEMs were mainly enriched in 6 pathways: MAPK signaling pathway, PI3K-Akt signaling pathway, Wnt signaling pathway, TGF-beta signaling pathway, Pathways in cancer, and Bacterial invasion of epithelial cells (Figure 3A).

miRNA-mRNA regulatory network

According to FunRich software, 1069 potential target mRNAs were obtained and only 1 of them showed different expression levels in GSE27651 (FAM83D). Based on the association between them, 1 essential microRNA-mRNA pair (microRNA-142-3p and FAM83D) was selected for the next research (Figure 3B, 3C).

genes expression and their associations with OC overall survival

KM Plot was used to analyze the overall survival of patients with OC. According to uploading the miRNA and target gene we identified, we downloaded survival curves. The pictures showed that microRNA-142-3p and FAM83D were associated with the overall survival of patients with OC (Figure 4).

Relationship between clinical characteristics and genes expression level of OC

Clinical and gene expression information of OC patients were downloaded in the TCGA database, such as patients' age, race, FIGO stage, and primary therapy outcome (Tables 1, 2). FAM83D and miR-142-3p expression of patients with Stage III and Stage IV was higher than that of patients with Stage I and Stage II ($P < 0.05$) according to the FIGO stage. Furthermore, associations between clinical characteristics and overall survival in OC were analyzed. According to medium FAM83D and miR-142-3p expression, patients were divided into two groups. Our results indicated that FAM83D mRNA and miR-142-3p expression level ($P < 0.05$), FIGO stage ($P < 0.05$), Primary therapy outcome ($P < 0.05$), and tumor stage ($P < 0.05$) was related to the OS of patients with OC (Tables 3, 4).

Validation of the expression with qRT-PCR and IHC

To deeply evaluate the expression of miR-142-3p and FAM83D, 20 pairs of normal ovarian tissues (NOT) and OC tissues (OCT) were enrolled as a validation cohort. The qRT-PCR approach was utilized to verify the differential expression levels from the patient's tissues. The same as the microarray data, hsa-miR-142-3p was significantly downregulated (Figure 5A) and FAM83D was overexpressed (Figure 5B) between 20 pairs of NOTs and OCTs which indicated that hsa-miR-142-3p and FAM83D could be the candidate

biomarkers for OC. Besides, this expression level of genes was detected by IHC. The staining intensity of FAM83D was divided into 0, 1, 2, or 3, corresponding to colorless, light yellow, light brown, and squid ink. In addition, the percentage score is defined as: 0% to 5%, 0; 6% - 25%, 1 point; 26-50%, 2 points; 50-75%, 3 points; 76% to 100%, 4 points. The final histochemical score was calculated by multiplying the intensity score by the percentage score. The final staining scores were negative (0), low (6), and strong (≥ 6). Statistically, the overall expression of FAM83D was much higher in OC tissues than in the adjacent noncancerous tissues ($P < 0.001$) (Figure 5C–5F).

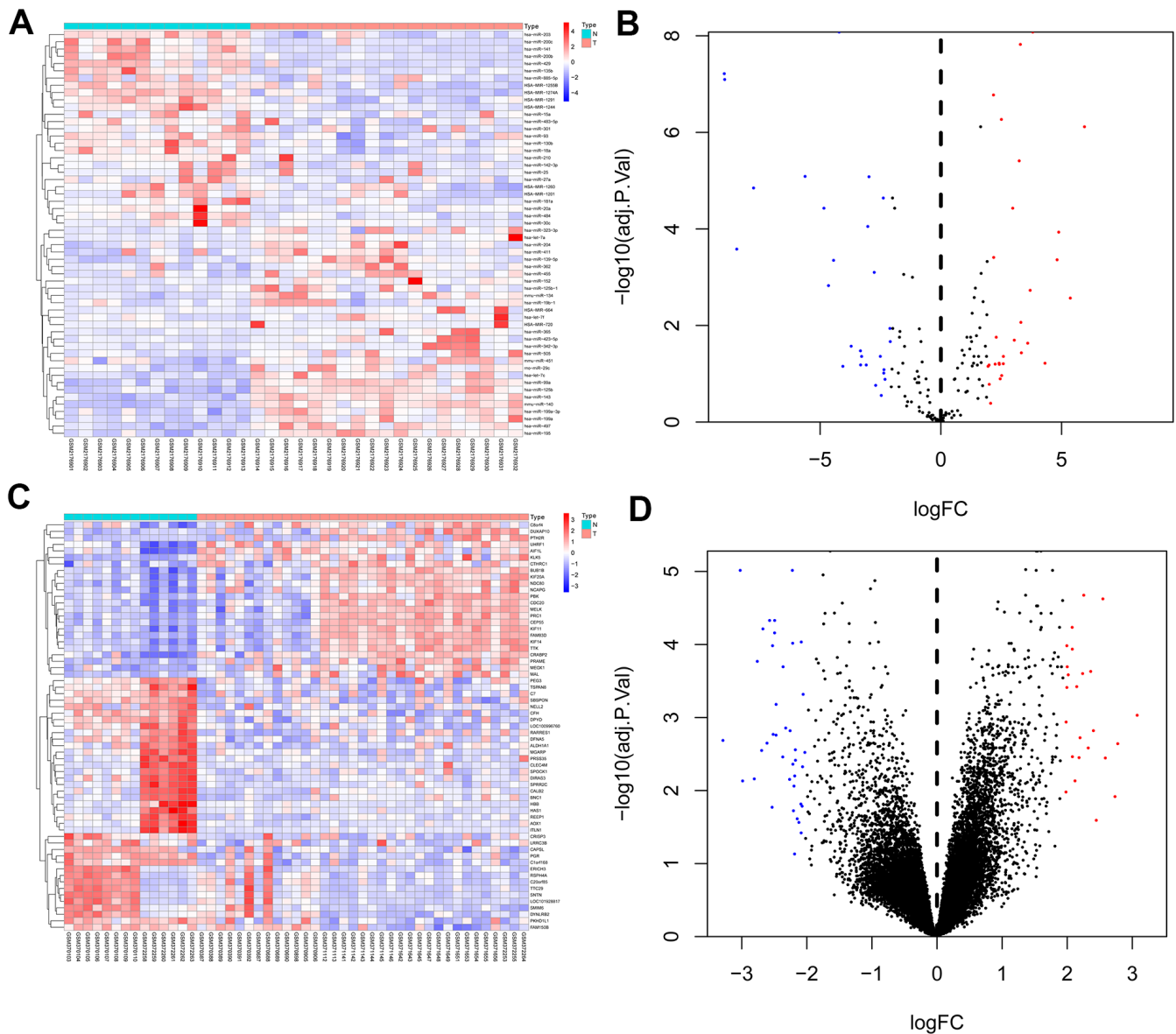


Figure 1. Heat map and volcano map of differentially expressed genes of GSE81873 and GSE27651. (A). Heat map of DEGs in GSE81873. **(B).** Volcano map of DEGs in GSE81873. **(C).** Heat map of DEGs in GSE27651. **(D).** Volcano map of DEGs in GSE27651. Red dots represent up-regulated genes and blue or green dots represent down-regulated genes.

Confirmation of the association between miR-142-3p and FAM83D

The Dual-Luciferase Reporter Assay System was utilized to evaluate the association between FAM83D and microRNA-142-3p. The FAM83D-WT activity of wild-type luciferase was 36.40%, and the FAM83D-MUT activity of mutant luciferase was 72.80%. These outcomes indicated that microRNA-142-3p reduced the luciferase activity of the wild-type FAM83D reporter gene (Figure 6).

DISCUSSION

In 2020, there were 19.29 million new cancer cases worldwide, including 10.06 million males and 9.23

million females; In 2020, there were 9.96 million cancer deaths worldwide, including 5.53 million males and 4.43 million females [11, 12]. In this research, GSE81873 and GSE27651 were obtained in the GEO database. 56 DEMs and 63 DEGs were identified. For deeply understanding the process of the 56 DEMs in OC, FunRich and R software were utilized for further study. GO and KEGG analysis indicated that these DEMs were primarily associated with the Cytoplasm, Nucleus, and Transcription factor activity. Previous studies have shown that Lysosomes and Nucleus may function as a vital role in plenty of human diseases, such as tumors, obesity, and infection [13–15]. Furthermore, KEGG analysis showed that DEGs were mainly enriched in 6 pathways such as MAPK signaling pathway, PI3K-Akt signaling pathway, Wnt signaling pathway, TGF-beta

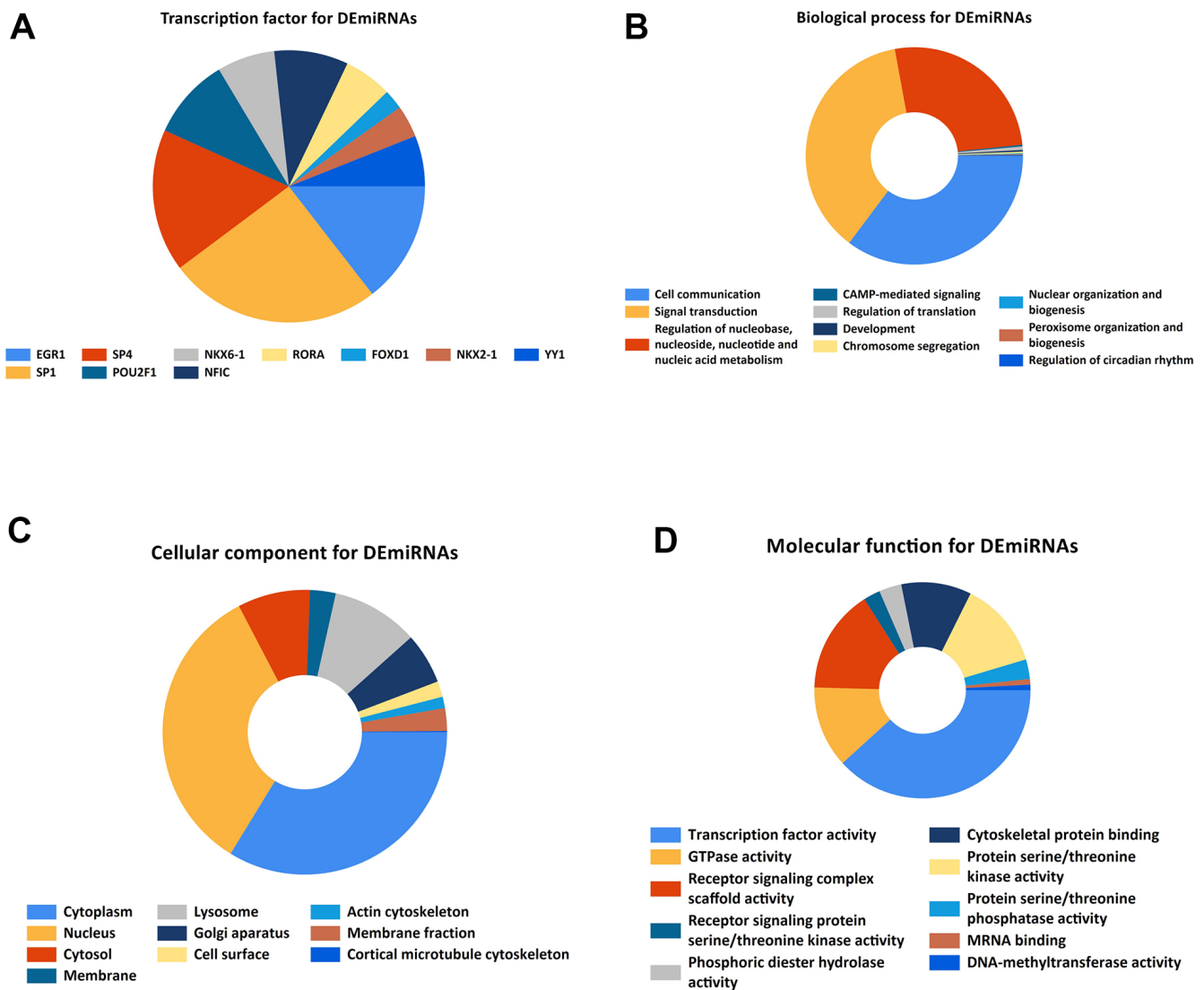


Figure 2. Gene ontology enrichment. (A). Identification of the potential transcription factors of DEMs by FunRich software. (B) biological process, (C) cellular component, and (D) molecular function enrichment analysis of the DEMs.

signaling pathway, Pathways in cancer, and Bacterial invasion of epithelial cells, which were indicated to influence migration and proliferation [16]. The MAPK signaling pathway is a common signaling pathway closely associated with carcinoma, which will not be

discussed here. Phosphatidylinositol-4,5-diphosphate-3-kinase (PI3K) is activated by many genes. In PI3K / Akt signal transduction pathway, phospholipid dependent kinase promotes the binding of protein kinase B (Akt) to the cell membrane. The phosphorylation of threonine

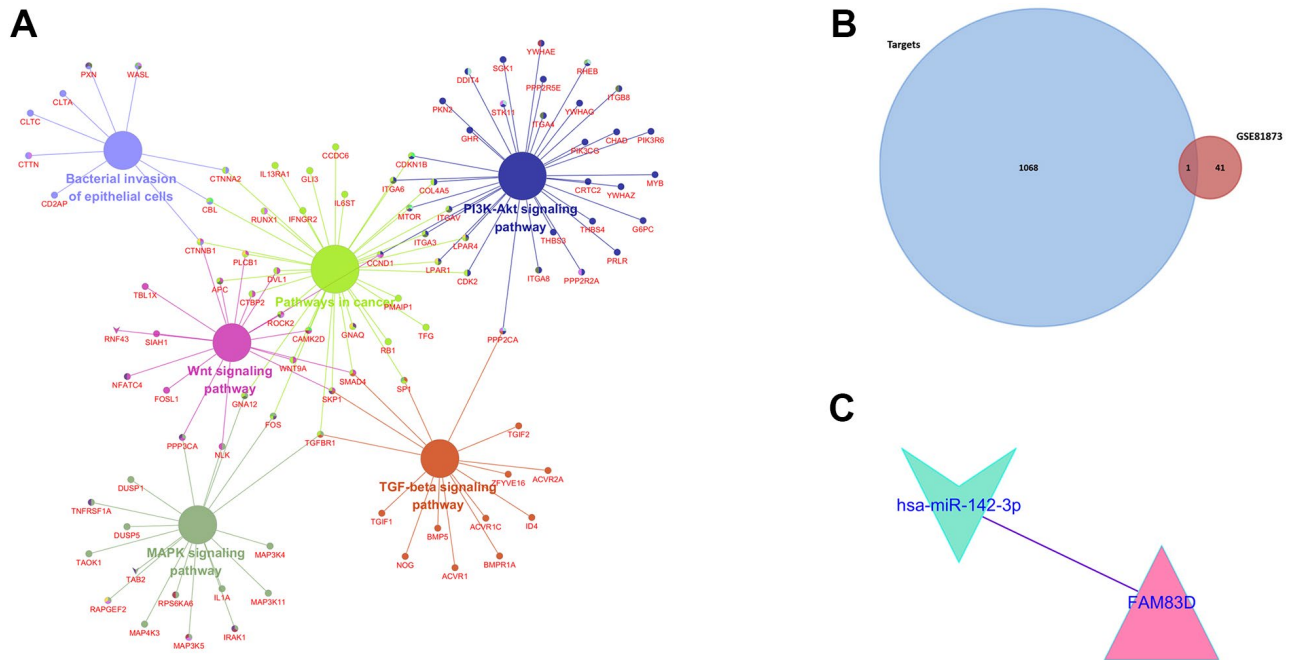


Figure 3. (A). KEGG pathway enrichment analysis of potential target mRNAs. (B). Venn Diagram of GSE81873 and GSE27651. (C). Identified target mRNAs and miRNA-mRNA regulatory network.

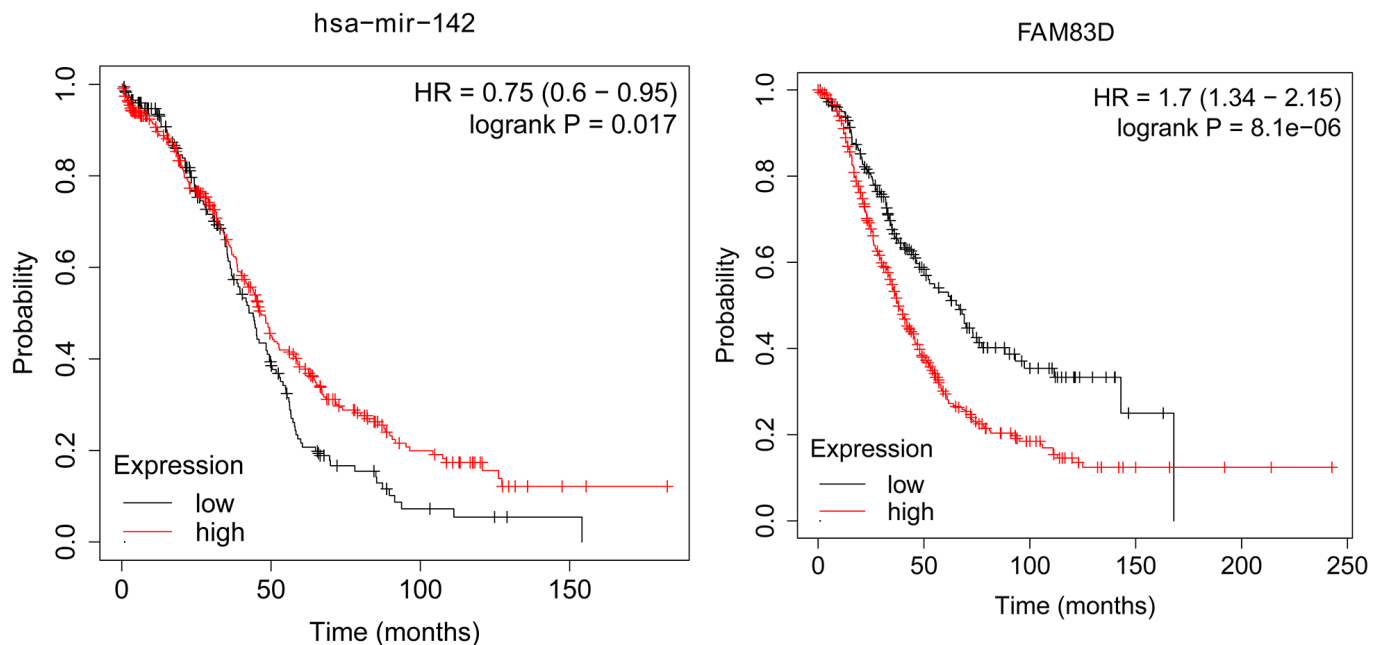


Figure 4. The association between the expression level of selected genes and overall survival of OC patients.

Table 1. Relationship between the expression level of FAM83D and clinical characteristics in OC.

Characteristic	Low expression of FAM83D	High expression of FAM83D	p
n	189	190	
FIGO stage, n (%)			0.007
Stage I	0 (0%)	1 (0.3%)	
Stage II	53 (13.9%)	10 (2.7%)	
Stage III	100 (26.3%)	155 (41.2%)	
Stage IV	35 (9.3%)	22 (5.9%)	
Primary therapy outcome, n (%)			0.484
PD	12 (3.9%)	15 (4.9%)	
SD	14 (4.5%)	8 (2.6%)	
PR	22 (7.1%)	21 (6.8%)	
CR	102 (33.1%)	114 (37%)	
Race, n (%)			0.840
Asian	5 (1.4%)	7 (1.9%)	
Black or African American	13 (3.6%)	12 (3.3%)	
White	161 (44.1%)	167 (45.8%)	
Age, n (%)			0.383
≤60	99 (26.1%)	109 (28.8%)	
>60	90 (23.7%)	81 (21.4%)	
Age, median (IQR)	60 (52, 68)	58 (50, 68)	0.390

Table 2. Relationship between the expression level of hsa-miR-142-3p and clinical characteristics in OC.

Characteristic	Low expression of hsa-miR-142-3p	High expression of hsa-miR-142-3p	p
n	248	248	
FIGO stage, n (%)			0.009
Stage I	0 (0%)	1 (0.2%)	
Stage II	13 (2.6%)	76 (15.3%)	
Stage III	199 (40.4%)	123 (24.8%)	
Stage IV	35 (7.1%)	45 (9.1%)	
Primary therapy outcome, n (%)			0.210
PD	21 (5.1%)	15 (3.7%)	
SD	16 (3.9%)	9 (2.2%)	
PR	24 (5.9%)	32 (7.8%)	
CR	139 (34.1%)	152 (37.3%)	
Race, n (%)			0.472
Asian	10 (2.1%)	6 (1.3%)	
Black or African American	14 (2.9%)	18 (3.8%)	
White	215 (44.9%)	216 (45.1%)	
Age, n (%)			0.786
≤60	139 (28%)	135 (27.2%)	
>60	109 (22%)	113 (22.8%)	
Age, median (IQR)	58.5 (51, 69)	59 (51.75, 68.25)	0.873

Table 3. Relationship between overall survival and the expression level of FAM83D researched by univariate and multivariate Cox regression.

Characteristics	Total(N)	Univariate analysis		Multivariate analysis	
		Hazard ratio (95% CI)	P value	Hazard ratio (95% CI)	P value
FIGO stage	374				
Stage I & Stage II	24	Reference			
Stage III	293	2.045 (0.905-4.621)	0.085	1.850 (0.670-5.108)	0.235
Stage IV	57	2.495 (1.057-5.889)	0.037	2.563 (1.541-4.517)	0.041
Primary therapy outcome	307				
PD	27	Reference			
SD	22	0.441 (0.217-0.895)	0.023	0.463 (0.222-0.967)	0.040
PR	42	0.652 (0.384-1.107)	0.113	0.637 (0.360-1.126)	0.121
CR	216	0.152 (0.093-0.247)	<0.001	0.203 (0.120-0.344)	<0.001
Race	364				
Asian & Black or African American	37	Reference			
White	327	0.637 (0.405-1.004)	0.052	0.738 (0.434-1.255)	0.262
FAM83D	377	1.645 (1.916-3.192)	0.011		
Tumor status	336				
Tumor free	72	Reference			
With tumor	264	9.576 (4.476-20.486)	<0.001	9.616 (3.875-23.866)	<0.001

Table 4. Relationship between overall survival and the expression level of hsa-miR-142-3p researched by univariate and multivariate Cox regression.

Characteristics	Total(N)	Univariate analysis		Multivariate analysis	
		Hazard ratio (95% CI)	P value	Hazard ratio (95% CI)	P value
FIGO stage	490				
Stage I & Stage II	30	Reference			
Stage III	380	2.179 (1.076-4.411)	0.031	1.513 (1.664-3.446)	0.004
Stage IV	80	2.785 (1.331-5.829)	0.007	1.333 (1.563-3.155)	0.013
Primary therapy outcome	407				
PD	36	Reference			
SD	25	0.453 (0.241-0.854)	0.014	0.452 (0.237-0.862)	0.016
PR	55	0.668 (0.426-1.047)	0.079	0.635 (0.400-1.010)	0.055
CR	291	0.168 (0.112-0.251)	<0.001	0.211 (0.139-0.319)	<0.001
Race	478				
Asian & Black or African American	48	Reference			
White	430	0.764 (0.513-1.138)	0.186		
hsa-miR-342-3p	494	0.835 (0.738-0.946)	0.005	1.910 (1.783-2.458)	0.019
Tumor status	442				
Tumor free	95	Reference			
With tumor	347	8.796 (4.784-16.170)	<0.001	8.362 (4.057-17.236)	<0.001

and serine promotes the transfer of Akt from the cytoplasm to the nucleus and further mediates the biological effects of enzymes, including cell proliferation, inhibition of apoptosis, cell migration, vesicle transport, and cell carcinogenesis [17]. Besides, it can influence the epithelial-mesenchymal transition in

plenty of methods to affect tumor aggressiveness [18]. As for OC, a previous study reported that it took an important part in OC tumorigenesis, proliferation and progression, and pre-clinical and clinical experience with several PI3K/AKT/mTOR pathway inhibitors [19]. Neurotrophins are produced by target tissues innervated

by developing neurons, so these factors act on the end of axons and produce signals that must be transmitted back to the cell body [20]. It can activate the PI3K/Akt signal transduction pathway and other oncogenic signaling pathways [21]. For example, it has been confirmed that in the early stage of cancer, the increase of nerve density is parallel to the increase of neurotrophin level, but it remains to be clarified which cells in TME are the source of neurotrophin and the nature of the stimulants that initiate the production of neurotrophin [22]. Besides, a previous study reported that Neurotrophin Receptor

TrkB (NTRK2) and Wnt β -Estradiol and MAPK signaling pathways are closely related to the worse prognosis of neuroblastoma [23]. Besides, the changes in neurotrophin signals are related to neurodegenerative diseases and mental diseases [24].

The regulated network was performed according to Cytoscape. 56 miRNAs (hsa-microRNA-142-3p, hsa-microRNA-429, hsa-microRNA-199a-3p, and hsa-microRNA-484) were selected for further research. After that, 1069 target genes were achieved and 1 of them

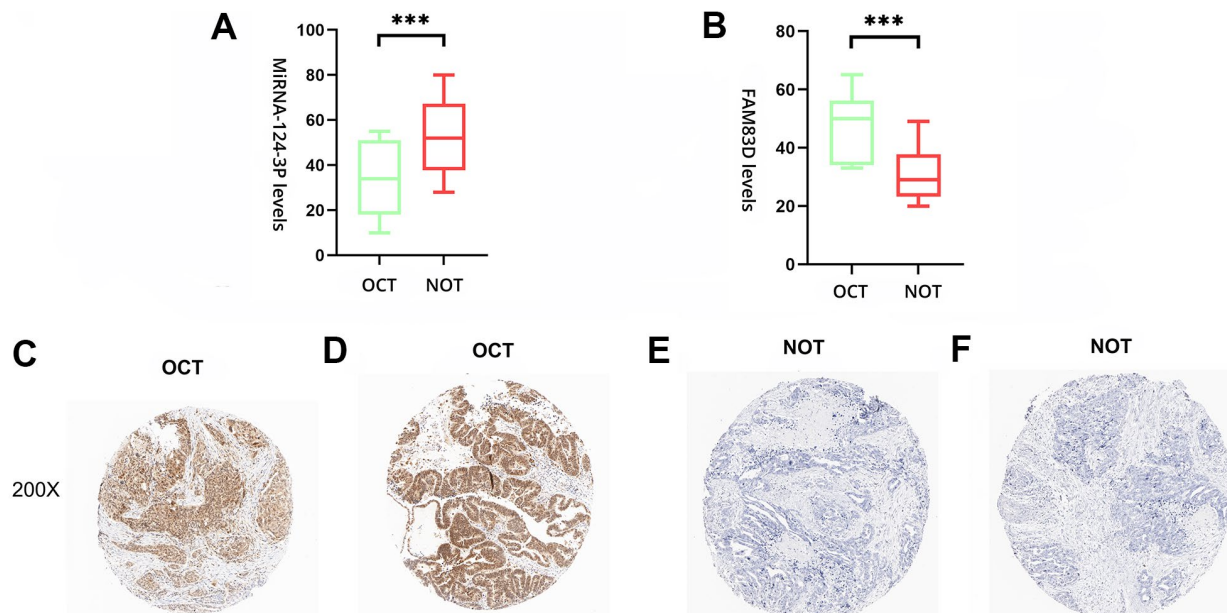


Figure 5. The expression level of hsa-miR-142-3p and FAM83D in normal ovarian tissues (NOTs) and OC tissues (OCTs). (A). Validation of hsa-miR-142-3p (***, $p < 0.001$). (B). Validation of FAM83D (***, $p < 0.001$). (C, D). The expression level of FAM83D in human OCTs. (E, F). The expression level of FAM83D in human NOTs (scale bar: 200 \times).

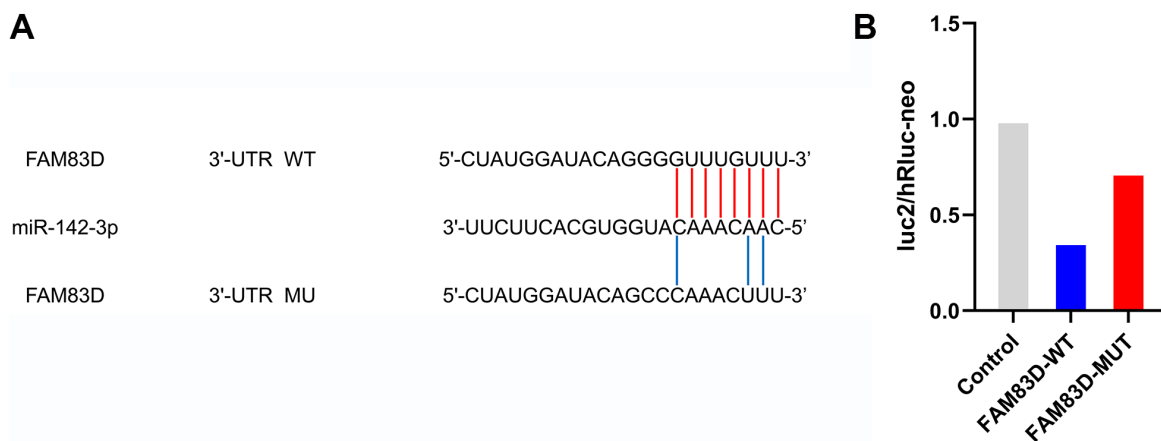


Figure 6. FAM83D is a direct target of miR-142-3p in OC cells. (A) Putative binding sites in FAM83D 3'UTR for miR-142-3p were predicted by bioinformatics analysis (microRNA.org). (B). Validation of luc2/hRluc-neo between miR-142-3p and FAM83D.

showed a different expression level in GSE27651 (FAM83D). MicroRNA-142-3p encoding human chromosome 17q22 is a new tumor suppressor factor, which is observed in many tumors including breast carcinoma, hepatocellular carcinoma, bladder carcinoma, and ovarian carcinoma [25–30]. The downregulation of microRNA-142-3p is related to tumorigenesis via regulation, cell migration, cell apoptosis, and invasion through various signaling pathways. Besides, microRNA-142-3p has been found as a carcinogenic microRNA in human T-cell acute lymphoblastic leukemia by acting on glucocorticoid receptors and cyclic adenosine monophosphate/protein kinase A pathway [31]. Upregulated microRNA-142-3p also monitors the characteristics of breast carcinoma stem cells, at least in section by sensitizing the WNT signaling pathway and microRNA-150 expression [32]. A previous study reported that upregulated microRNA-142-3p inhibited colorectal cancer cell migration and invasion, indicating that microRNA-142-3p may act as an oncogene during colorectal cancer tumorigenesis [33]. As for OC, another study concluded that microRNA-142-3p suppressed the proliferation and chemoresistance of OC cells by targeting SIRT1. This indicates that microRNA-142-3p may be a therapeutic target for the cure of OC [27].

FAM83D (family with sequence similarity 83, member D) is a mitosis-related gene located on chromosome 20q11 [34]. Previous studies have indicated that FAM83D may be amplified and upregulated in a variety of tumors, including hepatocellular tumors [35], ovarian carcinoma [36], colorectal carcinoma [37], and lung adenocarcinoma [38]. In addition, researches have demonstrated that FAM83D may act as a carcinogenic role by suppressing the invasion and proliferation of hepatocellular carcinoma and inhibiting the cell cycle of lung adenocarcinoma by suppressing FBXW7 in breast carcinoma [39–41]. These outcomes indicated that FAM83D may be widely taken part in process of tumors. Besides, FAM83D can advance epithelial-mesenchymal transition and metastasis of non-small cell lung carcinoma cells through the AKT/mTOR signal pathway, also improve the sensitivity of NSCLC cells to cisplatin [42]. Furthermore, FAM83D is highly expressed in invasive epithelial ovarian cancer and is related to tumor stage and grade [43]. Last but not least, FAM83D can also promote ovarian carcinoma cell invasion and proliferation, while suppressing autophagy through the PI3K/AKT/mTOR signaling pathway [44]. Therefore, we selected and tested whether microRNA-142-3p and FAM83D were differently expressed between NOTs and OCTs. qPCR results indicated that microRNA-142-3p and FAM83D were differentially expressed in NOTs and OCTs. Besides, IHC results indicated that FAM83D had a significant difference in OCTs compared with NOTs.

Many studies have shown that the abnormal expression of miRNAs is caused by gene aberrations (including genetic and epigenetic changes) of many cancer types, and plays a role in the occurrence and development of cancer through the imbalance of target gene expression. Therefore, many miRNAs and their target genes are closely related to the pathogenesis of tumors, including cell proliferation, cell survival, and cell invasion. Our study indicated that plenty of DEGs and DEMs were taken part in the process of OC by some pathways and had prognostic value. Therefore, suppression of FAM83D and upregulated miR-142-3p may have latent remedy worth in OC patients.

CONCLUSIONS

Our study indicated some reasons for the procession of OC. Plenty of DEMs and DEGs were selected between OC tissues and normal ovarian tissues. Besides, miR-142-3p and FAM83D were selected as latent biomarkers of OC. qPCR and IHC results indicated that microRNA-142-3p and FAM83D were differentially expressed in OC tissues. Besides, luciferase reporter assays verified that FAM83D was a direct target of miR-142-3p in OC cells. However, we need more cell experiments to prove it.

MATERIALS AND METHODS

Microarray data

The RNA-seq data of OC samples and corresponding normal ovarian tissues were retrieved from the GEO dataset (<https://www.ncbi.nlm.nih.gov/geo/>). The datasets of GSE81873 and GSE27651 were downloaded and divided into two groups.

Differently expressed miRNAs research

GEO2R is software for differential analysis of expression microarray based on the GEO database.

Limma R package was used to identify DEGs in the construction cohort. The screening standards of DEGs for functional enrichment analysis were $|\log_2FC| > 1$ and $FDR < 0.05$.

Gene ontology and pathway enrichment analysis

Transcription factors (TF), Kyoto Encyclopedia of Genes and Genomes (KEGG), and Gene Ontology (GO) enrichment analyses of the DEGs were performed by using R clusterProfiler package, including the package of "GOplot", "ggplot2", "stringi", "colorspace" and "digest". Then, the pathway and process enrichment analyses were carried out by using Cytoscape.

MicroRNA-mRNA regulatory network

At present, there are two generally recognized miRNA mechanisms: miRNA-mediated mRNA translation inhibition and miRNA-mediated mRNA-specific cleavage. In addition, researchers also found that miRNA may have other regulatory mechanisms, such as regulating the localization or stability of target mRNA, or acting on target molecules other than mRNAs, such as complementary binding with regulatory non-coding RNA or even miRNA, or competing with other RNAs to bind proteins to achieve its regulatory function. DEMs were uploaded to the FunRich software to achieve target mRNAs. Furthermore, GSE27651 was researched by utilizing R software. Based on the prediction conclusions of target mRNAs in FunRich software and the differentially expressed mRNAs of GSE27651, the microRNA-mRNA network was constructed.

The association between the expression level of identified genes and overall survival of patients with OC

Kaplan Meier plotter can assess the impact of 54K (mRNA, miRNA, protein) on the survival rate of 21 types of cancer (including breast cancer (n = 6234), ovarian cancer (n = 2190), lung cancer (n = 3452) and gastric cancer (n = 1440)). The sources of the Kaplan Meier plotter database include GEO, EGA, and TCGA. The main purpose of the tool is the discovery and validation of survival biomarkers based on a meta-analysis. In this study, patients with OC were divided into two groups. By uploading the DEGs we identified, corresponding survival curves were obtained.

DEGs expression and clinical characteristics in the cancer genome atlas

The associated statistics offered by The Cancer Genome Atlas. The data of 1037 patients with ovarian cancer were downloaded in the TCGA database. The expression level of mRNAs, clinicopathological information, and general information of patients with OC were achieved.

Immunohistochemical staining

20 pairs of OC tissues were prepared by buffering with 10% formalin for 24 hours. The study was approved by the Ethics Committee of the Second Affiliated Hospital of Soochow University and informed consent was obtained from all patients. 2 consecutive 5- μ m sections were taken from each formalin-fixed paraffin-embedded block and mounted on the glass slide treated with aminoalkyl silane, dewaxing with xylene, passing through graded alcohol, and then continue rinsing in deionized water and phosphate-buffered saline. It was

blocked by 3% non-immune horse serum. The sections were incubated with broad-spectrum anti-cytokeratin AE1 / 3 (Dako, Santa Barbara, CA, USA) in 1:50 dilution overnight at room temperature. After washing twice in buffer, an appropriate biotinylated secondary antibody was applied for 30 minutes. After two more washes in the buffer, appropriate biotinylated secondary antibodies were applied for 30 minutes. The sections were developed under the microscope in Tris HCl buffer (pH 7.4) and 0.03% hydrogen peroxide for 20 minutes. Application of light Mayer hematoxylin. The expressions of FAM83D and β - Catenin were detected by the Chi-square test or Fisher exact test. GraphPad Prism 9 software was utilized for statistical analysis. P-value < 0.05 was considered statistically significant.

Real-time quantitative polymerase chain reaction

Total RNA was extracted from OC tissues and normal tissues by utilizing TRIzol reagents (Invitrogen, Carlsbad, CA, USA) as per the manufacturer's instructions. The total RNA was reverse-transcribed into cDNA by utilizing a PrimeScriptTMRT kit with gDNA Eraser (TaKaRa, China). We also constructed Quantitative Real-time PCR (qRT-PCR) by using SYBR Select Master Mix for CFX (Invitrogen) and the CFX Connect Real-Time PCR System (BioRad). The amplification conditions are 95° C for 15s, then 40 cycles, 95° C for 5S, 60° C for the 30s. Primer sequences of FAM83D were as follows: primer F, 5'- GCACTTCCCTTTGTTGTA GTC -3', primer R, 5'-AGCACTTCCCTTAGG TTACTC -3'. Using glyceraldehyde-3-phosphate dehydrogenase (GAPDH) as endogenous control, the recorded data were analyzed and processed by 2- $\Delta\Delta$ Ct.

Luciferase reporter assay

The relationship between miR-142-3p and FAM83D was verified by performing a luciferase reporter assay. To construct a luciferase ratio vector, we amplified the wild or mutant fragment FAM83D 3' '- UTR containing the hypothetical binding site miR-142-3p and subcloned it into luciferase pLUC vector (Wuhan, Ruibo, China). OC cells were co-transfected with pLUC-FAM83D 3' '- UTR wild (WT) or pLUC-FAM83D 3' '- UTR (MU) mutants and miR-142-3p or NC analogues using Lipofectamine 2000 according to the manufacturer's instructions. After 48 hours of transfection, the relative activities of luciferase and double luciferase were detected by the analytical system (Promega, Madison, WI, USA). The luciferase activity of fireflies was normalized to *Renilla* luciferase activity.

Statistical methods

The data were expressed as mean \pm standard error. All data analyses were performed using R software (version 3.6.6) and GraphPad Prism 9 software package (GraphPad Software, Inc., La Jolla, California, USA). The differences between the two addiction groups were compared by student's t-test. All the experiments were made in triplicate.

Availability of data and materials

The datasets used and/or analyzed during the current study are available from the corresponding author on reasonable request.

Ethics approval and consent to participate

The study was conducted according to the guidelines of the Declaration of Helsinki, and approved by the Ethics Committee of the Soochow University.

AUTHOR CONTRIBUTIONS

Conceptualization, Xiaofei Guo; Methodology, Guangyu Gao; Software, Wenyong Gu; Validation, Guangyu Gao; Formal Analysis, Guangyu Gao.; Investigation, Yufeng Lu; Resources, Guangyu Gao; Data Curation, Guangyu Gao; Writing – Original Draft Preparation, Guangyu Gao; Writing – Review and Editing, Guangyu Gao; Visualization, Guangyu Gao; Supervision, Zhigang Chen; Project Administration, Zhigang Chen; Funding Acquisition, Zhigang Chen.

CONFLICTS OF INTEREST

The authors declare that they have no conflicts of interest.

FUNDING

This study was approved by Pre-Research Project of the National Natural Science Foundation of China (SDFEYGJ2014); Suzhou Science and Technology Development Project (SYSD2019108); Science and Technology Program of Suzhou City (SLJ2021012).

REFERENCES

1. Siegel RL, Miller KD, Jemal A. Cancer statistics, 2020. *CA Cancer J Clin.* 2020; 70:7–30. <https://doi.org/10.3322/caac.21590> PMID:31912902
2. Lheureux S, Gourley C, Vergote I, Oza AM. Epithelial ovarian cancer. *Lancet.* 2019; 393:1240–53. [https://doi.org/10.1016/S0140-6736\(18\)32552-2](https://doi.org/10.1016/S0140-6736(18)32552-2) PMID:30910306
3. Wilson MK, Pujade-Lauraine E, Aoki D, Mirza MR, Lorusso D, Oza AM, du Bois A, Vergote I, Reuss A, Bacon M, Friedlander M, Gallardo-Rincon D, Joly F, et al, and participants of the Fifth Ovarian Cancer Consensus Conference. Fifth Ovarian Cancer Consensus Conference of the Gynecologic Cancer InterGroup: recurrent disease. *Ann Oncol.* 2017; 28:727–32. <https://doi.org/10.1093/annonc/mdw663> PMID:27993805
4. Kossaï M, Leary A, Scoazec JY, Genestie C. Ovarian Cancer: A Heterogeneous Disease. *Pathobiology.* 2018; 85:41–9. <https://doi.org/10.1159/000479006> PMID:29020678
5. Bushati N, Cohen SM. microRNA functions. *Annu Rev Cell Dev Biol.* 2007; 23:175–205. <https://doi.org/10.1146/annurev.cellbio.23.090506.123406> PMID:17506695
6. Simonson B, Das S. MicroRNA Therapeutics: the Next Magic Bullet? *Mini Rev Med Chem.* 2015; 15:467–74. <https://doi.org/10.2174/1389557515666150324123208> PMID:25807941
7. Krol J, Loedige I, Filipowicz W. The widespread regulation of microRNA biogenesis, function and decay. *Nat Rev Genet.* 2010; 11:597–610. <https://doi.org/10.1038/nrg2843> PMID:20661255
8. Tong J, Lu J, Yin Y, Wang Y, Zhang K. microRNA-195 Promotes Small Cell Lung Cancer Cell Apoptosis via Inhibiting Rap2C Protein-Dependent MAPK Signal Transduction. *Technol Cancer Res Treat.* 2020; 19:1533033820977546. <https://doi.org/10.1177/1533033820977546> PMID:33302819
9. Wu Y, Shen Q, Chen X, Wu Y, Niu Y, Lv F. miR-1301-3p promotes the proliferation and migration of lung cancer cells via direct repression of polymerase I and transcript release factor. *Oncol Lett.* 2020; 20:286. <https://doi.org/10.3892/ol.2020.12149> PMID:33014164
10. Katakura S, Kobayashi N, Hashimoto H, Kamimaki C, Tanaka K, Kubo S, Nakashima K, Teranishi S, Manabe S, Watanabe K, Horita N, Hara Y, Yamamoto M, et al. MicroRNA-200b is a potential biomarker of the expression of PD-L1 in patients with lung cancer. *Thorac Cancer.* 2020; 11:2975–82. <https://doi.org/10.1111/1759-7714.13653> PMID:32893980
11. Laconi E, Marongiu F, DeGregori J. Cancer as a disease of old age: changing mutational and microenvironmental landscapes. *Br J Cancer.* 2020; 122:943–52.

- <https://doi.org/10.1038/s41416-019-0721-1>
PMID:[32042067](https://pubmed.ncbi.nlm.nih.gov/32042067/)
12. Thong MS, van Noorden CJ, Steindorf K, Arndt V. Cancer-Related Fatigue: Causes and Current Treatment Options. *Curr Treat Options Oncol*. 2020; 21:17.
<https://doi.org/10.1007/s11864-020-0707-5>
PMID:[32025928](https://pubmed.ncbi.nlm.nih.gov/32025928/)
 13. Ballabio A. The awesome lysosome. *EMBO Mol Med*. 2016; 8:73–6.
<https://doi.org/10.15252/emmm.201505966>
PMID:[26787653](https://pubmed.ncbi.nlm.nih.gov/26787653/)
 14. Pucino V, Cucchi D, Mauro C. Lactate transporters as therapeutic targets in cancer and inflammatory diseases. *Expert Opin Ther Targets*. 2018; 22:735–43.
<https://doi.org/10.1080/14728222.2018.1511706>
PMID:[30106309](https://pubmed.ncbi.nlm.nih.gov/30106309/)
 15. Payen VL, Hsu MY, Räddecke KS, Wyart E, Vazeille T, Bouzin C, Porporato PE, Sonveaux P. Monocarboxylate Transporter MCT1 Promotes Tumor Metastasis Independently of Its Activity as a Lactate Transporter. *Cancer Res*. 2017; 77:5591–601.
<https://doi.org/10.1158/0008-5472.CAN-17-0764>
PMID:[28827372](https://pubmed.ncbi.nlm.nih.gov/28827372/)
 16. Galli L, Marcelli G. [Water-electrolyte balances in urological surgery]. *Arch Ital Urol Nefrol*. 1968; 41:199–217.
PMID:[5737700](https://pubmed.ncbi.nlm.nih.gov/5737700/)
 17. Xie Y, Shi X, Sheng K, Han G, Li W, Zhao Q, Jiang B, Feng J, Li J, Gu Y. PI3K/Akt signaling transduction pathway, erythropoiesis and glycolysis in hypoxia (Review). *Mol Med Rep*. 2019; 19:783–91.
<https://doi.org/10.3892/mmr.2018.9713>
PMID:[30535469](https://pubmed.ncbi.nlm.nih.gov/30535469/)
 18. Xu W, Yang Z, Lu N. A new role for the PI3K/Akt signaling pathway in the epithelial-mesenchymal transition. *Cell Adh Migr*. 2015; 9:317–24.
<https://doi.org/10.1080/19336918.2015.1016686>
PMID:[26241004](https://pubmed.ncbi.nlm.nih.gov/26241004/)
 19. Ediriweera MK, Tennekoon KH, Samarakoon SR. Role of the PI3K/AKT/mTOR signaling pathway in ovarian cancer: Biological and therapeutic significance. *Semin Cancer Biol*. 2019; 59:147–60.
<https://doi.org/10.1016/j.semcancer.2019.05.012>
PMID:[31128298](https://pubmed.ncbi.nlm.nih.gov/31128298/)
 20. Hamanaka D, Suzuki T, Kawanishi K, Sakamoto T, Yamazaki T, Odori T, Ishii Y, Torizuka K. Two cases of primary isolated chylopericardium diagnosed by oral administration of 131I-triolein. *Radiat Med*. 1983; 1:65–9.
PMID:[6093198](https://pubmed.ncbi.nlm.nih.gov/6093198/)
 21. Hinz E. [Contribution to the standardization of experimental cysticercosis of the mouse as a model experiment for testing of agents effective against cysticercus]. *Z Tropenmed Parasitol*. 1965; 16:322–31.
PMID:[5885829](https://pubmed.ncbi.nlm.nih.gov/5885829/)
 22. Dittrich M, Thomas AK, Stelma FF, Talla I, Niang M, Decam C, Sow S, Mbaye A, Gryseels B, Ehrich JH, Doehring E. Preliminary ultrasonographical observations of intestinal lesions in a community with heavy *Schistosoma mansoni* infection in Richard Toll, Senegal. *Acta Trop*. 1994; 58:331–6.
[https://doi.org/10.1016/0001-706x\(94\)90026-4](https://doi.org/10.1016/0001-706x(94)90026-4)
PMID:[7709871](https://pubmed.ncbi.nlm.nih.gov/7709871/)
 23. Ruckes J, Stallkamp B. [On an unusually large neurinoma of the lung]. *Zentralbl Allg Pathol*. 1967; 110:306–13.
PMID:[5303304](https://pubmed.ncbi.nlm.nih.gov/5303304/)
 24. Watanabe M, Usui T, Shimizu M, Ito K, Okawara C. [Round table discussion; current status of the administrator of a nursing school and his problems]. *Kango Kyoiku*. 1968; 9:12–24.
PMID:[5187584](https://pubmed.ncbi.nlm.nih.gov/5187584/)
 25. Mansoori B, Mohammadi A, Gjerstorff MF, Shirjang S, Asadzadeh Z, Khaze V, Holmskov U, Kazemi T, Duijf PH, Baradaran B. miR-142-3p is a tumor suppressor that inhibits estrogen receptor expression in ER-positive breast cancer. *J Cell Physiol*. 2019; 234:16043–53.
<https://doi.org/10.1002/jcp.28263>
PMID:[30741415](https://pubmed.ncbi.nlm.nih.gov/30741415/)
 26. Hua S, Liu C, Liu L, Wu D. miR-142-3p inhibits aerobic glycolysis and cell proliferation in hepatocellular carcinoma via targeting LDHA. *Biochem Biophys Res Commun*. 2018; 496:947–54.
<https://doi.org/10.1016/j.bbrc.2018.01.112>
PMID:[29360449](https://pubmed.ncbi.nlm.nih.gov/29360449/)
 27. Gao J, Wu N, Liu X, Xia Y, Chen Y, Li S, Deng Z. MicroRNA-142-3p inhibits cell proliferation and chemoresistance in ovarian cancer via targeting sirtuin 1. *Exp Ther Med*. 2018; 15:5205–14.
<https://doi.org/10.3892/etm.2018.6107>
PMID:[29904404](https://pubmed.ncbi.nlm.nih.gov/29904404/)
 28. Godfrey JD, Morton JP, Wilczynska A, Sansom OJ, Bushell MD. MiR-142-3p is downregulated in aggressive p53 mutant mouse models of pancreatic ductal adenocarcinoma by hypermethylation of its locus. *Cell Death Dis*. 2018; 9:644.
<https://doi.org/10.1038/s41419-018-0628-4>
PMID:[29844410](https://pubmed.ncbi.nlm.nih.gov/29844410/)
 29. Lee YY, Yarmishyn AA, Wang ML, Chen HY, Chiou SH, Yang YP, Lin CF, Huang PI, Chen YW, Ma HI, Chen MT. MicroRNA-142-3p is involved in regulation of MGMT expression in glioblastoma cells. *Cancer Manag Res*. 2018; 10:775–85.

- <https://doi.org/10.2147/CMAR.S157261>
PMID:29695934
30. Li WQ, Zhao WC, Xin J, Niu TL, Chao YF, Zhou P, Zheng MH, Xu B. MicroRNA-142-3p suppresses cell proliferation and migration in bladder cancer via Rac1. *J Biol Regul Homeost Agents*. 2020. [Epub ahead of print].
<https://doi.org/10.23812/19-460-A> PMID:32107907
31. Lv M, Zhang X, Jia H, Li D, Zhang B, Zhang H, Hong M, Jiang T, Jiang Q, Lu J, Huang X, Huang B. An oncogenic role of miR-142-3p in human T-cell acute lymphoblastic leukemia (T-ALL) by targeting glucocorticoid receptor- α and cAMP/PKA pathways. *Leukemia*. 2012; 26:769–77.
<https://doi.org/10.1038/leu.2011.273>
PMID:21979877
32. Isobe T, Hisamori S, Hogan DJ, Zabala M, Hendrickson DG, Dalerba P, Cai S, Scheeren F, Kuo AH, Sikandar SS, Lam JS, Qian D, Dirbas FM, et al. miR-142 regulates the tumorigenicity of human breast cancer stem cells through the canonical WNT signaling pathway. *Elife*. 2014; 3:e01977.
<https://doi.org/10.7554/eLife.01977>
PMID:25406066
33. Gao X, Xu W, Lu T, Zhou J, Ge X, Hua D. MicroRNA-142-3p Promotes Cellular Invasion of Colorectal Cancer Cells by Activation of RAC1. *Technol Cancer Res Treat*. 2018; 17:1533033818790508.
<https://doi.org/10.1177/1533033818790508>
PMID:30064309
34. Deloukas P, Matthews LH, Ashurst J, Burton J, Gilbert JG, Jones M, Stavrides G, Almeida JP, Babbage AK, Bagguley CL, Bailey J, Barlow KF, Bates KN, et al. The DNA sequence and comparative analysis of human chromosome 20. *Nature*. 2001; 414:865–71.
<https://doi.org/10.1038/414865a>
PMID:11780052
35. Ramakrishna M, Williams LH, Boyle SE, Bearfoot JL, Sridhar A, Speed TP, Goringe KL, Campbell IG. Identification of candidate growth promoting genes in ovarian cancer through integrated copy number and expression analysis. *PLoS One*. 2010; 5:e9983.
<https://doi.org/10.1371/journal.pone.0009983>
PMID:20386695
36. van Dekken H, Paris PL, Albertson DG, Alers JC, Andaya A, Kowbel D, van der Kwast TH, Pinkel D, Schröder FH, Vissers KJ, Wildhagen MF, Collins C. Evaluation of genetic patterns in different tumor areas of intermediate-grade prostatic adenocarcinomas by high-resolution genomic array analysis. *Genes Chromosomes Cancer*. 2004; 39:249–56.
<https://doi.org/10.1002/gcc.20001>
PMID:14732926
37. Yan L, Yao J, Qiu J. miRNA-495 suppresses proliferation and migration of colorectal cancer cells by targeting FAM83D. *Biomed Pharmacother*. 2017; 96:974–81.
<https://doi.org/10.1016/j.biopha.2017.11.138>
PMID:29221726
38. Inamura K, Shimoji T, Ninomiya H, Hiramatsu M, Okui M, Satoh Y, Okumura S, Nakagawa K, Noda T, Fukayama M, Ishikawa Y. A metastatic signature in entire lung adenocarcinomas irrespective of morphological heterogeneity. *Hum Pathol*. 2007; 38:702–9.
<https://doi.org/10.1016/j.humpath.2006.11.019>
PMID:17376511
39. Wang Z, Liu Y, Zhang P, Zhang W, Wang W, Curr K, Wei G, Mao JH. FAM83D promotes cell proliferation and motility by downregulating tumor suppressor gene FBXW7. *Oncotarget*. 2013; 4:2476–86.
<https://doi.org/10.18632/oncotarget.1581>
PMID:24344117
40. Liao W, Liu W, Liu X, Yuan Q, Ou Y, Qi Y, Huang W, Wang Y, Huang J. Upregulation of FAM83D affects the proliferation and invasion of hepatocellular carcinoma. *Oncotarget*. 2015; 6:24132–47.
<https://doi.org/10.18632/oncotarget.4432>
PMID:26125229
41. Shi R, Sun J, Sun Q, Zhang Q, Xia W, Dong G, Wang A, Jiang F, Xu L. Upregulation of FAM83D promotes malignant phenotypes of lung adenocarcinoma by regulating cell cycle. *Am J Cancer Res*. 2016; 6:2587–98.
PMID:27904773
42. Yin C, Lin X, Wang Y, Liu X, Xiao Y, Liu J, Snijders AM, Wei G, Mao JH, Zhang P. FAM83D promotes epithelial-mesenchymal transition, invasion and cisplatin resistance through regulating the AKT/mTOR pathway in non-small-cell lung cancer. *Cell Oncol (Dordr)*. 2020; 43:395–407.
<https://doi.org/10.1007/s13402-020-00494-9>
PMID:32006253
43. Zhang Q, Yu S, Lok SI, Wong AS, Jiao Y, Lee LT. FAM83D promotes ovarian cancer progression and its potential application in diagnosis of invasive ovarian cancer. *J Cell Mol Med*. 2019; 23:4569–81.
<https://doi.org/10.1111/jcmm.14360> PMID:31037837
44. Zhu H, Diao S, Lim V, Hu L, Hu J. FAM83D inhibits autophagy and promotes proliferation and invasion of ovarian cancer cells via PI3K/AKT/mTOR pathway. *Acta Biochim Biophys Sin (Shanghai)*. 2019; 51:509–16.
<https://doi.org/10.1093/abbs/gmz028>
PMID:30939187

Wild type and gain of function mutant TP53 can regulate the sensitivity of pancreatic cancer cells to chemotherapeutic drugs, EGFR/Ras/Raf/MEK, and PI3K/mTORC1/GSK-3 pathway inhibitors, nutraceuticals and alter metabolic properties

James A. McCubrey¹, Akshaya K. Meher¹, Shaw M. Akula¹, Stephen L. Abrams¹, Linda S. Steelman¹, Michelle M. LaHair¹, Richard A. Franklin¹, Alberto M. Martelli², Stefano Ratti², Lucio Cocco², Fulvio Barbaro³, Przemysław Duda⁴, Agnieszka Gizak⁴

¹Department of Microbiology and Immunology, Brody School of Medicine at East Carolina University, Greenville, NC 27858, USA

²Department of Biomedical and Neuromotor Sciences, Università di Bologna, Bologna, Italy

³Department of Medicine and Surgery, Re.Mo.Bio.S. Laboratory, Anatomy Section, University of Parma, Parma, Italy

⁴Department of Molecular Physiology and Neurobiology, University of Wrocław, Wrocław, Poland

Correspondence to: James A. McCubrey; **email:** mccubreyj@ecu.edu

Keywords: TP53, targeted therapy, PDAC, chemotherapeutic drugs, metabolic properties

Received: December 3, 2021

Accepted: January 20, 2022

Published: April 27, 2022

Copyright: © 2022 McCubrey et al. This is an open access article distributed under the terms of the [Creative Commons Attribution License](https://creativecommons.org/licenses/by/3.0/) (CC BY 3.0), which permits unrestricted use, distribution, and reproduction in any medium, provided the original author and source are credited.

ABSTRACT

TP53 is a master regulator of many signaling and apoptotic pathways involved in: aging, cell cycle progression, gene regulation, growth, apoptosis, cellular senescence, DNA repair, drug resistance, malignant transformation, metastasis, and metabolism. Most pancreatic cancers are classified as pancreatic ductal adenocarcinomas (PDAC). The tumor suppressor gene *TP53* is mutated frequently (50–75%) in PDAC. Different types of TP53 mutations have been observed including gain of function (GOF) point mutations and various deletions of the TP53 gene resulting in lack of the protein expression. Most PDACs have point mutations at the *KRAS* gene which result in constitutive activation of KRas and multiple downstream signaling pathways. It has been difficult to develop specific KRas inhibitors and/or methods that result in recovery of functional TP53 activity. To further elucidate the roles of TP53 in drug-resistance of pancreatic cancer cells, we introduced wild-type (WT) TP53 or a control vector into two different PDAC cell lines. Introduction of WT-TP53 increased the sensitivity of the cells to multiple chemotherapeutic drugs, signal transduction inhibitors, drugs and nutraceuticals and influenced key metabolic properties of the cells. Therefore, TP53 is a key molecule which is critical in drug sensitivity and metabolism of PDAC.

INTRODUCTION

Pancreatic cancer—a disease associated with aging that is diagnosed late in development and difficult to successfully treat

When a patient is diagnosed with pancreatic cancer, the outcome is poor [1–7]. There are four

stages of pancreatic cancer. This cancer is often detected at stage IV, the most advanced stage [1, 2, 5]. The age of the patient will influence the survival rate as younger pancreatic cancer patients (15–49 years old) have a better survival rate than the older patients (50 and above) [7]. Thus, pancreatic cancer is a disease associated with aging [8, 9].

Therapeutic approaches for pancreatic cancer

Most pancreatic cancers consist of pancreatic ductal adenocarcinoma (PDAC). They are often refractive to classical chemotherapeutic drugs. PDAC patients undergo surgery to remove the diseased part of the pancreas. However, as PDAC is frequently diagnosed late in the course of the disease, the PDAC has often metastasized to other organs making therapy difficult and ineffective [10–12]. PDACs are often refractive to chemotherapeutic drugs and have modest effects in terms of treatments of the disease [13–17].

Genes implicated in PDAC

Many genes have been implicated in PDAC including *KRAS*, *TP53*, *CDKN2A*, *SMAD4* and *PDGFβR* [3, 8, 9, 18–22]. Changes in the expression of these genes has many different effects and contribute to PDAC progression and metastasis [23–26]. The *TP53* gene can become mutated by various genetic mechanisms. Two

of the most common mechanisms of mutation of *TP53* are point mutations and deletions of part or the entire *TP53* gene. Certain point mutations at the *TP53* gene alter the activity of the TP53 protein and give the TP53 protein different properties. This class of *TP53* mutation is referred to as a gain-of-function (GOF) mutation [27–31]. Another class of *TP53* mutation results in the lack of expression of the TP53. This class of *TP53* mutation is referred to TP53-null [27–31].

Interestingly, a novel class of compounds have been developed which alter the structure of mutant TP53 and restore some of its properties which are important in suppression of cell growth [32, 33]. APR-246 is one such compound which has been examined in clinical trials. A summary of the effects of TP53 on various processes important in cell growth and metastasis is present in Figure 1.

KRAS is another important gene which is mutated in >90% of PDAC. Although many potential Ras

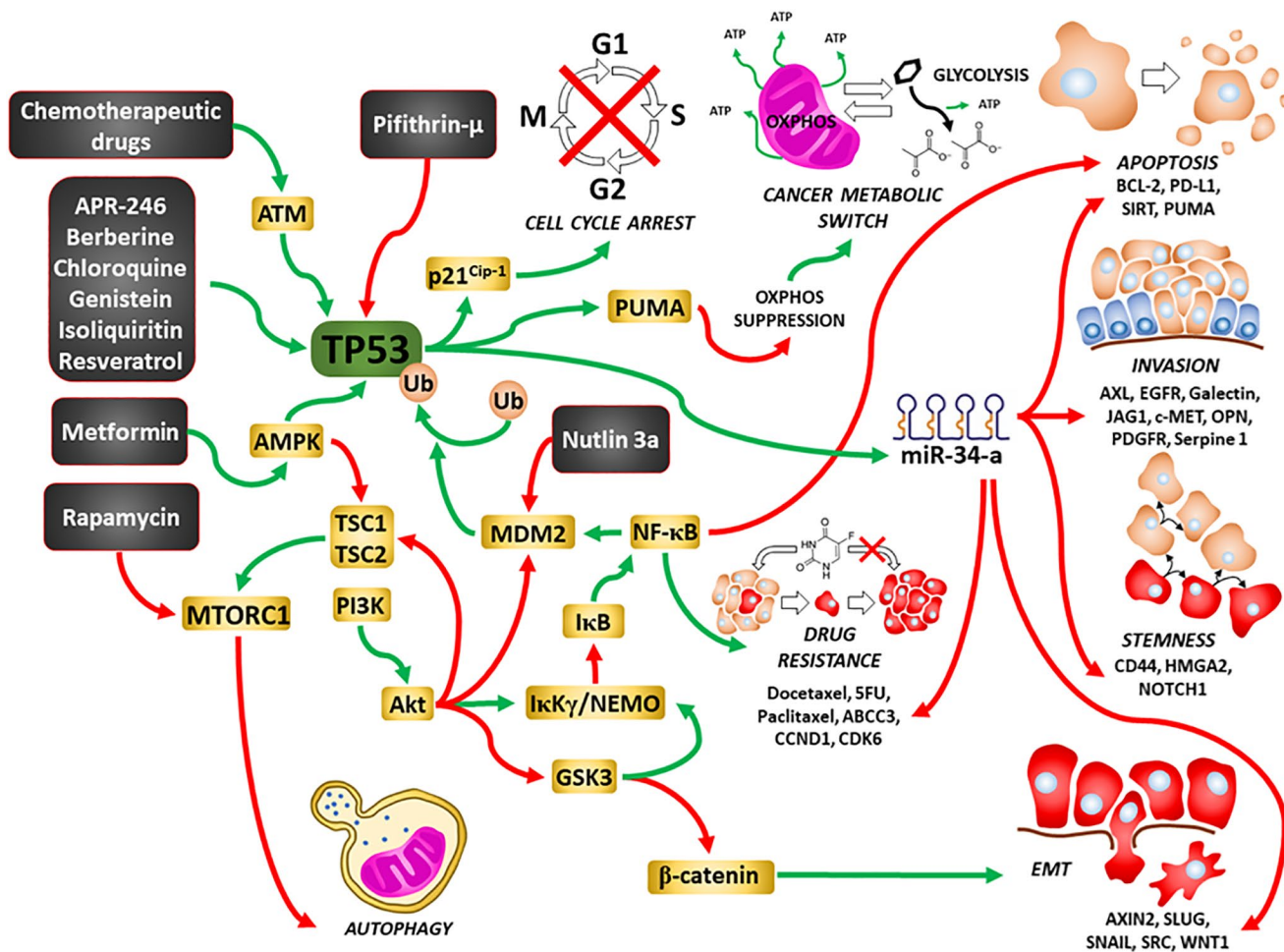


Figure 1. Illustration of TP53's interactions with other signaling pathways important in regulation of cell growth and sites of interaction for chemotherapeutic drugs, certain signal transduction inhibitors, natural products and nutraceuticals. Green arrows = induction of a pathway, red arrows = suppression of a pathway.

inhibitors were developed over the past 25 years, they were not specific to mutant KRas, recently, some have shown promise [34, 35]. As with most drugs, cancer cells have developed mechanisms to become resistant to these inhibitors [36]. In the following studies, we examined the consequences of introduction of WT-TP53 gene in two PDAC cell lines, one lacking TP53 expression (TP53-null) and one cell line with GOF-TP53 [37–39]. Earlier studies performed by us, indicated that inheritance of WT-TP53 increased the ability of some chemotherapeutic drugs, signal transduction inhibitors and natural products to inhibit cell proliferation [40, 41]. In the current studies, we examined the effects of inheritance of WT-TP53 on a larger panel of chemotherapeutic drugs as well the consequences of on other properties important in cancer progression such as clonogenicity, colony formation in soft agar and metabolic properties.

RESULTS

Restoration of WT-TP53 activity results in decreased resistance to various drugs, inhibitors, and natural products

MIA-PaCa-2 cells have GOF mutant TP53 alleles (R248W). A cDNA encoding WT-TP53 cDNA was inserted into the pLXSN vector [42]. MIA-PaCa-2 cells were transduced with the WT-TP53 vector and named MIA-PaCa-2 + WT-TP53 cells. As a negative control, the effects of the empty parental pLXSN plasmid [43] on MIA-PaCa-2 cells and named MIA-PaCa-2 + pLXSN.

Table 1 is a list of the various agents examined in this study as well as their targets and intersections with the TP53 pathway and a brief description of their mechanisms of action.

Docetaxel is a common chemotherapeutic drug used to treat various cancer types including PDAC. The IC₅₀ for docetaxel in MIA-PaCa-2 + WT-TP53 cells was 3.8-fold lower than in MIA-PaCa-2 + pLXSN cells (Figure 2A). The effects of WT-TP53 on the sensitivity to three topoisomerase inhibitors used in cancer therapy were also examined (Figure 2B–2D). The IC₅₀s for all the inhibitors were lower (~ 2-fold for etoposide and daunorubicin, and 5-fold for aclacinomycin) in MIA-PaCa-2 + WT-TP53 cells than in MIA-PaCa-2 + pLXSN cells.

Restoration of WT-TP53 activity in MIA-PaCa-2 cells resulted in increased sensitivity to chemotherapeutic drugs used to treat cancer patients. Table 2 summarizes the effects of addition of WT-TP53 into Mia-PaCa-2 cells. Restoration of WT-TP53 activity increased sensitivity to the KRAS inhibitor ARS-1620 [44] 125-fold (Figure 3A).

Various signaling cascades are located downstream of KRas. Two important kinase cascades are the Raf/MEK/ERK and PI3K/PTEN/Akt/mTORC1 pathways. They are often involved in regulation of cell growth and their aberrant regulation is often implicated in cancer [45–47]. Restoration of WT-TP53 activity in MIA-PaCa-2 cells increased the sensitivity to the MEK1 inhibitor PD0325901 3.3-fold. (Figure 3B).

Restoration of WT-TP53 activity in MIA-PaCa-2 cells led to a 33.3-fold lower IC₅₀ for the PI3K inhibitor LY294002 inhibitor than that observed in MIA-PaCa-2 cells lacking WT-TP53 (Figure 3C). Thus, addition of WT-TP53 activity in MIA-PaCa-2 cells increased their sensitivity to small molecule inhibitors which target the Ras/Raf/MEK/ERK and PI3K/PTEN/Akt/mTORC1 pathways.

Pifithrin- μ is a small molecule that inhibits the interactions of TP53 with either BCL2 or BCLXL at the mitochondrial membrane. This results in the induction of apoptosis. However, Pifithrin- μ does not inhibit the effects that TP53 has on transcription [48]. Restoration of WT-TP53 in MIA-PaCa-2 cells resulted in a pifithrin- μ IC₅₀ 240-fold lower than that detected in MIA-PaCa-2 cells which lack WT-TP53 activity (Figure 3D).

GSK-3 is a multifunctional kinase that is involved in the regulation of many processes both in normal physiological and malignant growth [49]. GSK-3 has been shown to be important for the interactions between KRas and NF- κ B [50, 51]. GSK-3 is an important target in many cancers. GSK-3 inhibitors have been suggested for the treatment of PDAC [52]. The effects of GSK-3 inhibitors BIO, CHIR99021 and SB415286 on MIA-PaCa-2 cells containing and lacking WT activity were examined. Restoration of WT-TP53 activity in MIA-PaCa-2 cells resulted in over 13-fold lower IC₅₀ for SB415286 and only about 2-fold lower IC₅₀ for BIO and CHIR99021 than in cells lacking WT-TP53 activity (Figure 4A–4C).

The mTORC1 complex plays critical roles in many processes, including: cell growth, metabolism, cancer and aging [53, 54]. Restoration of WT-TP53 activity in MIA-PaCa-2 cells resulted in a rapamycin IC₅₀ 6.7-fold lower than that observed in cells lacking WT-TP53 activity (Figure 4D).

EGFR, HER2, ALK, AXL, FLT3, PDGFR and other receptors and signal transducers (*e.g.*, Raf) are involved in the metastasis of various cancers [55–61]. The effects of: the AG1478 EGFR inhibitor, the multi-kinase ALK, AXL, FLT3 inhibitor gilteritinib and multi-kinase Raf, PDGFR, FLT3, VEGFR inhibitor sorafenib on the

Table 1. Chemotherapeutic drugs, signal transduction inhibitors, natural products used in this study and their targets, mode of action, and intersections with the TP53 pathway.^{1,2}

Chemotherapeutic drugs¹			
Drug↓	Target¹	Mode of action	Intersection with TP53 pathway
Docetaxel	Microtubule Binder	Blocks mitosis by inhibiting mitotic spindle assembly.	Docetaxel intersects with TP53 pathway. WT-TP53 increases sensitivity, increases phosphorylation of S15-TP53.
5-Fluorouracil (5FU)	Nucleoside Analogue	Blocks the activity of thymidylate synthase, thus, inhibits DNA synthesis/replication.	5FU intersects with TP53 pathway. WT-TP53 increases sensitivity to FU. 5FU induces TP53 stabilization by blocking MDM2.
Gemcitabine (Gem)	Nucleoside Analogue	Gemcitabine exerts its antitumor effects by promoting apoptosis of cells undergoing DNA synthesis.	Gem intersects with TP53 pathway. WT-TP53 increases sensitivity. Gem can induce TP53 targets such as PUMA and Bax which leads to apoptosis.
Aclacinomycin (Aclarubicin)	DNA intercalator, Topoisomerase II	Topoisomerase inhibitor (inh.) thus, inhibits DNA replication.	As an anthracycline it probably intersects with TP53 pathway. However, like most chemotherapeutic drugs, it can function in TP53 mutant cells.
Daunorubicin	DNA intercalators, Topoisomerase II	Topoisomerase inh. thus, inhibits DNA replication.	Daunorubicin intersects with TP53 pathway. It induces TP53 and downstream p21Cip1.
Doxorubicin (Dox)	DNA intercalator, Topoisomerase II	Topoisomerase inh. thus, inhibits DNA replication and induces many TP53-regulated genes, many induce apoptosis.	Dox intersects with TP53 pathway. It increases TP53 expression and phosphorylation at S15 and can induce p21Cip-1.
Etoposide	Binds to Topoisomerase II	Topoisomerase inh. thus, inhibits DNA replication and induces apoptosis. Complex form between etoposide and DNA and can prevent DNA repair.	Etoposide intersects with TP53 pathway. It increases TP53 and pro-apoptotic PUMA expression as well as Bax processing.
Cisplatin (Cis)	DNA	Crosslinks DNA to form DNA adducts. Preventing repair of DNA leading to DNA damage and subsequently apoptosis.	Cis intersects with TP53 pathway. Cis can enhance TP53, p21Cip-1, MDM2 and Fas expression.
Signal transduction inhibitors¹			
Drug↓	Target	Mode of action	Intersection with TP53 pathway
ARS-1620	Mutant KRas	KRas-mediated catalysis of the chemical reaction with Cys12 in KRASG12C.	KRas interacts with the TP53 pathway. TP53 and KRas interact to modulate CREB1 expression to promote metastasis and tumor growth.
PD0325901	MEK1	A highly selective allosteric inh. that does not compete with either ATP or ERK1/2.	MEK1 interacts with the TP53 pathway. Downstream ERK can phosphorylate and activate TP53, resulting in many cellular responses.
LY294002	PI3K and others	Competition with ATP for binding the PI3K active site.	PI3K and downstream molecules can interact with the TP53 pathway. Downstream of PI3K are PTEN and Akt and they can regulate the TP53 pathway at various steps and processes.
Pifithrin-μ	TP53	Inhibits some of TP53 activities by binding to BCLXL and BCL2 at the mitochondria without affecting TP53 transcriptional activities.	Pifithrin-μ inhibits some proteins regulated by the TP53 pathway (BCL-XL and BCL2).
6-bromindirubin-30-oxime (BIO)	GSK-3	BIO is a selective, reversible potent GSK-3 inh. It is an ATP-competitive inhibitor of GSK-3α/β. It interacts with ATP binding site of GSK-3.	GSK-3 interacts with TP53 pathway. GSK-3 phosphorylates sites on the proteasomal inhibitor MDM2. This phosphorylation is required for TP53 degradation. Inhibition of GSK-3 leads to an increase in TP53 levels.
SB415286	GSK-3	Targets ATP-binding site. It inhibits both GSK-3α and GSK-β.	GSK-3 interacts with TP53 pathway. GSK-3 phosphorylates sites on the proteasomal inhibitor MDM2. This phosphorylation is required for TP53 degradation. Inhibition of GSK-3 leads to an increase in TP53 levels.
CHIR99021	GSK-3	Targets ATP-binding site. It inhibits both GSK-3α and GSK-β.	GSK-3 interacts with TP53 pathway. GSK-3 phosphorylates sites on the proteasomal inhibitor MDM2. This phosphorylation is required for TP53 degradation. Inhibition of GSK-3 leads to an increase in TP53 levels.

Rapamycin	mTORC1	Binds and blocks mTORC1 complex.	mTORC1 interacts with the TP53 pathway. Activation of TP53 downregulates mTOR signaling. This occurs through AMPK.
AG1498	EGFR	AG1478 competitively binds to the ATP binding pocket in EGFR.	EGFR interacts with the TP53 pathway. TP53 mutations are associated with primary or acquired resistance to EGFR-tyrosine kinase inhibitors.
Gilteritinib	AXL/ALK/FLT3	Gilteritinib binds to the ATP binding site in the active pocket of the AXL/ALK/FLT3 kinases.	AXL/ALK/FLT3 interacts with the TP53 pathway. AXL suppresses TP53 expression by binding to DNA sequences upstream from the TP53 gene. AXL is also regulated by miR-34a which is regulated by TP53. ALK inhibitors are not as effective in lung cancer patients that have rearranged ALK genes and are also mutated at TP53 as in patients with germline genes. Also, FLT-3 and TP53 also interact.
Sorafenib	Multiple kinases (e.g., Raf, PDGFR, VEGFR, FLT-3 and others)	Sorafenib binds to the ATP binding site.	Many of these kinases and their downstream substrates interact with TP53 pathway by phosphorylating TP53 and other molecules regulated by TP53. Mutant TP53 can also regulate the expression of some of these kinases such as PDGFR.
OTX008	Galectin-1	OTX008 binds galectin-1 which leads to galectin-1 oxidation and proteasomal degradation.	Galectin-1 can interact with the TP53 pathway. TP53 can induce the expression of miRs which regulate galectin-1 expression.
Tiplaxtinin	Serpine-1	Tiplaxtinin binds to the active conformation of serpine-1 and induced reversible inactivation serpine-1.	TP53 regulates the expression of miR-34a which can down regulate serpine-1. Serpine1- is involvement of metastasis in various cancers.
Verapamil (Ver)	Calcium channel	Also, some transporters associated with chemotherapeutic drug resistance. Binds to sites on MDR1 glycoprotein preventing drug efflux. Also, downregulates MDR1 expression.	TP53 pathway and Ver interact. Ver interacts with the TP53 activator (MDM2 inhibitor) nutlin-3a which results in suppression of cell growth.
Vismodegib (Vis)	Hh pathway	Smoothened homologue (SMO) binds to Smoothened (SMO) and inhibits its activity.	Multiple interactions with TP53 pathway.

Natural products²

Cyclopamine	Sonic hedgehog (SHH) pathway	Cyclopamine binds to SMO and inhibits its activity.	Multiple interactions with TP53 pathway.
Parthenolide ²	NF-κB (other targets)	Inhibition of activation of IκB, and direct binding to NF-κB, preventing its interaction with DNA.	NF-κB interacts with the TP53 pathway TP53 and NF-κB inhibit each other's ability to stimulate gene expression.
Isoliquiritin ²	Induces apoptotic cell death through upregulating TP53 and p21Cip-1. Suppresses NF-κB, ERK and activation of other targets	Suppresses invasiveness and angiogenesis of cancer.	Isoliquiritin interacts with TP53 pathway. It induces TP53 and inhibits NF-κB and ERK. Both interact with TP53 pathway.
Genistein (isoflavone) ²	Multiple targets	Genistein triggers the ER stress to induce apoptosis and other mechanisms of cell death.	Genistein interacts with TP53 pathway. Genistein increases the phosphorylation and activation of ATM/ATR-TP53-p21Cip-1 pathway.
Daidzein (isoflavone) ²	Multiple targets	Daidzein and genistein induce cell cycle arrest in the G2/M phase. This is accompanied by activation of ATM/TP53, and p21Cip-1 and other cell cycle regulatory genes.	Daidzein interacts with TP53 pathway. Daidzein increases the phosphorylation and activation of ATM/ATR-TP53-p21Cip-1 pathway.

¹Many chemotherapeutic drugs and signal transduction inhibitors have other effects and targets. We describe the targets that are most closely related to TP53.

²Most natural products have multiple targets. We describe some of the targets that are more closely related to TP53.

Table 2. Effects of WT-TP53 and pLXSN on sensitivity of MIA-PaCa-2 pancreatic cancer cells on chemotherapeutic drugs, signal transduction inhibitors and natural products as determined by IC₅₀ analysis.¹

Drug/Agent↓	+ pLXSN	+ WT-TP53	Fold change WT vs. LXSN
Docetaxel (microtubule binder)	0.3 nM	0.08 nM	3.8 X↓
Etoposide (topoisomerase inh.)	750 nM	400 nM	1.9 X↓
Aclacinomycin (topoisomerase inh.)	1 nM	0.2 nM	5 X↓
Daunorubicin (topoisomerase inh.)	120 nM	60 nM	2 X↓
ARS-1620 (mutant KRas inh.)	10 nM	0.8 nM	12.5 X↓
PD0325901 (MEK1 inh.)	150 nM	45 nM	3.3 X↓
LY294002 (PI3K inh.)	5,000 nM	150 nM	33.3 X↓
Pifithrin-μ (TP53 inh.)	600 nM	2.5 nM	240 X↓
BIO (GSK-3 inh.)	210 nM	100 nM	2.1 X↓
SB415286 (GSK-3 inh.)	40 nM	3 nM	13.3 X↓
CHIR99021 (GSK-3 inh.)	500 nM	300 nM	1.7 X↓
Rapamycin (mTORC1 blocker)	2 nM	0.3 nM	6.7 X↓
AG1498 (EGFR inh.)	1,000 nM	200 nM	5 X↓
Gilteritinib (AXL/ALK/FLT3 inh.)	600 nM	220 nM	2.7 X↓
Sorafenib (multi-kinase inh.)	1,000 nM	700 nM	1.4 X↓
OTX008 (Galectin-1 inh.)	1,000 nM	10 nM	100 X↓
Tiplaxtinin (Serpine-1 inh.)	40 nM	10 nM	4 X↓
Cyclopamine (SHH inh.)	1,000 nM	500 nM	2 X↓
Parthenolide (NF-κB inh, other targets)	40 nM	3.5 nM	11.4 X↓
Isoliquiritin (multiple targets)	1,900 nM	600 nM	3.2 X↓
Genistein (isoflavone, many targets)	300 nM	70 nM	4.3 X↓
Daidzein (isoflavone, many targets)	1,000 nM	600 nM	1.7 X↓

¹Determined by MTT analysis as previously described [40, 41].

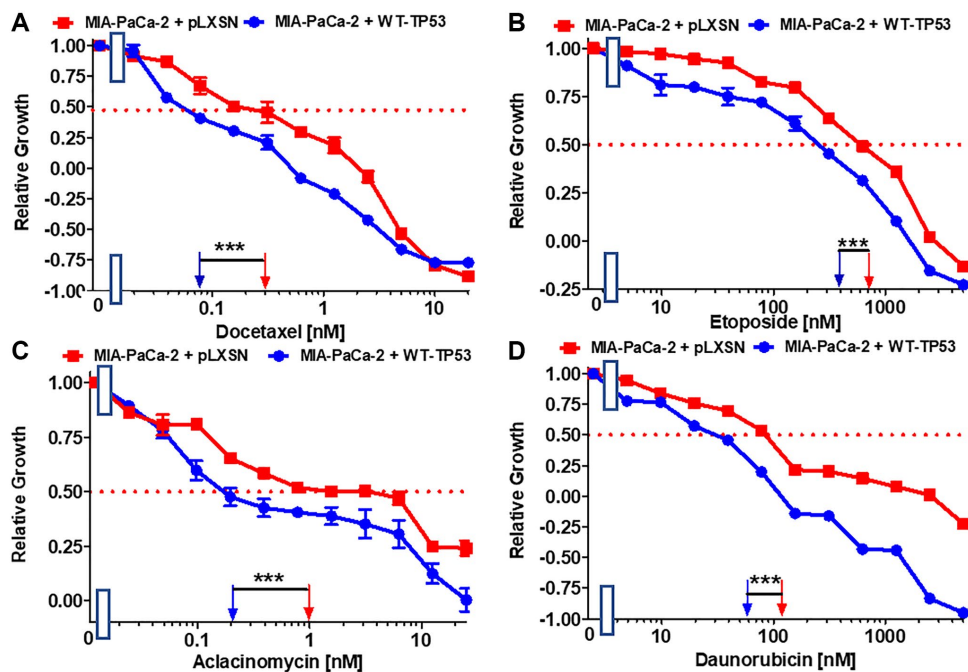


Figure 2. Effects of signal transduction inhibitors on the growth of MIA-PaCa-2 + WT-TP53 and MIA-PaCa-2 + pLXSN cells. The effects of docetaxel (A), etoposide (B) aclacinomycin (C) and daunorubicin (D) on MIA-PaCa-2 + pLXSN cells (solid red squares) and MIA-PaCa-2 + WT-TP53 cells (solid blue circles) were examined by MTT analysis. These experiments were repeated and similar results were obtained. Statistical analyses were performed by the Student *T* test on the means and standard deviations of various treatment groups. ****P* < 0.0001.

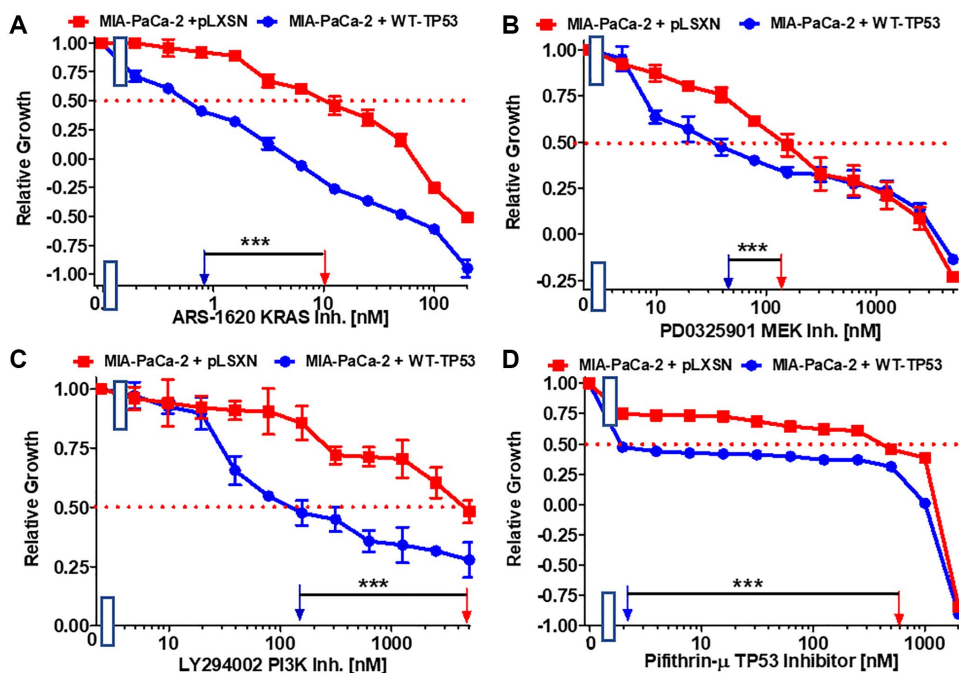


Figure 3. Effects of the Ras/MEK, PI3K/mTOR and TP53 inhibitors on the growth of MIA-PaCa-2 + WT-TP53 and MIA-PaCa-2 + pLXSN cells. The effects of the ARS-1620 mutant KRas inhibitor (A), the PD0325901 MEK1 inhibitor (B), the LY294002 PI3K inhibitor (C) and the TP53 inhibitor pifithrin- μ (D) on MIA-PaCa-2 + pLXSN cells (solid red squared) and MIA-PaCa-2 + WT-TP53 cells (solid blue circles) were examined by MTT analysis. The MIA-PaCa-2 + WT-TP53, and MIA-PaCa-2 + pLXSN cells in each panel were all examined at the same time period. These experiments were repeated and similar results were obtained. Statistical analyses were performed by the Student *T* test on the means and standard deviations of various treatment groups. ****P* < 0.0001.

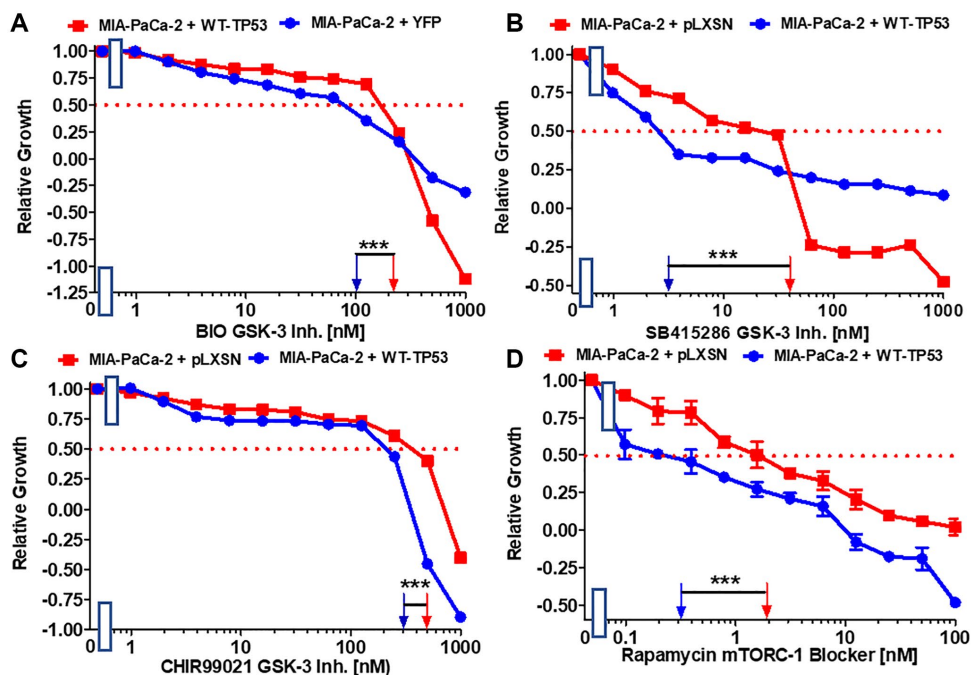


Figure 4. Effects of GSK-3 inhibitors and the mTORC1 blocker rapamycin on the growth of MIA-PaCa-2 + WT-TP53 and MIA-PaCa-2 + pLXSN cells. The effects of the BIO GSK-3 inhibitor (A), the SB415286 GSK-3 inhibitor (B), the CHIR99021 GSK-3 inhibitor (C) and the mTORC1 blocker rapamycin (D) on MIA-PaCa-2 + pLXSN cells (solid red squared) and MIA-PaCa-2 + WT-TP53 cells (solid blue circles) were examined by MTT analysis. The MIA-PaCa-2 + WT-TP53, and MIA-PaCa-2 + pLXSN cells in each panel were all examined at the same time period. These experiments were repeated and similar results were obtained. Statistical analyses were performed by the *T* test on the means and standard deviations of various treatment groups. ****P* < 0.0001.

growth of MIA-PaCa-2 cells expressing WT-TP53 or not were ascertained. Introduction of WT-TP53 into MIA-PaCa-2 cells resulted in reduction of the IC₅₀s for all the inhibitors in comparison to the IC₅₀s in MIA-PaCa-2 cells lacking WT-TP53 expression (Figure 5A–5C) but the reduction was most pronounced for the AG1478 EGFR inhibitor.

Galectin-1 is involved in hedgehog (Hh) signaling, stromal remodeling and metastasis of PDAC [62]. Galectin-1 is negatively regulated by WT TP53 [63]. OTX008 inhibits the activity of galectin-1. Restoration of WT-TP53 activity in MIA-PaCa-2 cells sensitized the cells 100-fold in comparison to MIA-PaCa-2 cells which lacked WT-TP53 activity (Figure 5D).

The plasminogen activator inhibitor (PAI-1), serpine1 is negatively regulated by miR-34a in MIA-PaCa-2 upon restoration of WT-TP53 activity [64]. The small molecule tiplaxtinin inhibits serpine1 activity [65]. Upon restoration of WT-TP53 activity in MIA-PaCa-2 cells resulted in 4-fold enhanced sensitivity to tiplaxtinin in comparison to MIA-PaCa-2 cells lacking WT-TP53 activity (Figure 6A).

Effects of WT-TP53 on sensitivity to natural products and nutraceuticals

The ability of various natural products and nutraceuticals to inhibit the proliferation in MIA-PaCa-2 cells in the presence and absence of WT-TP53 activity was determined. These compounds were selected on the basis of literature data suggesting their targets and their influence on the development of PDAC.

A natural product that inhibits the Hh signaling pathway is cyclopamine. The Hh pathway is very important in PDAC and metastasis [66, 67]. Restoration of WT-TP53 activity in MIA-PaCa-2 cells increased the sensitivity 2-fold to cyclopamine (Figure 6B).

Extracts from the plant fever few contain parthenolide. One of its targets is NF-κB [68]. Parthenolide has been observed to suppress PDAC progression [69]. Restoration of WT-TP53 activity in MIA-PaCa-2 cells increased the sensitivity to parthenolide 11.4-fold in comparison to cells lacking WT-TP53 activity (Figure 6C).

Licorice contains the flavonoid isoliquiritin which has various biological activities including anti-cancer

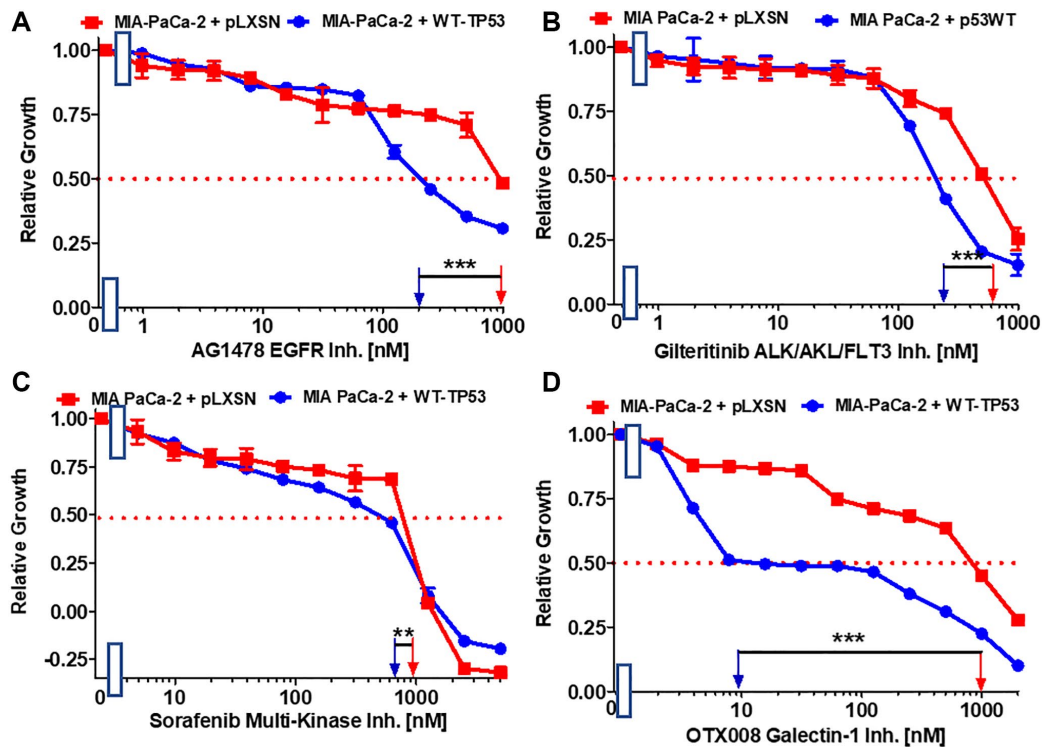


Figure 5. Effects of inhibitors which may suppress metastasis on the growth of MIA-PaCa-2 + WT-TP53 and MIA-PaCa-2 + pLXSN cells. The effects of the AG1478 EGFR inhibitor (A), the gilteritinib ALK/AXL/FLT3 inhibitor (B), the sorafenib multi-kinase inhibitor (C) and the galectin-1 inhibitor OTX008 (D) on MIA-PaCa-2 + pLXSN cells (solid red squares) and MIA-PaCa-2 + WT-TP53 cells (solid blue circles) were examined by MTT analysis. The MIA-PaCa-2 + WT-TP53, and MIA-PaCa-2 + pLXSN cells in each panel were all examined at the same time period. These experiments were repeated and similar results were obtained. Statistical analyses were performed by the *T* test on the means and standard deviations of various treatment groups. ****P* < 0.0001, and ***P* < 0.005.

activities [70, 71]. In lung cancer cells, it was shown that isoliquiritin can induce TP53 activity [71]. In pancreatic cancer cells it suppressed the invasiveness *in vitro* [72]. Restoration of WT-TP53 activity in MIA-PaCa-2 cells increased their sensitivity to isoliquiritin 3.2-fold (Figure 6D).

Genistein is an isoflavone. It possesses certain anti-cancer properties including inhibition of angiogenesis in PDAC [73]. It induces apoptosis in PDAC lines [74]. Restoration of WT-TP53 activity in MIA-PaCa-2 cells increased their sensitivity to genistein 4.3-fold in comparison to MIA-PaCa-2 cells lacking WT-TP53 (Figure 7A).

Daidzein is an additional isoflavone. It inhibited breast cancer growth in rodent models [75, 76]. Restoration of WT-TP53 activity in MIA-PaCa-2 cells increased the sensitivity to daidzein 1.7-fold (Figure 7B).

Summarizing, restoration of WT-TP53 activity in MIA-PaCa-2 cells increased the sensitivity to various chemotherapeutic drugs, signal transduction inhibitors and natural products.

Restoration of WT-TP53 decreases clonogenicity in the presence of chemotherapeutic drugs

The ability of WT-TP53 to suppress clonogenicity in 5-fluorouracil, gemcitabine and cisplatin was determined

in MIA-PaCa-2 and PANC-28 cell containing and lacking WT-TP53. Upon restoration of WT-TP53 activity in MIA-PaCa-2 and PANC-28 cells, clonogenicity decreased in a dose-dependent fashion more dramatically in cells containing WT-TP53 activity (Figure 8). Although gemcitabine inhibited clonogenicity in cells containing and lacking WT-TP53 activity. Thus, restoration of WT-TP53 suppressed clonogenicity in larger culture volumes containing chemotherapeutic drugs carried out for 14–21 days and it reduced the IC₅₀s for chemotherapeutic drugs in smaller cultures carried out over 5 days [40, 41].

Effects of WT-TP53 on the ability of cells to form colonies in medium containing soft agar

The ability of cells to form colonies in medium containing soft agar in the absence of adhesion to the bottom of the tissue culture plate (anchorage-independent growth) is often considered as a measure of the extent of transformation of malignant transformation as most “normal” cells do not [77].

The effects of restoration of WT-TP53 activity on the ability to form colonies in increasing concentrations of 5FU were compared. As documented in Figure 9, restoration of WT-TP53 activity in MIA-PaCa-2 cells inhibited their ability to form colonies in soft agar in the presence of 5FU.

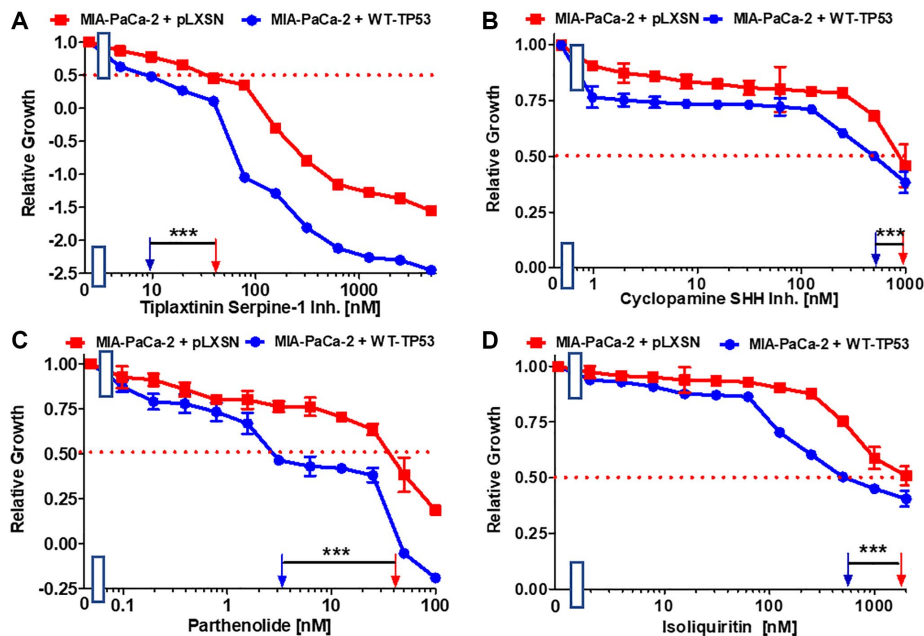


Figure 6. Effects of inhibitors/natural products which may suppress metastasis on the growth of MIA-PaCa-2 + WT-TP53 and MIA-PaCa-2 + pLXSN cells. The effects of the tiplaxtinin Serpine-1 inhibitor (A), the natural product cyclopamine, a SHH inhibitor (B), the natural product parthenolide, a NF-κB inhibitor (C), and the natural product/nutraceutical isoliquiritin (D) were examined by MTT analysis. The MIA-PaCa-2 + WT-TP53, and MIA-PaCa-2 + pLXSN cells in each panel were all examined at the same time period. These experiments were repeated and similar results were obtained. Statistical analyses were performed by the *T* test on the means and standard deviations of various treatment groups. ****P* < 0.0001.

Figure 10 presents photographs of colonies stained with crystal violet, not only were there less colonies in soft agar when WT-TP53 activity was restored to MIA-PaCa-2 cells but the colony sizes were also smaller. When there was no 5FU in the culture medium, MIA-PaCa-2 cells containing or lacking WT-TP53 formed similar numbers of colonies of roughly equal sizes. However, even at the lowest dose of 5FU (1.25 μ M), there was a massive drop in the number of colonies observed in MIA-PaCa-2 cells

containing WT-TP3 activity while the decline in MIA-PaCa-2 cells lacking WT-TP53 activity, was not as extreme.

Restoration of WT-TP53 activity in both MIA-PaCa-2 and PANC-28 cells decreased their ability to form colonies in soft agar containing docetaxel (Figure 11). Introduction of WT-TP53 activity decreased the ability of MIA-PaCa-2 cells to form colonies in soft agar containing doxorubicin (Figure 12A).

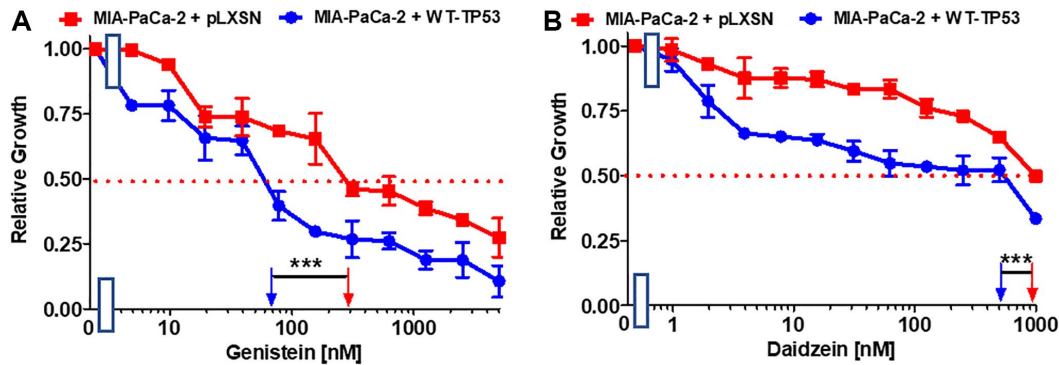


Figure 7. Effects of nutraceuticals on the growth of MIA-PaCa-2 + WT-TP53 and MIA-PaCa-2 + pLXSN cells. The effects of genistein (A), and daidzein (B), on MIA-PaCa-2 + pLXSN cells (solid red squares) and MIA-PaCa-2 + WT-TP53 cells (solid blue circles) were examined by MTT analysis. The MIA-PaCa-2 + WT-TP53, and MIA-PaCa-2 + pLXSN cells in each panel were all examined at the same time period. These experiments were repeated and similar results were obtained. Statistical analyses were performed by the *T* test on the means and standard deviations of various treatment groups. ****P* < 0.0001.

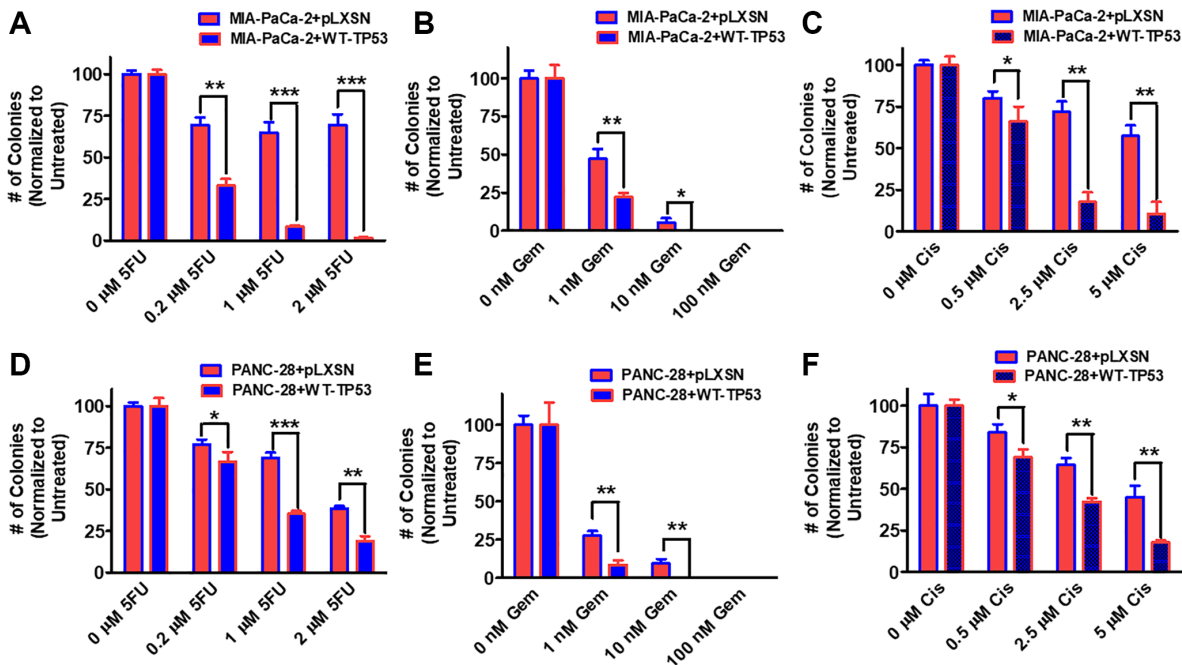


Figure 8. Effects of pLXSN and WT-TP53 on clonogenicity in the presence of 5-Fluorouracil, gemcitabine or cisplatin in two PDAC cell lines. The clonogenicity in the presence of increasing concentrations of 5-fluorouracil (5FU), gemcitabine (Gem) and cisplatin (Cis) were examined in: MIA-PaCa-2 + pLXSN and MIA-PaCa-2 + WT-TP53 (A–C), PANC-28 + pLXSN, and PANC-28 + WT-TP53 (D–F). Red horizontal bars = MIA-PaCa-2 or PANC-28 containing pLXSN. Blue horizontal bars = MIA-PaCa-2 or PANC-28 containing WT-TP53. These experiments were repeated and similar results were observed. The colonies for each cell line were normalized to untreated so that the results from pLXSN and WT-TP53 could be compared. ****P* < 0.0001, ***P* < 0.005 and **P* < 0.05.

Drug transporters such as MDR1 are often upregulated in drug resistant cells [78–80]. Verapamil will inhibit the activity of certain drug transporters such as MDR1. Addition of WT-TP53 activity to MIA-PaCa-2 cells increased their sensitivity to verapamil as determined by colony formation in soft agar (Figure 12B).

Hh signaling is critical in differentiation and in some cases, cancer metastasis [81]. Hh pathway inhibitors have been evaluated in PDAC patients [82]. Restoration of WT-TP53 activity in MIA-PaCa-2 cells made them more sensitive to the Hh pathway vismodegib in soft agar colony formation assays (Figure 12C). Thus,

restoration of WT-TP53 activity in both MIA-PaCa-2 and PANC-28 cells resulted in the cells becoming more sensitive to chemotherapeutic drugs.

Restoration of WT-TP53 activity in MIA-PaCa-2 cells alters their metabolic properties

For their rapid growth, cancer cells require a large amount of ATP that occurs by glycolysis and mitochondrial oxidative phosphorylation. To determine the consequence of restoration of WT-TP53 activity in energy metabolism in MIA-PaCa-2 cells, stress tests were done with the Seahorse analyzer. This machine determines the extent of glycolysis by determining the

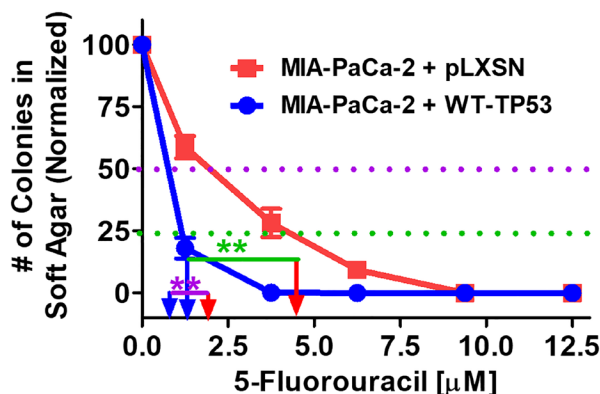


Figure 9. Effects of pLXSN and WT-TP53 on the colony formation in soft agar in the presence of 5-Fluorouracil. The effects of pLXSN and WT-TP53 on the colony formation in soft agar were examined. Red squares = MIA-PaCa-2 + pLXSN cells, blue circles = MIA-PaCa-2 + WT-TP53 cells. IC₅₀ is indicated with a purple dotted line and IC₂₅ is indicated with a green dotted line. IC₂₅ is a term to indicate inhibition of colony formation at 25%. These experiments were repeated performed and similar results were observed. The colonies for each cell line were normalized to untreated cells so that the results from the MIA-PaCa-2 + pLXSN and MIA-PaCa-2 + WT-TP53 could be compared. ***P* < 0.005.

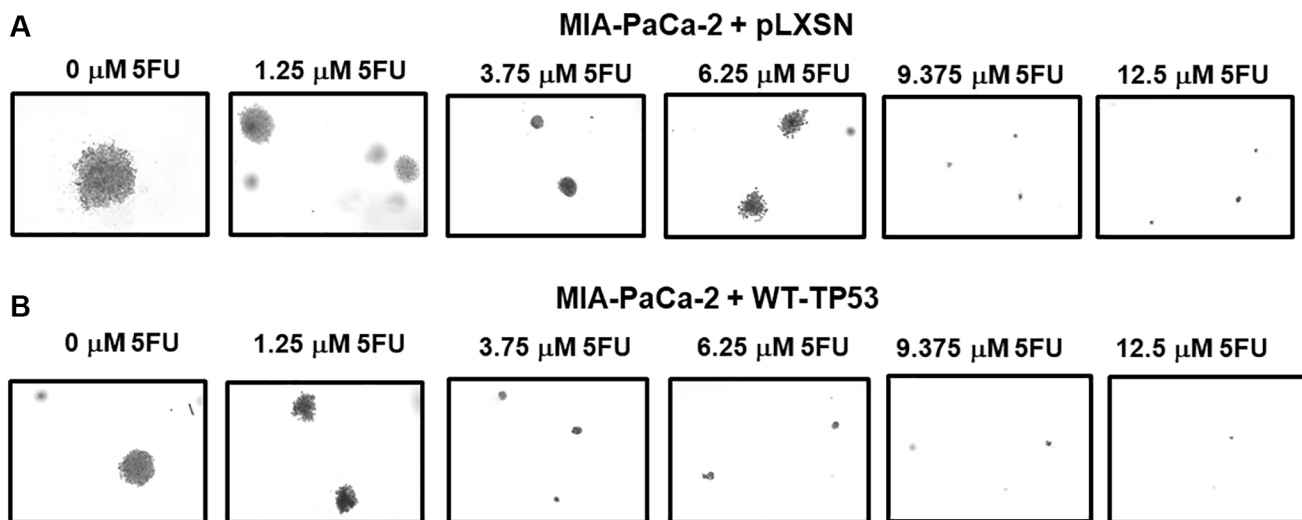


Figure 10. Crystal violet-stained colonies in soft agar in the presence of 5-Fluorouracil. The effects of pLXSN and WT-TP53 on the colony formation in soft agar were photographed after staining. Photographs were taken at the same day and at the same magnification on the microscope. (A) MIA-PaCa-2 + pLXSN cells treated with increasing concentration of 5FU, (B) MIA-PaCa-2 + WT-TP53 cells treated with increasing concentrations of 5FU.

extracellular acidification (ECAR) and can also analyze mitochondrial oxidative phosphorylation by measuring the real-time oxygen consumption rate (OCR).

TP53 has been shown to be a cellular energy metabolism regulator [83–88]. It can influence both glycolysis and mitochondrial metabolism through multiple mechanisms [88]. Some studies have shown that mutant TP53 can have more effects on mitochondrial metabolism than glycolysis [89]. The effects of restoration of WT-TP53 activity on mitochondrial activity in PDAC cells have not been documented well.

The effects of WT-TP53 activity on metabolic parameters were determined in MIA-PaCa-2 cells

containing and lacking WT-TP53 activity were determined as we previously described [90] using the Seahorse analyzer. The results presented here indicated that restoration of WT-TP53 activity led to a decrease in glycolytic capacity in comparison to cells lacking WT-TP53 activity (Figures 13–15). Moreover, the effects on mitochondrial respiration also were more pronounced in MIA-PaCa-2 cells containing WT-TP53 activity.

Upon restoration of WT-TP53 activity in MIA-PaCa-2 cells, the level of basal mitochondrial respiration was significantly lower than in MIA-PaCa-2 lacking WT-TP53 activity. Also, their maximal respiratory and spare respiratory capacity levels were significantly reduced in contrast to cells lacking WT-TP53 (Figures 13 and 14).

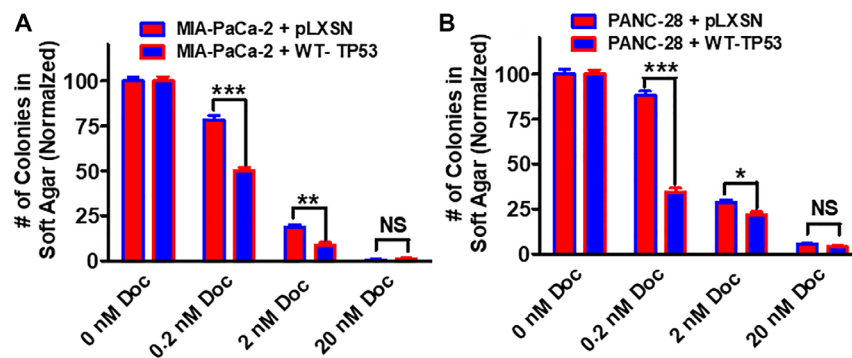


Figure 11. Effects of pLXSN and WT-TP53 on the colony formation in soft agar in the presence of docetaxel. The effects of pLXSN and WT-TP53 on the colony formation in soft agar in MIA-PaCa-2 and PANC-28 cells were examined. (A) MIA-PaCa-2 + pLXSN (red bars) and MIA-PaCa-2 + WT-TP53 (blue bars) were compared in response to docetaxel. (B) PANC-28 + pLXSN (red bars) and PANC-28 + WT-TP53 (blue bars) were compared in response to docetaxel. The colonies for each cell line were normalized to untreated so that the results from pLXSN and WT-TP53 could be compared. These studies were repeated and similar results were observed. $***P < 0.0001$, $**P < 0.005$ and $*P < 0.05$, NS = not statistically significant.

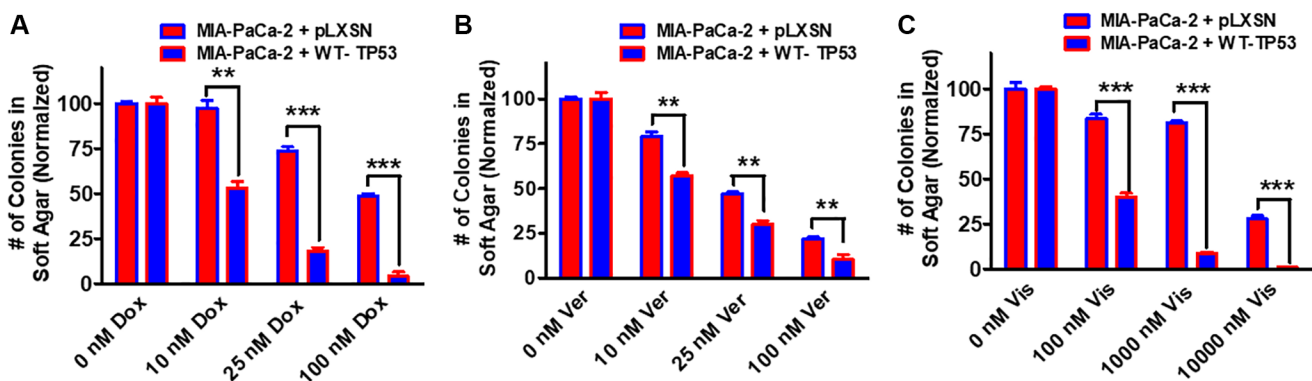


Figure 12. Effects of pLXSN and WT-TP53 on the colony formation in soft agar in the presence of doxorubicin, verapamil and vismodegib. The effects of pLXSN and WT-TP53 on the colony formation in soft agar in MIA-PaCa-2 in response to drugs was examined. (A) Colony formation abilities of MIA-PaCa-2 + pLXSN (red bars) and MIA-PaCa-2 + WT-TP53 (blue bars) were compared in response to treatment with doxorubicin. (B) Colony formation abilities of MIA-PaCa-2 + pLXSN (red bars) and MIA-PaCa-2 + WT-TP53 (blue bars) were compared in response to verapamil. (C) Colony formation abilities of MIA-PaCa-2 + pLXSN (red bars) and MIA-PaCa-2 + WT-TP53 (blue bars) were compared in response to treatment with vismodegib. The number of colonies for each cell line were normalized to untreated so that the results from pLXSN and WT-TP53 could be compared. These studies were repeated and similar results were observed. $***P < 0.0001$, and $**P < 0.005$.

DISCUSSION

TP53 is one of the most frequently mutated genes in human cancer, including pancreatic cancer. The *TP53* genes are altered in the two PDAC cell lines examined.

MIA-PaCa-2 cells have GOF *TP53* mutations and PANC-28 cells lack *TP53* expression. Both PDAC cell lines have activating mutations in the *KRAS* gene which results in constitutive *KRas* expression. Interactions between mutant *TP53* and *KRas* have been observed

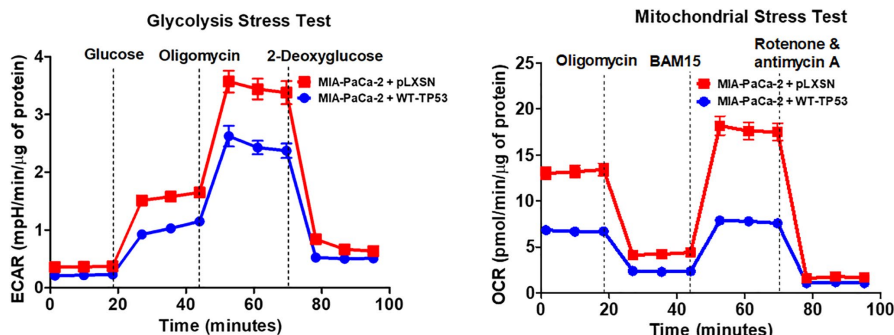


Figure 13. Effects of presence of WT-TP53 on glycolysis and mitochondrial respiration. The data for MIA-PaCa-2 + pLXSN is the same control as presented in [91]. Both MIA-PaCa-2 + pLXSN and MIA-PaCa-2 + WT-TP53 cells were examined the same time on the Seahorse machine as were MIA-PaCa-2 + WT-GSK-3 β and MIA-PaCa-2 + KD-GSK-3 β cells (all four cell lines done at same time). The data presented in Figure 14 are the means and standard error of the means (SEM).

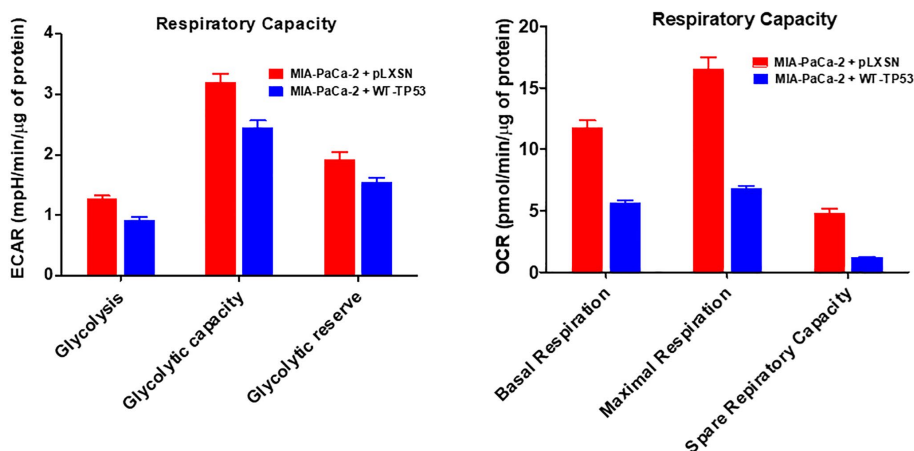


Figure 14. Effects of presence of WT-TP53 on respiratory capacity. The data for MIA-PaCa-2 + pLXSN is the same control as presented in [91]. Both MIA-PaCa-2 + pLXSN and MIA-PaCa-2 + WT-TP53 were examined the same time on the Seahorse machine. The measurements were made 5 times (5 replicates). The data presented in Figure 14 are the means and standard error of the means (SEM).

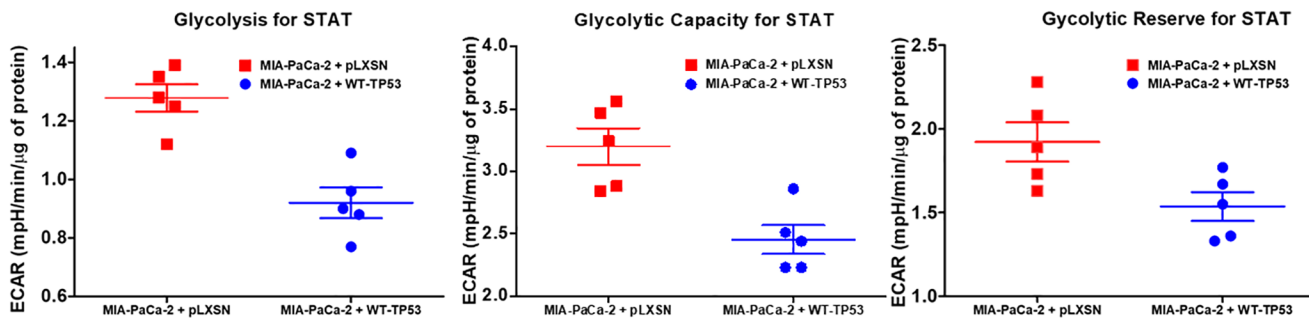


Figure 15. Effects of presence of WT-TP53 on glycolysis. Glycolysis for STAT, glycolytic capacity, and glycolytic reserve for STAT were measured by the Seahorse instrument. The data for MIA-PaCa-2 + pLXSN is the same control as presented in [91]. Both MIA-PaCa-2 + MIA-PaCa-2 + WT-TP53 were examined the same time on the Seahorse machine. STAT is an abbreviation for statistics used in study which was the Mann-Whitney test.

which led to increased KRas functions [51]. GSK-3 β may regulate KRas activity in these cells [51]. Thus, TP53 can interact with many signaling pathways important in cancer development.

In this manuscript, the consequences of restoration of WT-TP53 activity on the response to therapeutic agents have been documented. Restoration of WT-TP53 activity augmented the ability of PDAC cells to various agents used in the therapy of many different cancer types.

Interestingly, restoration of WT-TP53 activity augmented the responsive of MIA-PaCa-2 cells to multiple small molecule inhibitors which target critical signal molecules which are often aberrantly regulated in various cancers. These kinases and GTPases are often associated with cell growth and metastasis.

When WT-TP53 activity was restored to MIA-PaCa-2 cells they became more sensitive to small molecule inhibitors that target mutant KRas and downstream MEK1 than cells containing pLXSN. Thus, WT-TP53 could increase the sensitivity of cells which contain mutant KRas to MEK1 inhibitors. ERK1,2 lies downstream of MEK1. ERK1,2 phosphorylates many important substrates which are involved in various aspects of cell proliferation. Combination of ERK1,2 and autophagy inhibition with a MEK1 inhibitor and

chloroquine may be an additional treatment option for some PDAC patients [91].

The presence of functional WT-TP53 is important for the sensitivity of FL5.12 hematopoietic cells to the mTORC1 blocker rapamycin [92]. FL5.12 cells normally have WT-TP53 activity [93]. Upon insertion of dominant negative (DN) TP53 into FL5.12 cells, their sensitivity to rapamycin was eliminated [92]. Likewise, in this current study, restoration of WT-TP53 activity in MIA-PaCa-2 cells increased the sensitivity to rapamycin. Thus, TP53 intersects with the mTORC1 pathway.

Clearly, the presence of WT-TP53 is critical for the sensitivity of various cancers, including PDAC to many drugs used in cancer therapy [94]. Additional studies on methods and approaches to reactivate mutant TP53 and other mutated genes implicated cancer should be undertaken.

TP53 can influence glycolytic and mitochondrial metabolism both through transcriptional and non-transcriptional regulation. This influence is important for the tumor suppressor role of the protein. An overview of the effects of WT and mutant TP53 on metabolic properties, together with the effects of metformin and rapamycin, and drugs used to inhibit pancreatic cancer growth, is presented in Figure 16.

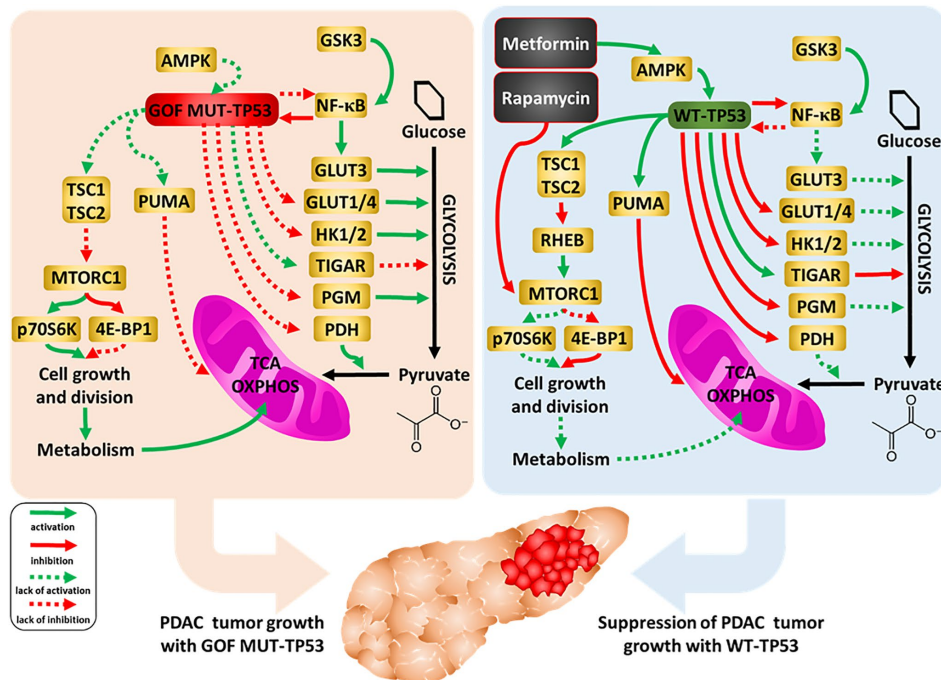


Figure 16. Influences of mutant and WT-TP53 on mitochondrial activity and glucose metabolism and effects of rapamycin and metformin. The effects of WT and mutant TP53 on key enzymes important in glycolysis and how they can influence metabolism and PDAC tumor growth. In our studies, we have examined the effect of GOF mutant TP53 and in some cases WT TP53. In addition, sites of interaction of the type 2 diabetes drug metformin and the immunosuppressive drug rapamycin and their effects on AMPK and mTORC1 are indicated. TP53 can induce mitochondrial apoptosis pathway by regulating the expression of PUMA and other proteins.

Enhanced glucose metabolism via glycolysis is the predominant source of ATP in numerous cancers. TP53 represses expression of, for example, glucose transporters, hexokinase and inhibits nuclear factor-kappa B cell (NF- κ B), a protein that regulates many genes, including genes encoding glycolytic enzymes. Thus, restoration of WT TP53 activity can lead to reduction of glycolysis and impairment of cancer cell growth. On the other hand, TP53 is known to induce oxidative phosphorylation and mitochondrial production of intermediates for biosynthesis [for review see 89]. In our work, however, we observed a decrease of both glycolysis and mitochondrial respiration after the restoration of WT TP53 activity in PDAC. Other studies with breast cancer cell lines, which differ in TP53 status as well as other genes, were observed to increase both glycolytic and mitochondrial activity when mutant TP53 was present [95]. Knock-in of certain TP53 GOF mutations in mice was observed to augment mitochondrial activity, promote survival, and increased maximal treadmill exercise times [96].

TP53 has been shown to induce pro-oxidant enzymes and mitochondrial apoptosis pathway (by regulating the expression of PUMA, BAK, BAX, BCL2, BCLXL), and block anti-oxidant pathways [88]. Thus, the observed reduction of mitochondrial respiration might result from the oxidative-stress-induced impairment of function of the organelles in the WT-TP53-expressing cells. The observed value of the maximum respiration of these cells, only slightly higher than the basal respiration, seems to confirm the impairment of mitochondrial function, but it should be kept in mind that the reduction of the glycolytic rate leads to a reduction in the number of mitochondrial substrates.

Regardless of which of the above processes contributes more to the reduction of mitochondrial metabolism in comparison with the same cells that only express GOF TP53, together the observed changes suggest restoration of WT-TP3 activity confers increased sensitization to various drugs and therapeutic molecules, natural products as well as nutraceuticals. Mutant TP53 can affect the activity of mTORC1 which is important in cellular growth and metabolism. Mutant TP53 may make the PDAC cells more resistant to rapamycin than cells containing WT-TP53. Rapamycin and metformin can interfere with some of the important pathways in the mitochondria, some of which are regulated by TP53 [96–98].

MATERIALS AND METHODS

Cell culture and sources of therapeutic agents

The MIA-PaCa-2 and PANC-28 cells have been described in previous publications [37, 39, 99]. Cell

culture conditions and sources of chemotherapeutic drugs, small molecule inhibitors, natural products and nutraceuticals have been described in our previous publications [40, 41, 47, 80, 90, 100]. Aclacinomycin was obtained from the US National Cancer Institute, (Bethesda, Maryland, USA).

Restoration of WT-TP53 activity

Restoration of WT-TP53 activity and sources of plasmid DNAs have been previously described [40, 41, 90].

Cell proliferation assays-MTT assays

MTT assays were performed as described previously [40].

Clonogenicity assays

Clonogenicity Assays were performed as described in our previous publication [100].

Semi-solid colony formation

Semi-solid colony formation in agar has been described in our previous publications [100, 101].

Analysis of cell metabolism

Cellular metabolism and statistical analysis were performed as described in our previous publication [90].

AUTHOR CONTRIBUTIONS

J.A.M., A.K.M., S.M.A., L.S.S., M.M.L., and R.A.F. researched various topics, carried out the experiments and analyzed some of the data, A.M.M., S.R., L.C., F.B., researched the many of the topics and wrote various sections, P.D. and A.G generated some of the artwork, researched various topics and wrote multiple sections. All of the authors have read the manuscript and accepted the final version of the manuscript.

CONFLICTS OF INTEREST

The authors declare no conflicts of interest related to this study.

FUNDING

J.A.M., S.L.A. and M.M.L were supported in part from East Carolina University Grants (#111104 and #111110-668715-0000). A.K.M. was supported in part by NIH grant (R01-HL146685).

REFERENCES

1. Rawla P, Sunkara T, Gaduputi V. Epidemiology of Pancreatic Cancer: Global Trends, Etiology and Risk Factors. *World J Oncol.* 2019; 10:10–27. <https://doi.org/10.14740/wjon1166> PMID:[30834048](https://pubmed.ncbi.nlm.nih.gov/30834048/)
2. Siegel R, Naishadham D, Jemal A. Cancer statistics, 2013. *CA Cancer J Clin.* 2013; 63:11–30. <https://doi.org/10.3322/caac.21166> PMID:[23335087](https://pubmed.ncbi.nlm.nih.gov/23335087/)
3. Hidalgo M, Cascinu S, Kleeff J, Labianca R, Löhner JM, Neoptolemos J, Real FX, Van Laethem JL, Heinemann V. Addressing the challenges of pancreatic cancer: future directions for improving outcomes. *Pancreatol.* 2015; 15:8–18. <https://doi.org/10.1016/j.pan.2014.10.001> PMID:[25547205](https://pubmed.ncbi.nlm.nih.gov/25547205/)
4. Fitzgerald TL, McCubrey JA. Pancreatic cancer stem cells: association with cell surface markers, prognosis, resistance, metastasis and treatment. *Adv Biol Regul.* 2014; 56:45–50. <https://doi.org/10.1016/j.jbior.2014.05.001> PMID:[24925031](https://pubmed.ncbi.nlm.nih.gov/24925031/)
5. McGuigan A, Kelly P, Turkington RC, Jones C, Coleman HG, McCain RS. Pancreatic cancer: A review of clinical diagnosis, epidemiology, treatment and outcomes. *World J Gastroenterol.* 2018; 24:4846–61. <https://doi.org/10.3748/wjg.v24.i43.4846> PMID:[30487695](https://pubmed.ncbi.nlm.nih.gov/30487695/)
6. Muniraj T, Jamidar PA, Aslanian HR. Pancreatic cancer: a comprehensive review and update. *Dis Mon.* 2013; 59:368–402. <https://doi.org/10.1016/j.disamonth.2013.08.001> PMID:[24183261](https://pubmed.ncbi.nlm.nih.gov/24183261/)
7. Wang H, Liu J, Xia G, Lei S, Huang X, Huang X. Survival of pancreatic cancer patients is negatively correlated with age at diagnosis: a population-based retrospective study. *Sci Rep.* 2020; 10:7048. <https://doi.org/10.1038/s41598-020-64068-3> PMID:[32341400](https://pubmed.ncbi.nlm.nih.gov/32341400/)
8. Morton JP, Timpson P, Karim SA, Ridgway RA, Athineos D, Doyle B, Jamieson NB, Oien KA, Lowy AM, Brunton VG, Frame MC, Evans TR, Sansom OJ. Mutant p53 drives metastasis and overcomes growth arrest/senescence in pancreatic cancer. *Proc Natl Acad Sci U S A.* 2010; 107:246–51. <https://doi.org/10.1073/pnas.0908428107> PMID:[20018721](https://pubmed.ncbi.nlm.nih.gov/20018721/)
9. Fitzgerald TL, Lertpiriyapong K, Cocco L, Martelli AM, Libra M, Candido S, Montalto G, Cervello M, Steelman L, Abrams SL, McCubrey JA. Roles of EGFR and KRAS and their downstream signaling pathways in pancreatic cancer and pancreatic cancer stem cells. *Adv Biol Regul.* 2015; 59:65–81. <https://doi.org/10.1016/j.jbior.2015.06.003> PMID:[26257206](https://pubmed.ncbi.nlm.nih.gov/26257206/)
10. Singh RR, O'Reilly EM. New Treatment Strategies for Metastatic Pancreatic Ductal Adenocarcinoma. *Drugs.* 2020; 80:647–69. <https://doi.org/10.1007/s40265-020-01304-0> PMID:[32306207](https://pubmed.ncbi.nlm.nih.gov/32306207/)
11. Skelton RA, Javed A, Zheng L, He J. Overcoming the resistance of pancreatic cancer to immune checkpoint inhibitors. *J Surg Oncol.* 2017; 116:55–62. <https://doi.org/10.1002/jso.24642> PMID:[28628715](https://pubmed.ncbi.nlm.nih.gov/28628715/)
12. Ruarus A, Vroomen L, Puijk R, Scheffer H, Meijerink M. Locally Advanced Pancreatic Cancer: A Review of Local Ablative Therapies. *Cancers (Basel).* 2018; 10:E16. <https://doi.org/10.3390/cancers10010016> PMID:[29320420](https://pubmed.ncbi.nlm.nih.gov/29320420/)
13. Conroy T, Desseigne F, Ychou M, Bouché O, Guimbaud R, Bécauarn Y, Adenis A, Raoul JL, Gourgou-Bourgade S, de la Fouchardière C, Bennouna J, Bachet JB, Khemissa-Akouz F, et al, and Groupe Tumeurs Digestives of Unicancer, and PRODIGE Intergroup. FOLFIRINOX versus gemcitabine for metastatic pancreatic cancer. *N Engl J Med.* 2011; 364:1817–25. <https://doi.org/10.1056/NEJMoa1011923> PMID:[21561347](https://pubmed.ncbi.nlm.nih.gov/21561347/)
14. Conroy T, Gavaille C, Samalin E, Ychou M, Ducreux M. The role of the FOLFIRINOX regimen for advanced pancreatic cancer. *Curr Oncol Rep.* 2013; 15:182–9. <https://doi.org/10.1007/s11912-012-0290-4> PMID:[23341367](https://pubmed.ncbi.nlm.nih.gov/23341367/)
15. Faris JE, Blaszkowsky LS, McDermott S, Guimaraes AR, Szymonifka J, Huynh MA, Ferrone CR, Wargo JA, Allen JN, Dias LE, Kwak EL, Lillemoe KD, Thayer SP, et al. FOLFIRINOX in locally advanced pancreatic cancer: the Massachusetts General Hospital Cancer Center experience. *Oncologist.* 2013; 18:543–8. <https://doi.org/10.1634/theoncologist.2012-0435> PMID:[23657686](https://pubmed.ncbi.nlm.nih.gov/23657686/)
16. Thota R, Pauff JM, Berlin JD. Treatment of metastatic pancreatic adenocarcinoma: a review. *Oncology (Williston Park).* 2014; 28:70–4. PMID:[24683721](https://pubmed.ncbi.nlm.nih.gov/24683721/)
17. Von Hoff DD, Ramanathan RK, Borad MJ, Laheru DA, Smith LS, Wood TE, Korn RL, Desai N, Trieu V, Iglesias JL, Zhang H, Soon-Shiong P, Shi T, et al. Gemcitabine plus nab-paclitaxel is an active regimen in patients

- with advanced pancreatic cancer: a phase I/II trial. *J Clin Oncol*. 2011; 29:4548–54.
<https://doi.org/10.1200/JCO.2011.36.5742>
PMID:21969517
18. Rasheed ZA, Yang J, Wang Q, Kowalski J, Freed I, Murter C, Hong SM, Koorstra JB, Rajeshkumar NV, He X, Goggins M, Iacobuzio-Donahue C, Berman DM, et al. Prognostic significance of tumorigenic cells with mesenchymal features in pancreatic adenocarcinoma. *J Natl Cancer Inst*. 2010; 102:340–51.
<https://doi.org/10.1093/jnci/djp535>
PMID:20164446
19. Klein AP. Genetic susceptibility to pancreatic cancer. *Mol Carcinog*. 2012; 51:14–24.
<https://doi.org/10.1002/mc.20855>
PMID:22162228
20. Klein AP. Identifying people at a high risk of developing pancreatic cancer. *Nat Rev Cancer*. 2013; 13:66–74.
<https://doi.org/10.1038/nrc3420>
PMID:23222481
21. McCubrey JA, Abrams SL, Fitzgerald TL, Cocco L, Martelli AM, Montalto G, Cervello M, Scalisi A, Candido S, Libra M, Steelman LS. Roles of signaling pathways in drug resistance, cancer initiating cells and cancer progression and metastasis. *Adv Biol Regul*. 2015; 57:75–101.
<https://doi.org/10.1016/j.jbior.2014.09.016>
PMID:25453219
22. Masetti M, Acquaviva G, Visani M, Tallini G, Fornelli A, Ragazzi M, Vasuri F, Grifoni D, Di Giacomo S, Fiorino S, Lombardi R, Tuminati D, Ravaioli M, et al. Long-term survivors of pancreatic adenocarcinoma show low rates of genetic alterations in KRAS, TP53 and SMAD4. *Cancer Biomark*. 2018; 21:323–34.
<https://doi.org/10.3233/CBM-170464>
PMID:29103024
23. Chen X, Ko LJ, Jayaraman L, Prives C. p53 levels, functional domains, and DNA damage determine the extent of the apoptotic response of tumor cells. *Genes Dev*. 1996; 10:2438–51.
<https://doi.org/10.1101/gad.10.19.2438>
PMID:8843196
24. Ko LJ, Prives C. p53: puzzle and paradigm. *Genes Dev*. 1996; 10:1054–72.
<https://doi.org/10.1101/gad.10.9.1054>
PMID:8654922
25. Olivier M, Eeles R, Hollstein M, Khan MA, Harris CC, Hainaut P. The IARC TP53 database: new online mutation analysis and recommendations to users. *Hum Mutat*. 2002; 19:607–14.
<https://doi.org/10.1002/humu.10081>
PMID:12007217
26. Saison-Ridinger M, DelGiorno KE, Zhang T, Kraus A, French R, Jaquish D, Tsui C, Erikson G, Spike BT, Shokhirev MN, Liddle C, Yu RT, Downes M, et al. Reprogramming pancreatic stellate cells via p53 activation: A putative target for pancreatic cancer therapy. *PLoS One*. 2017; 12:e0189051.
<https://doi.org/10.1371/journal.pone.0189051>
PMID:29211796
27. Dittmer D, Pati S, Zambetti G, Chu S, Teresky AK, Moore M, Finlay C, Levine AJ. Gain of function mutations in p53. *Nat Genet*. 1993; 4:42–6.
<https://doi.org/10.1038/ng0593-42>
PMID:8099841
28. Weissmueller S, Manchado E, Saborowski M, Morris JP 4th, Wagenblast E, Davis CA, Moon SH, Pfister NT, Tschaharganeh DF, Kitzing T, Aust D, Markert EK, Wu J, et al. Mutant p53 drives pancreatic cancer metastasis through cell-autonomous PDGF receptor β signaling. *Cell*. 2014; 157:382–94.
<https://doi.org/10.1016/j.cell.2014.01.066>
PMID:24725405
29. Stein Y, Rotter V, Aloni-Grinstein R. Gain-of-Function Mutant p53: All the Roads Lead to Tumorigenesis. *Int J Mol Sci*. 2019; 20:E6197.
<https://doi.org/10.3390/ijms20246197>
PMID:31817996
30. Roszkowska KA, Gizinski S, Sady M, Gajewski Z, Olszewski MB. Gain-of-Function Mutations in p53 in Cancer Invasiveness and Metastasis. *Int J Mol Sci*. 2020; 21:E1334.
<https://doi.org/10.3390/ijms21041334>
PMID:32079237
31. Vogiatzi F, Brandt DT, Schneikert J, Fuchs J, Grikscheit K, Wanzel M, Pavlakis E, Charles JP, Timofeev O, Nist A, Mernberger M, Kantelhardt EJ, Siebolts U, et al. Mutant p53 promotes tumor progression and metastasis by the endoplasmic reticulum UDPase ENTPD5. *Proc Natl Acad Sci U S A*. 2016; 113:E8433–42.
<https://doi.org/10.1073/pnas.1612711114>
PMID:27956623
32. Parrales A, Iwakuma T. Targeting Oncogenic Mutant p53 for Cancer Therapy. *Front Oncol*. 2015; 5:288.
<https://doi.org/10.3389/fonc.2015.00288>
PMID:26732534
33. Sallman DA. To target the untargetable: elucidation of synergy of APR-246 and azacitidine in TP53 mutant myelodysplastic syndromes and acute myeloid leukemia. *Haematologica*. 2020; 105:1470–2.
<https://doi.org/10.3324/haematol.2020.249060>
PMID:32482751

34. Janes MR, Zhang J, Li LS, Hansen R, Peters U, Guo X, Chen Y, Babbar A, Firdaus SJ, Darjania L, Feng J, Chen JH, Li S, et al. Targeting KRAS Mutant Cancers with a Covalent G12C-Specific Inhibitor. *Cell*. 2018; 172:578–89.e17.
<https://doi.org/10.1016/j.cell.2018.01.006>
PMID:[29373830](https://pubmed.ncbi.nlm.nih.gov/29373830/)
35. Goebel L, Müller MP, Goody RS, Rauh D. KRasG12C inhibitors in clinical trials: a short historical perspective. *RSC Med Chem*. 2020; 11:760–70.
<https://doi.org/10.1039/d0md00096e>
PMID:[33479673](https://pubmed.ncbi.nlm.nih.gov/33479673/)
36. Jiao D, Yang S. Overcoming Resistance to Drugs Targeting *KRASG12C* Mutation. *Innovation (N Y)*. 2020; 1:100035.
<https://doi.org/10.1016/j.xinn.2020.100035>
PMID:[32939510](https://pubmed.ncbi.nlm.nih.gov/32939510/)
37. Deer EL, González-Hernández J, Coursen JD, Shea JE, Ngatia J, Scaife CL, Firpo MA, Mulvihill SJ. Phenotype and genotype of pancreatic cancer cell lines. *Pancreas*. 2010; 39:425–35.
<https://doi.org/10.1097/MPA.0b013e3181c15963>
PMID:[20418756](https://pubmed.ncbi.nlm.nih.gov/20418756/)
38. Gradiz R, Silva HC, Carvalho L, Botelho MF, Mota-Pinto A. MIA PaCa-2 and PANC-1 - pancreas ductal adenocarcinoma cell lines with neuroendocrine differentiation and somatostatin receptors. *Sci Rep*. 2016; 6:21648.
<https://doi.org/10.1038/srep21648>
PMID:[26884312](https://pubmed.ncbi.nlm.nih.gov/26884312/)
39. Zhu J, Abbruzzese JL, Izzo J, Hittelman WN, Li D. AURKA amplification, chromosome instability, and centrosome abnormality in human pancreatic carcinoma cells. *Cancer Genet Cytogenet*. 2005; 159:10–7.
<https://doi.org/10.1016/j.cancergencyto.2004.09.008>
PMID:[15860351](https://pubmed.ncbi.nlm.nih.gov/15860351/)
40. Abrams SL, Lertpiriyapong K, Yang LV, Martelli AM, Cocco L, Ratti S, Falasca M, Murata RM, Rosalen PL, Lombardi P, Libra M, Candido S, Montalto G, et al. Introduction of WT-TP53 into pancreatic cancer cells alters sensitivity to chemotherapeutic drugs, targeted therapeutics and nutraceuticals. *Adv Biol Regul*. 2018; 69:16–34.
<https://doi.org/10.1016/j.jbior.2018.06.002>
PMID:[29980405](https://pubmed.ncbi.nlm.nih.gov/29980405/)
41. Abrams SL, Akula SM, Martelli AM, Cocco L, Ratti S, Libra M, Candido S, Montalto G, Cervello M, Gizak A, Rakus D, Steelman LS, McCubrey JA. Sensitivity of pancreatic cancer cells to chemotherapeutic drugs, signal transduction inhibitors and nutraceuticals can be regulated by WT-TP53. *Adv Biol Regul*. 2021; 79:100780.
<https://doi.org/10.1016/j.jbior.2020.100780>
PMID:[33451973](https://pubmed.ncbi.nlm.nih.gov/33451973/)
42. Eliyahu D, Michalovitz D, Eliyahu S, Pinhasi-Kimhi O, Oren M. Wild-type p53 can inhibit oncogene-mediated focus formation. *Proc Natl Acad Sci U S A*. 1989; 86:8763–7.
<https://doi.org/10.1073/pnas.86.22.8763>
PMID:[2530586](https://pubmed.ncbi.nlm.nih.gov/2530586/)
43. Miller AD, Rosman GJ. Improved retroviral vectors for gene transfer and expression. *Biotechniques*. 1989; 7:980-90.
PMID:[2631796](https://pubmed.ncbi.nlm.nih.gov/2631796/)
44. Padavano J, Henkhaus RS, Chen H, Skovan BA, Cui H, Ignatenko NA. Mutant K-RAS Promotes Invasion and Metastasis in Pancreatic Cancer Through GTPase Signaling Pathways. *Cancer Growth Metastasis*. 2015; 8:95–113.
<https://doi.org/10.4137/CGM.S29407>
PMID:[26512205](https://pubmed.ncbi.nlm.nih.gov/26512205/)
45. McCubrey JA, Steelman LS, Chappell WH, Abrams SL, Montalto G, Cervello M, Nicoletti F, Fagone P, Malaponte G, Mazzarino MC, Candido S, Libra M, Bäsecke J, et al. Mutations and deregulation of Ras/Raf/MEK/ERK and PI3K/PTEN/Akt/mTOR cascades which alter therapy response. *Oncotarget*. 2012; 3:954–87.
<https://doi.org/10.18632/oncotarget.652>
PMID:[23006971](https://pubmed.ncbi.nlm.nih.gov/23006971/)
46. Zhang Y, Liu JL, Wang J. KRAS gene silencing inhibits the activation of PI3K-Akt-mTOR signaling pathway to regulate breast cancer cell epithelial-mesenchymal transition, proliferation and apoptosis. *Eur Rev Med Pharmacol Sci*. 2020; 24:3085–96.
https://doi.org/10.26355/eurrev_202003_20673
PMID:[32271426](https://pubmed.ncbi.nlm.nih.gov/32271426/)
47. Candido S, Abrams SL, Steelman LS, Lertpiriyapong K, Martelli AM, Cocco L, Ratti S, Follo MY, Murata RM, Rosalen PL, Bueno-Silva B, de Alencar SM, Lombardi P, et al. Effects of the MDM-2 inhibitor Nutlin-3a on PDAC cells containing and lacking WT-TP53 on sensitivity to chemotherapy, signal transduction inhibitors and nutraceuticals. *Adv Biol Regul*. 2019; 72:22–40.
<https://doi.org/10.1016/j.jbior.2019.03.002>
PMID:[30898612](https://pubmed.ncbi.nlm.nih.gov/30898612/)
48. Strom E, Sathe S, Komarov PG, Chernova OB, Pavlovska I, Shyshynova I, Bosykh DA, Burdelya LG, Macklis RM, Skaliter R, Komarova EA, Gudkov AV. Small-molecule inhibitor of p53 binding to mitochondria protects mice from gamma radiation. *Nat Chem Biol*. 2006; 2:474–9.
<https://doi.org/10.1038/nchembio809>
PMID:[16862141](https://pubmed.ncbi.nlm.nih.gov/16862141/)

49. McCubrey JA, Steelman LS, Bertrand FE, Davis NM, Sokolosky M, Abrams SL, Montalto G, D'Assoro AB, Libra M, Nicoletti F, Maestro R, Basecke J, Rakus D, et al. GSK-3 as potential target for therapeutic intervention in cancer. *Oncotarget*. 2014; 5:2881–911. <https://doi.org/10.18632/oncotarget.2037> PMID:24931005
50. Ougolkov AV, Fernandez-Zapico ME, Savoy DN, Urrutia RA, Billadeau DD. Glycogen synthase kinase-3 β participates in nuclear factor kappaB-mediated gene transcription and cell survival in pancreatic cancer cells. *Cancer Res*. 2005; 65:2076–81. <https://doi.org/10.1158/0008-5472.CAN-04-3642> PMID:15781615
51. Kazi A, Xiang S, Yang H, Delitto D, Trevino J, Jiang RHY, Ayaz M, Lawrence HR, Kennedy P, Sebt SM. GSK3 suppression upregulates β -catenin and c-Myc to abrogate KRas-dependent tumors. *Nat Commun*. 2018; 9:5154. <https://doi.org/10.1038/s41467-018-07644-6> PMID:30514931
52. Ding L, Billadeau DD. Glycogen synthase kinase-3 β : a novel therapeutic target for pancreatic cancer. *Expert Opin Ther Targets*. 2020; 24:417–26. <https://doi.org/10.1080/14728222.2020.1743681> PMID:32178549
53. Morran DC, Wu J, Jamieson NB, Mrowinska A, Kalna G, Karim SA, Au AY, Scarlett CJ, Chang DK, Pajak MZ, Oien KA, McKay CJ, Carter CR, et al, and Australian Pancreatic Cancer Genome Initiative (APGI). Targeting mTOR dependency in pancreatic cancer. *Gut*. 2014; 63:1481–9. <https://doi.org/10.1136/gutjnl-2013-306202> PMID:24717934
54. Leontieva OV, Blagosklonny MV. DNA damaging agents and p53 do not cause senescence in quiescent cells, while consecutive re-activation of mTOR is associated with conversion to senescence. *Aging (Albany NY)*. 2010; 2:924–35. <https://doi.org/10.18632/aging.100265> PMID:21212465
55. Wu H, Zhu L, Zhang H, Shi X, Zhang L, Wang W, Xue H, Liang Z. Coexpression of EGFR and CXCR4 predicts poor prognosis in resected pancreatic ductal adenocarcinoma. *PLoS One*. 2015; 10:e0116803. <https://doi.org/10.1371/journal.pone.0116803> PMID:25679210
56. Xie ZB, Zhang YF, Jin C, Mao YS, Fu DL. LRG-1 promotes pancreatic cancer growth and metastasis via modulation of the EGFR/p38 signaling. *J Exp Clin Cancer Res*. 2019; 38:75. <https://doi.org/10.1186/s13046-019-1088-0> PMID:30760292
57. Raj D, Yang MH, Rodgers D, Hampton EN, Begum J, Mustafa A, Lorizio D, Garces I, Propper D, Kench JG, Kocher HM, Young TS, Aicher A, Heeschen C. Switchable CAR-T cells mediate remission in metastatic pancreatic ductal adenocarcinoma. *Gut*. 2019; 68:1052–64. <https://doi.org/10.1136/gutjnl-2018-316595> PMID:30121627
58. Avan A, Quint K, Nicolini F, Funel N, Frampton AE, Maftouh M, Pelliccioni S, Schuurhuis GJ, Peters GJ, Giovannetti E. Enhancement of the antiproliferative activity of gemcitabine by modulation of c-Met pathway in pancreatic cancer. *Curr Pharm Des*. 2013; 19:940–50. PMID:22973962
59. He X, Zheng Z, Li J, Ben Q, Liu J, Zhang J, Ji J, Yu B, Chen X, Su L, Zhou L, Liu B, Yuan Y. DJ-1 promotes invasion and metastasis of pancreatic cancer cells by activating SRC/ERK/uPA. *Carcinogenesis*. 2012; 33:555–62. <https://doi.org/10.1093/carcin/bgs002> PMID:22223849
60. Botla SK, Savant S, Jandaghi P, Bauer AS, Mücke O, Moskalev EA, Neoptolemos JP, Costello E, Greenhalf W, Scarpa A, Gaida MM, Büchler MW, Strobel O, et al. Early Epigenetic Downregulation of microRNA-192 Expression Promotes Pancreatic Cancer Progression. *Cancer Res*. 2016; 76:4149–59. <https://doi.org/10.1158/0008-5472.CAN-15-0390> PMID:27216198
61. Awasthi N, Zhang C, Hinz S, Schwarz MA, Schwarz RE. Enhancing sorafenib-mediated sensitization to gemcitabine in experimental pancreatic cancer through EMAP II. *J Exp Clin Cancer Res*. 2013; 32:12. <https://doi.org/10.1186/1756-9966-32-12> PMID:23497499
62. Martínez-Bosch N, Fernández-Barrena MG, Moreno M, Ortiz-Zapater E, Munné-Collado J, Iglesias M, André S, Gabius HJ, Hwang RF, Poirier F, Navas C, Guerra C, Fernández-Zapico ME, Navarro P. Galectin-1 drives pancreatic carcinogenesis through stroma remodeling and Hedgehog signaling activation. *Cancer Res*. 2014; 74:3512–24. <https://doi.org/10.1158/0008-5472.CAN-13-3013> PMID:24812270
63. Puchades M, Nilsson CL, Emmett MR, Aldape KD, Ji Y, Lang FF, Liu TJ, Conrad CA. Proteomic investigation of glioblastoma cell lines treated with wild-type p53 and cytotoxic chemotherapy demonstrates an association between galectin-1 and p53 expression. *J Proteome Res*. 2007; 6:869–75. <https://doi.org/10.1021/pr060302l> PMID:17269744

64. Akula SM, Ruvolo PP, McCubrey JA. TP53/miR-34a-associated signaling targets *SERPINE1* expression in human pancreatic cancer. *Aging (Albany NY)*. 2020; 12:2777–97.
<https://doi.org/10.18632/aging.102776>
PMID:31986125
65. Elokda H, Abou-Gharbia M, Hennen JK, McFarlane G, Mugford CP, Krishnamurthy G, Crandall DL. Tiplaxtinin, a novel, orally efficacious inhibitor of plasminogen activator inhibitor-1: design, synthesis, and preclinical characterization. *J Med Chem*. 2004; 47:3491–4.
<https://doi.org/10.1021/jm049766g>
PMID:15214776
66. Zhao J, Wang H, Hsiao CH, Chow DS, Koay EJ, Kang Y, Wen X, Huang Q, Ma Y, Bankson JA, Ullrich SE, Overwijk W, Maitra A, et al. Simultaneous inhibition of hedgehog signaling and tumor proliferation remodels stroma and enhances pancreatic cancer therapy. *Biomaterials*. 2018; 159:215–28.
<https://doi.org/10.1016/j.biomaterials.2018.01.014>
PMID:29331808
67. Rosow DE, Liss AS, Strobel O, Fritz S, Bausch D, Valsangkar NP, Alsina J, Kulemann B, Park JK, Yamaguchi J, LaFemina J, Thayer SP. Sonic Hedgehog in pancreatic cancer: from bench to bedside, then back to the bench. *Surgery*. 2012; 152:S19–32.
<https://doi.org/10.1016/j.surg.2012.05.030>
PMID:22770959
68. Sohma I, Fujiwara Y, Sugita Y, Yoshioka A, Shirakawa M, Moon JH, Takiguchi S, Miyata H, Yamasaki M, Mori M, Doki Y. Parthenolide, an NF- κ B inhibitor, suppresses tumor growth and enhances response to chemotherapy in gastric cancer. *Cancer Genomics Proteomics*. 2011; 8:39–47.
PMID:21289336
69. Liu W, Wang X, Sun J, Yang Y, Li W, Song J. Parthenolide suppresses pancreatic cell growth by autophagy-mediated apoptosis. *Onco Targets Ther*. 2017; 10:453–61.
<https://doi.org/10.2147/OTT.S117250>
PMID:28176967
70. Tang ZH, Li T, Tong YG, Chen XJ, Chen XP, Wang YT, Lu JJ. A Systematic Review of the Anticancer Properties of Compounds Isolated from Licorice (Gancao). *Planta Med*. 2015; 81:1670–87.
<https://doi.org/10.1055/s-0035-1558227>
PMID:26695708
71. Zhou Y, Ho WS. Combination of liquiritin, isoliquiritin and isoliquirigenin induce apoptotic cell death through upregulating p53 and p21 in the A549 non-small cell lung cancer cells. *Oncol Rep*. 2014; 31:298–304.
<https://doi.org/10.3892/or.2013.2849>
PMID:24247527
72. Kim A, Ma JY. Isoliquiritin Apioside Suppresses *in vitro* Invasiveness and Angiogenesis of Cancer Cells and Endothelial Cells. *Front Pharmacol*. 2018; 9:1455.
<https://doi.org/10.3389/fphar.2018.01455>
PMID:30618749
73. Tuli HS, Tuorkey MJ, Thakral F, Sak K, Kumar M, Sharma AK, Sharma U, Jain A, Aggarwal V, Bishayee A. Molecular Mechanisms of Action of Genistein in Cancer: Recent Advances. *Front Pharmacol*. 2019; 10:1336.
<https://doi.org/10.3389/fphar.2019.01336>
PMID:31866857
74. Bi YL, Min M, Shen W, Liu Y. Genistein induced anticancer effects on pancreatic cancer cell lines involves mitochondrial apoptosis, G₀/G₁ cell cycle arrest and regulation of STAT3 signalling pathway. *Phytomedicine*. 2018; 39:10–6.
<https://doi.org/10.1016/j.phymed.2017.12.001>
PMID:29433670
75. Liu X, Suzuki N, Santosh Laxmi YR, Okamoto Y, Shibutani S. Anti-breast cancer potential of daidzein in rodents. *Life Sci*. 2012; 91:415–9.
<https://doi.org/10.1016/j.lfs.2012.08.022>
PMID:23227466
76. Guo JM, Xiao BX, Dai DJ, Liu Q, Ma HH. Effects of daidzein on estrogen-receptor-positive and negative pancreatic cancer cells *in vitro*. *World J Gastroenterol*. 2004; 10:860–3.
<https://doi.org/10.3748/wjg.v10.i6.860>
PMID:15040033
77. Shin SI, Freedman VH, Risser R, Pollack R. Tumorigenicity of virus-transformed cells in nude mice is correlated specifically with anchorage independent growth *in vitro*. *Proc Natl Acad Sci U S A*. 1975; 72:4435–9.
<https://doi.org/10.1073/pnas.72.11.4435>
PMID:172908
78. Creemers SG, van Koetsveld PM, De Herder WW, Dogan F, Franssen GJH, Feelders RA, Hoffland LJ. MDR1 inhibition increases sensitivity to doxorubicin and etoposide in adrenocortical cancer. *Endocr Relat Cancer*. 2019; 26:367–78.
<https://doi.org/10.1530/ERC-18-0500>
PMID:30650062
79. Steelman LS, Abrams SL, Ruvolo P, Ruvolo V, Cocco L, Ratti S, Martelli AM, Neri LM, Candido S, Libra M, McCubrey JA. Drug-resistance in doxorubicin-resistant FL5.12 hematopoietic cells: elevated MDR1, drug efflux and side-population positive and decreased BCL2-family member expression. *Oncotarget*. 2017; 8:113013–33.

- <https://doi.org/10.18632/oncotarget.22956>
PMID:[29348885](https://pubmed.ncbi.nlm.nih.gov/29348885/)
80. Abrams SL, Ruvolo PP, Ruvolo VR, Ligresti G, Martelli AM, Cocco L, Ratti S, Tafuri A, Steelman LS, Candido S, Libra M, McCubrey JA. Targeting signaling and apoptotic pathways involved in chemotherapeutic drug-resistance of hematopoietic cells. *Oncotarget*. 2017; 8:76525–57.
<https://doi.org/10.18632/oncotarget.20408>
PMID:[29100331](https://pubmed.ncbi.nlm.nih.gov/29100331/)
81. Gu D, Schlotman KE, Xie J. Deciphering the role of hedgehog signaling in pancreatic cancer. *J Biomed Res*. 2016; 30:353–60.
<https://doi.org/10.7555/JBR.30.20150107>
PMID:[27346466](https://pubmed.ncbi.nlm.nih.gov/27346466/)
82. De Jesus-Acosta A, Sugar EA, O'Dwyer PJ, Ramanathan RK, Von Hoff DD, Rasheed Z, Zheng L, Begum A, Anders R, Maitra A, McAllister F, Rajeshkumar NV, Yabuuchi S, et al. Phase 2 study of vismodegib, a hedgehog inhibitor, combined with gemcitabine and nab-paclitaxel in patients with untreated metastatic pancreatic adenocarcinoma. *Br J Cancer*. 2020; 122:498–505.
<https://doi.org/10.1038/s41416-019-0683-3>
PMID:[31857726](https://pubmed.ncbi.nlm.nih.gov/31857726/)
83. Berkers CR, Maddocks OD, Cheung EC, Mor I, Vousden KH. Metabolic regulation by p53 family members. *Cell Metab*. 2013; 18:617–33.
<https://doi.org/10.1016/j.cmet.2013.06.019>
PMID:[23954639](https://pubmed.ncbi.nlm.nih.gov/23954639/)
84. Puzio-Kuter AM. The Role of p53 in Metabolic Regulation. *Genes Cancer*. 2011; 2:385–91.
<https://doi.org/10.1177/1947601911409738>
PMID:[21779507](https://pubmed.ncbi.nlm.nih.gov/21779507/)
85. Humpton TJ, Vousden KH. Regulation of Cellular Metabolism and Hypoxia by p53. *Cold Spring Harb Perspect Med*. 2016; 6:a026146.
<https://doi.org/10.1101/cshperspect.a026146>
PMID:[27371670](https://pubmed.ncbi.nlm.nih.gov/27371670/)
86. Kawauchi K, Araki K, Tobiume K, Tanaka N. p53 regulates glucose metabolism through an IKK-NF-kappaB pathway and inhibits cell transformation. *Nat Cell Biol*. 2008; 10:611–8.
<https://doi.org/10.1038/ncb1724>
PMID:[18391940](https://pubmed.ncbi.nlm.nih.gov/18391940/)
87. Matoba S, Kang JG, Patino WD, Wragg A, Boehm M, Gavrilova O, Hurley PJ, Bunz F, Hwang PM. p53 regulates mitochondrial respiration. *Science*. 2006; 312:1650–3.
<https://doi.org/10.1126/science.1126863>
PMID:[16728594](https://pubmed.ncbi.nlm.nih.gov/16728594/)
88. Flöter J, Kaymak I, Schulze A. Regulation of Metabolic Activity by p53. *Metabolites*. 2017; 7:E21.
<https://doi.org/10.3390/metabo7020021>
PMID:[28531108](https://pubmed.ncbi.nlm.nih.gov/28531108/)
89. Eriksson M, Ambroise G, Ouchida AT, Lima Queiroz A, Smith D, Gimenez-Cassina A, Iwanicki MP, Muller PA, Norberg E, Vakifahmetoglu-Norberg H. Effect of Mutant p53 Proteins on Glycolysis and Mitochondrial Metabolism. *Mol Cell Biol*. 2017; 37:e00328–17.
<https://doi.org/10.1128/MCB.00328-17>
PMID:[28993478](https://pubmed.ncbi.nlm.nih.gov/28993478/)
90. Abrams SL, Akula SM, Meher AK, Steelman LS, Gizak A, Duda P, Rakus D, Martelli AM, Ratti S, Cocco L, Montalto G, Cervello M, Ruvolo P, et al. GSK-3β Can Regulate the Sensitivity of MIA-PaCa-2 Pancreatic and MCF-7 Breast Cancer Cells to Chemotherapeutic Drugs, Targeted Therapeutics and Nutraceuticals. *Cells*. 2021; 10:816.
<https://doi.org/10.3390/cells10040816>
PMID:[33917370](https://pubmed.ncbi.nlm.nih.gov/33917370/)
91. Zhao H, Zheng B. Dual Targeting of Autophagy and MEK in KRAS Mutant Cancer. *Trends Cancer*. 2019; 5:327–9.
<https://doi.org/10.1016/j.trecan.2019.04.003>
PMID:[31208693](https://pubmed.ncbi.nlm.nih.gov/31208693/)
92. Abrams SL, Duda P, Akula SM, Steelman LS, Follo ML, Cocco L, Ratti S, Martelli AM, Montalto G, Emma MR, Cervello M, Rakus D, Gizak A, McCubrey JA. Effects of the Mutant TP53 Reactivator APR-246 on Therapeutic Sensitivity of Pancreatic Cancer Cells in the Presence and Absence of WT-TP53. *Cells*. 2022; 11:794.
<https://doi.org/10.3390/cells11050794>
PMID:[35269416](https://pubmed.ncbi.nlm.nih.gov/35269416/)
93. McCubrey JA, Abrams SL, Ligresti G, Misaghian N, Wong EW, Steelman LS, Bäsecke J, Troppmair J, Libra M, Nicoletti F, Molton S, McMahan M, Evangelisti C, Martelli AM. Involvement of p53 and Raf/MEK/ERK pathways in hematopoietic drug resistance. *Leukemia*. 2008; 22:2080–90.
<https://doi.org/10.1038/leu.2008.207>
PMID:[18685611](https://pubmed.ncbi.nlm.nih.gov/18685611/)
94. Balmer MT, Katz RD, Liao S, Goodwine JS, Gal S. Doxorubicin and 5-fluorouracil induced accumulation and transcriptional activity of p53 are independent of the phosphorylation at serine 15 in MCF-7 breast cancer cells. *Cancer Biol Ther*. 2014; 15:1000–12.
<https://doi.org/10.4161/cbt.29112>
PMID:[24801380](https://pubmed.ncbi.nlm.nih.gov/24801380/)
95. Harami-Papp H, Pongor LS, Munkácsy G, Horváth G, Nagy ÁM, Ambrus A, Hauser P, Szabó A, Tretter L, Gyórfy B. TP53 mutation hits energy metabolism and increases glycolysis in breast cancer. *Oncotarget*. 2016; 7:67183–95.
<https://doi.org/10.18632/oncotarget.11594>
PMID:[27582538](https://pubmed.ncbi.nlm.nih.gov/27582538/)

96. Kamp WM, Wang PY, Hwang PM. TP53 mutation, mitochondria and cancer. *Curr Opin Genet Dev.* 2016; 38:16–22.
<https://doi.org/10.1016/j.gde.2016.02.007>
PMID:[27003724](https://pubmed.ncbi.nlm.nih.gov/27003724/)
97. Abu El Maaty MA, Strassburger W, Qaiser T, Dabiri Y, Wölfl S. Differences in p53 status significantly influence the cellular response and cell survival to 1,25-dihydroxyvitamin D3-metformin cotreatment in colorectal cancer cells. *Mol Carcinog.* 2017; 56:2486–98.
<https://doi.org/10.1002/mc.22696>
PMID:[28618116](https://pubmed.ncbi.nlm.nih.gov/28618116/)
98. Agarwal S, Bell CM, Taylor SM, Moran RG. p53 Deletion or Hotspot Mutations Enhance mTORC1 Activity by Altering Lysosomal Dynamics of TSC2 and Rheb. *Mol Cancer Res.* 2016; 14:66–77.
<https://doi.org/10.1158/1541-7786.MCR-15-0159>
PMID:[26385560](https://pubmed.ncbi.nlm.nih.gov/26385560/)
99. Frazier ML, Fernández E, de Llorens R, Brown NM, Pathak S, Cleary KR, Abbruzzese JL, Berry K, Olive M, Le Maistre A, Evans DB. Pancreatic adenocarcinoma cell line, MDAPanc-28, with features of both acinar and ductal cells. *Int J Pancreatol.* 1996; 19:31–8.
<https://doi.org/10.1007/BF02788373>
PMID:[8656025](https://pubmed.ncbi.nlm.nih.gov/8656025/)
100. Sokolosky M, Chappell WH, Stadelman K, Abrams SL, Davis NM, Steelman LS, McCubrey JA. Inhibition of GSK-3 β activity can result in drug and hormonal resistance and alter sensitivity to targeted therapy in MCF-7 breast cancer cells. *Cell Cycle.* 2014; 13:820–33.
<https://doi.org/10.4161/cc.27728>
PMID:[24407515](https://pubmed.ncbi.nlm.nih.gov/24407515/)
101. Chappell WH, Candido S, Abrams SL, Russo S, Ove R, Martelli AM, Cocco L, Ramazzotti G, Cervello M, Montalto G, Steelman LS, Leng X, Arlinghaus RB, et al. Roles of p53, NF- κ B and the androgen receptor in controlling NGAL expression in prostate cancer cell lines. *Adv Biol Regul.* 2018; 69:43–62.
<https://doi.org/10.1016/j.jbior.2018.05.002>
PMID:[29861174](https://pubmed.ncbi.nlm.nih.gov/29861174/)